

2-2-2014

Maine Tidal Power Initiative: Environmental Impact Protocols for Tidal Power

Michael Peterson

University of Maine, Principal Investigator - Main, michael.peterson@maine.edu

Gayle Zydlewski

Co-Principal Investigator; University of Maine, Orono, gayle.zydlewski@umit.maine.edu

Huijie Xue

Co-Principal Investigator; University of Maine, Orono, huijie.xue@umit.maine.edu

Teresa R. Johnson

Co-Principal Investigator; University of Maine, Orono, teresa.johnson@maine.edu

Follow this and additional works at: https://digitalcommons.library.umaine.edu/orsp_reports

 Part of the [Energy Systems Commons](#), and the [Ocean Engineering Commons](#)

Recommended Citation

Peterson, Michael; Zydlewski, Gayle; Xue, Huijie; and Johnson, Teresa R., "Maine Tidal Power Initiative: Environmental Impact Protocols for Tidal Power" (2014). *University of Maine Office of Research and Sponsored Programs: Grant Reports*. 1.
https://digitalcommons.library.umaine.edu/orsp_reports/1

This Open-Access Report is brought to you for free and open access by DigitalCommons@UMaine. It has been accepted for inclusion in University of Maine Office of Research and Sponsored Programs: Grant Reports by an authorized administrator of DigitalCommons@UMaine. For more information, please contact um.library.technical.services@maine.edu.

Title Page: Final Technical Report

MAINE TIDAL POWER INITIATIVE: ENVIRONMENTAL IMPACT PROTOCOLS FOR TIDAL POWER

DOE Award Number: DE-EE0000298

Project Period 06:09 – 10:13 (June 2009 – October 2013)

Principal Investigators & Authors:

PI: Michael Peterson, 207-581-2129, Michael.peterson@maine.edu

Co-PI: Gayle Zydlewski, (207) 581-4365, gayle.zydlewski@umit.maine.edu

Co-PI: Huijie Xue, (207)581-4318, hxue@maine.edu

Co-PI: Teresa Johnson, (207) 581-4362, teresa.johnson@umit.maine.edu

Authors and Key Contributors:

M. Cameron, G. deBree, A. Demeo, J. S. Jansujwicz, R. Kimball, M. Maynard,
J. McCleave, J. Szillery, M. Swanger, R. Urbina, H. Viehman, ,

Name and address of recipient organization

The University System working through the University of Maine, Office of Research &
Sponsored Programs, 5717 Corbett Hall, Orono, Maine 04469-5717

Other project team member organizations:

Maine Maritime Academy, the Tidal Energy Device Evaluation Center, Ocean
Renewable Power Company, Maine Blue Stream, S.W. Cole Engineering, Inc.,
Chewonki Foundation, Pleasant Point Passamaquoddy

Date of Report: February 2, 2014

Final Report Maine Tidal Power Initiative

Acknowledgment, Disclaimer and Proprietary Data Notice – The next page(s) should contain following or similar statements:

Acknowledgment: “This report is based upon work supported by the U. S. Department of Energy under Award No. DE-EE0000298.

Disclaimer: “Any findings, opinions, and conclusions or recommendations expressed in this report are those of the author(s) and do not necessarily reflect the views of the Department of Energy”

Proprietary Data Notice: There is no patentable material or protected data in this report. The report also does not contain classified information, information subject to export control classification, or other information not subject to release. Appropriate attribution of data or results from this report is expected to conform to accepted ethical standards in science and applied research.

Table of Contents

<u>Section</u>	<u>Page</u>
List of Acronyms	4
List of Appendices	5
Executive Summary	6
Introduction	8
Background	10
Results and Discussion Task 1	15
Results and Discussion Task 2	21
Results and Discussion Task 3	33
Results and Discussion Task 4	46
Recommendations	50
Appendix 1	App-1
Appendix 2	App-2
Appendix 3	App-3
Appendix 4	App-4

List of Acronyms

The majority of the acronyms used in this document are specific to the subtasks. All acronyms in those areas will be defined since the majority of the material is in the appendices. All acronyms are defined in the subsections as well to facilitate readability of portions of the report by interested persons.

DEP: Maine Department of Environmental Protection

DMR: Maine Department of Marine Resources

FERC: Federal Energy Regulatory Commission (FERC)

FVM: free vortex model

MHK: Marine Hydrokinetic

MTPI: Maine Tidal Power Initiative

NMFS: National Marine Fisheries Services

ORPC: Ocean Renewable Power Company

TGU: Turbine Generator Unit

USACE: U.S. Army Corps of Engineering

USCG: U.S. Coast Guard

USFWS: U.S. Fish and Wildlife Service

List of Appendices

Appendix 1:

This appendix includes materials related to task 1, resource assessment. The material includes a manuscripts, a draft manuscript and an MS thesis

Appendix 2:

This appendix includes materials related to the environmental and fish studies on the tidal turbines. Manuscripts, reports and an MS thesis supported from this work are included.

Appendix 3:

This appendix includes the materials developed for the modeling and testing of scale model turbines for both ducted axial flow and cross flow designs. This appendix includes manuscripts, three M.S. theses and a draft Ph.D. dissertation

Appendix 4:

This appendix includes materials from the human and community response tasks. The materials included are manuscripts and reports related to this topic from the current research project.

Executive Summary

The Maine Tidal Power Initiative (MTPI), an interdisciplinary group of engineers, biologists, oceanographers, and social scientists, has been conducting research to evaluate tidal energy resources and better understand the potential effects and impacts of marine hydro-kinetic (MHK) development on the environment and local community. Project efforts include: 1) resource assessment, 2) development of initial device design parameters using scale model tests, 3) baseline environmental studies and monitoring, and 4) human and community responses. This work included in-situ measurement of the environmental and social response to the pre-commercial Turbine Generator Unit (TGU®) developed by Ocean Renewable Power Company (ORPC) as well as considering the path forward for smaller community scale projects.

The resource assessment task included modeling, scale model testing and field testing. Results from the modeling of tidal streams used field data and has shown that outer Cobscook Bay and Western Passage have a mean power density exceeding 1000 W/m^2 , with particularly high power density in several key locations. However, numerous eddies, both stationary and transient, induce significant variability in flow direction and speed, which can lead to apparent fluctuations in power density. Model testing of cross-flow turbines also showed that flow recovers slowly with the latitudinal velocity remaining at about 5-10 % at a distance of ten turbine diameters. Numerical models of turbine arrays, which used the distances from the physical model testing, were also developed. Although only small fractions of in-stream tidal energy are removed by the turbine arrays, changes in the flow, water level, as well as horizontal and vertical mixing coefficients were clearly detectable both in the near and far fields

Environmental studies established accepted protocols for assessing fish presence and interaction with an MHK device. Research focused on (1) baseline measurements of fish in tidally dynamic regions and (2) measuring the direct effects of the ORPC turbine on individual fishes. The first emphasis was on the effect of turbines on fish abundance and behavior resulting from the introduction of a tidal turbine to the natural environment. Down-looking hydroacoustics was found to be a reasonable approach to assessing potential impact on fishes of tidal energy development. This approach was shown to be transferrable between a commercial site (Cobscook Bay, Maine) to a small-scale site (Wiscasset, Maine). In Cobscook Bay, baseline fish densities were generally greater in May and June than in August and September, reflecting the high abundance of Atlantic herring with densities generally greatest near the sea floor. Behavior of fishes around a test turbine included: individuals milling up- and down-stream of the device, passing above or below the turbine, altering course to avoid the turbine and entering directly into the turbine. Night-time behavior was significantly different from behavior observed in the day. At night there was increased probability of entering the rotating turbine and lower probability of passing by. The results are promising with regard to the interaction of a low solidity turbine and fish. This work has established transferrable, scientifically peer-reviewed protocols for assessing fish presence and interaction with MHK devices in the natural environment.

A lifting line free vortex model (FVM) with dynamic stall correction was developed for a cross flow tidal turbine. This model provides reasonable power coefficient and blade force estimates. Results are for a larger range of solidities than is possible with traditional FVM. The analytical

model includes the effect of flow curvature on angle of incidence, an effect that was shown to be significant. The model is well suited for use in optimization schemes, and is also a useful tool for developing broad design parameters for the turbine. Validation was based on an extensive data set obtained for a range of solidity, blade profiles and toe angles and for a wide range of tip speed ratios including conditions with negative power output. The data will be made available for future model validation efforts as a part of our research publications.

The human dimensions research focused on community acceptance, stakeholder engagement, and the regulatory and permitting process. Research identified numerous and diverse stakeholders that affect and are affected by the process of tidal energy development in Cobscook Bay. Community and policy stakeholders generally perceived ORPC's engagement approach as effective. Responses placed an emphasis on direct economic benefits, indirect benefits to local businesses, and "hopeful" benefits such as cheaper electricity. General concerns associated with the project included potential environmental impacts and loss of fishing ground. However, given the nascent nature of the tidal power industry and the rapidly changing technology and permitting process, stakeholder salience is likely to change as the project unfolds. The regulatory and permitting process for tidal energy development mandates involvement by an array of federal and state agencies. Major laws structure the decision-making process and place power and authority with lead federal and state agencies. Responsibility shifts depending on the project and characteristics of the site. Regulatory changes at the federal and state level and a commitment by agencies to adaptive management facilitated and streamlined the permitting and regulatory process and will be important to the future success of tidal energy projects. Similar lessons arose from small site work in Wiscasset Maine. This work highlighted the importance of consultation in identifying information sources and knowledge gaps that required further study. Engagement strategies also need to adapt to the communication preferences and knowledge needs of the most salient stakeholder groups. However, financing and the research required to understand and quantify potential impacts of relatively new MHK technology may be prohibitive at the community scale. In practice, the Federal Energy Regulatory Commission (FERC) is not yet ready for the process to permit or license small or community scale hydrokinetic projects. The importance of an incremental approach on all fronts of a tidal power project development was demonstrated.

Development of this industry depends on continued engagement with the scientific community to understand the environmental and social impacts of emerging technologies. In particular, the monitoring of the devices is still in its infancy and will require continued research and development. Similarly, as turbine arrays are deployed, measurements and modeling of the local and long range impacts on flow, transport and biological responses must continue. The scale of the energy resource and location related costs such as environmental assessment and geotechnical issues remain as barriers for the industry. Because regulatory uncertainty and social acceptance remain critical barriers to industry development, research must continue to understand stakeholder questions, concerns, and information to better inform decision-making and move development forward in a socially acceptable and environmentally responsible manner. Our partner in the project, Ocean Renewable Power Company, is engaged in ongoing commercialization efforts for the technologies. Results from this work will be made available on an ongoing basis as a part of scientific literature and technical publications.

Introduction

As a result of ongoing climate change, the pressure for the development of new sources of renewable energy has increased. It is extremely likely that climate change is caused by anthropogenic activities¹. Thus even if dramatic gains are made in energy efficiency; the addition of novel renewable energy sources is critical to reducing fossil fuel emissions. Even current goals for a reduction in the growth of greenhouse gas emissions mean that all possible low-carbon or non-carbon emitting energy sources be considered. In the marine environment, energy in tidal currents, waves, and thermal structure may be extracted to produce electricity. These energy sources are a critical element in the overall renewable portfolio since, unlike wind and solar energy, both marine thermal and tidal energy are reliable additions to the overall electrical grid. In the case of tidal energy, the contribution of periodic but reliable sources of renewable energy becomes increasingly critical as wind and solar penetration in the grid increase. In a high renewable energy penetration grid, a resource like tidal energy does not provide the same base load capacity as, for example, a nuclear power plant. However, tidal energy can have the effect of reducing the size of either storage or peaking capacity that is required for grid stability by providing power for recovery of dispatchable loads². However, as an immature technology, significant questions remain regarding basic questions like the scale of the potential resource, the impact on sediment transport, the effects on fish populations and communities, and the ability to design a system which is acceptable by the people in the associated communities.

The objectives of the funded project were to examine tidal power development in Maine from all perspectives: engineering, resource assessment, biological effects, and social dimensions. Resource and environmental research focused on data collection for the Cobscook Bay/Western Passage, possibly the most viable commercial tidal energy site in the US, tidal power sites along with initial evaluation of the suitability of the approach for at least two other tidal development sites in Maine. Concomitantly, alternative energy research is used as a basis of education for a number of graduate and undergraduate students at the University of Maine and Maine Maritime Academy. The Maine Tidal Power Initiative has developed resource and environmental assessment protocols in conjunction with the deployment of a specific marine hydrokinetic device. The protocols are transferrable throughout Maine and the US to evaluate tidal energy resources and better understand the potential impact of this development on the environment. Again, site-specific social science and environmental research focused on the Cobscook Bay/Western Passage area near Eastport Maine. The protocols and methods developed at these sites have also been used to perform initial scoping reviews of locations in Castine Harbor and Wiscasset, Maine that represent a more modest and more typical small scale energy resource.

¹ "IPCC PRESS RELEASE". IPCC. 27 September 2013.

http://www.wmo.int/pages/mediacentre/press_releases/pr_978_en.html Retrieved 15 December 2013

² Anne E. Demeo and Michael L Peterson, "Community Smart Grid Utilizing Dynamic Demand Response and Tidal Power for Grid Stabilization", *Smart Grid and Renewable Energy*, 2013, 4, 465-472, <http://dx.doi.org/10.4236/sgre.2013.47053> Published Online October 2013

Final Report Maine Tidal Power Initiative

Specific barrier issues which have been addressed for the industry are technologies and protocols for measuring and modeling tidal flows, responses of fishes to those flows, and people interacting in these environments. Measuring tidal flows is critical to the key economic driver for this industry, the size of the potential resource. The second barrier issue is the need for methods for measuring the impact of marine hydrokinetic (MHK) devices on fish. Acoustic methods have been used with ground truth validation from trawls. The protocols developed in this project have already had a significant impact on the approach that has been taken at other sites. Finally the assessment of the human community response to these technologies and impact on community cohesion and participation is perhaps the largest single barrier to the acceptance of the projects. This work also has the potential to be replicated at other sites, although in both the case of the environmental effects and the social response to these projects, details of the species impacted and the economic and social environment are the ultimate determinants of impact and acceptance.

The technology focus for most of this work has been the cross-flow turbine developed by Ocean Renewable Power Company. Testing in the University of Maine tow tank has allowed a large design space to be explored for the optimization of the commercial turbine design. The design code developed for the project was validated using this data set. Both the design code and the data will be placed in a public repository. The most important outcome of the turbine design portion of the work is some general design parameters that can be used to assist in the site assessment and for benchmarking of proprietary designs. The design as well as the data is available for resource assessment and design comparisons. The appeal of this turbine design is that the potential exists for a low solidity turbine with lower tip speed ratios, which will have good performance. The low solidity and tip speed ratio is likely to reduce the risk of fish impacts and thus reduce environmental impact and community resistance to these technologies.

The need for low carbon energy sources is undeniable. Resistance to large-scale renewable energy development also continues to increase. The overall approach to this project, where the design of the system considers environmental impacts and social acceptance from the initial engineering design stages and continues with an adaptive management scheme, is the only option for addressing energy needs at the scale required.

Background

The goals of developing this new renewable energy resource are best served with a holistic approach to at least one location which can then be used as a template for others. This approach will allow technologies to be developed, facilitate assessment of other sites, as well as developing roadmaps for permitting by working with regulatory agencies and other stakeholders. The independence of the funding for this project has enabled an effective approach because of the honest broker role the local state university played in the process.

The project efforts included four tasks: 1) resource assessment, including development of initial array design parameters using scale model tests; 2) baseline environmental studies, including *in situ* measurement and monitoring of the beta pre-commercial Turbine Generator Unit (TGU) developed by Ocean Renewable Power Company (ORPC); 3) development of alternative tidal turbine designs; 4) application of initial test results to sites at different scales, in Maine and beyond while developing models for stakeholder participation.

The primary goal of resource assessment was to estimate the amount of extractable power from potential tidal power development sites. The University of Maine team and ORPC have jointly carried out the following four subtasks: (1) Tidal flow velocities were measured near the turbine deployment site in the outer Cobscook Bay. (2) A three-dimensional coastal circulation model was developed for the Quoddy region, which was validated with *in situ* observations. The model results were used to determine the power density, both the peak magnitude and the frequency distribution, which provided a baseline for selecting sites in Cobscook Bay and Western Passage. (3) Flow fields generated by model cross-flow turbines were measured in the University of Maine tow tank, from which a three-dimensional wake structure was reconstructed and the corresponding turbulent dissipation in the wake was estimated. (4) Feedbacks of turbines on tidal flows and other hydrodynamic conditions were examined using the regional circulation model by incorporating both kinematic and dynamic parameterizations of turbines. Moreover, efficiency of tidal arrays was studied for different operation criteria, density and layout of turbines.

The environmental task considered how, in areas of extreme tidal currents, marine hydrokinetic energy (MHK) devices—underwater turbines—may be deployed with unknown effects on marine vertebrates, especially fishes. Tidal currents in Cobscook Bay, Maine, Passamaquoddy Bay on the Maine-New Brunswick border, and the Bay of Fundy between New Brunswick and Nova Scotia are the strongest of anywhere in eastern North America. During this research Ocean Renewable Power Company (ORPC) was preparing to deploy MHK turbines in Cobscook Bay and lower Passamaquoddy Bay, having temporarily deployed pilot turbines in Cobscook Bay. The University of Maine undertook studies to assess the potential effects of the MHK devices on the fishes of Cobscook and Passamaquoddy Bays, focusing on Cobscook Bay. The objectives were threefold. (1) The first was to determine the abundance and vertical distribution of fishes at proposed deployment sites and control sites on tidal, diurnal, and seasonal scales. The abundance and distribution were assessed using active hydroacoustics and the verification of species identity was assessed by midwater and benthic trawling (discussed under Objective 3).

(2) The second was to characterize the behavioral interaction of fishes with a pilot turbine suspended below a moored barge at a potential deployment site. The approach was to use acoustic imaging cameras to capture sequences of the behavior of individuals and groups of fishes approaching and passing the turbine. No published work had examined fish interactions with MHK turbines in the open marine environment. MHK devices are free-standing, open structures installed in naturally flowing water currents, and fish may avoid these structures as they would other obstacles. (3) The third was to characterize the fish community structure of the entire Cobscook Bay on habitat, seasonal, and annual scales, in the absence of any prior bay-wide research. Distribution and abundance were assessed by seining and fyke netting in the intertidal zones and by midwater and benthic trawling in the subtidal zones of outer, central, and inner sub-bays.

Engineering research, task 3, was focused on the development of alternative tidal turbine designs with attention paid primarily to cross-flow turbine designs. The effect of ducting on axial flow turbines was also considered. The experimental work was focused on the development of data sets which would be useful for validating design codes. This tested variable for the tow tank studies included a wide range of critical design parameters such as toe angle and solidity as well as exploring the effect of blade design on efficiency. Using the data from the tow tank studies a vortex flow model was developed for cross-flow turbines. The vortex flow model extends prior work by including both dynamic stall and flow curvature effects. The lifting-line vortex method model with dynamic stall and flow curvature correction was shown to reasonably predict the hydrodynamic performance of cross-flow turbines at different toe angles for a range of solidity ratios. The dynamic stall correction is based on the Beddoes Leishman dynamic stall model and blade force solutions which are derived using conformal mapping³. The dynamic stall model has also been modified to provide predictions for a large range of angles of attack and Reynolds numbers, conditions under which cross-flow turbines operate. The model uses Sheng's consideration of the influence of reduced-pitch rate on the angle at which the blade stalls⁴. The dynamic stall model includes considerations for flow curvature effects. Parameters, such as blade thickness and camber, are considered in the derived formulae, which allow predictions of numerous turbine configurations and therefore make the model suitable for implementation on turbine optimization codes. This characteristic allows the method to better predict the performance of cross-flow turbines with high solidity ratios. The validation effort used experimental data for different blade profiles, a range of toe angles and multiple solidity ratios.

Task 4, considered the human dimensions of tidal energy development from a policy and community perspective. Research focused on issues of social acceptance and regulatory uncertainty both widely recognized as critical factors constraining ocean energy development. The human dimensions team engaged developers, regulators, local groups and citizens to: (1) identify and characterize the most salient stakeholders associated with MHK development, (2)

³ Leishman, J. G., Beddoes, T. S., "A Semi-Empirical Model for Dynamic Stall," *Journal of the American Helicopter Society*, Vol. 34, 1989, pp. 3-17.

⁴ Sheng, W., Galbraith, R. A., and Coton, F. N., "A Modified Dynamic Stall Model for Low Mach Numbers," *Journal of Solar Energy Engineering*, Vol. 130, August 2008, pp. 1-10.

Final Report Maine Tidal Power Initiative

determine the factors influencing community acceptability of tidal power, and (3) understand and inform the regulatory and permitting process for MHK development. In the process, the team identified effective and efficient engagement practices that allow stakeholders to shape the direction of research on MHK devices development and make informed decision about MHK development in their jurisdictions and communities. The engaged research process is also aimed at improving the use of research in future energy policymaking. Lessons learned from this study can assist regulators, policymakers, and developers to move renewable ocean energy development forward in a way that is socially acceptable and environmentally responsible.

Interest in developing tidal power is growing rapidly, yet little is known about the unique challenges of community-scale development. The Wiscasset Tidal Resources Project (also referred to as the Wiscasset Project) is a community-scale project initiated by the Town of Wiscasset and The Chewonki Foundation. The aim of the Project was to explore the feasibility for community-scale tidal power generation at one of the sites in Maine identified as having high potential for tidal power. The Wiscasset Tidal Resources Project shares the MTPI vision of balancing the potential for tidal power generation with the environmental and sociological impacts of tidal development on the resource and community.

Renewable energy is viewed as a potential solution to some of our most challenging social and environmental problems. However, while the long-term prospects for ocean energy appear promising, the developing industry is faced with significant challenges. Key factors constraining widespread deployment of new renewable energy technologies include engineering barriers, regulatory uncertainty, social acceptance, and uncertain impacts on the environment. Understanding basic design principles, effects on the physical and biological environment, and how humans respond is critically important to move renewable energy development forward in a socially and environmentally responsible manner.

Task 1. Tidal Resource Assessment

Acoustic Doppler current meters were deployed in Cobscook Bay and Western Passage and point measurements of velocities were obtained in 2010, 2011, and 2012. Lab experiments were conducted mostly in 2010 and 2011 in the University of Maine two tank to obtain velocity fields and turbulence dissipation associated with turbine wakes. Numerical simulations were carried out on computer clusters maintained by the University of Maine Advanced Computing Group. Estimations of tidal flow and power began in September 2010, which was transitioned into the study of tidal farm efficiency in 2012 and lately into a high-resolution simulation of flow fields near the ORPC TidGen unit in the outer Cobscook Bay with a follow-up funding from DOE.

The Task 1 research team consisted of Huijie Xue, Ph.D., Matthew Cameron, M.S. student, Min Bao, visiting student from Ocean Univ. of China, Stephen Cousins, M.S., and recently Shivanesh Rao, Ph.D. from the University of Maine as well as team members from Ocean Renewable Power Company. Xue, a Physical Oceanographer and Professor of Marine Sciences with extensive modeling experience of coastal Gulf of Maine, led the efforts in resource assessment. The ORPC team collected *in situ* measurements of currents in Cobscook Bay and Western Passage. Cameron and Xue designed the flow measurement experiments and analyzed the wake

structure. Bao, Cousins, and Xue developed a Quoddy regional circulation model that was used in estimating the tidal power distribution and studying the tidal farm efficiency. Rao took over the modeling work from Bao after she returned to China in 2012 and is continuing the tidal farm efficiency study and high-resolution (2-5 m) near field simulations.

Task 2. Assessment of potential effect on fishes and community analysis of fishes.

Hydroacoustic studies began in August of 2009, midwater netting studies started in 2010, and full fish community studies began in 2011. The original plan was that 2009-2013 would encompass pre- and post-deployment of turbine(s). However, delays encountered by ORPC meant that the only dates of data acquisition during deployment were in September 2010 for acoustic imaging of fish interactions with a test turbine suspended below a barge and August and September 2012 for hydroacoustics near a turbine sitting on the sea floor.

The Task 2 research team consisted of Gayle Zydlewski, Ph.D., James McCleave, Ph.D., Garrett Staines, M.S., Megan Altenritter, M.S., Haley Viehman, M.S., Ph.D. student, Jeffrey Vieser, M.S. student, and recently Haixue Shen, Ph.D., plus undergraduate students and other volunteer field crew members. Viehman, Staines, and Shen were principally responsible for hydroacoustic research, and Vieser, McCleave, and Altenritter were principally responsible for the fish community research. Zydlewski, an Associate Professor of Marine Sciences, led the team and participated fully in all aspects of the research. She has extensive experience in the biology of migratory fishes, including passive acoustic tracking and hydroacoustic surveying. She also was the primary liaison with other tidal research groups in the US and abroad. Staines and Shen brought field and analytical hydroacoustics experience to the team, and Vieman came with an engineering background, gathering background in hydroacoustics through an M.S. and a Ph.D. program. McCleave, an Emeritus Professor of Marine Sciences, has had a lengthy career involving quantitative surveys of fish communities in fresh waters, estuaries, and open oceans, plus tracking of acoustically tagged fishes and hydroacoustic surveying. Vieser and Altenritter both joined the team having previous experience in fish community studies.

Task 3. Development of alternative tidal turbine designs.

Both the tow tank and the modeling efforts began in 2009. The biggest effort in the first two years was the development of both the computational and testing infrastructure needed for the work.

The Task 3 research team consisted of Mick Peterson, Ph.D., Richard Kimball, Ph.D., Raul Urbina, M.S., Ph.D. student, Geoff DeBree, M.S. student, Thomas Lokocz, M.S. student and Megan Coleen Swanger, M.S. student. In addition a larger number of undergraduates were employed as a part of the project as well as several graduate students who did a portion of their work with support from this project, including Anna Demeo, Ph.D. student. All of the students have since completed their degree programs with the exception of Raul Urbina who has papers in review and is in the final stages of his dissertation. Peterson, a Professor of Mechanical Engineering, led the team and participated fully in all aspects of the research. Richard Kimball

brought expertise in the modeling and testing of propellers and turbines to the group. All of the graduate students worked on various aspects of the testing of turbines with the modeling carried out by Raul Urbina.

Task 4. Evaluation and Community Response and Small Scale Tidal Energy Sites.

The University of Maine undertook studies to examine stakeholder engagement in tidal energy development in Maine with a focus on Ocean Renewable Power Company's Cobscook Bay Project. Broadly, the purpose of this research was to understand the factors influencing the acceptability of tidal power development for different stakeholder groups (i.e., policy, technology, and community stakeholders) and to gather social data to inform more effective stakeholder engagement. More specifically, the research had two primary objectives. The first objective was to identify and characterize the most salient stakeholders associated with tidal energy development and the types of engagement strategies considered effective for these different stakeholders. The second objective was to understand and describe the regulatory and permitting process for marine hydrokinetic (MHK) development in Maine. This included an analysis of the various federal and state agencies involved, their jurisdictional authority, roles, and decision-making process. This research began in January 2010 and consisted primarily of semi-structured and informal interviews, discussions with key agency, industry, and community stakeholders, direct observations of the policy process, review of relevant documents, and a community mail survey.

In partnership with S. W. Cole Engineering, Inc. research aimed at tidal resource assessment, natural resource assessment, turbine design development, and feasibility assessment of tidal power for community-scale projects was also undertaken. Through site visits, attendance at meetings and workshops, document review, and discussions with key regulatory and community stakeholders, a framework was developed to assist prospective small-scale tidal power developers through the permitting process (full details of the framework are in Appendix Task 4A-1 and other appendices referenced therein). The report shares knowledge learned concerning the permitting and licensing of marine hydro-kinetic (MHK) projects and the Wiscasset Project covering topics such as agency requirements and timelines and provides links to useful resources.

The Task 4 research team which looked at the permitting and resource barriers associated with small scale tidal sites was led by Johanna Szillery, M.S., of CES, Inc. (formerly of S.W. Cole) and included Peter Arnold, M.S. (formerly of the Chewonki Foundation), James Churchill, Ph.D. (Woods Hole Oceanographic Institute), and Dot Kelly (Pleasant Cove Homeowners Association). The Task 4 research team working on the community response consisted of Teresa Johnson, Ph.D., Jessica Jansujwicz, Ph.D., Christopher Bartlett, Colleen Budzinski, M.S., Jeffrey Vieser, M.S. student, and undergraduate students Theodore Koboski, Mira Jordan, Katherine Doyen, and Ariadne Dimoulas. Assistant Professor of Marine Policy Teresa Johnson led the team and participated fully in all aspects of the research project. She has extensive experience in human dimensions research related to fisheries and coastal communities. Sustainability Solutions Initiative Postdoctoral Fellow Jessica Jansujwicz was primarily responsible for fieldwork and

Final Report Maine Tidal Power Initiative

data analysis and managed the team of staff and undergraduates. Sustainability Solutions Initiative Research Associate Colleen Budzinski assisted with undergraduate students, semi-structured interviews, data entry, and administrative aspects of the project. Christopher Bartlett, Maine Sea Grant/Cooperative Extension assisted with community interviews and provided valuable support for the team's research and outreach efforts in the communities of Eastport and Lubec Maine.

Results and Discussion

Task 1. Tidal Resource Assessment

Subtask 1.1

Acoustic Doppler current meters were deployed by the ORPC team at multiple locations near the demonstration sites in Outer Cobscook Bay as well as the potential development sites in the Western Passage during 2010, 2011 and 2012 (Table 1-1). Time series of velocity measurements were archived, from which the prevailing flow directions and frequency distributions of flow speed can be determined. For the site northwest of the Goose Island in Cobscook Bay (Figure 1-1), the flooding/ebb current centers at ~ 330° and 150° from north, respectively. This site is slightly ebb dominated with stronger and longer running ebb flows. Concurrent velocity profiles also showed gradual reductions in flow speed as well as small counterclockwise/clockwise rotations of flood/ebb flows with depth.

Table 1.1. List of ADCP measured time series in Cobscook Bay and Western Passage

Cobscook	File Name	Duration	Location
	TidGen001_north.000	9-26-2012 - 10-29-2012	44°54'36.90"N, 67°02'44.98"W
	TidGen001_south.000	9/26/2012 - 10-12-2012	44°54'35.47"N, 67°02'45.44"W
	HA11-4_ADCP.000	7/5/2011 - 8/5/2011	44°54'35.39"N, 67°02'44.67"W
	HA11-8_ADCP.000	11/9/2011 - 12/9/2011	44°54'35.03"N, 67°02'41.11"W
	HA11-10_ADCP.000	9/9/2011 - 10/4/2011	44°54'35.75"N, 67°02'45.80"W
	TidGen003_ADCP.000	10/11/2011 - 11/8/2011	44°54'37.00"N, 67°02'50.03"W
	TidGen004_ADCP.000	10/11/2011 - 11/8/2011	44°54'32.62"N, 67°02'39.33"W
	TidGen005_ADCP.000	12/9/2011 - 1/9/2012	44°54'34.22"N, 67°02'43.46"W
	CENTER60DAY.000	5/11/2010 – 7/8/2010	44°54'37.86"N, 67°02'43.62"W
	NE_000.000	6/24/2010 – 7/1/2010	44°54'37.86"N, 67°02'38.34"W
	NW_000.000	5/19/2010 – 5/26/2010	44°54'40.20"N, 67°02'46.68"W
	S_000.000	7/1/2010 – 7/8/2010	44°54'31.68"N, 67°02'45.00"W
	SE_000.000	6/16/2010 – 6/23/2010	44°54'32.70"N, 67°02'40.38"W
	SW_000.000	6/2/2010 – 6/9/2010	44°54'34.32"N, 67°02'48.24"W
Western Passage	WP_Deep_6-2012.000	5-24-2012 - 6-26-2012	44°55'18.60"N, 66°59'11.49"W
	WP_shallow_6-2012.000	5-24-2012 - 6-26-2012	44°55'18.64"N, 66°59'20.02"W
	WP_Dog_Is_shallow_5-16.000	4-17-2012 - 5-3-2012	44°55'18.64"N, 66°59'20.02"W
	WP_12-12_Shallow.000	11-28-2012 - 1-2-2013	44°55'12.25"N, 66°59'18.702"W
	WP_12-12_Deep.000	11-28-2012 - 1-2-2013	44°55'13.37"N, 66°59'12.677"W
	WP_2-2013.000	1-3-2013 - 2-4-2013	44°55'15.283"N, 66°59'21.072"W

Final Report Maine Tidal Power Initiative

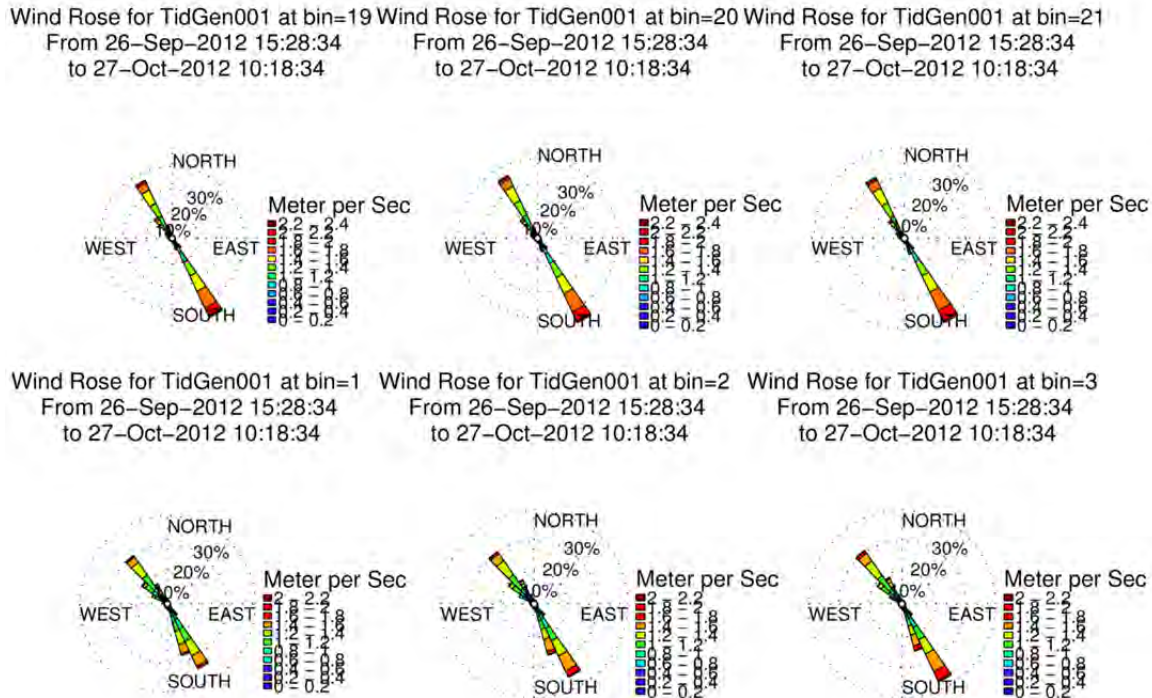


Figure 1-1. Example of rose diagrams from TidGen001_north.000 time series. Bin 1 is about 3 m above the seafloor. Each bin represents 0.8 m of water column.

Subtask 1.2.

In situ current measurements are indispensable in resource assessment, but because they are discrete and sparse they often cannot capture the full characteristics of the tidal stream across a tidal channel. Fortunately, modern coastal circulation models can attain sufficient accuracy to compliment the field observations if done correctly. A three-dimensional coastal ocean circulation model was set up to predict tide currents of the Quoddy region. The model uses unstructured triangle mesh in the horizontal with 25 m resolution in outer Cobscook Bay and Western Passage and it has 15 sigma levels in the vertical. 10 principal tidal constituents derived from WebTide (<http://www.bio.gc.ca/science/research-recherche/ocean/webtide/index-eng.php>) were specified along the open boundary in the Grand Manan Channel. The model simulation was first validated using the available observations, which was then used to calculate the spatial-temporal distribution of the power density (Figure 2-1).

Conclusions

- The tidal stream in the outer Cobscook Bay and Western Passage has the mean power density exceeding 1000 W/m^2 .
- Sites with the highest tidal power density include the area west of the Goose Island in the outer Cobscook Bay and the areas near the Dog Island and Kendall Head in the Western Passage.
- Numerous eddies, both stationary and transient, exist in and on the sides of the tidal stream. These eddies induce significant variability in flow direction and speed, which can

lead to apparent fluctuations in power density.

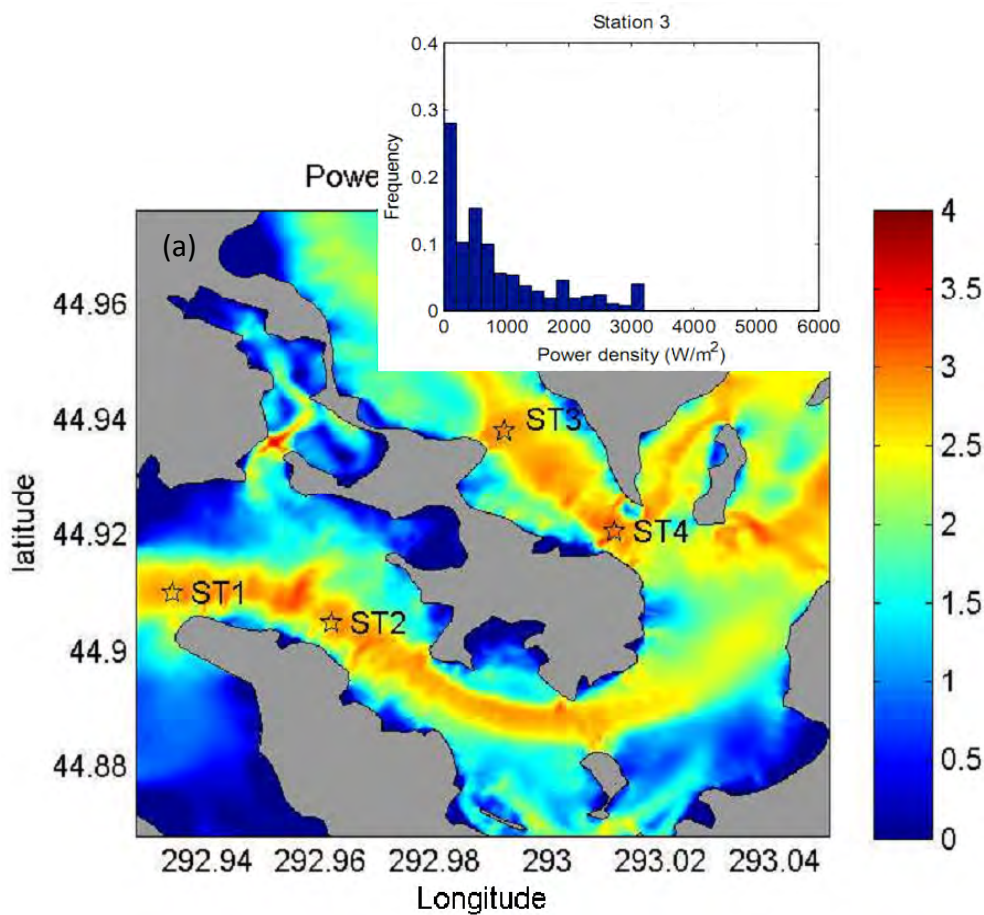


Figure 1-2. Distribution of the vertically averaged, mean power density in log10 scale (unit: Wm^{-2}). The inset shows the frequency distribution of the tidal power density at station 3

Subtask 1.3.

Flow fields around scaled models of cross-flow turbines were measured using a Nortek Acoustic Doppler Velocimeter (ADV) in the University of Maine tow tank. A measuring apparatus consisting of both the ADV and a pressure transducer on a weighted tripod was assembled and placed on the tank floor to allow the test turbine pass by overhead. By adjusting the angle between the ADV to the floor, measurements at different heights were obtained. Moreover, it was assumed that the flow field above the turbine centerline could be obtained by running the carriage backward. Measurements were obtained for different values of several key variables, including solidity, carriage speed, TSR, and blade positions (Table 1-2). The data were processed to produce composite flow fields. Figure 1-3 shows one of such composites for the 4-blade turbine at near optimum performance (test set A). Reynolds averaging was applied to separate the flow field into mean and fluctuations. The former was used to estimate bypass fraction while the latter was used to illustrate turbulence energy transfer and dissipation in the wake.

Conclusions

- The flow field can be divided into three stages, and they are the upstream effect, the entrained flow behind the turbine, and the flow recovery.
- The approach of the turbine drives the vertical velocity away from the turbine, and the bypass flow has the largest velocity outward at approximately -0.2 diameters in front of the turbine.
- Entrainment picks up dramatically around $x/D \approx -0.2$. Behind the turbine within a distance of 0.5 to 1 diameter the fluid travels at nearly the carriage speed, which decreases gradually to about 30% of the carriage speed at $x/D \approx 2$. Blockage effect can be noted during this stage in the outer layers where the latitudinal velocity travels in the opposite direction of the entrained flow.
- Composite TKE shows a front dispersing outward, indicating the expansion of the wake. Moreover, TKE attenuates relatively fast, usually within $3-4$ diameters downstream, where the flow recovery begins.
- Flow recovers slowly further downstream with the latitudinal velocity remaining at about $5-10\%$ for $x/D \approx 10$.

Table 1-2. Different sets of measurements and the corresponding values for key variables. Asterisks indicate a near optimum performance setting for the turbines.

Set	Solidity	Carriage Speed (m/s)	TSR	Blade Positions	Measurements
A*	0.32	1.0	1.4	Random	Free Surface & Velocity
B	0.32	1.0	0.9	Random	Free Surface & Velocity
C	0.32	1.0	1.9	Random	Free Surface & Velocity
D*	0.16	0.8	2.25	3 Different Blade Positions	Velocity
E	0.16	0.25-1.0	0.75-3.0	Random	Free Surface

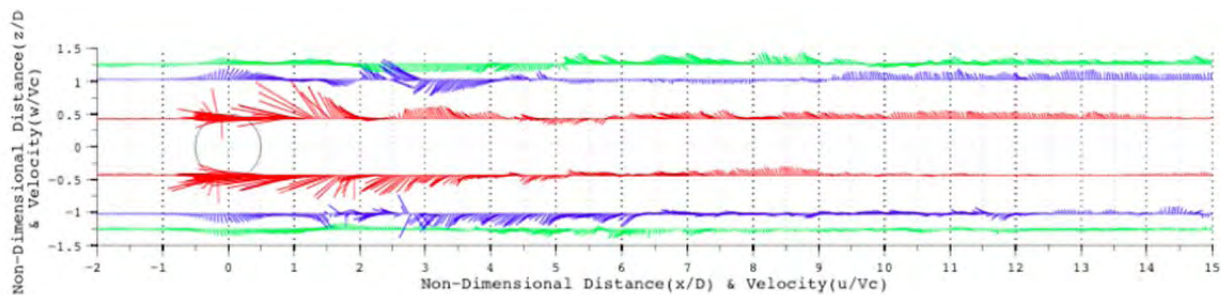


Figure 1-3. Composite of the measured flow field for test set A (see Table 1-2). The dashed circle represents the relative position of the turbine. D is the turbine diameter and $V_c = 1$ m/s is the carriage speed traveling in the negative x direction. u and w are velocity

components in the x and z (vertical) direction, and positive values are against the carriage traveling direction and upward, respectively.

Subtask 1.4.

Turbines were numerically implemented in the model as objects that extract energy to result in partial blocking and deflection of the tidal flow near Kendall Head in the Western Passage, where the coastline protrusion acts as a natural duct to concentrate in-stream kinetic energy.

Without specifying types of turbines and mounting structures, tidal devices were assumed to be in the mid-water column across the 7th, 8th and 9th sigma layers.

Because the water depth becomes increasingly shallower approaching the coasts, this is equivalent to having shorter turbines near the ends of the rows. Several experiments (Figure 1-4 and Table 1-3) were conducted to study the effects of turbines on the hydrodynamics in the near- and far-fields as well as how turbine densities and arrangements affect the efficiency of individual turbines and the farms as a whole.

Table 1-3. List of model experiments with different turbine allocations. See Figure 1-4 for locations of the rows.

Exp Cases	Turbine Distributions (Number of units/Approximate spacing)		
	Row 1:	Row 2	Row 3
1-1	10/100m		
1-2	19/50m		
1-3	29/25m		
1-4	58/0m		
2-1	10/100m	10/100m	
3-1	10/100m	10/100m	9/100m

Conclusions

- Even though only small fractions of in-stream tidal energy are taken out, changes in the flow, water level, as well as horizontal and vertical mixing coefficients were clearly detected both in the near and far fields

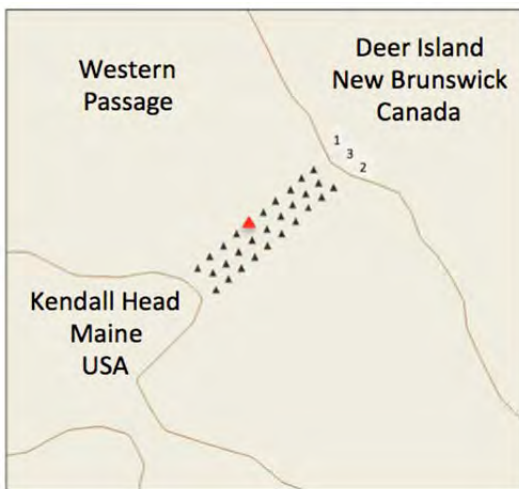


Figure 1-4. Schematic of turbine arrangements in the model cases 1-1, 2-1 and 3-1. The average distance is ~ 80 m between rows.

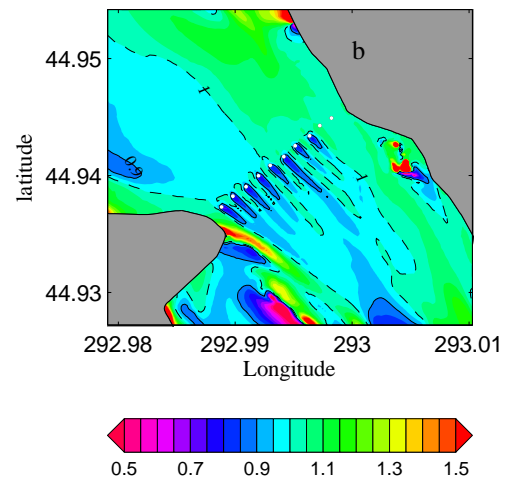


Figure 1-5. Ratio of the tidal current speed on the 8th sigma level in case 1-1 to its counterpart in the base case near the peak flood at 03:00 on 6 July 2004 (a) and near the peak ebb at 10:00 on 6 July 2004 (b).

(Figure 1-5).

- There is a delicate balance between having nearby turbines to benefit from the velocity gains in the turbine gaps (deflection effect) and having too many turbines so that the overall flux through the cross-section is substantially reduced (blockage effect) (Table 1-4).
- For a single row, the turbine array efficiency normalized by the BR (equivalent to a mean per-turbine-efficiency) is the highest when only one in every three cells is occupied by turbines. When turbines are arranged in multiple rows in the passage, significant reduction of the row efficiency is found when turbines are in the direct shadow of one to another because of the wakes. When turbines are set in a lattice form, the efficiency can benefit from the speed gain generated between turbine gaps from the neighboring rows.

Table 1-4. The extracted energy and efficiency during one spring-neap cycle for the six cases listed in Table 1-3. Π (row efficiency) is the ratio of the energy extracted by turbines on a given row to the naturally available in-stream energy from the cross-section at which the row of turbines resides.

Exp. Cases	# of units	Row 1			Row 2			Row 3		
		EE (MWh)	BR (%)	Π (%)	EE (MWh)	BR (%)	Π (%)	EE (MWh)	BR (%)	Π (%)
1-1	10	308.2	6.70	3.93						
1-2	19	866.1	12.09	11.04						
1-3	29	1149.6	18.46	14.66						
1-4	58	1716.8	37.76	21.89						
2-1	20	235.9	6.70	3.01	416.8	6.15	4.77			
3-1	29	225.8	6.70	2.88	427.5	6.15	4.89	494.9	5.80	5.81

List of Accomplishments for Task 1.

Publications

Xue, H., M. Bao, X. Bao, and M. Cameron, 2013: A numerical study of tidal farm efficiency in the Western Passage, US and Canada, Proceedings of MTS/IEEE OCEANS'13 Bergen, 130117-022.

Bao, M., H. Xue, X. Bao, in revision: Evaluating the Tidal Stream Power and Impacts of Energy Extraction on Hydrodynamics in Cobscook and Passamaquoddy Bays

Thesis

Cameron, M., 2012, Flow field measurements for a cross-flow turbine. M.S. thesis, University of Maine, pp. 113.

Task 2. Assessment of potential effect on fishes and community analysis of fishes.

Objective 1.

The abundance and vertical distribution of fishes was determined using down-looking single beam (Simrad ES60) and later single beam and split beam (Simrad EK60) echosounders mounted along the side of a boat moored in the tidal stream for 24 hours at each deployment site and control site (Table Task 2-1). A down looking acoustic imaging camera (DIDSON, Dual Frequency IDentification SONar) was also deployed on the echosounder mount. It was primarily used to help discriminate fish from turbulence in the water. For some surveys, an Acoustic Doppler Current Profiler recorded a water current profile every 30 min. Hydroacoustics data were analyzed using Echoview[®] software, omitting the top 10 m of the water column due to entrained turbulence.

Table Task 2-1. Months sampled for Fisheries Monitoring Plan (down-looking hydroacoustics). 1 and 2 indicate sampling in Cobscook Bay at CB1 and CB2, respectively; 1a, 1b, and 2 indicate sampling at CB1a (beside the turbine), CB1b (in-line with the turbine), and CB2 (control), respectively. W1-2 indicate sampling at two sites in lower Western Passage of Passamaquoddy Bay in 2009 and 2010. Light gray indicates presence of TidGen[®] bottom frame only; dark gray indicates presence of complete TidGen[®].

Year	Jan	Feb	Mar	April	May	June	July	Aug	Sept	Oct	Nov	Dec
2009								W1-2,2	W1-2, 2			
2010					W1-2,1, 2	W1-2,1,2		W1-2,1, 2	W1-2,1,2	1,2	1,2	
2011			1,2		1,2	1,2		1,2	1,2		1,2	
2012	1,2		1,2		1a,1b, 2	2		1a,1b,2	1a,1b,2			
2013			1a,1b,2		2	2		2	2			

In the single-beam system (presented here), fish density was represented on a relative scale using volume backscattering strength, S_v , which is a measure of the sound scattered by a unit volume of water and is assumed proportional to density. S_v is expressed in the logarithmic domain as decibels, dB re 1 m^{-1} . The vertical distribution of fish throughout the water column was

Final Report Maine Tidal Power Initiative

examined using the area backscatter coefficient, s_a , which is the summation of volume backscatter over a given depth range and is also proportional to fish density. s_a is expressed in the linear domain ($m^2 \cdot m^{-2}$) and is additive. Only results from 2010-June 2013 for Cobscook Bay sites are presented here.

Fish densities (mean water columns S_v) in 2010 and 2012 were significantly different from those of 2011 and 2013 (Figure Task 2-1). In 2012 and early 2013, there were no differences in water column fish densities in-line and beside the turbine (Figure Task 2-2). So CB1a and CB1b are combined as CB1 in the rest of the analyses.

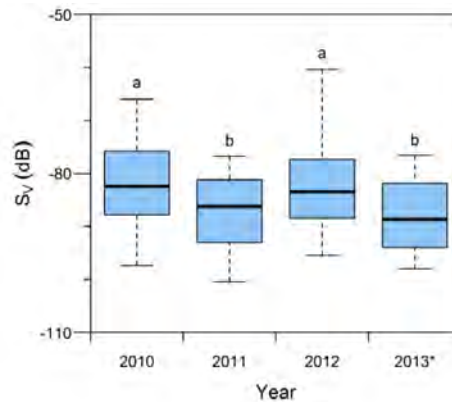


Figure Task 2-1. Water column S_v for all years sampled (CB1 and CB2 data pooled). Bold horizontal line indicates the median, boxes span the interquartile ranges, and whiskers extend to the 5th and 95th percentiles. Groups with different letters (a and b) are significantly different. In 2013 (*), only March, May, and June have been analyzed to date.

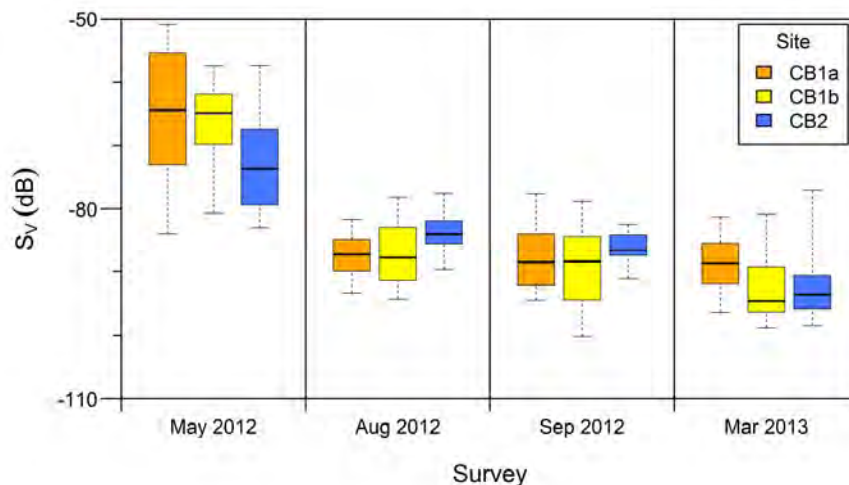


Figure Task 2-2. Water column S_v at CB1a, CB1b, and CB2 surveys in 2012 and 2013. Bold horizontal line indicates the median, boxes span the interquartile range, and whiskers extend to the 5th and 95th percentiles.

Final Report Maine Tidal Power Initiative

Fish density through the water column varied significantly by month, with May and June densities being greater than those in August and September, at least in 2010 and 2012 (Figure Task 2-3). Within surveys (months), densities at CB1 and CB2 were significantly different only in three months over three plus years. Thus, CB2 seems an appropriate control site to test differences between pre- and post-deployment surveys.

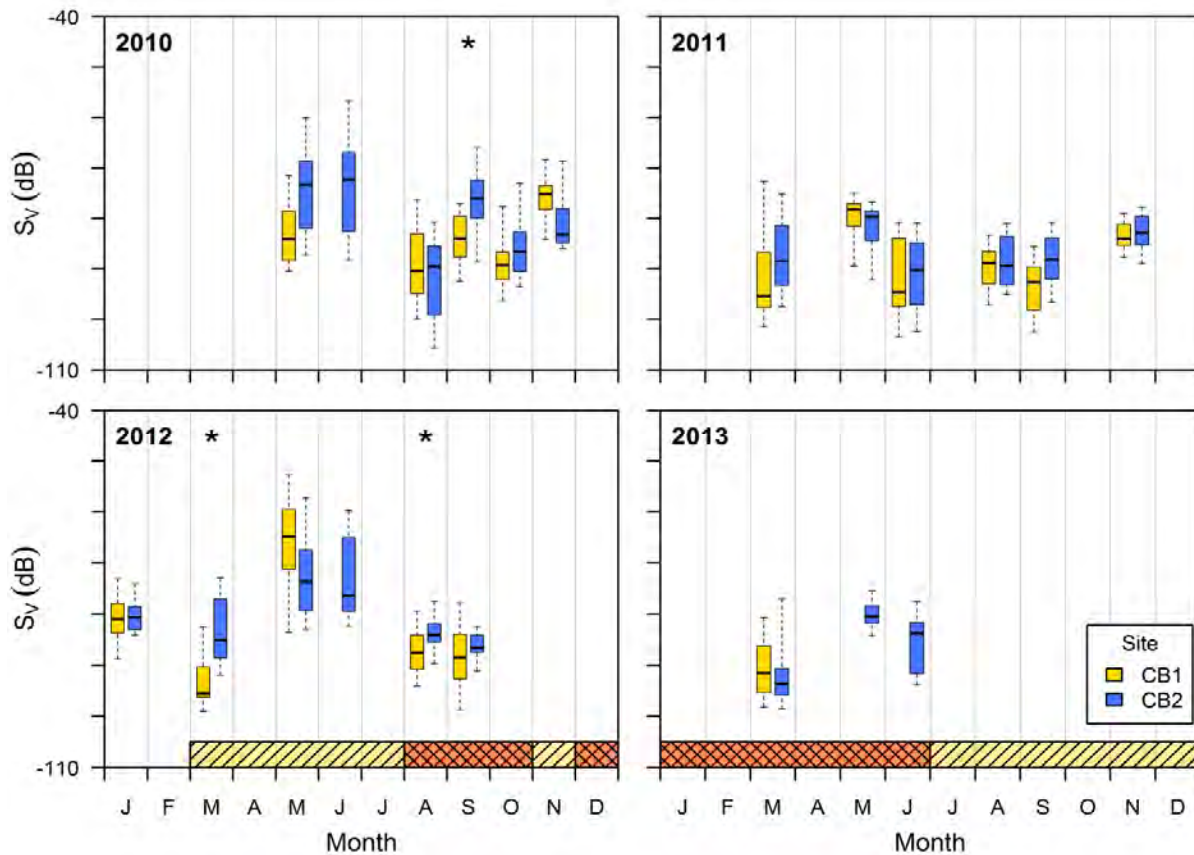


Figure Task 2-3. Water column S_v at CB1 (which includes CB1a and CB1b data) and CB2. Bold horizontal line indicates the median, boxes span the interquartile range, and whiskers extend to the 5th and 95th percentiles. Asterisks indicate significant differences between CB1 and CB2. Yellow hatched boxes indicate months when the TidGen[®] bottom frame was present on the seafloor; red hatched boxes indicate when the TidGen[®] turbine was also present. The turbine was braked (present but not spinning) starting mid-April until it was removed in July.

When CB1 and CB2 are combined, there is a seasonal trend in fish density, with fish densities highest in May and June, followed by November (when sampled), and generally lowest in August, September and March (when sampled) (Figure Task 2-4).

Whether the deployment of a turbine at CB1 affected the water column density of fishes is problematic depending on further post-deployment sampling. A significant difference between CB1 and CB2 was found only in the August 2012 post-deployment survey, when CB2 had a higher density index (water column S_v) than CB1 (Figure Task 2-3). A difference was seen in

Final Report Maine Tidal Power Initiative

March 2012, when the turbine's bottom support frame was in place. However, a similar difference occurred in August 2010, pre-deployment.

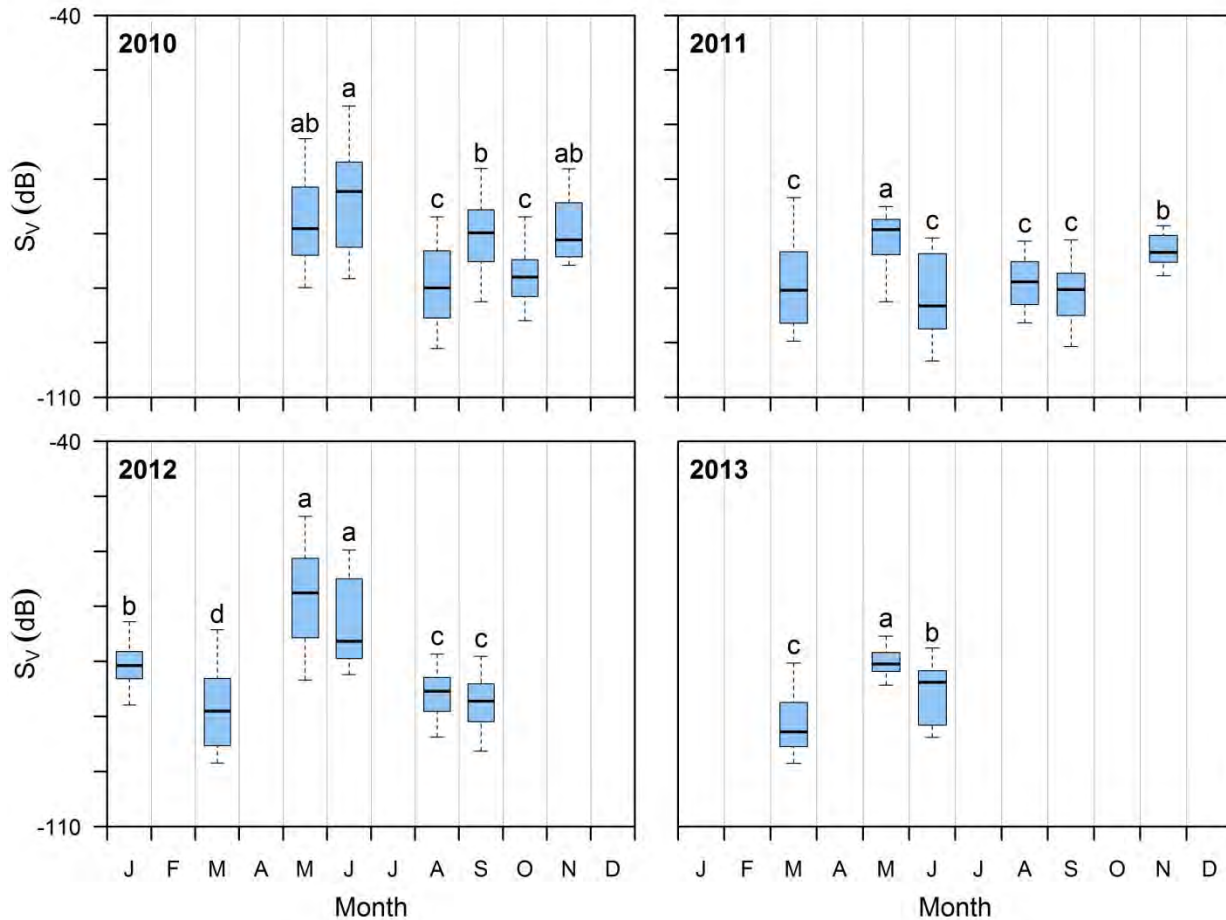


Figure Task 2-4. Water column S_v for all surveys (CB1 and CB2 data pooled together). Bold horizontal line indicates the median, boxes span the interquartile range, and whiskers extend to the 5th and 95th percentiles. Within each year, groups with different letters are significantly different.

Vertical distributions of fish were determined using the proportion of area backscatter coefficients, s_a , with depth. In most months throughout the study, the proportion of density was greatest near the bottom at all sites, but with considerable month to month variation (Figure Task 2-5). Departures from this pattern do not seem to be related to turbine deployment status, i.e., the control site showed a similar pattern. Significant differences in vertical distribution between CB1 and CB2 (only May 2011 and January 2012 pre-deployment) or between CB1a and CB1b (only March 2013 post-deployment) were rare.

For detailed analysis and discussion, see Viehman et al. in Appendix Task 2-3.

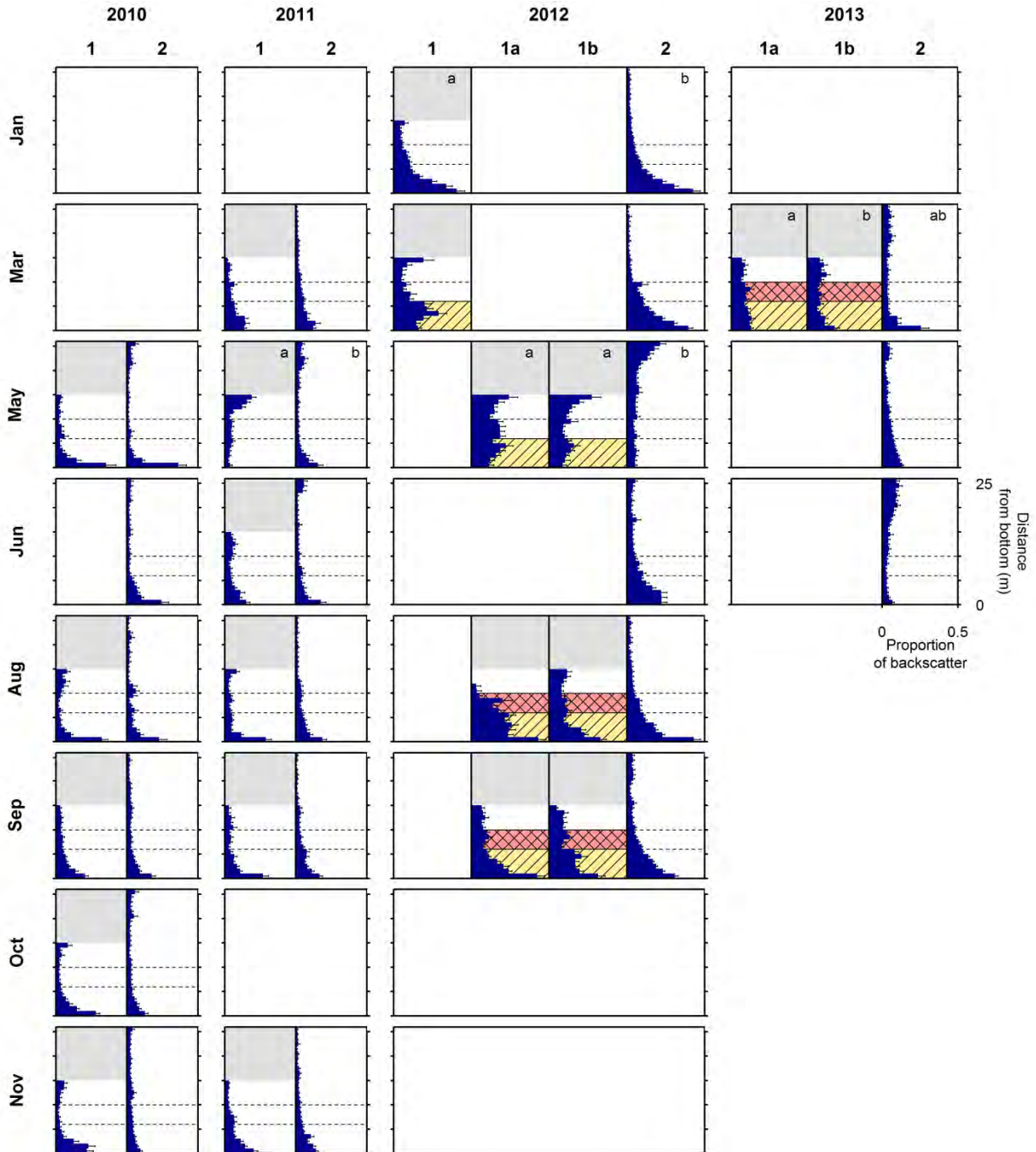


Figure Task 2-5. Mean proportion of area backscatter, S_a , contributed by each layer of the water column. All layers analyzed are shown for each site (0-15 m above the bottom at CB1, 0-26 m above the bottom at CB2). Depth of turbine is indicated by horizontal dashed lines. Yellow hatched areas indicate when the bottom support frame was deployed at the project site; red hatched areas indicate when the turbine was also present. Significantly different vertical distributions are indicated by different letters.

Conclusions

- Water column densities were higher overall in 2010 and 2012 than in 2011 and the first half of 2013.
- Densities estimated beside a turbine were not different from those in-line with the turbine.
- Densities at the chosen control location mirrored those at the deployment site.
- Fish densities were generally greater in May and June than in August and September, reflecting the high abundance of Atlantic herring (see Objective 3).
- Densities were generally greatest near the sea floor.
- Down-looking hydroacoustics is a reasonable approach to assessing potential impact on fishes of tidal energy development.

Objective 2.

At the time of the study, ORPC was testing its Turbine Generator Unit (TGU). The TGU was suspended approximately 5 m below the moored platform. It consisted of two helical-bladed cross-flow turbines (2.6 m diameter x 5.2 m length) and a permanent magnet generator on a single horizontal axis (Figure Task 2-6). The behavior of fish in front of, around, and behind the turbine was assessed using two DIDSON acoustic imaging cameras looking downward upstream and downstream of the turbine. The upstream DIDSON's viewing window included approximately 3 m of water upstream of the turbine, and the downstream DIDSON sampled approximately 3 m of water downstream of the turbine. Observations covered about 22 continuous hours, half during day and half during night on September 8-9, 2010.

Both individual fish (>20,000) and schools of fish (97) were observed. More than 90% of individuals and about 67% of schools were detected at night. Behaviors observed in the DIDSON recordings were described in seven categories (Table Task 2-2).

Milling behavior only occurred when the turbine was not rotating, i.e., near slack tide. Otherwise most fish moved in the same direction as the water current. About 50% of individual fish and about 33% of schools interacted with the turbine in some way. Less than 1% of individuals and about 15% of schools showed avoidance behavior, 35% versus 14% entered or exited the turbine, and 16% versus 2% remained in the wake. The rest of the individuals and schools passed above or below or milled about at slack tide.

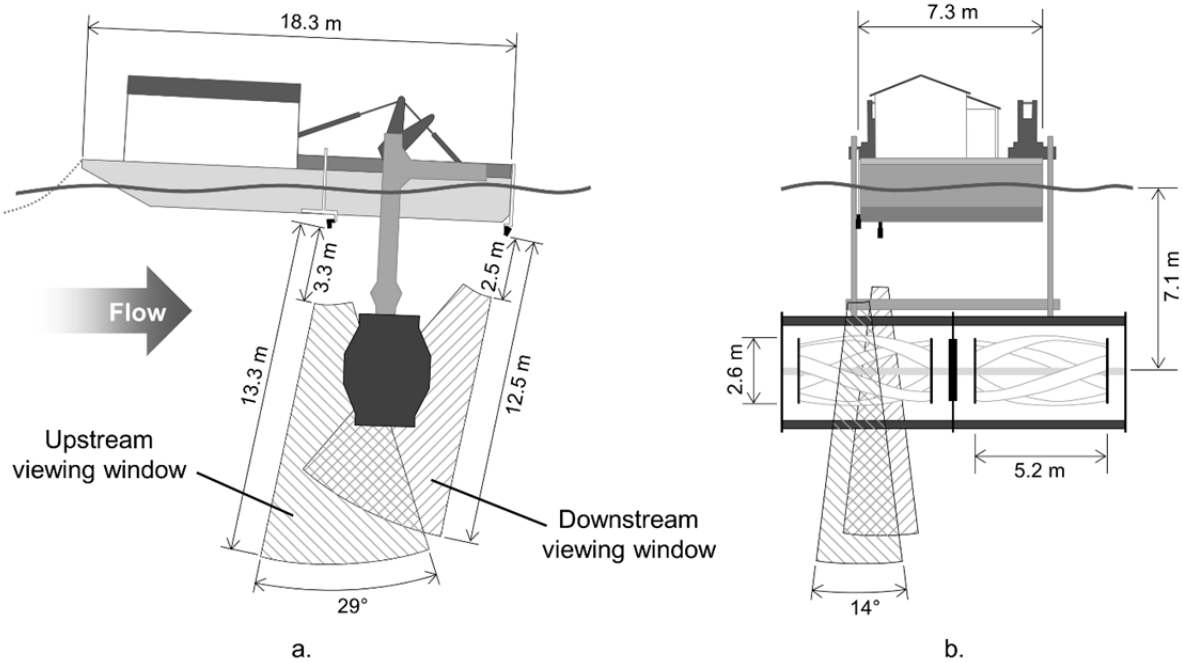


Figure Task 2-6. Schematic of Ocean Renewable Power Company’s turbine testing platform with the test turbine suspended below (adapted from schematic provided by Ryan Beaumont, RM Beaumont Corporation, Brunswick, ME): (a) side view, (b) front view. DIDSONs are shown in survey positions as small black boxes beneath the platform. The sampling volume for each DIDSON is marked by hatched areas. The turbine ceased rotating as the water current slowed approaching slack tide and resumed as the current speed increased after slack.

For individual fish, turbine rotation reduced the probability of entering the turbine by 35%, increased the probability of avoidance and passing by 120% and 97%, respectively, but avoidance was rare anyway. Diel condition affected small (≤ 10 cm long) and large (> 10 cm) individuals differently when the turbine was rotating. The probability of entering the turbine increased at night, by about 3.5 times for small fish and about 8 times for large fish. The probability of passing decreased about 40% at night for both size groups. The probability of avoiding decreased for small fish and increased for large fish at night, counterintuitively, but sample sizes were very small, especially in the daytime. Only about 3% of small fish remained in the wake during day, but about half did at night, while about 50% of large fish remained in the wake during day and about 40% did at night.

Final Report Maine Tidal Power Initiative

Table Task 2-2. Descriptions of the seven fish behaviors observed in DIDSON recordings.

Where observed	Behavior name	Description of behavior
Up- and downstream of turbine	Milling	Milling occurred during slack tide, when current speed was low. Fish ceased directed movement and instead moved in short bursts in random directions.
	Passing	Fish entered the field of view already above or below the turbine and passed across the view without diverting course, apparently unaffected by the turbine's presence.
Upstream of turbine	Avoiding	Fish altered course to avoid the turbine, swimming above or below it or reversing direction and moving against the current.
	Entering	Fish swam into the interior of the turbine. These were always fish that entered the field of view within the same depth range as the turbine.
Downstream of turbine	Exiting turbine, moving through wake	Fish exited the turbine, then swam directly through the wake of the turbine to re-enter the current.
	Exiting turbine, remaining in wake	Fish exited the turbine and then remained in the wake, showing behavior similar to milling for several seconds. Fish in the wake disappeared from view mid-wake, or returned to current and moved downstream and out of view.
	Appearing and remaining in wake	Same as above, but fish were not observed exiting the turbine. Previous location (inside the turbine, passing above or below, or in the wake but out of view) was unknown.

Fewer schools entered the turbine than individuals (21% versus 48%, respectively) and more schools avoided the turbine (28% versus 1%) and about 50% of both groups passed the turbine. Schools avoided the turbine from farther away than individuals (on average 2.5 m versus 1.7 m).

The DIDSON was a useful tool for monitoring fish interactions with the tidal turbine. It was especially well suited to sampling at night, when a video camera would not have been useful without artificial lighting that could alter the natural behavior of fish. As tidal turbines are likely to be placed in deep (dark) or turbid water, DIDSON and other acoustics equipment may be the most appropriate monitoring tools. However, there are shortcomings to using a DIDSON for this purpose. One was the boundaries of the viewing window; sampling a narrow slice of the water made it difficult to follow fish from upstream of the turbine to downstream, and may have resulted in some fish being counted multiple times (though this was unlikely unless fish were milling).

The largest shortcoming of the DIDSON in this study was the resolution. Although DIDSON image resolution is among the best available, fish with lengths under 10 cm were difficult to measure with certainty, and so fish had to be classified into broad size groups. This avoided introducing bias but also prevented more detailed analyses involving fish size. If the fish under

study were larger, length measurement error introduced by resolution would be a smaller proportion of fish length and would not be as much of an issue. The DIDSON could not provide information on direct blade strike of fish or the condition of fish exiting the turbine for the same reason.

For detailed analysis and discussion, see Viehman and Zydlewski in Appendix Task 2-2.

Conclusions.

- Milling behavior by individual fish occurred up- and down-stream of a test turbine.
- Some passed above or below the turbine.
- Some altered course to avoid the turbine.
- Some entered directly into the turbine.
- Some exited the turbine and left immediately or stayed in the wake.
- Some just appeared in the wake.
- A rotating turbine reduced the probability of entering the turbine and increased the probability of passing or avoiding the turbine.
- Night time increased the probability of entering the rotating turbine and decreased the probability of passing by.
- A smaller proportion of schools than individual fish entered the turbine.
- Acoustic camera imaging allowed equal quality observations day and night.
- The small field of view and the image resolution compromised the quality of observations.

Objective 3.

To characterize the fish community throughout Cobscook Bay, fishes were sampled at six open water sites by pelagic and benthic trawling from a commercial fishing vessel and at six intertidal sites by seining and fyke netting (Figure Task2-7). Samples were taken both day and night over the summer months (May, June, August, September) from 2011 through 2013, and the seining samples were supplemented in March, April, and November 2012 and November 2013 (Table Task 2-3). The outer bay pelagic trawl site and a nearby benthic trawl site provided some verification of targets seen in hydroacoustic sites (Objective 1). Only the four summer months are considered here. Midwater trawling, with funding under this award, was attempted in Western Passage and Outer Cobscook Bay in 2010 with little success, and is not considered here. However, that work was built upon to produce the results presented here, done with funding from a sub-award from a DOE award to Ocean renewable Power Company.

Trawls were nominally 20 minutes long. Pelagic and benthic trawling effort was slightly greater in 2012 and 2013 compared to 2011 by the addition of two night tows for each gear. Seine hauls usually were completed in 3-5 minutes, depending on substrate, and fyke net sets usually sampled most of an ebb tide. Seining effort during the four principal summer months of 2012 was more than double the effort in 2011 and slightly more than the effort of 2013. Fishes were

identified, counted, and subsets of each species measured and weighed in the laboratory or occasionally on the trawl boat.

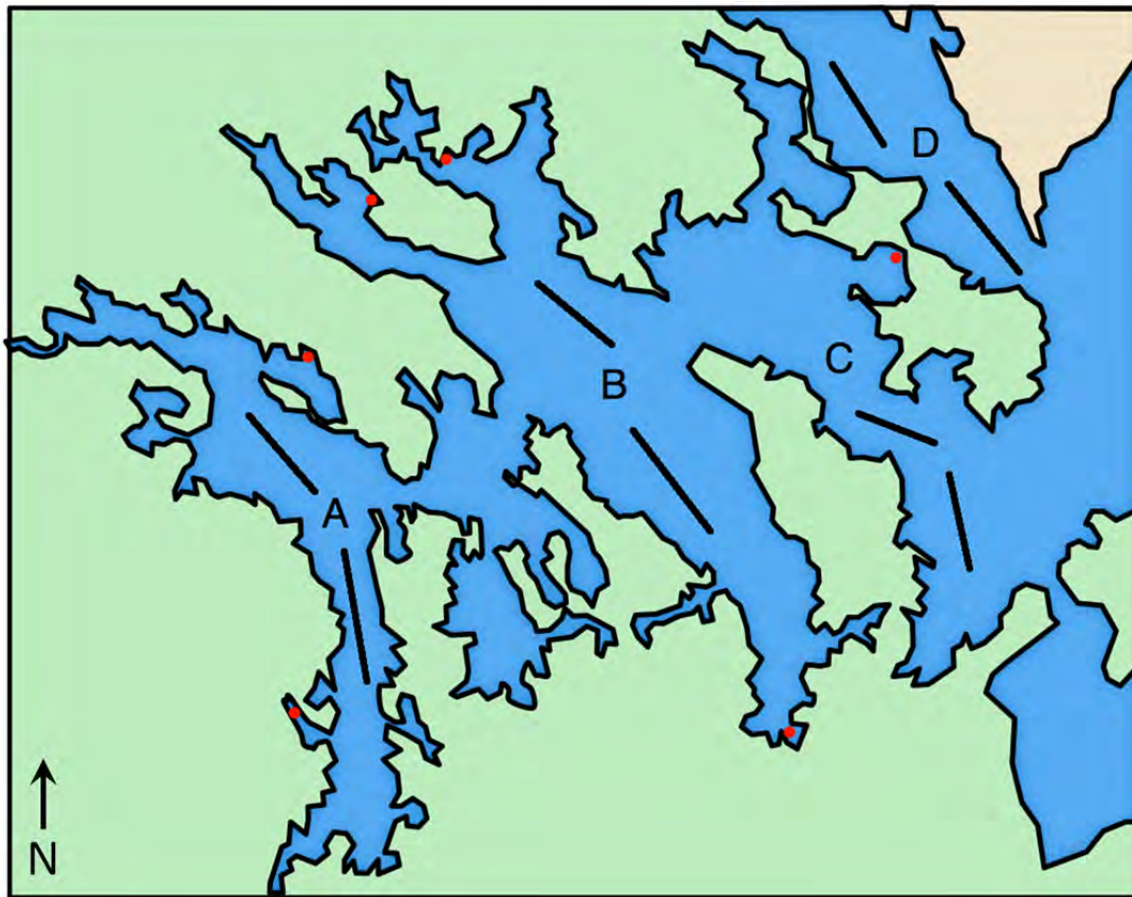


Figure Task 2-7. Map of Cobscook Bay and Western Passage of Passamaquoddy Bay showing mid-water and benthic trawl lines (black lines) fished and seine and fyke net sampling locations (red dots) for 2011-2013 (Cobscook Bay). Uppercase letters indicate the three sub-bays of Cobscook Bay sampled (A = inner; B = central; C = outer) and Western Passage in Passamaquoddy Bay (D). Both benthic and pelagic trawls occurred in the same location except in C, where midwater trawling occurred along the northerly line and benthic trawling occurred along the southerly line. C and D were sampled preliminarily with a midwater trawl in 2010 and are not considered in this report.

Forty six species and more than 60,000 individual fishes were captured by the various gears over the three years of the study. The overall species composition was dominated by four species, threespine stickleback (seining), Atlantic herring (pelagic trawling), winter flounder (benthic trawling), and Atlantic silverside (seining). Numbers of individuals caught per species ranged from about 20,000 down to several species represented by five or fewer individuals.

Final Report Maine Tidal Power Initiative

Year	Month	Pelagic trawl D/N	Benthic trawl D/N	Seine D/N	Fyke net D/N
2011	May	6/1	6/1	16/1	4/1
	June	7/2	6/2	16/4	5/2
	August	6/2	6/2	13/4	5/2
	September	6/2	6/2	22/3	0/3
2012	March			22/0	
	April			11/13	
	May	6/4	6/4	37/12	1/2
	June	6/4	6/4	42/6	5/2
	August	6/4	6/4	35/13	3/5
	September	6/4	6/4	28/8	3/4
	November			14/0	
2013	May	6/4	6/4	24/12	3/3
	June	6/4	6/4	26/13	3/3
	August	6/4	6/4	30/13	3/4
	September	6/4	6/4	27/12	3/3
	November			4/4	

Table Task 2-3. Number of day and night samples taken with various gears in Outer, Central, and Inner Cobscook Bays from 2011-2013. Principal months for interannual comparisons were May, June, August, and September. Night trawls were not done in Inner Cobscook Bay.

The Order Gadiformes (cods) was the most taxonomically diverse group represented by ten species: six Gadidae, including Atlantic cod and haddock, one Merlucciidae (silver hake), and three Phycidae (red and white hakes and fourbeard rockling). The Family Clupeidae was only represented by three species, including the second most abundant species (*in the catches*) overall, the Atlantic herring, plus alewife and blueback herring. Sticklebacks (Family Gasterosteidae) were represented by the most abundant species (*in the catches*) overall, the threespine stickleback, plus the abundant blackspotted stickleback and two rare species. There were four species in the Family Pleuronectidae, dominated by winter flounder, plus the related windowpane (Family Scopthalmidae). Four species of sculpins, mostly longhorn sculpins and grubbys (Family Cottidae), were present along with the related sea raven (Hemitripterae), lumpfish (Cyclopteridae), and Atlantic snailfish (Liparidae) in small numbers.

A number of seasonal trends occurred over the summer months. For example, rainbow smelt, mostly adults, were more abundant in May and June than in August and September, reflecting

their anadromous life cycle. Longhorn sculpin and grubby were also much more abundant in May and June than later in the summer. Butterfish, a species with a more southerly distribution, only appeared in Cobscook Bay in August and September, when water temperatures peaked. White hake were not caught in May, were rare in June and August and most abundant in September. Red hake were only abundant in 2013 and most were caught in June and August. Silver hake were only abundant in June 2012 and August 2013. Haddock, absent in 2012, were caught in low number in August and September 2011 and much larger numbers in August and September 2013. Fourspine sticklebacks were caught almost exclusively in August and September while the more abundant threespine and blackspotted sticklebacks were caught in all months.

Some of the observed interannual variability in abundance of some species may be related to the fact that 2012 was an extremely warm year compared with 2011 and 2013. Anomalously warm weather occurred early in the year. Atlantic herring illustrate this point well. In May and into June of 2011 and 2013, most of the herring caught were advanced larvae, and were under-sampled by the pelagic trawl because of mesh size. In contrast, in 2012 in May and June most of the herring had metamorphosed to the juvenile stage. Length-frequency distributions show the increased size of herring in May and June of 2012, and they had left the bay by August and September.

Butterfish, though not an abundant species overall, were much more abundant in trawls in August and September in 2012 than in 2011 and 2013, probably reflecting a seasonal migration farther north. Silver hake were most abundant in May and June of 2012, having mostly left by August. They were larger each month than those caught in 2013. Few alewives were caught in 2011 and in May of other years. In 2012, an older year class was present in June and then left. None were caught in June 2013. In August, young of the year alewives appeared as a cohort that was larger than the cohort in 2013, and the size differential carried into September.

Some species known to be present were under-sampled or not captured mostly because of low vulnerability to the sampling gears. Among cartilaginous fishes, only three spiny dogfish and a few little, smooth, winter, and clearnose skates were caught. Only one American eel was caught. Some Atlantic mackerel were caught, but observations of recreational fishing indicate a much greater abundance. No Atlantic salmon were caught, though wild salmon are very rare in a tributary to Inner Cobscook bay.

For details of methods, areas sampled, catches and results, see appendices to Appendix Task 2-4.

Conclusions.

- Forty six species were captured during the three-year study.
- Threespine sticklebacks dominated the catch in the intertidal zone.
- Atlantic herring dominated the catch in the open-water pelagic zone.
- Winter flounder dominated the catch in the open-water benthic zone.
- The Order Gadiformes was the most taxonomically diverse group with ten species.
- Five flatfish, four stickleback, and four sculpin species were caught.
- The anomalously warm year, 2012, altered the abundance, seasonal distribution, and growth of several species.

- Cartilaginous fishes, American eels and Atlantic mackerel were under-sampled by the gear types.

List of accomplishments for Task 2.

Viehman, H. A., and G. B. Zydlewski. (Accepted). Fish interactions with a commercial-scale tidal energy device in the natural environment. *Estuaries and Coasts*.

Viehman, H. A., G. B. Zydlewski, J. D. McCleave, and G. J. Staines. (Accepted). Using acoustics to understand fish presence and vertical distribution in a tidally dynamic region targeted for energy extraction. *Estuaries and Coasts*.

Task 3: Development of alternative tidal turbine designs

Objective 1.

The cross-flow turbines tested at the UMaine tow tank were modeled using a Free Vortex Method (FVM) model. FVM models were selected because they have a lower computational cost than Navier-Stokes equation methods, and are therefore better suited for use in conjunction with optimizers. FVM models can predict the hydrodynamic performance of cross-flow turbine using estimated blade forces generated by the fluid velocity field around the turbine. FVM models approximate the velocity field around the turbine by representing the wake created by the blades as shed vorticity at each time step. The FVM model tracks the shed vorticity position and its magnitude in time. A velocity field around the turbine can be approximated at each time step from the induced velocities estimation due to the shed vorticity and blade vorticity.

During operation, cross-flow turbine blades undergo large changes in their angles of attack, which cause the dynamic stall phenomenon. Dynamic stall is a phenomenon that results in the dynamic delay of stall of the blade due to unsteady motion, such as the motion a blade experiences in a cross flow turbine. Dynamic stall has been recognized as an important phenomenon to be considered when estimating the hydrodynamic performance of cross-flow turbines. The dynamic stall phenomenon was model in this work using a modified Sheng et al. (2008) Beddoes Leishman model for low Mach number flows (formulations can be found in Appendix 3). The three main components of the dynamic stall model are the calculation of the separation point function along the blade, a delayed angle of attack and the reduced pitch rate to estimate the blade forces. The dynamic stall model also considers cyclic variation of the Reynolds number due to rotation of the blade in the flow. All other variables to calculate the hydrodynamic performance of the cross-flow turbine are calculated using the method described in Strickland et al.(1980). Additionally, a Lamb-Oseen vortex model was used to represent the flow field created by the shed vorticity. As flow blockage is present in the experimental tests, a method of images was used in the FVM model to approximate the presence of boundaries, such as the seafloor or free surface. The method of images allowed for the FVM model calculations to be compared to the experimental data taken at the UMaine tow tank.

FVM results were compared with two published experimental data sets and experimental data taken at the University of Maine tow tank. The first set of data was developed by Strickland et al. (1980) and is reported for a turbine with two NACA 0012 blades, a chord to radius ratio, c/R , of 0.15 and an inflow velocity of 0.091 m/s. The second data set was developed by Shiono et al. (2000) and consisted of three NACA 63₃-018 blades with a chord-to-radius ratio of 0.375, an aspect ratio of 3.55 and an inflow velocity of 1 m/s. The tests performed at the University of Maine consisted of a turbine with two NACA 63₃-018 blades, a c/R of 0.461, an aspect ratio of 10, and inflow velocity of 0.60 m/s.

To improve the FVM model predictions for different conditions of toe angles, a flow curvature correction was implemented. Flow curvature is one of the most critical phenomena that affects the performance of a cross turbine. Flow curvature appears as a result of variation in the direction of the instantaneous relative velocity along the blade. This variation of the relative flow velocity direction affects the lift and drag forces on the blades. The flow curvature phenomenon was approximated by using a parabolic mean approximation of the velocity field along the blade. This flow curvature approximation calculates a virtual incidence angle and a virtual camber for the flow conditions. The blade forces are particularly sensitive to changes in the angle of incidence and camber. Because camber predictions for different conditions were needed, the blade forces model was improved so it could provide predictions of the blade forces for cambered blades. Additionally, improvements were also made to the dynamic stall model by implementing a limit on the movement of the separation point function along the blade.

FVM results were compared with one published experimental data set and experimental data taken at the University of Maine tow tank. The first set of data was developed by Li (2008) and is reported for a turbine with one and three NACA 63₍₄₎-021 blades, a chord to radius ratio, c/R , of 0.15 and an inflow velocity of 1.5 m/s to 2.0 m/s. The tests performed at the University of Maine consisted of a turbine with two NACA 63₃-018 blades, a chord-to-radius ratio of 0.30, an aspect ratio of 15, and inflow velocity of 0.80 m/s.

Examples of the experimental validation of the FVM are shown in Figure 3-1, Figure 3-2, and Figure 3-3. The non-dimensional tangential force shows good agreement with Strickland experimental data in the upstream region, but in the downstream region the tangential force is under-predicted. However, the dynamic stall model greatly improves the accuracy of torque and power coefficient values, as shown in Figure 3-2 and Figure 3-3. Figure 3-3 also shows that addition of the blockage effect to the FVM results in a higher peak power coefficient, which occurs at a higher tip speed ratio, as expected. The FVM with one wall blockage effect correction shows the best agreement with experimental data. Refer to Appendix 3 for more information on the modeling theory and complete results. Figure 3-4 shows improvements on the torque predictions by using the flow curvature correction. Figure 3.5 shows that improvements in the power coefficient predictions have been obtained for cross flow turbines with the blades mounted at different toe angles where flow curvature is considered.

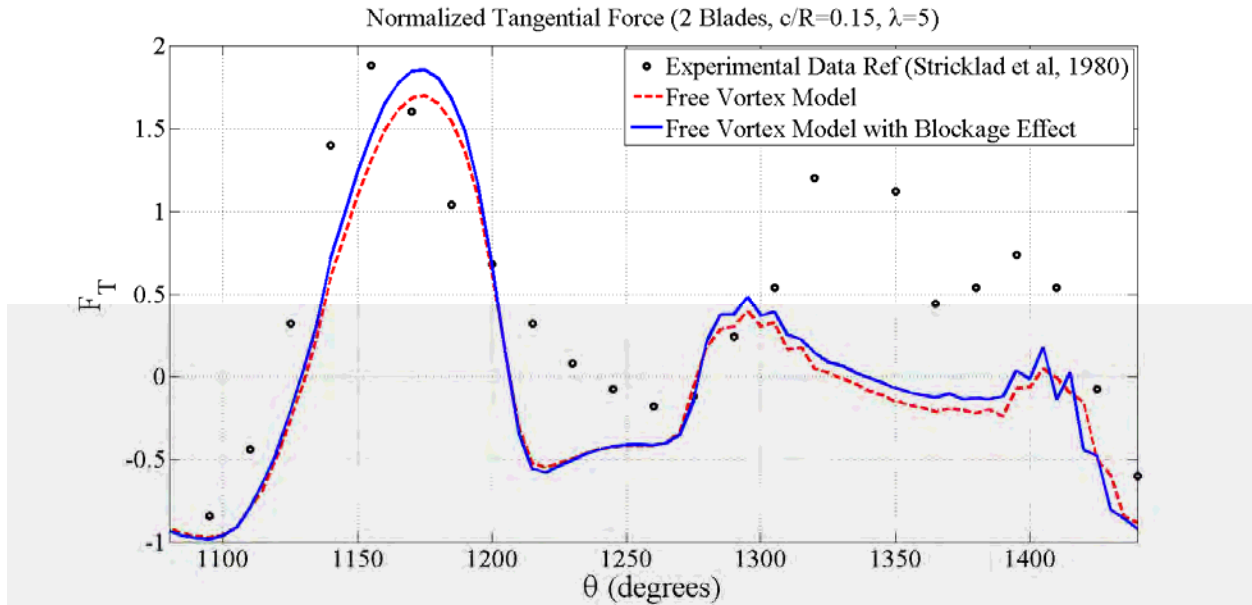


Figure Task 3-1. The nondimensional tangential force from Strickland et al.(1980) is compared to the results of the FVM.

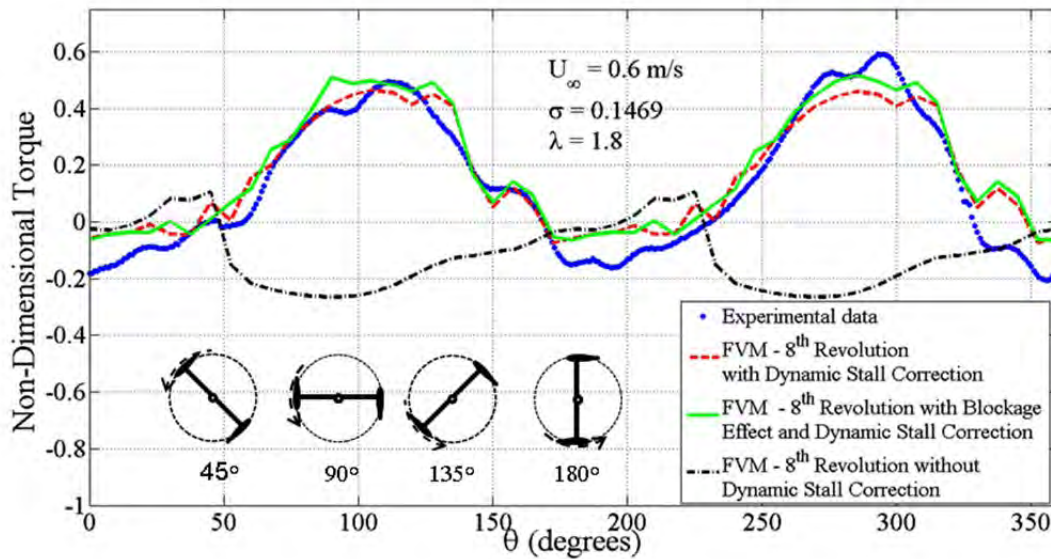


Figure Task 3-2. The unsteady nondimensional torque from UMaine tow tank tests is compared to the model with and without blockage and dynamic stall at a tip speed ratio of 1.5.

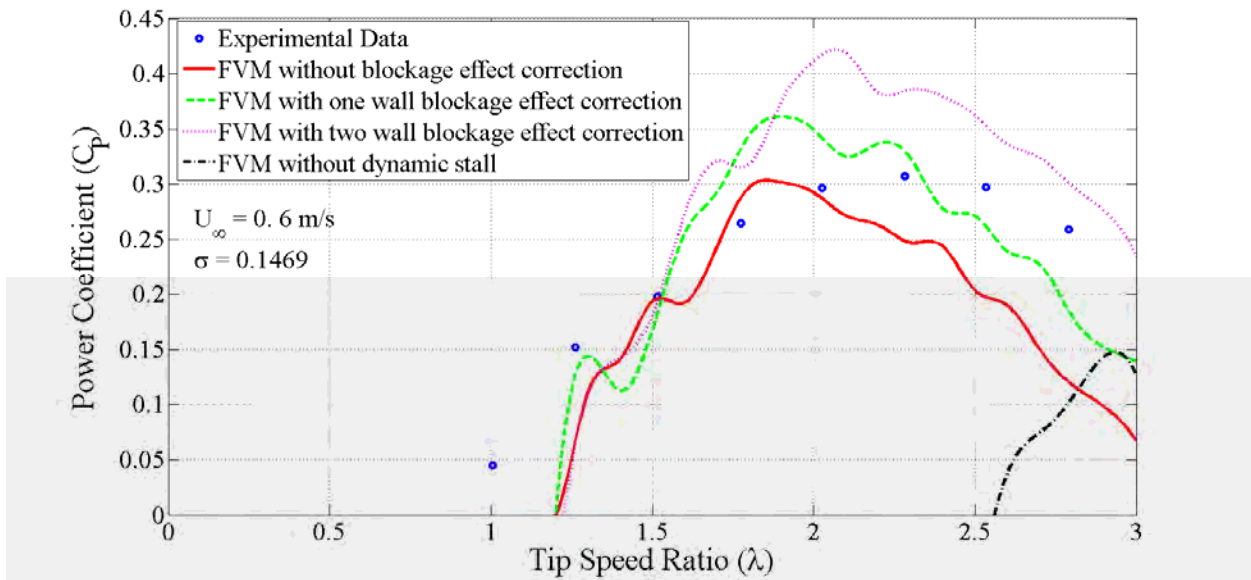


Figure Task 3-3. The power coefficient is compared to the model for 2 bladed tests with a chord to radius ratio of 0.46.

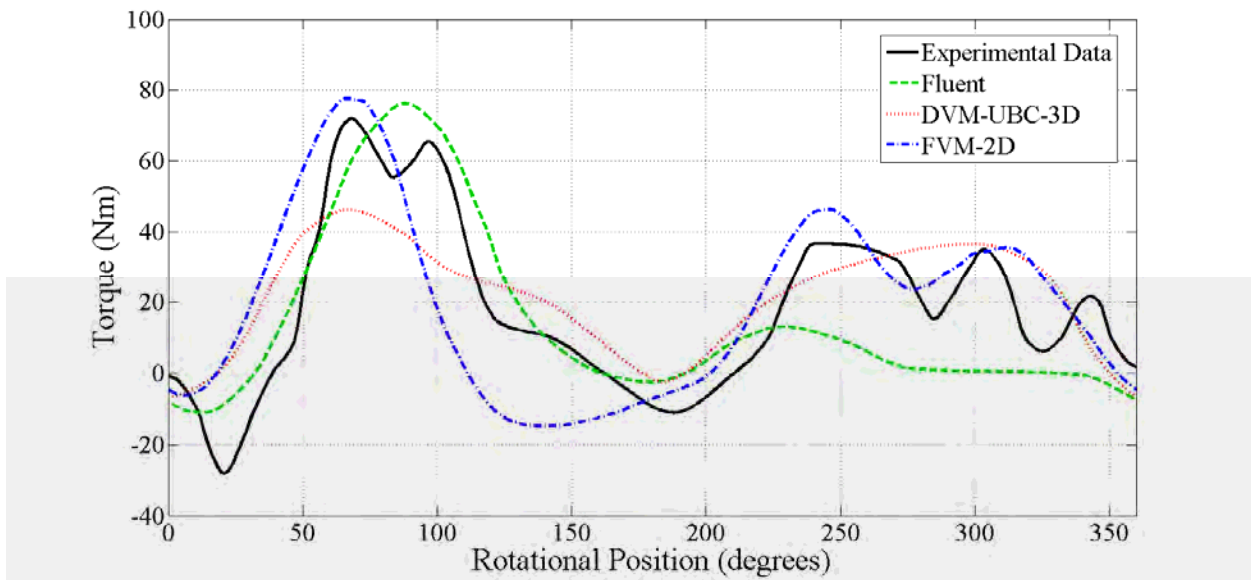


Figure Task 3-4. The calculated torque for a one bladed turbine with a chord to radius ratio of 0.15 at conditions of published results (Li, 2008) indicate improvements in the predictions.

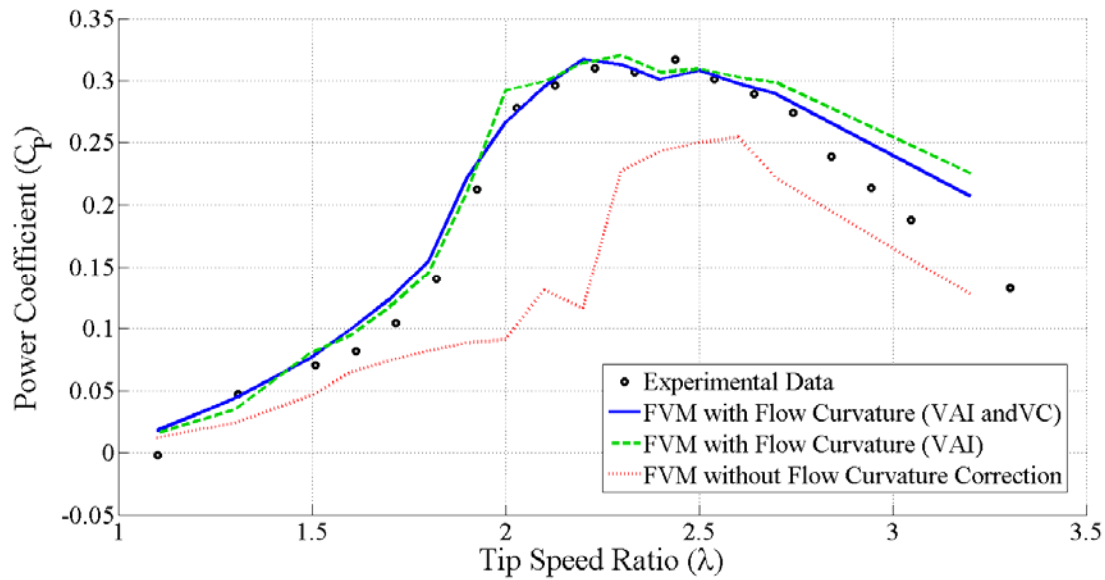


Figure Task 3-5. The analytical power coefficient results where flow curvature is considered show agreement with experimental data for a two-bladed turbine with a chord to radius ratio of 0.3 at a the toe angle of +4.

Conclusions:

- The lifting line FVM model with dynamic stall correction and flow curvature provides reasonable power coefficient predictions for cross flow turbines with blades mounted at different toe angles. The modified FVM model makes possible to obtain power coefficient predictions for a larger range of solidities and different toe angles than with traditional FVM models.
- The lifting line FVM model with dynamic stall correction and flow curvature provides improve predictions of the torque produced by cross flow turbines at low chord-to-radius ratios.
- The experiments show that dynamic stall is important for cases of relatively high stall regimes. The FVM was compared with data taken at the University of Maine and with data from several references.
- The analytical model was modified to model cross flow turbines with blades at different toe angles by using a flow curvature correction
- The one-walled boundary condition provided reasonable approximation of the flow blockage effects of the UMaine tow tank. The effects of flow blockage are not significant at low tip speed ratios.
- Further work may is needed to define onset criteria for dynamic stall, and to include considerations of the unsteady contributions, due to the changing vorticity on the blade, on the lift and drag coefficient calculations. These considerations will improve the torque predictions at larger chord-to-radius ratios.

- The model is well suited for use in optimization schemes, and it is also a useful tool for broad design parameters for the turbine. A basis for detailed optimization of the turbine using tools is provided to guide high computational cost approaches such as Navier-Stokes and lifting surface FVM methods.
- Inclusion of second order effects such as the boundary layer effects and countertorque may help provide better predictions.

Objective 2:

The first stage of the experimental campaign was designed to evaluate the performance of a cross-flow turbine with different blade profiles. The blades used in cross-flow turbines operate under conditions such as large angle of attack changes and curvilinear flows. These conditions affect the blade forces and consequently the hydrodynamic performance of the turbine. The hydrodynamic performance data of a scaled four-bladed cross flow turbine was acquired using seven different blade profiles. The blade profiles, which were tested in the cross flow turbine, were as follows: NACA 63₃-018 (NACA 6 digit series), NACA 0018, NACA 4418 (NACA 4 digit series), s809 (NREL profile), LNV109 (Douglas/Liebeck profile), and a modified NACA 63₃-018 with leading edge tubercles. The hydrodynamic performance was acquired for a range of toe angles and tip speed ratios to find the maximum power coefficient. The highest power coefficients were found when the four-bladed cross flow turbine was equipped with blades with NACA 63₃-018 and NACA 0018 profiles. During the first stage of testing in which symmetrical blade profiles were used, the maximum power coefficient was acquired at a toe angle of approximately +5 degrees.

The second stage of testing was performed for the turbine using NACA 63₃-018, NACA 0018 and NACA 4418 profile. Data was acquired for the turbine with blades set at toe angles from 0 degrees to +10 degrees. Data was also acquired for a cross flow turbine with two blades using the NACA 0018 and NACA 63₃-018 profiles. To further evaluate the camber effect on the hydrodynamic performance, data was acquired for the cross flow turbine with the NACA 4418 blades mounted inverted (referred to as reverse mounted), that is, with the camber and turbine circumference facing opposite directions.

The final stage of the experimental campaign was performed to evaluate the effects of varying blade variables such as number of blades, camber, and chord to radius ratio on the turbine performance. The two main variables in the tests were tip speed ratio and toe angle. The first series of tests were performed to evaluate the effect of varying the number of blades on the power coefficient. Data was acquired using a two-bladed turbine with NACA 0018 blades and a four-bladed turbine with NACA 0018 blades. The maximum power coefficient was acquired using a two-bladed turbine with NACA 0018 blades (Figure 3-8). The second set of tests were acquired for a two-bladed cross flow turbine using three-inch blades with NACA 0018 profiles, a two-bladed cross flow turbine using three-inch blades with NACA 4418 profiles and a two-bladed cross flow turbine using reverse mounted three-inch blades with NACA 4418 profiles.

The maximum power coefficient was acquired for the two-bladed cross flow turbine using three-inch blades with NACA 0018 profiles at a tip speed ratio of 1.7 and a toe angle of 5 degrees. The third set of tests was run to evaluate the effect of the chord to radius ratio on the turbine performance. The experimental data set was acquired for the turbine with two-inch blades using a NACA 63-3-018 profile and for the turbine with three-inch blades with a NACA 63-3-018 profile. The maximum power coefficient was acquired when the turbine was equipped with two-inch chord blades at a toe angle of 4 degrees.

Figure 3-6 shows the power coefficient as a function of tip speed ratio. In this case, the power coefficient for the turbine equipped with blades with NACA 0018 profile (straight blades) is compared to that of the turbine with cambered blades with NACA 4418 profile (cambered blades) at the same toe angle. The turbine with cambered blades has a lower power coefficient than the turbine with straight blades.

The hydrodynamic performance for the cross flow turbine was acquired for 20 different tip speed ratios and 9 different toe angles. The power coefficient results are shown in a single contour plot (Figure 3-7). Figure 3-7 shows that for the NACA 4418 profile, the maximum power coefficient was acquired when turbine had blades positioned at a toe angle of approximately +5 degrees.

The comparison of power coefficients for two-bladed and four-bladed tests show the difference in performance between two and four-bladed cross-flow turbines (Figure 3-8). The two-bladed turbine produced a significantly higher power coefficient. The maximum power coefficient for the two-bladed turbine was acquired at a higher tip speed ratio than maximum power coefficient of the four-bladed turbine. It is important to note that the maximum power coefficient was acquired at nearly the same toe angle for both the two and the four-bladed turbines. This suggests that the toe angle at which the maximum power coefficient was acquired was not a function of solidity, but it was most likely a function of the chord-to-radius ratio.

Figure 3-9 shows the experimental power coefficients for a two-bladed turbine equipped with blades with NACA 63-3-018 profile for different chord-to-radius ratios. The maximum power coefficient was acquired for the turbine using a lower chord-to-radius ratio. The loss of power coefficient was not as significant when the chord-to-radius ratio was increased as it was when the number of blades was increased. This fact may suggest that the solidity ratio cannot be used to accurately characterize cross-flow turbines.

Complete data, blade profiles, and experimental setup details are included in Appendix 3.

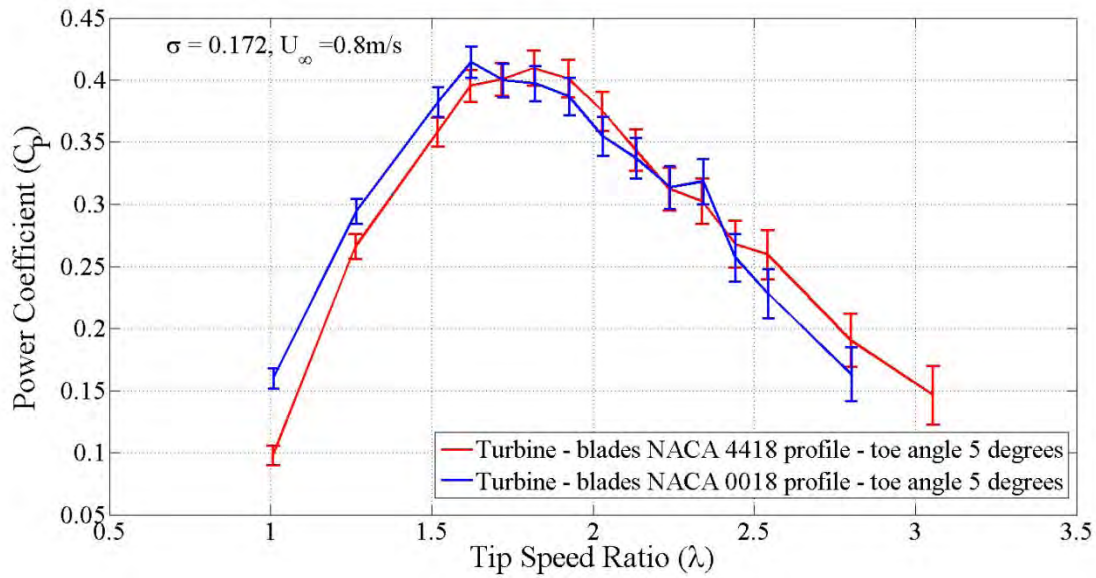


Figure Task 3-6. Power coefficient comparison curves for two-blade testing of 3-D printed NACA 4418 blades and NACA 0018 blades. The peak power coefficient occurred at +5° toe angle. Solidity ratio $\sigma = 0.171$ and inflow velocity $U_{\infty} = 0.8 \text{ m/s}$.

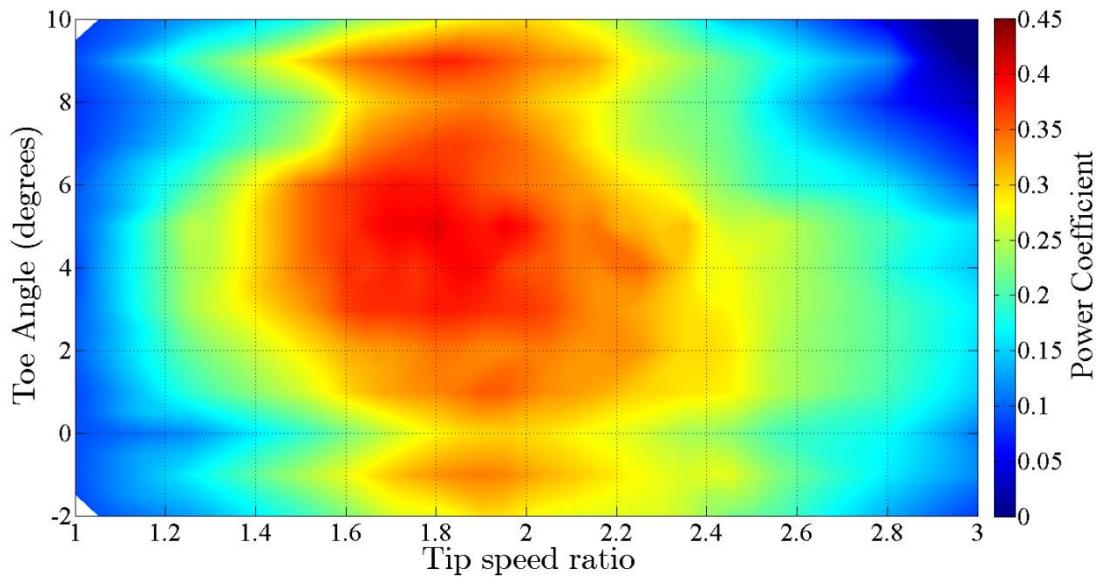


Figure Task 3-7. Power coefficient contour plot for two-blade testing of 3-D printed NACA 4418 blades with solidity ratio $\sigma = 0.171$ and inflow velocity $U_{\infty} = 0.8 \text{ m/s}$.

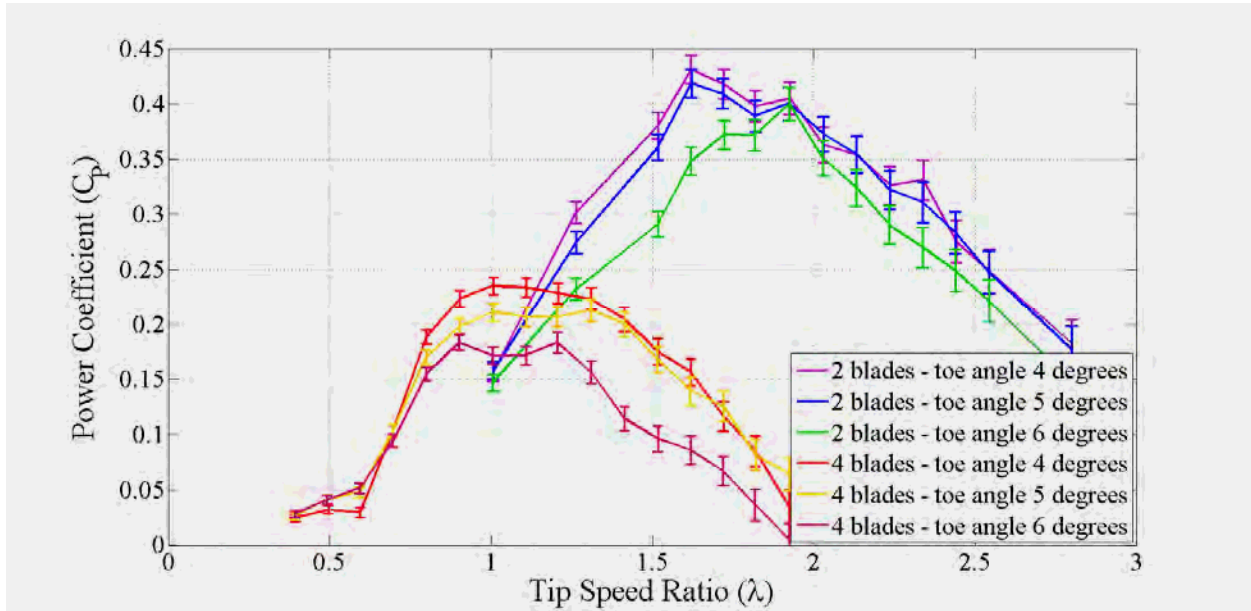


Figure Task 3-8. Power coefficient curve comparison for two-blade and four-blade testing of NACA 0018 blades from toe angles from +4° to +6° and inflow velocity $U_{\infty} = 0.8$ m/s.

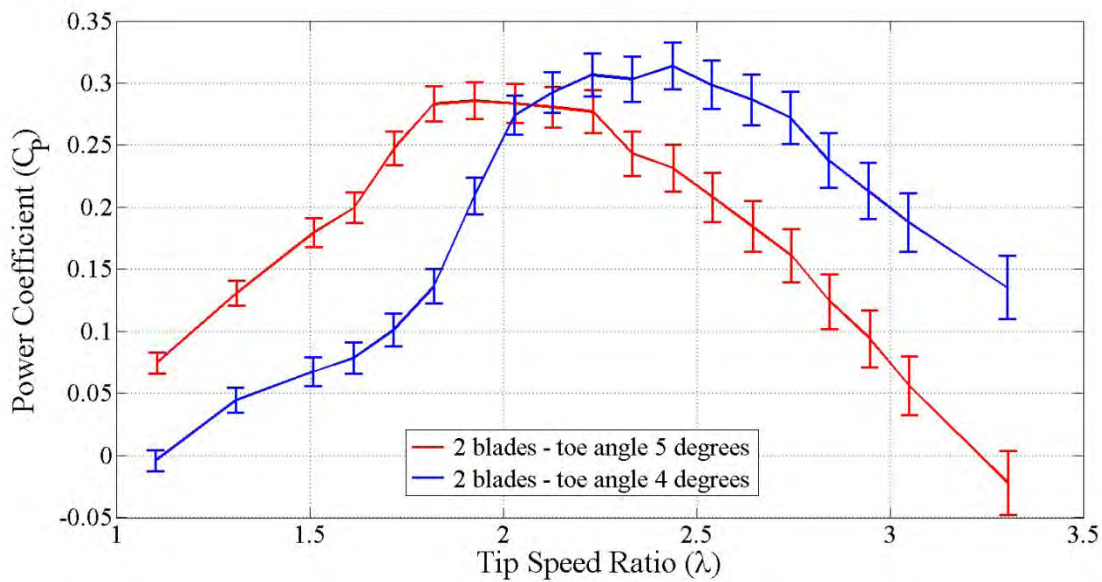


Figure Task 3-9. The experimental power coefficients for a two-bladed turbine using blades with NACA 63-3-018 profile are shown for different chord-to-radius ratios.

Conclusions:

- The test cross flow turbine had better hydrodynamic performance when equipped with blades with symmetric profiles than when equipped with blades with cambered profiles. The hydrodynamic performance of the turbine was considerably reduced when using cambered-blades with the camber and turbine circumference facing opposite directions.
- The highest efficiency was acquired with blades with NACA 63₃-018 and NACA 0018 profiles. The turbine efficiency was considerably reduced when the turbine was equipped with blades with other blade profiles as was the case when the LNV109, s809, and the NACA 63₃-018 with leading edge tubercles were used.
- The two-bladed turbine produced higher power coefficients than the four-bladed one. Additionally, the maximum power coefficient for the turbine with two blades was acquired at higher tip speed ratios than it was for the turbine with four blades.
- The maximum power coefficient was acquired when the blades were mounted at toe angles of +4 and +6 degrees.
- At the conditions under which the tests were performed, the toe angle had a significant effect on the turbine performance. The optimum turbine setup for the toe angle may be susceptible to scaling, specifically at particular chord-to-radius ratios. Full-scale devices will most likely have a lower chord-to-radius ratio which will consequently lower the effects of flow curvature. Changes in scale will also most likely result in a different optimum toe angle setup.
- Further study is needed to analyze the optimum blade camber necessary to maximize the turbine efficiency. The studies may also need to focus on how to minimize the flow separation at a wide range of angles of attack and in curvilinear flow.

Objective 3:

The key objective of this experimental program for axial flow turbines was to produce hydrodynamic-performance data to validate design codes for ducted and unducted axial-flow turbines. Similar experimental data sets for axial turbines had been acquired at MIT (Epps, 2010; Ketchum, 2010) using a two-bladed turbine design. The turbine had been designed using OpenProp, an open-source propeller and axial-flow turbine design code. These experimental data-sets demonstrated reasonable agreement between experimental data and OpenProp predictions for the tested conditions. However, for codes such as OpenProp to be validated for a larger range of operating conditions, additional experimental data sets are needed. For this reason, a scaled test turbine was designed and built using the existing systems developed for testing the scaled cross-flow turbine. Two configurations were considered, ducted and unducted.

The first part of the work was the acquisition of hydrodynamic performance data for a free-tip axial-flow turbine. A three-bladed free-tip axial-flow turbine was designed using OpenProp. The free-tip axial-flow turbine was tested at a range of tip speed ratios of $1 \lesssim \lambda \lesssim 10$ for two inflow velocities $V = 0.91$ m/s and $V = 1.25$ m/s. A maximum power coefficient of 0.44 was measured for the free-tip axial-flow turbine. This value is consistent with the maximum power coefficient

predicted by OpenProp (Figure Task 3-10) and is in line with published data on the free tip turbine designed with OpenProp (Ketchum, 2010).

The second part of the work was the acquisition of experimental data for a ducted turbine. It is important to note that the objective of this part of the work was not to compare the free tip turbine to a ducted turbine but to obtain experimental data for a ducted turbine. A ducted axial-flow turbine was designed using OpenProp. This ducted axial-flow turbine was tested at a range of tip speed ratios of $1 \lesssim \lambda \lesssim 10$ for two inflow velocities $V = 0.91 \text{ m/s}$ and $V = 1.25 \text{ m/s}$. A maximum power coefficient of 0.40 for the ducted axial-flow turbine was measured. This value is considerably lower than the power coefficient of 0.65 predicted with OpenProp (Figure Task 3-11). The ducted axial-flow turbine was also tested with the duct removed. The maximum power coefficient for this free-tip axial turbine did not change considerably when compared to the maximum power coefficient for the ducted axial-flow turbine (Figure Task 3-12). Refer to Lokocz in Appendix Task 3-4 Section 6.1.3 for more information.

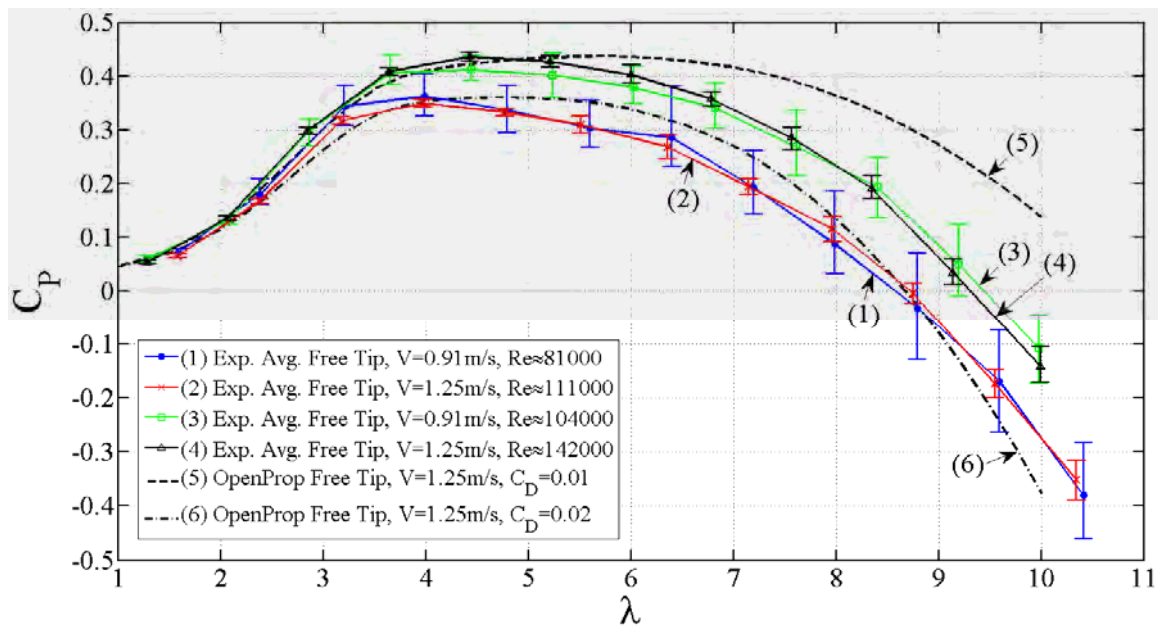


Figure Task 3-10. Free tip average C_p vs. tip speed ratio is shown for the two carriage speeds. The Reynolds numbers represent the change in both the velocity seen at the blade and water temperature.

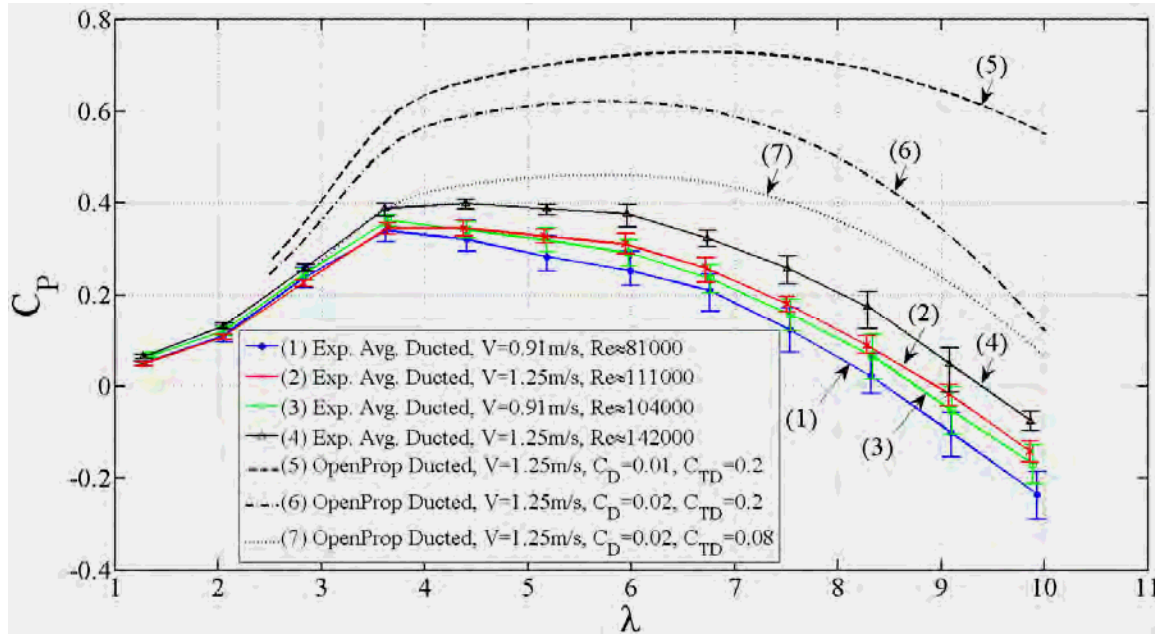


Figure Task 3-11. Ducted power coefficient vs. tip speed ratio of experimental data and OpenProp predictions. Curve (7) shows C_p from OpenProp adjusted with experimental $C_{TD} = .08$.

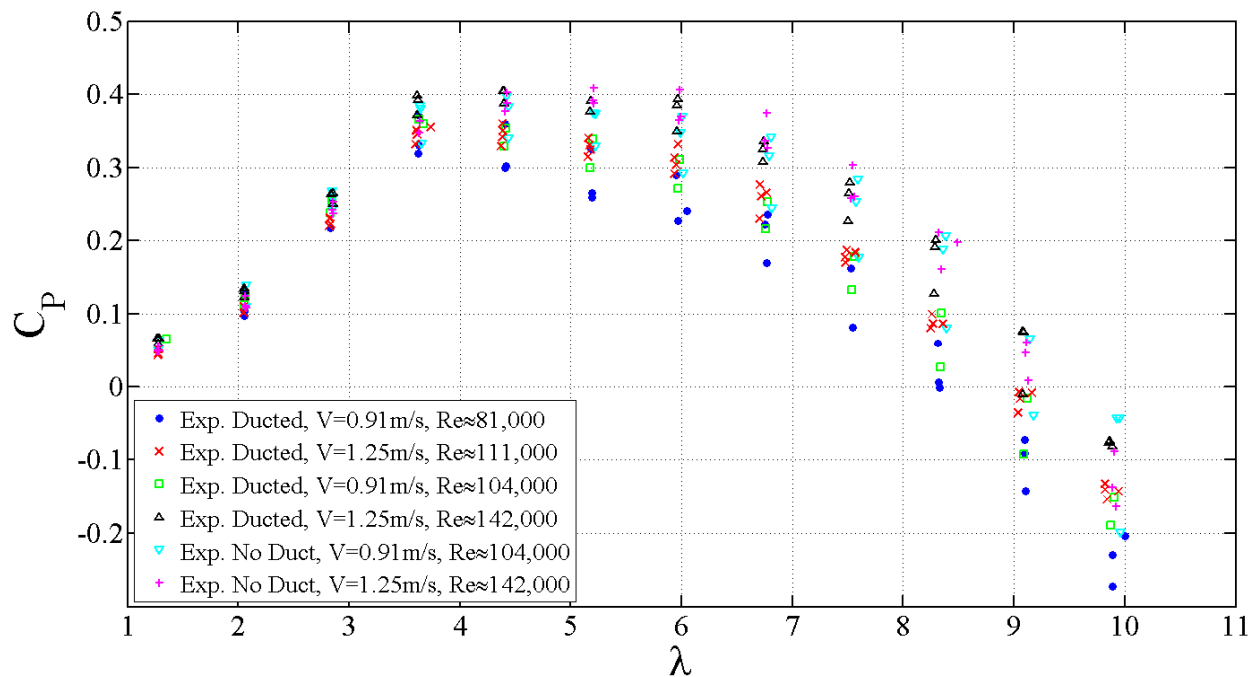


Figure Task 3-12. 5.6 Power coefficient vs. tip speed ratio for the ducted turbine rotor without the duct is shown with results of the same rotor with the duct.

Conclusions:

- Experimental data for the free-tip and ducted axial-flow tidal turbines was measured to facilitate validation of numerical design codes. The experimental data includes the power coefficient and thrust coefficient for a range of Reynolds numbers and inflow velocities.
- The free-tip turbine showed good agreement with the experimental data. This is consistent with published data on the free tip turbine designed with OpenProp (Epps, 2010)
- Higher power coefficients were acquired as the inflow velocity was increased. This finding is consistent with published data. Axial-flow turbines, at this scale, operate in the transitional region where Reynolds number and blade roughness play an important role in performance (Troost, 1948)(Muller, 2009).
- As the Reynolds number is a function of water temperature, water temperature has an effect on the hydrodynamic performance of axial-flow turbines at the scale tested.
- The ducted turbine did not increase the power coefficient as was expected. Despite the fact that ducting did not increase turbine power coefficients, the experimental data can be used to validate and improve design codes, such as OpenProp.
- Codes such as OpenProp could benefit from the implementation of a tip gap model, a duct optimization routine, and a function to analyze existing geometry for off-design conditions

List of Accomplishments for Task 3.

Publications

- Anne E. Demeo and Michael L Peterson, “Community Smart Grid Utilizing Dynamic Demand Response and Tidal Power for Grid Stabilization”, *Smart Grid and Renewable Energy*, 2013, 4, 465-472, <http://dx.doi.org/10.4236/sgre.2013.47053> Published Online October 2013
- Raul Urbina, Michael L. Peterson, Richard W. Kimball, Geoffrey S. DeBree, Matthew P. Cameron, “Modeling and validation of a cross flow turbine using free vortex model and a modified dynamic stall model”, *Renewable Energy* [Volume 50](#), February 2013, Pages 662–669

Theses

1. Colleen Swanger, M.S., “Testing, Scaling, and Optimization of a Cross-Flow Tidal Turbine” Summer 2013
2. Thomas Lokocz, M.S., “Testing of Ducted Axial Flow Tidal Turbines”, Summer 2012
3. Geoff DeBree, M.S., “Testing and Modeling of a High Solidity Cross Flow Turbine” Summer 2012

Task 4: Small Sites and People

Objective 1:

A mixed methods approach consisting of structured community interviews and in-depth ethnographic research (50 semi-structured interviews, three focus groups, numerous informal interviews, observations, and document review) was used to identify individuals, groups, and organizations that may affect or be affected by the development process and to document perceptions of the developer's stakeholder engagement process. Stakeholder characterization was facilitated using a framework by Mitchell et al. (The Academy of Management Review 22:853–886, 1997) that characterizes salient stakeholders using attributes of power, urgency, and legitimacy. In their typology, Mitchell et al. (1997) define salience as “the degree to which managers give priority to competing stakeholder claims.” Key stakeholders identified include fishermen, community members, native-American tribes, regulators, developers, and scientists. Fishermen and regulators are definitive stakeholders, with legitimacy, power, and urgency in the process. Tribes are considered dominant stakeholders; they have legitimacy and power, but their interests are, at this time, not viewed as urgent. Scientists are considered to have urgency and power. The developers viewed their stakeholder engagement strategy as open and transparent. Community stakeholders, regulators, and fishermen generally perceived the developer's approach as effective; they noted the company's accessibility and their efforts to engage stakeholders early and often.

Conclusions:

Numerous and diverse stakeholders affect and are affected by the process of tidal energy development in Cobscook Bay. Although evidence points to the benefits of the developer's current engagement approach, it is important to note that the tidal energy industry is still in its infancy, and changes will continue to occur as new information emerges. The dynamic nature of tidal energy development highlights the importance of the process, and the importance of continued engagement, transparency, and recognition of diverse stakeholder needs and communication preferences. This research and analysis using Mitchell et al. (1997) suggests that future stakeholder engagement should reflect the dynamic nature of salience. Given the nascent nature of the tidal power industry and the rapidly changing technology and permitting process salience is likely to change as the project unfolds, thereby requiring different levels of engagement. Some groups may become more or less important than others, and therefore, the appropriate engagement strategy would need to change as well. On-going research should track changes in typologies of salience.

Objective 2:

Using a social science approach of observation, interviews, and document analysis, this research study examined (1) agency roles and authority, (2) agency interactions, (3) regulatory change, and (4) challenges faced in the regulatory and permitting process for MHK development at the federal and state level. Sixteen semi-structured interviews with federal and state agency

representatives and industry developers were conducted. Agencies included the Federal Energy Regulatory Commission (FERC), the U.S. Fish and Wildlife Service (USFWS), the National Marine Fisheries Services (NMFS), U.S. Coast Guard (USCG), U.S. Army Corps of Engineering (USACE), Maine Department of Environmental Protection (DEP), and the Maine Department of Marine Resources (DMR). Interview questions were open-ended and designed to identify major themes related to the regulatory process and tidal energy development, particularly focused on the Cobscook Bay Tidal Energy Project. During the interviews, participants were asked about their role in the process, their interactions with agency and industry stakeholders, and their perceptions of the regulatory and permitting process as it has unfolded over time, including any knowledge gaps or challenges faced. Additionally, numerous informal interviews and discussions with agency regulators and project developers occurred throughout the research, and the team attended public meetings and consultation meetings related to the regulatory and permitting process. Key documents including government publications (e.g., agency guidance, FERC license applications, and biannual project progress reports), media articles from national, regional, and local papers, and audio from local broadcasts related to tidal energy development in Cobscook Bay were reviewed.

Conclusions:

The regulatory and permitting process for tidal energy development mandates involvement by an array of federal and state agencies. Major laws structure the decision-making process and place power and authority with lead federal and state agencies. Responsibility shifts depending on the project and unique characteristics of the site. Given the complexity of the process, interagency coordination and early proactive engagement with developers is important to avoid duplication of effort and streamline decision-making. Regulatory changes at the federal and state level and a commitment by agencies to “learn-by-doing” further facilitated and streamlined the permitting and regulatory process and will be important to the future success of tidal energy projects.

Adaptive management or “learning-by-doing” may be one approach to deal with uncertainty and inform permitting decisions for hydrokinetic projects such as the Cobscook Bay Tidal Energy Project. This study identified four institutional factors favorable to an adaptive approach. These included experimentation and learning, institutionalized choice to correct avoidable error, a strong commitment to interagency coordination, and an emphasis on early proactive engagement with project developers. Analysis also identified institutional challenges or vulnerabilities. These included conflicting agency cultures, high financial costs, and long timeframes associated with baseline data collection. Lessons learned from this study can assist regulators, policymakers, and project developers design and implement an actively adaptive management approach that can move new renewable ocean energy development forward in a way that is socially acceptable and environmentally responsible.

Objective 3:

Through site visits, attendance at meetings and workshops, document review, and discussions with key regulatory and community stakeholders, a framework was developed to assist

prospective small-scale tidal power developers through the permitting process (full details of the framework are in Appendix Task 4A-1 and other appendices referenced therein). The report shares knowledge learned concerning the permitting and licensing of marine hydro-kinetic (MHK) projects and the Wiscasset Project covering topics such as agency requirements and timelines and provides links to useful resources.

Conclusions:

Several key lessons were learned from the Wiscasset experience. The team learned the importance of consultation and the importance of sharing information with the broader hydrokinetic community. Consultation with stakeholders identified information sources and gaps in information that required the development of studies. For example, through the consultation process, the presence of protected species was identified early in the project. Early consultation facilitated collaboration with existing efforts, particularly with existing fisheries studies at the University of Maine and Maine Department of Marine Resources. The MHK field is an emerging industry and an emerging area of research. The importance of researchers, regulators, industry partners, and the public communicating throughout the process cannot be overstated. As the MHK industry develops, identifying partners, contractors, and device manufacturers will be aided through consultation.

The project team also learned that, in practice, the Federal Energy Regulatory Commission (FERC) does not have a process to permit or license small or community scale hydrokinetic projects. At this early stage of MHK device development and permitting process, there is no difference between a community scale project and commercial scale project in terms of FERC permitting requirements. Even more significant is that all hydrokinetic projects in navigable waters will trigger the involvement of either FERC or the U.S. Army Corps of Engineers, which then triggers the reviews of other federal and state agencies. With relatively new technologies which have environmental impacts that are not well understood or quantified, studies are required, which may be prohibitive for community scale hydrokinetic projects.

Finally, the research team learned the importance of an incremental approach on all fronts of a tidal power project development. The team worked concurrently on research and outreach in the areas that influenced project development: fisheries, community outreach, hydrodynamics and regulatory permitting. Using this incremental approach, the team was able to draw on comprehensive information to develop an understanding of the balance between the potential benefits and impacts to inform the next steps.

List of Accomplishments for Task 4.

Peer-Reviewed Publications

Johnson, T.R., J.S. Jansujwicz, and G. Zydlewski. 2013. Tidal power development in Maine: Stakeholder identification and perceptions of engagement *Estuaries and Coasts* DOI 10.1007/s12237-013-9703-3. (See Appendix Task 4-1)

Final Report Maine Tidal Power Initiative

Jansujwicz, J.S. and T.R. Johnson. 2013. Understanding and informing permitting decisions for tidal energy development using an adaptive management framework *Estuaries and Coasts*. DOI: 10.1007/s12237-013-9678-0. (See Appendix Task 4-2)

Johnson, T.R. and G.B. Zydlewski. 2012. Research for the sustainable development of tidal power in Maine *Maine Policy Review* 21(1): 58-64. (see Appendix Task 4-3)

Outreach

- Six community meetings (2010-2013) with fishermen and community members hosted by MTPI's Human Dimensions Team and Fish Assessment Team in Eastport and Lubec, Maine

Recommendations

Development of this industry depends on continued engagement with the scientific community to understand the environmental and social impacts of these emerging technologies. In particular, the monitoring of the devices is still in its infancy and will require continued research and development. Similarly, as turbine arrays are deployed, measurements and modeling of the local and long-range impacts on flow, transport and biological responses must continue. The scale of the energy resource and location related costs such as environmental assessment and geotechnical issues remain as barriers for the industry. Because regulatory uncertainty and social acceptance remain critical barriers to industry development, research must continue to track stakeholder salience over time as tidal power develops. Importantly, the dynamic nature of tidal energy development also highlights the importance of process and continued engagement, transparency, and recognition of diverse stakeholder needs and communication preferences. Identification of key stakeholders and their emerging questions, concerns, and information needs represents a critical first step toward informing the design of more effective stakeholder processes for tidal power. The complex interactions between the biophysical and social systems with respect to this emerging technology means that continued research is needed to find a socially acceptable and environmentally responsible manner way to develop this resource. Our partner in the project, Ocean Renewable Power Company, is engaged in ongoing commercialization efforts for the technologies. However there is currently no ongoing independent support for environmental, social and resource evaluation research.

The University of Maine Tidal Power Initiative has, over the course of this project, built a unique level of trust with the impacted communities. A key element of this trust was the independent funding of the research. It was clear in discussions in the community that the credibility of our research was demonstrated by our independence from the developer. As academic researchers the cost to our careers of misrepresentation of the observations was higher than the benefits of any relationship with the developer. This trust and the openness of our partner have led to a uniquely strong relationship with the community. The single greatest recommendation that we have for this industry is that government funding should include significant independent academic oversight of the developments. In the absence of the independent oversight by an honest broker the perception will always be that the conclusions related to impact are dependent on financial interests. The four critical areas of future work required for tidal energy in Maine are: 1) resource assessment, to determine the size of the energy resource, 2) environmental impact to determine what the effect of the devices will be on the marine environment and fish populations, 3) geotechnical and transport issues associated with the devices and foundations and 4) the social and cultural response of large and community scale ocean energy development. While research in these core areas is critically needed to address uncertainties and knowledge gaps, synergies among project components should also be supported. The Maine Tidal Power Initiative's holistic approach offers a framework for interdisciplinary integration and stakeholder engagement that can inform the design and conduct of similar research in other renewable energy context. However, the most critical lesson is that honesty and financially independent evaluation is the only reliable path forward for these technologies.

Appendix Task 4-1

A Numerical Study of Tidal Farm Efficiency in the Western Passage, US and Canada

Huijie Xue¹

1. School of Marine Sciences
University of Maine
Orono, ME 04469-5706, USA
hxue@maine.edu

Min Bao^{2,3} and Xianwen Bao²

2. College of Physical and Environmental Oceanography
Ocean University of China
Qingdao 266100, China

3. State Key Laboratory of Satellite Ocean Environment
Dynamics

2nd Institute of Oceanography, SOA
Hangzhou, China

Matthew Cameron⁴

4. Department of Mechanical Engineering
University of Maine
Orono, ME 04469, USA

Abstract— Turbines are implemented in the regional ocean circulation model to determine the energy extraction efficiency of tidal farms. A power curve is determined for different values of flow blockage when 10 turbines are distributed evenly across the Western Passage in the middle 1/3 of the water column. A speed reduction coefficient of 0.6 represents the most efficient case with ~ 3.95% of the undisturbed in-stream energy being taken. Efficiency is also estimated for different densities and distributions of turbines. The optimum density for a single row appears to be one turbine in every three cells. When turbines are allocated on parallel rows in the direct shadow of one to another the efficiency is reduced because of the wakes, whereas in the lattice form the efficiency is benefited from the speed gain in turbine gaps produced by the neighboring rows.

Keywords—tidal stream power, energy extraction, farm efficiency, ocean model

I. INTRODUCTION

The current development in marine hydrokinetic (MHK) device opens the opportunity of harvesting tidal in-stream energy as a reliable alternative energy source for the coastal regions where strong tidal currents are found because tidal power is more predictable compared to wind and solar power. However, a key piece of information needed prior to any tidal power development is the availability of tidal power resource, not only the naturally available amount but also the limit for extraction from a given tidal channel or tidal basin.

The naturally available amount is often measured by the in-stream power density, *i.e.*, the per unit area mass flux times the kinetic energy or $1/2\rho_oV^3$. Here ρ_o is the seawater density and V is the tidal flow speed. This formula needs to be modified in order to estimate the extractable power from a flow because turbines can block the flow so that less energy is available for further extraction [1, 2]. The limiting case of zero flow reduction corresponds to no energy being taken out and

the limiting case of the flow speed reduced to zero (*i.e.*, complete blockage) implies no more energy is available for further extraction. An upper bound of extractable power exists ranging from 1/3 to 2/3 of the naturally available energy flux depending on the blocking ratio in a tidal channel [2]. Here the blocking ratio (BR) is the percentage of the cross-sectional area occupied by turbines. Similarly, the peak production of power can be achieved in an idealized tidal channel that has a uniform rectangular cross-section and is partially blocked by a turbine fence when the transport through the fence is reduced to approximately 60-70% of the undisturbed transport [3]. The change in farm efficiency as a function of BR for a shallow channel is different from that for a deep and wide tidal strait, and higher efficiency is reached at much lower BR in the former than in the latter [4].

The power extraction limit was further analyzed in [5, 6] by taking into account the tidal head that drives the flow in the tidal channel, the natural friction from the channel, the additional drag imposed by MHK devices, as well as the effect of flow separation at the exit of the channel. Assuming the turbines occupy the choke section of the channel, the maximum extractable power can be estimated using an empirical formula of $\alpha\rho_o g\zeta_o Q_{max}$ with α ranging from 0.21 to 0.24, where ζ_o is the pressure head that drives the flow and Q_{max} is the maximum flux through the channel in the absence of turbines.

The complexities associated with the tidal basin and channel geometry as well as sheared flows in the channel have been ignored in the aforementioned theoretical studies. It was pointed out that the site-specific modeling is required to accurately determine the MHK resource [7]. Ocean models are capable of resolving the temporal and spatial patterns of flows in tidal basins and channels, although most of which don't resolve the flow variability at the scale of turbines. A retarding

force or speed reduction is specified in the models to approximate the effect of power extraction [8-12]. These studies focus on the effects of energy extraction on the tidal regime and hydrodynamics of the bays. Changes in the maximum and minimum water levels are often on the order of centimeters in the estuaries and bays [8, 12], but the flushing rate could be altered significantly for the residence time increases exponentially with the decrease in volume flux [10]. Far-field effects become less pronounced when power extraction is limited to the lower water column compared to when the extraction spans the entire water column [9]. Sensitivity of the maximum extractable energy to turbine hub height is examined in [10], but the study is carried out for a straight channel that connects an idealized bay to a shelf.

This study investigates the energy extraction and the efficiency of turbine arrays in a realistic coastal tidal channel, the Western Passage (WP) in the Quoddy region shared

between the state of Maine, US and the province of New Brunswick, Canada (Fig. 1). The tidal range in the Quoddy region varies from 5 to 8 m [13, 14], and the mean power density reaches 3-5 kWm^{-2} locally in several passages [12, 15]. While the outer Cobscook Bay (CB), where the Ocean Renewable Power Company has a test turbine running currently, offers moderate-scale development possibilities, the WP is chosen as the study site because the passage is deep and has the potential for commercial-scale development [16]. The Quoddy regional circulation model described in [12] is used in this study. Instead of the commonly adopted form drag or retarding force method, turbines are implemented in the water column as objects that partially block and deflect the flow at individual meshes where turbines are allocated. The energy deficit is then determined for experiments with different flow reduction rates, as well as densities and distributions of turbines.

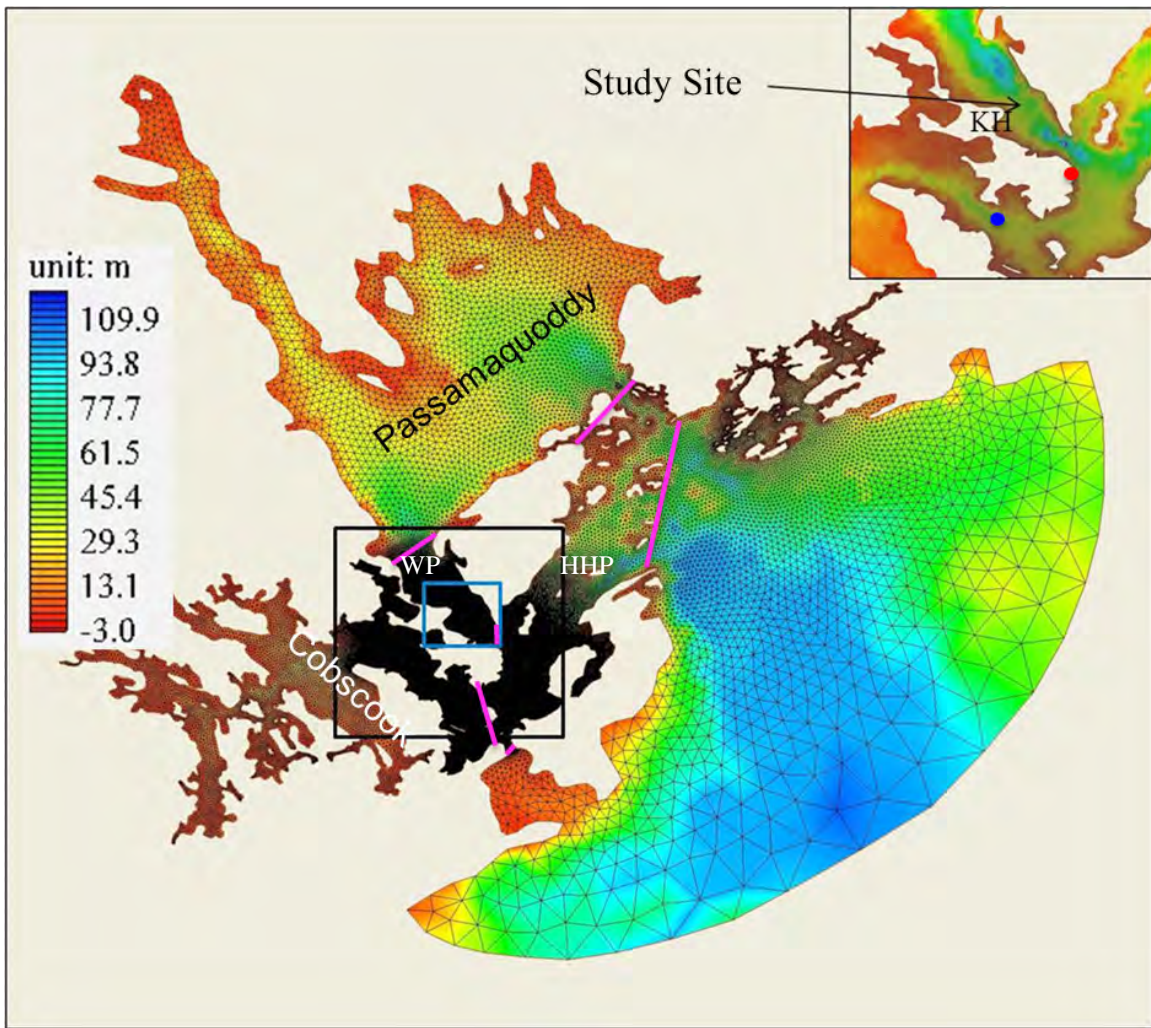


Fig. 1. Bathymetry (color) and mesh for the Quoddy regional model with locally refined resolution of ~ 25 m in the outer Cobscook Bay and the WP (the black box; the bathymetry in which is shown in the insert). The blue box is used for zoom-in of the near field in the WP. KH represents Kendall Head in ME, and HHP the Head Harbour Passage. Observations are available from the tide gauge in Eastport, ME (red dot) and the current meter mooring in the outer Cobscook (blue dot), which were compared with the model result in [12] and summarized in section II. The magenta lines define several subareas that are used to diagnose the volumes in Fig. 5.

II. CIRCULATION MODEL OVERVIEW

The Finite Volume Coastal Ocean Model (FVCOM) [17] is applied to the Quoddy region to simulate the tidal circulation and carry out energy extraction experiments. The model bathymetry and mesh are shown in Fig. 1. The maximum water depth in the model is 118.9 m below the undisturbed sea level. WP is a deep waterway with the maximum water depth near 100 m north and south of Kendall Head (KH). The model domain is divided into 197681 triangular elements in the horizontal, and there are 15 sigma layers in the vertical. The horizontal resolution in the outer CB and WP (areas of primary interest for tidal power development) is $\sim 20\text{-}25$ m. All simulations in this study are barotropic with a constant temperature and salinity, and there is no wind forcing. A total of 10 tidal constituents, namely, M_2 , N_2 , S_2 , K_2 , L_2 , M_4 , NU_2 , $2NU_2$, O_1 , and K_1 , are included in the simulations with the boundary condition derived from Webtide (<http://www.bio.gc.ca/science/research-recherche/ocean/webtide/index-eng.php>). The model time step is 1 s, and all runs cover the 30 day period from 00:00 on 1 July 2004 to 00:00 on 31 July 2004.

Detailed comparisons with the observations are available in [12]. Briefly, the modeled sea level agrees very well with the observations at the Eastport station (the red dot in Fig. 1), while the differences between the modeled tidal currents and observations at the CB mooring (the blue dot in Fig. 1) are more noticeable. Results of the harmonic analyses can be summarized as follows: 1) M_2 is the predominant tidal constituent; 2) the major axis of the tidal ellipses is 10 - 30 times longer than the minor axis; 3) the maximum absolute error for the tidal elevation is 4.3 cm for M_2 , corresponding to a relative error of 1.6 %; 4) phase differences in the elevation are $\leq 3^\circ$ for all constituents; 5) the largest difference in the major axis is 16.8 cms^{-1} for M_2 , corresponding to a relative error of 12.8 %, and 6) phase difference of the tidal ellipses for M_2 and S_2 are $\leq 2^\circ$, and the largest difference in phase is 20° for K_1 .

III. TURBINE ALLOCATIONS

Turbine arrays are allocated in the WP near KH (Fig. 2), where the coastline protrusion acts as a natural duct to concentrate in-stream kinetic energy. Although the power density is higher on the western side of the passage, turbines are evenly distributed in rows across the passage. Without specifying types of turbines and mounting structures, tidal devices are assumed to be in the mid-water column across the 7th, 8th and 9th sigma layers. Because the water depth becomes increasingly shallower approaching the coasts, this is equivalent to having shorter turbines near the ends of the rows. This may not be realistic, but it simplifies the calculation of row efficiency (see Section IV and V).

Many experiments have been conducted to study how turbine densities and arrangements affect the efficiency of individual turbines and the farms as a whole. Table 1 lists the few that are used in this paper. The first group of experiments includes 4 cases with different numbers of turbines all arranged in a single row: case 1-1 (1-2, 1-3, 1-4) has 10 (19, 29, 58) turbines placed one in every 5 (3, 2, 1) cells with an

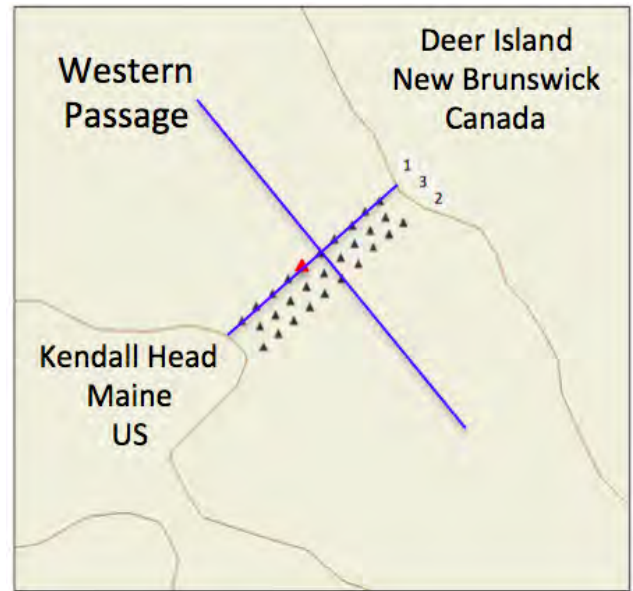


Fig. 2. Schematic of turbine arrangements in the model cases 1-1, 2-1 and 3-1. The average distance is ~ 80 m between rows. The highlighted turbine (red triangle) in element 126501 is used to show in Fig. 6 time series of extracted energy from different model experiments. The blue lines indicate the across- and the along-the-stream sections where changes to the flow speed induced by the turbines are shown in Fig. 9.

approximately equal spacing of 80 m (40m, 20m, 0m) between turbines (see Fig. 2 for the location of row 1). Only one case each from the second and the third group is included in this paper: case 2-1 has a total of 20 turbines split equally with 10 units on row 1 and another 10 units on row 2, while case 3-1 has a total of 29 turbines with 10 units on each of row 1 and row 2 and another 9 units on row 3 (Fig. 2).

IV. TURBINE IMPLEMENTATION METHODS

Turbines generate power by taking the mechanical energy from the tidal stream. The local impact on the hydrodynamics can be described in different ways, one of which is to add a

Table 1. List of model experiments with different turbine allocations. See Fig. 2 for locations of the rows.

Exp Cases	Turbine Distributions (Number of units/Approximate spacing)		
	Row 1:	Row 2	Row 3
1-1	10/80m		
1-2	19/40m		
1-3	29/20m		
1-4	58/0m		
2-1	10/80m	10/80m	
3-1	10/80m	10/80m	9/80m

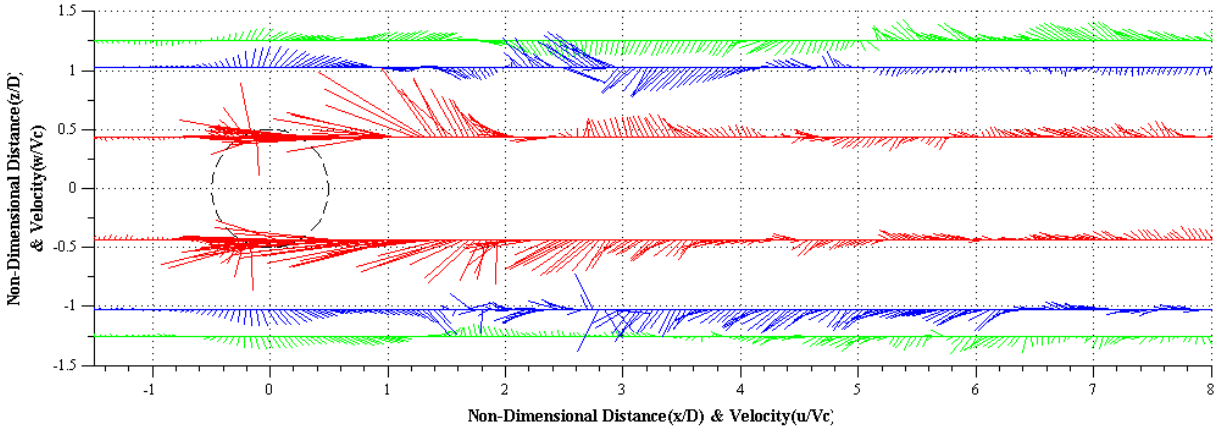


Fig. 3. Flow velocity measured during the peak performance test of a 4-blade cross-flow turbine ($A = 0.235 \text{ m}^2$, Tip Speed Ratio = 1.4). The dashed circle indicates the turbine location. D is the turbine diameter and $V_c = 1 \text{ ms}^{-1}$ is the carriage speed traveling in the negative x direction. u and w are velocity components in the x and z (vertical) direction, and positive values are against the carriage traveling direction and upward, respectively. (Adapted from [18]).

retarding force in the momentum equations [8-10]. Tidal flows exert a torque on the turbine. Ignoring possible shifting, rolling or heaving of the turbine, the same force also acts upon the tidal current in the opposite direction. The force in the direction of tidal current, often represented as a drag in the form $1/2 \rho_o C_{td} A |\vec{V}| \vec{V}$, is added to the horizontal momentum equations, while the force in the vertical direction is ignored to maintain the consistency with the hydrostatic approximation. Here, \vec{V} is the tidal velocity in the horizontal plane; C_{td} is a coefficient proportional to the drag imposed by turbines; and A is the turbine cross-sectional area facing the tidal current. The choices of C_{td} and A vary from application to application [8-10].

The approach adopted in this study is, however, to add turbines in the regional ocean model as objects that can block and deflect tidal flows to the surrounding of the devices. Specifically, the flow speed at the cells where turbines reside is reduced by a prescribed percentage. According to the theoretical derivation of [2], the flow reduces speed as it passes through the turbine, and the maximum power extraction corresponds to a definitive speed reduction (*i.e.*, u_1/u_0 in [2]) ranging from 1/3 to 2/3 of the undisturbed flow speed upstream in the tidal channel as the BR changes from near unity to near zero. Flows induced by towed cross-flow turbines were measured using a Nortek Vector Current Meter while the turbines were tested in the University of Maine tow tank [18]. Fig. 3 shows an example of the velocity field resulted from a 4-blade turbine (solidity of 0.32) near its peak performance. The speed reduction $(1+u/V_c)$ near the rim heights (at $z/D = \pm 0.43$) ranges from 30 to 100% right behind the turbine ($x/D \leq 2$), whereas the speed increases by about 10 to 20% at $z/D = \pm 1$, 0.5 diameters above or below the rim of the turbine.

The speed reduction method is effectively a boundary treatment. If the turbine were a solid object, one could simply set the velocity at the cell equal to zero and the fluid would be 100% deflected to the neighboring cells. For turbines, the fluid goes through partially with the rest being deflected. A concern associated with this treatment is the mass conservation. To address this, Fig. 4 shows the time series of the domain-integrated volume (the black line) and the difference between the case with a total of 29 turbines on 3 staggered rows (case 3-1, see Table 1 and Fig. 2) and the base case without any turbine (the red line). The magnitude of the red line is $5 \times 10^6 \text{ m}^3$, 4 orders smaller than the total volume, and it is comparable to the difference between two runs of the base case on two different computer clusters (the blue line). The latter has a magnitude on the order of $5 \times 10^6 \text{ m}^3$ as well. It is thus concluded that the mass conservation doesn't become an issue to affect this study.

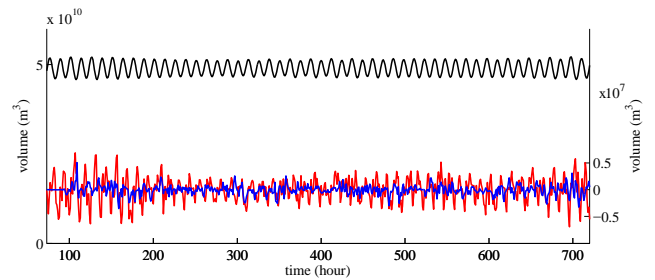


Fig. 4. Time series of the entire domain water volume (black) and the difference of the total volume between case 3-1 and the base case without any turbine (red). Also shown is the time series of the difference of the total volume between two runs of the base case on two computer clusters (blue).

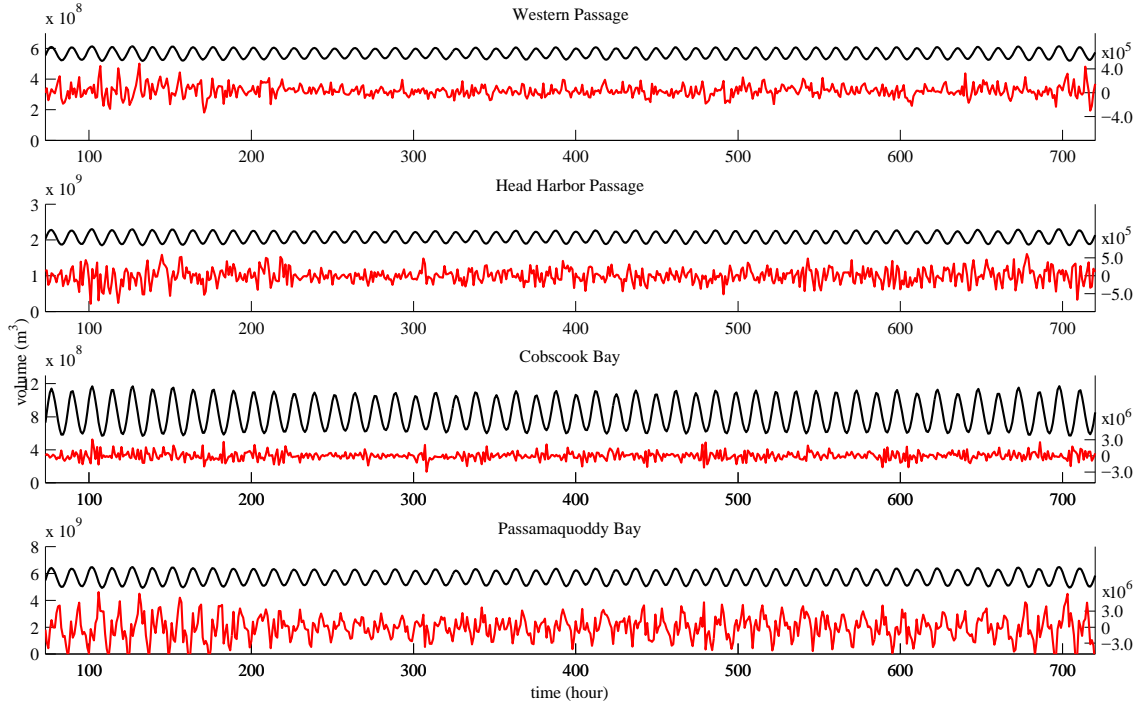


Fig. 5. Similar to the black and red curves in Fig. 4 but for the 4 subdomains delineated by the magenta lines in Fig. 1.

It is, however, interesting to follow the temporal changes of these curves. When the domain-integrated volume is at the lowest (low tide), the difference in volume between the case with turbines and the case without turbine reaches the positive maximum, and vice versa. This suggests the barricade effect of the turbines with less water reaching the bays during the flood and less water leaving the bays during the ebb. The magnitude is consistent not only with the spring and neap cycle but also increases gradually as the number of turbines increases (not shown). To diagnose this more clearly, the model domain is subdivided to illustrate the changes in volume from the WP, Head Harbour Passage (HHP), CB and Passamaquoddy Bay (PB). Obviously PB has the largest volume among the 4 subdomains and the change in the total volume seen in Fig. 4 comes mostly from the changes in PB, which is easily understood such that the blockage affects mostly the water body inside the turbine fences. However, it is obvious from Fig. 5, the volume changes in WP, HHP, and CB are not phase locked with the tide during most of the time unlike that in PB. This is most likely related to the numerous, intense eddies seen in the WP, HHP and outer CB [12], which tend to respond to the turbine arrays in less predictable manners. The volume changes least in the HHP when compared to the total volume of this subarea. On the other hand, having turbines in the WP appears to induce volume variabilities in CB comparable to those in PB percentage wise, and this is consistent with equal magnitude of sea level responses seen in CB and PB [12] albeit the changes in CB are not monotonic as the number of turbines increases.

The relationship between the turbine efficiency and the speed reduction was derived for a single turbine in a uniform channel flow in [2] and for a turbine fence in [3]. A power curve is obtained for the WP with highly sheared flows and distributed turbines. Fig. 6 shows how the extraction efficiency varies as a function of the speed reduction ratio when a group of 10 turbines is arranged in a single row and evenly distributed across the channel (see case 1-1 in Table 1 and Fig. 2). A total of 6 experiments have been run with the turbines so tuned that the speed through the turbines decreases to a fraction of the instantaneous speed at the cells. The change of the kinetic energy from all turbine-occupied cells (designated as the extracted energy (EE) by the turbines) can be estimated using the formula below.

$$EE = \sum_{n=1}^N \sum_{m=1}^M \sum_{k=7}^9 \beta \times \frac{\Delta T}{2} \times \rho_o \times [V_1^2(k, m, n) - V_2^2(k, m, n)] \times volume(k, m, n) \quad (1)$$

Here $V_1(k, m, n)$ is the instantaneous tidal current speed before the energy being extracted from a cell where a turbine resides; $V_2(k, m, n) = \gamma V_1(k, m, n)$ is the instantaneous tidal current speed after extracting energy from the same cell (in the 6 experiments $\gamma = 0.4, 0.5, 0.6, 0.7, 0.8,$ and 0.9 , respectively); $volume(k, m, n)$ is the volume of the cell; M is the number of turbines; $\Delta t = 1s$ and $N = 1292400$ is the number of seconds for a 15-day period from 01:00 on 16 July 2004 to 00:00 on 31 July 2004, which is used to tally the total energy from the section in the base case (no turbines) and the energy yields estimated using eqn. 1. β is used to represent the cut-in speed of different turbines, and the threshold chosen in

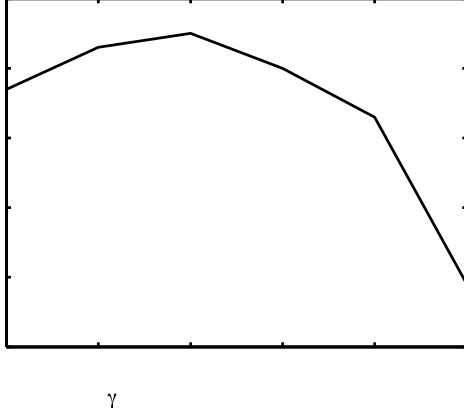


Fig. 6. Distribution of the energy extraction efficiency for different values of speed reduction coefficient in case 1-1.

this study is that β equals to 1 when $V_I(k, m, n) \geq 1 \text{ ms}^{-1}$ but equals to 0 otherwise. In actuality, β isn't zero even when the current speed falls below the threshold as a stalled turbine can deflect part of the fluid, albeit at lower percentage, which is similar to choosing a different C_{td} when turbines are not running at low flow speeds.

The efficiency of the turbine row is measured as the ratio of EE to E_{total} , and the latter is the total energy in the base experiment from the same section where row 1 would be but for every cell of the section and over the same time period used to estimate EE:

$$E_{total} = \sum_{n=1}^N \sum_{m=1}^{MS} \sum_{k=1}^{15} \frac{\Delta T}{2} \times \rho_o \times V_I^2(k, m, n) \times \text{volumn}(k, m, n) \quad (2)$$

Here MS is the number of cells across the section. The maximum efficiency is reached when the flow speed is reduced to approximately 60% (Fig. 6). The blocking ratio with 10 turbines on this section is $\sim 6.70\%$ only (Table 2) so that where the maximum efficiency is attained (*i.e.*, the reduced speed at 60%) is closer to the limit of near zero BR in [2]. The efficiency decreases from 3.95% to 3.93% and 3.87% when the speed is reduced to 50% and 40%, respectively. However, the decrease in efficiency is faster on the right hand side, and the efficiency decreases to 3.90% (3.83%, 3.59%) when the speed is reduced to 70% (80%, 90%). The asymmetry of the curve is similar to the one shown in [3], but the decrease in efficiency away from the peak isn't as fast until the last leg.

V. TURBINE DISTRIBUTIONS AND EFFICIENCY

Not only the turbine operation parameters can affect the extraction efficiency, so can the turbine density and distribution. For the model cases listed in Table 1, time series of the extracted energy from the same turbine near the center of the passage (the red triangle in Fig. 2 located in element 126501) are shown in Fig. 7. Because there isn't a turbine in the same element in case 1-3, this case is excluded. Despite all

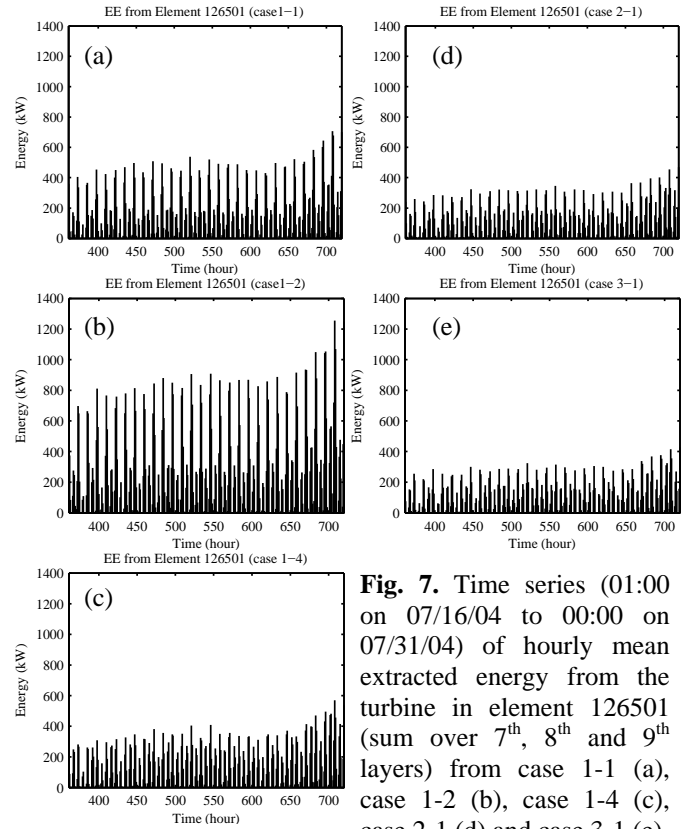


Fig. 7. Time series (01:00 on 07/16/04 to 00:00 on 07/31/04) of hourly mean extracted energy from the turbine in element 126501 (sum over 7th, 8th and 9th layers) from case 1-1 (a), case 1-2 (b), case 1-4 (c), case 2-1 (d) and case 3-1 (e).

cases listed in Table 1 have the same γ value of 0.5, this particular turbine appears to take considerably more energy from the tidal stream from case 1-1 to 1-2, but much less from case 1-2 to case 1-4. The latter is even lower than in case 1-1. The comparison suggests that this turbine can benefit from having neighboring turbines only when there are sufficient gaps between turbines, and that too many turbines can actually be counter-productive. On the other hand, the amount of extracted energy decreases from case 1-1 to case 2-1 and to case 3-1, demonstrating the adverse effect by having turbines in neighboring rows. The decrease from case 1-1 to case 2-1 is larger than that from case 2-1 to case 3-1 although the distance between rows is halved in the latter case. The reason is the turbines in row 3 are staggered with respect to turbines in row 1 and 2.

This gain/loss of efficiency can be explained by the changes in flow speed due to turbines. Fig. 8 and 9 show the responses in the flow field in case 1-1. The most noticeable difference is the velocity reduction surrounding the turbines especially in the downstream direction. The wakes are asymmetric with stronger reduction in Fig. 8a, *i.e.*, at a time near peak flood. The tails measured by the 0.9 contours (the flow speed is at 90% of that in the base case) can reach 1000 m downstream. The asymmetric wakes are resulted partly from the flooding tide being stronger than the ebbing tide, but it is also obvious that the wakes in Fig. 8a are affected by the cyclonic eddy formed north of KH during the flood. Increases in flow speed between the turbines can be seen more clearly in Fig. 8b,

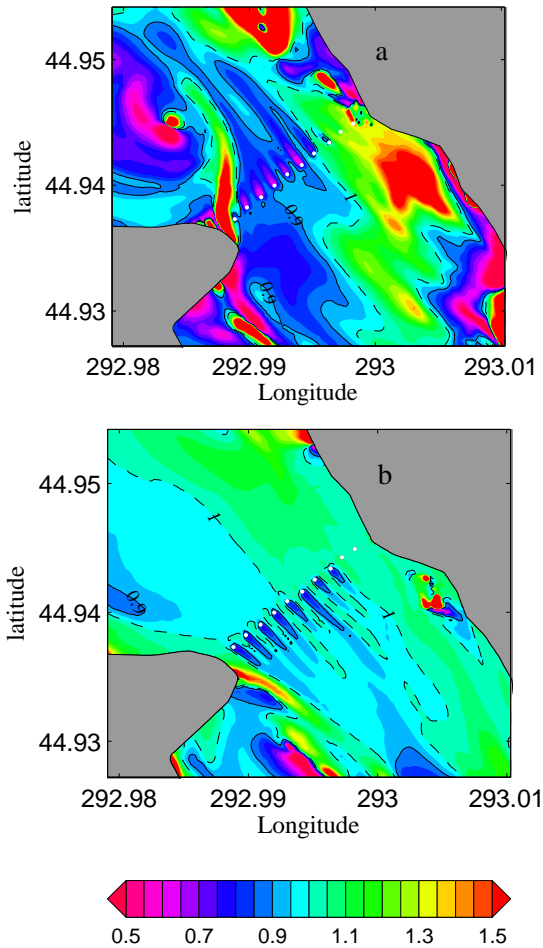


Fig. 8. Ratio of the tidal current speed on the 8th sigma level in case 1-1 to its counterpart in the base case near the peak flood at 03:00 on 6 July 2004 (a) and near the peak ebb at 10:00 on 6 July 2004 (b).

corresponding to a time near peak ebb. The tails at this instant (again using the 0.9 contours) are mostly less than 200 m in the downstream direction.

Increases in speed occur not only between turbines at hub heights but also in the upper and lower 1/3 of the water column (Fig. 9). Large changes are seen near both ends of the cross-stream section (Fig. 9a and b) because the speed is small there in the base experiment. What is more interesting is the asymmetry seen in the along-stream section (Fig. 9c and d). On the downstream side, the speed decreases in the mid water column in contrast to the increase seen above and below near the peak flood (Fig. 9c) and near the peak ebb (Fig. 9d), but the former has a secondary decrease about 300 m downstream. This secondary decrease spans more extensively in the vertical. Immediately upstream of the turbine there appears to be a convergence zone with the speed approaching the turbine being slightly higher than that in the base case followed by the quick decrease at the turbine, whereas 400-500 m upstream the responses appear to show a decrease in the upper half but increase in the lower half of the water column as seen in Fig.

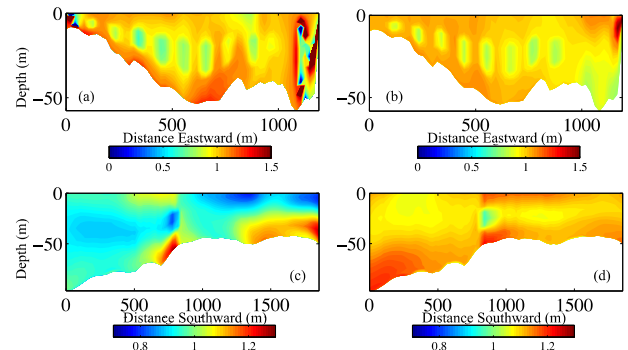


Fig. 9. Similar to Fig. 8 but for the speed on the cross-channel section (a and b) and the along-channel section (c and d) (see Fig. 2 for the locations). (a) and (c) are near the peak flood at 03:00 on 6 July 2004, while (b) and (d) are near the peak ebb at 10:00 on 6 July 2004.

9c. Near the peak ebb, although the speed increases throughout the water column upstream, the increase is much more in the lower water column.

It is worthwhile to note that the decreases/increases of flow speed change constantly throughout a tidal cycle not only in terms of the magnitude but also the location. Particularly the relatively large increases in flow speed near the coasts can result in different proportional gain in efficiency for turbines placed close to the ends of the row. Different quantities measuring the overall efficiency for various layouts of tidal farms and individual rows within the farms are thus valuable metrics.

The total energy (EE) from all turbines are summed according to rows in each of the 6 different experiments, which is listed as column 3, 6, and 9 in Table 2. The absolute values of EE can vary depending on specifications of the turbines and operational parameters, but it is instructive to compare between experiments because $\gamma = 0.5$ and cut-in speed = 1.0 ms^{-1} are not changed for all these experiments. First of all, among the 4 experiments with turbines allocated all in a single row, more and more energy is extracted as the number of turbines increases and Π (the ratio of the extracted energy to the naturally available energy from the cross-section) also increases. However, the per-turbine-yield is the highest at 45.6 MWh in case 1-2, so is the ratio between Π and BR. In case 1-1, although BR is at 6.70%, Π is only 3.93% because close to 40% of the time the flow speed is below the cut-in speed [12] during which the turbines are not taking any energy, but the amount of energy is much higher at higher speeds. The farm efficiency normalized by the BR reaches 58.7%. In case 1-2, 12.09% of the cross-section is occupied by a total of 19 turbines, but a total of 11.04% of the energy available from the natural tidal stream is extracted. Hence the normalized farm efficiency reaches 91.3%. Given the same values of γ and cut-in speed, the only explanation is turbines benefit from the presence of neighboring devices when they are close enough. However, in case 1-3 and 1-4 although the turbines are increasingly closer to each other, the normalized farm

Table 2. The extracted energy and efficiency during one spring-neap cycle for the six cases listed in Table 1. Π (row efficiency) is the ratio of the energy extracted by turbines on a given row to the naturally available in-stream energy from the cross-section at which the row of turbines resides.

Exp. Cases	# of units	Row 1			Row 2			Row 3		
		EE (MWh)	BR (%)	Π (%)	EE (MWh)	BR (%)	Π (%)	EE (MWh)	BR (%)	Π (%)
1-1	10	308.2	6.70	3.93						
1-2	19	866.1	12.09	11.04						
1-3	29	1149.6	18.46	14.66						
1-4	58	1716.8	37.76	21.89						
2-1	20	235.9	6.70	3.01	416.8	6.15	4.77			
3-1	29	225.8	6.70	2.88	427.5	6.15	4.89	494.9	5.80	5.81

efficiency drops to 79.4% and 58.0%, respectively, suggesting the adverse effect of having turbines too close to each other. In summary, there is an optimum density of turbines for a given cross-section so that a maximum per turbine energy yield can be obtained.

When turbines are added in parallel rows, Π for row 1 decreases from 3.93% in case 1-1 to 3.01% in case 2-1. It is easy to understand this decrease in Π because the turbines in row 1 and 2 are lined up in the flow direction so that row 2 turbines are in the tails of speed reduction caused by row 1 turbines during the ebb tide (see Fig. 8b) and vice versa during the flood tide. The normalized efficiency for row 2 is higher than row 1 most likely due to the positioning of the turbines relative to the core of the tidal stream on this cross-section. What this implies is that the Π for row 2 might be even higher if row 1 were not present. From case 2-1 to case 3-1, Π for row 1 decreases further from 3.01% to 2.88%. Although the distance from row 3 is only half of the distance from row 2, the decrease in Π is much smaller because the turbines in row 3 are added in a lattice form so that some of the turbines in row 1 actually benefit from the speed gain created by turbines in row 3. This gain is further illustrated by Π for row 2 and 3 in case 3-1 such that it increases for row 2 from case 2-1 to case 3-1, indicating the asymmetry of the near field responses during the ebb and the flood as seen in Fig. 8a and b. Row3 appears to benefit most from the lattice form of turbine distribution because the normalized efficiency exceeds 1.

VI. DISCUSSION AND SUMMARY

The Quoddy region located at the mouth of the Bay of Fundy has attracted multiple applications and proposals of tidal power development both in US and in Canada in the last 5 years. In this study the site near KH, a choking point in the WP, is chosen to investigate the feedbacks between the tidal stream and the MHK devices in determining the extractable power resource and the tidal farm efficiency. A regional ocean model with unstructured meshes is used to simulate the tidal circulation of the Quoddy region, and the model prediction compares favorably with the limited observations [12]. Turbines are then implemented in the model as objects that extract in-stream energy to result in partial blocking and

deflection of the tidal flow. Even at 20 m resolution, the model cannot depict structure details of tidal devices and any impact on the hydrodynamics due to foundations or anchoring systems is ignored so that the turbines are prescribed in the model for the three middle sigma layers only. Furthermore, turbine operation status is simplified by considering only the following two parameters: the flow reduction ratio γ and the cut-in speed. Sensitivities to turbine densities and distributions are examined as well.

For a group of 10 turbines placed evenly apart across the WP, the highest efficiency for the group as a whole is found as the flow speed through the turbines is reduced to 60 % if the cut-in speed is set at 1 ms^{-1} . There is a wide window of tuning the flow reduction rate (from 0.4 to 0.8) such that the change to the array efficiency is within 3% of the maximum efficiency. However, further decrease of speed reduction (*e.g.*, γ increases to 0.9) causes a steep decrease in efficiency by $\sim 10\%$. Experiments with a cut-in speed of 0.7 ms^{-1} have also been conducted [19]. The overall energy extraction and Π increase with γ until γ reaches about 0.9.

The farm efficiency is also shown for several cases with different densities and distributions of turbines. For a single row, as the density of turbines increases from one in five, to one in three, to one in two, and finally to one in every cells, the array efficiency normalized by the BR (equivalent to a mean per-turbine-efficiency) is the highest when only one in every three cells is occupied by turbines. This implies a delicate balance between having closeby turbines to benefit from the velocity gains in the turbine gaps (deflection effect) and having too many turbines so that the overall flux through the cross-section is substantially reduced (blockage effect). When turbines are arranged in multiple rows in the passage, significant reduction of the row efficiency (Π) is found when turbines are in the direct shadow of one to another because of the wakes, and the wake effects can be asymmetric depending on the tidal flow characteristics. In the WP, the flooding tide is stronger so that the decline in efficiency is felt more heavily for the row on the bay side (*i.e.*, row 1 in these experiments). When turbines are set in a lattice form, the efficiency can

benefit from the speed gain generated between turbine gaps from the neighboring rows. An interesting scenario is row 3 in case 3-1 at which the normalized row efficiency exceeds 1. However, this isn't to break the Betz limit as studied in [20] because the total EE from all three rows in case 3-1 is similar to that in case 1-3 (the two cases have exactly the same number of turbines). Hence the total EE is still less than 15% of the naturally available in-stream energy from the KH section.

In summary, the model experiments have revealed complex relationships between the turbine array efficiency and turbine operation parameters as well as the number and distribution of turbines. This list of experiments is by no means all-inclusive. For example, experiments can be conducted with unevenly distributed turbines, *e.g.*, more turbines near the core of the tidal stream. Gains in flow speed is also seen in the portions of the water column above and below the turbines (Fig. 9), which can affect the extraction efficiency of neighboring rows as the water depth and hub height change in the channel. Hence experiments should also be carried out with higher densities in multiple row setting, as well as with more rows and different distances between rows that are both in-line and stacked. Nevertheless, there are already some general guidelines demonstrated by this limited number of experiments: such as allowing sufficient distances between turbines both in a row and from one row to another as well as the preference for turbines in lattice distributions even in the real world tidal channel with highly sheared flows. Project specific optimization, however, needs to be done in case-by-case basis not only considering the the spatial and temporal variability of the project site but also the actual turbine technology (type, size, operation criteria, etc).

Another interesting aspect of research is to compare the turbine implementation methods. The retarding force method is based on the actuator disc theory, and as explained in [21] the coefficient C_{td} isn't the thrust coefficient C_t . However, C_{td} is related to C_t as given by eqn. 27 in [21], which is

$$C_{td} = 4 \times \frac{1 - \sqrt{1 - C_t}}{1 + \sqrt{1 - C_t}} \quad (3)$$

Several numerical experiments using the Quoddy regional model have been conducted with C_{td} varies from 0.6 to 0.9. The extracted energy is much lower with the efficiency being about 1/3-1/2 of those shown in Fig. 5 [19] It can be derived from [21], the corresponding values of $u_d/u_\infty = 4u/(4+C_{td})$ change from 0.870 to 0.816. As C_t increases from a commonly chosen value of 0.85 towards 1, C_{td} increases quickly from 1.77 to 4 (eqn. 3) and u_d/u_∞ reduces from 0.693 to 0.5. Because of the ocean model resolution, it is not straightforward to pick a value of γ from the velocity deficit curve such as the one shown in [21] or Fig. 3 in this paper. Nevertheless, more experiments with C_{td} ranging from 2 to 4 are being conducted and comparisons with the results from the speed reduction experiments will be reported in a future paper.

It is pointed out in [21] that turbine blades shed vortices and rotational motions in the wake can induce additional turbulence. The model simulation appears to agree better with

the experimental data from a flume after introducing additional production and dissipation of turbulence in the closure model [21]. However, isolating the turbulence effects related to these modifications from the turbulence induced by velocity shears due to wakes would be challenging in the field, which warrants further research in the future. Lastly, when the ocean model has cell sizes several times smaller than the turbine size, how to best represent turbine and energy extraction should be researched.

ACKNOWLEDGMENT

Computations in this work were conducted using the super clusters both at the University of Maine and at the Ocean University of China. The authors thank Mr. Stephen Cousins and Dr. Jun Song for providing frequent computational assistance. This work was supported by the Department of Energy grant DE-EE0000298 to the University of Maine and the Special Fund for Marine Renewable Energy Project from Ministry of Finance, China (GHME2010ZC11) to Ocean University of China. Min Bao was supported by the China Scholarship Council for her Ph.D. research work at the University of Maine.

REFERENCES

- [1] C. Garrett and P. Cummins, "Generating power from tidal currents," *Journal of waterway, Port, Coastal and Ocean Engineering*, vol. 130, pp.114-118, 2004.
- [2] C. Garrett and P. Cummins, "The efficiency of a turbine in a tidal channel," *Journal of Fluid Mechanics*, vol. 588, pp. 243-251, 2007.
- [3] R. Vennell, "Estimating the power potential of tidal currents and the impact of power extraction on the flow speeds," *Renewable Energy*, vol. 36, pp. 3558-3565, 2011.
- [4] R. Vennell, "Realizing the potential of tidal currents and the efficiency of turbine farms in a channel," *Renewable Energy*, vol. 47, pp. 95-102, 2012.
- [5] C. Garrett and P. Cummins, "The power potential of tidal currents in channels," *Proc. R. Soc. A*, vol. 461, pp. 2563-2572, 2005.
- [6] C. Garrett and P. Cummins, "Limits to tidal current power," *Renewable Energy*, vol. 33, pp. 2485-2490, 2008.
- [7] B. L. Polagye and P. C. Malte, "Far-field dynamics of tidal energy extraction in channel networks," *Renewable Energy*, vol. 36, pp. 222-224, 2011.
- [8] Z. Define, K. A. Haas, and H. M. Fritz, "Numerical modeling of tidal currents and the effects of power extraction on estuarine hydrodynamics along the Georgia coast, USA," *Renewable Energy*, vol. 36, pp. 3461-3471, 2011.
- [9] D. Hasegawa, J. Sheng, D. A. Greenberg, and K. R. Thompson, "Far-field effects of tidal energy extraction in the Minas Passage on tidal circulation in the Bay of Fundy and Gulf of Maine using a nested-grid coastal circulation model," *Ocean Dynamics*, vol. 61, pp. 1845-1868, 2011.
- [10] Z. Yang, T. Wang, and A. Copping, "Modeling tidal stream energy extraction and its effects on transport processes in a tidal channel an bay system using a three-dimensional coastal ocean model," *Renewable Energy*, vol. 50, pp. 605-613, 2013.
- [11] D. R. Plew and C. L. Stevens, "Numerical modeling of the effect of turbins on currents in a tidal channel – Tory Channel, New Zealand", vol. 57, pp. 269-282, 2013.
- [12] M. Bao, H. Xue, and X. Bao, "Evaluating the tidal power and impacts of energy extraction on hydrodynamics in Cobscook and Passamaquoddy Bays," *Estuaries and Coasts*, unpublished.

- [13] D. A. Brooks, "Tides and tidal power in Passamaquoddy Bay: A numerical simulation," *Continental Shelf Research*, vol. 12, pp. 675-716, 1992.
- [14] D. Xu, H. Xue, and D. A. Greenberg, "A numerical study of the circulation and drifter trajectories in Cobscook Bay," *Proceedings of the 9th International Conference on Coastal & Estuarine Modeling*, doi: [http://dx.doi.org/10.1061/40876\(209\)11](http://dx.doi.org/10.1061/40876(209)11), 2006.
- [15] D. A. Brooks, "Tidal-stream energy resource in Passamaquoddy-Cobscook Bays: A fresh look at an old story," *Renewable Energy*, vol. 31, pp. 2284-2295, 2006.
- [16] M. Previsic, B. Polagye, and R. Bedard, "System level design, performance, cost, and economic assessment – Maine Western Passage tidal in-stream power plant," Electric Power Research Institute, EPRI-TP-006-ME. June 10, 2006
- [17] C. Chen, G. Cowles, and R.C. Beardsley, "An unstructured grid, finite volume coastal ocean model: FVCOM User Manual, Second Edition," SMASST/UMASSD Technical Report-06-0602, pp. 315, 2006.
- [18] M. Cameron, "Flow field measurements for cross-flow turbines," MS thesis, University of Maine, pp. 113, 2012.
- [19] M. Bao, "Tidal turbine array optimization – Using the Quoddy region as an example", Ph.D. dissertation, Ocean University of China, pp. 98, in Chinese, 2013.
- [20] R. Vennell, "Exceeding the Betz limit with tidal turbines," *Renewable Energy*, vol. 55, pp. 277-285, 2013.
- [21] T. Roc, D. C. Conley, and D. Greaves, "Methodology for tidal turbine representation in ocean circulation model," *Renewable Energy*, vol. 51, pp. 448-464, 2013.

Appendix Task 1-2

Evaluating the Tidal Stream Power and Impacts of Energy Extraction on Hydrodynamics in Cobscook and Passamaquoddy Bays

Min Bao^{1,2}, Huijie Xue², Xianwen Bao¹

1. College of Physical and Environmental Oceanography, Ocean University of China, Qingdao
266100, China

Email: minbao1985@gmail.com

2. School of Marine Science, University of Maine, Orono, ME 04469-5706, U.S.A.

Abstract

Cobscook and Passamaquoddy bays are located at the mouth of the Bay of Fundy. This area is known for its high tidal range and has long been regarded as a premier location for tidal power development. In this study a three-dimensional coastal ocean circulation model was set up to predict tide currents in this region, and the result was validated using the available observations. Strong tidal currents were present in the outer Cobscook Bay and Western Passage. However, numerous eddies were embedded in the tidal stream, which often resulted in fluctuations in tidal current direction. Locations with high tidal power density in this area were identified where the tidal current speed reached 1 ms^{-1} for 40-60% of time. Energy extraction at high power density sites was implemented in the model by reducing the flow speed in the mid-water column when the speed exceeded the threshold of 1 ms^{-1} . The amount of extracted energy and the extraction efficiency were determined for different distributions of turbine arrays in the Western Passage near Kendall Head. Although only small fractions of in-stream tidal energy were taken out,

25 changes in the flow, water level, and horizontal and vertical mixing coefficients were clearly
26 detected both in the near and far fields.

27

28 **Keywords:** tidal stream power - power extraction - impact – model

29

30 **1. Introduction**

31 Tidal in-stream power, a viable member of renewable energy, has a great potential for
32 electricity generation in the near future. It is a strong candidate for alternative energy source
33 especially in the coastal regions where strong tidal currents exist, because tidal power is more
34 predictable compared to wind and solar power. However, the tidal power reserves should be
35 evaluated prior to the development. It is easier to study a single turbine, but to make a noticeable
36 contribution to power grid many turbines need to be grouped into turbine farms. Any evaluation
37 method should also account for the effect of turbines on the flows in the tidal channel, as
38 otherwise would lead to a significant overestimate of the tidal power available for power
39 production.

40 The maximum available power given by Lanchester-Betz limit is 59% of the undisturbed
41 in-stream kinetic energy flux. However, extracting energy from tidal currents affects the flow
42 through the channel by enhancing the drag that could retard the flow, which in turn limits the
43 extractable power. By considering the reduction of current speed through the turbine Garrett and
44 Cummins (2004) suggested that the maximum power output could only be 38% of the
45 undisturbed energy flux in a tidal channel. In this case, the flow speed through the turbine is
46 reduced to 58% of the undisturbed flow speed upstream. In a follow-up study, Garrett and
47 Cummins (2007) showed that the maximum available power decreases as the blocking ratio (*i.e.*,

48 the fraction of the channel occupied by turbines) increases. Correspondingly, the flow speed
49 through the turbines reduces from $2/3$ of the undisturbed speed upstream at zero blocking to $1/3$
50 of the undisturbed speed upstream at 100% blocking. Using a one-dimension model for idealized
51 channels with rectangular sections, Vennell (2011) showed the peak production of power by
52 turbines could be achieved when the transport through the turbines is reduced to approximately
53 60-70 % of the undisturbed transport. Vennell (2012) further pointed out that the changing of
54 farm efficiency as a function of blocking ratio for a shallow channel is different from that for a
55 deep and wide tidal strait. Moreover, the farm efficiency approaches an asymptote with much
56 fewer rows in the shallow channel than in the deep and wide tidal strait.

57 The aforementioned studies ignore all the complexity associated with the channel
58 geometry and sheared flows in tidal channels. Moreover, impacts of power extraction can occur
59 not only in the immediate area around turbines, but also far upstream and downstream (Bryden
60 2006; Hasegawa et al. 2011), which may modify the tidal stream entering the channels or straits
61 (*i.e.*, to alter the so called “undisturbed energy flux ” upstream). It is thus of great interest to
62 understand the available tidal power resource in realistic settings of coastal bays or estuaries as
63 power extraction and the device may also have consequences on the local ecosystem (Pearce
64 2005; Scott 2007).

65 Ocean models are powerful tools to resolve the temporal and spatial patterns of flows at
66 an estuary scale and in tidal channels, most of which, however, don't resolve turbines. To
67 approximate the effect of power extraction, a retarding force or an energy loss is often specified
68 in the models (*e.g.*, Bryden and Couch 2006; Define et al. 2011; Hasegawa et al. 2011). Define et
69 al. (2011) used the three-dimensional Regional Ocean Modeling System to model the tidal
70 currents and effects of power extraction off the coast of the state of Georgia. A retarding force

71 based on the depth-averaged velocity and a constant extraction coefficient was added to the
72 governing momentum equations at every depth layer at the computational cells that contain
73 turbines. The model showed changes in the maximum and minimum water levels on the order of
74 centimeters even when 45% of the power from a cross-section was extracted. Of course, turbines
75 do not necessarily occupy the entire water column because tidal channels are often important
76 shipping pathways, and turbines should be located at depths where the interference with ship
77 traffics is minimized. Hence a step function was introduced in Hasegawa et al. (2011) to specify
78 the depth layers where energy extraction is assumed to take place, and it was found that the
79 impact becomes less if energy extraction takes place only in the lower water column compared to
80 the case with energy extraction throughout the water column.

81 The area of interest for this study is Cobscook Bay (CB) in US and Passamaquoddy Bay
82 (PB) shared between US and Canada, which is more compactly known as the ‘Quoddy Region’
83 located in the eastern Gulf of Maine near the mouth of the Bay of Fundy (Fig.1). The tidal range
84 in the Quoddy region is ~ 5-6 m on the average (Brooks 1992; Greenberg et al. 2005), but can
85 exceed 8 m during the spring tide. Tidal currents essentially determine the exchanges between
86 CB and PB as well as between CB and the Bay of Fundy (Xu et al 2006; Xu and Xue 2011).
87 With relatively low resolution, Brooks (2006) showed that the Letete Passage (LP) and Lubec
88 Narrows (LN) have the highest power density ($\sim 3.5 \text{ kW m}^{-2}$). Although the power density
89 appears to be somewhat lower than that in LP and LN, Western Passage (WP) has been regarded
90 as a prime site for tidal power development [Previsic et al. 2006] because the passage is much
91 deeper and more suitable for installing marine hydrokinetic energy devices. The outer CB and
92 Head Harbor Passage (HHP) offer additional possibilities of moderate scale development.

93 A three-dimensional numerical circulation model is set up for the Quoddy region with the
94 implementation of power extraction. Unlike in previous studies where the power extraction was
95 realized by increasing the drag (Garrett and Cummins 2004; Blanchfield 2008a, b; Karsten et al.
96 2008) or adding a retarding force (Define et al. 2011; Hasegawa et al. 2011), the approach
97 adopted in the present study is to reduce the velocity at individual meshes where turbines are
98 allocated. Because the present model has higher resolution, ~ 25 m around potential development
99 sites, which is comparable to the size of actual turbines, it is possible to take this point-wise
100 approach so that wake effects associated with the power extraction can develop accordingly in
101 the model. The distribution of the tidal power potential in the Quoddy region is examined, and
102 the locations with high tidal power density in this area are identified. More importantly, effects
103 on the near- and far-field are diagnosed if tidal power is removed from the hydrodynamic
104 system.

105 **2. Model and Validation**

106 **2.1. The model and set-up**

107 The numerical experiments in this paper were conducted by using the Finite Volume
108 Coastal Ocean Model (FVCOM) (Chen et al. 2006). FVCOM is a prognostic, unstructured grid,
109 finite-volume, free-surface, three-dimensional (3D) primitive equation coastal ocean and
110 estuarine model. It solves the hydrostatic primitive equations by calculating fluxes, which
111 provides a good numerical representation of momentum and mass. FVCOM utilizes a modified
112 Mellor and Yamada level 2.5 (MY-2.5) and Smagorinsky turbulent closure schemes for vertical
113 and horizontal mixing, respectively (Smagorinsky 1963; Mellor and Yamada 1982; Galperin et

114 al. 1988). This model has been widely applied to coastal oceans and estuaries since it can better
115 describe the complex shoreline using unstructured triangular meshes.

116 The FVCOM was configured in a domain that includes Cobscook and Passamaquoddy
117 bays and the offshore water at the mouth of Bay of Fundy (Fig. 2). The water depth in the model
118 ranged from 118.9 m below to 2.8 m above the undisturbed sea surface. Most of CB is shallow
119 except for the outer bay where the depth is deeper than 20 m. On the other hand, the WP is a
120 deep waterway with the water depth exceeding 70 m in many places. There were 15 vertical
121 sigma layers with higher resolutions near the surface and bottom. The model domain was divided
122 into 197681 elements that were connected by 102447 nodes. The meshes in the outer CB and
123 WP were refined locally to ~ 25 m since these areas appeared to be the primary tidal
124 development sites based on previous studies (Brooks 2006; Xu and Xue unpublished). The
125 coarsest meshes were ~ 3500 m, near the open boundary of the domain.

126 The external forcing conditions included the tidal elevation computed using Webtide
127 (<http://www.bio.gc.ca/science/research-recherche/ocean/webtide/index-eng.php>) with 10 tidal
128 constituents, O_1 , K_1 , N_2 , M_2 , S_2 , K_2 , L_2 , M_4 , NU_2 , and $2NU_2$, on the boundary and the runoff
129 from the Dennys River and St. Croix River obtained from US Geological Survey
130 (<http://waterdata.usgs.gov/me/nwis/rt>). River effects were minimal during the simulation because
131 discharge from both rivers were very low on the order of several m^3s^{-1} for Dennys River and
132 dozens m^3s^{-1} for St. Croix River for the simulation period. Because this study focused on tidal
133 currents and the corresponding tidal power density, the temperature and salinity were fixed
134 throughout the domain, and the temperature and the salinity of the river runoff were constant and
135 the same as the ocean. For all model runs, the model time step was 1 s.

136 2.2. Model validation

137 The Quoddy region is well known for especially high tidal range and vigorous tidal
138 currents. Model simulations used in this study depicted the period from 01:00 07/01/2004 to
139 00:00 07/31/2004 because the previous simulations for the same period (Xu et al. 2006; Xu and
140 Xue 2011) had been compared well with directly measured currents in the outer CB
141 (<http://gyre.umeoce.maine.edu/buoyhome.php>), sea level at the tide gauge station in Eastport,
142 ME (<http://tidesonline.nos.noaa.gov/geographic.html>), and drifter trajectories. It should be noted
143 the previous simulations were based on a different model at much coarser resolutions.

144 The base case simulated the undisturbed tidal regime without any turbine. The modeled
145 sea level agreed very well with the observations at the Eastport gauge station (Fig. 3a). Harmonic
146 analyses were carried out for both the observed and modeled sea surface height using MATLAB
147 code `t_tide.m` from http://www.eos.ubc.ca/~rich/#T_Tide, which indicated good agreement for
148 the four main tidal constituents, M_2 , S_2 , K_1 , and O_1 (Table 1). The maximum absolute error was
149 4.3 cm for M_2 , while the maximum relative error was 4.7% for S_2 . Phase differences were all \leq
150 3° . Comparisons between the modeled tidal currents and observations at the CB mooring are
151 presented in Fig. 3b and c. Tidal flows at the location were mostly back-and-forth with the
152 flooding tide coming at $\sim 300^\circ$ and the ebbing tide at $\sim 120^\circ$. The magnitude of the minor axis
153 was less than 7% of the magnitude of the corresponding major axis for all 4 principal tidal
154 constituents (Table 2). The flooding tide was stronger than the ebbing tide, but the ebbing tide
155 lasted a bit longer. The agreement between the modeled and observed magnitudes wasn't as
156 good as in Xu et al. (2006), but the wind forcing was excluded from the experiment. The largest
157 difference in the major axis was 16.82 cms^{-1} for M_2 , corresponding to a relative error of 12.8 %.
158 The phase of the modeled tidal current agreed better with the observations than the speed (Fig.

159 3c). The phase difference was $\leq 2^\circ$ for M_2 and S_2 , and the largest difference in phase was 20° for
160 K_1 .

161 Some sharp changes were found in the tidal current direction, which happened more often
162 when the tide switched directions. Eddies appeared to be responsible for the sharp changes in
163 directions. It can be seen from aerial photos (Fig. 4) that there were numerous small vortices on
164 both sides of the swift current in the outer CB. Vorticity fields computed from the modeled tidal
165 currents demonstrated that eddies were ubiquitous in the outer CB and WP during the flood (Fig.
166 5a) as well as at slack tide (Fig. 5b). Eddies existed not only near headlands and capes, but were
167 also embedded in the swift currents in the central tidal channels. The latter tended to be visually
168 masked by the strong tidal flows as seen in Fig. 4, but were detected at the mooring as the
169 directional changes during the flood and ebb (see Fig. 3c). The sharp changes in the model didn't
170 always coincide with the observed because small-scale eddies are sensitive to minor changes in
171 the forcing condition such as the detailed topography and wind. However, the model was able to
172 show their existence.

173 3. Power Density

174 The tidal power density is the tidal power per unit area (unit: Wm^{-2}), which can be
175 evaluated using the formula below:

$$176 \quad P = \frac{1}{2} \cdot \rho \cdot V^3 \quad (1)$$

177 where P is the tidal power density, ρ is the seawater density, and V is the tidal current speed.

178 The model simulated tidal in-stream power density averaged over 30 tidal cycles in CB and
179 WP is shown in Fig. 6. The locations with high power density were in the outer CB, WP, and

180 HHP, where the power density could reach several thousand Wm^{-2} . The power density was
181 usually higher in the mid-channel, but can shift laterally during a tidal cycle and be affected by
182 the aforementioned eddies (not shown). Frequency distribution of the in-stream power density at
183 four locations with high power density, ST1, ST2, ST3 and ST4 in Fig. 6, was analyzed and
184 shown in Fig. 7 using a bin size of 200 Wm^{-2} . The first bin of 200 Wm^{-2} corresponding to the
185 current magnitude less than $\sim 0.75 \text{ ms}^{-1}$ happened most frequently. For example, the power
186 density was less than 200 Wm^{-2} at ST1 for 35% of this month hours and it was less than 400
187 Wm^{-2} for $\sim 50\%$ of this month hours. Bins with power density greater than 400 Wm^{-2}
188 (corresponding to current speeds $> 0.9 \text{ ms}^{-1}$) occurred for about 50 – 60 % of this month hours at
189 ST2 – 4. Among the four stations, ST3 and ST4 had a significant amount of time ($> 15\%$ of this
190 month hours) with the power density exceeding 2000 Wm^{-2} . The monthly averaged power
191 density at ST1, ST2, ST3, and ST4 were 556, 715, 878, and 1029 Wm^{-2} , respectively.

192 **4. Energy Extraction Experiments**

193 **4.1. Experiment design**

194 Turbines were placed in the mid water column, namely the 7th 8th and 9th layer in the
195 model, which implied the in-stream power would be extracted from and only from these three
196 layers in this hypothetical study. Secondly, the power was extracted by reducing the flow speed
197 by half when the speed exceeded the threshold of 1 ms^{-1} . In order to produce an appreciable
198 amount of electricity, many turbines would need to be grouped as a turbine farm, which could
199 have many possible arrangements. On the other hand, removing energy from the tidal stream
200 might retard the flow considerably and could in turn limit the power to be extracted.

201 To explore the relationship between the number of turbines and the power extraction,
 202 three experiments were conducted in this study with multiple rows of turbines added sequentially
 203 in the WP (Fig. 8), where the power density was relatively high as seen in Figure 6 and 7. Case 1
 204 considered 10 turbines in row 1 only. Case 2 added another 10 turbines in row 3, and case 3
 205 included a total of 29 turbines arranged in three rows. Because of the relatively high rate of
 206 reduction in speed, the wake signal might be amplified and be tracked more easily in the model.
 207 However, with relatively few turbines the overall power extraction was still a small percentage
 208 of the total power at the given section (see Table 3) so that the overall impacts were not
 209 exaggerated. Of course, the operation criteria should be rectified if the goal were to optimize
 210 turbine arrays.

211 4.2. Results

212 Given the turbine implementation method described above, different measures were used
 213 to quantify power extraction and the results were listed in Table 3. The first measure was the
 214 total energy taken out of the system over a given period of time from all meshes that occupied by
 215 turbines.

$$216 E_{total} = \sum_{n=1}^N \sum_{m=1}^M \sum_{k=7}^9 \alpha \times \frac{1}{2} \times \rho \times (V_1^2(k, m, n) - V_2^2(k, m, n)) \times \text{volume}(k, m, n) \quad (2)$$

217 $V_1(k, m, n)$ was the instantaneous tidal current speed before energy extraction from a
 218 triangular mesh where a turbine resided; $V_2(k, m, n)$ was the instantaneous tidal current speed
 219 from the same mesh after energy extraction; M was the number of turbines at a particular row;
 220 $\text{volume}(k, m, n)$ is the water volume; $\Delta t = 1\text{s}$ and $N = 1292400$ was the number of seconds for
 221 the period from 01:00 on 16 July 2004 to 00:00 on 31 July 2004. $\alpha = 1$ when $V_1(k, m, n) \geq 1 \text{ ms}^{-1}$

222 but 0 otherwise. The total output for one spring-neap tide from case 1 (10 turbines), 2 (20
223 turbines), and 3 (29 turbines) was 308.2, 652.7, and 1148.1 MWh, respectively.

224 Another measure was the ratio between the extracted energy and the base kinetic energy
225 (BKE) at these cross-sections. The overall efficiency for case 1, 2, and 3 was 3.93, 3.94, and
226 4.57 %, respectively. Note that the total BKE over the half-month period increased from 7.8
227 GWh for the section that traversed row 1 to 8.7 GWh for the sections that traversed row 2 or 3.
228 The efficiency was the highest at row 2 (~5.81%) in case 3; the efficiency of row 1 decreased
229 from 3.93% in case 1 to 3.01% in case 2 to 2.88% in case 3, suggesting the adverse effect of row
230 3 and 2 turbines on the turbines in row 1; while the efficiency of row 3 increased from 4.77% in
231 case 2 to 4.89% in case 3.

232 **5. Impact on hydrodynamics**

233 **5. 1. Flows in the near field**

234 The changes of row efficiency in different experiments could be explained by the
235 modification of tidal flows by the turbines. Fig. 9 shows the ratio of the tidal current speed in
236 case 1-3 to its counterpart in the base case at near maximum flooding and ebbing. Most turbines
237 generated a wake in the downstream. Individual wakes were easily discernable in case 1 during
238 the ebb (Fig 9b) with the 80% contours extending as far as ~ 160 m and the 90% contours
239 reaching ~ 650 m in length. Longer tails were found in the middle and on the western side of the
240 WP, indicative of higher power density there. During the flood, the protruding Kendall Head
241 induced a large cyclonic eddy apparent in all experiments, which squeezed the individual wakes
242 towards the middle of the WP and the area of immediate impact reached more than 1000 m
243 downstream. Moreover, the flooding tide was stronger than the ebbing tide so that the combined

244 effect appeared asymmetric with the stronger impacts emerging during the flood tide. As more
245 turbines were added to the WP, some of the wakes overlapped each other to result in stronger
246 impacts both in terms of the magnitude and the area of speed reduction.

247 Because the turbines in row 1 were in the wakes of row 3 during the flooding tide (Fig.
248 9c) the efficiency of row 1 decreased from 3.93% in case 1 to 3.01% in case 2. Nevertheless, the
249 overall efficiency for case 2 increased to 3.94%. This was because the turbine locations relative
250 to flow conditions allowed higher efficiency of row 3 (4.77%) compared to row 1 (Table 3), but
251 one would expect even higher efficiency for row 3 if row 1 were absent because the turbines in
252 row 3 were in the wakes of row 1 turbines during the ebb (Fig. 9d). From case 2 to case 3, the
253 rising in the overall efficiency was bigger (0.63%) although the distances between rows were
254 almost halved. This was partly because the turbines in row 2 were farther away from both shores
255 so that the efficiency of row 2 was the highest despite it had one turbine fewer. This case also
256 benefited from the fact that the turbines in row 2 were added in a lattice form so that turbines
257 benefited from speed gains created by turbines from neighboring rows so that the efficiency of
258 row 1 only decreased slight from 3.01% in case 2 to 2.88% in case 3 but the efficiency of row 3
259 increased from 4.77% in case 2 to 4.89% in case 3.

260 Speed reduction also occurred immediate upstream of the turbines (the areas were largely
261 masked by the back bots), while further upstream the current speed decreased in the middle of
262 the passage, which was compensated by increase in the current speed near the side walls. The
263 increase was more obvious on the eastern side of the passage where the undisturbed flows were
264 weaker.

265 **5.2. A_m & K_m**

266 Besides the changes in the flow field, energy extraction could affect other aspects of
267 hydrodynamics, such as the mixing and sea level. Changes in A_m and K_m , the horizontal and
268 vertical mixing coefficients in the model, showed not only how soon the turbulence generated by
269 turbines can be dissipated in the tidal stream but also how much and where in the bays the
270 mixing can be affected. A_m was calculated using the Smagorinsky eddy parameterization method
271 as the following:

$$272 \quad A_m = 0.5C\Omega^u \sqrt{\left(\frac{\partial u}{\partial x}\right)^2 + 0.5\left(\frac{\partial v}{\partial x} + \frac{\partial u}{\partial y}\right)^2 + \left(\frac{\partial v}{\partial y}\right)^2} \quad (3)$$

273 where $C=0.4$ is a constant, and Ω^u is the area of the individual momentum control element. K_m
274 is determined using the MY-2.5 modified by Galperin et al (1988).

275 Without the turbines, the horizontal mixing coefficient (A_m) was generally low except near
276 coastline protrusions (Fig. 10a and b). For example, there appeared to be a jet emanating from
277 Kendall Head to the southeast during ebb and to the north during flood with the values ranging
278 from 1-2 m^2s^{-1} . A similar feature could be seen near the opposite shore. In contrast the vertical
279 mixing coefficient (K_m) had significant values only in the middle of the passage, both upstream
280 and downstream of Kendall Head (Fig. 11a and b). Because the turbines were added in the
281 mid-water column, changes to A_m and K_m in the near field were small close to the surface and
282 bottom (not shown). However, in the mid water column the changes in A_m and K_m were clearly
283 seen as tails upstream (downstream) of the turbines in all three cases (Fig. 10 and 11c-h) because
284 the velocity tails seen in Fig. 9 increased shears hence enhanced turbulence production and
285 mixing. In all cases the magnitude of A_m and K_m changes was as large as the A_m and K_m itself,
286 respectively. However, the areas of significant changes were relatively small such that most of
287 the tails were on the order of 100-200 m in length. Tails from individual turbines were almost

288 isolated from each other in case 1 and 2 (Fig. 10c-f and 11c-f), but some of them were close
289 enough to overlap in case 3 and formed a broader envelop that affected several hundreds of
290 meters downstream (Fig. 10g-h and 11g-h). Outside of this area of influence, both A_m and K_m
291 were generally reduced except near the jets emanating from Kendall Head where A_m and K_m
292 increased in a streak on the left side but decreased in another streak to the right, suggesting the
293 jets were pushed towards the western shore.

294 **5.3. The water level**

295 Any significant change in sea level would be of great concern. If the energy extraction
296 were to cause a considerable drop of the water level, wetlands would be reduced even disappear,
297 whereas if the energy extraction resulted in a rise of the mean water level shoreline recession
298 would happen, which would be hazardous to beach buildings and put more stress on shore
299 protection structures.

300 For all three cases, averaged changes of high tide water level and low tide water level
301 were both less than 1 cm almost everywhere of the bays except in the WP immediately north and
302 south of the turbine arrays where the changes reached 2 cm (figures not shown). However, a
303 safer measure could be the extreme changes to the maximum and minimum water levels, which
304 were the differences between the highest water level (Fig. 12 a, c and e) and the lowest water
305 level (Fig. 12 b, d and f) recorded over the one-month simulation period in case 1-3 and their
306 counterparts in the base case. Again, the magnitude of the extreme changes was on the order of 6
307 cm only, which was ~ 2% of the mean tidal amplitude of the Quoddy region. What could cause
308 potential concern was where the high water level became higher as in the inner CB in case 1 (Fig.
309 12a) and the upper reach of PB in case 2 (Fig. 12c) as well as where the low water level became

310 lower as in the out CB in case 3 (Fig. 12f). Since the changes didn't increase monotonically as
311 the number of turbines increased from case 1 to case 3, they might be affected by aliasing
312 associated with the hourly interval of archived model output. One place where the consistent
313 changes occurred was in the WP. There was a band north of the turbine arrays where the high
314 water level became increasingly higher from case 1 to case 3. Similarly, there was a band south
315 of the turbine arrays where the low water level became increasingly lower from case 1 to case 3.

316 **6. Discussion and Summary**

317 In this study, a 3D numerical circulation model based on FVCOM was developed for
318 Cobscook and Passamaquoddy bays. The model results were compared with the observed sea
319 level in Eastport, Maine and the direct current observations from a mooring in the outer CB.
320 Harmonic analyses showed the maximum error in tidal constants was 4.3 cm in height and 16.8
321 cms^{-1} in major axis for M_2 , corresponding to a relatively error of 1.6 and 12.8%, respectively.
322 Eddies widely existed in this region, which caused the sharp switches in the current direction.
323 Eddies like these might be important to the engineering design of turbines and platforms because
324 they could change the force distributions on the blades and structures. As well, they might affect
325 the power production as animated model results suggest that the power density fluctuated
326 noticeably as eddies evolved. Furthermore, the exact location and timing of eddies were sensitive
327 to the power extraction, which could affected the dispersion characteristics of the bays (Xu and
328 Xue 2011). Hence these small-scale features would warrant further investigations in the future.

329 Based on the model results, the outer CB, WP and HHP were identified as the locations
330 with high tidal in-stream energy where the power density reached several thousand Wm^{-2} .
331 Frequency distribution of the in-stream power density at four high power density locations was
332 analyzed. The monthly averaged power density reached 556, 715, 878, and 1029 Wm^{-2} for ST1,

333 ST2, ST3 and ST4, respectively. With the turbines implemented in the circulation model, the
334 energy extraction can be quantified, which amounted to 308.2, 652.7 and 1148.1 MWh for a
335 half-month period in July 2004, equivalent to an average of 86, 91, and 110kW per turbine from
336 case 1, 2 and 3, respectively. Because of weaker currents and shallower water depth near the
337 coasts, the maximum production was attained for the turbines near the middle of the passage on
338 the US side with 57.9, 73.8, and 97.9 MWh over the half-month period (see Fig. 8 for the
339 turbines with the maximum yield in case 1-3, respectively).

340 The ratios between the extracted energy and the BKE at these cross-sections varied from
341 3.93% in case 1 to 3.94% in case 2 to 4.57% in case 3. The increase from case 1 to case 2 was
342 because of the higher ratio for row 3 as the wake effect actually reduced the efficiency of row 1
343 from 3.93% in case 1 to 3.01% in case 2 as expected. The larger increase from case 2 to case 3,
344 however, came from both the higher efficiency from row 2 (with turbines farther away from the
345 coasts) and the turbines being in a lattice form. The latter allowed the turbines to be benefited
346 from the speed gain produced by turbines from neighboring rows as the efficiency for row 3
347 increased from 4.77 % in case 2 to 4.89 % in case 3. The lattice form also benefited the turbines
348 in row 1 as the decrease in efficiency from case 2 to case 3 was much smaller than that from case
349 1 to case 2 despite the distances between rows were halved. However, the responses were not
350 symmetric, likely due to the asymmetry between the flooding and ebbing currents. Although not
351 surprising, the demonstrated benefit of a turbine array in the lattice form was significant, which
352 could be an important guideline for engineering design and further research.

353 The impacts of power extraction on the hydrodynamics were evaluated in terms of the
354 changes in the water level and the mixing coefficients, A_m and K_m . The changes to A_m and K_m
355 were clearly seen as tails in the downstream direction at the depths where turbines were

356 implemented. The changes had the similar magnitude as A_m and K_m itself, but tails with
357 significant changes of A_m and K_m reached $\sim 200\text{m}$ in case 1 and 2 to $\sim 400\text{ m}$ in case 3. Eddies
358 away from the turbine arrays were affected in location and timing, which altered the A_m and K_m
359 in the far field (e.g., the cyclonic eddy behind Kendall Head). Changes to the water level were on
360 the order of a few centimeters only, much smaller than the mean tidal amplitude in the Quoddy
361 region. A band of increase (decrease) in the high (low) water level was detected north (south) of
362 the turbine arrays in the WP, where the impact was enhanced as the number of turbines increased
363 from case 1 to 3. If the maximum changes to the highest/lowest water levels would be adopted as
364 a “minimum regret” measure, yearlong simulations and continuously tracking over the
365 integration period are needed to obtain more accurate estimates.

366 This study was an initial attempt at simulating energy extraction by MHK turbines and
367 evaluating the corresponding impacts on hydrodynamics in the Quoddy region. Only three array
368 designs were examined. In this study, the energy extraction by turbines was implemented by
369 reducing the flow speed to one half at the model cells where turbines were allocated. This
370 approach was based on the theoretical derivation of Garrett and Cummins (2004) that there is a
371 definite reduction in speed corresponding to the maximum power extraction. According to
372 Garrett and Cummins (2007), the speed through the turbines can be reduced from $2/3$ of the
373 undisturbed flow when the blocking ratio is near zero to $1/3$ of the undisturbed flow when the
374 blocking ratio is near 1. In this study, the blocking ratio for each of the rows was about 3%. How
375 to quantify the blocking ratio with multiple rows hasn't been as obvious. Nevertheless,
376 experiments have been conducted with a single row of turbines (as in case 1) but at different
377 speed reduction rates and the results shall be summarized in a follow-up study, along with other

378 aspects of the methodology (such as mass conservation) and the comparison with the more
379 widely adopted approach of adding a retarding force to represent individual turbines.

380 The energy loss to turbines was relatively minor compared to the baseline kinetic energy
381 in each of the three cases. If the goal is to optimize turbine farm arrangements and derive
382 guidelines for commercial-size tidal power development, more numerical experiments with
383 different specifications of the cut-in speed (instead of 1 ms^{-1} used in this study) and efficiency,
384 explicit designs of framing and anchoring structures, as well as difference sizes and densities of
385 turbine arrays should be conducted in the future to determine not only the maximum potential in
386 power generation, but also impacts on hydrodynamics as well as on living marine resources.

387 **Acknowledgements**

388 Computations in this work were conducted at the High Performance Computing Center at the University
389 of Maine, and the authors thank Mr. Stephen Cousins for providing frequent technical assistance. We
390 greatly appreciate the constructive comments and suggestions from three anonymous reviewers, which
391 have led to a significant improvement of this paper. This work was supported by the Department of
392 Energy grant DE-EE0000298 to the University of Maine and National Natural Science Foundation of
393 China (41206013) . Min Bao was supported by the China Scholarship Council for her Ph.D. research
394 work in US.

395

396 **References**

397 Blanchfield, J., C. Garrett, P. Wild, and A. Rowe. 2008a. The extractable power from a channel
398 linking a bay to the open ocean. *Proceeding of the Institution of Mechanical Engineers, Part*
399 *A: Journal of Power and Energy* 222:289-297.

400 Blanchfield, J., C. Garrett, A. Rowe and P. Wild. 2008b. Tidal stream power resource assessment
401 for Masset Sound, Haida Gwaii. *Proceeding of the Institution of Mechanical Engineers, Part*
402 *A: Journal of Power and Energy* 222:485-492.

403 Brooks, D. A., 2006. The tidal-stream energy resource in Passamaquoddy-Cobscook Bays: A
404 fresh look at an old story. *Renewable Energy* 31: 2284-2295.

405 Bryden, I. G., and S. J. Couch. 2006. ME1—marine energy extraction tidal resource analysis.
406 *Renewable Energy* 31:133-139.

407 Chen, C., G. Cowles, and R.C. Beardsley. 2006. An unstructured grid, finite volume coastal
408 ocean model: FVCOM User Manual, Second Edition. SMAST/UMASSD Technical
409 Report-06-0602, pp. 315.

410 Define, Z., K.A. Haas, and H.M. Fritz. 2011. Numerical modeling of tidal currents and the
411 effects of power extraction on estuarine hydrodynamics along the Georgia coast, USA.
412 *Renewable Energy* 36:3461-3471.

413 Galperin, B., L.H. Kantha, S. Hassid, and A. Rosati. 1988. A quasi-equilibrium turbulent energy
414 model for geophysical flows. *Journal of Atmospheric Sciences* 45:55-62.

415 Garrett, C., and P. Cummins. 2004. Generating power from tidal currents. *Journal of waterway,*
416 *Port, Coastal and Ocean Engineering* 130:114-118.

417 Garrett, C., and P. Cummins. 2007. The efficiency of a turbine in a tidal channel. *Journal of*
418 *Fluid Mechanics* 588:243-251.

419 Greenberg, D.A., J.A. Shore, F.H. Page, and M. Dowd. 2005. A finite element circulation model
420 for embayments with drying intertidal areas and its application to the Quoddy region of the
421 Bay of Fundy. *Ocean Modelling* 10:211-231.

422 Hasegawa, D., J. Sheng, D. A. Greenberg, and K. R. Thompson. Far-field effects of tidal energy
423 extraction in the Minas Passage on tidal circulation in the Bay of Fundy and Gulf of Maine
424 using a nested-grid coastal circulation model. 2011. *Ocean Dynamic* 61:1845-1868.

425 Karsten, R.H., J.M. McMillan, M.J. Lickley, and R.D. Haynes. 2008. Assessment of tidal current
426 energy in the Minas Passage, Bay of Fundy. *Proceeding of the Institution of Mechanical*
427 *Engineers, Part A: Journal of Power and Energy* 222:493-507.

428 Mellor, G.L., and T. Yamada. 1982. Development of a turbulence closure model for geophysical
429 fluid problem. *Reviews of Geophysics and space physics* 20:851-875.

430 Pearce, N. 2005. Worldwide tidal current energy developments and opportunities for Canada's
431 Pacific coast. *International Journal of Green Energy* 2:365-86.

432 Previsic, M., B. Polagye, and R. Bedard. 2006. System level design, performance, cost, and
433 economic assessment – Maine Western Passage tidal in-stream power plant. Electric Power
434 Research Institute, EPRI-TP-006-ME. June 10, 2006

435 Scott, B.E. 2007. A renewable engineer's essential guide to marine ecology. *Proceedings Oceans*
436 *2007 - Europe International Conference* doi: 10.1109/OCEANSE.2007.4302218

437 Smagorinsky, J. 1963. General circulation experiments with the primitive equations, I. The basic
438 experiment. *Monthly Weather Review* 91:99-164.

439 Vennell, R. 2011. Estimating the power potential of tidal currents and the impact of power
440 extraction on the flow speeds *Renewable Energy* 36:3558-3565.

- 441 Vennell, R. 2012. Realizing the potential of tidal currents and the efficiency of turbine farms in a
442 channel. *Renewable Energy* 47:95-102.
- 443 Xu, D., H. Xue, and D.A. Greenberg. 2006. A numerical study of the circulation and drifter
444 trajectories in Cobscook Bay. *Proceedings of the 9th International Conference on Coastal &*
445 *Estuarine Modeling* doi: [http://dx.doi.org/10.1061/40876\(209\)11](http://dx.doi.org/10.1061/40876(209)11).
- 446 Xu, D., and H. Xue. 2011. Numerical study of horizontal dispersion in a macro tidal basin.
447 *Ocean Dynamics* doi: 10.1007/s10236-010-0371-6.

448 **Tables**

449 Table 1. Comparison of amplitudes and phases of tidal elevation for O₁, K₁, M₂ and S₂ in
 450 Eastport, ME (red dot in Fig. 1).

Tidal Constituent	Amplitude (cm)				Phase (°)		
	obs	model	Diff.	Rel. diff.	obs	model	Diff.
O1	11.35	11.7	0.35	2.64%	180	180	-1
K1	17.41	18.0	0.59	2.87%	205	208	3
M2	263.65	259.34	-4.31	-1.63%	100	103	3
S2	26.36	27.59	1.23	4.67%	160	162	2

451

452

453 Table 2. Comparison of major and minor axes, orientations and phases of tidal ellipses for O₁, K₁,
 454 M₂ and S₂ at the CB mooring (blue dot in Fig. 1).

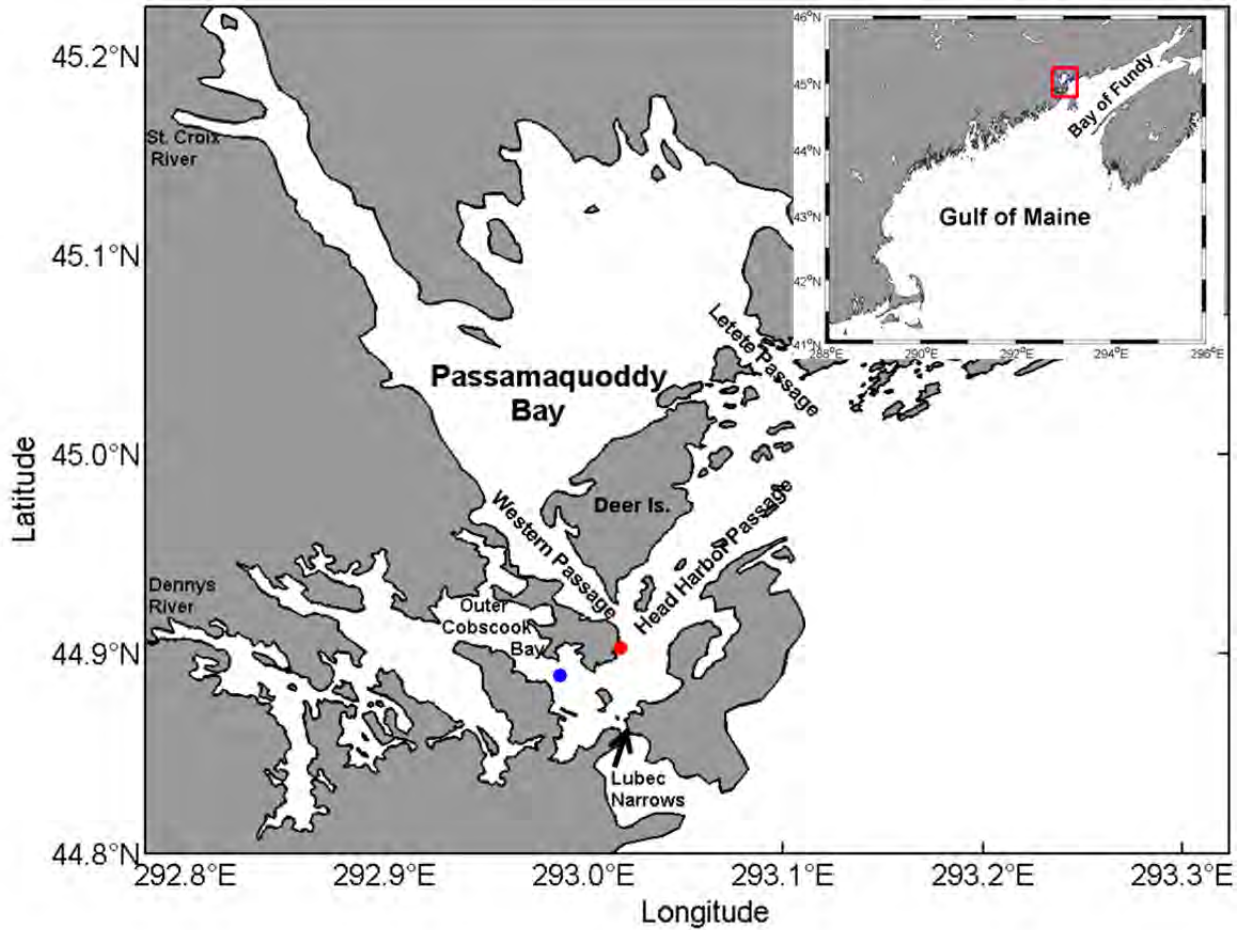
	O1		K1		M2		S2	
	obs	model	obs	model	obs	model	obs	model
Major Axis (cm/s)	3.96	3.40	4.48	5.74	131.25	148.07	15.37	16.33
Minor Axis (cm/s)	0.12	0.09	0.14	0.51	5.09	3.25	1.04	0.67
Ellipse Orienta. (°)	159	165	148	164	151	154	155	155
Phase (°)	90	80	127	107	33	33	92	90

455

456 Table 3. The energy loss during one spring-neap cycle in three different cases.

Case	Row 1		Row 2		Row 3	
Number	Extracted Energy (MWh)	Efficiency %	Extracted Energy (MWh)	Efficiency %	Extracted Energy (MWh)	Efficiency %
1	308.2	3.93	—	—	—	—
2	235.9	3.01	—	—	416.8	4.77
3	225.8	2.88	494.9	5.81	427.5	4.89

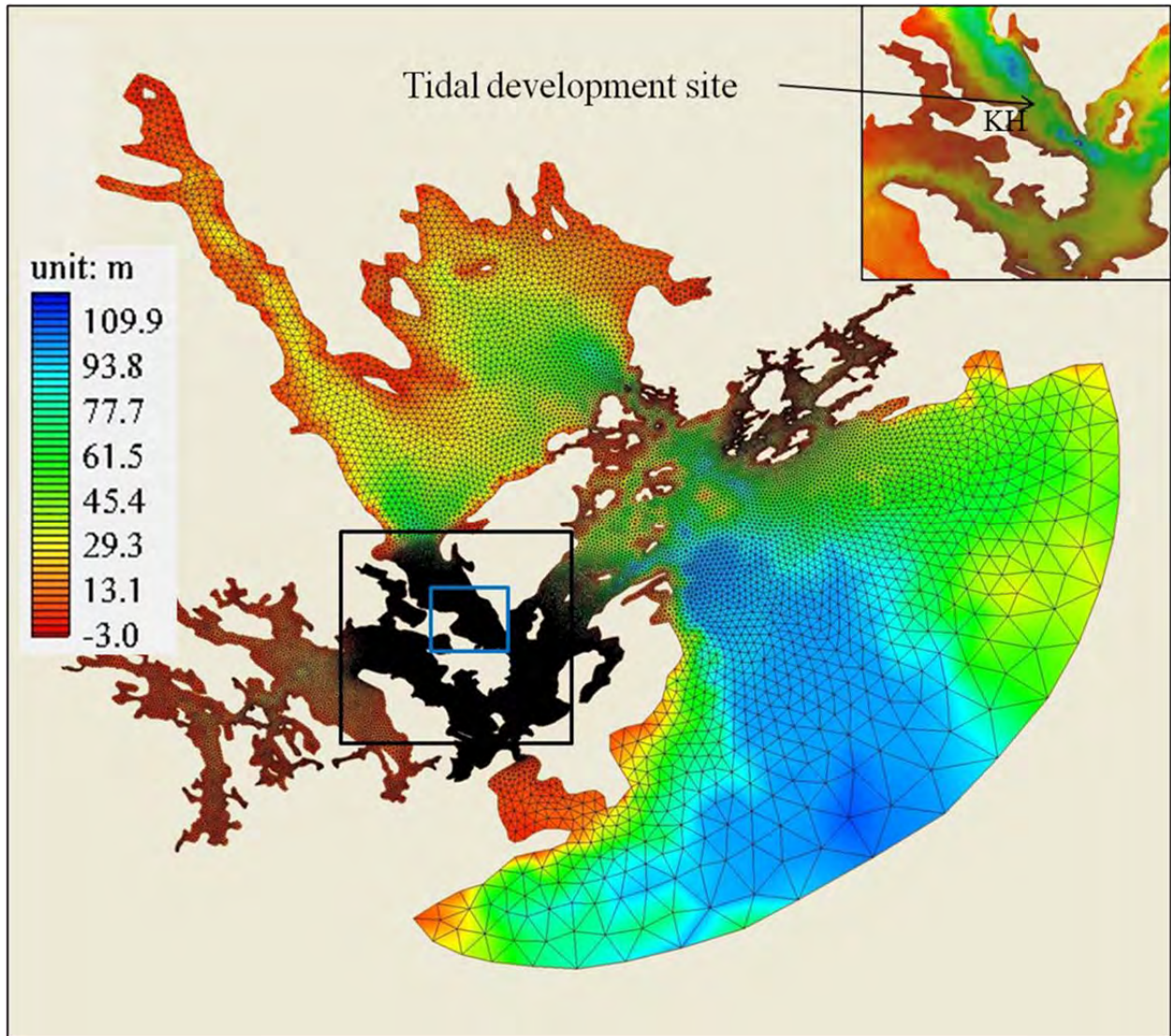
457



458

459 **Fig. 1** A map of the Quoddy region, located in the eastern Gulf of Maine near the mouth of the
 460 Bay of Fundy (see the red box in the inset), showing the tidal channels suitable for potential tidal
 461 power development. Marked in circles are locations for the tidal gauge station in Eastport (red)
 462 and the current meter mooring in the outer CB (blue), where the data are used in Fig. 3 for
 463 comparison with the model result.

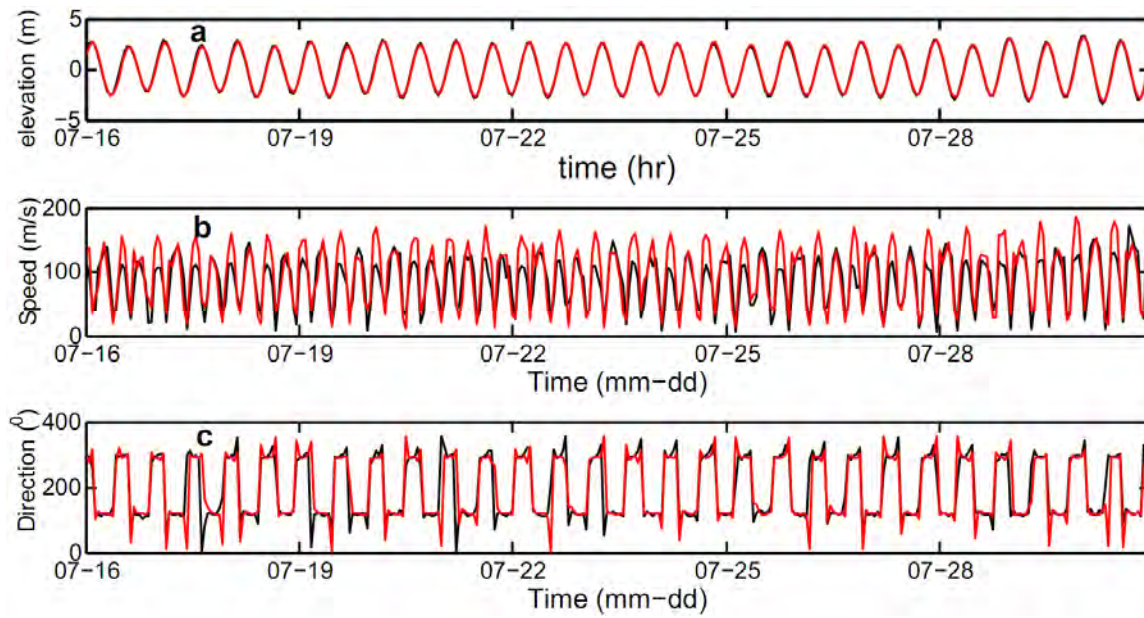
464



465

466 **Fig. 2** Bathymetry (color) and mesh for the Quoddy regional model with locally refined
 467 resolution of ~ 25 m in the outer Cobscook Bay and the Western Passage (the black box and the
 468 bathymetry of which is shown in the insert). The blue box is used for zoom-in of the near field in
 469 the Western Passage. KH represents Kendall Head in Eastport, ME.

470



471

472 **Fig. 3** Comparisons between the modeled (red) and observed (black) water elevation (a), tidal
 473 current speed (b) and direction (c). Only the second half of the simulation period is shown for
 474 clarity, which is also the period used to calculate the power extraction by turbine arrays shown in
 475 Table 3.

476

477

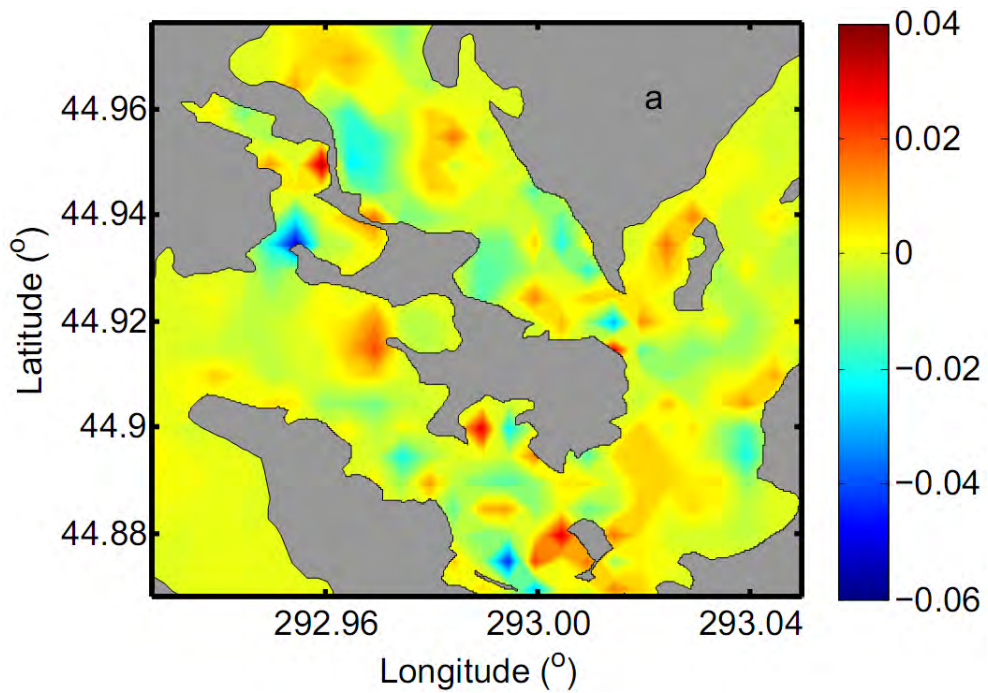


478

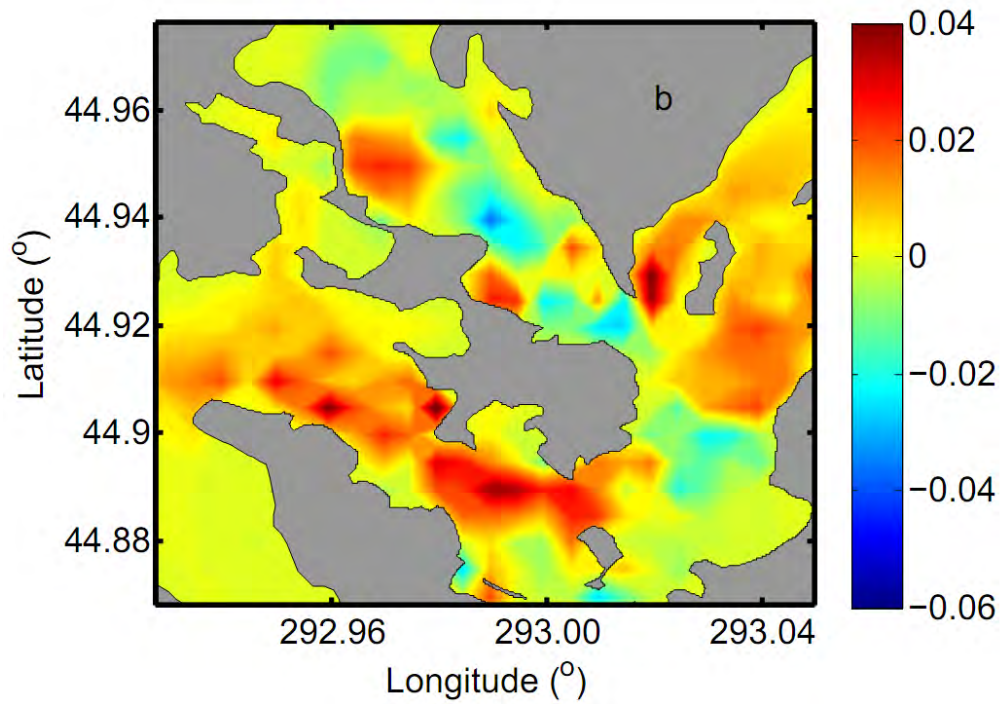
479 **Fig. 4** An aerial photo showing the tidal stream and swirls along its sides in the outer CB during
480 flooding tide (taken by H. Xue on 23 November 2009).

481

482



483

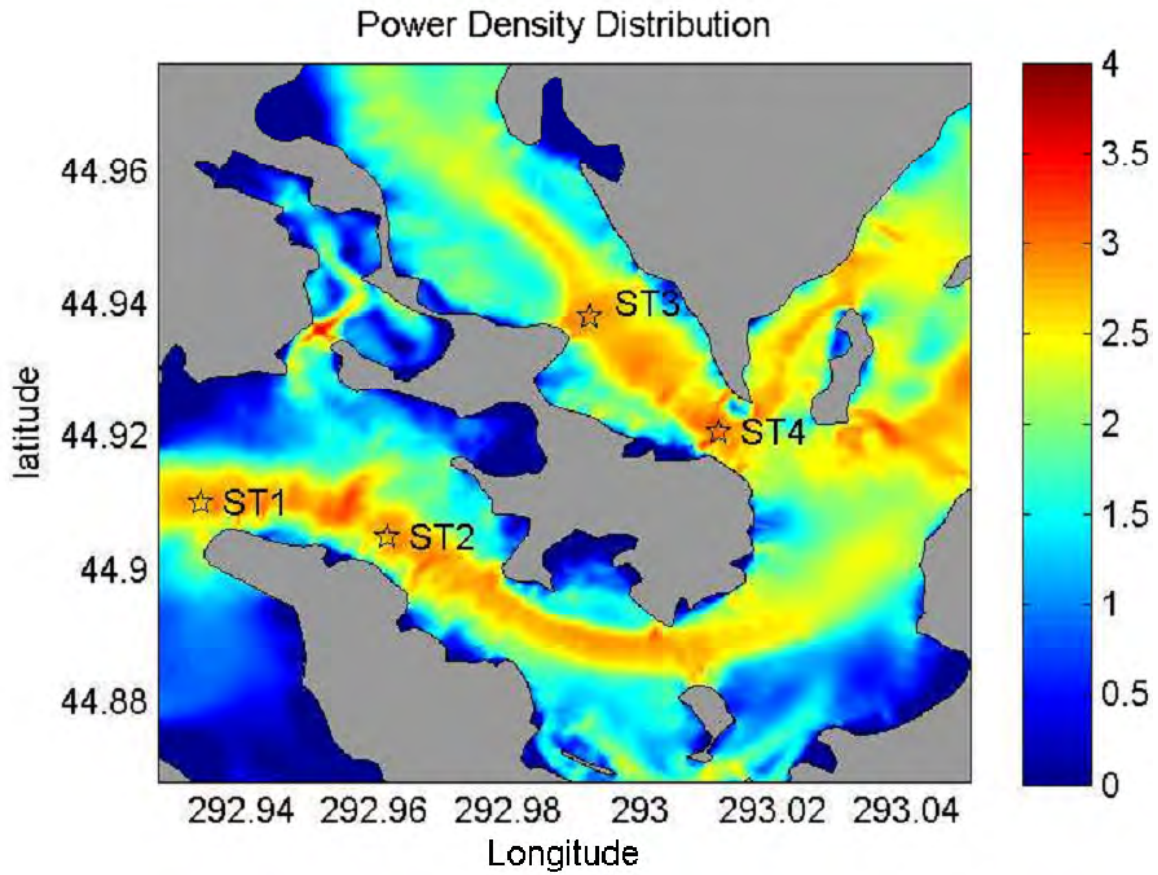


484

485 **Fig. 5** The surface vorticity field (unit: s^{-1}) in the outer CB and WP (a) near the maximum
 486 flooding tide at 02:00 on 6 July 2004 and (b) near the switch from flood to ebb at 05:00 on 6 July
 487 2004.

488

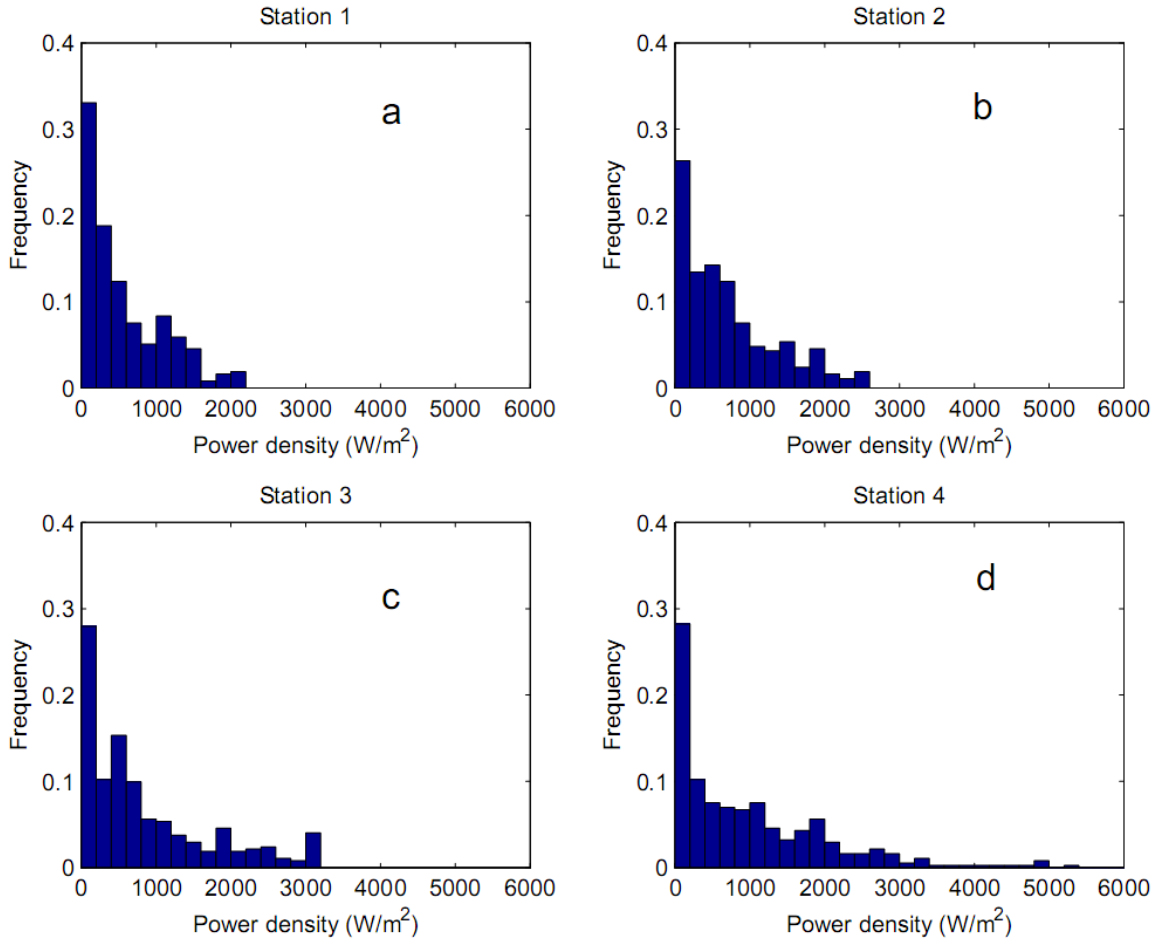
489



490

491 **Fig. 6** Distribution of the vertically averaged, mean power density over 30 tidal cycles in log10

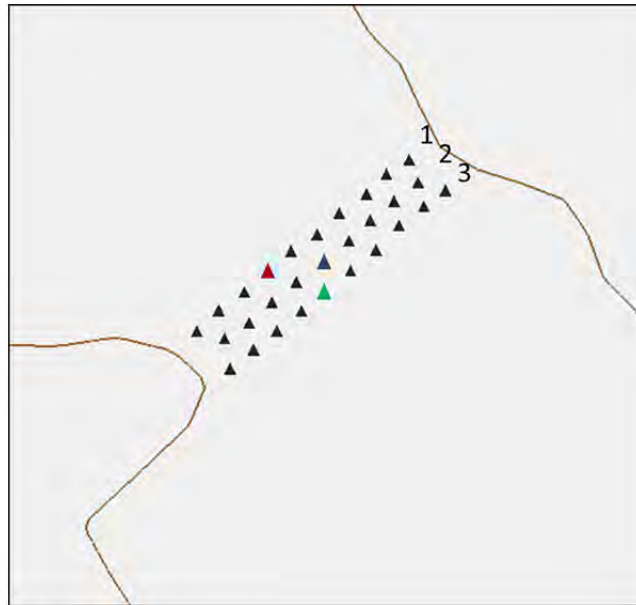
492 scale (unit: Wm^{-2}).



493

494 **Fig. 7** Frequency distribution of the power density during the one-month modeling period (bin
 495 size: 200 Wm⁻²) at (a) station 1 (ST1), (b) station 2 (ST2), (c) station 3 (ST3), and (d) station 4
 496 (ST4).

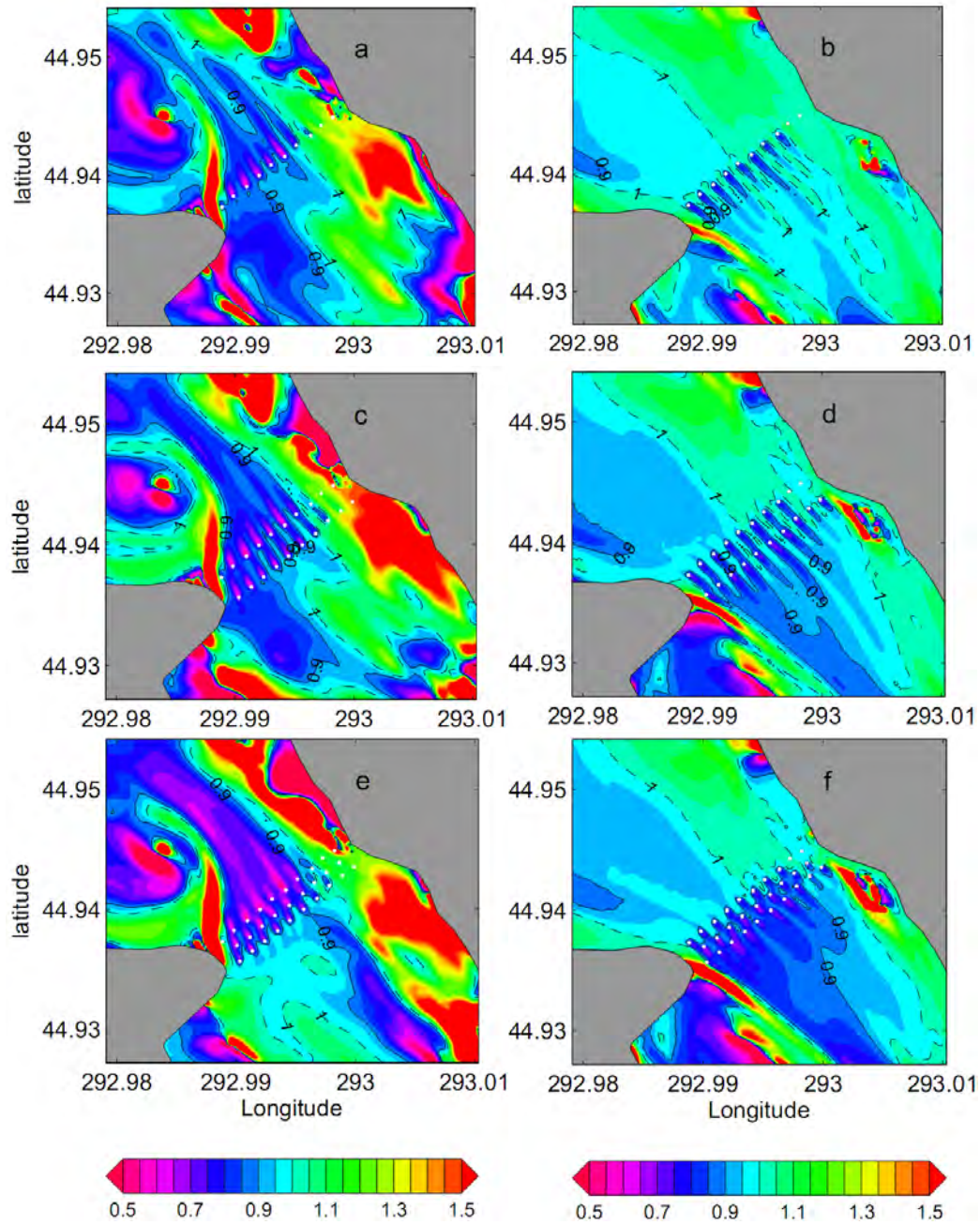
497



498

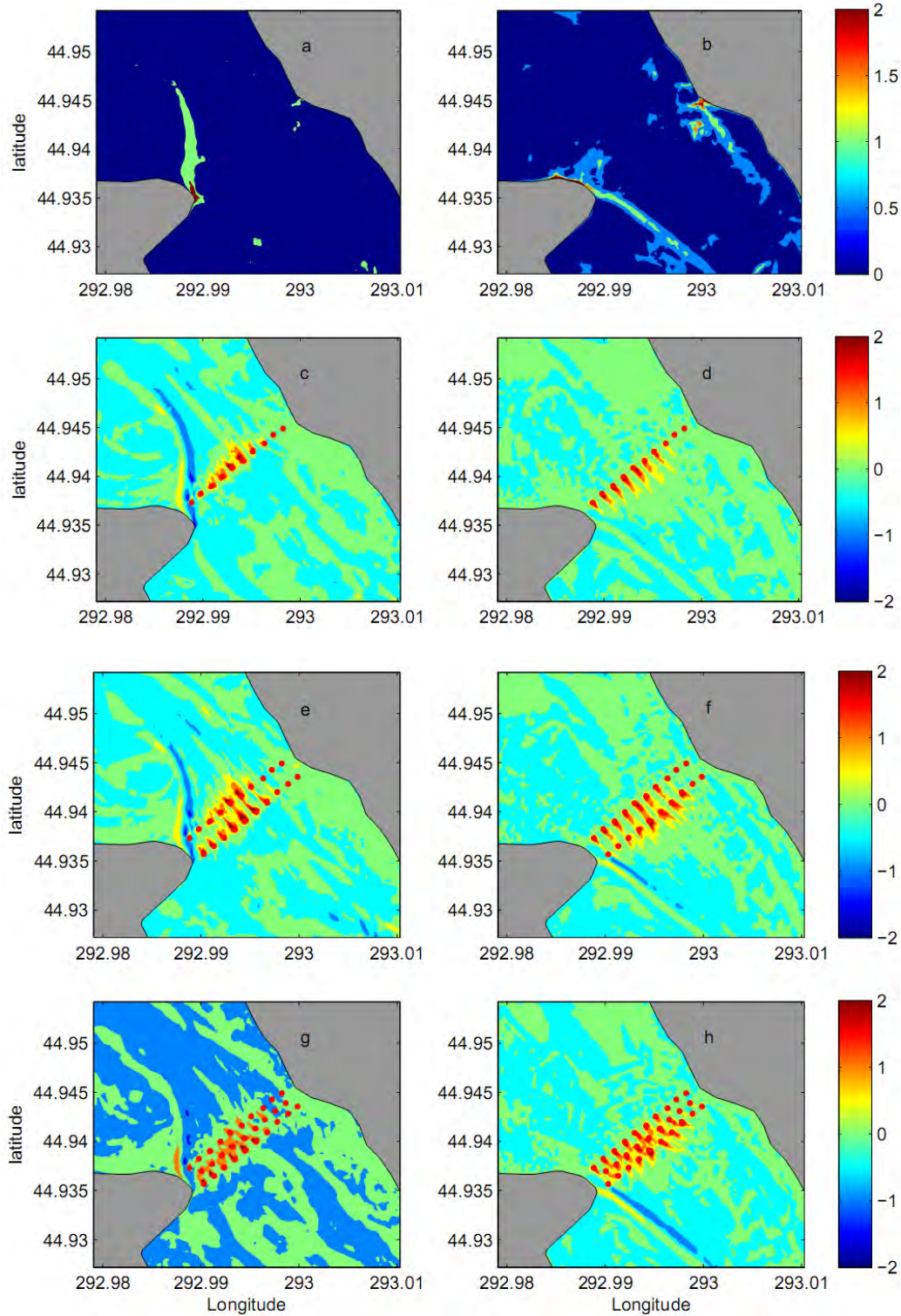
499 **Fig. 8** Turbine arrangements in the model experiments. Row 1 and 3 have 10 turbines, and row
500 2 has 9. The average distance is ~ 80 m between rows and ~ 100 m between turbines in a given
501 row. Red, green and blue triangles indicate the turbines with maximum energy yield in case 1, 2
502 and 3, respectively.

503



504

505 **Fig. 9** Ratio of the tidal current speed in case 1 (a and b), case 2 (c and d), and case 3 (e and f) to
 506 its counterpart in the base case near the peak flood at 03:00 on 6 July 2004 (a, c, and e) and near
 507 the peak ebb at 10:00 on 6 July 2004 (b, d, and f).

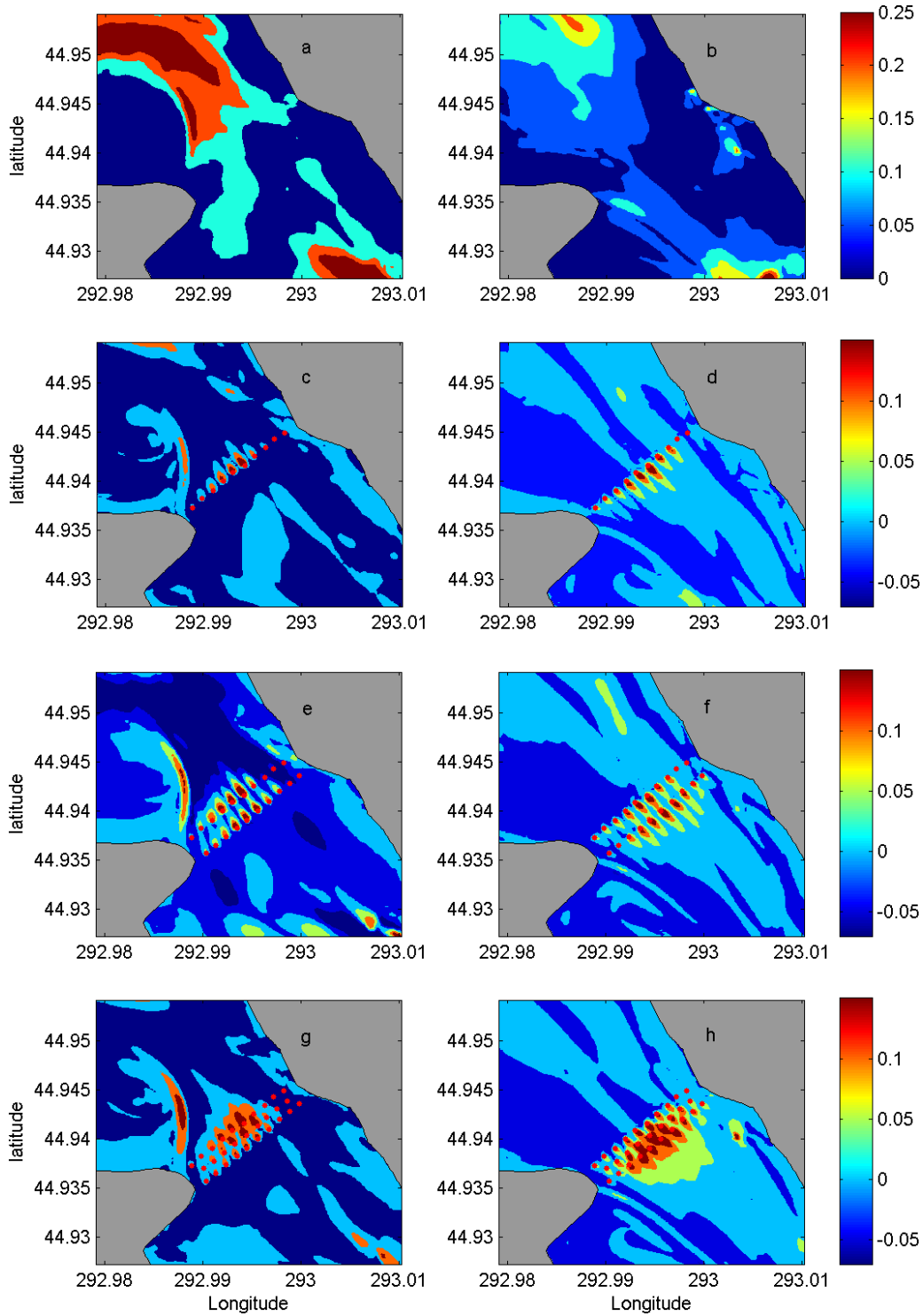


508

509

510 **Fig. 10** Distribution of the horizontal mixing coefficient, A_m (unit: m^2s^{-1}), in the 8th layer in base
 511 case near the peak flood at 03:00 on 6 July 2004 (a) and near the peak ebb at 10:00 on 6 July
 512 2004 (b) as well as their changes due to energy extraction in case 1 (c and d), case 2 (e and f),

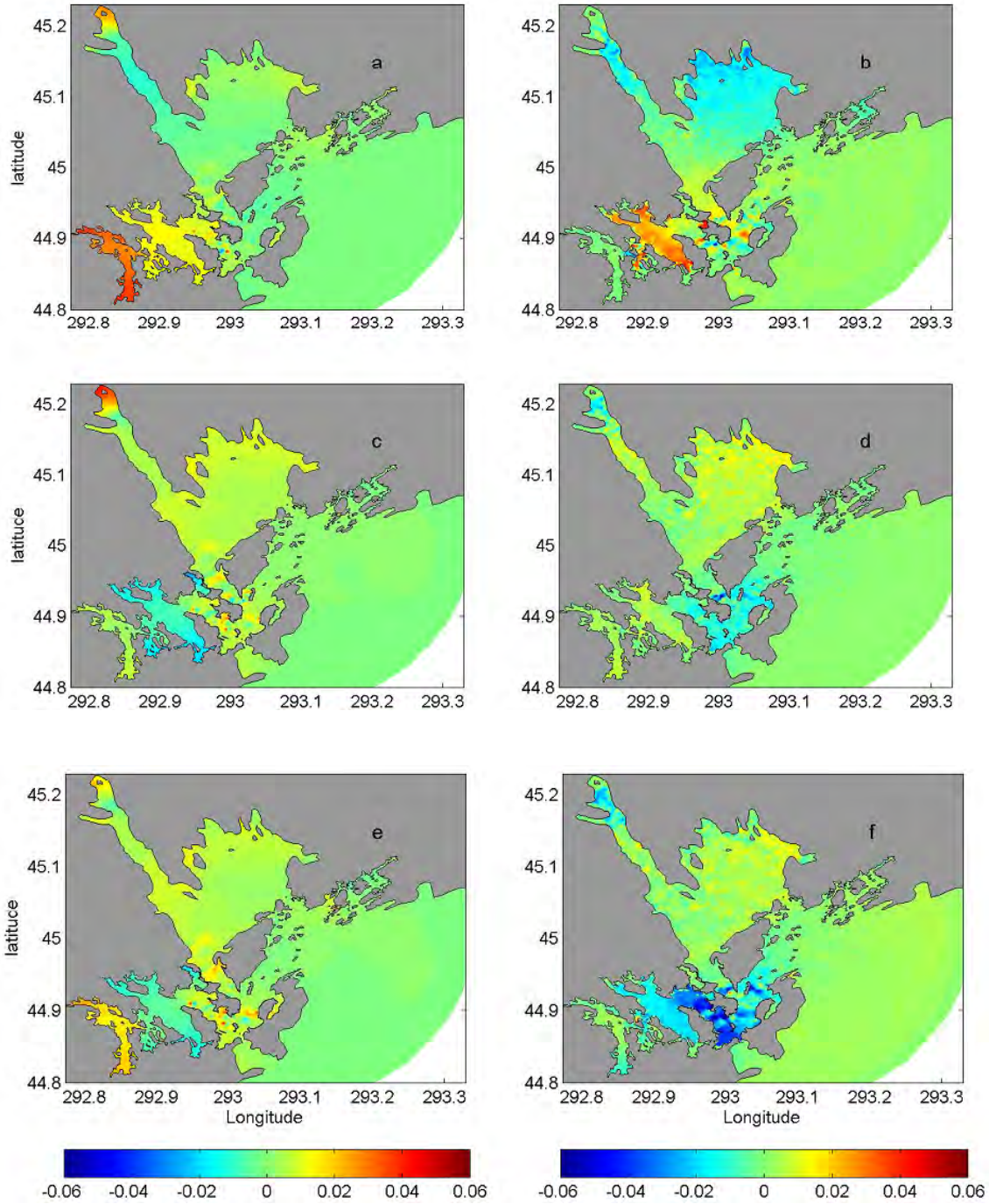
513 and case 3 (g and h), respectively. Positive values in c-h correspond to higher A_m in case 1-3
 514 than in the base case.



515

516

517 **Fig. 11** Similar to Fig. 10 but for the vertical mixing coefficient, K_m (unit: $m^2 s^{-1}$).



518

519

520 **Fig. 12** Difference in the maximum (a, c, and e) and minimum (b, d, and f) water level (unit: m)
 521 between the base case and case 1 (a and b), case 2 (c and d), and case 3 (e and f). Positive values
 522 correspond to higher water levels in case 1-3 than in the base case.

Appendix Task 1-3

FLOW FIELD MEASUREMENTS FOR A CROSS FLOW TURBINE

By

Matthew Cameron

B.S. University of Maine, 2009

A THESIS

Submitted in Partial Fulfillment of the

Requirements for the Degree of

Master of Science

(in Mechanical Engineering)

The Graduate School

The University of Maine

August 2012

Advisory Committee:

Michael L. Peterson, Professor of Mechanical Engineering, Advisor

Huijie Xue, Professor of Marine Sciences

Richard Kimball, Professor, of Maine Maritime Academy

THESIS ACCEPTANCE STATEMENT

On behalf of the Graduate Committee for Matthew Cameron I affirm that this manuscript is the final and accepted the thesis. Signatures of all committee members are on file with the Graduate School at the University of Maine, 42 Stodder Hall, Orono, Maine.

Chair's Name, & Title

Date

LIBRARY RIGHTS STATEMENT

In presenting this thesis in partial fulfillment of the requirements for an advanced degree at The University of Maine, I agree that the Library shall make it freely available for inspection. I further agree that permission for "fair use" copying of this thesis for scholarly purposes may be granted by the Librarian. It is understood that any copying or publication of this thesis for financial gain shall not be allowed without my written permission.

Signature:

Date:

FLOW FIELD MEASUREMENTS FOR A CROSS FLOW TURBINE

By Matthew Cameron

Thesis Advisor: Dr. Michael L. Peterson

An Abstract of the Thesis Presented
in Partial Fulfillment of the Requirements for the
Degree of Master of Science
(in Mechanical Engineering)
August 2012

Understanding the flow pattern around hydrokinetic devices is important for the development of tidal energy technology. The objective of the research is to provide the wake characteristics from laboratory measurements, including wake structure, and flow recovery in the near and far fields of a cross-flow turbine. The data can be used to assist in optimization of an array of turbines by providing experimental results for numerical models validation and industrial developers of tidal energy. Another critical use of this data will be to provide a basis for parameterization of energy extraction in coastal ocean models in resource assessment. The experimental flow field measurements presented were obtained in a tow tank. Measurements were performed with an Acoustic Doppler Velocity meter on a scale model of a cross-flow turbine. The turbine was operated near the predicted optimum efficiency with varying solidity and tip speed ratios. The shape and recovery of the wake were seen in the near field and the decay of the induced turbulence was observed to continue into the far field. This work represents a step toward the full characterization of the flow patterns induced by the cross-flow turbine with near and far field effects.

ACKNOWLEDGMENTS

This author sincerely thanks Dr. Huijie Xue and Dr. Michael L. Peterson for the opportunity to do the research as well as patients and technical leadership throughout this research. Thanks to Dr. Richard Kimball for the useful technical discussions. Thanks to the faculty of the mechanical engineering department and fellow graduate students for the many interesting discussions regarding the experimental aspects of this research. This research was supported by the Department of Energy through a research grant (DE-DD0000298) to the University of Maine.

TABLE OF CONTENTS

ACKNOWLEDGMENTS.....	iii
LIST OF TABLES.....	vii
LIST OF FIGURES.....	viii
Chapters	
1. Introduction.....	1
2. Objectives.....	3
3. Experiment Set-up	4
3.1 Tow Tank and Testing Facilities.....	4
3.2 Turbine.....	5
3.2.1 Turbine Non-Dimensional Variable.....	7
3.2.2 Turbine and Dynamometer.....	9
3.2.3 Confirmation of Measurements.....	12
3.2.4. Turbine Measurement.....	14
3.3 Acoustic Doppler Velocity Meter (ADV)	17
3.4 Pressure transducer.....	21
3.5 Test configurations.....	22
3.6 Programmable Controller and Data Acquisition.....	27
3.7 Synchronization.....	29
4. Data Acquisition and Post Processing.....	33
4.1 Analog I/Os.....	33
4.2 ADV Measurements.....	36
4.3. Test Matrix.....	39

	52
4.4. Post-Processing.....	39
4.4.1 Coordinate Rotation	39
4.4.2 Velocity Measurement Range	40
5. Wake Characteristics	43
5.1 Reynolds' Time Averaging Concept.....	43
5.2 Turbulent Kinetic Energy.....	43
5.3 Reynolds Stress.....	44
5.4 Numerical Processing.....	44
5.4.1 Running Window	45
5.4.2 Weighting Function	45
5.4.3 Window Size.....	47
5.5 Wavelet Transforms.....	50
5.6 Visualization techniques	50
6. Results.....	51
6.1 Composite Flow Field.....	51
6.1.1 High Solidity Turbine.....	52
6.1.2 Low Solidity Turbine	54
6.2 Reynolds time averaging	57
6.3 Wavelet Spectrum.....	63
6.4 Turbulence Kinetic Energy and Reynolds Stress.....	67
6.5 Surface Elevation	72
7. Discussion.....	73
7.1 Entrained Fluid and Flow Recovery.....	73
7.2 Upstream Effects	77
7.3 Surface Elevation and Blockage Effect.....	80
7.4 Flipped Reference Frame	83

8. Conclusion	85
REFERENCES	86
APPENDICES	88
Appendix A: Reynolds Decomposition	88
Appendix B: High Solidity turbine Wake Characteristics at different TSR.....	94
Appendix C: Low Solidity Turbine Wake Characteristics	97
BIOGRAPHY OF THE AUTHOR.....	100

LIST OF TABLES

Table 3.1 Dimensions of tow tank	4
Table 3.2 List of different turbine solidity tested	8
Table 3.3 Reynolds number numerical values for different effects and max for data sets	9
Table 3.4 Force coefficients form dynamo results form the two data with different solidity	14
Table 4.1 List of test preformed with turbine and measurement variables	39
Table 6.1 Qualitative comparisons wake energy spectrum for the three different positions	65
Table 7.1 Flow Bypass for High Solidity for high solidity turbine over increasing TSR	79
Table 7.2 Flow Bypass for Low Solidity for low solidity turbine	79

LIST OF FIGURE

Figure 3.1	University of Maine’s tow tank	4
Figure 3.2	Test Turbine on carriage and side illustration of cross flow turbine operation.....	6
Figure 3.3	Three-dimensional forces assassinated with the turbines dynamo.....	9
Figure 3.4	Two view of test turbines upper assembly	10
Figure 3.5	Test turbines lower assembly with two blades and the NACA 63018 blade profile.....	11
Figure 3.6	Multiple Fourier transform for increasing motor rotational speed show the torque response of a freely rotating turbine.....	13
Figure 3.7	Dynamometer results as a function of blade position for low solidity with different inflow directions.....	15
Figure 3.8	Torque and drag force coefficients as a function of blade position and tip speed ratio.....	16
Figure 3.9	Torque and drag force coefficients as a function of blade position and inflow speed (V_c)	17
Figure 3.10	The acoustic doppler velocity meter ADV.....	18
Figure 3.11	ADV’s acoustic Head and sample volume with detail drawing of the acoustic head and sample volume with coordinate system.....	19
Figure 3.12	Pressure transducer and flow shroud configuration to measure the surface elevation on the floor of the tow tank.....	22
Figure 3.13	ADV’s carriage mount setup with two degrees of freedom.....	23
Figure 3.14	ADV and pressure transducer with flow shroud mounted to the adjustable floor tripod.....	24
Figure 3.15	Illustration of side and top view of experimental configuration.....	25
Figure 3.16	Approximation of flow field drawing of different ADV sample volume height with respect to turbine.....	26
Figure 3.17	Flow diagram of controller and data acquisition.	29
Figure 3.18	The three variables needed to determine position of the sample volume relative to each blade.....	30

Figure 3.19 Calibration data used to measure position of turbine relative to the ADV sample volume	31
Figure 3.20 Tracking Blades with respect to ADV'S sample volume	32
Figure 4.1 Encoder curves from turbine and carriage from a test starting at rest.....	34
Figure 4.2 Steps for processing the carriage encoder signal.....	35
Figure 4.3 The raw three-dimensional velocity data from the ADV's internal memory.....	37
Figure 4.4 Validation of speed measurements using three different methods.....	38
Figure 4.5 Combination of two data sets to form a composite wake.....	41
Figure 4.6 Results from the repeatability study concerning blade position and fluid velocity.....	42
Figure 5.1 Functionality of running window.....	45
Figure 5.2 The Hamming weighting functions and their effects on the frequency domain.....	46
Figure 5.3 Effect of running window size on Reynolds decomposition.....	48
Figure 5.4 Results of Reynolds decomposition for different window sizes	49
Figure 6.1 Near flow field for high solidity turbine operating on design	54
Figure 6.2 Far flow Field for high solidity turbine operating on design.....	54
Figure 6.3 Near flow fields for low solidity turbine over three-blade position.....	56
Figure 6.4 Far flow fields for low solidity turbine over three-blade position.....	57
Figure 6.5 The magnitude of fluctuation for the high solidity turbine.....	60
Figures 6.6 Three mean velocity component of Reynolds averaging for the low solidity turbine.....	60
Figure 6.7 The magnitude of fluctuation for the high solidity turbine.....	61
Figures 6.8 The three-dimensional mean velocity component of Reynolds decomposition for the low solidity turbine for three-blade position.....	61
Figures 6.9 Time and frequency response for the sample volume adjacent to the top of turbine at blade position 1.....	64

Figure 6.10 Two time and frequency responses stacked with the sample volumes on the top of turbine at blade position 1.....	64
Figures 6.11 Time and frequency response from wavelet analysis for high solidity turbine operating on design.....	65
Figures 6.12 Wavelets for each height and blade position showing the fluctuation intensity as a function of frequency and distance to turbine.....	66
Figure 6.13 Turbulence kinetic energy terms for high solidity with optimum TSR.....	68
Figure 6.14 Turbulence kinetic energy for low solidity turbine over three blade positions.....	69
Figure 6.15 The three Reynolds shear terms for four blades with optimum TSR.....	70
Figure 6.16 The three Reynolds shear terms for low solidity turbine over three blade positions.....	71
Figure 6.17 Vector plot with the upper and lower surface elevation for the high solidity turbine.....	72
Figure 7.1 Mean velocity for each direction for high solidity turbine.....	74
Figure 7.2 Mean velocity magnitude and fluctuation velocities for high solidity turbine.....	74
Figure 7.3 Mean and fluctuation velocities for low solidity test over three blade positions.....	76
Figure 7.4 Visualization of the bypass flow and volumetric flow fraction.....	78
Figure 7.5 Change in surface elevations for two different solidities.....	81
Figure 7.6 Fourier transform of measured surface elevation for the low solidity turbine over different TSR values.....	82
Figure 7.7 Surface elevation for high solidity test with three different TSR for power side on top.....	83
Figure 7.8 Surface elevation for high solidity test with three different TSR for return side on top.....	83
Figure 7.9 Actuator Disk principle from the Bitz momentum theory.....	84
Figure A.1 Reynolds decomposition for low solidity at blade position 1.....	88
Figure A.2 Reynolds decomposition for low solidity at blade position 2.....	89
Figure A.3 Reynolds decomposition for low solidity at blade position 3.....	90
Figure A.4 Reynolds decomposition for high solidity at 1.4 TSR.....	91

Figure A.5 Reynolds decomposition for high solidity at 0.9 TSR.....	92
Figure A.6 Reynolds decomposition for high solidity at 1.9 TSR.....	93
Figure B.1 Flow Field for high solidity turbine operating at different TSR.....	94
Figure B.2 Turbulent kinetic energy for high solidity turbine operating at different TSR.....	95
Figure B.3 Reynolds shear for high solidity turbine operating at different TSR.....	96
Figure C.1 Velocity magnitude for blade position 1.....	97
Figure C.2 Velocity components for blade position 1.....	97
Figure C.3 Velocity magnitude for blade position 2.....	98
Figure C.4 Velocity components for blade position 2.....	98
Figure C.5 Velocity magnitude for blade position 3.....	99
Figure C.6 Velocity components for blade position 3.....	99

1. INTRODUCTION

The present need for renewable energy has led researchers to investigate the development of wind, wave, and tidal energy sources. This international surge in demand for renewable energy resources and the subsequent investment in research have produced a wide range of hydrokinetic technology for tidal developers to consider for implementation. Two major challenges faced by the tidal industry are locating favorable sites and understanding the amount of the energy that can be extracted from the sites. Less favorable sites are more abundant, but are prone to flow instability and other issues resulting impede recovery of significant amounts of power. As a whole, developing the technology for the available sites provides engineering challenges that will determine the success of the growing industry. Fortunately, lessons learned from past developments in wind energy have resulted in a number of different turbine types, which can be explored in order to exploit an assortment of technologies of various designs and concepts.

The two main types of turbines are lift- and drag-dependent devices, respectively. An example of a drag-dependent device is a savonius turbine, which produces power by the change in fluid inertia. Lift-dependent devices include axial-flow turbines and cross-flow turbines; and the latter is the focus of this study. Lift-dependent devices produce power depending on blade shape and angle of attack to produce a pressure difference resulting in lift. Each type of turbine, and their respective power production, has different advantages. The savonius and cross-flow turbines are mechanically simple and unaffected by changes in inflow direction normal to the axis of rotation. A distinct advantage of a drag-dependent device is that its operational performance is unaffected by turbulence. In comparison, lift-dependent devices are affected by turbulence. The axial-flow out performs the cross-flow and savonius in efficiency, but has structural and mechanical disadvantages. The ability of different turbines to convert inflow velocity into mechanical energy has been shown analytically, in which the ideal turbine has efficiency of

~59%, with an ideal drag device converting ~20% of the energy (Hau, 2006). The cross-flow turbine typically performs at a efficiency that is between the axial-flow and savonius turbines; however, these numbers are for a single turbine operating in a steady and uniform flow. A single turbine in uniform flow is not how the turbine is used in practical applications. While understanding the amount of power to be extracted from a single turbine is a critical part of the engineering design, a larger question remains regarding to how much power can be produced economically from any tidal energy site.

To extract appreciable amounts of power, an array of turbines will need to be deployed at a given site. Since favorable sites are limited in number and often cover a small region, developers must consider the turbine array power density. A high-density turbine array both increases the amount of energy that can be extracted and minimizes cost by reducing the amount of underwater cabling and potentially reducing foundation costs. However, the turbine wake can cause the array power density to be lower compared to an array of turbines chosen for optimum array output. In fact, the maximization of turbine power density may be more important to the overall performance of an installation than the efficiency of a single turbine. One demonstration of the importance of this design parameter is the recent work on the cross-flow wind turbines, which suggests that higher density arrays can be used with this type of turbines (*Dabiri J., 2010*). To address the knowledge gap in tidal power development, we have obtained and analyzed the wake data from a cross-flow turbine in a steady and uniform flow. We have focused on two flow characteristics: the mean flow recovering behind the turbine and the behavior of turbulence. This study is the first step to understand the impacts of turbines on tidal flows, which will lead to enhanced understanding of optimization of turbine array design and the potential size of this renewable energy resource.

2. OBJECTIVES

The objective of the study is to understand the flow field around a cross-flow turbine using a scaled experimental turbine and a single point three-dimensional Acoustic Doppler Velocimeter (ADV). The research explores the concept of turbine spacing by examining a single turbine's effect on a uniform flow. A cross-flow turbine belongs to a class of turbines that depends on lift to produce power. Power production depends on the inflow velocity of the fluid as well as the amount of turbulence present in the inflow. The subjects of interest are the flow recovery and the magnitude of induced turbulence as a function of distance from the turbine. To acquire the experimental results, experimental methods were developed to gather repeatable velocity measurements relative to the turbine. This method produces a composite flow field using multiple positions of ADV, which measures the turbine approach and departure in a quasi-two dimensional flow field. In addition to measuring the turbine's influence on the flow, operational coefficients that describe the forces are associated with the three degrees of freedom related to the turbine flow field.

The experimental method presented provides the ability to measure the recovery of the flow, particularly the collapse of the entrained region immediately behind the turbine as well as the full flow recover in the far field. For the analysis, the Reynolds time averaging concept is used as a turbulence model to classify and describe turbulent flow. From the turbulence model, other relevant variables can be computed to describe different characteristics of the wake. For example, the Reynolds averaging separates the measurement into the mean and turbulent components, from which one can calculate the quantity and the transfer of the turbulent energy through turbulent shear and turbulent kinetic energy. To further examine different attributes of the velocity measurements, a wavelet analysis was performed providing both frequency and location information relative to the turbine.

3. EXPERIMENT SET-UPS

3.1 Tow Tank and Testing Facilities

The University of Maine tow tank (Figure 3.1) is maintained and operated by the Mechanical Engineering Department. The tank is used for a variety of projects, most of which are currently related to turbine testing. The dimensions of the tow tank are given in Table 3.1.



Figure 3.1 The University of Maine's tow

30m (Length)	2.4m (Width)	1.1m (Max Water Depth)
-----------------	-----------------	---------------------------

Table 3.1 Dimensions of
the tow tank

The tow tank also has a wave making capabilities and was used in the past for research related to aquaculture. The system includes a wire pulled carriage, a wave maker, an artificial shore, and wave dampening structures. The artificial shore and wave damping structure is a valuable asset for the flow study by reducing the wave reflection allowing for long test durations and increasing the quality of both turbine and ADV data.

The carriage is the only utility available to push or pull different devices including turbines, floating and submersible structures. The wire-pull is coiled around a drive drum. The drive drum is connected to a gearbox and a motor that pulls the carriage in both directions. The carriage suspension and wheel arrangement provides a platform for hydrodynamic tests. The carriage can accelerate up to 1.5 ms^{-1} . An encoder is used to measure the position as the carriage travels down the tank. The encoder is attached to an axle, which has a rubber wheel that rides on the rail. With the recently improved suspension and a spring-loaded hinge providing downward force, the encoder wheel maintains consistent contact with the rail when the carriage travels in either direction.

3.2 Turbine

The test turbine is a cross-flow turbine in which the entire blade is parallel to the center of rotation as opposed to an axial flow turbine where blades span the radius normal to the axis of rotation. The turbine's distinctive operational characteristics of the turbine are its cylindrical shape and the direction of the inflow necessary to maintain optimal performance. The two features contribute to practical advantages in the field. The shape of the turbine facilitates a rectangular active area and better utilizes the space in the flow channel by stacking individual turbines together. The inflow only needs to be normal to the axis of rotation, which eliminates the need to realign the turbine with the flow. Both of these characteristics reduce the turbine's overall complexity of construction and hardware.

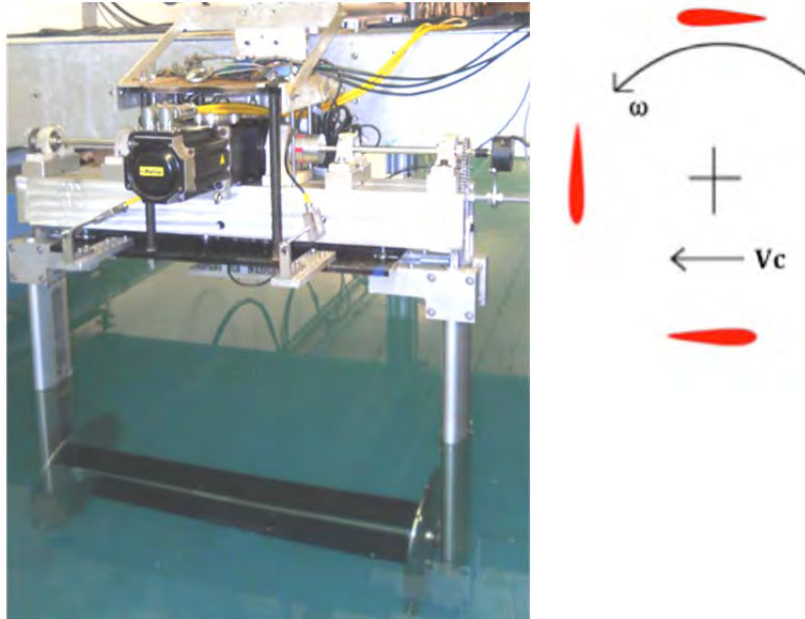


Figure 3.2 Test Turbine on carriage and side illustration of cross flow turbine

A cross-flow turbine is designed to produce maximum torque because the entire lifting surface is at the outer radius thus fully utilizing the distance between the lifting surface to the center of rotation. Figure 3.2 shows the drawing of the cross section and a picture of the test turbine in the tow tank. The torque curve can be altered by using either straight or helical blades. Straight blades produce lift and stall intermittently along the span of a blade causing the torque curve to fluctuate with position, while a section of helical blade always produces lift resulting in a steadier torque curve. Practical cross-flow turbines usually use helical blades, providing more constant torque output, as well as the ability to self-start. The blades used in this testing are straight not helical. While straight blades do not match a practical turbine, this is not a major discrepancy because the method used to measure the flow field is performed in a two-dimensional plane. The ADV sample volume measures the three-dimensional velocity within the plane depicted in Figure 3.2.

3.2.1 Non-Dimensional Variables of the Turbine

Three forces torque, drag, and heave provide the sum of all the forces acting on the turbine. The coefficients use force, fluid density, inflow velocity, and swept area to define the configuration for a turbine's mechanical characteristics. Independent of specific design factors as blade type or rotational speed. The coefficients are determined by measuring the force acting on the turbine and relating it to the available energy or power.

$$\text{Performance Coefficient} \quad C_P = \frac{\omega T}{\frac{1}{2} \rho A V_C^3} \quad (1)$$

$$\text{Drag Coefficient} \quad C_D = \frac{F_H}{\frac{1}{2} \rho A V_C^2} \quad (2)$$

$$\text{Heave Coefficient} \quad C_H = \frac{F_V}{\frac{1}{2} \rho A V_C^2} \quad (3)$$

Tip Speed Ratio: Tip speed ratio (TSR) is a non-dimensional variable used to define the rotational speed of a turbine in relation to the free stream velocity. TSR strongly affects the performance of a turbine, and is the only variable easily altered once the turbine is set up.



(4)

Solidity: Solidity is a non-dimensional variable describing the ratio of blade cord length to the circumference of the turbine. A basic and useful property of the solidity is its effect on the TSR. A lower solidity turbine requires a higher TSR to maintain near-optimal performance, and conversely, a higher solidity turbine requires a lower TSR.

$$\begin{aligned}
 C_P &= \frac{\omega T}{\frac{1}{2} \rho A V^3} \\
 C_D &= \frac{F_H}{\frac{1}{2} \rho A V^2} \\
 C_H &= \frac{F_V}{\frac{1}{2} \rho A V^2}
 \end{aligned}
 \tag{5}$$

Data Set	Blade Number	Solidity
A	2	0.16
B	4	0.32

Table 3.2 List of different turbines solidity tested

Reynolds Number The magnitude of the Reynolds number influences the turbine's performance by affecting its behavior. However, the Reynolds number is complex calculations due to blades that are constantly changing their direction relative to the incoming flow. This results in a large periodic oscillation. To add to the complexity of the problem, the blade can travel back through its own wake. As the solidity number decreases, the range of angles of attack narrows and enters a region where the lift and drag characteristics are well understood, stabilizing the Reynolds number. However, a steady Reynolds number does not translate to a practical cross-flow turbine that often has a solidity and TSR chosen for high efficiency and low environmental impact. Due to the complicated blade-fluid interaction, there is no absolute value for Reynolds number. Therefore, the components; inflow and rotation as well as maximum values, are shown in Table 3.3. Other variables, such as the angle of the blades and the chord to diameter ratio, are not significant to this study, but are relevant in operation and performance of the turbine.

Data Set	Reynolds Number		
	Inflow	Rotation	Max
	$\frac{c V_C}{\nu}$	$\frac{\omega R c}{\nu}$	$\frac{c (\omega R + V_C)}{\nu}$
A	47,000	105,000	152,000
B	58,000	82,000	140,000

Table 3.3 Reynolds number numerical values for different effects and max for data sets

3.2.2 Turbine and Dynamometer

One purpose of the test turbine is to measure torque, vertical and horizontal forces on the turbine over a range of inflow speed, TSR, blade angle, blade shape, or blade profile. The dynamometer data is used to calculate turbine efficiency in converting inflow velocity to mechanical energy and to determine the drag and heave coefficients. The three coefficients, measuring relative magnitude of torque, drag, and heave, can be used to quantify the amount of energy removed from the fluid with respect to the amount of available energy (Hau, 2006). The forces seen by a cross-flow turbine with straight blade are uneven and dependent on blade position. The forces are measured as a function of blade position providing information on the specific response of the foils fluid interactions.

The three forces of entrance drag, heave, and torque are labeled below in Figure 3.4. The three forces are measured by load cells, located in positions on the turbine where the force of interest is isolated.

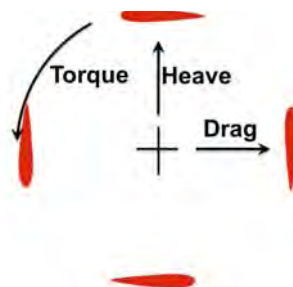


Figure 3.4 Three-dimensional forces associated with the turbine's dynamometer

The upper assembly supports the motor, drive train, and turbine. The purpose of the upper assembly is to isolate the three turbine forces through slender strut to load cells to measure only relevant forces. The motor is connected to a gearbox with dual output shafts containing a bearing that is bolted to the inner beam. A link with a load cell from the inner beam to the motor provides the motor with the resistance to rotations and provides a direct torque measurement. Due to fluctuations with the carriage's speed near the frequency range of the torque oscillation, the motor was mounted horizontally to shield the torque measurements from the carriage's oscillation. Mounting the motor horizontally exposed the load cell to the high frequency rolling noise, which was removed by a digital filtering of the data.

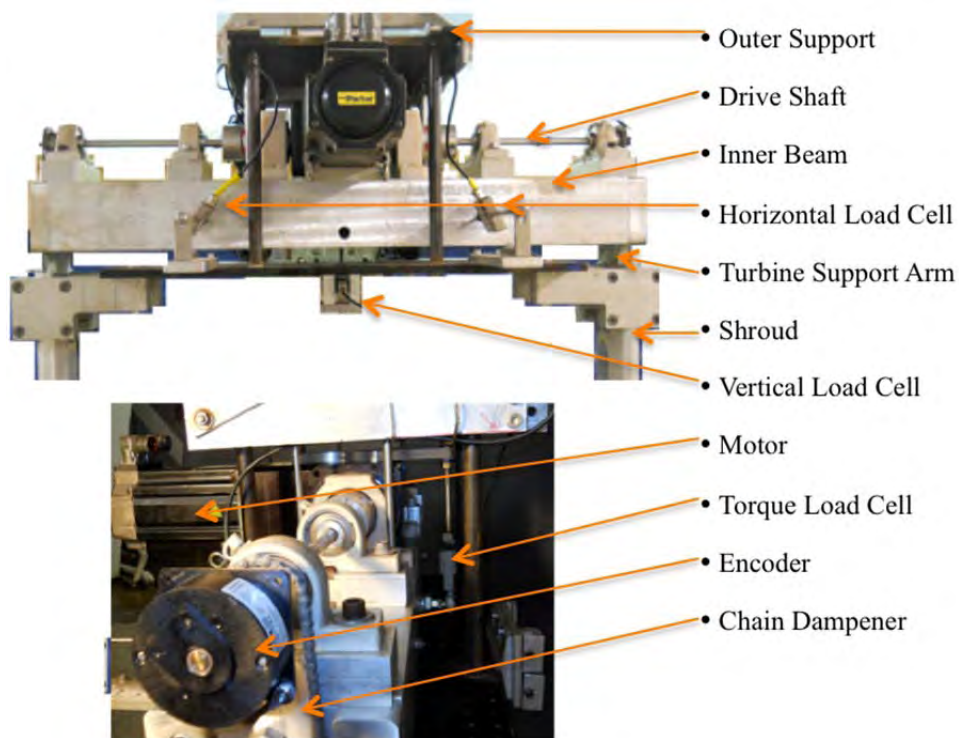


Figure 3.4 Two view of the test turbines upper assembly

The lower assembly consists of the mounting plates, the submerged portion of the drive train, and the removable blades. The turbine is supported on either side by two sleeve bearings that are bolted to the inner support arms. The inner arms are shielded from the water flow by

faired shrouds. The shrouds serve to reduce the effect of the arms on the flow field and because they are independently mounted, they prevent the drag of the arms from being included in the drag measurement. As a result, the drag measurements only measure the forces from the blades and mounting plates.

The design of the blade profile and angle of attack used for this research were selected to maximize the coefficient of performance from the test turbine based on available data. The blade shape is a NACA 63-0018, a symmetric profile developed by the National Advisory Committee for Aeronautics (Lokocz, 2010). The blade is 7.6cm in length and 76.2cm long and is constructed from carbon fiber, which produces a blade able to resist deformation under load. The rigidity of the blade and angle of attack at +5 degrees were the factors, which caused this blades' performance output to be superior to other blade types. The optimum setting does not change with different solidity ratios, thus, all tests were done using the same type of blade and angle of attack.

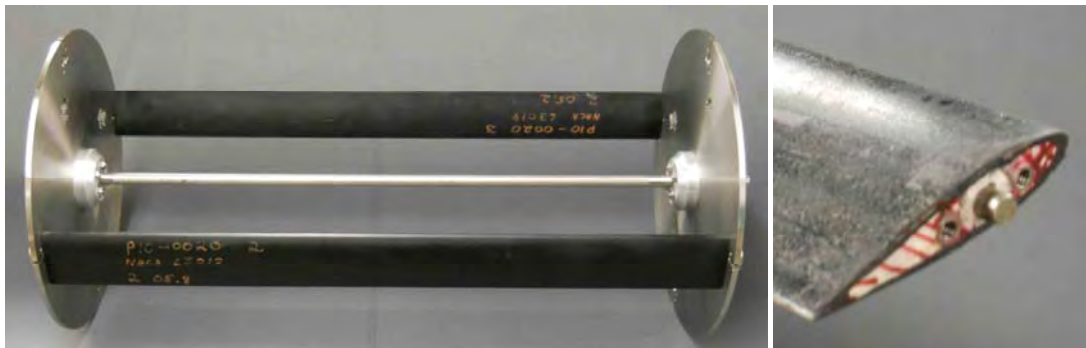


Figure 3.5 Test turbines lower assembly with two blades and NACA 63018 blade profile.

The maximum performance coefficient from the test turbine is small compared to that of the large-scale turbines used by renewable energy developers. This discrepancy in performance is due in part to the nature of scaled testing, in which the Reynolds number and drag coefficient do not scale equally. The drag on individual blades of small-scale turbines is proportionally higher than large-scale turbines, leading to reduce overall performance.

3.2.3 Confirmation of Measurements

Initial trials of the test turbine were conducted with the objective of determining the accuracy and repeatability of the measurements. Shake down testing revealed significant vibration present in the drive train that could potentially mask the torque measurement. To confirm that the measured forces reflect the forces acting on the turbine, a series of tests were performed to determine the frequency response of the drive train and support structure. The same load cells used for normal testing were used in this frequency analysis. The drive train was disconnected incrementally from the turbine blades to the motor bearings to determine each component's effect on the measured forces. The motor was run at test speeds during the test to measure the drive noise. Further trials included an impact excitation test that measured the drive train's response to a sudden impulse typical of straight blades testing. From the data gathered, the amplitude and fundamental frequency from rolling noise was determined for each component in the drive train. These results were used to dampen the largest contributors.

The largest source of noise, which was also the easiest to eliminate, was the chain connecting the upper and lower drive trains. Chain oscillations were being amplified when the motor switched from braking to driving. The noise was removed by developing an improved chain pretension technique and adding a chain dampener. The chain dampener consists of plastic wedges to stop oscillations from propagating through the chain to the upper drive train. Upon completion of the drive train evaluation, a number of other smaller issues were identified and the effects on the drive train addressed. For example, the alignment of the blades and plates was addressed by introducing improved alignment techniques as well as refashioning the blades to tighter dimensions and improving the end connection.

The refined drive train performance improved the results of the harmonic analysis of the torque measurements as a function of motor speed. The improved consistency is shown in Figure 3.7. Results are for the entire drive train with all components used during a test connected. In

Figure 3.7, the first three harmonics dominate the torque measurement with the magnitude of the response, seen in the z-axis, within allowable limits. Identification of noise sources was aided by a linear response to motor operational speed. The linear response of the noise confirmed the result from the incremental test, which concluded that the majority of the remaining noise was from inside the motor and gearbox. The linear progressions match the output shaft rotation, shown by the red line, and the internal rotations of the motor. The motor uses a three to one gear ratio, shown by the green line. The harmonic analysis also provided information necessary for post-processing the force measurement. The most useful information acquired from the analysis was the cut-off frequency for the digital filter used to determine the force coefficients. The vibrations of the structure had a higher fundamental frequency response, than the data of interest so that a low pass filter could be used to prevent any adverse issues.

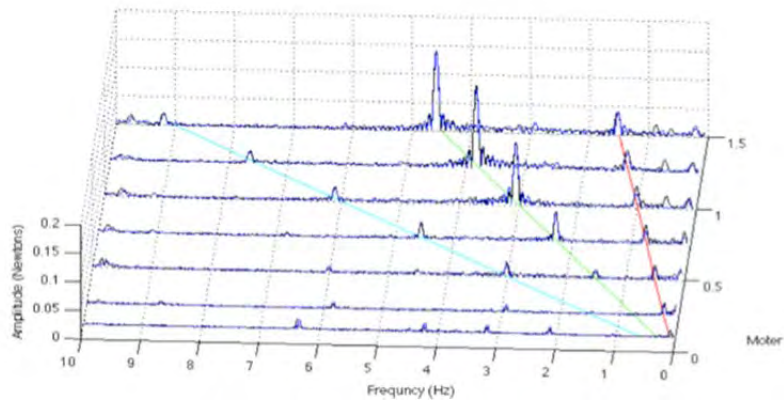


Figure 3.6 Multiple fourier transform for increasing motor rotational speed show the torque response of a freely rotating turbine.

3.2.4. Turbine Measurement

Two different turbine setups with resulting operational characteristics are shown in Table 3.4. The results are within five percent of other measurements which were primarily focused on determining the efficiency of the turbine (Debree, 2012).

(Hz)

Turbine Coefficients NACA 63018, $\alpha=+5^\circ$					
	Solidity	TSR	Cp	Ct	Ch
Set A	0.16	2.25	0.26 ±0.006 (Reverse & Forward)	0.30 ±0.012 (Reverse & Forward)	0.16 ±0.02 (Forward) 0.02 ±0.02 (Reverse)
Set B	0.32	0.9	0.12 ±0.006	0.29±0.012	NA
		1.4	0.24 ±0.006	0.32±0.012	
		1.9	0.15 ±0.006	0.34±0.012	

Table 3.4 Force coefficients form dynamo results form the two data with different solidity

The drag data showed a linear correlation with the TSR. However, the data set was insufficient to draw broad conclusions. The effects of the floor and the free surface were presumed to be the cause for the two different heave results. The carriage runs both forward and backward, while the turbine rotates the same direction, which reverses the turbine's operational orientation relative to the surface and floor. During the forward run the power side is closer to the floor, and during a reverse run the power side is closest to the surface.

The low solidity dynamometer results are shown as a function of blade position in Figure 3.8. The low solidity turbine used two blades, which resulted in each force having a period of one half of a rotation. Figure 3.8 also includes two independent tests of the same configuration to display the repeatability of the measurements. The figure shows that the drag forces are the most consistent, with the highest drag force occurring when the blades are perpendicular to the flow. The torque curve varies slightly in shape, but it integrates to approximately the power coefficient.

The shape difference between the two directions can be correlated to the standard wave patterns: the solid line is similar to the square wave, and the dotted line resembles the triangle wave. The graph shows a different shape for the heave measurements in each direction and from the table 3.4 shows the integration does not converge to one value. The differences in the torque measurement between forward and reverse runs are unexpected however, possible cause is from the change in boundary conditions with the floor and surface relative to the turbine.

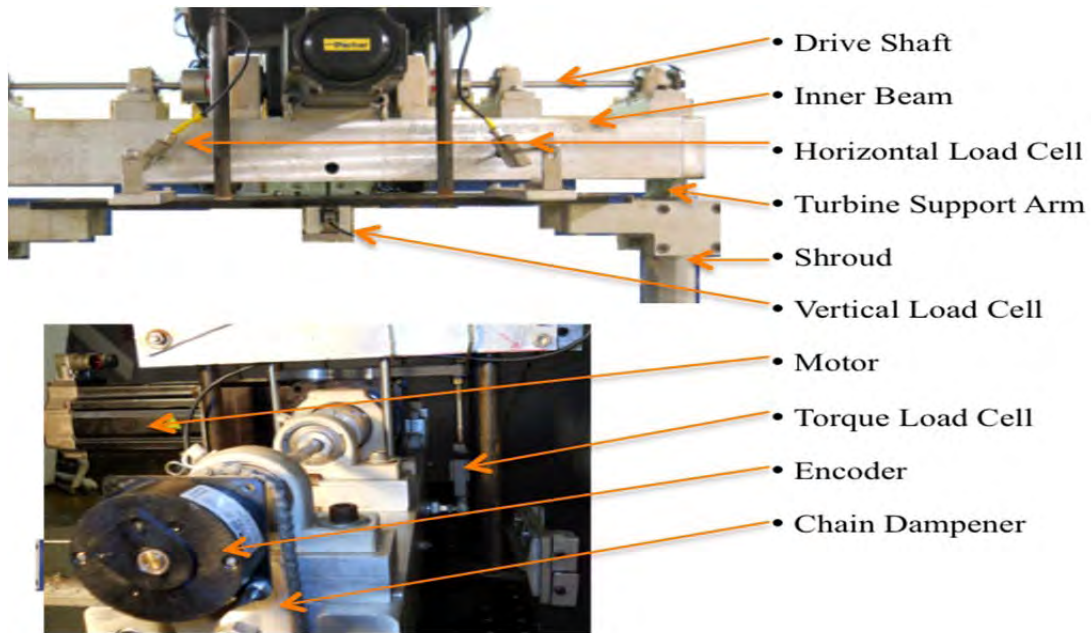


Figure 3.7 Dynamometer results as a function of blade position for low solidity with different inflow directions

The significance of the force measurement for this wake study is to show the force acting on the fluid in all test configurations. To illustrate the complexity of analyzing the wake, tests were performed over a range of inflow speeds and TSR. This behavior illustrates how the coefficients change with different inflow speeds and TSR. Variation in TSR and the effect on performance is a well-known characteristic of any hydrokinetic device, and is not within the scope of this paper. However, the turbine's method of interaction with the fluid is subject of this study. Figure 3.9 shows how the instantaneous non-dimensional form of torque and drag change with blade position and TSR. The torque demonstrates a phase shift as the TSR increases from 1

to 3 units. There are no measurements significantly distant from the optimum TSR of 2.25. The lines above the optimum performance show a growing trend in which more power is needed to maintain the rotational rate compared to low TSR. The forces do not exhibit any change in terms of the drag coefficient. All line in Figure 3.9 has a corresponding black dashed line with a height of zero along its TSR value to aid visibility.

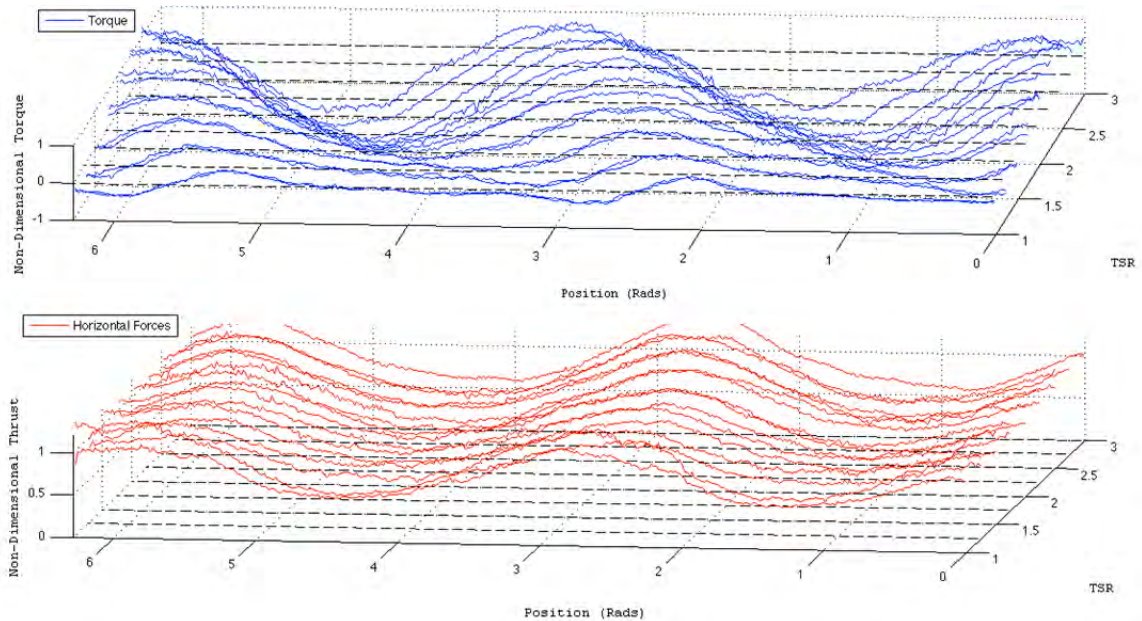


Figure 3.8 Torque and drag force coefficients as a function of blade position and tip speed ratio (TSR)

To further investigate how the turbines' interaction changes, TSR is maintained at the optimum level and the inflow speed is varied. The dependent variable from the previous test becomes the independent variable in order to evaluate these two turbine variables. The results for the varied inflow speed, seen in Figure 3.10, exhibited a different response compared to the result obtained by varying the TSR. These results show decay in the drag coefficient as the speed increased. The shape and amplitude of the curves remained constant; the only effect is on the offset. The torque curve remained constant if the maximum and minimum inflow speeds are

ignored. The blockage effect might have caused the discrepancy at the highest speed in the Figure 3.10. The blockage effect is discussed in the discussion section.

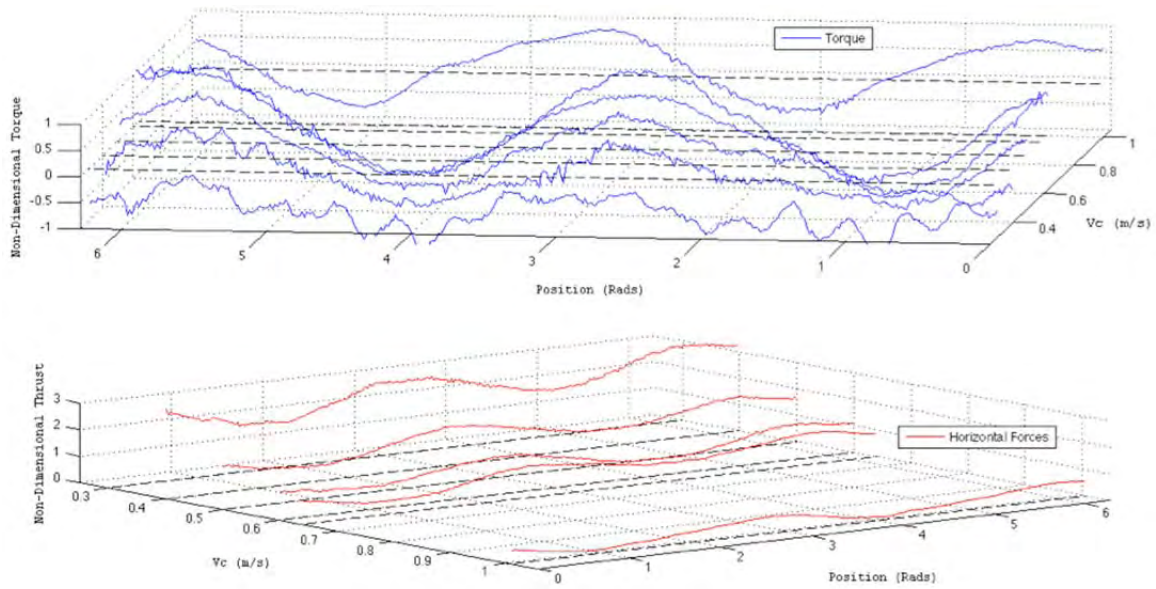


Figure 3.9 Torque and drag force coefficients as a function of blade position and inflow speed (V_C)

3.3. Acoustic Doppler Velocity meter (ADV)

The ADV used in this study is the Nortek Vector Velocity Meter (NortekUSA, Vector Field Velocimeter, Boston) (Figure 3.11). The device has been proven effective in measuring fluid velocity in a wide range of environments when deployed appropriately. The functionality and the accuracy of the device has been addressed elsewhere (Lohrmann, 1994; Rusello, 2006; Blanckaert, 2006). The ADV measures three-dimensional flow while providing minimal flow unobstructed at a reasonable high sampling rate, and are commonly used to study velocity fluctuations, turbulent shear, and other disturbances.

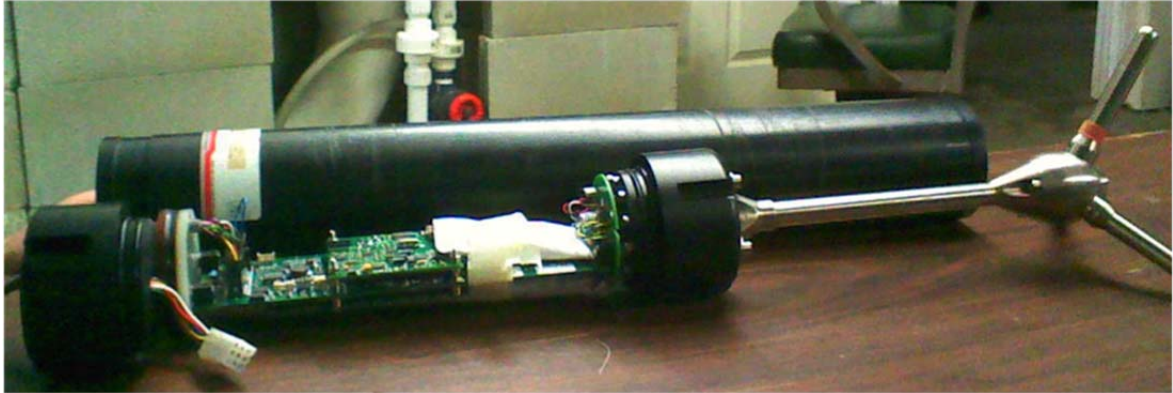


Figure 3.10 The acoustic doppler velocity meter ADV. The Nortek Vector Current Meter with its circuit board exposed.

In the field, ADVs can be operated in both salt- and freshwater environments and are typically deployed in the bottom boundary layer using a tripod or hanging from a moored buoy. This type of deployment provides a rugged structure to support the device in a harsh environment. In the lab setting, the ADV can be operated in a similar fashion, with the option of including an additional communication connection to allow for real-time monitoring and reprogramming.

The signal repetition rate for the ADV is higher than the rate at which data is stored to the memory. The ADV internal software is used to average the data and/or eliminate readings that are classified as irregular based phase-space algorithm. The velocity measurements are stored at a rate of 64 samples per second and the ping rate varies with the expected flow velocity. The ADV measures the three-dimensional velocity from acoustic Doppler shift in a region, referred to as the sample volume, ~15.7 mm in front of the ADV. The shape and size of the sample volume can be approximated by a cylinder with dimensions that can be changed with the internal setting of the ADV. Each reflection is measured by three acoustic receivers located around the sample volume (Figure 3.12). The velocity along the beam to each receiver is determined by comparing the source beam to its respective beam reflection. Using the position and orientation of the three receivers, the three-beam velocity can be converted to velocities in a Cartesian coordinate system, with the axes relative to the acoustic head (see Figure 3.12). The geometry of the three beams'

angles yields a greater resolution and range of velocity measurements in the z-direction compared to the x and y directions shown in Figure 3.12. The asymmetrical velocity resolution was considered in experimental setup to capture the higher velocity and higher fluctuations with the more sensitive direction.

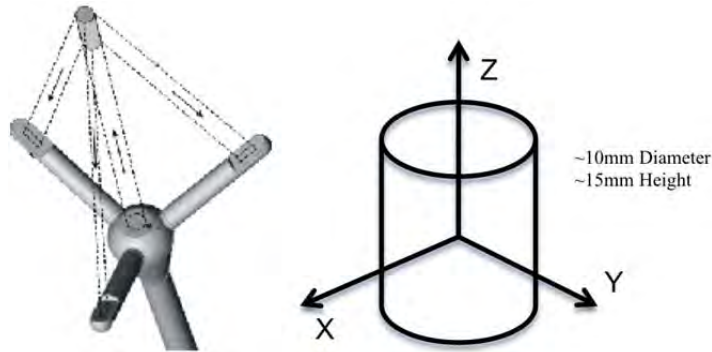


Figure 3.11 ADV's acoustic Head and sample volume with detail drawing of the acoustic head and sample volume with coordinate system

The quality of data depended on the acoustic properties of the measured fluid. For quality data, the water needs to have suspended particulates with high acoustic reflectance. The strength of the return signal is measured as the signal to noise ratio (SNR). The SNR is a non-dimensional number that compares the returning signal strength to the background noise. An arbitrary signal to noise ratio was determined through testing experience to be greater than 20.



(6)

In order to obtain the required signal to noise ratio in the field lipids in plankton and other suspended matters provide the necessary reflection for acceptable signal strength. However, the tow tank water did not have a significant amount of biomass or suspended particles. To obtain high SNR, the water in the tow tank was seeded with neutrally buoyant hollow glass spheres. The spheres are provided strong acoustic reflections in the water. The addition of glass spheres enhanced the signal strength to acceptable levels. However, the SNR declined over time and had to be monitored.

The velocity data from the ADV is the average velocity of a sample volume over a period of time. The sample volume is cylindrical, 10 mm in diameter and 15 mm in height (see Figure 3.12). The height of the sample volume is related to the amount of time the receiver is active: the longer the receivers are active, the stronger the signal becomes. The ADV is very accurate in measuring creep flows with little velocity fluctuation, such as the laminar boundary layer found near river or sea bottom. On the other hand, with a change to the ADV settings, the ADV is capable of measuring velocities up to 7 m sec^{-1} . The precision of the measurements suffers in this high velocity range. The experiments in the tow tank covered a wide range of velocities and large accelerations, so an additional step was implemented in post-processing that will be discussed in section 4.1.4.

Several modifications to the ADV were needed in order to position the device in the tow tank and synchronize the ADV data acquisition with the turbine data acquisition system. The size of the ADV with the large battery bank was problematic in the tow tank. The ADV's original configuration consists of a waterproof cylindrical tube attached to an acoustic probe. The tube section is 0.55 m long and has an outside diameter of 7,5 cm. The tube cavity houses the circuit board and the large battery needed for long deployment. With the addition of the acoustic probe, the overall length of the ADV is 0.85 m. A shorter tube used to reduce the ADV's size in the tow tank. While this approach addressed the size issue, however created challenges for the communication.

There are three options for communication to the shore powered ADV. The options are 20-meter RS-422, a 6-meter RS-232 with auxiliary inputs, and a modified RS 232, which was ultimately used. The RS-422 cable uses two wires transmit the serial communication and the third powers the ADV from shore. The ability of this channel to power the ADV from shore makes it possible to remove the large battery and use the shorter tube. However, the RS-422

cable does not provide analog channels, leaving the ASCII mode as the only means for communication apart from the proprietary software. However, the ASCII mode has proven unreliable in synchronization. An alternative for communication was explored by connecting the RS-422 cable to a second computer independent of turbine and carriage system, which led to a new problem when synchronizing the ADV measurements with carriage and turbine data. The computers were synchronized to a single clock across a network connection. However, after several attempts to synchronize the ADV's internal clock with the computer it became clear it lacks sufficient accuracy.

The second option was to use a 6-meter-long RS-232 cable with three auxiliary input/output analog channels, providing the means to easily synchronize multiple systems. Two major disadvantages to this method: are the RS-232 cable does not provide the option of powering from the shore, so the ADV has to use the internal battery. This causes the length of the device to be cumbersome in the confined space of the tow tank. Second, the short cable length of the RS-232 cable limits the distance between the ADV and the carriage, placing the equipment at risk during testing.

Ultimately, the RS-232 cable was selected with a modification to the ADV's internal wire harness and the function of the communication wire. The modification enabled the ADV to be powered from shore removing the battery and shortening the ADV's length. Three lines were used to carry an analog signal to the surface. This modification combines the best features, shore power and analog channels, from both options.

3.4. Pressure transducer

In addition to velocity measurements, the surface elevation was also measured to characterize the hydraulic jump caused by the turbine. The equipment used to measure elevation was a pressure transducer mounted to the ADV tripod under the ADV sample volume. The

pressure transducer must be sensitive enough to resolve millimeters of change in surface height (1 mm water height is equal to 9.8 Pa) while operating in less than 1.2 m of water (11.7 kPa). The selected hardware for this study was a pressure transducer PX409-2.5GI (Omega Engineering inc., Stamford CT.) with a full-scale pressure of 17.2 Pa and an accuracy of 0.05%, providing a resolution better than one millimeter. A flow shroud, an aluminum pipe with a series of relief holes and a sealed bottom, was utilized to prevent erroneous surface elevation measurement associated with the Bernoulli's effect. The shroud and pressure transducer can be seen in Figure 3.13 with the pressure transducer. Sequences of tests were performed to check the effectiveness of the flow shroud by exposing it to a water jet. The results revealed that the shroud was effective at nearly all angles, with the only exception when the jet was pointed into the pipe. We estimated this effect to be negligible since a strong downward jet of fluid rarely occurred near the floor of the tow tank during the tests. The pressure signal needed to reach the data acquisition system located on the moving carriage through an 8 m long wire. The wire connection to the carriage limited the carriage travel to 15m. The output from the sensor was 4-20mA to prevent noise effect.



Figure 3.12 Pressure transducer and flow shroud configuration to measure the surface elevation on the floor of the tow tank.

3.5. Test configurations

The ADV was initially fixed underneath the carriage with the acoustic head pointed downward, partially submerging the lower half. The addition of a two-dimensional traverse was added to allow the ADV to move behind the turbine during and in-between tests. The traverse

consisted of two actuators that moved the ADV horizontally and vertically. During a test, the vertical actuator would be triggered automatically and slide downward until the end of the test. This configuration allowed the measurements of velocity profiles in the wake at short distances behind the turbine. Figure 3.15 shows a data sample with three-dimensional velocities from six traverses at different horizontal distances from the turbine. The vertical velocity is represented by the color of the dot located at the ADV's point of origin, which represent velocity magnitude. Due to the space limitation underneath the carriage and the length of the ADV, the bottom half of the wake could not be measured. The data shows a section behind the turbine where a large mass of water was entrained vertically through the water column.

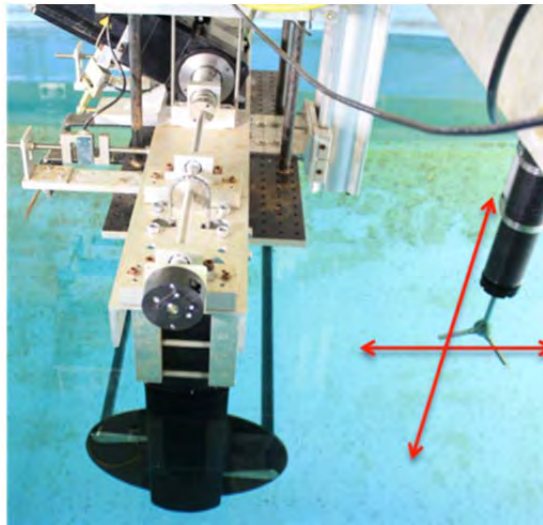


Figure 3.13 ADV's carriage mount setup with two degrees of freedom. ADV was capable of moving in two dimensions in a plane normal to the turbine axis of rotation.

Carriage vibrations, coupled with the flexibility of the ADV mount, which led to uncertainties in the velocity data. Accelerometers were attached to the carriage to address determined the severity of the vibration. The accelerometer results were processed by a discreet Fourier transforms to convert the acceleration measurements to the frequency demand. The strongest amplitudes were in the measured in the vertical direction with the dominant frequencies between 1.5 to 2 kHz. The acceleration results where high enough to potentially contaminate ADV recordings, therefore, this mounting method was abandoned.

One alternative to mounting the ADV to the carriage is an overpass method, in which the ADV is mounted on a tripod and placed on the floor of the tow tank (Figure 3.15). Having the ADV stationary on the concrete floor alleviated the problem of data contamination by carriage vibration. As mentioned above in Section 3.3.1, the velocity component in the direction emanating from the acoustic source to the sample volume (z-axis in Figure 3.12) is more robust and reliable. Given this characteristic, the ADV was placed in the x-z plane, pointing the direction down the length of the tank (x-axis in Figure 3.16). The ADV also created the smallest flow obstruction in this configuration. Due to the confined space of the tow tank, the ADV had to be mounted at an angle from the floor to clear the turbine overpass. The angle of the ADV in the stand could be changed to vary the distance between the ADV's sample volume and the center of the turbine. The pressure transducer was mounted on the same stand as the ADV, and was situated underneath the acoustic sample volume Figure 3.13. Given the sample volume location relative to the ADV acoustic head, it was possible to measure the velocity a few centimeters into the turbine-swept area. This configuration became the favored method for this study because it also measured the entire wake at a constant height, as well as the flow field as the turbines approached the ADV. A full outline of the deployment procedure is given in Appendix A.



Figure 3.14 ADV and pressure transducer with flow shroud mounted to the adjustable floor tripod.

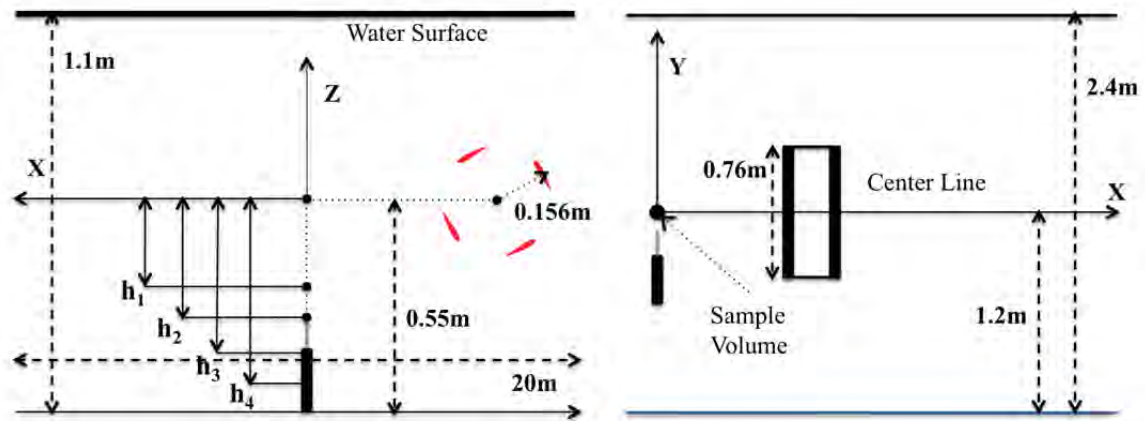


Figure 3.15 Illustration of side and top view of experimental configuration. Two view drawing of experimental setup . X-Y Plane (Left) and X-Z plane (Right).

The mounting fixture used in the overpass configuration was a weighted tripod. The function of this tripod was to provide a rigid stand for the ADV and to provide the ability to change the ADV angle easily while the ADV was on the bottom of the tank (Figure 3.13). Being able to change the sample volume height without needing to remove the entire apparatus simplified the calculation of the relative position of the ADV to the turbine during data processing. The series of vertical positions of the sample volume were measured outside of the tank and were cataloged for post-processing. Changing the height enabled the construction of flow field in a two-dimensional x-z plane. The three-dimensional velocities were measured with the ADV converted from the reference coordinate of the sample volume (see Figure 3.12) to the reference coordinate chosen for the tow tank (see Figure 3.16) later in post processing. The archive data included three or four different heights. These heights, coupled with the ability to run the carriage backward, made it possible to create a data set both above and below the centerline of the turbine. The final data arrangement, seen in Figure 3.17, shows the two different carriage directions combined to produce the upper and lower portion of the wake. Note that the composite image may distort the actual characteristics of the upper portion of the wake because of the different condition for a free surface and the floor. This will be discussed further in subsequent chapters.

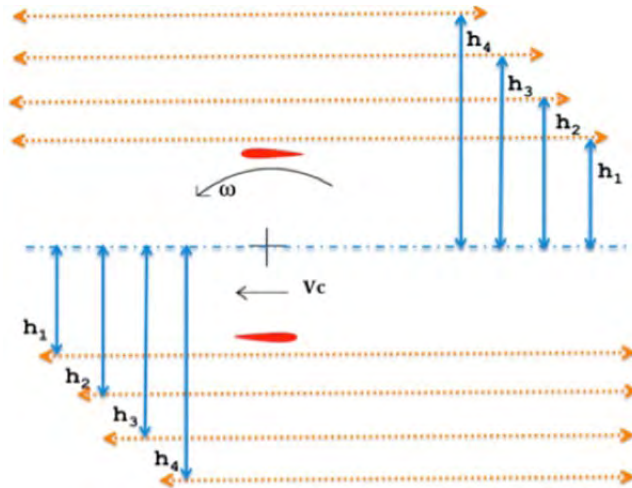


Figure 3.16 Approximation of flow field drawing of different ADV sample volume height with respect to turbine

A large number of tests were necessary in order to obtain meaningful results. We considered a number of variables, including ADV velocity range, the carriage direction, the sample volume height, the horizontal distance from the turbine center to the sample volume, and the blade position over the sample volume. All of the variables except the blade position were easily controlled and monitored. The objective of the repeatable blade position was to have the turbine blade positioned at a particular angle (± 5 degrees) when the turbine passed over the ADV sample volume. Three methods were attempted, with different degrees of success. The first method returned the blade to its original angular position before the turbine and carriage were accelerated to their test speeds. This method yielded a repeatability of 20 to 40 degrees and was not significantly better than a random blade position test performed without constraining the initial angular position. The next iteration used a feedback control loop in addition to the initial controlled blade. The control algorithm monitored the distance traveled by the blades and turbine and provided feedback to the motor control array. This second method did not produce any significant improvements in blade angle repeatability. The limit to the feedback control was diagnosed from process programming: the time when the carriage and turbine were accelerating was a period of high speed and was the major cause of variation in the repeatability. To mitigate

variation, a feedback controller was utilized to develop the final experimental design. The turbine remains at rest until the carriage traveled a certain distance from the starting point. This final method resulted in a repeatability of ± 3.5 degrees.

3.6. Programmable Controller and Data Acquisition

A programmable real-time controller was used to control, record, and integrate the carriage, turbine, and ADV operation and data collection. The hardware consisted of a controller (NI cRIO 9073) from National Instruments (Austin Texas) that was connected to its host computer, which ran the NI LabView software. The cRIO was an independent controller with one processing unit and memory designed to run input and output (I/O) utilities. For simplicity and reliability, all I/O signals connected to the cRIO were analog. The digital encoder used was connected to analog converters then to cRIO.

Programs for the cRIO and host computer, and the architecture of the hardware were designed to meet three specific criteria: high sampling rate, continuous test time, and the ability to update graphical output in real time. These criteria were met by splitting the tasks between the host computer and cRIO through a shared memory network, which allowed data to be streamed without interruption and at high throughput. The cRIO was programmed to run the I/O utilities by updating the outputs while writing the inputs to the shared memory. The host computer updated the graphics for users and removed data from the shared memory to stay within memory limits. While the test was running, the host computer wrote the data to a binary file on the host hard-drive and converted the binary file to a text-file once the test ended. The cRIO memory size was a limiting feature of the device with 250 KB overall and 20 KB free space after programs and drivers were installed. With the limited memory, and a high sampling rate, long test times, and ten input channels, the cRIO was not capable of independently handling data storage alone.

The host computer was monitored by an operator, who input test parameters. The host computer generated the acceleration curves to be used by the cRIO during the ramp-up and ramp-down stage. The acceleration curves were sent to the cRIO, which supplied the turbine and carriage output channels with an analog signal to a variable frequency drive. Once a test was initiated, the cRIO began to record data from six channels from carriage-turbine system, and four channels from the ADV. The primary objective at this stage was to accelerate the turbine and carriage to the target speed. During the acceleration stage, the cRIO was run at a lower rate to reduce the size of the control curves. In the ramp down stage of testing, the data acquisition was stopped, and the same curve from the acceleration was used but read in the opposite direction.

The acceleration stage was followed by the constant speed test period where data acquisition was performed at high sample rate. The sample rate for the cRIO was raised to 2 kHz during this period, and since the ADV had a significantly lower rate of 64Hz a second independent data stream was added for the ADV. The high sample rate for the pressure transducer, turbine, and carriage became unnecessary once the shakedown tests were finished and the system dynamics were well understood. The two streams of data were sent to their independent memory buffers. To avoid both computers accessing the same memory at the same time, the cRIO signaled the host computer when to clear the memory. The host removed the data and sent it to a binary file, and updated the user screen for a near real time display for the operator to watch and confirm the data quality. Figure 3.18 shows the bidirectional flow of data from the carriage computer to the three systems.

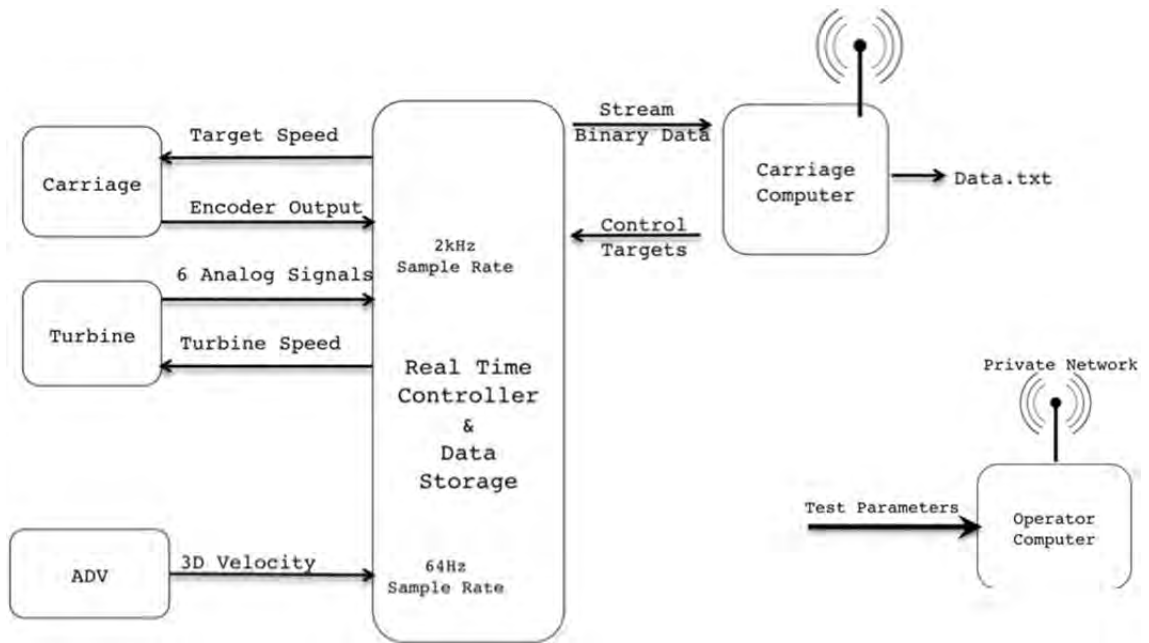


Figure 3.17 Flow diagram of controller and data acquisition. Flow chart of operator inputs and I/O data through the automation system

3.7. Synchronization

Multiple methods were tried to synchronize the systems, which resulted in a final method that is simple, reliable and accurate but requires a large amount of post processing. The final method linked the systems together by connecting carriage computer to the ADV located on the floor of the tow tank. A tether carried the command from the operator as well as data communications to the DAQ. The DAQ recorded both the turbine and ADV data in different files and were synched by a shared time array. However, by comparing both internal and analog data the analog signals did not match the internal files thus the analog signal was only used to synchronize the internal ADV data to the DAQ's clock.

Post processing of the signals used Matlab (Math Works 2009b) to handle the data unpacking, sorting, and data saving from the two Labview files and ADV internal file. The first step in the process is to unpack the data, performs basic conversions of the analog signals to physical units, and performs filtering on the load cell data. In the first synchronization step, the two velocity files were plotted next to each other and a corresponding point was identified in both

files. At this point, the process of matching the Labview and ADV internal files has not been done with automation. Each file was identified at an indicial point using the MATLAB's graphical tool and combined to form a synchronize date. This data is then synched with the turbine to identical data stored in the ADV internal memory. Each file was thus marked with a data stamp that corresponded to the data mark. Once all the files were marked, the second m-file was used to repack all the ADV internal files and associate each ADV with the corresponding turbine file.

With the turbine and ADV files linked, the instantaneous position of the blade can be calculated from three degrees of freedom with respect to ADV's sample volume. The three degrees of freedom consist of the vertical position of the ADV, the horizontal position of the carriage, and the angular position of the turbine (see Figure 3.19).

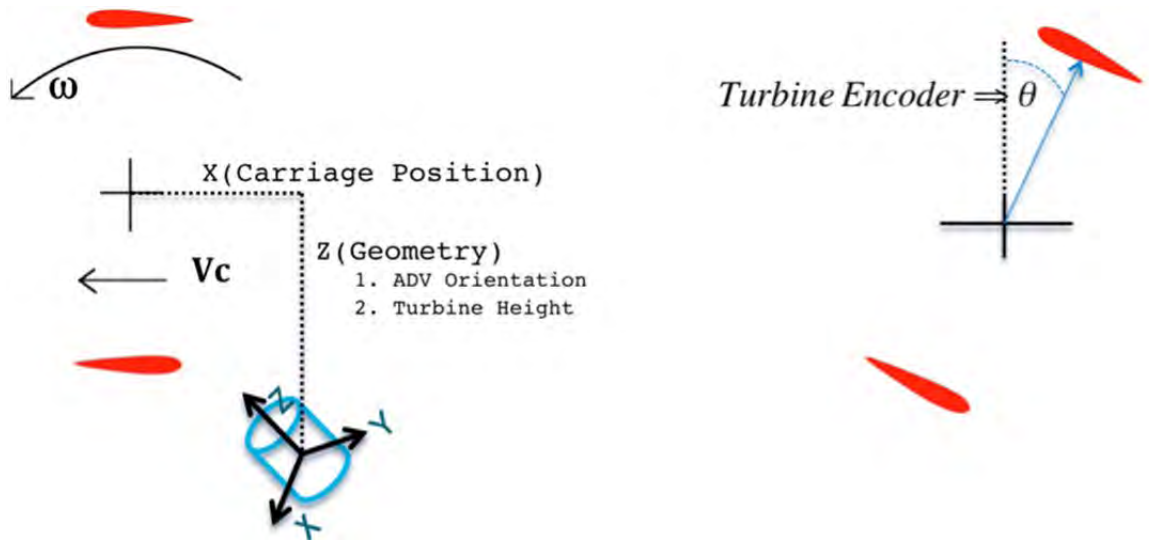


Figure 3.18 The three variables needed to determine position of the sample volume relative to each blade.

In order to determine and incorporate the relative position of the ADV into the synchronization of the data, a constant starting position for the carriage was used. For each carriage direction, a separate calibration run was conducted. Unlike normal runs, the system was controlled manually during the calibration run and the turbine was fixed at a predetermined

angular position. The carriage was moved until the lower blade intersected with the sample volume, causing a drop in the ADV's signal-to-noise ratio. At the point of intersection, the carriage was stopped and the carriage encoder data was integrated to find the horizontal distance from the starting point to the ADV sample volume. The angular position of the turbine was held constant at a predetermined angle, allowing the leading edge of the blade, located at the center, to maintain the measured distance from the sample volume to the turbine center.

To find the relative vertical distance from the sample volume to the turbine center two measurements were taken. The vertical position of the sample volume was measured outside the tank, while the vertical position of the turbine centerline was measured in the tank, and the difference was the relative vertical distance. The measured values were logged and retrieved later during data processing.

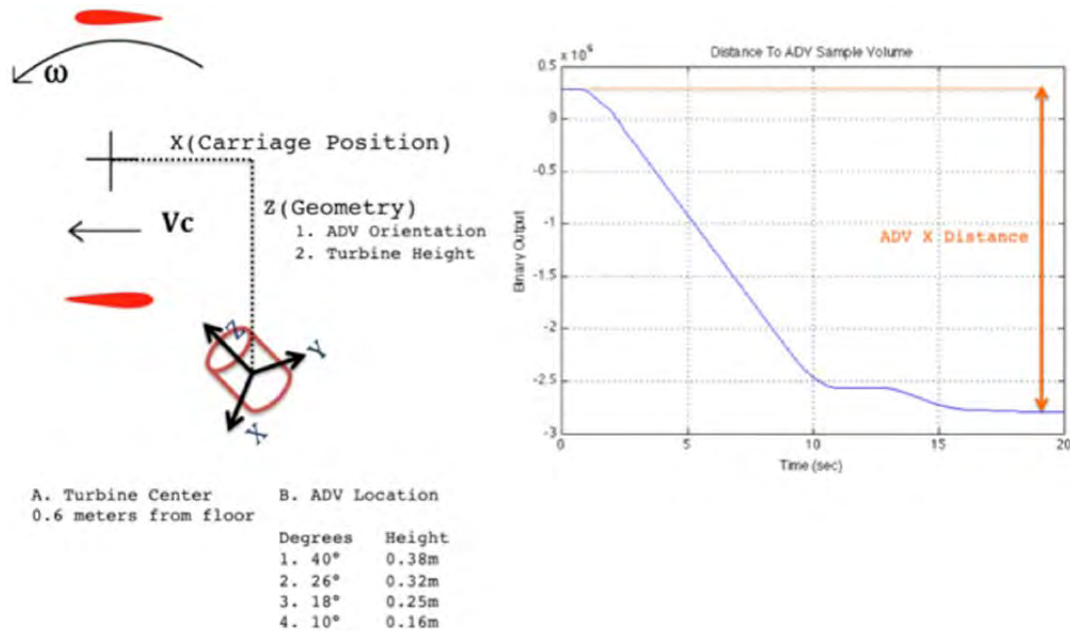


Figure 3.19 Calibration data used to measure position of turbine relative to the ADV sample volume.

The angular position of the blade was recorded by the cRIO and then converted to radians. The value was then used to calculate its instantaneous position in the chosen reference frame. The position of each blade was converted in to x and z components, with the center of the turbine

at the origin. The addition of the carriage position to the x-component yielded the relative position of each blade to the sample volume. As seen in Figure 3.21 below, the two-blade path was represented with two lines as it passed the sample volume located at zero distance.

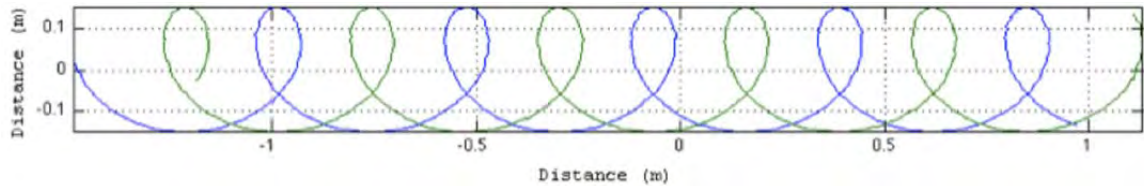


Figure 3.20 Tracking Blades with respect to ADV'S sample volume. Path of two-blade over the ADV's sample volume where x-axis represents the blade's horizontal distance to the ADV sample volume and the y-axis distance relative to the center of turbine

The blade path was repeatable over many tests, maintaining an accuracy of ± 3.5 degrees over the sample volume. The method used to calculate the blade path is described in Section 3.3.2. The blade path is not relevant in the analysis; only the instantaneous position of the blades over the sample volume is needed.

4. DATA ACQUISITION AND POST PROCESSING

4.1 Analog I/O

To develop a means of tracking the individual blades during a test the measurements of the angular position of the turbine and movement of the carriage along the track were required. An absolute encoder was installed on the upper assembly and attached to one of the two drive shafts located on the upper assembly. The upper-drive train was geared one-to-one with the turbine. As a result, one rotation of the absolute encoder corresponds to one rotation of the turbine. The signal from the absolute encoder is a linear signal from zero to five volts, which corresponds to a position between 0 to 2π radians. Hence, the encoder curve consisted of a saw-tooth signal (Figure 4.1), and only a calibration constant was required to convert analog signal to the angular position.

To standardize the blade position for all tests a procedure of alignment the turbine encoder to a blade position was established. The turbine and encoder were placed at the zero position by manually rotating the turbine until one blade was located at the top dead center. Then, the encoder was spun until its output was reading zero volts, putting the blades and encoder at a known position. With the turbine and encoder synced this way, the blade location could be determined at any time during a test.

Analog Position Measurements

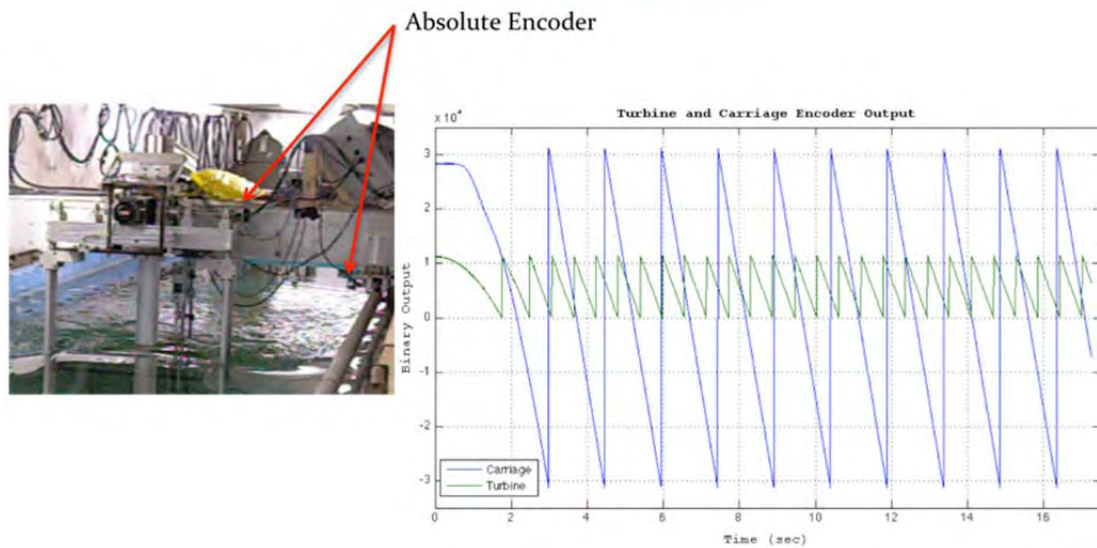


Figure 4.1 Encoder curves from turbine and carriage from a test starting at rest.

The method used to measure the carriage position was similar, to the blade position measurements. However, the method needed to be refined due to the distance and the required accuracy of tracking the carriage position within millimeters. Unlike the turbine encoder, which measures the position directly, it was impractical to measure the carriage position directly because of the long distance traveled. A series of solutions were implemented by using a digital encoder augmented with a digital-to-analog converter. The converter maintained a data acquisition system that used only analog signals as well as providing a reliable and adaptable signal to best fit the experiment objectives. The result from the encoder and converter was an analog signal of a saw-tooth wave similar to a rotary potentiometer. The saw-tooth wave ranged from -10 to 10 volts (Figure 4.1), with one tooth equal to 8.3 revolutions of the carriage encoder. This broadens signal range made it possible to obtain the carriage position measurements accurate to within ± 2 mm.

A numerical processing procedure was needed to convert the saw-tooth signal into a curve that represents the actual carriage position with respect to time. The saw-tooth signal had

discontinuities where the value jumped from 10 to -10, which needed to be removed to reconstruct the actual position. To find the discontinuity the derivative of the signal was evaluated. If an exceptionally large change or sudden change of sign occurred, the derivative was replaced with the mean value. The new continuous signal was then passed through a zero phase shift digital filter with a cutoff frequency of 40Hz to remove any electrical noise. The steps of converting the encoder data to the carriage position are shown in Figure 4.2. The filter did not affect the carriage position measurements since its velocity oscillations are much lower, ranging from 0.1 to 20 Hz. At this stage, the filtered data had the unit of volts per unit time.

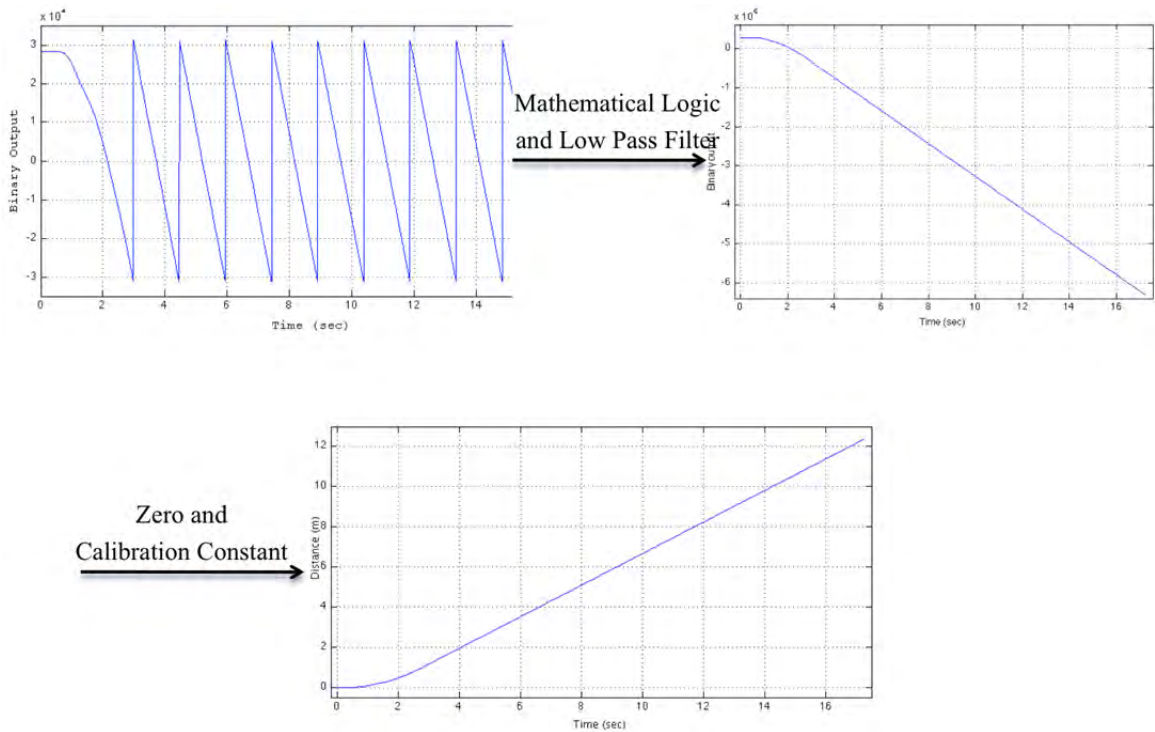


Figure 4.2 Steps for processing the carriage encoder signal. Raw data (upper left), steps removed (upper right), and final instantaneous position curve (bottom).

The filtered derivative term from the position was used to reconstruct the carriage velocity. The carriage and turbine speeds are shown in Figure 4.4. The calculated carriage speed was not directly used in the wake analysis, but it provided to better understanding of the system speed control. For example, certain combinations of carriage and turbine speeds for a low solidity turbine would produce an unstable speeds for both the turbine and carriage. The fluctuations

could reach as much as 20% of the target speeds. Fortunately, the unstable oscillation became more prevalent far from the peak performance and was thus of little immediate interests.

4.2 ADV measurements

The ADV data were saved in two ways. The simplest and most reliable method to obtain acceptable velocity was to save the data internally to the ADV. However, the internal data was not synchronized with other systems, leaving the ADV data isolated from with the turbine and carriage data. The ADV memory files consisted of 12 columns of data, four of which were relevant including the signal to noise ratio (SNR) and three velocity columns. The ADV internal timer was not accurate enough to be useful in synchronization. To overcome this synchronization problem, a second data stream was sent from the ADV to the cRIO via the three analog channels contained in the RS-232 communication cable. The analog output contained the same data, which was not only saved internally in the ADV but also saved synchronously with the turbine and carriage data. To maintain high quality velocity measurement the SNR and the velocities were checked before saving. With the system synchronized, it was then possible to determine the turbine and blade positions relative to the ADV.

The raw data taken from a given experiment consists of three files: two files from the LabView program (the analog output of the turbine and ADV), and one from the ADV internal memory. The ADV internal memory was downloaded later, after subsets of test were completed. The LabView files pertaining to individual experiments contained only approximately 10 seconds of data. In contrast, the ADV's internal memory was used repeatedly over many experiments and became large, often containing 30 to 60 minutes worth of data. Figure 4.4. shows a segment of the raw velocity data from the ADV internal memory.

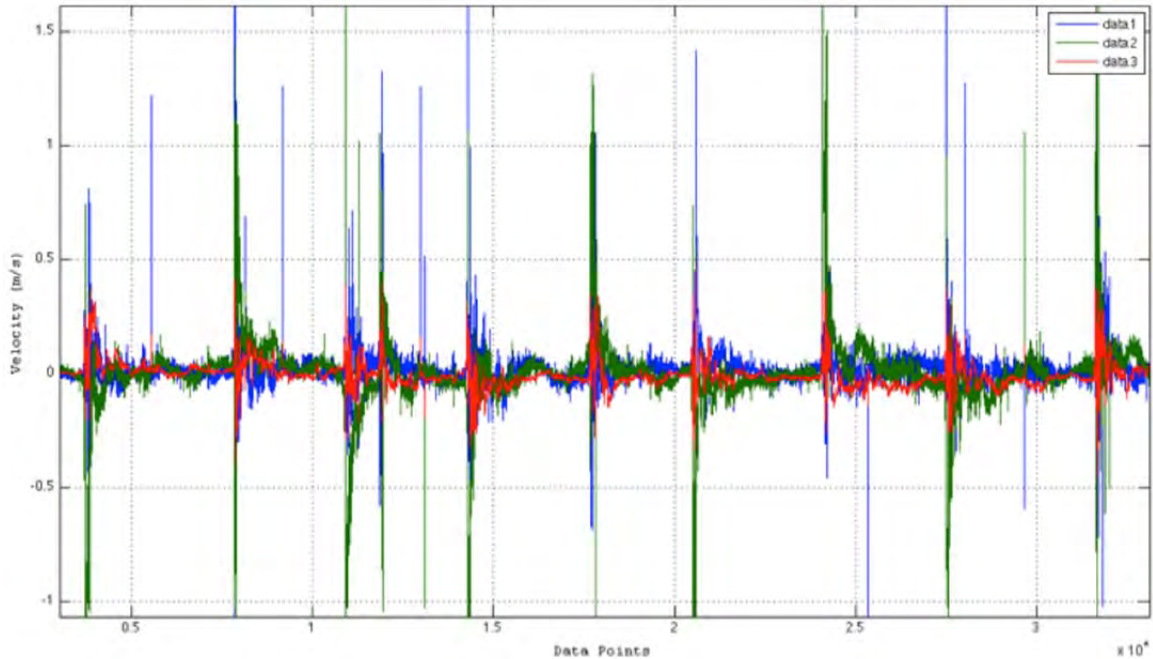


Figure 4.3 The raw three-dimensional velocity data from the ADV's internal memory

Tests were done in increments, such as a single ADV height or a single velocity range. Once a single ADV height and velocity range was complete, the data was downloaded and checked for any unobserved problem as a precaution. LabView and ADV internal files were both accounted for and checked for quality and missing data before moving forward to the next subset of data. The velocity measurements were checked to confirm that the velocity range and the SNR were acceptable. The two velocity files, one from the ADV internal files and one from LabView, were then compared to each other. It was found that the analog output of the ADV did not always match the data in the internal memory of the ADV. The ADV files from LabView were determined to be less precise than the ADV internal files, and were therefore not used for the final analysis. Consequently, the LabView ADV files were only used as a reference to synchronize the timing from the ADV internal memory files with the turbine data.

To validate velocity measurements from the ADV and the carriage encoder, a series of tests were performed in order to compare the two devices to an independent estimate, based on the time required for the carriage to travel a known distance. To perform this test, the ADV was

mounted to the carriage to measure the undisturbed flow and a 15-m section of rail was measured and marked. The tests series were done over a range of speeds. Figure 4.5 shows an example of the result that captures the carriage's initial speed oscillations as it gradually approached the target speed of 0.8 m s^{-1} . The clock time began only after the carriage reached a stable speed so the acceleration and oscillation period was not included in the time measurement. The figure does show how well the carriage encoder system worked and that the two independent measurements co-varied with time.

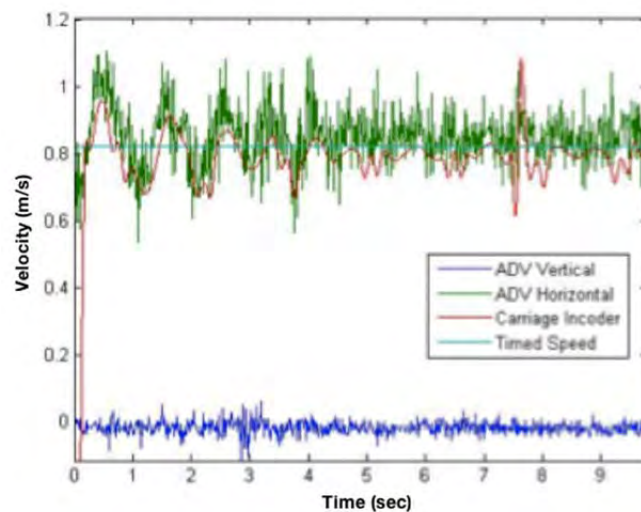


Figure 4.4 Validation of speed measurements using three different methods. Comparison of three independent speed measurements from the ADV, carriage encoder, and stopwatch during an unsteady acceleration.

4.3 Test Matrix

Measurements were obtained for different values of several key variables, including solidity, carriage speed, TSR, and blade positions. Table 4.1 shows the operating variables, corresponding performance coefficient (C_p), and the measured variables.

Set	Solidity	Carriage Speed (m/s)	TSR	Performance (C_p)	Wake Variable	Blade Position
A	0.32	1.0	1.4	Optimal	Surface Elevation & ADV	Random
B	0.32	1.0	0.9	Off Optimal	Surface Elevation & ADV	Random
C	0.32	1.0	1.9	Off Optimal	Surface Elevation & ADV	Random
D	0.16	0.8	2.25	Optimal	ADV	Three Different Blade Positions
E	0.16	0.25-1.0	0.75-3.0	All Points	Surface Elevation	Random

Table 4.1 List of test performed with turbine and measurement variables

4.4 Post-Processing

A post-processing procedure to analyze the velocity data was developed to transform these data into a usable form. This procedure included three steps: 1) rotating the ADV measurements to align with the reference coordinate of the tow tank (see Figure 3.16); 2) combining data from multiple runs of identical tests in order to produce a complete wake; and 3) running weighted windows to obtain statistical quantities with which to characterize the wake.

4.4.1 Coordinate rotation

In the first step, the three-dimensional velocity data had to be rotated from the sample volume reference coordinate (see Figure 3.12) to align with the reference coordinate of the tow tank (see Figure 3.16). As discussed above, the ADV angle changed with the orientation and vertical distance from the turbine center. There are two rotation matrices $R_i(f)$ because the ADV had two different orientations with different axes parallel to the reference coordinates. With one of the ADV directions symmetric with the reference coordinates the angle at which the ADV is

resting in the tripod was predetermined outside the tow tank. The angle (ϕ) for each vertical distance is recorded and used in the post processing.

Rotation Matrixes

$$R_x = \begin{bmatrix} 1 & 0 & 0 \\ 0 & \cos(\phi) & -\sin(\phi) \\ 0 & \sin(\phi) & \cos(\phi) \end{bmatrix}$$

$$R_y = \begin{bmatrix} \cos(\phi) & 0 & \sin(\phi) \\ 0 & 1 & 0 \\ -\sin(\phi) & 0 & \cos(\phi) \end{bmatrix}$$

$$\begin{Bmatrix} u \\ v \\ w \end{Bmatrix}_{Ref} = R_i \begin{Bmatrix} u \\ v \\ w \end{Bmatrix}_{ADV}$$

(7)

The ADV was used in two different orientations, which is why there are two rotation matrixes seen above. Only two coordinates need to be adjusted for each case. In set A, the ADV was oriented to measure the true velocity in the x direction, so the R_x matrix was used. Similarly, set B measured the true velocity in the Y direction so that the matrix R_y was used. With all the velocity data transformed to a common reference frame, data from multiple runs were compiled to form a composite two-dimensional wake field.

4.4.2 Velocity measurement range

The second step compiled measurements using different ADV measuring ranges that were obtained from multiple (usually two) runs of the same test set up. Two measurement ranges were needed because the lower measurement range was more sensitive to small velocity fluctuations but could not capture the highest velocities measured during testing. The low setting was able to measure a maximum velocity of 0.3 m s^{-1} with an accuracy of $\pm 5 \text{ mm s}^{-1}$. As a result, the lower measurement range was used to capture the flow during the approach of the turbine and the dissipation in the far field. The higher measurement range sacrificed accuracy at low velocities, but performed well in the high velocity range when the turbine was close by, where the lower

measurement range was not usable. The high velocity range allowed a maximum of 1.0 m s^{-1} with an accuracy of $\pm 10 \text{ mm s}^{-1}$. Therefore, the two measurement ranges were necessary to produce one composite set of data that represent accurately the full range of velocities during a testing.



Figure 4.5 Combination of two data sets to form a composite wake. (Left) Two curves show the velocity measurements based on identical tests but using different ADV ranges. (Right) The composite wake

The procedure for producing a composite wake was similar to the process used to synchronize the ADV data file with the turbine data file. The two velocity ranges in the file pair were plotted together and the points that required a change in velocity range were marked. The two files were then patched together to produce one complete measurement of the wake. The differences between the two time series of different measurement ranges, however, complicated the merging process. Differences were partly due to random positions of the blade as the turbine passed the ADV, which caused poor correlations between the velocity magnitude and the distance to the turbine. Moreover, abnormal readings could result from a number of things occurring when the turbine was near the sample volume. One common cause for an abnormal reading occurred when the blades passing through the sample volume resulted in the signal-to-noise ratio going to zero and led to an unrealistic spike in velocity. Another cause for a corrupted point was the fact that velocity near the blade was out of range of the ADV. Figure 4.6 illustrates the process from the file pair to the result.

The repeatability of velocity measurement as well as the measurement with respect to four test variables (velocity range, blade position, ADV height, and carriage position) was validated by

comparing identical tests. The velocity measurements were compared and found to demonstrate strong repeatability over multiple tests with identical variables. The data set was shown not only to match the velocity magnitudes, but also to repeat small fluctuations at the same carriage and blade positions. Figure 4.7 shows the result from the blade controlled directly over the ADV as well as strong repeatability between a high and a low velocity range verses carriage position.

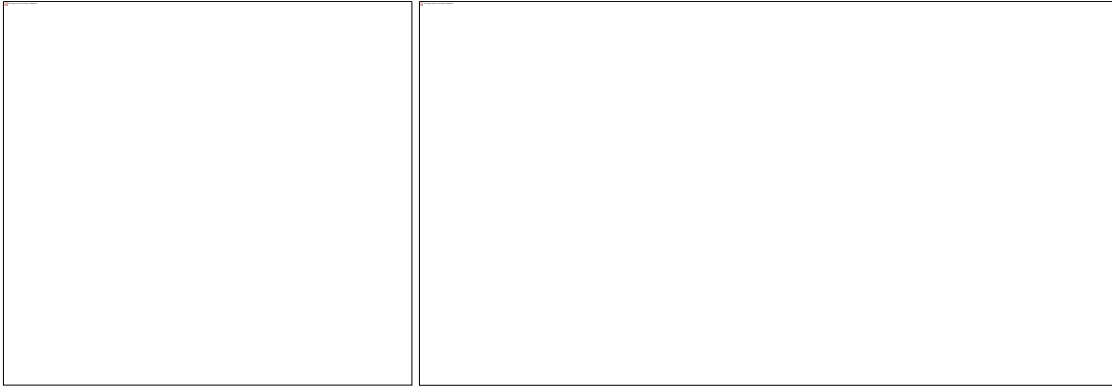


Figure 4.6. Results from the repeatability study concerning blade position and fluid velocity. (a) Results of blade position directly over the ADV, where each dot represents a blade position at $x=0$ (b) Velocity magnitudes of two independent tests showing strong repeatability from controlled blade position

5. WAKE CHARACTERISTICS

A numerical procedure was developed to process the raw data into four variables that describe the wake characteristics. The procedure utilizes the Reynolds turbulence model, in which the velocity measurements were converted into two time-dependent components, known as the mean and fluctuation terms. From the Reynolds concept other important variables and by acquired to determine the quantity, location and dispersion of turbulent energy in the wake.

5.1. Reynolds' Time Averaging Concept

Reynolds decomposition is a mathematical tool used to derive a fluctuation and mean term from single point velocity observations. The mean \bar{U} and fluctuation \hat{U} terms are two components that differentiate between steady and turbulent flow. The velocity was decomposed into the following form:

$$U_{\text{measured}} = \bar{U} + \hat{U} \quad (8)$$

The mean was calculated as a moving average over time (the averaging period will be defined in Section 5.2) and the fluctuation term was the difference between the measured value and the calculated mean. The need for the second equation is that the turbulence intensity (TI) analysis requires a modification to the standard Reynolds decomposition to avoid a mean nearing zero, in which case the mean is replaced by the root mean squared (RMS) to avoid singular points. The decomposition yielded four Reynolds terms for each of u, v, and w components and the magnitude U. The individual terms were used in the analysis and shown in the next chapter.

5.2. Turbulence Kinetic Energy (TKE)

The calculation of turbulence kinetic energy used the fluctuation term from the Reynolds decomposition to quantify the amount of kinetic energy per unit mass associated with the turbulent flow. The TKE is equal to the sum of the squares of the three-dimensional velocity fluctuations from the Reynolds time averaging concept:

$$\text{TKE} = \frac{1}{2}(u'^2 + v'^2 + w'^2) \quad (9)$$

In addition to describing the amount of turbulence present in the water, the distribution of TKE also shows where the turbulence occurs with respect to the turbine and where dissipation occurs behind the turbine.

5.3. Reynolds Stress

Velocity fluctuations can also be used to determine the rate of momentum transfer across a boundary. Momentum transfer is equivalent to the application of stress (see equation 5.3), which also shows the transfer of energy through the flow field. Together with the turbulent kinetic energy and Reynolds stress show the amount of the turbulence energy and is direction of transfer. The Reynolds stress is shown below as Equation 10. The equations are simplified by introducing two statements that result in three relevant terms. The laminar shear was calculated for a few random samples and was shown to be consistently smaller in magnitude than the turbulent contribution.

$$\tau_{RS} = \begin{pmatrix} u' & w' \\ u' & v' \\ w' & v' \end{pmatrix} \quad (10)$$

All the stress variables have units of force per unit area, and dimensions of $ML^{-1}T^{-2}$. The correlation between two orthogonal velocity components leads is defined as the Reynolds stress. A three-by-three matrix representing the three-dimensional velocity measurements is usually used to depict the Reynolds stress. However, due to the large amount of data, the stress was represented by the magnitude of the traction vector, the last expression in equation 5.6.

5.4. Numerical Processing

To obtain the wake characteristics, the following numerical procedure was developed. The objective of this process was to decompose the observed velocity data into mean and fluctuations while maintaining a level of resolution as well as a degree of dynamic range in conjunction with applying a running window to a segment of single point data.

5.4.1. Running window

The running window is a statistical operator that evaluates a segment of data within a much larger sample array. The numerical tool calculates the mean and fluctuation components from the raw data based on the Reynolds time averaging concept. This is achieved by using a significantly smaller number of data points to produce a single value assigned to the middle point in the window. The window then runs through the entire sample array to result in a new processed array. Figure 5.1 illustrates the running window for a single data point.

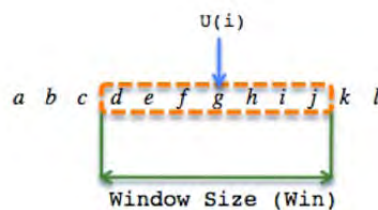


Figure 5.1. Functionality of running window

The running window is a type of low-pass filter, or more precisely, a finite impulse response filter, in which the cut-off frequency relates to the size of the running window. The numerical operation used to convert the measured velocity to its time-averaged components resulted in unintended effects of reduced Nyquist frequency. Since one of the objectives of this research is to study the fluctuation in the flow caused by the turbine, a low Nyquist frequency could threaten the relevancy of the research. For example, if the windows were wide and constant (i.e., box-car), the moving operation would produce filtered data for which the Nyquist frequencies were significantly lower than the original. Additional numerical techniques were explored and implemented to reduce the effect on the cut-off frequency and are discussed in section 5.5.2 and 5.5.3.

5.4.2. Weight Function

A weight function is a mathematical operation used during convolution in order to give specific elements more influence on the result over less relevant elements in the same segment of

data. Constant weight functions are characterized with a low dynamic range, as a result a poor choice for turbulence analysis, which requires a high dynamic range. Conversely, a weight function that is designed to handle the presence of fluctuations in frequency and amplitude suffers from low resolution and a high sensitivity to random noise. Spectral analysis shows the tradeoff between resulting signals' strength with comparable frequencies, and resolving dissimilar strength of signals with dissimilar frequencies. The Hamming function, seen in Figure 5.2 below, is a compromise of these two extremes that provided a favorable frequency response. How to choose the size of the window will be addressed below.

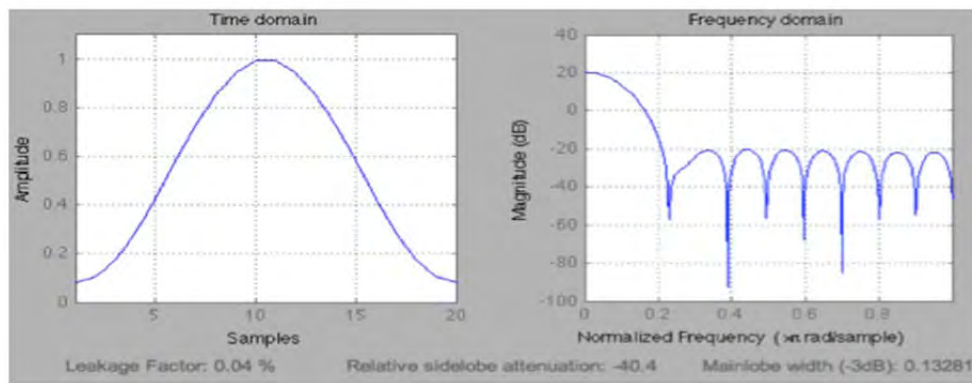


Figure 5.2. The Hamming weighting functions and their effects on the frequency domain

The advantage of the Hamming window is low aliasing, and the tradeoff is the decrease in resolution through lowering and widening the main lobe. For the Hamming window shown in Figure 5.2, the effective Nyquist frequency was lowered to 10 Hz from 32 Hz after the application of the weighted running window. If the weighting function were constant, the resulting cut-off frequency would have been drastically smaller, at approximately 1 Hz. All the calculations were done by producing a signal of know frequencies and amplitude and looking at the frequency response of the running weighted window.

5.4.3. Window Size

The size of the weighted running window had a significant effect on the results. Figure 5.3 shows the magnitude of the velocity converted into the Reynolds time-averaged mean (\bar{u}) and fluctuations (\hat{u}), in which the window size was incrementally increased from 4 to 64 data points. Figure 5.3 depicts the strong variability of the results, indicating the importance of finding the ideal window size. Two methods were utilized in order to determine the best size of the window: using the experimental results and assuming certain physical attributes.

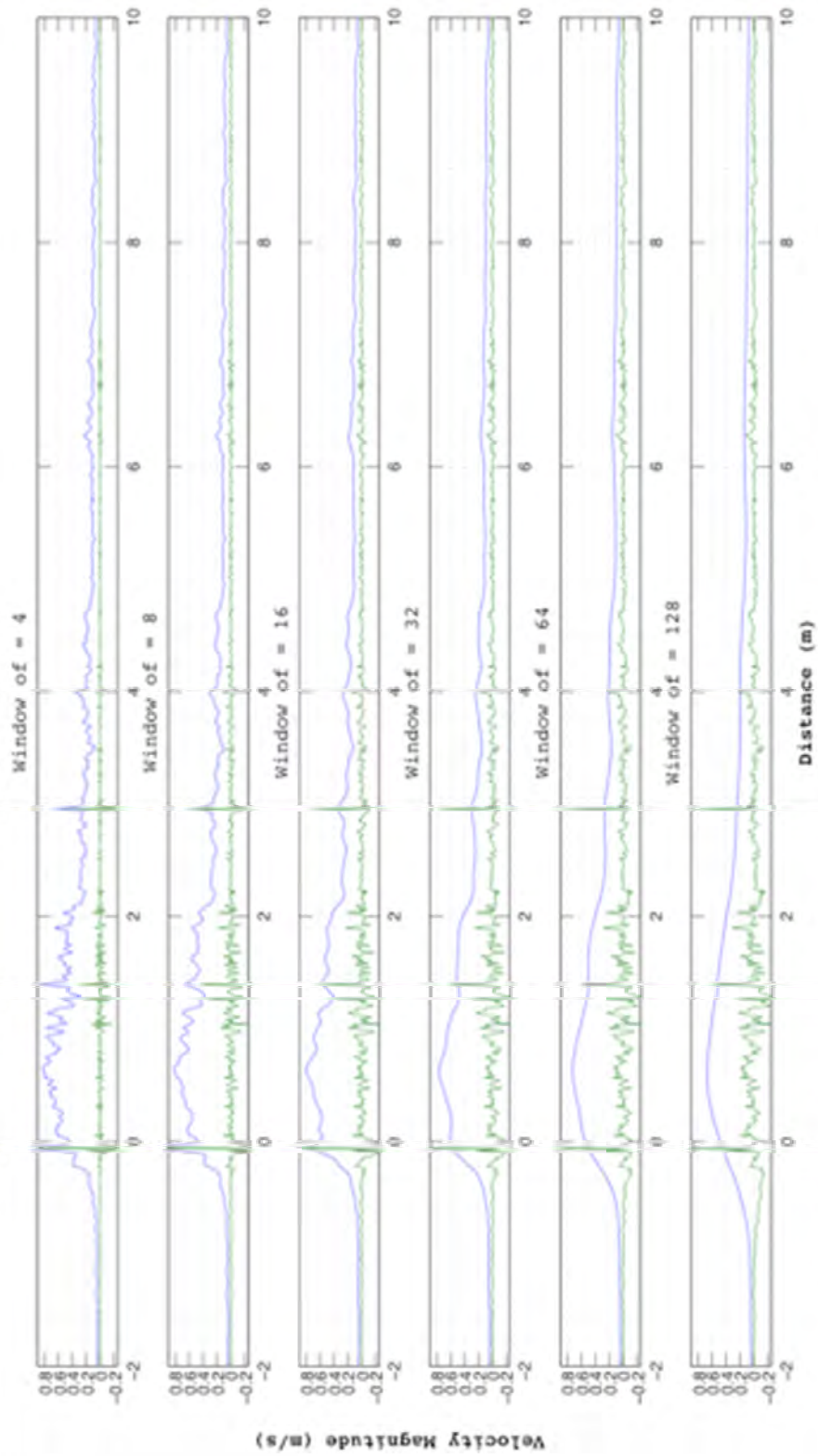


Figure 5.3. Mean and Fluctuation results of Reynolds decomposition for different window sizes

The first method examined the effect of a changing window size on the Reynolds components. The window size was incrementally reduced over a segment of measurements of a creep flow. The results from the algorithm produced average fluctuations and mean values for one window size through the entire segment. Figure 5.3 shows the change in the mean and fluctuations quantities as a function of window sizes. The result yield a region of stability with a point of inflection and constant height at a window size between 15 to 25 which suggested a range to set the window size. Other assumption can be applied to further understand the effect of a changing window size to determine the optimal size.

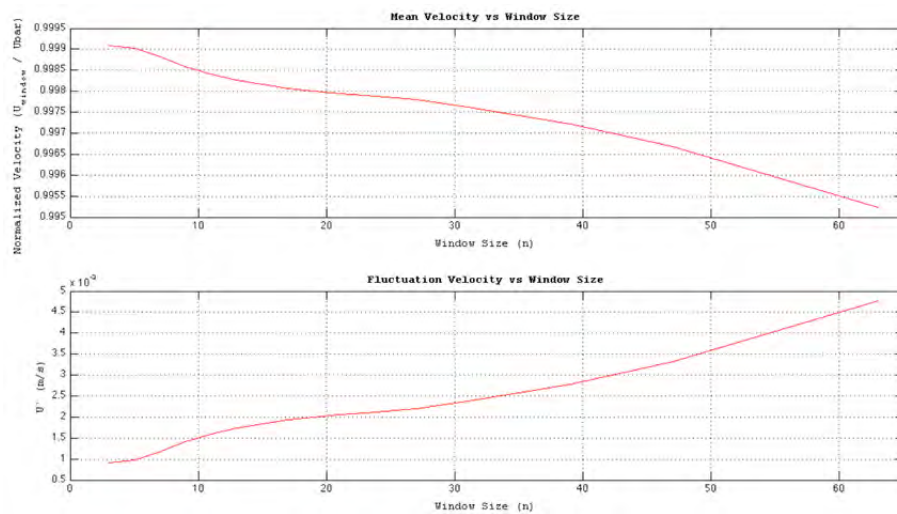


Figure 5.4 Results of Reynolds decomposition for different window sizes

The second method used to determine an optimal window size focused on the energetic and turbulent period behind the turbine. The second method assumed that the velocity in the y-direction are only the fluctuations (v') components. In a process similar to the first method, window size was varied and v' and \bar{v} were studied, where the objective was to return \bar{v} to zero. The variation of the window size from 4 to 128 significantly reduced \bar{v} with the largest effect seen below 40, however, \bar{v} only approached zero resulting in a horizontal asymptote as a function of window size. With the results from both methods and the effect of the Nyquist frequency calculated from the weighted running window, the window size of 25 data points was chosen as the ideal size for this study.

5.5 Wavelet transforms

An additional numerical tool used for analysis was a discrete wavelet transforms use to capture both frequency and time information associated with flow field. Other experimental fluid studies have used similar time-frequency spectrum methods to examine turbulent behavior (Rinoshika 2007, LI 1999). The analysis was used to capture both frequency and time/distance information associated with the flow field. The time-frequency spectrum has additional advantage of temporal/spatial evolution over the traditional Fourier transform, which is needed for highly time-dependent structure of a wake. The frequency range of the spectrum, from 0.03 Hz at the base to 32 Hz at the top, was determined by the experimental method and equipment. The analysis was done on the velocity magnitude, $(u^2+v^2+w^2)^{1/2}$, from all sampling heights

5.6 Visualization techniques

The results are presented in a non-dimensional format to provide a unified representation of the data, independent of the physical shape and operation settings of the experiments. Segments of data were presented as a distance between the turbine and the velocity of the fluid, and were measured in length and velocity units. In order to utilize a non-dimensional format distance, the unit of length was converted to length per turbine diameter. As a result, the horizontal and vertical distances are depicted in terms of turbine diameters. Similarly, the fluid velocities are presented in a non-dimensional format normalized by the carriage speed.

The velocity measurements are presented to generate a flow field in two forms. The simplest is the vector plots to better understand both the near-field and far-field characteristics. Each vector was calculated from a mean of four individual unprocessed three dimensional velocity points. A reference circle is used in to represent the turbine in all the figures and blade position is marked for the low solidity turbine. The aspect ratio, which can be inferred from the shape of the circle, was used to maintain the correct representation of the data.

6. RESULTS

The differences in the flow field over two different solidity ratios as well as additional measurements on the effect of TSR and blade position were acquired to examine the dynamic flow behaviors of a cross flow turbine. The two different turbine solidity and their arrangements are defined in the turbine Section 3.2 as well as the results from the dynamometer for the different turbines are shown in Table 3.4. For the two different turbine configurations, one variable was altered at a time to examine different effects of the controlled variable on the flow field, and the variables are listed in the test matrix in Table 4.1.

6.1. Composite Flow Fields

The results for the flow field are illustrated as a vector plot showing the magnitude and direction of the two velocity components as the turbine approaches and departs. The flow field is shown in the x-z plane where the third velocity component (v) is not represented in the vector plot. The flow fields are shown twice to highlight different stages in the wake showing the two regions referred to as the near field and the far field. The far field displays the flow decay down stream while the near field shows two stages of the wake in the region close to the turbine.

Overall, the responses were the strongest near the turbine depth and decreased with the distance away from the turbine centerline. Furthermore, the responses were almost symmetric about the centerline before the turbine passed overhead the ADV ($x/D = 0.5$), but the symmetry gradually disappeared downstream. The entire flow fields can be divided into three stages. The first stage is the turbine approach when the u-velocity gradually increased while w-velocity was upward above the centerline (ACL) and downward below the centerline (BCL), indicating the water being pushed away as the turbine approaches. The second stage shows the entrained flow. During this stage, the u-velocity near the turbine heights accelerated quickly to a peak speed about the speed of the carriage, which then decelerated between 1 and 3 turbine diameters. Away from the turbine ($z/D \geq 0.75$), the u-velocity was opposite to the carriage moving direction in the

beginning of this stage, but the direction reversed as the entrainment spreading towards the surface and the bottom to reach the depths. The w-velocity during the second stage first decreased at all depths followed by a small collapse towards the centerline then even stronger expansion towards the surface and the bottom. After the collapse of the entrained flow the third and final stage is the wake tail that consisted of small fluctuations. These fluctuations decayed rather slowly over a large distance, and their magnitude could still be 10 percent of V_c at $x/D = 14$.

6.1.1 High Solidity Turbine

The high solidity turbine used a four-blade configuration and measurements were obtained over three different TSR values. The optimal TSR of 1.4 was the focus of the high solidity data set with velocity measurements at three different distances from the turbine center to the sample volume: 0.43, 1.0 and 1.3 diameters. A high solidity turbine, with a value above 0.2, has been shown in this and other studies (Shiono 2000) to be less efficient than a low solidity turbine, by as much as ten percent on comparison with a similar turbine setup. As a result, a raised solidity requires a lower TSR to achieve its optimum performance. The lower TSR reduces fish strikes, resulting in conservational incentives for turbine developers to use a higher solidity turbine (Polagye 2011).

The experimental work for the four-blade turbine was performed before the repeatability of the blade position was addressed. As a result, the blade position in test set A was random, i.e., the blade position was recorded, but not controlled. However, the data demonstrated a strong degree of repeatability and correlation between different runs of identical tests when the two-velocity ranges were combined to form a composite wake profile. The correlation between different runs only matched the velocity magnitude and direction. Small variations existed with the mean components between matching velocity range, thus, the tests were concluded to be first-order repeatable. The repeatability across runs suggested that the blade position was not a large

factor on the flow field for the high solidity turbine. From the correlation across equivalent wake results, the wake appeared to be stable in size and intensity. This hypothesis was further supported by the turbine forces through a rotation having an amplitude and frequency associated with each force, however the high solidity and most notably the high number of blades produce small amplitudes in all the forces. The mean of the osculating forces are the coefficients seen in table 3.4. The force frequency is four time higher then the rotational frequency.

The results seen in Figure 6.1 and 6.2 show the different stages of the wake, approach, entrained flow, and flow recovery with respect to the turbine. The level of symmetry between the opposite sides of the turbine, suggests that the blade position and the turbine rotation were not strong factors in the wake and the turbine acted similarly to a cylinder in a uniform flow.

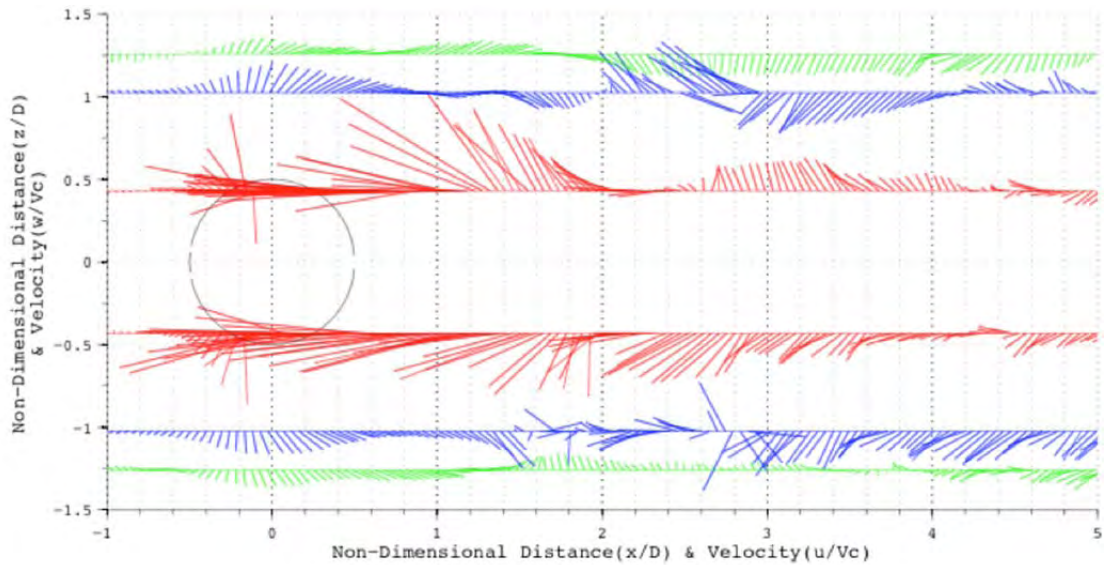


Figure 6.1 Near flow field for high solidity turbine operating on design

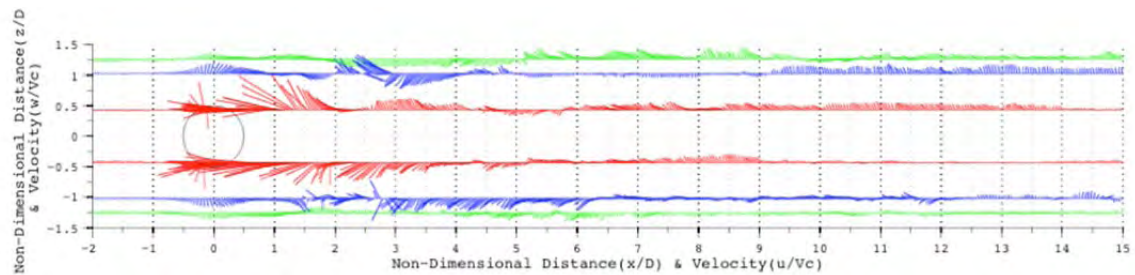


Figure 6.2 Far flow Field for high solidity turbine operating on design

In addition to the optimum TSR at 1.4, two off design TSR were tested with the four-blade turbine and the results for the off design turbine are shown in Appendix B. The results for the off design show similar traits such as the bypass flow entrained flow and flow recovery.

6.1.2 Low Solidity Turbine

The low solidity turbine wake data includes three different blade positions for a carriage speed at 0.8 m/s and the optimal TSR of 2.25 for maximum C_p . The low solidity turbine used only two blades that reduces the solidity by half compared to the high solidity arrangement. The reduction in the number of blades caused significant differences in the flow pattern through the 180° rotations, which led to the control of blade positions over the ADV instead of random blade

position in the high solidity data set. The data set includes three-blade position at 45° intervals, as well as the four different locations for the ADV's sample volume to the turbine center: 0.51, 0.77, 1.1, and 1.5 diameters.

In all cases shown in Figure 6.3, the different stages of the wake were noticeable: the first was the gradual diversion in front of the turbine, beginning at about 0.5 diameter in front of the turbine. The second stage was the entrained region behind the turbine that traveled in the direction of the carriage at speeds close to that of the carriage. With the final stage, the dispersion and decay of the wake.

In all cases of different blade position for the low solidity turbine show an asymmetrical structure between upper and lower sections in Figure 6.3. The asymmetry of the wake was not observed with the high solidity turbine (see Figure 6.1 and 6.2). During the turbine approach, the wake below the centerline (BCL) showed more flow activities in comparison to above the centerline (ACL), resulting in a higher bypass flow BLC. Additionally, the ACL area experienced a stronger response in flow magnitude and variability, emphasized by an upwelling through all levels. The blade travels with or against the inflow; depending on which side of the centerline the blade is located. Since the TSR is equal to 2.25, the blades at top will travel into the flow with a maximum speed at top dead center of 3.25 times faster than the inflow. As for the lower blade located at bottom dead center the flow passes from the leading edge to the trailing edge at a speed of 1.25 times the inflow.

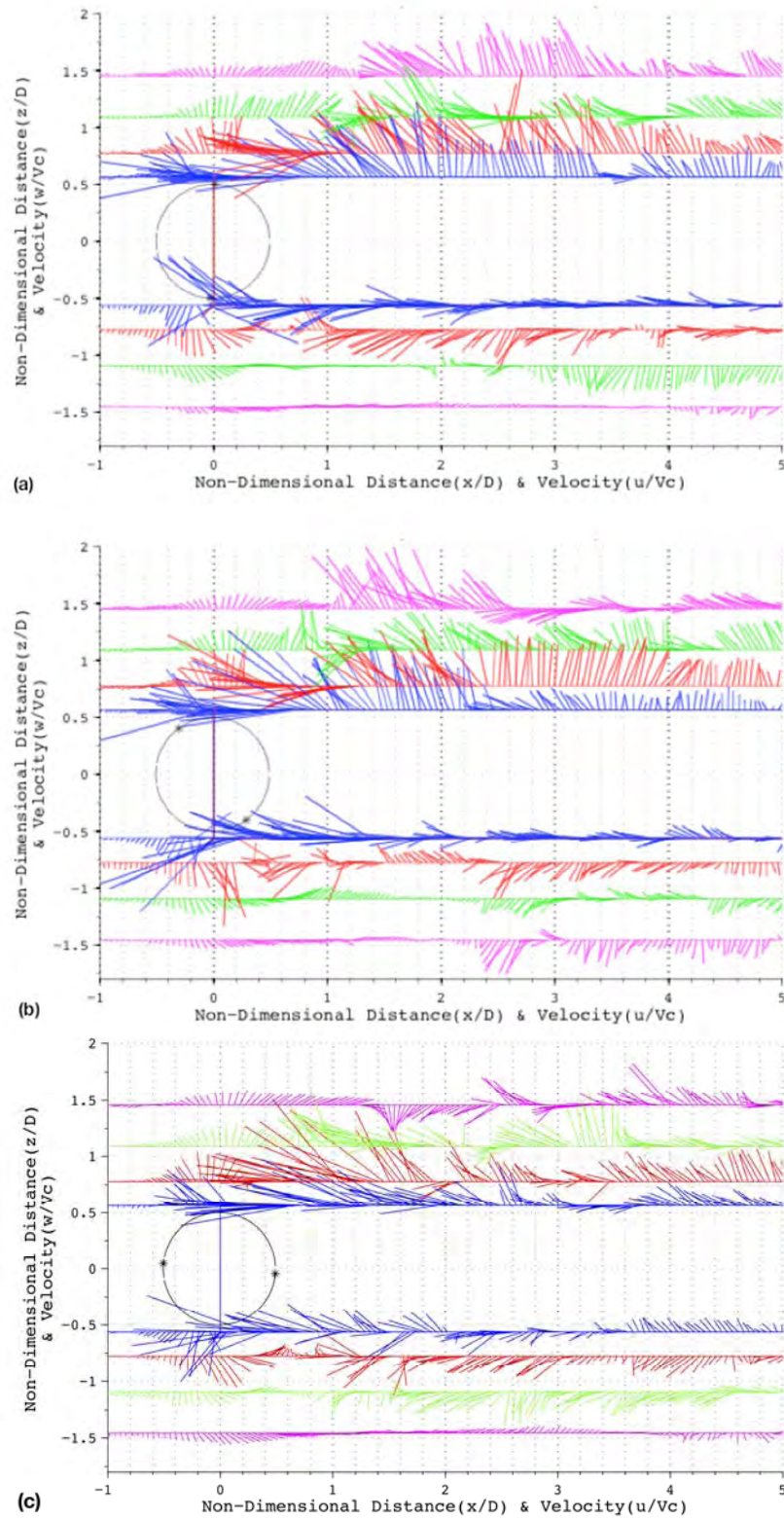


Figure 6.3 Near flow fields for low solidity turbine over three-blade position.
 (a) Position 1 (b) Position 2 (c) Position 3

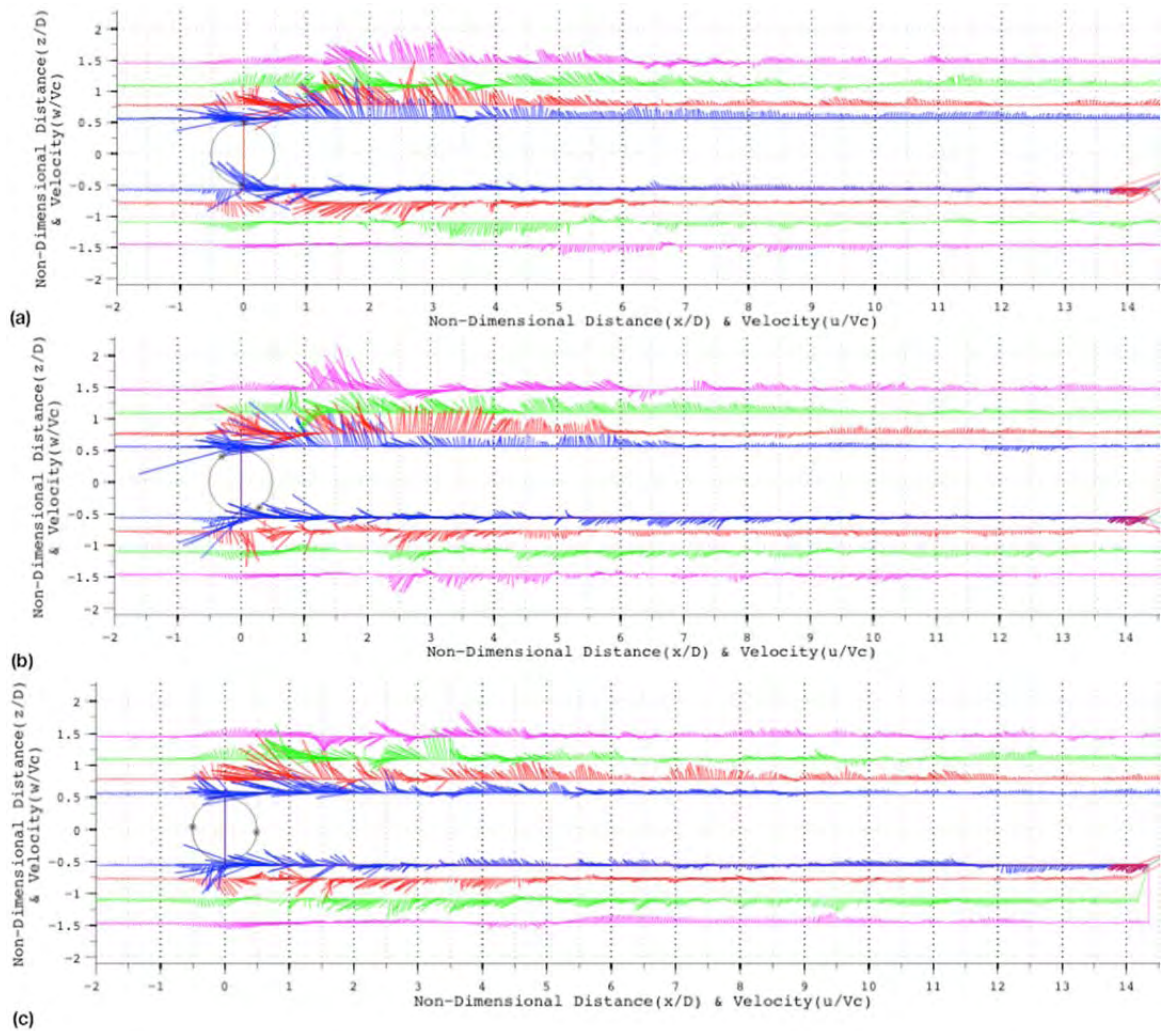


Figure 6.4 Far flow fields for low solidity turbine over three-blade position.
 (a) Position 1 (b) Position 2 (c) Position 3

6.2 Reynolds Time Averaging

To further examine the wake, the data has been separated into the mean and the fluctuation components. The separation of the two components made it possible to examine the connection between the mean and fluctuation terms, with respect to the distance from the turbine. The connections between the mean and fluctuation terms are examined in more detail in section 7.1. The velocity measurements for the high solidity turbine are shown in Figure 6.5 and 6.6. The two figures together show the structure and behavior of the flow field with the velocity magnitude shown in Figure 6.5 and the three-dimensional components in Figure 6.6. The

velocity magnitude demonstrates the average influence of the turbine over the quasi two-dimensional field where the separation of three velocity components shows how the flow translates through a three-dimensional space. The individual velocity components display a phase relationship between the u, w, and v, especially during the flow accelerations. The phase relationship was measured throughout all layers as the momentum disperses outward, affecting the outer layers to a lesser extent. The figures shown include only the near field in order to illustrate the behavior of flow recovery as the momentum transfers out from the x-direction and into all other directions. To see the details of the interior wake measurements, additional figures for each velocity component are provided in Appendix B.

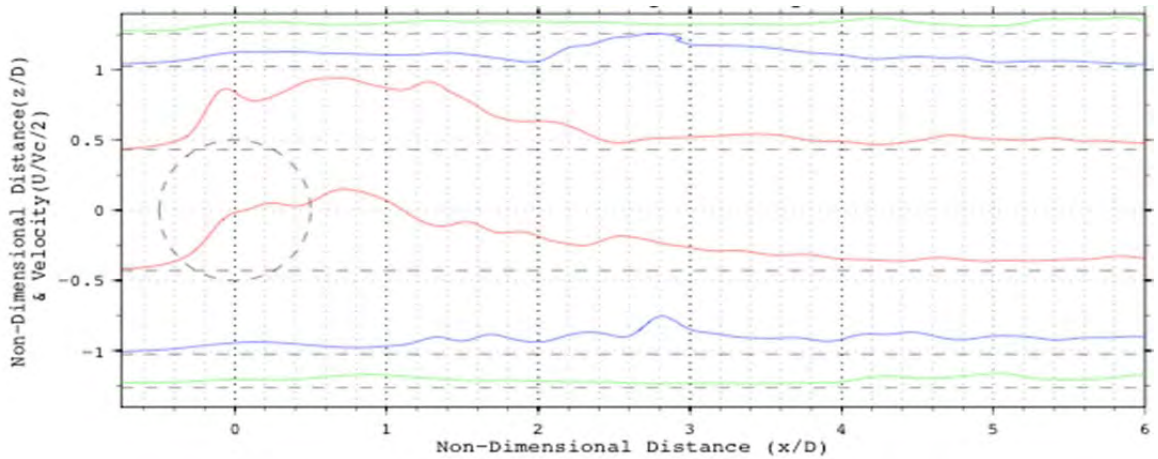
Small oscillations still exist in the case of high solidity turbines but are lower in amplitude and higher in frequency due to the large number of blades. Therefore, the velocity fluctuations in general are considered relatively stable. With the fluid interaction being steady, the wake should have steady size and shape. The steady wake structure was further supported during the process of making a composite wake, in which different files of the same test demonstrated a repeatable pattern in the mean flow.

Other physical properties such as the bypass flow, the shear front, and the blockage effect can be seen in Figure 6.5 and 6.6.

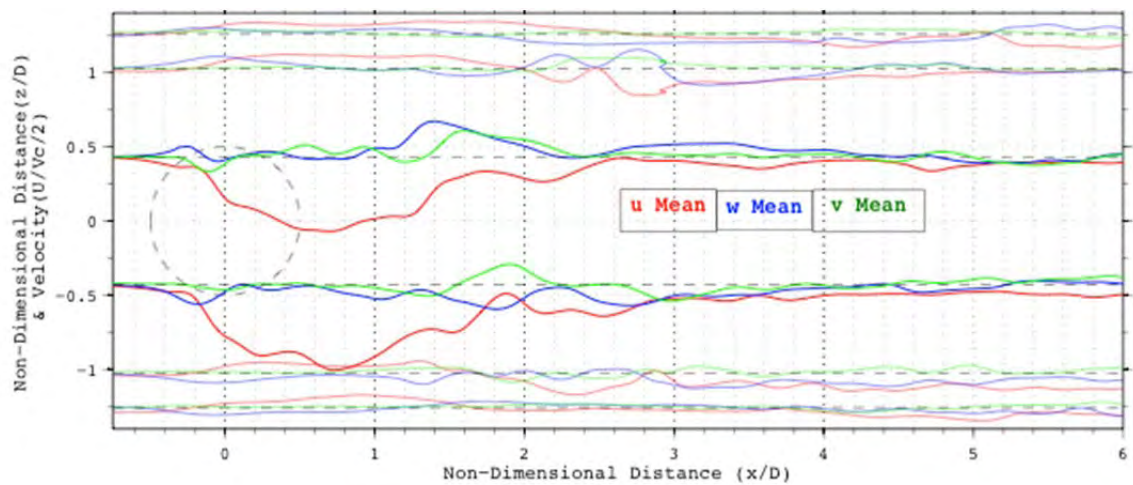
- As the turbine approached a steady flow around the turbine is observed w components with the largest velocity outward at approximately -0.2 diameters in front of the turbine. Followed an abrupt change in direction. The velocities upstream are predominantly in the w but after the abrupt change, w goes to near zero and velocity in the u dominates.
- Through the different heights, two different fronts are observed as the wake propagates outward and dissipates. The first is the steady flow as the turbine approaches dominated by u and w velocity components with diminishing strength in the outer layers occurring simultaneously throughout the layers. The second is the turbulent front dispersing

outward by oscillating w and v components, that are apparent in the time-frequency spectra analysis where.

- A feature of the blockage effect can be noted in the outer layers where the u -mean velocity is travels in the opposite direction of the entrained flow.

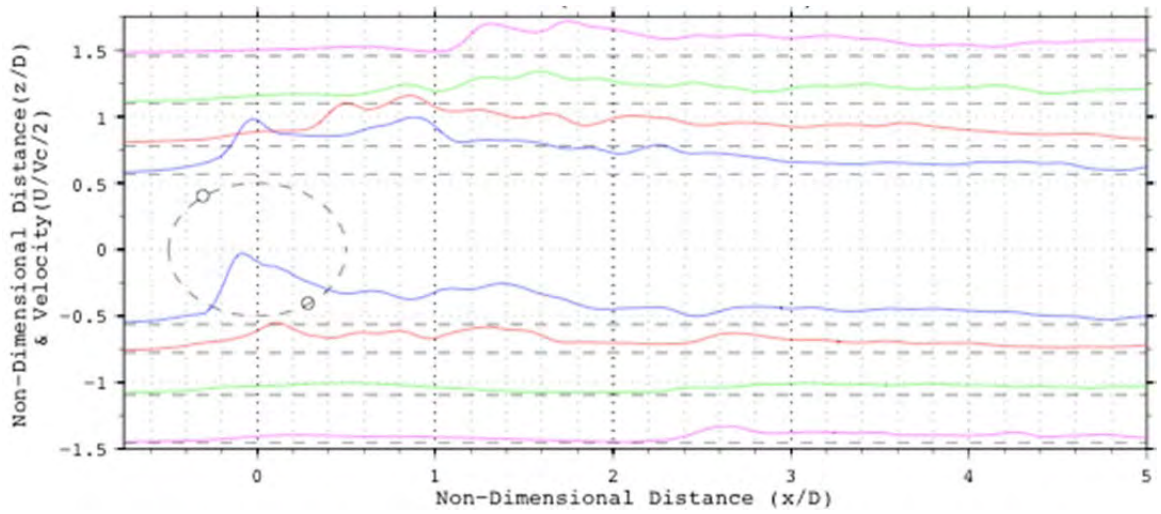


Figures 6.5. The velocity magnitude mean from the Reynolds decomposition for the high solidity turbine.

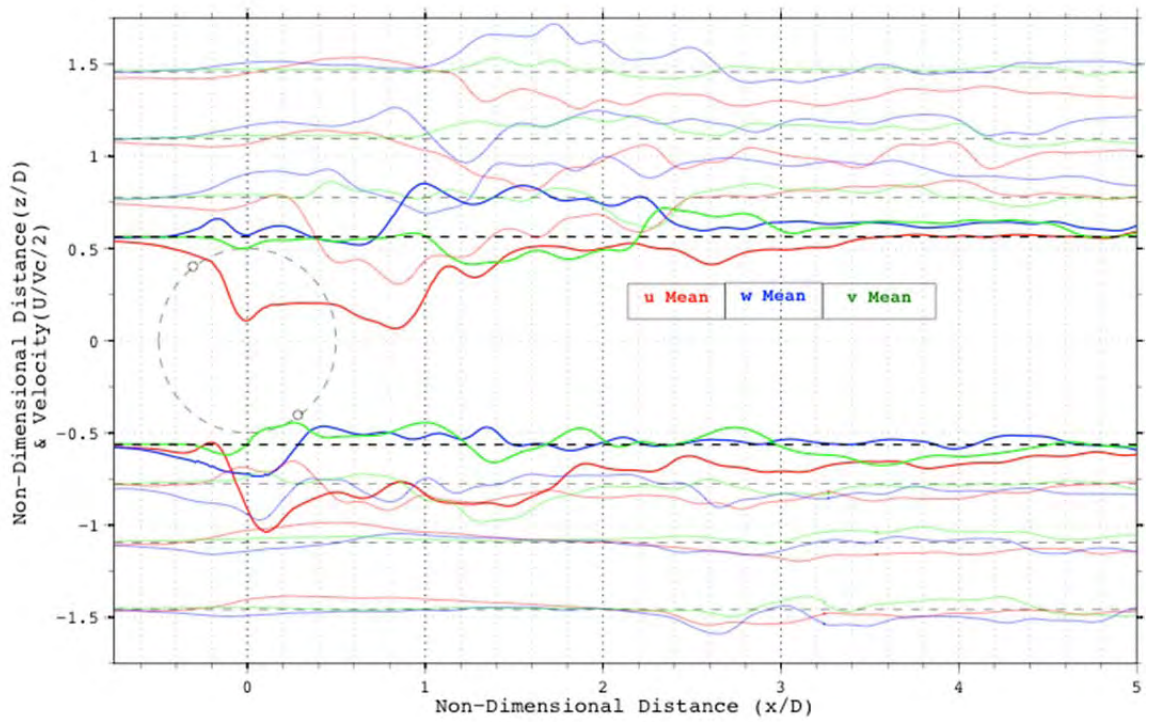


Figures 6.6 The three (u, w, v) mean velocity component of Reynolds decomposition for the high solidity turbine.

Similar features seen in the high solidity turbine is observed in the low solidity turbine's mean velocity components in Figure 6.7 and 6.8. The two turbines share similar flow recovery at the distance of 10 diameters downstream, approximately 10 to 15 percent of inflow speed in \bar{U} (at all heights) remained while the velocity in the u remains below 5 percent. The remaining flow persisted for a long distance, and did not begin to dissipate until approximately 30 to 35 diameters away (not shown). However, one major difference is the low solidity turbine's wake is asymmetric compared to the high solidity. Unsteady flow pattern are seen through the different blade position where the velocity in front of the turbine dependent on the blade position.



Figures 6.7. The velocity magnitude of Reynolds decomposition for the low solidity turbine for blade position 2.



Figures 6.8. The three-dimensional mean velocity component (u w v) of Reynolds decomposition for the low solidity turbine for blade position 2.

- ACL at $z/D = 0.5$, \bar{u} increases quickly to V_c ; away from the turbine, the flow starts by moving towards left, but reverses immediately behind the turbine, then changes to leftward again when the first wave of upward spreading disturbance from the blade reaches the sampling height and the magnitude decreases as the distance from the centerline increases; the decay further downstream is slower and the decay rate decreases with the distance from the centerline.
- For \bar{w} : Water is pushed away from the centerline as the turbine approaches so that \bar{w} is positive ACL and negative BCL. Conversely, the water rushes back towards the centerline immediately behind the turbine. However, the expanding wake is associated with upward motions ACL and downward motions BCL.
- \bar{v} oscillates: A phase relationship exist between in the three mean velocity components in the flow recovery region one to two diameters downstream. As \bar{u} recovers downstream generate a negative acceleration resulting in positive acceleration in \bar{v} and \bar{w} showing the velocity to be redirected into other direction. This phase relationship between the three velocity components are seen in best in Figure 6.8 and from the phase relationship between \bar{v} and \bar{w} being in phase with each other, it can be best described by an eddy. Furthermore, the final significant decrease in all velocity components is marked by sudden flash of fluctuation velocity.

6.3 Wavelet Spectrum

A time and frequency analysis was done on the velocity magnitude using a discrete time frequency spectra. Figure 6.9 shows the time and frequency response for the single sample volume adjacent to the top of the turbine ($z/D \approx 0.5$) at Blade Position 1. Figure 6.9 is the only figure that includes the second frequency axis from 0 to 32 Hz on a linear scale. Figure 6.9 also shows three distinct bands in the time domain associated with the turbine overpass collapse of the entrained flow, and the turbulence. The first band, located at zero distance, is associated with the turbine passing over the sensor, and exhibits the largest response over a large frequency range. The first band was followed by a brief period of low intensity fluctuations at 15Hz and above. Fluctuations at while the 15Hz and below does not occur until approximately two diameters past the turbine. The second band had only a few frequencies present over the frequency range due to the abrupt acceleration from the flow recovery. The third and other bands are typically observed at high frequencies near to the Nyquist frequency and are typical with large fluctuations over a brief period. These fluctuations are the result of random turbulence and has no significant on this analysis.

Figure 6.10 shows two wavelets stacked together using the same visual arrangement with the x-axis of the wavelet located at the respective sample volume height. The stacked time-frequency spectra show the propagation of the fluctuation energy away from the turbine with a distinct shear front. In addition to the propagation outward, the decay of the energy fluctuation is also apparent. The scale chosen is log based 10 scale providing a wide amplitude range.

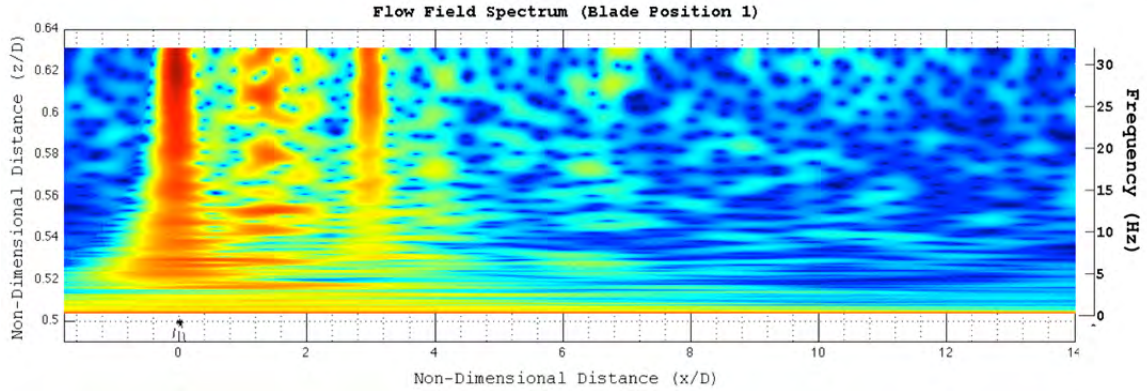


Figure 6.9 Time and frequency response for the sample volume adjacent to the top of turbine at blade position 1.

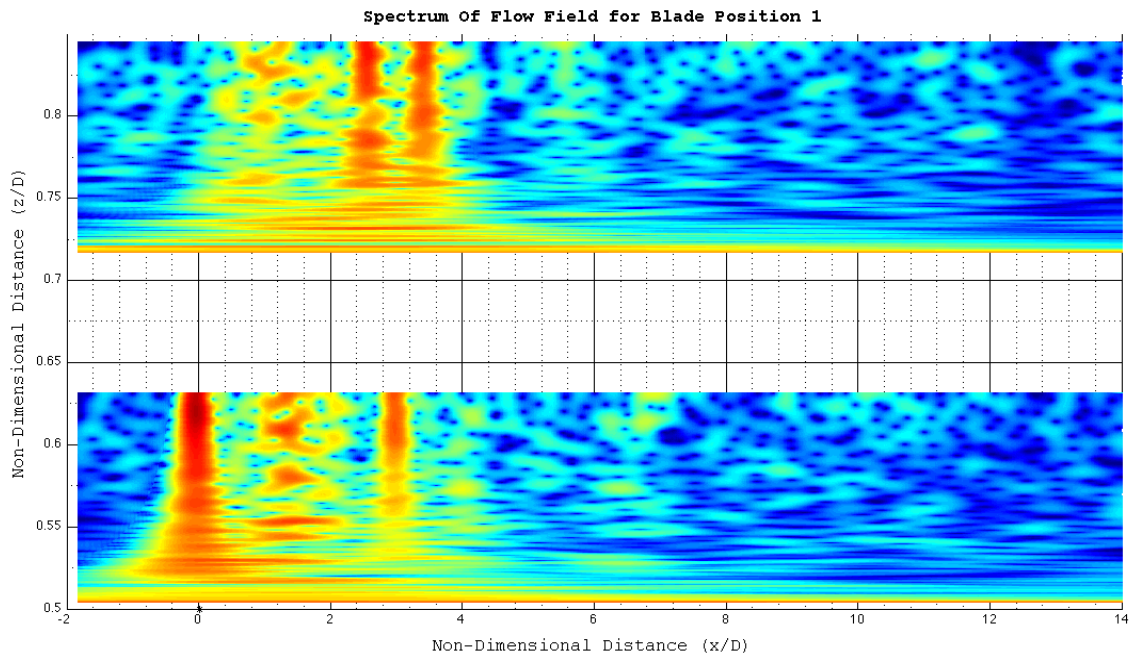


Figure 6.10 Two time and frequency responses stacked with the sample volumes on the top of turbine at blade position 1.

The wavelet spectra were placed together with respect to the sample heights. Although the visualization technique in Figure 6.11 sacrifices the resolution of each individual peak, it allows all the information to be viewed in a single reference frame. Figure 6.11 shows the spread of fluctuation from the centerline and the dissipation behind the turbine for the high solidity turbine operating at an optimal TSR.

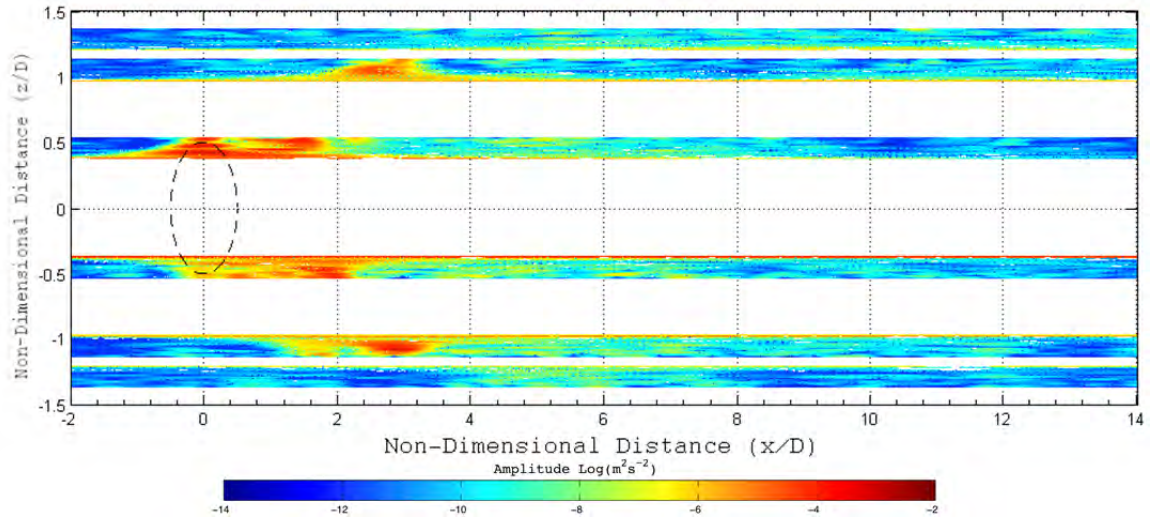


Figure 6.11 Time and frequency response from wavelet analysis for high solidity turbine operating on design.

For the low solidity turbine three time-frequency spectra are shown for each blade position in Figure 6.12. The figures also show constantly shifting behavior of the turbulent energy as the blades change position, resulting in different shear planes throughout the wake. For example, blade position 1 and 2 have the largest responses at zero distance to the turbine, as would be expected with the blade's proximity to the sample volume. On the other hand, blade position 3 has the largest area with high fluctuation. A real integration of the spectra shows that blade position 2 has the largest amount of energy, as seen in Table 6.1 below. As the table shows, there is a large variation in measured energy, further demonstrating a continuously changing wake.

Position	1	2	3
$\frac{\iint A(x, f, i) dxdf}{[\iint A(x, f, i) dxdf]_{\text{Max}(i)}}$	0.75	1.0	0.65

Table 6.1 Qualitative comparisons wake energy spectrum for the three different positions

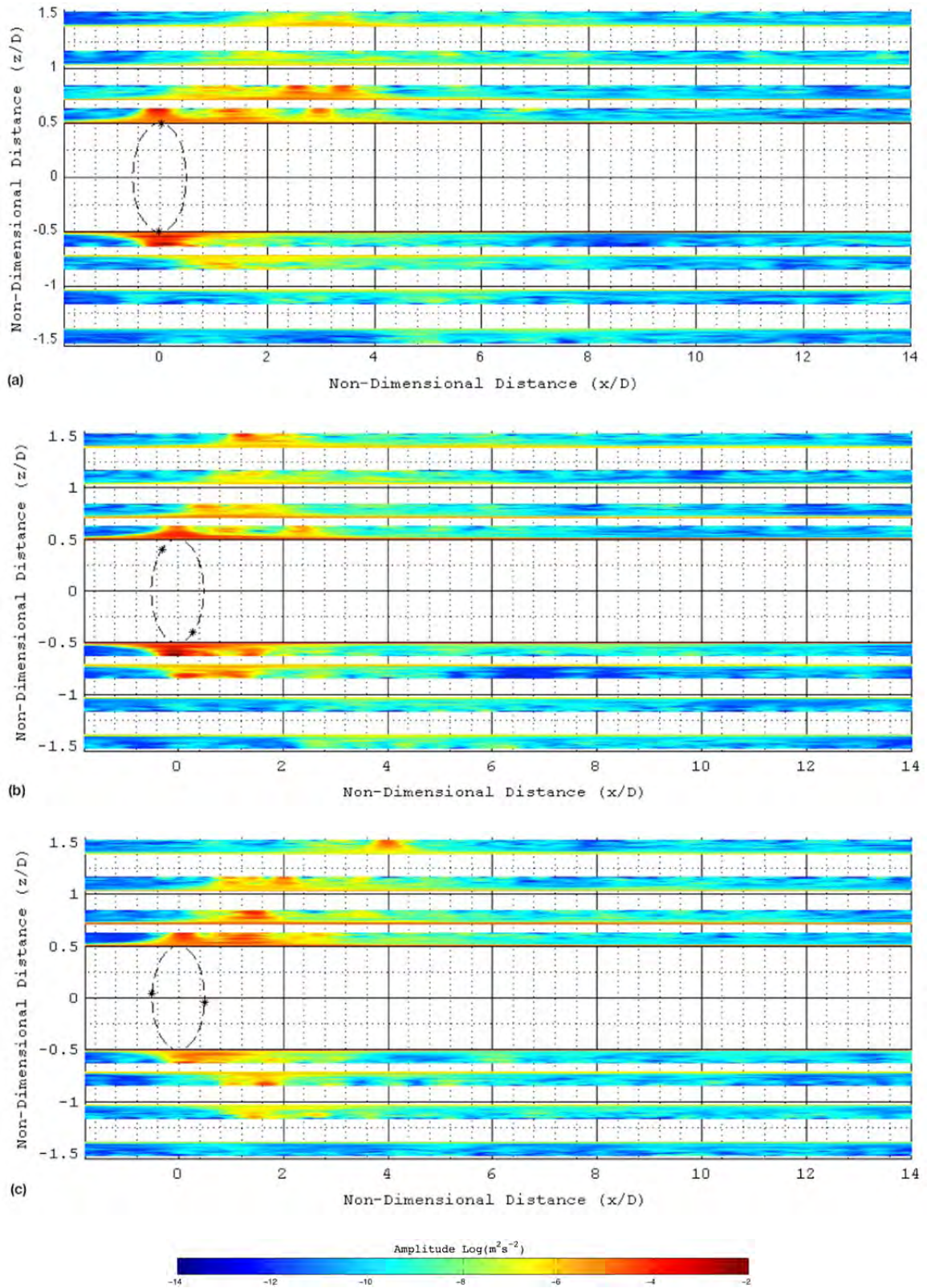


Figure 6.12 Wavelets for each height and blade position showing the fluctuation intensity as a function of frequency and distance to turbine. (a) Position 1 (b) Position 2 (c) Position 3

6.4 Turbulence Kinetic Energy and Reynolds Stress

Turbulence commonly contains coherent structures such as eddies, however, point measurements can only acquire fluctuations from the turbulence. The resolution of equipment and methodology used in this study will not show individual eddies instead focusing on the distribution of turbulence in a quasi two-dimensional regions. The measurements have shown localize regions near the turbine and the dispersion of the TKE outward. The results for the high and low solidity turbine show different behavior between each other but maintain a general simultaneity in size, intensity, and dispersion of the TKE. However, a notably difference was measured in the decay rate down stream of the turbine.

The high solidity turbine exhibited a highly organized and symmetrical TKE also seen above in the velocity results. The TKE showed a distinct connection to the flow recovery seen in Figure 6.6 where the flow recovers in the same region as TKE go to zero. The high solidity turbine results in Figure 6.13 shows how the TKE is confined to a small region over three diameters in length with two well-defined peaks. The TKE for the inner layers are contained within a small region but are bounded by a rapid increase in energy at approximately zero as well as a rapid decrease between 1.5 and 2.5 diameters. The results also show the dispersion of the turbulent energy outward through the layers, exhibiting the shear front. As the TKE disperses to the outer layers the peak and boundaries are reduced.

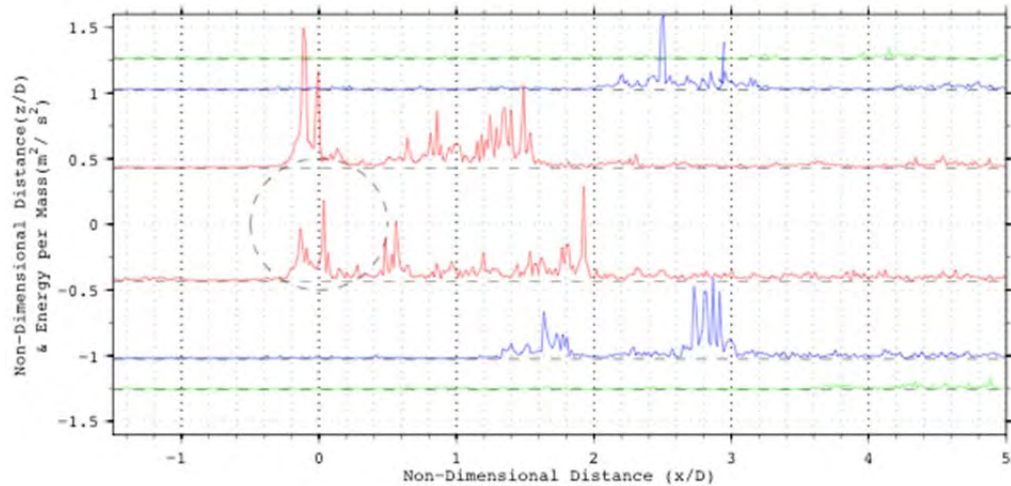


Figure 6.13 Turbulence kinetic energy terms for high solidity with optimum TSR

The TKE results for the low solidity turbine did not show a confined region of turbulent energy with a rapid decay as seen in the high solidity measurements. The TKE results demonstrate an asymmetrical feature of the wake favoring the ACL region. The low solidity turbine also showed little to no disturbance in the bottom two heights of the sensor. The different blade positions show that the fluctuation in magnitude at the strongest area of turbulence depended on the blade's position. The low solidity turbine's TKE shows similarities to the high solidity: the general structure of approximately two regions of high activity associated with the overpass and the flow recovery. However, unlike in Figure 6.13 where the TKE has a sharp decline near zero, Figure 6.14 shows a fluctuation in distance and magnitude at approximately two diameters, with addition regions of high activity. The results for the TKE show a slower approach to zero compared to the high solidity with approximately one diameter long required to reach a similar energy level.

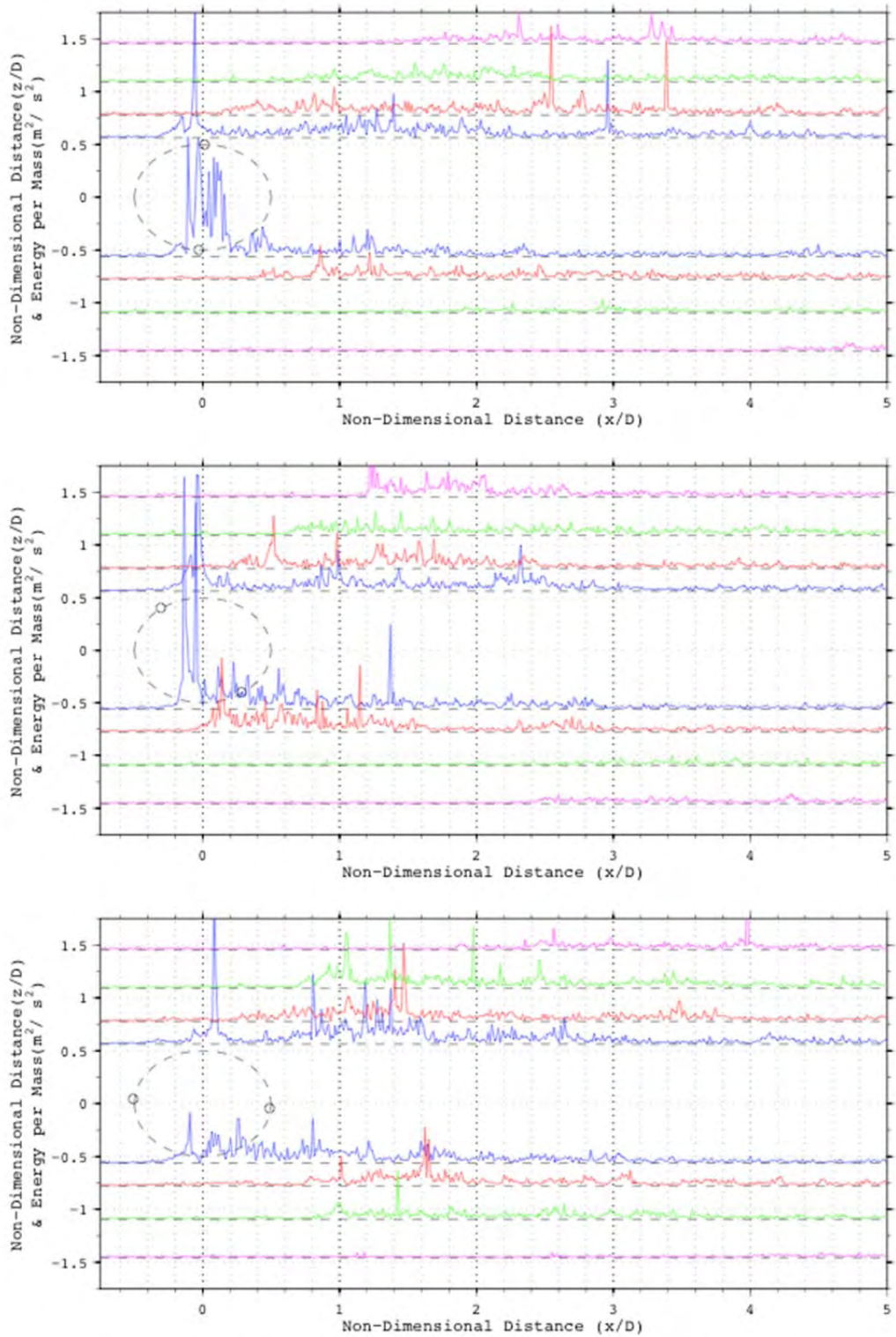


Figure 6.14 Turbulence kinetic energy for low solidity turbine over three blade positions.
 (a) Position 1 (b) Position 2 (c) Position 3

The transfer of turbulent energy can be seen with the Reynolds shear. Data from the ADV was well suited for measuring the turbulent shear by using its internal software and the procedure used for data collection. The results, seen in Figure 6.15, demonstrate the transfer of momentum from the turbulent motion across the three orthogonal planes in Cartesian coordinates for at each height. The Reynolds shear components are the dominant quantities responsible for momentum transfer in turbulent and transitional flow. The nature of the cross flow turbine operating over a range of angles of attaches that introduces dynamic stall over a rotation produces a turbulent wake.

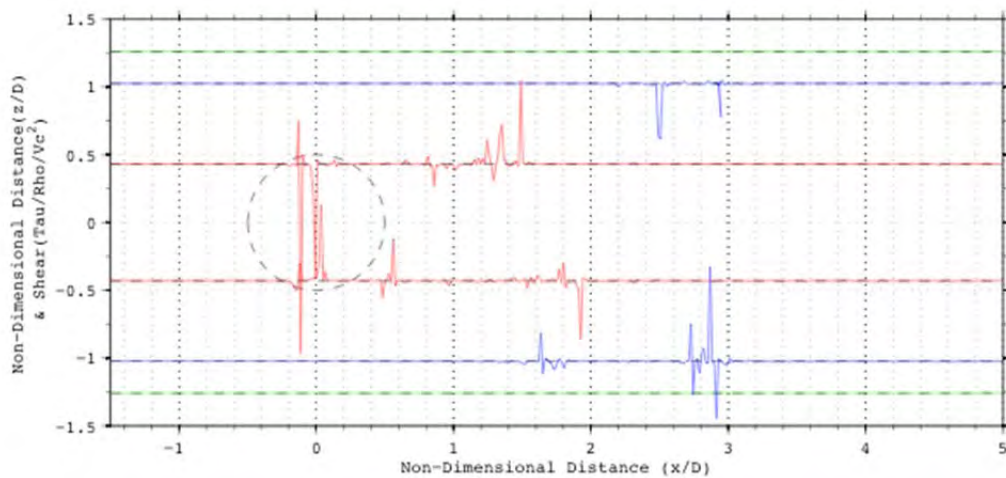
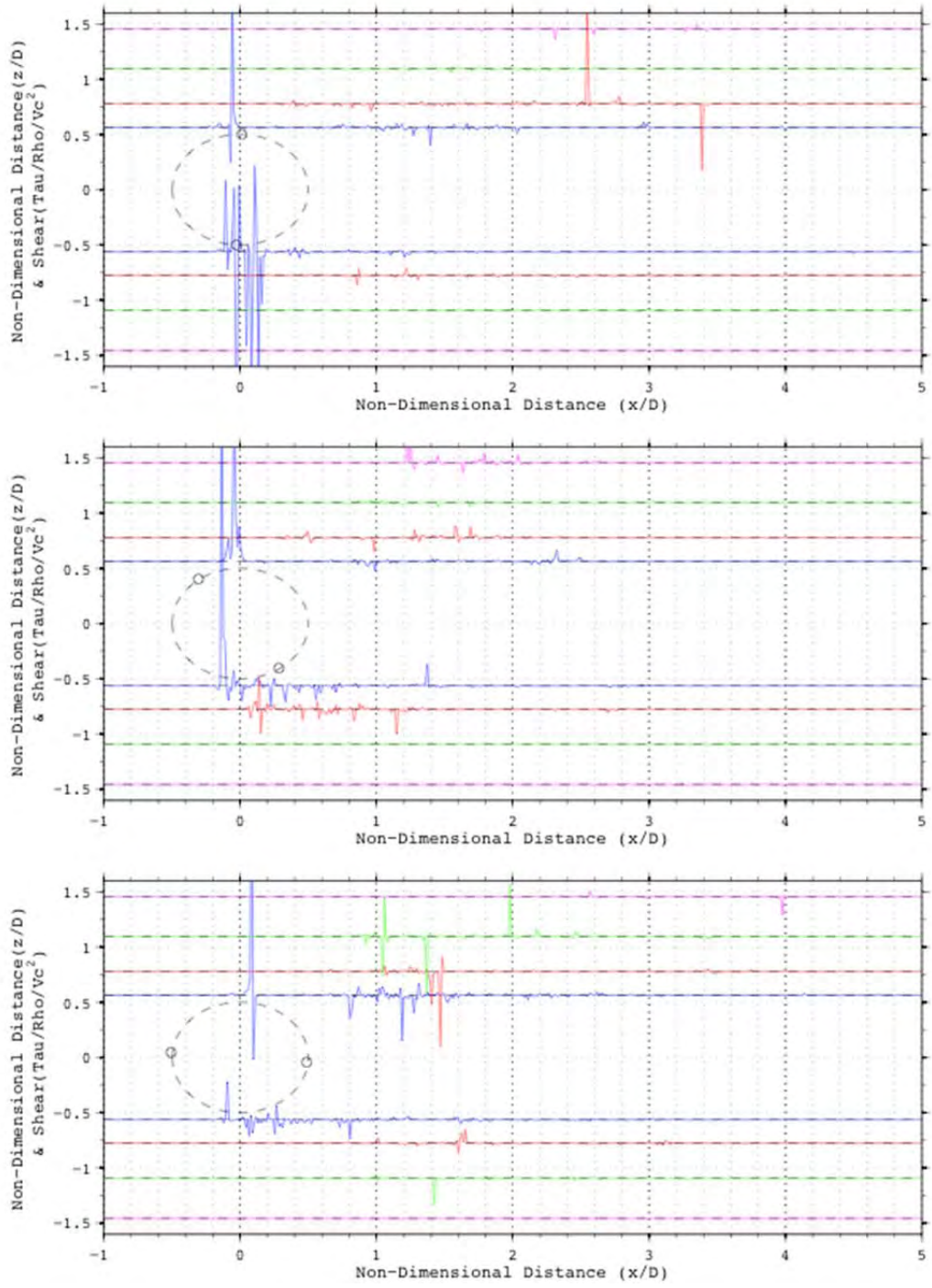


Figure 6.15 The $u'w'$ Reynolds shear component for four blades with optimum TSR

The results for the low solidity turbine are seen in Figure 6.16 which constantly changed due to the changing rotation of the turbine. For instance, the distance between the peaks of both Reynolds shear and TKE changed as the turbine rotated, while the magnitude of both remained relatively constant.



Figures 6.16 The three Reynolds shear terms for low solidity turbine over three blade positions.
 (a) Position 1 (b) Position 2 (c) Position 3

6.5 Surface Elevation

The surface elevation from the forward and reverse runs for the high solidity turbine displayed with the vector plot in Figure 6.19 show the relationship of the flow field and the surface elevation. The changes in elevation are shown in non-dimensional units with respect to the turbine diameter, and the distance from the turbine centerline is proportional to the real measurement, however, in non-dimensional units of diameters.

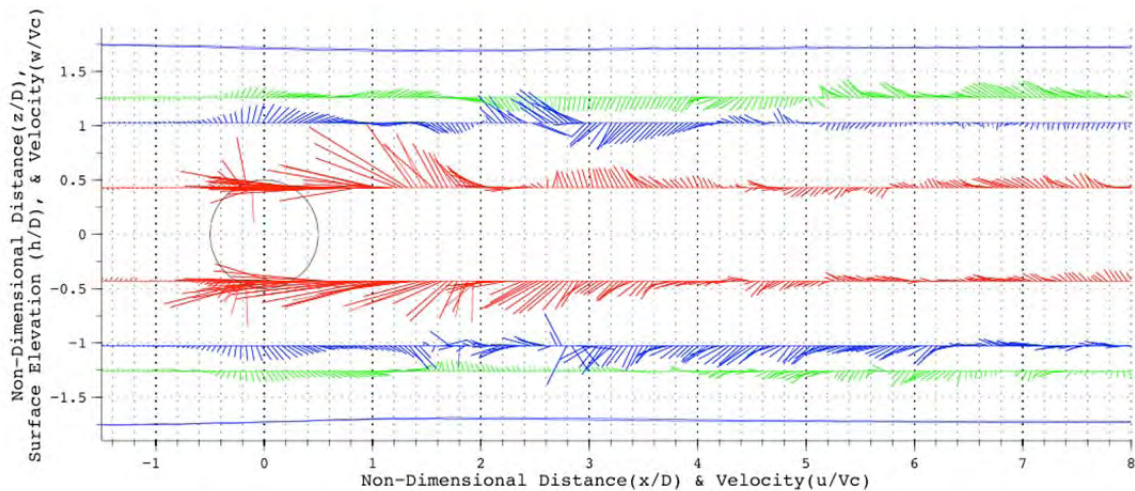


Figure 6.17 Vector plot with the upper and lower surface elevation for high solidity turbine.

Hydrodynamic testing in a semi-confined region with a large tank to turbine area ratio can amplify in the surface elevation as well as turbine performance. The effect is known as the blockage effect and has been discussed earlier in other papers, (Bahaja 2007, Whelan 2009). The amplified elevation change was observed by measuring a rise in surface elevation far up and down stream with the assumption that at large distances only the passing wave and the hydraulic pressure are present. The amplification of the elevation change was found in front of the turbine as well as behind the turbine with the larger drop downstream. The blockage effect is present in all tow tank and flume tests, particularly for devices with large drag and with large turbine to tank area ratio. A closer look at the surface elevation and blockage effect will be discussed in section 7.3.

7. DISCUSSION

The results from this study have shown four distinct stages in the flow field around a cross flow turbine. The stages are dependent on general viscous flow around any hydro-kinetics device in a uniform flow. Therefore, the stages will be present in either a lift dependent turbine or drag dependent turbine. However, the characteristics of each stage are strongly dependent on the type of turbine, solidity, TSR, and inflow velocity. The four stages are the up stream effects, the entrained flow behind the turbine, the connection between the entrainment to turbulence, and flow recovery. The stages are examined in this section as well as surface effects and the flipped reference frame of the tow tank.

7.1 Entrained Flow and Flow Recovery

One of the most important unanswered questions associated with marine hydrokinetics is the flow recovery behind the turbine. In this study the flow recovery is going to be analyzed using measurements of the mean velocity components, velocity magnitudes and velocity fluctuations for the different cross flow turbines. The high solidity case was analyzed first because of the uniform shape of the wake and simple flow patterns.

The recovery of the flow is divided into two regions of full and partial recovery. A partial recover is defined by flow within 80% of the initial velocity. A full recovery is more difficult to determine and is defined in this study as velocity within five percent of inflow velocity. The velocity magnitude for the high solidity turbine in Figure 7.1 demonstrates a partial recovery at ~3 diameters. The full recovery was measured at approximately 8 to 12 diameters downstream depending on the sample height for the high solidity turbine. A connection between the three velocity components was measured showing a phase relationship in accelerations. A rapid change in u-velocity is reflected by a large increase in w and v velocities. These changes are associated with the entrained flow seen in Figure 7.1 and 7.2 where the dominant velocity in the u-direction decays rapidly. A comparison of the velocity magnitude for the three components

shows conservation of energy until the occurrence of a spike in turbulence activity. The collapse of the entrained flow occurs at approximately 1.1 to 1.5 diameters. The flow recover is marked by a sudden increase in velocity fluctuation. The sudden increase in velocity fluctuation is seen as a second spike in TKE and Reynolds shear. The turbulent variables also show an abrupt end to the fluctuations as the large acceleration in the u-direction end. The second region of high velocity fluctuation appears to serve as a good indicator of transition between the entrained flow and a region of partial recovery.

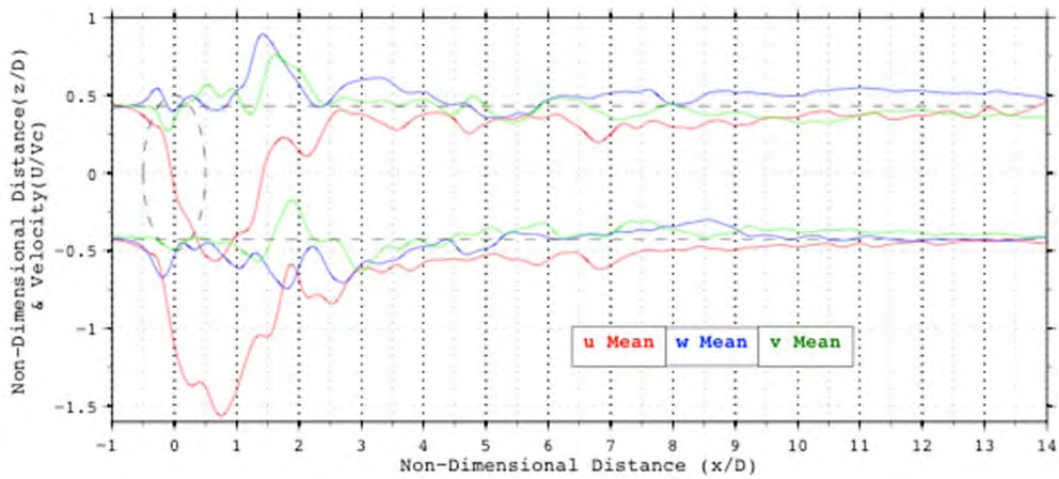


Figure 7.1 Mean velocity for each direction for high solidity turbine. The change momentum in x-direction shows equal change reflected into two orthogonal planes.

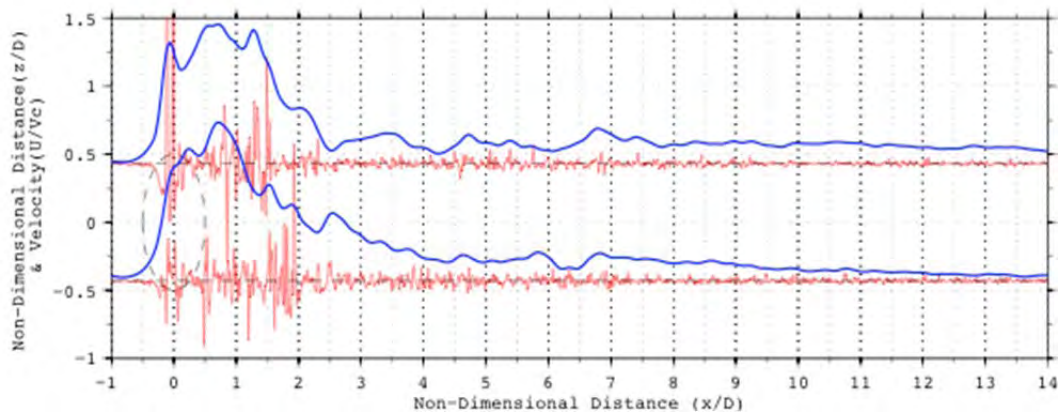


Figure 7.2 Mean velocity magnitude (red curves) and velocities fluctuation (blue curves) for high solidity turbine

The u-velocity fluctuations behavior down stream of the turbine show a consistent pattern through all acquired data. The velocity fluctuations have a brief period of high variability at

approximately zero distance followed by a sudden reduction seen in Figure 7.2. The decay rates of the two components are quite different: behind the turbine the fluctuations lasts only a short distance. In contrast to the slower decay of the mean component persists past ten diameters. The turbulent analysis shows the same trend measured for the high solidity turbine. A coupled behavior is thus demonstrated between flow recovery and turbulence. Where a connections between flow accelerations are associated with regions of high TKE and Reynolds shear are observed. Precise measurements of turbulent behavior are seen in the Reynolds shear and turbulence kinetic energy in Figure 6.13 and 6.15.

The entrained flow for the low solidity turbine appears uniform compared to the high solidity turbine. The u-mean velocity in Figure 7.3 shows that the entrained flow had different configuration through blade position as well as from ACL to BCL. Although the flow is unstable, the low solidity turbine entrained flow collapse can be determined from the data series using the turbulence variables. The second spike marks the vicinity of major velocity change as seen in the high solidity test. The full mean and turbulent variables are shown in Appendix A. For the low solidity turbine, the collapse occurs between 1.5 and 2.5 diameters downstream from the turbine, followed by the partial flow recovery between 2.5 and 10 diameters.

A relationship of the difference in flow recovery between the high and low solidity can be inferred from the measured blade forces. The flow variation of the low solidity turbine can be attributed to the oscillation of the blade forces because of the changing angle of attack. The forces for the low solidity case seen in Figure 3.8 show oscillations in all three degrees of freedom producing non-uniform flow. In comparison, the high solidity turbine has a more uniform wake and results in a less variable forces measured between the fluid and turbine demonstrating the relationship between the turbine and fluid has an effect on the overall flow field.

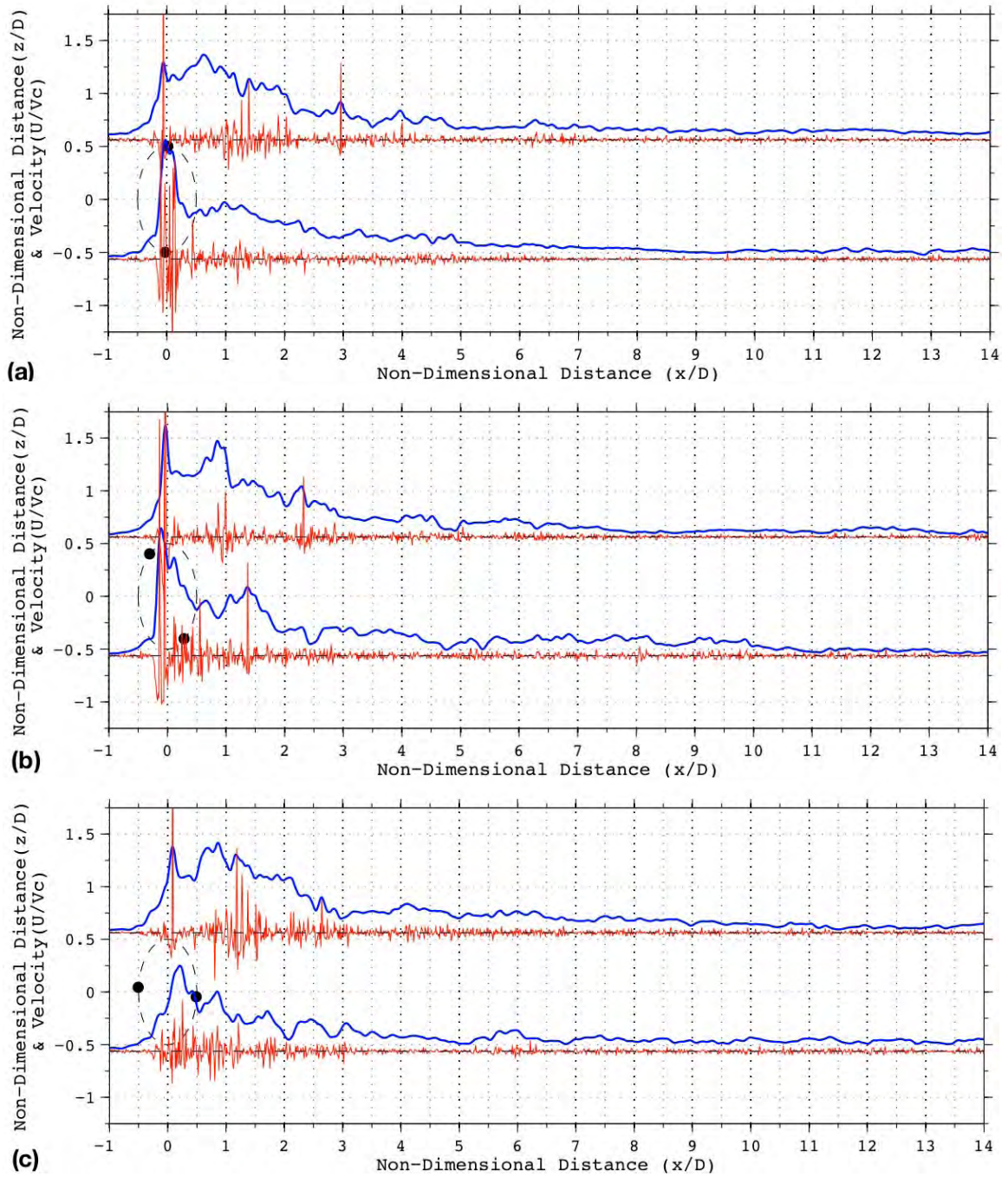


Figure 7.3 Mean (Blue) and fluctuation (Red) velocities for low solidity test over three blade positions

(a) Position 1 (b) Position 2 (c) Position 3

7.2. Upstream Effects

The approach of the turbine causes deceleration in the u-velocities while accelerating w-velocities away from the turbine. This upstream effect produces a flow around the turbine producing a bypass flow. The amount diverted from the turbine has significance relative to the environmental impact. The first environmental issue is that a turbine with high bypass will reduce the probability of fish strike. The amount of bypass flow determines the probability of wildlife will pass through or around forced around the swept area. Another environmental concern for developers is the effect of turbine scour on the seabed. Scour is a consequence of the turbine bypass flow increasing seafloor erosion. In addition to the impact on benthic ecology of the site scour can also compromise the turbine foundation.

Velocity measurements upstream of the turbine allow of the fraction of fluid forced away from the active area before the turbine arrives to be calculated. The bypass fraction is defined as the amount of flow diverted away from the turbine divided by the total flow. With no turbine, the ratio would be zero and a ratio of one if the turbine were solid. To convert the measurements into a non-dimensional bypass fraction the two volumetric flow rates are determined from the incoming flow (V_C) and measured vertical velocity (w) of the two inner sample heights. The distances between the two inner heights were included in the calculation as well as the distances between individual velocity sample volumes. The resulting quantity is the ratio representing the fraction of the fluid bypassing the turbine seen in Equation 12. Figure 7.3 depicts the physical principle.

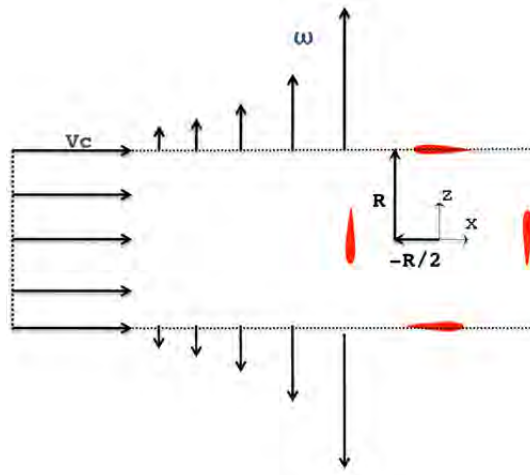


Figure 7.4 Visualization of the bypass flow and volumetric flow fraction

$$\dot{V}_{\text{Bypass}} = \int_{-\infty}^{\frac{R}{2}} \omega \, dx$$

$$\dot{V}_{\text{Ref}} = \int_{-R}^R u \, dz = 2 R V_c$$

$$\text{BPF} = \frac{\dot{V}_{\text{Bypass}}}{\dot{V}_{\text{Ref}}} \quad (12)$$

Bypass fraction for each side is presented and summed to obtain the total bypass fraction for both turbines. The bypass fraction results for the high solidity turbine are over three different TSR values are shown in Table 7.1. The results show a consistent increase of bypass with an increase in TSR. Due to the rotation of the turbine, both sides performed differently consistently showing a larger fraction ACL. For example, the topside for 0.9 and 1.4 TSR remained constant and the bottom side increases by an order of magnitude. If the turbine had no resistance to limit the rotational speed, then the turbine would free spin at the point near the zero performance at high TSR. The value for zero performance at a high TSR for the high solidity turbine is approximate 2.2 TSR. The bypass fraction for this point of operation was predicted using the assumption that the fraction is a function of the drag coefficient. The predicted bypass fraction for a free spin turbine is included in Table 7.1.

TSR	Bypass		
	Top	Bottom	Total
0.9	~0.033	~0.013	~0.05
1.4 (On Design)	~0.033	~0.10	~0.13
1.9	~0.223	~0.152	~0.38
2.2 <i>(Free Spin)</i>	<i>Predicted</i>		<i>~0.65 – 0.75</i>

Table 7.1 Flow Bypass for High Solidity for high solidity turbine over increasing TSR

The bypass fraction for low solidity turbine is shown in table 7.2 for each blade position. There is a measurable difference in bypass fraction for each blade position. A 20% shift on the mean was measured which clearly dominates the unsteady flow field for the low solidity wake. The mean bypass fraction is the average of the three positions and is remarkably similar to the high solidity turbine, with only 15% less bypass than the high solidity. In both cases, the bypass fractions are a relatively small portion of the overall volume.

TSR	Blade Position	Bypass Fraction		
		Top	Bottom	Total
2.25	1	~0.032	~0.052	~0.08
	2	~0.043	~0.091	~0.13
	3	~0.045	~0.068	~0.11
			Mean	~0.11

Table 7.2 Flow Bypass for Low Solidity for low solidity turbine

The two turbines of different solidity set to a TSR producing maximum performance divert approximately the same amount of fluid away from the active area. The two turbines have similar thrust coefficients (Table 3.6) when the two turbines were operating at optimal output. It thus can be concluded that the bypass factor is related to the drag coefficient even for the less conventional cross flow turbine.

Connection between the turbine forces and the flow field are present with the opportunity to simplify wake characterization. The two solidity turbines have solidity values of 0.16 and 0.32 and their measured drag coefficients are 0.30 and 0.32, respectfully. The bypass fraction only

changes slightly between the low and high solidity from 0.11 to 0.13 however the drag coefficient correlates well with the measured bypass fraction. This is further enforced by the measurements when TSR increases resulting in higher drag coefficients and the bypass flow.

7.3 Surface Elevation and Blockage Effect

An important factor to consider in hydrodynamic testing is that the turbine in the tow tank cannot be considered as an ideal infinite fluid. The ratio between the area of the turbine and the area of the tow tank is ~ 0.10 in the cross sectional y-z plane. The tank is relatively wide and shallow compared to the turbine, resulting in only 1.3 diameters of water above and below the turbine. The flow field is also influenced by the type of flow around the turbine. Flow in a restricted area can be either supercritical or subcritical and is determined by the Froude number, Equation 13. The Froude-number is the ratio of the flow velocity over the speed of surface wave.

The behavior of the free surface depends on whether the approaching flow being subcritical or supercritical. A subcritical flow ($Fr < 1$) will cause the water level to decrease around an obstruction. Conversely, a supercritical flow ($Fr > 1$) will cause the water level to increase over a obstruction. For tow tank test the Fr number is below supercritical flow value. A depression in the water level over the turbine occurred as expected. The height from the top of the turbine to the water surface was 0.33m and the largest inflow speed of 1.0ms^{-1} . Supercritical flow will only occurs if the speed is increased to 1.8ms^{-1} with the same depth or the depth is reduced to 0.1m.

$$Fr = \frac{V_c}{\sqrt{g h}} = 0.55 \quad (13)$$

However, depending on the test configuration a buildup of a hydraulic head can occur. The higher solidity turbine is more likely to produce a hydraulic head due to its higher number of blades and the low variability in turbine forces. The blockage effect was previously introduced in section 6.5. The tests in this study were performed at a relatively high TSR and carriage speed producing a measurable hydraulic head only for the high solidity turbine. The blockage effect

appeared in the surface data for the high solidity turbine as an elevated surface as soon as the carriage started to accelerate from rest. The blockage effect is also present down stream from the turbine where the effect is negative change in elevation. As the turbine neared the end of the tow tank, the elevation begins to recover due to the reduced tank volume ahead of the turbine. Due to the reduced blade area of the low solidity turbine the blockage effect is much smaller and is considered negligible.

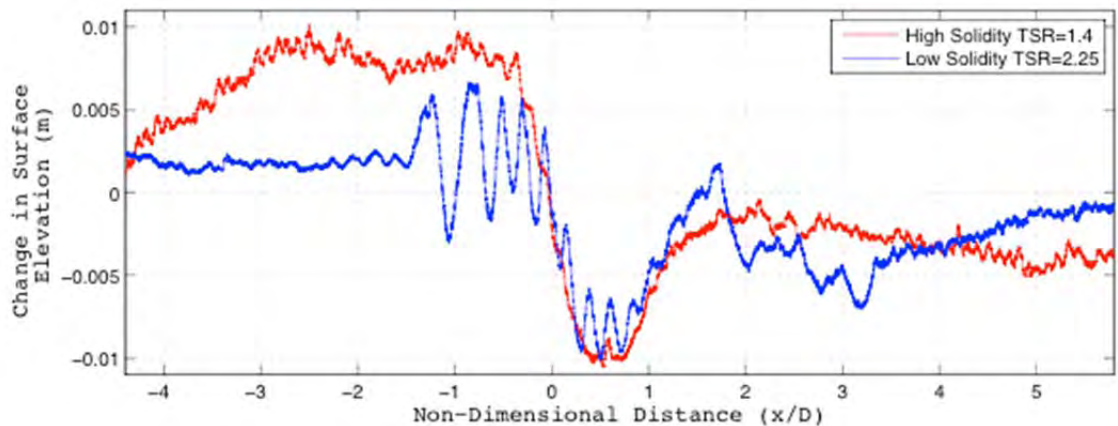


Figure 7.5 Change in surface elevations for two different solidities. Tests were done with the constant carriage speed at 0.8ms^{-1} for the high and low solidity at optimum TSR.

The surface effects from the low solidity turbine show a different response with a region dominated by gravity waves near the turbine. The fewer number of blades for the low solidity turbine allowed individual blade effects to be measured in the surface elevation. The waves occur 1.5 diameters in front and 1 diameter behind the turbine. The increase elevation at 1 to 1.5 diameters in Figure 7.5 is associated with the second hydraulic jump to return to the water level to equilibrium. The waves also occur at the same rate as the blade frequency. A Fourier transform on the surface elevation measurements (Figure 7.6) confirmed the blade frequency was equal to the surface wave frequency. Thus, the surface elevations differ according to TSR showing individual blade effects on the surface.

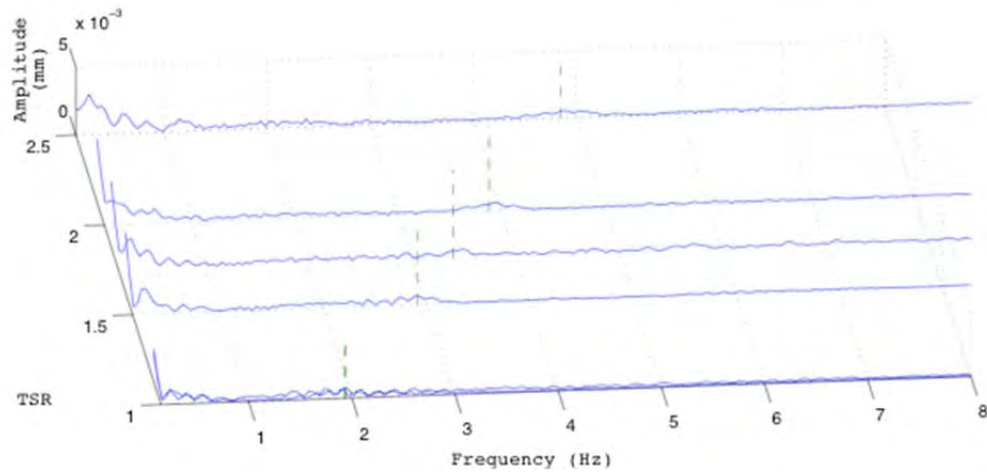


Figure 7.6 Fourier transform of measured surface elevation for the low solidity turbine over different TSR values. The blade frequency is marked by green dash line.

Surface elevation measurements were also collected for different TSR using the high solidity turbine. Three different TSR were used 0.9, 1.4, and 1.9. A 1.4 TSR yielded the maximum performance. The increase in TSR causes an increase in the drag coefficient affecting the hydraulic jump of the turbine. In Figure 7.7 and 7.8 the measurements of surface elevation three TSR are shown with the carriage traveling in opposite directions in the two figures. These measurements show the difference in the hydraulic jump as the TSR changes. As a result, a larger pressure drop occurs across the turbine, which is seen in the hydraulic jump.

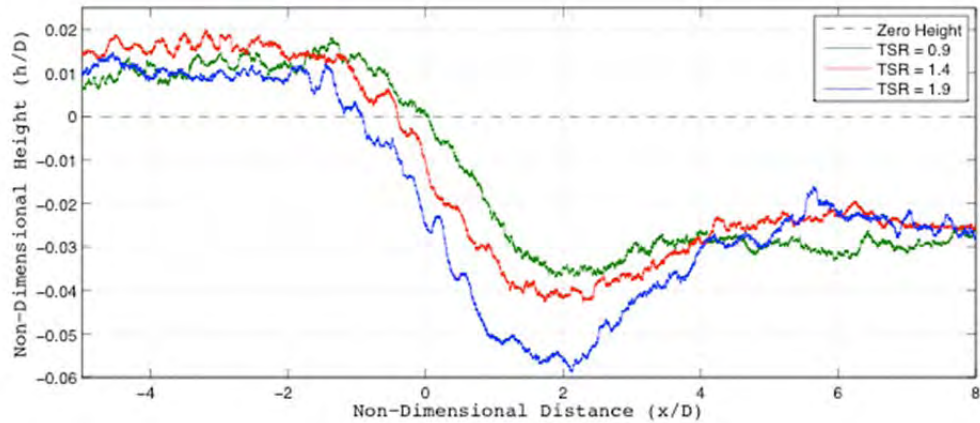


Figure 7.7 Surface elevation for high solidity test with three different TSR for power side on top

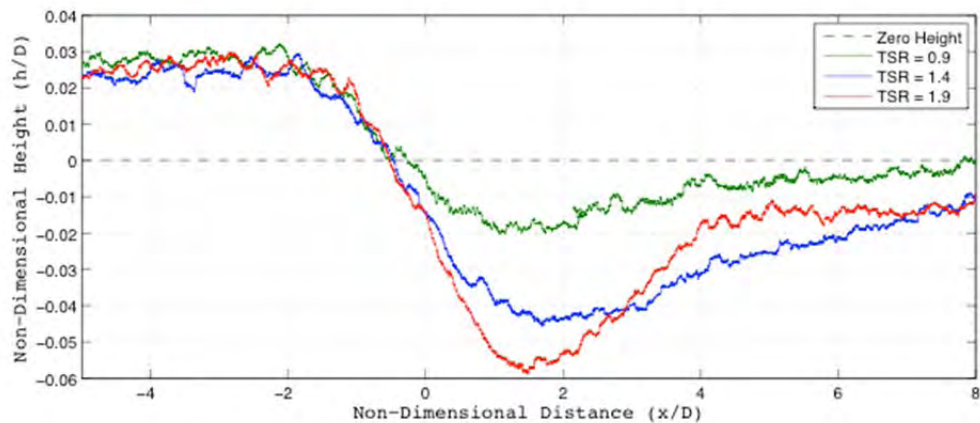


Figure 7.8 Surface elevation for high solidity test with three different TSR for return side on top

7.4. Flipped Reference Frame

In addition to the direction and blockage another effect is evident in the testing. A fundamental principle of a tow tanks the turbine move through a fluid at rest. For test of a turbine in a tow tank the result is a flipped reference frame. The fluid is at rest while work is done to move the turbine through the fluid. The flipped reference frame creates a discrepancy between the velocities in the wake and in the surrounding fluid. For a stationary turbine the flow decelerates relative to the surrounding unaffected flow, resulting in a pressure gradient which forces the wake to expand. The expansion of the wake is described by Bitz's momentum theory. In the Bitz theory a simplified analysis can predict the cross sectional area of the wake seen in the

flow diagram in Figure 7.6. However, the theory assumes steady inviscid laminar flow. The theory also ignores the blade section lifts and drag forces associated with wing theory. If the momentum theory is compared to the tow tank reference frame, differences appear both in wake and in the surrounding fluid. In contrast to the actual turbine, in the tow tank the flow is accelerated and moves with the turbine. The surrounding fluid is at rest and the result is that a pressure gradient develops in the opposite direction if Bernoulli's principle is considered.

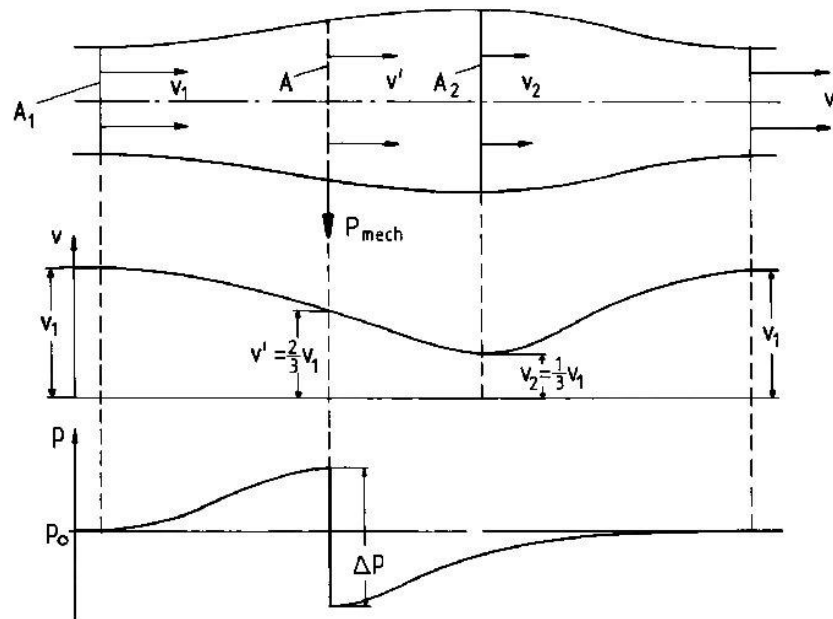


Figure 7.9 Actuator Disk principle from the Betz momentum theory (Hau, E., 2006)

The validity of Bernoulli's principle to the understanding of the wake is dependent on the introduction of unsteady viscous turbulent flow. A derivation of Reynolds stress shows that the three turbulent components that cause momentum transfer across a boundary introduce an unsteady time-dependent term. Because of time-dependent term the turbulent momentum transfer dominates. Therefore, the tow tank may in fact be useful for wake measurements. Since turbulence is primarily responsible for the wake in both the actual application and the tow tank tests. The flipped reference frame is not a concern.

8. CONCLUSION

This study extends previous work on the flow recovery of marine hydrokinetic devices to cross flow turbines. This experimental work was performed using a reduced scaled cross-flow turbine to analyze the wake changes as the blade rotates for different blade solidities, tip speed ratios and blade mounting angles.

The results show four distinct regions of the flow field around a cross flow turbine. These regions are dependent on the general viscous flow around any hydro-kinetic device in a uniform flow. These flow in these regions are to be strongly dependent on the solidity, TSR, and inflow velocity of the cross-flow turbine. Since the regions are dependent on the turbine configuration, they may be an important factor to consider with regards to turbine designs and installations. In particular, the measurements of the location where the flow is fully recovered are particularly useful for turbine array design.

Major factors such as the bypass flow are also important characteristics to identify. The bypass flow for the low solidity and high solidity cases was measured since it is an important factor for calculating the probability of the turbines striking marine fauna. Results of the bypass flow in the terms of Reynolds shear and TKE are presented for consideration of future studies of bottom scour. Finally, the entrained flow is analyzed to provide information for future work on the impacts on marine fauna and on the sediment transport for the low and high velocity regions.

Overall, what has been demonstrated is the ability to characterize some of the most important features of the flow field around and behind a cross flow turbine. While this type of study is intended to provide information for turbine array design, the information presented is also a useful tool to understand the impact that a cross flow turbine will have on marine fauna. This study can also help to provide the basis for a statistical analysis to define the flow field regions around a cross-flow turbine.

REFERENCES

- Bahaja, A. S., & Mollandb, A. F., Chaplin, J. R., Batten, W. M. (2007). *Power and thrust measurements of marine current turbines under various hydrodynamic flow conditions in a cavitation tunnel and a towing tank. Renewable energy*, 32, 407-426
- Blanckaert, R. H., & Lemmin, U. (2006). Means of noise reduction in acoustic turbulence measurements. *Journal of Hydraulic Research*, 44, 3-18.
- Charlier, R. H. (2006). *Tidal energy*. New York: Van Nostrand Reinhold Company.
- Dabiri, J. (2010). *Order-of-magnitude enhancement of wind farm power density via counter-rotating vertical-axis wind turbine arrays*. Informally published manuscript, Graduate Aeronautical Laboratories & Bioengineering, California Institute of Technology, Pasadena, CA.
- deBree, G. S. (2012). *Testing and Modeling of High Solidity Cross-Flow Tidal Turbines*. Master's Thesis, University of Maine, Orono, ME.
- Goring1 D., Nikora V. (2002). Despeaking acoustic doppler velocimeter data. *Journal of Hydraulic Engineering*, 117-126.
- Hau, E. (2006). *Wind turbines: Fundamentals, technologies, application, economics*. Berlin: Springer.
- Harris, F. J. (1978). On the use of windows for harmonic analysis with the discrete fourier transform. *IEEE*, 66(1), 51-83.
- Li, L., Xu, C., & Zhang, Z. (1999). Measurement of mean burst period in wall turbulence by wavelet analysis. *Communications in Nonlinear Science & Numerical Simulation*, 4(3), 200-206.
- Lohrmann A., Cabrera R., Kraus N.C. (1994). Acoustic Doppler velocimeter (ADV) for laboratory use. *Proceedings of the Symposium on Fundamentals and Advancements in Hydraulic Measurements and Experimentation*. 351-365.
- Lokocz, T., 2010, "Solid Mechanics of Cross Flow Tidal Turbine Blades," University of Maine.
- Myers L., Bahaj A. (2009, March). Experimental analysis of the flow field around horizontal axis tidal turbines by use of scale mesh disk rotor simulators. *Ocean Engineering*, 219-227.
- Polagye B., Cleve B.V., Copping A., Kirkendall K. (2011). Environmental Effects of Tidal Energy. U.S. Department of Commerce National Oceanic and Atmospheric Administration National Marine Fisheries Service
- Rinoshika A., Zhou Y. (2007). Effects of initial conditions on wavelet-decomposed structures in a turbulent far-wake. *International Journal of Heat and Fluid Flow*, 948-962

- Rusello, P.J., Lohrmann, A., Siegel, E., Maddux, T. (2006). Improvements in acoustic doppler velocimetry. *Proceedings of the Seventh International Conference on Hydroscience and Engineering*, Sept.
- Shiono, M., Suzuki, K., and Kiho, S. (2000). An Experimental Study of the Characteristics of a Darrieus Turbine for Tidal Power Generation, *Electrical Engineering in Japan*. 132(3) 38-47
- Thorpe, S., (2007). *An Introduction to Ocean Turbulence*. Cambridge MA: Cambridge Press.
- Tropea C., Yarin A. L., Foss J.F., (Eds.), (2007) *Springer Handbook Experimental Fluid Mechanics*, Berlin Heidelberg: Springer-Verlag
- Urbina, R., Peterson, M.L., Kimball, R.W., DeBree, G.S., and Cameron, M.P., (2011), Modeling and Validation of a Cross Flow Turbine Using Free Vortex Model and a Modified Dynamic Stall Model, Submitted to: *Renewable Energy*.
- Voulgaris G., Trowbridge H., (1997). Evaluation of the Acoustic Doppler Velocimeter (ADV) for Turbulence Measurements. *Journal of Atmospheric and Oceanic Technology*. 272-289
- Whelan J. I., Graham J. M. R., Peiro J. (2009) A free-surface and blockage correction for tidal turbines. *Journal of Fluid Mechanics*. 624, 281–291

APPENDICES

Appendix A: Reynolds Decomposition

Complete set of Reynolds decomposition for all tested turbine arrangements. The low solidity turbine Reynolds decomposition is shown in Figure B.1 through B.3 for the three blade positions. Figure B.4 through B.6 show the components for the high solidity turbine.

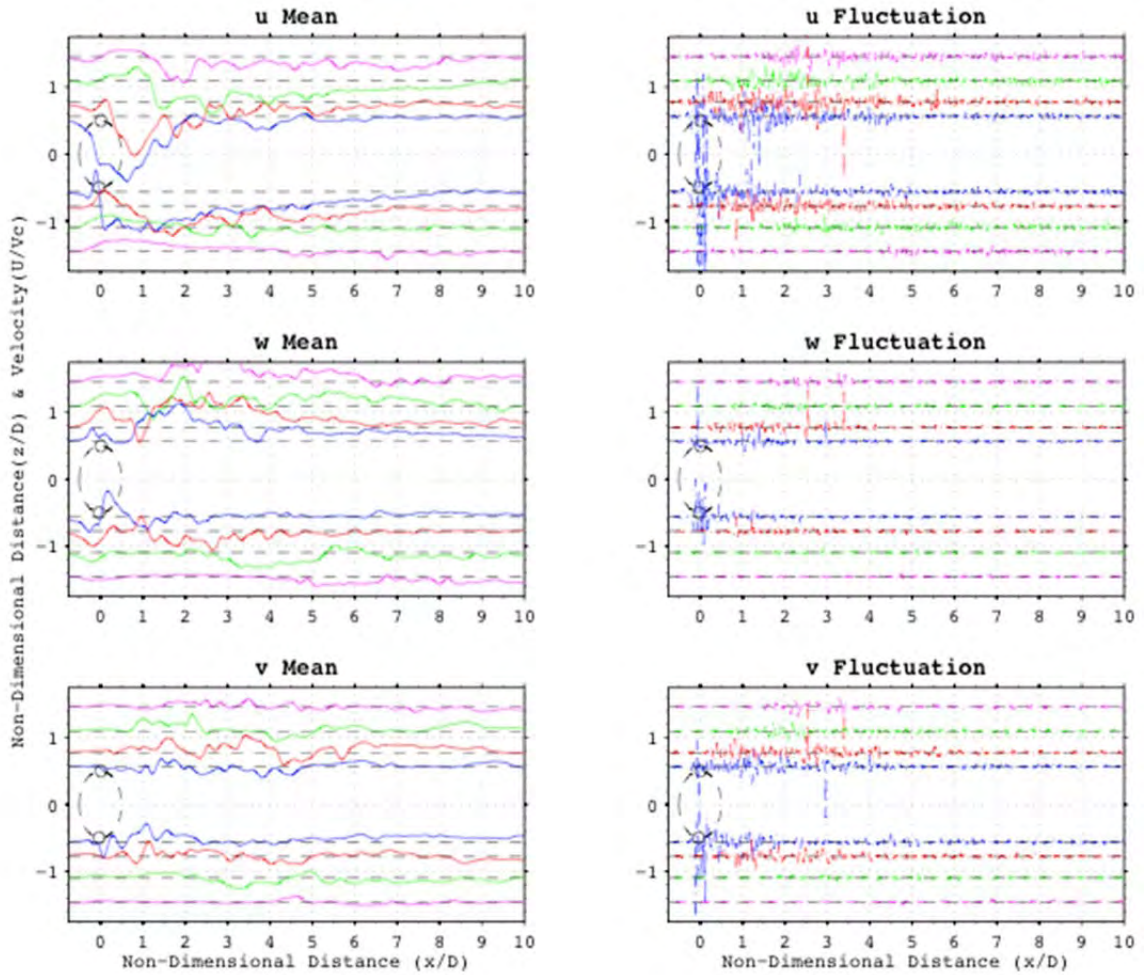


Figure A.1 Reynolds decomposition for each velocity component for low solidity at blade position 1

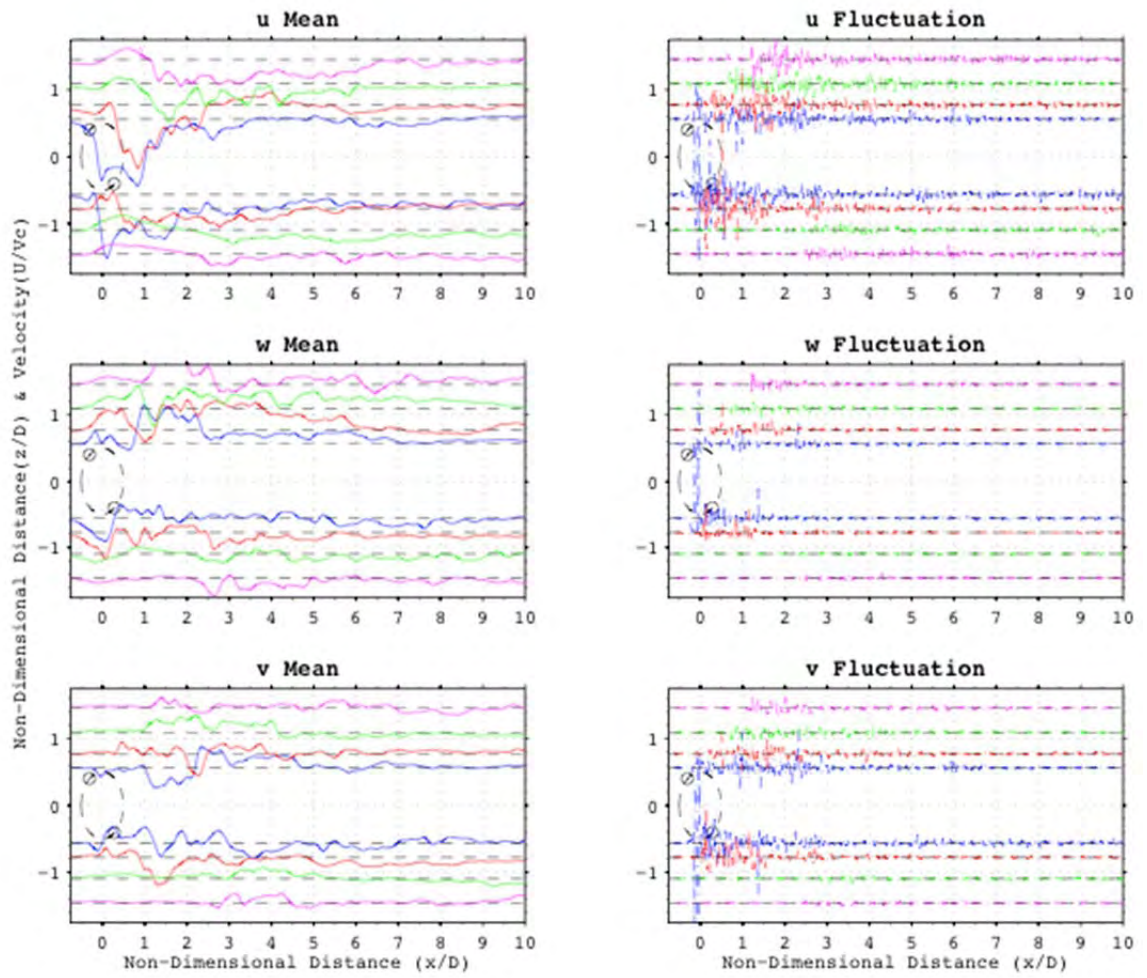


Figure A.2 Reynolds decomposition for each velocity component for low solidity at blade position 2

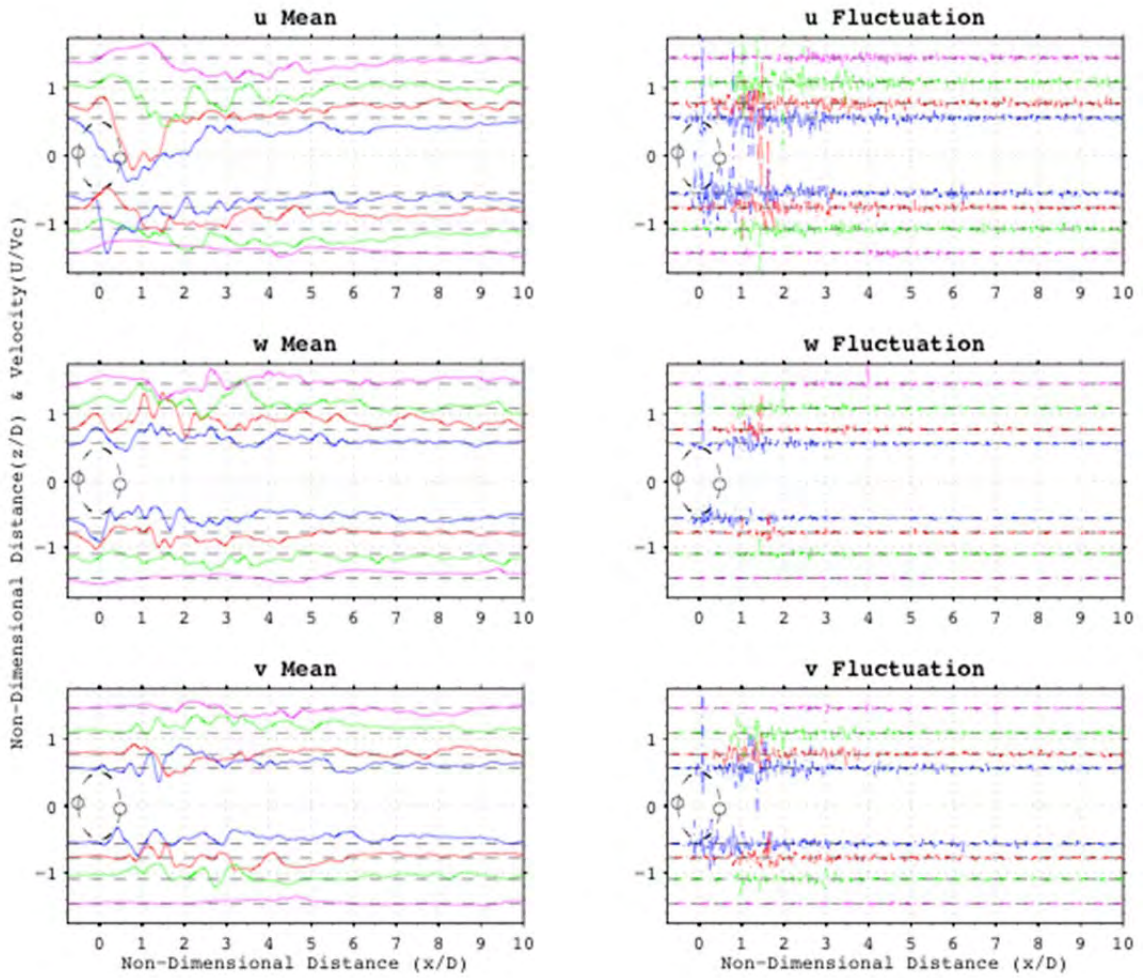


Figure A.3 Reynolds decomposition for each velocity component for low solidity at blade position 3

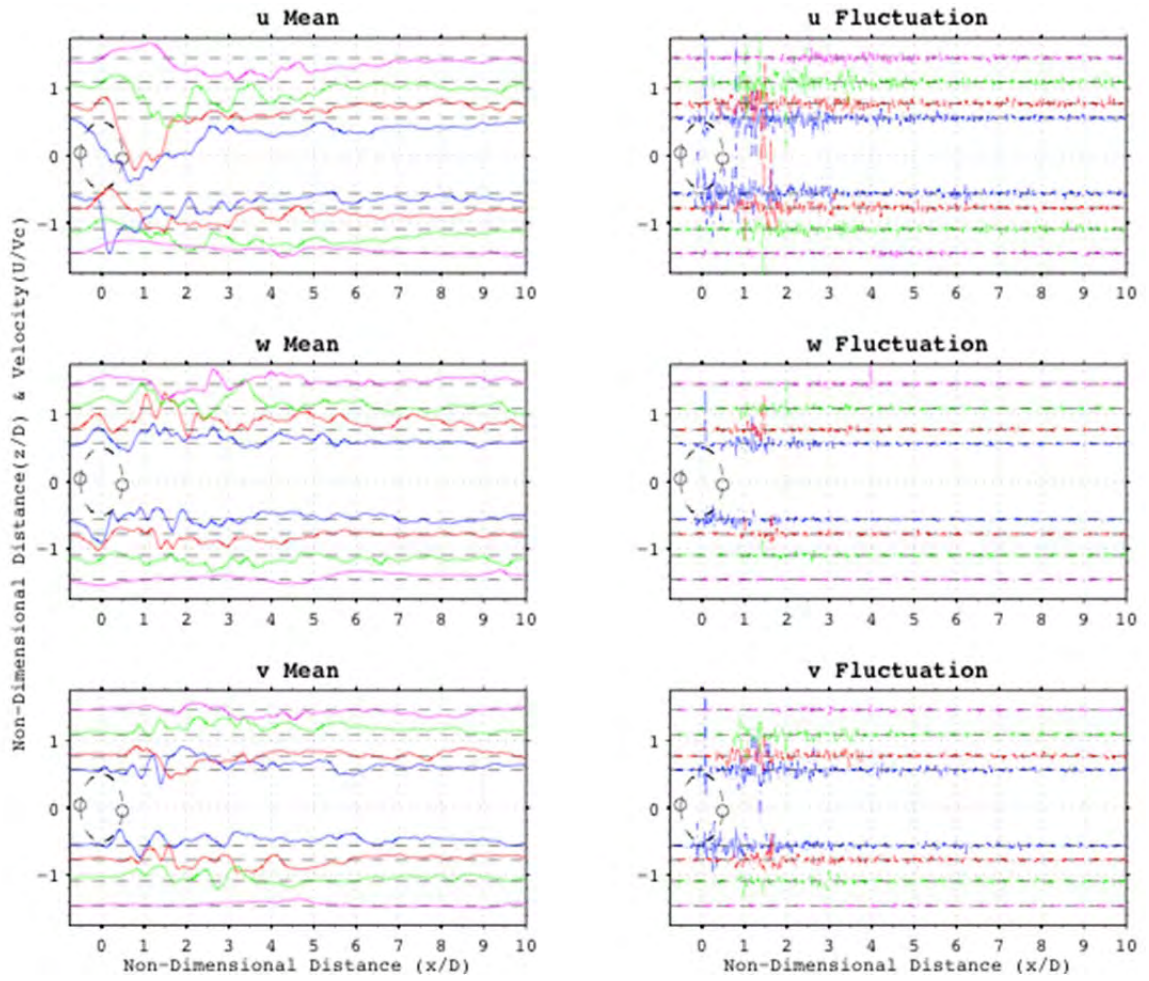


Figure A.4 Reynolds decomposition for each velocity component for high solidity at 1.4 TSR



Figure A.5 Reynolds decomposition for each velocity component for high solidity at 0.9 TSR



Figure A.6 Reynolds decomposition for each velocity component for high solidity at 1.9 TSR

Appendix B: High Solidity Wake Characteristics at different TSR

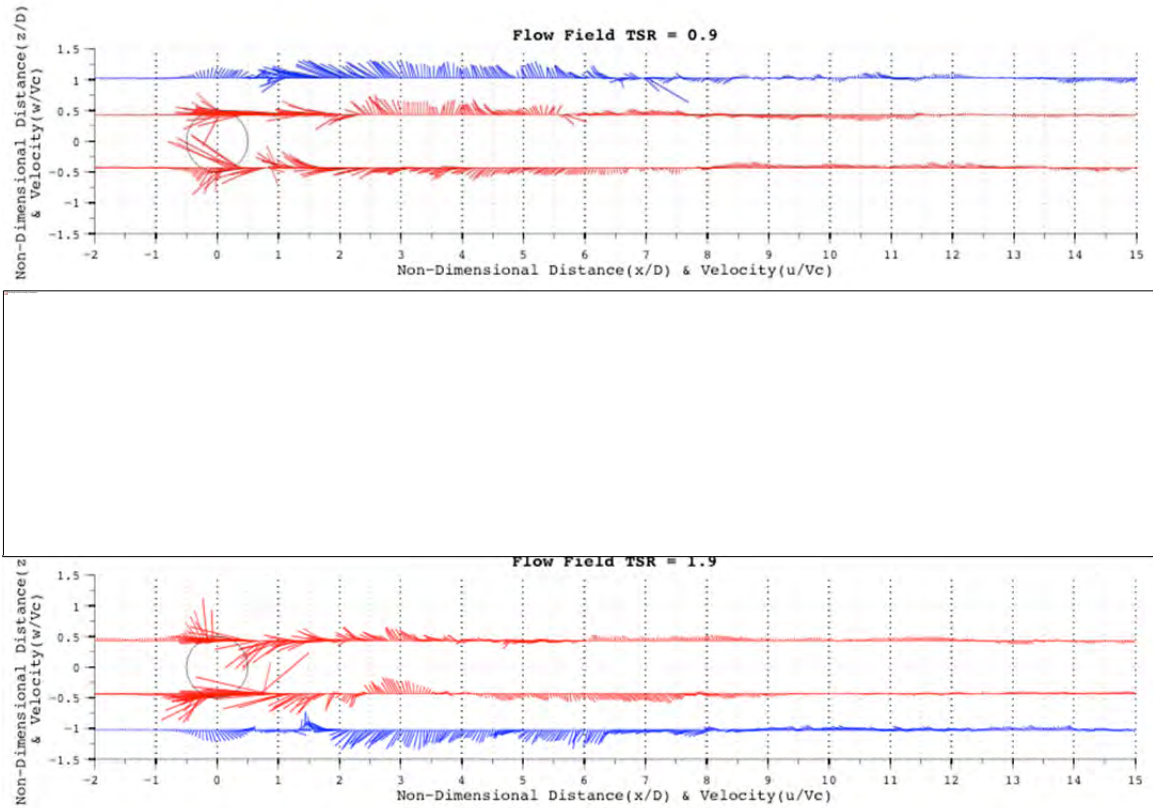


Figure B.1 Flow Field for high solidity turbine operating at different TSR..
0.9 TSR Top, 1.4 TSR middle, and 1.9 TSR bottom



Figure B.2 Turbulent kinetic energy for high solidity turbine operating at different TSR.
0.9 TSR Top, 1.4 TSR middle, and 1.9 (Bottom) TSR



Figure B.3 Reynolds shear for high solidity turbine operating at different TSR.
0.9 TSR Top, 1.4 TSR middle, and 1.9 (Bottom) TSR

Appendix C: Low Solidity Turbine Wake Characteristics

Full velocity results for low solidity turbine for different blade positions. The results shown below are velocity magnitude and the three velocity components.

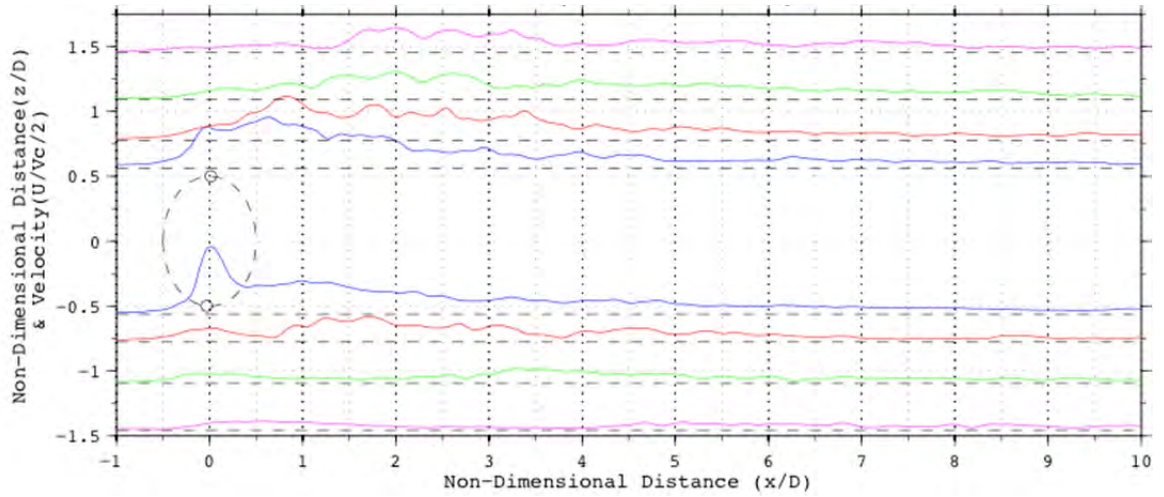


Figure C.1 Velocity magnitude for blade position 1

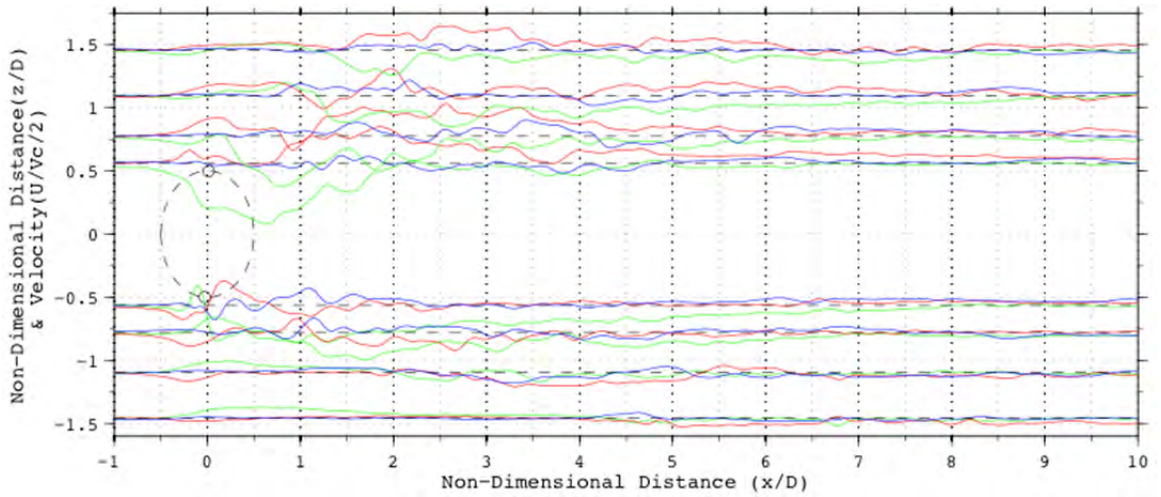


Figure C.2 Velocity components for blade position 1

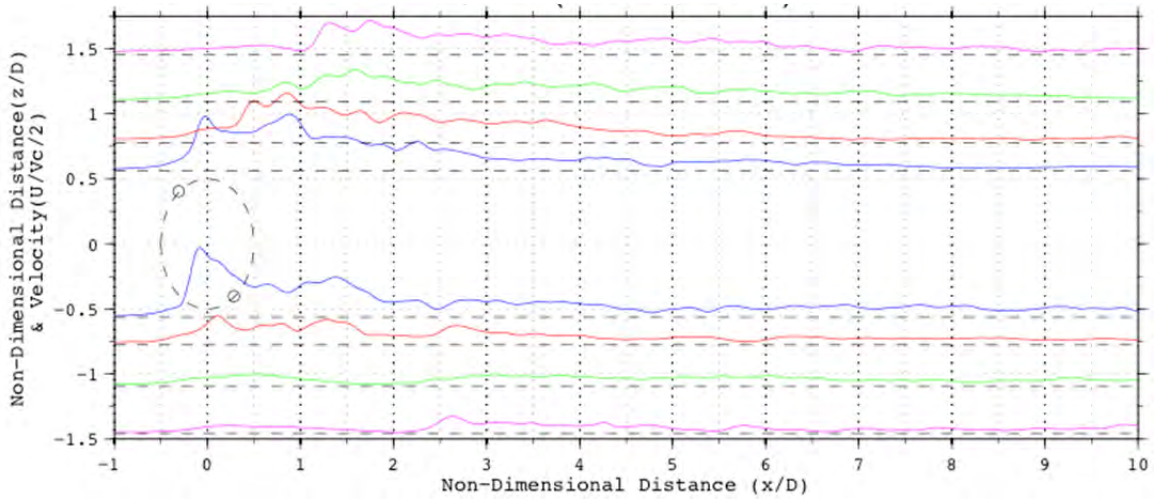


Figure C.3 Velocity magnitude for blade position 2

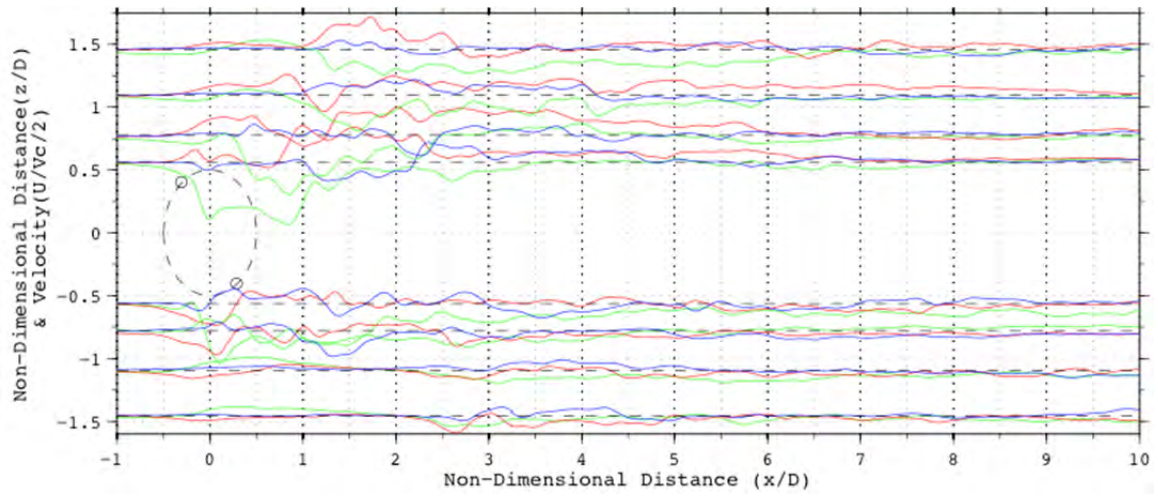


Figure C.4 Velocity components for blade position 2

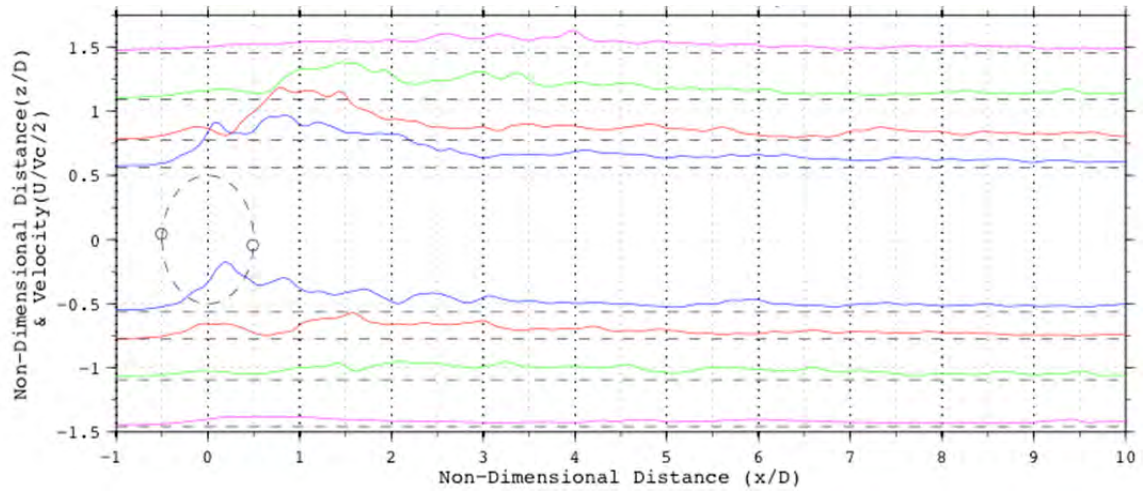


Figure C.5 Velocity magnitude for blade position 3

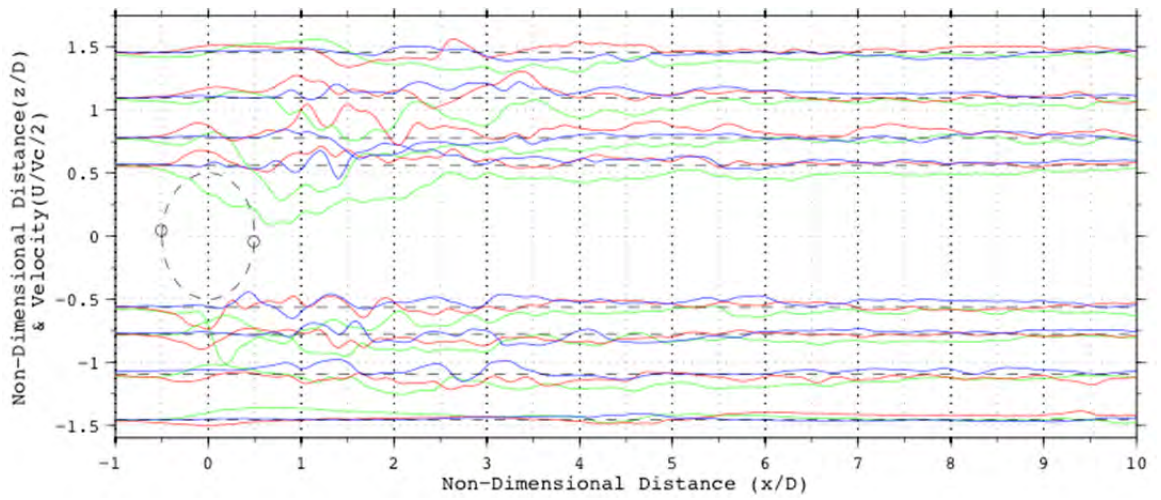


Figure C.6 Velocity components for blade position 3

BIOGRAPHY OF THE AUTHOR

Matthew Cameron attended the University of Maine, Orono, as an undergraduate from 2005 to 2009, whereupon he graduated with a Bachelor's degree in Mechanical Engineering. He decided to further his education and entered the Mechanical Engineering graduate program at The University of Maine in the fall of 2010. After receiving his degree, Matthew intends to pursue a career of invention and innovation. Matthew is a candidate for the Master of Science degree in Mechanical Engineering from The University of Maine in August, 2012.

Appendix Task 2-1

FISH IN A TIDALLY DYNAMIC REGION IN MAINE: HYDROACOUSTIC ASSESSMENTS IN RELATION TO TIDAL POWER DEVELOPMENT

By

Haley A. Viehman

B.S. Cornell University, 2009

A THESIS

Submitted in Partial Fulfillment of the

Requirements for the Degree of

Master of Science

(in Marine Bioresources)

The University of Maine

May, 2012

Advisory Committee:

Gayle Zydlewski, Assistant Professor of Marine Science, Advisor

Michael Peterson, Professor of Mechanical Engineering

James McCleave, Professor Emeritus of Marine Science

LIBRARY RIGHTS STATEMENT

In presenting this thesis in partial fulfillment of the requirements for an advanced degree at the University of Maine, I agree that the Library shall make it freely available for inspection. I further agree that permission for "fair use" copying of this thesis for scholarly purposes may be granted by the Librarian. It is understood that any copying or publication of this thesis for financial gain shall not be allowed without my written permission.

Signature:

Date:

**FISH IN A TIDALLY DYNAMIC REGION IN MAINE: HYDROACOUSTIC
ASSESSMENTS IN RELATION TO TIDAL POWER DEVELOPMENT**

By Haley A. Viehman

Thesis Advisor: Dr. Gayle Zydlewski

An Abstract of the Thesis Presented
in Partial Fulfillment of the Requirements for the
Degree of Master of Science
(in Marine Bioresources)
May, 2012

Fish ecology in regions of extreme tidal flows is poorly understood, but as these areas link on- and off-shore habitats, they are important to many marine and diadromous fish species. Strong tidal currents are also being targeted for energy extraction, but the effects of tidal energy devices on fish are unknown. The probability of fish encountering a tidal energy turbine is highly dependent on the vertical distribution of fish at the project site. In extremely tidal coastal areas, fish presence and distribution is heavily influenced by tidal, diel, and seasonal cycles. Understanding the vertical distribution of fish therefore requires sampling on a fine temporal and spatial scale. Stationary hydroacoustic surveys may be used to gather these data, as part of a BACI (Before, After, Control, Impact) type study design, to predict then monitor the effects of tidal energy devices on fishes.

Starting in May 2010, a down-looking, single-beam SIMRAD echosounder and a DIDSON (Dual-frequency IDentification SONar) unit were used to document the

relative density of fish throughout the water column at a targeted pilot project site and a control site in Cobscook Bay, Maine. Stationary 24-hour surveys were carried out each season to examine variation in fish density and vertical distribution. Relative fish density was highest in spring and fall, and almost always increased near the bottom, regardless of tide or time of day. Tide and day/night had some effect on the vertical distribution of fish, but the effect was not the same each month. Results from these analyses will be used to predict the likelihood of fish encountering the turbine and to create a basis for comparison of data collected after device installation.

Direct observation of fish reactions to a full-scale test device was carried out in September of 2010. A test turbine suspended below a floating research platform was monitored for 24 hours using two DIDSON units. A higher proportion of fish interacted with the device when it was still than when it was rotating. A greater portion interacted at night, and the type of interaction shifted from avoidance during the day to passing into the turbine at night. This behavioral shift was most obvious in small fish (<10 cm), nearly all of which passed through the device at night; most large fish (>20 cm) still avoided the turbine. Most fish were present at night during the slack tide.

Combining the baseline knowledge of where fish are in the water column with knowledge of how they behave in close proximity to an operating tidal device will

provide a more complete picture of the potential effects these devices could have once installed.

THESIS/DISSERTATION/PROJECT

ACCEPTANCE STATEMENT

On behalf of the Graduate Committee for Haley A. Viehman I affirm that this manuscript is the final and accepted thesis. Signatures of all committee members are on file with the Graduate School at the University of Maine, 42 Stodder Hall, Orono, ME.

Dr. Gayle Zydlewski, Assistant Professor of Marine Science

Date

ACKNOWLEDGEMENTS

I would like to thank my advisory committee, Drs. Gayle Zydlewski, Michael Peterson, and James McCleave, for the opportunity to participate in this research, and for their continuous enthusiasm and dedication to the project. This work would not have been possible without the unlimited guidance and patience of Dr. Zydlewski.

I would also like to thank the other members of the Maine Tidal Power Initiative for their insights and support. Thanks go out to Garrett Staines and Alexander Jensen, who provided invaluable support in the lab and the field, and to Amy Wyman for her close attention to hours of DIDSON footage. Thanks as well to the other members of the Zydlewski lab who aided in field work preparation or took shifts on the acoustics boat.

The employees of Ocean Renewable Power Company were essential to this project, generously contributing time and resources to the work in Cobscook Bay. The input of Donald Degan and Anna-Maria Mueller was invaluable in shaping acoustic analyses.

None of this work could have taken place without the knowledge and skill of Captain Butch Harris and his crew, and I thank them for their boundless generosity and support through many long hours of acoustic surveys, and for the countless times they have gone out of their way to assist us during this process.

Funding was provided by the United States Department of Energy project
#DE-EE0000298.

Finally, I wish to thank my family for their unlimited love and support.

TABLE OF CONTENTS

ACKNOWLEDGEMENTS.....	7
LIST OF TABLES.....	14
LIST OF FIGURES.....	15

Chapter

AN APPROACH FOR ASSESSING FISH PRESENCE IN RELATION TO TIDAL

POWER DEVELOPMENT	16
1.1 Abstract	16
1.2. Introduction	17
1.3. General Methodology.....	20
1.4. Sampling Gears	22
1.4.1. Benthic and Pelagic Trawling.....	22
1.4.2. Seines, Fyke nets, Weirs	23
1.4.3. Acoustic Telemetry	24
1.4.4. Hydroacoustics.....	25
1.4.5. Acoustic Imaging: the Dual-frequency IDentification SONar (DIDSON).....	28

1.5. Case study: Cobscook Bay	28
1.5.1 Site Considerations	29
1.5.2 Sampling Gear	30
1.5.3 Data Analysis.....	31
1.6. Discussion	32
1.6.1. Sampling Schedule.....	32
1.6.2. BACI Approach.....	33
1.6.3. Sampling Gear	33
1.7. Recommendations.....	35
VERTICAL DISTRIBUTION OF FISH AT A TIDALLY DYNAMIC REGION	
TARGETED FOR ENERGY EXTRACTION	110
2.1. Abstract	111
2.2. Introduction	147
2.3. Methods.....	151
2.3.1. Site	41
2.3.2. Equipment.....	43
2.3.3. Field Sampling.....	45
2.3.4. Data Analysis.....	153
2.3.4.1. Acoustic Data Processing.....	47

2.3.4.2. Analysis of variance in total area backscatter of the entire water column.....	51
2.3.4.3. Analysis of the distribution of area backscatter within the water column.....	52
2.4. Results.....	156
2.4.1. Does the density of fish in the water column vary year to year?.....	53
2.4.2. Does total water column fish density vary among months of the year?.....	54
2.4.3. Does fish density vary spatially?	54
2.4.4. What is the vertical distribution of fish density in the water column?	54
2.4.5. Does the vertical distribution of fish density vary seasonally and annually?	55
2.4.6. Does the vertical distribution of fish density vary with day and night or tidal stage?	58
2.5. Discussion	158
FISH INTERACTIONS WITH A COMMERCIAL-SCALE TIDAL ENERGY DEVICE IN A FIELD SETTING	69

3.1. Abstract	69
3.2. Introduction	111
3.3. Methods.....	114
3.3.1. Site	73
3.3.2. Equipment.....	74
3.3.3. Survey Sampling.....	76
3.3.4. Data Analysis.....	116
3.3.4.1. Classification of Fish Behavior	117
3.3.4.2. Analysis of Factors Affecting Fish Behavior	78
3.4. Results.....	119
3.4.1. Fish Schools.....	81
3.4.2. Individual Fish	83
3.4.3. What affects fish-turbine interactions?	83
3.4.3.1. Turbine Rotating vs. Still:	83
3.4.3.2. Effects on Initial Behavioral Response to Turbine: Fish Fore of Turbine.....	84
3.4.3.3. Departure from Turbine: Fish Aft of Turbine.....	87
3.5. Discussion	122
REFERENCES.....	99
BIOGRAPHY OF THE AUTHOR.....	109

LIST OF TABLES

Table 1.1	Hydroacoustic sampling schedule	31
Table 2.1	Hydroacoustic survey information	47
Table 2.2	Expected fish and target strengths	50
Table 2.3	Vertical distributions of fish at CB1, 2010 v. 2011	56
Table 2.4	Vertical distributions of fish, day v. night.....	58
Table 2.5	Vertical distributions of fish, ebb tide v. flood tide	59
Table 3.1	Fish reactions to test turbine.....	79

LIST OF FIGURES

Figure 2.1	Pilot tidal energy device.....	40
Figure 2.2	Map of Cobscook Bay and locations of hydroacoustic surveys.....	42
Figure 2.3	Acoustic survey setup and sample data	44
Figure 2.4	Water column total area backscatter v. sampling	53
Figure 2.5	Vertical distributions of fish at CB1	57
Figure 3.1	Map of Cobscook Bay	73
Figure 3.2	Research platform	75
Figure 3.3	Survey setup	76
Figure 3.4	Fish reactions to test turbine.....	79
Figure 3.5	Current speed and number of fish detected v. time	80
Figure 3.6	Fish size distribution	81
Figure 3.7	Effects of turbine state on fish behavior	84
Figure 3.8	Effects of day/night on fish behavior	85
Figure 3.9	Effects of day/night on fish behaviors in front of turbine, by size class	87
Figure 3.10	Effects of day/night on fish behaviors behind turbine, by size class	88

CHAPTER 1

AN APPROACH FOR ASSESSING FISH PRESENCE IN RELATION TO TIDAL POWER DEVELOPMENT

1.1 Abstract

This paper seeks to guide fish assessment studies related to tidal power development because the lack of installed projects to date has prevented the creation of any standard protocols. A before-after-control-impact (BACI) study design is suggested to examine changes in the presence and vertical distribution of fishes. Changes in these aspects of fish behavior occur on small (tidal) and large (seasonal) temporal scales, and sampling must occur at similar scales. Fine temporal and spatial resolution is required to characterize fish movements associated with tide or diel cycle, but surveys must be conducted across long periods of time in order to identify seasonal trends. Several tools for the collection of such data are described and discussed. One approach that provides the high-resolution data necessary for these analyses is hydroacoustics. A fish assessment study related to tidal power developments in Cobscook Bay, Maine is presented as an example. This study used stationary hydroacoustic surveys to collect baseline data on fish presence and distribution during every season over the course of two years. The methods and results of the study are discussed, and recommendations for future assessments are made.

1.2. Introduction

Little is known of fish ecology in the regions of extreme tidal flows that are currently targeted for tidal power development. These sites are often the interface between deep-ocean habitats and inshore foraging, spawning, and nursery areas essential to the life history of many marine fishes. In addition to sustaining resident fish species year-round, these areas are frequented seasonally by diadromous fishes, marine species spawning on- or off-shore and using the coastal zone as nursery grounds, and marine species making seasonal visits to the coastal zone as adults (Zijlstra 1988).

Extreme tidal currents such as those sought for tidal power generation (on the order of $2.5 \text{ m}\cdot\text{s}^{-1}$; Polagye et al. 2011) have a major influence on the behavior of these species.

Currents are an integral part of a fish's environment, effecting migrations, habitat selection, foraging behaviors, and predator-prey interactions (Auster 1988, Montgomery et al. 2000). Several migratory species utilize selective tidal stream transport to move on- or off-shore (or in and out of freshwater), rising up in the water column when the current is flowing in the desired direction but moving to the bottom, where the current is slower, when it changes direction. Some examples include American eel, *Anguilla rostrata* (McCleave and Kleckner 1982); Atlantic cod, *Gadus morhua* (Arnold et al. 1994); sockeye salmon, *Oncorhynchus nerka* (Levy and Cadenhead 1995); sea trout, *Salmo trutta* (Moore et al. 1998); and plaice, *Pleuronectes platessa* (de Veen 1978, Greer Walker et al. 1978). Castonguay and Gilbert (1995) found that Atlantic mackerel (*Scomber scombrus*)

avoided opposing tidal flows but moved with favorable ones as they migrated into the Gulf of St. Lawrence, though vertical migrations were not observed. Atlantic herring, *Clupea harengus*, have been found to swim with favorable tides but against opposing ones in order to maintain position (Lacoste et al. 2001), and some fish simply move back and forth with both flow directions, traversing up to several kilometers per tidal cycle (Sakabe and Lyle 2009). Sampling tidal flats, lagoons, and estuaries at slack tides has demonstrated that multiple species use the tides to gain access to intertidal foraging, spawning, and sheltering grounds (Gibson et al. 1996, Marshall and Elliott 1998, Morrison et al. 2002, Hartill et al. 2003, Krumme 2004, Ribeiro et al. 2006, Jovanovic et al. 2007).

Tidal turbines placed in the water column have the potential to affect fish using tidal currents. Potential effects of tidal devices on fish have been hypothesized by various groups (Gill 2005, DOE 2009, Polagye et al. 2011), with the highest priority concerns being fish interaction with moving parts of the device. Effects of such interactions range from mortality or injury of individuals due to direct blade strike, to interference with fish movements and migrations, whether due to strike, velocity changes, or noise generation (Polagye et al. 2011). The quantity and magnitude of these “dynamic” effects are highly uncertain, as very few devices have been installed to enable field studies (Polagye et al. 2011).

Understanding these effects depends on understanding the movements and migrations of fish at a site, particularly of pelagic fishes, which are most likely to be within range of turbine blades. Any tidal device will be placed in a specific part of the water column, so how fish use the water column during the moving tide, specifically their vertical distribution, will greatly affect their probability of interaction with a device. Fish vertical distribution is not constant. Apart from vertical migrations linked to tidal currents, many fish species also exhibit diel vertical migrations linked to changing light intensity (Bohl 1980, Janssen and Brandt 1980, Levy 1990, Nilsson et al. 2003). Tide and diel factors together can affect fish behavior; for example, fish may wait for nightfall to travel with the rising tide into shallow intertidal foraging grounds (Morrison et al. 2002, Ribeiro et al. 2006, Jovanovic et al. 2007). These vertical movements are site- and species-specific, and may also vary with age or size class within a species (Imbrock et al. 1996, Jovanovic et al. 2007, Ellis and Bell 2008, Becker et al. 2011).

Few studies examine the vertical distribution of fish in high-velocity flows, especially those strong enough for tidal power generation. Many studies of tidally dynamic areas have focused on species composition and habitat use at low and high tides, which has shown that fish move with the tides but does not reveal anything about their use of the water column during that time (Morrison et al. 2002, Ribeiro et al. 2006, Jovanovic et al. 2007). Tracking individual fish using acoustic tags has provided

detailed information on horizontal tidal migrations of individuals, and in some cases vertical distribution as well (Parker and McCleave 1997, Barbin 1998). Others provide depth information by passively sampling tidal currents with nets placed at discrete depths (McCleave and Kleckner 1982, Rijnsdorp et al. 1985), or depth and horizontal distribution by using hydroacoustics (Castonguay and Gilbert 1995, Levy and Cadenhead 1995). The vertical distribution of fish in strong tidal currents remains poorly understood for most species and locations, which increases the uncertainty surrounding the dynamic effects of tidal turbines.

As very few tidal energy devices have been installed, no standard protocols exist to guide the collection of data for effect assessment. The purpose of this chapter, therefore, is to act as a starting point for assessing the effects of a tidal power installation on fishes. General methodology is suggested, tools available for sampling tidally dynamic areas are reviewed and discussed, and a study of fish in Cobscook Bay in relation to a pilot tidal power project is presented as an example, along with recommendations for future work.

1.3. General Methodology

Any approach chosen will need to suit the location and scale of the tidal power project under investigation. For most project installations, a Before-After-Control-Impact (BACI) study design is recommended. This design reduces sampling to a limited number of points, and may be applied over a wide range of spatial and

temporal scales. BACI designs are meant to quantify the effects of a change to the local environment, and has been used successfully in several offshore applications, including wind power (Carstensen et al. 2006), oil drilling (Currie and Isaacs 2005), and pipeline construction (Lewis et al. 2002). The use of a control site aids in identifying variation in the data that is not due to the “impact” and is a particularly useful aid in extremely variable environments.

Pre-deployment information (“before” data) on fish at a tidal energy site is essential, creating the baseline for comparison of post-installation (“impact”) data. Pre-deployment data can also aid in predicting the effects of a tidal device. This may be useful for device placement or risk assessment involved with the permitting process. The amount of information that must be gathered as part of the “before” study of a site will depend on the amount of information already available for the location. Studies should naturally begin with a thorough literature review, focusing on the species present at the site and considering seasonal, diel, and tidal patterns in their presence and vertical distribution.

The goal for the site should then be to characterize the presence and vertical distribution of fish at project and control areas, before installation and when it is in place. It is important to survey shortly after device installation if installation-related effects are also of interest. Construction-related changes can be short-lived in marine

environments and can be lost if using a temporally coarse sampling regime (Smith 2002).

Fish movements occur on a large range of time scales, from small movements that take place in a matter of minutes (vertical migration at slack tide) to large movements that take place seasonally, such as offshore migration. Surveys must sample with fine enough resolution to capture small-scale movements of fish associated with tide and diel cycles (multiple samples per tidal stage), and surveys must be spaced adequately to also capture longer-term trends associated with seasonally changing fish communities (multiple surveys per season).

1.4. Sampling Gears

A wide array of sampling gears and techniques exist for the observation and characterization of fish presence and distribution. Not all can be used successfully in the difficult working conditions often present at tidal power sites. Those that may aid the assessment of tidal energy devices are listed and discussed below. It is unlikely that any single gear will provide all the necessary information, and a combination of multiple sampling methods is likely to be the best solution.

1.4.1. Benthic and Pelagic Trawling

Physical sampling techniques such as benthic and pelagic trawls are useful for acquiring the species and size composition of a fish community. Spreader doors are useful for keeping the net open and herding fish into it. If the depth of a trawl can be known and controlled, it may also be useful for obtaining a measure of the vertical

distribution of fish within the water column. The capacity in this sense is limited because the depth of a trawl can be difficult to control, and a trawl can only sample a small portion of the water column at one time. Trawls are difficult to fish in high current speeds, which can limit available sampling time in tidal channels to a small window surrounding slack tide. Gibson et al. (1996) used a beam trawl (a form of benthic trawl) to sample at slack water in a rapidly changing tidal environment, and pointed out that making repeated hauls in a short amount of time and obtaining replicates for each tidal state can be challenging. Other issues to consider include gear avoidance by fish, size selectivity of the gear, fish injury or mortality, and, in the case of benthic trawls, destruction of bottom habitat (Nielsen and Johnson 1983).

1.4.2. Seines, Fyke nets, Weirs

Seine, fyke nets, and weirs can be used effectively to characterize the components of a fish community on relatively fine temporal and spatial scales, but in limited habitats. They have been used extensively to study the use of habitats in shallow intertidal areas, including the study of behaviors related to tidal and diel cycles (Gibson et al. 1996, Morrison et al. 2002, Ribeiro et al. 2006, Jovanovic et al. 2007). However, these sampling methods are generally limited to shallow areas, and are not useful for sampling deep, fast tidal channels.

1.4.3. Acoustic Telemetry

Acoustic telemetry allows the tracking of individual fish with a great range of spatial and temporal resolution (Hartill et al. 2003). Acoustic tags have been used with success to investigate the tidal and diel movements of fish within estuaries and other coastal zones, some of which examine vertical as well as horizontal movements (Parker and McCleave 1997, Barbin 1998), and some that look only at horizontal ones (Greer Walker et al. 1978, Moore et al. 1998, Lacoste et al. 2001, Childs et al. 2008). Tagged fish can be tracked manually from a boat, or an array of acoustic receivers can be placed throughout a study area to detect tags moving within range of the receivers. The latter option is better suited to longer-term studies of a relatively limited region, such as a tidal power project site and surrounding areas. In the case of extremely tidal locations, which vary greatly in space and time, telemetry has a significant advantage over netting techniques because it provides more than just a “snapshot” of fish behavior. However, acoustic tags can be expensive, which may limit the number of individuals that may be tagged. Tagging individual fish can be logistically demanding, and fish must be large enough for the tag to be attached or implanted, which limits the species and age classes that can be studied. Battery life of tags are dependent on size, the frequency of transmission, and the amount of data that is collected (Lucas and Baras 2000, Hartill et al. 2003). Noisy underwater areas, such as those with high current speeds or complex physical structures, greatly limit the detection range of acoustic receivers (Lucas and

Baras 2000), and this may make them unsuitable for monitoring tidal energy projects at close range.

1.4.4. *Hydroacoustics*

Hydroacoustics encompasses a broad range of methods that use active sonar to detect, identify, and quantify fish presence. Hydroacoustic surveys have been used for many purposes, including monitoring vessel avoidance by fish (Vabø et al. 2002, Draščík and Kubečka 2005), characterizing diel vertical migrations (Bohl 1980, Janssen 1980) and tidal stream transport (Levy and Cadenhead 1995), and quantifying upstream salmonid migrations (Ransom et al. 1998). Most echosounder systems used in fisheries assessments can detect objects much smaller than most fish at ranges of hundreds of meters, with resolution on the order of centimeters.

Echosounding systems range in complexity and cost and come with a wide variety of frequencies and beam widths and shapes, but there are three basic configurations: single-, dual-, split-, and multi-beam. All of them can be used to obtain the distance of sound-reflecting objects, such as fish, from the acoustic transducer, as well as volume backscattering strength, which is generally assumed to be a relative measure of fish density. This is all that the single-beam echosounder can provide directly, though additional methods such as deconvolution can be used to obtain target strength approximations (Simmonds and MacLennan 2005). Target strength is necessary to estimate the numbers of fish contributing to the acoustic signal, and to

estimate the sizes of individual fish. Dual- and split-beam echo sounders provide target strength, and additional information provided by split-beam echosounders can include fish swimming speed and direction (Simmonds and MacLennan 2005).

Hydroacoustic survey sampling designs are flexible, numerous, and adaptable to a number of situations (Lucas and Beras 2000, Simmonds and MacLennan 2005).

Acoustic beams can be oriented horizontally, as in shallow water (Draštík and Kubečka 2005) or in some riverine passage studies (Ransom et al. 1998), or they can be oriented vertically, as in studies of diel vertical migrations (Bohl 1980, Janssen and Brandt 1980), tidal stream transport (Levy and Cadenhead 1994), or horizontal fish distribution (Simard et al. 2002). Surveys can include mobile transects across an area of interest (Levy and Cadenhead 1994, Simard et al. 2001), or they can be stationary (Ransom et al. 1998, Krumme 2004, Chapter 2). While many surveys are carried out from the surface, it is also possible to mount hydroacoustic equipment on the sea floor. Bottom-mounted, upward-looking acoustics have been used to examine diel migrations at a site (Axenrot et al. 2004, Jensen et al. 2011) and can help to reduce effects of vessel motion or hull-induced turbulence, though sampling volume near the bottom is decreased. These types of deployments can be connected to shore via underwater cables or be completely self-contained, with batteries and data storage included in the unit.

Overall, hydroacoustics offers diverse, adaptable, and non-invasive methods to sample large volumes of water in a nearly continuous manner, regardless of current

speed or light levels. This is extremely useful in highly variable tidal environments, and fish presence and vertical distribution may be studied with extremely high temporal and spatial resolution. However, external noise sources or entrained air (common in high velocity environments) can affect the quality of hydroacoustic data (Simmonds and MacLennan 2005). Additionally, sampling can be limited by acoustic “deadzones” which occur near boundaries such as the seafloor or surface, in which fish or other targets cannot be distinguished from the surface or substrate (Ona and Mitson 1996). Also, the echo strengths of fish are affected by fish physiology (with or without swim bladder) and behavior (e.g., tilt angle or dense schooling), which can influence number and size/species estimates (Simmonds and MacLennan 2005). Equipment costs can be high, especially for complex systems such as split- or multi-beam echosounders. Data storage can become an issue for long-term surveys, especially for autonomous deployments.

Data processing must be kept in mind when designing acoustic surveys. Huge volumes of data are produced by continuous sampling, and though processing can be automated to some extent, manual inspection is always required and is time consuming. Additionally, acoustics data alone are generally not enough for species identification, especially in environments with highly diverse fish communities. Surveys are usually be combined with physical sampling, such as trawling, to verify the species of fish detected (Simmonds and MacLennan 2005).

1.4.5. Acoustic Imaging: the Dual-frequency IDentification SONar (DIDSON)

DIDSON is a form of multi-beam acoustic equipment which uses the feedback from multiple stacked sound beams to construct a video-like image of a fan-shaped sampling volume. DIDSON operates in very high frequencies (1.1 or 1.8 MHz) and as such has a relatively short sampling range (approximately 40 m at 1.1 MHz and 12 m at 1.8 MHz). DIDSON data are particularly helpful for providing accurate length measurements of fish and has been used in applications such as detecting the passage of migrating salmon (Ransom et al. 1998) and characterizing the diel movements of different size classes of fish in an estuary (Becker et al. 2011). DIDSON also offers the unique opportunity to observe fish behaviors in detail and has been used to study the reactions of fish to a pelagic trawl (Rakowitz et al. 2011) and to a hydrokinetic tidal turbine (Chapter 3). As the DIDSON uses sound to create an image rather than light, it is effective in dark or turbid environments where cameras have limited utility. This is especially appealing for tidal applications, where nighttime monitoring of fish-turbine interactions is important. DIDSON could be very useful for applications such as turbine monitoring (Chapter 3) or for verification of fish targets in other acoustic data (Chapter 2). Unfortunately, DIDSON units are much more expensive than other acoustic systems, such as single- and split-beam echosounders.

1.5. Case study: Cobscook Bay

Cobscook Bay, Maine, is currently host to the largest commercial tidal energy project in the United States. In March 2012, Ocean Renewable Power Company (ORPC) started

installing a pilot tidal energy device on the sea floor. This device consists of four cross-flow turbines aligned end-to-end on a horizontal axis, with a permanent magnet generator in the center. Each turbine contains four helical blades and is approximately 6 feet (1.8 m) in diameter and 20 feet (6.1 m) in length. The entire turbine structure is 102 feet (31.1 m) long, and is held approximately 24 feet (7.3 m) above the sea floor by a solid steel frame. Plans for this deployment prompted the start of the fish assessment study, and baseline data collection started in 2010, two years before the expected installation date. The literature review conducted at the outset revealed that little was known of the fishes of Cobscook Bay. Most studies had taken place in adjacent Passamaquoddy Bay and were dated (Tyler 1971, MacDonald et al. 1984). Furthermore, these studies were not always in agreement on seasonality or presence of species. While they identified several key species in the area, none of these studies considered the vertical distribution of pelagic species in relation to season, tide, or diel cycles (except for Atlantic herring in Passamaquoddy Bay; Brawn 1960a).

1.5.1 Site Considerations

Cobscook Bay is located at the mouth of the Bay of Fundy, and consists of three smaller bays joined by narrow channels. The bay's nearly enclosed nature combines with its high tidal range (mean range of 5.7 m; Brooks 2004) to generate tidal current speeds in excess of $2.5 \text{ m}\cdot\text{s}^{-1}$ in the outer bay, the site of the pilot tidal energy project. Here, tidal mixing is very strong, resulting in nearly uniform salinity and temperature

throughout the outer bay (Brooks 2004). The outer bay is the only link between deeper ocean waters and the inner bays, which have expansive intertidal zones that could serve as nurseries and feeding grounds for many species during the summer months.

Surveys were carried out at an impact site and a control site. The impact site was chosen to be as close as possible to the future pilot project, located mid-channel location at the upper end of the outer bay, where the minimum low-tide depth was 24 m and the maximum high-tide depth was 35 m. The control site was chosen to be as similar as possible in depth and flow pattern, though it was slightly deeper (31 m to 45 m, minimum and maximum) and had current speeds that were slightly less constant with depth than at the project site. Current speeds over the course of a tidal cycle were relatively well matched, however.

1.5.2 Sampling Gear

Stationary, down-looking hydroacoustic surveys were chosen as the primary means of data collection, given the desire to characterize fish present at the project site with fine vertical and temporal resolution, during all tidal stages. A wide-angle, single-beam echosounder system was used to sample as large a volume as possible, especially near the surface. Another goal of the project was to develop a cost-effective method for initial site assessments related to marine renewable energy, and single beam echosounders were best suited for that need. A DIDSON acoustic camera was used in conjunction with the single-beam echo sounder to obtain acoustic images of the upper

10 m of the water column. Though species identification was not one of the initial goals of this project, the DIDSON provided length and behavior information that could not be extracted from single beam data and aided in distinguishing entrained air or krill from schools of fish in the upper water column (Chapter 2), all of which appear similar in the single-beam echosounder data.

Sampling was carried out at least once per season, beginning in May of 2010 (Table 1.1). Each site was surveyed continuously for 24 hours, with survey dates chosen to ensure two tidal cycles during the day and two at night. This was not always possible when nights or days were very short.

Year	Winter	Spring	Summer	Fall
2010		May	June, Aug	Sept, Oct, Nov
2011	Jan, Mar	May	June, Aug	Sept, Nov

Table 1.1. Hydroacoustic sampling schedule. Months sampled by 24-hour stationary hydroacoustic surveys at project and control sites in Cobscook Bay in 2010 and 2011.

1.5.3 Data Analysis

Volume backscatter and total area backscatter were used as relative estimates of fish density, but fish were not enumerated or sized since target strength values could not be obtained from the single beam data. Total water column backscatter was assumed proportional to overall fish abundance, and the vertical distribution of backscatter throughout the water column was assumed indicative of fish distribution. DIDSON data were primarily used to distinguish between fish and non-fish

aggregations in the upper water column, but the upper 10 m of hydroacoustic data were excluded due to interference from entrained air.

Relative abundance (density) and vertical distribution of fish could be obtained for any span of time, from minutes to the entire 24 hours sampled in a survey. Distributions for ebb and flood tides during the day and night were compared, revealing distinct effects in many surveys. By examining the relative abundance of fish in each survey over time, seasonal patterns in fish presence were also apparent and were similar at both sites for both years, though overall density changed substantially between years.

1.6. Discussion

1.6.1. Sampling Schedule

The sampling schedule, involving a one-day survey at each site for 8 months of the year proved logistically simple but time intensive. Running acoustic equipment over the side of a vessel moored mid-channel required the constant presence of at least two people. This sampling scheme resulted in points of extremely high-resolution data spread across two years (Chapter 2); however, increasing survey frequency and sampling multiple times per month would greatly increase the ability to better distinguish patterns within natural daily variability. Operation costs limited the ability to increase the temporal sampling regime. However, increased cost could be mitigated by applying those funds to deploy an autonomous acoustic system on the sea floor, programmed to record data at intervals over a longer period of time (on the order of a

month or more, depending on battery life). This would spread sampling more evenly across longer time spans, increasing overall resolution without requiring as many hours of boat time and allowing time series analyses. However, autonomous systems are not readily available and are costly.

+1.6.2. *BACI Approach*

Despite the hydrodynamic and geographic differences between the control and impact site, similar seasonal patterns in relative fish abundance were found at both locations. This pattern was the same in both years, and both sites also showed similar changes in overall fish density from 2010 to 2011. The similarity in trends at both sites supports the role of the control site for distinguishing natural variation from turbine effects, despite the highly variable environment of the bay.

1.6.3. *Sampling Gear*

As the project progressed, it became clear that more information on the species present was necessary. An additional study was initiated to characterize the fishes of the bay, using trawls where possible in all three bays, and extensive beach seining. This sampling effort has added greatly to what was gleaned from the literature review, revealing some species that were not expected and confirming the presence or absence of others. Though the amount of trawling that can be carried out alongside the acoustic surveys was limited, it will likely aid in verifying the species detected with down-looking hydroacoustics. However, it is suspected that some of the faster fish known to be in the area are avoiding the trawl, including Atlantic mackerel. The addition of more

nighttime trawls may reduce net avoidance and allow a more complete picture of species presence.

The relative density measurements obtained with the single-beam acoustic system are useful, but it became clear that for this study, more information is required. Without reliable target strength values, it could not be certain that omitted signals were not from fish. As the reality of the tidal device deployment progressed, the focus of the fish assessments shifted toward species identification and movements of the various components of the fish community. For this, accurate target strength values are necessary. As such, a split-beam echo sounder has been purchased, and will be integrated into surveys beginning in May 2012. Changing equipment just before beginning the “impact” phase of sampling may complicate before-after comparisons. However, calibration of the two systems (single- and split-beam) and comparison of concurrent data will help mitigate any effects of equipment change. Examination of the vertical distributions of fish by size groups should reveal more species- or size-specific diel and tidal behaviors, and on- and off-shore movements, many of which are likely not discernible when species must be grouped into a single metric.

Though a split-beam system will overcome many of the analytical limits of the single-beam system currently in use, all acoustics surveys are subject to interference from a myriad of external noise sources. In Cobscook Bay, there is a significant amount of entrained air in the upper 10 m of the water column, sometimes extending nearly to

the bottom in rough weather conditions. This masks a good deal of signals from fish, which can be seen amidst these clouds in the DIDSON. The upper 10 m of the water column had to be omitted from analysis of single beam data because of this (Chapter 2), which constitutes nearly half of the water column at low tide. This issue has yet to be resolved.

1.7. Recommendations

A BACI design is recommended for the assessment of tidal power devices' affects on fish, focusing on changes in fish presence and vertical distribution at project and control sites. Stationary hydroacoustic surveys can obtain data with the high temporal and spatial resolution necessary for these analyses. A split-beam echosounder should be used, if possible, due to the greater ability to identify detected fish and examine the movements of different groups. Autonomous acoustic data collection will likely allow for much more thorough sampling over a longer time frame. Acoustic surveys should be accompanied by physical sampling methods (using a trawl with spreader doors) to verify acoustic targets, but this may be difficult for most sites of interest. If concurrent fish tagging studies are ongoing in a region, at least one acoustic receiver should be deployed somewhere in the study area; however, these should not be located too near the tidal power device, as structure noise will decrease the receiver's detection range. Regardless of the methods or sampling gear chosen, high-resolution information on fish use of the water column at a tidal project site should be the result.

The ability to analyze fish presence and vertical distribution on a wide range of time scales is necessary for the assessment of extremely tidal regions, where fish behavior is largely governed by cyclical environmental changes over widely different scales.

CHAPTER 2

VERTICAL DISTRIBUTION OF FISH AT A TIDALLY DYNAMIC REGION TARGETED FOR ENERGY EXTRACTION

2.1. Abstract

The use of tidal currents by fish for movements to and from onshore spawning, foraging, and nursery grounds is well documented. However, fish use of the water column in extremely tidal areas, where current speeds are frequently in excess of 1.5-2 m·s⁻¹, is largely unknown. This information is necessary to determine the environmental effects of tidal energy devices, which are installed in high-current areas at fixed locations within the water column. A pilot tidal energy device will be installed in outer Cobscook Bay, Maine in 2012. To assess its effects on fish, in 2010 and 2011, down-looking hydroacoustic surveys were used to collect pre-deployment data on the presence and vertical distribution of fish at the proposed pilot project site and at a control site. Twenty-four-hour stationary surveys were conducted at each at least once every season. Relative fish density and distribution were analyzed with respect to annual, seasonal, diel, and tidal cycles. In both years and both sites, fish density increased in the spring (May) and late fall (November). Fish density nearly always increased toward the sea floor, and there was evidence of vertical movements related to diel and tidal cycles, though these were not consistent from survey to survey. This work has established a baseline dataset for the comparison of similar acoustic data that will be collected post-deployment of the pilot tidal device.

2.2. Introduction

The importance of tidal flows to fish ecology is well documented. Several migratory species utilize selective tidal stream transport to move on- or off-shore (or in and out of freshwater), moving into the water column when the current is flowing in a favorable direction but moving to the bottom, where the current is slower, when it changes direction. Some examples include American eel, *Anguilla rostrata* (McCleave and Kleckner 1982); Atlantic cod, *Gadus morhua* (Arnold et al. 1994); sockeye salmon, *Oncorhynchus nerka* (Levy and Cadenhead 1995); sea trout, *Salmo trutta* (Moore et al. 1998); and plaice, *Pleuronectes platessa* (de Veen 1978, Greer Walker et al. 1978). Atlantic salmon, *Salmo salar*, migrating upriver (Stasko 1975) and Atlantic mackerel, *Scomber scombrus*, migrating into the Gulf of St. Lawrence (Castonguay and Gilbert 1995) have been observed moving with flood tides more than ebbs, and so may also use selective tidal stream transport, though associated vertical migrations have not been observed. Atlantic herring, *Clupea harengus*, have been found to swim with favorable tides but against opposing ones in order to maintain position (Lacoste et al. 2001), and fish have also been shown to simply move back and forth with both flow directions, traversing up to several kilometers per tidal cycle (Sakabe and Lyle 2009). Beyond the vertical migrations involved in selective tidal stream transport, fish use of the water column in extreme tidal currents remains largely unknown.

Cobscook Bay is a highly productive bay located at the mouth of the Bay of Fundy, consisting of an inner, central, and outer bay joined by narrow channels. The bay is known for its high biodiversity, which is largely due to the extreme tidal mixing that takes place there (Larsen and Campbell 2004). The mean tidal range is 5.7 meters, and current speeds in the bay can exceed $2 \text{ m}\cdot\text{s}^{-1}$ in the channel of the outer bay (Brooks 2004), making this area extremely attractive for tidal power development. In March 2012, Ocean Renewable Power Company (ORPC) began installing a pilot tidal energy device in the outer bay; however, the effects of the device on fish are unknown, and little information exists to aid in predicting these effects. The presence and composition of pelagic fishes of the bay are poorly understood because most studies of the region have focused on benthic species vulnerable to trawling. Additionally, many of these studies are dated and were conducted not in Cobscook but in the adjacent Passamaquoddy Bay (Tyler 1971, MacDonald et al. 1984). Key species in the area include alewife (*Alosa pseudoharengus*), Atlantic herring (*Clupea harengus*), blueback herring (*Alosa aestivalis*), rainbow smelt (*Osmerus mordax*), silver hake (*Merluccius bilinearis*), white hake (*Urophycis tenuis*), and Atlantic mackerel (*Scomber scombrus*), though studies do not always agree on species seasonality (Tyler 1971, MacDonald et al. 1984, Saunders et al. 2006, Athearn and Bartlett 2008). Vertical distribution of fishes in the water column is unknown, apart from one study of the vertical distribution of

Atlantic herring in Passamaquoddy Bay (Brawn 1960a). These missing data are critical to assessing the potential effects of any tidal power device on fishes.

The pilot device that will be installed in outer Cobscook Bay is ORPC's TidGen™ power system, which consists of four cross-flow turbines aligned end-to-end on a horizontal axis, with a permanent magnet generator in the center (www.orpc.co; Figure 2.1). Each turbine contains four helical blades, and is approximately 6 feet (1.8 m) in diameter and 20 feet (6.1 m) in length. The entire turbine structure is 102 feet (31.1 m) long, and is held approximately 24 feet (7.3 m) above the sea floor by a solid steel frame. The TidGen™ has a peak power output of 180 kW in a $3 \text{ m}\cdot\text{s}^{-1}$ (6 knot) current, and operates at a maximum of 40 rotations per minute, which corresponds to a tip speed of approximately $5.5 \text{ m}\cdot\text{s}^{-1}$.

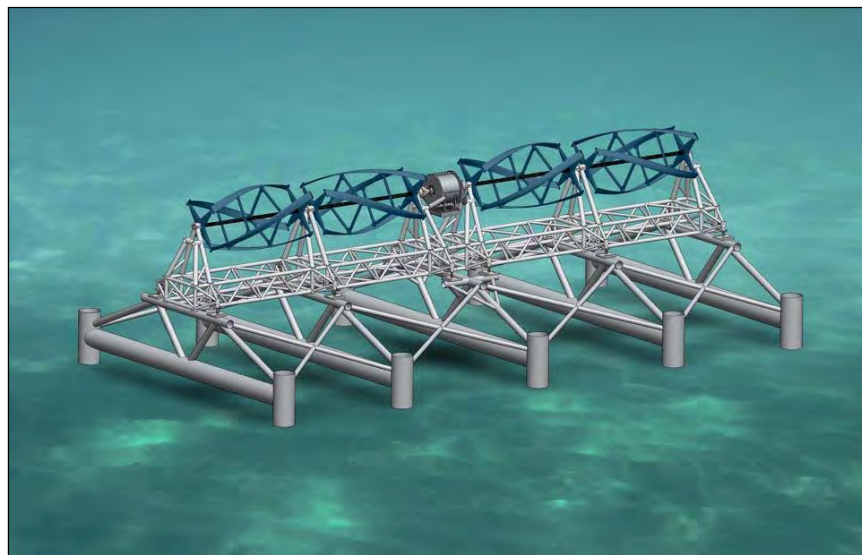


Figure 2.1. Pilot tidal energy device. Drawing of Ocean Renewable Power Company's TidGen™ Power System, the pilot project to be installed in outer Cobscook Bay.

Hydroacoustic technologies allow continuous observation of the entire water column regardless of current speed, with high spatial resolution and low disturbance to fish or other organisms (Simmonds and MacLennan 2005). A downward-looking, single beam echosounder was therefore used to examine the presence and vertical distribution of fish in the water column prior to device deployment, in order to provide a baseline for assessing the effects of the pilot tidal power device on fishes after deployment. Two years of pre-deployment data were collected at the pilot project site and at a control site nearby, addressing the following:

1. Does the density of fish in the water column vary year to year?
2. Does total water column fish density vary among months of the year?
3. Does fish density vary spatially (between sites)?
4. What is the vertical distribution of fish density in the water column?
5. Does the vertical distribution of fish density vary seasonally and annually?
6. Does the vertical distribution of fish density vary with day and night or tidal stage?

2.3. Methods

2.3.1. Site

Data were collected in outer Cobscook Bay at the future pilot project site and a control site (Figure 2.2). The future project site, CB1, was located mid-channel at 44°54.60' N, 67°2.74' W; the control site, CB2, was approximately 1.6 km farther seaward, mid-channel at 44°54.04' N, 67°1.71' W. The vessel was moored at these two

sites and swung around its mooring as the direction of tidal flow changed at each slack water. This movement was minimal for most months (205 m mean difference at CB1, 147 m mean difference at CB2), though positioning of the mooring at CB1 in May and June of 2010 caused the boat to swing over a very deep region during most of the ebbing tide. Ebb tide data were subsequently omitted from analyses for these months. Under normal conditions, water depth at CB1 ranged from an average of 24.5 m at low tide to 32.3 m at high tide, and from 33.8 m to 41.3 m at CB2. At CB1, average current speed (water column mean) was $1.01 \text{ m}\cdot\text{s}^{-1}$ (2.0 knots), with a maximum of $2.06 \text{ m}\cdot\text{s}^{-1}$ (4.0 knots). At CB2, average current speed was $0.87 \text{ m}\cdot\text{s}^{-1}$ (1.7 knots), with a maximum of $1.78 \text{ m}\cdot\text{s}^{-1}$ (3.5 knots).

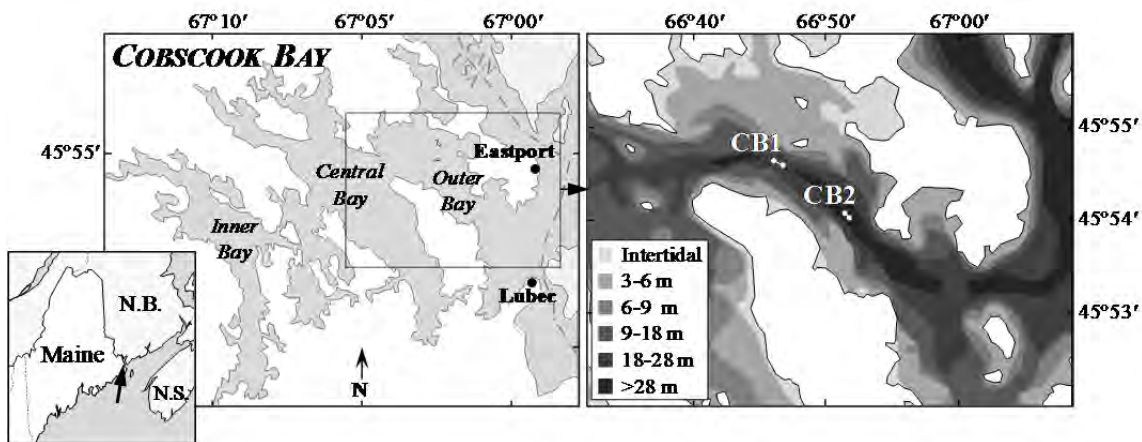


Figure 2.2. Map of Cobscook Bay and locations of hydroacoustic surveys.

Left: Cobscook Bay, Maine. Right: Sampling sites in the outer bay, showing bottom depth (from Kelley and Kelley 2004). Mean ebb and flood positions are indicated by the white-filled circles.

2.3.2. *Equipment*

Surveys were carried out from a moored, 40-foot (12.2 m) fishing vessel (Figure 2.3). A dual-frequency (38 kHz and 200 kHz) single beam Simrad EK60 echo sounder was used with a 31° (half power beam angle) circular transducer. The echo sounder was operated at 2 pings per second with a pulse duration of 0.512 ms for all surveys except May and June 2010, when 1.024 ms and 0.256 ms pulse durations were used, respectively. The transducer insonified a 31° conical volume of water from the surface to the sea floor, though it is likely that some fish near the surface and seafloor were not detected due to the acoustic deadzones (Ona and Mitson 1996, Horne 2000). The vertical resolution of the transducer was approximately 38 cm when using the 0.512 ms pulse length (most surveys), and resolution was 19 cm and 76 cm with the 0.256 ms and 1.024 ms pulse lengths, respectively.

The Simrad echo sounder was calibrated using standard copper calibration spheres as recommended by Foote et al. (1987). In-situ on-axis calibrations were carried out at slack tide at least once during each sampling session. The position of the spheres within the beam was approximate because the water was rarely completely still. Therefore, calibration values obtained in this manner were only used to assure continued equipment functionality. To obtain accurate calibration offsets, in January 2011 and February 2012 the echo sounder was taken to a frozen lake, where the water was still, to be sure of the location of the spheres in the echosounder beam. On-axis

calibrations were performed for both frequencies at all power and pulse length settings used during surveys, and corrected transducer gains and volume backscatter calibration constants were calculated for each setting. During the 2011 calibration, the beam pattern was also characterized and found similar to that provided by the manufacturer.

A DIDSON (Dual-frequency IDentification SONar) was used in conjunction with the Simrad echo sounder. The DIDSON operated at 1.8 MHz frequency and captured approximately 8 frames per second, producing video-like images of a $29^{\circ} \times 14^{\circ}$ sampling volume with a range of 10.8 m. Vertical resolution (along the length of the viewing window) was 2.0 cm. Horizontal resolution was 0.5 cm at the start of the viewing window (1.0 m from the DIDSON lens) and 7.0 cm at its maximum range. Both the Simrad transducer and the DIDSON were mounted 1 meter below the surface over the port side of the vessel, facing downward (Figure 2.3).

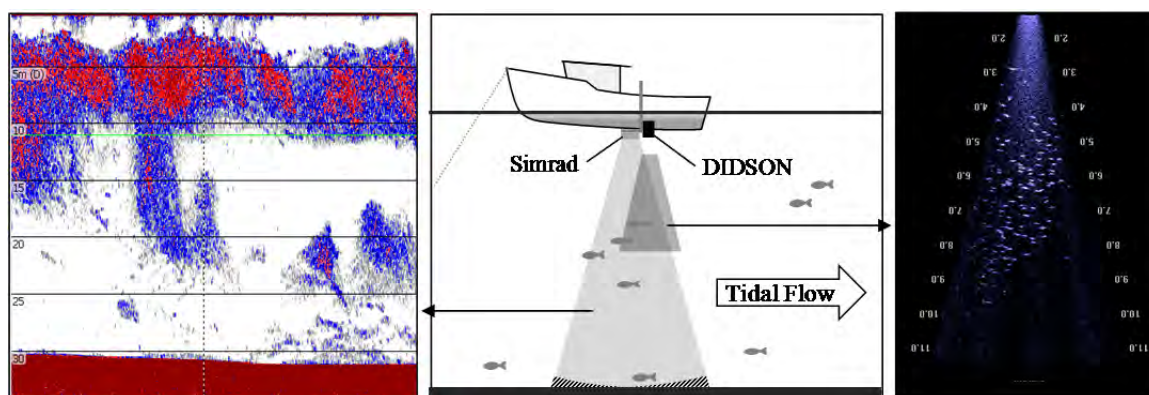


Figure 2.3. Acoustic survey setup and sample data. Stationary acoustic survey setup (center). Light grey filled area represents volume insonified by the Simrad echosounder; hatched lines indicate the acoustic deadzone. Dark grey area indicates field of view of DIDSON. Left: Sample segment of data from Simrad echosounder. Right: sample frame from DIDSON footage, showing individuals in the upper portion of the aggregation seen in the Simrad data.

Current speed readings were obtained with either a Marsh-McBirney (MM) flow meter (May 2010-May 2011) or an Acoustic Doppler Current Profiler (ADCP) (June 2011-November 2011). These were also mounted over the side of the vessel about 1 meter below the surface (MM flow meter to starboard; ADCP to port, just aft of the DIDSON and Simrad transducer). The MM flow meter recorded surface current speed only, while the ADCP recorded current speeds throughout the water column with vertical resolution of 1 m.

2.3.3. Field Sampling

Twenty-four-hour stationary surveys were carried out at the two sites at least once each season, beginning in May of 2010 (Table 2.1). Surveys were scheduled with the goal of sampling nearly two complete tidal cycles: one at night and one during the day. Depending on the time of year, this was not always possible; in May and June, nights encompassed only one tidal stage, and in March, this was true for days. Environmental data were recorded every half hour, and included cloud cover, precipitation, sun/moon visibility, qualitative wind speed and wave height, and current speed (when using the MM flow meter). When using the ADCP, current speed was automatically recorded every half hour. Salinity was 32 ± 0.45 ppt in May, June, August, and September surveys in 2011 (unpublished data), and was assumed to vary little over the course of the year in this very well-mixed area (Brooks 2004, Larsen and Campbell 2004).

2.3.4. Data Analysis

The raw data used in analyses were volume backscatter. Volume backscatter is the total contribution of acoustic backscatter from all the targets within the volume of water sampled, expressed in units of $\text{m}^2 \cdot \text{m}^{-3}$ in the linear domain or in decibels (dB) in the logarithmic domain (Simmonds and MacLennan 2005). When sampling fish, volume backscatter can generally be assumed a relative measure of fish density. It can be used to estimate the number of fish detected if combined with accurate target strength readings or detailed knowledge of the fish being sampled. This was beyond the scope of our analyses because target strength values obtained with the single-beam echosounder could not be corrected for losses associated with beam pattern. Instead, total area backscatter was chosen to represent fish density in various layers of the water column. Total area backscatter is the summation of volume backscatter over a range of depths, and is expressed linearly in $\text{m}^2 \cdot \text{m}^{-2}$ (s_a) or in dB (s_A). Linear values were used in analyses and figures.

For each site (analyzed separately), acoustic data were processed then analyzed. Data analyses consisted of two main parts: a) analysis of the variance in total water column backscatter (i.e., fish density) in relation to year, month, and diel and tidal cycles; and b) analysis of the vertical distribution of backscatter (i.e. fish density) within the water column in relation to year, month, and diel and tidal cycles.
























Year	Month	Site	Days	Start – end time	Mean surface temp. (°C)	Tidal depth range (m)	Moon phase
2010	5	CB1	19 – 20	06:30 – 06:00	7.5	25 – 49	
		CB2	21 – 22	09:00 – 09:00	7.8	31 – 41	
	6	CB2	13 – 14	06:40 – 07:40	9.4	33 – 40	
	8	CB1	5 – 6	08:15 – 08:30	13.3	25 – 30	
		CB2	4 – 5	07:45 – 08:00	13.3	35 – 40	
	9	CB1	6 – 7	06:10 – 06:10	14.3	24 – 31	
		CB2	7 – 8	07:00 – 07:40	13.9	34 – 45	
	10	CB1	17 – 18	13:40 – 13:40	11.9	26 – 35	
		CB2	19 – 20	17:20 – 14:00	11.7	36 – 42	
	11	CB1	20	07:30 – 16:10	9.6	24 – 31	
		CB2	17 – 18	06:00 – 07:30	9.6	36 – 45	
2011	3	CB1	15 – 16	07:00 – 06:30	2.9	25 – 30	
		CB2	16 – 17	22:15 – 22:00	3.0	34 – 41	
	5	CB1	28 – 29	08:00 – 08:00	7.9	24 – 30	
		CB2	27 – 28	07:45 – 07:45	7.8	32 – 41	
	6	CB1	26 – 27	08:00 – 08:00	10.2	24 – 30	
		CB2	27 – 28	08:50 – 08:50	10.4	33 – 40	
	8	CB1	22 – 23	05:45 – 05:45	13.8	25 – 30	
		CB2	23 – 24	06:20 – 06:00	13.5	35 – 40	
	9	CB1	22 – 23	06:20 – 06:30	13.0	24 – 29	
		CB2	23 – 24	07:00 – 06:30	12.9	33 – 40	
	11	CB1	16 – 17	14:00 – 14:00	10.5	24 – 30	
CB2		18 – 19	14:40 – 14:40	10.5	33 – 40		

Table 2.1. Hydroacoustic survey information. Sampling dates, times, and basic environmental data.

2.3.4.1. Acoustic Data Processing

Acoustic data processing was carried out using Echoview software (5.1, Myriax Pty. Ltd., Hobart, Australia), and data values were exported for statistical analyses in MATLAB (r2011b, The MathWorks, Inc., Natick, MA, USA). In Echoview, data processing began with calibration of the data using the correct gain and volume backscatter calibration constants obtained during the winter ice calibrations (section

2.1). The volume backscatter data were then visually scrutinized, and areas of noise (for instance, from a passing boat's depth sounder) or high boat motion (for example, during slack tides, when the boat was rotating about its mooring) were identified and excluded from analyses. The upper 10 m of the water column were similarly excluded from analyses because large quantities of entrained air frequently obscured the acoustic backscatter from fish within that layer, especially during rough water. Any backscatter that showed clear evidence of entrained air that extended below 10 m was manually excluded from analyses, as were any times that indicated excessive boat movement. DIDSON footage was used to verify that excluded signals were from non-fish targets, which included entrained air as well as occasional aggregations of krill. Acoustic returns beyond the range of the DIDSON could not be verified in this way, and were not excluded unless clearly abiotic in origin (e.g., electrical interference).

A threshold was then set for the volume backscatter data, which eliminated any targets with on-axis target strengths (TS) less than -60 dB. This was done to exclude backscatter signals from non-fish targets (such as plankton, krill, and fish larvae) from analyses, while keeping signals from fish, though some fish were probably also excluded. Of fishes known to be in the region, Atlantic mackerel are among the few pelagic species lacking a swimbladder; therefore, they are likely to have some of the weakest target strengths detected. A 20-cm Atlantic mackerel (the lower size limit expected, based on local knowledge and hook-and-line sampling) would have a target

strength of approximately -60 dB according to several equations converting TS to length (Foote 1980, Misund and Beltestad 1996, Simmonds and MacLennan 2005). For comparison, a 10-cm Atlantic herring, which has a swim bladder, would have a much stronger target strength of approximately -52 dB (Foote 1987). For single-beam data, setting the TS threshold at -60 dB means that a fish with TS of -60 dB is included in analyses if it swims through the central axis of the beam. However, since the acoustic beam is weaker near the edges, the same -60 dB fish swimming through the beam off-axis will appear to have a lower TS, and will be excluded from analyses. For the single-beam echosounder used in this survey, this means that Atlantic mackerel 26 cm long (TS \approx 54 dB) are only included if swimming within 15.5° of the beam's central axis, but a herring 15 cm long would be included if within 23° of the central axis. Basically, the sampling volume is lower for fish with weaker acoustic signals than for those with stronger ones, and setting a universal threshold will exclude fishes from analyses somewhat disproportionately. Fishes that may have been present at the sampling locations and their expected minimum and maximum lengths are shown in Table 2.2, along with their theoretical target strengths.

Species	Expected length (cm)		Estimated TS (dB)		TS-length equation source
	Min.	Max.	Min.	Max.	
Atlantic herring <i>Clupea harengus</i>	10	30	-51.9	-42.4	Foote 1987
Atlantic mackerel <i>Scomber scombrus</i>	20	40	-60.3	-44.2	Foote 1980
Threespine stickleback <i>Gasterosteus aculeatus</i>	5	10	-58.5	-52.5	Jurvelius et al. 1996
Atlantic cod <i>Gadus morhua</i>	10	20	-44.8	-40.1	Foote 1987

Table 2.2. Expected fish and target strengths. Four fishes expected to be seen in the water column within the survey area, with expected lengths and target strengths calculated using equations from sources at right.

Slack tide start and end times were determined using the mean water column current speed. If current speed data were collected with the ADCP, mean water column current speed was obtained by averaging from surface to seafloor. If a survey's current speed data were surface measurements taken with the MM flow meter, a correction was applied in order to approximate the water column mean using surface measurements. This correction was obtained for each site using data collected concurrently with the ADCP and the MM flow meter in August of 2011. Slack tides were defined as periods of time when the turbine would not be rotating, beginning when the current speed fell below $0.5 \text{ m}\cdot\text{s}^{-1}$ and ending when it rose above $1.0 \text{ m}\cdot\text{s}^{-1}$. On average (\pm standard error), periods of slack tide were 2.9 ± 0.1 hours long at CB1 and 2.2 ± 0.1 hours at CB2. Slack tides were removed from each survey's acoustic dataset, since during these times the

boat was swinging about its mooring, and the increased motion lowered the quality of the data. Also, when a turbine would not be rotating, it would pose a lesser threat to fishes encountering it.

Remaining acoustic data were divided into analysis cells spanning 30 minutes in the time dimension and 1 m in the depth dimension. Half-hour time bins were chosen in order to capture the variability in vertical distribution over time, and to assure minimal autocorrelation of successive bins and a sample size of at least 6 time bins for each tidal stage (the shortest of which was approximately 3 hours). Depth divisions were measured upward from the seafloor rather than downward from the surface because the tidal turbine will be installed at a fixed distance above the bottom (it will span the range of 7 to 9 m above the bottom). Because the depth of the water column changes with the tide, for each survey the highest layer included in analyses was determined by the water depth at low tide minus the 10 m that were excluded due to entrained air. This value was 15 m for CB1 and 27 m for CB2, and any layers that rose above this level were ignored. Echoview was used to calculate and export the total area backscatter, in units of $\text{m}^2 \cdot \text{m}^{-2}$, of each analysis cell.

2.3.4.2. Analysis of variance in total area backscatter of the entire water column

Total area backscatter, s_a , of the water column (sea floor to highest layer analyzed) was obtained for each half-hour time bin by summing the s_a values from each layer. Each time bin was associated with a site, year, month, day or night, and a tidal

stage (ebb or flood). The s_a data were not normally distributed and did not meet the assumptions of the ANOVA without transformation (Box-Cox method), so permutation tests were used to confirm ANOVA p-values. If factors were found to have significant effects, Scheffe multiple comparison tests were used on transformed data to determine which groups of means, if any, were different.

2.3.4.3. Analysis of the distribution of area backscatter within the water column

The vertical distribution of backscatter (i.e., relative fish density) within the water column was obtained for multiple time spans of interest by calculating the mean backscatter for each layer of analysis cells within a time span. Time spans depended on the comparisons being made: for each survey, vertical distributions were calculated for the entire 24 hours sampled, day and night, and day ebb, day flood, night ebb, and night flood. The effects of factors such as year, month, day and night, and tidal stage on vertical distribution were determined by comparing the corresponding distributions. Comparison consisted of analyzing the similarity of the shapes of the distributions, as well as the offset between them (i.e., the difference between their means). To quantify the similarity of shape, one distribution was linearly regressed onto the other. The significance of this regression and the slope of the regression line were used as parameters indicative of shape similarity. If the fit was significant ($p \leq 0.05$) and the slope was not negative, the shapes were considered similar. If the fit was not significant or the slope was negative (which would indicate opposite trends), the shapes were

considered dissimilar. In many comparisons, one stage had consistently higher backscatter throughout the water column than the other (offset). The significance of this offset was evaluated using a two-sample, two-tailed Student t-test ($p \leq 0.05$).

2.4. Results

2.4.1. Does the density of fish in the water column vary year to year?

Analysis of the water column s_a revealed that year had no significant effect on overall fish density at CB1 ($p = 0.12$), but that 2010 had significantly higher density than 2011 at CB2 ($p = 0.001$; Figure 2.4).

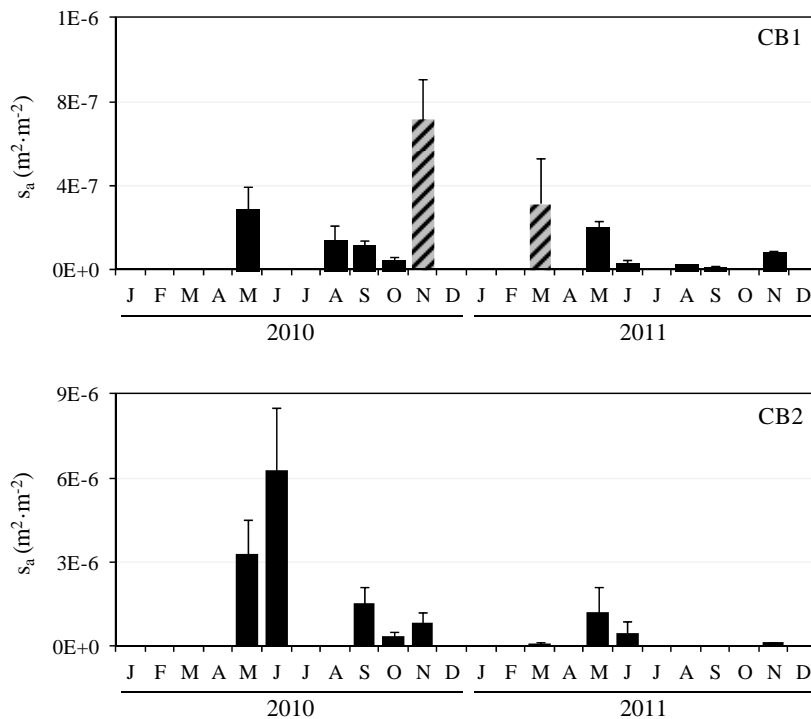


Figure 2.4. Water column total area backscatter v. sampling month. Average total area backscatter (s_a) for months in 2010 and 2011, at CB1 (top) and CB2 (bottom). Error bars are 1 standard error, crosshatched bars denote potentially abnormal values (section 4). Months lacking bars were not sampled.

2.4.2. Does total water column fish density vary among months of the year?

Relative fish density changed significantly from month to month at both sites in 2010 (CB1: $p = 0.013$, CB2: $p = 0.004$), but only at CB1 in 2011 (CB1: $p = 0.005$, CB2: $p = 0.181$) (Figure 2.4). At CB1 in 2010, November had a significantly higher fish density than the other months in multiple comparisons tests, followed by May and September, then August and October. At CB1 in 2011, May and November had the highest densities, followed by the four other months, which were not significantly different from each other. At CB2 in 2010, there was less distinction among the months. May and June had higher densities than August, October, and November; September spanned these two groups, having greater fish density than August and October but not having significantly different density than the other months. At CB2 in 2011, the separation among months was more clear: May and November had significantly higher fish densities than all other months, followed by March, June, August, and September.

2.4.3. Does fish density vary spatially?

Relative fish density varied significantly from site to site only in 2010, when fish were an order of magnitude less dense at CB1 than at CB2 ($p = 0.001$; CB1: $2 \cdot 10^{-7} \pm 3.5 \cdot 10^{-8}$; CB2: $2.1 \cdot 10^{-6} \pm 4.9 \cdot 10^{-7}$). In 2011, relative density was not significantly different at the two sites ($p = 0.613$).

2.4.4. What is the vertical distribution of fish density in the water column?

Backscatter from fish was observed in all parts of the water column (Figure 2.5). Fish density almost always increased with depth, except for three surveys in which fish

density increased in the upper layers analyzed. These surveys included all tides in May 2011 and the daytime ebb tide in August 2010 and June 2011. Fish were sometimes concentrated in one or two layers in the middle of the water column (e.g., day flood in September 2011). These mid-column increases in density were generally associated with the passage of several small, dense schools of fish during that time span.

2.4.5. Does the vertical distribution of fish density vary seasonally and annually?

At CB1, the vertical distribution of fish varied from month to month in both years (left-hand blocks, Figure 2.5). For those months that were sampled in both years, survey distributions from 2010 were compared to the corresponding surveys in 2011. Fish had similarly shaped distributions in both years in August and November, but were distributed differently in May and September (Table 2.3). May was strongly bottom-oriented in 2010, but top-oriented in 2011 (Figure 2.5). September 2010 and 2011 were similar when compared visually, except that in 2011 there was an increase in density in the 10-11 m layer (Figure 2.5). Differences in the magnitudes of the distributions in 2010 and 2011 were more obvious, as can be clearly seen in the unscaled distributions in the left blocks of Figure 2.5. Fish densities throughout the water column were higher in 2010 than in 2011 in all months surveyed besides May, in which magnitude did not change significantly between years (Table 2.3). These differences reflect what was shown by the analysis of total water column backscatter (section 3.2).

Month	Distribution shape: Significance of linear fit (p-value)	Distribution mean: 2010 or 2011 greater?
May	0.243	Same
Aug	0.003	2010
Sept	0.274	2010
Nov	$1.78 \cdot 10^{-5}$	2010

Table 2.3: Vertical distributions of fish at CB1, 2010 v. 2011. Similarity of 2010 and 2011 entire-survey vertical distributions of fish at CB1. Shaded cells indicate significant difference. For shape, insignificance of the linear regression ($p > 0.05$) or negative slope indicate dissimilarity.

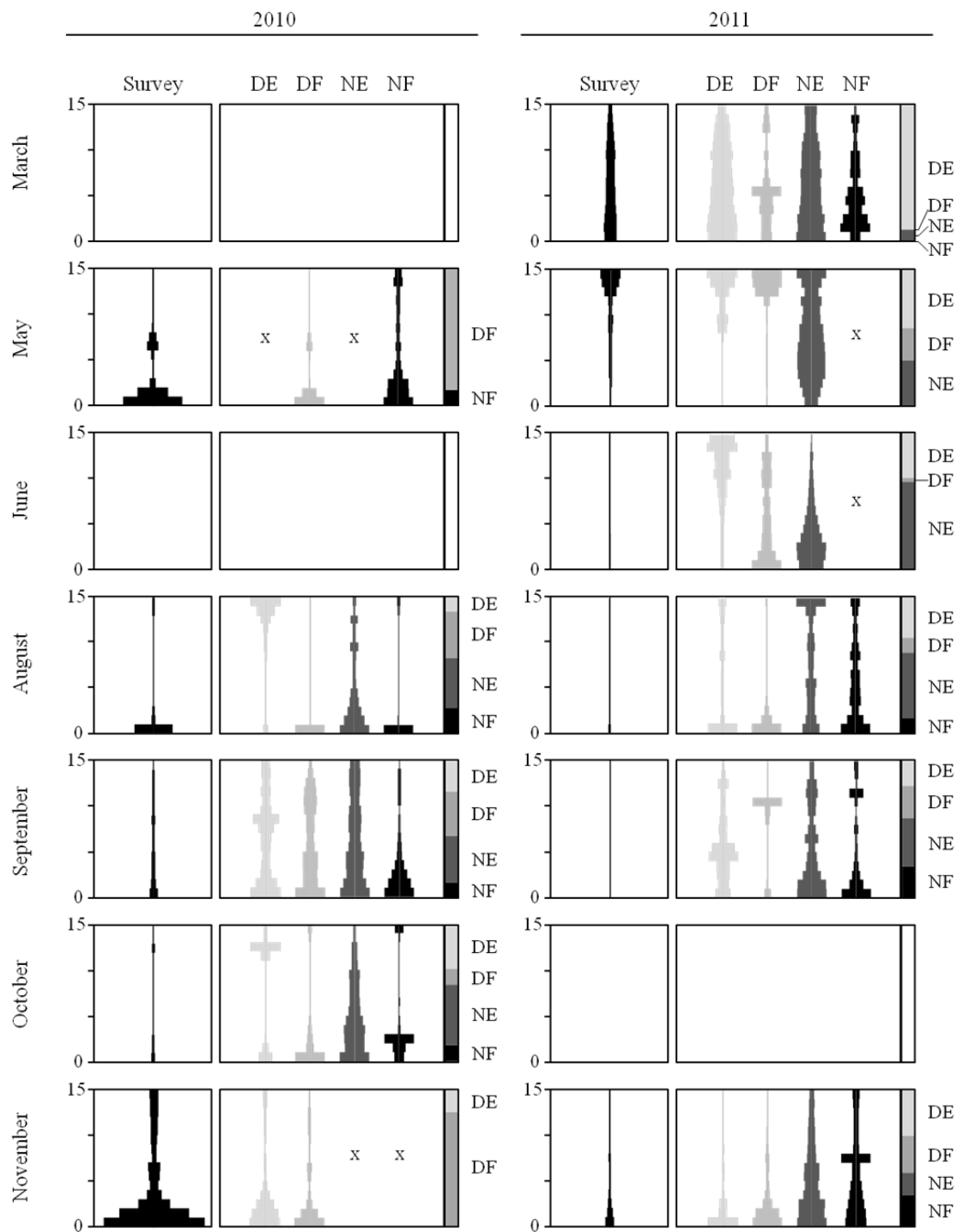


Figure 2.5. Vertical distributions of fish at CB1. Relative vertical distribution of fish within the water column at CB1 for 2010 (left column) and 2011 (right column). The vertical axes are distance from sea floor in m, the horizontal axes are relative total area backscatter (s_a), proportional to fish density. In each column, entire-survey distributions are shown in the left block, in black. These are to scale to allow visual comparison of relative density in different surveys. The right blocks contain the relative distributions for each tidal stage, separated into day ebb (DE), day flood (DF), night ebb (NE), and night flood (NF). These distributions are normalized to show small backscatter values. The vertical bar to the right shows the relative backscatter (fish density) of each stage. X's indicate unavailable data.

2.4.6. Does the vertical distribution of fish density vary with day and night or tidal stage?

Fish distributions changed shape with day and night in 4 of the 11 surveys, including October 2010 and May, June, and September of 2011. In Figure 2.5, this can be seen in general as a more filled water column during at least one of the night tides. While the shape of fish distributions differed in 4 of the surveys, overall magnitude differed in 3: fish density was less during the day than the night in August of 2010 and June of 2011, but greater during the day in March of 2011 (Table 2.4).

Year	Month	Distribution shape: significance of linear fit (p-value)	Distribution mean: day or night greater? (D/N)
2010	May	< 0.001	Same
	Aug	< 0.001	N
	Sept	< 0.001	Same
	Oct	0.689	Same
	Nov	–	–
2011	Mar	< 0.001	D
	May	0.935	Same
	June	0.002	N
	Aug	0.036	Same
	Sept	0.903	Same
	Nov	< 0.001	Same

Table 2.4. Vertical distributions of fish, day v. night. Similarity of day and night vertical distributions of fish at CB1. Shaded cells indicate significant difference. For shape, insignificance of the linear regression ($p > 0.05$) or negative slope indicate dissimilarity.

Fish distributions also varied with tide (Table 2.5). The shapes of the distributions were affected by tide more often during the day (August and October

2010, March, June, and September 2011) than at night (October 2010, August 2011). In 10 of the 13 instances when offsets between distributions were significant, densities were greater during the ebb tide than the flood tide.

Year	Month	Day or Night	Significance of linear fit (p-value)	Greater density in ebb or flood? (E/F)
2010	May	D	-	-
		N	-	-
	Aug	D	0.932	Same
		N	0.001	E
	Sept	D	0.039	F
		N	< 0.001	E
	Oct	D	0.373	Same
		N	0.068	E
	Nov	D	< 0.001	F
		N	-	-
2011	Mar	D	0.132	E
		N	0.006	E
	May	D	< 0.001	E
		N	-	-
	June	D	0.072	E
		N	-	-
	Aug	D	< 0.001	E
		N	0.120	E
	Sept	D	0.406	Same
		N	< 0.001	E
Nov	D	< 0.001	Same	
	N	0.016	F	

Table 2.5. Vertical distributions of fish, ebb tide v. flood tide. Similarity of tidal stage vertical distributions of fish at CB1. Shaded cells indicate significant difference. For shape, insignificance of the linear regression ($p > 0.05$) or negative slope indicate dissimilarity.

2.5. Discussion

Primary features of Cobscook Bay are its high biological productivity and its extreme tidal currents (Brooks 2004, Larsen and Campbell 2004). The bay has complicated geography, which combines with its large tidal range to create high current speeds and flow that vary greatly with location and tide (Brooks 2004, Huijie Xue, unpublished data). Multiple fish species pass through the strong currents of the outer bay to move between deeper ocean habitats and the extensive inshore nurseries and foraging grounds of the inner bays. These include migratory fish species, such as alewives, blueback herring, rainbow smelt, silver hake, white hake, and Atlantic mackerel, as well as year-round residents, such as Atlantic herring and threespine stickleback (Tyler 1971, MacDonald et al. 1984, Saunders et al. 2006, Athearn and Bartlett 2008). Given the extreme variation in currents over time and space, as well as the mixed seasonal and year-round fish community, acoustic estimates of relative abundance and vertical distribution were expected to show high variation.

Though acoustic backscatter (i.e., fish density) at the control site, CB2, was an order of magnitude greater than that of the project site, CB1, similar yearly and seasonal trends were seen at both sites. At both sites, fish density increased in the spring and fall. The largest difference between the seasonal patterns at the two sites were November 2010 and March 2011, which had much higher fish densities relative to the other surveys at CB1 than at CB2 (Figure 2.4). Both instances can be linked to

unusual circumstances. The November 2011 survey occurred during a storm, and fish density during the partial flood tide sampled was much greater than it was during the ebb of that survey as well as any of the other surveys at CB1. Abnormality of this high backscatter was verified by comparison with fish densities at CB2, which was sampled just two days prior but in good weather conditions. The increase in relative density was much more modest there. The storm is the best explanation for this great difference. Relative density in March 2010 was greatly affected by the passage of two large schools in an otherwise nearly empty water column. The same schools did not pass through CB2, and backscatter there was much less in March than in other months. If these two surveys are eliminated from CB1 data, CB1 and CB2 both show significantly higher fish densities in 2010 relative to 2011 ($p = 0.001$). It is beyond the scope of this study to explain this yearly variation, but the fact that both sites show similar trends on an annual and seasonal scale (despite large differences in magnitude) supports the use of CB2 as a control site, and its importance in identifying variation that may be out of the ordinary.

Given the seasonal pattern in total fish density at each site, and the seasonal variation in both species and size composition of the fish community, patterns in vertical distribution on seasonal, diel, and tidal cycles were expected. Atlantic herring, alewives, and juvenile Atlantic cod are all species present in the area that are known to exhibit diel vertical migrations (Brawn 1960a, Janssen and Brandt 1980, Blaxter 1985,

Perry and Neilson 1988, Nilsson et al. 2003), and tidal flows can be selectively used by adult and juvenile fish of many species (Stasko 1975, de Veen 1978, Greer Walker et al. 1978, Arnold et al. 1994, Castonguay and Gilbert 1995, Levy and Cadenhead 1995, Moore et al. 1998, Lacoste et al. 2001). While patterns in vertical distribution of fish associated with these factors were not consistent from survey to survey at either CB1 or CB2, there were distinct differences associated with day/night, tide, or a combination of the two factors in several surveys.

Diel changes in fish distribution were observed in several surveys, including August and October 2010 and May, June, September, and November of 2011 (Figure 2.5, Table 2.4). In these surveys, fish were more evenly distributed at night than during the day. The strongest example of diel changes in distribution was seen in May of 2011, when during the day, fish were concentrated in the upper few layers of the water column analyzed, but at night they spread throughout the water column. In this case, fish were near enough to the surface to clearly observe this behavior with the DIDSON. Almost all fish observed in the DIDSON footage were small (on the order of 5 cm) and aggregated in tight, small schools during the day that remained in the upper half or so of the water column. At night, these schools dispersed throughout the water column, extending downward from the upper layers. This is obvious in the vertical distributions, and is consistent with known diel behavioral patterns in fish (Janssen and Brandt 1980, Luecke and Wurtsbaugh 1993, Nilsson et al. 2003). These small fish are

also unlikely to have much control over their horizontal movements in the strong tidal currents throughout the outer bay, which may explain why they were seen in abundance during the ebb as well as the flood tides. The unusually low variety in fish sizes in the DIDSON footage from this survey, though not necessarily representative of the entire water column, may indicate that on this day a more uniform group of fish was sampled than usual. This is perhaps one reason the diel behavior is so obvious. As many diel patterns are species- and site-specific (Weinstein et al. 1980, Levy and Cadenhead 1995, Neilson and Perry 2001), the more mixed the fish community, the less clear these patterns will appear. This is likely to be a common problem faced in Cobscook Bay, given its diverse and variable fish community. This problem is exacerbated by the inability to estimate fish size from the single-beam acoustic data; for this, a split-beam echo sounder is required.

Significant changes in distribution with tidal stage were relatively common at CB1 (Table 2.5), however, as with diel variation, differences were not consistent from one survey to another. August 2010 is one example. During the daytime ebb, fish were concentrated in the upper 4 m analyzed (though in low densities in comparison to the other stages), and during the night ebb, fish were spread throughout the water column, increasing in density in the lower 5 m. These distributions contrasted sharply with those of flood tides, in which fish were almost entirely concentrated in the lowest water layer, regardless of day or night. This could indicate that fish sought the slower-

moving boundary layer near the sea floor during the inflowing tide, perhaps indicative of an offshore movement. Differences between tidal stages, such as these, were seen in multiple surveys.

Relative fish densities were not always the same during the ebb and flood tides. Of the 13 instances when densities were unequal, fish densities were higher during the ebb than the flood (Table 2.6). This difference may indicate a general outward flux of fish at CB1, which could be true without suggesting a net outward flux of fish from the inner bays. The flow in Cobscook Bay is highly variable, and the nature of its route changes with the ebb and flood tide (Brooks 2004; Huijie Xue, unpublished data). Fish carried out through CB1 on the ebb tide could easily return to locations up-bay of CB1 via a completely different route. Less than 2% of the width of the channel is sampled at the acoustic beam's greatest diameter, and variability in flow pattern likely obscured some tidally-related fish behaviors. However, the presence and behavior of fish at this particular location with reference to the pilot tidal device were the focus of this study.

In nearly every survey, there was an obvious increase in fish density in the lower layers of the water column, regardless of day/night or tidal stage. This may be attributable to demersal feeding habits of fishes, and may also be related to the decrease in current speed near the sea floor, which was evident in ADCP data. Regardless of cause, this preference for lower layers appears to outweigh the influence of tidal stage or daylight on fish distribution at CB1, as it is apparent during most surveys and other

behaviors are inconsistent. Preference for the bottom-most layers is therefore likely a behavior common to multiple species and size classes. If current speed plays a role in the distribution of fish in the water column, it may be beneficial to examine fish behavior during the slack tides. With strong currents removed, certain behaviors (e.g. diel movements) and distinct groups of fish (e.g. pelagic or benthic) may become more apparent.

Observing the changes in fish presence and distribution was complicated by the properties of the acoustic system used. The use of a single-beam echo sounder has several limitations which make pattern identification within a mixed fish community difficult. First, the acoustic threshold of -60 dB target strength (TS) eliminated backscatter from most larval fish and small invertebrates, such as krill, but it also likely eliminated backscatter from some fishes, especially those lacking swimbladders, such as Atlantic mackerel (as explained in the methods). This difference could result in under-sampling certain fish species in relation to others, which may affect the behaviors seen. A further limitation of the acoustic system was the inability to correct TS values for beam pattern, therefore neither size nor number of fish detected could be estimated. Without the ability to distinguish between groups of fish, movements of the various components of the community are impossible to distinguish from each other, and instead may serve to mask each other from detection. Additionally, without the knowledge of fish size, the ability to identify differences in the fish species sampled at

the ebb and flood tides is limited. With such variable flow patterns throughout the bay and the large amount of flushing that occurs with each tidal cycle (Brooks 2004), the fish within the ebb and flood tides could be very different, making a consistent effect of tide on the vertical distribution of fish unlikely.

The omission of the upper 10 m of data due to excessive acoustic interference may also have removed evidence of diel or tidal changes in the vertical distribution of fish. During low tide at CB1, the excluded layers constituted nearly the entire upper half of the water column. If fish underwent vertical migrations, a large part of the movement was likely omitted. Analyses of the DIDSON footage collected during these surveys would aid in quantifying this effect. The DIDSON footage from May 2011 has been reviewed in more detail than other surveys, and many small schools were seen in the upper 10 m during the day but spread throughout the rest of the water column at night. Future work will include quantifying fish in the omitted layers through full analyses of the DIDSON data collected at CB1 and CB2.

The timing of surveys each month likely affected the data collected. Sampling continuously for one day per month provided a wealth of information for that particular day on a fine time scale, useful for behavioral analyses. However, the data collected over 24 hours are not necessarily representative of a larger span of time, such as an entire month or season. In such a dynamic environment, there is a high degree of day-to-day variability which is difficult to identify unless multiple days are sampled.

November 2010 and March 2011 surveys at CB1 provided examples of the type of error that can be introduced by sampling just one day. While sampling at a control site helped identify these two surveys as abnormal, to achieve a more accurate understanding of the patterns in vertical distribution and how they change over time would likely require sampling multiple days spread throughout the month. Continuous monitoring is probably unnecessary, and the quantity of data would be difficult to manage due to limited data storage in the field and the high level of manual processing that it must undergo. A compromise of shorter periods of continuous sampling, occurring more often over a larger time scale, would greatly improve the interpretation of patterns within the data, while remaining realistic in terms of analysis. One option for future consideration would be to deploy a bottom-mounted unit that automatically collects data on a preset, semi-continuous schedule. This would solve issues such as boat motion at slack tide, reduce the effort and cost required to collect the data, and allow high-resolution data collection over a much longer time.

Regardless of these issues, the results obtained provide valuable information for the assessment of the pilot tidal power device. While the omission of 10 m of water column and the limitations of the single-beam acoustic system may not be ideal for quantifying the drivers of biological processes, it is certainly sufficient to characterize fish use of the region that will be directly affected by the installation of a tidal turbine. The rotating foils will be located approximately 7 to 9 m above the sea floor, directly in

the center of the analysis range (0-15 m). This study showed that within that range, fish were generally denser near the bottom (0-5 m). This is below the layers spanned by the rotating turbine, but these fish are likely to encounter the solid support frame and foundation. If the number and size of detected fish could be approximated, the potential rate of fish encounters with the turbine and its supporting structures, as well as the likely reactions of those fish (which have been found to be affected by fish size; Chapter 3) could be estimated.

As this study progresses, continued data collection at the pilot project and control sites will improve understanding of the seasonal movements of fish through the region, fish use of the water column during periods of high flow, and any changes associated with the introduction of the pilot device. The use of a split-beam echosounder in place of the current single-beam system will allow estimation of fish numbers and size, as well as direction of movement. Analyzing the vertical distribution of various size groups will greatly improve knowledge of which species are present, when they are present, and which parts of the water column they utilize with respect to various environmental factors. This information is of particular interest to environmental regulators concerned for endangered species, such as Atlantic salmon, that may be present at tidal sites, and can aid in management efforts as tidal power development continues.

CHAPTER 3

FISH INTERACTIONS WITH A COMMERCIAL-SCALE TIDAL ENERGY DEVICE IN A FIELD SETTING

3.1. Abstract

Fish are a key part of the marine ecosystem likely to be affected by marine hydrokinetic tidal turbines, but little is known about fish behavior around a hydrokinetic turbine in the natural environment. In September of 2010, two DIDSON acoustic cameras were used to observe fish interactions with a test turbine mounted below a floating platform in Cobscook Bay, Maine. Twenty-four hours of footage were collected, fish behaviors were classified (e.g., avoidance, entrance, passing by), and the effects of turbine movement (rotating or still), day and night, and fish size (small, ≤ 10 cm; medium, > 10 and ≤ 20 cm; and large > 20 cm) on behaviors were analyzed. A greater proportion of fish interacted with the turbine when it was still rather than rotating, and at night rather than day. Fish reacted further away from the device during the day than at night. For small and medium fish, the type of interaction shifted from avoidance of the turbine during the day to entrance at night; large fish mainly avoided the turbine. Given the poor visibility in the bay and the need for both day and night observation, the DIDSON was a useful tool for turbine assessment.

3.2. Introduction

Tidal currents play an essential role in the life cycles of marine and diadromous fishes, but humans are increasingly interested in extracting energy from the same currents. Many fishes are known to use the tides for on- and off-shore movements

related to foraging, spawning, and sheltering (Dadswell and Rulifson 1994, Hartill et al. 2003, Krumme 2004, Ribeiro et al. 2006). Several migratory species actively seek currents when the tide is flowing in their desired direction of movement, including American eel, *Anguilla rostrata* (McCleave and Kleckner 1982); Atlantic cod, *Gadus morhua* (Arnold et al. 1994); sockeye salmon, *Oncorhynchus nerka* (Levy and Cadenhead 1995); sea trout, *Salmo trutta* (Moore et al. 1998); plaice, *Pleuronectes platessa* (de Veen 1978, Greer Walker et al. 1978); Atlantic salmon, *Salmo salar* (Stasko 1975); Atlantic mackerel, *Scomber scombrus* (Castonguay and Gilbert 1995), and Atlantic herring, *Clupea harengus* (Lacoste et al. 2001). Areas of extreme tidal currents are being targeted for tidal energy development, which utilizes large, in-stream hydrokinetic (HK) turbines to extract energy from the fast, predictable flow (Charlier and Finkl 2010). Due to the spatial overlap of tidal energy devices with fish populations, interactions between the two should be expected. However, this has yet to be studied in the United States due to the lack of installed HK turbines. Most of what is known of fish interactions with turbines is from conventional hydropower plants, where water flows at high speeds through turbines installed within dams or other barrages. To move upstream past these obstacles fish must use fishways if available, or when moving downstream, pass over a spillway or (more likely) through a turbine (Čada et al. 2006). When passing through a hydropower turbine, fish are subjected to rapid pressure changes, cavitation, shear stress, and blade strike, all of which can cause injury or mortality (Dadswell and

Rulifson 1994, Čada et al. 2006). At the Annapolis estuary low-head tidal barrage in the Bay of Fundy, mortality rates among fish passing through turbines were found to range from 20% to 80% (Dadswell and Rulifson 1994). HK turbines are fundamentally different from conventional hydropower designs because they do not require a barrage. Instead, HK devices are free-standing, open structures installed in areas with strong currents. Rather than being channeled through turbines, fish may be able to avoid them entirely. While studies have examined the survival of fish passing through tidal turbines in laboratory flumes (Amaral et al. 2008, Jacobson 2011), the probability of fish interactions with tidal turbines when in their natural environment is unknown.

The choices fish make when presented with a tidal energy device in the open marine environment must be examined in order to assess the potential effects of these devices on fish. To date, most tidal devices are composed of a stationary support structure and foundation, a generator, and moving turbine components. The attraction of fish to underwater anthropogenic structures is well documented, and turbine support structures and foundations have the potential to act as artificial reefs. This has been the case for the foundations of offshore wave power devices (Langhamer et al. 2009), the monopiles of offshore wind farms (Wilhelmsson et al. 2006), and decommissioned oil platforms (Soldal et al. 2002). Additionally, in high-flow channels where low-flow areas are sparse, the lower-energy area downstream of the support structure and turbine could provide refuge from the high speed currents for a number

of fish species (Čada and Bevelhimer 2011). On the other hand, the turbine will be a large, moving object, and the generator will produce a certain level of noise, potentially repelling fish from the area. The ability of fish to avoid objects perceived as threatening is as well known as their attraction to solid structures: fish have shown avoidance behaviors to vessels at ranges of 100-200 m, or as far as 400 m if the vessel is particularly noisy (Mitson 1995, Vabø et al. 2002, de Robertis and Wilson 2007). Rakowitz et al. (2011) observed strong avoidance reactions of several fish species to trawls at close ranges as well, with fish darting away when as close as 1 m to the advancing net. Jacobson (2011) documented a strong aversion of fish to entering a tidal turbine in the laboratory, even when introduced at very close range.

Polagye et al. (2011) identified several potential “dynamic” effects of HK tidal turbines on fish. These are effects involving the moving portion of the turbine (the blades), including direct strike and pressure changes around the blades. These effects have been hypothesized to lead to fish death or injury, increased stress, alterations of migratory pathways, or even changes in predator-prey relationships. To evaluate the potential for any of these effects, the behavior of fish around a device in a field setting must be better understood.

This study was designed to answer that question by monitoring a test HK turbine deployed in Cobscook Bay, Maine by Ocean Renewable Power Company. Goals were to classify fish behaviors in reaction to the turbine when encountered in the

natural environment, to quantify the behaviors observed, and assess the effects of day or night, fish size, and turbine movement on their behaviors.

3.3. Methods

3.3.1. Site

Cobscook Bay is the eastern-most bay of the United States, at the mouth of the Bay of Fundy, and it consists of three smaller bays joined by narrow channels (Figure 3.1). The mean tidal range is 5.7 m (Brooks 2004), and current speeds within the outer bay regularly surpass $2 \text{ m}\cdot\text{s}^{-1}$. The depth at the site of the research platform ranged from 17 m to 31 m over the course of a tidal cycle.

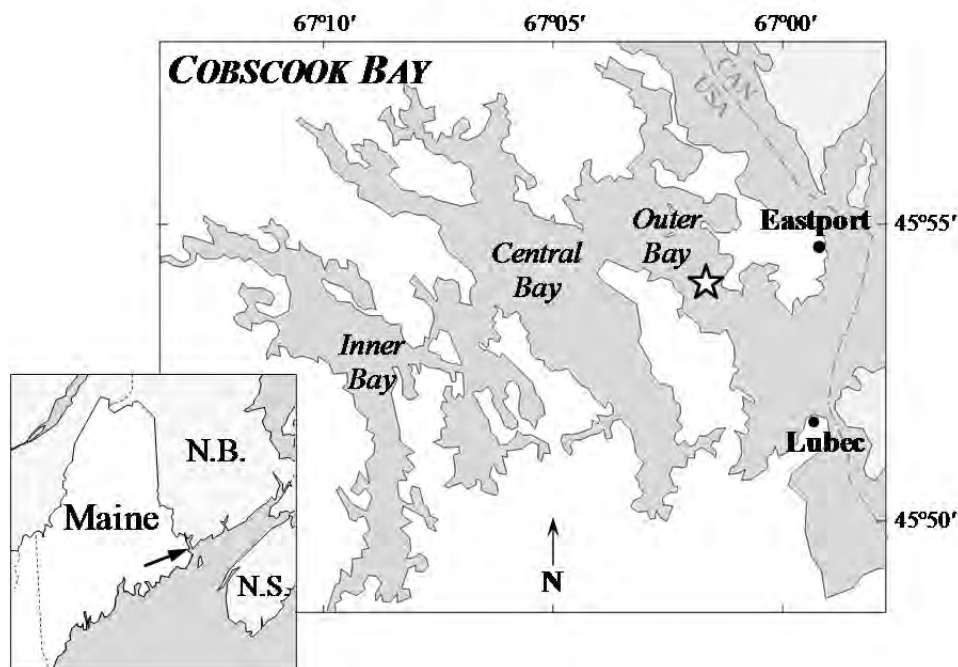


Figure 3.1. Map of Cobscook Bay. ORPC research platform, the Energy Tide II, mooring location at ☆.

3.3.2. *Equipment*

Two DIDSON (Dual Frequency IDentification SONar) acoustic cameras were used to observe a test turbine suspended below ORPC's research platform, the Energy Tide II (Figure 3.2). The Energy Tide II is a modified 56 ft (17 m) x 23 ft (7 m) barge, with two large, hydraulic arms that rotate 90° to suspend the turbine below at a depth of approximately 5 m (Figure 3.3). The test turbine was ORPC's basic device module, the Turbine Generator Unit (TGU), which consists of two helical-bladed, cross-flow turbines sharing a central axis with a permanent magnet generator. The turbine started to rotate when current speeds exceeded 1 m·s⁻¹, and stopped rotating when current speeds fell below 0.5 m·s⁻¹. The maximum rotational speed of the turbine observed during this survey was 27 rpm at a current speed of 2.8 m·s⁻¹ (5.4 knots), at which point the blade tip speed was approximately 2.6 m·s⁻¹. The maximum rotational speed of the turbine is 40 RPM, at which point the blade-tip speed is approximately 5.5 m·s⁻¹. The research platform was moored in place, and turned on its mooring with each turn of the tide.

The two DIDSON units were mounted fore and aft of the TGU and angled in order to view a cross section of each side of the turbine and support structure (Figure 3.3). The DIDSON combines the feedback from 96 individual, high-frequency (1.8 MHz) acoustic beams, each 0.3° x 14° and divided into 512 equal range segments, to build an image of a 29° by 14° volume of water.



Figure 3.2. Research platform. ORPC's Energy Tide II, showing test turbine in raised position.

These images are produced in rapid succession, between 4 and 21 frames per second, to create "video" footage of the insonified area. The viewing windows were aligned as closely as possible with one another on each side of the turbine, each oriented with the long axis of its cross-sectional viewing area parallel to the flow. Fish swimming or drifting with the flow passed through as many of the 96 beams as possible, providing the best view of the fish's behavior as it approached and departed from the turbine. Fish swimming at an angle to the current were harder to visualize. In high-frequency (1.8 MHz) mode, each DIDSON had a range of 13.3 m. The viewing window was set to begin at 3.3 m in the fore DIDSON and 2.5 m in the aft to eliminate areas of noise due to reflection off of the support structures and to better view the turbine. The DIDSONs sampled a partial cross-section of turbine approximately 0.75 m wide at its top and 1 m wide at its base, and each captured approximately 1/3 of the turbine's cross section. The fore DIDSON's viewing window extended 2.5 m upstream of the turbine, 1 m above it,

and 5 m below it. The aft DIDSON was held at more of an angle due to its mount location, and insonified a region extending approximately 3 m above, behind, and below the turbine. Vertical resolution of each DIDSON (along the length of the viewing window) was 2.0 cm. Horizontal resolution ranged from 1.3 cm at a range of 2.5 m to 8.3 cm at its maximum range. A frame rate of at least 7 frames·s⁻¹ was maintained throughout the sampling period.

Current speed was recorded using a Valeport model 803 ROV current meter attached to the support frame of the turbine.

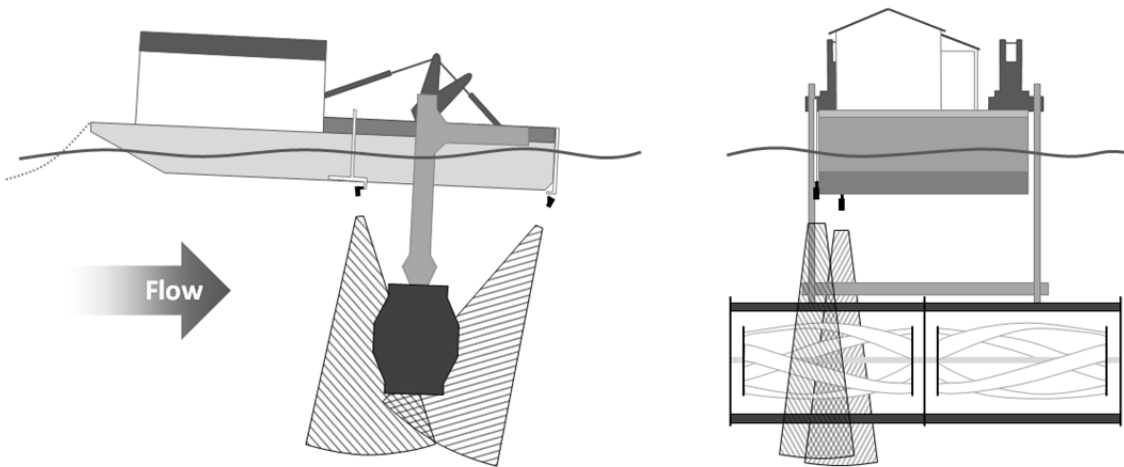


Figure 3.3. Survey setup. Schematic of the ORPC research platform, the Energy Tide II, with the test turbine suspended below (adapted from schematic provided by Ryan Beaumont, RM Beaumont Corporation, Brunswick, ME). Left: side view. Right: front view. DIDSONs are shown in survey positions by black boxes. Volume insonified by each DIDSON is indicated by hatched areas.

3.3.3. Survey Sampling

The survey began at 10 am on September 8th, and acoustic video was recorded with both DIDSONs continuously for 24 hours. Sampling included 13 hours of daylight

and 11 hours of darkness, and spanned two tidal cycles. Current speed was recorded every half hour along with environmental observations that included wave height, wind speed, cloud cover, precipitation, and sun and moon visibility.

3.3.4. Data Analysis

DIDSON footage was analyzed manually using DIDSON software, which allowed frame-by-frame viewing of the footage along with measurement tools. Information was collected for each fish viewed, including time of detection, range from the DIDSON, fish length, whether the fish was part of a school (and how many individuals were in the school), turbine state (rotating or still), and fish behavior (see section 3.4.1). If fish avoided the turbine, the distance between the fish and the turbine at the time of the avoidance reaction (“reaction distance”) was recorded. Often, long spans of time would pass in which same-sized fish would pass through at the same depth, showing similar behaviors and at a roughly constant frequency. At these times, the number of individual fish was estimated by multiplying the rate of fish passage by the duration of time for which that rate remained constant. Behavior, depth, and the other descriptors were then assigned to each of those fish.

3.3.4.1. Classification of Fish Behavior

Seven fish behavior categories were identified (Table 3.1 and Figure 3.4). Five of these behaviors were interactions with the turbine, and two were not. Interactions fore of the turbine were considered encounter behaviors, or initial reactions, as they

occurred during a fish's first approach to the turbine. Behaviors aft of the turbine were considered departure behavior, or secondary responses. Encounter and departure behaviors were analyzed separately.

3.3.4.2. Analysis of Factors Affecting Fish Behavior

The effects of day, night, fish size, and current speed on the proportion of fish interacting with the turbine and the type of interaction were examined. The category of day or night was assigned to each fish using its time of detection and known times of sunset and sunrise. Current speed data were interpolated to obtain the current speed at each fish's time of detection. Fish were classified by their length as small (≤ 10 cm), medium (> 10 cm and ≤ 20 cm), or large (> 20 cm). Schools in which fish were too densely packed or too numerous to be counted accurately were omitted from analyses and described qualitatively instead. Fish detected within 3.3 m of the aft DIDSON were omitted from analyses in order to assure that sampling areas fore and aft were similar. The number of fish exhibiting each behavior (Table 3.1) was counted for each factor category or combination of categories examined (e.g., large fish avoiding the turbine at night, large fish avoiding the turbine during the day). The proportions obtained were compared using two-sample z-tests for difference of proportions. The effects of factors on reaction distance was examined using one-way ANOVA permutation tests, with a significance level (alpha) of 0.05.

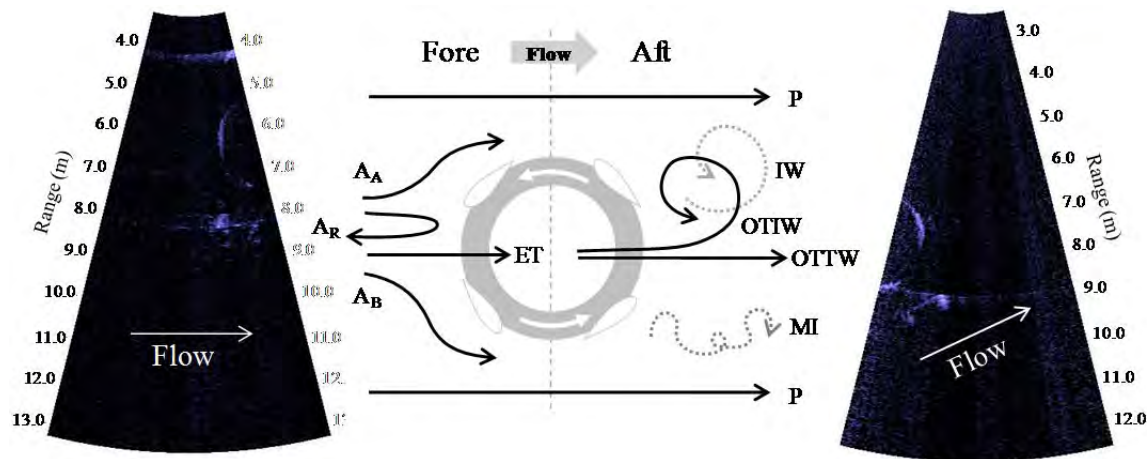


Figure 3.4. Fish reactions to test turbine. (Center) Schematic of the seven behaviors observed in DIDSON footage of ORPC test turbine. (Left) Frame from fore DIDSON. (Right) Frame from aft DIDSON. Cross-section of turbine and support frame can be seen in both frames. Flow direction is indicated is slanted in the aft view due to the tilt of the DIDSON.

Where seen	Name of Behavior	Description of behavior
In front of and behind turbine	MI	Milling – milling occurred during slack tide, when current speed was low. Fish ceased directed movement and instead moved in short bursts in random directions.
	P	Pass by – fish entered the field of view already above or below the turbine and passed across the view without diverting course, apparently unaffected by the turbine’s presence.
In front of turbine	A	Avoidance – fish noticeably altered course to avoid the turbine, swimming above or below it (A _A or A _B), or reversing direction against the current (A _R).
	ET	Enter Turbine – fish swam into the interior of the turbine. These were always fish that entered the field of view within the same depth range as the turbine.
Behind turbine	OTTW	Out of Turbine, Through Wake – fish were seen exiting the turbine, then swam directly through the wake of the turbine to re-enter the current.
	OTIW	Out of Turbine, Into Wake – fish were seen to exit the turbine and then remained in the wake, generally moving in and out of sight in a spiral pattern.
	IW	In Wake – fish appeared within the wake of the turbine and remained for several seconds, though previous location (inside the turbine or travelling above or below with the current) was unknown.

Table 3.1. Fish reactions to test turbine. Categorization and description of fish behaviors observed near ORPC test turbine in Cobscook Bay, ME.

3.4. Results

Fish were within view of the two DIDSONs during every hour of the survey, and were present 45% of the time analyzed (Figure 3.5). More fish were present aft of the turbine than fore (18,991 fore; 20,262 aft), and many more fish were present at night than during the day (4,511 day; 34,742 night). There was a large increase in numbers of fish during the nighttime slack tide (12 to 3 am), which accounted for over 77% of the total fish detected (Figure 3.5).

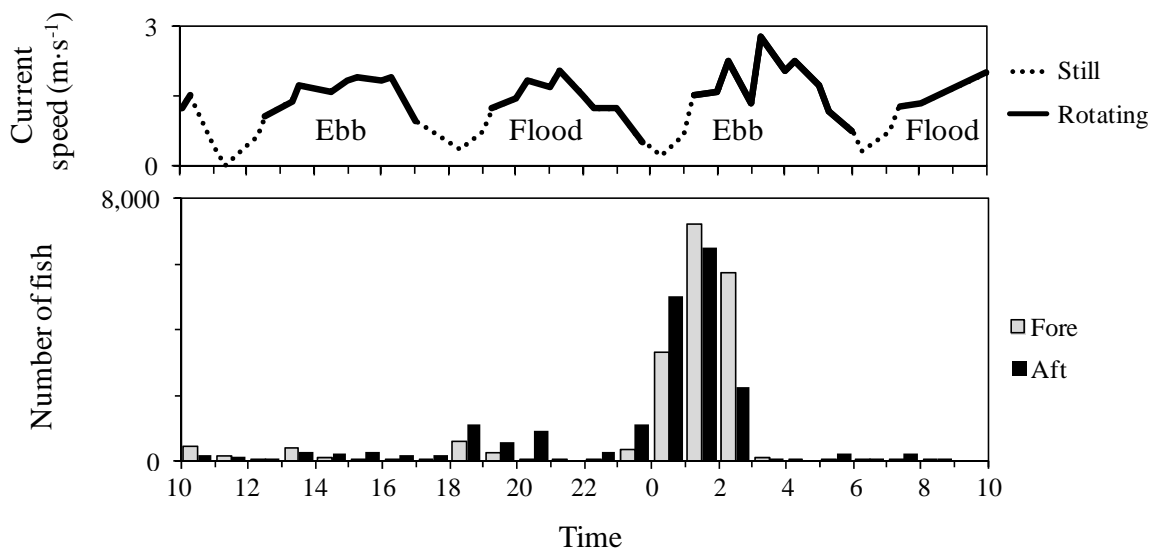


Figure 3.5. Current speed and number of fish detected v. time. Top: Surface current speed at ORPC research platform in Cobscook Bay, September 8-9, 2010. Solid lines indicate time when test turbine was rotating, dashed lines indicate time when turbine was still. Bottom: Number of fish detected at research platform per hour, fore and aft of test turbine. Shaded grey region indicates night.

Most fish were small (28,951), with fewer medium fish (9,851), and very few large fish (451). Fish aft of the turbine were slightly larger than those fore of it (permutation test $p = 0.001$) (Figure 3.6).

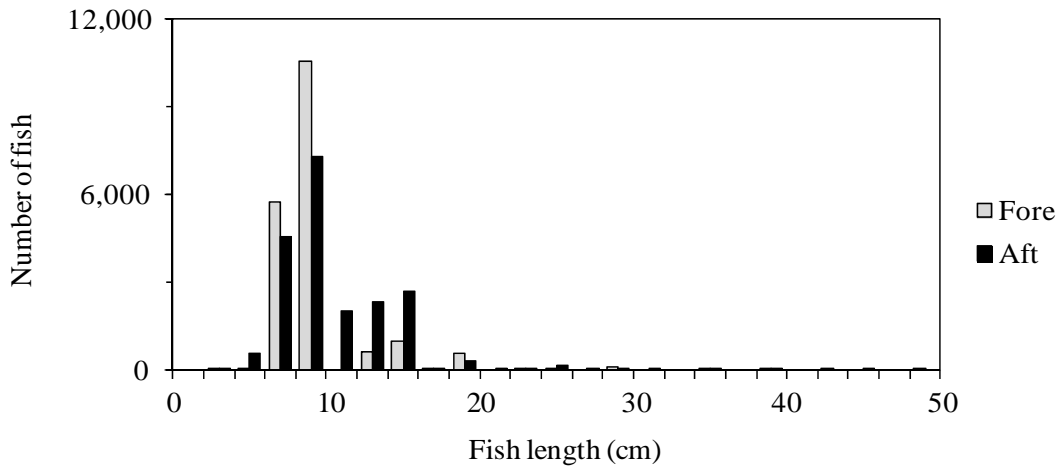


Figure 3.6. Fish size distribution. Distribution of fish sizes observed fore and aft of the ORPC test turbine in Cobscook Bay, Maine.

3.4.1. Fish Schools

Seventy schools were observed within the viewing zone of the two DIDSONs. Most schools were composed of less than 20 individuals (54 schools, 77.1%). Nine schools were estimated as having more than 50 individuals, and two had more than 100. These large schools (>50 individuals) were excluded from quantitative individual-based analyses, given the difficulty in distinguishing individual fish. When the tide was flowing, most schools (47) passed by either above or below the turbine (P), apparently unaffected. Individuals from 23 schools interacted with the turbine in some way, either avoiding it (A, 16 schools), passing into it (ET, 2 schools), passing out of it (OTTW/OTIW, 3 schools), or appearing in its wake (IW, 2 schools). When the current

speed was low, schools moved slowly with no clear direction (milling behavior, MI), and did not appear to interact with the turbine (which was not rotating).

The large schools (> 50 individuals) were seen primarily during the day, with only two occurring at night. Three of the 50+ schools and both 100+ schools were seen only when the DIDSON had been temporarily switched into long-range mode in order to view them. None of these schools came within 2 m of the turbine, whether rotating or still, and only one of them needed to divert its course downward to maintain that distance. The only other sign of interaction between these large schools and the tidal turbine was at one point during the daytime slack tide, when a 100+ school approximately 7 m across gathered below the stationary turbine. This school consisted of small (≤ 10 cm), tightly-aggregated fish (most likely herring), and it rose up from the lower limits of the view, milled below the turbine for several seconds, then slowly moved out of view.

Other schools did not remain near the turbine for long, and only five of the 70 entered the turbine (ET or OTTW/OTIW). Of the 16 that avoided the turbine, 14 altered course to swim below it and 2 reversed direction, swimming upstream and out of sight. The mean reaction distance for these schools was 2.52 ± 0.21 m. One school entering the turbine (15 fish, 20 cm long) swam directly in without altering course. The other (six fish, each 10 cm long) broke apart just before reaching the turbine: four individuals managed to dart upstream, while the remaining two passed into the turbine. Neither

school was seen to emerge from the turbine downstream, but this is not surprising, since a small movement to either side would carry fish outside the volume sampled by the aft DIDSON. The 3 schools observed leaving the turbine on the aft side were small (three, six, and seven fish apiece), with fish lengths ranging from 10 to 15 cm. Two of these (three- and seven-fish) emerged together as a tight group and passed directly through the wake and into the current (OTTW). The other school (six fish) emerged from the turbine slightly scattered, but quickly aggregated in the wake and returned to the current together (OTIW).

3.4.2. *Individual Fish*

Individuals include all non-schooling fish as well as those fish in schools with fewer than 50 members, which could be counted reliably. Nearly 40% of the total fish observed interacted with the turbine, either avoiding it (A), passing into it (ET), passing out of it (OTTW/OTIW), or appearing in its wake (IW).

3.4.3. *What affects fish-turbine interactions?*

3.4.3.1. Turbine Rotating vs. Still.

More fish interacted with the turbine (A, ET, OTTW, OTIW, or IW) when it was still (39.2%) than when it was rotating (35.1%) (z-test $p < 0.001$). More interactions were fish passing through the turbine (ET) when it was still (91.1%) than when it was rotating (43.2%) (z-test p -value < 0.001 , Figure 3.7). Whether the turbine was rotating or still also had a significant effect on the reaction distance of fish. The mean reaction distance

(\pm standard error) while the turbine was rotating and still was 1.50 ± 0.02 m and 2.42 ± 0.07 m, respectively (permutation test $p = 0.001$).

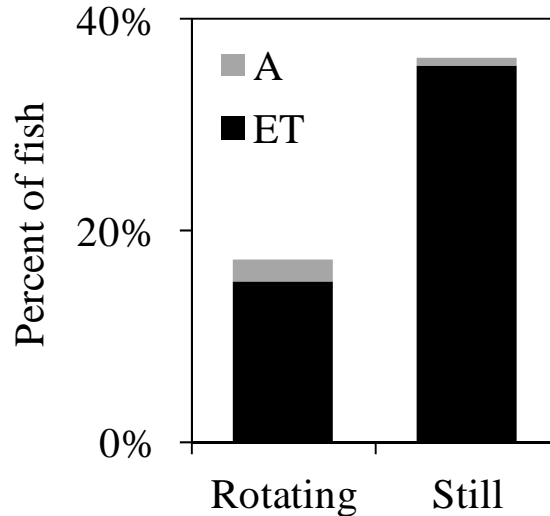


Figure 3.7. Effects of turbine state on fish behavior. Proportions of fish that interacted with the test turbine in Cobscook Bay while it was rotating and still (includes fish fore and aft of turbine). Interactions are split into proportions of fish that avoided the turbine (A) and fish that passed into it (ET).

3.4.3.2. Effects on Initial Behavioral Response to Turbine: Fish Fore of Turbine

Results from this point forward focus on times when the turbine was rotating and excludes fish in schools with 50 or more members.

A higher proportion of fish interacted with the turbine during the night than during the day (day: 20.5%; night: 35.5%; z -test $p < 0.001$). Of those fish to interact with the turbine, avoidance was higher during the day than during the night (day: 81.8%; night: 8.5%; z -test $p < 0.001$, Figure 3.8). Reaction distance was also greater during the day than during the night: 2.95 ± 0.04 m and 1.25 ± 0.02 m, respectively (permutation test $p = 0.001$).

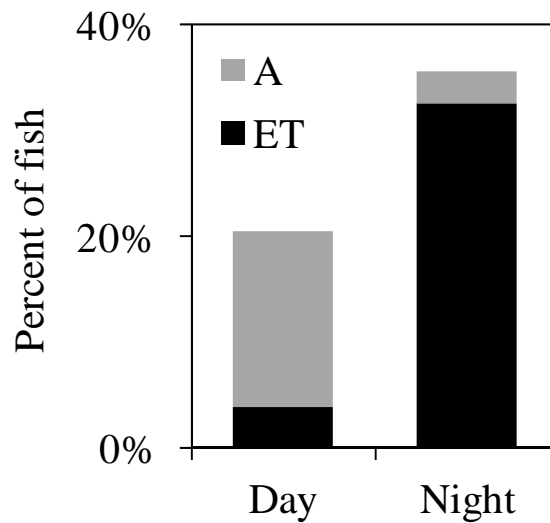


Figure 3.8. Effects of day/night on fish behavior. Proportions of fish that interacted with the test turbine in Cobscook Bay during the day and night (fore of turbine only). Interactions are split into proportions of fish that avoided the turbine (A) and fish that passed into it (ET).

The relative numbers of fish in the three size classes changed considerably between day and night. During the day, 34.8% of the fish were small, 52.5% were medium, and 12.7% were large. During the night, proportions were dominated by small fish (85.0%), followed by medium fish (14.4%), then very few large fish (0.6%).

The proportion of small fish to interact with the turbine did not change significantly between night and day (33.1% day; 33.3% night; z-test p-value = 0.969; Figure 3.9). A significantly higher proportion of medium fish interacted with the turbine at night than during the day (16.7% day; 49.2% night; z-test $p < 0.001$), and the same was true for large fish (1.9% day, 23.4% night, z-test $p < 0.001$). The type of interaction was found to change significantly for both small and medium fish, but not

enough large fish interacted with the turbine to test this effect. During the day, 76.8% of small-fish interactions with the turbine were avoidance, with the remainder passing into the turbine. At night, avoidance dropped to only 5.0% (z-test p-value < 0.001). A similar pattern was seen for the medium-sized fish: during the day, 89.8% avoided the turbine instead of passing through, but at night only 20.7% avoided the turbine (z-test p-value < 0.001). Size had a significant effect on the reaction distance (permutation test $p = 0.001$). Medium fish reacted furthest from the turbine, with mean reaction distance of 3.54 ± 0.08 m during the day and 2.57 ± 0.06 m at night. Small and large fish reacted to the turbine at significantly shorter distances, during both the day and night. During the day, small fish had a mean reaction distance of 2.64 ± 0.03 m. Only one large fish was detected avoiding the turbine during the day, and it did so at 0.8 m away. At night, small and large fish reaction distances were not significantly different, with a mean of 1.12 ± 0.02 m.

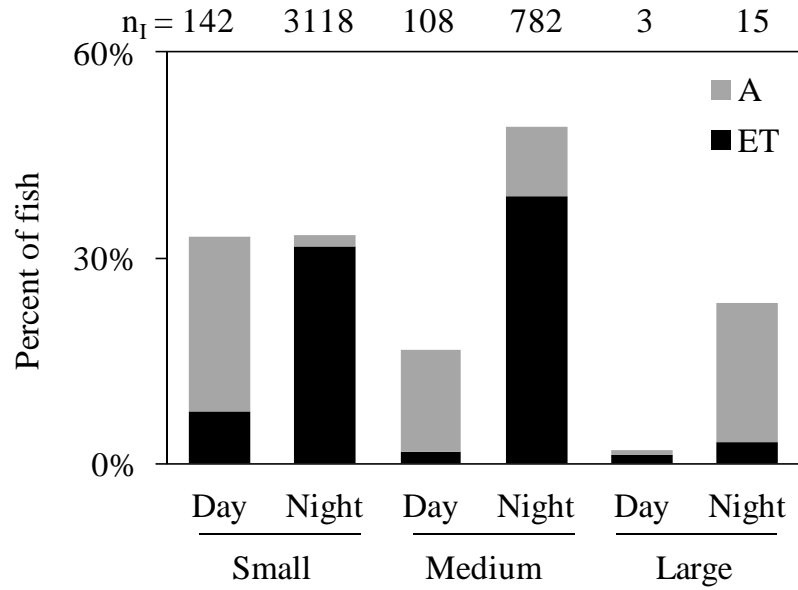


Figure 3.9. Effects of day/night on fish behaviors in front of turbine, by size class.

Proportions of each fish size class that interacted with the test turbine in Cobscook Bay during the day and night (fore of turbine only). The total number of interactions is shown along the top edge of the plot area (n_i). Interactions are split into proportions of fish that avoided the turbine (A) and fish that passed into it (ET).

3.4.3.3. Departure from Turbine: Fish Aft of Turbine

Interactions aft of the turbine included passing through the wake (TW) and pausing within the wake (IW), but almost all fish (97.5%) paused in the wake. Of those that passed straight through the wake, more did so during the day than the night (4.7 % and 1.0%, respectively; z -test $p < 0.001$). Within each size class, there was a large difference in the proportion of fish interacting during the day and at night, though the difference was not the same for each size (Figure 3.10). During the day, most fish in the wake were medium (62.6%), followed by small (31.3%) and large (0.9%). At night, most were small (69.7%), followed by medium (29.1%), then large (0.2%). This change was independent of the overall shift in size proportions seen between night and day, when

all fish (interacting and passing by) were included (z-test p-value < 0.001 for small and medium, < 0.03 for large).

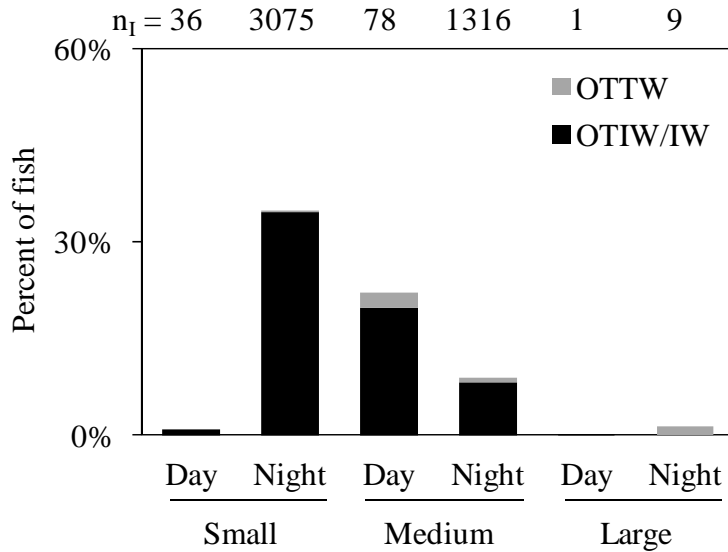


Figure 3.10. Effects of day/night on fish behaviors behind turbine, by size class. Proportions of each fish size class that interacted with the test turbine in Cobscook Bay during the day and night (aft of turbine only). The total number interactions is shown along the top edge of the plot area (n_I). Interactions are split into proportions of fish that passed directly through the wake of the turbine (OTTW) and fish that paused within the wake (OTIW/IW).

3.5. Discussion

A possible outcome from this study could have been fish avoiding the barge and turbine entirely, but they clearly did not. Thousands of fish were seen in the immediate area of the turbine, passing above, below, and through it, actively avoiding it, or pausing in its wake. Their presence does not necessarily support the attraction of fish to the turbine, but they were observed to approach it quite closely. The only potential

evidence of the structure attracting fish occurred when the very large school gathered below it for several seconds during the day.

Only 5 of 70 schools entered the turbine, suggesting that schooling fish may be better able to detect and avoid it. This would be in agreement with Domenici and Batty (1997), who observed that schooling herring reacted to a sound stimulus with more consistent directional movement away from the stimulus than individuals. Rosen et al. (2012) noted that the diving speed of shoaling Atlantic cod in response to a pelagic trawl was positively correlated with shoal size. Godø et al. (1999) studied the effects of density on the catchability of Atlantic cod (*Gadus morhua*), haddock (*Melanogrammus aeglefinus*), and American plaice (*Hippoglossoides platessoides*) using video observations and noted that individual cod and haddock swam erratically in front of the trawl, but fish that formed schools swam at a steady pace ahead of the trawl and in the same direction. Schooling fish may therefore be more capable of avoiding an obstacle such as the test turbine than individual fish.

Most fish detected were already above or below the turbine when they entered the field of view, and most of these were above the turbine. This was at least partially due to a combination of decreasing resolution with range, increasing acoustic beam attenuation with range, and the acoustic “shadow” effect below the turbine structure. These fish passed straight across the view without changing course. It is possible that they had already detected the obstacle and adjusted their trajectories farther upstream.

This type of behavior was observed in bream (*Abramis brama*), bleak (*Alburnus alburnus*), and silver carp (*Hypophthalmichthys molitrix*), and others avoiding a trawl in the Czech reservoir, Želivka, where they reacted as far as 7 m away from the advancing net (Rakowitz et al. 2011). However, behavioral response at that spatial scale would not be detected in this study, since the DIDSON viewing window extended only 2.5 m upstream of the turbine.

Fish were almost always present in the wake of the turbine, but it was not always clear whether they originated from within the turbine or had diverted into the wake from the stream of fish passing above and below. Many fish were observed exiting the turbine on the downstream side, after which a small proportion (approximately 1%) passed directly back into the uninterrupted current, and most fish paused within the wake of the structure. Fish travelling straight across above or below the turbine would also sometimes depart from their trajectories to pause in the wake. This was not a frequent behavior, but there were much greater numbers of fish counted in the wake than were counted entering the turbine. This would indicate that either many more fish passed through points of the turbine beyond the section viewed, or more were entering the wake after passing the turbine, also outside the insonified volume. As less than 1 m of the total length of the turbine was insonified (Figure 3.3), both of these are likely scenarios. Fish in the turbulent waters of the wake would have a good deal of lateral

movement within the eddies, and fish could have been counted multiple times as they passed back and forth through the volume sampled.

Though their origins were not clear and their numbers may be inflated, the frequent presence of fish in the wake of the turbine could indicate a preference for lower-energy regions within this high-velocity channel, a rheotactic response to a stationary reference point, or a need to rest and re-orient to the flow after passing through the turbine. Since this behavior was evident even when the turbine was still as well as moving, the former are more likely. This is consistent with results from acoustic studies carried out at a nearby site, where fish were most commonly found to be concentrated in the lower 3-4 m of the water column, where current speeds were lowest (Chapter 2). While there is not much literature on the use of low-velocity areas by marine pelagic fish, several migratory species have been found to seek out low-flow areas for rest and for more efficient progress through high-velocity periods during upriver migration, e.g. sea trout (Linnik et al. 1998); Pacific lamprey, *Lampetra tridentata* (Keefer et al. 2011); and sockeye salmon (Hinch and Rand 1998). Atlantic herring have been shown to be positively rheotactic under certain flow regimes when near a stationary reference point (Brawn 1960b), and therefore it is possible that sensing the device (either visually or through other senses, such as the lateral line system) could cause fish to swim against the current in its wake. This may be an important

consideration for the design and placement of large-scale tidal turbine arrays, especially when located on migratory fish routes.

There was a marked difference between fish behavior during the day and night: fish avoided the turbine much more often during the day than at night and at a farther distance away. These results indicate that visibility may be an important factor in determining a fish's response to an obstacle. Relying on vision during the day, fish may have detected the turbine from a greater distance and adjusted their courses earlier; at night, they may have used other sensory systems to detect and avoid it, which resulted in closer-range reactions or none at all. Blaxter and Batty (1985) observed similar behaviors in herring in a tank, where objects of varying opacity were introduced with and without light. Fish did not collide with opaque obstacles in the light, only transparent ones, and at night, both transparent and opaque obstacles were hit in similarly high proportions. Rakowitz et al. (2011) also concluded that ambient light affected trawl avoidance behaviors: during the day, 44% of fish showed avoidance reactions to the trawl, whereas at night, this number dropped to only 6%.

The sizes of fish detected also varied noticeably between night and day. Many more fish were detected at night than during the day, and these were predominantly small. During the day, fish were mostly medium in length. This is likely due to a diel vertical migration of small fish from the more sheltered layers near the sea floor to the upper layers at night. This type of behavior is well documented in many fish species,

including Atlantic herring, alewives (*Alosa pseudoharengus*), and juvenile Atlantic cod (Brawn 1960a, Janssen and Brandt 1980, Blaxter 1985, Perry and Neilson 1988). It is particularly prevalent among small and juvenile fish, and is usually the product of predator avoidance (i.e., seabirds) and the tracking of planktonic food sources (Bohl 1980, Levy 1990, Axenrot et al. 2004). In this case, the vertical migration was also likely related to the low current speeds of the slack tide, which are more manageable for small fish and allowed them to use the entire water column, rather than just the low-current layers near the bottom (Auster 1988). Hydroacoustic studies at a nearby site just two days prior to this study (Chapter 2) confirmed this migration, showing backscatter transfer between the deep, slow-moving layers of water and the mid-water column corresponding to the start and end of this time span (however, the upper 10 m of the water column were not sampled in that case). Vertical fish migrations such as this will greatly affect which fishes encounter a tidal energy device and when. The importance of light to obstacle avoidance is important to consider when designing and placing tidal energy devices. Most HK tidal turbines are designed to be placed in the mid-water column or to be bottom-mounted, and therefore patterns in the number of fish encounters would be very different than in this study.

Fish size also had a significant effect on their interactions with the turbine independently of day and night. A higher proportion of medium fish avoided the turbine than the small ones. Though there were not enough large fish that interacted

with the turbine to include in statistical analyses, a much higher proportion of the large fish passed by or avoided the turbine than was seen in either small or medium fish. It was apparent that larger fish were more able to avoid the turbine, most likely due to their greater maneuverability in fast currents (Auster 1988). These results are in agreement with Rakowitz et al. (2011), who found that the fish showing the least avoidance reaction to the trawl were the smallest (mean total length approximately 19 cm), swimming at low speeds and showing no change in direction. The fish that avoided the trawl the most were the largest (mean total length of approximately 42 cm, maximum near 70 cm), which showed complex swimming behaviors, faster swimming speeds, and a high average reaction distance. The distribution of fish reaction distances in Rakowitz et al. was bimodal, with the larger fish changing course 5-7 m away from the trawl and smaller fish reacting 1-2 m away. The fish observed in this study would fall mostly within the small and medium categories of Rakowitz et al., and their reaction distances agreed well with the shorter group of distances reported there. No reaction distances on the order of 5-7 m were seen in this study because the viewing window extended only 2.5 m upstream of the turbine.

If fish entered the field of view in line with the turbine, they either avoided the turbine by adjusting their course (diverting up, down, or upstream) or passed directly into it. It was not possible to determine whether fish entering the turbine were struck by the blades or not, as the resolution of the DIDSONs and a slight blurring of the

moving turbine parts made anything within approximately 5 cm of the blades difficult to discern. However, if fish are known to be entering the turbine, results from laboratory studies may be applied to predict the likelihood of their survival, and their behavior upon exiting. For instance, flume studies discussed by Jacobson (2011) indicated high survival rates, on the order of 98-100%, for fish passed through a similar form of cross-flow turbine. If relative scale and turbine design are similar, laboratory and field observations may be combined for a more complete understanding of fish interactions with tidal HK turbines. This would be especially useful for improving understanding of fish behaviors near the turbine at higher current speeds, which can only be sampled in the field for the short time that they exist, at mid-tide.

The operational state of the turbine, which is closely linked to current speed, had a significant effect on fish behavior. A higher proportion of fish passed through the turbine when it was still than when it was rotating. As night and day made little difference to these proportions, this is likely related to the fish's abilities to detect moving objects via senses other than vision, such as the lateral line system. For example, Blaxter and Batty (1985) found that herring avoided vibrating objects with more success than stationary ones, in the dark as well as light. Moving objects may therefore be easier for fish to detect than still ones, and may also be perceived as a higher threat.

Another possible explanation for the increased avoidance of the rotating turbine could be its effect on the nearby flow field. Recent work by Cameron (2012) has shown that flowing water tends to be diverted around fast-spinning cross-flow turbines, flowing above and below the turbine rather than passing through. While this is not optimal for turbine performance, it may be beneficial to fish, especially those with limited maneuverability within the current. This may have been related to some of the more gradual avoidance reactions shown by fish, such as the unhurried downward movement of schools to pass below the turbine. Additionally, the very close-range flow- and pressure-fields around the blades of the turbine may have a significant effect on how fish interact with them (Amaral 2008). Some small fish appearing to enter the turbine may have shown last-minute deflection downward along the outer surface of the passing blade (within 5 cm). Again, resolution was not high enough to be certain of this effect without further processing, but this behavior is consistent with how a passive particle would travel through the flow field generated near the surface of a moving hydrofoil (Chang 1970). The flow fields around the turbine as a whole and around its individual components are important aspects of fish-turbine interaction that should be investigated in the future. The fine-scale interactions of fish, turbines, and flow fields are likely to be best understood through a combination of computer models, laboratory flume studies, and high resolution field sampling techniques.

Even given the DIDSON's limited resolution for viewing fine-scale interactions of fish with the moving blades, it is clearly a useful tool for evaluating the interactions between fish and tidal HK turbines. This is especially true when considering the need for nighttime monitoring (as there is an obvious effect of day and night on fish behavior near the turbine), and when remembering that most devices will be installed at depths with poor light, in areas that are often too turbid for light-dependent cameras to work well.

In this study, DIDSON footage could not reveal how fish were behaving further away from the research platform. Any fish avoidance of the observation area could be quantified with the addition of side-looking acoustics to the research platform, or potentially the use of DIDSON units in low-frequency mode (1.1 MHz), which increases the maximum range to 40 m but reduces resolution.

The combination of varying scales of study is crucial to understanding the effects of tidal turbines. Laboratory studies provide accurate estimates of the survival of fish when passing through HK turbines. Field observations of fish interactions with turbines, such as the one presented here, are necessary to obtain the probability of fish encountering and either passing through or avoiding the device, and how this changes with biological and environmental factors. Combining the results of both study types will allow more accurate prediction of fish survival when encountering a device in the natural environment, but this information must then be placed in the context of a

project site. The horizontal and vertical movements of fishes in relation to seasonal, diel, and tidal cycles will be unique to each project site, and will determine what fish are likely to encounter the device and when this is likely to occur.

REFERENCES

- Amaral SV, Hecker GE, Stacy P, Dixon DA. Effects of leading edge turbine blade thickness on fish strike survival and injury. HydroVision 2008. Paper No. 250. 14 p.
- Arnold GP, Greer Walker M, Emerson LS, Holford BH. 1994. Movements of cod (*Gadus morhua* L.) in relation to the tidal streams in the southern North Sea. ICES J. Mar. Sci. 51: 207-232.
- Athearn K, Bartlett C. 2008. Saltwater fishing in Cobscook Bay: Angler profile and economic impact. Marine Research in Focus. 6.
- Auster PJ. 1988. A review of the present state of understanding of marine fish communities. J. Northw. Atl. Fish. Sci. 8: 67-75.
- Axenrot T, Didrikas T, Danielsson C, Hansson S. 2004. Diel patterns in pelagic fish behaviour and distribution observed from a stationary, bottom-mounted, and upward-facing transducer. ICES J. Mar. Sci. 61: 1100-1104.
- Barbin, GP. 1998. The role of olfaction in homing and estuarine migratory behavior of yellow-phase American eels. Can. J. Fish. Aquat. Sci. 55: 564-575.
- Becker A, Cowley PD, Whitfield AK, Järnegren J, Næsje TF. 2011. Diel fish movements in the littoral zone of a temporarily closed South African estuary. J. Exp. Mar. Biol. Ecol. 406: 63-70.
- Blaxter JH. 1985. The herring: a successful species? Can. J. Fish. Aquat. Sci. 42(Suppl. 1): 21-30.
- Blaxter JHS, Batty RS. 1985. Herring behaviour in the dark: responses to stationary and continuously vibrating obstacles. J. Mar. Biol. Ass. U.K. 65: 1031-1049.
- Bohl E. 1980. Diel pattern of pelagic distribution and feeding in planktivorous fish. Oecologia (Berl.). 44: 368-375.
- Bos AR. 1999. Tidal transport of flounder larvae (*Platichthys flesus*) in the Elbe River, Germany. Arch. Fish. Mar. Res. 47(1): 47-60.
- Brawn VM. 1960a. Seasonal and diurnal vertical distribution of herring (*Clupea harengus* L.) in Passamaquoddy Bay, N.B. J. Fish. Res. Bd. Canada. 17(5): 699-711.

- Brawn VM. 1960b. Underwater television observations of the swimming speed and behaviour of captive herring. *J. Fish. Res. Bd. Canada.* 17(5): 689-698.
- Brooks DA. 2004. Modeling tidal circulation and exchange in Cobscook Bay, Maine. *Fish. Bull.* 11 (Special Issue 2): 23-50.
- Burke JS, Masahiro U, Tanaka Y, Walsh H, Maeda T, Kinoshita I, Seikai T, Hoss DE, Tanaka M. 1998. The influence of environmental factors on early life history patterns of flounders. *J. Sea Res.* 40: 19-32.
- Čada G, Loar J, Garrison L, Fisher R Jr., Neitzel D. 2006. Efforts to reduce mortality to hydroelectric turbine-passed fish: locating and quantifying damaging shear stresses. *Environ. Manage.* 27(6): 898-906.
- Čada GF, Bevelhimer MS. 2011. Attraction to and avoidance of instream hydrokinetic turbines by freshwater aquatic organisms. Oak Ridge (TN): Oak Ridge National Laboratory; Report No.: ORNL/TM-2011/131. Available from: U.S. Department of Energy Information Bridge.
- Cameron MP. 2012. Flow field measurements for a cross flow turbine. [master's thesis]. [Orono, (ME)]: University of Maine.
- Carstensen J, Henriksen OD, Teilmann J. 2006. Impacts of offshore wind farm construction on harbour porpoises: acoustic monitoring of echolocation activity using porpoise detectors (T-PODs). *Mar. Ecol.-Prog. Ser.* 321: 295-308.
- Castonguay M, Gilbert D. Effects of tidal streams on migrating Atlantic mackerel, *Scomber scombrus* L. *ICES J. Mar. Sci.* 52(6): 941-954.
- Castro-Santos T. 2011. Applied Aspects of Fish Swimming Performance. In: Farrell AP, editor-in-chief. *Encyclopedia of Fish Physiology.* San Diego: Academic Press, 1652-63 p.
- Chang PK. 1970. Separation of flow. New York: Pergamon. 777 p.
- Charlier RH, Finkl CW. 2010. Ocean energy: tide and tidal power. Berlin: Springer-Verlag. 262 p.
- Childs A-R, Cowley PD, Næsje TF, Booth AJ, Potts WM, Thorstad EB, Økland F. 2008. Do environmental factors influence the movement of estuarine fish? A case study using acoustic telemetry. *Estuar. Coast. Shelf S.* 78: 227-236.

- Crittenden RN, Thomas L, Marino DA, Bhorne RE. 1988. A weighted duration-in-beam estimator for the volume sampled by a quantitative echosounder. *Can. J. Fish. Aquat. Sci.* 45: 1249-1 256.
- Currie DR, Isaacs LR. 2005. Impact of exploratory offshore drilling on benthic communities in the Minerva gas field, Port Campbell, Australia. *Mar. Env. Res.* 59: 217-233.
- Dadswell MJ, Rulifson RA. 1994. Macrotidal estuaries: a region of collision between migratory marine animals and tidal power development. *Biol. J. of the Linn. Soc.* 51: 93-113.
- de Robertis A, Wilson CD. 2006. Walleye pollock respond to trawling vessels. *ICES J. Mar. Sci.* 63: 514-522.
- de Veen JF. 1978. On selective tidal transport in the migration of North Sea Plaice (*Pleuronectes platessa*) and other flatfish species. *Netherlands J. Sea Res.* 12(2): 115-147.
- Domenici P, Batty RS. 1997. Escape behaviour of solitary herring (*Clupea harengus*) and comparisons with schooling individuals. *Mar. Bio.* 128: 29-38.
- Drašík V, Kubečka J. 2005. Fish avoidance of acoustic survey boat in shallow waters. *Fish. Res.* 72: 219-228.
- Ellis WL, Bell SS. 2008. Tidal influence on a fringing mangrove intertidal fish community as observed by in situ video recording: implications for studies of tidally migrating nekton. *Mar. Ecol. Prog. Ser.* 370: 207-219.
- Foote KG. 1980. Importance of the swimbladder in acoustic scattering by fish: A comparison of gadoid and mackerel target strengths. *J. Acoust. Soc. Am.* 67(6): 2084-2089.
- Foote KG. 1987. Fish target strengths for use in echo integrator surveys. *J. Acoust. Soc. Am.* 82(3): 981-987.
- Foote KG, Knudsen HP, Vestnes G, MacLennan DN, Simmonds EJ. 1987. Calibration of acoustic instruments for fish density estimation: a practical guide. *ICES Coop. Res. Rep.* 144.

- Forward RB, Reinsel KA, Peters DS, Tankersley RA, Churchill JH, Crowder LB, Hettler WF, Warlen SM, Green MD. 1999. Transport of fish larvae through a tidal inlet. *Fish. Oceanogr.* 8(Suppl. 2): 153-172.
- Forward RB, Tankersley RA, Reinsel KA. 1998. Selective tidal stream transport of spot (*Leiostomus xanthurus* Lacepede) and pinfish [*Lagodon rhomboids* (Linnaeus)] larvae: Contribution of circatidal rhythms in activity. *J. Exp. Mar. Biol. Ecol.* 226: 19-32.
- Gibson RN, Robb L, Burros MT, Ansell AD. 1996. Tidal, diel and longer term changes in the distribution of fishes on a Scottish sandy beach. *Mar. Ecol. Prog. Ser.* 130: 1-17.
- Gibson RN. 1973. Tidal and circadian activity rhythms in juvenile plaice, *Pleuronectes platessa*. *Mar. Biol.* 22(4): 379-386.
- Gill AB. 2005. Offshore renewable energy: ecological implications of generating electricity in the coastal zone. *J. Appl. Ecol.* 42: 605-615.
- Godø OR, Walsh SJ, Engås A. 1999. Investigating density-dependent catchability in bottom-trawl surveys. *ICES J. Mar. Sci.* 56: 292-298.
- Graham JJ. 1972. Retention of larval herring within the Sheepscot Estuary of Maine. *Fish. Bull.* 70(2): 299-305.
- Greer Walker M, Harden Jones FR, Arnold GP. 1978. The movements of plaice (*Pleuronectes platessa* L.) tracked in the open sea. *J. Cons. Int. Explor. Mer.* 38(1): 58-86.
- Guillard J. 1998. Daily migration cycles of fish populations in a tropical estuary (Sine-Saloum, Senegal) using a horizontal-directed split-beam transducer and multibeam sonar. *Fish. Res.* 35: 23-31.
- Hartill BW, Morrison MA, Smith MD, Boubée J, Parsons DM. 2003. Diurnal and tidal movements of snapper (*Pagrus auratus*, Sparidae) in an estuarine environment. *Mar. Freshwater Res.* 54: 931-940.
- Hinch SG, Rand PS. 1998. Swim speeds and energy use of upriver-migrating sockeye salmon (*Oncorhynchus nerka*): role of local environment and fish characteristics. *Can. J. Fish. Aquat. Sci.* 55: 1821-1831.

- Horne JK. 2000. Acoustic approaches to remote species identification: a review. *Fish Oceanogr.* 9(4): 356-371.
- Imbrock F, Appenzeller A, Eckmann R. 1996. Diel and seasonal distribution of perch in Lake Constance: a hydroacoustic study and in situ observations. *J. Fish Biol.* 49: 1-13.
- Jacobson P. 2011. *Fish Passage Through Turbines: Applicability of Conventional Hydropower Data to Hydrokinetic Technologies*. Palo Alto (CA): Electric Power Research Institute. Report No.: 1024638.
- Janssen J, Brandt SB. 1980. Feeding ecology and vertical migration of adult alewives (*Alosa pseudoharengus*) in Lake Michigan. *Can. J. Fish. Aquat. Sci.* 37: 177-184.
- Jensen OP, Hansson S, Didrikas T, Stockwell JD, Hrabik TR, Axenrot T, Kitchell JF. 2011. Foraging, bioenergetic and predation constraints on diel vertical migration: field observations and modeling of reverse migration by young-of-the-year herring *Clupea harengus*. *J. Fish Bio.* 78: 449-465.
- Jovanovic B, Longmore C, O'Leary A, Mariani S. 2007. Fish community structure and distribution in a macro-tidal inshore habitat in the Irish Sea. *Estuar. Coast. Shelf S.* 75: 135-142.
- Jurvelius J, Leinikki J, Mamylov V, Pushkin S. 1996. Stock assessment of pelagic three-spined stickleback (*Gasterosteus aculeatus*): A simultaneous up- and down-looking echo-sounding study. *Fish. Res.* 27: 227-241.
- Keefer ML, Peery CA, Lee SR, Daigle WR, Johnson EL, Moser ML. 2011. Behaviour of adult Pacific lamprey in near-field flow and fishway design experiments. *Fisheries Manag. Ecol.* 18: 177-189.
- Kelley JT, Kelley AR. 2004. Controls on surficial materials distribution in a rock-framed, glaciated, tidally dominated estuary: Cobscook Bay, Maine. *Northeast. Nat.* 11(Special Issue 2): 51-74.
- Krumme U. 2004. Patterns in tidal migration of fish in a Brazilian mangrove channel as revealed by a split-beam echosounder. *Fish. Res.* 70(1): 1-15.
- Lacoste KN, Munro J, Castonguay M, Saucier FJ, Gagné JA. 2001. The influence of tidal streams on the pre-spawning movements of Atlantic herring, *Clupea harengus* L., in the St Lawrence estuary. *ICES J. Mar. Sci.* 58: 1286-1298.

- Langhamer O, Wilhelmsson D. 2009. Colonisation of fish and crabs of wave energy foundations and the effects of manufactured holes—a field experiment. *Mar. Env. Res.* 68: 151-157.
- Larsen PF and Campbell DE. 2004. Ecosystem modeling in Cobscook Bay, Maine: a summary, perspective, and look forward. *Northeast. Nat.* 11(Special Issue 2): 425-438.
- Levy DA. 1990. Reciprocal diel vertical migration behavior in planktivores and zooplankton in British Columbia lakes. *Can. J. Fish. Aquat. Sci.* 47: 1755-1764.
- Levy DA and Cadenhead AD. 1995. Selective tidal stream transport of adult sockeye salmon (*Oncorhynchus nerka*) in the Fraser River Estuary. *Can J. Fish. Aquat. Sci.* 52: 1-12.
- Lewis LJ, Davenport J, Kelly TC. 2002. A study of the impact of a pipeline construction on estuarine benthic invertebrate communities. *Estuar. Coast. Shelf S.* 55: 513-221.
- Linnik VD, Malinin LK, Wozniowski M, Sych R, Dembowski P. 1998. Movements of adult sea trout *Salmo trutta* L. in the tailrace of a low-head dam at Włocławek hydroelectric station on the Vistula River, Poland. *Hydrobiologia.* 371/372: 335-337.
- Lucas MC, Baras E. 2000. Methods for studying spatial behaviour of freshwater fishes in the natural environment. *Fish Fish.* 1: 283-316.
- Luecke C, Wurtsbaugh WA. 1993. Effects of moonlight and daylight on hydroacoustic estimates of pelagic fish abundance. *T. Am. Fish. Soc.* 122: 112-120.
- MacDonald JS, Dadswell MJ, Appy RG, Melvin GD, Methven DA. 1984. Fishes, fish assemblages, and their seasonal movements in the lower Bay of Fundy and Passamaquoddy Bay, Canada. *Fish. Bull.* 82(1): 121-139.
- Marshall S and Elliott M. 1998. Environmental influences on the fish assemblage of the Humber Estuary, U.K. *Estuar. Coast. Shelf S.* 46: 175-184.
- McCleave JD, Kleckner RC. 1982. Selective tidal stream transport in the estuarine migration of glass eels of the American eel (*Anguilla rostrata*). *J. Cons. Int. Explor. Mer.* 40: 262-271.

- Metcalfe JD, Arnold GP, Webb PW. 1990. The energetics of migration by selective tidal stream transport: an analysis for plaice tracked in the southern North Sea. *J. Mar. Biol. Assoc. U.K.* 70: 149-162.
- Misund, OA, Beltestad AK. 1996. Target-strength estimates of schooling herring and mackerel using the comparison method. *ICES Mar. Sc.*, 53: 281-284.
- Mitson RB. 1995. Underwater noise of research vessels: review and recommendations. *ICES Coop. Res. Rep.* 209. 61 pp.
- Montgomery J, Carton G, Voigt R, Baker C, Diebel C. 2000. Sensory processing of water currents by fishes. *Phil. Trans. R. Soc. Lond. B.* 355: 1325-1327.
- Moore A, Ives M, Scott M, Bamber S. 1998. The migratory behavior of wild sea trout (*Salmo trutta* L.) smolts in the estuary of the River Conwy, North Wales. *Aquaculture.* 198: 57-68.
- Morrison MA, Francis MP, Hartill BW, Parkinson DM. 2002. Diurnal and tidal variation in the abundance of the fish fauna of a temperate tidal mudflat. *Estuar. Coast. Shelf S.* 54: 793-807.
- Neilson JD, Perry RI. 2001. Fish Migration, Vertical. In: Steele JH, Thorpe SA, Turekian KK, editors. *Encyclopedia of Ocean Sciences.* 1st ed. Boston: Elsevier Academic Press. Vol. 2, p. 955-961.
- Nielson LA, Johnson DL, editors. 1985. *Fisheries techniques.* 2nd ed. Blacksburg: Southern Printing Company. 468 p.
- Nilsson LAF, Thygesen UH, Lundgren B, Nielsen BF, Nielsen JR, Beyer JE. 2003. Vertical migration and dispersion of sprat (*Sprattus sprattus*) and herring (*Clupea harengus*) schools at dusk in the Baltic Sea. *Aquat. Living Resour.* 16: 317-324.
- Ona E, Mitson RB. 1996. Acoustic sampling and signal processing near the seabed: the deadzone revisited. *ICES J. Mar. Sci.* 53: 677-690.
- Parker SJ, McCleave JD. 1997. Selective tidal stream transport by American eels during homing movements and estuarine migration. *J. Mar. Biol. Ass. U.K.* 77: 871-889.
- Perry R I, Neilson J D. 1988. Vertical distributions and trophic interactions of age-0 Atlantic cod and haddock in mixed and stratified waters of Georges Bank. *Mar. Ecol. Prog. Ser.* 49: 199-214.

- Polagye B, Van Cleve B, Copping A, Kirkendall K. 2010. Environmental effects of tidal energy development. U.S. Dept. Commerce, NOAA Tch. Memo. F/SPO-116. 181 p.
- Rakowitz G, Tušer M, Říha M, Jůza T, Balk H, Kubečka J. 2011. Use of high-frequency imaging sonar (DIDSON) to observe fish behavior towards a surface trawl. *Fish. Res.* 123-124: 37-48.
- Ransom BH, Johnston SV, Steig TW. 1998. Review on monitoring adult salmonid (*Oncorhynchus* and *Salmo* spp.) escapement using fixed-location split-beam hydroacoustics. *Fish. Res.* 35: 33-42.
- Ribeiro J, Bentes L, Coelho R, Gonçalves JMS, Lino PG, Monteiro P, Erzini K. 2006. Seasonal, tidal and diurnal changes in fish assemblages in the Ria Formosa lagoon (Portugal). *Estuar. Coast. Shelf S.* 67: 461-474.
- Rijnsdorp AD, Stralen MV, Van der Veer HW. 1985. Selective tidal transport of North Sea Plaice larvae *Pleuronectes platessa* in coastal nursery areas. *T. Amer. Fish. Soc.* 114(4): 461-470.
- Rosen S, Engås A, Fernö A, Jörgensen T. 2012. The reactions of shoaling adult cod to a pelagic trawl: implications for commercial trawling. *ICES J. Mar. Sci.* 69(2): 303-312.
- Rowe PM, Epifanio CE. 1994. Tidal stream transport of weakfish larvae in Delaware Bay, USA. *Mar. Ecol. Prog. Ser.* 110: 105-114.
- Sakabe R and Lyle JM. 2010. The influence of tidal cycles and freshwater inflow on the distribution and movement of an estuarine resident fish *Acanthopagrus butcheri*. *J. Fish Biol.* 77(3): 643-660.
- Saunders R, Hachey M, Fay CW. 2006. Maine's diadromous fish community. *Fisheries.* 31(11): 537-547.
- Simard Y, Lavoie D, Saucier FJ. 2002. Channel head dynamics: capelin (*Mallotus villosus*) aggregation in the tidally driven upwelling system of the Saguenay – St. Lawrence Marine Park's whale feeding ground. *Can. J. Fish. Aquat. Sci.* 59: 197-210.
- Simmonds J, MacLennan D. 2005. *Fisheries Acoustics: Theory and Practice*. 2nd ed. Oxford: Blackwell Science. 437 p.

- Smith EP. 2002. BACI design. In: El-Shaarawi AH, Piegorisch WW, editors. Encyclopedia of environmetrics. Chichester: John Wiley & Sons. p 141-148.
- Soldal AV, Svellingen I, Jørgensen T, Løkkeborg S. 2002. Rigs-to-reefs in the North Sea: hydroacoustic quantification of fish in the vicinity of a "semi-cold" platform. ICES J. Mar. Sci. 59: S281-S287.
- Thorne RE. 1988. An empirical evaluation of the duration-in-beam technique for hydroacoustic estimation. Can. J. Fish. Aquat. Sci. 45: 1244-1248.
- Trump CL, Leggett WC. 1980. Optimum swimming speeds in fish: the problem of currents. Can. J. Fish. Aquat. Sci. 37:1086-1092.
- Tyler AV. 1971. Periodic and resident components in communities of Atlantic fishes. J. Fish. Res. Bd. Canada. 28: 935-946.
- USDOE 2009. Report to Congress on the Potential Environmental Effects of Marine and Hydrokinetic Energy Technologies: Prepared in Response to the Energy Independence and Security Act of 2007, Section 633(B). Wind and Hydropower Technologies Program, Energy Efficiency and Renewable Energy, U.S. Department of Energy. December, 2009.
- Vabø R, Olsen K, Huse I. 2002. The effect of vessel avoidance of wintering Norwegian spring spawning herring. Fish. Res. 58: 57-77.
- Weinstein MP, Weiss SL, Hodson RG, Gerry LR. 1980. Retention of three postlarval fishes in an intensively flushed tidal estuary, Cape Fear River, North Carolina. Fish. Bull. 78(2): 419-436.
- Willhelmsson D, Malm T, Öhman MC. 2006. The influence of offshore windpower on demersal fish. ICES J. Mar. Sci. 63: 775-784.
- Wills JC, Bremigan MT, Hayes DB. 2004. Variable effects of habitat enhancement structures across species and habitats in Michigan reservoirs. T. Am. Fish. Soc. 133(2): 399-411.
- Wilson B, Batty RS, Daunt F, Carter C. 2007. Collision risks between marine renewable energy devices and mammals, fish and diving birds. Oban (Scotland): Scottish Association for Marine Science; Report No.: PA37 1QA.

Wroblewski JS, Nolan BG, Rose GA, deYoung B. 2000. Response of individual shoaling Atlantic cod to ocean currents on the northeast Newfoundland Shelf. *Fish. Res.* 45: 51-59.

Zijlstra JJ. 1988. Fish migrations between coastal and offshore areas. *Lect. Notes Coast. Estuar. Interact.* 22: 257-272.

BIOGRAPHY OF THE AUTHOR

Haley Viehman was born in Allentown, PA in December 1987. She spent most of her childhood in Camden, ME but spent part of middle and high school in Quakertown, PA. She and her family returned to Maine in 2003, and she graduated from Camden Hills Regional High School in 2005. Haley has always loved animals, the outdoors, and building things. Her interest in marine biology began in Maine's tide pools, and in her junior year of high school she was selected to participate in the Keller Bloom Program at the Bigelow Laboratory for Ocean Sciences. She studied Civil Engineering at Cornell University, spending her junior year abroad at the University of Cantabria in Santander, Spain. During her years at Cornell, Haley became fascinated with work at the intersection of engineering, society, and the environment, particularly related to sustainable development and renewable energy. She participated in the AguaClara sustainable water treatment research project during her senior year, and in the organization Engineers for a Sustainable World. Haley graduated with a Bachelor of Science in Civil Engineering in May of 2009. Her passion for invention, the environment, and multidisciplinary work led her to a graduate position at the University of Maine the following fall, researching the effects of novel tidal energy technology on fishes. Haley is a candidate for the Master of Science degree in Marine Bioresources from the University of Maine in May, 2012.

Appendix Task 2-2

**Fish interactions with a commercial-scale tidal energy device
in the natural environment**

Haley A. Viehman

University of Maine, School of Marine Sciences, 5741 Libby Hall, Orono, ME 04469-5741

Phone: 207-581-4356; Email: haley.viehman@umit.maine.edu

Gayle Barbin Zydlewski

University of Maine, School of Marine Sciences, 5741 Libby Hall, Orono, ME 04469-5741

Abstract

Fish are a key part of the marine ecosystem likely to be affected by hydrokinetic tidal turbines, but little is known about their behavior around such obstacles in the natural environment. In September 2010, two DIDSON acoustic cameras were used to observe fish interactions with a commercial-scale turbine in Cobscook Bay, Maine. Twenty-two hours (nearly two tidal cycles) of footage were collected. Behaviors of individual fish and schools were classified (e.g., entering, avoiding, passing, or remaining in the wake of the turbine). We analyzed the effects of turbine motion (rotating or not rotating), diel condition (day or night), and fish size (small, ≤ 10 cm; large, >10 cm) on individual fish behaviors, and compared behaviors of individual fish to schools of fish. When the turbine was rotating, the probability of fish entering the turbine decreased by over 35% from when it was not. The probability that fish would enter the turbine was higher at night than during the day, and this difference was greater for small fish than for large fish (probability of small fish entering: 0.147 day, 0.513 night; large fish: 0.043 day, 0.333 night). Fish were almost always present in the wake of the turbine. Schools of fish had a 56% lower probability of entering the turbine than individual fish, and reacted at greater distances from the turbine (median distance of 2.5 m for schools, 1.7 m for individuals). This study indicates that fish behavior in response to tidal turbines appears to be similar to responses to obstacles such as trawls, and highlights the importance of environmental context in determining the effects of a tidal turbine on fish.

Key Words

Tidal energy, fish, DIDSON, marine hydrokinetic, turbine, semidiurnal tides

Introduction

Tidal currents play an essential role in the life cycles of many marine and diadromous fishes. Many fishes are known to use the tides for on- and off-shore movements related to foraging, spawning, and sheltering (Dadswell and Rulifson 1994, Hartill et al. 2003, Krumme 2004, Ribeiro et al. 2006) and several migratory species actively seek currents when the tide is flowing in their desired direction of movement (e.g., *Anguilla rostrata*, McCleave and Kleckner 1982; *Pleuronectes platessa*, Greer Walker et al. 1978; *Clupea harengus*, Lacoste et al. 2001).

There is increasing interest in extracting energy from the same currents exploited by fishes. Large, in-stream hydrokinetic (HK) turbines can be used to convert the energy of fast tidal currents to electric power (Charlier and Finkl 2010). Due to the spatial overlap of tidal energy devices and fishes, interactions between the two should be expected. However, field studies of fish interactions with HK turbines have yet to be carried out in the United States due to the lack of installed devices.

Most of what is known of fish interactions with turbines comes from studies of conventional hydropower facilities, where water flows at high speeds through turbines installed within dams or other barrages. When moving downstream, fish must pass over a spillway or through a turbine (Čada et al. 2006). When passing through a conventional hydropower turbine, fish are subjected to rapid pressure changes, cavitation, shear stress, and blade strike, all of which can cause injury or mortality (Dadswell and Rulifson 1994, Čada et al. 2006). Mortality of juvenile Coho salmon (*Oncorhynchus kisutch*) passing through the turbines at conventional hydropower dams was found to exceed 30% (Čada et al. 2006). At the Annapolis estuary low-head tidal barrage in the Bay of Fundy, mortality rates were 21% to 46% for adult American shad (*Alosa sapidissima*) and 52% for juvenile clupeids (American shad, alewife *Alosa pseudoharengus*, and blueback herring *Alosa aestivalis*; Dadswell and Rulifson 1994). HK

turbines are fundamentally different from conventional or tidal barrage hydropower designs, and are therefore likely to affect fish differently (Polagye et al. 2011; EPRI 2011b).

HK devices are free-standing, open structures installed in naturally flowing water currents, and fish may avoid these structures as they would any other obstacle, such as a trawl or a boat. Fish have shown avoidance of boats at ranges of 100-200 m, or as far as 400 m if the vessel is particularly noisy (Mitson 1995, Vabø et al. 2002, de Robertis and Wilson 2007). Rakowitz et al. (2012) observed strong avoidance reactions of several fish species to trawls at close ranges, as well, with fish reacting as close as 1 m from the advancing net. EPRI (2011a) documented fish actively avoiding a tidal turbine in a flume, even when introduced at very close range.

HK turbines and their support structures also have the potential to act as fish aggregation devices. Other anthropogenic structures have been shown to attract fish for multiple reasons. For instance, the foundations of offshore wave power devices (Langhamer et al. 2009), the monopiles of offshore wind farms (Wilhelmsson et al. 2006), and decommissioned oil platforms (Soldal et al. 2002) create new habitats that can attract fish. Čada and Bevelhimer (2011) suggest that HK devices could offer refuge from high speed currents by providing a lower-energy area downstream of the turbine and supporting structure.

The behavioral responses of fishes to HK turbines are likely to include some combination of avoidance and attraction. However, while there have been studies of fish survival through down-scaled HK turbines in laboratory flumes (Amaral et al. 2008, EPRI 2011a), no published work has examined fish interactions with these in the open marine environment. The choices fish make when encountering an HK device in their natural environment must be better understood to assess the effects of these devices on fish. We monitored a commercial-scale test

turbine deployed in Maine, U.S.A., to classify and quantify fish behaviors in reaction to the turbine and to assess the effects of turbine motion (rotating or not), diel condition (day or night), and fish size (small or large) on those behaviors.

Methods

Cobscook Bay is the eastern-most bay of the United States. It is located at the mouth of the Bay of Fundy and consists of three smaller bays joined by narrow channels (Fig. 1). The Bay has semidiurnal tides with a mean tidal range of 5.7 m (Brooks 2004), and current speeds within the outer bay regularly surpass $2 \text{ m}\cdot\text{s}^{-1}$. Cobscook Bay is known for its high biodiversity, which is largely due to the extreme tidal mixing that takes place (Larsen and Campbell 2004). Little is known of the marine fish of the bay, but recent findings have indicated that Atlantic herring (*Clupea harengus*), Atlantic mackerel (*Scomber scombrus*), alewife (*Alosa pseudoharengus*), and threespine stickleback (*Gasterosteus aculeatus*) are among the most common pelagic species present (J. Vieser, unpublished information, 2013, University of Maine, School of Marine Sciences, Orono, ME 04469).

This study was carried out on Ocean Renewable Power Company's (ORPC's) turbine testing platform, a modified 18.3 m x 7.3 m barge (Fig. 2). The survey began at 9:45 am on 8 September 2010 and ended at 8 am on 9 September 2010. This time span included approximately 11 hours of daylight and 11 hours of darkness, and nearly two tidal cycles. The only exterior source of illumination at night was the pilot light located above the cabin, and light did not reach the water's surface. The depth at the site of the research platform ranged from 34 m at low tide to 43 m at high tide.

At the time of the study, ORPC was testing its Turbine Generator Unit (TGU). The TGU was suspended approximately 5 m below the platform. It consisted of two helical-bladed cross-

flow turbines (2.6 m diameter x 5.2 m length) and a permanent magnet generator on a single horizontal axis (Figure 2b). The turbine began rotating (and generating power) when current speeds exceeded $1 \text{ m}\cdot\text{s}^{-1}$, and ceased rotating when current speeds fell below $0.5 \text{ m}\cdot\text{s}^{-1}$. The research platform was moored in place and turned on its mooring with each turn of the tide. Therefore, the bow was consistently facing into the current (upstream) with the stern facing downstream, except while the platform swung around at slack tide. Current speed was recorded each half hour using a Valeport model 803 ROV current meter attached to the support frame of the turbine.

Two DIDSON (Dual Frequency IDentification SONar, Sound Metrics Corp., Seattle, WA) acoustic cameras were operated continuously to observe the TGU (Fig. 2). The DIDSONs were operated in high-frequency mode (1.8 MHz), which provides better resolution at short ranges ($< 20 \text{ m}$) than low-frequency mode (1.1 MHz). The DIDSON samples a 29° by 14° volume of water by combining data from 96 stacked acoustic beams, each 0.3° by 14° . The result is a 2D image, 29° wide. These images are produced in rapid succession at a user-defined frame rate between 4 and 21 frames per second, which creates “video” footage of the sampled volume with high temporal resolution. The start range and length of the viewing window are set by the user, but maximum window length in high-frequency mode is limited to 10 m. The viewing window is divided into 512 samples in the range dimension, and therefore resolution along the central beam axis (along the length of the window) is constant (2.0 cm for a 10 m viewing window). Due to the spreading of the 96 acoustic beams, resolution perpendicular to the central beam axis decreases with range.

The two DIDSON units were mounted upstream (forward) and downstream (aft) of the TGU and angled in order to view a vertical cross section of the turbine and support structure

(Fig. 2). The DIDSON mounts were placed so that the sampled volumes were aligned as closely as possible with one another, upstream and downstream of the turbine. Each DIDSON was oriented with its larger beam angle parallel to the current (perpendicular to the turbine). This orientation ensured that fish moving with the current passed through as many of the 96 acoustic beams as possible, providing the best profile view of individual fish. Fish swimming at an angle to the current were harder to visualize and were unlikely to be detected. The viewing window was set to begin at a range of 3.3 m in the upstream DIDSON and 2.5 m in the downstream DIDSON, and extended for 10 m. These settings eliminated areas of noise due to reflection from the TGU support structures and provided a better view of the turbine. Image resolution ranged from 1.3 cm at 2.5 m range to 7.0 cm at 13.3 m range. Together, the DIDSONs sampled a nearly complete vertical cross-section of the turbine that spanned approximately 1 m of its length (Fig. 2). A frame rate of approximately $7 \text{ frames} \cdot \text{s}^{-1}$ was maintained throughout the sampling period. The rotation of the turbine caused a slight blurring around the blade edges, so everything within approximately 5 cm of the blades was not discernible. The upstream DIDSON's viewing window included approximately 3 m of water upstream of the turbine, and the downstream DIDSON sampled approximately 3 m of water downstream of the turbine.

Data Processing

DIDSON footage was processed manually using DIDSON control and display software (5.25.32, Sound Metrics Corp., Lake Forest Park, WA, USA), which allowed frame-by-frame viewing of the footage and provided measurement tools. Schools and individual fish were identified and assessed separately. Schools were defined as three or more fish within 1 body length of each other, swimming in the same direction and behaving similarly (Pitcher 2001). Information collected for each school or individual fish included time of detection, the turbine

motion at that time (rotating or not), individual size (for schools, the mean length of up to 10 randomly selected individuals was used), mean range from the DIDSON, behavior (discussed below, see Table 1), and reaction distance if behavior included avoidance. Additional information collected for schools included the number of individuals visible. Often, similarly-sized but non-schooling fish would pass through the view at an approximately constant rate, exhibiting the same behavior (e.g., passing by the turbine). To aid in manual fish detection at these times, the number of individual fish was estimated by multiplying the rate of fish passage by the duration of time for which that rate remained constant. Behavior, depth, and the other descriptors were then assigned to each of those fish.

Classification of Fish Behavior

The fish observed moved from upstream to downstream in straight trajectories (unless avoiding the turbine or milling, as discussed below). Behaviors of individual fish and schools were classified into seven categories (Table 1 and Fig. 3). Two of these categories involved no interaction with the turbine, and were observed in both the upstream and downstream views: *passing* either above or below the turbine with no change of course, and *milling* in place, which occurred only at slack tide (though similar behavior was observed in the wake of the turbine). Upstream of the turbine, behaviors also included *avoiding* the turbine and *entering* the turbine. A fish (or school of fish) was classified as avoiding the turbine if it altered its initial trajectory to move around the turbine. Avoidance included full reversal of path to move upstream, or altering the path to moving upward or downward while still moving with the current. The shortest distance from the fish (or school) to the turbine at the start of the avoidance maneuver (when the fish departed from its initial trajectory) was defined as the *reaction distance*. Downstream of the turbine, behaviors involved the wake of the device. Fish that were observed exiting the turbine

either *remained in its wake* showing milling behavior before moving out of sight, or moved straight *through the wake* without pausing. Many fish milling within the wake were not observed exiting the turbine; these were also counted as remaining in the wake.

Behaviors upstream of the turbine were considered *encounter behaviors*, as they occurred during a fish's first approach to the turbine; behaviors downstream of the turbine were considered *departure behaviors*. Encounter and departure behaviors were analyzed separately due to their limited overlap and the inability to reliably track fish from upstream to downstream across DIDSON views (except for some of the larger schools).

The diel condition (day or night) was assigned to each fish or school using its time of detection and known times of sunset and sunrise. Individual fish were classified by their measured length as small (≤ 10 cm) or large (> 10 cm). These somewhat coarse length categories were chosen to account for the uncertainty introduced to length measurements because of DIDSON's decreasing resolution with range. Fish and schools detected within the first 3.3 m of the downstream DIDSON view were omitted from analyses to best align the sampled volumes.

Data Analysis

We examined whether encounter behaviors of individual fish depended on turbine motion (rotating or not), and then whether behaviors exhibited while the turbine was rotating depended on diel condition (day/night) and fish size (small/large). These effects could not be analyzed for schools due to the low sample size in each group. However, we compared the encounter behaviors of schools and individual fish, as schooling and shoaling have been shown to influence avoidance in the past (Domenici and Batty 1997, Rosen et al. 2012, Godø et al. 1999).

R software (version 2.15.2, R Foundation for Statistical Computing) was used for all statistical analyses. Binomial logistic regression (function *glm* in the *stats* package in R; R Core Team 2013) was used to examine factors affecting the probability that a fish would exhibit each behavior. Each behavior (entering, avoiding, passing, or remaining in wake) was assessed individually by assigning each fish a 0 if it did not exhibit the behavior or a 1 if it did. Factors tested included turbine motion (non-rotating, 0; or rotating, 1), diel condition (day, 0; or night, 1), and fish size (small, 0; or large, 1). Significant model coefficient estimates indicated either a decrease (if negative) or increase (if positive) in the probability of a fish exhibiting a given behavior when the factor category increased by one (e.g., from day to night, or small to large). For example, using the coefficients from Table 2.2, the probability of avoidance for a large fish during the day (probability of 0.020; Table 4) would be computed as $P = \text{logit}[-3.784 - 2.164 \cdot (0) - 0.124 \cdot 1 + 3.968 \cdot (0) \cdot (1)]$.

The effect of turbine motion was analyzed first. Diel condition and fish size were not included as factors because sample sizes were too low for each factor group when the turbine was not rotating (e.g., no large fish were observed avoiding the non-rotating turbine during the day). Similarly, the effects of diel condition, fish size, and their interaction on behaviors were then tested for only the rotating turbine. The encounter behaviors of schools were then compared to those of individuals using school (no, 0; yes, 1) as a factor. Effects of diel condition and fish size could not be tested with schooling due to the low number of schools. The effect of schooling on reaction distance was also examined using a non-parametric ANOVA permutation test with significance level 0.05 (R package *lmPerm*; Wheeler 2010).

Results

Fish were observed during most of the survey, but not after 4 am on 9 September (Fig. 4). Most fish were detected at night (91.5%), with a peak in numbers from the nighttime slack through the first half of the ebb tide (Fig. 4). The number of fish observed upstream and downstream of the turbine were similar (14,444 downstream; 14,544 upstream). Fish sizes ranged from 3 to 50 cm in length (Figure 5). Most fish observed were small (82.8%). Sizes were similar during the day and night (day: 80.4% small, 19.6% large; night: 83.0% small, 17.0% large). 11,377 fish were detected while the turbine was not rotating, and 17,611 were detected while it was rotating. When the turbine was rotating, the average current speed was $1.6 \text{ m}\cdot\text{s}^{-1}$ (3.1 knots), the average rotational speed of the turbine was 21.4 rpm, and the average tip speed of the turbine was $2.1 \text{ m}\cdot\text{s}^{-1}$.

While resolution was generally too low to determine if a fish was facing into the current or not, its net movement was discernible (i.e., upstream, right to left; or downstream, left to right). All fish observed moved with the current, unless they avoided the turbine by swimming upstream or remained within the turbine's wake. Milling behavior was observed only when the current speed was below approximately $0.5 \text{ m}\cdot\text{s}^{-1}$ (turbine not rotating). Over 50% of all individual fish observed interacted with the turbine in some way: avoiding it (0.4%), entering or exiting it (34.8%), or remaining in its wake (16.4%).

Ninety-seven schools of fish were observed during this study. The smallest school contained 3 fish; the largest contained over 300 within the viewing window. The size of schooling individuals was larger than those detected individually (schools: 22.7% small, 77.3% large; individuals: 82.8% small, 17.2% large). Thirty-two schools were detected during the day, 65 at night. Approximately one-third of schools interacted with the turbine in some way, either

avoiding it (15.5%), entering or exiting it (14.4%), or remaining in its wake (2.1%). The rest passed above or below the turbine (63.9%), or were milling at slack tide (4.1%).

During the day when the turbine was rotating, 4 schools avoided the turbine, none entered it, none remained in the wake, and 13 passed it by. At night, 8 schools avoided the turbine, 13 entered, 2 remained in the wake, and 35 passed it by. Most schools behaved as one unit, with individuals remaining in cohesive groups and showing the same behavior. At night, however, 11 of the 65 detected schools split, showing more than one behavior. Eight of these schools were in the upstream view, and these were large enough to span from above the turbine to the bottom of it. School members that were above the turbine passed by it while those level with the turbine entered it. Three of the 11 schools were in the downstream view, and their timing indicated that they may have been three of the schools that entered the turbine. In two of these schools, fish that exited the turbine showed milling behavior in the wake before continuing downstream, while all fish in the third school moved immediately through the wake and out of sight.

Behaviors of Individual Fish

Turbine motion significantly affected the probability of fish entering, avoiding, and passing by the turbine (Table 2.1). When the turbine was rotating, the probability of fish entering decreased by 35%, the probability of avoiding increased by 120%, and the probability of passing increased by 97% from when the turbine was not rotating.

While the turbine was rotating, diel condition, fish size, and their interaction all affected fish behavior (Table 2.2). The probability of fish entering the turbine was greater at night than during the day, and small fish had a higher probability of entering than large fish (Table 4). The pattern was similar for fish passing the turbine (Table 4). The interaction of factors indicated a different effect of diel condition for small and large fish (Table 2.2), but the difference was very

small: the probability for small fish to pass the turbine decreased by 42% at night, while the probability for large fish decreased by 40% (Table 4). Small and large fish showed significantly different trends in avoidance behavior. During the day, small and large fish had nearly equal probabilities of avoiding the turbine (0.022 and 0.020, respectively). From day to night, the probability of avoiding the turbine decreased for small fish (0.022 to 0.002) but increased for large fish (0.020 to 0.109; Table 4).

Departure behavior (i.e., remaining in the wake or not) also depended on diel condition, fish size, and the interaction of these factors (Table 2.3). Small fish had a higher probability of remaining in the wake at night (0.518) than during the day (0.026), but the opposite was true for large fish (probability of 0.509 day, 0.387 night; Table 5).

Behavior of Individual Fish vs. Schools

Schooling affected fish behavior (Table 2.4). Schools had a lower probability of entering the turbine and a lower probability of avoiding it than individuals, but schools and individuals had equal probabilities of passing by the turbine (Table 6).

Schools of fish that were observed avoiding the turbine reacted farther from the turbine than did individual fish (p-value < 0.05). The median reaction distance of schools was 2.5 m (minimum = 1 m, maximum = 4.5 m) from the turbine, and that of individuals was 1.7 m (minimum = 0.2 m, maximum = 3.9 m). While diel condition and fish size were also likely to affect reaction distance, sample size was too low to test the effects of these factors on schools.

Discussion

During the 22-hour observation period, thousands of fish were observed in the immediate area of the turbine, passing above, below, and through it, actively avoiding it, or pausing in its

wake. Clearly, fish did not entirely avoid the area of the test turbine. However, many fish could have responded to the turbine farther upstream and avoided our view altogether. Given the limits of our viewing window, behavioral responses at that spatial scale could not have been detected. Since most fish and schools observed were above or below the turbine when they entered the upstream view, they may have already responded to the turbine or platform. Some portion of the passing behavior observed could therefore be the result of previous avoidance behavior. This connection may be supported by the similar responses of the probabilities of avoiding and passing to diel condition and turbine motion.

When the turbine was rotating, the probability that fish would avoid or pass the turbine increased and the probability of fish entering decreased. The numbers of fish exhibiting each behavior (Table 3) indicated that turbine motion had similar effects during the day and night, though this could not be tested statistically. The effect of turbine motion may therefore be related to the fishes' abilities to detect moving objects via senses other than vision, e.g., the lateral line. Blaxter and Batty (1985) found that herring avoided vibrating objects with more success than stationary ones, in the dark as well as the light. Moving objects may be easier for fish to detect than still ones, and may also be perceived as a higher threat, resulting in greater avoidance.

The turbine's effect on the nearby flow field may also explain increased avoidance while the turbine was rotating. Cameron (2012) indicated that water flow is partially diverted around a fast-spinning cross-flow turbine, i.e., flowing above and below the turbine rather than through it. Flow diversion around the turbine could contribute to some of the gradual upward or downward avoidance maneuvers of fish approaching the turbine. The very close-range flow- and pressure-fields around the blades of the turbine may also have a significant effect on how fish interacted

with them (Amaral 2008, EPRI 2011b). Though DIDSON resolution was not high enough for us to analyze this effect, there were several instances when small fish, on course to enter the turbine, appeared to turn downward at the last instant, skimming along the outer surface of the passing blade. This behavior would be consistent with how a passive particle would travel in response to the flow field generated near the surface of a moving hydrofoil (Chang 1970). In addition, laboratory studies have demonstrated that small fish are swept aside by turbine blades (EPRI 2011). The flow fields around the turbine as a whole and around its individual components are important aspects of fish-turbine interaction that should be investigated in the future.

Small fish had a greater chance of entering the turbine than did large fish. As swimming power increases with length (Wardle 1986), larger fish may have a greater ability to maneuver in strong currents than smaller ones, and therefore a greater ability to avoid obstacles like tidal turbines. Rakowitz et al. (2012) observed avoidance behaviors of bream (*Abramis brama*), bleak (*Alburnus alburnus*), silver carp (*Hypophthalmichthys molitrix*), and other species to a trawl. They also found that the smallest fish in their study (mean total length approximately 19 cm) showed the least avoidance reaction to the trawl, swimming at lower speeds and not changing direction. The largest fish (mean total length of approximately 42 cm, maximum near 70 cm) avoided the trawl the most, swimming faster, using complex swimming behaviors, and having a longer average reaction distance than small fish. The larger fish changed course 5-7 m away from the trawl while smaller fish reacted 1-2 m away. While the reaction distances of fish we observed agreed well with the smaller fish of Rakowitz et al. (2012), the reaction distance of large fish in that study were well beyond the range of our upstream viewing window. This could be one

reason for the absence of larger fish from our observations and highlights the need for monitoring fish behavior at greater distances from tidal turbines.

Environmental and biological factors (turbine motion, diel condition, and fish size) had opposite effects on the probability of fish passing as they had on fish entering the turbine, which is to be expected if passing is related to avoidance taking place upstream of our view.

Avoidance, on the other hand, did not show the same pattern. During the day, large and small fish had equal probabilities of avoiding the turbine. At night, the probability of avoiding decreased for small fish (as would be expected), but increased for large ones. This counterintuitive result is likely because observing avoidance behavior depends on the extent of our viewing window and the reaction distance of fish. Rakowitz et al. (2012) found that the fishes they observed reacted closer to the trawl during the night than during the day. If this is true for fish reacting to a turbine, then the probability of the reaction taking place within our viewing window would increase at night, and therefore the probability of avoidance would also appear to increase. As fish entering the turbine were always within our viewing window, it is a more reliable (inverse) measure of avoidance.

The importance of fish size to the probability of turbine entrance indicates that tidal turbines could affect fish differently depending on fish species and life stage. Juvenile fish may be at higher risk of entering turbines than adults, for example. Placement of tidal devices should therefore take into account local species composition and the role of the site in important life history stages. Higher risk of entering the turbine does not necessarily correlate to higher fish injury or mortality, however. Blade strike studies have shown survival rates of over 90% for fish with lengths similar to or less than the thickness of the blade (Amaral 2008, EPRI 2011a and 2011b). Though small fish may have higher probabilities of entering the turbine, they may also

be more likely to survive passage. Different species may also be more resilient to blade strike than others due to physical features (e.g., higher flexibility or cartilaginous skeletons), and blade shape (e.g., semi-circular or elliptical) that can greatly affect survival (Amaral 2008, EPRI 2011 and 2011b).

The influence of diel condition on the probability of fish entering the turbine may indicate that visibility was also an important factor in determining a fish's response to the turbine. During the day, increased visibility would allow fish to see the turbine in time to adjust course; at night, fish are likely to rely on other sensory systems (e.g., hearing and the lateral line), which may result in a much shorter reaction distance (Plachta and Popper 2003, Popper and Higgs 2009) and fewer avoidances. Blaxter and Batty (1985) observed similar behaviors in herring in a tank when introducing objects of varying opacity in light and dark conditions. In the light, fish did not collide with opaque obstacles but did collide with transparent ones. In the dark, collisions with both transparent and opaque obstacles occurred in similarly high proportions. Rakowitz et al. (2012) found that trawl avoidance was also affected by ambient lighting conditions. During the day, 44% of fish they observed showed avoidance reactions to the trawl, and at night only 6% reacted. It is possible that the effect of diel condition on fish behavior that we observed was due to random temporal variation over the 22 hours sampled (one day period and one night period). However, given the importance of visual cues to obstacle avoidance and the consistency of our results with other studies, turbine visibility should be considered when assessing effects on fish.

We observed many more individual fish at night than during the day, mostly due to a peak in fish numbers that occurred during and just after the nighttime slack tide. This increase may be related to a diel vertical movement of fish from the darker, more sheltered water near the

sea floor (beyond our viewing window) to the upper water column at night. This study spanned only a single 22-hour period and alone cannot support a diel vertical movement of fish in the area. However, diel vertical movements have been well documented in many fish species, including Atlantic herring (*Clupea harengus*; Brawn 1960a), alewives (*Alosa pseudoharengus*; Janssen and Brandt 1980), and juvenile Atlantic cod (*Gadus morhua*; Perry and Neilson 1988). Additionally, a 24-hour hydroacoustic survey of the entire water column took place at a nearby site two days prior to this study (Viehman et al., in revision) and also showed this pattern of movement: fish biomass shifted from the lower water column to the upper water column during the nighttime slack tide, followed by the reverse movement after the slack tide. The coincidence of this nighttime movement with the slack tide may indicate a link to current speed. Most fish we detected were small (84% were 10 cm or less, and 98% were less than 20 cm), so they may normally shelter in the low-current layers near the bottom and wait for the current to slow before moving to the upper layers (Auster 1988). Vertical fish movements such as this will greatly affect which fishes encounter a tidal energy device and when, depending on where the device is located in the water column. The type and timing of fish encounters with bottom-mounted or mid-water column tidal energy devices are likely to differ greatly from those observed in this study of a surface-mounted turbine.

In this study, fish were almost always present in the wake of the turbine, exhibiting behavior similar to the milling which occurred during the slack tide. Some fish in the wake were observed exiting the turbine; however, many simply appeared there, indicating that fish entering the wake at other points along the turbine were then moving laterally along its length. Lateral movement of fish back and forth could have resulted in multiple counting of some fish, which could have inflated the numbers observed within the wake of the turbine. Even if numbers were

inflated, the frequent presence of fish in the wake could indicate a preference of fish for lower-energy regions within this high-velocity channel (as suggested by Čada and Bevelhimer, 2011), a rheotactic response to a stationary reference point, or a need to re-align with the flow after becoming disoriented within the rotating turbine. In-wake milling behavior was evident even when the current was fast enough to generate a wake but not fast enough to rotate the turbine, so the former two options are more likely. While there is not much literature on the use of low-velocity areas by marine pelagic fishes, several migratory species have been found to seek out low-flow areas for rest and for more efficient movement against high-velocity currents for upstream migration, e.g. sea trout (*Salmo trutta*; Linnik et al. 1998), Pacific lamprey (*Lampetra tridentata*; Keefer et al. 2011), and sockeye salmon (*Oncorhynchus nerka*; Hinch and Rand 1998). Fish have been shown to be positively rheotactic under certain flow regimes when near a stationary reference point (Arnold 1981), including Atlantic herring (Brawn 1960b).

While the behavior of pausing within flows is not uncommon, the differences we observed between small and large fish at day and night were interesting. At night, the departure behavior of both small and large fish appeared to be related to turbine entrance, as the probability of fish entering the turbine was almost equal to the probability of fish remaining within the wake. During the day, this was not the case. Small fish had a lower probability of remaining in the wake than of entering the turbine, and the opposite was true for large fish. Large fish may have actively chosen to remain in the wake of the turbine regardless of their behavior upstream of it. As this pattern was not observed at night, the choice could be linked to visibility (e.g., recognizing a stationary reference point, or seeking shelter from currents or predators). As small and large fish had opposite trends, size may also influence this behavior. This could be due to larger fish having a greater ability to direct their movement in strong flows, or perhaps the

behavior varies with species. Regardless, fish presence in the wakes of turbines may be an important consideration for the design and placement of large-scale tidal turbine arrays, especially when located on migratory fish routes. This behavior could have implications for local ecology: if fish aggregate in the wake of turbines, these areas could become attractive to predators, as well, including larger fish, some marine mammals, and diving birds. More work is needed to determine if HK turbines or their structural supports act as fish aggregation devices.

Schools of fish may be better able to detect and avoid tidal turbines than individual fish. Schools had a lower probability of entering the turbine, a higher probability of avoiding it, and reacted at greater distances from the turbine than individuals. This could be related to the size of schooling fish, which were mostly large whereas the majority of individual fish were small. However, these results are also consistent with Domenici and Batty's (1997) observation that schooling herring reacted to a sound stimulus with more consistent directional movement away from the stimulus than did individuals. Rosen et al. (2012) also noted that the diving speed of shoaling Atlantic cod in response to a pelagic trawl was positively correlated with shoal size. Godø et al. (1999) used video to study the effects of density on the catchability of Atlantic cod (*Gadus morhua*), haddock (*Melanogrammus aeglefinus*), and American plaice (*Hippoglossoides platessoides*) and noted that individual cod and haddock swam erratically in front of the trawl, but fish that formed schools swam at a steady pace ahead of the trawl and in the same direction. This improved collective decision making agrees with the behavior of schools observed in this study, though this effect also appeared to be dependent on diel condition. Many more schools entered the turbine at night than during the day, compared to avoiding or passing it by (although sample size was too low to analyze statistical significance). Also, the only instances when schools showed divided behavior (e.g., the upper part of the school passed above the turbine

while the lower part went through the turbine) occurred at night, possibly indicating poor perception of the device.

The DIDSON was a useful tool for monitoring fish interactions with the tidal turbine. It was especially well suited to sampling at night, when a video camera would not have been useful without artificial lighting that could alter the natural behavior of fish. As tidal turbines are likely to be placed in deep (dark) or turbid water, DIDSON and other acoustics equipment may be the most appropriate monitoring tools. However, we identified several shortcomings of using a DIDSON for this purpose. One was the boundaries of the viewing window: sampling a narrow slice of the water made it difficult to follow fish from upstream of the turbine to downstream, and may have resulted in some fish being counted multiple times (though this is unlikely unless fish were milling).

The largest shortcoming of the DIDSON in this study was the resolution. Although DIDSON image resolution is among the best available, fish with lengths under 10 cm were difficult to measure with certainty, and so fish had to be classified into broad size groups. This avoided introducing bias but also prevented more detailed analyses involving fish size. If the fish under study were larger, length measurement error introduced by resolution would be a smaller proportion of fish length and would not be as much of an issue. The DIDSON could not provide information on direct blade strike of fish or the condition of fish exiting the turbine for the same reason. If blade strike is the focus of a study, video (as in EPRI 2011a) may be a more useful tool, though the advantage of sampling in dark or turbid water is lost.

Acoustic imaging cameras continue to improve and may soon be capable of video-quality images, but it should be noted that processing DIDSON footage using the methods presented here is extremely time consuming. For multi-day studies, it may be more practical to analyze

short clips of data collected periodically than a long, continuous dataset. Automating fish detection would drastically reduce processing time; however, this can be difficult to achieve due to moving turbine parts, variable fish sizes, and intermittent, unwanted sound reflection obscuring the image. Unwanted sound reflection came from the turbine support structure in the upstream view and from clouds of entrained air from the wake of the test platform in the downstream view. This noise was sometimes strong enough to obscure sound reflected by fish, causing disagreement between the numbers of fish observed in the upstream and downstream viewing windows.

This study made the best use of the available space and time on the turbine research platform, but future studies should seek to monitor fish at greater ranges from the turbine, as well as to each side. This would capture any longer-range reactions we suspect may be occurring (particularly for larger fish than those observed in this study), and would allow quantification of any general avoidance, attraction, or indifference shown by fish toward the turbine and support structure. The DIDSON can sample only short ranges in high frequency mode (window lengths up to approximately 10 m), but other hydroacoustic devices, such as split beam echosounders, would allow the tracking of fish at much greater ranges. However, identifying echoes from fish and estimating fish size are much more difficult when using split-beam hydroacoustic systems compared to imaging sonars like the DIDSON.

The combination of varying scales of study is crucial to understanding the effects of tidal turbines on fishes. The fine-scale interactions of fish, tidal turbines, and flow fields are likely to be best understood through a combination of computer models, laboratory flume studies, and high resolution field sampling techniques. Observations of fish interactions with turbines under realistic conditions in the natural environment, such as those presented here, are necessary to

obtain the probability of fish encountering a device and then entering or avoiding it, and how this changes with biological and environmental factors. Combining the results of laboratory and field studies will allow more accurate prediction of fish survival when encountering an HK device in the natural environment, but this information must then be placed in the context of a project site. The horizontal and vertical movements of fishes in relation to seasonal, diel, and tidal cycles will be unique to each site, and will determine what fish are likely to encounter the device and when this may occur. While results of single-turbine studies are scalable to some extent, new monitoring methods will need to be developed to understand the ecological implications of large arrays of HK turbines.

Acknowledgments

We thank Dr. James McCleave, Garrett Staines, Jeffrey Vieser, Kaitlyn Harmon, Amy Wyman, and Alexander Jensen for their assistance with this work, in the field and in the laboratory. We also thank the employees of Ocean Renewable Power Company for their generous contribution of time and resources, Captain George Harris, Jr. and crew for their invaluable assistance in the field, and Donald Degan and Dr. Anna-Maria Mueller for their acoustics advice. We thank the members of the Maine Tidal Power Initiative and Dr. Michael Peterson for their assistance. This work was supported by an award from the United States Department of Energy, project #DE-EE0003647. The views expressed herein are those of the authors and do not necessarily reflect the views of Ocean Renewable Power Company or any of its sub-agencies.

References

- Amaral, S.V., G.E. Hecker, P. Stacy, and D.A. Dixon. 2008. Effects of leading edge turbine blade thickness on fish strike survival and injury. Proceedings of Hydrovision 2008. HCI Publications, St. Louis, Missouri.
- Arnold, G.P., M. Greer Walker, L.S. Emerson, and B.H. Holford. 1994. Movements of cod (*Gadus morhua* L.) in relation to the tidal streams in the southern North Sea. *ICES Journal of Marine Science* 51: 207-232.
- Arnold, G. P. 1981. Movements of fish in relation to water currents. In *Animal migration*, ed. D. J. Aidley. Society for Experimental Biology, Seminar Series 13. USA: Cambridge University Press.
- Auster, P.J. 1988. A review of the present state of understanding of marine fish communities. *Journal of Northwest Atlantic Fishery Science* 8: 67-75.
- Axenrot, T., T. Didrikas, C. Danielsson, and S. Hansson. 2004. Diel patterns in pelagic fish behaviour and distribution observed from a stationary, bottom-mounted, and upward-facing transducer. *ICES Journal of Marine Science* 61: 1100-1104.
- Blaxter, J.H.S. and R.S. Batty. 1985. Herring behaviour in the dark: responses to stationary and continuously vibrating obstacles. *Journal of the Marine Biological Association of the United Kingdom* 65: 1031-1049.
- Bohl, E. 1980. Diel pattern of pelagic distribution and feeding in planktivorous fish. *Oecologia (Berlin)* 44: 368-375.
- Brawn, V.M. 1960a. Seasonal and diurnal vertical distribution of herring (*Clupea harengus* L.) in Passamaquoddy Bay, N.B. *Journal of the Fisheries Research Board of Canada* 17(5): 699-711.
- Brawn, V.M. 1960b. Underwater television observations of the swimming speed and behaviour of captive herring. *Journal of the Fisheries Research Board of Canada* 17(5): 689-698.
- Brooks, D.A. 2004. Modeling tidal circulation and exchange in Cobscook Bay, Maine. *Fishery Bulletin* 11(Special Issue 2): 23-50.
- Čada, G., J. Loar, L. Garrison, R. Fisher Jr., and D. Neitzel. 2006. Efforts to reduce mortality to hydroelectric turbine-passed fish: locating and quantifying damaging shear stresses. *Environmental Management* 27(6): 898-906.
- Čada, G.F. and M.S. Bevelhimer. 2011. Attraction to and avoidance of instream hydrokinetic turbines by freshwater aquatic organisms. Oak Ridge (TN), Oak Ridge National Laboratory. Report no. ORNL/TM-2011/131.

- Cameron, M.P. 2012. Flow field measurements for a cross flow turbine. M.S. Thesis. University of Maine, Orono, ME.
- Castonguay, M. and D. Gilbert. 1995. Effects of tidal streams on migrating Atlantic mackerel, *Scomber scombrus* L. *ICES Journal of Marine Science* 52(6): 941-954.
- Chang, P.K. 1970. *Separation of flow*. New York: Pergamon.
- Charlier, R.H. and C.W. Finkl. 2010. *Ocean Energy: Tide and tidal power*. Berlin: Springer-Verlag.
- Dadswell, M.J. and R.A. Rulifson. 1994. Macrotidal estuaries: a region of collision between migratory marine animals and tidal power development. *Biological Journal of the Linnean Society* 51: 93-113.
- de Robertis, A. and C.D. Wilson. 2006. Walleye pollock respond to trawling vessels. *ICES Journal of Marine Science* 63: 514-522.
- de Veen, J.F. 1978. On selective tidal transport in the migration of North Sea Plaice (*Pleuronectes platessa*) and other flatfish species. *Netherlands Journal of Sea Research* 12(2): 115-147.
- EPRI (Electric Power Research Institute). 2011a. Evaluation of fish injury and mortality associated with hydrokinetic turbines. Palo Alto (CA): EPRI. Report no. 1024569.
- EPRI (Electric Power Research Institute). 2011b. Fish passage through turbines: application of conventional hydropower data to hydrokinetic technologies. Palo Alto (CA): EPRI. Report no. 1024638.
- Domenici, P. and R.S. Batty. 1997. Escape behaviour of solitary herring (*Clupea harengus*) and comparisons with schooling individuals. *Marine Biology* 128: 29-38.
- Godø, O.R., S.J. Walsh, and A. Engås. 1999. Investigating density-dependent catchability in bottom-trawl surveys. *ICES Journal of Marine Science* 56: 292-298.
- Greer Walker, M., F.R. Harden Jones, G.P. Arnold. 1978. The movements of plaice (*Pleuronectes platessa* L.) tracked in the open sea. *Conseil international pour l'exploration de la mer* 38(1): 58-86.
- Hartill, B.W., M.A. Morrison, M.D. Smith, J. Boubée, and D.M. Parsons. 2003. Diurnal and tidal movements of snapper (*Pagrus auratus*, Sparidae) in an estuarine environment. *Marine & Freshwater Research* 54: 931-940.
- Hinch, S.G. and P.S. Rand. 1998. Swim speeds and energy use of upriver-migrating sockeye salmon (*Oncorhynchus nerka*): role of local environment and fish characteristics. *Canadian Journal of Fisheries and Aquatic Sciences* 55: 1821-1831.

- Janssen, J., S.B. Brandt. 1980. Feeding ecology and vertical migration of adult alewives (*Alosa pseudoharengus*) in Lake Michigan. *Canadian Journal of Fisheries and Aquatic Sciences* 37: 177-184.
- Keefer, M.L., C.A. Peery, S.R. Lee, W.R. Daigle, E.L. Johnson, and M.L. Moser. 2011. Behaviour of adult Pacific lamprey in near-field flow and fishway design experiments. *Fisheries Management and Ecology* 18: 177-189.
- Krumme, U. 2004. Patterns in tidal migration of fish in a Brazilian mangrove channel as revealed by a split-beam echosounder. *Fisheries Research* 70(1): 1-15.
- Lacoste, K.N., J. Munro, M. Castonguay, F.J. Saucier, and J.A. Gagné. 2001. The influence of tidal streams on the pre-spawning movements of Atlantic herring, *Clupea harengus* L., in the St Lawrence estuary. *ICES Journal of Marine Science* 58: 1286-1298.
- Langhamer, O. and D. Wilhelmsson. 2009. Colonisation of fish and crabs of wave energy foundations and the effects of manufactured holes—a field experiment. *Marine Environmental Research* 68: 151-157.
- Levy, D.A. and A.D. Cadenhead. 1995. Selective tidal stream transport of adult sockeye salmon (*Oncorhynchus nerka*) in the Fraser River Estuary. *Canadian Journal of Fisheries and Aquatic Sciences* 52: 1-12.
- Linnik, V.D., L.K. Malinin, M. Wozniowski, R. Sych, and P. Dembowski. 1998. Movements of adult sea trout *Salmo trutta* L. in the tailrace of a low-head dam at Włocławek hydroelectric station on the Vistula River, Poland. *Hydrobiologia* 371/372: 335-337.
- McCleave, J.D. and R.C. Kleckner. 1982. Selective tidal stream transport in the estuarine migration of glass eels of the American eel (*Anguilla rostrata*). *Conseil international pour l'exploration de la mer* 40: 262-271.
- Mitson, R.B. 1995. Underwater noise of research vessels: review and recommendations. ICES Cooperative Research Report 209.
- Moore, A., M. Ives, M. Scott, and S. Bamber. 1998. The migratory behavior of wild sea trout (*Salmo trutta* L.) smolts in the estuary of the River Conwy, North Wales. *Aquaculture* 198: 57-68.
- Perry, R.I. and J.D. Neilson. 1988. Vertical distributions and trophic interactions of age-0 Atlantic cod and haddock in mixed and stratified waters of Georges Bank. *Marine Ecology Progress Series* 49: 199-214.
- Pitcher, T. J. 2001. Fish Schooling. In *Encyclopedia of ocean sciences (2nd edition)*, ed. J. H. Steel, K. K. Turekian, S. A. Thorpe. 2: 432-444. Oxford: Academic Press.

- Plachta, D. T. T. and A. N. Popper. 2003. Evasive responses of American shad (*Alosa sapidissima*) to ultrasonic stimuli. *Acoustics Research Letters Online* 4: 25-30.
- Polagye, B., B. Van Cleve, A. Copping, and K. Kirkendall. 2010. Environmental effects of tidal energy development. U.S. Dept. Commerce, NoAA Tch. Memo. F/SPO-116.
- Popper, A. N. and D. M. Higgs. 2009. Fish: hearing, lateral lines (mechanisms, role in behavior, adaptations to life underwater). In *Encyclopedia of ocean sciences (2nd edition)*, ed. J. H. Steel, K. K. Turekian, S. A. Thorpe. 476-482. Oxford: Academic Press.
- R Core Team. 2013. R: A language and environment for statistical computing. R Foundation for Statistical Computing. Vienna, Austria. ISBN 3-900051-07-0. <http://www.R-project.org>.
- Rakowitz, G., M. Tušer, M. Říha, T. Jůza, H. Balk, and J. Kubečka. 2012. Use of high-frequency imaging sonar (DIDSON) to observe fish behavior towards a surface trawl. *Fisheries Research* 123-124: 37-48.
- Ribeiro, J., L. Bentes, R. Coelho, J.M.S. Gonçalves, P.G. Lino, P. Monteiro, and K. Erzini. 2006. Seasonal, tidal and diurnal changes in fish assemblages in the Ria Formosa lagoon (Portugal). *Estuarine, Coastal and Shelf Science* 67: 461-474.
- Rosen, S., A. Engås, A. Fernö, and T. Jørgensen. 2012. The reactions of shoaling adult cod to a pelagic trawl: implications for commercial trawling. *ICES Journal of Marine Science* 69(2): 303-312.
- Soldal, A.V., I. Svellingen, T. Jørgensen, and S. Løkkeborg. 2002. Rigs-to-reefs in the North Sea: hydroacoustic quantification of fish in the vicinity of a “semi-cold” platform. *ICES Journal of Marine Science* 59: S281-S287.
- Stasko, A.B. 1975. Progress of migrating Atlantic salmon (*Salmo salar*) along an estuary, observed by ultrasonic tracking. *Journal of Fish Biology* 7: 329-338.
- Vabø, R., K. Olsen, and I. Huse. 2002. The effect of vessel avoidance of wintering Norwegian spring spawning herring. *Fisheries Research* 58: 57-77.
- Viehman, H., G.B. Zydlewski, J.D. McCleave, G. Staines. In revision. Using acoustics to understand fish presence and vertical distribution in a tidally dynamic region targeted for energy extraction. *Estuaries and Coasts*.
- Wardle, C.S. 1986. Fish behavior and fishing gear. In *The behavior of teleost fishes*, ed. T. J. Pitcher. Baltimore: Johns Hopkins University Press.
- Wheeler, B. 2010. lmPerm: Permutation tests for linear models. R package version 1.1-2. <http://CRAN.R-project.org/package=lmPerm>.
- Willhelmsson, D., T. Malm, and M.C. Öhman. 2006. The influence of offshore windpower on demersal fish. *ICES Journal of Marine Science* 63: 775-784.

Figure Legends

Fig. 1 Map of Cobscook Bay, Maine. Ocean Renewable Power Company's turbine testing platform was located at the closed circle in Outer Bay.

Fig. 2 Schematic of Ocean Renewable Power Company's turbine testing platform with the test turbine suspended below (adapted from schematic provided by Ryan Beaumont, RM Beaumont Corporation, Brunswick, ME): (a) side view, (b) front view. DIDSONs are shown in survey positions as small black boxes beneath the platform. Dimensions are indicated, and the sampling volume for each DIDSON is marked by hatched areas.

Fig. 3 Sample frames from upstream (left) and downstream (right) DIDSON units, showing cross-section of the test turbine and its support frame. Fish behaviors illustrated are (A) passing, (B) avoiding, (C) entering, (D) milling, (E) exiting and remaining in wake, and (F) exiting and moving through the wake. Water flow in the downstream view is angled upward due to the angle of the DIDSON.

Fig. 4 Number of individual fish (bars) and schools (triangles) observed upstream and downstream of the test turbine at Ocean Renewable Power Company's turbine testing platform. Current speed is shown by the line plot and the right-hand vertical axis. The shaded grey background indicates the night period.

Fig. 5 Distribution of lengths of observed fish, measured with DIDSON control and display software.

Tables

Table 1 Descriptions of the seven fish behaviors observed in DIDSON footage at the ORPC test turbine in Cobscook Bay, ME.

Where observed	Behavior name	Description of behavior
Up- and downstream of turbine	Milling	Milling occurred during slack tide, when current speed was low. Fish ceased directed movement and instead moved in short bursts in random directions.
	Passing	Fish entered the field of view already above or below the turbine and passed across the view without diverting course, apparently unaffected by the turbine's presence.
Upstream of turbine	Avoiding	Fish altered course to avoid the turbine, swimming above or below it or reversing direction and moving against the current.
	Entering	Fish swam into the interior of the turbine. These were always fish that entered the field of view within the same depth range as the turbine.
Downstream of turbine	Exiting turbine, moving through wake	Fish exited the turbine, then swam directly through the wake of the turbine to re-enter the current.
	Exiting turbine, remaining in wake	Fish exited the turbine and then remained in the wake, showing behavior similar to milling for several seconds. Fish in the wake disappeared from view mid-wake, or returned to current and moved downstream and out of view.
	Appearing and remaining in wake	Same as above, but fish were not observed exiting the turbine. Previous location (inside the turbine, passing above or below, or in the wake but out of view) was unknown.

Table 2. Coefficient estimates (95% confidence intervals) and p-values from binomial logistic analyses of fish behavior. Asterisks indicate statistical significance (p-value < 0.05).

Parameter	Coefficient estimate (95% CI)		
1. Does turbine motion affect encounter behavior of individual fish?			
	Entering	Avoiding	Passing
Intercept	1.020 (0.956, 1.084) p-value < 0.001 *	-5.299 (-5.700, -4.898) p-value < 0.001 *	-1.046 (-1.110, -0.981) p-value < 0.001 *
Turbine Motion	-1.110 (-1.187, -1.034) p-value < 0.001*	0.776 (0.326, 1.226) p-value = 0.001 *	1.093 (1.016, 1.170) p-value < 0.001 *
2. Does diel condition or fish size affect encounter behavior of individual fish?			
	Entering	Avoiding	Passing
Intercept	-1.761 (-2.130, -1.392) p-value < 0.001 *	-3.784 (-4.671, -2.898) p-value < 0.001 *	1.594 (1.245, 1.942) p-value < 0.001 *
Diel condition (day/night)	1.811 (1.439, 2.183) p-value < 0.001 *	-2.164 (-3.153, -1.175) p-value < 0.001 *	-1.654 (-2.006, -1.303) p-value < 0.001 *
Size (small/large)	-1.334 (-2.042, -0.626) p-value < 0.001 *	-0.124 (-1.377, 1.129) p-value = 0.846	1.106 (0.491, 1.721) p-value < 0.001 *
Diel condition x Size	0.588 (-0.142, 1.318) p-value = 0.114	3.968 (2.615, 5.320) p-value < 0.001 *	-0.810 (-1.448, -0.173) p-value = 0.013 *
3. Does diel condition or fish size affect departure behavior of individual fish?			
	Pausing in wake		
Intercept	-3.655 (-4.060, -3.250) p-value < 0.001 *		
Diel condition (day/night)	3.662 (3.253, 4.072) p-value < 0.001 *		
Size (small/large)	3.690 (3.186, 4.194) p-value < 0.001 *		
Diel condition x Size	-4.162 (-4.674, -3.649) p-value < 0.001 *		
4. Does schooling affect encounter behavior of fish?			
	Entering	Avoiding	Passing
Intercept	-0.092 (-0.134, -0.050) p-value < 0.001 *	-4.524 (-4.727, -4.321) p-value < 0.001 *	0.049 (0.007, 0.091) p-value = 0.022 *
School (no/yes)	-1.237 (-1.972, -0.502) p-value = 0.001 *	3.575 (2.878, 4.271) p-value < 0.001 *	-0.003 (-0.602, 0.597) p-value = 0.993

Table 3 Effect of turbine motion on probability of individual fish entering, avoiding, or passing the turbine. Parentheses indicate number of fish.

Turbine motion	Probability of			Total number of fish
	Entering	Avoiding	Passing	
Not rotating	0.735 (77 day, 5,688 night)	0.005 (0 day, 24 night)	0.260 (782 day, 2,803 night)	9,374
Rotating	0.477 (61 day, 4,280 night)	0.011 (10 day, 84 night)	0.512 (1,420 day, 8,140 night)	13,995
Total number of fish	10,106	118	13,145	23,369

Table 4 Effect of fish size and diel condition on probability of individual fish entering, avoiding, or passing the rotating turbine. Parentheses indicate number of fish.

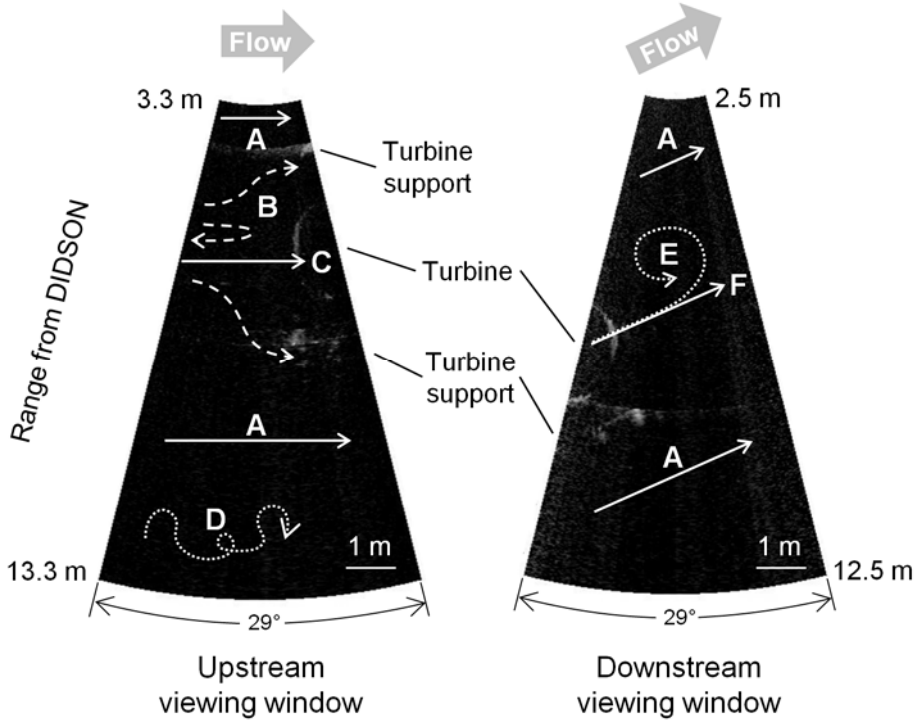
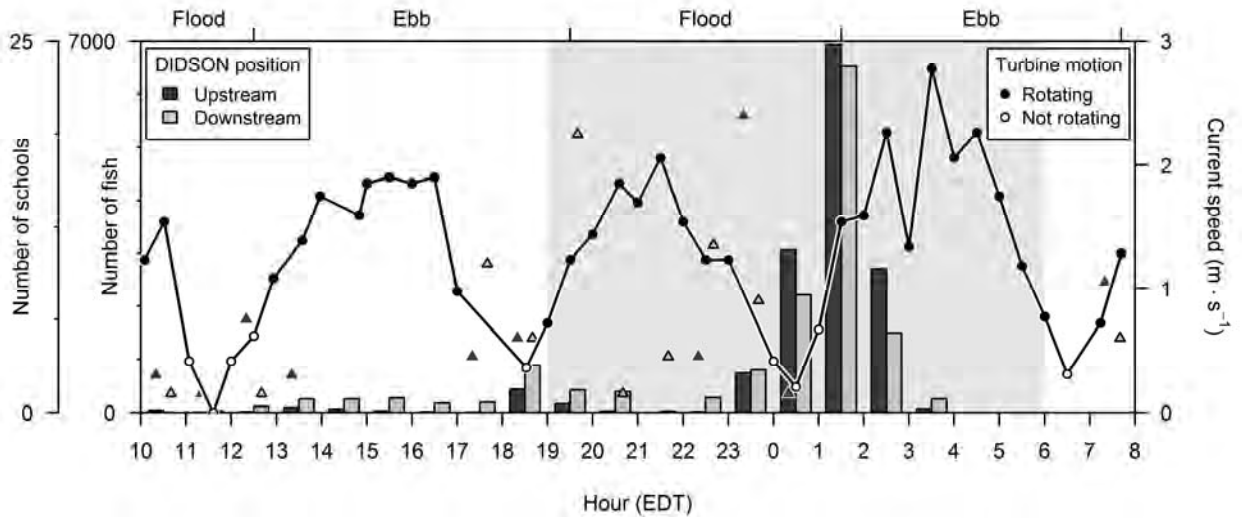
Size	Diel condition	Probability of			Total number of fish
		Entering	Avoiding	Passing	
Small	Day	0.147 (37)	0.022 (5)	0.831 (1,111)	1,153
	Night	0.513 (4,061)	0.002 (20)	0.485 (5,834)	9,915
Large	Day	0.043 (87)	0.020 (5)	0.937 (309)	401
	Night	0.333 (1,257)	0.109 (64)	0.559 (2,306)	3,627
Total number of fish		5,542	94	9,560	15,096

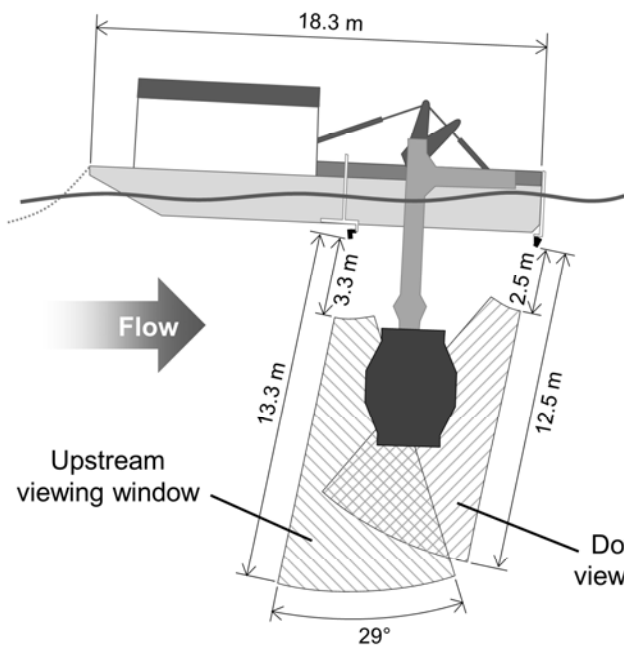
Table 5 Effect of fish size and diel condition on probability of individual fish remaining in the wake of the rotating turbine. Parentheses indicate number of fish.

Size	Day/Night	Probability of Remaining in wake
Small	Day	0.026 (24)
	Night	0.518 (2,248)
Large	Day	0.509 (24)
	Night	0.387 (219)
Total number of fish		2,515

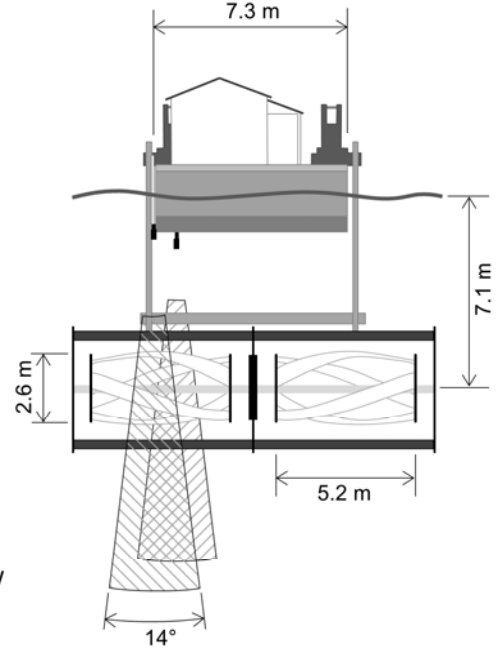
Table 6 Effect of schooling on probability of fish (individuals or schools) entering, avoiding, or passing the turbine. Parentheses indicate number of fish.

	Probability of		
	Entering	Avoiding	Passing
Individuals	0.477 (10,106)	0.011 (118)	0.512 (13,145)
Schools	0.209 (14)	0.279 (15)	0.512 (73)

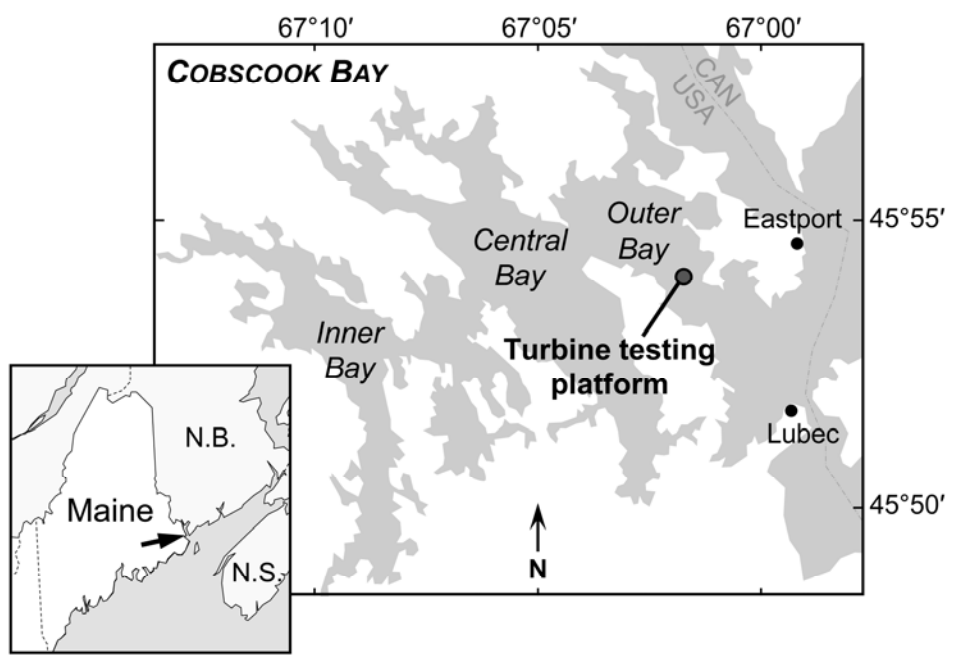


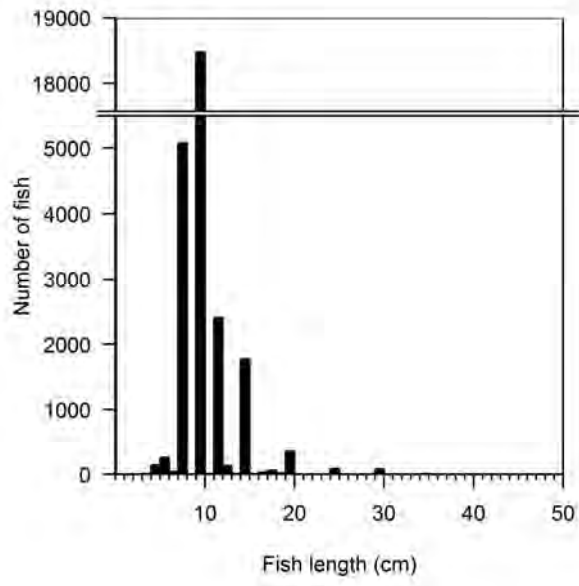


a.



b.





Appendix Task 2-3

Using Acoustics to Understand Fish Presence and Vertical Distribution in a Tidally Dynamic Region Targeted for Energy Extraction

Haley A. Viehman

University of Maine, School of Marine Sciences, 5741 Libby Hall, Orono, ME 04469-5741

Gayle Barbin Zydlewski

University of Maine, School of Marine Sciences, 5741 Libby Hall, Orono, ME 04469-5741

Phone: 207-581-4365; FAX: 207-581-4990; Email: gayle.zydlewski@maine.edu

James D. McCleave

University of Maine, School of Marine Sciences, 5741 Libby Hall, Orono, ME 04469-5741

Garrett J. Staines

University of Maine, School of Marine Sciences, 5741 Libby Hall, Orono, ME 04469-5741

Abstract

The use of tidal currents by fishes for movements to and from onshore spawning, foraging, and nursery grounds is well documented. However, fishes' use of the water column in tidal currents frequently exceeding $1.5 \text{ m}\cdot\text{s}^{-1}$ is largely unknown. With growing interest in extracting energy from the tides, understanding animal use of these dynamic environments has become essential to determining environmental effects of tidal energy devices. To assess the effects of a tidal energy device on fishes, we used down-looking single beam hydroacoustic technology to collect pre-deployment data on the presence and vertical distribution of fishes at a pilot project site and a control site in Cobscook Bay, Maine. Twenty-four-hour stationary surveys were conducted in each season of 2010 and 2011. Relative fish density and vertical distribution were analyzed for variation with respect to site, year, month, and diel and tidal cycles. A seasonal pattern in fish density was apparent in both years at both sites, with maxima in spring and late fall. Fish density was generally highest near the sea floor. Diel changes in vertical distribution were frequently observed, but changes in distribution related to tidal cycle were inconsistent. Results from the project and control sites were very similar, demonstrating that the control site provides a reference for quantifying changes in fish density and vertical distribution related to the tidal device. This approach and baseline dataset will be used to compare hydroacoustic data collected at the project and control sites after device deployment.

Keywords

hydroacoustics, tidal, fish, density, vertical distribution, Cobscook Bay

Introduction

Tidal currents help shape coastal marine environments and play an essential role in the life cycles of many marine and diadromous fishes. Numerous fish species use the tides to gain access to valuable intertidal foraging habitat (Dadswell and Rulifson 1994, Hartill et al. 2003, Krumme 2004, Ribeiro et al. 2006), actively feed when moving against the tidal flow (Krumme and Saint-Paul 2003), or traverse several kilometers over the course of a tidal cycle by moving with the current (Aprahamian et al. 1998, Sakabe and Lyle 2010). Species demonstrated to select tides to aid their movements include American eel (*Anguilla rostrata*; McCleave and Kleckner 1982), Atlantic cod (*Gadus morhua*; Arnold et al. 1994), Atlantic salmon (*Salmo salar*; Stasko 1975, Aprahamian et al. 1998), sea trout (*Salmo trutta*; Moore et al. 1998), plaice (*Pleuronectes platessa*; de Veen 1978, Greer Walker et al. 1978), Atlantic mackerel (*Scomber scombrus*; Castonguay and Gilbert 1995), and Atlantic herring (*Clupea harengus*; Lacoste et al. 2001).

Areas of extreme tidal currents are also targeted by humans for energy extraction. Harvesting tidal energy involves large, in-stream hydrokinetic (HK) turbines installed in areas with fast tidal flows (Charlier and Finkl 2010). Unlike conventional or tidal barrage hydropower designs, HK turbines are free-standing, open structures installed in naturally flowing water currents. These devices have the potential to affect fishes using the same currents but, because of a scarcity of installed projects, effects on fishes remain unknown. Some high-priority unknowns include direct strike by turbine blades and injury because of pressure changes near the blades (Polagye et al. 2011). More indirectly, fish behavior in response to a device may result in a modified distribution of individuals in the water column, ultimately affecting the magnitude of more direct effects like blade strike. While tidal currents are used by many fish species, the

distribution of fish within the flow are largely unstudied, partly because of the difficulty of working in these challenging environments (Gill 2005; Shields et al. 2008; Shields et al. 2009).

Cobscook Bay is located at the mouth of the Bay of Fundy. It has a mean tidal range of 5.7 m (Brooks 2004) and current speeds exceeding $2 \text{ m}\cdot\text{s}^{-1}$ (4 knots) in the outer bay. A pilot tidal energy device, Ocean Renewable Power Company's (ORPC's) TidGen[®] Power System (Fig. 1), was installed in outer Cobscook Bay, Maine in August of 2012 (Fig. 2). The entire turbine structure is 31.2 m (102.3 ft) long and is positioned approximately 8.1 m (26.5 ft) above the sea floor by a solid steel frame. As with other tidal energy devices, the effects of the TidGen[®] system on fishes are unknown.

Cobscook Bay is a productive ecosystem (Larsen and Campbell 2004), but the annual and seasonal presence and composition of pelagic fishes of the bay have not been studied. Most studies of the region have focused on benthic species vulnerable to trawling, and many of these studies are dated (Brawn 1960, Tyler 1971, MacDonald et al. 1984), therefore community composition could have changed and all of these surveys were conducted, not in Cobscook Bay, but in the adjacent Passamaquoddy Bay (Brawn 1960, Tyler 1971, MacDonald et al. 1984) or the Bay of Fundy proper (AECOM 2009). Key pelagic species expected to be in Cobscook Bay include Atlantic and blueback herring (*Clupea harengus* and *Alosa aestivalis*), alewife (*Alosa pseudoharengus*), rainbow smelt (*Osmerus mordax*), red, white, and silver hake (*Urophycis chuss*, *Urophycus tenuis*, and *Merluccius bilinearis*), threespine and blackspotted stickleback (*Gasterosteus aculeatus* and *Gasterosteus wheatlandi*), American eel (*Anguilla rostrata*), and Atlantic mackerel (*Scomber scombrus*) (Tyler 1971, MacDonald et al. 1984, Saunders et al. 2006, Athearn and Bartlett 2008, J. Vieser, unpublished information, 2013, University of Maine, School of Marine Sciences, Orono, ME 04469). Studies do not always agree on species

seasonality, and the vertical distribution of species in the water column and use of tidal currents is unknown. These missing data are critical to assessing the effects of tidal power devices on fishes in Cobscook Bay.

Few studies have examined the vertical distribution of fishes in tidal flows strong enough for tidal power generation. Many studies of tidally dynamic areas have focused on species composition and habitat use at low and high slack tides, to demonstrate that fishes move with the tides, but details about their use of the water column during those movements are lacking (Morrison et al. 2002, Ribeiro et al. 2006, Jovanovic et al. 2007). The best details concerning vertical distribution of fishes in tidal currents comes from studies of selective tidal stream transport. These studies show that certain species move into the water column during tides that flow in the desired direction of movement, and out of the water column during opposing tides to avoid being swept in an undesirable direction (Greer Walker et al. 1978, de Veen 1978, McCleave and Kleckner 1982). Other studies of fish vertical distribution have been carried out at ocean sites with little current (Brawn 1960, Neilson et al. 2003, Jensen et al. 2011), estuaries with moderate current (Bennett et al. 2002), lakes (Clark and Levy 1988, Levy 1990), and rivers (Kubecka and Duncan 1998). Many of these studies document significant diel or tidal differences in the vertical distribution of fish, with additional variation related to time of year, location, and species.

We conducted stationary, down-looking hydroacoustic surveys to characterize patterns in fish presence and vertical distribution, with fine vertical and temporal resolution, at the Cobscook Bay project area. A preliminary study conducted in Minas Passage concluded that hydroacoustic technology could be used for this purpose (Melvin and Cochrane 2012). Using hydroacoustics allows non-invasive, continuous sampling of nearly the entire water column

despite this difficult, high-velocity environment. Our study design included a project site (where the device has been located since August 2012) and a control site, with data collected prior to and after device installation. The use of a control site and before-and-after data collection are both critical to detecting the effects of the device on fish density and vertical distribution over time; the use of a control site will allow the assessment of any changes due to turbine installation to be discriminated from natural variation.

We hypothesize that the overall density and vertical distribution of fishes at the project site will change when the device is installed. Therefore, effects of the turbine will be assessed as statistically detectable differences in fish density or vertical distribution. For example: (1) overall reduced fish density at the project site compared to density recorded previously at the project site (e.g., in the same month of the previous year) and compared to data collected concurrently at the control site; or (2) a detectable change in vertical distribution of fish in the water column after turbine installation, compared to previously collected data at the project site, or compared to data collected at the control site. This manuscript details natural variation in these parameters prior to turbine deployment.

Two years of pre-deployment data from the project site and the control site were collected and analyzed. Our goals were to describe the patterns in fish density and vertical distribution at the test and control sites on varying temporal scales (seasonal, diel, and tidal cycles), and to verify that the control site is similar to the project site and therefore useful for detecting effects of the device.

Methods

Data were collected in outer Cobscook Bay at the proposed pilot project site and a control site (Fig. 2). The project site, CB1, was located mid-channel at 44°54.60' N, 67°2.74' W; the control site, CB2, was approximately 1.6 km seaward, also mid-channel, at 44°54.04' N, 67°1.71' W. For data collection, a 12.2 m boat was moored at these two sites. The boat swung around its mooring at each slack tide as the direction of tidal flow changed; this movement was minimal for most months (205 m mean difference at CB1, 147 m mean difference at CB2). Under normal conditions, water depth at CB1 averaged 24.5 m at low tide to 32.3 m at high tide, and at CB2 depth averaged 33.8 m to 41.3 m. However, positioning of the mooring at CB1 in May 2010 caused the boat to swing into much deeper water during most of the ebbing tide; ebb tide data for that month were subsequently omitted from analyses. At CB1, average current speed (water column mean) was $1.01 \text{ m}\cdot\text{s}^{-1}$ (2.0 knots), with a maximum of $2.06 \text{ m}\cdot\text{s}^{-1}$ (4.0 knots). At CB2, average current speed was $0.87 \text{ m}\cdot\text{s}^{-1}$ (1.7 knots), with a maximum of $1.78 \text{ m}\cdot\text{s}^{-1}$ (3.5 knots).

A single beam Simrad ES60 echosounder was used with a circular transducer (38/200 Combi W) mounted 1 meter below the surface over the port side of the vessel, facing downward. The transducer insonified a volume of water approximately conical in shape, extending from the transducer to the sea floor. The echosounder operated at 200 kHz and 38 kHz simultaneously, at a rate of 2 pings per second, with a half-power beam angle of 31° for both frequencies. A wide beam angle was used to maximize the volume sampled. The pulse duration was 0.512 ms for all surveys except the first two (May and June 2010; 1.024 ms and 0.256 ms pulse lengths, respectively), when trial and error were used to reduce electrical noise in the dataset.

The echosounder was calibrated using copper calibration spheres (13.7 mm diameter with -45.00 dB nominal target strength for 200 kHz; 60 mm diameter with -33.60 dB nominal target

strength for 38 kHz) as recommended by Foote et al. (1987). On-axis calibrations were conducted in situ at slack tide during each sampling session to ensure consistent system functionality. To obtain accurate calibration offsets for use during data processing, on-axis calibrations were carried out each winter (January 2011 and February 2012) on a frozen lake, where the water was sufficiently still to allow precise positioning of the sphere within the acoustic beam. These calibrations were carried out for each pulse duration used during the surveys.

Current speed measurements were obtained using a Marsh-McBirney flow meter from May 2010 to May 2011, and an Acoustic Doppler Current Profiler (ADCP) from June 2011 to November 2011. These devices were also mounted over the side of the vessel, 1 m below the surface (flow meter to starboard; ADCP to port, aft of the Simrad transducer). The flow meter recorded surface current speed only, while the ADCP recorded current speeds throughout the water column with 1 m vertical resolution.

Data collection

Twenty-four-hour stationary surveys were carried out at the two sites at least once each season, beginning in May 2010 (Table 1). Surveys were scheduled in order to sample nearly two complete tidal cycles: one at night and one during the day. Depending on the time of year, this was not always possible; in May and June, nights encompassed only one tidal stage, and in March, this was true for days. Surface current speed was manually recorded every half hour when using the flow meter; current speed throughout the water column was automatically measured and recorded every half hour for one minute when using the ADCP. Surface salinity was measured using a handheld refractometer in all months surveyed in 2011, and was 32.00 ± 0.45 (average \pm standard error). It was assumed that salinity variation with depth and over the

course of the year would be negligible in this very well-mixed area (Brooks 2004, Larsen and Campbell 2004, G. Staines, unpublished information, 2013, University of Maine, School of Marine Sciences, Orono, ME 04469).

Data Analyses

Data collected with the 200 kHz frequency were used in this study, as smaller objects may be detected with 200 kHz than with 38 kHz, and we were interested in all sizes of fish. Hydroacoustic data were processed using Echoview[®] software (5.1, Myriax Pty. Ltd., Hobart, Australia), and statistical analyses were carried out in R (2.15.2, R Core Team, Vienna, Austria).

Hydroacoustic data processing began with calibrating the raw data according to results from the winter calibration sessions. The Simrad ES systematic triangle wave error was investigated in calibration files and determined to be negligible. The bottom line was automatically detected with the Echoview best-bottom-line-pick algorithm, then manually corrected for errors and offset by 0.5 m. Backscatter data were then visually scrutinized, and areas of noise (for instance, from electrical interference, a passing boat's depth sounder, or interference from the ADCP) or high boat motion were manually excluded from analyses. June 2010 data collected at CB1 were excluded because of excessive electrical interference. Acoustic interference from entrained air was common in the upper 10 m of the water column. Data analyses were therefore limited to the lowest 15 m of the water column at both sites (though CB2 was deeper). The lower 15 m of water spanned the future position of the TidGen[®] turbine, which occupies the space from 6.7 m to 9.5 m above the sea floor.

Acoustic signals from unwanted targets (such as plankton, krill, and fish larvae) were then excluded by eliminating acoustic returns with target strengths (TS) less than -60 dB. Most

fish have TS between -60 dB and -20 dB, but this varies greatly with fish anatomy and orientation (Simmonds and MacLennan 2005). This variability, combined with the TS uncertainty inherent in single beam systems, meant that some fish with actual TS greater than the -60 dB threshold may have been excluded, depending on their position within the beam (Simmonds and MacLennan 2005).

Data from slack tides were removed from analyses because flowing tides (when the turbine would be rotating) were the focus of this study. Focusing on flowing tides also greatly reduced the potential for the same fish to make multiple passes through the hydroacoustic beam, and eliminated periods of time when the boat was swinging around its mooring (and therefore moving over the seafloor, instead of remaining stationary). The ORPC TidGen[®] stops rotating when current speeds fall below $0.5 \text{ m}\cdot\text{s}^{-1}$, and remains non-rotating until current speeds rise above $1.0 \text{ m}\cdot\text{s}^{-1}$. These non-rotating periods were considered slack tides, and mean water column current speed was used to define slack tide start and end points. Mean current was obtained for each half hour by averaging ADCP current data from surface to seafloor. When only surface current data were available (collected with the flow meter), a correction was applied to approximate the water column average. This correction was obtained for each site using data collected concurrently with the ADCP and the flow meter in August of 2011. The average slack tide spanned 2.9 hours (± 0.1 standard error) at CB1 (the project site) and 2.2 hours (± 0.1) at CB2.

Once slack tide data were removed, the remaining hydroacoustic data were divided into a grid with columns 30 minutes wide and rows 1 meter high. Thirty minute time segments were large enough to minimize autocorrelation but obtain an accurate measure of the variation in density that occurred over the course of each survey. The 1 m water column layers were

measured upward from the sea floor, rather than downward from the surface, as the turbine is located at a fixed distance above the bottom. Echoview was used to calculate the mean volume backscatter strength (S_v) of each 30 min column of the grid, and the area backscattering coefficient (s_a) for each 30 min x 1 m grid cell. Volume backscatter is a measure of the sound scattered by a unit volume of water, and is an index of fish density (Foote 1983). It is represented in the linear scale as the volume backscattering coefficient (s_v , with units of $m^2 \cdot m^{-3}$), or in the logarithmic scale as volume backscattering strength (S_v , with units of decibels: dB re $1 m^{-1}$; Simmonds and MacLennan 2005). The area backscattering coefficient, s_a , is the acoustic energy returned from a given layer within the water column, and has units of $m^2 \cdot m^{-2}$. s_a is the integration of s_v with respect to depth, and so is also an index of fish density. The normalized vertical distribution of fish was constructed for each 30-min grid column by calculating the proportion of the column's total s_a contributed by each 1-m layer of water.

Permutation ANOVA tests (R package *lmPerm*; Wheeler 2010) were done to assess variation in water column S_v , as the data did not meet the assumption of normality (significance level = 0.05). When significant factor effects were found, nonparametric Tukey-type multiple comparisons (R package *nparcomp*; Konietzschke 2012) were used to determine significant differences among groups (significance level, $p = 0.05$). After testing for the effect of year on S_v , 2010 and 2011 were treated separately, as we believe the year effect was largely due to an improved electrical system used in 2011. We then tested for the effect of month and site on water column S_v in each year, and for effects of diel condition (day or night) and tidal stage (ebb or flood) on water column S_v in 2011 only.

To assess changes in fish vertical distribution, the mean vertical distribution of s_a was obtained for each survey in 2010 and 2011, as well as for each diel and tidal stage of each survey

in 2011 (day, night; day ebb, day flood, night ebb, and night flood). Survey distributions from the project site were compared to those from the control site to test for site differences. Diel and tidal stage comparisons were done for each 2011 survey. Statistical testing consisted of the linear regression of one mean vertical distribution onto the other. If distributions were similar, the fitted line was significant ($p < 0.05$) and had a positive slope. If distributions were not similar, the fitted line had either a non-significant fit ($p > 0.05$) or a negative slope (indicating opposite distributions).

Results

Fish Density Index: Water column S_v

Water column S_v (an index of fish density) was significantly greater in 2010 than 2011 at both sites ($p < 0.05$). In 2010, S_v was significantly affected by month and month's interaction with site ($p < 0.05$), indicating that fish density varied significantly over the course of the year, but not in the same way at both sites. Multiple comparisons for 2010 data indicated that sites were significantly different from each other only in September. At CB1 (project), water column fish density was highest in November, followed by May, then September, August and October (Fig. 3). At CB2 (control), May, June, and September had the greatest density, followed by November, October, and August (Fig. 3). The effects of diel and tidal stage on water column fish density were not tested for 2010.

In 2011, S_v varied significantly by month and site ($p < 0.05$), but the interaction had no effect. S_v was slightly higher at CB2 when all surveys were grouped together; however, multiple comparisons revealed that within each survey, densities at CB1 and CB2 were never significantly different. Fish density was highest in May, followed by November (Fig. 3). Diel condition, tidal stage, and their interaction with month significantly affected S_v , indicating diel condition and

tidal stage had different effects on fish density in different months (Fig. 4). Multiple comparisons carried out within each survey showed fish density during the ebb tide was equal to or higher than during flood tide (Fig. 4). Density also appeared more variable during the day than at night (except March 2011 at CB2; Fig. 4). Water column S_V at CB1 and CB2 showed similar patterns with respect to tidal stage during most surveys (Fig. 4).

Vertical distribution: proportional s_a

The proportion of backscatter (fish density) contributed by each layer of water generally increased toward the sea floor (0-5 m above the bottom) at both sites in both years (Fig. 5). This was true in all months surveyed, except May 2011 CB1, when fish density was highest in the upper layers analyzed (11-15 m above the bottom). This was the only month in which vertical distributions at the test and control sites were significantly different (though note that only the lower 15 m of CB2 could be used in the statistical comparison to CB1; density increased near the upper layers at CB2, as well).

Vertical distributions of fish in 2011 differed significantly between day and night in May and June at CB1, but not at CB2 (Fig. 6). In these instances, the fish density index was higher in the upper layers analyzed during the day, but shifted towards the sea floor during the night (Fig. 6). Though the difference between day and night was not statistically significant in the other surveys, fish appeared to be more evenly distributed throughout the water column at night than during the day, with generally lower variation and fewer peaks in density (Fig. 6).

In 2011, the vertical distributions of fish were affected by tidal stage during the day in March and June at CB1 and June at CB2 (Fig. 6). In March at CB1, fish density was higher near the bottom during the daytime ebb, but more evenly distributed in the water column during the daytime flood. In June at CB1, fish density was highest between 10 and 15 m above the bottom

during the ebb, but highest between 1 and 5 m above the bottom during the flood. At CB2 in June, fish were more evenly distributed in the water column during the daytime ebb (with variable peaks mid-column), but closer to the bottom during the flood.

Discussion

Understanding the interactions between the environment and its biological constituents in tidally dynamic coastal regions is essential for informing tidal power development. Research and monitoring in these areas is limited because of the strong tidal currents. Recent interest in tidal power extraction in Cobscook Bay provided the opportunity to develop an approach to investigate variation in fish abundance (density index) and vertical distribution, both expected to change with the installation of an obstacle (e.g., tidal turbine) occupying a specific layer within the water column. The Bay's complicated bathymetry combines with a large tidal range to create high current speeds and flow patterns that vary greatly with location and tide (Brooks 2004, H. Xue, unpublished information, 2013, University of Maine, School of Marine Sciences, Orono, ME 04469). Multiple fish species pass through the strong currents of the outer bay to move between deeper ocean habitats and the extensive inshore habitats of the inner bays. Given the extreme variation in currents over time and space and the mixed seasonal and year-round fish community structure, hydroacoustic measures of fish density were expected to vary widely in relation to season and location. Our two years of hydroacoustic assessment demonstrate that while fish density is indeed variable, changes in fish density and vertical distribution on seasonal, diel, and tidal time scales are similar at the project and control sites. Therefore, site comparisons in the future can be used to statistically examine the effects of devices on overall fish density and vertical distribution at the project site.

Water column fish density varied by year and month in a similar manner at both sites. The decrease in density and its variability related to site and month from 2010 to 2011 may have been natural variation. However, it is also likely related to changes to the electrical system used in 2011 that resulted in cleaner data, especially at greater depths. This is supported by preliminary data collected in 2012 (unpublished) which appear very similar to 2011, with little difference between sites. Despite the change from 2010 to 2011, similar seasonal patterns were discernible at both sites in both years, with fish density higher in May and November than other months. The increase in May is likely linked to the springtime movements of anadromous fish (e.g., alewife; Saunders et al. 2006) and other species (e.g. threespine and blackspotted stickleback) into the bay, and the presence of large schools of larval and juvenile Atlantic herring (J. Vieser, unpublished information, 2013, University of Maine, School of Marine Sciences, Orono, ME 04469). The slight increase in November may reflect an inverse movement of summer residents out of the bay.

The vertical distribution of fish did not show a distinct seasonal pattern. Fish density almost always increased toward the sea floor, regardless of time of year. The main exception was May 2011 at CB1 (project), when dense schools were present in the middle and upper water column (mostly during the day), causing the density index to increase toward the surface. This effect was also seen during the daytime ebb tide in June 2011 at CB1, and during the day in May and June 2011 at CB2. These higher densities in the upper water column were likely due to the large numbers of larval and juvenile herring that were present in the spring, which have been found to move toward the surface during the day and toward the bottom at night (Jensen et al. 2011).

A relatively consistent difference between day and night was observed in the vertical distributions, though only two of the surveys tested showed a significant difference. At night, fewer peaks in density throughout the water column and lower variation in each layer reflected a general dispersal of dense clusters (e.g., schools of fish). This was also evidenced by the higher variation in water column density during the day than during the night (Fig. 4). The dispersion of fish at night has been observed by others (Gauthier and Rose 2002, Knudsen et al. 2009), and may be linked to visibility as schooling fish often depend on vision to remain in formation (Pitcher 2001). Regardless of the reason, this diel change in fish use of the water column may be important to consider when assessing the potential effects of tidal turbines on fishes. Viehman and Zydlewski (this issue) found that schooling fish may have a greater likelihood of avoiding a test tidal turbine than individual fish, and that fish were more likely to enter the turbine at night than during the day. If fish in the area of a tidal device spread out at night, a fish's chance of entering the turbine may increase.

The vertical distribution of fish lacked a consistent pattern related to tidal stage. This was not surprising, considering different species of fish may be using different tidal currents depending on the time of year, or even time of day (Tyler 1971, Morrison et al. 2002). Diel and tidal fish behaviors are often species- and age-specific (Weinstein et al. 1980, Levy and Cadenhead 1995, Neilson and Perry 2001), and the fish community of Cobscook Bay is composed of many species and age classes which change over the course of the year. The species composition of sampled fish may even differ between ebb and flood tides due to the difference in flow pattern through the bay. The ability to isolate a specific group of fish within a mixed fish community is limited when using hydroacoustics. This is especially true for single-beam systems, which cannot provide accurate target strength values without detailed knowledge

of the beam pattern and additional data processing methods (such as deconvolution; Simmonds and MacLennan 2005). Without isolating groups of fish, movement patterns of one group may be obscured by the movements of others. In this study, one of the best examples of a diel pattern in vertical fish distribution occurred in May 2011 at CB1 and CB2, and in June 2011 at CB2, when fish were in the upper layers of the water column during the day but spread throughout the lower layers at night (Fig. 6). This difference may have been because of large numbers of larval and juvenile herring during these surveys compared to other fish species. The fish community was likely to be more evenly mixed during the other surveys.

Fish density almost always increased near the sea floor, regardless of any diel or tidal variation in the vertical distribution of fish. Therefore, factors besides diel condition and tidal stage may have been shaping the vertical distribution of fish. The increase in fish density in the lower layers may correspond to the species present, which include winter flounder (*Pseudopleuronectes americanus*), tomcod (*Microgadus tomcod*), red, white, and silver hake, sculpins, and other species generally associated with the bottom (J. Vieser, unpublished information, 2013, University of Maine, School of Marine Sciences, Orono, ME 04469).

Pelagic fish might also seek shelter in the lower current speeds near the sea floor in the same way that species exhibiting selective tidal stream transport resist backward movement (McCleave and Kleckner 1982, Auster 1988). Auster (1988) described this behavior in cunner (*Tautoglabrus adspersus*) feeding on current-exposed surfaces: increasing current speed resulted in increasingly larger fish remaining above the seabed to forage, while smaller fish moved toward shelter on the bottom. If fish seek refuge near the sea floor during strong currents at the sites studied, analyzing behaviors during the slack tide (when pelagic species may leave the bottom layers) could aid in distinguishing diel behavioral patterns suppressed during the flowing tide. This

could allow the identification of pelagic and benthic species based on behavior as well as acoustic properties.

The timing of these surveys within each month likely affected the data collected and the patterns observed. Sampling continuously for one day per month provided a wealth of information for that day on a fine time scale, but data collected over 24 hours may not be representative of an entire month or season. In such a dynamic environment, there is likely to be variability from one day to the next which is difficult to quantify without sampling multiple sequential days. To achieve a more accurate understanding of fish vertical distribution and what causes it to change over time would likely require sampling multiple days throughout each month, although sampling the control site should help identify abnormal occurrences at the project site. One option for consideration in future studies is to deploy a surface- or bottom-mounted echosounder that automatically collects data on a preset, semi-continuous schedule. This would reduce the long-term cost and effort required to collect the data, while allowing the collection of high-resolution data over a long period of time. High-resolution data collected over long time periods is essential for quantifying natural variability and separating it from turbine effects.

Data collected to date were sufficient to characterize the relative abundance and vertical distribution of fish at the site that could be affected by the installation of a tidal turbine, despite any influence of survey timing and natural variation. The use of a control site, which has exhibited similar changes in fish density and vertical distribution as the project site (especially in 2011 and 2012; unpublished data), overcomes the potential for natural variation to mask effects of the turbine. The rotating blades of ORPC's TidGen[®] span the area between 6.7 and 9.5 m above the sea floor, directly in the center of the range analyzed (0-15 m above the bottom).

Within this range, fish density was generally greatest near the bottom (0-5 m). While this is below the height of the rotating turbine, these fish are still likely to interact with the solid support frame and foundation, and this could affect their vertical distribution post-deployment. Using the tests presented, we should be able to detect such changes in the future.

Continued data collection at the pilot project and control sites will improve understanding of the seasonal movements of fishes through the region, fishes' use of the water column in fast tidal currents, and any changes to fish density or vertical distribution associated with the introduction of the pilot device. The use of a split-beam echosounder (as in Melvin and Cochrane 2012) concurrently with the single-beam system (which must continue to be used for comparison to past data) will allow estimation of fish abundance and length, as well as direction of movement. Fish size has been found to affect their reactions to a hydrokinetic turbine (Viehman and Zydlewski this issue), so if the number and length of detected fish could be approximated, the potential rate of fish encounters with the turbine and supporting structures as well as their likely reactions could be estimated. Furthermore, analyzing the vertical distribution of various size groups may improve knowledge of the temporal and spatial use of the water column by different fish species relative to various environmental factors. This information is of particular interest to federal and state agencies making decisions concerning habitat protection (e.g., Essential Fish Habitat) and species regulations (e.g., the U.S. Endangered Species Act) in coastal zones, and can aid in management efforts as tidal power development continues.

Acknowledgements

We thank the employees of Ocean Renewable Power Company for their generous contribution of time and resources, Captain George Harris, Jr. and crew for their invaluable assistance in the field, and Donald Degan, Anna-Maria Mueller, and Michael Jech for their acoustics advice. We thank everyone who volunteered field time, Jeffrey Vieser for sharing his unpublished data, and the members of the Maine Tidal Power Initiative and Michael Peterson for their assistance. This work was supported by an award from the United States Department of Energy, project #DE-EE0003647. The views expressed herein are those of the authors and do not necessarily reflect the views of Ocean Renewable Power Company or any of its sub-agencies.

References

- AECOM. 2009. Appendix 9: Commercial Fisheries Studies-Phase I and Phase II. In: *Fundy Ocean Research Centre for Energy (Minas Basin Pulp and Power Co. Ltd.) Environmental Assessment*.
- Aprahamian, M.W., G.O. Jones, and P.J. Gough. 1998. Movement of adult Atlantic salmon in the Usk estuary, Wales. *Journal of Fish Biology* 53: 221-225.
- Arnold, G.P., M. Greer Walker, L.S. Emerson, and B.H. Holford. 1994. Movements of cod (*Gadus morhua* L.) in relation to the tidal streams in the southern North Sea. *ICES Journal of Marine Science* 51: 207-232.
- Athearn, K. and C. Bartlett. 2008. Saltwater fishing in Cobscook Bay: Angler profile and economic impact. *Maine Sea Grant Marine Research in Focus* 6.
- Auster, P. J. 1988. A review of the present state of understanding of marine fish communities. *Journal of Northwest Atlantic Fishery Science* 8: 67-75.
- Bennett, W.A., W.J. Kimmerer, J. R. Burau. 2002. Plasticity in vertical migration by native and exotic estuarine fishes in a dynamic low-salinity zone. *Limnology and Oceanography* 47(5): 1496-1507.
- Brawn, V.M. 1960. Seasonal and diurnal vertical distribution of herring (*Clupea harengus* L.) in Passamaquoddy Bay, N.B. *Journal of the Fisheries Research Board of Canada* 17: 699-711.
- Brooks, D.A. 2004. Modeling tidal circulation and exchange in Cobscook Bay, Maine. *Fisheries Bulletin* 11: 23-50.
- Castonguay, M. and D. Gilbert. 1995. Effects of tidal streams on migrating Atlantic mackerel, *Scomber scombrus* L. *ICES Journal of Marine Science* 52: 941-954.
- Charlier, R.H. and C.W. Finkl. 2010. Ocean energy: tide and tidal power. Berlin: Springer-Verlag.
- Clark, C.W. and D. A. Levy. 1988. Diel vertical migrations by juvenile sockeye salmon and the antipredation window. *The American Naturalist* 131(2): 271-290.
- Dadswell, M.J. and R.A. Rulifson. 1994. Macrotidal estuaries: a region of collision between migratory marine animals and tidal power development. *Biological Journal of the Linnean Society* 51: 93-113.

- de Veen, J.F. 1978. On selective tidal transport in the migration of North Sea plaice (*Pleuronectes platessa*) and other flatfish species. *Netherlands Journal of Sea Research* 12: 115-147.
- Foote, K.G. 1983. Linearity of fisheries acoustics, with addition theorems. *Journal of the Acoustical Society of America* 73(6): 1932-1940.
- Foote, K.G., H.P. Knudsen, G. Vestnes, D.N. MacLennan, and E.J. Simmonds. 1987. Calibration of acoustic instruments for fish density estimation: a practical guide. *ICES Cooperative Research Report* 144.
- Gauthier, S. and G.A. Rose. 2002. Acoustic observation of diel vertical migration and shoaling behavior in Atlantic redfishes. *Journal of Fish Biology* 61: 1135-1153.
- Gill, A.B. 2005. Offshore renewable energy: ecological implications of generating electricity in the coastal zone. *Journal of Applied Ecology* 42: 605-615.
- Greer Walker, M., F.R. Harden Jones, and G.P. Arnold. 1978. The movements of plaice (*Pleuronectes platessa* L.) tracked in the open sea. *Journal du Conseil International pour l'Exploration de la Mer* 38: 58-86.
- Hartill, B.W., M.A. Morrison, M.D. Smith, J. Boubée, and D.M. Parsons. 2003. Diurnal and tidal movements of snapper (*Pagrus auratus*, Sparidae) in an estuarine environment. *Marine and Freshwater Research* 54: 931-940.
- Jensen, O. P., S. Hansson, T. Didrikas, J. D. Stockwells, T. R. Hrabik, T. Axenrot, J. F. Kitchell. 2011. Foraging, bioenergetic and predation constraints on diel vertical migration: field observations and modeling of reverse migration by young-of-the-year herring *Clupea harengus*. *Journal of Fish Biology* 78: 449-465.
- Jovanovic, B., C. Longmore, A. O'Leary, and S. Mariani. 2007. Fish community structure and distribution in a macro-tidal inshore habitat in the Irish Sea. *Estuarine, Coastal and Shelf Science* 75: 135-142.
- Kelley, J.T. and A.R. Kelley. 2004. Controls on surficial materials distribution in a rock-framed, glaciated, tidally dominated estuary: Cobscook Bay, Maine. *Northeast Naturalist* 11: 51-74.
- Knudsen, F.R., A. Hawkins, R. McAllen, and O. Sand. 2009. Diel interactions between sprat and mackerel in a marine lough and their effects upon acoustic measurements of fish abundance. *Fisheries Research* 100: 140-147.

- Konietschke, F. 2012. nparcomp: Perform multiple comparisons and compute simultaneous confidence intervals for the nonparametric relative contrast effects. R package version 2.0. <http://CRAN.R-project.org/package=nparcomp>.
- Krumme, U. 2004. Patterns in tidal migration of fish in a Brazilian mangrove channel as revealed by a split-beam echosounder. *Fisheries Research* 70: 1-15.
- Krumme, U. and U. Saint-Paul. 2003. Observations of fish migration in a macrotidal mangrove channel in Northern Brazil using a 200-kHz split-beam sonar. *Aquatic Living Resources* 16: 175-184.
- Kubecka, J. and A. Duncan. 1998. Diurnal changes of fish behavior in a lowland river monitored by a dual-beam echosounder. *Fisheries Research* 35: 55-63.
- Lacoste, K.N., J. Munro, M. Castonguay, F.J. Saucier, and J.A. Gagné. 2001. The influence of tidal streams on the pre-spawning movements of Atlantic herring, *Clupea harengus* L., in the St Lawrence estuary. *ICES Journal of Marine Science* 58: 1286-1298.
- Larsen, P.F. and D.E. Campbell. 2004. Ecosystem modeling in Cobscook Bay, Maine: a summary, perspective, and look forward. *Northeast Naturalist* 11: 425-438.
- Levy, D.A. 1990. Reciprocal diel vertical migration behavior in planktivores and zooplankton in British Columbia lakes. *Canadian Journal of Fisheries and Aquatic Sciences* 47: 1755-1764.
- Levy, D.A. and A.D. Cadenhead. 1995. Selective tidal stream transport of adult sockeye salmon (*Oncorhynchus nerka*) in the Fraser River Estuary. *Canadian Journal of Fisheries and Aquatic Sciences* 52: 1-12.
- MacDonald, J.S., M.J. Dadswell, R.G. Appy, G.D. Melvin, and D.A. Methven. 1984. Fishes, fish assemblages, and their seasonal movements in the lower Bay of Fundy and Passamaquoddy Bay. *Fishery Bulletin* 82: 121-139.
- McCleave, J.D. and R.C. Kleckner. 1982. Selective tidal stream transport in the estuarine migration of glass eels of the American eel (*Anguilla rostrata*). *ICES Journal of Marine Science* 40: 262-271.
- Melvin, G.D. and N.A. Cochrane. 2012. A preliminary investigation of fish distributions near an in-stream tidal turbine in Minas Passage, Bay of Fundy. *Canadian Technical Report of Fisheries and Aquatic Sciences* 3006. St. Andrews, New Brunswick.
- Moore, A., M. Ives, M. Scott, and S. Bamber. 1998. The migratory behavior of wild sea trout (*Salmo trutta* L.) smolts in the estuary of the River Conwy, North Wales. *Aquaculture* 198: 57-68.

- Morrison, M.A., M.P. Francis, B.W. Hartill, and D.M. Parkinson. 2002. Diurnal and tidal variation in the abundance of the fish fauna of a temperate tidal mudflat. *Estuarine, Coastal and Shelf Science* 54: 793-807.
- Neilson, J.D. and R.I. Perry. 2001. Fish Migration, Vertical. In *Encyclopedia of Ocean Sciences (second edition)*, eds. J. H. Steel, K. K. Turekian, S. A. Thorpe. 2: 411-416. Oxford: Academic Press.
- Neilson, J.D., D. Clark, G. D. Melvin, P. Perley, and C. Stevens. 2003. The diel vertical distribution and characteristics of pre-spawning aggregations of Pollock (*Pollachius virens*) as inferred from hydroacoustic observations: the implications for survey design. *ICES Journal of Marine Science* 60: 860-871.
- Pitcher, T.J. 2001. Fish Schooling. In *Encyclopedia of Ocean Sciences (second edition)*, eds. J. H. Steel, K. K. Turekian, S. A. Thorpe. 2: 432-444. Oxford: Academic Press.
- Polagye, B., B. Van Cleve, A. Copping, and K. Kirkendall. 2011. Environmental effects of tidal energy development. U.S. Dept. Commerce, NOAA Tech. Memo. F/SPO-116.
- Ribeiro, J., L. Bentes, R. Coelho, J.M.S. Gonçalves, P.G. Lino, P. Monteiro, and K. Erzini. 2006. Seasonal, tidal and diurnal changes in fish assemblages in the Ria Formosa lagoon (Portugal). *Estuarine, Coastal and Shelf Science* 67: 461-474.
- Sakabe, R. and J.M. Lyle. 2010. The influence of tidal cycles and freshwater inflow on the distribution and movement of an estuarine resident fish *Acanthopagrus butcheri*. *Journal of Fish Biology* 77: 643-660.
- Saunders, R., M. Hachey, and C.W. Fay. 2006. Maine's diadromous fish community. *Fisheries* 31: 537-547.
- Shields, M. A., A. T. Ford, and D. K. Woolf. 2008. Ecological considerations for tidal energy development in Scotland. 10th World Renewable Energy Conference, 19-25 July, Glasgow, Scotland.
- Shields, M. A., L. J. Dillon, D. K. Woolf, and A. T. Ford. 2009. Strategic priorities for assessing ecological impacts of marine renewable energy devices in the Pentland Firth (Scotland, UK). *Marine Policy* 33:635-642.
- Simmonds, J. and D. MacLennan. 2005. Fisheries Acoustics: Theory and Practice. 2nd ed. Oxford: Blackwell Science.
- Stasko, A.B. 1975. Progress of migrating Atlantic salmon (*Salmo salar*) along an estuary, observed by ultrasonic tracking. *Journal of Fish Biology* 7: 329-338.

Tyler, A.V. 1971. Periodic and resident components in communities of Atlantic fishes. *Journal of the Fisheries Research Board of Canada* 28: 935-946.

Weinstein, M.P., Weiss SL, Hodson RG, Gerry LR. 1980. Retention of three postlarval fishes in an intensively flushed tidal estuary, Cape Fear River, North Carolina. *Fisheries Bulletin* 78: 419-436.

Wheeler, B. 2010. ImPerm: Permutation tests for linear models. R package version 1.1-2. <http://CRAN.R-project.org/package=ImPerm>.

Figure Captions

Fig. 1 Ocean Renewable Power Company's TidGen[®] device (drawing courtesy of ORPC), installed in outer Cobscook Bay in August 2012.

Fig. 2 Left: Map of Cobscook Bay, Maine. Right: Sampling sites in the outer bay, showing bottom depth (adapted from Kelley and Kelley 2004). Mean ebb and flood positions are indicated by the circles at each end of the white lines. CB1 is the Cobscook Bay 1 “project” site and CB2 is the Cobscook Bay 2 “control” site.

Fig. 3 Mean water column (0-15 m above sea floor) volume backscatter, S_v , of each survey. Horizontal lines are median S_v , filled rectangles indicate the interquartile range, and whiskers extend to the 5th and 95th percentile. Month of survey is shown along horizontal axis. Significant differences between the sites (project, CB1; control, CB2) are indicated by *.

Fig. 4 Mean water column (0-15 m above sea floor) volume backscatter, S_v , of each tidal stage sampled (day ebb, day flood, night ebb, and night flood) in 2011. Horizontal lines are median S_v ; filled rectangles indicate the interquartile range, and whiskers extend to the 5th and 95th percentile. Month of survey is shown along the horizontal axis. Significant differences, determined for each survey using multiple comparisons, are indicated with letters *a* and *b*, with group *a* having the highest values and group *b* having the lowest. May and June lack night flood data because nights were too short to encompass two complete tidal stages.
























Fig. 5 Mean vertical distribution of fish for each survey in 2010 and 2011, at CB1 and CB2. Vertical axis is distance above bottom (m). Each horizontal bar represents the proportion of the water column's total area backscatter (s_a) within each 1 m layer. Error bars show one standard error. Data are for the lower 15 m at CB1 and for the lower 26 m at CB2, which is a deeper site. Horizontal dashed lines indicate the depth spanned by the tidal energy device's turbine (not

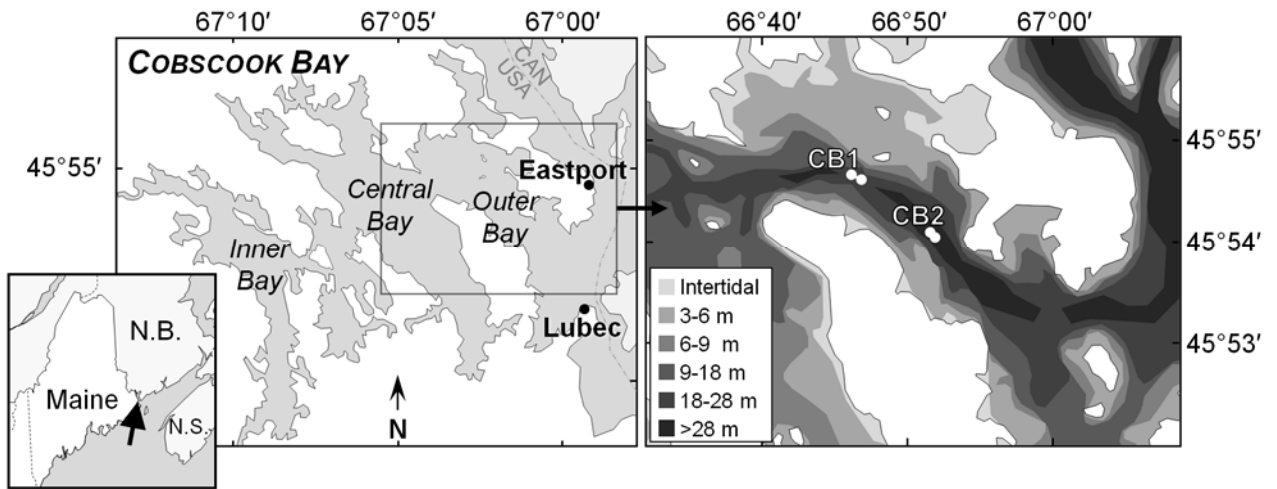
present during this study). A blank box indicates no data collected; 'X' indicates data were collected, but not usable (June 2010, CB1). May 2010 (†) data were limited to the flood tides, and in November 2010 (‡), only the first half of the CB1 survey was conducted due to inclement weather. The mean water column s_a for each survey is shown in the upper right of each box (units of $m^2 \cdot m^{-2}$).

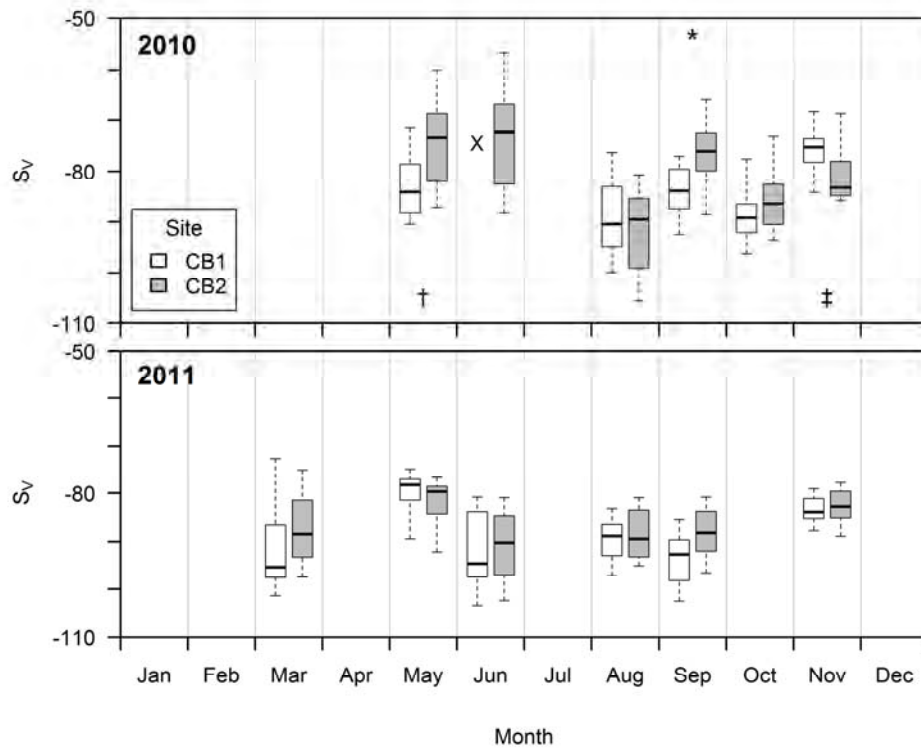
Fig. 6 Mean vertical distribution of fish for each tidal stage at CB1 and CB2 in 2011: day ebb (DE), day flood (DF), night ebb (NE) and night flood (NF). Day distributions are shown in gray; night, in black. Vertical axis is distance above bottom. Each horizontal bar represents the proportion of the water column's total area backscatter (s_a) within each 1 m layer during that tidal stage. Error bars show one standard error. Data are for the lower 15 m at CB1 and for the lower 26 m at CB2, which is a deeper site. Horizontal dashed lines indicate the depth spanned by the tidal energy device's turbine (not present during this study). Blank boxes in May and June indicate no data collected during that time period because nights were too short. The mean water column s_a for each time period is shown in the upper right of each box (units of $m^2 \cdot m^{-2}$).

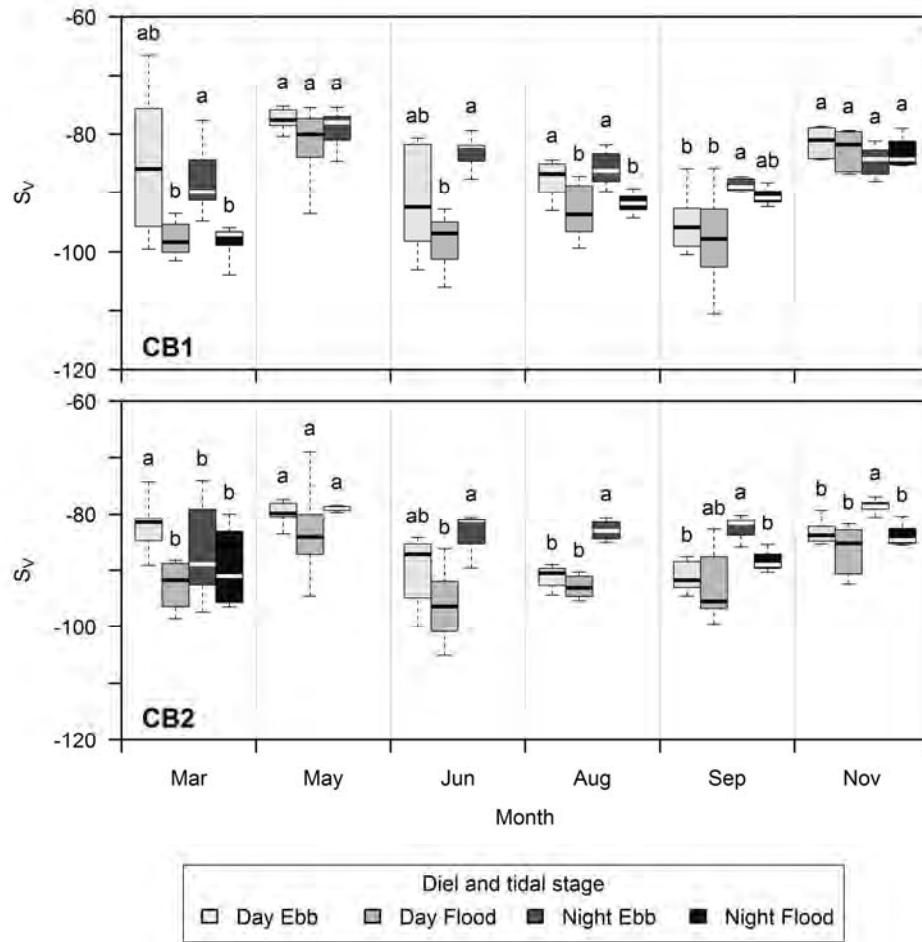
Tables

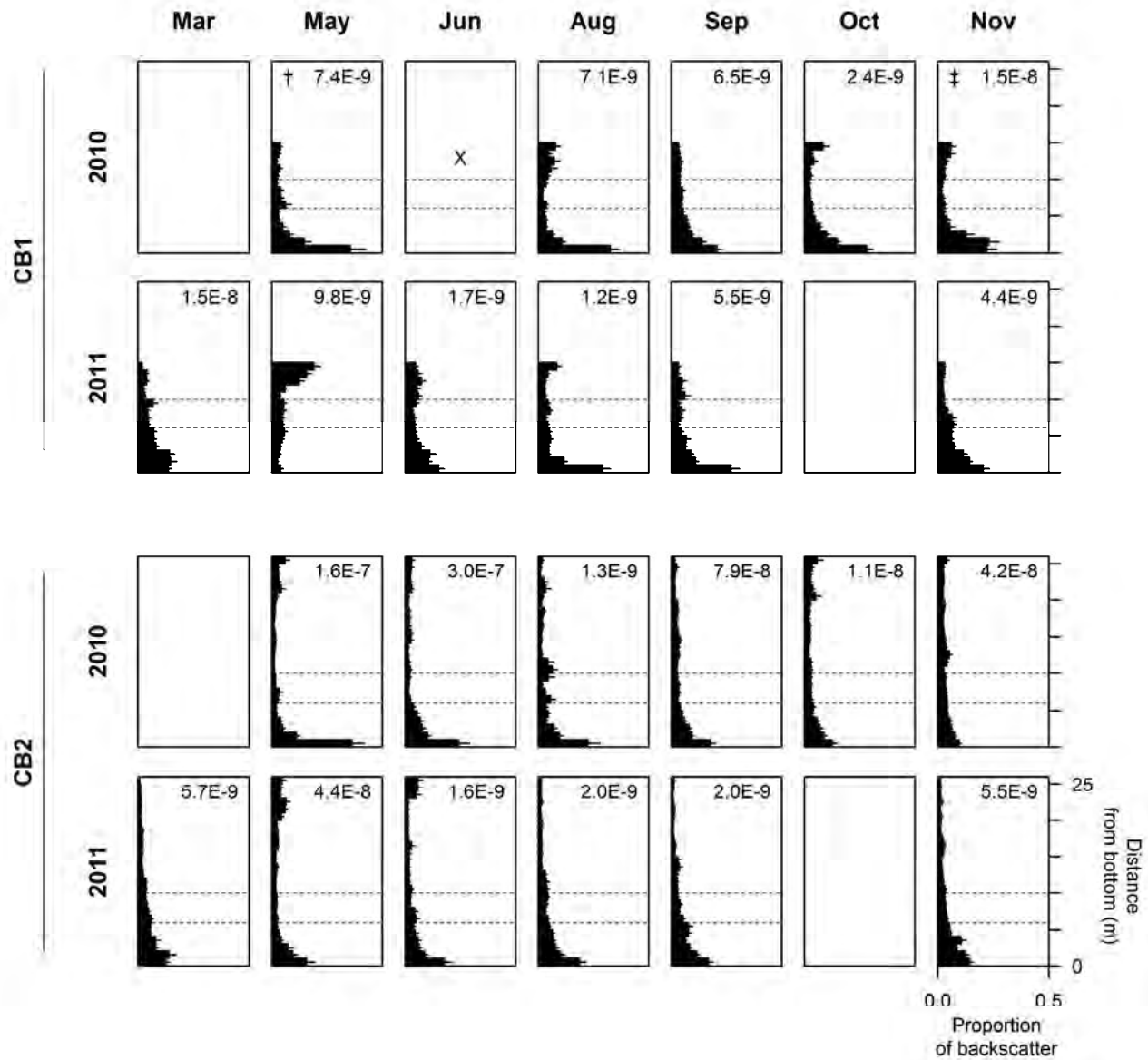
Table 1 Sampling dates, times, and basic environmental data for each survey.

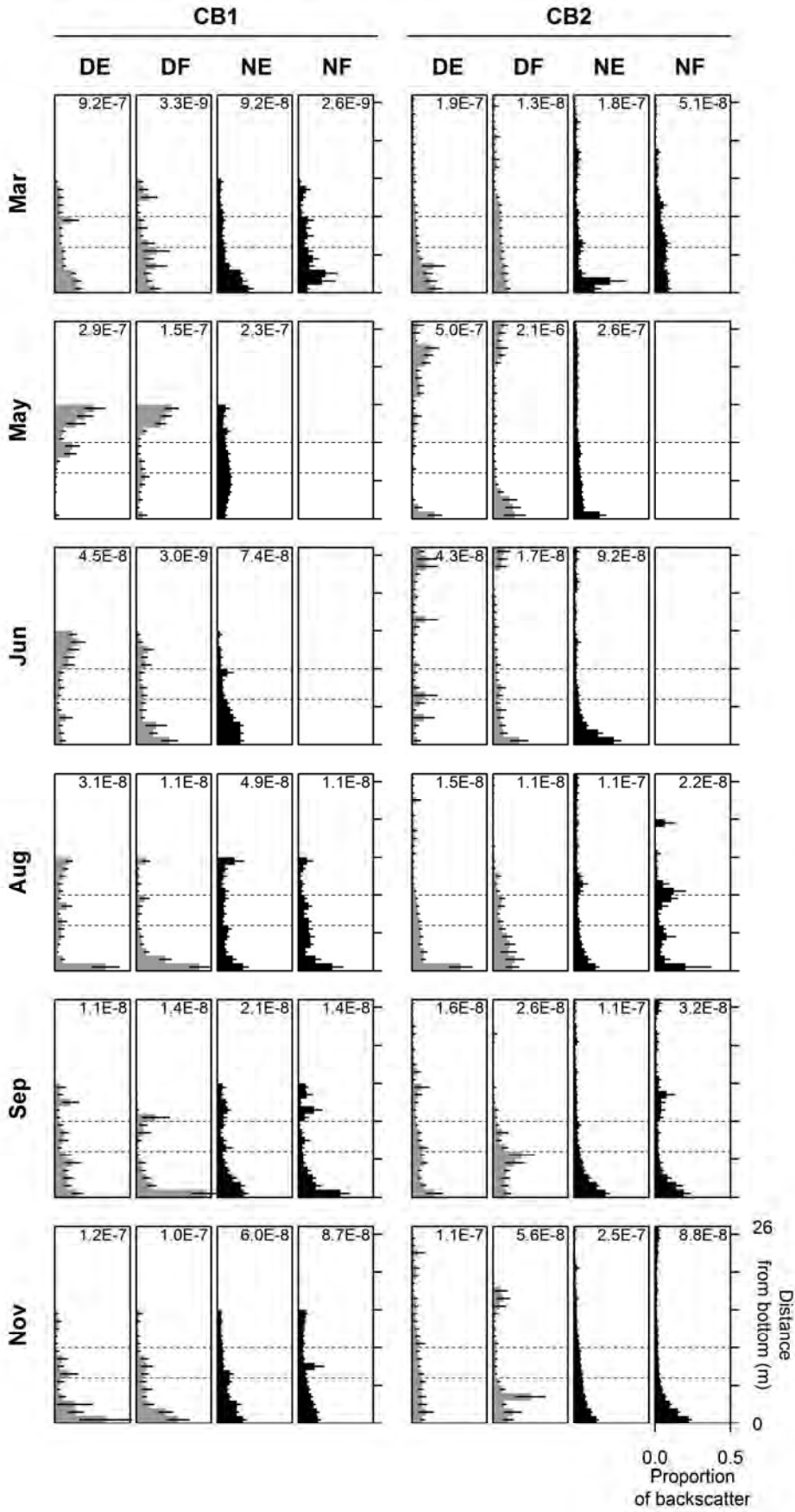
Year	Month	Site	Start Day	Start time	Survey duration (hrs)	Mean surface temp. (°C)	Tidal depth range (m)	Moon phase
2010	May	CB1	19	06:30	24	7.5	25 – 49	
		CB2	21	09:00	24	7.8	31 – 41	
	Jun	CB2	13	06:40	25	9.4	33 – 40	
	Aug	CB1	5	08:15	24	13.3	25 – 30	
		CB2	4	07:45	24	13.3	35 – 40	
	Sep	CB1	6	06:10	24	14.3	24 – 31	
		CB2	7	07:00	24	13.9	34 – 45	
	Oct	CB1	17	13:40	24	11.9	26 – 35	
		CB2	19	17:20	21	11.7	36 – 42	
	Nov	CB1	20	07:30	9	9.6	24 – 31	
CB2		17	06:00	25	9.6	36 – 45		
2011	Mar	CB1	15	07:00	24	2.9	25 – 30	
		CB2	16	22:15	24	3.0	34 – 41	
	May	CB1	28	08:00	24	7.9	24 – 30	
		CB2	27	07:45	24	7.8	32 – 41	
	Jun	CB1	26	08:00	24	10.2	24 – 30	
		CB2	27	08:50	24	10.4	33 – 40	
	Aug	CB1	22	05:45	24	13.8	25 – 30	
		CB2	23	06:20	24	13.5	35 – 40	
	Sep	CB1	22	06:20	24	13.0	24 – 29	
		CB2	23	07:00	24	12.9	33 – 40	
Nov	CB1	16	14:00	24	10.5	24 – 30		
	CB2	18	14:40	24	10.5	33 – 40		











Appendix Task 2-4

An initial assessment of fish presence and vertical distribution at two sites (control and proposed tidal power site) in Cobscook Bay

Report prepared for:
Ocean Renewable Power Company

By

Gayle Zydlewski¹, James McCleave¹, Haley Viehman¹, and Kaitlyn Harmon²

1: University of Maine, School of Marine Sciences

2: Maine Maritime Academy, Corning School of Ocean Studies

December 2010

Table of Contents

Table of Contents.....	179
Executive Summary	181
1.1 Study Context	182
1.2 Study Purpose	183
1.3 Study Design.....	185
1.3a Fish presence, pre-deployment of the TidGen™ Power System.....	185
1.3b. Direct observation of interactions with Beta TGU	186
1.4 Acoustic target identification.....	187
2. Methods	188
2.1 Fish presence, pre-deployment of the TidGen™ Power System.....	188
2.1a Hydroacoustics data collection.....	188
2.1b Research platform.....	190
2.1c Sampling design	191
2.1d Hydroacoustics data analysis.....	193
2.2 Acoustic target identification.....	197
2.2a DIDSON.....	197
2.2b Netting.....	197
3. Results.....	198
3.1 Fish presence, pre-deployment of the TidGen™ Power System	198
3.1a Statistical assessment of environmental factors	203
3.1ai. Intra-annual (2010) factors.....	204
Response variable: Count	204
Counts at depth of interest (proposed depth of TidGen™ Power System: foils between 5 and 10 m above seafloor)	207
Response variable: Median height off the seafloor and IQR (i.e., vertical extent).....	208
3.1aii Interannual effects.....	210
4. Conclusions	217

4.1 Fish presence pre-deployment of TidGen™ Power System	217
4.2 Direct observation of interactions with Beta TGU	218
4.3 Final considerations.....	219
5. Future Work	219
5.1 Reducing the time from data collection to interpretation.....	219
5.2 Hydroacoustics for species (or target size) validation.....	219
5.3 Netting for species validation.....	220
5.4 Expanded fish assessments	220
6. Acknowledgements	220
7. References	222
Appendix 1. Summary of midwater net tows made in Outer Cobscook Bay.....	224
Appendix 2. Species and numbers of fishes netted.....	225
Appendix 3. Table of data contained in Figure 13.....	226
Appendix 4. Table of data contained in Figure 14.....	227
Appendix 5. Summary of effects for 2010 comparisons at CB2.	229

Executive Summary

This project was initiated in the summer of 2009 when the University of Maine received funding from the US Department of Energy to conduct research associated with the development of tidal power. A primary focus of the research was to develop an understanding of how fish would be affected by tidal power development. At the time, Ocean Renewable Power Company (ORPC) had initiated planning for an in-stream tidal power deployment in the Cobscook and Passamaquoddy Bays of eastern Maine. There was little information concerning fishes in this region of eastern Maine, particularly those that may be in the water column where a tidal device would be placed. ORPC needed this information to move their project forward, and University of Maine researchers saw scientific value in helping close the information gap. From 2009 to date, the goal of the University's research in eastern Maine has been to gather baseline (pre-deployment) data concerning fish distribution in the water column. Studies are being conducted at potential tidal power locations as well as control locations, with the intent of ultimately assessing effects during device deployment. A secondary goal has been to observe interactions of fish with a commercial scale test device (called the Beta Turbine Generator Unit or Beta TGU) prior to long-term deployment; including validation of previously untested methods for assessment.

This report details the presence and distribution of acoustic targets (fish) in the water column at two sites in Cobscook Bay over four months in 2010 (one of these sites was also assessed during two months in 2009). One site is the location of the planned deployment of an in-stream tidal power system mounted on a bottom support frame (ORPC's TidGen™ Power System). This would occur under a Pilot Project License to be obtained from the Federal Energy Regulatory Commission (FERC) and a General Permit for Tidal Testing to be obtained from the Maine Department of Environmental Protection. The other site is a control site. Analyses of these data indicate that fish were present at both locations in all months examined (May, June, August, and September of 2010). There were more individual targets and fewer schools detected at the proposed deployment site than at the control site. In all months schools and individuals were primarily in the upper 25 m ($89 \pm 11\%$) of the water column (though in June the distribution of schools was slightly deeper). More than 50% of the schools and individual targets detected were 20 – 25 m above the seafloor. The proposed TidGen™ Power System deployment will encompass the lowest 10 m ($35 \pm 4\%$) of the water column. Fish number and distribution in the water column were examined with respect to diel and tidal cycles and were found to vary

with site, month, and year. As research continues, it is possible that more specific daily or seasonal patterns will arise. These patterns will provide a better understanding of the probability of fish interacting with the TidGen™ Power System during different tides and seasons. To date, numbers of schools and individual targets at the depth of the proposed deployment are low compared to the remainder of the water column. Targets near the seafloor are primarily individuals, not abundant schooling species, and depending on population status, every individual can be important at the population level. Future work includes further analyses of the baseline data collected to date, those data collected in fall and winter (2010 and 2011), data to be collected in 2011, and those collected during deployment (through 2013). Future analyses include extraction of individual target sizes, target species validation (as possible), and streamlining data collection and analyses.

Results from work conducted at the Beta TGU (observation of responses to a test device) are preliminary but have indicated two different behavioral responses to the device. Individual fish have responded to the Beta TGU with avoidance and some moved through the device and continued to move with the water current. However, data analysis is not complete enough to determine if these will be the only interactions at a tidal power device. Future work includes assessment of all device interaction data collected.

1. Introduction

1.1 Study Context

Ocean Renewable Power Company (ORPC) plans to deploy tidal energy technology in Cobscook Bay, Maine. In anticipation, University of Maine researchers initiated a sampling design to acquire a better understanding of the fish resources in the region. Studies were initiated in summer 2009 with funding from the US Department of Energy to the University of Maine's Maine Tidal Power Initiative (MTPI).

Maine Tidal Power Initiative

MTPI is developing resource and environmental assessment protocols associated with tidal power development. The protocols will be transferrable throughout Maine and the US to evaluate tidal energy resources and better understand the potential impact of this development on the environment. Site-specific work is focused on Cobscook Bay/Western Passage near Eastport, Maine, which has been identified as potentially the most viable tidal energy development area on the East Coast of the US. A smaller scale site in another part of Maine will also

be used for some initial demonstrations of methodology. MTPI efforts are designed around a four-pronged approach: (1) resource assessment; (2) environmental assessment; (3) development of tidal turbine designs; and (4) community assessment.

Relevant to this report are the details related to approach (2), environmental assessment, which focuses on fishes and other pelagic macrofauna (marine life). Active acoustic, or hydroacoustic, surveys are being used in tidal regions at multiple locations in Maine in a standard study design that includes data collection prior to tidal device deployment, during device deployment and at control sites during all collection periods. Surveys use low frequency echosounder equipment (SIMRAD single beam systems) to look at the entire water column and a higher frequency Dual-Frequency Identification Sonar (DIDSON) to look at the top 10 m of water for target verification and to aid in species identification. Acoustic survey data need to be validated/verified with visual observations, rod and reel fishing, midwater trawling (netting), and local knowledge. Acoustic surveys are performed from a moored platform (vessel) to determine presence and depth distribution of fish and schools during seasons of high abundance. This work has been initiated in Western Passage and Cobscook Bay and will continue there.

The sheer quantity of data accumulated from active acoustic surveys with multiple acoustic technologies over multiple years and seasons can create a bottleneck in data analysis that can slow the progress of the industry relying on these datasets to make forward-looking decisions. We are working to streamline the link between data collection and decision-making by using specialized analysis software and developing an automated processing routine.

1.2 Study Purpose

Potential environmental effects of tidal power development have been hypothesized by multiple groups, including the US Department of Energy (2009). Two potential effects are strike and interference with animal movements and migrations. UMaine's work at ORPC sites will provide a more completely understanding of the impact of tidal energy devices since studies to date are not based on actual deployment experience. Understanding any of these effects will be dependent on the receptor of the effect, e.g. the "animal." To understand the impact of tidal energy devices on animal movement and migration, migration and movement patterns must be understood prior to the deployment of devices.

With the pending deployment of an ORPC tidal energy device in Cobscook Bay, a literature review of the movement and migration patterns of fishes in the region was conducted. The presence and composition of pelagic fishes, i.e., those most likely to be affected by hydro-kinetic power generation, are poorly understood. Most studies have concentrated on near-bottom species, vulnerable to trawling. In addition, most trawling studies in the literature occurred in the adjacent Passamaquoddy Bay and are dated (Tyler 1971, MacDonald et al. 1984). Unfortunately, even these studies are not always in agreement on seasonality or presence of key species. Known key species in the area are alewife and blueback herring (Koch 1974 and others), rainbow smelt, silver hake, white hake (Tyler 1971); and Atlantic mackerel (Athearn & Bartlett 2008). Studies reported in the literature have not considered the relative abundance and vertical distribution of pelagic species in relation to year, season, time of day, and stage of tide (except for juvenile Atlantic herring; Brawn 1960).

Acoustic surveys, when coupled with pelagic mid-water trawling, could overcome deficiencies in available information. Results provide estimates of the likelihood of fish being in the depth bin of the turbine on seasonal, diel, and tidal frequencies. Inclusion of a control site along with the potential deployment site provides an account of variability on various time scales (inter-annual, seasonal, diel, and tidal).

Future studies, i.e., during the deployment of ORPC's TidGen™ Power System, will provide a unique opportunity to examine the potential effects of commercial-scale turbine operation on fish behavior (turbine site vs. control site). This sampling, to be conducted under a pilot project license issued by FERC, will provide data for assessing the impacts of a FERC-licensed project.

Specific project objectives include the assessment of indirect and direct impacts of tidal power devices. To document indirect impacts, we quantified (pre-deployment) the spatial and temporal changes in fish vertical distribution in the water column (seasonal, diel, and tidal) at the proposed deployment site in Cobscook Bay. To document potential direct impacts of tidal power devices, limited monitoring was conducted on ORPC's Beta Turbine Generator Unit (TGU), which was mounted on a test platform. This project involved the largest ocean energy device ever deployed in the US. Limited data from this portion of the study are included in this report.

1.3 Study Design

The study consisted of two parts: (1) pre-deployment baseline documentation of fish presence and distribution in the water column, and (2) observations of fish response to the ORPC Beta TGU. Data reported for part one is pre-deployment and therefore does not involve a tidal device. However, reference to the bottom-mounted ORPC TidGen™ Power System (Figure 1a) is made to provide an idea of the area of the water column where impacts may occur. Data reported for part two are preliminary and directly involve assessments at the ORPC's Beta TGU (Figure 1b).

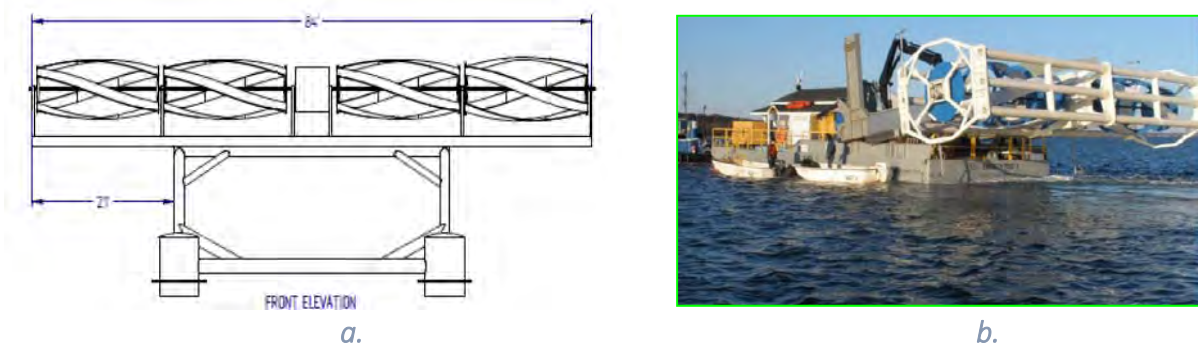


Figure 1. Schematic drawing of the Ocean Renewable Power Company proposed bottom-mounted ORPC TidGen™ Power System (a) and photograph of the Beta TGU (b).

1.3a Fish presence, pre-deployment of the TidGen™ Power System

Fish presence and depth distribution in the water column were documented at sites chosen for tidal device deployment, i.e., high energy, channel habitats. The “impact” site (which is pre-deployment for this report) is the site ORPC designated for deployment of their first bottom-mounted TidGen™ Power System (Figure 2, CB1). A control site was also chosen for pre-deployment comparison and post-deployment assessment of effects (Figure 2, CB2).

Single beam hydroacoustics were used to provide the vertical distribution of all fish species. Species identification and population estimates were beyond the scope of this project. Data provided are relative abundance (density per volume of water) and vertical distribution of fishes in the water column in two locations in Cobscook Bay (Table 1). Variation in fish presence and distribution were assessed based on year, site, season, tide, and diel factors (Table 2).

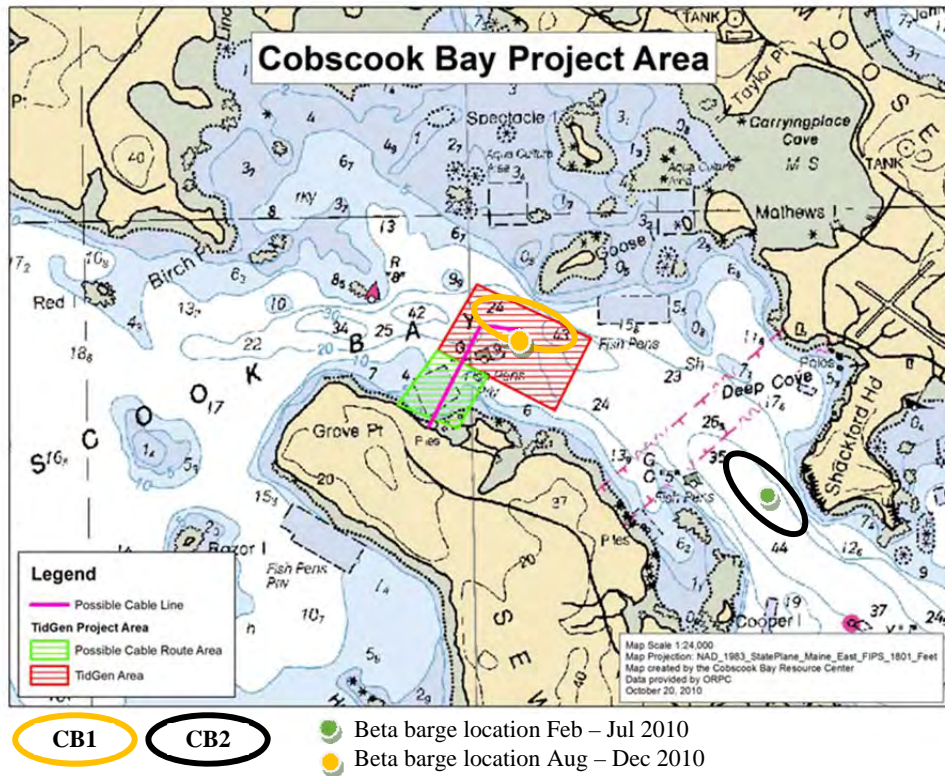


Figure 2. Chart showing Lower Cobscook Bay and the Ocean Renewable Power Company proposed project deployment site and

Table 1. Sampling frequency by year, sampling type, number of sites and season. Each site was sampled for 24 hours, resulting in samples from two tidal cycles, day and night.

Year	Sampling type	Number of sampling locations	Season (month)
2009	Active hydroacoustics	1 site (control)	Aug, Sep
2010	Active hydroacoustics	2 sites (project and control)	May, June, Aug, Sep
2010	Mid-water netting	2 sites (project and control)	May, June, August

1.3b. Direct observation of interactions with Beta TGU

Study plans included sampling monthly at the ORPC test platform (Figure 3). Data collection was opportunistic and dependent on the turbine being in the water over a 24-hour period to assess day/night differences. Acoustic gear was

used to assess individual and group behavior upstream and downstream of the device.

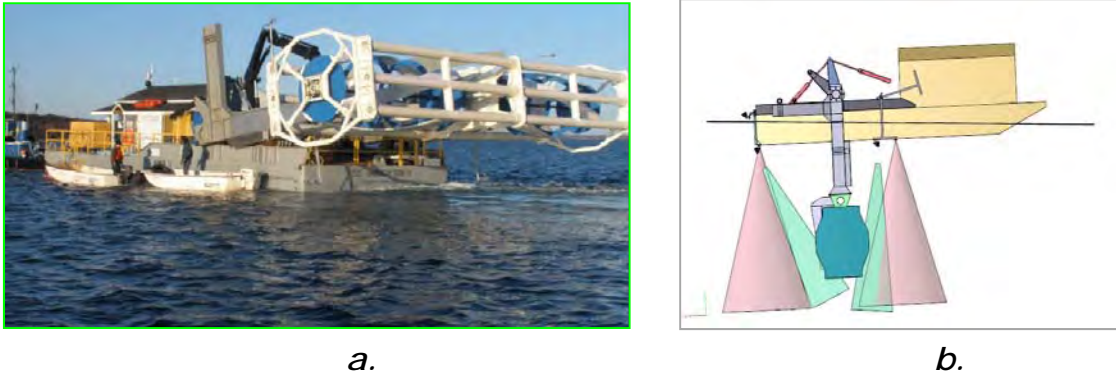


Figure 3. ORPC Beta TGU and platform photograph (a) and schematic (b). In (b) the pink cones indicate the SIMRAD sampling area and green cones indicate DIDSON sampling cones.

1.4 Acoustic target identification

Targets detected using active hydroacoustic echo sounders (e.g., SIMRAD) represent a discontinuity in density within the medium (seawater, in this case). An acoustic signal is returned when sound reflects off the boundary between regions of different densities. Entrained air bubbles can return a strong signal, since the air has a very different density than water. The surface of an animal reflects some sound, though the echo strength of a fish is dominated by returns from its gas-filled swimbladder, if it has one. An Atlantic mackerel, which does not have a swim bladder, will return a weaker signal than a herring of equivalent size, which does have a swimbladder. The size of the smallest detectable object is dependent on the frequency of sound produced (discussed later) and the speed of sound in the acoustic medium. For these reasons, acoustic target identification (and species validation) is confounded by many factors. In order to get an idea of the identity of an acoustic target, physical capture (netting) and visual observation (DIDSON) were used. A mid-water net was proposed for fishing in spring and summer 2010. The goal of the netting was to evaluate species composition of hydroacoustic targets. DIDSON, an acoustic imaging system, was used to provide a visual presentation of fish shape and size for fish in the upper 10 m of the water column.

2. Methods

2.1 Fish presence, pre-deployment of the TidGen™ Power System

2.1a Hydroacoustics data collection

A SIMRAD ES60 commercial fisheries echo sounder (General Purpose Transceiver, GPT) and a dual-frequency (38kHz and 200kHz) Combi W transducer (Figure 4) were used for acoustic surveys of the water column from surface to bottom, up to a range of 200 meters. A wide angle (31°x31°), single-beam transducer was chosen because it is significantly less expensive and covers more area at shallower depths than a split-beam transducer. However, it provides no information on a target's location within the beam, introducing uncertainty in target strength analysis (since targets appear stronger in the middle of the beam than at the edge).

The GPT was operated at 1 to 2 pings per second and pulse widths of 0.256 to 1 millisecond. A Sound Metrics Corporation DIDSON US300 acoustic imaging camera, operating at 1.8 MHz, was used to survey the upper 10-12 meters of the water column in detail.

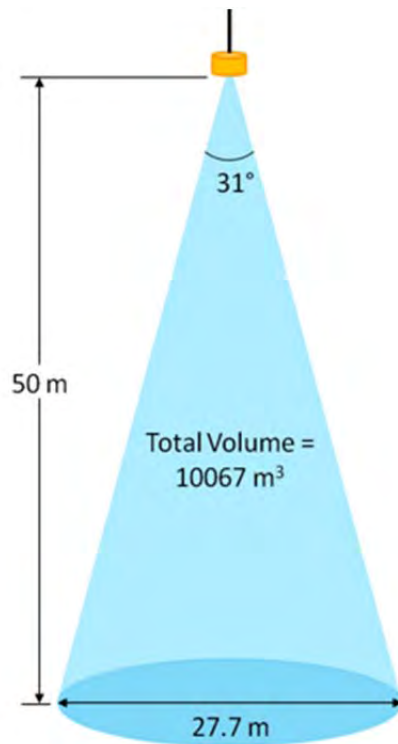


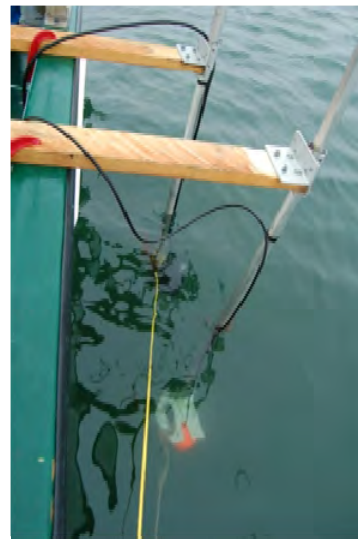
Figure 4. Region ensounded by the SIMRAD 38/200 Combi W transducer at the maximum observed depth (50 m).

2.1b Research platform

Acoustic surveys were conducted from a 36-foot fishing vessel. The SIMRAD and DIDSON transducers were mounted on the port side of the vessel, approximately 1 m below the surface with transducers aimed vertically downward (Figure 5). The DIDSON was mounted so the 29° beam angle was oriented parallel to the vessel's axis, therefore approximately parallel to the current. Both units were operated using deep-cycle marine batteries and laptops were powered with a DC-AC inverter (Figure 6).



a.



b.

Figure 5. (a) Transducer mount arrangement on research vessel showing mounting boards clamped across the gunwales and the SIMRAD (orange) and DIDSON (black) transducers above the water. (b) SIMRAD and DIDSON transducers in operating position, 1 m below the water surface.



Figure 6. Arrangement of DIDSON control computer, SIMRAD control computer and transceiver unit behind (right), and storage batteries for operation of the DIDSON and SIMRAD transceivers.

2.1c Sampling design

The vessel was moored at selected sites (Figure 2, CB1 and CB2) for 24-hour periods (Table 2). The tidal flow replaced the need for transects that are typical of lake and open ocean hydroacoustic surveys. In our case, instead of passing the vessel over acoustic targets, the current carried them past the vessel. Furthermore, the goal of the project was to assess fish presence and distribution at a specific location, e.g., where a tidal device may be deployed. The twenty-four hour survey period covered day and night, and one tidal cycle (ebb and flood) for each. This provided an estimate of the number of fish moving past the location, with respect to both tidal stage and diel cycle.

Weather and water observations were made approximately every half hour during each survey. These observations included cloud cover, sun or moon visibility, estimated wind speed and direction, estimated wave height, surface current speed, surface temperature, and (in 2009 only) surface salinity. Occasionally, observations of aquatic birds or marine mammal activity were recorded.

Table 2. Summary of acoustic surveys conducted in 2009 and 2010 at the proposed deployment site (CB1) and control site (CB2) in Cobscook Bay. Latitudes and longitudes are listed and reflect the swing of the vessel on its mooring line. Tidal phase categorization listed with “spring” being the predicted spring tide date \pm 2 days; and “neap” being predicted neap tide date \pm 2 days; tidal phases that were not \pm 2 days of spring or neap are categorized as “between”.

Nominal	Location		Date	Time (EDT)		Full tide during		Tidal phase
	Latitude, N	Longitude, W		Start	End	Day	Night	
off Shackford Head CB2	44° 54' 04" 44° 54' 09"	67° 01' 39" ebb 67° 01' 42" flood	8/18-19 2009	0735	0655	ebb	ebb	between
off Shackford Head CB2	44° 54' 05" 44° 54' 08'	67° 01' 38" ebb 67° 01' 43" flood	9/10-11 2009	1720	1650	flood	flood	neap
off Goose Island CB1	44° 54' 31" 44° 54' 37" 44° 54' 32"	67° 02' 33" ebb 67° 02' 45" flood 67° 02' 33" ebb	5/19-20 2010	0620	0600	flood	flood	neap
off Shackford Head CB2	44° 54' 00" 44° 54' 09" 44° 54' 01" 44° 54' 09'	67° 01' 42" ebb 67° 01' 50" flood 67° 01' 41" ebb 67° 01' 50" flood	5/21-22 2010	0900	0902	ebb & flood	-	neap
off Goose Island CB1	44° 54' 33" 44° 54' 36" 44° 54' 37"	67° 02' 35" ebb 67° 02' 46" flood 67° 02' 51" flood	6/12-13 2010	0630	0600	ebb & flood	-	spring
off Shackford Head CB2	44° 54' 03" 44° 54' 05' 44° 54' 05'	67° 01' 43" ebb 67° 01' 48" flood 67° 01' 47" flood	6/13-14 2010	0630	0630	ebb & flood	-	spring
off Shackford Head CB2	44° 54' 01" 44° 54' 01" 44° 54' 04' 44° 54' 04'	67° 01' 41" ebb 67° 01' 41" ebb 67° 01' 45" flood 67° 01' 45" flood	8/4-5 2010	0740	0756	ebb & flood	-	neap
off Goose Island CB1	44° 54' 34" 44° 54' 38" 44° 54' 38"	67° 02' 42" ebb 67° 02' 54" flood 67° 02' 54" flood	8/5-6 2010	0830	0830	ebb & flood	-	neap
off Goose Island CB1	44° 54' 34" 44° 54' 35" 44° 54' 38"	67° 02' 44" ebb 67° 02' 43" ebb 67° 02' 56" flood	9/6-7 2010	0945	0900	ebb	ebb	spring
off Shackford Head CB2	44° 54' 01" 44° 53' 58" 44° 54' 01' 44° 54' 04'	67° 01' 41" ebb 67° 01' 29" flood 67° 01' 42" ebb 67° 01' 45" flood	9/7-8 2010	0700	0600	ebb	ebb	spring

2.1d Hydroacoustics data analysis

EchoView software by Myriax was used to analyze the acoustic data returned by the SIMRAD and DIDSON units, using the base, bathymetric, analysis export, stationary sonar, and school detection modules. All data files were compiled by 24-hour station for processing. Processing began with scrutinization, which included visual inspection of the data and removal of background noise, intermittent noise, gaps in the data, and other irregularities (Figure 7). Schools were then detected using the schools module (Figure 7b). Any targets greater than 1 meter high and 1 m long were considered schools, while all other targets were classified as individual targets. Surface schools were separated from turbulence by cross-referencing DIDSON data. Individual targets were then detected with EchoView's fish-tracking capabilities, using approximate cone diameter and current speed to determine the appropriate track length parameters in different parts of the water column. Detected schools and individual targets were manually checked and edited, and those within the upper 10 m of the water column were verified using records from the DIDSON. Counts of schools and individual targets (any target detectable by the transducer) were obtained for each 5 m depth bin, and these numbers are reported.

For this report, only data from the 200 kHz transducer were analyzed. This higher frequency is more typically used by fisheries biologists in marine environments, for it detects acoustic returns from targets in the relevant range for juvenile as well as adult fishes. The detection limit of the system is dependent upon the frequency of the transducer, the dynamic range of the instrument, and the environment. The 200 kHz frequency is sufficiently high to detect targets of less than 1 cm, about the size of a juvenile herring's swim bladder. Though this higher-frequency signal weakens more quickly with distance than lower frequencies, SIMRAD has provided data indicating the echosounder can detect a 20 cm cod at 200 m. The target-strength-to-length relationship of a cod is comparable to that of a herring (Ona 2003, Foote 1987, Nielsen and Lundgren 1999), so it is reasonable to assume that the majority of targets within the depth of interest (usually less than 50 m in Cobscook Bay) will be detected at the 200 kHz frequency, and that these targets will be sufficiently differentiable from the background noise to be characterized effectively. The impacts of the higher turbidity in the bay, as well as the effects of fish depth and sexual maturity, on target strength will be considered in continuing work (Ona 2003).

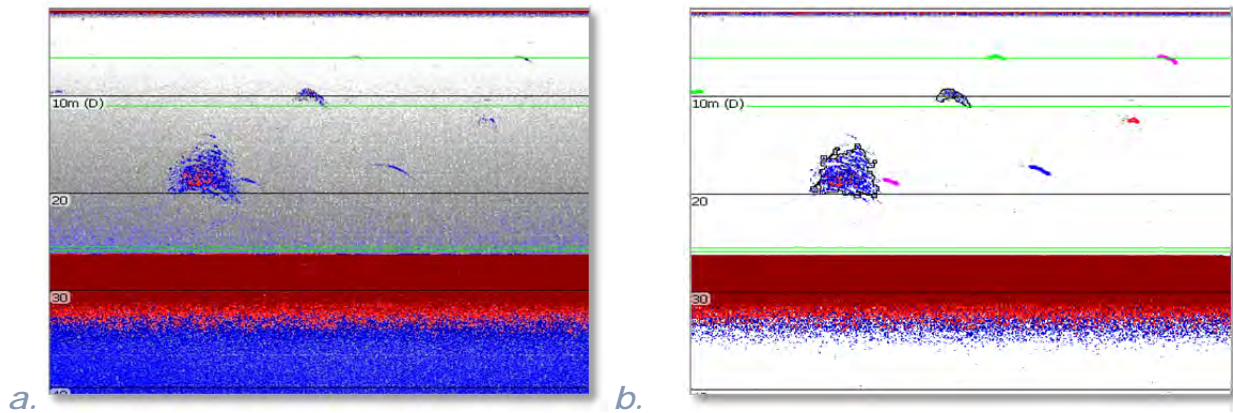


Figure 7. (a) Echogram of active acoustics data collected with SIMRAD ES60 and the CombiWide 200 kHz transducer. (b) Same echogram after noise removal; schools and individual targets have been detected (schools outlined in black, individuals in colored lines).

Approximate transducer calibrations using solid copper calibration spheres (diameters of 60 and 13.1 mm) were performed at slack tide during each survey to detect any obvious equipment malfunctions. The same transducer was used during every survey and transducer reliability over time has been shown (Knudsen 2009), so data collected in each month are relative to each other. However, during surveys, tidal currents were always too high to allow accurate transducer calibration. This rendered target strength analysis or application of a minimum threshold impractical. A careful calibration will be conducted under more manageable conditions in the near future.

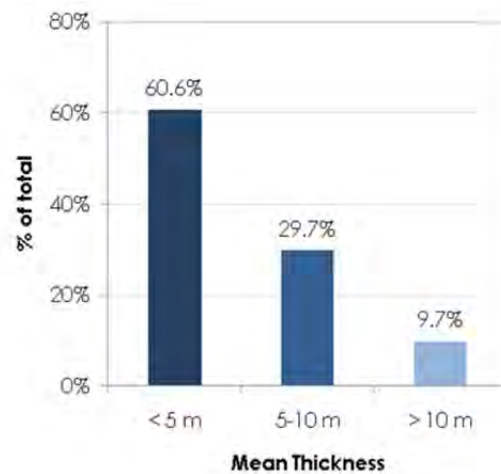


Figure 8. Categorization by thickness of all schools detected at CB1. “% of total” is the total percent of schools documented in each thickness bin.

Counts of individual targets and schools were obtained by grouping the data first into half-hour time bins (beginning at the start of the survey), and then by 5-m depth bins measured from the sea floor. The choice of the sea floor as a reference point relates the data to the tidal application: with the bottom as the zero line, we can visualize changes in the specific regions of the water column

occupied by bottom-mounted devices without having to account for water levels that rise and fall with the tide. Five meter bins were chosen because the majority of schools were less than 5 m thick (Figure 8), where school ‘thickness’ is the vertical depth the school encompassed in the water column.

Data were further described based on their depth distribution. The depth of greatest concern was where the proposed ORPC TidGen™ Power System foils will be turning, 7-10 m up from the bottom, within depth bin 2 (which encompasses 5 – 10 m above the bottom) (Figure 9).

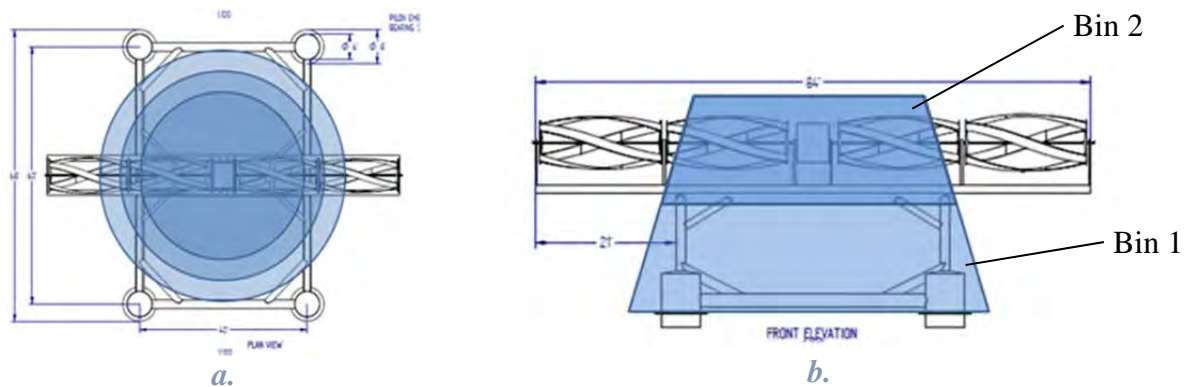


Figure 9. Relative size of lower two depth bins of SIMRAD sampling volume with respect to proposed TidGen™ Power System, from above (a) and side (b).

For comparisons across time and depth bins, data were standardized with respect to sample volume and current speed. The sample area is conical in shape, and therefore the volume of water sampled near the sea floor is larger than the volume sampled near the surface (Figure 10a). Standardization by current speed was required because of the range in tidal currents: faster currents move more water (and possibly more fish) through the ensonified space (Figure 10b). To account for changing sample volume and compare numbers in different depth bins, the count obtained in each depth bin was converted to a density (number per 100 m³ of water) by dividing the count in that bin by its corresponding volume of water. To allow comparison across time (and therefore across varying current speeds, see Figure 10b), the densities obtained for each time bin were divided by the linear distance of water that passed below the boat during that time (Figure 10c). This distance is effectively the length of the transect the boat would have made had it been moving over still

water at the measured current speed for the same duration. Although current speed decreases near the seafloor, the count standardization is primarily driven by the correction for volume; therefore, variation in current speed at the seafloor was assumed negligible. The final unit of measurement used for comparison of school and individual numbers was a density per unit distance, (number/100m³)/km.

For example, if 100 fish were detected in Bin 3 and in Bin 6 (Figure 10a), in order to compare these numbers to each other, they need to be divided by the volume of their respective bins: 372.5 m³ and 10m³. This yields two densities: 26.8 fish/100m³ in bin 3 and 1000 fish/100m³ in bin 6. When comparing, for instance, the June and August densities obtained for the highlighted time bin during night flood (shown in Figure 10b), the June density must be divided by 3.41 km and the August one by 2.31 km (Figure 10c). This step removes the impact of the higher current speeds in the June sampling session.

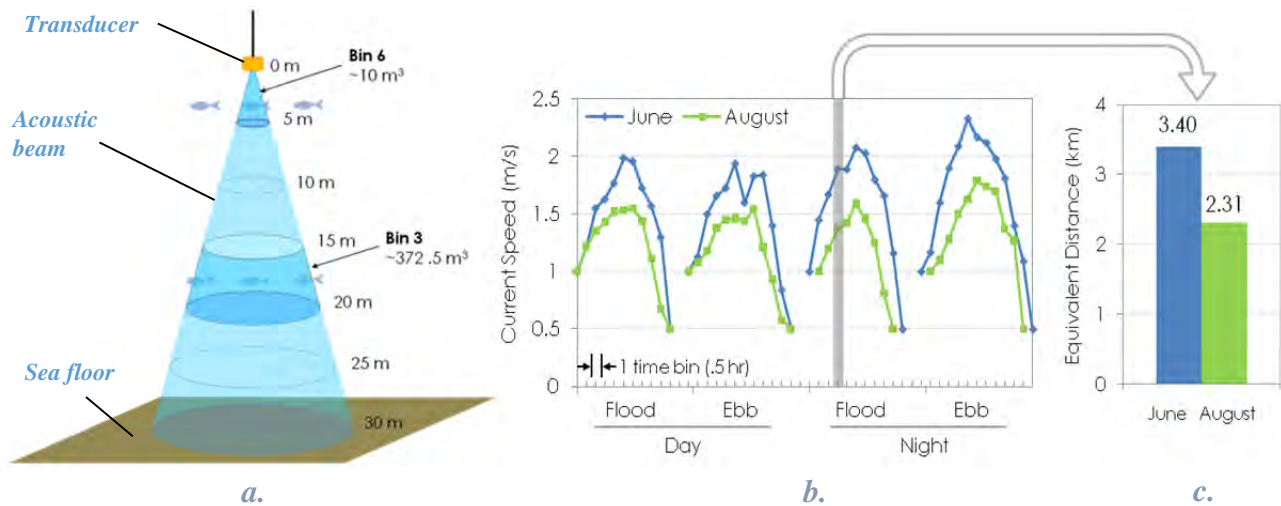


Figure 10. Graphical depiction of the need for count standardization. (a) Sampling volume varies with depth in the water column. (b) Current speed (collected in the top 1 m of the water column) varies with time, within and between sampling months. (c) Amount of water traversed during highlighted region of (b) expressed as a linear distance, which is used to standardize data to the changing current speeds.

2.1e Statistical analyses

For statistical analyses we examined: (1) standardized counts of schools and individual targets, grouped in 30 minute intervals; and (2) depth distribution (position) of schools and individual targets in the water column, grouped by 30 minute intervals. Twenty-four hour survey data from each station were used to

examine statistically the factors that describe fish presence (schools and individuals) at each location. Factors examined were site, tidal cycle, diel cycle, and all possible factor interactions (e.g., tide and diel, site and diel, site and tide). Year and season were treated as fixed blocks.

2.2 Acoustic target identification

2.2a DIDSON

The surface 10 m of all acoustics data reported were validated using the DIDSON's acoustic imaging. DIDSON videos were synchronized with echograms, and targets in the upper 10 m were visually confirmed as fish (as opposed to turbulence or krill). Further analyses of these images can be made to size fish in the acoustic images and more accurately describe fish species/groups present in the echograms, but these analyses are beyond the scope of this report.

2.2b Netting

A 3.5 x 3.05 m frame of aluminum pipe with a net of graded mesh size (0.1m, 0.08m, 0.05m, and 0.01m) was fished in May and June 2010 (Appendix 1). Net tows were approximately 30 or 45 minutes. Tows were made mostly at night with some in daytime on both ebb and flood tides (Appendix 1). In May, the net consisted of a white nylon graded mesh net (4", 3", 2", 1.5", 0.75", 0.5" mesh) fastened to a frame of 2" aluminum pipe. Floats were attached to the top pipe and weights to the bottom pipe to provide vertical stability. In June, the net was modified by dyeing it dark green, adding a 0.75" mesh liner to the 2" and 1.5" mesh sizes, and replacing the side aluminum pipe with steel pipe. Later in June, the pipe frame was replaced by a welded stainless steel frame for rigidity and resistance to bending. Various bridle arrangements were tried. A Sensus Ultra[®] depth sensor was attached to the top right corner of the net frame to record depth. Current speed was recorded before and after net deployment.

Acoustic surveys conducted simultaneously confirmed the presence of numerous individual fish targets and schools of fishes during many of the tows. To compare netting data to hydroacoustic data, an echogram was produced using the 200 kHz data (Figure 11). Acoustic noise (extraneous to individual fish targets or schools) was estimated and subtracted. Schools present during the netting periods were counted. Individual target tracks were detected and counted. The data set was separated into specific times and depths for each net deployment to provide a visual assessment of the individual targets and schools. Schools were masked from the data set in order to then detect and

count the individual targets. Individual target counts were used for statistical comparison between netting data (number of fish captured) and hydroacoustic data (number of individual targets present).

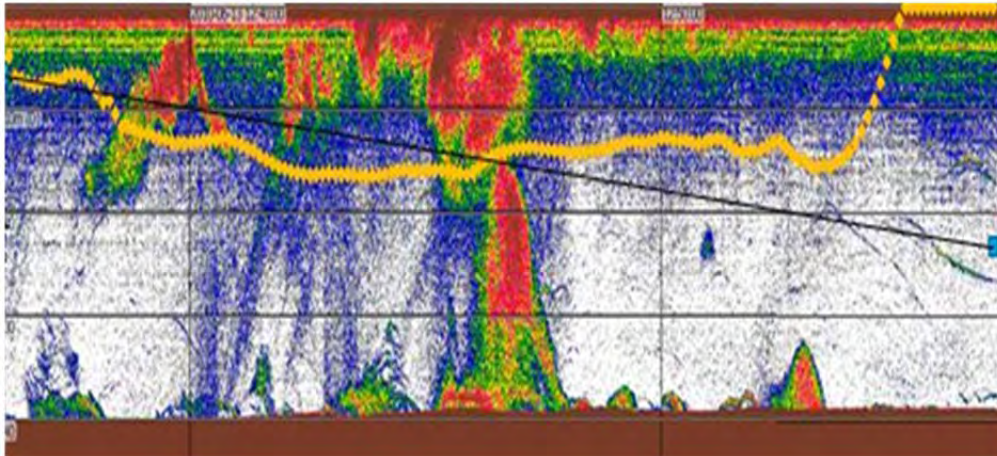


Figure 11. Sample echogram showing net deployment (yellow dashed line) during June 2010 in Cobscook Bay at CB2.

3. Results

3.1 Fish presence, pre-deployment of the TidGen™ Power System

Fish presence was quantified at two sites in Cobscook Bay: the proposed deployment area near Goose Island (CB1), and at the control site near Shackford Head (CB2; Figure 2). Fish (individual targets and schools) were present at both sites during all survey periods. Over the entire study period (24-h periods in May, June, August, and September 2010, approximately two tidal cycles per 24-h period), 74,579 individual targets and 1,978 schools were documented at CB1. At CB2, 31,040 individual targets and 7,246 schools were documented. Both sites were sampled for a similar number of tidal cycles (8 each) and hours (95.4 h each). More individual targets were observed at CB1 and more schools at CB2. However, differences were also dependent on season (Figure 12). The data shown in Figure 12 were not standardized (by cone volume or depth) in order to provide an indication of how many individual targets and schools were detected. There were obvious differences observed at the two sites that required statistical comparison (see statistical analyses below).

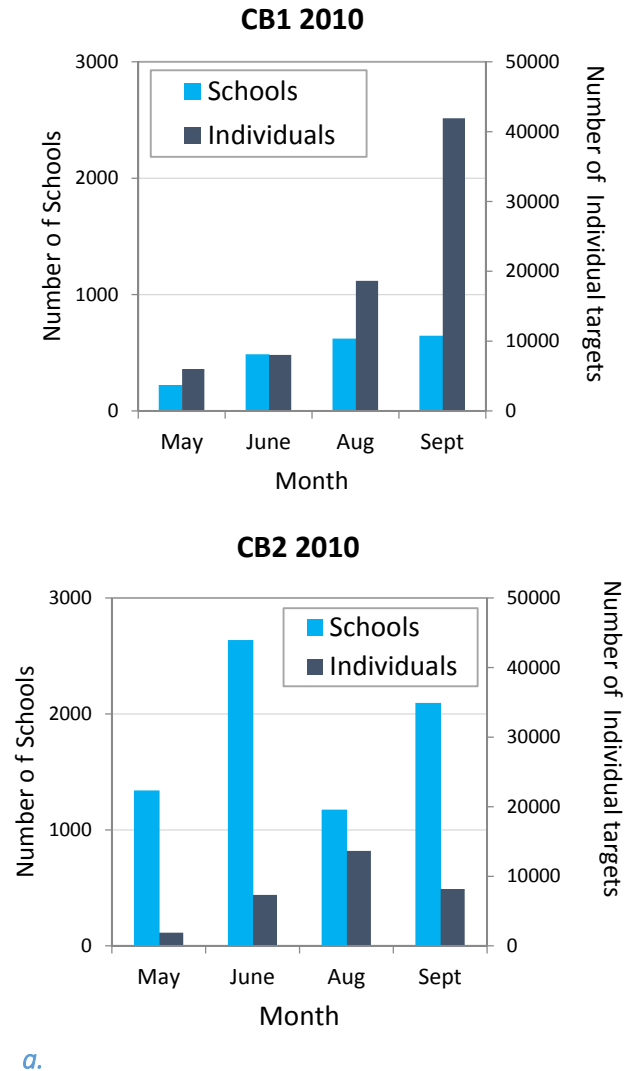


Figure 12. Total counts of individual targets and schools detected at CB1 (a) and CB2 (b) during all months sampled in 2010.

Scrutiny of preliminary data indicated that the vertical distribution of schools and individual targets in the water column varied. The relative distribution of individual targets and schools over all months were plotted to provide an idea of the proportion of individual targets and schools in each 5-meter height bin (distance off the bottom; Figure 13). At the proposed deployment site, CB1, more than 50% of the schools and individual targets detected were in the fifth bin up from the seafloor, 20 – 25 meters off the bottom (Figure 13a). A similar pattern was observed at CB2 (Figure 13b), though the bulk of detections were slightly higher, in bin 7 (30 - 35 meters above the bottom).

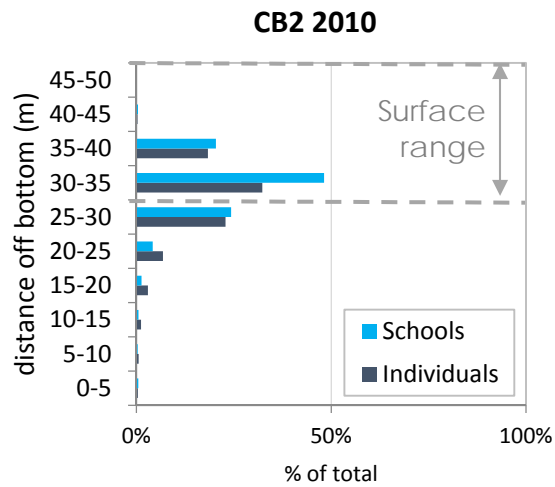
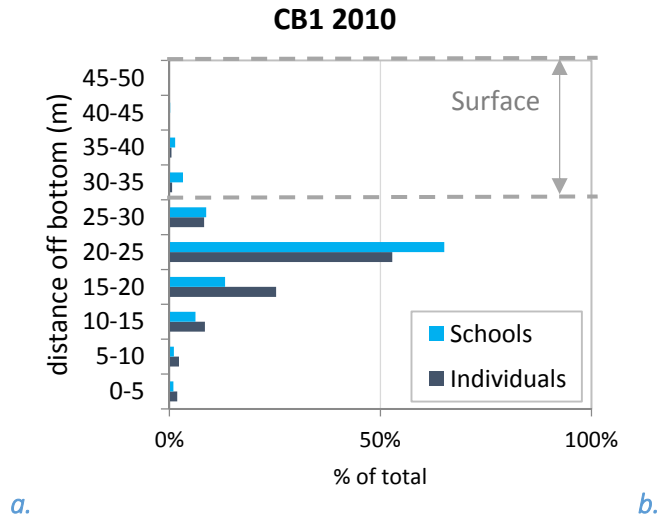
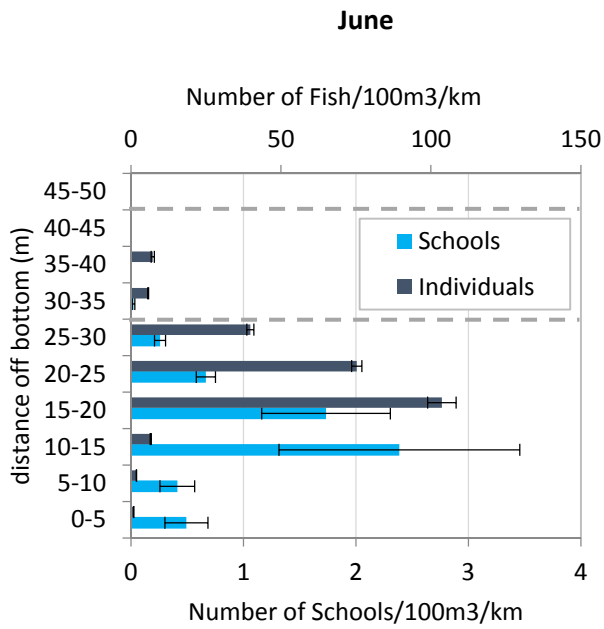
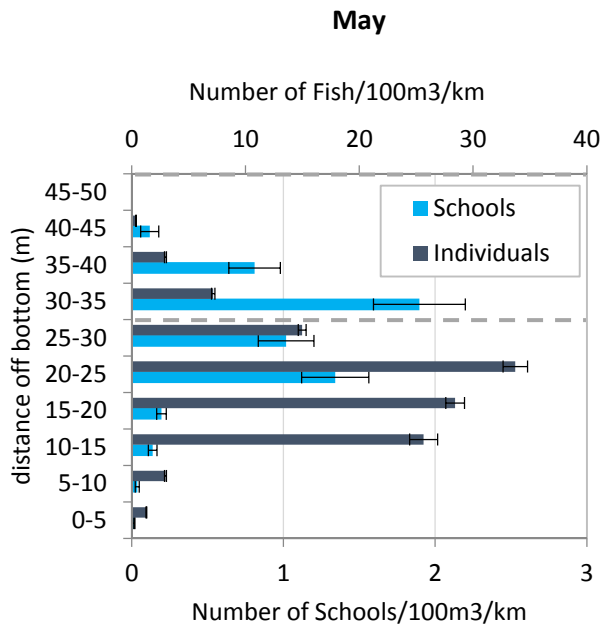


Figure 13. Vertical distribution of individual targets and schools pooled for all months sampled in 2010, for CB1 (a) and CB2 (b). Data by distance bin are included in Appendix 3.

As with total counts (Figure 12), vertical distribution of targets varied by month. This variation is shown in Figure 14, where distributions of individual targets and schools detected at CB1 in 2010 were plotted by month, again in 5-meter distance bins. Peaks and spreads of the distributions changed among seasons (months). Individual target counts were generally highest between 15-30 meters above the seafloor, and school counts were highest between 15 and 40 meters above the seafloor.

Vertical distributions pooled by month and binned by depth (Figure 14) do not allow analysis of tidal or diel variation. To examine this variation, a statistical approach was applied.



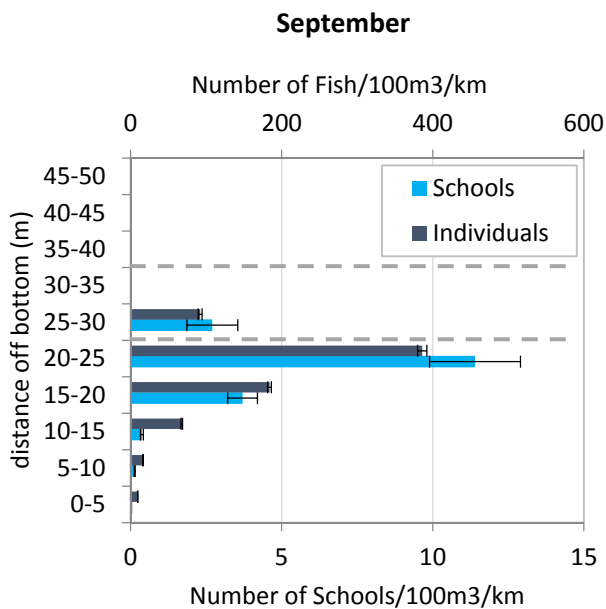
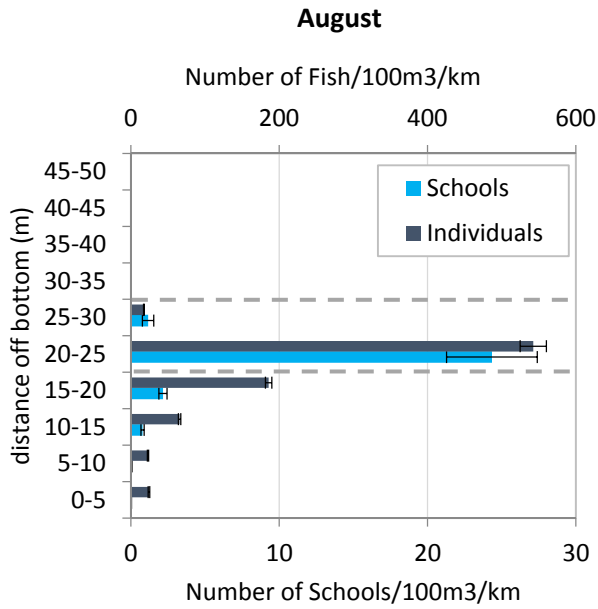


Figure 14. Vertical distributions of individual targets and schools at CB1 in 2010. Data are pooled by 30-minute time bins and 5-m depth bins. Counts are standardized to sampling volume and current speed. Data by distance bin are included in Appendix 4.

3.1a Statistical assessment of environmental factors

A randomized complete block design was used to assess potential factors affecting counts and distribution of individual targets and schools. Three response variables tested were: (1) standardized count; (2) median normalized height off the seafloor; and (34) normalized interquartile range (IQR).

Median height (distance off the seafloor) of an individual or a school is the general center of its distribution in the water column, and the IQR provides an indication of the vertical span of the distribution (Figure 15).

Median normalized height and normalized IQR were obtained by dividing each height measurement by total water column depth at the time of the target's detection. Using these normalized variables eliminated variation in height above the seafloor due to changing water levels, as illustrated by Figure 16. These normalized values were used for statistical comparisons.

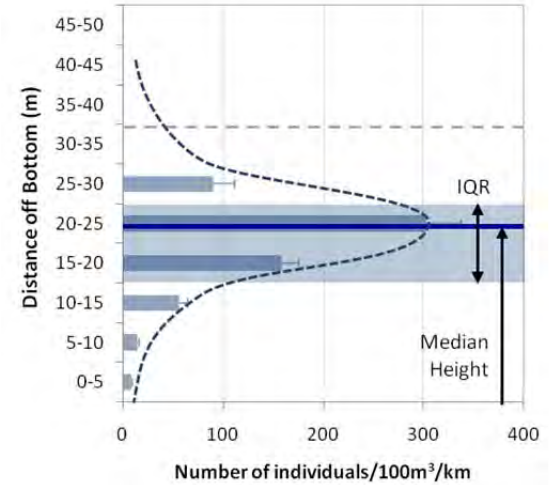


Figure 15. Median height (blue horizontal line) and interquartile range (shaded area) of the vertical distribution of schools in September at CB1 during a peak tide (when the turbine would be turning).

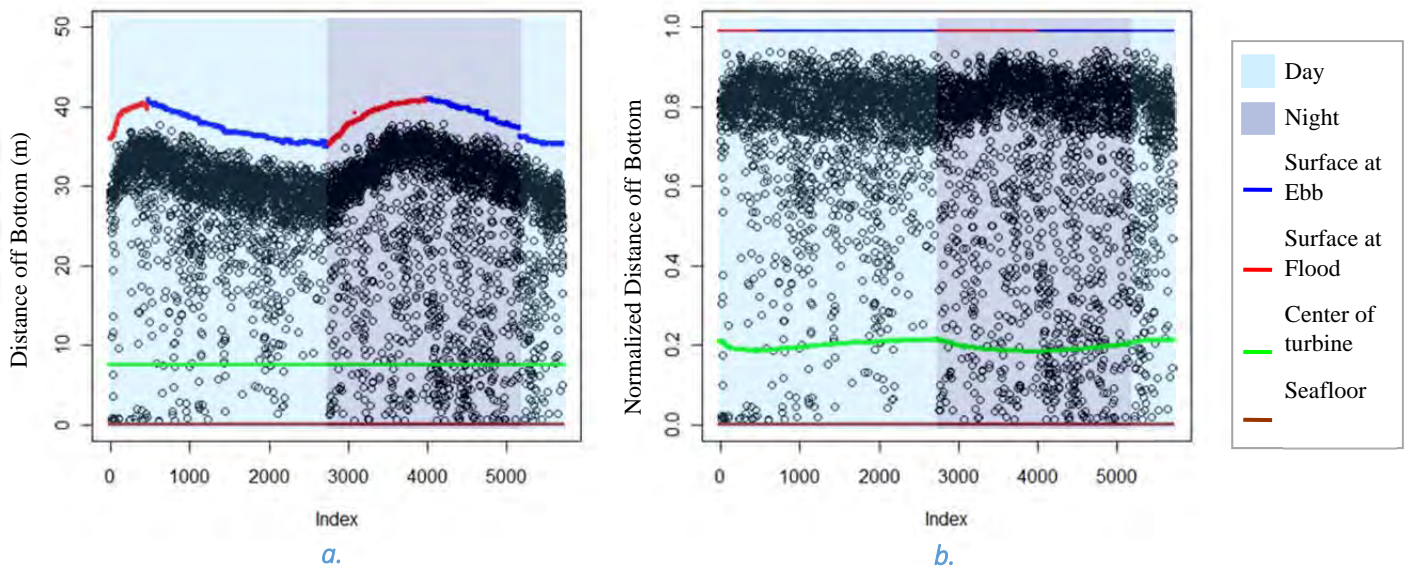


Figure 16. Actual (a) and normalized (b) height data for individuals detected in June at CB2. Note that the apparent change in target height relative to the seafloor becomes insignificant when normalized with respect to water depth. Indices are sequential numbers assigned to each school in time order.

3.1ai. Intra-annual (2010) factors

Site and month had significant effects on all response variables (counts and depth distribution variables); therefore, these effects were treated as fixed blocks in order to examine effects of tidal (ebb and flood only) and diel cycles. Results of the statistical analyses of intra-annual (2010) comparisons are summarized in Tables 3 (CB1) and Appendix 1 (CB2). Schools and individual targets were assessed separately. Though assumptions of normality and constant variance could not be met for the ANOVA models, permutation tests performed on the data yielded similar p-values; therefore, the ANOVA model p-values were assumed approximately correct. Statistical comparisons of effects at CB1 (proposed deployment site) are detailed in the text, figures for both sites are provided, and statistical comparisons for CB2 are included in the appendix. Figures are included to show relative numbers (and associated variability) of individual targets and schools based on factors (day/night, ebb/flood) examined.

Response variable: Count

The number of schools present was influenced by location (CB1 or CB2) and month. CB2 generally had higher numbers of schools than CB1. Numbers of schools were generally highest in August at CB1. At CB1 tidal effects were apparent in May ($p = 0.014$, Table 3) and August (Figure 17). In both of these months, more schools were detected on the ebb tide than on the flood tide. In August this effect varied with the diel cycle (Table 3). In September there were more schools during the day than at night ($p = 0.026$, Table 3).

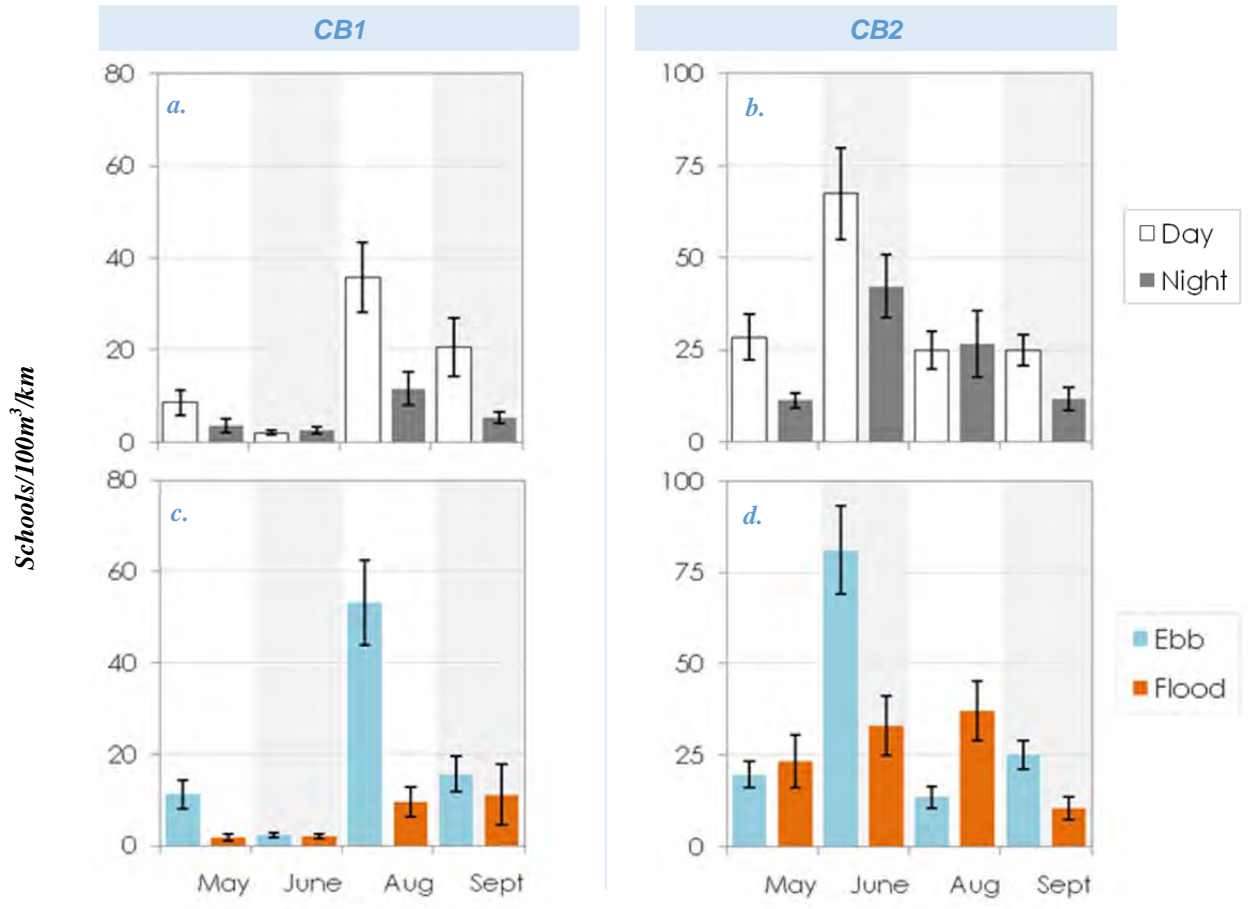


Figure 17. Mean school numbers by site and month. Error bars are standard error.

Table 3. Summary of effects for 2010 comparisons at CB1. Empty boxes indicate no significance. Values are p-values from 2-way ANOVA comparisons.

Response	Treatment	May		June		August		September	
		Schools	Indiv.	Schools	Indiv.	Schools	Indiv.	Schools	Indiv.
Count	Tide	0.014				<.001			
	Diel				0.036	<.001		0.026	
	Inter.					.005			

The number of individual targets present was influenced by location (CB1 or CB2) and month. CB1 generally had higher numbers of individual targets than CB2. Numbers of targets were generally highest in September at CB1. There was no significant difference in the numbers of individual targets at CB1 during the ebb or flood tide during any month (Table 3, Figure 18). In June there were more individual targets in the water column during the night than day (Figure 18a).

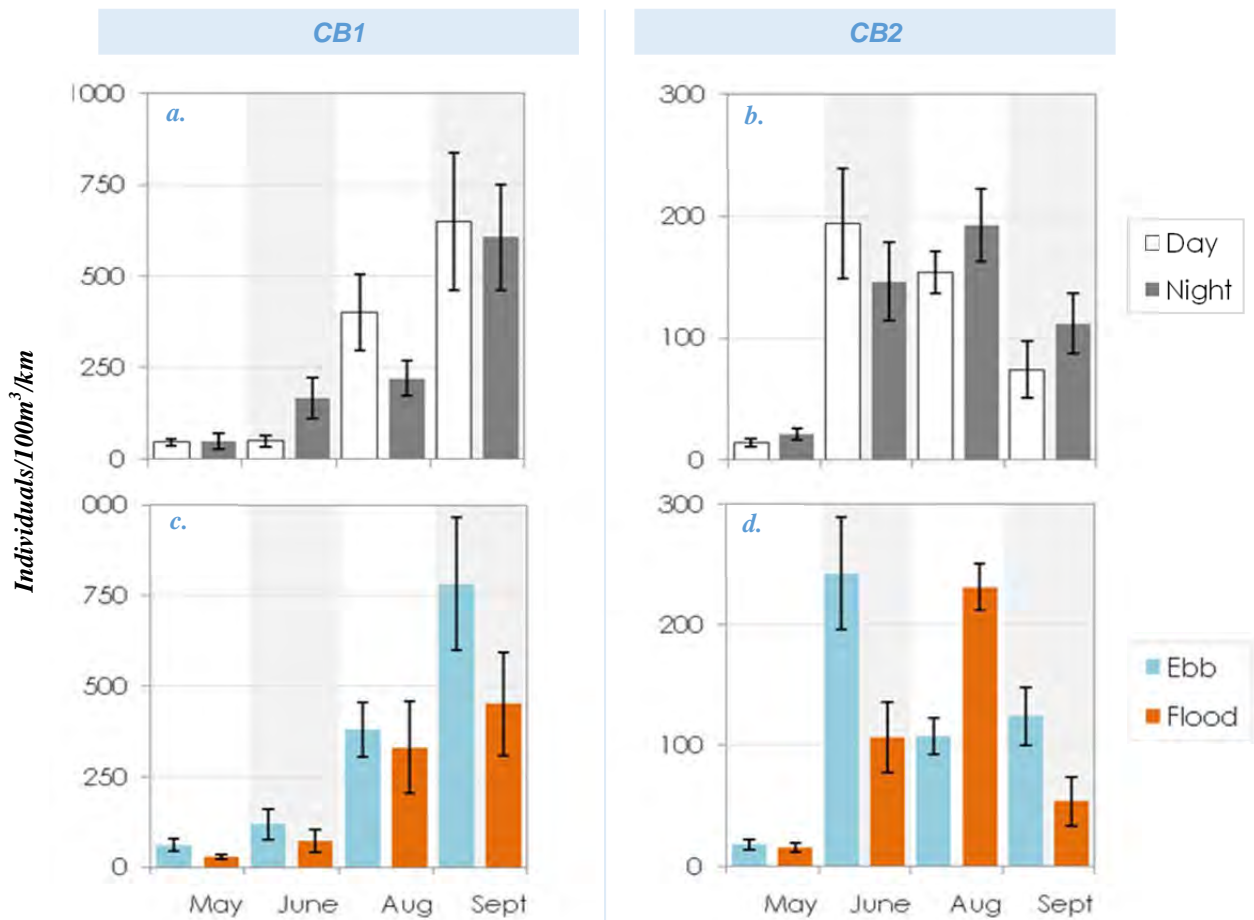


Figure 18. Mean standardized counts of individual targets, 2010. Error bars are standard error.

Counts at depth of interest (proposed depth of TidGen™ Power System: foils between 5 and 10 m above seafloor)

At the proposed depth of the TidGen™ Power System, school numbers were affected by tidal and diel cycles differently than for the entire water column. Numbers of schools were generally highest in September (while August had the highest numbers when pooled for the entire water column). Similar to the overall distribution, tidal effects were apparent at this depth in May ($p = 0.01$, Table 4, Figure 19c). In June ($p = 0.04$, Table 4) there were more schools during the day than at night. Numbers of individual targets were generally highest in September, particularly during the ebb tide (Figure 19b&d). In May and August, there were more individual targets in the water column at night (Figure 19b).

Table 4. Summary of effects for height bin 2, CB2 2010. Empty boxes indicate no significance. Values are p-values from 2-way ANOVA comparisons.

Response	Treatment	May		June		August		September	
		Schools	Indiv.	Schools	Indiv.	Schools	Indiv.	Schools	Indiv.
Count	Tide	0.01					.01		<.001
	Diel		.007	.04			<.001		
	Interaction						.01	.01	

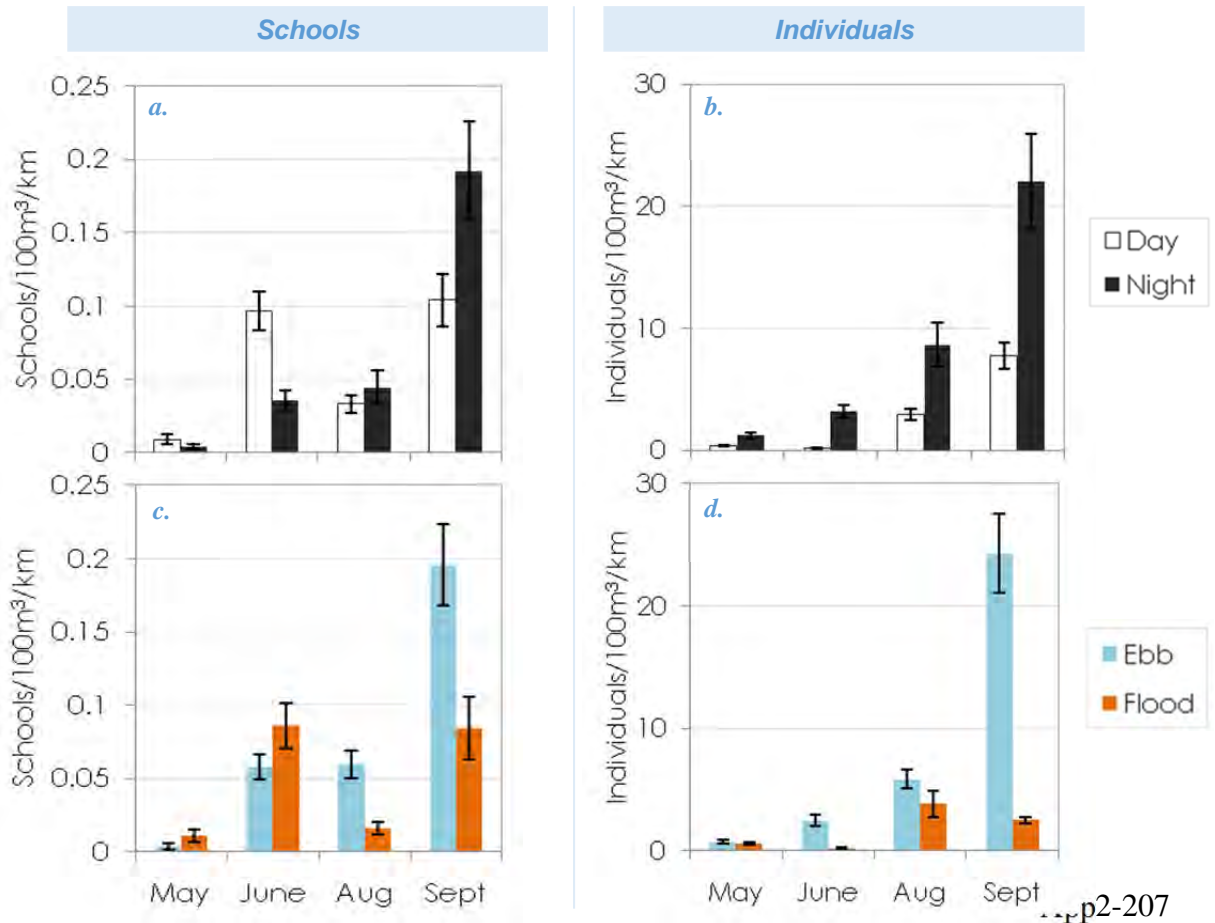


Figure 19. Mean counts of schools and of individual targets in height bin 2 (location of TGU) at CB1 for 2010, showing standard error.

Response variable: Median height off the seafloor and IQR (i.e., vertical extent)

The distribution of schools in the water column at CB1 varied month to month with tide and diel cycle, where tidal effects were apparent in May ($p = .017$) and August ($p = 0.003$) (Table 5, Figure 20c). Distance off the bottom was effected by diel cycle in June ($p = .025$) and August ($p = .009$) (Table 5, Figure 20a). In May and August the distribution of schools was significantly further off the seafloor during the ebb tide than during the flood. The spread of school distribution was not significantly affected by tidal or diel cycles (Table 5).

Table 5. Summary of effects on fish distributions at CB1 in 2010. Empty boxes indicate no significant effect. Values are p-values from 2-way ANOVA comparisons.

Response	Treatment	May		June		August		September	
		Schools	Indiv.	Schools	Indiv.	Schools	Indiv.	School	Indiv.
Height	Tide	0.017				0.003	0.001		
	Diel			0.025		0.009	<.001		0.009
	Inter.						0.008		
IQR	Tide						0.043		0.029
	Diel		<.001				<.001		
	Inter.								

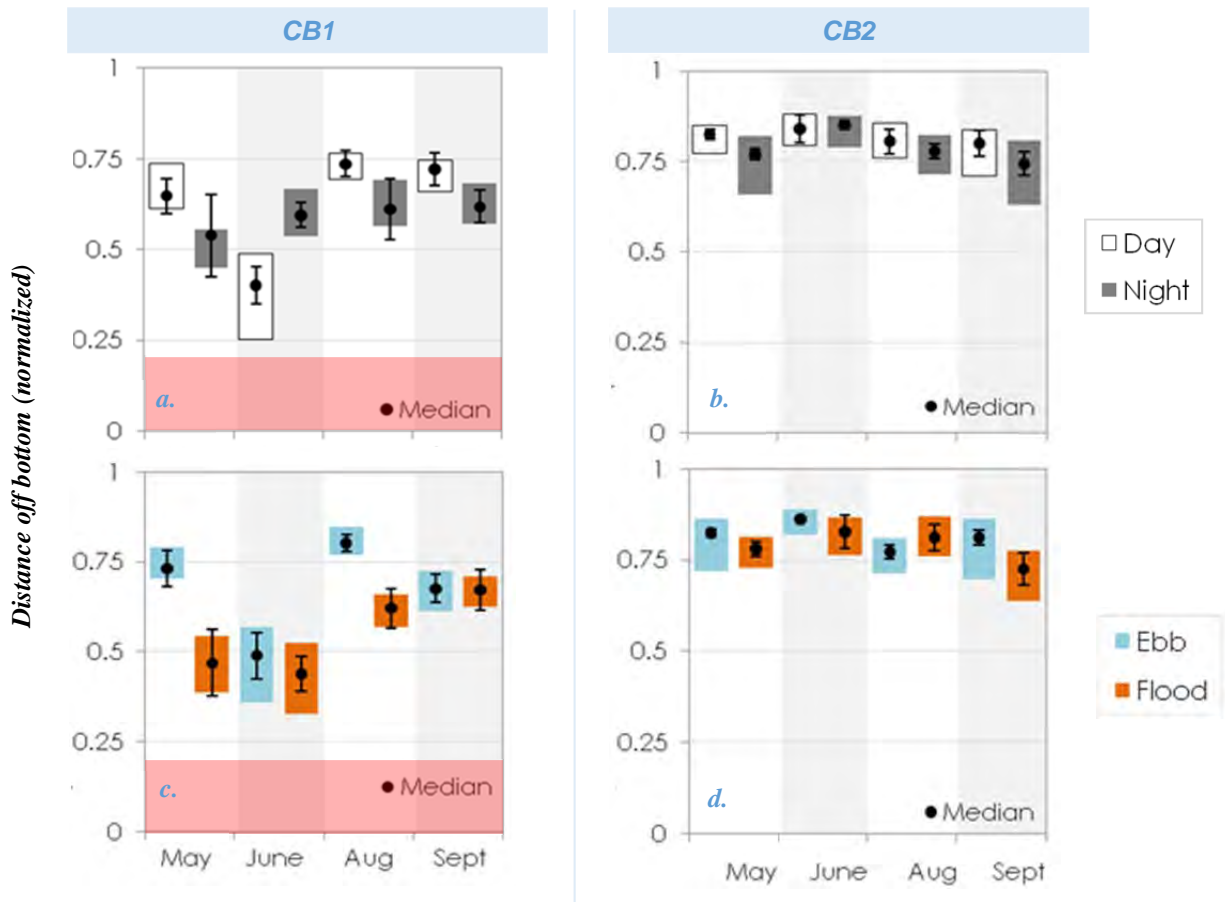


Figure 20. Mean of the median distance of schools off the seafloor (filled circle) and its standard error (error bars), IQR (shaded box), by site and by month. Distance off seafloor is normalized for depth changes associated with tidal cycle. Red shaded area shows region of the proposed deployment at CB1.

The distribution of individual targets in the water column varied by month for tidal and diel cycle (Table 5, Figure 21). In September, diel cycle had an effect on individuals' distance off the bottom ($p = .009$, respectively), and in August both tidal and diel cycle as well as their interactions were significant (Table 5, Figure 21a&c). In May, the spread of individual targets in the water column was significantly greater at night. In August, both tidal and diel cycles influenced the portion of the water column used by individuals: they were more spread out during ebb tide than during flood, as well as at night than during the day. In September, individuals were spread further during the ebb tide than during flood (Figure 21c).



Figure 21. Mean of the median distance of individual targets off the seafloor (filled circle) and its standard error (error bars), IQR (shaded box), by site and by month. Distance off seafloor is normalized for depth changes associated with tidal cycle. Red shaded area shows region of the proposed deployment at CB1.

3.1aⁱⁱⁱ Interannual effects

Differences between years could only be assessed for August and September at the control site, CB2. When the model assumptions of normality and constant variance of error could not be met, ANOVA p-values were confirmed using permutation tests.

Response variable: Count

In 2010 counts were affected by more factors than in 2009 (Table 6). In 2009, only September school counts were affected by the interaction of tidal and diel cycles. In 2010, school and individual counts were affected by tidal cycle in

both months, and in September, school numbers were also affected by the diel cycle (Table 6). In August 2010, there were significantly more schools and individual targets detected during the flood tide than during the ebb, while the opposite was true in September 2010 (Figure 22 c&d). In September, there were also significantly more schools during the day than at night (Figure 22a).

Table 6. Summary of effects for 2009/2010 comparisons at CB2. Empty boxes indicate no significance. Values are p-values from 2-way ANOVA comparisons.

Response	Treatment	2009				2010			
		August		September		August		September	
		Schools	Indiv.	Schools	Indiv.	Schools	Indiv.	Schools	Indiv.
Count	Tide					.014	<.001	.005	.039
	Diel							.012	
	Inter.			.036			.003		

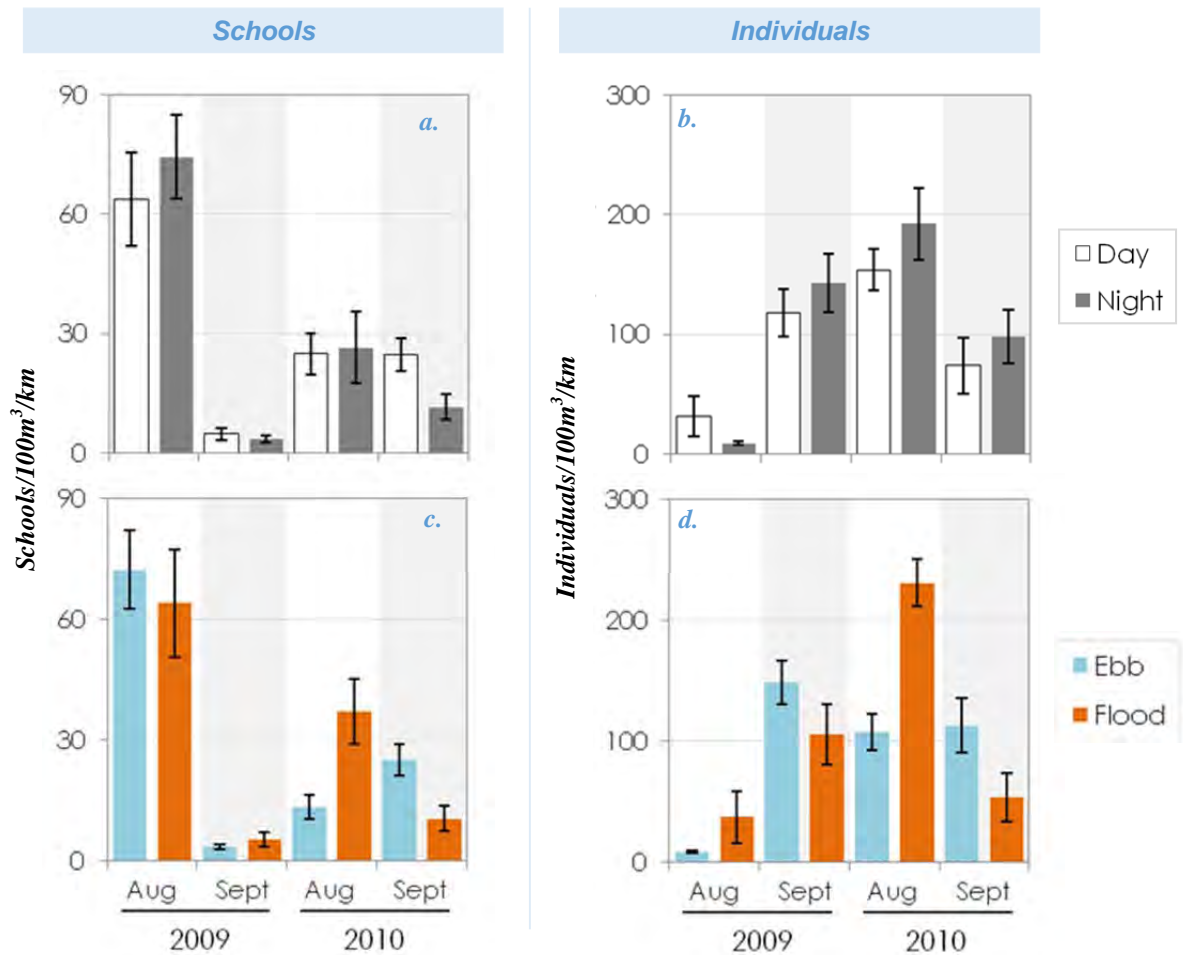


Figure 22. Counts of schools and individual targets at CB2 for August and September of 2009 and 2010. Standard error shown.

Response variable: Height off the seafloor and IQR (i.e., vertical extent)

There was limited influence of tidal and diel cycles on school use of the water column: only the spread of school distribution was affected by diel cycle, in August 2009 (Table 7). Schools did appear significantly deeper in September 2009 than in August 2009, however in 2010 there was little overall difference in depth between August and September (Figure 23).

Individual targets showed an inverse pattern: though there was still little change in depth between months in 2010, in 2009 targets were deeper in August than in September. The distance of individuals off the sea floor was impacted by tide in August 2010 and day/night in August 2009. In August of 2009, distance above the bottom was significantly higher during the day than at night, while in August 2010, distance above the bottom was significantly greater during the ebb tide than the flood (Figure 23).

Table 7. Summary of effects for 2009/2010 comparisons at CB2. Empty boxes indicate no significance. Values are p-values from 2-way ANOVA comparisons.

Response	Treatment	2009				2010			
		August		September		August		September	
		Schools	Indiv.	Schools	Indiv.	Schools	Indiv.	Schools	Indiv.
Height	Tide						.03		
	Diel		.003						
	Inter.								
IQR	Tide								
	Diel	.02					.008		
	Inter.								

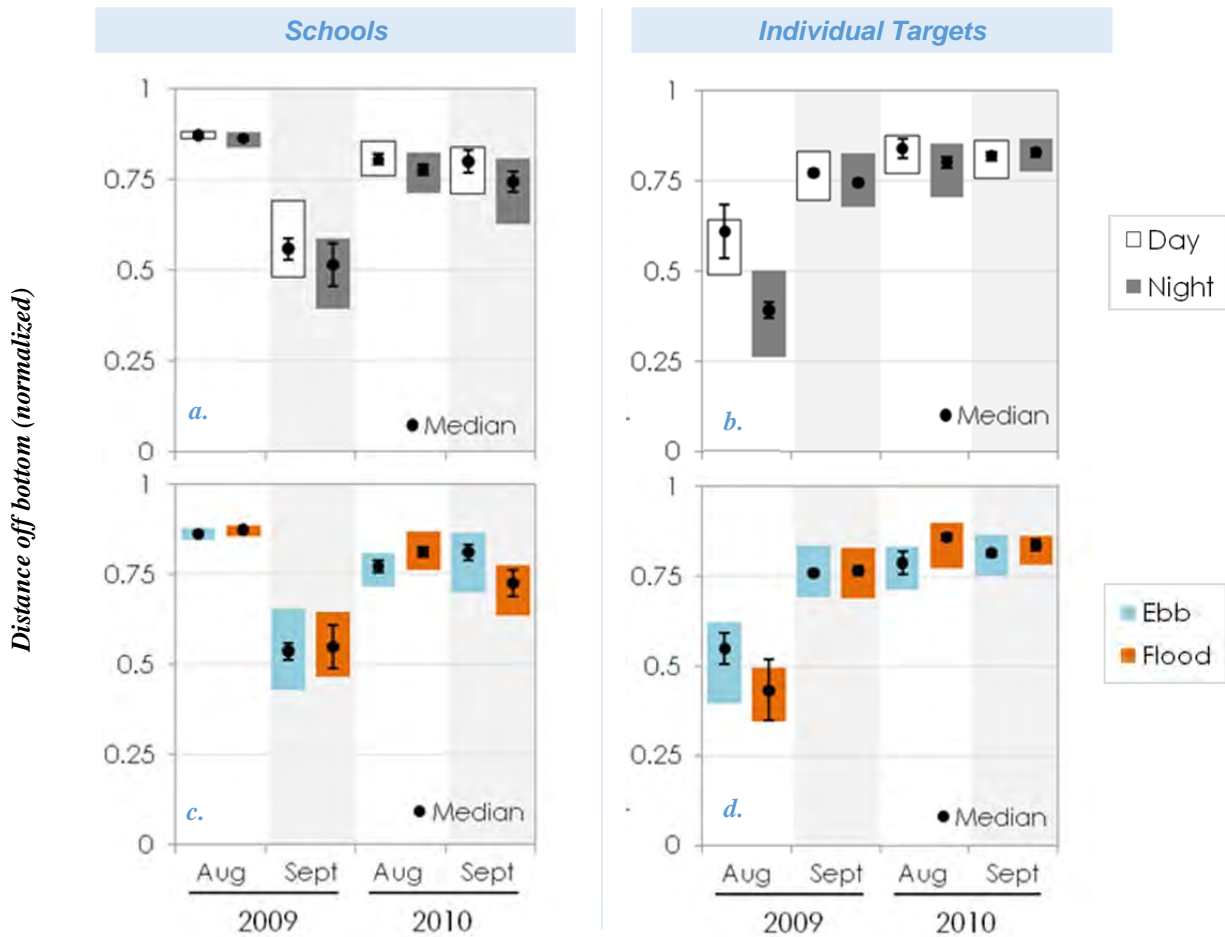


Figure 23. Mean of the median distance off the seafloor (filled circle) and its standard error (error bars), IQR (shaded box), by month and year for schools and individual targets at CB2. Distance off seafloor is normalized for depth changes associated with tidal cycle.

3.2 Acoustic target identification: netting

Seventeen net deployments were made in May 2010 in Cobscook Bay. Three tows were made during the daytime ebb tide; three during daytime flood tide; five during nighttime ebb tide; and six during nighttime flood tide. The average depth of the deployments was 14.5 m and ranged from 1m at surface to depths of 37.7m. There were ten deployments in the upper (< 15 m) water column, six deployments in the middle (> 15 m, < 30 m) water column, and one deployment in the lower (> 30 m) water column. Eight of the 17 deployments resulted in captures of fish. For deployments that captured fish, the minimum number of fish captured was one and the maximum was nine. There were three species

captured: *Gasterosteus aculeatus*, *Raja ocellata*, and *Pseudopleuronectes americanus*. The first two species were captured in the upper water column; two tows in the lower half of the water column captured *Gasterosteus aculeatus* and *Pseudopleuronectes americanus*. Few schools were present when netting in May.

Sixteen net deployments were made in June 2010. Five were made during the day, ebb tide; one during the day, flood tide; two during night, ebb tide; six during night, flood tide; and two during slack tide. The average depth of deployments was 13.04 m and ranged from 1m at surface to depths of 39.55m. There were 11 deployments in the upper (< 15 m) water column, five deployments in the middle (> 15 m, < 30 m) water column, and no deployments in the lower (> 30 m) water column. Seven of the 16 deployments resulted in captures of fish. The minimum number of fish captured was one and the maximum was five. There were six species captured: *Cyclopterus lumpus*, *Scophthalmus americanus*, *Myoxocephalus octodecimspinosus*, *Hemitripteris americanus*, *Zoarces americanus*, and *Gasterosteus wheatlandi*. Of the tows near the surface all six species were captured; of tows in the lower water column, one species (*Cyclopterus lumpus*) was captured. Nets were fished when schools were present in the water column.

In most cases there was an inverse relationship between the number of schools present in the water column and the number of fish caught while netting. There was a significant difference between the counts of fish from netting (2.1 ± 2.4) and the count of individual targets using hydroacoustics (5.5 ± 6.6) (Figure 24). Counts were significantly higher using hydroacoustics, but the targets identified using hydroacoustics were more likely those associated with schools, e.g. mackerel and herring, than those captured in the net (poor-swimming, benthic fishes).

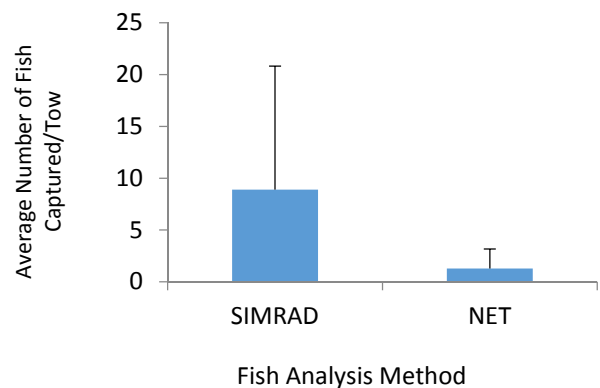


Figure 24. Mean values of individual targets observed during hydroacoustic analysis (SIMRAD) and amount of fish capture while netting (NET) \pm standard deviation. There was a significant difference (t-test, t critical=1.67, $p=0.000425$, $f_{df}= 60$).

3.3 Direct observation of interactions with Beta TGU

Over 100 hours of acoustic imaging and hydroacoustic data were collected with the test device operating in 2010 (Table 8). Note that the location of the test device changed in September, from CB2 to CB1.

Table 8. Sampling at the test ORPC Beta TGU.

Month	Location of test device	Hours of observation
February	CB2	48 (no Beta TGU)
March	CB2	12
May	CB2	24
June	CB2	24
September	CB1	24
October	CB1	24

During each 12 – 48 hour observation period, researchers remained with the equipment as data were recorded. During these periods, two specific events were observed when fish interacted with the device. These events were more thoroughly examined to assess the response. By no means are these observations a complete assessment of the data collected or of all possible animal responses to tidal energy devices. Approximately 2 hours of 108 h collected have been analyzed, leaving 98% of the collected data to be analyzed.

Two basic responses were observed: (1) movement over and through the device and (2) device approach and flee. In both of these cases image resolution was not fine enough to determine if the fish came into physical contact with the foils. The first response was observed when at least 20 individuals (approximately 100 mm in length) were observed moving over and through the device on September 9th 2010 (Figure 25a). On the downstream side of the device, these individuals appeared to pass through the device and pause in the turbulent region behind it before re-orienting themselves to the flow and continuing downstream. This occurred during the flood tide at night, at a slight decline in the peak current speed. Current speed was 1.3 knots (between periods of 4 and 5 knots), and turbine rotational speed was approximately 23 rotations per minute (RPM).

The second response to the device was observed on October 16th 2010 (Figure 25b). A ~25 cm fish was observed on the upstream side of the device swimming downward in the water column; it approached the lower half of the device, turned away abruptly and swam upstream against the current. Tidal current and

device rotational speed were 3.2 knots and 33 RPM. This response occurred during the ebb tide at night.

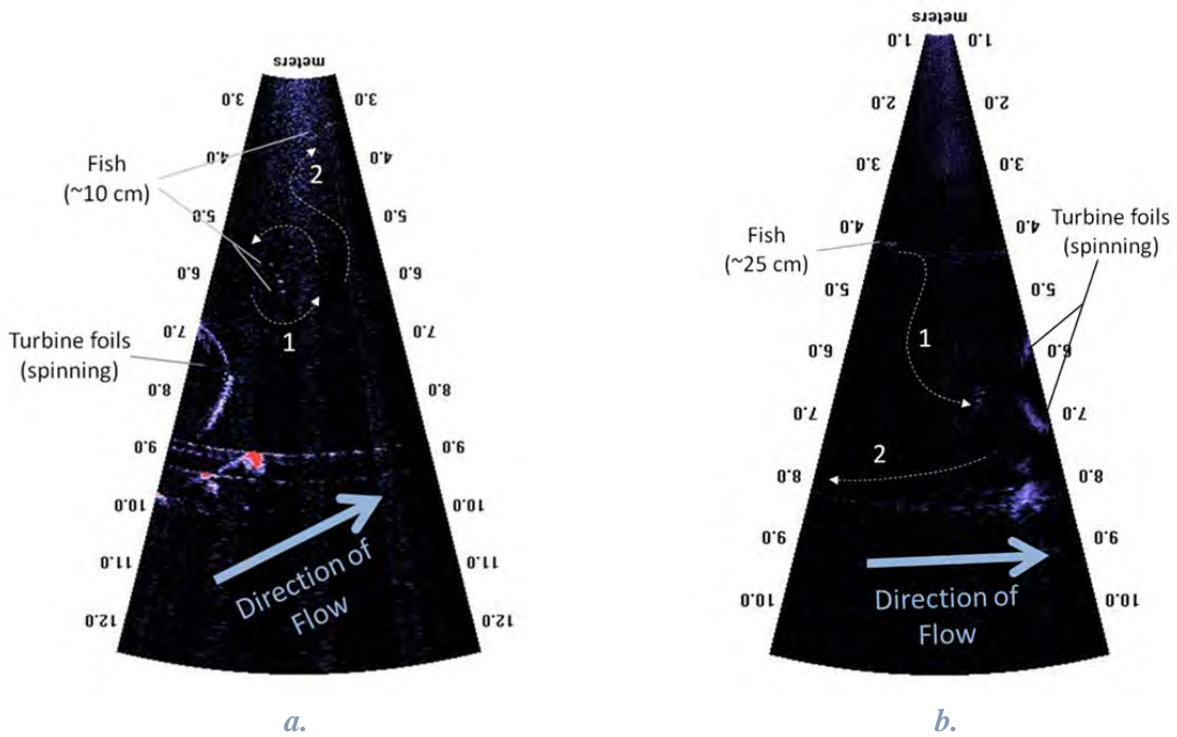


Figure 25. (a) Still shot of ~ 20 fish (approximately 100 mm long). Arrows show path of motion (re-orientation to flow, aft of turbine); (b) Still shot of a ~25 cm fish approaching turbine. Arrows show path of motion (approach to turbine, disappearance, quick change of direction).

4. Conclusions

4.1 Fish presence pre-deployment of TidGen™ Power System

There were differences in school and fish presence at the two sites studied in Cobscook Bay. Differences were likely linked to channel morphology and water flow at the sites. CB2 was generally deeper and likely had more laminar flow than at CB1, where the shape of the Bay changes and there is a major turn in the water flow. Relative differences between the two sites will likely not change annually, but data collected thus far are not complete enough (only one site and two months were available for inter-annual comparisons) to examine these differences. Future work and analyses will further inform inter-annual comparisons.

There were obvious seasonal differences in school and fish presence which were unique at each of the sites. At the deployment site there were more individual targets and schools present in August and September than in May and June. Based on data from 2010, there will likely be more individuals and schools present at the deployment site in late-summer and fall than in late-spring and early summer. These differences likely reflect the movement of different species in the bay during these seasons. For example, in early summer, diadromous species (such as salmon and river herring) would move upstream through bays as adults migrate toward spawning areas in freshwater (Saunders et al. 2006).

School presence at the deployment site, CB1, varied with tide (ebb and flood) in May and August 2010, while at CB2 tide affected presence in June, August, and September, 2010. More schools were present at the proposed deployment site during the ebb tide in May and August, but in August this difference also interacted with diel influences and more schools were present during the day than at night. School presence varied with diel cycle in September, when there were more schools in the water column during the day than at night at the proposed deployment site. While the number of schools was greater during the day, the size of the schools may vary and result in larger or smaller schools during different tidal or diel stages. Tidal and diel differences are likely related to the presence of schooling species that move in and out of the bay at different times of year, as explained above.

The presence of individuals, while influenced by season, was not influenced by tidal cycle. Only in June 2010 did individual target presence vary with diel cycle, where there were more targets present at the proposed deployment site during the night than at day.

When combined over all seasons and months, more than 50% of all schools and individual targets were detected 20-25 m above the seafloor. The center (median) of school and individual target distributions each month was at heights off the seafloor that were greater than 15 m, except in June 2010. The vertical distribution of schools off the seafloor was influenced by tidal cycle in May and August, 2010, and by day/night differences in June, 2010. The distance of individual targets off the seafloor was influenced by tide in August and September, and by diel factors in August. In May, August, and September, the amount of the water column used (IQR) was influenced by tide or diel cycle. At the proposed deployment depth (0 – 10 m above the seafloor), specifically where the foils will be moving (5 – 10 m), school and individual presence was highest in September, during the night and ebb tides (individuals). In May and June, 2010, relationships of individuals and schools with tidal and diel cycles were different from September.

Knowing when targets are lower in the water column (e.g., June at the proposed deployment site) and when they are spread out far enough for a significant proportion of them to be within the zone of the pilot turbine will be useful in analyzing risk posed by the project. As research continues, daily and seasonal patterns may provide a better understanding of fish interactions with the tidal power system. The next steps in our research involve examining how each factor influences fish activity, across and between months and sites, and identifying other possible influences on fish presence and distribution. Further analyses of these data, along with collection and analyses of new data, may elucidate factor effects.

The netting conducted in this study was not effective under these environmental conditions. Further knowledge of school composition would not only aid in target strength analysis for hydroacoustic assessments but would also allow an understanding of what species may be affected by the presence of a turbine in the water column. Other anecdotal information collected during the study (hook and line) indicated school composition was mixed in some cases and consisted of single species in others. Hook and line results confirmed the presence of Atlantic herring (*Clupea harengus*) and Atlantic mackerel (*Scomber scombrus*) at both sites in Cobscook Bay. However, netting results indicated the presence of primarily benthic fishes, which are weak swimmers (Scott *et al.* 1988 and Robbins *et al.* 1986) that probably could not avoid the net.

4.2 Direct observation of interactions with Beta TGU

Interactions of individual fishes with the ORPC Beta TGU are preliminary and require further analyses. Thus far two behaviors have been identified:

avoidance of and movement over and through the turbine. The fish observed were different in size and likely in species.

4.3 Final considerations

A bottom-mounted tidal power device would be located in the bottom 10 m (roughly $35 \pm 4\%$) of the water column at certain tidal stages. The presence of individual targets and schools in that portion of the water column is generally low and varies with the tidal cycle in May, August, and September. While numbers of schools and individual targets in this region are low, species remains unknown. More individual targets are present at the proposed deployment site than the control site. Any effect at the turbine will likely be on individual fishes that move in the bottom 10 m in that region. The presence of solitary, bottom-oriented species and their interaction with structures placed on the bottom should be considered further.

5. Future Work

5.1 Reducing the time from data collection to interpretation

A scrutinization and analysis routine is being created using MATLAB and EchoView's scripting module to allow automated processing of these types of data. This routine will reduce the amount of visual inspection and manual adjustments required to choose effective data thresholds, remove noise, and discriminate between noise, fish, schools, and turbulence. We are using analysis software and scripting to streamline the link between data collection and decision-making. This involves developing a method to determine the optimum data threshold that eliminates acoustic noise from the data while preserving actual targets, with limited human inspection. Since Echoview's fish tracking algorithm performs poorly when fish are densely aggregated, our routine must also be able to determine school detection parameters and change the quantification procedure accordingly. We will analyze existing and newly collected datasets to automate the process of determining the spatial and temporal patterns of fish distribution and how the introduction of tidal energy devices may impact those distributions.

5.2 Hydroacoustics for species (or target size) validation

Several procedures will be combined to extract species information from the acoustic data. First, knowledge of the life cycles of the region's fish combined

with the acoustic observations of their use of the tidal cycles will help to identify likely species. For example, fish known to spawn in rivers in the spring may be observed as an increase in numbers during the flood tides of those months as they use that flow to move upstream, and those species leaving in the fall will be detected as an increased number during ebb tides. Any distinct patterns will inform the target strength analysis of the acoustic data. Once a careful calibration of the SIMRAD transducer has been conducted, known target strengths of the expected species will be compared to target strengths of detected targets. The two frequencies of the SIMRAD transducer will aid in this analysis, since some species can be distinguished by their differing acoustic signatures at different frequencies. The DIDSON acoustic camera will be used to directly view species in the upper 10 meters of the water column, which can sometimes result in identification of targets to the species level. More generally, the DIDSON will provide information such as fish length and school density that can be used in conjunction with the acoustic returns obtained with the SIMRAD to narrow down likely species and develop length-target strength relationships that can be applied to detections beyond the DIDSON's range.

5.3 Netting for species validation

Net modifications and discussions with local fishermen are being considered to successfully deploy and fish midwater nets successfully in Cobscook Bay. We may switch to bottom trawling to provide some indication of fish species presence in the region. These changes will be subject to acquiring a new research permit.

5.4 Expanded fish assessments

It is worth noting that future study plans include further hydroacoustic assessments (additional months, specifically October, November, January, March) at the same sites as well as an expanded assessment of fish communities in the region. The expansion will include assessment of fish communities along in-shore regions and in other parts of the Bay (outer, middle, and upper).

6. Acknowledgements

This work was funded by the US Department of Interior, grant DE-EE0000298. We thank the Maine Tidal Power Initiative, particularly Mick Peterson, for supporting (and emphasizing) this part of the project and its importance for achieving a balance for the natural resources and development of tidal power in Maine. Our work could not have been completed without the incredible Downeast

spirit and work ethic of our field support: captains and crews of the Lady H and Brayden's Future (Butch Harris, Scott MacNichol, Darius Neptune, Robert Gordon, Skip Harris, and others) and ORPC staff (Bob Lewis, David Turner, Ryan Beaumont, Sean Anderton, and Seth Gray). General encouragement and support was provided by University of Maine School of Marine Sciences (Huijie Xue, Pete Jumars) and ORPC (Chris Sauer, Jarlath McEntee, John Ferland, Herb Scribner, and Ernie Hauser).

7. References

- Athearn, K. and C. Bartlett. 2008. Saltwater fishing in Cobscook Bay: Angler profile and economic impact. *Marine Research in Focus*. Volume 6, 6 pp.
- Brawn, V.M. 1960. Temperature tolerance of unacclimated herring (*Clupea harengus* L.). *Journal of the Fisheries Research Board of Canada*. 17(5): 721-723.
- Foote, K.G. 1987. Fish target strengths for use in echo integrator surveys. *Journal of the Acoustical Society of America*. 82: 981-987.
- Knudsen, H. P. 2009. Long-term evaluation of scientific-echosounder performance. *ICES Journal of Marine Science*. 66: 1335-1340.
- Koch, P. 1974. Distribution of pelagic fishes in a Maine estuary subject to thermal pollution. M.S. Thesis, University of Maine, Orono, ME. 51 pp.
- Macdonald, J. S., M. J. Dadswell, R. G. Appy, G. D. Melvin, and D. A. Methven. 1983. Fishes, fish assemblages, and their seasonal movements in the lower Bay of Fundy and Passamaquoddy Bay, Canada. *Fishery Bulletin*. 82: 121-139.
- Nielsen, J. R. and B. Lundgren. 1999. Hydroacoustic *ex situ* target strength measurements on juvenile cod (*Gadus morhua* L.). *ICES Journal of Marine Science*. 56 (5): 627-639.
- Ona, E. 2003. An expanded target-strength relationship for herring. *ICES J. Mar. Sci.* 60 (3): 493-499.
- Robins, C.R., G.C. Ray, J. Douglass, and R. Freund. 1986. *A field guide to the Atlantic coast fishes of North America*. Houghton Mifflin, Boston.
- Saunders, R., M.A. Hachey, and C.W. Fay. 2006. Maine's diadromous fish community: past, present, and implications for Atlantic salmon recovery. *Fisheries*. 31: 537-547.
- Scott, W.B. and M.G. Scott. 1988. Atlantic fishes of Canada. *Canadian Bulletin of Fisheries and Aquatic Sciences*. 219: 731.
- Tyler, A.V. 1971. Periodic and resident components in communities of Atlantic fishes. *Journal of the Fisheries Research Board of Canada*. 28: 935-946.

USDOE 2009. *Report to Congress on the Potential Environmental Effects of Marine and Hydrokinetic Energy Technologies: Prepared in Response to the Energy Independence and Security Act of 2007, Section 633(B)*. Wind and Hydropower Technologies Program, Energy Efficiency and Renewable Energy, U.S. Department of Energy. December, 2009.

Appendix 1. Summary of midwater net tows made in Outer Cobscook Bay.

Tows were conducted in May and June 2010. *Boat was moored on these tows, letting the tide flow through the net.

Tow number	Latitude, deg, min	Longitude, deg, min	Date	Start time	Duration, min	Tidal stage	Fish caught?
1	44 54	67 01	20 May	8:13am	30	Ebb	Yes
2	44 54	67 01	20 May	9:03am	30	Ebb	No
3	45 00	67 01	20 May	9:43am	33	Ebb	No
4	44 54	67 02	20 May	1:01pm	30	Flood	No
5	44 54	67 02	20 May	1:40pm	30	Flood	No
6	44 54	67 02	20 May	2:15pm	30	Flood	Yes
7	44 54	67 02	20 May	8:22pm	31	Ebb	Yes
8	44 54	67 02	20 May	9:05pm	30	Ebb	Yes
9	44 54	67 02	20 May	9:45pm	30	Ebb	No
10	44 54	67 02	21 May	0:55am	30	Flood	No
11	44 54	67 02	21 May	1:32am	30	Flood	Yes
12	44 54	67 02	21 May	2:08am	30	Flood	No
13	44 54	67 02	21 May	8:56pm	30	Ebb	No
14	44 54	67 02	21 May	9:35pm	30	Ebb	Yes
15	44 54	67 02	21 May	10:15pm	30	Ebb	No
16	44 54	67 02	22 May	2:10am	30	Flood	Yes
17	44 54	67 02	22 May	2:47am	30	Flood	Yes
18	44 55	67 01	13 June	12:35pm	22	Flood	No
19	44 54	67 01	13 June	2:10pm	30	Ebb	No
20*	44 54	67 02	13 June	6:40pm	12	Ebb	No
21	44 54	67 02	13 June	7:06pm	45	Slack	Yes
22*	44 54	67 02	13 June	8:15pm	45	Flood	Yes
23*	44 54	67 02	13 June	9:10pm	45	Flood	Yes
24*	44 54	67 02	13 June	11:25pm	45	Flood	Yes
25	44 54	67 02	14 June	0:45am	15	Ebb	Yes
26*	44 54	67 02	14 June	2:20am	45	Ebb	No
27*	44 54	67 02	14 June	3:10am	45	Ebb	Yes
28*	44 54	67 02	14 June	4:10am	45	Ebb	Yes

Appendix 2. Species and numbers of fishes netted.

Species and numbers of fishes caught in midwater net tows in Outer Cobscook Bay May and June.

Tow number/ Species	1	6	7	8	11	14	16	17	21	22	23	24	25	27	28	Total
Blackspotted stickleback														1		1
Hake sp.													1			1
Longhorn sculpin				3?						1						4
Lumpfish									1			1	1	3	1	8
Ocean pout														1		1
Sea raven												1				1
Threespine stickleback	9	1		3		2	2	2								19
Windowpane											1					1
Winter flounder					3											3
Winter skate			1													1
Total	9	1	1	6	3	2	2	2	1	1	1	2	2	5	1	40

Appendix 3. Table of data contained in Figure 13.

Percent of individual targets and schools in associated depth bins (distance off the seafloor). Numbers are standardized totals encountered in all seasons in 2010. Percentages are calculated using the total for all bins. Red shaded areas are those that the proposed deployment will encompass.

For proposed deployment site (CB1):

Distance off the seafloor	Individual targets		Schools	
	Number (#/100m ³ /km)	Percent	Number (#/100m ³ /km)	Percent
0-5	1783.4	1.8	27.2	1.0
5-10	2195.5	2.3	30.5	1.1
10-15	8145.6	8.4	176.0	6.1
15-20	24538.7	25.3	377.0	13.2
20-25	51206.9	52.8	1859.9	65.1
25-30	7982.7	8.2	248.9	8.7
30-35	611.5	0.6	92.1	3.2
35-40	484	0.5	38.9	1.4
40-45	18.4	0.02	5.7	0.2
45-50	0	0	0	0

For control site (CB2):

Distance off the seafloor	Individual targets		Schools	
	Number (#/100m ³ /km)	Percent	Number (#/100m ³ /km)	Percent
0-5	157.8	0.4	39.4	0.5
5-10	150.1	0.4	26.4	0.3
10-15	319.2	0.7	40.8	0.5
15-20	807.3	1.9	107.5	1.3
20-25	1927.8	4.4	344.0	4.2
25-30	8171.3	18.9	1998.0	24.3
30-35	17911.2	41.3	3959.6	48.1
35-40	13810.3	31.9	1677.1	20.4
40-45	68.2	0.1	32.0	0.4
45-50	0	0	0	0

Appendix 4. Table of data contained in Figure 14.

Number of individual targets and schools in associated depth bins (distance off the seafloor). Numbers are standardized totals encountered in all seasons in 2010, \pm standard error. Red shaded areas are those that the proposed deployment will encompass (turbine foils located in the 5-10 m bin).

For proposed deployment site (CB1):

Distance off the seafloor (m)	Individual targets				Schools			
	May	June	Aug	Sept	May	June	Aug	Sept
0-5	1.24 \pm 0.51	0.81 \pm 0.28	24.34 \pm 15.60	9.27 \pm 1.62	15.60 \pm 0.02	1.62 \pm 0.46	0.00 \pm 0.04	0.00 \pm 0.03
5-10	2.85 \pm 1.15	1.71 \pm 0.58	23.12 \pm 12.49	16.22 \pm 3.98	12.49 \pm 0.04	3.98 \pm 0.39	0.00 \pm 0.05	0.00 \pm 0.13
10-15	24.63 \pm 16.34	6.20 \pm 2.13	65.61 \pm 22.11	66.47 \pm 15.02	22.11 \pm 0.13	15.02 \pm 2.24	0.00 \pm 0.79	0.00 \pm 0.36
15-20	27.29 \pm 11.00	97.43 \pm 61.41	185.74 \pm 60.12	180.31 \pm 33.32	60.12 \pm 0.19	33.32 \pm 1.63	0.00 \pm 2.16	0.00 \pm 3.56
20-25	32.36 \pm 14.33	70.77 \pm 22.22	542.61 \pm 249.66	378.40 \pm 84.69	249.66 \pm 1.29	84.69 \pm 0.63	0.00 \pm 24.34	0.00 \pm 10.94
25-30	14.39 \pm 4.55	37.40 \pm 15.24	17.55 \pm 6.65	90.32 \pm 34.78	6.65 \pm 0.98	34.78 \pm 0.24	0.00 \pm 1.16	0.00 \pm 2.60
30-35	6.88 \pm 1.93	5.35 \pm 2.14		0.00 \pm 0.00	0.00 \pm 1.82	0.00 \pm 0.02		0.00 \pm 0.00
35-40	2.86 \pm 1.15	6.83 \pm 6.75			0.00 \pm 0.78	0.00 \pm 0.00		
40-45	0.37 \pm 0.20	0.00 \pm 0.00			0.00 \pm 0.11	0.00 \pm 0.00		
45-50	0.00 \pm 0.00				0.00 \pm 0.00			

For control site (CB2):

Distance off the seafloor (m)	Individual targets				Schools			
	May	June	Aug	Sept	May	June	Aug	Sept
0-5	0.16 ± 0.12	0.26 ± 0.05	1.87 ± 0.48	0.86 ± 0.22	0.48 ± 0.19	0.22 ± 0.37	0.00 ± 0.05	0.00 ± 0.18
5-10	0.37 ± 0.26	0.24 ± 0.06	1.48 ± 0.45	0.91 ± 0.23	0.45 ± 0.08	0.23 ± 0.14	0.00 ± 0.11	0.00 ± 0.21
10-15	0.59 ± 0.23	0.44 ± 0.11	2.06 ± 0.56	3.30 ± 1.52	0.56 ± 0.18	1.52 ± 0.23	0.00 ± 0.14	0.00 ± 0.26
15-20	1.97 ± 0.90	1.11 ± 0.26	4.99 ± 0.94	8.08 ± 4.32	0.94 ± 0.61	4.32 ± 0.61	0.00 ± 0.31	0.00 ± 0.62
20-25	6.69 ± 2.26	3.84 ± 1.00	14.34 ± 1.84	13.69 ± 6.44	1.84 ± 2.18	6.44 ± 2.14	0.00 ± 1.29	0.00 ± 1.28
25-30	24.64 ± 12.11	46.80 ± 11.53	42.55 ± 5.94	49.44 ± 20.95	5.94 ± 22.43	20.95 ± 10.02	0.00 ± 3.56	0.00 ± 3.96
30-35	14.79 ± 5.81	193.09 ± 88.16	109.01 ± 16.48	41.33 ± 9.52	16.48 ± 18.03	9.52 ± 37.67	0.00 ± 16.11	0.00 ± 7.38
35-40	3.63 ± 2.55	182.52 ± 125.37	73.13 ± 30.78	16.93 ± 5.58	30.78 ± 2.08	5.58 ± 22.20	0.00 ± 5.13	0.00 ± 4.13
40-45	0.00 ± 0.00	0.00 ± 0.00	0.00 ± 0.00	1.36 ± 0.86	0.00 ± 0.00	0.86 ± 0.00	0.00 ± 0.00	0.00 ± 0.64
45-50	0.00 ± 0.00	0.00 ± 0.00	0.00 ± 0.00	0.00 ± 0.00	0.00 ± 0.00	0.00 ± 0.00	0.00 ± 0.00	0.00 ± 0.00

Appendix 5. Summary of effects for 2010 comparisons at CB2.

Empty boxes indicate no significance. Values are p-values from 2-way ANOVA comparisons.

Response	treatment	May		June		August		September	
		Schools	Indiv.	Schools	Indiv.	Schools	Indiv.	Schools	Indiv.
Count	Tide			.005	.03	.01	<.001	.005	.04
	Diel	.04					<.001	.01	
	Inter.						<.001		
Height	Tide	.035			.032		.03		
	Diel	.002							
	Inter.								
IQR	Tide				.016				
	Diel						.008		
	Inter.								

Appendix Task 2-5

Fisheries and Marine Life Interaction Monitoring Plans Annual Report

March 2013

University of Maine, School of Marine Sciences
Haley Viehman, Garrett Staines, Gayle Zydlewski

1.0 Introduction

1.1 Study Context and Purpose

Ocean Renewable Power Company, LLC (ORPC) has deployed a TidGen™ Power System in outer Cobscook Bay, Maine, as the first stage of the Cobscook Bay Tidal Energy Project (Figure 1). This installation requires monitoring to assess potential effects of the TidGen™ Power System on the marine environment. ORPC's monitoring plan regarding marine life has two parts: 1) Fisheries Monitoring Plan and 2) Marine Life Interaction Monitoring Plan.

1.2 Study Design

1.2.1 Fisheries monitoring plan

The Fisheries Monitoring Plan is a continuation of research started by the University of Maine's School of Marine Science researchers in 2009. The study was designed to capture tidal, seasonal and spatial variability in the presence and relative abundance of fish in the area of interest (near the TidGen™ deployment site). The design involves down-looking hydroacoustic surveys during several months of the year, and examines the vertical distribution and relative abundance of fish at the project and control site (for relative comparison). Pre-deployment data were collected in 2010, 2011, and early 2012, and will be compared to post-deployment data to quantify changes in fish presence, biomass, and vertical distribution associated with the installation of the TidGen™ power system. Surveys are planned through the year 2017.

1.2.2 Marine life interaction monitoring plan

The Marine Life Interaction Monitoring Plan uses side-looking hydroacoustics collected by ORPC at the TidGen™ project site to assess the interaction of marine life (fish, mammals, and diving birds) with the TidGen™ device. This monitoring focuses on the behavior of marine life (primarily fish) as they approach or depart from the region of the turbine, and will attempt to quantify changes in behavior in response to the TidGen™ unit. Side-looking hydroacoustic data will be collected for three years after the deployment of the TidGen™ Power System.

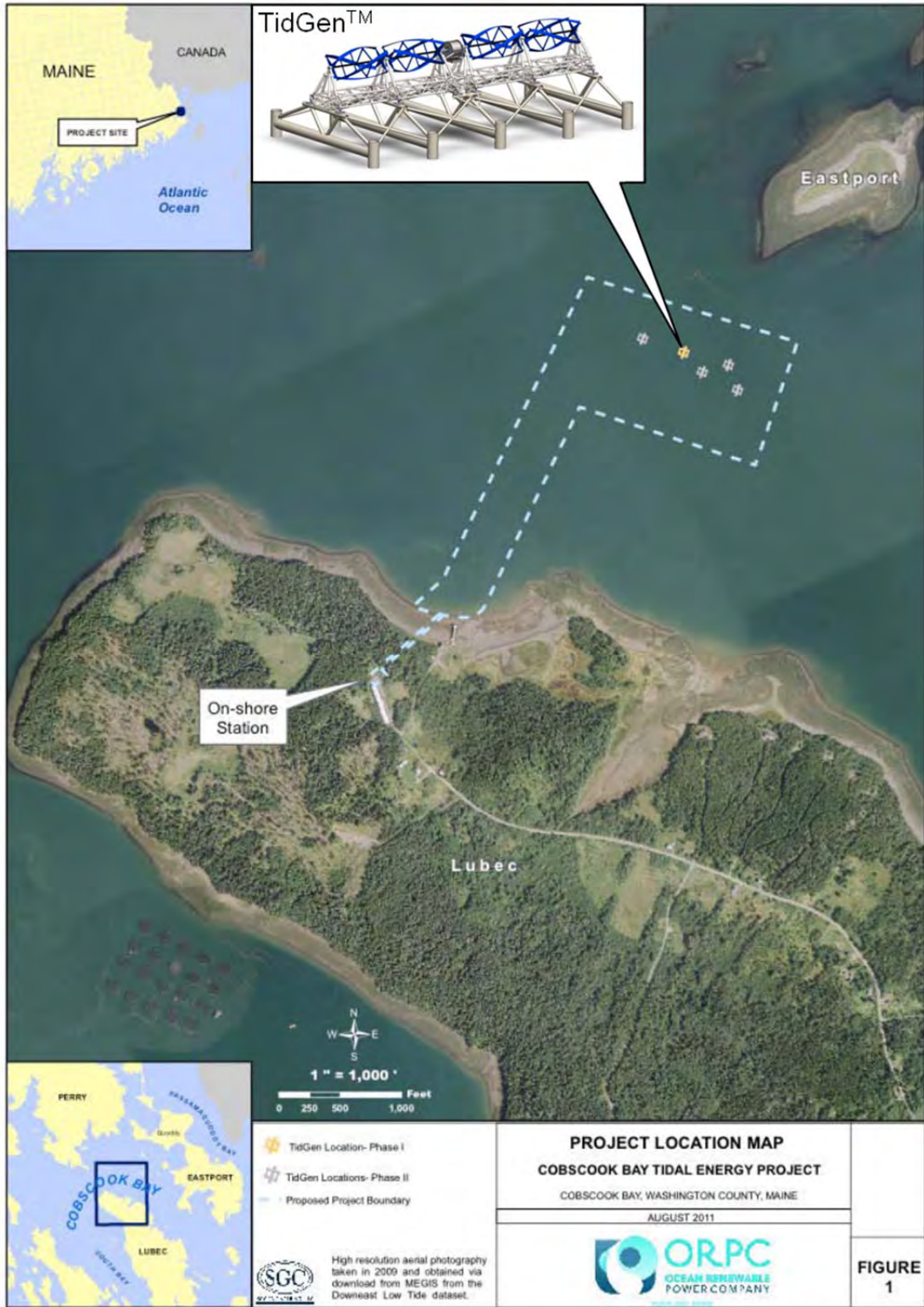


Figure 1. Cobscook Bay Tidal Energy Project location map and TidGen™ device drawing (ORPC monitoring plan/pilot license application). The yellow icon represents the present location of a TidGen™ device. The grey icons represent potential TGU locations to complete an array in the future.

1.3 In This Report

This first report details: (1) approach to date; (2) preliminary results; (3) challenges to date, how they are being addressed and future work.

2.0 Approach

2.1 Fisheries Monitoring Plan (down-looking hydroacoustic surveys)

2.1.1 Study design

To compare the relative abundance and vertical distribution of fish at the project site and a control site nearby, both before and after turbine deployment, down-looking hydroacoustic surveys are conducted from a research vessel for one 24-hour period several times per year at each site (Table 1). Locations during pre-deployment sampling include one site at the project location (CB1) and one control site, approximately 1.6 km seaward of the project site (CB2) (Figure 2). During post-deployment, two sites were sampled at the project location: CB1a, beside the turbine, and CB1b, in line with the turbine, and the same single location at the control site (CB2) (Figure 2). Sampling locations at the project sites in 2012 varied geographically because of construction activity and related safety concerns around the TidGen™. January and March were pre-deployment, so only CB1b and CB2 were sampled. CB1b in March was only sampled for 12 hours due to extreme weather. There was no November sample because the TGU was removed for maintenance.

The down-looking surveys are carried out using a single-beam Simrad ES60 commercial fisheries echosounder, with a wide-angle (31° half-power beam angle), dual-frequency (38 and 200 kHz) circular transducer. In May 2012, a Simrad EK60 200 kHz split beam echosounder was added to the previous sampling protocol. The transducers are mounted over the side of the research vessel 1.8 meters below the surface, and they ensonify (alternately, every 0.5 seconds) an approximately conical volume of water extending to the sea floor. A 600 kHz Workhorse Sentinel acoustic Doppler current profiler (ADCP) is set to record mean current speed in 1 meter bins to the sea floor every 30 minutes during the survey. ADCP data are used to determine slack tide periods during sampling.

The single-beam transducer, used for relative comparison to baseline data collected in 2010 and 2011, does not provide information on an acoustic target's location within the ensonified beam cross-section. This lack of angular data prevents meaningful target strength (TS) (size) data from being acquired. Therefore, a relative hydroacoustic measure of fish biomass, rather than an absolute fish count, is used to examine changes in fish biomass over time. This relative measure is also used to assess vertical distribution of fish biomass in the water column.

Table 1. Months sampled for Fisheries Monitoring Plan (down-looking hydroacoustics). 1,2 indicate sampling at CB1 and CB2, 1a,1b,2 indicates sampling at CB1a, CB1b, and CB2. Shaded blocks indicate presence of TidGen™. * TidGen™ support frame installed.

	Jan	Feb	Mar	April	May	June	July	Aug	Sept	Oct	Nov	Dec
2010					1,2			1,2	1,2	1,2	1,2	
2011			1,2		1,2	1,2		1,2	1,2		1,2	
2012	1,2		1,2*		1a,1b, 2	2		1a,1b, 2	1a,1b, 2			

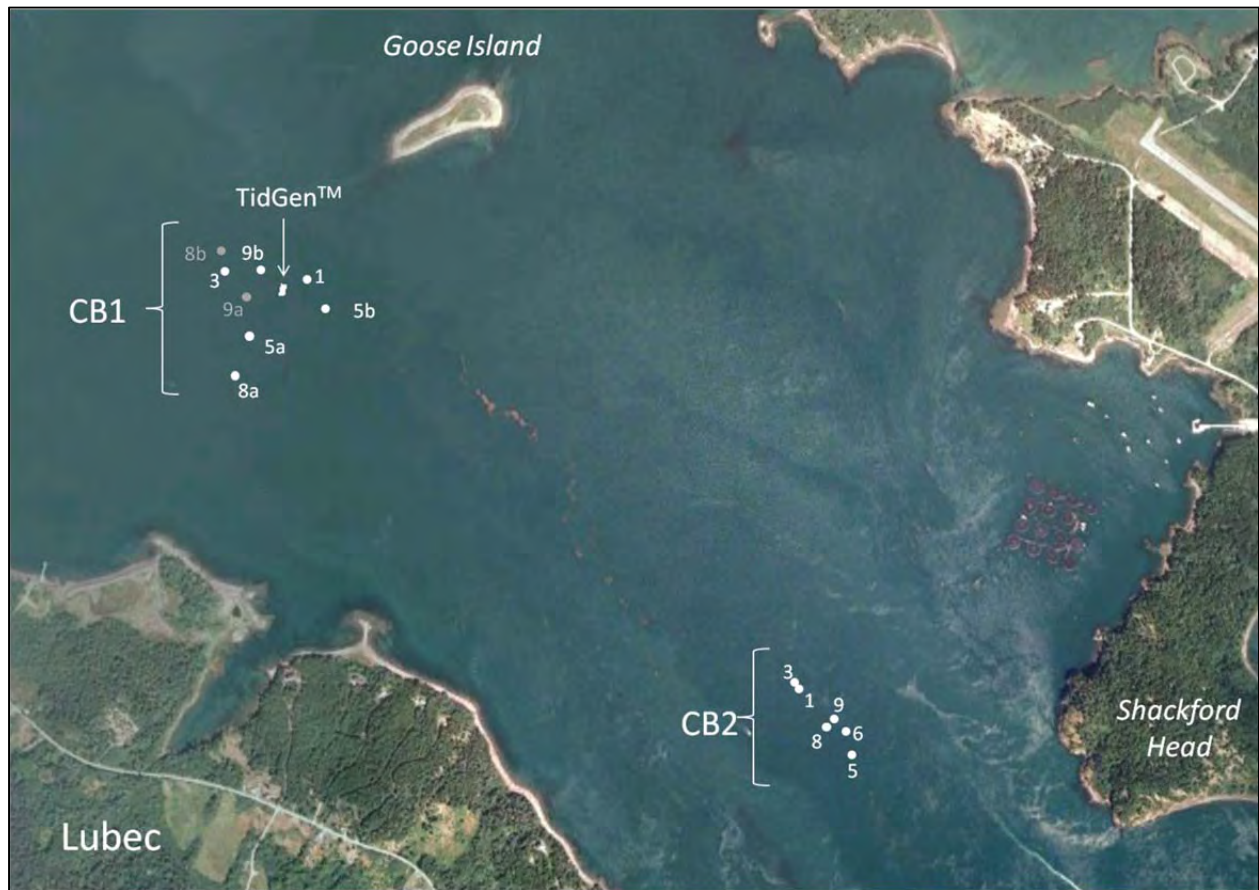


Figure 2. Fisheries Monitoring Plan study area and down-looking hydroacoustic survey locations for 2012. Each point represents the mooring location for one 24-hour survey. Numbers indicate the month of each survey; a and b indicate CB1a or CB1b, if applicable. Darker points (8b and 9a at CB1) are approximate due to GPS error.

Comparisons of fish biomass and vertical distribution are made among the control site and project site(s) and among different months at each site. Sampling before and after turbine deployment at the project as well as at a control site improves the ability to distinguish changes that may be related to the presence of the turbine from changes due to annual, seasonal, daily, and tidal variation. These methods are consistent with a before-after-control-impact (BACI) statistical design. In the future, split beam data will be used to provide accurate TS on single fish and potentially allow quantitative measures of fish movement.

2.1.2 Data processing

Hydroacoustic data are processed using Echoview® software (5.3, Myriax Pty. Ltd., Hobart, Australia), and statistical analyses are carried out in MATLAB (r2011b, The MathWorks, Inc., Natick, MA, USA). Only 200 kHz frequency data are used in analyses. Processing includes scrutinizing the data and removing areas of noise (e.g., from electrical interference, a passing boat's depth sounder, high boat motion). Hydroacoustic interference from entrained air is common in the upper 10 m of the water column; analyses are therefore limited to the lowest 15 m of the water column. Unwanted hydroacoustic signals (such as plankton, krill, and fish larvae) are excluded by eliminating backscatter from targets with TS less than -60 dB. Most fish have a TS between -60 dB and -20 dB but TS varies greatly with fish anatomy and orientation (Simmonds and MacLennan 2005). This variability, combined with the TS uncertainty inherent in single beam systems, means that some fish will be excluded from analyses. Fish presence is measured on a relative scale using volume backscatter (S_v), which is a measure of the sound scattered by a unit volume of water and is assumed proportional to biomass (Simmonds and MacLennan 2005). S_v is expressed in the logarithmic domain as decibels, dB re 1 m^{-1} . S_a is a measure of biomass scaled to unit area of water expressed in the linear domain and is used for vertical distribution comparisons (Simmonds and MacLennan 2005).

Because flowing tides are the focus of this study, hydroacoustic data during slack tides were not included in analyses. Slack tides span one hour, centered at the time of low or high water. Mean current speed is obtained for each half hour by averaging ADCP data from surface to seafloor. The recorded time with the lowest water flow value was deemed slack. The half hour before and after this time was then removed from hydroacoustics data processing and analyses.

Inspected hydroacoustic data are divided into 30-minute segments. Echoview is used to calculate the mean S_v of the water column for each 30-min interval. For each interval, the area backscattering coefficient, S_a , is calculated for 1-m layers within the water column. S_a is the summation of volume backscatter over a given depth range, and is also proportional to fish biomass. By calculating the proportion of S_a contributed to each 1-m layer of water, the vertical distribution of fish is constructed for each 30-min time interval. Layers are measured upward from the sea floor, rather than downward from the surface, as the turbine is installed at a fixed distance above the bottom. In the future, split beam data will be processed similarly to determine whether it can be used for comparison to previously collected single beam data. At minimum, split beam data will be used to (1) make meaningful comparisons of the vertical distribution of fish using S_a ; (2) quantify the number of fish tracks observed in 1-m layers measured up from the

sea floor; and (3) provide accurate TS for those targets. Analyses comparing S_v between the single and split beam systems are underway.

Statistical comparisons of overall fish biomass and vertical distribution can be conducted among survey dates using t-test and linear regression analyses, as in Viehman 2012. Briefly, mean water column S_v values for each entire 24 h survey can be compared to other 24 h surveys using t-tests (significance level = 0.05). Vertical distributions can be compared by linear regression of one distribution onto the other. Shape similarity is indicated by a significant fit (significance level of 0.05) and a positive slope. Negative slope or insignificant fit indicates dissimilar distributions. For a full description of single-beam data analyses methods used and results from pre-deployment data collected, see Viehman 2012.

2.2 Marine Life Interaction Monitoring Plan (side-looking hydroacoustics)

2.2.1 Study design

ORPC has mounted a Simrad EK60 split beam echosounder (200 kHz, 7° half-power beam width) to a steel frame located 44.5 m from the southern edge of the TidGenTM (Figure 3). This frame holds the transducer 3.4 m above the sea floor, with the transducer angled 9.6° above the horizontal with a heading of 23.3°. The echosounder samples an approximately conical volume of water extending approximately 100 m, directly seaward of the TidGenTM device (Figure 3). The actual sampled volume used in data analysis is smaller, extending to the far edge of the turbine (78.1 m) rather than beyond. This is because after that point, interference from sound reflection off the water's surface becomes too great to reliably detect fish. The sampled volume is upstream of the device during the flood tide and downstream of the device during the ebb tide. The echosounder is powered and controlled via undersea cables from the ORPC shore station in Lubec, where data files are stored on a server and collected periodically by the University.

The echosounder records data continuously (though to date, collection has been intermittent; see Sections 3.1.2 and 4.2). Continuous data collection at a fast sample rate (4 to 6 per second) allows each fish or other marine animal that passes through the beam to be detected several times, recording information on the echo strength and 3D location within the beam (Figure 4). These data are used to track fish movement during their approach to the turbine (flood tide) as well as during their departure (ebb tide) on a fine spatio-temporal scale. The sampled volume is divided into three zones: the turbine zone, where fish would be likely to encounter the turbine; above the turbine zone (A, Figure 3a); and beside the turbine zone (B, Figure 3a). Fish numbers and movement in each zone provide indicators of turbine avoidance. The total sampling volume to 78.1 m range (for a 7° cone) is 1,866 m³, and of this, 607m³ are within the turbine zone, 345 m³ are beside the turbine zone, and 914 m³ are above the turbine zone.

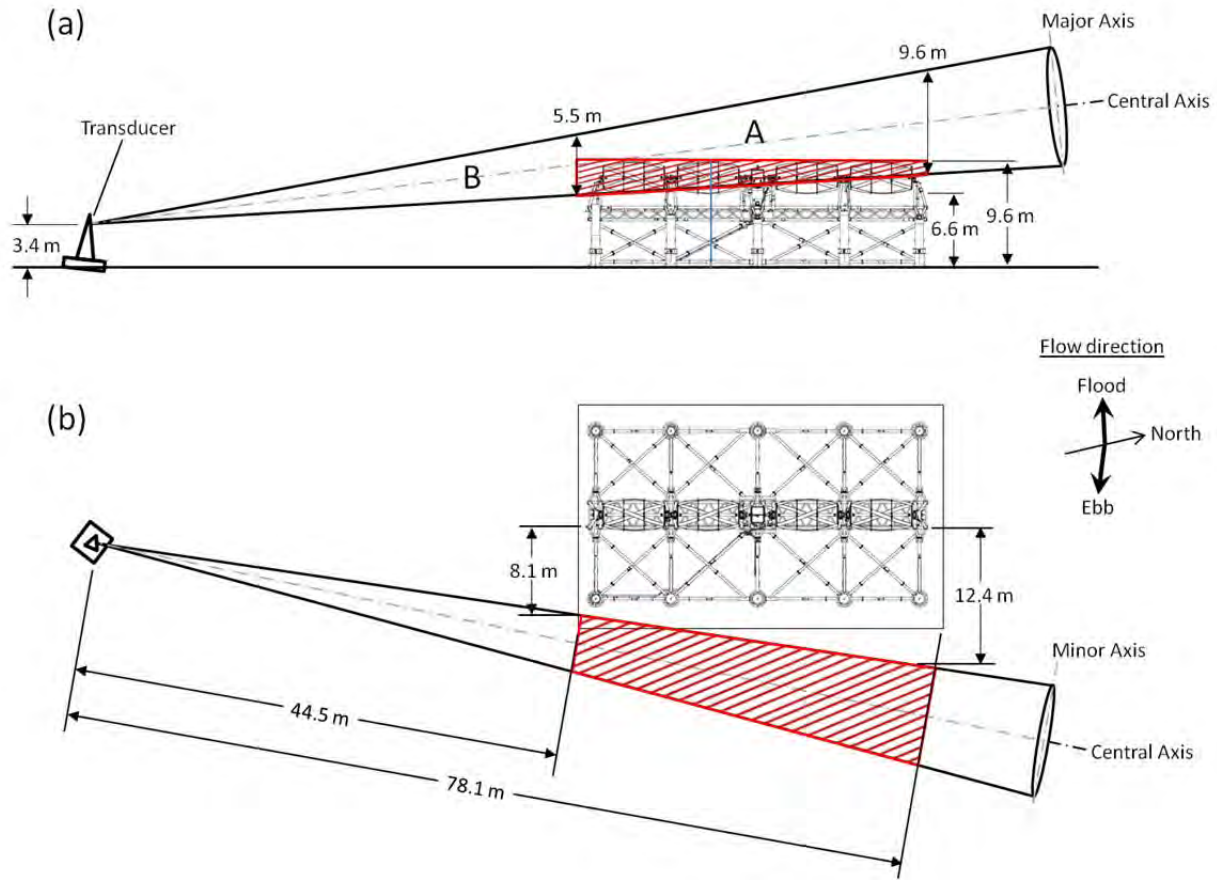


Figure 3. Marine Life Interaction Monitoring Plan setup. TidGen™ device and Simrad EK60 support structure shown from (a) the seaward side and (b) above. Hydroacoustic beam represented as 7° cone (half-power beam width) in solid black lines. Red hatched area indicates sampled volume within the turbine zone; A indicates the volume sampled above the turbine, and B indicates the volume sampled beside the turbine.

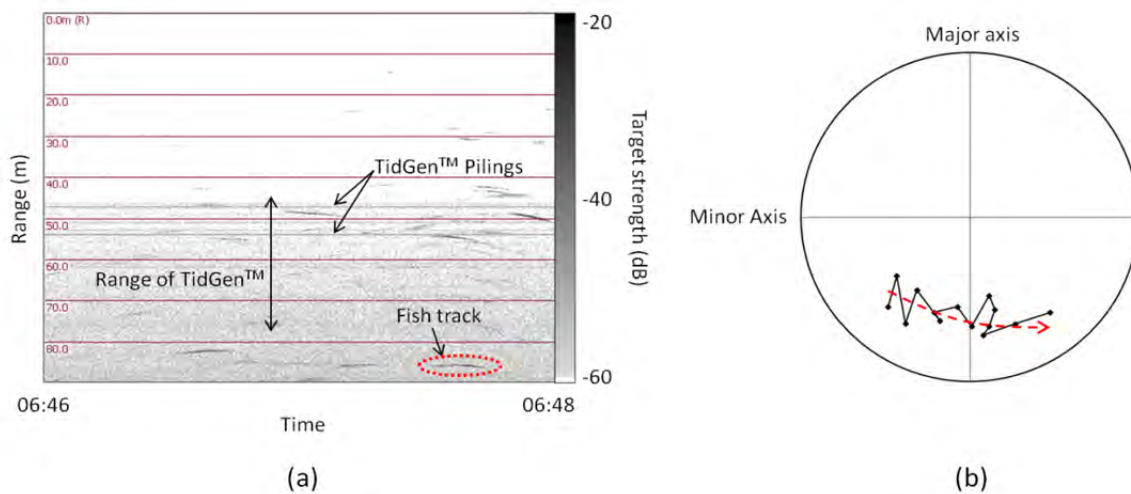


Figure 4. (a) Sample of side-looking hydroacoustic data from 9/30/2012. (b) Fish in red dashed oval in (a) tracked through beam cross section. Outer circle represents 3.5° off-axis, or 5.3 m at this range. Each diamond is a single detection of the fish. Red dashed arrow indicates direction of movement.

2.2.2 Data processing

Echoview is used to process raw side-looking split beam hydroacoustic data. Processing in Echoview begins with manually inspecting the data to identify and exclude unwanted noise (e.g., interference from depth sounders, entrained air from the surface, reflection from surface waves), and setting a TS threshold of -60 dB (consistent with down-looking approach) to exclude plankton and other small objects from analyses. Echoes from single targets are detected, excluding those more than 3.5° from the central axis of the beam or beyond 78.1 m from the transducer (due to the increase in surface noise interference). Single target detection parameters are summarized in Table 2. Echoview's fish tracking module is then used to trace the paths of individual fish through the sampled volume; schools of fish are excluded from analyses. Fish track data are then exported from Echoview to be further analyzed using MATLAB. The data for each fish track include time of fish detection, location of the fish within the beam over time (range, depth, major and minor off-axis angles), fish TS, and fish swimming speed and direction. Data can then be grouped by month for further analyses.

Table 2. Single target detection settings in Echoview.

Parameter	Value
Target strength threshold	-60.00 dB
Pulse length determination level	6.00 dB
Minimum normalized pulse length	0.60
Maximum normalized pulse length	1.50
Beam compensation model	Simrad LOBE
Maximum beam compensation	6.00 dB
Maximum standard deviation of minor-axis angles	1.000°
Maximum standard deviation of major-axis angles	1.000°

Flood and ebb tide data are treated separately for all but overall summary data (e.g., total fish TS distribution and fish numbers). This is because a fish's approach to the turbine is sampled during the flood tide while its departure from the turbine is sampled during the ebb tide, and behaviors during each are assumed to differ (Viehman 2012; Viehman and Zydlewski submitted).

Target strength

Target strength is a point source measure and is the relative amount of hydroacoustic energy reflected back toward the transducer by an object, represented in decibels (dB; Simmonds and MacLennan 2005). Though TS is dependent on several factors, including fish anatomy (e.g., swim bladder or none) and orientation to the hydroacoustic beam, it is generally proportional to fish size (Simmonds and MacLennan 2005). Depending on the species known to be in the area, TS may be used to identify with some probability the species of a detected fish and approximate its size. The TS distribution is therefore extracted for each month of data in order to provide information on the size of fish sampled. The fish community of Cobscook Bay is also being assessed by UMaine and will aid in identifying probable species represented by hydroacoustic targets.

Number and location of fish tracks

The total number of fish tracks detected in Echoview for each month of hydroacoustic data provides an index of the abundance of fish in the sampled volume over time.

The location of each fish at the time of entry into the sampled volume is used to place it in one of the three zones (in the turbine zone, beside the turbine zone, or above the turbine zone; Figure 3). Density of fish in each zone is calculated for each ebb and flood tide by dividing the total number of fish detected in each zone by the volume sampled within the zone. This volume is calculated by multiplying the area of the zone's vertical cross-section (Figure 3a) by the approximate linear distance of water to pass through it during the time sampled (ebb tide or flood tide, slack to slack). The linear distance of water is the median of current speed during the time spanned multiplied by the sampling duration. In this way, fish counts were normalized for varying sample times and volumes, allowing the direct comparison of densities from different tidal stages. Densities obtained from each tidal stage are then grouped by month and can be compared to those from other months using a t-test (significance level = 0.05).

Fish swimming speed and direction of movement

The speed and direction of movement of each fish is compared to the current speed and direction at the time of fish detection (when available). Higher deviation from the current speed or direction within the turbine zone than in other zones may indicate avoidance behavior. For each month, the difference in fish speed and direction from current speed and direction in each zone is calculated for each tidal stage (flood or ebb) and can be compared to corresponding values from other months using t-tests (significance level = 0.05).

If current speed and direction information is not available (see section 3.1.2), the distributions of fish swimming direction and speed and their variance can be used as indicators of avoidance. More variable movement directions are associated with avoidance reactions (e.g., diverting

above, below, or to the side of the turbine, or reversing direction; Viehman 2012). Variance in speed and direction within each zone can be compared using one-way ANOVA tests (significance level of 0.05).

3.0 Results to Date

3.1 Fisheries monitoring plan (down-looking hydroacoustics)

Down-looking hydroacoustics data for the Fisheries Monitoring Plan have been collected as outlined in Section 2.1. Total water column fish biomass was determined at each site for each month (Figure 5). Vertical distribution of fish biomass by 1 meter depth layers (measured upward from the sea floor) was determined at each site for each month (Figure 6 and Appendices B and C). Pre-deployment data from 2010 and 2011 were analyzed previously and are not included here, but full analyses are available in Viehman 2012. March had the lowest biomass and May had the highest. As the summer months progressed, biomass decreased.

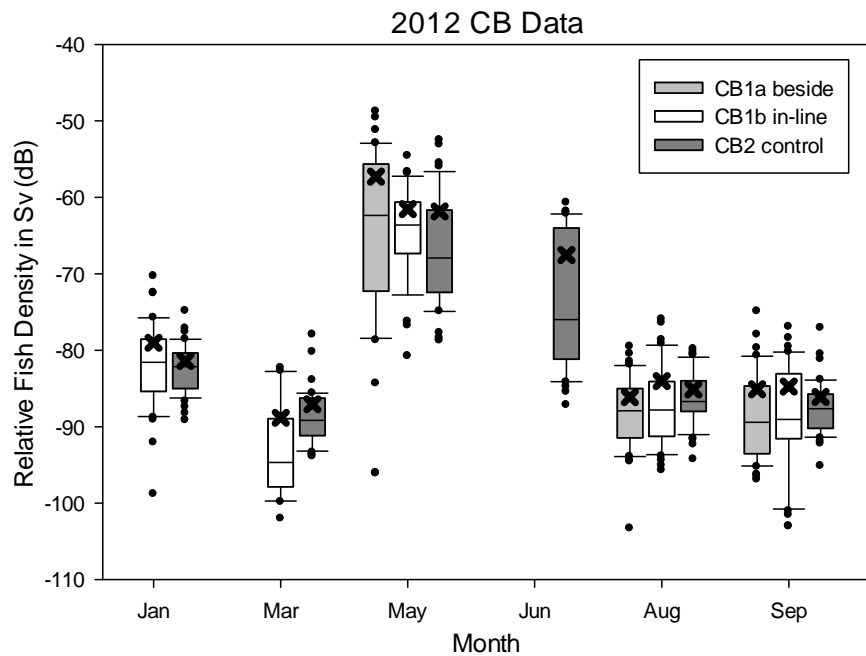


Figure 5. Total water column fish biomass recorded in Cobscook Bay at three sites in 2012. Sv (in dB) is displayed on the y-axis. Each site is represented for each month that data were collected. The box plot shows the 25th, 50th, and 75th percentiles. Each whisker represents the 10th and 90th percentile. The "x" on each is the overall mean. Dots outside the whiskers are outliers and display the variability in fish biomass over a 24 hour period.

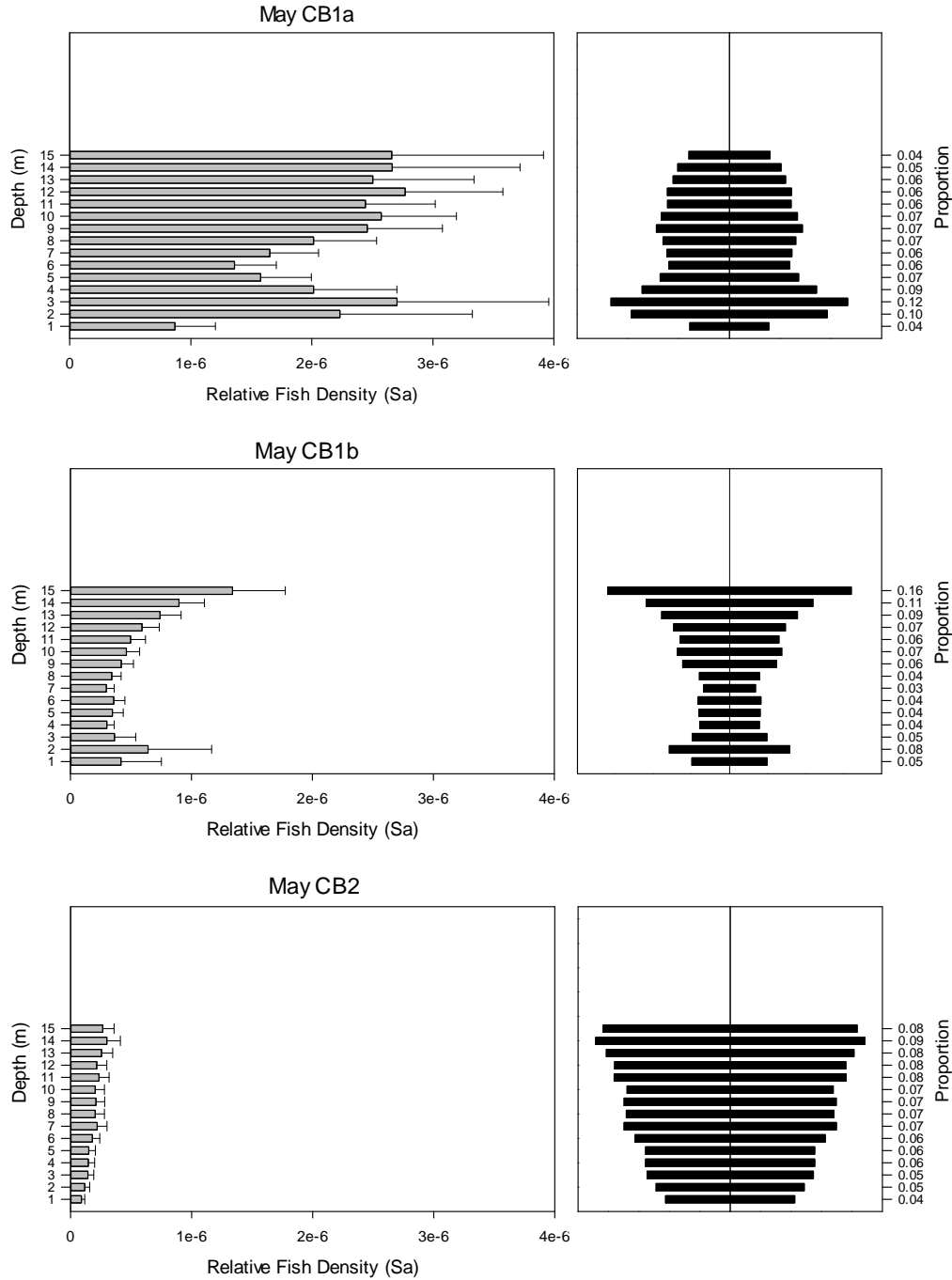


Figure 6. Relative fish densities + 1 standard error) for Cobscook Bay in May 2012. S_a is an area-relative measure of biomass. Depth strata start at the ocean floor. Note the upper depth strata were not sampled due to changing tidal levels and entrained air in the upper water column close to the surface (<10 m). Graphs on right are for visual display of how fish are proportionally distributed in the water column. Depth strata are on the left y-axis and proportions of fish density are shown on the right y-axis. Data for Jan, Mar, Jun, Aug, and Sep are included in Appendices.

3.2 Marine life interaction monitoring plan (side-looking hydroacoustics)

3.2.1 Data availability

Data collection for the Marine Life Interaction Monitoring Plan began on August 29, 2012. The echosounder can be remotely accessed, acoustic data collection is automated, and data are stored on an ORPC server that is backed up periodically at the University. Due to various other operational constraints since the start of data collection, collection has not been continuous (Figure 7). Gaps exist in the side-looking hydroacoustic data whenever the turbine or acoustic system was being repaired or adjusted, during periods of turbine deployment or removal, and whenever divers were present near the echosounder support structure. Additionally, hydroacoustic data have not yet been collected when the turbine was generating power, though collection has been possible while the turbine was free-spinning (moving but not generating power) or still (brake applied). This was because of electrical interference between the data and power transmission cables running together along the seabed to the shore station, and resulted in data gaps 3 to 5 hours in length on days when the turbine was generating. This issue is currently being addressed (see Sections 4 and 5) but, to date, side-looking hydroacoustic data exist only for times when the turbine was free-spinning or still. As echosounder communication issues are resolved, data collection will become more continuous and reliable. For a discussion of these issues and remedial measures taken or planned, see Section 4.2.

Water current speed and direction data collection has also been intermittent. For times when data are available, current direction is not reliable due to the alignment of the flow meter, and therefore was not used in the following analyses. Turbine operational data provided by ORPC included rotations-per-minute (RPM), to determine if the turbine was still or moving, and whether or not the turbine was generating power. Small gaps exist in both data sets, and the first set of RPM data is not useful due to a communication error (Figure 7).

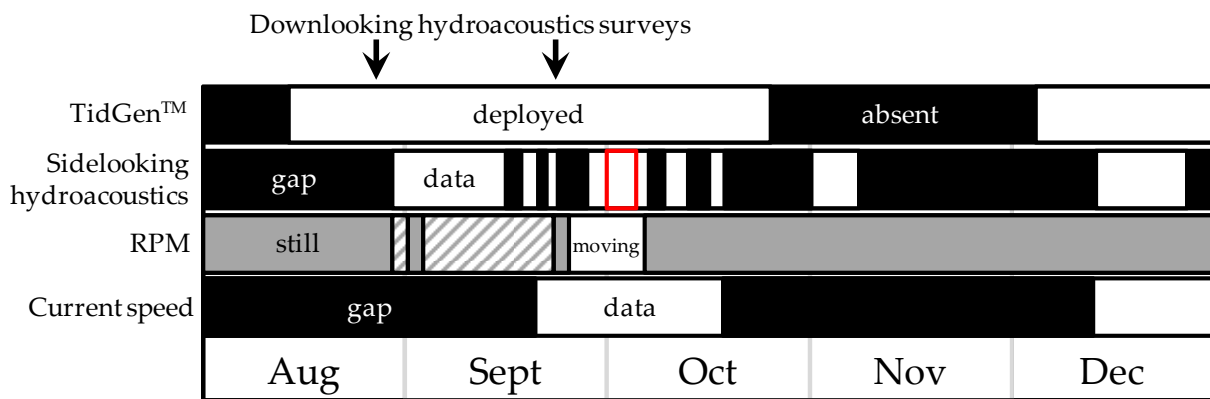


Figure 7. Summary of Marine Life Interaction Monitoring Plan data availability. Hatch lines represent revolutions per minute (RPM) data that are not accurate, but indicate that the turbine was free-spinning. Red box highlights data subset analyzed for this report.

Given these gaps in information, a subset of the data (Figure 8) collected since August 2012 was analyzed for this report. This subset spans October 1st to October 5th, when the turbine was present and fully operating (that is, the brake was not applied, and the turbine would spin at

sufficient current speeds, sometimes generating power; Figure 8). Current speed, RPM, and power generation data are also available for this time. The turbine was free-spinning for several tidal stages, resulting in approximately 13 hours of ebb tide data and 9 hours of flood tide data to analyze (Table 2).

As full months of data are not yet available, monthly comparisons have not been carried out as described in the methods section. The distribution of fish TS was created, and fish density was calculated for each zone during flood and ebb tide to carry out example comparisons. The direction of fish movement was examined qualitatively. Sample size is low (4 ebb tides and 3 flood tides), so statistical analyses were not carried out; however, this provides an example of future results.

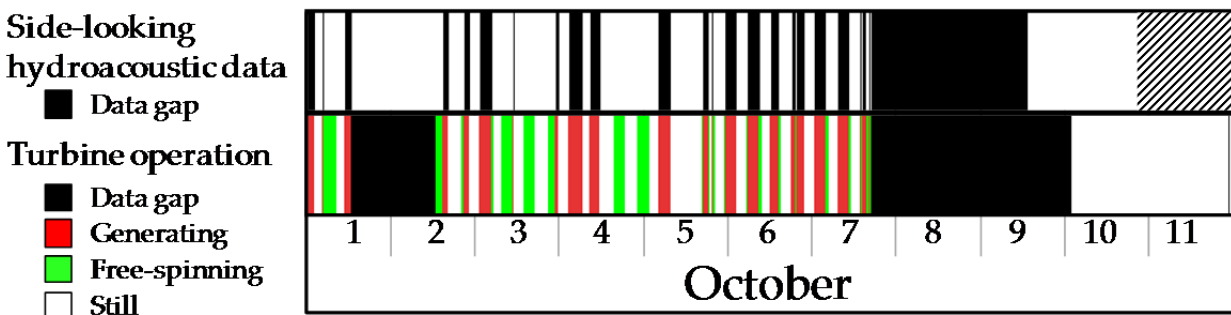


Figure 8. Turbine operational state and side-looking hydroacoustic data availability on dates analyzed for this report. Hatch lines represent hydroacoustic data that is present, but could not be used due to interference from rough surface conditions. The green (free-spinning) segments in October 1-5 were analyzed for this report.

Table 2. Summary of data subset analyzed to date.

Fileset	Date	Start time	End time	Tidal stage	Median current speed ($\text{m}\cdot\text{s}^{-1}$)	Duration (hrs)	Total fish tracked
1	10/1/2012	02:06	06:11	Ebb	-1.35	4.08	2,538
2	10/2/2012	09:20	11:12	Flood	0.44	1.85	247
3	10/3/2012	03:19	06:27	Ebb	-0.06	3.15	3,681
4	10/3/2012	09:47	12:36	Flood	0.31	2.82	1,300
5	10/3/2012	16:20	18:18	Ebb	-0.36	1.97	1,873
6	10/4/2012	10:22	13:38	Flood	0.35	3.27	1,644
7	10/4/2012	16:47	20:27	Ebb	-0.62	3.67	2,360

3.3.1 Results from subset analyzed

A total of 13,643 fish tracks were detected in the acoustic data subset. 3,191 of these were detected during flood tides, and 10,452 detected during ebb tides.

Target strength

The TS distribution of these fish is shown in Figure 9. The distribution is slightly bimodal, with peaks at -57 dB and -50 dB and most detections lying near these values.

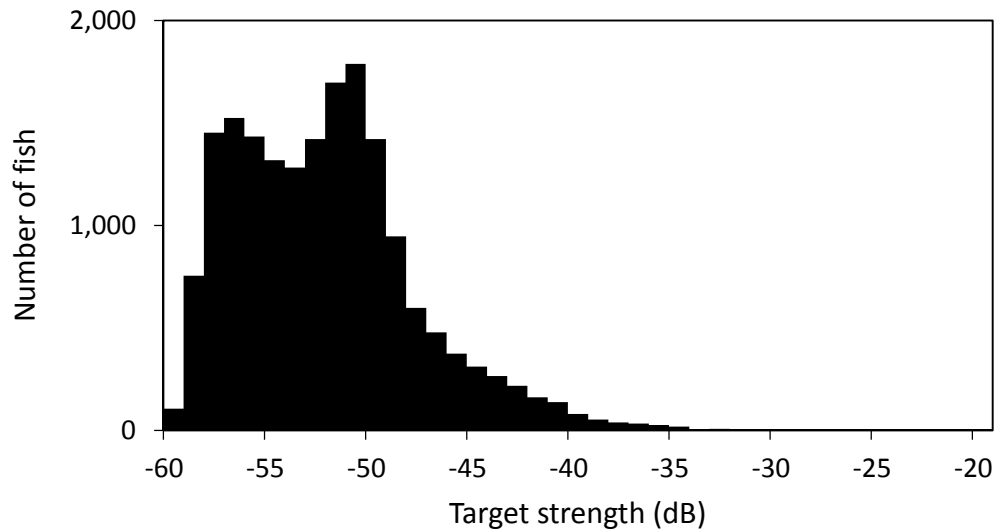


Figure 9. Target strength distribution of all fish detected in data subset.

Fish density

The mean density of fish in each sampling zone is shown in Figure 10. Density appeared to be greater beside and above the turbine than in the turbine zone, though no tests for statistical significance have been carried out due to the low sample size. At this point, densities in the zone beside the turbine may be disproportionately large compared to the densities above and in the turbine zone, possibly due to noise reducing the number of fish detected.

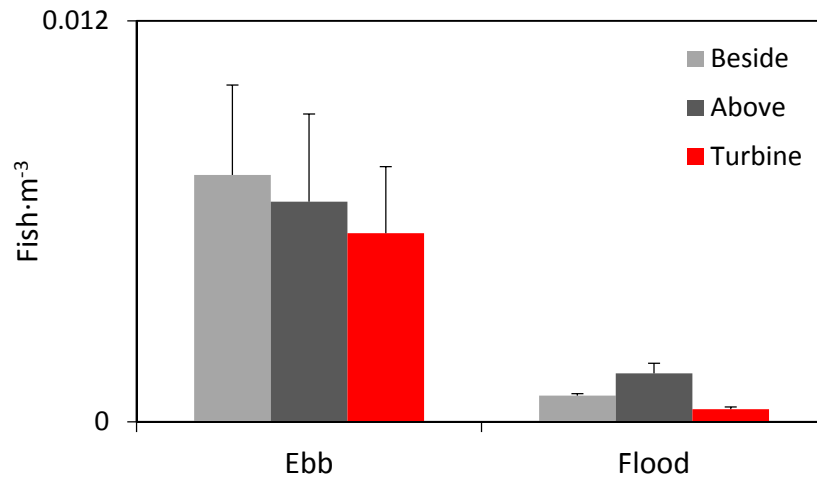


Figure 10. Mean fish density (+1 standard error) in each sampling zone during flood and ebb tide.

Direction of fish movement

The compass heading distribution for fish in each sampling zone was bimodal with peaks at the predominant current directions (Figure 11). Due to the small sample size, statistical significance was not tested. More fish were tracked with the prevailing current, though some were tracked moving directly against it. Against-current tracks were nearly as prevalent as with-current tracks in the region beside the turbine. Above the turbine, fish moved with the prevailing current almost exclusively. In the turbine zone during the flood tide, a greater proportion of fish were tracked moving against the current than with it. Overall, variance in direction of tracks above the turbine and in the turbine zone appeared greater during flood tide than during ebb tide. However, without current direction data, fish track directions cannot be attributed to fish behavior alone. Vertical heading of fish tracks have not yet been analyzed.

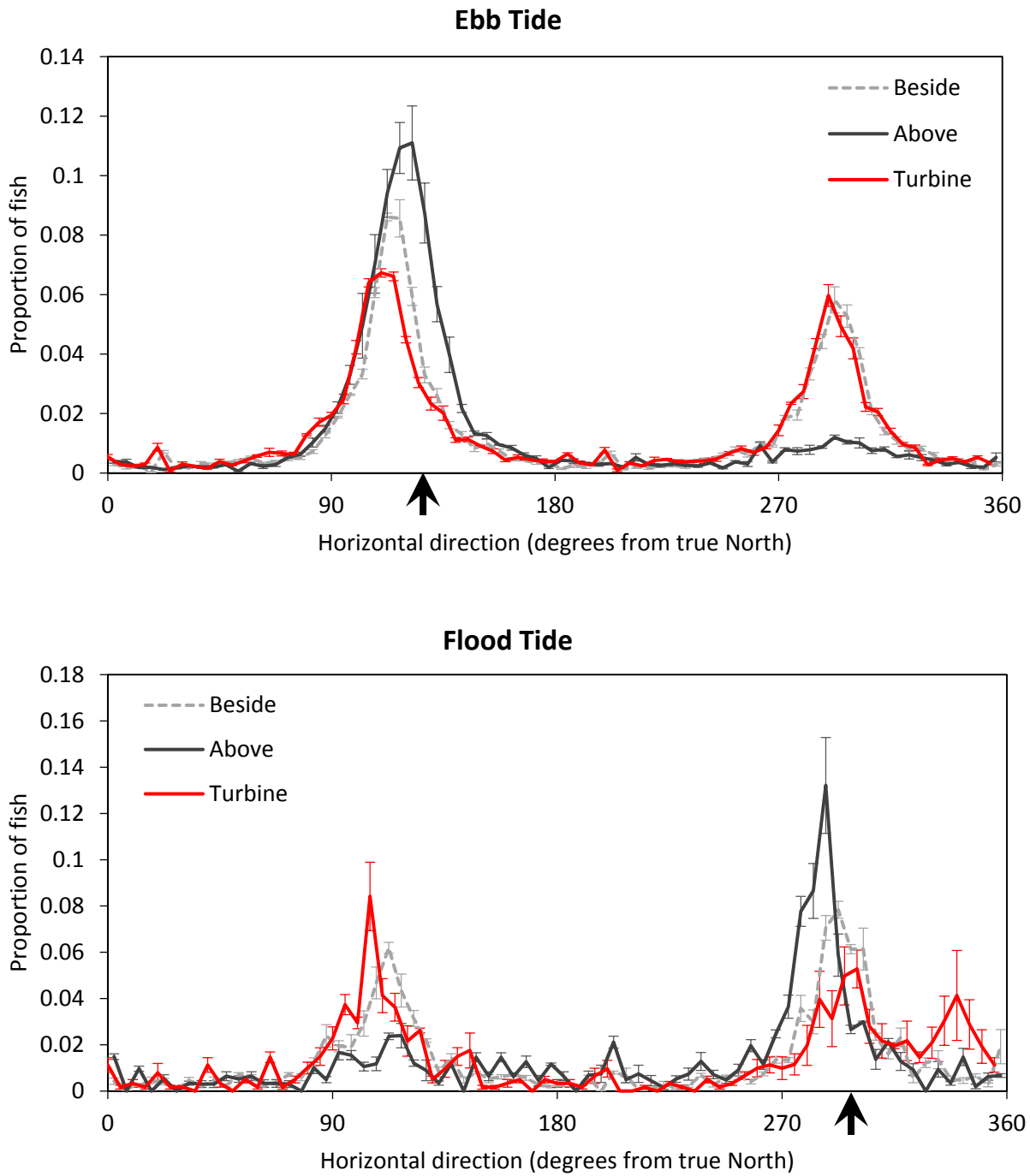


Figure 11. Distribution of fish horizontal swimming direction in each turbine zone for ebb and flood tides. Mean proportion of fish shown on vertical axis. Error bars represent standard error. Arrows show predominant direction of tidal flow, obtained by ORPC.

4.0 Challenges & Future: Operational Constraints and Reconciliation

Ideal data collection is difficult under the best circumstances, and the highly dynamic environment of Cobscook Bay combined with construction activities associated with the TidGen™ project have affected data collection to date. Outlined below are the obstacles encountered within each monitoring plan and a discussion of how these have been or will be addressed as data collection continues.

4.1 Fisheries Monitoring Plan (down-looking hydroacoustic surveys)

As shown in Figure 2, sampling locations have so far been highly variable. Ideally, these locations would be consistent over time. This variability mainly has been due to construction activities surrounding the deployment, maintenance, and retrieval of the TidGen™ device, and the safety protocols involved (e.g., minimum safe distances for moorings). Additionally, November 2012 and January 2013 down-looking surveys were cancelled due to re-deployment and retrieval of the turbine, causing sampling dates to deviate from the proposed schedule. Sampling locations and times will become more consistent with what was initially proposed as activity in the project area decreases. In addition, there has been a recent deployment of a large mooring block near the TGU that will be a permanent mooring for CB1b, eliminating spatial variation at that site. Site CB1a spatial variation will be decreased with the use of a more precise GPS unit.

4.2 Marine Life Interaction Monitoring Plan (side-looking hydroacoustics)

The goal of this plan is to collect and assess continuous data on the behavior of fish and other marine life in the vicinity of the turbine while it is operating. However, the operation of the side-looking echosounder at the turbine site is largely dependent on work carried out on the turbine. As discussed in Section 3.1.2, gaps exist in the hydroacoustic data collected to date which limit possible analyses. The largest gaps correspond to turbine operations (e.g., work on the undersea cables, retrieval or redeployment of the turbine). Smaller gaps occur when communication with the echosounder from shore is interrupted. These interruptions occur when the turbine is generating power, as the electric current in the undersea cables interferes with the neighboring data transmission cable of the echosounder. ORPC has taken several steps to remedy this issue and continues to work towards continuous data transfer. As construction activity in the area decreases and communication issues are resolved, the dataset will become more continuous and will be processed as described in this report.

Increased noise within the turbine zone, from reflection off of support structure and the surface, may affect fish detection and must be examined. Clear gaps exist in the detected fish tracks at the range of each piling and even at the intervening crossbars (visible as faint horizontal lines in Figure 4a). It is likely that the detection of fish echoes at these ranges is confounded by the sound reflected by the turbine support structure. To help determine the extent of this effect, the number of fish tracks obtained by Echoview must be compared with the number of fish tracks obtained by manually counting. Fish tracks may be obvious to the eye even when surrounded by

interference that limits their detectability in Echoview. Comparing a manual count of fish tracks to the Echoview-generated count will determine if this is indeed an issue that must be addressed.

If so, there are several options available to explore:

1. Re-aim the transducer until the noise from the turbine no longer interferes with fish tracking. The disadvantage to this is that this will move the beam even farther from the turbine face, and will therefore limit the usefulness of behavioral analyses. This method also does not help to reduce the effect of surface noise on the data at greater ranges.
2. Increase the threshold to -50 dB to eliminate most noise from the echogram altogether. Unfortunately, this method will also result in the exclusion of fish with weaker acoustic signatures, such as mackerel or small herring. However, small fish are those that tend to interact with turbine blades (Viehman 2012), and most of the fish tracked so far have target strength less than -50 dB (Figure 9). Also, this option is not immune to the effects of surface noise and does not address the effect of very strong targets (such as the pilings) confounding Echoview's fish detection process.
3. Alter the method of fish detection. Image processing techniques may be useful when tracking fish in noisy data (e.g. Balk and Lindem 2000).

These options will be assessed as data collection and data quality continue to improve.

Current speed and direction are being collected by ORPC using a flow meter on the turbine support frame. While current speed data collected thus far have been accurate, direction data cannot be used due to the alignment of the flow meter. Once this is corrected, future data analyses will be carried out using both current speed and direction.

Since the implementation of the Fisheries and Marine Life Interaction Monitoring Plans, great progress has been made in the setup and collection of data. New sampling locations and survey equipment have been integrated into the continuing down-looking acoustic surveys, and the side-looking Simrad echosounder has been successfully installed at the TidGen™ site and it can be remotely operated from shore. Several obstacles remain to be addressed. For the Fisheries Monitoring Plan, these include achieving constant survey locations and further automation of data processing. Issues facing the Marine Life Interaction Plan include continuous data collection, noise reduction, processing automation, and full analyses of data collected to date. All of these concerns are currently being addressed, or will be, in the near future. Results presented here are preliminary analyses of a subset of data collected to date, and analyses in future reports will follow a similar approach. As data collection becomes more continuous and quality improves, we will continue to adopt and refine our analysis techniques.

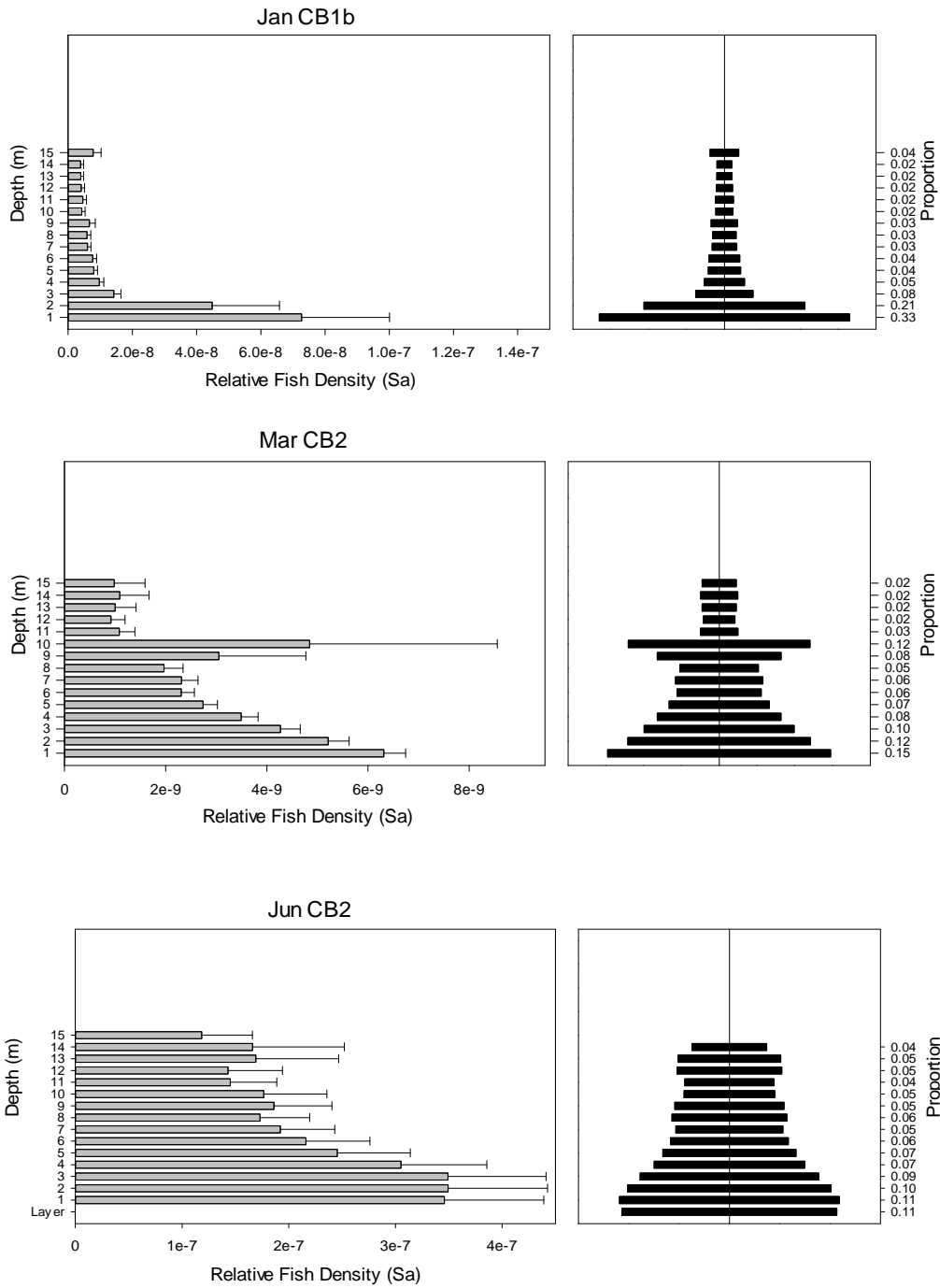
5.0 References

Balk, H. and T. Lindem. 2000. Improved fish detection in data from split-beam sonar. *Aquatic Living Resources* 13: 297-303.

- Simmonds, J. and D. MacLennan. 2005. Fisheries Acoustics: Theory and Practice. 2nd ed. Oxford: Blackwell Science. 437 p.
- Viehman, H. 2012. Fish in a tidally dynamic region in Maine: hydroacoustic assessments in relation to tidal power development. [master's thesis]. [Orono, (ME)]: University of Maine.
- Viehman, H. and G. B. Zydlewski. 2012. Fish interactions with a commercial-scale tidal energy device in the natural environment. Estuaries and Coasts. Submitted.

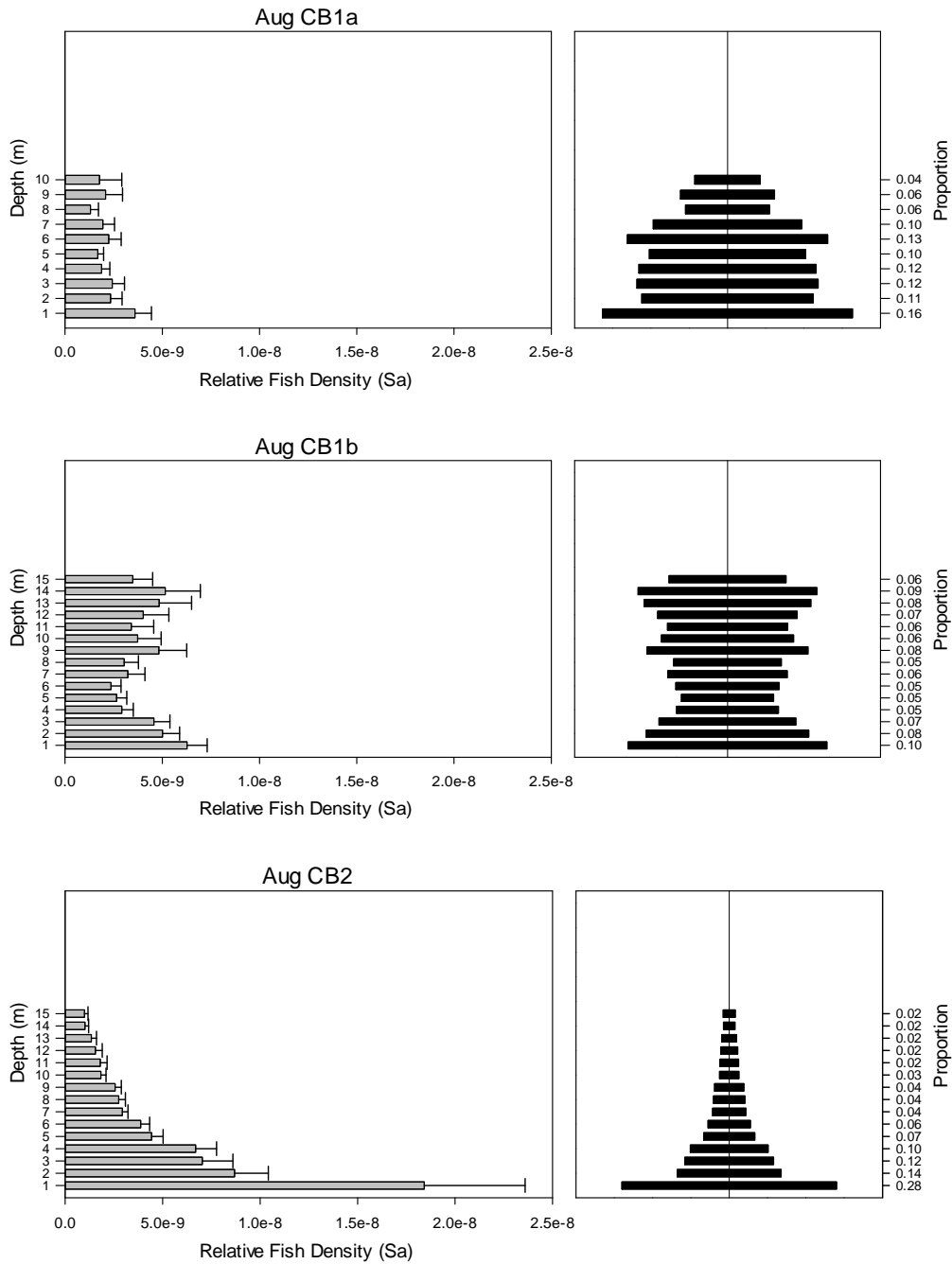
Appendix A

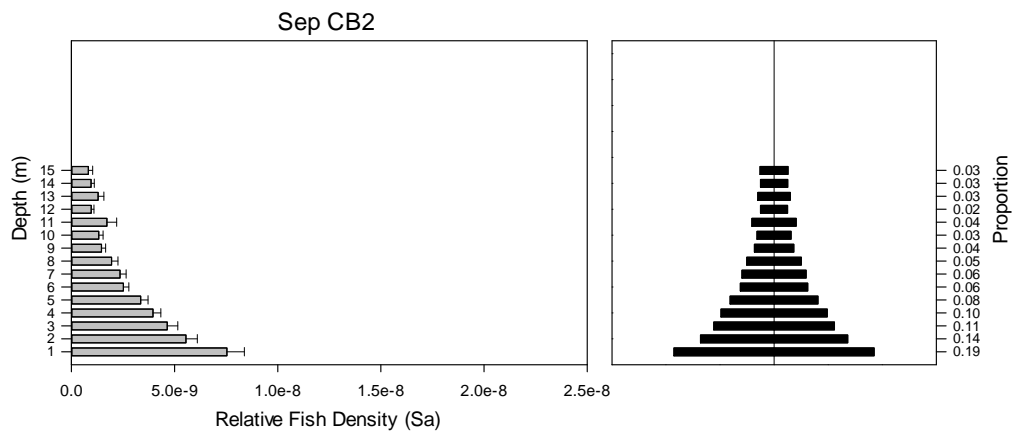
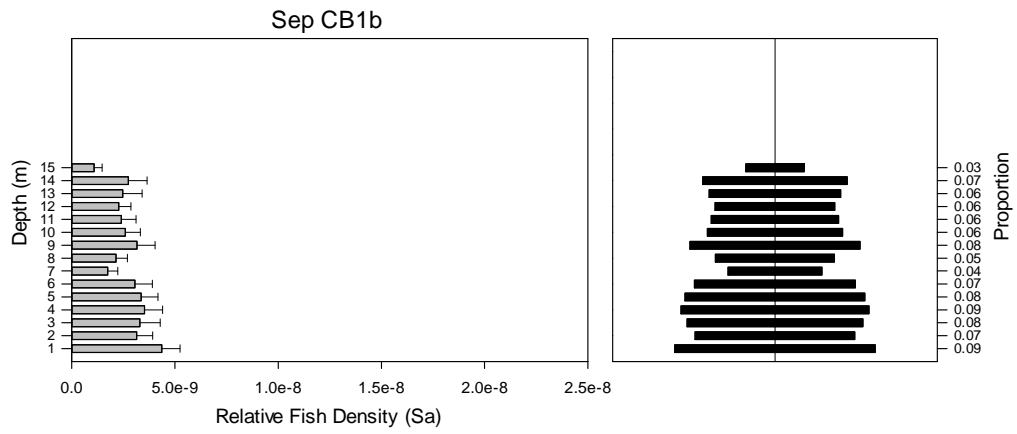
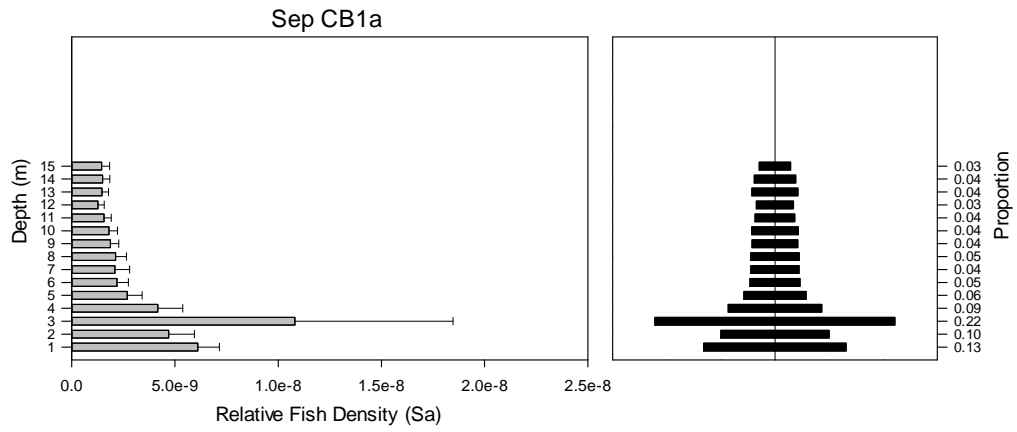
Vertical fish distributions for Cobscook Bay 2012, pre-deployment (Jan – Jun). Note that x-axes are not standardized across graphs. CB1a is ‘next to’, CB1b is ‘in-line with’ the turbine and CB2 is the control site.



Appendix B

Vertical fish distributions for Cobscook Bay 2012, post-deployment (Aug and Sep). Note that x-axes are not standardized across graphs. CB1a is 'next to', CB1b is 'in-line with' the turbine and CB2 is the control site.





Appendix Task 2-6

Fisheries and Marine Life Interaction Monitoring

Bi-Annual Report

September 2013

University of Maine, School of Marine Sciences
Haley Viehman, Garrett Staines, Gayle Zydlewski

Contents

1.0 Introduction: Study Context and Purpose 254

2.0 Fisheries Monitoring (downlooking hydroacoustics) 254

 2.1 Methods..... 255

 2.2 Results 258

3.0 Marine life interaction monitoring (side-looking hydroacoustics) 264

 3.1 Methods..... 264

 3.2 Results..... 272

4.0 Summary 276

 4.1 Fisheries monitoring (down-looking hydroacoustics) 276

 4.2 Marine life interaction monitoring (side-looking hydroacoustics) 278

5.0 References..... 280

Appendix 1: Fish Community Assessment in Cobscook Bay, Maine **Error! Bookmark not defined.**

1.0 Introduction: Study Context and Purpose

Ocean Renewable Power Company, LLC (ORPC) deployed a TidGen[®] Power System in outer Cobscook Bay, Maine, as the first stage of the Cobscook Bay Tidal Energy Project (CBTEP) (Figure 1). This installation requires monitoring to assess potential effects of the TidGen[®] Power System on the marine environment. ORPC's marine life monitoring plan has two parts: 1) Fisheries Monitoring and 2) Marine Life Interaction Monitoring.



Figure 1. Cobscook Bay Tidal Energy Project location map and TidGen[®] device drawing (CBTEP Fisheries and Marine Life Interaction Plan, 2012). The yellow icon represents the location of the TidGen[®] device. The grey icons represent potential TGU locations to complete an array in the future.

2.0 Fisheries Monitoring (downlooking hydroacoustics)

The Fisheries Monitoring Plan is a continuation of research started by the University of Maine's School of Marine Science researchers in 2009. The study was designed to capture annual, seasonal, tidal, and spatial variability of fish presence in the area of interest (near the TidGen[®] deployment site). The design involves down-looking hydroacoustic surveys during several months of the year, and examines the relative density and vertical distribution of fish at the project site and a control site. Pre-deployment data were collected in 2010, 2011, and early

2012, and post-deployment data were collected from August 2012 through September 2013 (August 2012 through June 2013 are reported here). Data from the project site were compared to the control site to quantify changes in fish presence, density, and vertical distribution that may be associated with the installation of the TidGen[®] power system. ORPC plans to conduct surveys through the year 2017.

2.1 Methods

2.1.1 Study design

Down-looking hydroacoustic surveys were conducted from an anchored research vessel for one 24-hour period several times per year at a project site (CB1) and a control site (CB2) (Table 1, Figure 2). During the time when the complete TidGen[®] (bottom support structure and the dynamic turbine) was in the water (from here on referenced as "deployment"), three sites were sampled: two at the project location (CB1a, beside the turbine, and CB1b, in line with the turbine) and one at the same control site (CB2) (Figure 2). Sampling locations at the project sites in 2012 varied geographically because of construction activities and related safety concerns around the TidGen[®]. January and March 2012 were pre-deployment surveys, so only CB1 and CB2 were sampled. In January, CB1 was only sampled for 12 hours due to unsafe weather conditions. There was no November 2012 survey because the dynamic part of the TidGen[®] was removed for maintenance at the time.

The down-looking surveys were carried out using a single-beam Simrad ES60 commercial fisheries echosounder, with a wide-angle (31° half-power beam angle), dual-frequency (38 and 200 kHz) circular transducer. The transducer was mounted over the side of the research vessel 1.8 meters below the surface, and ensonified an approximately conical volume of water extending to the sea floor. Current speed was measured every half-hour of each survey using a Marsh-McBirney flow meter (May 2011 to May 2012) or a Workhorse Sentinal Acoustic Doppler Current Profiler (ADCP) (June 2011 onward). A 300 kHz ADCP was used in 2011 and 2012, and a 600 kHz ADCP was used in 2013. Every 30 minutes, the ADCP operated for 1 minute, recording mean current speed in 1 m depth bins from 3 m below the surface to the sea floor.

Table 1. Months sampled for Fisheries Monitoring Plan (down-looking hydroacoustics). 1 and 2 indicate sampling at CB1 and CB2, respectively; 1a, 1b, and 2 indicate sampling at CB1a (beside), CB1b (in-line), and CB2 (control), respectively. Light gray indicates presence of TidGen[®] bottom frame only; dark gray indicates presence of complete TidGen[®].

Year	Jan	Feb	Mar	April	May	June	July	Aug	Sept	Oct	Nov	Dec
2010					1, 2			1, 2	1, 2	1, 2	1, 2	
2011			1, 2		1, 2	1, 2		1, 2	1, 2		1, 2	
2012	1, 2		1, 2		1a, 1b, 2	2		1a, 1b, 2	1a, 1b, 2			
2013			1a, 1b, 2		2	2						



Figure 2. Fisheries Monitoring Plan study area and down-looking hydroacoustic survey locations for 2010-2013. CB1 and CB2 are indicated by dashed ovals. CB1a and CB1b are indicated by small round points. CB1 current directions are averages provided by Ocean Renewable Power Company.

The single-beam transducer was used to obtain an index of fish density, which allowed us to examine changes in fish density over time. This relative measure was also used to assess vertical distribution of fish throughout the water column.

Comparisons of fish density and vertical distribution were made among the control site and project site(s) and among different months at each site. Sampling before and after turbine deployment at the project as well as at a control site improves the ability to distinguish changes that may be related to the presence of the turbine from changes due to annual, seasonal, daily, and tidal variation. These methods are consistent with a before-after-control-impact (BACI) study design.

2.1.2 Data processing

Hydroacoustic data were processed using Echoview® software (5.3, Myriax Pty. Ltd., Hobart, Australia), and statistical analyses were carried out in R (2.15.2, R Core Team, Vienna, Austria). The data collected at the 200 kHz frequency were used in analyses. Processing included scrutinizing the data and manually removing areas of noise (e.g., from electrical interference, a passing boat's depth sounder, high boat motion, or interference from the ADCP). Hydroacoustic interference from entrained air was common in the upper 10 m of the water column, so the top 10 m of the water column were excluded from analyses. Weak hydroacoustic signals, such as

plankton, krill, and fish larvae, were excluded by eliminating backscatter with target strength (TS) less than -60 dB. Most fish have TS between -60 dB and -20 dB but TS varies greatly with fish anatomy and orientation (Simmonds and MacLennan 2005). This variability, combined with the TS uncertainty inherent in single beam systems, means that some fish with TS higher than -60 dB were likely excluded from analyses (Simmonds and MacLennan 2005).

In March and June of 2013, some weak background noise from electrical interference could not be eliminated using the -60 dB threshold. Echoview's background subtraction tool (based on the algorithm developed by de Robertis and Higginbottom, 2007) was used to remove this interference.

Because flowing tides were the focus of this study, hydroacoustic data during slack tides were not included in analyses. Slack tides were defined as the hour centered at the time of low or high water. The time of low and high tide was determined using the depth of the bottom line detected in Echoview. Thirty minutes to either side of these time points was then removed from the hydroacoustic dataset.

Fish density was represented on a relative scale using volume backscattering strength, S_v , which is a measure of the sound scattered by a unit volume of water and is assumed proportional to density (Simmonds and MacLennan 2005). S_v is expressed in the logarithmic domain as decibels, dB re 1 m^{-1} . The vertical distribution of fish throughout the water column was examined using the area backscatter coefficient, s_a , which is the summation of volume backscatter over a given depth range and is also proportional to fish density (Simmonds and MacLennan 2005). s_a is expressed in the linear domain ($\text{m}^2 \cdot \text{m}^{-2}$) and is additive.

The inspected and cleaned hydroacoustic data were divided into 30-minute time segments, which were large enough to minimize autocorrelation but maintain variation in density that occurred over the course of each survey. Echoview was used to calculate the mean S_v of the entire water column for each 30-min interval. Then, for each interval, s_a was calculated for 1-m layers of water. Layers were measured upward from the sea floor, rather than downward from the surface, because the turbine is installed at a fixed distance above the bottom (the top of the turbine is 9.6 m above the sea floor). By calculating the proportion of total water column s_a contributed by each 1-m layer of water, the vertical distribution of fish was constructed for each 30-min interval.

2.1.2 Statistical analyses

To examine annual, seasonal, tidal, and spatial variability of fish density in the area of interest, comparisons of water column fish density index (S_v) were made using permutation ANOVAs (R package *lmPerm*; Wheeler 2010), followed by nonparametric Tukey-type multiple comparisons to determine significant differences (R package *nparcomp*; Konietzschke 2012). Five questions were asked:

- 1) Inter-annual variability: was fish density constant across years? We tested the effect of year on fish density in outer Cobscook Bay, combining data for all sites.
- 2) Beside vs. in-line with the turbine: were densities similar at the two project sites (CB1a and CB1b)? We tested the effect of site on mean water column S_v for surveys in which

CB1a and CB1b were both sampled (May, August and September 2012, and March 2013). If CB1a and CB1b have similar fish densities, they may be grouped for comparison to CB1 surveys carried out in previous years.

- 3) Project site vs. control site: is fish density similar at CB1 and CB2, and is CB2 therefore a useful control site? To validate the utility of CB2 as a control site, differences between the project site (CB1) and control site (CB2) were evaluated using month and site as factors.
- 4) Seasonal variability: is there a consistent seasonal pattern to fish density in outer Cobscook Bay? The effect of month on fish density was tested, combining data for CB1 and CB2.
- 5) Did deployment of the TidGen[®] affect fish density at the project site (CB1)? Results from the tests in (2) were used to compare differences before and after device deployment.

The vertical distribution of fish was compared between sites within each survey, with the goal of detecting differences potentially related to the presence of the turbine. To test the similarity of two distributions, one was fit to the other with linear regression. Similar vertical distributions were indicated by a significant fit (significance level of 0.05) and a positive slope. Negative slope or insignificant fit indicated dissimilar distributions. If distributions at the project and controls sites were similar before the turbine was installed, differences afterward may indicate an effect of the turbine on how fish use the water column (e.g., avoidance of the depths spanned by the turbine). Differences between CB1a and CB1b may also indicate behaviors altered by the turbine's presence.

2.2 Results

2.2.1 Relative fish density

1) Inter-annual variability: was fish density constant across years? Fish density (mean water column S_v) changed significantly each year. Density was significantly higher in 2010 and 2012 than 2011 and 2013 (Figure 3). Because of these differences, years were analyzed separately in subsequent statistical analyses.

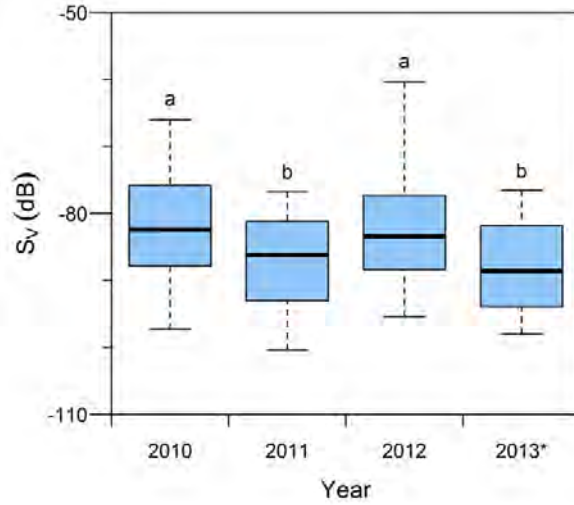


Figure 3. Water column S_v for all years sampled (CB1 and CB2 data pooled together). Bold horizontal line indicates the median, boxes span the interquartile range, and whiskers extend to the 5th and 95th percentiles. Significantly different groups are indicated by letters a and b. (*) In 2013, only March, May, and June have been analyzed.

2) Beside vs. in-line with the turbine: were densities similar at the two project sites (CB1a and CB1b)? There were no differences in fish density (total water column S_v) between CB1a and CB1b (Figure 4). As such, we grouped these two sites as CB1 in further analyses of water column S_v .

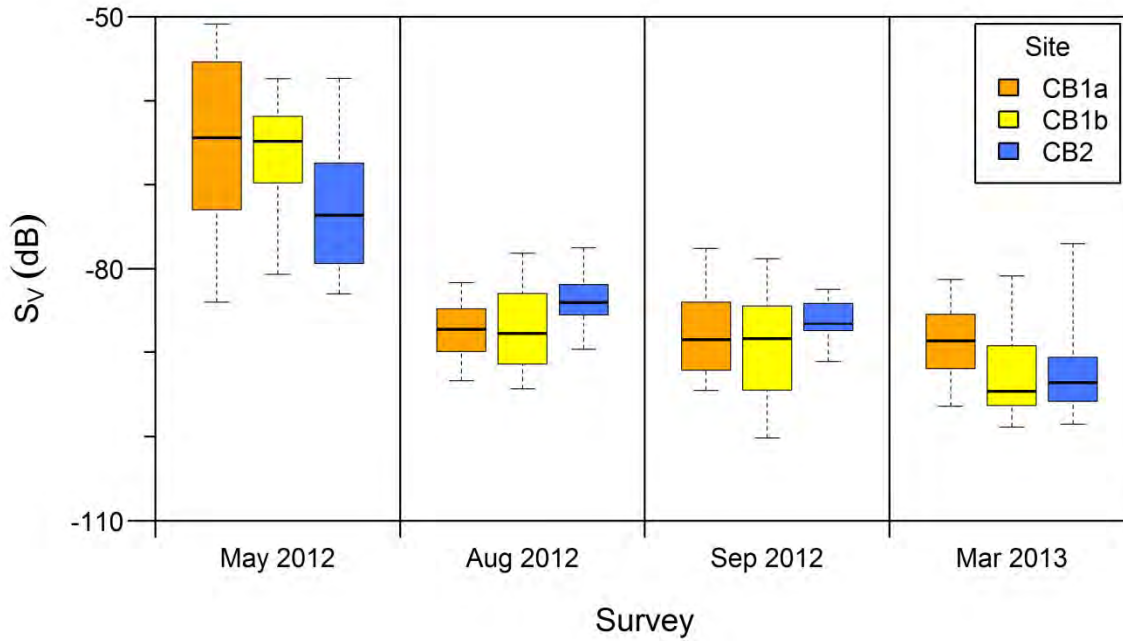


Figure 4. Water column S_v at CB1a, CB1b, and CB2 surveys in 2012 and 2013. Bold horizontal line indicates the median, boxes span the interquartile range, and whiskers extend to the 5th and 95th percentiles.

3) Project site vs. control site: is fish density similar at CB1 and CB2, and is CB2 therefore a useful control site? In each year, fish density varied significantly with month (Figure 5). Site had a significant effect on fish density in 2011, meaning density was greater at CB2 when data from all surveys were grouped together. However, within surveys (months), densities at CB1 and CB2 were not significantly different. The interaction of site and month significantly affected fish density in 2010 and 2012, indicating that site had a different effect on density in the different months. Multiple comparisons showed that fish density was significantly different at CB1 and CB2 in September 2010 and in March and August of 2012, but that there was no effect of site in the other surveys. Interaction effects could not be tested in 2013 since CB1 was only sampled in only one of three months.

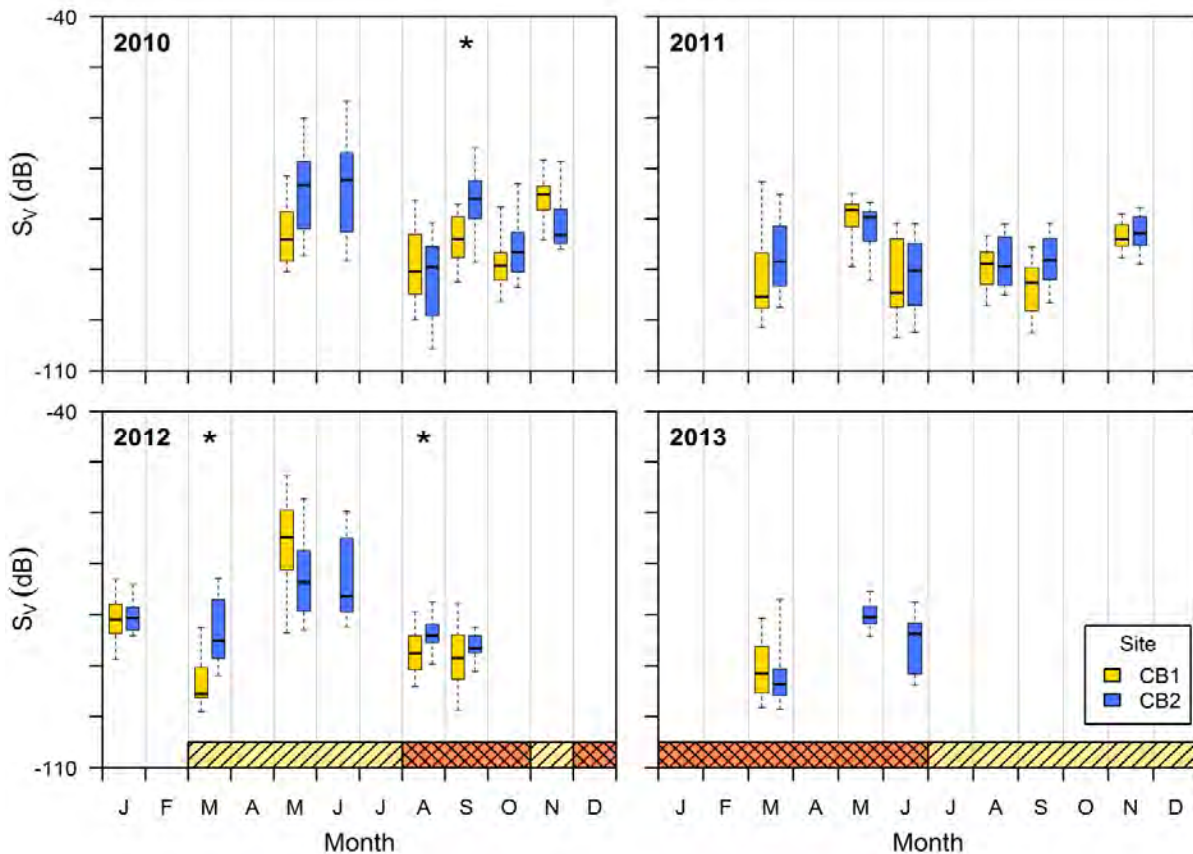


Figure 5. Water column S_v at CB1 (which includes CB1a and CB1b data) and CB2. Bold horizontal line indicates the median, boxes span the interquartile range, and whiskers extend to the 5th and 95th percentiles. Asterisks indicate significant differences between CB1 and CB2. † indicates surveys when only ebb tide data were sampled; ‡ indicates surveys when only daytime was sampled. Yellow hatched box indicates surveys when the TidGen[®] bottom frame was present on the seafloor; red hatched boxes indicate when the TidGen[®] turbine was also present. The turbine was braked (present but not spinning) starting mid-April until it was removed in July.

4) Seasonal variability: is there a consistent seasonal pattern to fish density in outer Cobscook Bay? Results of multiple comparisons indicated highest fish densities in May and June, followed by November (Figure 6).

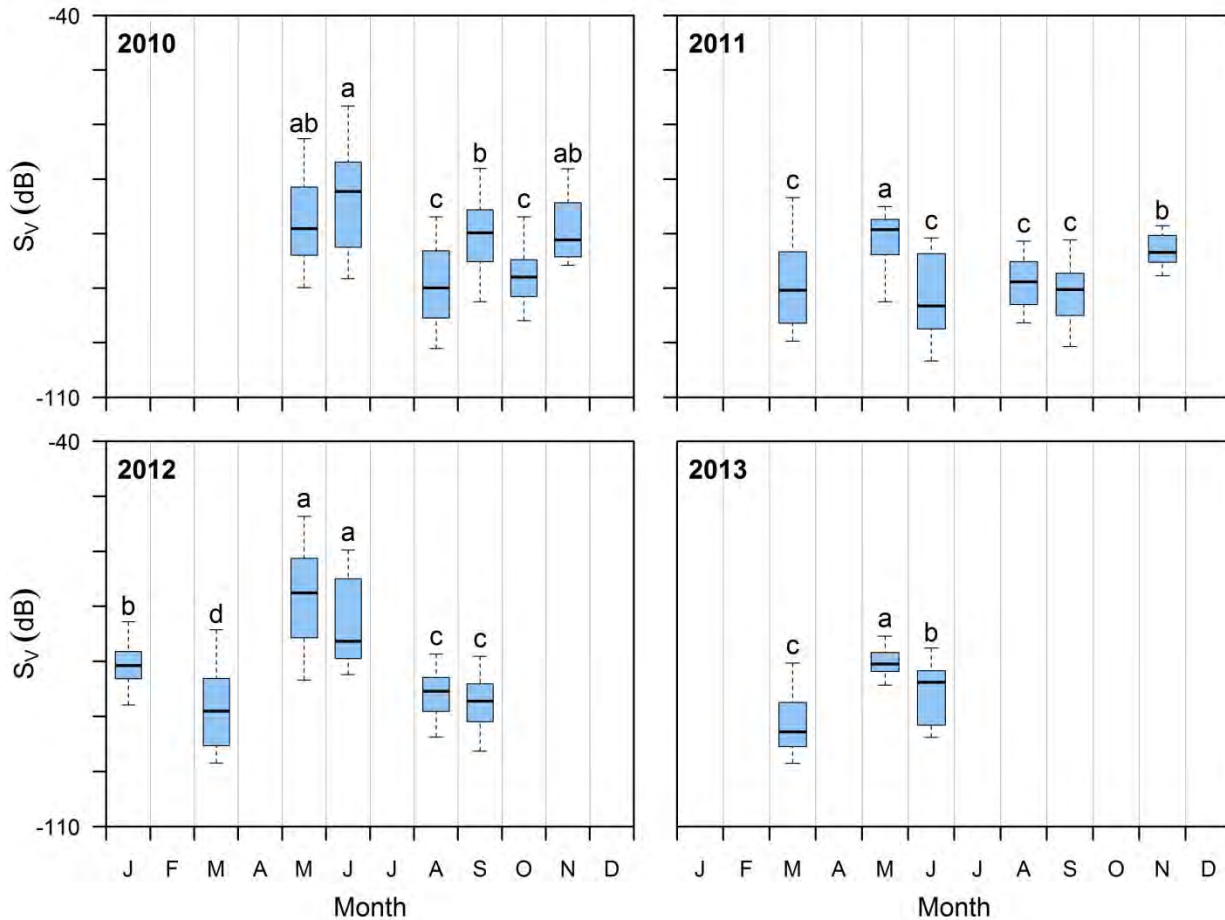


Figure 6. Water column S_v for all surveys (CB1 and CB2 data pooled together). Bold horizontal line indicates the median, boxes span the interquartile range, and whiskers extend to the 5th and 95th percentiles. Significantly different groups within each year are indicated by letters a through d (group a is the highest, d is the lowest).

5) Did deployment of the TidGen[®] affect fish density at the project site (CB1)? A significant difference between CB1 and CB2 was found only in the August 2012 survey, when CB2 had a higher density index (water column S_v) than CB1 (Figure 5). A similar difference was seen in March 2012, when the turbine's bottom support frame was deployed.

2.2.2 Vertical Distribution

Significant differences were only found between sites CB1 and CB2 in May 2011, CB1 and CB2 in March 2012, CB1a and CB2 in May 2012, CB1b and CB2 in May 2012, and CB1a and CB1b in March 2013 (Figure 7).

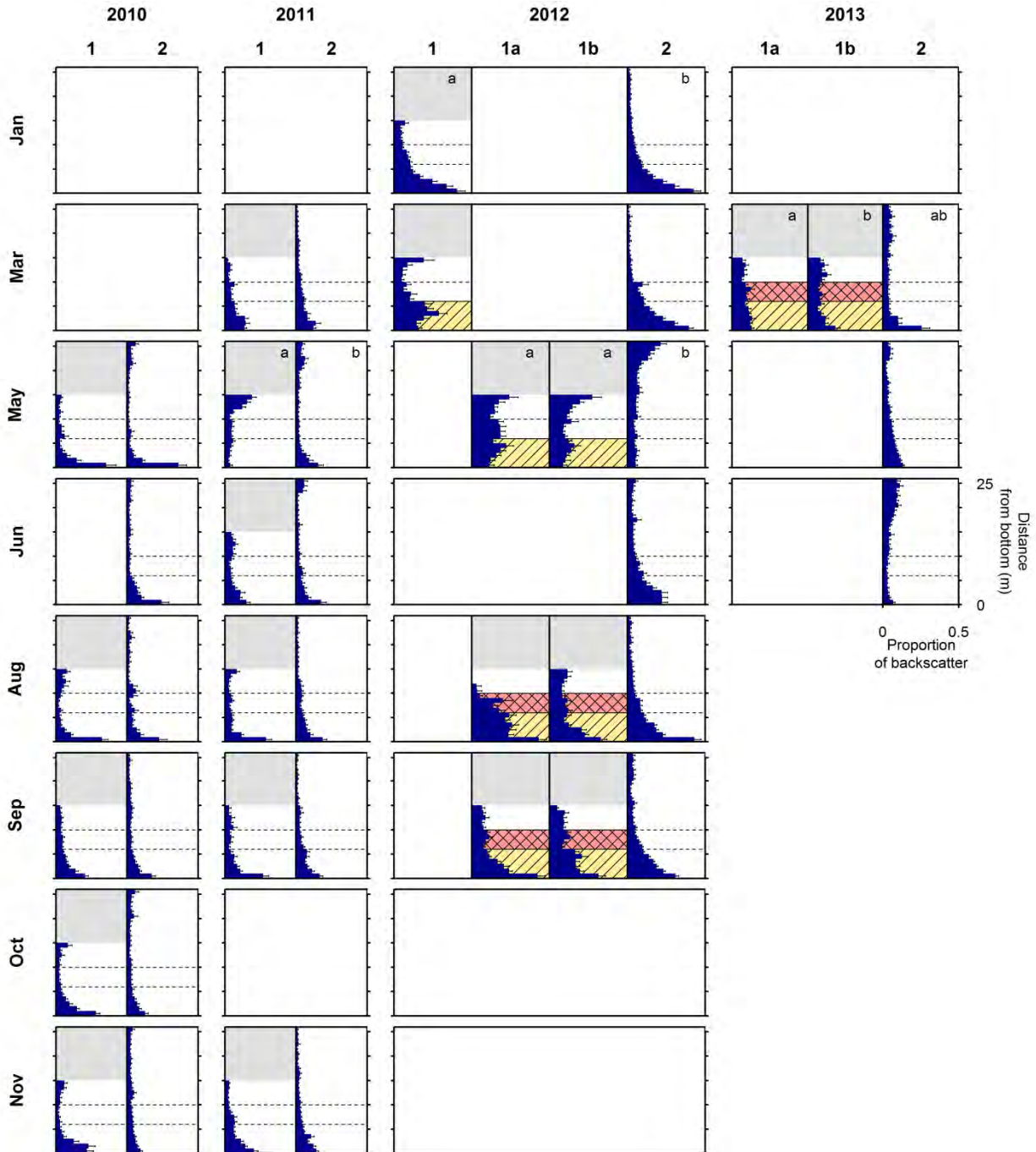


Figure 7. Mean proportion of S_a contributed by each layer of the water column. All layers analyzed are shown for each site (0-15 m above the bottom at CB1, 0-26 m above the bottom at CB2). Whiskers are one standard error. Depth of turbine is indicated by horizontal dashed lines. Yellow hatched areas indicate when the bottom support frame was deployed at the project site; red hatched areas indicate when the turbine was also present. Significantly different distributions between sites are indicated by letters "a" and "b" in the upper right of the graph.

3.0 Marine life interaction monitoring (side-looking hydroacoustics)

The Marine Life Interaction Monitoring Plan uses side-looking hydroacoustics collected by ORPC at the TidGen[®] project site to assess the interaction of marine life (fish, mammals, and diving birds) with the TidGen[®] device. This monitoring focuses on the behavior of marine life (primarily fish) as they approach or depart from the region of the turbine, to document variation in behavioral responses related to the TidGen[®] unit. ORPC plans to collect side-looking hydroacoustic data for three years after the deployment of the TidGen[®] Power System.

3.1 Methods

3.1.1 Study design

ORPC has mounted a Simrad EK60 split beam echosounder (200 kHz, 7° half-power beam width) to a steel frame located 44.5 m from the southern edge of the TidGen[®] (Figure 8). This frame holds the transducer 3.4 m above the sea floor, with the transducer angled 9.6° above the horizontal with a heading of 23.3°. The echosounder samples an approximately conical volume of water extending for 100 m, directly seaward (southeast) of the TidGen[®] device (Figure 8). The actual sampled volume used in data analysis does not include the entire beam. The sampled volume extends to the far edge of the turbine (78.1 m), not beyond because after that point, interference from sound reflection off the water's surface becomes too great to reliably detect fish. The sampled volume is upstream of the device during the flood tide (examining approach behaviors) and downstream of the device during the ebb tide (examining departure behaviors). The echosounder is powered and controlled via undersea cables from the ORPC shore station in Lubec, where data files are stored on a server and collected periodically by the University.

When operational, the echosounder records data continuously. Continuous data collection at a sample rate of 4 to 6 pings per second allows each fish or other marine animal that passes through the beam to be detected several times, recording information on the echo strength and 3D location of targets within the beam (Figure 9). These data are used to track fish movement during their approach to the turbine (flood tide) as well as during their departure (ebb tide) on a fine spatio-temporal scale. The sampled volume is divided into three zones: the turbine zone (red hatched area, Figure 8a), where fish would be likely to encounter the moving turbine; above the turbine zone (A, Figure 8a); and beside the turbine zone (B, Figure 8a). Fish numbers and movement in each zone provide indicators of turbine avoidance. The total sampling volume to 78.1 m range (for a 7° hydroacoustic cone) is 1,866 m³, and of this, 607m³ (33%) are within the turbine zone, 345 m³ (18%) are beside the turbine zone, and 914 m³ (49%) are above the turbine zone.

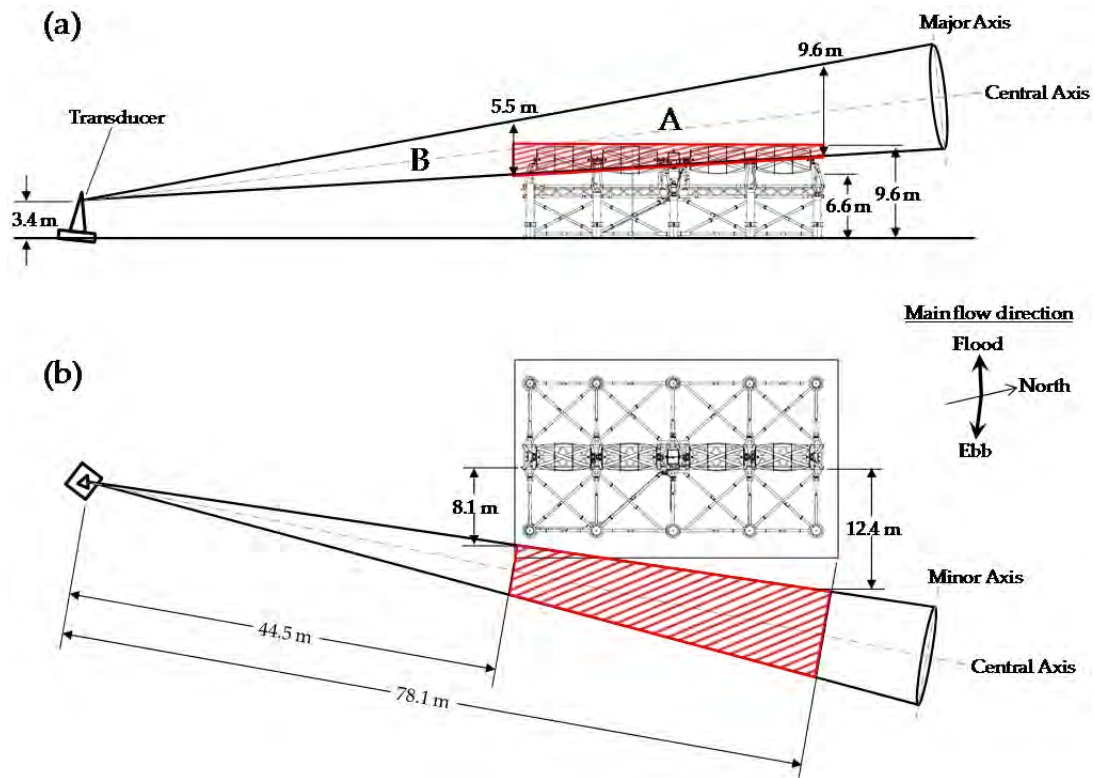


Figure 8. Marine Life Interaction Monitoring Plan setup. TidGen[®] device and Simrad EK60 support structure shown from (a) the seaward side and (b) above. Hydroacoustic beam represented as 7° cone (half-power beam width) in solid black lines. Red hatched area indicates sampled volume within the turbine zone, A indicates the volume sampled above the turbine, and B indicates the volume sampled beside the turbine. Current directions shown are project site averages provided by ORPC.

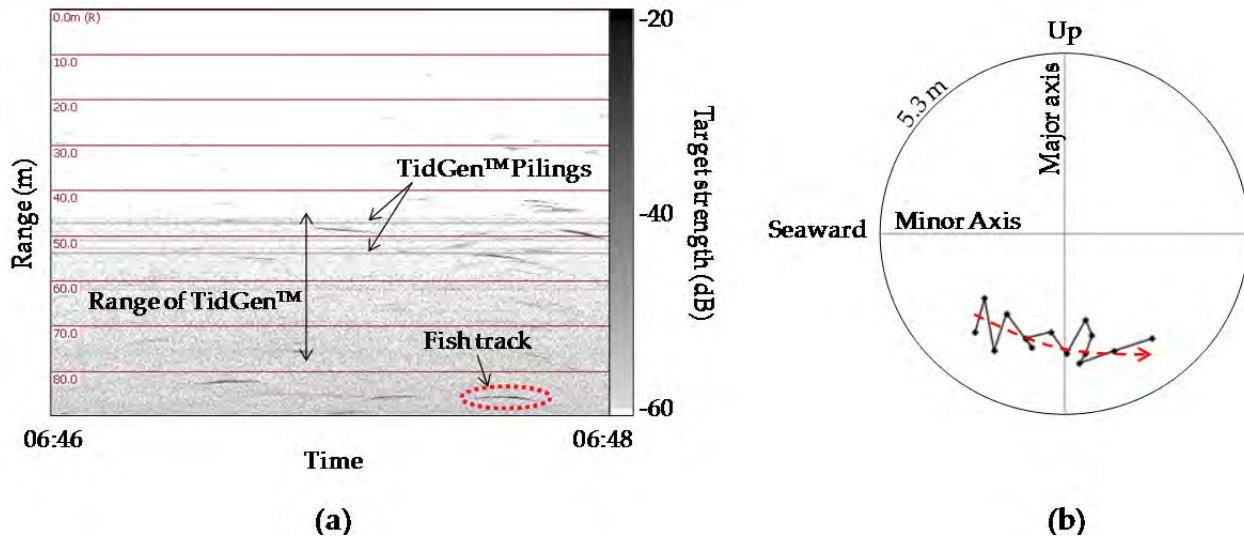


Figure 9. (a) Sample of side-looking hydroacoustic data from 9/30/2012 during the flood tide. (b) Fish in red dashed oval in (a) tracked through beam cross section. Outer circle represents 3.5° off-axis, or 5.3 m at this range. Each dot is a single detection of the fish. Red dashed arrow indicates direction of movement.

ORPC also collected current speed, direction (intermittently; see section 3.1.2), turbine movement in rotations per minute (RPM), and turbine operation state (generating or not).

3.1.2 Data Availability

Data collection began on August 29, 2012. Data could not be collected while the turbine was generating power due to electrical interference between the data and power transmission cables running together along the seabed to the shore station. Therefore, hydroacoustic data have been collected only for periods of time when the turbine was not rotating (either during slack tides when the current was too weak, or when the brake was applied), or when it was free-spinning (rotating but not generating power). Gaps also exist in the dataset whenever the turbine or hydroacoustic system was being repaired or adjusted, during periods of turbine deployment or removal, and whenever divers were present near the echosounder.

Collection of current speed and direction data by sensors mounted on the TidGen® Power System frame has been intermittent. For times when data are available, current direction is not useful for fish behavior analysis due to the placement of ORPC's flow meters, which are oriented to collect information in the plane parallel to the TidGen®. At times, ORPC has collected current speed and direction information with an Acoustic Doppler Current Profiler (ADCP) placed approximately 4.6 m from the turbine, between the turbine and hydroacoustic transducer. This ADCP would operate for various lengths of time (spanning days), obtaining current speed and direction readings every second. When ADCP deployment overlaps with hydroacoustic data collection, the information may be used to analyze fish swimming direction and speed in relation to the current.

Given these constraints to data collection and availability, three subsets of the data collected since August 2012 were analyzed for this report (Table 2). The first two subsets spanned March 19th to 21st and April 18th to April 20th, when ORPC ceased normal power generation to allow continuous hydroacoustic data collection with the turbine free-spinning. These dates were chosen because there were nearly two complete tidal cycles during each day and night. While a free-spinning turbine does not have the same hydraulic signature as one generating power, these data should provide a better idea of fish behavior around an operating turbine than data collected while the turbine is held stationary by its brake. Current speed and RPM (range 8.22-16.73) data were available for these time segments. More free-spinning data collection periods had been planned for May, June, July, and August 2013; however, unforeseen circumstances caused turbine operation to cease in April 2013, just after the free-spinning data presented here were collected. The turbine brake was then applied and the turbine held motionless until it was removed in July 2013.

Hydroacoustic data collection continued after the turbine brake was applied, so a third time period was selected from these data for comparison to the free-spinning datasets from March and April. This 'braked' dataset spans April 26th to April 28th. These dates were chosen for comparison because they were the closest data available to the April free-spinning period that had similar timing of tides (e.g., nearly two complete cycles during each day and night). Current speed data were not available for this time, however, and were instead estimated using previous current speed data (see section 3.1.3).

Table 2. Summary of data subset analyzed to date.

Data subset	Tidal stage	Start Date	Start time	End time	Mean current speed ($\text{m}\cdot\text{s}^{-1}$)	Duration (hrs)	Mean turbine rotation speed (rpm)*
March Free-spinning	Ebb	3/19/13	17:00	22:20	0.82	5.33	11.80
	Flood	3/19/13	23:15	4:50	0.91	5.58	12.95
	Ebb	3/20/13	5:50	10:40	0.86	4.83	13.52
	Flood	3/20/13	11:40	17:20	0.93	5.67	13.28
	Ebb	3/20/13	18:20	23:20	0.81	5.00	11.95
	Flood	3/21/13	0:20	5:30	0.99	5.17	15.05
	Ebb	3/21/13	6:30	11:40	0.86	5.17	8.22
	Flood	3/21/13	12:40	18:30	0.95	5.83	–
	Ebb	3/21/13	19:30	0:30	0.85	5.00	–
	Flood	3/22/13	1:30	7:00	1.01	5.50	–
Ebb	3/22/13	8:00	13:00	0.95	5.00	–	
April Free-spinning	Ebb	4/18/13	5:00	10:20	0.94	5.33	15.82
	Flood	4/18/13	11:20	16:40	1.02	5.33	16.24
	Ebb	4/18/13	17:40	22:40	0.84	5.00	–
	Flood	4/18/13	23:40	4:50	1.03	5.17	16.24
	Ebb	4/19/13	5:50	11:15	0.91	5.42	15.24
	Flood	4/19/13	12:15	17:30	1.01	5.25	16.22
	Ebb	4/19/13	18:30	23:40	0.86	5.17	14.51
Flood	4/20/13	0:40	6:00	1.01	5.33	16.73	
April Braked	Flood	4/26/13	7:00	12:00	1.22*	5.00	0.00
	Ebb	4/26/13	13:00	18:20	1.24*	5.33	0.00
	Flood	4/26/13	19:20	0:15	1.22*	4.92	0.00
	Ebb	4/27/13	1:15	6:45	1.24*	5.50	0.00
	Flood	4/27/13	7:45	12:45	1.22*	5.00	0.00
	Ebb	4/27/13	13:45	19:05	1.24*	5.33	0.00
	Flood	4/27/13	20:05	1:55	1.22*	5.83	0.00
	Ebb	4/28/13	2:55	7:35	1.24*	4.67	0.00

* Turbine rotation speed while free-spinning is faster than rotation speed during normal operation.

3.1.3 Data processing and analysis

Echoview software (5.3, Myriax Pty. Ltd., Hobart, Australia) was used to process side-looking split beam hydroacoustic data. Processing in Echoview began with manually inspecting the data to identify and exclude unwanted noise (e.g., interference from depth sounders, entrained air from the surface, reflection from surface waves, reflection from fish schools), and setting a target strength threshold of -50 dB to exclude background noise, plankton, and other small objects from analyses. Target strength (TS) is a measure of the relative amount of acoustic energy reflected back toward the transducer by an object, compensating for transmission and signal losses and

represented in decibels (dB re 1 m²; Simmonds and MacLennan 2005). Though TS is dependent on several factors, including fish anatomy (e.g., swim bladder or none) and orientation relative to the transducer, it is generally proportional to fish size (Simmonds and MacLennan 2005). A threshold of -50 dB should eliminate most fish less than 8.7 cm in length (Lilja et al. 2004), assuming they have air-filled swim bladders (e.g., Atlantic herring). For fish lacking a gas-filled swimbladder, such as Atlantic mackerel, this threshold may eliminate larger fish to an unknown degree.

Echoes from single targets were then detected, excluding data collected beyond 78.1 m from the transducer (far edge of the turbine) due to frequent interference from the surface. Single target detection parameters (Table 3) were set liberally to allow a large number of single targets to be detected among the noise, though this also allowed more false detections to occur. Echoview's fish tracking module was then used to trace the paths of individual fish through the sampled volume. Fish track parameters (Table 4) were chosen to limit the effect of false single target detections on the number of detected fish. Fish track data (including time of detection, target strength, and direction of movement) were exported from Echoview to be further analyzed using MATLAB.

Table 3. Single target detection settings in Echoview

Parameter	Value	Units
Target strength threshold	-50.00	dB
Pulse length determination level	6.00	dB
Minimum normalized pulse length	0.24	Unitless
Maximum normalized pulse length	10.00	Unitless
Beam compensation model	Simrad LOBE	
Maximum beam compensation	35	dB
Maximum standard deviation of minor-axis angles	1.000	Degrees
Maximum standard deviation of major-axis angles	1.000	Degrees

Table 4. 4D fish track detection settings in Echoview.

		Major Axis	Minor Axis	Range
Algorithm	Alpha	0.5	0.5	0.7
	Beta	0.1	0.2	0.1
	Exclusion distance (m)	2.25	2.25	0.2
	Missed ping expansion (%)	0	0	100
Weights	Major axis	0		
	Minor axis	0		
	Range	1		
	TS	0		
	Ping gap	0		
Track Acceptance	Min number single targets in track	5		
	Min number of pings in track (pings)	5		
	Max gap between single targets	8		

In MATLAB, fish tracks that had been contaminated by false single targets were removed based on track properties, including minor and major axis angle, tortuosity, and change in depth and range (Table 5). These settings helped eliminate fish tracks affected by noise from the turbine and other environmental factors. However, one effect of the turbine that could not be removed without drastically limiting the dataset was its apparent masking of weaker fish echoes within its range (i.e., between 44.5 and 78.1 m from the transducer; Figure 8). This masking is apparent in the distribution of fish track TS from beside the turbine and within the turbine's range (Figure 10). As weaker fish tracks were not detected in the range of the turbine, the numbers of fish detected on either side of the turbine were likely to be inflated with respect to numbers of fish detected within the turbine zone or above it, and included more of the weaker echoes (e.g., smaller fish).

Table 5. Fish track acceptance parameters used in MATLAB processing.

Fish track property	Value required for track acceptance
Minor axis angle	< 3.0°
Major axis angle	< 3.0°
Change in range	> 0.05 m
Change in depth	> 0.05 m
2D and 3D tortuosity	< 5.0

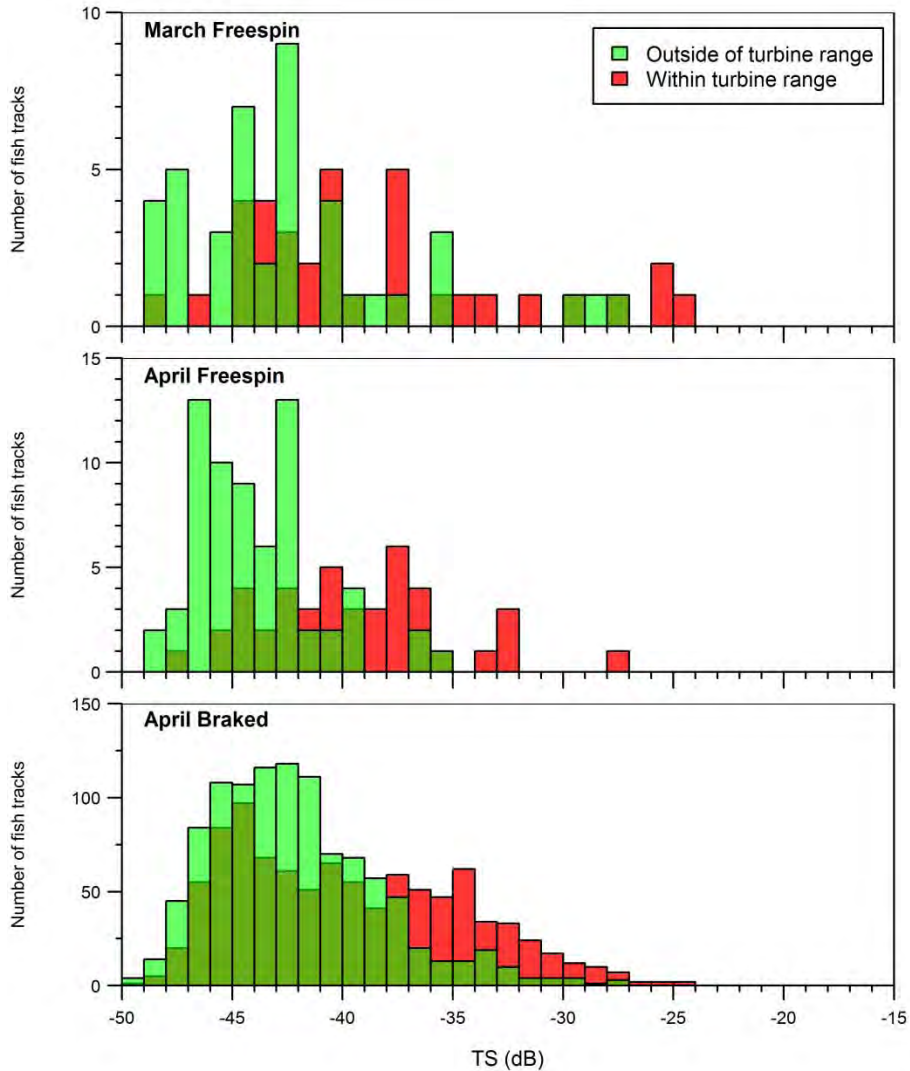


Figure 10. Target strength (TS) distribution from before the turbine range (< 44.5 m from transducer) and within the turbine range (> 44.5 m and \leq 78.1 m from transducer).

Accepted fish tracks were grouped by tidal stage for analysis of target strength and direction of movement. Flood and ebb tide data were treated separately because a fish's approach to the turbine is sampled during the flood and its departure from the turbine is sampled during the ebb, and behaviors during each are assumed to differ (Viehman 2012; Viehman and Zydlewski accepted).

3.1.5 Fish density and location of tracks

The total number of fish tracks detected in the hydroacoustic data provided an estimate of the density of fish in the sampled volume over time. The location of each fish in the sampled volume was used to place it in one of the three zones near the turbine (Figure 8). Density of fish in a zone (in fish per cubic hectometer, hm^3) was calculated for each time span of interest (e.g., each ebb and flood tide) by dividing the total number of fish detected in the zone by the volume

of water to pass through that zone. This volume was calculated by multiplying the area of the zone's vertical cross-section by the approximate linear distance of water to pass through it during the analysis period. The linear distance of water was determined using the mean current speed of each 10-minute time increment. Using 10-minute averages greatly reduced the effect of the noise in the ADCP current speed data. In this way, fish counts were normalized for varying sampling duration and current speed, allowing the direct comparison of densities from different datasets.

Current speed data were not available for the braked turbine dataset, so current speeds from the nearest free-spinning data (April 18-20) were used to obtain an approximation. Since free-spinning data were collected at neap tide (first quarter moon) and braked data were collected at spring tide (full moon), the mean flood tide current speed was multiplied by a factor of 1.2 and the mean ebb tide speed was multiplied by 1.4. These factors were determined using ADCP data collected during spring and neap tides in 2012. While this is a coarse approximation, some estimate was needed in order to make any comparisons between fish numbers obtained from the free-spinning data to those of the braked data.

3.1.6 Direction of movement

The direction of movement (heading, degrees from North; inclination, degrees from horizontal) of each fish was compared to the current direction at the time of fish detection (when data were available). Higher deviation from the water current direction within the turbine zone than in other zones may indicate avoidance behavior during approach (flood tides), or milling during departure (ebb tides).

3.2 Results

A total of 68 fish tracks were detected during the March free-spinning period, 87 were detected during the April free-spinning period, and 1,827 were detected during the April braked period (Figure 11). The number of flood and ebb tides sampled was too low to carry out statistical analyses of the differences between these sampling periods (5 tidal cycles in March, 4 in each April dataset). The large number of fish in the braked dataset in April compared to the other two datasets is unlikely related to turbine operation. To investigate this, the number of fish detected during the slack tides were also compared across datasets, and showed a similar pattern (Figure 12). As the turbine was not moving (and therefore assumed not to be a contributing factor) during the slack tides in either dataset, this comparison supports a natural increase in fish numbers between the free-spinning periods and the braked period. This would also be in line with results from down-looking hydroacoustic surveys (Section 2.2.1), which have shown a large increase in fish density between March and May.

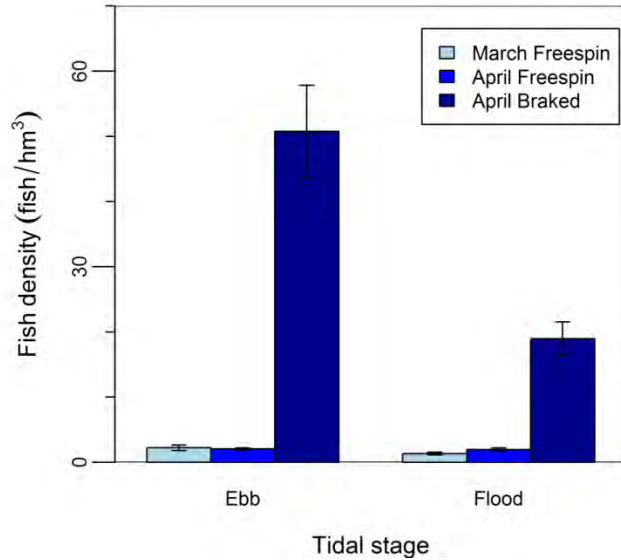


Figure 11. Mean fish density (fish/hm³) of each tide of each dataset. Whiskers are one standard error.

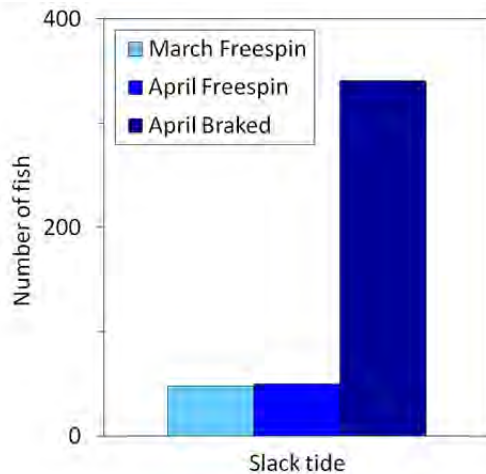


Figure 12. Number of fish detected during the slack tides in each dataset.

3.2.3 Fish density by zone

The mean density of fish in each sampling zone is shown in Figure 13. Density appears greatest beside the turbine and lowest in the turbine zone, though no tests for statistical significance have been carried out due to the low sample sizes (5 tides in March, 4 tides in each April dataset). This is unlikely to be entirely natural or a response to the turbine; rather, it is likely largely due to the masking of weaker fish echoes within the range of the turbine (see section 3.1.3). Though fish track filtering removed much of this effect, the target strength distributions of accepted fish tracks (Figure 10) show that the lower end of the TS spectrum (-50 dB to -41 dB) appear undersampled in the turbine range compared to beside the turbine.

In the braked dataset, more fish were detected during the ebb tide than during the flood tide. This could be explained by the natural movements of fish in the area (e.g., an outward movement of species at the time of the data collection), or may be related to fish sheltering in the lee of the device and its supporting structure. This behavior was previously observed within approximately 3 m of a test turbine (Viehman and Zydlewski, accepted) but more data are necessary before this behavior can be identified in these datasets, especially as the sampling volume of this study is approximately 10 m from the device. The low sample size and the few fish detected to date result in a high degree of variability that makes further comparison of fish counts not useful.

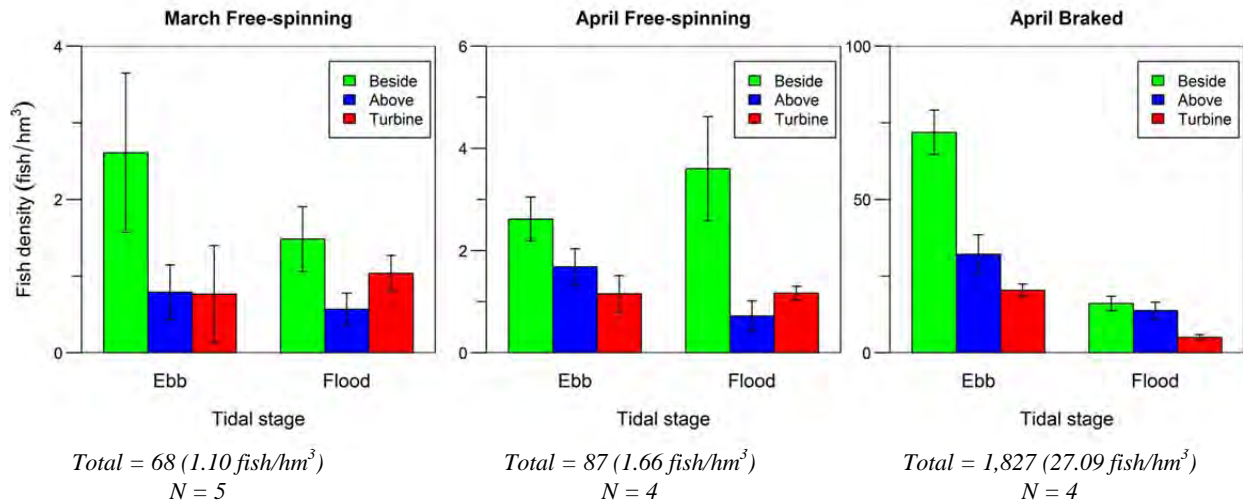


Figure 13. Mean fish density (fish/hm³) in each zone (+/- 1 standard error).

3.2.4 Direction of movement

The distribution of the headings of fish in each sampling zone peaked at the predominant current direction, indicating fish moved primarily with the prevailing current (Figure 14). Due to the small sample size, statistical significance was not tested. The low number of fish detected in March and April free-spinning periods made interpretation of distributions unconstructive. However, in the braked dataset, enough fish were detected to make slight differences in each zone visible. During the flood tide (approach to the device), more fish were swimming in directions other than that of the main current. During the ebb (departure from the device), more fish swam with the current. The greater variation in fish direction during their approach indicates higher variability in behavior, though sample sizes were too low to draw any conclusions associated with avoidance. Additionally, some of this variation may be due to variable current direction, but this cannot be confirmed without current direction data.

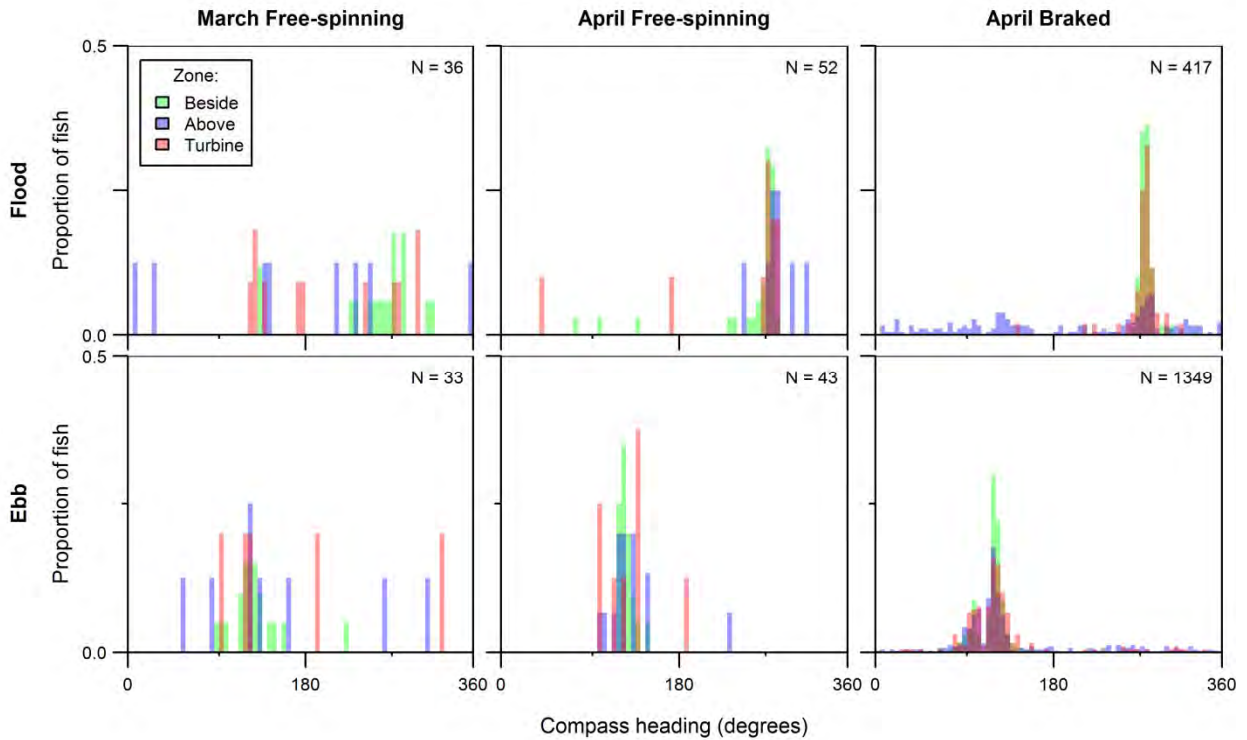


Figure 14. Distribution of fish headings during each dataset (0 = North). Values are scaled to number of fish detected in each zone.

The distribution of inclination angles of fish peaked between -10° and 0° , indicating that most fish were swimming horizontally or slightly downward (Figure 15). Again, the March and April free-spinning datasets did not yield enough fish to draw conclusions. In the braked dataset, variation in inclination angle appeared higher during the flood tide than the ebb tide, as indicated by the wider spread of the distribution. This increased variation could be linked to the fewer numbers of fish detected during the flood tide.

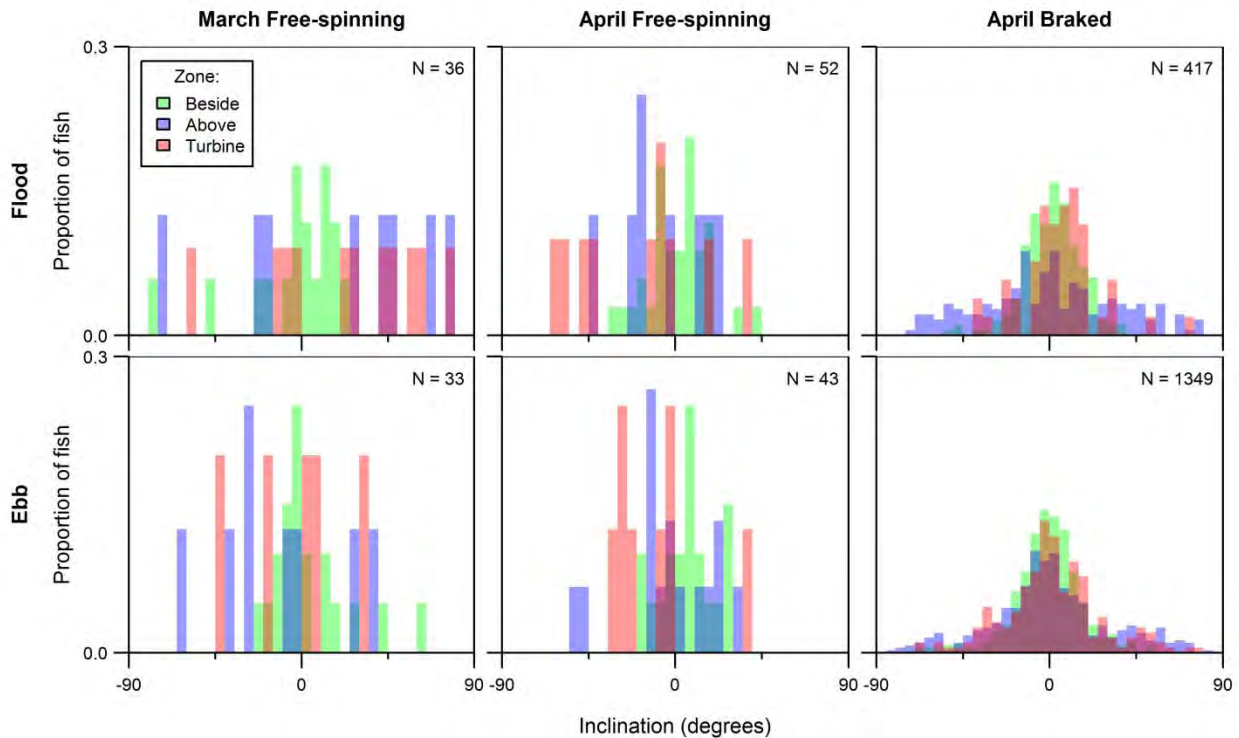


Figure 15. Distribution of fish inclination during each dataset (-90 = down, 0 = horizontal, 90 = up). Values are scaled to number of fish detected in each zone.

4.0 Summary

4.1 Fisheries monitoring (down-looking hydroacoustics)

Understanding the interactions between the environment and its biological constituents in tidally dynamic coastal regions is essential for informing tidal power development. Research and monitoring in these areas is limited because of the physical dynamics. Recent interest in tidal power extraction in Cobscook Bay provided the opportunity to develop an approach to assess such areas. The Bay's complicated bathymetry combines with a large tidal range to create high current speeds and flow patterns that vary greatly with location and tide (Brooks 2004, Huijie Xue, unpublished data). Multiple fish species pass through the strong currents of the outer bay to move between deeper ocean habitats and the extensive inshore habitats of the inner bays. Given the extreme variation in currents over time and space and the mixed seasonal and year-round fish community (Appendix 1), hydroacoustic measures of relative fish density were expected to vary widely in relation to season and location. Our hydroacoustic assessments demonstrate that while fish density is indeed variable, patterns are repeatable and will be useful in understanding the effects of devices.

4.1.1 Overall Fish Density

1. Inter-annual variability: was fish density constant across years? Differences in overall annual mean S_v with sites combined was discernible. The years 2010 and 2012 had higher fish density than 2011 and 2013. These differences display natural annual variation occurring within the years we have sampled. This highlights the importance of a useful control site in distinguishing changes in density due to turbine deployment from natural variation in fish density over time.

2. Beside vs. in-line with the turbine: were densities similar at the two project sites (CB1a and CB1b)? Both sites were similar and not statistically significantly different. The similarity between data collected at these two sites to date indicates that the inline site, CB1b, is representative of fish passage on a large lateral scale in the area of deployment. In addition, their similarity allowed us to combine them for analyses. It is important to note that the similarity between the inline and beside sites do not represent similarity of fish behavior in these locations. The beside site had little consistency in geographic location month to month and was often hundreds of meters away from the TidGen[®], which could have resulted in similar data collected, not truly reflecting fish distribution beside the turbine. Further data closer to the turbine for the “beside” monitoring is necessary.

3. Project site vs. control site: is fish density similar at CB1 and CB2, and is CB2 therefore a useful control site? The utility of the control site becomes apparent when examining the variation between the experimental site CB1 and the control site CB2 within each month sampled. These two sites typically had no significant differences with the exception of CB2 having significantly higher mean S_v in September 2010 and March and August 2012. With only these three exceptions to significant differences, we feel that the utility of the respective sites is valid. The difference in September 2010 could be linked to electrical noise in the hydroacoustic system during that year. The differences in March and August 2012 may be related to construction activities around the TidGen[®]: in March, the bottom support frame was being installed, and in August, the turbine was being deployed.

4. Seasonal variability: is there a consistent seasonal pattern to fish density in outer Cobscook Bay? Consistent monthly differences were found for all years, with peaks in density in May and June, followed by November. May of 2012 had much higher mean S_v than other years. This peak may have been related to elevated water temperatures, which affect the movements and growth of fish. For example, midwater trawls carried out near CB2 at this time found fully metamorphosed herring, while in other years the same trawls found larval herring or none at all (Vieser unpublished data). This early growth of herring would have caused a greater increase in mean S_v than normally seen. It is important to be able to distinguish this type of natural variation from turbine effects.

5. Did deployment of the TidGen[®] affect fish density at the project site (CB1)? The turbine was deployed during the August and September 2012 and March 2013 surveys. Only August 2013 had a significantly lower fish density at the project site than the control site. This may have been related to increased boat traffic and construction activities at the project site as the device was deployed. These activities included deploying and retrieving ADCPs, divers performing

observation or maintenance on the device, or deployment and adjustment of the deployment area marker buoys. At times, there was also a large construction barge over the TidGen[®]. A similar difference between densities at the project and control sites was seen in March 2012, which was just after the bottom support frame was installed. This installation included pile driving, divers, a large barge, and high boat traffic at the project site, all of which may have led to fish avoiding the area. Unfortunately, only three surveys were carried out while the turbine was operating. While there was no difference between project and control sites in the September 2012 and March 2013 surveys (carried out post-deployment and during normal turbine operation), this is not enough information to conclude that the turbine had negligible effect on fish density at the site.

4.1.2 Vertical Distribution

The vertical distribution of fish was rarely different among sites. Distributions showed that fish density generally increased toward the sea floor regardless of time of year. This trend of higher density near the bottom could possibly be related to the decrease in current speed in the boundary layer against the sea floor. Fish may be using this area as a refuge from faster current speeds found higher in the water. There are exceptions to this trend of fish density increasing toward the sea floor in May 2011 at CB1, May 2012 at all sites, and June 2013 at CB2, potentially related to the large numbers of larval and juvenile herring utilizing the upper layers of the water column at those times.

4.2 Marine life interaction monitoring (side-looking hydroacoustics)

The original goal of this monitoring was to collect data continuously during turbine operation (while generating power). A power-generating turbine has a different hydraulic and acoustic signature than a turbine that is free-spinning or braked. As such, fish response under these conditions may differ and it is important to collect fish response data while the turbine is generating power.

The dataset analyzed is limited to a few days of free-spinning and braked conditions. It is difficult to draw conclusions about fish behavior with so few fish detected during each tide, particularly during free-spinning periods. Down-looking hydroacoustic survey results indicate that fish densities are low in March compared to other months sampled, which is supported by the low numbers detected during the free-spinning periods in March and mid-April. The braked dataset in late April had many more fish than the earlier two datasets, perhaps linked to the springtime peak in density that was apparent in down-looking data. More data should be collected during times of the year when fish abundance is higher (e.g., May and June), which would provide datasets with higher sample sizes and allow quantitative statistical analyses. Higher sample sizes and statistical testing would lead to more constructive conclusions about effects of the TidGen[®] on fish behavior. This was originally planned, and will hopefully occur once the turbine has been re-deployed.

Available data allowed us to identify some key issues that should be addressed in the future.

1. Data should be collected while the turbine is generating power.
2. Current speed and direction data are necessary for accurate estimation of fish density and for analyses of fish movement through the beam. Without speed information, the volume of water sampled over time may be miscalculated. In this report, we estimated water speeds based on past data. This is unlikely to be accurate, but in this case even a large miscalculation in current speed would not account for the huge increase in fish density between the free-spinning datasets and the braked dataset. Current direction data is necessary for the identification of fish behaviors related to the turbine, as opposed to those related to current. This can be accomplished by adjusting or adding sensors on the TidGen[®] or more regularly deploying an ADCP near the TidGen[®].
3. The turbine appears to be masking echoes from smaller fish within its range. This renders the TS distributions obtained incomplete, and excludes analyses of the behaviors of smaller size classes of fish. This could be solved by orienting the hydroacoustic beam further away from the device or focusing analyses on larger targets.
4. When more data are collected, more thorough analyses can be carried out. For now, the numbers of fish detected, their estimated densities, and their direction of movement are qualitative at best.

The fish community of Cobscook Bay is also being assessed by UMaine. In the future, results from that study will aid in identifying probable species represented by hydroacoustic targets. However, for now, the masking effect of the turbine on fish must be more carefully examined before target strength distributions will be useful.

5.0 References

- Balk, H. and T. Lindem. 2000. Improved fish detection in data from split-beam sonar. *Aquatic Living Resources* 13: 297-303.
- Brooks, D. A. 2004. Modeling tidal circulation and change in Cobscook Bay, Maine. *Northeastern Naturalist* 11: 23-50.
- De Robertis, A. and I. Higginbottom. 2007. A post-processing technique to estimate the signal-to-noise ratio and remove echosounder background noise. *ICES Journal of Marine Science* 64: 1282-1291.
- Konietschke, F. 2012. nparcomp: Perform multiple comparisons and compute simultaneous confidence intervals for the nonparametric relative contrast effects. R package version 2.0. <http://CRAN.R-project.org/package=nparcomp>.
- Lilja, J., T. J. Marjomäki, J. Jurvelius, T. Rossi, E. Heikkola. 2004. Simulation and experimental measurement of side-aspect target strength of Atlantic salmon (*Salmo salar*) at high frequency. *Canadian Journal of Fisheries and Aquatic Sciences* 61: 2227-2236.
- Ocean Renewable Power Company. 2012. License Article 407, Fisheries and Marine Life Interaction Plan. Federal Energy Regulatory Commission Pilot Project No. 12711.
- Simmonds, J. and D. MacLennan. 2005. *Fisheries Acoustics: Theory and Practice*. 2nd ed. Oxford: Blackwell Science. 437 p.
- Viehman, H. 2012. Fish in a tidally dynamic region in Maine: hydroacoustic assessments in relation to tidal power development. [master's thesis]. [Orono, (ME)]: University of Maine.
- Viehman, H. and G. B. Zydlewski. accepted. Fish interactions with a commercial-scale tidal energy device in the natural environment. *Estuaries and Coasts*.
- Wheeler, B. 2010. lmPerm: Permutation tests for linear models. R package version 1.1-2. <http://CRAN.R-project.org/package=lmPerm>.

Appendix Task 2-7

2011 Annual Report: Special License Number ME 2011-63-01 University of Maine, School of Marine Sciences Gayle Zydlewski, James McCleave, Jeffrey Vieser

Introduction

The first objective of the project requiring the special license was to use midwater trawling to provide species verification to accompany acoustic assessment of pelagic fish abundance in Outer Cobscook Bay and Western Passage, near Eastport, Maine. The acoustic assessment was conducted independently of the special license. The acoustic assessment and midwater trawling are parts of an overall project to assess the seasonal, daily, and tidal abundance and distribution of pelagic fishes in locations proposed for deployment of electricity generating tidal turbines.

The second objective of the project requiring the special license was to use midwater trawling, benthic trawling, intertidal seining, and intertidal fyke netting to characterize the fish community of the entire Cobscook Bay and the midwater fish community of Western Passage. This study provides a wider ecosystem perspective against which to consider deployment of arrays of electricity generating tidal turbines.

Methods

Midwater and benthic trawling was done with the commercial fishing vessel *Pandalus* (147YV), owned and operated by Stephen W. Brown. The midwater net mouth dimensions were: headrope, footrope and breastlines 40 feet. Mesh sizes were: belly, square and side panels 4 inch, tapers 2 inch, and extensions and codend 1 inch. The benthic net mouth dimensions were: headrope 45 feet, headrope 35 feet, no breastlines. Stretch mesh sizes were: net body 2 inch, codend 1 inch. Tows were nominally 20 minutes, but sometimes varied, especially to shorter times because towable distance was too short. Tows were mostly made during daytime, but some night tows were made, mostly in East and South Bays, subbays of middle Cobscook Bay (Figure 1, Tables 1, 2).

Two 100 foot x 6 foot seines with 0.25-inch diamond mesh were used to sample shallow intertidal habitats including cobble fields, mud flats, rockweed patches, and grass beds (Figure 1, Tables 3a, b). Two fyke nets with 30 foot wings, 4 foot tall square hoops, and 1.5-inch stretch mesh were used to sample larger rock piles (Table 4). Sampling of intertidal habitats was conducted mostly in day time, with some night sampling.

Trawling and intertidal sampling were conducted during neap tides in May, June, August and September, 2011.

Results

Benthic trawling and intertidal seining were quite successful in capturing a variety of fish species, but midwater trawling and fyke netting were less successful. Approximately 6,000 individual fish of 31 species were caught (all gears and dates combined) (Table 5). Individuals of many species were primarily smaller (juvenile) specimens, but a few adult Atlantic herring (*Clupea harengus*) and Atlantic mackerel (*Scomber scombrus*) were caught in pelagic trawls (Table 6). Atlantic herring dominated the pelagic catch, but most in May were still in the larval stage and not sampled well by the pelagic trawl. Unexpected was the capture of adult threespine

sticklebacks (*Gasterosteus aculeatus*) in midwater trawls in all four months, but especially in May. Winter flounder (*Pseudopleuronectes americanus*) juveniles dominated the catch in benthic trawls, but species richness was greatest in the benthic trawls (24 species caught at least once) (Table 7).

Threespine stickleback, Atlantic herring, mummichog (*Fundulus heteroclitus*), and blackspotted stickleback (*Gasterosteus wheatlandi*) were all common in intertidal seine tows, but in widely varying proportions in different months (Table 8). Only four species represented by few individuals were caught in fyke nets (Table 9).

No Atlantic salmon (*Salmo salar*), shortnose sturgeon (*Acipenser brevirostrum*), or Atlantic sturgeon (*A. oxyrinchus*) were captured in any gear.

Discussion

Visual observation, hook and line recreational fishing, acoustic fish finder records, and local fishers' knowledge indicates the presence of large numbers of Atlantic herring and Atlantic mackerel throughout the water column in the study area, especially in August and September. The inability of our gear to capture these highly mobile pelagic species is a problem. We suspect that the ability of highly mobile fish to detect the presence of the net, through visual and other sensory clues, allows them to avoid it in most cases. When capture did occur, it was primarily at night, when visual cues are restricted. Additional sampling at night, especially with midwater trawls, is desirable but must be balanced against safety considerations in strongly tidal locations.

It is expected that larger benthic species, e.g., spiny dogfish (*Squalus acanthius*), succeeded in avoiding capture, though there is less anecdotal evidence to support their presence in the bays. A number of other species are probably under sampled as well in various gears, e.g., river herring (alewife *Alosa pseudoharengus* and blueback herring *A. aestivalis*), rainbow smelt (*Osmerus mordax*) except for one targeted seine tow, skates and flatfish species (other than winter flounder).

An application for an extension of our special license for 2012 will be forthcoming involving a few small changes to our scope of work.

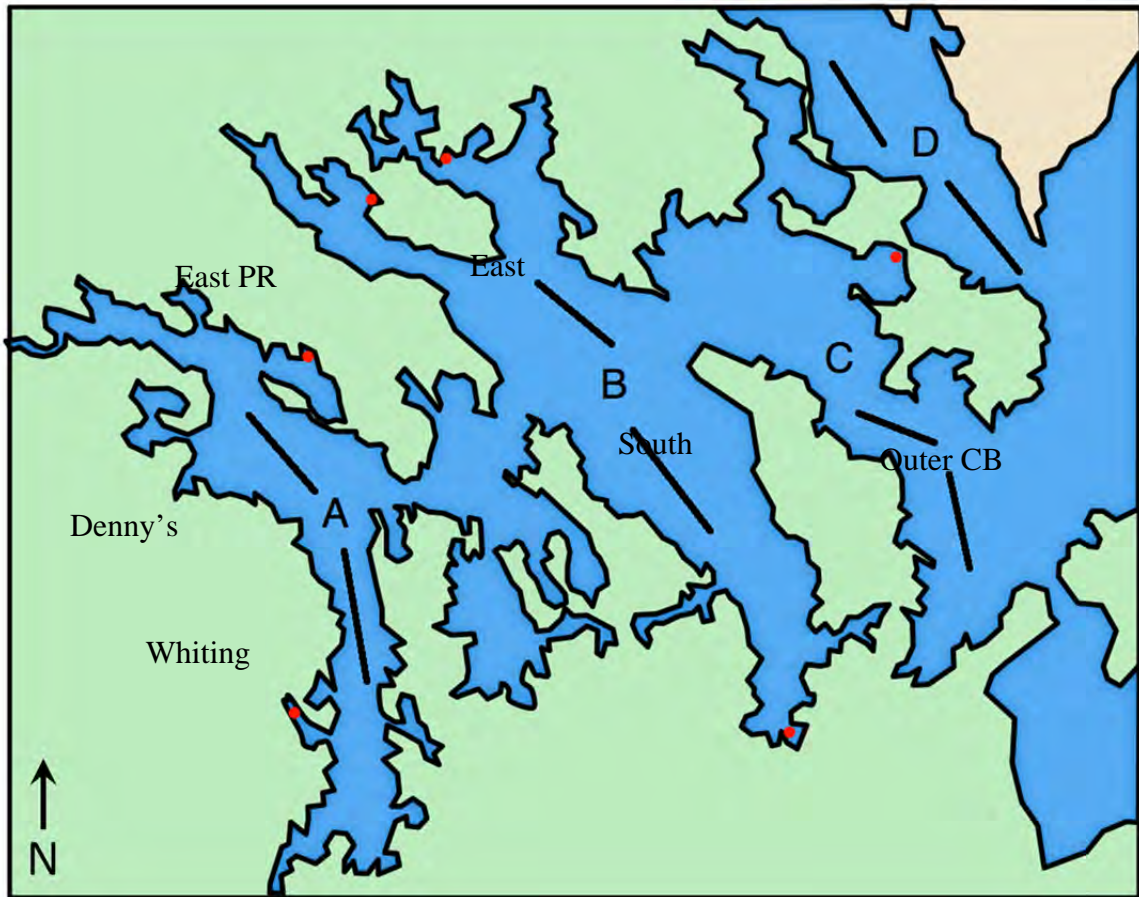


Figure 1. Map of Cobscook Bay and Western Passage of Passamaquoddy Bay showing mid-water and benthic trawl lines (black lines) fished in 2011 and planned for 2012, as well as seine and fyke net sampling locations (red dots). Both benthic and pelagic trawls occurred in the same location. Uppercase letters indicate the center of each of the three sub-bays of Cobscook Bay (A = inner; B = middle; C = outer) and Western Passage in Passamaquoddy Bay (D). Smaller bays of each sub-bay are also named.

Table 1. Date and location of pelagic trawl samples in Cobscook Bay during May, June, August and September of 2011. Tide is the tidal stage when nets were fished. GPS Begin and GPS End are latitude and longitude where nets were deployed and retrieved, respectively. Tow is tow number. Begin and End are times (EDT) when the trawls were deployed and retrieved, respectively. Night samples are highlighted in gray. CB is Cobscook Bay.

Month	Day	Bay	GPS Begin	GPS End	Tide	Tow	Begin	End
May	26	East	N 44 54.884 W 67 55.590	N 44 55.538 W 67 5.333	EBB	5	9:48	10:08
May	26	South	N 44 53.575 W 67 4.645	N 44 52.930 W 67 3.903	EBB	6	10:47	11:08
May	27	Outer CB Lower	N 44 53.847 W 67 1.449	N 44 54.025 W 67 1.543	EBB	7	11:05	11:28
May	27	Outer CB Upper	N 44 54.604 W 67 3.257	N 44 54.536 W 67 3.302	EBB	8	12:02	12:28
May	27	Outer CB Upper	N 44 53.798 W 67 1.355	N 44 54.293 W 67 2.097	FLOOD	9	20:31	20:52
May	28	Denny's	N 44 53.125 W 67 9.486	N 44 52.310 W 67 8.706	EBB	10	9:20	9:40
May	28	Whiting	N 44 51.880 W 67 8.735	N 44 51.113 W 67 8.600	EBB	11	9:55	10:15
Jun	25	South	N 44 53.543 W 67 4.747	N 44 52.784 W 67 3.935	EBB	5	10:36	10:57
Jun	26	East	N 44 54.841 W 67 5.383	N 44 55.488 W 67 6.142	EBB	6	10:20	10:41
Jun	26	South	N 44 53.428 W 67 4.471	N 44 52.677 W 67 3.858	EBB	7	11:13	11:34
Jun	26	South	N 44 52.918 W 67 4.160	N 44 53.594 W 67 4.807	EBB	8	22:31	22:51
Jun	26	East	N 44 54.845 W 67 5.540	N 44 55.417 W 67 6.130	EBB	9	23:17	23:37
Jun	27	Outer CB Lower	N 44 52.313 W 66 59.921	N 44 52.988 W 67 0.472	EBB	10	12:24	12:45
Jun	27	Outer CB Upper	N 44 53.376 W 67 0.600	N 44 53.554 W 67 .819	EBB	11	13:04	13:24
Jun	28	Whiting	N 44 51.879 W 67 8.719	N 44 51.069 W 67 8.568	EBB	12	10:45	11:06
Jun	28	Denny's	N 44 52.860 W 67 8.987	N 44 53.311 W 67 9.733	EBB	13	11:40	12:00
Aug	23	Outer CB	N 44 53.557 W 67 0.935	N 44 53.986 W 67 1.708	EBB	1	12:08	12:30
Aug	23	Outer CB	N 44 53.893 W 67 1.405	N 44 53.369 W 67 0.287	LOW	2	12:43	13:03
Aug	24	South	N 44 52.387 W 67 5.505	N 44 53.106 W 67 4.277	EBB	5	22:01	22:20
Aug	24	East	N 44 54.902 W 67 5.527	N 44 55.470 W 67 6.204	EBB	6	22:45	23:05
Aug	25	East	N 44 54.922 W 67 5.617	N 44 55.602 W 67 6.207	EBB	7	12:47	13:07

Aug	25	South	N 44 53.169 W 67 4.232	N 44 52.439 W 67 3.567	EBB	8	13:43	14:03
Aug	26	Whiting	N 44 52.086 W 67 8.755	N 44 51.231 W 67 8.605	EBB	9	10:08	10:28
Aug	26	Denny's	N 44 52.876 W 67 9.057	N 44 53.308 W 67 9.719	EBB	10	10:53	11:10
Sep	23	Outer CB	N 44 52.213 W 66 59.919	N 44 53.030 W 67 0.404	EBB	1	13:11	13:31
Sep	23	Outer CB	N 44 53.566 W 67 1.017	N 44 54.009 W 67 1.789	EBB	2	13:48	14:08
Sep	24	East	N 44 55.852 W 67 6.426	N 44 55.205 W 67 5.967	FLOOD	5	18:53	19:13
Sep	24	South	N 44 53.570 W 67 4.667	N 44 52.903 W 67 4.081	FLOOD	6	19:38	19:58
Sep	25	South	N 44 53.020 W 67 4.202	N 44 53.715 W 67 4.783	FLOOD	7	16:08	16:28
Sep	25	East	N 44 54.884 W 67 5.663	N 44 55.620 W 67 6.300	FLOOD	8	16:48	17:08
Sep	26	Denny's	N 44 53.321 W 67 9.657	N 44 52.887 W 67 9.071	FLOOD	9	10:19	10:36
Sep	26	Whiting	N 44 52.041 W 67 8.727	N 44 51.078 W 67 8.625	FLOOD	10	10:54	11:14

Table 2 Date and location of benthic trawl samples in Cobscook Bay during May, June, August and September of 2011. Tide is the tidal stage when nets were fished. GPS Begin and GPS End are latitude and longitude where nets were deployed and retrieved, respectively. Tow is tow number. Begin and End are times (EDT) when the trawls were deployed and retrieved, respectively. Night samples are highlighted in gray. CB is Cobscook Bay.

Month	Day	Bay	GPS Begin	GPS End	Tide	Tow	Begin	End
May	26	South	N 44 52.795 W 67 3.739	N 44 53.513 W 67 4.501	EBB	1	11:54	12:15
May	26	East	N 44 55.001 W 67 5.681	N 44 55.67 W 67 6.236	LOW	2	12:39	13:00
May	27	Outer CB Upper	N 44 53.523 W 67 1.655	N 44 53.975 W 67 1.655	LOW	3	13:29	13:50
May	27	Outer CB Lower	N 44 52.182 W 67 0.44	N 44 52.458 W 67 0.043	LOW	4	14:12	14:32
May	27	Outer CB Upper	N 44 53.903 W 67 1.55	N 44 53.434 W 67 0.818	EBB	5	19:43	20:04
May	28	Whiting	N 44 42.036 W 67 8.793	N 44 51.281 W 67 8.568	EBB	6	10:52	11:12
May	28	Denny's	N 44 52.89 W 67 9.038	N 44 53.16 W 67 9.487	EBB	7	12:46	12:58
Jun	26	South	N 44 52.578 W 67 3.726	N 44 53.355 W 67 4.423	EBB	1	12:01	12:22
Jun	26	East	N 44 54.805 W 67 5.451	N 44 55.491 W 67 6.170	EBB	2	12:43	13:03
Jun	26	East	N 44 54.780 W 67 5.507	N 44 55.443 W 67 6.148	EBB	3	20:47	21:07
Jun	26	South	N 44 53.400 W 67 4.464	N 44 52.726 W 67 3.915	EBB	4	21:38	21:58
Jun	27	Outer CB Lower	N 44 52.444 W 67 0.107	N 44 53.207 W 67 0.359	EBB	5	14:14	14:35
Jun	27	Outer CB Upper	N 44 53.899 W 67 1.470	N 44 53.390 W 67 0.692	FLOOD	6	15:27	15:48
Jun	28	Denny's	N 44 53.196 W 67 9.518	N 44 52.850 W 67 8.969	FLOOD	7	9:08	9:22
Jun	28	Whiting	N 44 51.350 W 67 8.630	N 44 52.135 W 67 8.706	FLOOD	8	9:47	10:07
Aug	23	Outer CB	N 44 52.787 W 67 0.304	N 44 52.085 W 66 59.634	EBB	1	10:43	11:04
Aug	23	Outer CB	N 44 52.137 W 66 59.695	N 44 52.894 W 67 0.143	EBB	2	11:17	11:37
Aug	24	East	N 44 54.790 W 67 5.482	N 44 55.484 W 67 6.142	HIGH	3	19:48	20:09
Aug	24	South	N 44 53.582 W 67 4.664	N 44 52.926 W 67 4.031	EBB	4	20:43	21:04
Aug	25	South	N 44 52.341 W 67 3.452	N 44 53.018 W 67 4.131	LOW	5	14:30	14:50
Aug	25	East	N 44 54.852 W 67 5.621	N 44 55.620 W 67 6.196	FLOOD	6	15:14	15:34

Aug	26	Denny's	N 44 52.938 W 67 9.038	N 44 53.390 W 67 9.820	FLOOD	7	8:28	8:45
Aug	26	Whiting	N 44 51.297 W 67 8.612	N 44 52.079 W 67 8.730	HIGH	8	9:14	9:34
Sep	23	Outer CB	N 44 52.239 W 66 59.220	N 44 53.073 W 67 0.406	EBB	1	11:51	12:13
Sep	23	Outer CB	N 44 53.045 W 67 0.353	N 44 52.270 W 66 59.959	EBB	2	12:24	12:45
Sep	24	South	N 44 52.725 W 67 4.046	N 44 53.422 W 67 4.619	HIGH	3	20:22	20:42
Sep	24	East	N 44 54.794 W 67 5.550	N 44 55.478 W 67 6.213	EBB	4	21:11	21:31
Sep	25	East	N 44 54.730 W 67 5.435	N 44 55.470 W 67 6.210	LOW	5	14:33	14:54
Sep	25	South	N 44 53.638 W 67 4.760	N 44 52.919 W 67 4.097	FLOOD	6	15:18	15:38
Sep	26	Whiting	N 44 51.308 W 67 8.632	N 44 52.152 W 67 8.759	HIGH	7	11:35	11:55
Sep	26	Denny's	N 44 52.900 W 67 9.100	N 44 53.374 W 67 9.831	HIGH	8	12:11	12:28

Table 3a. Date and location of seine samples in Cobscook Bay during May and June of 2011. Tide is the tidal stage when nets were pulled, Tow is tow number, and Time (EDT) indicates the beginning time for each tow. Night samples are highlighted in gray. Bay locations are also shown in Figure 1. PR indicates Pennamaquan River and CB is Cobscook Bay.

Month	Day	Bay	Latitude and longitude	Tide	Tow	Time
May	25	South	N 44 50.142 W 67 2.890	EBB	1	6:52
May	25	South	N 44 50.142 W 67 2.891	EBB	2	9:00
May	25	South	N 44 50.142 W 67 2.892	EBB	3	10:04
May	26	East	N 44 56.435 W 67 7.472	EBB	4	7:05
May	26	East	N 44 56.435 W 67 7.473	EBB	5	8:52
May	27	Outer CB	N 44 55.432 W 67 0.941	EBB	6	7:45
May	27	Outer CB	N 44 55.432 W 67 0.942	EBB	7	8:11
May	27	Outer CB	N 44 55.432 W 67 0.942	EBB	8	9:32
May	27	Outer CB	N 44 55.432 W 67 0.943	EBB	9	9:48
May	27	Outer CB	N 44 55.432 W 67 0.943	EBB	10	21:40
May	27	Outer CB	N 44 55.432 W 67 0.944	EBB	11	12:53
May	28	East PR	N 44 55.99 W 67 8.277	EBB	12	9:28
May	28	East PR	N 44 55.99 W 67 8.278	EBB	13	9:40
May	29	Whiting	N 44 50.380 W 67 8.901	EBB	14	10:17
May	29	Denny's	N 44 50.380 W 67 8.902	EBB	16	9:45
May	29	Denny's	N 44 50.380 W 67 8.903	EBB	17	10:02
June	24	South	N 44 50.142 W 67 2.890	HIGH	1	7:31
June	24	South	N 44 50.142 W 67 2.891	EBB	2	8:17
June	25	East	N 44 56.435 W 67 7.472	HIGH	3	8:39
June	25	East	N 44 56.435 W 67 7.473	EBB	4	8:51
June	25	East	N 44 56.435 W 67 7.474	EBB	5	9:48
June	25	East	N 44 56.435 W 67 7.475	HIGH	6	19:36
June	25	East	N 44 56.435 W 67 7.476	EBB	7	19:53
June	25	East	N 44 56.435 W 67 7.477	EBB	8	21:08
June	25	East	N 44 56.435 W 67 7.478	EBB	9	21:19
June	26	Outer CB	N 44 55.432 W 67 0.944	EBB	10	8:56
June	26	Outer CB	N 44 55.432 W 67 0.945	EBB	11	9:14
June	26	Outer CB	N 44 55.432 W 67 0.946	EBB	12	10:28
June	27	Whiting	N 44 50.380 W 67 8.901	EBB	13	11:01
June	27	Whiting	N 44 50.380 W 67 8.902	EBB	14	11:38
June	27	Whiting	N 44 50.380 W 67 8.903	EBB	15	13:21
June	28	Denny's	N 44 50.380 W 67 8.903	EBB	16	12:46
June	28	Denny's	N 44 50.380 W 67 8.904	EBB	17	13:56
June	28	East PR	N 44 55.99 W 67 8.278	EBB	18	11:05
June	28	East PR	N 44 55.99 W 67 8.279	EBB	19	11:41
June	28	East PR	N 44 55.99 W 67 8.280	EBB	20	11:56

Table 3b. Date and location of seine samples in Cobscook Bay during August and September of 2011. Tide is the tidal stage when nets were pulled, Tow is tow number, and Time (EDT) indicates the beginning time for each tow. Night samples are highlighted in gray. PR indicates Pennamaquan River and CB is Cobscook Bay.

Month	Day	Bay	Latitude and longitude	Tide	Tow	Time
August	22	East	N 44 56.435 W 67 7.473	HIGH	1	18:27
August	22	East	N 44 56.435 W 67 7.474	HIGH	2	18:41
August	22	East	N 44 56.435 W 67 7.475	EBB	3	20:53
August	23	Whiting	N 44 50.380 W 67 8.902	EBB	4	9:11
August	23	Whiting	N 44 50.380 W 67 8.903	EBB	5	10:36
August	23	Whiting	N 44 50.380 W 67 8.904	EBB	6	12:20
August	24	Outer CB	N 44 55.432 W 67 0.946	EBB	7	8:15
August	24	Outer CB	N 44 55.432 W 67 0.947	EBB	8	8:55
August	24	Outer CB	N 44 55.432 W 67 0.948	EBB	9	10:37
August	24	Denny's	N 44 50.380 W 67 8.904	EBB	10	9:43
August	24	Denny's	N 44 50.380 W 67 8.905	EBB	11	10:24
August	24	Denny's	N 44 50.380 W 67 8.906	EBB	12	11:36
August	25	South	N 44 50.142 W 67 2.891	EBB	13	9:41
August	25	South	N 44 50.142 W 67 2.892	EBB	14	10:31
August	25	Outer CB	N 44 55.432 W 67 0.948	EBB	15	23:17
August	26	East PR	N 44 55.99 W 67 8.280	EBB	16	11:01
August	26	East PR	N 44 55.99 W 67 8.280	EBB	17	12:01
September	22	Outer CB	N 44 55.432 W 67 0.943	EBB	1	7:48
September	22	Outer CB	N 44 55.432 W 67 0.944	EBB	2	8:34
September	22	Outer CB	N 44 55.432 W 67 0.945	EBB	3	9:18
September	22	Denny's	N 44 50.380 W 67 8.903	HIGH	4	7:39
September	22	Denny's	N 44 50.380 W 67 8.904	EBB	5	8:24
September	22	Denny's	N 44 50.380 W 67 8.905	EBB	6	8:39
September	22	Denny's	N 44 50.380 W 67 8.906	EBB	7	9:39
September	23	Whiting	N 44 50.380 W 67 8.903	EBB	8	9:32
September	23	Whiting	N 44 50.380 W 67 8.904	EBB	9	10:31
September	23	Whiting	N 44 50.380 W 67 8.905	EBB	10	11:21
September	23	Whiting	N 44 50.380 W 67 8.906	EBB	11	12:01
September	24	East	N 44 56.435 W 67 7.474	HIGH	12	9:15
September	24	East	N 44 56.435 W 67 7.475	EBB	13	9:22
September	24	East	N 44 56.435 W 67 7.476	EBB	14	10:36
September	24	East	N 44 56.435 W 67 7.477	EBB	15	11:32
September	24	East	N 44 56.435 W 67 7.478	EBB	16	20:46
September	24	East	N 44 56.435 W 67 7.479	EBB	17	23:16
September	25	East	N 44 56.435 W 67 7.480	EBB	18	0:16
September	25	South	N 44 50.142 W 67 2.892	EBB	19	10:46
September	25	South	N 44 50.142 W 67 2.893	EBB	20	11:26
September	25	South	N 44 50.142 W 67 2.894	EBB	21	11:41

September	27	East PR	N 44 55.99 W 67 8.280	EBB	22	12:41
September	27	East PR	N 44 55.99 W 67 8.281	EBB	23	12:59
September	27	East PR	N 44 55.99 W 67 8.282	EBB	24	13:16
September	27	East PR	N 44 55.99 W 67 8.283	EBB	25	13:41

Table 4. Date and location of fyke net samples in Cobscook Bay during May, June, August and September of 2011. Tide is the tidal stage when nets were set. Tow is tow number. Begin and End are times (EDT) when the fyke net was set and pulled, respectively. Night samples are highlighted in gray. PR indicates Pennamaquan River and CB is Cobscook Bay.

Month	Day	Bay	Latitude and longitude	Tide	Tow	Begin	End
May	25	South	N 44 50.142 W 67 2.890	EBB	1	9:29	9:50
May	26	East	N 44 56.435 W 67 7.472	EBB	2	9:47	10:17
May	27	Outer CB	N 44 54.882 W 67 1.101	EBB	3	9:05	10:12
May	27	Outer CB	N 44 54.882 W 67 1.102	EBB	4	21:28	22:34
May	28	East PR	N 44 55.99 W 67 8.278	EBB	5	10:40	11:45
June	24	South	N 44 50.142 W 67 2.891	EBB	1	7:05	9:05
June	25	East	N 44 56.435 W 67 7.472	EBB	2	7:40	10:15
June	26	Outer CB	N 44 55.432 W 67 0.945	EBB	3	8:10	11:05
June	26	East	N 44 55.432 W 67 0.944	EBB	4	20:55	23:59
June	27	Whiting	N 44 50.380 W 67 8.903	EBB	5	9:45	12:40
June	27	Outer CB	N 44 55.432 W 67 0.945	EBB	6	15:00	1:05
June	28	East PR	N 44 55.99 W 67 8.280	EBB	7	10:00	12:00
August	22	East	N 44 56.435 W 67 7.474	EBB	1	18:00	20:30
August	23	Whiting	N 44 50.380 W 67 8.904	EBB	2	8:00	12:30
August	24	Outer CB	N 44 55.432 W 67 0.947	EBB	3	7:33	10:10
August	24	Denny's	N 44 50.380 W 67 8.905	EBB	4	9:05	12:12
August	24	Outer CB	N 44 55.432 W 67 0.947	EBB	5	20:10	22:45
August	25	South	N 44 50.142 W 67 2.892	EBB	6	9:25	11:30
August	26	East PR	N 44 55.99 W 67 8.280	EBB	7	10:45	13:00
September	22	Outer CB	N 44 55.432 W 67 0.945	EBB	1	19:30	22:15
September	22	Denny's	N 44 50.380 W 67 8.906	EBB	2	20:45	23:00
September	24	East	N 44 56.435 W 67 7.479	EBB	3	22:00	0:35

Table 5. Capture data, by month, all gear types combined, for sampling in Cobscook Bay in 2011.

Month	May	June	August	September	Total
Species	Number of individuals				
Atlantic herring, <i>Clupea harengus</i>	351	1,091	545	24	2,011
Threespine stickleback, <i>Gasterosteus aculeatus</i>	259	428	437	308	1,432
Winter flounder, <i>Pleuronectes americanus</i>	156	251	461	286	1,154
Rainbow smelt, <i>Osmerus mordax</i>	238	14	12	33	297
Mummichog, <i>Fundulus heteroclitus</i>	29	25	148	70	272
Black spotted stickleback, <i>Gasterosteus wheatlandi</i>	43	109	68	11	231
Atlantic tomcod, <i>Microgadus tomcod</i>	0	17	24	28	69
Longhorn sculpin, <i>Myoxocephalus octodecemspinosus</i>	27	13	21	1	62
Grubby, <i>Myoxocephalus aeneus</i>	47	10	1	3	61
Atlantic silverside, <i>Menidia menidia</i>	3	10	18	25	56
Fourspine stickleback, <i>Apeltes quadracus</i>	0	1	21	33	55
White hake, <i>Urophycis tenuis</i>	0	2	20	28	50
Haddock, <i>Melanogrammus aeglefinus</i>	0	0	40	8	48
Pollock, <i>Pollachius virens</i>	0	10	12	3	25
Sea raven, <i>Hemitripterus americanus</i>	12	1	6	3	22
Atlantic cod, <i>Gadus morhua</i>	4	9	2	3	18
Butterfish, <i>Peprilus triacanthus</i>	0	0	7	10	17
Alewife, <i>Alosa pseudoharengus</i>	0	1	1	14	16
Silver hake, <i>Merluccius bilinearis</i>	1	7	8	0	16
Shorthorn sculpin, <i>Myoxocephalus scorpius</i>	3	6	1	1	11
Atlantic mackerel, <i>Scomber scombrus</i>	0	0	10	0	10
Red hake, <i>Urophycis chuss</i>	0	2	2	4	8
Snakeblenny, <i>Lumpenus lampraeformis</i>	0	4	3	0	7
Lumpfish, <i>Cyclopterus lumpus</i>	0	2	1	1	4
Winter skate, <i>Raja ocellatus</i>	2	0	2	0	4
Radiated shanny, <i>Ulvaria subbifurcata</i>	0	1	1	0	2
Rock gunnel, <i>Pholis gunnellus</i>	0	1	1	0	2

Ninespine stickleback, <i>Pungitius pungitius</i>	0	1	1	0	2
American sand lance, <i>Ammodytes americanus</i>	0	1	0	0	1
Little skate, <i>Raja erinacea</i>	0	0	0	1	1
Atlantic halibut, <i>Hippoglossus hippoglossus</i>	0	0	0	1	1
Total	1,175	2,017	1,874	899	5,965

Table 6. Capture data, by month, for pelagic trawl sampling in Cobscook Bay in 2011.

Month	May	June	August	September	Total
Species	Number of individuals				
Atlantic herring	351	880	39	12	1282
Threespine stickleback	209	3	1	6	219
Atlantic mackerel			10		10
Butterfish			2	4	6
Blackspotted stickleback	4	1			5
Rainbow smelt		3	1	1	5
Grubby	1	2			3
Lumpfish		1		1	2
Shorthorn sculpin		1	1		2
Alewife			1		1
American sand lance		1			1
Winter flounder			1		1
Total	565	892	56	24	1,537

Table 7. Capture data, by month, for benthic trawl sampling in Cobscook Bay in 2011.

Month	May	June	August	September	Total
Species	Number of individuals				
Winter flounder	156	251	461	285	1,153
Atlantic herring		211	21	4	236
Longhorn sculpin	27	13	21	1	62
Grubby	46	8	1	3	58
Rainbow smelt		9	10	32	51
White hake		2	20	28	50
Haddock			40	8	48
Atlantic tomcod			9	13	23
Sea raven	12	1	6	3	22
Atlantic cod	4	9	2	3	18
Silver hake	1	7	8		16
Butterfish			5	6	11
Shorthorn sculpin	3	5		1	9
Alewife		1		7	8
Red hake		2	2	4	8
Snakeblenny		4	3		7
Pollock		2	4	1	7
Winter skate	2		2		4
Radiated shanny		1	1		2
Rock gunnel		1	1		2
Lumpfish		1	1		2
Threespine stickleback		1			1
Atlantic halibut				1	1
Little skate				1	1
Total	251	529	618	402	1,800

Table 8. Capture data, by month, for intertidal seine sampling in Cobscook Bay in 2011.

Month	May	June	August	September	Total
Species	Number of individuals				
Threespine stickleback	50	424	436	302	1,212
Atlantic herring			485	8	493
Mummichog	29	24	148	70	271
Rainbow smelt	231*	1			239
Blackspotted stickleback	39	108	88	11	226
Atlantic silverside	3	10	18	25	56
Fourspine stickleback		1	21	33	55
Atlantic tomcod		17	9		26
Pollock		8			8
Alewife				7	7
Ninespine stickleback		1	1		2
Total	359	594	1,186	456	2,595

*This seine tow targeted a school of adult rainbow smelt swimming along the shoreline.

Table 9. Capture data, by month, for intertidal fyke net sampling in Cobscook Bay in 2011.

Month	May	June	August	September	Total
Species	Number of individuals				
Atlantic tomcod			6	14	20
Pollock			8	2	10
Rainbow smelt		1	1		2
Mummichog		1			1
Total	0	2	15	16	33

Appendix Task 2-8

2012 Annual Report: Special License Number ME 2012-36-02
University of Maine, School of Marine Sciences
Gayle Zydlewski, James McCleave, Jeffrey Vieser
16 November 2012

Introduction

The first objective of the project requiring the special license was to use midwater trawling to provide species verification to accompany acoustic assessment of pelagic fish abundance in Outer Cobscook Bay, near Eastport, Maine. The acoustic assessment was conducted independently of the special license. The acoustic assessment and midwater trawling are parts of an overall project to assess the seasonal, daily, and tidal abundance and distribution of pelagic fishes in locations proposed for deployment of electricity generating tidal turbines.

The second objective of the project requiring the special license was to use midwater trawling, benthic trawling, intertidal seining, and intertidal fyke netting to characterize the fish community of the entire Cobscook Bay. This study provides a wider ecosystem perspective against which to consider deployment of arrays of electricity generating tidal turbines.

Methods

Midwater and benthic trawling was done with the commercial fishing vessel *Pandalus* (147YV), owned and operated by Stephen W. Brown. The midwater net mouth dimensions were: headrope, footrope and breastlines 40 feet. Mesh sizes were: belly, square and side panels 4 inch, tapers 2 inch, and extensions and codend 1 inch. The benthic net mouth dimensions were: headrope 45 feet, footrope 35 feet, no breastlines. Stretch mesh sizes were: net body 2 inch, codend 1 inch. Tows were nominally 20 minutes, but sometimes varied, especially to shorter times because towable distance was too short in inner Cobscook Bay (Figure 1, Tables 1, 2).

Two 100 foot x 6 foot seines with 0.25-inch diamond mesh were used to sample shallow intertidal habitats including cobble fields, mud flats, rockweed patches, and sea grass beds (Figure 1, Table 3). Two fyke nets with 30 foot wings, 4 foot tall square hoops, and 1.5-inch stretch mesh were used to sample larger rockweed covered rock piles (Table 4). Sampling of intertidal habitats was conducted mostly in day time, with some night sampling.

Trawling and intertidal sampling were conducted during neap tides primarily in May, June, August and September, 2012. Forty midwater tows and 40 benthic tows were made over the four months, with 16 tows of each type being at night in central and outer Cobscook Bay (Tables 1, 2). One hundred eighty one seine hauls were made over the four months, with 36 hauls being at night (Table 3). Twenty five fyke net sets were made, with each set being two fyke nets nearby at the same location; 14 sets were at night (Table 4). Sixty additional seine hauls were made at a subset of locations in March, April, and November, with 13 being at night (Table 3).

Results

Benthic trawling and intertidal seining were quite successful in capturing a variety of fish species, but midwater trawling and fyke netting were less successful. More than 28,000 individual fish of 36 species were caught (all gears and dates combined) (Table 5).¹ Individuals of many species were primarily smaller (juvenile) specimens, but a few adult Atlantic herring (*Clupea harengus*) were caught in pelagic trawls (Table 6). Atlantic herring dominated the pelagic catch, and most were early juveniles. Winter flounder (*Pseudopleuronectes americanus*) juveniles dominated the catch in benthic trawls, but species richness was greatest among gears in the benthic trawls (26 species caught at least once) (Table 7).

Threespine stickleback (*Gasterosteus aculeatus*), Atlantic silverside (*Menidia menidia*), blackspotted stickleback (*Gasterosteus wheatlandi*), and alewife (*Alosa pseudoharengus*) dominated the catches in intertidal seine tows, but in widely varying proportions in the four primary months of sampling (Table 8). Only six species represented by few individuals were caught in fyke nets (Table 9).

In both 2011 and 2012, four species comprised about 82% of the total catch. In 2012, these were, in rank order, threespine stickleback, Atlantic herring, Atlantic silverside, and winter flounder (Table 5), while in 2011, they were Atlantic herring, threespine stickleback, winter flounder, and rainbow smelt. Threespine sticklebacks were 10 times more abundant and blackspotted sticklebacks seven times more abundant in 2012 than 2011, but seining effort only increased threefold. Likewise, the 40-fold increased abundance of Atlantic silverside cannot be explained on increased seining effort. The decrease in abundance of winter flounder is probably real, as benthic trawling effort was similar in the two years.

Atlantic herring were abundant in both years, but those caught in May and June 2011 were mostly advanced larvae, while those caught in May and June 2012 were mostly juveniles. This may have been due to the mild winter of 2011-2012 and early warming in March 2012.

No Atlantic salmon (*Salmo salar*), shortnose sturgeon (*Acipenser brevirostrum*), or Atlantic sturgeon (*A. oxyrinchus*) were captured in any gear. One harbor seal entered a fyke net on June 28, 2012, and drowned; it was reported through the proper channels. Excluder bars were installed in the mouths of the fyke nets before August and September sampling periods following a design suggested by NOAA.

Discussion

Visual observation, hook and line recreational fishing, acoustic fish finder records, and local fishers' knowledge indicates the presence of large numbers of Atlantic herring and Atlantic mackerel throughout the water column in the study area, especially in August and September. The inability of our gear to capture these highly mobile pelagic species in proportion to their probable abundance is a problem. We suspect that the ability of highly mobile fish to detect the presence of the trawls, through visual and other

¹ Catch numbers in Tables 5-9 are provisional.

sensory clues, allows them to avoid it in most cases. When capture did occur, it was primarily at night, when visual cues are restricted. Sampling effort at night with both midwater and benthic trawls was increased in 2012 compared with 2011.

It is expected that larger benthic species, e.g., spiny dogfish (*Squalus acanthius*), succeeded in avoiding capture, though there is less anecdotal evidence to support their presence in the bay. However, three were caught in one benthic trawl in 2012. A number of other species are probably under sampled as well in various gears, e.g., adult river herring (alewife and blueback herring), skates and flatfish species (other than winter flounder).

An application for an extension of our special license for 2013 will be forthcoming involving a few modest changes to our scope of work.

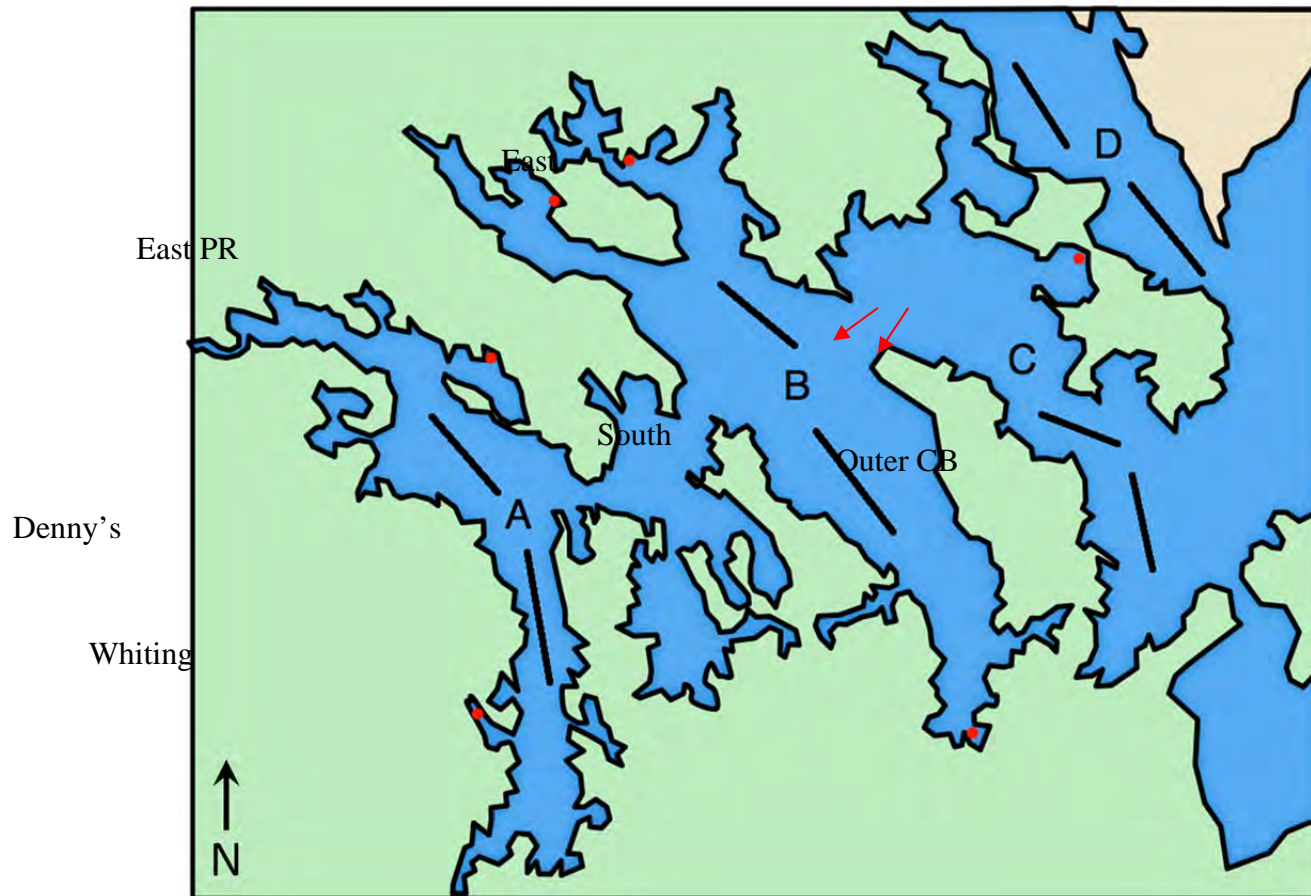


Figure 1. Map of Cobscook Bay and Western Passage of Passamaquoddy Bay showing mid-water and benthic trawl lines (black lines) fished in 2012 (Cobscook Bay) and planned for 2013 (all), as well as regular seine and fyke net sampling locations (red dots) and seining locations specifically for sticklebacks (red arrows). Both benthic and pelagic trawls occurred in the same location. Uppercase letters indicate the center of each of the three sub-bays of Cobscook Bay (A = inner; B = central; C = outer) and Western Passage in Passamaquoddy Bay (D). Smaller bays of each sub-bay are also named. PR is Pennamaquan River.

Table 1. Date and location of pelagic trawl samples in Cobscook Bay during May, June, August, and September, 2012. Tide is the tidal stage when nets were fished. GPS Begin and GPS End are latitude (N) and longitude (W) where nets were deployed and retrieved, respectively. Tow is tow number. Begin and End are times (EDT) when the trawls were deployed and retrieved, respectively. Night samples are highlighted in gray. CB is Cobscook Bay.

Month	Day	Bay	GPS Begin	GPS End	Tide	Tow	Begin	End
May	25	Outer CB	44°53.543' 67°00.968'	44°53.943' 67°01.712'	Low	P401	21:38	21:53
	25	Outer CB	44°55.837' 67°01.371'	44°53.454' 67°00.762'	Low	P402	22:06	22:26
	26	East	44°55.025' 67°05.773	44°54.453 67°04.631	Low	P403	21:52	22:12
	26	South	44°53.744' 67°04.827'	44°52.985' 67°04.123'	Flood	P404	22:29	22:49
	27	Outer CB	44°53.950' 67°01.470'	44°53.417' 67°00.278	High	P405	16:02	16:22
	27	Outer CB	44°53.415' 67°00.535'	44°53.925' 67°01.628'	Ebb	P406	16:39	16:59
	28	Whiting	44°52.483' 67°08.739'	44°51.029' 67°08.599'	Flood	P407	16:47	17:08
	28	Dennys	44°53.388' 67°09.843'	44°52.825' 67°08.841'	Ebb	P408	18:30	18:46
	29	South	44°53.165' 67°04.310'	44°54.061' 67°05.209'	Low	P409	11:24	11:45
	29	East	44°54.518' 67°05.121'	44°55.282' 67°06.025'	Low	P410	12:00	12:23
June	24	Outer CB	44°53.767' 67°01.407'	44°53.248' 66°59.576'	Flood	P501	21:10	21:30
	24	Outer CB	44°53.356' 67°00.484'	44°54.263' 67°02.066'	Flood	P502	23:10	23:30
	25	East	44°55.208' 67°05.936'	44°54.505' 67°04.824'	Ebb	P503	21:25	21:50
	25	South	44°53.897' 67°04.961'	44°53.118' 67°04.251'	Low	P504	22:10	22:30

	26	Outer CB	44°53.370' 67°00.313'	44°53.957' 67°01.696'	High	P505	16:45	17:05
	26	Outer CB	44°53.762' 67°01.321'	44°53.357' 66°59.773	Ebb	P506	17:20	17:43
	27	South	44°53.004' 67°03.985'	44°53.890' 67°04.810'	Low	P507	11:20	11:41
	27	East	44°54.490' 67°05.315'	44°55.456' 67°06.109'	Low	P508	11:54	12:15
	28	Whiting	44°52.545' 67°08.771'	44°51.288' 67°08.576'	Low	P509	06:33	06:53
	28	Dennys	44°53.362' 67°09.890'	44°52.715' 67°08.794'	Ebb	P510	08:12	08:27
August	26	Outer CB	44°53.923' 67°01.531'	44°53.333' 66°59.941'	Ebb	P601	19:42	20:02
	26	Outer CB	44°53.694' 67°01.347'	44°53.280' 66°59.487'	Ebb	P602	20:30	20:50
	27	East	44°55.423' 67°06.086'	44°54.395' 67°04.881'	Ebb	P603	20:45	21:05
	27	South	44°52.901' 67°04.005'	44°53.807' 67°04.394	Ebb	P604	22:00	22:20
	28	Outer CB	44°53.337' 66°59.895'	44°53.761' 67°01.076'	High	P605	09:00	09:23
	28	Outer CB	44°53.736' 67°01.410'	44°59.886 66°59.883'	Ebb	P606	09:35	09:55
	29	Whiting	44°52.113' 67°08.655'	44°50.941' 67°08.671'	Flood	P607	09:52	10:12
	29	Dennys	44°53.361' 67°09.839'	44°52.771' 68°08.832'	Ebb	P608	11:27	11:49
	30	South	44°53.490' 67°04.709'	44°52.566' 67°03.655'	Flood	P609	10:00	10:20
	30	East	44°55.376' 67°06.265'	44°54.443' 67°04.885'	Ebb	P610	11:45	12:10
September	23	Outer CB	44°54.081' 67°01.827'	44°53.416' 66°59.280'	Ebb	P701	10:14	10:35

	23	Outer CB	44°53.262' 66°59.760'	44°53.816' 67°01.311'	Flood	P702	12:19	12:39
	24	East	44°55.241' 67°06.214'	44°54.463' 67°05.039'	Low	P703	12:45	13:06
	24	South	44°53.711' 67°04.768'	44°52.898' 67°04.129'	Flood	P704	13:22	13:42
	25	Outer CB	44°53.335' 67°00.201'	44°54.161' 67°02.083'	Flood	P705	19:04	19:25
	25	Outer CB	44°53.956' 67°01.661'	44°53.531' 67°00.854'	Flood	P706	19:44	20:05
	26	Whiting	44°52.099' 67°08.660'	44°50.946' 67°08.680'	Flood	P707	08:30	08:56
	26	Dennys	44°53.179' 67°09.323	44°52.771' 67°08.626'	Ebb	P708	10:13	10:28
	26	East	44°54.712' 67°05.550'	44°55.535' 67°06.321'	Flood	P709	18:50	19:10
	26	South	44°52.903' 67°04.045'	44°53.704' 67°04.796'	High	P710	20:40	21:00

Table 2. Date and location of benthic trawl samples in Cobscook Bay during May, June, August, and September, 2012. Tide is the tidal stage when nets were fished. GPS Begin and GPS End are latitude (N) and longitude (W) where nets were deployed and retrieved, respectively. Tow is tow number. Begin and End are times (EDT) when the trawls were deployed and retrieved, respectively. Night samples are highlighted in gray. CB is Cobscook Bay.

Month	Day	Bay	GPS Begin	GPS End	Tide	Tow	Begin	End
May	25	Outer CB	44°53.030' 67°00.337'	44°52.275' 66°59.878'	Ebb	B401	20:22	20:44
	25	Outer CB	44°52.330' 66°59.842'	44°53.190' 67°00.359'	Ebb	B402	20:54	21:04
	26	East Bay	44°54.770' 67°05.401'	44°55.400' 67°06.111'	Ebb	B403	21:03	21:23
	26	South Bay	44°52.754' 67°04.045'	44°53.587' 67°04.893'	Flood	B404	23:03	23:23
	27	Outer CB	44°53.107' 67°00.467'	44°52.347' 66°59.939'	Flood	B405	14:50	15:10
	27	Outer CB	44°52.253' 66°59.859'	44°53.080' 67°00.123'	Flood	B406	15:21	15:41
	28	Whiting	44°51.104' 67°08.602'	44°52.087' 67°08.646	High	B407	17:25	17:47
	28	Dennys	44°52.899' 67°08.966'	44°53.378' 67°09.864'	High	B408	18:01	18:18
	29	South	44°53.917' 67°04.891'	44°52.002' 67°04.211'	Ebb	B409	10:50	11:10
	29	East	44°55.450' 67°06.223'	44°54.665' 67°05.334'	Flood	B410	12:32	12:53
June	24	Outer CB	44°52.961' 67°00.207'	44°52.187' 66°59.630'	Flood	B501	21:50	11:17
	24	Outer CB	44°52.401' 66°59.834'	44°53.223' 67°00.608'	Flood	B502	22:30	23:00
	25	East	44°54.721' 67°05.387'	44°55.367' 67°06.007'	Ebb	B503	20:50	21:10
	25	South	44°52.692' 67°03.975'	44°53.444' 67°04.637'	Flood	B504	22:50	23:10

	26	Outer CB	44°52.982' 67°00.336'	44°52.241' 66°59.870'	Flood	B505	15:30	15:50
	26	Outer CB	44°52.231' 66°59.897'	44°53.019' 67°00.173'	Flood	B506	16:08	16:28
	27	South	44°53.789' 67°04.787'	44°53.145' 67°03.959'	Ebb	B507	10:42	11:02
	27	East	44°55.559' 67°06.199'	44°54.747' 67°05.348'	Flood	B508	12:28	12:49
	28	Whiting	44°51.147' 67°08.580'	44°52.081' 67°08.692'	High	B509	07:05	07:26
	28	Dennys	44°52.793' 67°08.844'	44°53.327' 67°09.787'	Ebb	B510	07:40	08:00
August	26	Outer CB	44°53.140' 67°00.395'	44°52.112' 66°59.759'	Ebb	B601	21:16	21:36
	26	Outer CB	44°52.077' 66°59.705'	44°52.929' 67°00.314'	Ebb	B602	21:51	22:12
	27	East	44°54.788' 67°05.574'	44°55.505' 67°06.260'	High	B603	20:05	20:25
	27	South	44°53.716' 67°04.737'	44°52.917' 67°03.788'	Ebb	B604	21:25	21:45
	28	Outer CB	44°52.863' 67°00.195'	44°52.038' 66°59.667'	Ebb	B605-B	10:35	10:55
	28	Outer CB	44°52.177' 66°59.762'	44°53.020' 67°00.337'	Ebb	B606	11:05	11:25
	29	Whiting	44°51.158' 67°08.591'	44°52.051' 67°08.668'	High	B607	10:27	10:47
	29	Dennys	44°52.970' 67°09.093'	44°53.372' 67°09.817'	Ebb	B608	11:00	11:20
	30	South	44°52.622' 67°03.775'	44°53.453' 67°04.545'	High	B609	10:32	10:54
	30	East	44°54.766' 67°05.531'	44°55.455' 67°06.139'	Ebb	B610	11:10	11:30
September	23	Outer CB	44°52.079' 66°59.684'	44°52.950' 67°00.285'	Ebb	B701	11:00	11:20

	23	Outer CB	44°52.999' 67°00.389'	44°52.187' 66°59.811'	Low	B702	11:33	11:53
	24	East	44°54.648' 67°05.501'	44°55.487' 67°06.181'	Ebb	B703	12:06	12:26
	24	South	44°52.729' 67°03.890'	44°53.514' 67°04.642'	Flood	B704	13:54	14:15
	25	Outer CB	44°52.916' 67°00.294'	44°52.148' 66°59.731'	High	B705	20:22	20:43
	25	Outer CB	44°52.238' 66°59.887'	44°53.110' 67°00.446'	Ebb	B706	20:55	21:15
	26	Whiting	44°51.204' 67°08.578'	44°52.070' 67°08.681'	Flood	B707	09:07	09:28
	26	Dennys	44°52.956' 67°09.123'	44°53.344' 67°09.840'	High	B708	09:44	09:59
	26	East	44°55.488' 67°06.212'	44°54.705' 67°05.507'	Flood	B709	19:20	19:40
	26	South	44°53.632' 67°04.853'	44°52.835' 67°04.034'	Flood	B710	20:00	20:20

Table 3. Date and location of regular intertidal seine samples in Cobscook Bay during May, June, August, and September, and additional seine samples at a subset of regular stations in March, April, and November, 2012. Tide is the tidal stage when nets were fished. Tow is tow number. Time is the time when each tow (EDT) began; each tow takes <10 minutes. Night samples are highlighted in gray. CB is Cobscook Bay.

Month	Day	Bay	Locale	Tide	Habitat	Tow	Time
March	8	Outer CB	Broad Cove	Ebb	Not recorded	W1	12:00
	8	Outer CB	Broad Cove	Ebb	Not recorded	W2	12:30
	8	Outer CB	Deep Cove	Ebb	Not recorded	W3	13:15
	8	Outer CB	Deep Cove	Ebb	Not recorded	W4	13:45
	8	Outer CB	Deep Cove	Ebb	Not recorded	W5	14:15
	9	East	Sipp Cove	High	Not recorded	W6	11:49
	9	East	Sipp Cove	Ebb	Not recorded	W7	11:55
	9	East	Sipp Cove	Ebb	Not recorded	W8	12:20
	9	Outer CB	Carrying Place Cove	Ebb	Not recorded	W9	13:25
	9	Outer CB	Carrying Place Cove	Ebb	Not recorded	W10	13:40
	9	Outer CB	Carrying Place Cove	Ebb	Not recorded	W11	13:55
	9	East	Sipp Cove	Ebb	Not recorded	W12	14:20
	9	East	Sipp Cove	Ebb	Not recorded	W13	14:55
	10	Pennamaquan	Hersey Cove	Ebb	Not recorded	W14	13:40
	10	Pennamaquan	Hersey Cove	Ebb	Not recorded	W15	13:45
	10	Pennamaquan	Hersey Cove	Ebb	Not recorded	W16	13:50
	10	Pennamaquan	Hersey Cove	Ebb	Not recorded	W17	14:10
	10	Pennamaquan	Hersey Cove	Ebb	Not recorded	W18	14:15
	10	Dennys	Youngs Cove	Ebb	Not recorded	W19	14:50
	10	Dennys	Youngs Cove	Ebb	Not recorded	W20	14:55
	10	Dennys	Youngs Cove	Ebb	Not recorded	W21	15:00
	10	Dennys	Youngs Cove	Ebb	Not recorded	W22	15:25
April	13	Pennamaquan	Hersey Cove	High	Not recorded	A1	17:55
	13	Pennamaquan	Hersey Cove	High	Not recorded	A2	18:00
	13	Pennamaquan	Hersey Cove	Ebb	Not recorded	A3	18:25
	13	Pennamaquan	Hersey Cove	Ebb	Not recorded	A4	18:40
	13	Pennamaquan	Hersey Cove	Ebb	Not recorded	A5	18:50
	13	Dennys	Youngs Cove	Ebb	Not recorded	A6	19:45

Month	Day	Bay	Locale	Tide	Habitat	Tow	Time
	13	Dennys	Youngs Cove	Ebb	Not recorded	A7	20:00
	13	Dennys	Youngs Cove	Ebb	Not recorded	A8	20:40
	13	Dennys	Youngs Cove	Ebb	Not recorded	A9	20:50
	14	Outer CB	Broad Cove	High	Not recorded	A10	06:30
	14	Outer CB	Deep Cove	Ebb	Not recorded	A11	07:00
	14	Outer CB	Deep Cove	Ebb	Not recorded	A12	07:10
	14	Outer CB	Broad Cove	Ebb	Not recorded	A13	07:50
	14	Outer CB	Broad Cove	Ebb	Not recorded	A14	08:20
	14	Outer CB	Deep Cove	Ebb	Not recorded	A15	08:50
	14	Outer CB	Deep Cove	Ebb	Not recorded	A16	09:10
	14	Outer CB	Broad Cove	Ebb	Not recorded	A17	09:30
	14	East	Sipp Cove	High	Not recorded	A18	18:20
	14	East	Sipp Cove	High	Not recorded	A19	18:30
	14	East	Sipp Cove	High	Not recorded	A20	18:40
	14	Outer CB	Carrying Place Cove	Ebb	Not recorded	A21	20:30
	14	Outer CB	Carrying Place Cove	Ebb	Not recorded	A22	21:00
	14	East	Sipp Cove	Ebb	Not recorded	A23	22:10
	14	East	Sipp Cove	Ebb	Not recorded	A24	22:30
May	25	South	Case Cove	Ebb	Cobble	S401	15:55
	25	South	Case Cove	Ebb	Mudflat	S402	16:20
	25	South	Case Cove	Ebb	Sea grasses	S403	16:45
	26	Outer CB	Broad Cove	High	Cobble	AS401	15:53
	26	Outer CB	Broad Cove	High	Cobble	AS402	16:14
	26	Outer CB	Deep Cove	Ebb	Not recorded	AS403	16:48
	26	Outer CB	Deep Cove	Ebb	Rockweed/cobble	AS404	17:07
	26	Pennamaquan	Hersey Cove	Ebb	Cobble	S404	16:10
	26	Pennamaquan	Hersey Cove	Ebb	Cobble	S405	16:35
	26	Pennamaquan	Hersey Cove	Ebb	Sea grasses	S406	16:52
	26	Pennamaquan	Hersey Cove	Ebb	Rockweed	S407	17:25
	26	Pennamaquan	Hersey Cove	Ebb	Rockweed	S408	17:45
	27	Whiting	Burnt Cove	Ebb	Rockweed	S409	06:40

Month	Day	Bay	Locale	Tide	Habitat	Tow	Time
	27	Whiting	Burnt Cove	Ebb	Rockweed	S410	07:10
	27	Whiting	Burnt Cove	Ebb	Mudflat	S411	07:35
	27	Whiting	Burnt Cove	Ebb	Mudflat	S412	08:15
	27	Whiting	Burnt Cove	Ebb	Mudflat	S413	08:35
	28	Outer CB	Carrying Place Cove	Ebb	Sea grasses	S414	06:05
	28	Outer CB	Carrying Place Cove	Ebb	Sea grasses	S415	06:15
	28	Outer CB	Carrying Place Cove	Ebb	Mudflat	S416	07:00
	28	Outer CB	Carrying Place Cove	Ebb	Mudflat	S417	07:15
	28	Outer CB	Carrying Place Cove	Ebb	Sea grasses	S418	–
	28	Outer CB	Carrying Place Cove	Ebb	Cobble/grasses	S419	–
	28	Outer CB	Carrying Place Cove	Ebb	Mudflat	S420	–
	29	East	Sipp Bay	Ebb	Sea grasses	S421	06:12
	29	East	Sipp Bay	Ebb	Cobble	S422	06:25
	29	East	Sipp Bay	Ebb	Rockweed	S423	06:35
	29	East	Sipp Bay	Ebb	Cobble	S424	07:26
	29	East	Sipp Bay	Ebb	Not recorded	S425	07:34
	29	East	Sipp Bay	Ebb	Rockweed	S426	08:35
	29	East	Sipp Bay	Ebb	Rockweed	S427	08:55
	29	East	Sipp Bay	Ebb	Sea grasses	S428	19:00
	29	East	Sipp Bay	Ebb	Cobble	S429	19:08
	29	East	Sipp Bay	Ebb	Sea grasses	S430	19:40
	29	East	Sipp Bay	Ebb	Sea grasses	S431	19:50
	29	East	Sipp Bay	Ebb	Rockweed	S432	20:20
	29	East	Sipp Bay	Ebb	Rockweed	S433	20:35
	30	Dennys	Youngs Cove	Ebb	Cobble	S434	08:15
	30	Dennys	Youngs Cove	Ebb	Rockweed	S435	08:28
	30	Dennys	Youngs Cove	Ebb	Sea grasses	S436	08:42
	30	Dennys	Youngs Cove	Ebb	Cobble	S437	09:15
	30	Dennys	Youngs Cove	Ebb	Rockweed	S438	09:40
	30	Dennys	Youngs Cove	Ebb	Mudflat	S439	10:30
	30	Dennys	Youngs Cove	Ebb	Sea grasses	S440	21:14
	30	Dennys	Youngs Cove	Ebb	Cobble	S441	21:27

Month	Day	Bay	Locale	Tide	Habitat	Tow	Time
	30	Dennys	Youngs Cove	Ebb	Not recorded	S442	21:42
	30	Dennys	Youngs Cove	Ebb	Cobble	S443	22:05
	30	Dennys	Youngs Cove	Ebb	Rockweed	S444	22:20
	30	Dennys	Youngs Cove	Ebb	Not recorded	S445	22:40
	30	Dennys	Youngs Cove	Ebb	Mudflat	S446	23:15
June	23	South	Case Cove	Ebb	Cobble	S501	15:56
	23	South	Case Cove	Ebb	Mudflat	S502	16:25
	23	South	Case Cove	Ebb	Sea grasses	S503	16:50
	23	Pennamaquan	Hersey Cove	Ebb	Cobble	S504	14:46
	23	Pennamaquan	Hersey Cove	Ebb	Cobble	S505	15:00
	23	Pennamaquan	Hersey Cove	Ebb	Cobble	S506	15:15
	23	Pennamaquan	Hersey Cove	Ebb	Sea grasses	S507	15:30
	23	Pennamaquan	Hersey Cove	Ebb	Cobble	S508	15:55
	24	Outer CB	Carrying Place Cove	Ebb	Sea grasses	S509	04:49
	24	Outer CB	Carrying Place Cove	Ebb	Mudflat	S510	05:20
	24	Outer CB	Carrying Place Cove	Ebb	Sea grasses	S511	16:41
	24	Outer CB	Carrying Place Cove	Ebb	Sea grasses	S512	16:50
	24	Outer CB	Carrying Place Cove	Ebb	Mudflat	S513	~17:00
	24	Outer CB	Carrying Place Cove	Ebb	Mudflat	S514	~17:20
	25	East	Sipp Cove	Ebb	Cobble	S515	04:00
	25	East	Sipp Cove	Ebb	Cobble	S516	04:15
	25	East	Sipp Cove	Ebb	Sea grasses	S517	04:26
	25	East	Sipp Cove	Ebb	Cobble	S518	04:50
	25	East	Sipp Cove	Ebb	Rockweed	S519	05:12
	25	East	Ipp Cove	Ebb	Rockweed	S520	05:30
	25	East	Sipp Cove	Ebb	Rockweed	S521	06:15
	25	East	Sipp Cove	Ebb	Sea grasses	S522	16:36
	25	East	Sipp Cove	Ebb	Sea grasses	S523	16:45
	25	East	Sipp Cove	Ebb	Sea grasses	S524	17:10
	25	East	Sipp Cove	Ebb	Cobble	S525	17:45
	25	East	Sipp Cove	Ebb	Rockweed	S526	18:50
	26	Outer CB	Broad Cove	Ebb	Cobble	AS501	17:09

Month	Day	Bay	Locale	Tide	Habitat	Tow	Time
	26	Outer CB	Broad Cove	Ebb	Cobble	As502	17:20
	26	Outer CB	Broad Cove	Ebb	Cobble	AS503	18:05
	26	Outer CB	Broad Cove	Ebb	Cobble	AS504	18:27
	26	Outer CB	Deep Cove	Ebb	Not recorded	AS505	19:06
	26	Outer CB	Deep Cove	Ebb	Nor recorded	AS506	19:27
	26	Outer CB	Deep Cove	Ebb	Cobble/mudflat	AS507	19:50
	26	Outer CB	Deep Cove	Ebb	Not recorded	AS508	20:12
	27	Whiting	Burnt Cove	Ebb	Rockweed	S532	08:55
	27	Whiting	Burnt Cove	Ebb	Rockweed	S533	09:25
	27	Whiting	Burnt Cove	Ebb	Mudflat	S534	10:10
	27	Whiting	Burnt Cove	Ebb	Mudflat	S535	10:25
	28	Dennys	Youngs Cove	Ebb	Sea grasses	S527	08:45
	28	Dennys	Youngs Cove	Ebb	Rockweed	S528	08:57
	28	Dennys	Youngs Cove	Ebb	Cobble	S529	09:30
	28	Dennys	Youngs Cove	Ebb	Rockweed	S530	09:40
	28	Dennys	Youngs Cove	Ebb	Not recorded	S531	10:00
	28	Dennys	Youngs Cove	Ebb	Cobble	S536	–
	28	Dennys	Youngs Cove	Ebb	Rockweed	S537	21:03
	28	Dennys	Youngs Cove	Ebb	Cobble	S538	21:15
	28	Dennys	Youngs Cove	Ebb	Sea grasses	S539	21:35
	28	Dennys	Youngs Cove	Ebb	Mudflat	S540	21:40
August	25	Outer CB	Deep Cove	High	Cobble	AS601	18:00
	25	Outer CB	Deep Cove	Ebb	Cobble	AS602	18:27
	25	Outer CB	Deep Cove	Ebb	Cobble/grasses	AS603	18:55
	25	Outer CB	Deep Cove	Ebb	Cobble/grasses	AS604	19:10
	25	Outer CB	Broad Cove	Ebb	Not recorded	AS605	19:30
	25	Outer CB	Broad Cove	Ebb	Cobble	AS606	19:50
	25	Outer CB	Broad Cove	Ebb	Cobble	AS607	20:10
	26	Outer CB	Carrying Place Cove	Ebb	Sea grasses	S601	07:39
	26	Outer CB	Carrying Place Cove	Ebb	Sea grasses	S602	07:48
	26	Outer CB	Carrying Place Cove	Ebb	Sea grasses	S603	08:07
	26	Outer CB	Carrying Place Cove	Ebb	Sea grasses	S604	08:20

Month	Day	Bay	Locale	Tide	Habitat	Tow	Time
	26	Outer CB	Carrying Place Cove	Ebb	Mudflat	S605	08:36
	26	Outer CB	Carrying Place Cove	Ebb	Mudflat	S606	08:51
	26	Outer CB	Carrying Place Cove	Ebb	Sea grasses	S607	20:23
	26	Outer CB	Carrying Place Cove	Ebb	Sea grasses	S608	20:35
	26	Outer CB	Carrying Place Cove	Ebb	Sea grasses	S609	20:50
	26	Outer CB	Carrying Place Cove	Ebb	Mudflat	S610	21:15
	27	East	Sipp Cove	Ebb	Sea grasses	S611	08:16
	27	East	Sipp Cove	Ebb	Rockweed	S612	08:25
	27	East	Sipp Cove	Ebb	Not recorded	S613	08:42
	27	East	Sipp Cove	Ebb	Cobble	S614	09:20
	27	East	Sipp Cove	Ebb	Sea grasses	S615	09:35
	27	East	Sipp Cove	Ebb	Rockweed	S616	10:04
	27	East	Sipp Cove	Ebb	Rockweed	S617A	10:15
	27	East	Sipp Cove	High	Cobble	S617B	20:15
	27	East	Sipp Cove	Ebb	Sea grasses	S618	20:30
	27	East	Sipp Cove	Ebb	Cobble	S619	21:20
	27	East	Sipp Cove	Ebb	Sea grasses	S620	21:40
	27	East	Sipp Cove	Ebb	Rockweed	S621	22:25
	27	East	Sipp Cove	Ebb	Cobble	S622	22:40
	28	Pennamaquan	Hersey Cove	High	Cobble	S623	09:30
	28	Pennamaquan	Hersey Cove	Ebb	Cobble	S624	09:41
	28	Pennamaquan	Hersey Cove	Ebb	Sea grasses	S625	10:00
	28	Pennamaquan	Hersey Cove	Ebb	Sea grasses	S626	10:18
	28	Pennamaquan	Hersey Cove	Ebb	Cobble	S627	10:34
	28	Pennamaquan	Hersey Cove	Ebb	Cobble	S628	10:44
	29	Dennys	Youngs Cove	Ebb	Cobble	S629	11:47
	29	Dennys	Youngs Cove	Ebb	Sea grasses	S630	12:10
	29	Dennys	Youngs Cove	Ebb	Rockweed	S631	12:35
	29	Dennys	Youngs Cove	Ebb	Mudflat	S632	13:45
	30	Dennys	Youngs Cove	Ebb	Cobble	S633	00:55
	30	Whiting	Burnt Cove	Ebb	Rockweed	S634	13:49
	30	Whiting	Burnt Cove	Ebb	Rockweed	S635	14:21

Month	Day	Bay	Locale	Tide	Habitat	Tow	Time
	30	Whiting	Burnt Cove	Ebb	Mudflat	S636	14:52
	30	Whiting	Burnt Cove	Ebb	Mudflat	S637	15:35
	31	South	Case Cove	Ebb	Cobble	S638	13:00
	31	South	Case Cove	Ebb	Rockweed	S639	13:27
	31	South	Case Cove	Ebb	Sea grasses	S640	13:35
September	22	Outer CB	Deep Cove	Ebb	Not recorded	AS701	17:32
	22	Outer CB	Deep Cove	Ebb	Not recorded	AS702	18:10
	22	Outer CB	Broad Cove	Ebb	Not recorded	AS703	18:48
	23	Whiting	Burnt Cove	Ebb	Rockweed	S701	08:47
	23	Whiting	Burnt Cove	Ebb	Rockweed/flat	S702	09:25
	23	Whiting	Burnt Cove	Ebb	Rockweed	S703	09:35
	23	Whiting	Burnt Cove	Ebb	Mudflat	S704	09:43
	24	Outer CB	Carrying Place Cove	Ebb	Sea grasses	S705	07:40
	24	Outer CB	Carrying Place Cove	Ebb	Sea grasses	S706	08:05
	24	Outer CB	Carrying Place Cove	Ebb	Mudflat	S707	08:30
	24	Outer CB	Carrying Place Cove	Ebb	Mudflat	S708	09:00
	24	Outer CB	Carrying Place Cove	Ebb	Sea grasses	S709	20:00
	24	Outer CB	Carrying Place Cove	Ebb	Sea grasses	S710	20:30
	24	Outer CB	Carrying Place Cove	Ebb	Mudflat	S711	21:30
	25	East	Sipp Cove	High	Sea grasses	S712	07:48
	25	East	Sipp Cove	High	Cobble	S713	08:10
	25	East	Sipp Cove	Ebb	Cobble	S714	08:40
	25	East	Sipp Cove	Ebb	Sea grasses	S715	09:00
	25	East	Sipp Cove	Ebb	Rockweed	S716	09:40
	25	East	Sipp Cove	Ebb	Cobble	S717	20:20
	25	East	Sipp Cove	Ebb	Sea grasses	S718	20:45
	26	Dennys	Youngs Cove	Ebb	Rockweed	S719	10:30
	26	Dennys	Youngs Cove	Ebb	Cobble	S720	11:05
	26	Dennys	Youngs Cove	Ebb	Sea grasses	S721	11:30
	26	Dennys	Youngs Cove	Ebb	Rockweed	S722	23:00
	26	Dennys	Youngs Cove	Ebb	Cobble	S723	23:35
	26	Dennys	Youngs Cove	Ebb	Mudflat	S724	01:27

Month	Day	Bay	Locale	Tide	Habitat	Tow	Time
	27	South	Case Cove	Ebb	Cobble	S751	11:10
	27	South	Case Cove	Ebb	Sea grasses	S752	11:37
	27	Pennamaquan	Hersey Cove	High	Cobble	S761	10:03
	27	Pennamaquan	Hersey Cove	Ebb	Cobble	S762	10:13
	27	Pennamaquan	Hersey Cove	Ebb	Sea grasses	S763	10:24
	27	Pennamaquan	Hersey Cove	Ebb	Sea grasses	S764	10:37
	27	Pennamaquan	Hersey Cove	Ebb	Rockweed/cobble	S765	11:35
	27	Pennamaquan	Hersey Cove	Ebb	Rockweed/cobble	S766	11:48
November	2	Outer CB	Deep Cove	High	Cobble	N1	13:35
	2	Outer CB	Deep Cove	Ebb	Cobble	N2	13:54
	2	Outer CB	Deep Cove	Ebb	Not recorded	N3	14:10
	2	Outer CB	Broad Cove	Ebb	Sea grasses	N4	15:12
	2	Outer CB	Broad Cove	Ebb	Not recorded	N5	16:00
	2	Outer CB	Broad Cove	Ebb	Rockweed	N6	16:15
	2	Outer CB	Broad Cove	Ebb	Rockweed/cobble	N7	16:40
	2	East	Sipp Cove	High	Sea grasses	6#1	14:10
	2	East	Sipp Cove	Ebb	Cobble	6#2	14:15
	2	East	Sipp Cove	Ebb	Cobble	6#3	14:20
	2	East	Sipp Cove	Ebb	Not recorded	6#4	14:30
	2	Dennys	Youngs Cove	Ebb	Sea grasses	6#5	15:20
	2	Dennys	Youngs Cove	Ebb	Cobble/mix	6#6	15:30
	2	Dennys	Youngs Cove	Ebb	Sea grasses	6#7	15:40

Table 4. Date and location of intertidal fyke net samples in Cobscook Bay during May, June, August, and September, 2012. Fyke is fyke set number; each set is composed of two fyke nets. Begin and End are the approximate times (EDT) when each set began and ended. Each fyke net was assumed to begin effective fishing at the time of high tide and to end effective fishing when the water level was low in the net. Samples partially or completely at night are highlighted in gray. BT is baited minnow trap that caught fish. CB is Cobscook Bay.

Month	Day	Bay	Locale	Fyke	Begin	End	BT
May	28	Outer CB	Carrying Place Cove	F401	17:15	20:00	
	29	East	Sipp Cove	F402	18:30	21:45	
	30	Dennys	Youngs Cove	F403	19:00	21:30	
June	24	Outer CB	Carrying Place Cove	F501	03:30	06:15	
	24	Outer CB	Carrying Place Cove	F502	16:00	18:15	
	25	East	Sipp Cove	F503	03:30	07:00	
	25	East	Sipp Cove	F504	16:00	19:00	
	27	Dennys	Youngs Cove	F505	18:30	23:00	
	28	Dennys	Youngs Cove	F506	06:00	10:30	
	28	Dennys	Youngs Cove	F507	18:30	23:15	
August	25	Outer CB	Carrying Place Cove	F601	18:00	21:00	
	26	Outer CB	Carrying Place Cove	F602	06:30	10:00	
	26	Outer CB	Carrying Place Cove	F603	19:00	22:15	
	27	East	Sipp Bay	F604	07:45	09:30	
	27	East	Sipp Bay	F605	20:15	23:00	X
	28-29	Dennys	Youngs Cove	F606	21:15	00:00	X
	29	Dennys	Youngs Cove	F607	10:45	13:15	X
	29-30	Dennys	Youngs Cove	F608	23:00	02:00	
September	23	Outer CB	Carrying Place Cove	F701	18:40	21:00	
	24	Outer CB	Carrying Place Cove	F702	06:20	09:45	
	24	Outer CB	Carrying Place Cove	F703	18:50	22:10	
	25	East	Sipp Bay	F704	07:30	10:00	X
	25	East	Sipp Bay	F705	20:00	22:45	
	26	Dennys	Youngs Cove	F706	09:30	12:30	
	26-27	Dennys	Youngs Cove	F707	22:00	01:20	

Table 5. Capture data, by month, all gear types combined, for sampling in Cobscook Bay in 2012.

Month	March	April	May	June	August	September	November	Total
Species	Number of individuals							
Threespine stickleback, <i>Gasterosteus aculeatus</i>	5	>4	895	903	8439	4631	77	>14954
Atlantic herring, <i>Clupea harengus</i>			2558	1231		3		3792
Atlantic silverside, <i>Menidia menidia</i>		>75	70	52	37	1858	>335	>2427
Winter flounder, <i>Pleuronectes americanus</i>			1119	892	130	162		2303
Black spotted stickleback, <i>Gasterosteus wheatlandi</i>	1	5	221	237	716	331	32	1543
Alewife, <i>Alosa pseudoharengus</i>				735	289	92	7	1123
Mummichog, <i>Fundulus heteroclitus</i>		11	188	195	133	298	5	830
Silver hake, <i>Merluccius bilinearis</i>			32	216	8	2		258
Rainbow smelt, <i>Osmerus mordax</i>			31	118	16	18		183
Longhorn sculpin, <i>Myoxocephalus octodecemspinosus</i>			87	86	4	6		183
Grubby, <i>Myoxocephalus aeneus</i>			46	54	6	8		114
Atlantic tomcod, <i>Microgadus tomcod</i>			2	16	26	22		66
Butterfish, <i>Peprilus triacanthus</i>					53	11		65
Fourspine stickleback, <i>Apeltes quadracus</i>					33	10		43
White hake, <i>Urophycis tenuis</i>				5	8	28		41
Red hake, <i>Urophycis chuss</i>			6	7		11		24
Snakeblenny, <i>Lumpenus lampraeformis</i>			15	6				21
Sea raven, <i>Hemitripterus americanus</i>			8	6	1			15
Ninespine stickleback, <i>Pungitius pungitius</i>					12	3		15
Atlantic cod, <i>Gadus morhua</i>			7	4				11
Atlantic halibut, <i>Hippoglossus hippoglossus</i>			2	5	1	1		9
Blueback herring, <i>Alose aestivalis</i>				2	2	3		7
Atlantic mackerel, <i>Scomber scombrus</i>					4	2		6
Pollock, <i>Pollachius virens</i>						5		5
Shorthorn sculpin, <i>Myoxocephalus scorpius</i>				3				3
Radiated shanny, <i>Ulvaria subbifurcata</i>				1	1	1		3
Spiny dogfish, <i>Squalus acanthias</i>					3			3

Month	March	April	May	June	August	September	November	Total
Winter skate, <i>Raja ocellatus</i>				2				2
Smooth skate, <i>Malacoraja senta</i>			2					2
Lumpfish, <i>Cyclopterus lumpus</i>				1				1
Rock gunnel, <i>Pholis gunnellus</i>				1				1
Little skate, <i>Raja erinacea</i>				1				1
Goosefish, <i>Lophius americanus</i>				1				1
Fourbeard rockling, <i>Enchelyopus cimbrius</i>			1					1
Windowpane, <i>Scophthalmus aquosus</i>				1				1
Clearnose skate, <i>Raja eglanteria</i>						1		1
Total	6	>95	5290	4782	9922	7507	>456	>28058

Table 6. Numbers of individuals caught by month in pelagic trawling in Cobscook Bay, 2012

Species	May	June	August	September	Total
Atlantic herring	2539	726	0	1	3266
Rainbow smelt	4	4	0	0	8
Butterfish	0	0	3	1	4
Silver hake	1	2	0	0	3
Threespine stickleback	1	1	0	0	2
Alewife	0	1	0	0	1
Goosefish	0	1	0	0	1
Atlantic mackerel	0	0	1	0	1
Total	2545	735	4	2	3286

Table 7. Numbers of individuals caught by month in benthic trawling in Cobscook Bay, 2012

Species	May	June	August	September	Total
Winter flounder	1119	890	125	162	2296
Silver hake	31	214	8	2	255
Longhorn sculpin	87	86	4	6	183
Rainbow smelt	13	100	1	0	114
Grubby	46	54	6	8	114
Butterfish	0	1	50	10	61
Atlantic herring	8	50	0	0	58
White hake	0	5	8	28	41
Red hake	6	6	0	11	23
Snakeblenny	15	6	0	0	21
Sea raven	8	6	1	0	15
Atlantic cod	7	4	0	0	11
Atlantic halibut	2	5	1	1	9
Alewife	0	5	3	1	9
Atlantic mackerel	0	0	3	2	5
Shorthorn sculpin	0	3	0	0	3
Radiated shanny	0	1	1	1	3
Spiny dogfish	0	0	3	0	3
Smooth skate	2	0	0	0	2
Winter skate	0	2	0	0	2
Fourbeard rockling	1	0	0	0	1
Windowpane	0	1	0	0	1
Lumpfish	0	1	0	0	1
Rock gunnel	0	1	0	0	1
Little skate	0	1	0	0	1
Clearnose skate	0	0	0	1	1
Total	1345	1442	214	233	3234

Table 8. Numbers of individuals caught by month in intertidal seining in Cobscook Bay, 2012.

Species	March	April	May	June	August	September	November	Total
Threespine stickleback	5	>4	894	902	8333	4623	77	14838
Atlantic silverside	0	>75	70	52	37	1858	>335	2427
Blackspotted stickleback	1	5	221	237	716	331	32	1543
Alewife	0	0	0	728	286	91	7	1112
Mummichog	0	11	188	195	133	298	5	830
Atlantic herring	0	0	11	455	0	1	0	467
Fourspine stickleback	0	0	0	0	32	10	0	42
Rainbow smelt	0	0	14	14	6	7	0	41
Ninespine stickleback	0	0	0	0	12	3	0	15
Blueback herring	0	0	0	2	2	3	0	7
Atlantic tomcod	0	0	0	5	0	0	0	5
Red hake	0	0	0	1	0	0	0	1
Total	6	>95	1398	2591	9557	7225	>456	21328

Table 9. Numbers of individuals caught by month in fyke netting and limited baited minnow trapping in Cobscook Bay, 2012. Only those baited trap sets that caught fish are included.

Gear	Species	May	June	August	September	Total
Fyke net	Atlantic tomcod	2	11	25	22	60
	Alewife	0	1	0	0	1
	Winter flounder	0	2	5	0	7
	Rainbow smelt	0	0	9	11	20
	Atlantic herring	0	0	0	1	1
	Pollock	0	0	0	5	5
	Total	2	14	39	39	94
Baited trap	Threespine stickleback			106	8	114
	Atlantic tomcod			1		1
	Fourspine stickleback			1		1
	Total	0	0	108	8	116

Appendix Task 2-9

2013 Annual Report: Special License Number ME 2013-02-03
Issued January 4, 2013; amended October 22, 2013
University of Maine, School of Marine Sciences
Gayle Zydlewski, James McCleave, Jeffrey Vieser
February 5, 2014

Introduction

The first objective of the project requiring the special license was to use midwater trawling to provide species verification to accompany acoustic assessment of pelagic fish abundance in Outer Cobscook Bay, near Eastport, Maine. The acoustic assessment was conducted independently of the special license. The acoustic assessment and midwater trawling are parts of an overall project to assess the seasonal, daily, and tidal abundance and distribution of pelagic fishes in locations proposed for deployment of electricity generating tidal turbines (marine hydrokinetic energy devices, MHK).

The second objective of the project requiring the special license was to use midwater trawling, benthic trawling, intertidal seining, and intertidal fyke netting to characterize the fish community of the entire Cobscook Bay. This study provides a wider ecosystem perspective against which to consider deployment of arrays of electricity generating tidal turbines.

Methods

Midwater and benthic trawling was done with the commercial fishing vessel *Pandalus* (147YV), owned and operated by Stephen W. Brown. The midwater net mouth dimensions were: headrope, footrope and breastlines 40 feet. Mesh sizes were: belly, square and side panels 4 inch, tapers 2 inch, and extensions and codend 1 inch. The benthic net mouth dimensions were: headrope 45 feet, footrope 35 feet, no breastlines. Stretch mesh sizes were: net body 2 inch, codend 1 inch. Tows were nominally 20 minutes, but sometimes varied, especially to shorter times because towable distance was too short in Inner Cobscook Bay (Figure 1, Tables 1, 2). Trawling was done both day and night in Outer Cobscook Bay and Central Cobscook Bay but only during day in Inner Cobscook Bay for safety reasons (Tables 1, 2).

Two 100 foot x 6 foot seines with 0.25-inch diamond mesh were used to sample shallow intertidal habitats including cobble fields, mud flats, rockweed patches, and sea grass beds (Figure 1, Table 3). Two fyke nets with 30 foot wings, 4 foot tall square hoops, and 1.5-inch stretch mesh were used to sample larger rockweed covered rock piles (Table 4). Excluder bars were present in the mouths of the fyke nets to prevent capture of marine mammals. Sampling of intertidal habitats was conducted both during day and during night (Tables 3, 4).

Trawling and intertidal sampling were conducted during neap tides primarily in May, June, August and September, 2013. Thirty nine midwater tows and 40 benthic tows were made over the four months, with 15 midwater tows and 16 benthic tows being at night in Central and Outer Cobscook Bays (Tables 1, 2). One hundred fifty four seine hauls were made over the four months, with 51 hauls being at night (Table 3). Twenty four fyke net sets were made, with each set being two fyke nets nearby at the same location; 11 sets were at night (Table 4). Eight

additional seine hauls were made at a subset of locations in November, with 4 being at night (Table 3).

Results

Benthic trawling and intertidal seining were quite successful in capturing a variety of fish species, but midwater trawling and fyke netting were less successful. More than 27,000 individual fish of 41 species were caught (all gears and dates combined) (Table 5). Eight species were caught in 2013 that had not been caught previously: American eel, American plaice, Atlantic sea snail, cusk, moustache sculpin, ocean pout, smooth flounder, and white perch, each represented by 1-5 individuals (Table 5). Individuals of many species were primarily smaller (juvenile) specimens, but a few adult Atlantic herring were caught in pelagic trawls (Table 6). Threespine and blackspotted sticklebacks and mummichogs were caught as both adults and juveniles in seines (Table 8). Longhorn sculpin, grubby (Table 7), and Atlantic tomcod (Tables 8, 9) were caught as adults and juveniles.

Atlantic herring dominated the pelagic catch, and most were early juveniles. Atlantic herring and winter flounder juveniles dominated the catch in benthic trawls, but species richness was greatest among gears in the benthic trawls (31 species caught at least once) (Table 7).

Threespine stickleback, Atlantic silverside, blackspotted stickleback, and alewife dominated the catches in intertidal seine tows, but in widely varying proportions in the four primary months of sampling (Table 8). For example, alewives were absent in May and June, but their juveniles dominated the catch in August. Threespine sticklebacks were much more abundant in June than in other months. Only six species represented by few individuals were caught in fyke nets (Table 9). However, fyke nets caught adult Atlantic tomcod, while seining captured the juveniles.

In 2011, 2012, and 2013 four species comprised about 82% of the total catch. In rank order these were:

<u>2011</u>	<u>2012</u>	<u>2013</u>
Atlantic herring	Threespine stickleback	Atlantic herring
Threespine stickleback	Atlantic herring	Winter flounder
Winter flounder	Atlantic silverside	Threespine stickleback
Rainbow smelt	Winter flounder	Alewife

The increase in proportion of threespine stickleback and Atlantic silverside in 2012 over 2011 is in part due to increased effort on intertidal seining in 2012. In 2013, the appearance of alewife in the top four species was due to the outmigration of large numbers of juveniles especially in August.

Atlantic herring were abundant in all years, but those caught in May and June 2011 and 2013 were mostly advanced larvae, while those caught in May and June 2012 were mostly already metamorphosed into juveniles. This was probably due to the mild winter of 2011-2012 and early warming in March 2012. Butterfish, a species with more southerly distribution, were more abundant in 2012 than 2011 or 2013, probably reflecting the same phenomenon. Of note, juvenile haddock were present (48 individuals caught) in 2011, absent in 2012, and more abundant in 2013 (343 caught).

No Atlantic salmon (*Salmo salar*), shortnose sturgeon (*Acipenser brevirostrum*), or Atlantic sturgeon (*A. oxyrinchus*) were captured in any gear.

Discussion

Visual observation, hook and line recreational fishing, acoustic fish finder records, and local fishers' knowledge indicates the presence of large numbers of Atlantic herring and Atlantic mackerel throughout the water column in the study area, especially in August and September. The inability of our gear to capture these highly mobile pelagic species in proportion to their probable abundance is a problem. We suspect that the ability of highly mobile fish to detect the presence of the trawls, through visual and other sensory clues, allows them to avoid it in most cases. When capture did occur, it was primarily at night, when visual cues are restricted. Sampling effort at night with both midwater and benthic trawls was increased modestly in 2012 and 2013 compared with 2011.

It is expected that larger species, e.g., spiny dogfish, succeeded in avoiding capture, though there is less anecdotal evidence to support their presence in the bay. However, three were caught in one benthic trawl in 2012. A number of other species are probably under sampled as well in various gears, e.g., American eels, adult river herring (alewife and blueback herring), skates and flatfish species (other than winter flounder). Other species expected to be able to avoid the trawling gear used, e.g., striped bass (*Morone saxatilis*), have been rare or absent in recent years according to local knowledge.

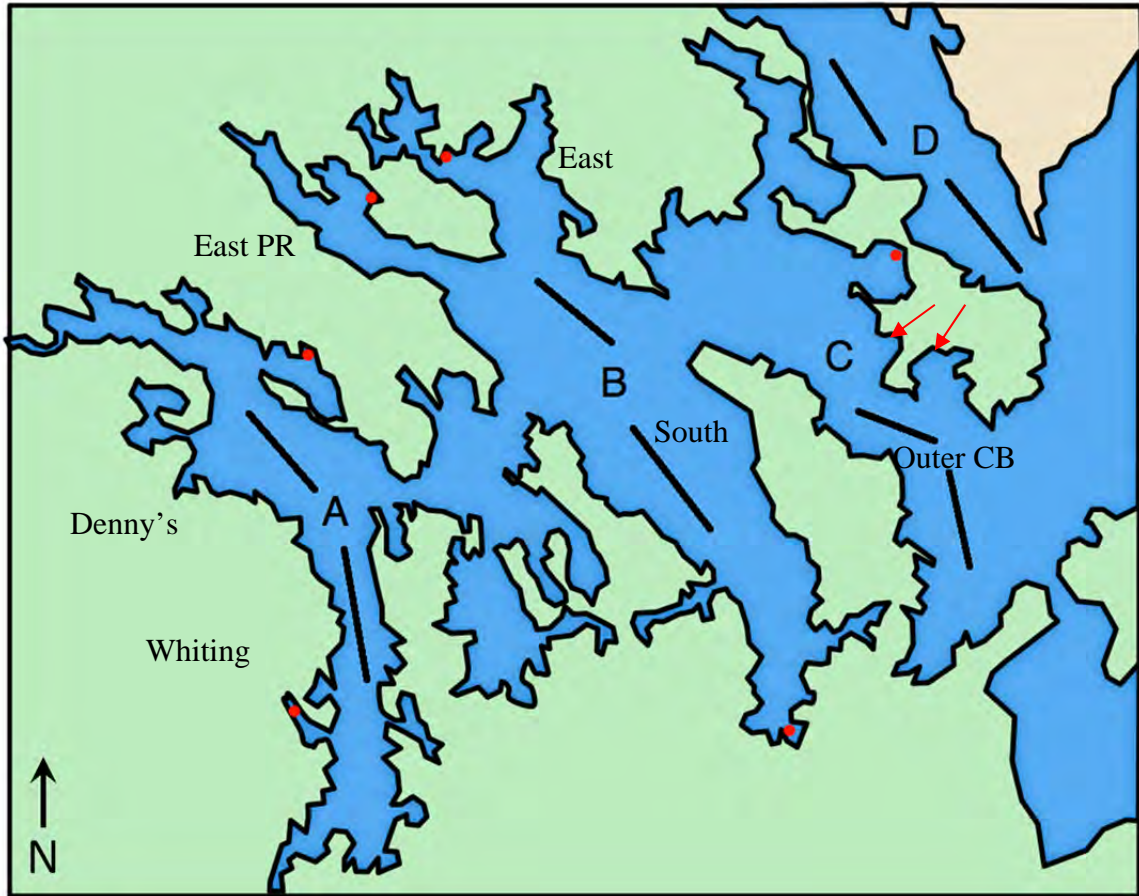


Figure 1. Map of Cobscook Bay and Western Passage of Passamaquoddy Bay showing mid-water and benthic trawl lines (black lines) fished in 2013 (Cobscook Bay only) and regular seine and fyke net sampling locations (red dots). Both benthic and pelagic trawls occurred in the same location. Uppercase letters indicate the center of each of the three sub-bays of Cobscook Bay (A = inner; B = central; C = outer) and Western Passage in Passamaquoddy Bay (D). Western Passage was sampled with some preliminary midwater trawling in 2011 but not later. Smaller bays of each sub-bay are also named. PR is Pennamaquan River.

Table 1. Date and location of pelagic trawl samples in Cobscook Bay during May, June, August, and September, 2013. Tide is the tidal stage when nets were fished. GPS positions where nets were deployed and retrieved are similar to those presented in the 2012 report and are not included here. Tow is tow number. Begin and end times (EDT) are when the trawls were deployed and retrieved, respectively. Night samples are highlighted in gray.

Month	Day	Bay	Tide	Tow	Begin time	End time
May	6	Outer Bay	Ebb	P801	8:31	8:56
May	6	Outer Bay	Ebb	P802	9:08	9:35
May	6	Outer Bay	Ebb	P810	21:40	22:10
May	6	Outer Bay	Ebb	P811	22:23	22:50
May	7	South Bay	Flood	P830	8:50	9:17
May	7	East Bay	High	P831	10:15	10:35
May	8	Whiting Bay	Ebb	P841	9:55	10:17
May	8	Dennys Bay	Flood	P842	11:15	11:35
May	8	East Bay	Flood	P851	20:27	20:47
May	8	South Bay	Flood	P852	21:41	22:01
June	2	Outer Bay	Flood	P901	6:10	6:30
June	2	Outer Bay	Ebb	P902	7:07	7:27
June	3	Outer Bay	Ebb	P911	20:50	21:10
June	3	Outer Bay	Ebb	P912	21:40	22:00
June	4	East Bay	Flood	P921	8:30	8:50
June	4	South Bay	Ebb	P922	10:15	10:35
June	5	Whiting Bay	High	P931	9:46	10:06
June	5	Dennys Bay	Ebb	P932	11:27	11:42
June	5	East Bay	Flood	P941	21:05	21:25
June	5	South Bay	Ebb	P942	22:55	23:15
August	4	Outer Bay	High	P1001	22:10	22:30
August	4	Outer Bay	High	P1002	22:45	23:05
August	5	Outer Bay	Flood	P1011	10:22	10:42
August	5	Outer Bay	Flood	P1012	10:58	11:18
August	6	South Bay	Flood	P1021	10:40	11:00
August	6	East Bay	Ebb	P1022	12:56	13:16
August	6	East Bay	Flood	P1031	21:50	22:10
August	7	Whiting Bay	Flood	P1041	11:13	11:33
August	7	Dennys Bay	High	P1042	12:56	13:16
September	1	Outer Bay	High	P1101	20:58	21:18
September	1	Outer Bay	High	P1102	21:35	21:55
September	2	Outer Bay	High	P1111	10:09	10:29
September	2	Outer Bay	High	P1112	10:43	11:03
September	3	South Bay	Flood	P1131	9:46	10:06
September	3	East Bay	Ebb	P1132	11:30	11:50
September	3	South Bay	Ebb	P1141	21:38	21:58
September	4	East Bay	Flood	P1142	20:05	20:25
September	4	Whiting Bay	Flood	P1151	10:58	11:18
September	4	Dennys Bay	Ebb	P1152	12:34	12:51

Table 2. Date and location of benthic trawl samples in Cobscook Bay during May, June, August, and September, 2012. Tide is the tidal stage when nets were fished. GPS positions where nets were deployed and retrieved are similar to those presented in the 2012 report and are not included here. Tow is tow number. Begin and end times (EDT) are when the trawls were deployed and retrieved, respectively. Night samples are highlighted in gray.

Month	Day	Bay	Tide	Tow	Begin time	End time
May	5	Outer Bay	High	B801	7:20	7:42
May	5	Outer Bay	Ebb	B802	7:53	8:18
May	6	Outer Bay	Flood	B810	20:20	20:45
May	6	Outer Bay	High	B811	21:00	21:27
May	7	South Bay	Flood	B830	9:35	9:55
May	7	East Bay	Ebb	B831	10:49	11:10
May	8	Whiting Bay	Flood	B841	10:35	10:55
May	8	Dennys Bay	High	B842	11:50	12:07
May	8	East Bay	Flood	B851	21:01	21:21
May	8	South Bay	Flood	B852	22:15	22:35
June	2	Outer Bay	Ebb	B901	9:38	9:58
June	2	Outer Bay	Ebb	B902	10:10	10:30
June	3	Outer Bay	Ebb	B911	22:16	22:36
June	3	Outer Bay	Ebb	B912	22:55	23:15
June	4	East Bay	Ebb	B921	9:05	9:25
June	4	South Bay	Ebb	B922	9:40	10:00
June	5	Whiting Bay	Ebb	B931	10:19	10:39
June	5	Dennys Bay	Ebb	B932	10:53	11:13
June	5	East Bay	High	B941	21:40	22:00
June	5	South Bay	Ebb	B942	22:16	22:36
August	4	Outer Bay	Flood	B1001	20:50	21:10
August	4	Outer Bay	Flood	B1002	21:30	21:50
August	5	Outer Bay	Ebb	B1011	11:35	11:55
August	5	Outer Bay	Ebb	B1012	12:08	12:28
August	6	South Bay	High	B1021	11:14	11:34
August	6	East Bay	High	B1022	12:18	12:38
August	6	East Bay	Flood	B1031	21:04	21:24
August	6	South Bay	Flood	B1032	22:23	22:43
August	7	Whiting Bay	Flood	B1041	11:49	12:09
August	7	Dennys Bay	Flood	B1042	12:25	12:40
September	1	Outer Bay	Flood	B1101	19:49	20:09
September	1	Outer Bay	Flood	B1102	20:23	20:43
September	2	Outer Bay	Flood	B1111	8:53	9:13
September	2	Outer Bay	Flood	B1112	9:33	9:53
September	3	South Bay	High	B1131	10:18	10:38
September	3	East Bay	Ebb	B1132	10:57	11:17
September	3	South Bay	Flood	B1141	22:14	22:34

September	4	East Bay	Flood	B1142	20:43	21:03
September	4	Whiting Bay	Flood	B1151	11:28	11:48
September	4	Dennys Bay	Ebb	B1152	12:05	12:22

Table 3. Date and location of regular intertidal seine samples in Cobscook Bay during May, June, August, and September, and additional seine samples at a subset of regular stations in November, 2013. Tide is the tidal stage when nets were fished. GPS positions and locales within bays where seines were deployed are similar to those presented in the 2012 report and are not included here. Tow is tow number. Time is the time (EDT) when each tow began; each tow takes <10 minutes. All tows were made on ebb tides. Night samples are highlighted in gray.

Month	Day	Bay	Locale	Habitat	Tow	Time
May	4	Dennys Bay	Youngs Cove	Rockweed	S800	21:30
May	4	Dennys Bay	Youngs Cove	Cobble	S801	21:45
May	4	Dennys Bay	Youngs Cove	Grass	S802	22:00
May	4	Dennys Bay	Youngs Cove	Mudflat	S803	23:22
May	5	Dennys Bay	Youngs Cove	Unknown	S810	9:57
May	5	Dennys Bay	Youngs Cove	Cobble	S811	10:06
May	5	Dennys Bay	Youngs Cove	Unknown	S812	10:23
May	5	Dennys Bay	Youngs Cove	Unknown	S813	11:33
May	5	East Bay	Sipp Bay	Unknown	S820	21:05
May	5	East Bay	Sipp Bay	Unknown	S821	21:20
May	5	East Bay	Sipp Bay	Unknown	S822	21:55
May	5	East Bay	Sipp Bay	Unknown	S823	22:10
May	5	East Bay	Sipp Bay	Unknown	S824	23:00
May	6	East Bay	Sipp Bay	Unknown	S830	9:50
May	6	East Bay	Sipp Bay	Unknown	S831	10:00
May	6	East Bay	Sipp Bay	Unknown	S832	10:29
May	6	East Bay	Sipp Bay	Unknown	S833	10:45
May	6	Outer Bay	Carrying Place Cove	Unknown	S840	23:02
May	6	Outer Bay	Carrying Place Cove	Unknown	S841	23:30
May	6	Outer Bay	Carrying Place Cove	Mudflat	S842	23:41
May	7	Pennamaquan River	Hersey Cove	Cobble	S851	10:45
May	7	Pennamaquan River	Hersey Cove	Cobble	S852	10:55
May	7	Pennamaquan River	Hersey Cove	Unknown	S853	11:23
May	7	Pennamaquan River	Hersey Cove	Unknown	S854	11:21
May	7	Pennamaquan River	Hersey Cove	Unknown	S855	12:12
May	7	Pennamaquan River	Hersey Cove	Unknown	S856	12:25
May	7	Outer Bay	Carrying Place Cove	Grass	S861	10:58
May	7	Outer Bay	Carrying Place Cove	Mudflat	S862	11:50
May	7	Outer Bay	Carrying Place Cove	Unknown	S863	12:05
May	8	South Bay	Case Cove	Unknown	S880	12:17
May	8	South Bay	Case Cove	Grass	S881	12:31
May	8	South Bay	Case Cove	Rockweed	S882	13:02
May	9	Whiting Bay	Burnt Cove	Rockweed	S891	14:10
May	9	Whiting Bay	Burnt Cove	Rockweed	S892	14:40
May	9	Whiting Bay	Burnt Cove	Unknown	S893	15:39
May	9	Whiting Bay	Burnt Cove	Unknown	S894	15:52

June	1	Dennys Bay	Youngs Cove	Rockweed	S900	20:20
June	1	Dennys Bay	Youngs Cove	Cobble	S901	20:30
June	1	Dennys Bay	Youngs Cove	Grass	S902	20:55
June	1	Dennys Bay	Youngs Cove	Grass	S903	21:48
June	2	Dennys Bay	Youngs Cove	Rockweed	S910	8:50
June	2	Dennys Bay	Youngs Cove	Cobble	S911	9:01
June	2	Dennys Bay	Youngs Cove	Grass	S912	9:13
June	2	Dennys Bay	Youngs Cove	Mudflat	S913	10:08
June	2	Outer Bay	Carrying Place Cove	Grass	S920	21:08
June	2	Outer Bay	Carrying Place Cove	Grass	S921	21:15
June	2	Outer Bay	Carrying Place Cove	Mudflat	S922	21:47
June	3	Outer Bay	Carrying Place Cove	Grass	S931	9:25
June	3	Outer Bay	Carrying Place Cove	Mudflat	S932	9:48
June	3	Outer Bay	Carrying Place Cove	Mudflat	S933	10:05
June	3	East Bay	Sipp Bay	Grass	S940	20:41
June	3	East Bay	Sipp Bay	Cobble	S941	20:53
June	3	East Bay	Sipp Bay	Grass	S942	21:35
June	3	East Bay	Sipp Bay	Cobble	S943	21:46
June	3	East Bay	Sipp Bay	Rockweed	S944	22:35
June	3	East Bay	Sipp Bay	Rockweed	S945	22:48
June	4	East Bay	Sipp Bay	Grass	S950	9:14
June	4	East Bay	Sipp Bay	Cobble	S951	9:23
June	4	East Bay	Sipp Bay	Grass	S952	10:00
June	4	East Bay	Sipp Bay	Unknown	S953	10:08
June	4	East Bay	Sipp Bay	Unknown	S954	10:44
June	4	East Bay	Sipp Bay	Unknown	S955	11:04
June	4	Pennamaquan River	Hersey Cove	Unknown	S960	9:25
June	4	Pennamaquan River	Hersey Cove	Unknown	S961	9:32
June	4	Pennamaquan River	Hersey Cove	Unknown	S962	9:47
June	4	Pennamaquan River	Hersey Cove	Grass	S963	10:02
June	4	Pennamaquan River	Hersey Cove	Unknown	S964	10:45
June	4	Pennamaquan River	Hersey Cove	Unknown	S965	10:54
June	5	South Bay	Case Cove	Cobble	S971	10:50
June	5	South Bay	Case Cove	Grass	S972	11:00
June	5	South Bay	Case Cove	Rockweed	S973	11:30
June	6	Whiting Bay	Burnt Cove	Rockweed	S981	13:05
June	6	Whiting Bay	Burnt Cove	Rockweed	S982	13:51
June	6	Whiting Bay	Burnt Cove	Unknown	S983	14:15
June	6	Whiting Bay	Burnt Cove	Mudflat	S984	14:37
August	3	Dennys Bay	Youngs Cove	Cobble	S1001	11:35
August	3	Dennys Bay	Youngs Cove	Unknown	S1002	11:52
August	3	Dennys Bay	Youngs Cove	Grass	S1003	12:06
August	3	Dennys Bay	Youngs Cove	Cobble	S1004	12:45
August	3	Dennys Bay	Youngs Cove	Unknown	S1005	13:06
August	3	Dennys Bay	Youngs Cove	Mudflat	S1006	13:30

August	4	Dennys Bay	Youngs Cove	Rockweed	S1011	0:06
August	4	Dennys Bay	Youngs Cove	Cobble	S1012	0:32
August	4	Dennys Bay	Youngs Cove	Grass	S1013	0:55
August	4	Dennys Bay	Youngs Cove	Mudflat	S1014	1:50
August	4	East Bay	Sipp Bay	Grass	S1021	11:00
August	4	East Bay	Sipp Bay	Cobble	S1022	11:17
August	4	East Bay	Sipp Bay	Grass	S1023	11:30
August	4	East Bay	Sipp Bay	Cobble	S1024	11:48
August	4	East Bay	Sipp Bay	Rockweed	S1025	12:28
August	4	East Bay	Sipp Bay	Rockweed	S1026	12:58
August	4	East Bay	Sipp Bay	Unknown	S1031	23:00
August	4	East Bay	Sipp Bay	Unknown	S1032	23:10
August	5	East Bay	Sipp Bay	Unknown	S1033	0:08
August	5	East Bay	Sipp Bay	Unknown	S1034	0:20
August	5	East Bay	Sipp Bay	Unknown	S1035	1:00
August	5	Outer Bay	Carrying Place Cove	Unknown	S1041	12:19
August	5	Outer Bay	Carrying Place Cove	Unknown	S1042	12:47
August	5	Outer Bay	Carrying Place Cove	Mudflat	S1043	13:00
August	5	Outer Bay	Carrying Place Cove	Mudflat	S1044	13:14
August	6	Outer Bay	Carrying Place Cove	Unknown	S1051	0:53
August	6	Outer Bay	Carrying Place Cove	Unknown	S1052	1:10
August	6	Outer Bay	Carrying Place Cove	Mudflat	S1053	1:23
August	6	Outer Bay	Carrying Place Cove	Unknown	S1054	1:43
August	6	South Bay	Case Cove	Cobble	S1061	13:21
August	6	South Bay	Case Cove	Unknown	S1062	13:30
August	6	South Bay	Case Cove	Rockweed	S1063	13:41
August	7	Whiting Bay	Burnt Cove	Rockweed	S1071	15:01
August	7	Whiting Bay	Burnt Cove	Rockweed	S1072	15:41
August	7	Whiting Bay	Burnt Cove	Mudflat	S1073	16:29
August	7	Whiting Bay	Burnt Cove	Mudflat	S1074	16:46
August	8	Pennamaquan River	Hersey Cove	Cobble	S1081	14:35
August	8	Pennamaquan River	Hersey Cove	Cobble	S1082	14:42
August	8	Pennamaquan River	Hersey Cove	Grass	S1083	14:51
August	8	Pennamaquan River	Hersey Cove	Cobble	S1084	15:03
August	8	Pennamaquan River	Hersey Cove	Rockweed	S1085	15:21
August	8	Pennamaquan River	Hersey Cove	Unknown	S1086	15:31
August	31	Whiting Bay	Burnt Cove	Rockweed	S1101	11:00
August	31	Whiting Bay	Burnt Cove	Rockweed	S1102	11:27
August	31	Whiting Bay	Burnt Cove	Mudflat	S1103	12:20
August	31	Whiting Bay	Burnt Cove	Mudflat	S1104	12:30
August	31	Dennys Bay	Youngs Cove	Rockweed	S1111	22:30
August	31	Dennys Bay	Youngs Cove	Cobble	S1112	23:00
September	1	Dennys Bay	Youngs Cove	Unknown	S1121	10:50
September	1	Dennys Bay	Youngs Cove	Unknown	S1122	11:00
September	1	Dennys Bay	Youngs Cove	Grass	S1123	11:10

September	1	Dennys Bay	Youngs Cove	Mudflat	S1124	12:44
September	1	East Bay	Sipp Bay	Grass	S1131	21:37
September	1	East Bay	Sipp Bay	Cobble	S1132	21:48
September	1	East Bay	Sipp Bay	Grass	S1133	22:26
September	1	East Bay	Sipp Bay	Cobble	S1134	22:33
September	1	East Bay	Sipp Bay	Rockweed	S1135	23:02
September	1	East Bay	Sipp Bay	Rockweed	S1136	23:40
September	2	East Bay	Sipp Bay	Cobble	S1141	10:15
September	2	East Bay	Sipp Bay	Grass	S1142	10:24
September	2	East Bay	Sipp Bay	Grass	S1143	10:55
September	2	East Bay	Sipp Bay	Cobble	S1144	11:01
September	2	East Bay	Sipp Bay	Unknown	S1145	11:40
September	2	East Bay	Sipp Bay	Unknown	S1146	12:00
September	2	Outer Bay	Carrying Place Cove	Unknown	S1151	23:15
September	2	Outer Bay	Carrying Place Cove	Grass	S1152	23:35
September	3	Outer Bay	Carrying Place Cove	Mudflat	S1153	0:25
September	3	Outer Bay	Carrying Place Cove	Unknown	S1154	0:45
September	3	Outer Bay	Carrying Place Cove	Grass	S1161	12:00
September	3	Outer Bay	Carrying Place Cove	Unknown	S1162	12:22
September	3	Outer Bay	Carrying Place Cove	Unknown	S1163	12:32
September	3	Outer Bay	Carrying Place Cove	Mudflat	S1164	12:44
September	4	South Bay	Case Cove	Cobble	S1171	12:30
September	4	South Bay	Case Cove	Grass	S1172	12:41
September	4	South Bay	Case Cove	Unknown	S1173	13:00
September	5	Pennamaquan River	Hersey Cove	Cobble	S1180	13:05
September	5	Pennamaquan River	Hersey Cove	Cobble	S1181	13:15
September	5	Pennamaquan River	Hersey Cove	Unknown	S1182	13:40
September	5	Pennamaquan River	Hersey Cove	Grass	S1183	13:50
September	5	Pennamaquan River	Hersey Cove	Unknown	S1184	14:21
September	5	Pennamaquan River	Hersey Cove	Rockweed	S1185	14:40
November	18	Pennamaquan River	Hersey Cove	Unknown	3 tows	11:30
November	18	Dennys Bay	Youngs Cove	Unknown	1 tow	14:00
November	19	East Bay	Sipp Bay	Unknown	2 tows	0:15
November	19	Outer Bay	Carrying Place Cove	Unknown	2 tows	1:30

Table 4. Date and location of intertidal fyke net samples in Cobscook Bay during May, June, August, and September, 2013. Fyke is fyke set number; each set is composed of two fyke nets. Begin and End are the approximate times (EDT) when each set began and ended. Each fyke net was assumed to begin effective fishing at the time of high tide and to end effective fishing when the water level was low in the net. Samples partially or completely at night are highlighted in gray. CB is Cobscook Bay.

Month	Day	Bay	Locale	Fyke	Begin	End
May	4	Dennys Bay	Youngs Cove	F800	20:00	23:59
May	5	Dennys Bay	Youngs Cove	F810	9:02	11:53
May	5	East Bay	Sipp Cove	F820	20:42	23:30
May	6	East Bay	Sipp Cove	F830	9:30	11:43
May	6	Outer Bay	Carrying Place Cove	F840	21:20	0:00
May	7	Outer Bay	Carrying Place Cove	F850	9:47	13:20
June	1	Dennys Bay	Youngs Cove	F900	19:15	22:15
June	2	Dennys Bay	Youngs Cove	F901	7:45	10:45
June	2	Outer Bay	Carrying Place Cove	F903	19:02	22:30
June	3	Outer Bay	Carrying Place Cove	F904	7:31	11:00
June	3	East Bay	Sipp Bay	F905	20:30	23:00
June	4	East Bay	Sipp Bay	F910	9:00	11:30
August	3	Dennys Bay	Youngs Cove	F1001	13:00	19:03
August	3/4	Dennys Bay	Youngs Cove	F1011	19:03	02:45
August	4	East bay	Sipp Cove	F1021	~10:00	13:15
August	4/5	East Bay	Sipp Cove	F1031	~22:30	01:30
August	5	Outer Bay	Carrying Place Cove	F1041	11:00	15:00
August	6	Outer Bay	Carrying Place Cove	F1051	23:00	02:30
Aug-Sep	31/1	Dennys Bay	Youngs Cove	F1101	21:10	00:20
September	1	Dennys Bay	Youngs Cove	F1111	9:45	13:20
September	1	East Bay	Sipp Cove	F1131	9:15	23:58
September	2	East Bay	Sipp Bay	F1146	9:40	12:20
September	2/3	Outer Bay	Carrying Place Cove	F1501	22:00	01:15
September	2/3	Outer Bay	Carrying Place Cove	F1160	10:20	13:45

Table 5. Number of individuals caught by all gears combined in Cobscook Bay, 2013. Limited sampling in November is not included in this table, but see Table 8.

Scientific name	Common name	May	June	August	September	Total
<i>Clupea harengus</i>	Atlantic herring	52	6153	1042	5417	12664
<i>Pseudopleuronectes americanus</i>	Winter flounder	2443	1600	798	365	5206
<i>Gasterosteus aculeatus</i>	Threespine stickleback	112	1848	157	362	2479
<i>Alosa pseudoharengus</i>	Alewife	5	0	1738	474	2217
<i>Fundulus heteroclitus</i>	Mummichog	133	394	796	46	1369
<i>Menidia menidia</i>	Atlantic silverside	79	26	17	536	658
<i>Gasterosteus wheatlandi</i>	Blackspotted stickleback	62	143	153	72	430
<i>Melanogrammus aeglefinus</i>	Haddock	0	0	208	135	343
<i>Myoxocephalus octodecemspinosus</i>	Longhorn sculpin	140	123	61	9	333
<i>Merluccius bilinearis</i>	Silver hake	5	59	207	47	318
<i>Myoxocephalus aenaeus</i>	Grubby	138	66	36	29	269
<i>Urophycis tenuis</i>	White hake	0	0	120	76	196
<i>Urophycis chuss</i>	Red hake	23	52	84	15	174
<i>Microgadus tomcod</i>	Atlantic tomcod	3	26	65	46	140
<i>Osmerus mordax</i>	Rainbow smelt	9	55	17	22	103
<i>Pungitius pungitius</i>	Ninespine stickleback	0	0	5	20	25
<i>Scophthalmus aquosus</i>	Windowpane	13	9	3	0	25
<i>Pollachius virens</i>	Pollock	0	2	5	6	13
<i>Peprilus triacanthus</i>	Butterfish	0	0	1	8	9
<i>Lumpenus lumpretaeformis</i>	Snakeblenny	5	0	2	0	7
<i>Hemirhamphus americanus</i>	Sea raven	0	3	1	2	6
<i>Hippoglossus hippoglossus</i>	Atlantic halibut	0	0	3	3	6
<i>Myoxocephalus scorpius</i>	Shorthorn sculpin	0	4	2	0	6
<i>Pleuronectes putnami</i>	Smooth flounder	0	0	4	1	5
<i>Cyclopterus lumpus</i>	Lumpfish	0	1	1	2	4
<i>Gadus morhua</i>	Atlantic cod	2	0	0	2	4
<i>Zoarces americanus</i>	Ocean pout	0	2	2	0	4
<i>Alosa aestivalis</i>	Blueback herring	2	0	0	1	3
<i>Leucoraja ocellata</i>	Winter skate	1	1	0	1	3
<i>Liparis atlanticus</i>	Atlantic sea snail	2	1	0	0	3
<i>Malacoraja senta</i>	Smooth skate	0	0	3	0	3
<i>Ulvaria subbifurcata</i>	Radiated shanny	2	1	0	0	3
<i>Apeltes quadricus</i>	Fourspine stickleback	2	0	0	0	2
<i>Hippoglossoides platessoides</i>	American plaice	1	1	0	0	2
<i>Triglops murrayi</i>	Moustache sculpin	0	2	0	0	2
<i>Anguilla rostrata</i>	American eel	0	0	0	1	1
<i>Brosme brosme</i>	Cusk	1	0	0	0	1
<i>Leucoraja erinacea</i>	Little skate	0	0	0	1	1
<i>Morone americana</i>	White perch	0	0	0	1	1
<i>Scomber scombrus</i>	Atlantic mackerel	0	0	1	0	1
Total		3235	10572	5532	7700	27039

Table 6. Numbers of individuals caught by month by pelagic trawling in Cobscook bay, 2013.

Species	May	June	August	September	Total
Atlantic herring	50	6150	470	41	6711
Winter flounder	6	46	0	0	52
Silver hake	0	4	2	1	7
Alewife	0	0	0	6	6
Shorthorn sculpin	0	1	1	1	3
Lumpfish	1	1	0	0	2
Atlantic sea snail	1	0	0	0	1
Threespine stickleback	0	1	0	0	1
Blackspotted stickleback	1	0	0	0	1
Windowpane	1	0	0	0	1
Total	50	6150	470	41	6711

Table 7. Numbers of individuals caught by month by benthic trawling in Cobscook Bay, 2013.

Species	May	June	August	September	Total
Atlantic herring	2	3	566	5376	5947
Winter flounder	2442	1600	798	363	5203
Haddock	0	0	208	135	343
Longhorn sculpin	140	123	61	9	333
Silver hake	5	55	205	46	311
Alewife	4	0	29	237	270
Grubby	138	66	36	29	269
White hake	0	0	120	76	196
Red hake	23	52	84	15	174
Rainbow smelt	7	5	7	11	30
Windowpane	12	9	3	0	24
Atlantic tomcod	0	0	2	7	9
Butterfish	0	0	1	8	9
Snakeblenny	5	0	2	0	7
Sea raven	0	3	1	2	6
Atlantic halibut	0	0	3	3	6
Shorthorn sculpin	0	3	2	0	5
Atlantic cod	2	0	0	2	4
Ocean pout	0	2	2	0	4
Winter skate	1	1	0	1	3
Smooth skate	0	0	3	0	3
Radiated shanny	2	1	0	0	3
American plaice	1	1	0	0	2
Pollock	0	0	0	2	2
Moustache sculpin	0	2	0	0	2
Blueback herring	0	0	0	1	1
Cusk	1	0	0	0	1
Lumpfish	0	0	0	1	1
Little skate	0	0	0	1	1
Atlantic sea snail	1	0	0	0	1
Atlantic mackerel	0	0	1	0	1
Total	2786	1926	2134	6325	13171

Table 8. Numbers of individuals caught by month by intertidal seining in Cobscook Bay, 2013. For November, only those individuals kept for examination for sea lice are included. Other catch was released and not recorded. November catch not included in table totals or in Table 5.

Species	May	June	August	September	November	Total
Threespine stickleback	106	1802	157	362	(123)	2427
Alewife	0	0	1709	231		1940
Mummichog	133	394	796	46		1369
Atlantic silverside	79	26	17	536		658
Blackspotted stickleback	61	143	153	72	(104)	429
Atlantic tomcod	1	22	62	5		90
Rainbow smelt	2	50	9	4		65
Ninespine stickleback	0	0	5	20	(7)	25
Pollock	0	2	4	1		7
Atlantic herring	0	0	6	0		6
Smooth flounder	0	0	4	1		5
Fourspine stickleback	2	0	0	0		2
American eel	0	0	0	1		1
Winter flounder	0	0	0	1		1
Blueback herring	0	0	0	0		0
American eel	0	0	0	1		1
Total	384	2439	2922	1281	(234)	7026

Table 9. Numbers of individuals caught by month by fyke netting in Cobscook Bay, 2013.

Species	May	June	August	September	Total
Atlantic tomcod	2	4	1	34	41
Rainbow smelt			1	7	8
Pollock			1	3	4
Blueback herring	2				2
Alewife	1				1
Winter flounder				1	1
Total	5	4	3	45	57

Appendix 3-1

**TESTING OF A DUCTED AXIAL FLOW
TIDAL TURBINE**

By

Thomas A. Lokocz

B.S University of Maine, 2010

A THESIS

Submitted in Partial Fulfillment of the

Requirements for the Degree of

Masters of Science

(in Mechanical Engineering)

The Graduate School

University of Maine

August, 2012

Advisory Committee:

Michael Peterson Jr., PhD, Libra Foundation Professor of Mechanical Engineering,

Advisor

Richard Kimball, PhD, Associate Professor, Maine Maritime Academy

Krish P Thiagarajan, PhD, Correll Presidential Chair in Energy and Professor of

Mechanical Engineering

LIBRARY RIGHTS STATEMENT

In presenting this thesis in partial fulfillment of the requirements for an advanced degree at the University of Maine, I agree that the Library shall make it freely available for inspection. I further agree that permission for “fair use” copying of this thesis for scholarly purposes may be granted by the Librarian. It is understood that any copying or publication of this thesis for financial gain shall not be allowed without my written permission.

Signature:

Date:

**TESTING OF A DUCTED AXIAL FLOW
TIDAL TURBINE**

By: Thomas A. Lokocz

Thesis Advisor: Dr. Michael Peterson

An Abstract of the Thesis Presented
in Partial Fulfillment of the Requirements for the
Degree of Master of Science
(in Mechanical Engineering)
August, 2012

Energy independence and a reduction on the reliance on fossil fuels is a critical area of current research and development. Utilizing the energy in the world's oceans can help the world move towards a more sustainable energy supply. One of the most promising sources of ocean energy is tidal energy or marine hydrokinetics, the topic of this thesis.

This research analyzes the performance of a ducted axial flow tidal turbine and compares the result to an unducted turbine. While the focus of this research is on experimental results obtained in tow tank tests, the turbine and duct were designed using the open source software code, OpenProp. OpenProp was used because of the suitability of the design approach for the optimization of a turbine design and its modeling capability for ducted propellers. While OpenProp has the capability to analyze ducted turbines this capability has been added only recently and has not been validated. Thus the duct used in the experimental work could not be optimized and was intended to provide data which could be used as a part of the validation of the ducted portion of the

code. Literature reviews indicate that limited experimental data exists for the performance of comparable ducted and unducted turbines.

The design used is a three-bladed, ducted turbine with blade shapes optimized in OpenProp. For the unducted case, an optimal C_p of 0.44 was measured at a tip speed ratio of 4.43. The duct was shown to have a detrimental effect on the performance of the turbine with a maximum $C_p = .4$ at a tip speed ratio of 4.4. This result demonstrates the challenges associated with the design of an efficient ducted turbine

THESIS ACCEPTANCE STATEMENT

On behalf of the Graduate Committee for Thomas A. Lokocz I affirm that this manuscript is the final and accepted thesis. Signatures of all committee members are on file with the Graduate School at the University of Maine, 42 Stodder Hall, Orono, Maine.

Dr. Michael Peterson Jr., Professor of Mechanical Engineering,

Date

ACKNOWLEDGEMENTS

There are many people who made this thesis possible. I would like to thank my wife, Claire and son, Cabot for their patience and support. I would also like to thank my advisors Dr. Michael “Mick” Peterson and Dr. Richard Kimball for their guidance, insight and editing. Thank you to Dr. Brenden Epps whose experience and advice were always valuable.

This thesis would not be possible without the support of my fellow graduate students who helped in the lab and data processing, especially: Geoffrey deBree for data processing, Matthew Cameron for help with the tow tank, Raul Urbina for numerical modeling and writing advice, and Melissa Colleen Swanger for being a good lab mate. I would also like to thank the following undergraduate students for help with fabrication, testing and coding: Samuel Sayen for machining, Tom McKay for testing and James Staszko for both testing and creating figures.

Finally, I would like to thank the University of Maine, Department of Mechanical Engineering and the U.S. Department of Energy (grant EE-000298) for their financial support to make this project possible.

TABLE OF CONTENTS

ACKNOWLEDGEMENTS	6
LIST OF TABLES	11
LIST OF FIGURES	12
NOMENCLATURE	15
PERFORMANCE EQUATIONS	16
CHAPTER 1. INTRODUCTION	17
1.1 Motivation	17
1.2 Background	18
1.2.1 OpenProp	19
1.2.2 Free Tip Turbines	20
1.2.3 Ducted Turbines	20
1.3 Thesis Overview	20
CHAPTER 2. TURBINE DESIGN AND FABRICATON	21
2.1 Free Tip Turbine Design	22
2.2 Ducted Turbine Design	23
2.2.1 Duct Geometry	24
2.3 Turbine Fabrication	25

CHAPTER 3. EXPERIMENTAL TESTING	27
3.1 Experimental Setup	27
3.1.1 Tow Tank.....	27
3.1.2 Axial Flow Turbine Test Platform.....	28
3.1.3 Measured Quantities	30
3.1.3.1 Torque.....	31
3.1.3.2 Rotor Thrust.....	32
3.1.3.3 Duct Thrust	32
3.1.3.4 Turbine Frequency.....	34
3.1.3.5 Inflow Velocity.....	34
3.2 Test Methods	35
3.2.1 Calibration	35
3.2.1.1 Torque Calibration.....	35
3.2.1.2 Rotor Thrust Calibration.....	37
3.2.1.3 Duct thrust Calibration	38
3.2.2 Turbine Test Procedure	38
CHAPTER 4. DATA PROCESSING.....	40
4.1 Filtering	40

CHAPTER 5. RESULTS	43
5.1 Free Tip Results	43
5.1.1 Free Tip C_p	44
5.1.2 Free Tip C_T	45
5.2 Ducted Results.....	45
5.2.1 Ducted C_p	46
5.2.2 Ducted C_T	46
5.2.3 Duct Thrust Coefficient	47
5.2.4 Ducted Turbine Rotor Without Duct	48
5.2.4.1 C_p For Ducted Turbine Rotor Without Duct	48
5.2.4.2 C_T For Ducted Turbine Without Duct	49
CHAPTER 6. DISCUSSION AND CONCLUSIONS	50
6.1 Discussion	50
6.1.1 Reynolds Number and Water Temperature Effects.....	52
6.1.1.1 Free tip turbine.....	53
6.1.1.2 Ducted Turbine	54
6.1.2 Duct Thrust	54
6.1.3 OpenProp Validation	57
6.1.4 Free Tip and Ducted C_T Discussion	58

6.2 Conclusions	60
6.3 Future Work	62
6.3.1 Experimental.....	62
6.3.2 Modeling.....	63
WORKS CITED	64
APPENDIX A: Free tip input code	67
APPENDIX B: Free tip blade Geometry file	71
APPENDIX C: Ducted input code	72
APPENDIX D: Ducted Blade Geometry File	74
APPENDIX E: Uncertainty and Repeatability	75
APPENDIX F: Tip Gap Study.....	78
APPENDIX G: Free Tip Turbine Picture	83
BIOGRAPHY OF THE AUTHOR.....	84

LIST OF TABLES

Table 2.1 Axial flow turbine design parameters	21
Table E.1 Uncertainty Equations	77
Table F.1 Tip Gap Case Definitions	80

LIST OF FIGURES

Figure 2.1 Non-dimensional geometry of the free tip and ducted turbine plotted against the non dimensional local radius divided by the full turbine radius.	22
Figure 2.2 The OpenProp output of the free tip turbine plotted in MATLAB [9].....	23
Figure 2.3 The ducted turbine geometry from OpenProp demonstrates the graphics plotted in MATLAB [9]......	24
Figure 2.4 NACA 4412 in Xfoil	25
Figure 2.5 A SolidWorks [16] model of the ducted turbine created from the OpenProp output text file.	26
Figure 3.1 A dimensioned schematic of the UMaine tow tank with the axial flow turbine in place.	27
Figure 3.2 UMaine tow tank with ducted turbine installed ready for testing.	28
Figure 3.3 An isometric view of the ducted turbine on the axial flow test platform showing the major components of the test platform.....	30
Figure 3.4 A schematic drawing of the axial flow test platform viewed from one end.	31
Figure 3.5 Schematic drawing showing the end and profile views of the axial flow turbine.....	33
Figure 3.6 Details AA and BB show a blown up view of the schematic in Figure 3.5.	34
Figure 3.7 Calibration graph of load cell for measuring torque vs. load cell output.	36
Figure 3.8 Torque friction as a function of turbine frequency.....	37

Figure 4.1 This figure shows a single sided Fourier transform of Q during hammer test.....	41
Figure 4.2 This figure shows the torque vs. samples before and after applying 30 Hz low-pass Butterworth filter.	41
Figure 4.3 A typical set of data for Q vs. samples is shown before and after filtering.	42
Figure 5.1 The free tip power coefficient vs. tip speed ratio is shown for the range of velocities and Reynolds numbers tested.....	44
Figure 5.2 The free tip thrust coefficient vs. tip speed ratio is shown for the range of velocities and Reynolds numbers tested.....	45
Figure 5.3 The ducted power coefficient vs. tip speed ratio is shown for the range of velocities and Reynolds numbers tested.....	46
Figure 5.4 The thrust coefficient vs. tip speed ratio of the ducted turbine is shown for the range of velocities and Reynolds numbers tested.	47
Figure 5.5 The duct thrust coefficient vs. tip speed ratio is shown for the range of velocities and Reynolds numbers tested.	47
Figure 5.6 C_p vs. tip speed ratio for the ducted turbine rotor without the duct is shown with results of the same rotor with the duct.	48
Figure 5.7 C_T vs. tip speed ratio for the ducted turbine without the duct is shown with results of the same rotor without the duct.	49
Figure 6.1 Free tip average C_p vs. tip speed ratio is shown for the two carriage speeds.....	50

Figure 6.2 Ducted average C_P vs. tip speed ratio is shown for the two carriage speeds.....	51
Figure 6.3 Duct thrust coefficient vs. tip speed ratio is shown for the two carriage speeds. $C_D = .02$ are also shown.	55
Figure 6.4 C_L & C_D for the duct as a function of Re.	56
Figure 6.5 This figure shows the upper half of a duct with the relevant force vectors drawn in.....	57
Figure 6.6 Ducted power coefficient vs. tip speed ratio of experimental data and OpenProp predictions..	58
Figure 6.7 Free tip average C_T vs. tip speed ratio is shown for the two carriage speeds.....	59
Figure 6.8 Ducted average C_T vs. tip speed ratio is shown for the two carriage speeds.....	60
Figure E.1 Shows the uncertainty in C_P for the free tip and ducted turbines.	75
Figure E.2 Shows the uncertainty in C_T for the free tip and ducted turbines.	76
Figure F.1 Measuring tip gap on ducted turbine.....	79
Figure F.2 C_P as a function of t/D ($V = 1.25$ m/s)	80
Figure F.3 Percent difference in C_P	81
Figure G.1 Picture of the free tip turbine.	83

NOMENCLATURE

c/D	chord length to rotor diameter ratio
c	chord length
c_D	cord length of duct
C_d	drag coefficient
C_L	lift coefficient of rotor
C_{LD}	lift coefficient of duct
D	diameter
Q	torque
T_D	duct thrust
T_R	rotor thrust
V	inflow velocity
Q	torque
r	local radius
R	radius of rotor
α	angle of attack of rotor
α_D	angle of attack of duct
β_i	inflow angle as seen by rotor
β_{iD}	inflow angle as seen by duct

PERFORMANCE EQUATIONS

$$C_P = \frac{Q\omega}{\frac{1}{2}\rho V^3 \pi R^2} \quad \text{power coefficient}$$

$$C_T = \frac{T_r}{\frac{1}{2}\rho V^2 \pi R^2} \quad \text{thrust coefficient for rotor (no duct)}$$

$$C_{TD} = \frac{T_D}{\frac{1}{2}\rho V^2 \pi R^2} \quad \text{thrust coefficient of duct}$$

$$\lambda = \frac{R\omega}{V} \quad \text{tip speed ratio}$$

CHAPTER 1. INTRODUCTION

As we use more and more of earth's petroleum reserves and learn about the effects of global warming, it has become critical that we find alternative energy sources to meet our electricity needs. However, no single source is likely to meet the growing global demand. The benefits and drawbacks of nuclear, solar, wind, hydro and tidal energy must all be carefully weighed, and assessments made based on thorough, research.

1.1 MOTIVATION

While in all likelihood moving water has been a power source since humans invented machines, relatively little research has been performed on axial flow tidal turbines and even less on ducted axial flow turbines. As of the date of this writing there is only one deployed, grid connected, commercial-scale tidal turbine in the world [1] . One of the most important characteristics of a turbine is the overall efficiency, which is usually reported as a coefficient of performance (C_p), or the percentage of total kinetic power that can be removed from the flow. Free tip axial flow turbines are capable of $C_p \approx .46$ [2]. In theory, ducted axial flow turbines have the potential to exceed the Betz limit of $C_p \approx .59$ [3] making them the most efficient style of hydrokinetic turbine for use in free stream flows. However, to date these efficiency claims have not been tested except with theoretical models. The key objective of this thesis is to provide a data set to be used as a part of a validated design code for ducted and unducted axial flow turbines. The actual optimization of the turbine and evaluation of efficiency claims is well beyond the scope of this thesis.

1.2 BACKGROUND

The key objective of this thesis is to provide data to be used as a part of a validated design code for ducted and unducted axial flow turbines. A substantial amount of setup and infrastructure was required to meet this end goal. Many parts of that infrastructure were in place at the University of Maine from ongoing testing of cross-flow tidal turbines [4]. A decision was made early on in this thesis to design and build as much of the experimental system around the existing facilities as possible without compromising the quality of results. This decision reduced overhead costs, setup time and expanding the knowledge base of our current systems. The major components of the infrastructure in place included:

- Tow tank
- Data acquisition system programmed in LABVIEW [5]
- Turbine motor controller setup for a Parker servo motor

This left the turbine test rig, the turbines themselves and the duct to be designed, fabricated and tested.

For several reasons a decision was also made to start testing with the free tip turbine case, which has some experimental data for marine applications but has not been exhaustively tested. The most directly applicable experiments were performed at MIT [6][7] using a 2 blade turbine designed in OpenProp and demonstrate reasonable agreement between experimental data and OpenProp predictions but further validation was desirable. The other purpose, and perhaps the dominant one for starting with the free tip turbine, was to gain benchmark data with the test rig built at the University of Maine. This benchmark data could be compared to previous work from other experiments to see

if our test rig yielded similar results. Our free tip data could then be compared to the ducted case to see if a performance increase was realized.

OpenProp was selected as the basic design tool since it is computationally efficient. The program can be run on a basic laptop computer in a matter of minutes and thus is suitable for the optimization necessary in developing an efficient turbine.

1.2.1 OpenProp

OpenProp is an open source propeller and turbine design code [8]. The design code is written in MATLAB [9] and utilizes lifting line theory and a prescribed helical wake to model the blades. A system of ring vortices and an image model are used for the hub and duct. The code was initially developed to design free tip marine propellers and then extended to include the design of ducted propellers [10] [8]. The code was later modified and has been at least partially validated for modeling of turbines. Essentially no data exists for the ducted turbine case.

For the case of the free tip propeller OpenProp was validated with experimental data and is in good agreement [6]. The ducted propeller model has been validated with the MIT Propeller Lifting Line program and is in good agreement [11] but has not been validated with experimental data. The free tip turbine case has been validated with experimental data as well and is in reasonable agreement but not as well as the propeller [6]. The ducted turbine portion of the code is still under development in OpenProp and has not been validated.

1.2.2 Free Tip Turbines

Free tip (unducted) axial flow turbines are primarily used in the wind industry for commercial applications. The designs are well developed with extensive experimental data and multiple numerical codes to optimize their design and evaluate performance.

Marine turbines are not as well developed, however several companies are working on developing codes for this purpose. There are a couple of test deployments, perhaps the most notable by Marine Current Turbines [12] owned by Siemens [13]. Currently, Marine Current Turbines has the only grid-tied commercial scale turbine in the world [1].

1.2.3 Ducted Turbines

Ducted propellers are widely applied in marine propulsion for a variety of reasons, one of which is improved efficiency [14]. Ducts are typically employed when high thrust at a relatively low ship speed (less than 5 m/s) is required [14]. Tugboats are a good example of this. Typically, marine current turbines operate under a similar operating condition, relatively low current velocity. It is therefore reasonable to investigate whether or not adding a duct to an axial flow turbine increases its efficiency as well.

1.3 THESIS OVERVIEW

The purpose of this thesis is to provide experimental data which can be used for validation of ducted and unducted axial flow tidal turbine models. The basic infrastructure used was in place from ongoing testing of cross-flow tidal turbines [4]. To the extent possible the existing experimental facilities were used. For this work the mechanical portions of the turbine test rig, the turbines and the duct had to be designed and built. The contribution of this work is to highlight the challenges of proper duct design and to provide an unducted data set for future optimization studies.

CHAPTER 2. TURBINE DESIGN AND FABRICATON

The basic parameters for the turbine design were determined largely by the capabilities of our testing apparatus. The turbine needed to provide enough torque and thrust to facilitate measurement but sufficiently small to fit in the tank. The tank dimensions are limited by both blockage and free surface effects. The design parameters for both the free tip and ducted turbines and can be seen in Table 2.1.

Table 2.1 Axial flow turbine design parameters.

Parameter	Symbol	Value	Units
Turbine Diameter	D	.254	m
Carriage speed	V	1.25	m/s
Lift Coefficient (Blades)	C_L	.5	
Lift Coefficient (Duct)	C_{LD}	.5	
Drag Coefficient	C_d	.02	

It is important to note that the free tip and ducted turbines do not have the same geometry; they are both optimized by OpenProp for their respective case. The objective of this thesis is not to compare a free tip turbine to a ducted turbine but rather to obtain experimental data from a ducted turbine. The free tip turbine is however a useful way of checking the design and testing methods. To illustrate the differences of the two blades Figure 2.1 shows both the free tip and ducted turbine geometry. Table of the non-dimensional geometry can also be seen in Appendices B and D.

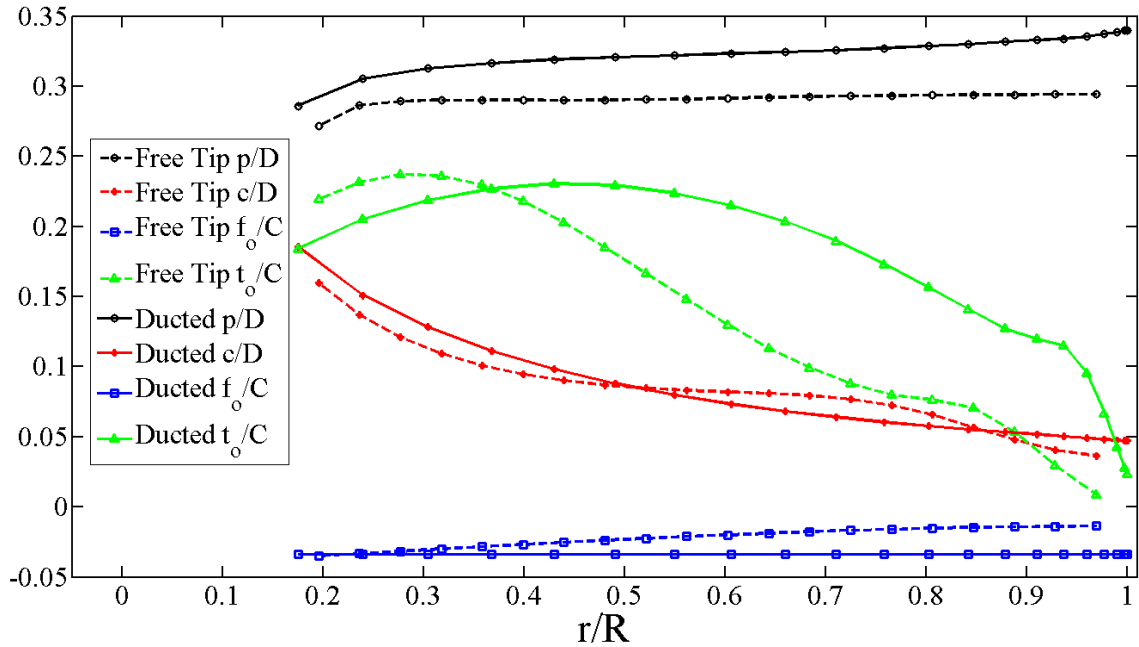


Figure 2.1 Non-dimensional geometry of the free tip and ducted turbine plotted against the non dimensional local radius divided by the full turbine radius.

2.1 FREE TIP TURBINE DESIGN

The free tip turbine was designed using OpenProp. No code modifications were required for the unducted turbine case. The code was run directly using a MATLAB [9] script, not the OpenProp GUI. Use of the GUI limits the number of parameters that can be modified. Plots from OpenProp were also customized which is not possible with the GUI. An example of the output is the turbine geometry shown in Figure 2.2. The input for OpenProp can be seen in Appendix A.

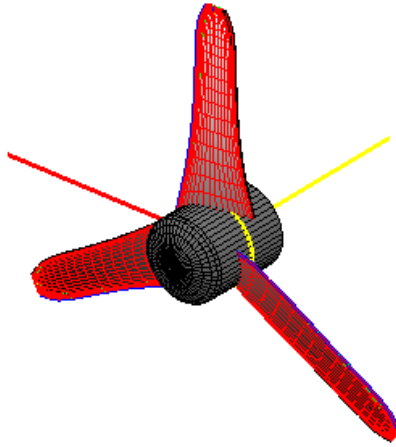


Figure 2.2 The OpenProp output of the free tip turbine plotted in MATLAB [9].

2.2 DUCTED TURBINE DESIGN

The rotor for the ducted turbine was also designed using OpenProp, but the duct was only partially designed with this code. OpenProp optimizes the blades for the ducted turbine but does not optimize the duct. The code calculates the circulation of the blades and the duct, finds the influence of the duct and the blades on each other and then iterates until the blade circulation converges [11][8]. The code also calculates the lift coefficient of the duct (C_{LD}) required to obtain the correct duct circulation as well as the inflow angle for the duct (β_{iD}). The duct thrust coefficient (C_{TD}), and the duct chord length (C_D), are entered as inputs. The rotor was placed at the $\frac{1}{4}$ chord of the duct (from leading edge). This location was chosen by moving the location of the rotor along the duct chord in OpenProp and selecting the location that corresponded with the highest C_p . Figure 2.3 shows MATLAB [9] graphic of the ducted turbine. The input code for OpenProp can be seen in Appendix C.

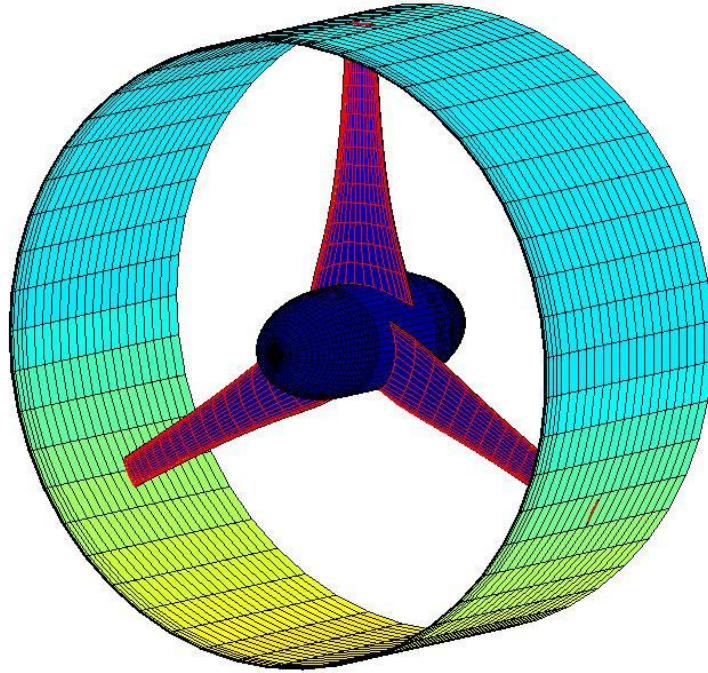


Figure 2.3 The ducted turbine geometry from OpenProp demonstrates the graphics plotted in MATLAB [9].

2.2.1 Duct Geometry

Since the duct geometry is not modeled in OpenProp it must be designed separately. OpenProp outputs basic parameters for the duct, specifically the inflow angle as seen by the duct (β_{iD}) and the required lift coefficient of the duct (C_{LD}). Based on these values and the duct cord length (C_D) a duct profile and angle of attack can be determined. A duct foil profile that supplies the correct C_{LD} is then selected. For the current case OpenProp provide, $C_{LD} = .5$, $\beta_{iD} = -1^\circ$ and $C_d = .127m$. A NACA 4412 was selected as the profile and XFOil [15] was used to obtain the lift coefficient at a zero degree angle

of attack (Figure 2.4 NACA 4412 in XFOil). The profile was then set at $\beta_{iD} = -1^\circ$ to maintain a zero degree attack angle as specified in XFOil.

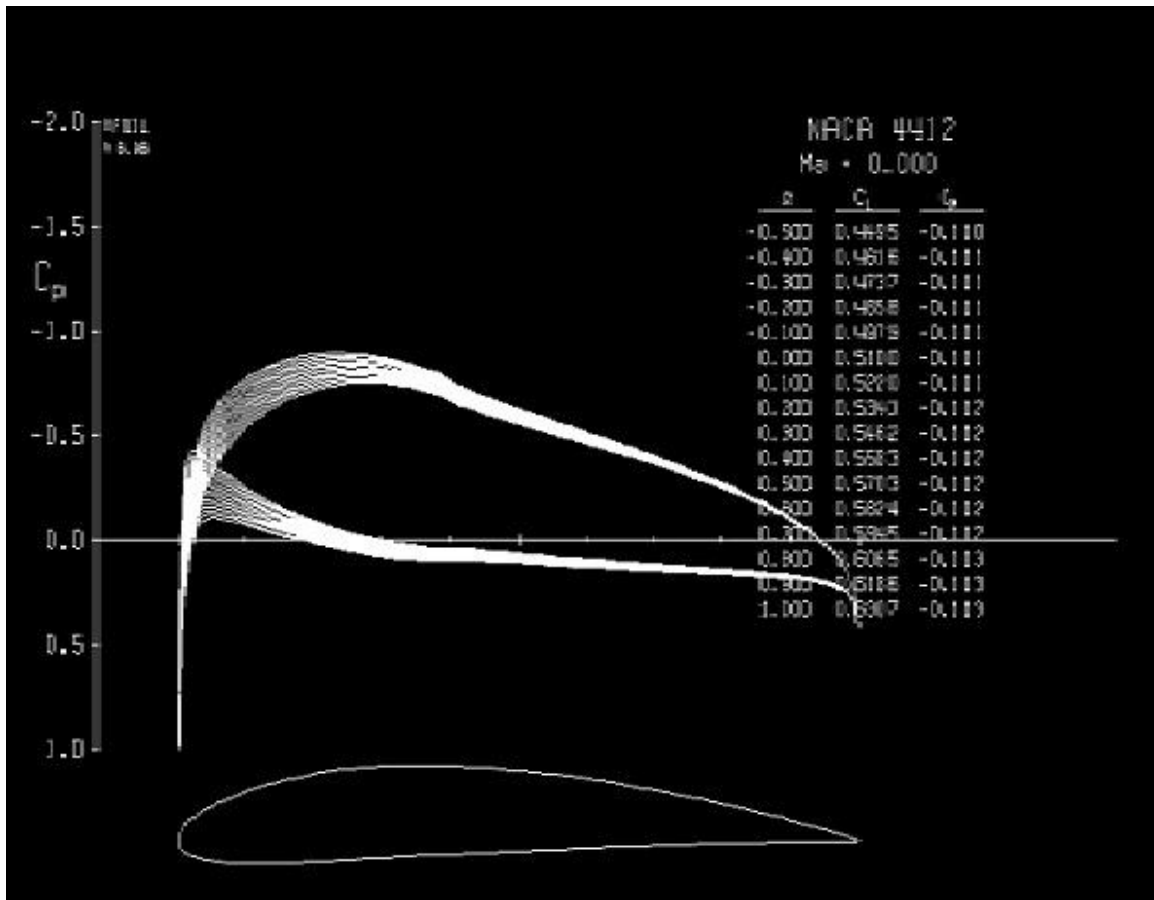


Figure 2.4 NACA 4412 in XFOil

2.3 TURBINE FABRICATION

Several methods of producing the turbine blades were considered; 3D printing was selected for these turbine blades. OpenProp outputs a text file of 3D points for the blade geometry, which can be imported into SolidWorks [16] to create a part. The duct was also modeled in SolidWorks [16] using the profile of a NACA 4412. The ducted turbine model can be seen in Figure 2.5.

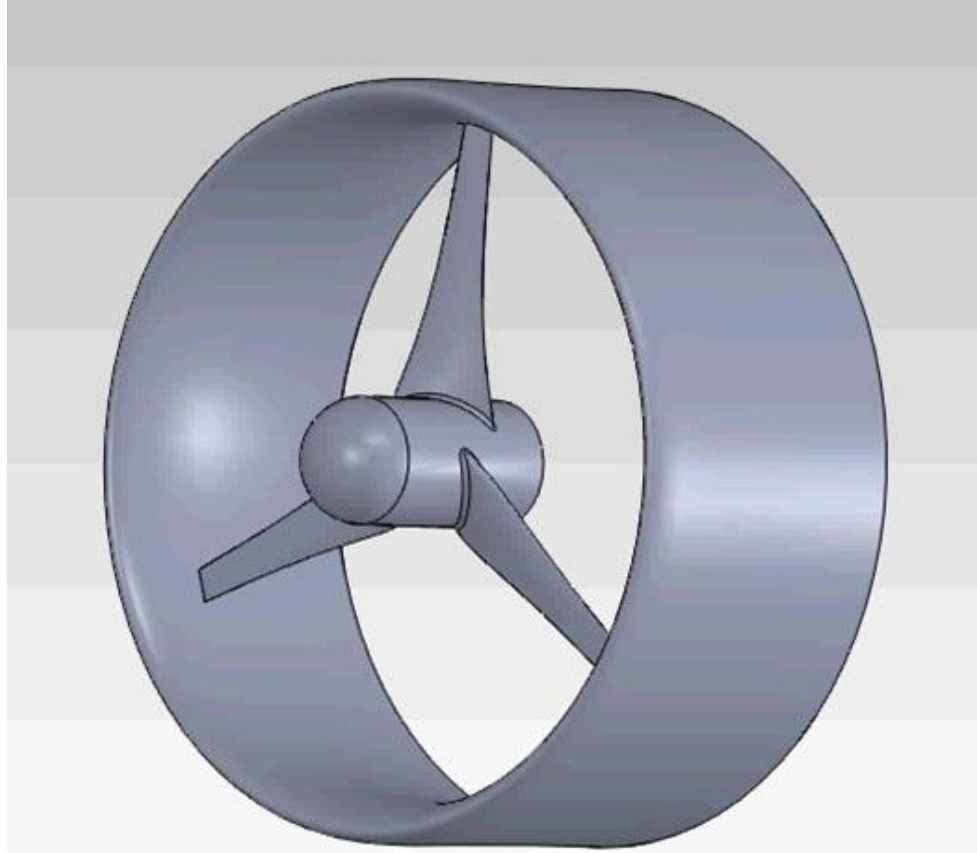


Figure 2.5 A SolidWorks [16] model of the ducted turbine created from the OpenProp output text file.

CHAPTER 3. EXPERIMENTAL TESTING

3.1 EXPERIMENTAL SETUP

This chapter describes the infrastructure and procedures used for collecting data. The tow tank, motor controller and data acquisition were in place from previous testing performed for a cross-flow turbine [4].

3.1.1 Tow Tank

UMaine's tow tank was utilized for all data collection. The tank is 2.44 meters wide, 1 meter deep and 30 meters long, and is capable of carriage speeds up to 1.5 meters per second. The carriage is mounted on sided rails and driven by an endless wire rope wrapped around a drive drum [4]. Figure 3.1 shows the dimensions of the tow tank and the position of the axial flow turbine. Figure 3.2 shows the tow tank with the ducted turbine during testing.

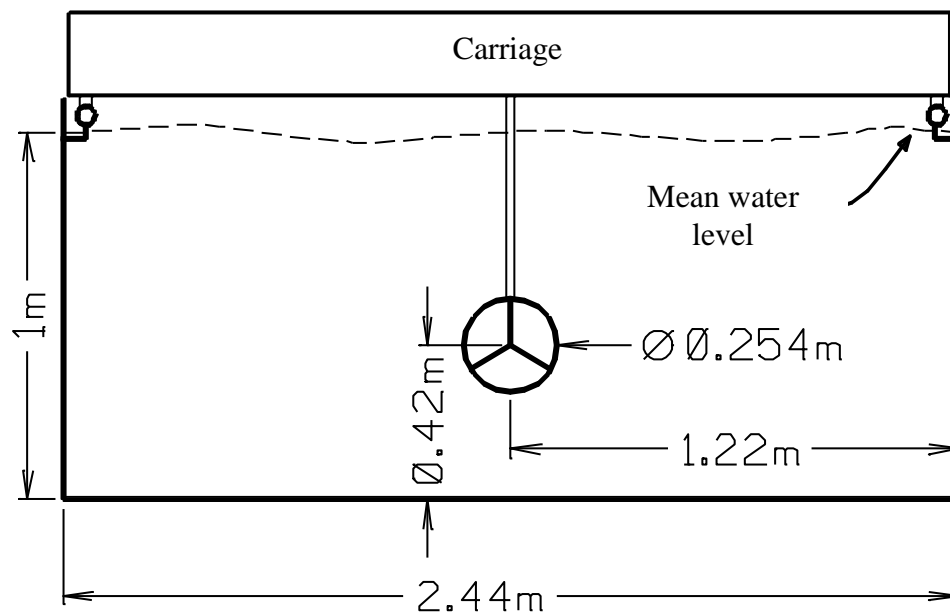


Figure 3.1 A dimensioned schematic of the UMaine tow tank with the axial flow turbine in place.



Figure 3.2 UMaine tow tank with ducted turbine installed ready for testing.

3.1.2 Axial Flow Turbine Test Platform

The turbine test platform was fabricated at UMaine. The turbine testing system consists of a wet hub and shaft connected via a chain to an above-water shaft. The chain drive is a one-to-one ratio with the chain running in water for most of its length. The dry upper shaft is connected to a Parker [17] servo motor to regulate turbine frequency. The servo motor controller is configured to either drive the turbine or absorb energy. This flexibility eliminates self starting issues and allows the turbine to be operated at negative power coefficients if required.

The entire motor drivetrain is suspended on slender rods attached to a mounting frame. This allows a small amount of motion in the horizontal direction unrestrained by friction. A load cell is in place to prevent the horizontal motion and to record thrust from the underwater body. Schematic drawings illustrating this may be seen in Figure 3.4 Figure 3.5 and Figure 3.6. The other two load cells shown in Figure 3.5 and Figure 3.6 are for measuring torque and duct thrust. They are explained in the following section.

Data is collected in real time using LABVIEW [5] and a National Instruments CRIO [5] data acquisition system. The test platform was designed to be compatible with the existing data collection and control systems in place [4]. Figure 3.3 shows the axial flow test platform with major components labeled.

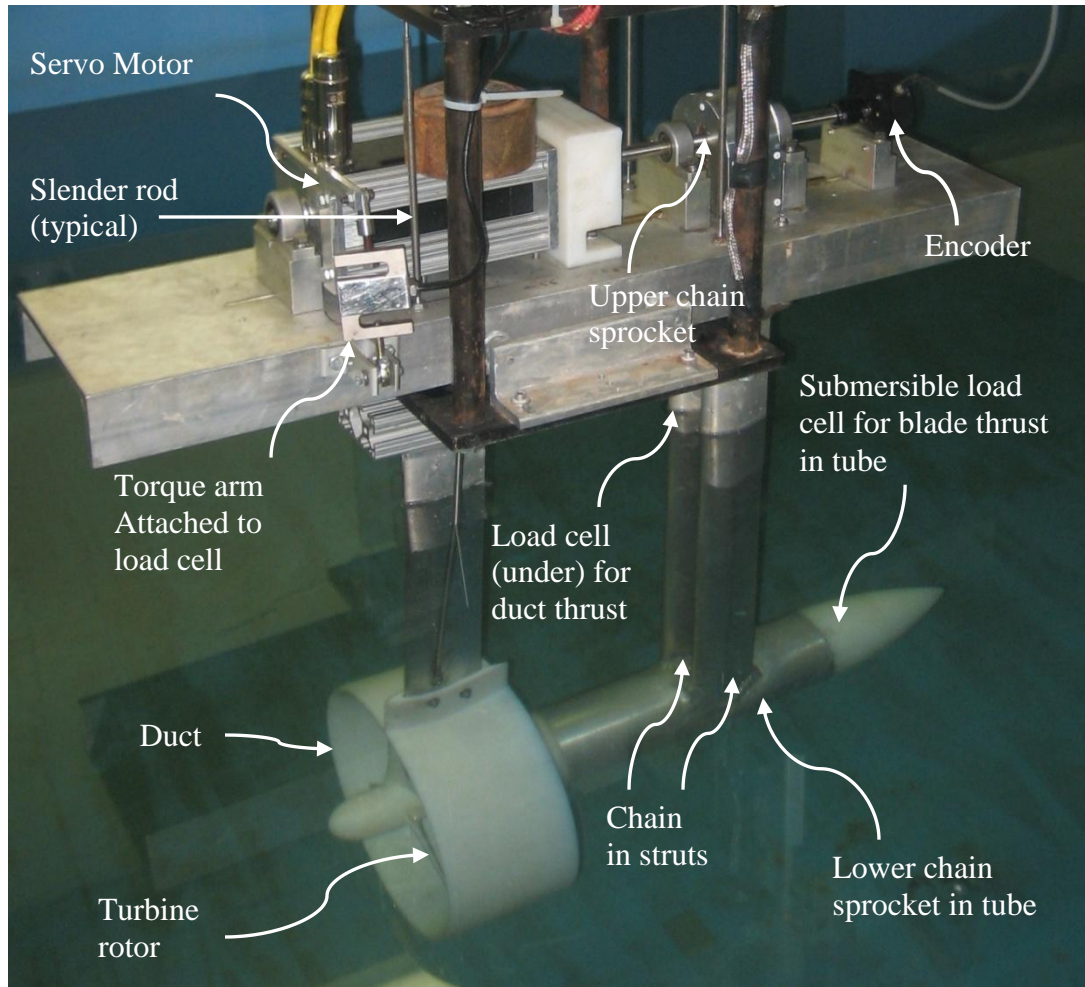


Figure 3.3 An isometric view of the ducted turbine on the axial flow test platform showing the major components of the test platform.

3.1.3 Measured Quantities

Controlled parameters were measured to track variations in desired settings. Additional measurements were also taken to perform a full range of performance characterization. All measured quantities were recorded at a sample rate of 1 kHz. The measured quantities were recorded simultaneously to allow for correlation at each time step. Data acquisition starts after the acceleration period of the tow tank carriage and the data acquisition is stopped before the ramp-down or deceleration period to simplify post

processing. This is consistent with normal tow tank practice and the signal procession discussed in Chapter 4 applies only to the time period when the carriage is at the test speed. Time is recorded in the data acquisition system using a 266 MHz clock speed [4].

3.1.3.1 Torque

Torque is used in calculating the power coefficient (C_p). Torque data is acquired from an S-type load cell mounted on a lever arm at a known distance from the upper shaft's center of rotation. Figure 3.4 shows the orientation of the load cell and motor on the axial flow test bed.

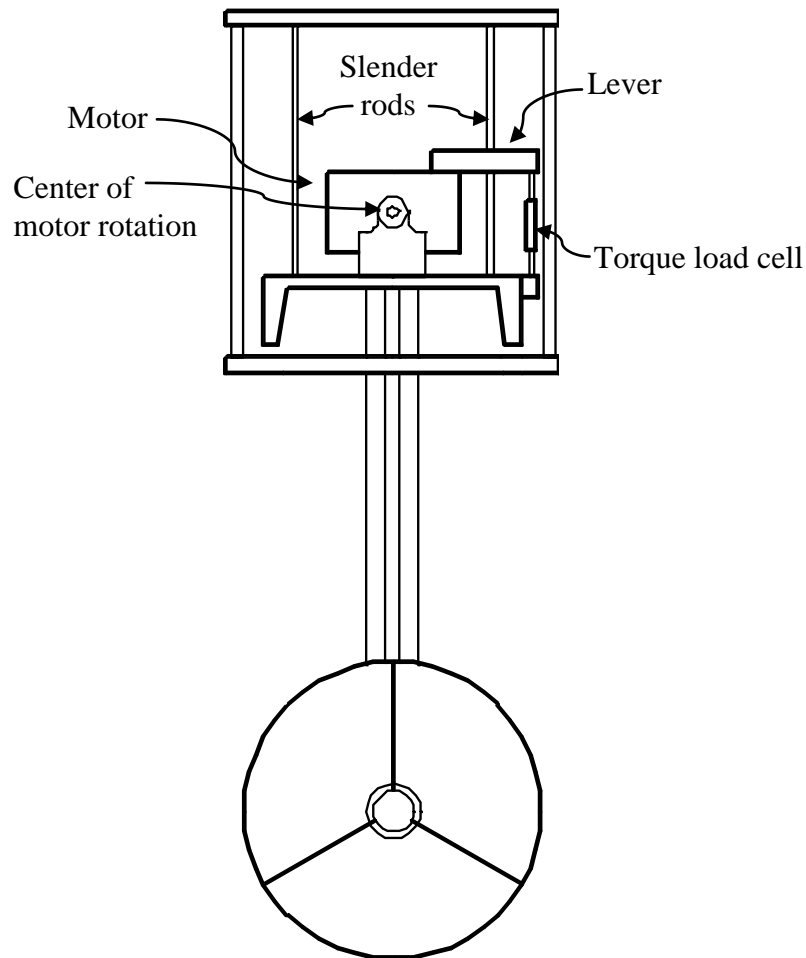


Figure 3.4 A schematic drawing of the axial flow test platform viewed from one end. The load cell to measure torque is shown.

3.1.3.2 Rotor Thrust

Rotor thrust is used in calculating the thrust coefficient (C_T). Rotor thrust is measured using a submersible S-type load cell mounted in the downstream side of test platform hub. The lower shaft pushes on the load cell via a thrust bearing. Figure 3.5 and Figure 3.6 illustrate the load cell and shaft.

3.1.3.3 Duct Thrust

Duct thrust is used in calculating the duct thrust coefficient (C_{TD}). Duct thrust is measured from an S-type load cell. The load cell measures lateral force on the entire underwater apparatus. This includes drag from the support struts, blade thrust and turbine thrust. The blade thrust and drag are then subtracted during post processing from the overall thrust to obtain the duct thrust. Figure 3.5 and Figure 3.6 illustrate the load cell that measures duct thrust.

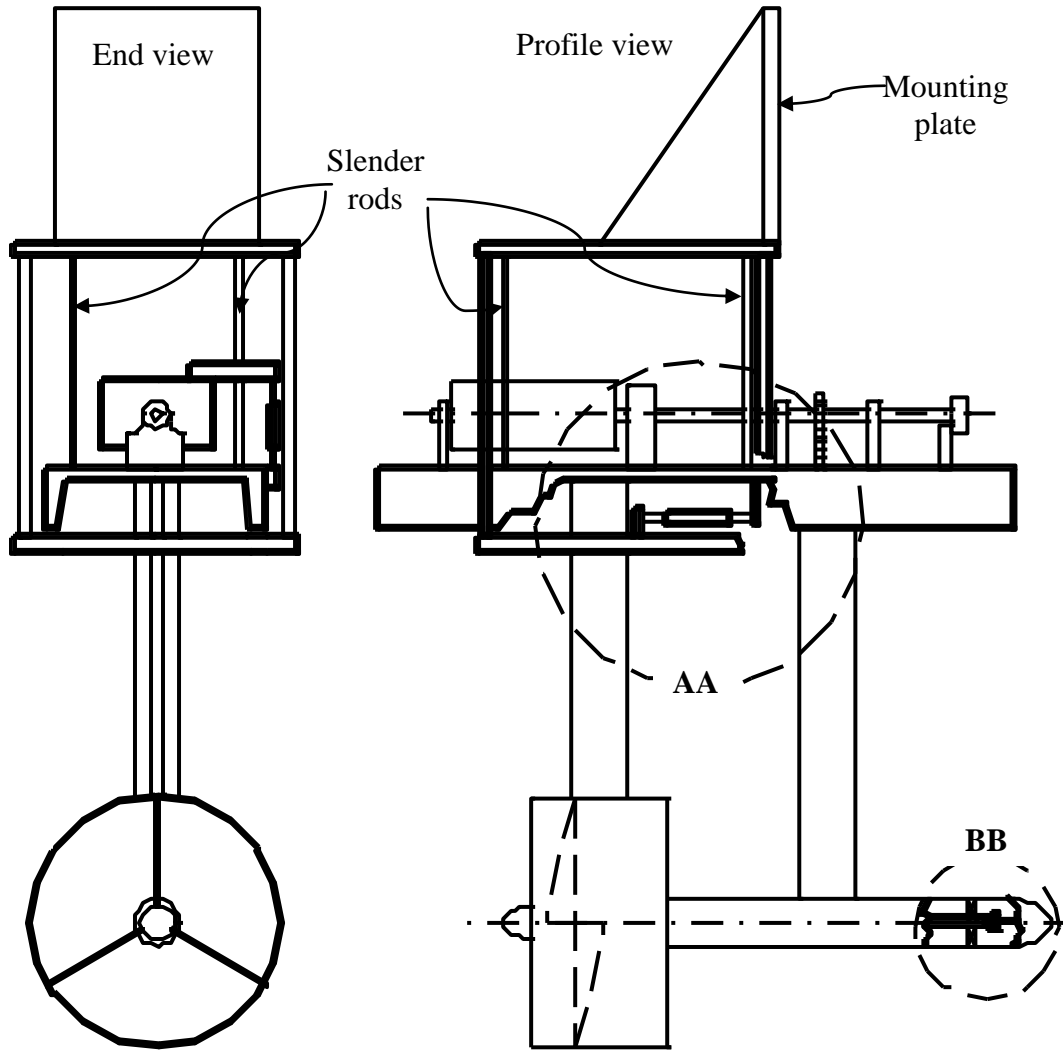


Figure 3.5 Schematic drawing showing the end and profile views of the axial flow turbine. Also shown are the load cells for the duct thrust and blade thrust.

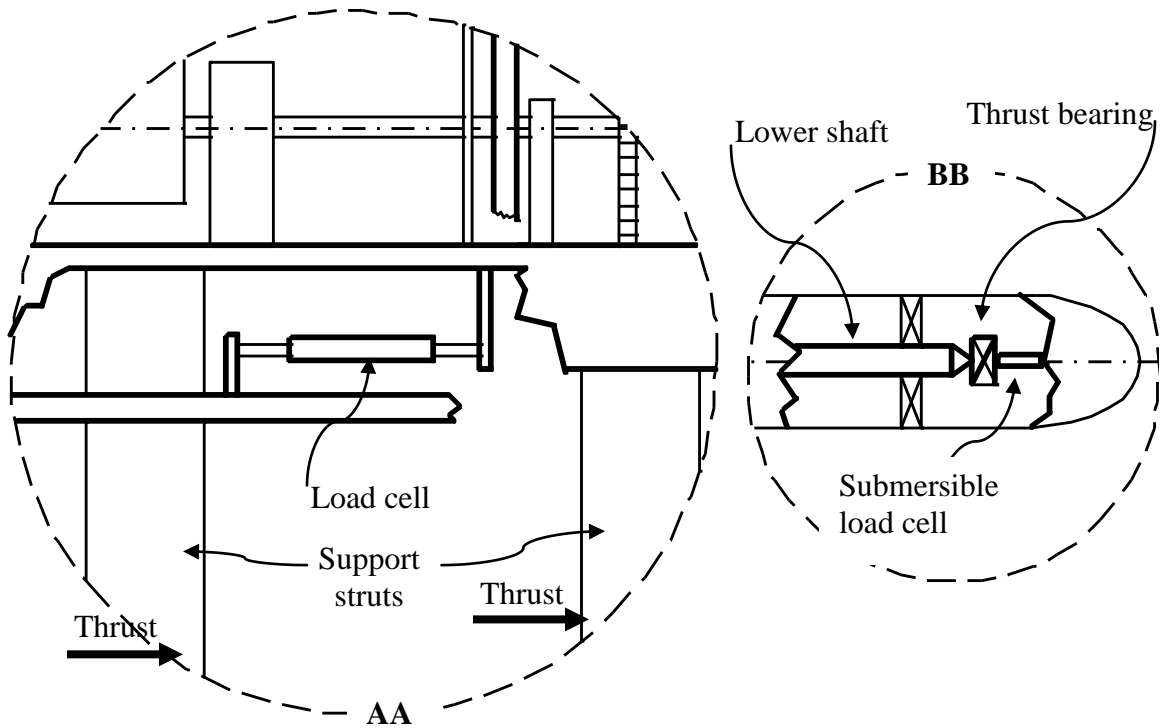


Figure 3.6 Details AA and BB show a blown up view of the schematic in Figure 3.5. AA shows the load cell used for measuring duct thrust. BB shows the load cell used for blade thrust.

3.1.3.4 Turbine Frequency

Turbine frequency (ω) is used in calculating the tip speed ratio (λ). The drivetrain utilizes a position encoder to calculate the turbine frequency from the derivative of the position with respect to time [4].

3.1.3.5 Inflow Velocity

Inflow velocity (V) is also used in calculating the tip speed ratio (λ). The inflow velocity is measured with a position encoder mounted on the tow tank carriage. A rubber wheel rides on the carriage and drives the encoder. The velocity is obtained by taking the derivative of the position with respect to time [4].

3.2 TEST METHODS

Consistent methodical tests were required to obtain usable data from these experiments. This section explains the calibrations and testing methods performed for this thesis.

3.2.1 Calibration

Calibrating the load cells and accounting for friction losses were the most difficult and essential steps for this thesis. Friction losses, especially for torque, are significant and without properly accounting for it, the resulting data is of little value.

3.2.1.1 Torque Calibration

Torque calibration is crucial to obtain meaningful power coefficient results. A calibration of the torque was performed by placing weights on a lever arm attached to the motor. The motor is free to rotate on its bearings, and the force on the torque load cell was recorded. Three trials were performed, each trial consisting of five incrementally heavier weights. The average of the data from each trial was used to obtain an equation for the torque (Q). The data points and curve fit can be seen in Figure 3.7.

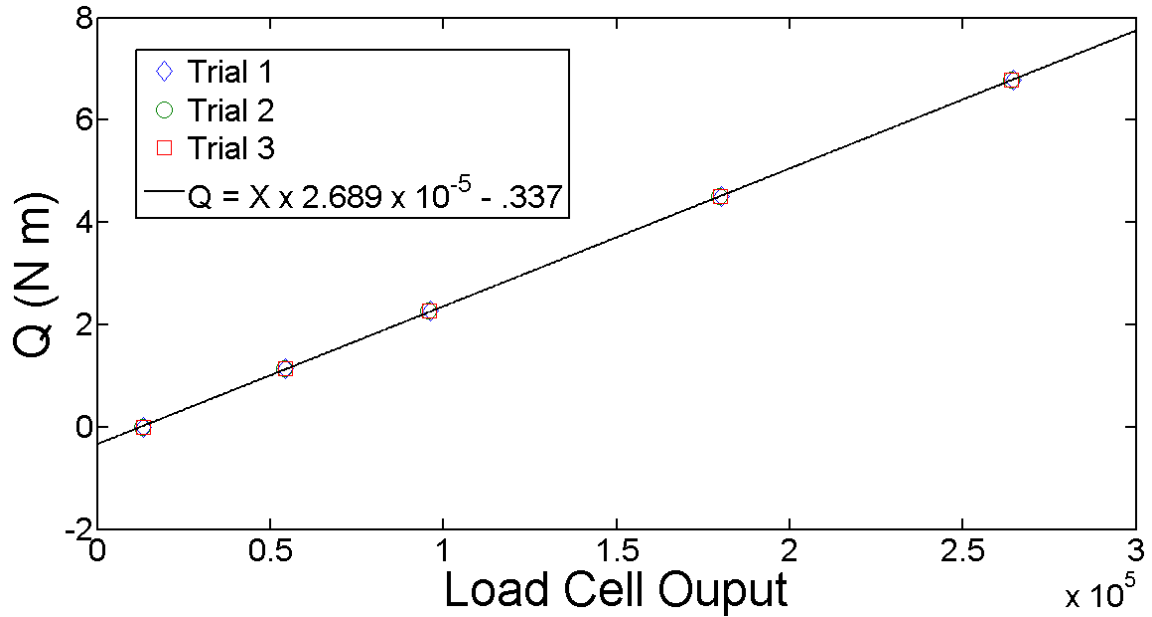


Figure 3.7 Calibration graph of load cell for measuring torque vs. load cell output.

The friction in the drivetrain was measured as a function of turbine frequency. Water acted as a lubricant to the turbine making friction losses in the system significantly lower when the turbine was in the water compared to out of the water. Therefore, friction losses from the drivetrain were measured “wet”. By placing the test platform in the tank without a rotor and creating a torque curve (which is important to create a C_p curve) only the parasitic losses were measured. A third order polynomial ($Q = -5.01 \times 10^{-8}\omega^3 + 1.44 \times 10^{-5}\omega^2 + 1.33 \times 10^{-4}\omega + Q_o Nm$) fit to the data gave the frictional loss in torque as a function of turbine frequency where Q_o is the offset and ω is in rad/s. Figure 3.8 shows the calculated curve along with two sets of experimental data.

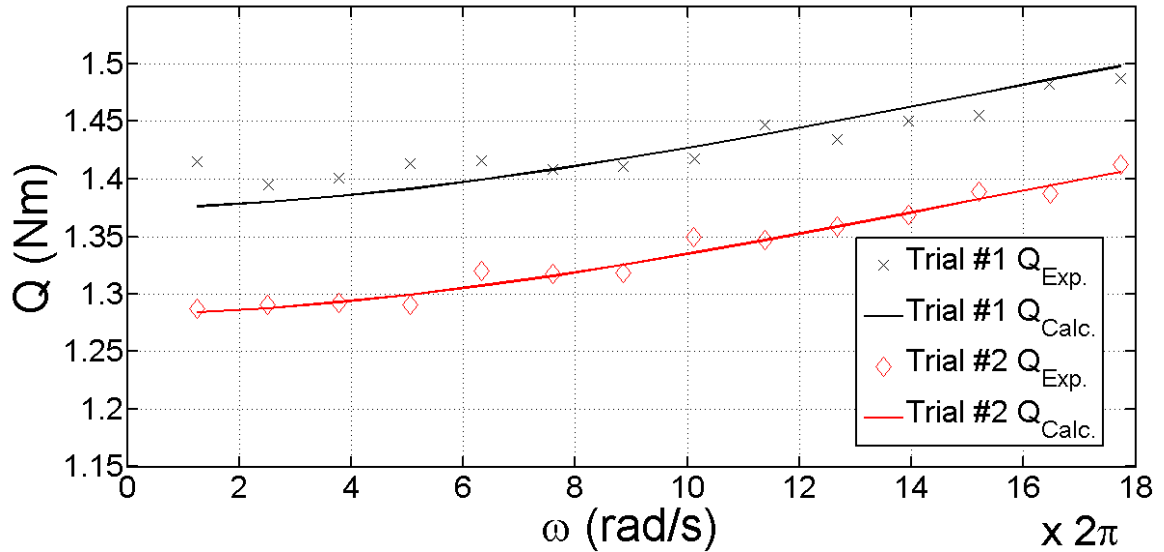


Figure 3.8 Torque friction as a function of turbine frequency. Two sets of data are shown plotted with the calculated curve using two different offsets.

The offset term in Q_o was measured often during testing to ensure any irregularities in rotational friction were accounted for. Due to the difficulty of removing the turbine from the test platform during testing the torque offset was measured by operating the test platform with the turbine in place at a very slow rotational speed. The low turbine speed was not sufficient to create any lift in the turbine blades to contribute to the torque. The torque offset term was measured at least three times (sometimes more) for every C_p curve, at the beginning, middle and end of each data set. The average of these three values was used as the offset term Q_o . Figure 3.8 shows a typical variation in offset before correction.

3.2.1.2 Rotor Thrust Calibration

A calibration equation for the rotor thrust (T_R) load cell was determined in a similar fashion to the equation for the torque load cell. Incrementally heavier, known weights

were applied to the load cell and the output recorded. A polynomial was then fitted to the experimental data. The offset for the polynomial was established by performing a tow tank run with the free tip turbine in place at a low carriage speed (0.0762 m/s). The force on the load cell is negligible at a low carriage speed so the offset could be established for zero force. Since the load cell for the rotor thrust is mounted in the test platform hub and pushed on directly by the rotor via the lower shaft there was no drag force to account for with this measurement. Figure 3.5 and Figure 3.6 illustrate the load cell and lower shaft.

3.2.1.3 Duct thrust Calibration

The load cell for the duct thrust (T_D) was also calibrated in a similar manner to the rotor thrust calibration. An additional complication to measuring the duct thrust was that the duct thrust load cell measured the force for the entire underwater body (T_{OA}). The sum of the rotor thrust, the duct thrust and the test platform drag (D_{OA}) created by the support struts was measured. The rotor thrust and strut drag from previous tests was subtracted to obtain the duct thrust as seen in (3.1).

$$T_D = T_{OA} - T_R - D_{OA} (N) \quad (3.1)$$

3.2.2 Turbine Test Procedure

A standard operating procedure was established for testing. All testing in the tow tank was performed in the same sequence each time to minimize variations in the data. Each data point shown in a performance curve (C_p , C_T etc.) was obtained from a complete carriage run at a fixed tip speed ratio. The carriage and turbine were

accelerated to the desired velocity before data recording started. A minimum of 28 turbine revolutions were obtained for each data point (typically about 15 seconds).

Recording ended prior to carriage deceleration [4].

The range of tip speed ratios for a typical curve in this testing is $1 \leq \lambda \leq 10$ at $\lambda = 0.75$ increments. The turbine is operated at a very low frequency, typically 0.19 Hz, at the beginning, middle and end of testing for the range of tip speed ratios. These low frequency tests are averaged to obtain the offset in the torque load cell. The offset is applied to the measured C_p for these tip speed ratios.

Performance is expressed non-dimensionally. However, it was desirable to perform testing at different inflow velocities (V). Two inflow velocities, $V = 0.91 \text{ m/s}$ and the design velocity, $V = 1.25 \text{ m/s}$ were chosen. This was done to see what affect changing the Reynolds number would have on performance.

Blockage effects were not corrected for in the data and are not considered substantial since the ratio of tow tank area to turbine area, $\frac{A_{tank}}{A_{turbine}} = 48$. This is a much larger ratio than is generally considered significant for blockage effects to be considered [18]. Figure 3.1 shows the dimensions of the axial flow turbine and tow tank.

For the ducted turbine the tip gap ratio ($\frac{t_g}{D}$) was limited to 0.0039 or less based on a tip gap study performed for this thesis (Appendix F) and previously published data for propellers [19][20]. For this turbine $\frac{t_g}{D} = .0039$ translates to 1mm of gap between the rotor tip and duct.

CHAPTER 4. DATA PROCESSING

The data acquisition programmed in LABVIEW [5] provided a binary raw data file that was post processed in MATLAB [9]. Processing the data consisted of separating the binary file into data vectors and calculating calibrated quantities of interest. Filtering was used to remove noise. The mean value of the filtered data is used for calculating performance parameters.

4.1 FILTERING

Noise from the system consisted of mechanical electrical and other sources. Filtering of the data was accomplished in MATLAB [9] using a low-pass Butterworth filter. A hammer test was performed to determine the natural frequency of the system. The natural frequency for this system was in the 38 Hz range as seen in Figure 4.1. A range of filter cutoff levels between 18 Hz to 38 Hz was tried with virtually no change to the mean value of the performance parameters before and after filtering. 30 Hz was chosen as a good middle ground for the cutoff since it provides an adequately clean signal with no risk of over filtering; particularly as mean values were used for calculations. The filtered results of the hammer test can be seen in Figure 4.2. Figure 4.3 shows a typical set of data for Q before and after filtering along with the mean value for both the filtered and unfiltered data. The mean of Q before filtering is -1.201Nm compared to the mean after filtering of -1.200Nm.

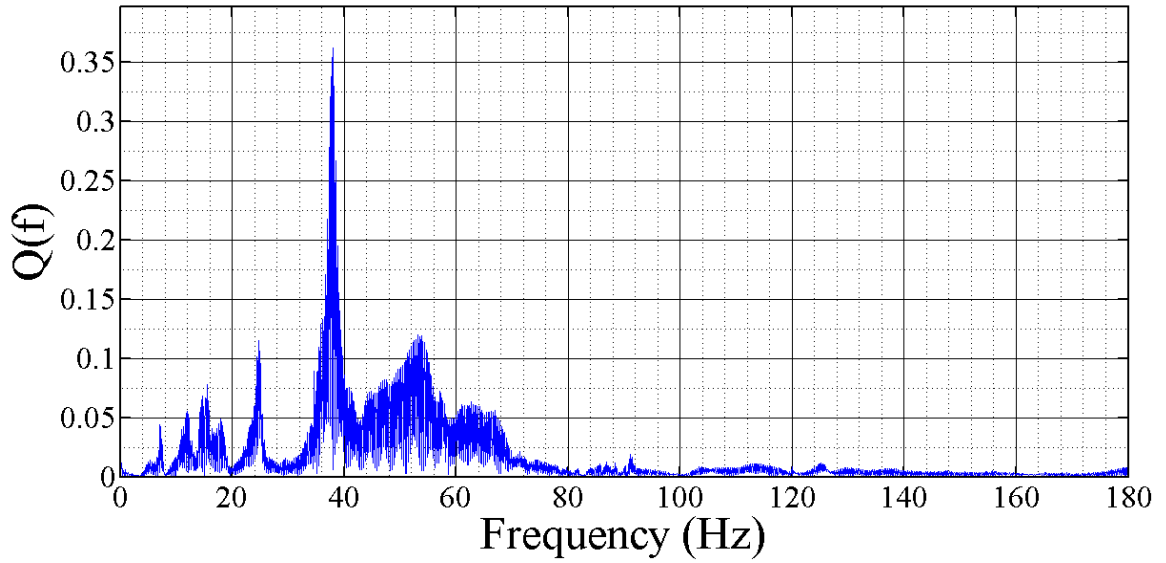


Figure 4.1 This figure shows a single sided Fourier transform of Q during hammer test.

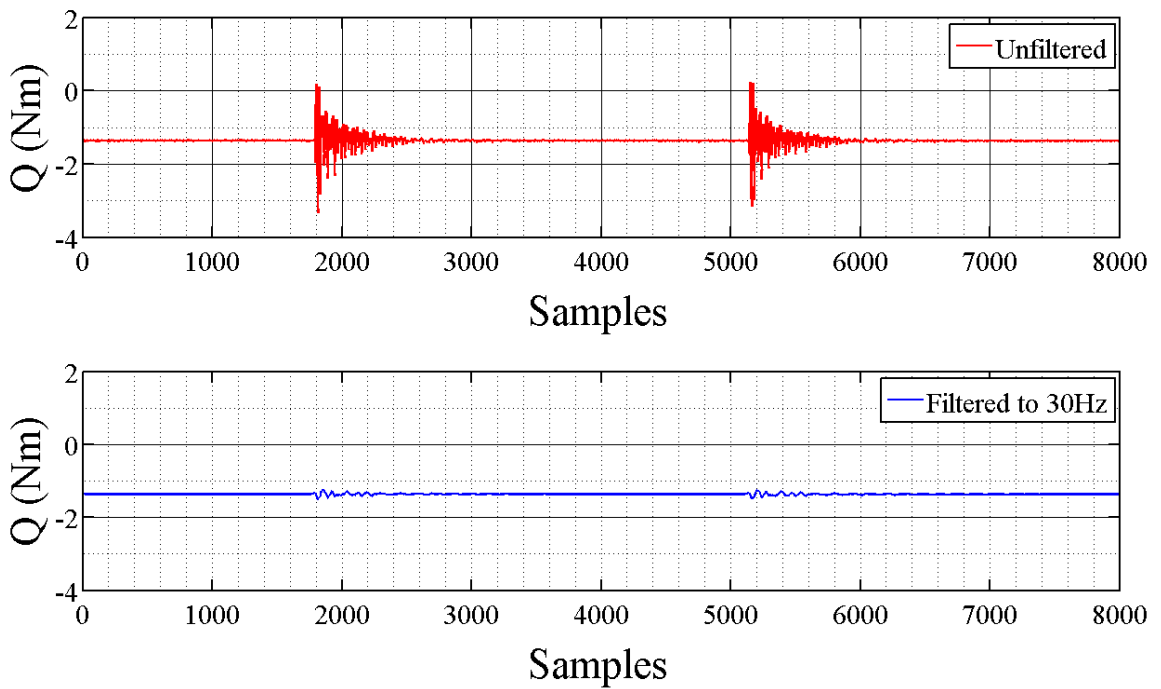


Figure 4.2 This figure shows the torque vs. samples before and after applying 30 Hz low-pass Butterworth filter.

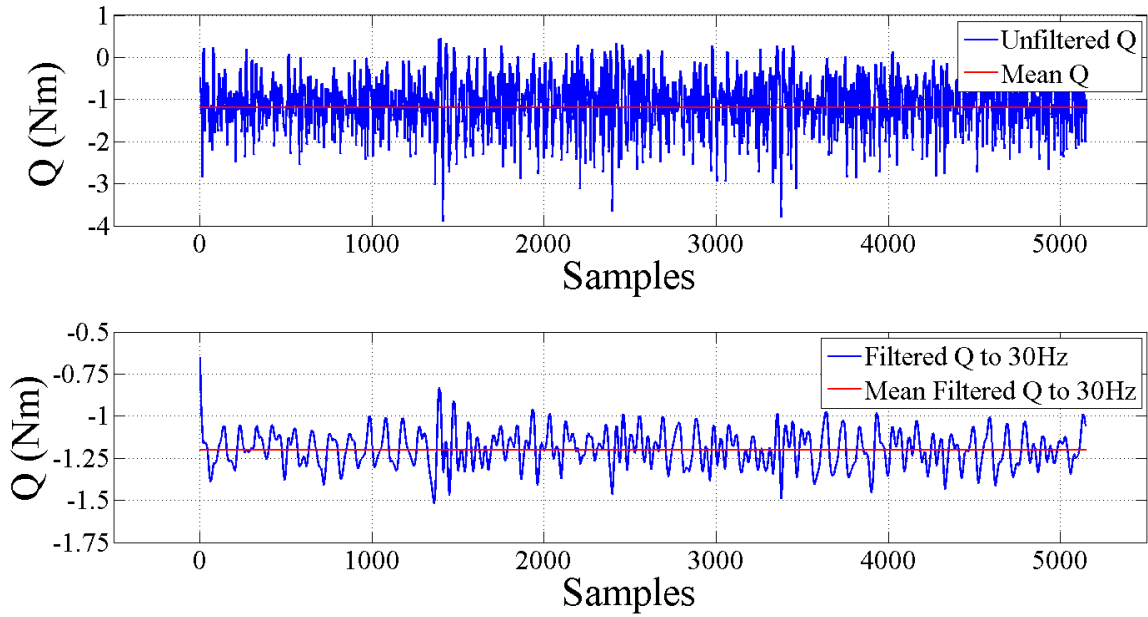


Figure 4.3 A typical set of data for Q vs. samples is shown before and after filtering. The mean values for the filtered and unfiltered data are also displayed.

Figure 4.3 shows the entire data set acquired for a single carriage run. It was not necessary to remove data from the beginning or the end of the run when the carriage is accelerating or decelerating in post processing since that data is not acquired with the data acquisition system.

CHAPTER 5. RESULTS

The results from the experimental work performed for this thesis are presented and described in this chapter. The actual data points instead of mean and range are plotted in order to provide raw data for other researchers. The most important objective of this work is to provide data for model validation. This type of validation data set with an open source turbine is currently lacking, in particular ducted turbine data is currently very limited. Further discussion of the results and conclusions are reserved for Chapter 6.

Results are grouped by estimated Reynolds number. The tests were performed at two different times of the year and consequently at two different water temperatures, the water in the tow tank changed by approximately $9.5^{\circ} C$ over this period. This change in temperature was sufficient to have impacted the testing results. In addition, the two carriage velocities tested display different performance which is also likely to be related to the Reynolds number. Thus, it was determined to be reasonable to group the data by the approximate Reynolds number.

5.1 FREE TIP RESULTS

The free tip turbine was designed to optimize output and as such the blade chord length tapers towards the tips with increasing radius as shown in Figure 2.1. The turbine was tested at a range of tip speed ratios for four different conditions shown in Figure 5.1. The data is non-dimensionalized so would ideally lay on top of each other for all of the conditions. This is in fact the case at lower tip speed ratios. The data was taken at two different times with a difference of 9.5 degrees in water temperature increase. In

addition, between test sessions the tips of the blades were chipped during handling. The effect of this is primarily evident in the C_p data.

5.1.1 Free Tip C_p

In Figure 5.1 the coefficient of performance is shown for the free tip turbine. The maximum of the averaged C_p for $V = 0.91 \text{ m/s}$ is $C_p = 0.41$ and occurred at $\lambda = 4.45$, $Re \approx 104000$. The maximum of the averaged C_p for the designed inflow velocity, $V = 1.25 \text{ m/s}$ is $C_p = 0.44$ and occurred at $\lambda = 4.43$, $Re \approx 142000$. The data in Figure 5.1 for $Re \approx 10400$ appears to be higher than expected when compared to $Re \approx 111000$. Increased blade roughness would explain this difference by causing the flow to be moved out of the transitional region thus having the same effect as increasing Reynolds number. A picture of the turbine with damaged blade tips can be seen in Appendix G.

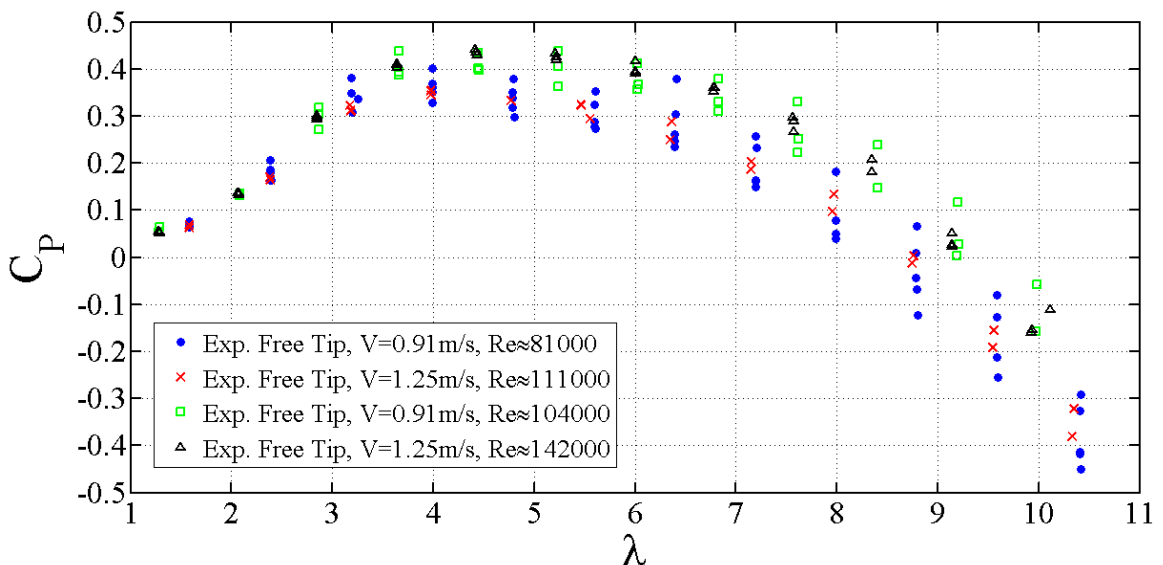


Figure 5.1 The free tip power coefficient vs. tip speed ratio is shown for the range of velocities and Reynolds numbers tested.

5.1.2 Free Tip C_t

The data in Figure 5.2 is for the thrust coefficient (C_t) results of the free tip turbine. The turbine was tested at $V = 0.91 \text{ m/s}$ and $V = 1.25 \text{ m/s}$. The maximum of the averaged C_t for $V = 0.91 \text{ m/s}$ is $C_t = 0.72$ and occurred at $\lambda = 5.24$, $Re \approx 104000$. The maximum of the averaged C_t for $V = 1.25 \text{ m/s}$ is $C_t = 0.74$ and occurred at $\lambda = 5.22$, $Re \approx 142000$.

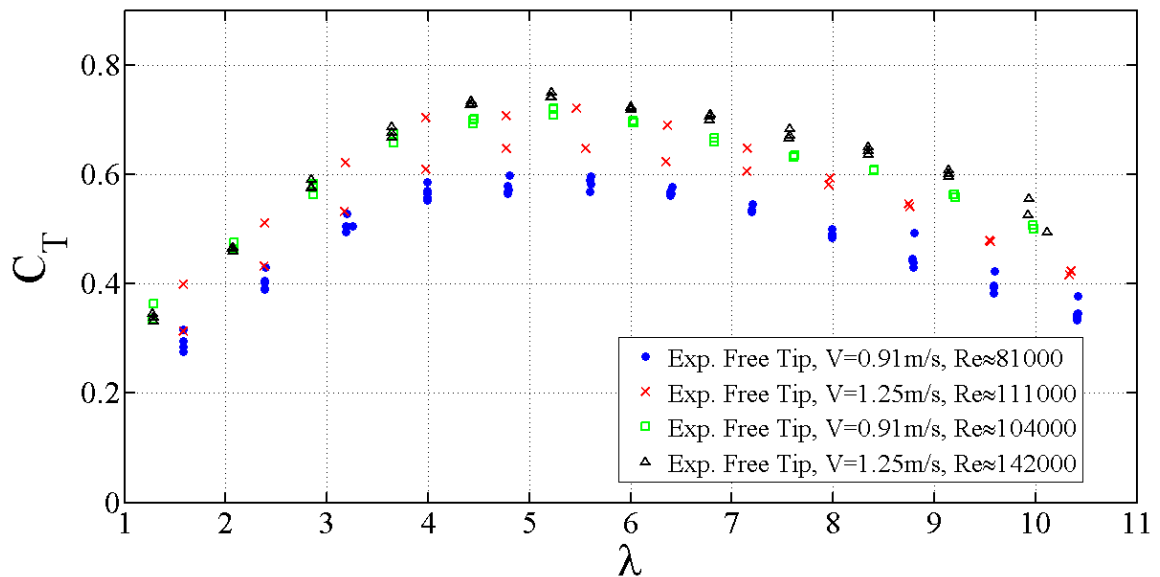


Figure 5.2 The free tip thrust coefficient vs. tip speed ratio is shown for the range of velocities and Reynolds numbers tested.

5.2 DUCTED RESULTS

The second turbine that was developed for this thesis was a ducted turbine for which the design was optimized to work with the duct. The ducted turbine chord length does not taper with increasing radius like the free tip turbine as shown in Figure 2.1. The testing for the ducted turbine was carried out for the same conditions as used for the free tip turbine. The data is also non-dimensionalized with similar Reynolds number effects due to water temperature changes as seen in the free tip turbine.

5.2.1 Ducted C_p

Figure 5.3 shows the C_p results of the free tip turbine at $V = 0.91 \text{ m/s}$ and $V = 1.25 \text{ m/s}$. The maximum of the averaged C_p for $V = 0.91 \text{ m/s}$ is $C_p = 0.36$ and occurred at $\lambda = 3.65$, $Re \approx 104000$. The maximum of the averaged C_p for the designed inflow velocity, $V = 1.25 \text{ m/s}$ is $C_p = 0.40$ and occurred at $\lambda = 4.40$, $Re \approx 142000$.

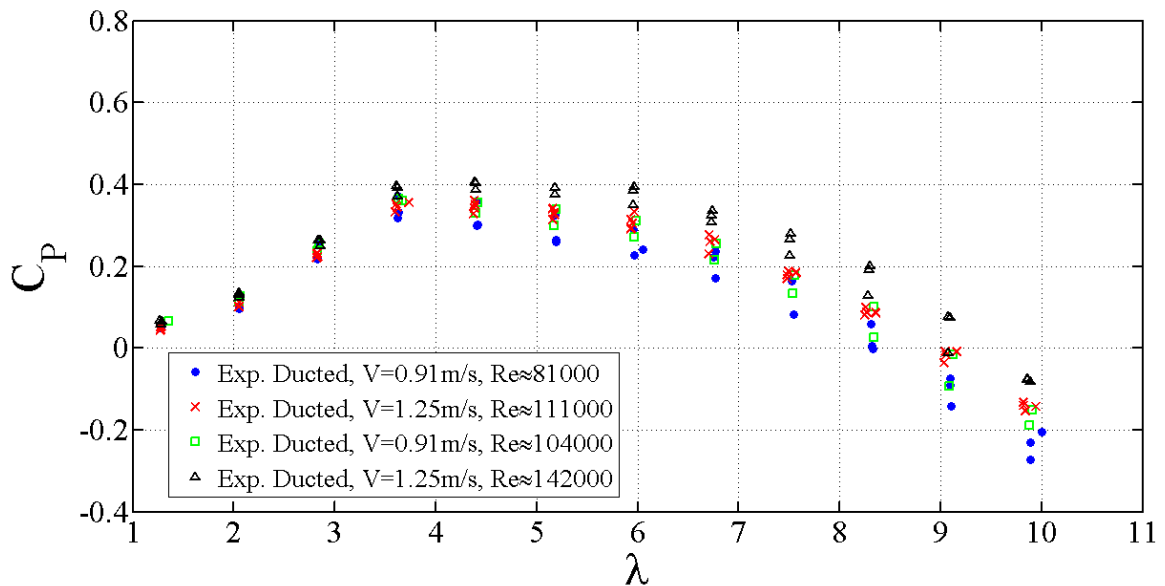


Figure 5.3 The ducted power coefficient vs. tip speed ratio is shown for the range of velocities and Reynolds numbers tested.

5.2.2 Ducted C_t

Figure 5.4 shows the C_t results of the ducted turbine at $V = 0.91 \text{ m/s}$ and $V = 1.25 \text{ m/s}$. The maximum of the averaged C_t for $V = 0.91 \text{ m/s}$ is $C_t = 0.67$ and occurred at $\lambda = 5.94$, $Re \approx 104000$. The maximum of the averaged C_t for $V = 1.25 \text{ m/s}$ is $C_t = 0.68$ and occurred at $\lambda = 5.96$, $Re \approx 142000$.

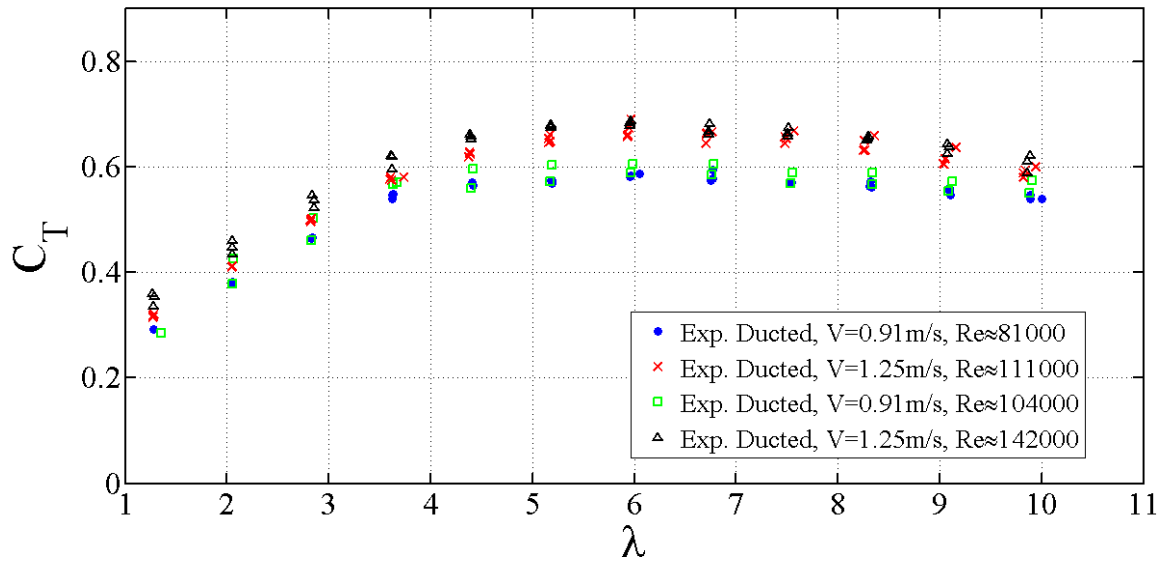


Figure 5.4 The thrust coefficient vs. tip speed ratio of the ducted turbine is shown for the range of velocities and Reynolds numbers tested.

5.2.3 Duct Thrust Coefficient

The duct thrust coefficient (C_{TD}) is shown below in Figure 5.5 Note that C_{TD} has an average of about at $C_{TD} \approx .08$ and remains almost flat through the range of λ .

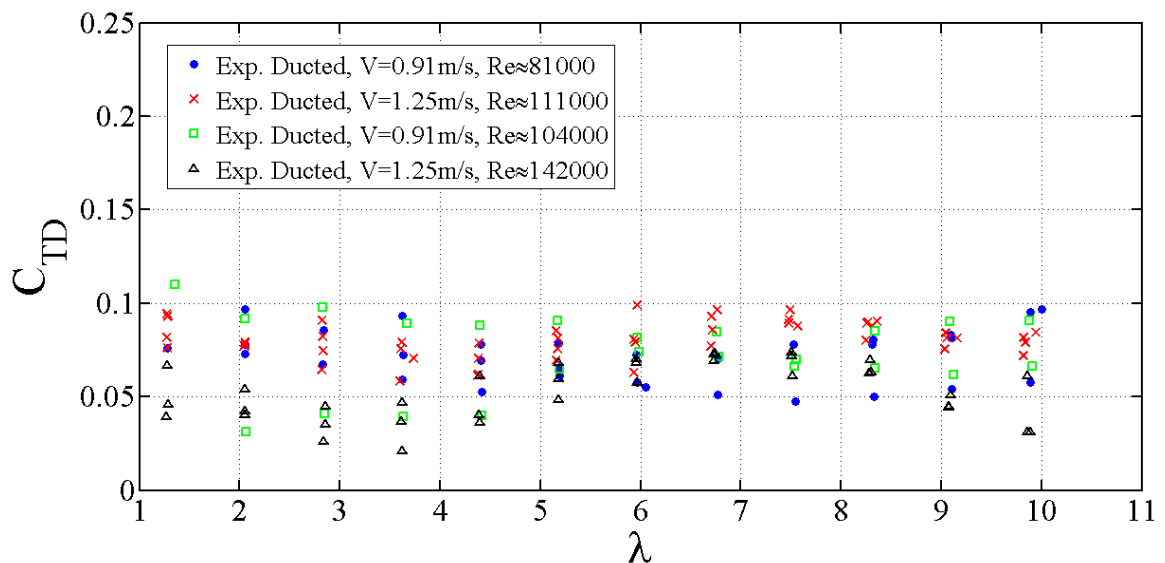


Figure 5.5 The duct thrust coefficient vs. tip speed ratio is shown for the range of velocities and Reynolds numbers tested.

5.2.4 Ducted Turbine Rotor Without Duct

Testing was performed on the ducted turbine to examine what effect the duct had on the rotor. This was accomplished by testing the rotor used for ducted turbine testing with the duct removed. While this is not the focus of this thesis it is useful in ascertaining the overall effect of the duct.

5.2.4.1 C_p For Ducted Turbine Rotor Without Duct

Figure 5.6 shows that the duct had very little effect on C_p . The results from the two Reynolds numbers tested ($Re \approx 104000$ and $Re \approx 142000$) compared to the tests with the duct in place are within the range of uncertainty defined in Appendix E and therefore statistically the same. The Reynolds number effects seen throughout the other results can also be seen here.

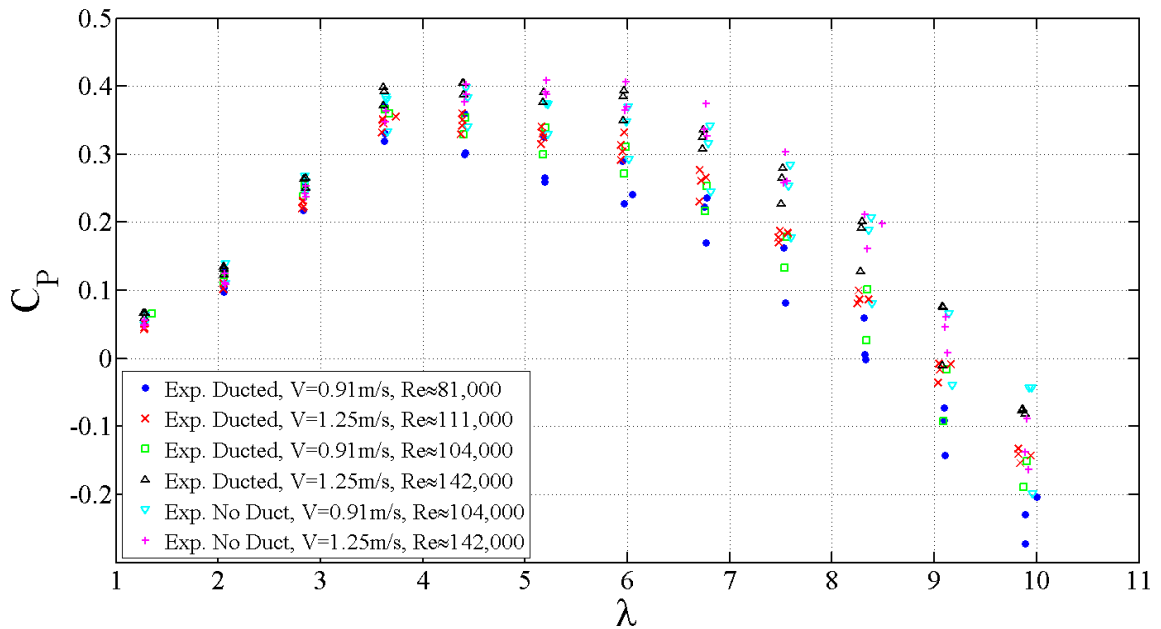


Figure 5.6 C_p vs. tip speed ratio for the ducted turbine rotor without the duct is shown with results of the same rotor with the duct.

5.2.4.2 C_t For Ducted Turbine Without Duct

Figure 5.7 show the results of the thrust coefficient for the ducted turbine without the duct plotted with the results for the ducted turbine with the duct. The thrust coefficient shows a small overall increase without the duct verses with the duct.

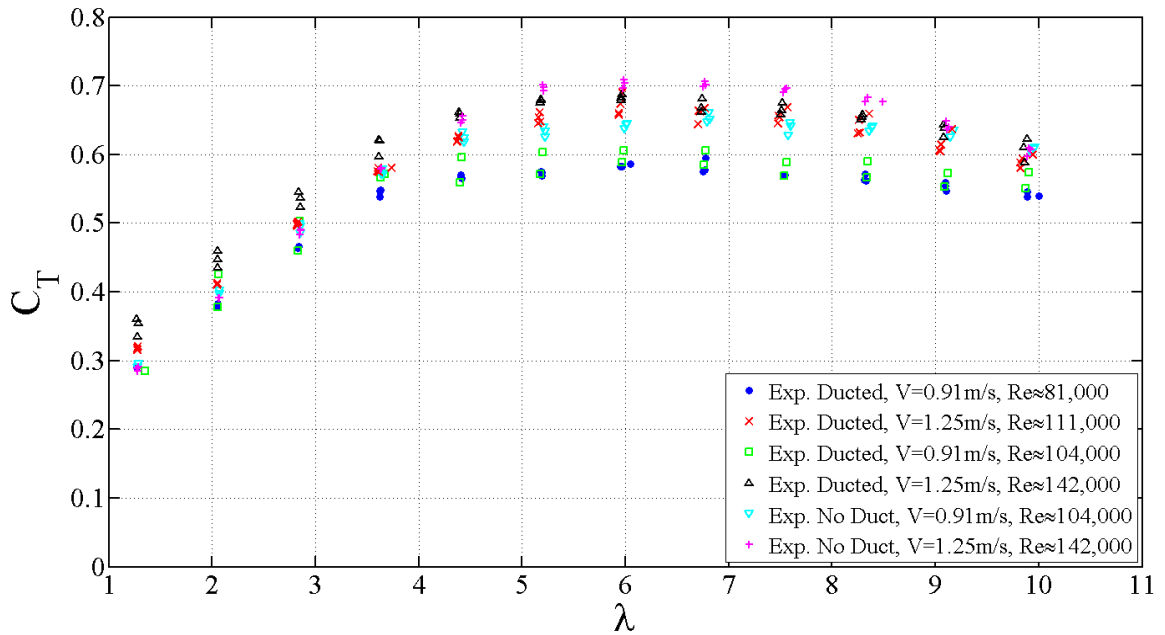


Figure 5.7 C_T vs. tip speed ratio for the ducted turbine without the duct is shown with results of the same rotor without the duct.

CHAPTER 6. DISCUSSION AND CONCLUSIONS

This section discusses the results and compares the experimental data to predictions from the OpenProp program for both the free tip and ducted turbines. Several factors were found to play important roles in this testing. They include temperature related Reynolds number effects, blade roughness, uncertainty and repeatability of the instrumentation and duct optimization.

6.1 DISCUSSION

The free tip turbine performed close to predictions but the ducted turbine did not perform as was expected. The underperformance of the ducted turbine may have been a result of inadequate duct lift force. The lack of lift force requires further study but some hints to its possible causes are in the data and will be discussed in the coming sections.

Results of C_p for the two turbines are shown in Figure 6.1 and Figure 6.2.

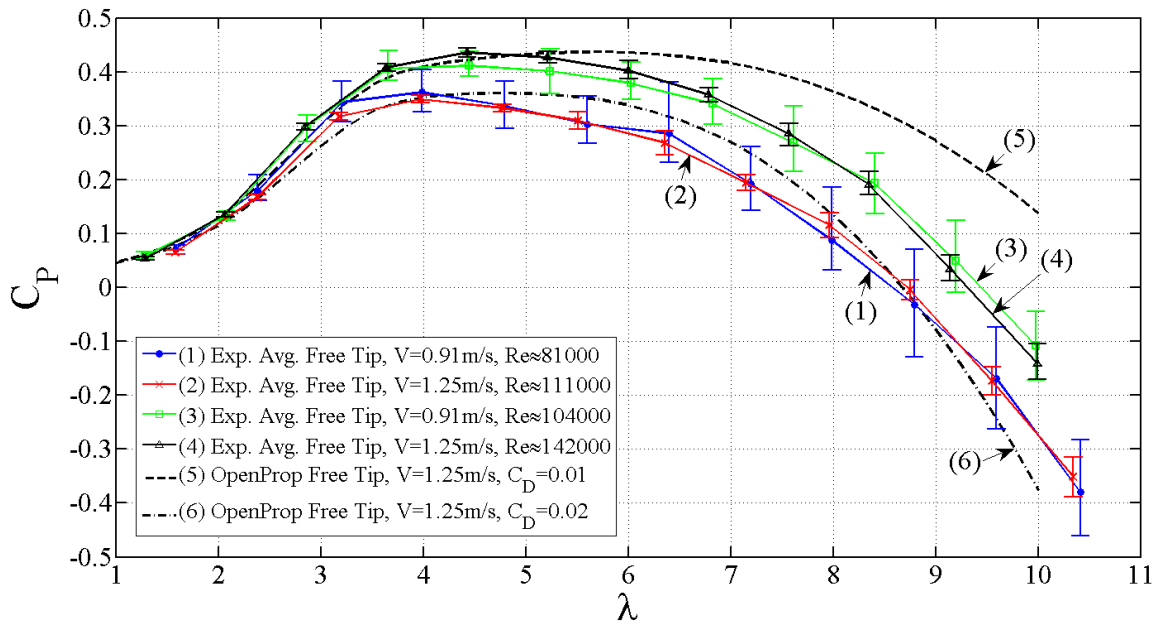


Figure 6.1 Free tip average C_p vs. tip speed ratio is shown for the two carriage speeds. The Reynolds numbers represent the change in both the velocity seen at the blade and water temperature.

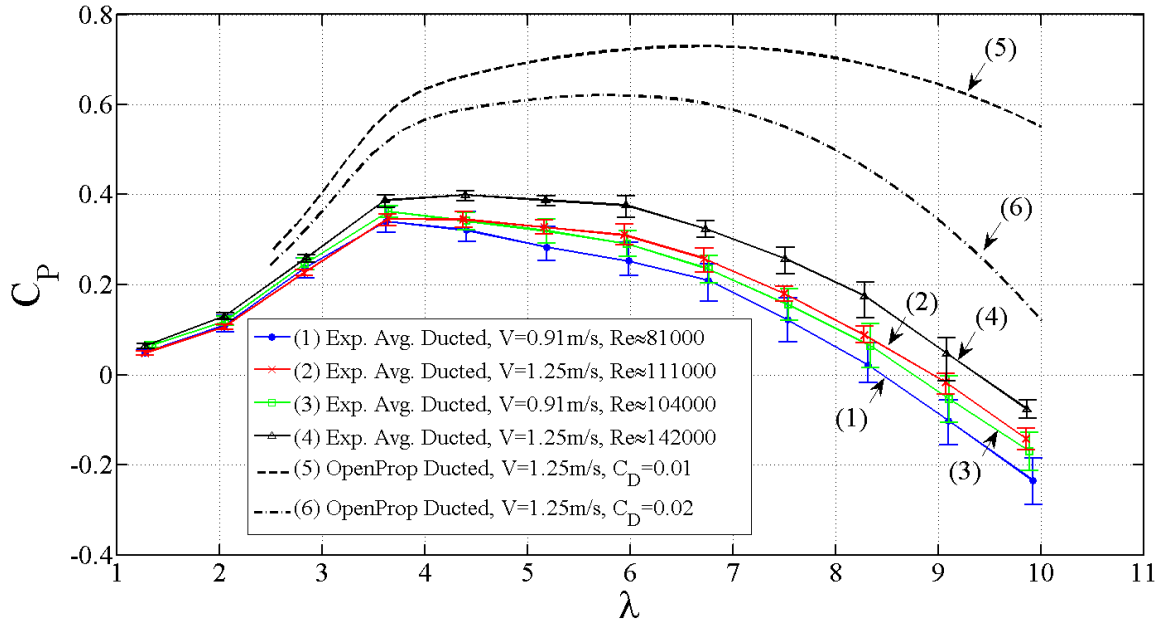


Figure 6.2 Ducted average C_p vs. tip speed ratio is shown for the two carriage speeds. The Reynolds numbers represent the changes in the velocity seen at the blade and in the water temperature.

To more easily see the trends, results in this chapter are displayed as averages with error bars are added to show the quality of the data. Error bars (E) include instrumentation uncertainty (w) and experimental repeatability (Δ). The method used to calculate w and Δ can be found in Appendix E. The error bars were found by combining w and Δ , $E = \sqrt{w^2 + \Delta^2}$.

As discussed in Chapter 5 the acquired data has shown that the Reynolds number has an influence on blade forces [21] [22] which in turn effects C_p and C_T . This explains the variations between OpenProp predictions and experimental data as shown for the free tip case in figure Figure 6.1. This also holds true for the data from the ducted case (Figure 6.2) but with added complication of the duct fluid dynamics.

6.1.1 Reynolds Number and Water Temperature Effects

Reynolds number (Re) effect is an important factor to consider for this scale of testing. It has a major effect on the lift and drag (blade forces) of the turbine. The lift and drag in turn affects the torque and thrust created by the turbine, which are needed to calculate C_p and C_T . For the range of Reynolds numbers shown for this testing ($81000 \lesssim Re \lesssim 142000$) the blades are operating in the transitional range and could be at least partially stalling up to $Re \approx 140000$ thereby reducing performance [21] [22].

The Reynolds numbers displayed for this study are approximations based on common practice and the best information available. The Reynolds numbers were found using $Re = \frac{\rho V^* C}{\mu}$ where ρ = density, V^* = local velocity, C = blade chord length and μ = viscosity. By convention the chord length and local velocity is taken at $r/R = .7$ [21][22]. The blade chord length was found from the OpenProp geometry file. V^* for both the free tip and ducted turbine were found using free tip OpenProp code and includes radial, axial and induced velocity components [6].

V^* from the free tip code was used for the ducted turbine since OpenProp over predicts the performance for ducted turbine by more than 50% (Figure 6.2) but comes closer to the experimental performance with the free tip turbine code (Figure 6.1). The velocity for the ducted turbine should therefore be a closer approximation using the free tip code.

The Reynolds number, Re, is highly dependent on the water temperature in the tow tank because of the effect on viscosity, μ , and to a lesser degree on the density, ρ . Water temperature records for the tow tank began in March and do not exist for all of the first set data shown at $Re \approx 81000$ and $Re \approx 111000$. Some of the data for those

Reynolds numbers was taken when the water was colder during the month of January while the rest was taken in March and April when water temperatures were recorded at about 10°C. The temperature of the water for testing done in January was conservatively estimated to be 10°C and could have been colder since the ambient temperature was colder in January. Temperature records for the tow tank for later testing at $Re \approx 104000$ and $Re \approx 142000$ show the water at 19.5°C. The 9.5°C temperature change accounts for the change in Re at the same inflow velocity (V).

6.1.1.1 Free tip turbine

C_p for the free tip turbine (Figure 6.1) shows reasonably good agreement with OpenProp. The maximum experimental $C_p = .44$ which occurred at the design velocity of $V = 1.25 \text{ m/s}$. This compares to the maximum $C_p = .44$ from OpenProp. Results from the lower Reynolds numbers ($Re \approx 81000$ and $Re \approx 11000$) show reasonable correlation with OpenProp predictions and with previous experimental data at $C_D = .02$ [6].

Testing at higher Reynolds number ($Re \approx 104000$ and $Re \approx 142000$) shows an increase in efficiency over the lower Reynolds numbers that could indicate at least part of the turbine is operating in the transition range. The peak experimental data of $C_p = .44$ matches the peak prediction of C_p from OpenProp at $C_D = .01$. The lower drag coefficient is consistent with drag coefficients typically used for marine propeller testing [6]. It is also consistent with published data for marine propellers showing that at least some testing was performed in the transition range [21] [22].

As discussed in Chapter 5 the data in Figure 6.1 for $Re \approx 10400$ appears to be higher than expected when compared to $Re \approx 111000$. Increased blade roughness explains this

difference by causing the flow to be moved out of the transitional region thus having the same effect as increasing Reynolds number. This is consistent with published data on wind turbines showing the effects of blade roughness on C_p [23]. A picture of the damaged blade can be seen in Appendix G.

6.1.1.2 Ducted Turbine

Results from the ducted turbine while informative are not as expected. The ducted turbine is affected by the Reynolds number in the same way as the free tip turbine. Curves (1-4) in Figure 6.2 show a trend of increased C_p along with increased Reynolds number. Curve (4) shows the best performance of $C_p = .40$ for the ducted turbine, it also represents the data for the highest Reynolds number. This is well below the predictions of OpenProp. Reynolds number effects and blade roughness do not explain the low performance for the ducted turbine, however some other data collected from this research helps.

6.1.2 Duct Thrust

Some insight to performance of the ducted turbine can be gained from looking at the duct thrust coefficient. As stated in section 2.2, OpenProp does not optimize the duct but provides a duct lift coefficient and inflow angle to aid in duct design. These values are based in part, on the duct thrust coefficient that is entered in OpenProp ($C_{TD} = .2$ as designed). The duct thrust coefficient (Figure 6.3) plays an important role in understanding why ducted C_p falls short of predictions. The duct thrust coefficient (Figure 6.3) shows very little change in experimental C_{TD} , while OpenProp predicts that C_{TD} should rise.

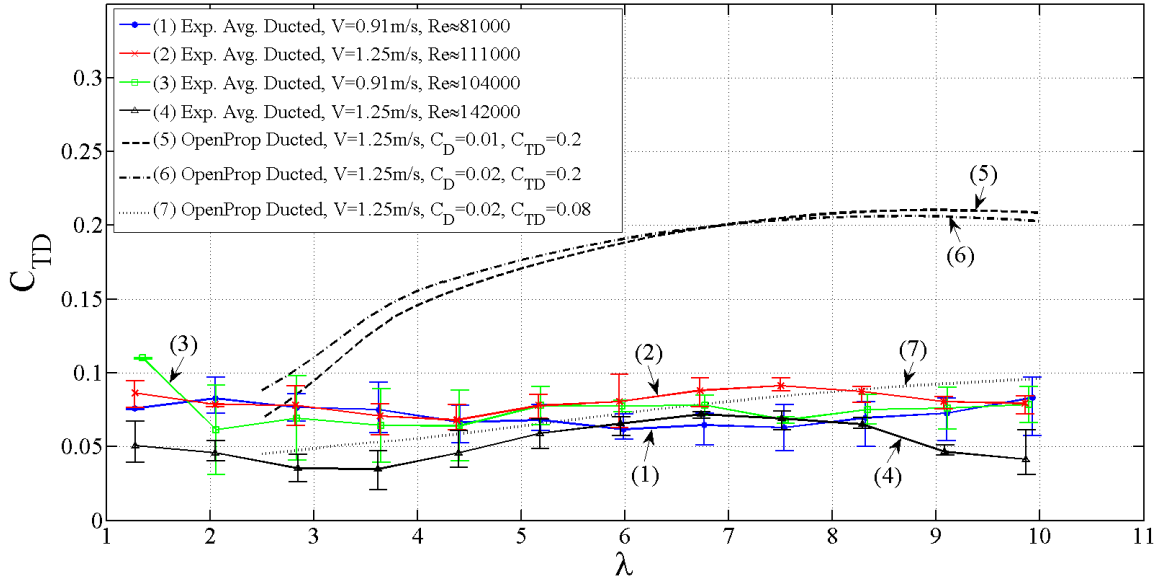


Figure 6.3 Duct thrust coefficient vs. tip speed ratio is shown for the two carriage speeds. The Reynolds numbers represent the changes in the velocity seen at the blade and in the water temperature. OpenProp predictions at $C_D = .01$ and $C_D = .02$ are also shown.

This relatively flat value of $C_{TD} \approx .08$ throughout the range of λ is indicative that the duct is not providing a contributing lift force and that C_{TD} is due only to drag. λ is varied by changing the frequency of the turbine at a given carriage speed (V) which would lead to a constant duct thrust coefficient if the duct produced no lift and C_{TD} was only due to drag. There are several possible causes for the duct to underperform. They include:

- Separation of the boundary layer on the duct caused by an adverse pressure gradient created by the rotor inside the duct [24][18].
- Lower than expected inflow velocity (V^*) to the duct as found by OpenProp.
- Incorrect inflow angle (β_{iD}) to the duct as found by OpenProp.
- Incorrect assumption made about the duct drag coefficient that was entered into OpenProp.

To examine what qualitative affect an incorrect duct drag coefficient would have on duct performance XFOil [15] was used to find the drag coefficient of the duct (C_D). Figure 6.4 shows the range of lift and drag coefficients for the range of Reynolds numbers that the duct might see. At the designed inflow velocity of $= 1.25 \text{ m/s}$ $C_D \approx .012$.

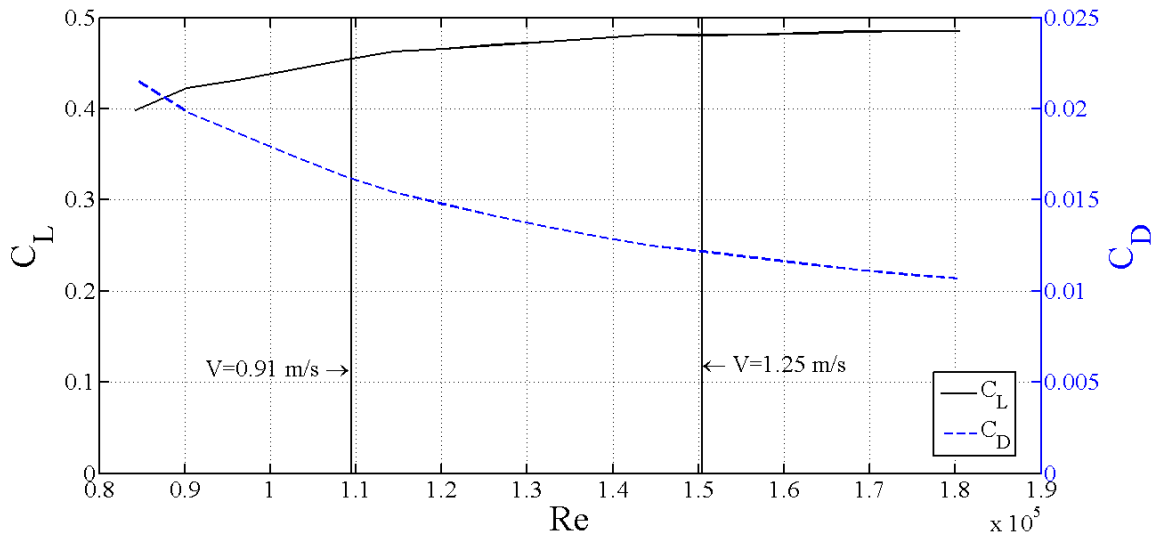


Figure 6.4 C_L & C_D for the duct as a function of Re.

The duct drag coefficient is entered into OpenProp by the user. The design for the duct was done with $C_D = .02$ (see Appendix C). If the value of $C_D = .012$ from XFOil [15] is used as the input to OpenProp it changes the output parameters used in the duct design, as explained in Chapter 2, substantially. The duct lift coefficient changes from $C_{LD} = .5$ to $C_{LD} = .2$ and the duct inflow angle changes from $\beta_{iD} = -1^\circ$ to $\beta_{iD} = 0^\circ$. These parameters substantially change the design of the duct. For instance the importance of β_{iD} can be by examining Figure 6.5 .

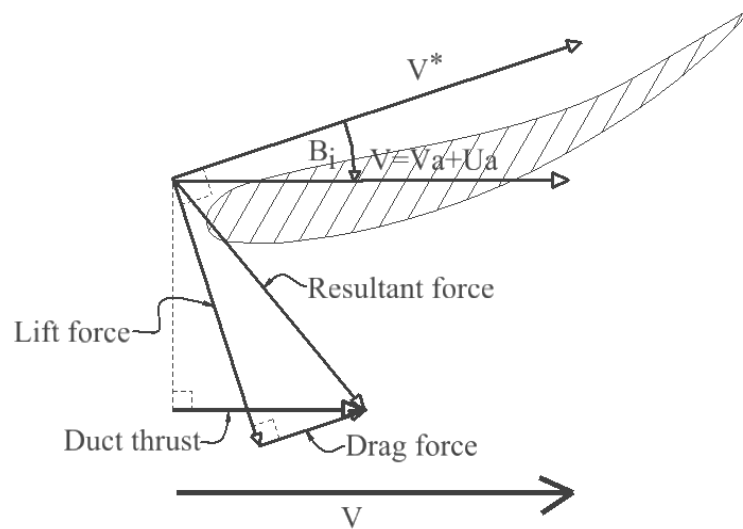


Figure 6.5 This figure shows the upper half of a duct with the relevant force vectors drawn in. It is representative only and is not to scale.

Figure 6.5 shows that the duct lift force acts perpendicular to V^* [25]. If $\beta_{iD} = 0^\circ$ then the lift force would act perpendicular to V and not contribute to the duct thrust as shown in Figure 6.5. This means that the duct thrust coefficient (C_{TD}) would be a function of only drag force and not of lift force leading to a constant C_{TD} as exhibited in Figure 6.3.

6.1.3 OpenProp Validation

Even though the ducted turbine did not perform as expected, it does not necessarily follow that the data is not useful for validation of the ducted turbine in OpenProp. While the design of the duct was not optimal a robust code should work off-design as well as for an optimal design. Given that C_{TD} was provided as an input to OpenProp, an investigation was made to see if OpenProp would predict a more accurate C_p curve if the experimental value of C_{TD} was provided as the input. Figure 6.6 shows OpenProp's prediction of C_p , curve (7), using experimental $C_{TD} = .08$.

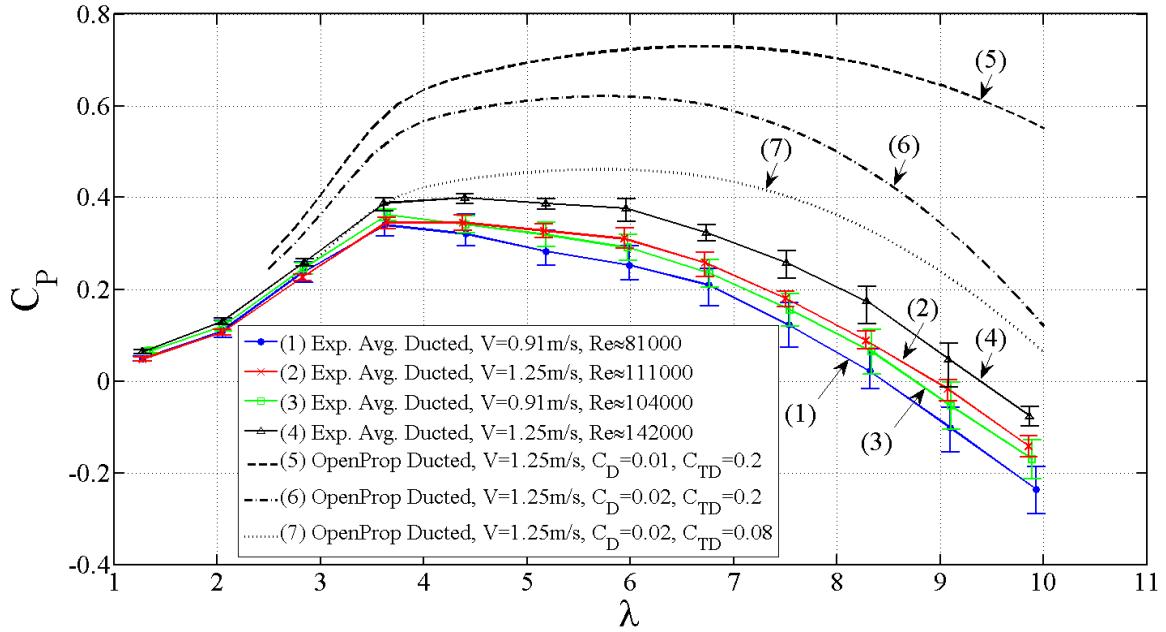


Figure 6.6 Ducted power coefficient vs. tip speed ratio of experimental data and OpenProp predictions. Curve (7) shows C_p from OpenProp adjusted with experimental $C_{TD} = .08$.

Figure 6.6 shows that C_p has a much closer match at low tip speed ratios but is still not a good fit at higher tip speed ratios entering experimental $C_{TD} = .08$ as the input to OpenProp.

It is important to note that currently OpenProp does not provide the ability to analyze existing turbine geometry. For the ducted turbine case the code always optimizes the geometry of the turbine. The difference in the output files for the turbine geometry was examined from $C_{TD} = .2$ to $C_{TD} = .08$ and found to be very small. So, curve (7) is an approximation but is a reasonable one.

6.1.4 Free Tip and Ducted C_T Discussion

The average thrust coefficients with uncertainty bars for the free tip and ducted turbines are shown below in Figure 6.7 and Figure 6.8. These figures do not agree well

with OpenProp for either case but are consistent with the Reynolds number effects discussed in this chapter. Figure 6.8 also includes OpenProp's prediction using the experimental value of $C_{TD} = .08$ as input. No published data for thrust coefficients of marine turbines could be found for comparison purposes.

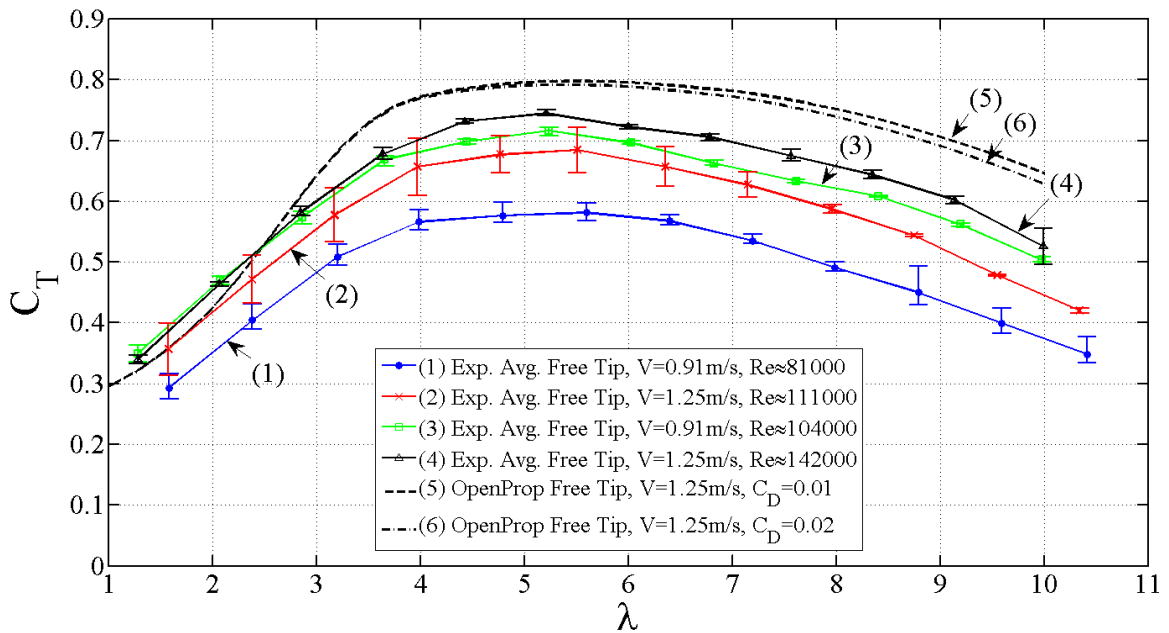


Figure 6.7 Free tip average C_T vs. tip speed ratio is shown for the two carriage speeds. The Reynolds numbers represent the changes in the velocity seen at the blade and in the water temperature.

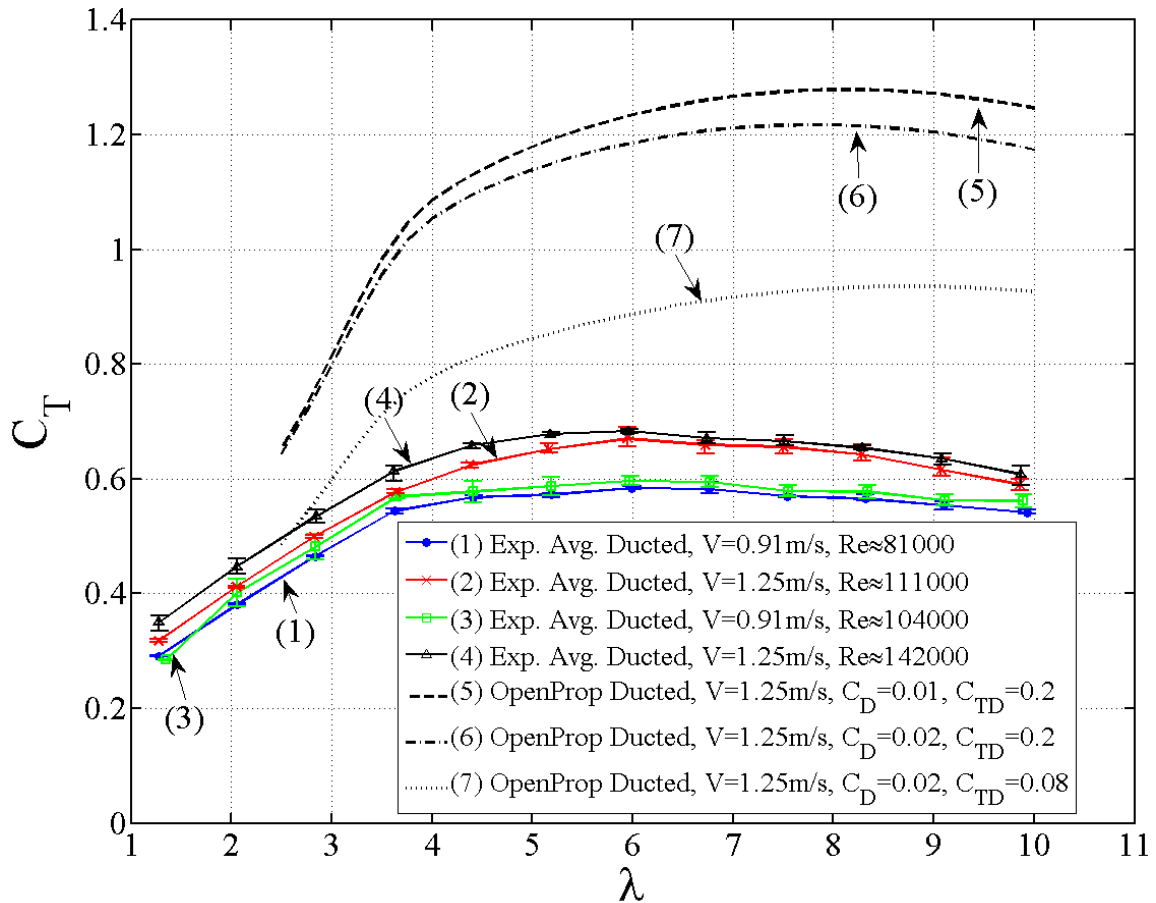


Figure 6.8 Ducted average C_T vs. tip speed ratio is shown for the two carriage speeds. The Reynolds numbers represent the changes in the velocity seen at the blade and in the water temperature. OpenProp prediction with $C_{TD} = .08$ is added for comparison.

6.2 CONCLUSIONS

A free tip and ducted turbine was designed, built and tested at a range of tip speed ratios of $1 \lesssim \lambda \lesssim 10$ for two inflow velocities $V = .91 \text{ m/s}$ and $V = 1.25 \text{ m/s}$. The free tip turbine performed as expected with a maximum $C_p = .44$, the same as OpenProp's prediction of maximum $C_p = .44$. This is consistent with published data on the free tip turbine designed with OpenProp [26] and provides a benchmark against which to check both the design method and testing procedure. The overall power coefficient obtained

from the ducted turbine reached a maximum of $C_p = .40$. The measured C_p is considerably lower than the $C_p = .65$ predicted with OpenProp. The ducted turbine was also tested with the duct removed and displayed very little change in C_p when compared to tests performed with the duct in place (Figure 5.6).

The primary goal of this thesis was to provide ducted axial flow tidal turbine data for other researchers to validate numerical design codes against. This goal has been met by providing C_p , C_T and C_{TD} for a range of Reynolds numbers and inflow velocities as shown in Figure 5.3, Figure 5.4 and Figure 5.5 respectively.

Both turbines exhibited performance changes based on Reynolds number by showing higher values of C_p with at higher Reynolds numbers. This is consistent with published data showing that the turbines are operating in the transitional region at this scale of testing and Reynolds number effects as well as blade roughness play an important role in performance [27] [28]. Water temperature played a significant role in performance because Reynolds numbers is a function of temperature.

The duct did not perform as expected and had very little impact on turbine performance. Examination of the duct thrust coefficient provides some insight into why the duct did not perform as expected by displaying a nearly constant value of $C_{TD} \approx .08$ throughout the range of tip speed ratios. The nearly constant value of the duct thrust indicates that the duct is not providing the lift component that contributes to the duct thrust. In the absence of a lift component the duct does not increase the C_p . No specific cause for the lack of lift was determined but several possibilities explanations are presented in Chapter 6.

The fact that the data for the free tip model matches OpenProp reasonably well suggests that the approach to taking the data is a reasonable way to validate the code. OpenProp should prove to be a useful design tool for free tip turbines. Data for the ducted turbine demonstrates the challenges associated with designing a ducted turbine. Continuing development of OpenProp is needed in order for the code to be useful for ducted turbine designs. Further validation with optimized ducts will also be needed prior to making extensive use of the design code.

6.3 FUTURE WORK

There are several areas that could be improved in modeling and testing. The ones this author suggests beginning with are stated below, in no particular order of importance.

6.3.1 Experimental

The turbine test platform requires carefully calibration for frictional losses. Some of the measured values for this testing are very small, in some cases much smaller than the frictional loss, i.e., the measured torque is smaller than the tare. This correction is inherently difficult. A new test platform should be developed to minimize friction from the experimental setup. The new platform should be designed to use a dry hub and a six-axis load cell. A control motor in line with the shaft will minimize the number of parts but will introduce additional seal problems. However, assuming that a proper shaft seal can be found this system should produce more repeatable results.

6.3.2 Modeling

The modeling of the ducted turbine in OpenProp has not been previously validated.

Some areas that the ducted turbine model could benefit from include:

- Implement tip gap model
- Implement duct optimization routine
- Implement a function for ducted turbines to analyze existing geometry for off-design conditions
- The design tip speed ratio for the testing in this thesis is $\lambda = 7$. For both the free tip and ducted cases the maximum power coefficient occurs between $\lambda = 4$ and $\lambda = 5$; this is also supported by previous work [26]. This critical aspect of the turbine design is also in need of additional work in the model

WORKS CITED

- [1] [Online]. Available: <http://www.marineturbines.com/>. [Accessed 4 June 2012].
- [2] A. J. W. B. A.S. Bahaj, "Power and thrust measurements of marine current turbines under various hydrodynamic flow conditions in a cavitatoin tunner and towing tank," *RENEWABLE ENERGY*, 2005.
- [3] B. Kirke, "Developments in Ducted Water Current Turbines," www.cyberaid.net, Sustainable Energy Centre, University of South Australia, Mawson Lakes, SA 5095, Austrailia, 2003.
- [4] G. S. deBree, "Testing and Modeling of High Solidity Cross-Flow Tidal Turbines," University of Maine, Orono, Maine, 2012.
- [5] *Labview, National Instruments*, North Mopac Expressway, Austin, TX 78759.
- [6] B. P. Epps, "PhD Thesis, An Impulse Framework for Hydrodynamic Force Analysis:," MIT, Cambride, MA, 2010.
- [7] J. W. Ketchum, "Design, Build and Test of an Axial Flow Hydrokenetic Turbine with Fatigue Analysis," MIT, Cambride, MA, 2010.
- [8] R. Kimball, "'OpenProp v2.4 Propeller/Turbine Design Code," <http://openprop.mit.edu>, 2010.," [Online]. Available: http://openprop.mit.edu/~openprop/wiki/index.php?title=Main_Page. [Accessed 11 January 2012].
- [9] *Mathworks, Natick MA. USA*.
- [10] W. B. Coney, "A Method for the Design of A Class of Optimum Marien Propulsors," MIT, Cabridge, MA, 1989.
- [11] J. M. Stubblefield, "Numerically-Based Ducted Propeller Design," MIT, Cabridge, MA, 2008.
- [12] *Marine Current Turbines Limited, Stoke Gifford, Bristol, UK*.
- [13] *Siemens AG, Munich, Germany*.
- [14] V. B. H. Schneekluth, *Ship Design for Efficiency and Economy*, Oxford, UK: Butterworth-Heinemann, 1998.

- [15] M. Drela, "XFOIL," [Online]. Available: <http://web.mit.edu/drela/Public/web/xfoil/>. [Accessed 8 June 2012].
- [16] *Dassault Systèmes SolidWorks Corporation*, 175 Wyman Street, Waltham, MA 02451.
- [17] *Parker Hannifin Corporation*, Rohnert Park, CA..
- [18] R. Kimball, *Personal Communication*, June 2012.
- [19] R. W. Kimball, "Experimental Investigation and Numerical Modelling of a Mixed Flow Marine Waterjet; Ph.D. Thesis," Massachusetts Institute of Technology, Cambridge MA, 2001.
- [20] S. L. B. S. V. M. F. M. C. F. Gaggero Stefano, "Comparison of experimental measurements and numerical calculations for a propellor in axial cylinder," in *First International Symposium on Marine Propulsors*, Trondheim, Norway, 2009.
- [21] P. L. Troost, "Reynolds Number for Model Propeller Experiments," Netherlands Model Basin, 1948.
- [22] M. A.-M. G. H. Sven-Brian Muller, "Scale Effects on Propellers for Large Container Vessels," in *First Internatioal Symposium on Marine Propulsors*, Trondheim, Norway, June 2009.
- [23] H. R. Martin, "Development of a Scale Model Wind Turbine for Testing of Offshore Floating Wind Turbine Systems," University Of Maine, Orono, Maine, 2011.
- [24] B. Epps, *Personal Communication*, June 2012.
- [25] J. E. Kerwin, *13.04 Lecture Notes, Hydrofoils and Propellers*, MIT, 2001.
- [26] B. P. Epps, "PhD Thesis, An impulse framework for hydrodynamic force analysis:," MIT, Cambride, MA, 2010.
- [27] P. L. Troost, "Reynolds Number for Model Propeller Experiments," Netherlands Model Basin, 1948.
- [28] M. A.-M. G. H. Sven-Brian Muller, "Scale effects onpropellers for large container vessels," in *First Internatioal Symposium on Marine Propulsors*, Trondheim, Norway, June 2009.
- [29] J. P. Holman, *Experimental Methods for Engineers*, McGraw-Hill, 2007.

- [30] W. B. Coney, "A Method for the Design of A Class of Optimum Marine Propulsors," MIT, 1989.
- [31] M. R. Shives, "Hydrodynamic Modeling, Optimization and Performance Assessment for Ducted and Non-Ducted Tidal Turbines," Carleton University, 2008.
- [32] G. P. M. Hugh, "Advances in Ducted Propulsor Analysis using Vortex-Lattice Lifting-Surface Techniques," MIT, 1997.

APPENDIX A: FREE TIP INPUT CODE

```
Using OpenProp V2.4.4
% ----- Example_input.m
% Created: 3/2/2010, Brenden Epps, bepps@mit.edu
%
% This script creates an "input" data structure for use in OpenProp.
%
% To design a propeller using these inputs, run:
%           design = EppsOptimizer(input)
%
% -----
clear, %close all, clc

filename = 'OpenProp Tom unducted Aug_11_2012'; % filename prefix
notes    = 'Ducted propeller from Sutbblefield (2008) M.S. thesis';

% ----- Design parameters
Z      = 3;          % number of blades
% N     = 72*(60/2/pi); % propeller speed [RPM]
N=650;
D      = 0.254;      % (approx 10 in) propeller diameter [m] (Note: 39.37 in/m )

THRUST = 0;          % (11.240 lb) required thrust [N] (0.2248 lb/N)
% Vs   = .915;%1.25; % ship velocity [m/s]
Vs     = 1.25;
Dhub   = .04445;    % hub diameter [m] (must be greater than 0.15*D)

Mp     = 20;        % number of vortex panels over the radius
Np     = 20;        % number of points along the chord
ITER   = 75;        % number of iterations in wake alignment
Rhv    = 0.5;       % hub vortex radius / hub radius
HUF    = 0;         % Hub Unloading Factor (0 == no unloading, 1 == reduced loading)
TUF    = 0;         % Tip Unloading Factor (0 == no unloading, 1 == reduced loading)
SCF    = 1;         % Swirl Cancellation Factor (1 == no cancellation)
rho    = 1000;      % water density [kg/m^3]

H      = 1;         % Shaft centerline depth [m]
dV     = 0.2;       % Inflow variation [m/s]
Np     = 20;        % Number of points over the chord for geometry plots [ ]

% ----- Duct parameters
% Inputs for no duct: Duct_flag = 0; TAU = 1; Rduct_oR = 1; CDd = 0;
TAU    = .9;        % thrust ratio
Rduct  = D/2;       % duct radius [m]
Cduct  = D/3;       % duct chord length [m]
CDd    = 0.008;     % duct viscous drag coefficient

% ----- Blade 2D section properties
Meanline = 'NACA a=0.8'; % Meanline type (1 == NACA a=0.8, 2 == parabolic)
Thickness = 'NACA 65A010'; % Thickness form (1 == NACA 65A010, 2 == elliptical, 3 ==
parabolic)
```

```

alpha = 1.54; % [deg] ideal angle of attack (should match with Meanline type)
CLI = 1.0; % [ ], ideal lift coefficient (should match with Meanline type)

XR = [0.2 0.3 0.4 0.5 0.6 0.7 0.8 0.9 0.95 1.0]; % radius / propeller radius
XCoD = [0.1600 0.1818 0.2024 0.2196 0.2305 0.2311 0.2173 0.1806...
        0.1387 0.000001]; % chord / diameter unducted

% XCoD = [0.2600 0.2321 0.2109 0.1957 0.1900 0.1845 0.1800 0.1800 0.1800 0.1800]; % (old) chord /
diameter ducted
XCD = .02;%[0.0080 0.0080 0.0080 0.0080 0.0080 0.0080 0.0080 0.0080 0.0080 0.0080]; % section
drag coefficient
% XCD = [0.18 0.018 0.018 0.018 0.018 0.0180 0.01800 0.0180 0.01800 0.01800];
XVA = [1 1 1 1 1 1 1 1 1 1 ]; % axial inflow velocity / ship velocity
XVT = [0 0 0 0 0 0 0 0 0 0 ]; % tangential inflow velocity / ship velocity
t0oc0 = [0.2056 0.1551 0.1181 0.0902 0.0694 0.0541 0.0419 0.0332 0.0324 0.0000]; % max section
thickness / chord
skew0 = [0 0 0 0 0 0 0 0 0 0 ]; % skew [deg]
rake0 = [0 0 0 0 0 0 0 0 0 0 ]; % rake / diameter

% ----- Flags
Propeller_flag = 0; % 0 == turbine, 1 == propeller
Viscous_flag = 1; % 0 == viscous forces off (CD = 0), 1 == viscous forces on
Hub_flag = 1; % 0 == no hub, 1 == hub
Duct_flag = 0; % 0 == no duct, 1 == duct
Wake_flag = 0; % 0 == Horseshoe(...,Wrench(...)), 1 == Wake_Horseshoe(...)
Plot_flag = 1; % 0 == do not display plots, 1 == display plots
Chord_flag = 1; % 0 == do not optimize chord lengths, 1 == optimize chord lengths
Optimizer_flag = 2; % 1 == Lerbs optimizer, 2 == Epps optimizer
Lagrange_flag = 0; % 0 == do not fix Lagrange multiplier, 1 == fix Lagrange multiplier

LM0 = -1; % [1 x 1] fixed value of Lagrange multiplier

Make2Dplot_flag = 1; % 0 == do not make a 2D plot of the results, 1 == make plot
Make3Dplot_flag = 1; % 0 == do not make a 3D plot of the results, 1 == make plot
Make_Rhino_flag = 0; % 0 == do not make Rhino files, 1 == make Rhino files
% ----- Compute derived quantities
n = N/60; % revolutions per second [rps]
R = D/2; % propeller radius [m]
Rhub = Dhub/2; % hub radius [m]
Rhub_oR = Rhub/R;
Js = Vs/(n*D); % advance coefficient
L = pi/Js; % tip-speed ratio
CTDES = THRUST/(0.5*rho*Vs^2*pi*R^2); % CT thrust coefficient required

dVs = dV/Vs; % axial inflow variation / Vs
CDoCL = mean(XCD)/CLI;

ALPHAstall = 8*pi/180; % [rad], stall angle of attack - ideal angle of attack
dCLdALPHA = 2*pi; % d(CL)/d(alpha)

% =====
% ===== Pack up input variables
input.filename = filename; % filename prefix for output files

```

```

input.date = date; % today's date

input.part1 = '----- Performance inputs -----';
input.Z = Z; % [1 x 1], [ ] number of blades
input.N = N; % propeller speed [RPM]
input.D = D; % propeller diameter [m]
input.Vs = Vs; % [1 x 1], [m/s] ship speed
input.Js = Js; % [1 x 1], [ ] advance coefficient,  $J_s = V_s/nD = \pi/L$ 
input.L = L % [1 x 1], [ ] tip speed ratio,  $L = \omega R/V$ 
input.THRUST = THRUST; % required thrust [N]
input.CTDES = CTDES; % [1 x 1], [ ] desired thrust coefficient

input.part2 = '----- Geometry inputs -----';
input.Mp = Mp; % [1 x 1], [ ] number of blade sections
input.Np = Np; % [1 x 1], [ ] number of points along the chord
input.R = R; % [1 x 1], [m] propeller radius
input.Rhub = Rhub; % [1 x 1], [m] hub radius
input.XR = XR; % [length(XR) x 1], [ ] input radius/propeller radius
input.XVA = XVA; % [length(XR) x 1], [ ] input axial inflow velocity at XR
input.XVT = XVT; % [length(XR) x 1], [ ] input swirl inflow velocity at XR
input.XCD = XCD; % [length(XR) x 1], [ ] input drag coefficient at XR
input.XCoD = XCoD; % [length(XR) x 1], [ ] input chord / diameter at XR
input.t0oc0 = t0oc0; % [length(XR) x 1], [ ] input thickness / chord at XR
input.skew0 = skew0; % [length(XR) x 1], [ ] input skew [deg] at XR
input.rake0 = rake0; % [length(XR) x 1], [ ] input rake X/D at XR
input.Meanline = Meanline; % 2D section meanline flag
input.Thickness = Thickness; % 2D section thickness flag
input.ALPHAstall = ALPHAstall; % [rad], stall angle of attack - ideal angle of attack
input.alphaI = alphaI; % [1 x 1], [deg] input ideal angle of attack at XR
input.dCLdALPHA = dCLdALPHA; % d(CL)/d(alpha)
input.CLI = CLI; % [1 x 1], [ ] input ideal lift coefficient at XR
input.CDoCL = CDoCL; % [1 x 1], [ ] blade section drag coefficient / lift coefficient

input.part3 = '----- Computational inputs -----';
input.ITER = ITER; % [ ] number of iterations
input.Propeller_flag = Propeller_flag; % 0 == turbine, 1 == propeller
input.Viscous_flag = Viscous_flag; % 0 == viscous forces off (CD = 0), 1 == viscous forces on
input.Hub_flag = Hub_flag; % 0 == no hub, 1 == hub
input.Duct_flag = Duct_flag; % 0 == no duct, 1 == duct
input.Plot_flag = Plot_flag; % 0 == do not display plots, 1 == display plots
input.Chord_flag = Chord_flag; % 0 == do not optimize chord lengths, 1 == optimize chord lengths
input.Wake_flag = Wake_flag; % 0 == Horseshoe(...,Wrench(...)), 1 == Wake_Horseshoe(...)
input.Optimizer_flag = Optimizer_flag; % 1 == Lerbs optimizer, 2 == Epps optimizer
input.Lagrange_flag = Lagrange_flag; % 0 == do not fix Lagrange multiplier, 1 == fix Lagrange multiplier
input.Make2Dplot_flag = Make2Dplot_flag;
input.Make3Dplot_flag = Make3Dplot_flag;
input.Make_Rhino_flag = Make_Rhino_flag;
input.LM0 = LM0; % [1 x 1] fixed value of Lagrange multiplier
input.HUF = HUF; % [1 x 1], [ ] Hub Unloading Factor (0 == no unloading, 1 == reduced loading)
input.TUF = TUF; % [1 x 1], [ ] Tip Unloading Factor (0 == no unloading, 1 == reduced loading)
input.SCF = SCF; % [1 x 1], [ ] Swirl Cancellation Factor (1 == no cancellation)
input.Rhv = Rhv; % [1 x 1], [ ] hub vortex radius / hub radius

input.part4 = '----- Cavitation inputs -----';

```

```

input.rho    = rho;    % [1 x 1], [kg/m^3] fluid density
input.dVs    = dVs;    % [1 x 1], [ ] ship speed variation / ship speed
input.H      = H;      % [1 x 1]

input.part5  = '----- Duct inputs -----';
input.TAU    = TAU;    % [1 x 1], [ ] propeller thrust / total thrust
input.Rduct  = Rduct;  % [1 x 1], [m] duct radius
input.Cduct  = Cduct;  % [1 x 1], [m] duct chord length
input.CDd    = CDd;    % [1 x 1], [ ] duct drag coefficient

% ----- Pack up propeller/turbine data structure, pt
pt.name      = filename; % (string) propeller/turbine name
pt.date      = date;    % (string) date created
pt.notes     = notes;   % (string or cell matrix) notes
pt.input     = input;   % (struct) input parameters
pt.design    = [];      % (struct) design conditions
pt.geometry  = [];      % (struct) design geometry
pt.states    = [];      % (struct) off-design state analysis

% ----- Save input data
save OPinput pt input

clear, clc,
pause(0.01),
pause(0.01),

load OPinput,

pause(0.01),
pause(0.01),

input

```

APPENDIX B: FREE TIP BLADE GEOMETRY FILE

OpenProp Tom unducted Aug_11_2012_Geometry.txt

Propeller Geometry Table

Date and time: 11-Jun-2012

Propeller Diameter = 0.2540 m
Number of Blades = 3
Propeller Speed = 650 RPM
Propeller Hub Diameter = 0.0445 m
Meanline Type: NACA a=0.8
Thickness Type: NACA 65A010

r/R	P/D	Skew	Xs/D	c/D	f0/c	t0/c
0.1954	0.2716	0.0000	0.0000	0.1597	-0.0350	0.2193
0.2361	0.2861	0.0000	0.0000	0.1370	-0.0333	0.2317
0.2769	0.2894	0.0000	0.0000	0.1209	-0.0317	0.2372
0.3176	0.2902	0.0000	0.0000	0.1093	-0.0300	0.2363
0.3583	0.2902	0.0000	0.0000	0.1008	-0.0284	0.2297
0.3991	0.2901	0.0000	0.0000	0.0946	-0.0268	0.2179
0.4398	0.2900	0.0000	0.0000	0.0901	-0.0253	0.2026
0.4806	0.2902	0.0000	0.0000	0.0869	-0.0238	0.1851
0.5213	0.2905	0.0000	0.0000	0.0847	-0.0224	0.1668
0.5620	0.2910	0.0000	0.0000	0.0832	-0.0211	0.1483
0.6028	0.2915	0.0000	0.0000	0.0821	-0.0199	0.1299
0.6435	0.2921	0.0000	0.0000	0.0810	-0.0187	0.1131
0.6843	0.2926	0.0000	0.0000	0.0794	-0.0177	0.0991
0.7250	0.2930	0.0000	0.0000	0.0767	-0.0167	0.0878
0.7657	0.2934	0.0000	0.0000	0.0724	-0.0159	0.0797
0.8065	0.2937	0.0000	0.0000	0.0659	-0.0152	0.0763
0.8472	0.2939	0.0000	0.0000	0.0568	-0.0146	0.0707
0.8880	0.2940	0.0000	0.0000	0.0477	-0.0142	0.0535
0.9287	0.2941	0.0000	0.0000	0.0406	-0.0138	0.0296
0.9694	0.2942	0.0000	0.0000	0.0364	-0.0136	0.0085

r/R [], radial position of control points / propeller radius.

P/D [], section pitch / diameter.

c/D [], section chord-length / diameter.

fo/C [], section camber / section chord-length.

to/C [], section thickness / section chord-length.

APPENDIX C: DUCTED INPUT CODE

```

Using OpenProp V3.2.0
% -----
% Ducted turbine design example:
% -----

% -----
clear, close all, clc,

filename = 'turbine'; % filename prefix
notes   = 'Tom Lokocz ducted turbine';

% -----
i.part1 = '----- Performance inputs -----';

i.Z      = 3;      % number of blades
i.N      = 650;    % propeller speed [RPM]
i.Vs     = 1.25;   % free-stream speed [m/s]

i.D      = 0.254;  % rotor diameter [m] (Note: 39.37 in/m)
i.Dhub   = .04445; % hub diameter [m] (must be greater than 0.15*D)

i.L      = pi*(i.N/60)*i.D/i.Vs; % tip-speed ratio

% -----
input.part2 = '----- Geometry inputs -----';
i.Mp      = 20;    % number of vortex panels over the radius

i.XR      = [0.2  0.3  0.4  0.5  0.6  0.7  0.8  0.9  0.95  1.0]; % radius / propeller radius

% XCoD    = [0.1600 0.1818 0.2024 0.2196 0.2305 0.2311 0.2173 0.1806 0.1387 0.000001]; % chord /
diameter unducted
i.XCoD    = [0.1600 0.1818 0.2024 0.2196 0.2305 0.2311 0.2173 0.19 0.17 0.15]; % (use this one) chord /
diameter ducted
% XCoD    = [0.2600 0.2321 0.2109 0.1957 0.1900 0.1845 0.1800 0.1800 0.1800 0.1800]; % (old) chord /
diameter ducted

i.XCD     = .02;%[0.0080 0.0080 0.0080 0.0080 0.0080 0.0080 0.0080 0.0080 0.0080 0.0080]; % section
drag coefficient
i.XVA     = [1  1  1  1  1  1  1  1  1  1 ]; % axial inflow velocity / ship velocity
i.XVT     = [0  0  0  0  0  0  0  0  0  0 ]; % tangential inflow velocity / ship
velocity
i.t0oc0   = [0.2056 0.1551 0.1181 0.0902 0.0694 0.0541 0.0419 0.0332 0.0324 0.0000]; % max section
thickness / chord
i.skew0   = [0  0  0  0  0  0  0  0  0  0 ]; % skew [deg]
i.rake0   = [0  0  0  0  0  0  0  0  0  0 ]; % rake / diameter

i.Meanline = 'NACA a=0.8'; % Meanline type (1 == NACA a=0.8, 2 == parabolic)
i.Thickness = 'NACA 65A010'; % Thickness form (1 == NACA 65A010, 2 == elliptical, 3 ==
parabolic)

i.ALPHAstall = 8*pi/180; % [rad], stall angle of attack - ideal angle of attack
i.dCLdALPHA = 2*pi; % d(CL)/d(alpha)

```

```

i.XCLmax = .5;

% -----
i.part3 = '----- Computational inputs -----';

i.Propeller_flag = 0; % 0 == turbine, 1 == propeller
i.Viscous_flag = 1; % 0 == viscous forces off (CD = 0), 1 == viscous forces on
    i.Hub_flag = 1; % 0 == no hub, 1 == hub
    i.Duct_flag = 1; % 0 == no duct, 1 == duct
    i.Plot_flag = 1; % 0 == do not display plots, 1 == display plots
    i.Chord_flag = 1; % 0 == do not optimize chord lengths, 1 == optimize chord lengths

i.ITER = 50; % number of iterations in wake alignment

% -----
i.part4 = '----- Duct inputs -----';
i.Rduct = i.D/2;%+.00159; % duct radius [m]
i.Cduct = i.D/2; % duct chord length [m]
i.Xduct = i.Cduct*.25; % duct axial displacement downstream [m]
i.CDd = .02;%0.008; % duct viscous drag coefficient
i.CTD = -0.2; % duct thrust coefficient

% -----
i.part5 = '----- Cavitation inputs -----';
i.rho = 1000; % water density [kg/m^3]
i.H = 1; % Shaft centerline depth [m]
i.dV = 0.2; % Inflow variation [m/s]

% =====
% ----- Pack up propeller/turbine data structure, pt
pt.name = filename; % (string) propeller/turbine name
pt.date = date; % (string) date created
pt.notes = notes; % (string or cell matrix) notes
pt.i = i; % (struct) input parameters
pt.d = []; % (struct) design conditions
pt.g = []; % (struct) design geometry
pt.s = []; % (struct) off-design state analysis

% ----- Save input data
save OPinput pt

clear, clc,
pause(0.01),
pause(0.01),

load OPinput pt

pause(0.01),
pause(0.01),

pt.i

```

APPENDIX D: DUCTED BLADE GEOMETRY FILE

Date and time: 15-Apr-2012

Propeller Diameter = 0.2540 m
 Number of Blades = 3
 Propeller Speed = 650 RPM
 Propeller Hub Diameter = 0.0445 m
 Meanline Type: NACA a=0.8
 Thickness Type: NACA 65A010

r/R	P/D	Skew	Xs/D	c/D	f0/c	t0/c
0.1750	0.2859	0.0000	0.0000	0.1855	-0.0340	0.1840
0.2397	0.3054	0.0000	0.0000	0.1509	-0.0340	0.2053
0.3041	0.3126	0.0000	0.0000	0.1282	-0.0340	0.2186
0.3676	0.3165	0.0000	0.0000	0.1112	-0.0340	0.2271
0.4299	0.3190	0.0000	0.0000	0.0982	-0.0340	0.2307
0.4907	0.3207	0.0000	0.0000	0.0880	-0.0340	0.2293
0.5495	0.3220	0.0000	0.0000	0.0799	-0.0340	0.2239
0.6061	0.3233	0.0000	0.0000	0.0734	-0.0340	0.2149
0.6599	0.3245	0.0000	0.0000	0.0682	-0.0340	0.2035
0.7108	0.3257	0.0000	0.0000	0.0640	-0.0340	0.1895
0.7584	0.3270	0.0000	0.0000	0.0605	-0.0340	0.1730
0.8023	0.3285	0.0000	0.0000	0.0577	-0.0340	0.1567
0.8424	0.3300	0.0000	0.0000	0.0553	-0.0340	0.1408
0.8784	0.3316	0.0000	0.0000	0.0533	-0.0340	0.1272
0.9101	0.3328	0.0000	0.0000	0.0517	-0.0340	0.1196
0.9372	0.3339	0.0000	0.0000	0.0503	-0.0340	0.1152
0.9596	0.3355	0.0000	0.0000	0.0492	-0.0340	0.0954
0.9772	0.3372	0.0000	0.0000	0.0483	-0.0340	0.0667
0.9898	0.3386	0.0000	0.0000	0.0476	-0.0340	0.0427
0.9975	0.3397	0.0000	0.0000	0.0472	-0.0340	0.0280
1.0000	0.3400	0.0000	0.0000	0.0471	-0.0340	0.0232

r/R [], radial position of control points / propeller radius.
 P/D [], section pitch / diameter.
 c/D [], section chord-length / diameter.
 fo/C [], section camber / section chord-length.
 to/C [], section thickness / section chord-length.

APPENDIX E: UNCERTAINTY AND REPEATABILITY

Uncertainty and repeatability in instrumentation were calculated as follows. The uncertainty in C_p , C_t and λ were calculated using a MATLAB [9] function written by

$$\text{deBree [4], } w_R = \sqrt{\left(\frac{\partial R}{\partial x_1}\right)^2 w_{x_1}^2 + \left(\frac{\partial R}{\partial x_2}\right)^2 w_{x_2}^2 + \left(\frac{\partial R}{\partial x_3}\right)^2 w_{x_3}^2 + \dots + \left(\frac{\partial R}{\partial x_n}\right)^2 w_{x_n}^2} \quad [29].$$

Where $R = f(x_1, x_2, x_3 \dots x_n)$, w_R is the uncertainty in R, w_{x_n} is the uncertainty in x_n and $\frac{\partial R}{\partial x_n}$ is the partial derivative with respect to x_n .

Table E.1 shows the partial derivatives used herein. The uncertainty of the tip speed ratio for all cases, $(w\lambda) \leq \pm 0.009$ and can therefore be neglected. Figure E.1 and Figure E.2 show the uncertainty bars applied to the averages of C_p and C_T for both the free tip and ducted cases. The uncertainties are fairly small, much smaller than the repeatability of the data.

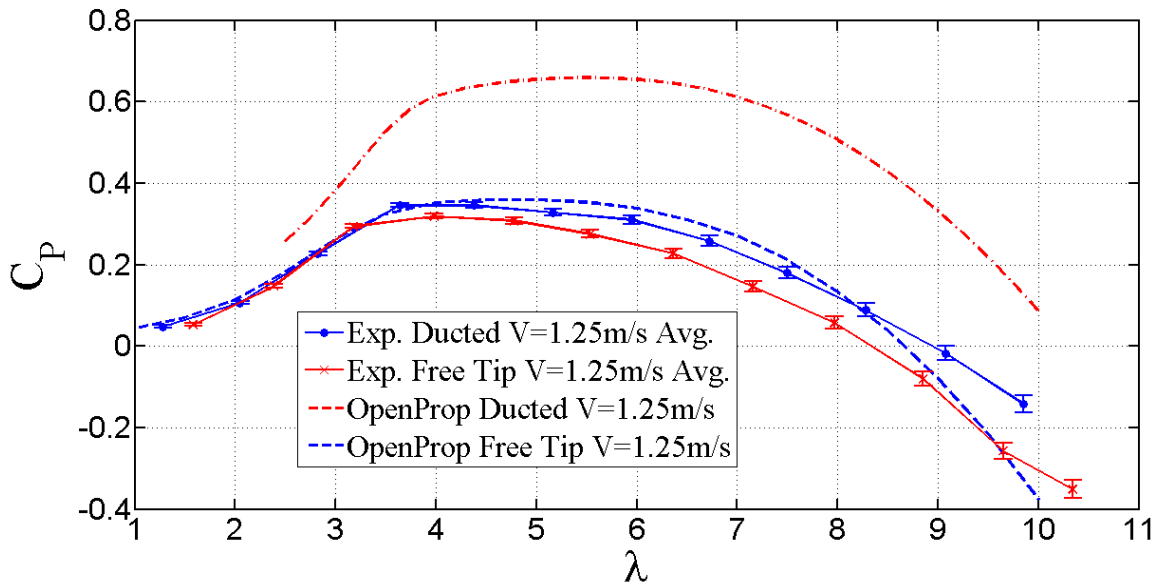


Figure E.1 Shows the uncertainty in C_p for the free tip and ducted turbines.

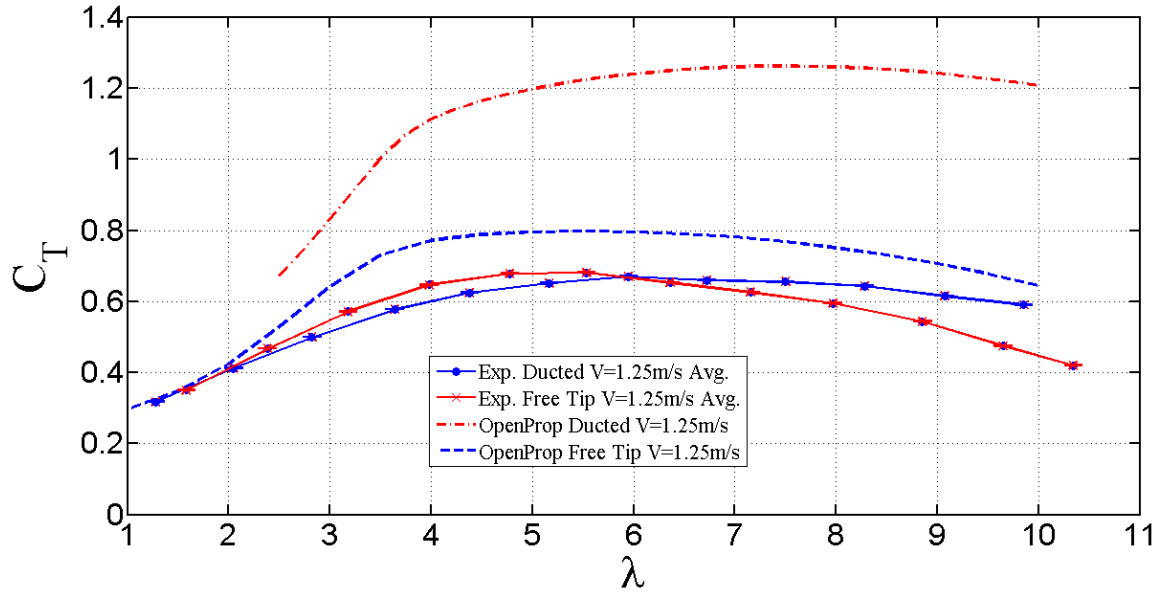


Figure E.2 Shows the uncertainty in C_T for the free tip and ducted turbines.

Table E.1 Uncertainty Equations

Partial differential equation	Equation variables in MATLAB
$C_p = \frac{FlW}{\frac{1}{2} rV_s^3 \rho \frac{D^2}{4}}$	$Cp_{-av} = \frac{(avg_F)l(avg_omega)}{.5(rho)(avg_v)^3 .25(pi)D^2}$
$\frac{\partial C_p}{\partial F} = \frac{lW}{\frac{1}{2} rV_s^3 \rho \frac{D^2}{4}} = \frac{8lW}{rV_s^3 \rho D^2}$	$part_F = \frac{l(avg_omega)}{.5(rho)(avg_v)^3 .25(pi)D^2}$
$\frac{\partial C_p}{\partial l} = \frac{FW}{\frac{1}{2} rV_s^3 \rho \frac{D^2}{4}} = \frac{8FW}{rV_s^3 \rho D^2}$	$part_l = \frac{(avg_F)(avg_omega)}{.5(rho)(avg_v)^3 .25(pi)D^2}$
$\frac{\partial C_p}{\partial W} = \frac{Fl}{\frac{1}{2} rV_s^3 \rho \frac{D^2}{4}} = \frac{8Fl}{rV_s^3 \rho D^2}$	$part_omega = \frac{(avg_F)l}{.5(rho)(avg_v)^3 .25(pi)D^2}$
$\frac{\partial C_p}{\partial dx} = \frac{-3FlW}{\frac{1}{2} rV_s^3 dx \rho \frac{D^2}{4}} = \frac{-24FlW}{rV_s^3 dx \rho D^2}$	$part_dx = \frac{3(avg_F)l(avg_omega)}{.5(rho)(avg_v)^3 (dx) .25(pi)D^2}$
$\frac{\partial C_p}{\partial D} = \frac{-2FlW}{\frac{1}{2} rV_s^3 \rho \frac{D^3}{4}} = \frac{-16FlW}{rV_s^3 \rho D^3}$	$part_D = \frac{2(avg_F)l(avg_omega)}{.5(rho)(avg_v)^3 .25(pi)D^3}$

Repeatability (Δ) was found by taking difference of the maximum and minimum values to the mean value of the data.

APPENDIX F: TIP GAP STUDY

Introduction

Maintaining sufficient tip gap is important to prevent interference between the blades and duct. This tip gap study will be used to answer the question of how much gap is allowable without adverse affect of ducted turbine performance.

This research is accomplished experimentally in the UMaine tow tank using the same test platform, data acquisition system, duct and rotor as previously described in this thesis. By varying the tip gap over a range of tip speed ratios a C_p curve was obtained for each tip gap ratio. The results are plotted with the results from the minimum tip gap for comparison purposes.

The theory behind the affects of tip gap is the subject of numerous papers and theses and is beyond the scope of this study [30][25].

Experimental Setup

After the duct and rotor were assembled and aligned to ensure the rotor was concentric to the hub, the blade tips were “ground in” to the duct to ensure an even tip clearance. This was done using emery cloth laid on the duct and turning the rotor by hand on its shaft. The tip gap was adjusted using feeler gauges and sliding the rotor in or out of the duct to achieve the desired clearance (Figure F.1).

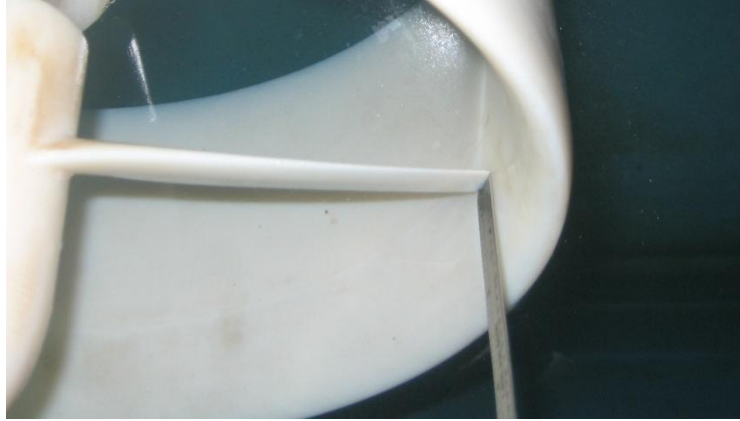


Figure F.1 Measuring tip gap on ducted turbine.

This method is reasonably accurate in terms of the tip gap but ideally one would manufacture a series of rotors each with different blade lengths. For this work fabricating three rotors was prohibitively expensive. The problem with using one rotor is that as the rotor is moved out of the duct to increase the tip gap it also changes its chordwise position along the duct. The duct rotor combination was designed in OpenProp at the $\frac{1}{4}$ chord of the duct, the affect of this change in position is not expected to be significant because the change in circulation along the relatively small change in position (approximately 2.5% of the duct length) is not significant.

Results

Based on published data [2] [31] [32] [19] 3 tip gaps ratios were chosen to test

$\frac{t_g}{D} = 0.00197; 0.0039; 0.0059$. The experimental C_p curves are shown in Figure F.2

C_p as a function of t/D ($V = 1.25$ m/s)

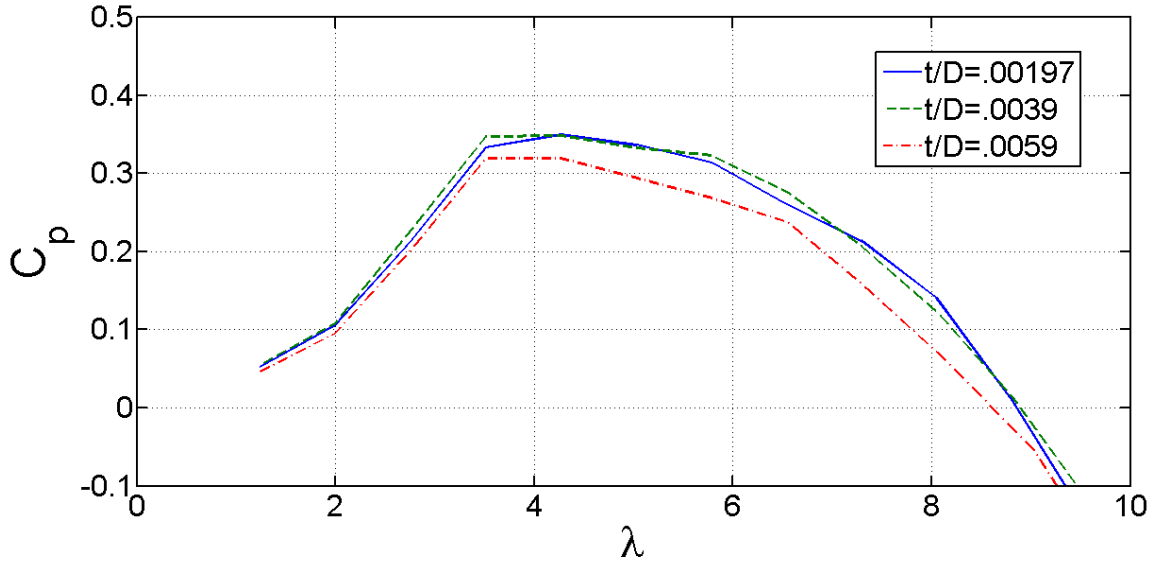


Figure F.2 C_p as a function of t/D ($V = 1.25$ m/s)

For the remainder of this study we will define the following cases as follows in Table F.1

Tip Gap Case Definitions.

Table F.1 Tip Gap Case Definitions

Case #1	Percent Difference between $t/D = .00197$ and $t/D = .0039$
Case #2	Percent Difference between $t/D = .00197$ and $t/D = .0059$

It was expected from previous work[2] [32] [20][19] that C_p would not change significantly for case #1 but would drop by 10% to 15% for case #2. The percent differences in C_p show that the change for case #1 varies from 0.35% to 12.5% with an average of 4.49% and the change for case #2 varies from 4.1% to 50% with an average of 14.96% (Figure F.3 Percent difference in C_p).

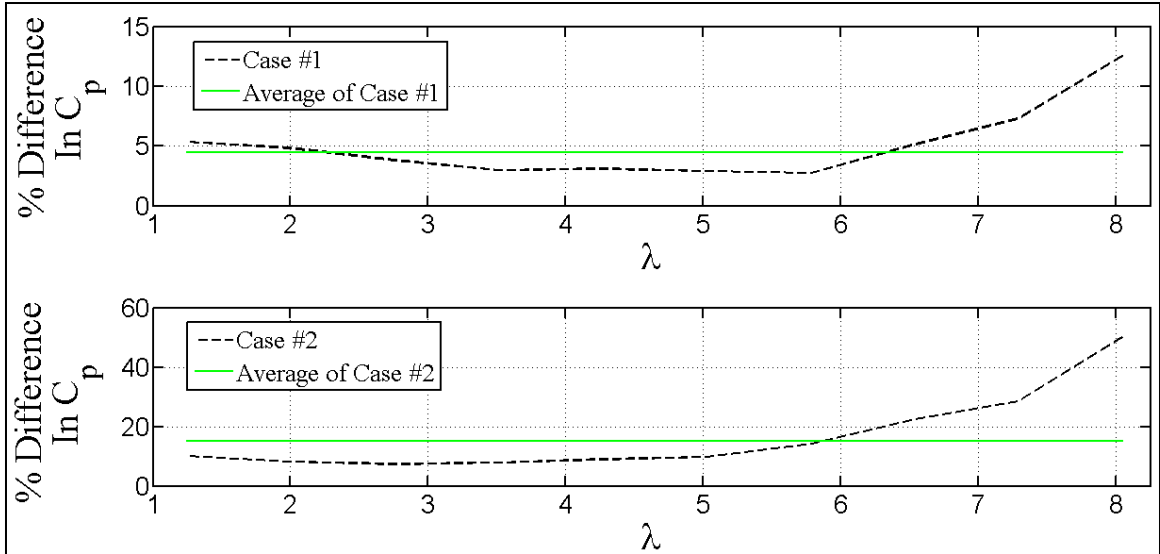


Figure F.3 Percent difference in C_p

Discussion

The results of this tip gap study are consistent with previously published experimental data on similar devices [20] [19].

Case #1

At first glance the experimental data in case #1 looks larger than expected with ranges of 0.35% to 12.5% variation in C_p with an average of 4.49% (Figure F.3 Percent difference in C_p). These values in and of themselves constitute a significant change in performance but the percentages are not necessarily significant when also considering Figure F.2 C_p as a function of t/D ($V = 1.25$ m/s). The plot of $t/D = .00197$ and the plot of $t/D = .0039$ are identical when viewed from the standpoint of repeatability. It is clear from this plot that no trend can be ascertained, this in turn makes the percent difference in case #1 insignificant.

Case #2

Unlike case #1 (Figure F.2 C_p as a function of t/D ($V = 1.25$ m/s) clearly demonstrates a lower trend in C_p with increased tip gap. As predicted the experimental average of 14.96% difference in C_p falls within the expected range of 10% to 15%.

Conclusion

The experimental data shows that maintaining $t/D \leq .0039$ does not significantly degrade the quality of the data in comparison to the tighter tolerance of $t/D \leq .00197$.

APPENDIX G: FREE TIP TURBINE PICTURE

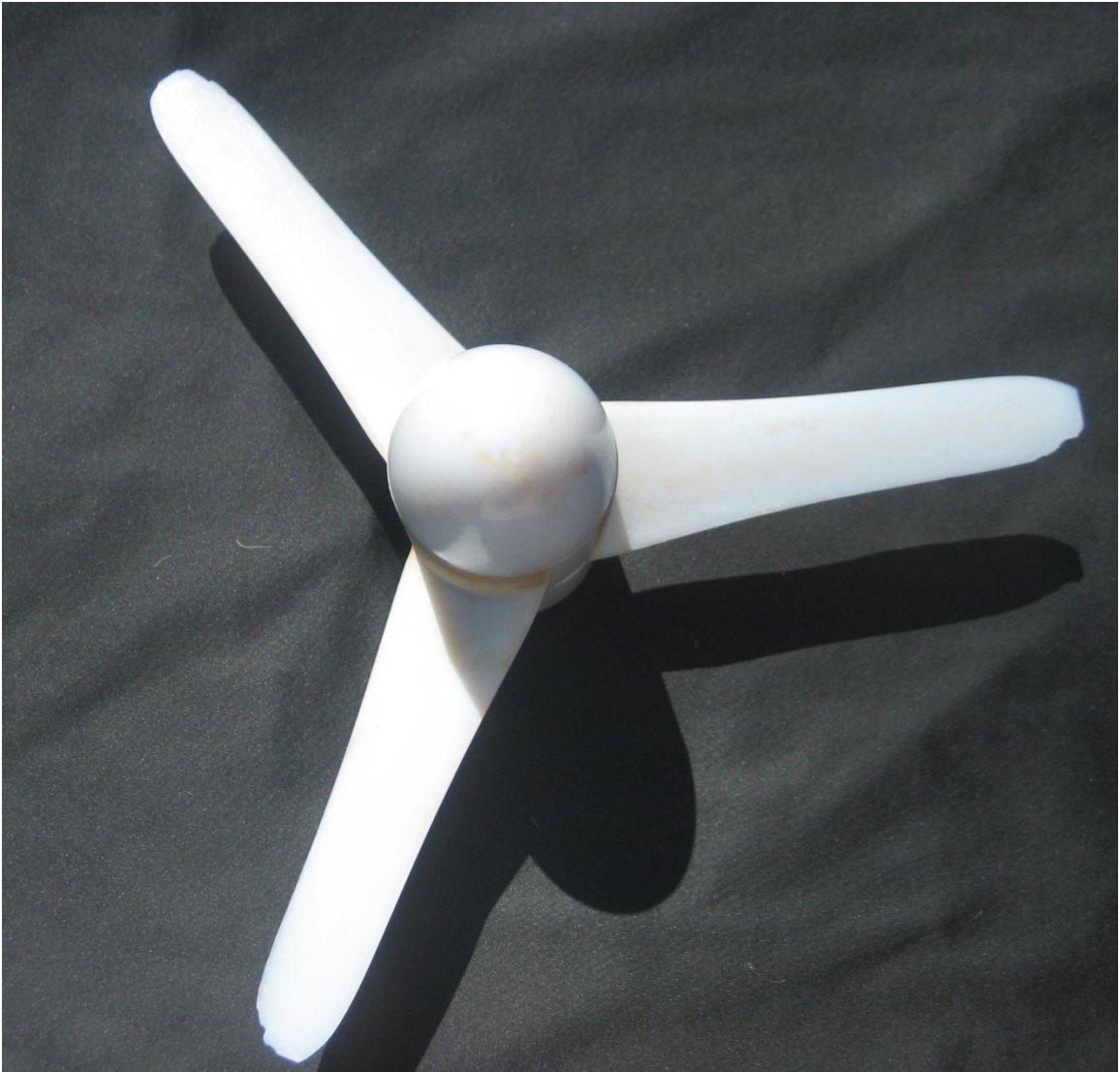


Figure G.1 Picture of the free tip turbine. Note the damaged blade tips.

BIOGRAPHY OF THE AUTHOR

Thomas A Lokocz graduated from the University of Maine in 2010 with a B.S in Mechanical Engineering. He spent several years prior to college working as a professional sailor, boat builder and yacht designer. Tom plans to pursue a career in engineering and continue living in Maine with his wife and son. Tom is a candidate for the Master of Science degree in Mechanical Engineering from the University of Maine in August, 2012.

Appendix 3-2

**TESTING AND MODELING OF HIGH SOLIDITY
CROSS-FLOW TIDAL TURBINES**

By

Geoffrey Steven deBree

B.S. University of Maine, 2005

A THESIS

Submitted in Partial Fulfillment of the

Requirements for the Degree of

Master of Science

(in Mechanical Engineering)

The Graduate School

The University of Maine

May, 2012

Advisory Committee:

Michael L. Peterson, Libra Foundation Professor of Mechanical Engineering,
Advisor

Richard W. Kimball, Assistant Professor, Maine Maritime Academy

Gayle Zydlewski, Assistant Professor of Marine Sciences

LIBRARY RIGHTS STATEMENT

In presenting this thesis in partial fulfillment of the requirements for an advanced degree at the University of Maine, I agree that the Library shall make it freely available for inspection. I further agree that permission for “fair use” copying of this thesis for scholarly purposes may be granted by the Librarian. Is it understood that any copying or publication of this thesis for financial gain shall not be allowed without my written permission.

Signature:

Date:

TESTING AND MODELING OF HIGH SOLIDITY CROSS-FLOW TIDAL TURBINES

By Geoffrey deBree

Thesis Advisor: Dr. Michael Peterson

An Abstract of the Thesis Presented
in Partial Fulfillment of the Requirements for the
Degree of Master of Science
(in Mechanical Engineering)
May, 2012

Hydro-kinetic tidal energy is a novel renewable resource with many potential sites located throughout the world. This thesis considers high solidity cross-flow turbines which are likely to be more fish friendly than axial flow turbines because they operate at low tip speed ratios while maintaining reasonable performance. At this time, limited experimental data exists that compares high solidity cross-flow turbine performance for different blade profiles. A cross-flow tidal turbine test bed was developed with power coefficient, thrust coefficient, and wake velocity measurement capabilities. Tow tank testing was performed for seven different blade profiles over a range of inflow velocities, tip speed ratios, and blade toe angles, with a constant blade number of four. Two-bladed tests were also performed for one of the profiles. Turbine rotational speed was controlled to eliminate the problem of turbine starting, allowing for testing at low tip speed ratios and conditions with negative power coefficients. Power coefficient results compared well with published data under similar test conditions; peak efficiencies were located at tip

speed ratios consistent with modeling and had reasonable magnitudes that did not exceed the Betz limit.

A free vortex model was modified to include two effects: variation of blade toe angle, and a virtual incidence angle correction, which is an effect of flow curvature. These flow curvature effects were shown to be significant when the curvature index (blade chord length/turbine radius) was high, the case for the turbine geometries tested. Addition of the flow curvature correction significantly improved the comparison of the model with experimental data, specifically for the case of varying blade toe angle. These results are being used to validate the free vortex model, which can then be used to optimize the performance of cross-flow turbines.

On behalf of the Graduate Committee for Geoffrey Steven deBree I affirm that this manuscript is the final and accepted thesis. Signatures of all committee members are on file with the Graduate School at the University of Maine, 42 Stodder Hall, Orono, Maine.

Michael L. Peterson, Ph. D, Professor of Mechanical Engineering

Date

ACKNOWLEDGMENTS

I would like to thank my advisor, Dr. Michael “Mick” Peterson, for his constant encouragement, guidance, and countless hours spent editing this thesis. I would also like to thank my advisory committee: Dr. Richard Kimball, for his knowledge and guidance in the areas of fluid dynamics and propeller design, and Dr. Gayle Zydlewski, for her knowledge of the tidal power industry and the environmental effects of tidal power development. I am grateful for all of your help in revising this thesis.

I would like to thank the Maine Tidal Power Initiative for their support of research in all areas of Tidal Power development. This group has helped show me the importance of developing technology in a sensible manner, and the importance of studying all aspects of a project, from environmental effects of technology installations to the reaction of the local communities where the technologies are being launched.

I would like to thank my fellow graduate students: Matthew Cameron, for his work developing the experimental setup, Raul Urbina, for contributing the Free Vortex Model used in this thesis, for helping with the model modifications, and for many fruitful discussions on cross-flow turbine theory, Thomas Lokocz, for designing and building the carbon fiber turbine blades, and Colleen Swanger, for running experimental tests. I would also like to thank undergraduate Thomas McKay for his help at the tow tank.

I would like to thank Ocean Renewable Power Company for providing the 3-D printed plastic blades, and for funding of the experimental work. I would like to thank Jarlath

McEntee for his help with the entire experimental process. I would also like to thank Patrick Pottle for running many turbine tests.

I would also like to thank Alexander's Welding and Machine for manufacturing the test turbine, and Ryan Beaumont for providing assistance with the experimental process and data analysis.

Finally, I am grateful for the financial support from the U.S. Department of Energy through grant EE-000298.

TABLE OF CONTENTS

ACKNOWLEDGMENTS	iii
LIST OF TABLES	ix
LIST OF FIGURES	x
1. INTRODUCTION	1
1.1 Motivation.....	1
1.2 Background.....	5
1.2.1 Fundamental Definitions.....	6
1.2.1.1 Foil Shape.....	6
1.2.1.2 Turbine Geometry	11
1.2.1.3 Performance Parameters	13
1.2.2 Literature.....	16
1.2.3 Thesis Overview	20
2. NUMERICAL MODELING	21
2.1 Free Vortex Model.....	21
2.2 Flow Blockage and Model Boundary Conditions Using Images	26
2.2.1 Two Walls Using Images.....	27
2.2.2 One Wall and Infinite Fluid Using Images	28
2.3 Model Modifications for Blade Toe Angle Variation and Virtual Incidence Angle	28
2.3.1 Toe Angle Orientation	29
2.3.2 Coordinate Transformation.....	30
2.4 Model Results for Various Boundary Conditions.....	31
2.5 Free Vortex Model Results with Variable Toe Angle	33

3.	EXPERIMENTAL TESTING	38
3.1	Experimental Setup.....	40
3.1.1	Apparatus	40
3.1.2	Motor Control	44
3.1.3	Measured Quantities	45
3.1.3.1	Torque.....	45
3.1.3.2	Inflow Velocity.....	47
3.1.3.3	Turbine Angular Position and Angular Velocity.....	48
3.1.3.4	Thrust.....	48
3.1.3.5	Time.....	49
3.2	Test Methods.....	49
3.2.1	Drive Train Friction and End Plate Drag Determination.....	50
3.2.2	Turbine Test Procedure.....	51
3.3	Test Matrix Variables	52
3.3.1	Inflow Velocity	53
3.3.2	Solidity Ratio and Number of Blades	54
3.3.3	Tip Speed Ratio and Toe Angle.....	55
3.3.4	Blade Profiles.....	56
3.3.4.1	NACA 63 ₃ -018.....	58
3.3.4.2	NACA 63 ₃ -018 B	58
3.3.4.3	NACA 0018.....	60
3.3.4.4	NACA 4418.....	60
3.3.4.5	S809.....	61
3.3.4.6	LVN109.....	62

4.	RESULTS AND DISCUSSION	64
4.1	Four-Bladed Test Results at Three Different Toe Angles	64
4.1.1	Symmetric Foil Results.....	65
4.1.2	Cambered Foil Results.....	69
4.2	Effect of Blade Profile on Power Coefficient.....	72
4.3	Effect of Toe Angle on Power Coefficient	74
4.4	Two-Bladed Tests	77
4.4.1	Testing Results for $\theta_t = 0^\circ$	78
4.4.2	Testing Results for $\theta_t = +5^\circ$	80
4.5	Uncertainty in Experimental Results	80
4.5.1	Uncertainty in Power Coefficient	81
4.5.2	Uncertainty in Nondimensional Torque.....	83
4.6	Comparison of Numerical and Experimental Results.....	83
4.6.1	Comparison at $\theta_t = 0^\circ$	84
4.6.2	Comparison at $\theta_t = +5^\circ$	87
4.6.3	Dependence of Maximum Power Coefficient on Toe Angle.....	90
4.7	Conclusions.....	91
4.8	Recommendations.....	95
4.8.1	Experimental Recommendations	95
4.8.2	Modeling Recommendations	96
4.8.3	Summary.....	97
	REFERENCES	99
	APPENDICES	101
A.	TEST METHODS, DATA ANALYSIS AND FILTERING	102
B.	UNCERTAINTY ANALYSIS AND REPEATABILITY STUDY	122
C.	FLOW CURVATURE COORDINATE SYSTEM.....	130

D.	ADDITIONAL TEST RESULTS.....	131
E.	TOW TANK GEOMETRY	133
	BIOGRAPHY OF THE AUTHOR.....	135

LIST OF TABLES

Table 3.1.	Test matrix for four-bladed testing at $U_\infty = 1.00$ m/s for nine tip speed ratios between $\lambda \approx 0.75$ and $\lambda \approx 1.65$. CF designates carbon fiber blades and B designates tubercles	53
Table 3.2.	Test matrix for four-bladed testing at $U_\infty = 1.22$ m/s for nine tip speed ratios between $\lambda \approx 0.75$ and $\lambda \approx 1.65$. CF designates carbon fiber blades and B designates tubercles	53
Table 4.1.	Maximum C_P and λ_{\max} are shown for each toe angle from symmetric foil testing results taken at an inflow velocity of $U_\infty = 1.22$ m/s. Note that the carbon fiber blade set has a chord length of $c = 0.0762$ m, which was truncated to $c = 0.0699$ m during manufacturing. The chord length of 0.0762 m was used to calculate the turbine solidity ratio	69
Table 4.2.	Maximum C_P and λ_{\max} are shown for each toe angle from asymmetric foil testing results taken at an inflow velocity of $U_\infty = 1.22$ m/s	72
Table 4.3.	The maximum C_P and λ_{\max} are shown for the carbon fiber NACA 63 ₃ -018 blade profile over the extended toe angle range. Four-bladed data was taken at a solidity of $\sigma = 0.294$ and an inflow velocity of $U_\infty = 1.00$ m/s.....	77
Table A.1.	Manual carriage speed measurements are compared to the results obtained using the data acquisition	105
Table B.1.	Sample standard deviation of power coefficient is compared to the uncertainty in power coefficient calculated using uncertainty propagation equations. The uncertainties are larger than three standard deviations for every point except one. The uncertainty is still close to three standard deviations in magnitude for this point.....	128

LIST OF FIGURES

Figure 1.1.	A tidal barrage, the Rance Tidal Power Station, is shown installed across an estuary in France	2
Figure 1.2.	A cross-flow hydrokinetic turbine is shown above water.....	2
Figure 1.3.	The straight bladed model Darrieus turbine rotor is shown with NACA 63 ₃ -018 blades installed and rod across the center	4
Figure 1.4.	The operation of a cross-flow turbine is depicted with example force and velocity vectors. U_{∞} is the inflow velocity, ω is the turbine angular velocity, U_R is the relative velocity at the foil, α is the angle of attack between the foil and relative velocity vector U_R , F_L is the lift force on the foil, F_D is the drag force on the foil, F_R is the resultant force from the lift and drag forces, and F_T and F_N are the components of the resultant force that are tangential and normal to the chord length of the foil, respectively	5
Figure 1.5.	A sample profile is shown with annotations including chord length, maximum thickness, maximum camber, mean line, leading edge (LE) and trailing edge (TE). Mean line is the camber of the foil at each position x along the chord. The thickness distribution of the foil is the thickness of the foil at each position x along the chord	7
Figure 1.6.	The configuration for a static lift and drag test is shown, where F_L is the lift force, F_D is the drag force, U_R is relative velocity of the fluid, and α is the angle of attack, or the angle between the blade chord length and the relative velocity. A moment term exists along with the lift and drag forces, but it was not included in the theory in this thesis, so it is not shown.....	9
Figure 1.7.	The experimental lift curve for a NACA 0018 blade profile was taken at a Reynolds number of $Re = 1,000,000$ (Sheldahl and Klimas, 1981).....	9
Figure 1.8.	The experimental drag curve for a NACA 0018 blade profile was taken at a Reynolds number of $Re = 1,000,000$ (Sheldahl and Klimas, 1981).....	10
Figure 1.9.	A cross-flow turbine blade is shown mounted at a positive toe angle, θ_t . The turbine rotates with turbine angular velocity ω . The toe angle is referenced from the tangent to the turbine circumference at the blade mounting point	12

Figure 1.10.	The concept of solidity ratio is demonstrated by varying the blade chord length for turbines with the same turbine radius, R , and same number of blades. The example low solidity and high solidity turbines have solidity ratios of $\sigma \approx 0.090$ and $\sigma \approx 0.25$, respectively	13
Figure 1.11.	A foil is shown in a curvilinear flow (top) and a rectilinear flow (bottom). The foil in the rectilinear flow has been transformed from the curvilinear coordinate system to a rectilinear coordinate system, with virtual angle of incidence, α_i , and virtual camber. The virtual camber is indicated by the curved mean line, with a maximum value of f_v	18
Figure 2.1.	(a) The coordinate system from Strickland et al. (1980) was used for the FVM. (b) The relative velocity at the blade, U_R , is a vector sum of the inflow velocity U_∞ , the tangential blade velocity, U_T , and the induced velocities U and W	22
Figure 2.2.	The angle of attack as a function of turbine blade angular position from the FVM results is shown for turbines with a high solidity ratio ($\sigma = 0.147$) and low solidity ratio ($\sigma = 0.0477$). The angle of attack for turbines with high and low solidity ratios is significantly different. The blades in turbines with high solidity ratios reach angles of attack much higher than the static stall angle of attack. Turbines with a low solidity ratio tend to operate at angles of attack under the static stall angle of attack.	24
Figure 2.3.	Orientation of turbine wake images used to model two-walled case. Image A' is necessary to maintain symmetry about the upper wall, and image B' is necessary to maintain symmetry about the lower wall	28
Figure 2.4.	The orientation of the angle of attack from Strickland et al. (1980) is shown with the orientation of the toe angle, θ_t , and relative angle of attack, α_r . Note that in order to obtain the relative angle of attack between the foil and the flow, α_r , the toe angle, θ_t , must be subtracted from the angle of attack, α . Turbine angular velocity, ω , is shown for reference.....	30
Figure 2.5.	Example normal and tangential coefficients are shown in the turbine and blade coordinate systems. C_R is the resultant force coefficient for the normal and tangential force coefficients in either coordinate system	31
Figure 2.6.	Power coefficient results from the free vortex model are shown for the three model boundary conditions. Results are for two blades, where $\sigma = 0.147$ and $U_\infty = 0.60$ m/s.....	32

Figure 2.7.	Two-bladed nondimensional torque results from the free vortex model are shown for $\lambda = 1.50$, $\sigma = 0.147$ and $U_\infty = 0.60$ m/s	33
Figure 2.8.	FVM results are shown for $\theta_t = -5^\circ$, $\theta_t = -2^\circ$, $\theta_t = 0^\circ$, $\theta_t = +2^\circ$ and $\theta_t = +5^\circ$ with no blockage effect and without angle of incidence correction. Results are for two blades, $\sigma = 0.147$, $R = 0.165$ m, and $U_\infty = 0.60$ m/s.....	35
Figure 2.9.	FVM results with incidence angle correction and no blockage effect are shown for $\theta_t = -5^\circ$, $\theta_t = 0^\circ$, $\theta_t = +5^\circ$, $\theta_t = +7^\circ$ and $\theta_t = +9^\circ$. Results are for two blades, $\sigma = 0.147$, $R = 0.165$ m, and $U_\infty = 0.60$ m/s.....	36
Figure 2.10.	FVM results with incidence angle correction and one wall blockage effect are shown for $\theta_t = 0^\circ$ and $\theta_t = +5^\circ$. Results are for two blades, $\sigma = 0.147$, $R = 0.165$ m, and $U_\infty = 0.60$ m/s	37
Figure 2.11.	Maximum power coefficient as a function of toe angle is shown for the FVM with no blockage effect and the FVM with angle of incidence correction and no blockage effect. Results are for two blades, $\sigma = 0.147$, $R = 0.165$ m, and $U_\infty = 0.60$ m/s	37
Figure 3.1.	The University of Maine tow tank with rails and carriage in the distance	39
Figure 3.2.	Cross-flow turbine installed in the tow tank with instrumentation.....	39
Figure 3.3.	The model cross-flow turbine test bed is shown mounted in the tow tank.....	41
Figure 3.4	A solid model of the upper assembly of the cross-flow turbine is shown with measurement axes. The torque in the driveshaft is measured with a load cell mounted perpendicular to the motor, at a certain distance from the driveshaft. Torque is calculated using the force in the load cell and this distance. The rotor torque is transferred to the driveshaft with a chain-drive (not shown). The thrust load cells measure the force parallel to the direction of turbine motion	42
Figure 3.5.	The lower turbine assembly (turbine rotor) is shown with blades, end plates, and angle indicators	43
Figure 3.6.	The center hole in the angle indicator accepts the blade mounting rod. The center hole protrudes out of the page, and when installed in the indicator mounting hole, it extends all the way through the end plate. This section transfers the blade loads from the blade to the end plate	44

Figure 3.7.	A solid model of the upper turbine drive system is shown with the torque load cell, torque load cell lever arm, load cell bracket, motor, and rectangular tube. The system is shown without the frame and other components for clarity	47
Figure 3.8.	The upper turbine assembly is shown with dynamometer, thrust load cells, and hydrodynamic shrouds	49
Figure 3.9.	Drive-train friction and end plate drag curves are shown as a function of turbine angular velocity. Drive-train friction curves were obtained outside the tow tank, while end plate drag tests were performed inside the tank.....	51
Figure 3.10.	The NACA 63 ₃ -018 carbon fiber turbine blade is shown with locating rod and tapped mounting holes	57
Figure 3.11.	The NACA 63 ₃ -018 profile resists flow separation at high angles of attack. Cross-flow testing has been performed by Shiono et al. (2000) using a modified version of this profile	58
Figure 3.12.	The side view of the NACA 63 ₃ -018 blade is shown with tubercles added to the leading edge.....	59
Figure 3.13.	The top view of the NACA 63 ₃ -018 blade profile is shown with tubercles added to the leading edge	59
Figure 3.14.	The NACA 0018 profile has been used in cross-flow tidal and wind turbine testing.....	60
Figure 3.15.	The NACA 4418 profile has the same thickness distribution as the NACA 0018 but with added camber.....	61
Figure 3.16.	The S809 profile, which is commonly used in the axial-flow wind turbine industry, has a large maximum thickness compared to the rest of the tested profiles.....	62
Figure 3.17.	The LNV109 profile has a very high lift-to-drag ratio while resisting separation	63
Figure 4.1.	The power coefficient curves for $\theta_t = +3^\circ$ and $\theta_t = -2^\circ$ are shown for the carbon fiber NACA 63 ₃ -018 blade set. Four-bladed testing was performed at the toe angles $\theta_t = +3^\circ$ and $\theta_t = -2^\circ$, at an inflow velocity of $U_\infty = 1.22$ m/s, and at a solidity ratio of $\sigma = 0.294$	67

Figure 4.2.	The power coefficient curves for $\theta_t = +3^\circ$ and $\theta_t = -2^\circ$ are shown for the 3-D printed NACA 63 ₃ -018 blade set. Four-bladed testing was performed at the toe angles $\theta_t = +3^\circ$ and $\theta_t = -2^\circ$, at an inflow velocity of $U_\infty = 1.22$ m/s, and at a solidity ratio of $\sigma = 0.269$67
Figure 4.3.	The power coefficient curves for $\theta_t = +3^\circ$ and $\theta_t = -2^\circ$ are shown for the 3-D printed NACA 63 ₃ -018 B blade set. NACA 63 ₃ -018 B refers to the profile with tubercles or bumps. Four-bladed testing was performed at the toe angles $\theta_t = +3^\circ$ and $\theta_t = -2^\circ$, at an inflow velocity of $U_\infty = 1.22$ m/s, and at a solidity ratio of $\sigma = 0.269$. Note the difference in scale in this figure.....68
Figure 4.4.	The power coefficient curves for $\theta_t = +3^\circ$ and $\theta_t = -2^\circ$ are shown for the 3-D printed NACA 0018 blade set. Four-bladed testing was performed at the toe angles $\theta_t = +3^\circ$ and $\theta_t = -2^\circ$, at an inflow velocity of $U_\infty = 1.22$ m/s, and at a solidity ratio of $\sigma = 0.343$68
Figure 4.5.	The power coefficient curves for $\theta_t = +3^\circ$ and $\theta_t = -2^\circ$ are shown for the 3-D printed NACA 4418 blade set. Four-bladed testing was performed at the toe angles $\theta_t = +3^\circ$ and $\theta_t = -2^\circ$, at an inflow velocity of $U_\infty = 1.22$ m/s, and at a solidity ratio of $\sigma = 0.343$70
Figure 4.6.	The power coefficient curves for $\theta_t = +3^\circ$ and $\theta_t = -2^\circ$ are shown for the 3-D printed S809 blade set. Four-bladed testing was performed at the toe angles $\theta_t = +3^\circ$ and $\theta_t = -2^\circ$, at an inflow velocity of $U_\infty = 1.22$ m/s, and at a solidity ratio of $\sigma = 0.289$71
Figure 4.7.	The power coefficient curves are shown for the 3-D printed LNV109 blade set. Four-bladed testing was performed at the toe angles $\theta_t = +3^\circ$ and $\theta_t = -2^\circ$, at an inflow velocity of $U_\infty = 1.22$ m/s, and at a solidity ratio of $\sigma = 0.269$71
Figure 4.8.	The testing results for each blade profile, excluding the LNV109, are compared for $U_\infty = 1.22$ m/s and $\theta_t = +3^\circ$. Uncertainties are included at the point with maximum power coefficient for each profile. NACA 63 ₃ -018 B refers to the profile with tubercles or bumps.....73
Figure 4.9.	The maximum power coefficient from four-bladed experimental testing is shown for each blade profile at $\theta_t = +3^\circ$ and $U_\infty = 1.22$ m/s74
Figure 4.10.	Power coefficient curves are shown for NACA 63 ₃ -018 carbon fiber blades for $\theta_t = +3^\circ$, $\theta_t = +5^\circ$, and $\theta_t = +7^\circ$. These four-bladed tests were taken at a solidity of $\sigma = 0.294$ and an inflow velocity of $U_\infty = 1.00$ m/s. Uncertainties are included at the peak power coefficient from each toe angle.....75

Figure 4.11.	Power coefficient curves are shown for NACA 63 ₃ -018 carbon fiber blades for $\theta_t = +0.5^\circ$ and $\theta_t = -2^\circ$. These four-bladed tests were taken at a solidity of $\sigma = 0.294$ and an inflow velocity of $U_\infty = 1.00$ m/s. Uncertainties are included at the peak power coefficient from each toe angle	76
Figure 4.12.	The maximum power coefficient for the carbon fiber NACA 63 ₃ -018 blade profile is shown as a function of toe angle. Four-bladed data was taken at a solidity of $\sigma = 0.294$ and an inflow velocity of $U_\infty = 1.00$ m/s.....	77
Figure 4.13.	Power coefficient results are shown for two-bladed NACA 63 ₃ -018 testing taken at a solidity of $\sigma = 0.147$, inflow velocity of $U_\infty = 0.6$ m/s and toe angle of $\theta_t = 0^\circ$. Testing was performed four times at each tip speed ratio. The same data is shown with uncertainty in C_P in Fig. 4.17	79
Figure 4.14.	Bin-averaged nondimensional torque from two-bladed NACA 63 ₃ -018 experimental data is shown for $\lambda = 2.00$. Data was taken at a solidity of $\sigma = 0.147$, inflow velocity of 0.6 m/s, and toe angle of $\theta_t = 0^\circ$	79
Figure 4.15.	Two bladed experimental testing results are shown for the NACA 63 ₃ -018 profile, taken at $\sigma = 0.147$, inflow velocity of 0.6 m/s, and $\theta_t = +5^\circ$. Only one data point was taken for each tip speed ratio, and the error bars were calculated using the uncertainty propagation equations outlined in Appendix B.....	80
Figure 4.16.	Uncertainty in power coefficient is compared with multiple experimental data points at each tip speed ratio taken with the same turbine geometry and flow conditions. Data was taken using the NACA 63 ₃ -018 blade profile, with four blades, $\sigma = 0.269$, $\theta_t = 0^\circ$, and $U_\infty = 1.00$ m/s	82
Figure 4.17.	Uncertainty in power coefficient is compared with multiple experimental data points at each tip speed ratio taken with the same turbine geometry and flow conditions. Data was taken using the NACA 63 ₃ -018 blade profile, with two blades, $\sigma = 0.147$, $\theta_t = 0^\circ$, and $U_\infty = 0.60$ m/s	82
Figure 4.18.	Two-bladed experimental data at a solidity of $\sigma = 0.147$, inflow velocity of 0.6 m/s, and $\theta_t = 0^\circ$ is compared to the FVM with one wall blockage effect, and the FVM with virtual incidence angle correction and one wall blockage effect	85

Figure 4.19.	Experimental nondimensional torque taken at $\sigma = 0.147$, $\theta_t = 0^\circ$, $\lambda = 1.80$, and $U_\infty = 0.6$ m/s is compared to the FVM with virtual incidence angle correction and one wall blockage, as well as the FVM with no blockage effect and without the virtual incidence angle correction. The eighth revolution refers to the first turbine revolution that has reached convergence.....	86
Figure 4.20.	Experimental nondimensional torque taken at $\sigma = 0.147$, $\theta_t = 0^\circ$, $\lambda = 2.40$, and $U_\infty = 0.6$ m/s is compared to the FVM with virtual incidence angle correction and one wall blockage, as well as the FVM with no blockage effect and without the virtual incidence angle correction. The eighth revolution refers to the first turbine revolution that has reached convergence.....	86
Figure 4.21.	Two-bladed experimental data at a solidity of $\sigma = 0.147$, inflow velocity of 0.6 m/s, and $\theta_t = +5^\circ$ is compared to the FVM with no blockage effect, and the FVM with virtual incidence angle correction and one wall blockage effect.....	88
Figure 4.22.	Experimental nondimensional torque taken at $\sigma = 0.147$, $\theta_t = +5^\circ$, $\lambda = 1.80$, and $U_\infty = 0.6$ m/s is compared to the FVM with virtual incidence angle correction and one wall blockage, as well as the FVM with no blockage effect and without the virtual incidence angle correction. The eighth revolution refers to the first turbine revolution that has reached convergence.....	89
Figure 4.23	Experimental nondimensional torque taken at $\sigma = 0.147$, $\theta_t = +5^\circ$, $\lambda = 2.40$, and $U_\infty = 0.6$ m/s is compared to the FVM with virtual incidence angle correction and one wall blockage, as well as the FVM with no blockage effect and without the virtual incidence angle correction. The eighth revolution refers to the first turbine revolution that has reached convergence.....	90
Figure 4.24	The maximum power coefficient as a function of toe angle is shown for two-bladed experimental data, FVM with virtual incidence angle correction and no blockage effect, and FVM with virtual incidence angle correction and one wall blockage effect. Two-bladed experiment and modeling was performed at a solidity of $\sigma = 0.147$ and inflow velocity of 0.6 m/s. Four-bladed data is included for reference. Uncertainties are included in the two-bladed and four-bladed experimental data	91
Figure A.1.	The carriage velocity encoder wheel assembly is shown riding on the tow tank rail	104

Figure A.2.	The configuration of the torque load cell is shown during the slope calibration process. The applied load F and applied load lever arm l determine the torque applied in the calibration, according to eqn. 3.1	106
Figure A.3.	Torque load cell calibration results are shown. Raw torque load cell output refers to the unconverted binary format of the resulting data. The data was not converted to voltage because the output could be calibrated in this format. Error estimates for the linear regression line are included in Appendix B.2	107
Figure A.4.	Drive train friction as a function of turbine angular velocity is shown for four separate groups of tests, which were performed before and after disassembling and assembling the drive train several times	108
Figure A.5.	The straight bladed model Darrieus turbine rotor is shown with NACA 63 ₃ -018 blades installed and rod across the center	109
Figure A.6.	Drive train friction as a function of turbine angular velocity is shown for four separate tests. End plate drag as a function of turbine angular velocity is shown. Two data points were taken at each turbine angular velocity, and a polynomial was fit to the data	109
Figure A.7.	The instantaneous turbine angular velocity is entered in the end plate drag and drive train friction function, and the instantaneous torque can be calculated. This torque term represents all of the losses the system resulting from end plate drag and drive train friction	110
Figure A.8.	Example power coefficient results are shown for two-bladed testing taken at a solidity of $\sigma = 0.147$, inflow velocity of $U_{\infty} = 0.6$ m/s and toe angle of $\theta_t = 0^{\circ}$. Testing was performed four times at each tip speed ratio	111
Figure A.9.	Unfiltered and filtered turbine rotational frequency (in Hz) are compared. Note the difference in the y-scale between the two graphs....	112
Figure A.10.	The angular position of an encoder signal is shown before and after the modifications. A signal with no discontinuities was necessary for filtering before differentiation.....	113
Figure A.11.	Filtered and unfiltered angular position over an elapsed time are compared. Note the chatter in the unfiltered data compared to the unfiltered data	113

Figure A.12.	Filtered inflow velocity is shown from a four-bladed test at $\lambda = 1$ and $U_\infty = 1$ m/s. Filtering significantly improved the accuracy of the inflow velocity and turbine angular velocity calculations	114
Figure A.13.	Sample unfiltered torque data from a four-bladed test is shown after application of eqn. A.5. Note the significant fluctuations in the unfiltered torque data that is a result of vibrations	115
Figure A.14.	An FFT of the torque in the measurement system is shown. The test turbine was run down the tow tank with the turbine motor control turned off in order to capture structural vibrations in the absence of hydrodynamic forces.....	116
Figure A.15.	An FFT of the turbine torque is shown for a four-bladed test. Comparing with Fig. A.14 shows the hydrodynamic frequency range and the structural vibration frequency range.....	117
Figure A.16.	An FFT was performed on filtered and unfiltered torque data from a four-bladed test. Note the significant decrease in the structural vibration frequency range (above 17 Hz) that results from application of the filter.....	118
Figure A.17.	Unfiltered and filtered torque data from a four-bladed test are shown in the time domain. Note the significant decrease in noise after application of the filter.....	118
Figure A.18.	C_p results from a series of four-bladed tests are shown with low-pass filter cut-off frequencies of 2 Hz, 17 Hz, and 45 Hz. The C_p results were not significantly affected by changes in the cut-off frequency of the low-pass filter	119
Figure A.19.	An example bin-averaged non-dimensional torque curve from a two-bladed test is shown. Results are from the NACA 63 ₃ -018 profile at $\theta_t = 0^\circ$, $U_\infty = 0.6$ m/s, and $\lambda = 2.30$	120
Figure A.20.	Bin-averaged non-dimensional torque from a two-bladed test is shown with and without accounting for the inertial term, $T_{inertia}$. Results are from the NACA 63 ₃ -018 profile at $\theta_t = 0^\circ$, $U_\infty = 0.6$ m/s, and $\lambda = 2.30$	121
Figure B.1.	The power coefficient curves for $\theta_t = +3^\circ$ and $\theta_t = -2^\circ$ are shown with uncertainty error bars for the carbon fiber NACA 63 ₃ -018 blade set. Four-bladed testing was performed at the toe angles $\theta_t = +3^\circ$ and $\theta_t = -2^\circ$, at an inflow velocity of $U_\infty = 1.22$ m/s, and at a solidity ratio of $\sigma = 0.294$	124

Figure B.2.	The C_P results of the repeatability study are shown for four-bladed testing of the NACA 63 ₃ -018 profile at $\theta_t \approx +5^\circ$ and $U_\infty = 1.00$ m/s. The spline interpolation used the average CP value at a given tip speed ratio from the repeatability study, as well as some data points from Fig. B.3.....	127
Figure B.3.	Uncertainty in C_P is shown for four-bladed testing of the NACA 63 ₃ -018 profile at $\theta_t \approx +5^\circ$ and $U_\infty = 1.00$ m/s. Additional tests were taken for the repeatability study (shown in Fig. B.2) under the same test conditions, but not at all of the tip speed ratios in this curve	128
Figure C.1.	The coordinate systems used by Strickland and Migliore were different, so it was necessary to modify the turbine angular position, θ , input to the conformal mapping calculations in order to apply the virtual incidence angle at the correct turbine angular position	130
Figure D.1.	Four-bladed testing results are shown for five of the blade sets. Testing was performed at $\theta_t = -7^\circ$ at an inflow velocity of $U_\infty = 1.22$ m/s for a range of blade solidity ratios. The NACA 0018 profile was set at the incorrect angle of $\theta_t = -5^\circ$, but is included for comparison nonetheless	131
Figure D.2.	Four-bladed testing results are shown for the NACA 63 ₃ -018 carbon fiber and 3-D printed blade sets. Testing was performed at $\theta_t = +3^\circ$, at an inflow velocity of $U_\infty = 1.22$ m/s.....	132
Figure E.1	A schematic of the cross-flow turbine installed in the tow tank shows the geometry used for testing. The turbine direction of motion corresponds to out of the page	134

CHAPTER 1

INTRODUCTION

1.1 Motivation

In an age of climate change and dependence on fossil fuels, the need for affordable, clean, renewable, and environmentally friendly energy sources is becoming increasingly important. Tidal energy is one potential source that is currently being developed worldwide. Tidal energy is an appealing source of carbon free electricity. While tidal energy is periodic in availability, it is available on a predictable schedule, which is desirable for grid operation.

Tidal energy devices can be divided into two separate categories: marine hydrokinetics (MHK) and barrages. Examples are shown in Fig. 1.1 and Fig 1.2. Tidal barrages are essentially dams installed across tidal inlets. Because barrages extract energy from velocity and pressure head, they can produce large amounts of power, but have been proven to significantly alter the surrounding environment (Charlier, 1982). Barrages also force organisms to travel directly through tidal turbines, which greatly increases the chances of mechanical strike, injury and mortality. Hydrokinetic devices produce power from the velocity of the tidal flow only. These devices have lower power densities, but because of the reduced environmental impact and the number of sites, marine hydrokinetic devices have the potential to produce significant power in some regions. It has been generally accepted that impacts will be more localized with MHK, but a large number of questions remain unanswered. Far-field effects of pilot-scale deployments are anticipated to be negligible, but the cumulative effects resulting from the installation of commercial-scale arrays are expected to be substantial (Polagye et al., 2010). Potential

cumulative effects include changes in water quality, sediment transport, and the nature of inter-tidal areas. All of these changes could potentially affect the population of organisms in near-field and far-field habitats. The eventual scale of commercial projects will likely depend on the magnitude of these region-wide impacts (Polagye et al., 2010).

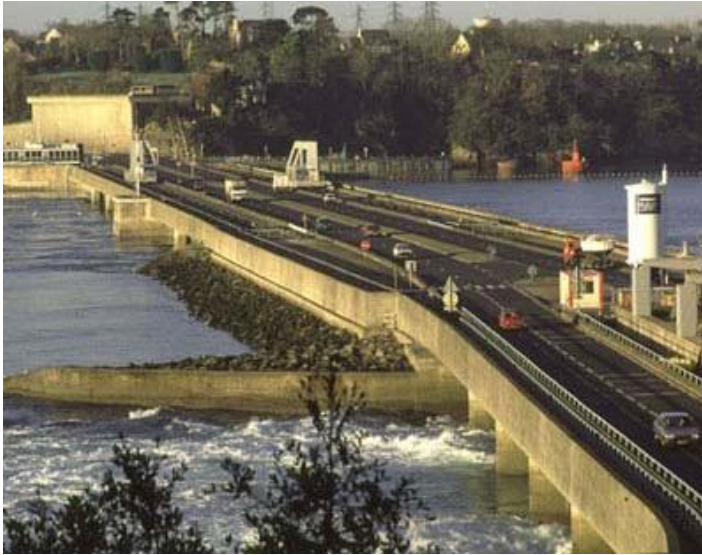


Figure 1.1 – A tidal barrage, the Rance Tidal Power Station, is shown installed across an estuary in France (Image Source: <http://www.solarpowernotes.com/renewable-energy/tidal-energy/tidal-energy.html>).



Figure 1.2 - A cross-flow hydrokinetic turbine is shown above water (Image Source: http://www.orpc.co/newsevents_photogalleryDetails.aspx?Aid=i1%2bgAhwr%2boY%3d).

Two primary types of hydrokinetic turbines are expected to have acceptable efficiencies. Axial flow turbines are the most common and resemble a wind turbine or ship propeller. While these devices are efficient, additional mechanical complexity is required in order for the devices to generate power for flow in both directions. Either the turbine must be reoriented or the blade pitch must be altered during turbine operation. These devices also operate at a high tip speed ratio. Tip speed ratio is the blade tip velocity divided by the inflow velocity, and is the standard nondimensional quantity for characterizing turbine operational speed. High tip speed ratios create a flow condition where the tips of the blades move much faster than the water. For an axial flow turbine to develop optimum efficiency, the tip speed ratios range from 5 to 7 at peak output (Lokocz, 2012).

Operation at high tip speed ratios may pose a risk to fish and marine mammals that swim near turbines with fast moving blade tips (Polagye et al., 2010). Finally, depending on the shape of a site, the circular cross section of an axial flow turbine can make it difficult to utilize a channel with devices of a reasonable size, without interfering with the navigation channel. Thus an alternative design, such as a cross-flow turbine, can be appealing for many applications.

There are several advantages to using cross-flow turbines in the MHK industry, including environmental and logistical reasons. Figure 1.3 shows an example model cross-flow turbine rotor. The axis of rotation of a cross-flow turbine is perpendicular to the flow direction (Fig. 1.4). Because of this orientation, cross-flow turbines can operate with flow in either direction, so when the tide changes from ebb to flood and vice versa, a system is not needed to align it to generate power. Cross-flow turbines would be expected to operate with an efficiency slightly below axial turbines (Paraschivoiu, 2002). However,

the peak efficiency is achieved when rotating at low tip speed ratios, such as between 1 and 2, which is likely to reduce the risk of blade strike (Polagye et al., 2010). Cross-flow turbines can also cover large areas while maintaining navigational channels by increasing the width of the turbine or using an array of turbines installed side by side. Any of these factors could make the cross-flow turbine a desirable choice for a specific site.



Figure 1.3 – The straight bladed model Darrieus turbine rotor is shown with NACA 63₃-018 blades installed and rod across the center.

While some data exists regarding the performance of cross-flow turbines, such as Shiono et al. (2000), Strickland et al. (1980), and Li (2008), these devices have not been as widely studied as axial flow turbines. Currently, insufficient data exists for a turbine to be optimized for a specific application. The goal of this thesis is to examine changes in cross-flow turbine performance as a function of changes to two variables in the turbine geometry: blade profile and blade toe angle. Experimental data was obtained and is compared to a numerical model developed in related work by Urbina (2011a) that was modified to include additional theoretical concepts. This validated model then allows turbine optimization work to be performed.

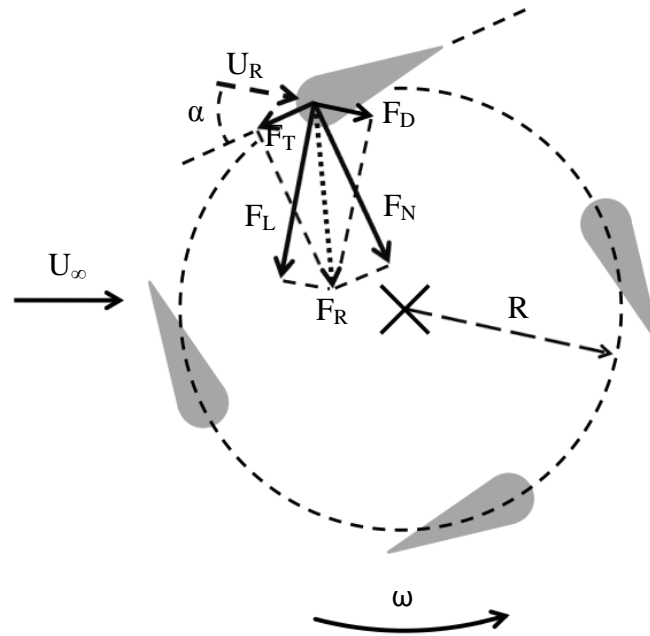


Figure 1.4 – The operation of a cross-flow turbine is depicted with example force and velocity vectors. U_∞ is the inflow velocity, ω is the turbine angular velocity, U_R is the relative velocity at the foil, α is the angle of attack between the foil and relative velocity vector U_R , F_L is the lift force on the foil, F_D is the drag force on the foil, F_R is the resultant force from the lift and drag forces, and F_T and F_N are the components of the resultant force that are tangential and normal to the chord length of the foil, respectively.

1.2 Background

Several types of cross-flow turbine designs currently exist. The simplest type of cross-flow turbine and the easiest to manufacture is the straight bladed Darrieus turbine (Fig. 1.3). The simplicity of the straight bladed Darrieus turbine made it the obvious choice for this research. Because the numerical model is two-dimensional, straight bladed model turbines are also the best option for experimental validation, specifically for comparison of the torque between the model and experiment. In MHK applications helical blades are typically used because the torque output is steadier. A steady torque output is preferred to reduce dynamic bearing loading. Straight bladed cross-flow turbines may also not self-

start at all blade positions, with helical turbines much less sensitive to blade position in self-starting.

Figure 1.4 shows the operation of a cross-flow turbine. The operation of the cross-flow turbine is in some ways complex compared to other types of turbines. The theory of operation may not be apparent from appearance. The turbine is made up of foils mounted at a distance R (the turbine radius) from the axis of rotation (Fig. 1.4). When water passes through a rotating turbine, the foils produce lift and drag forces. Depending on the rotational position of the foil, the lift and drag forces can produce positive or negative rotor torque. For a useful design the average torque over an entire revolution must be positive, so the turbine produces power. The cross-flow turbine is classified as a lift device, because the power produced is primarily from lift forces. In Fig. 1.4, the resultant force from the lift and drag can be reduced to tangential and normal force components, which are more useful for determining the rotor torque and turbine efficiency. In Fig. 1.4, a positive tangential force, F_T , results in a positive rotor torque.

1.2.1 Fundamental Definitions

This thesis will make use of a number of geometric definitions associated with the cross-flow turbine. These definitions describe aspects of the turbine that have an impact on performance. This thesis includes a parametric study of two geometric characteristics, however, all of these geometrical parameters impact turbine performance to some degree.

1.2.1.1 Foil Shape

Foil or blade profile selection is one of the most important aspects of cross-flow turbine design (Migliore and Wolfe, 1980). The blade profile is a primary part of the turbine design, and significantly affects turbine performance. Figure 1.5 shows a sample blade profile. The base reference for the blade profile is the blade chord length, which extends from the leading edge (LE) to the trailing edge (TE). The other main geometric parameters of a blade profile are the thickness profile and mean line, or camber line. The thickness profile is simply the thickness of the blade profile at each position along the chord line. The camber line is the distance from the center of the foil to the chord line at each point along the chord length. Both numbers are nondimensionalized by the chord length so that one profile can be used to describe a foil regardless of physical size. Foils with no camber are called symmetric foils, and foils with camber are called asymmetric foils and appear “bent”. The addition of camber to a foil can significantly change the lift and drag characteristics of the foil (Abbott and von Donhoff, 1959). This can improve or detract from overall turbine performance.

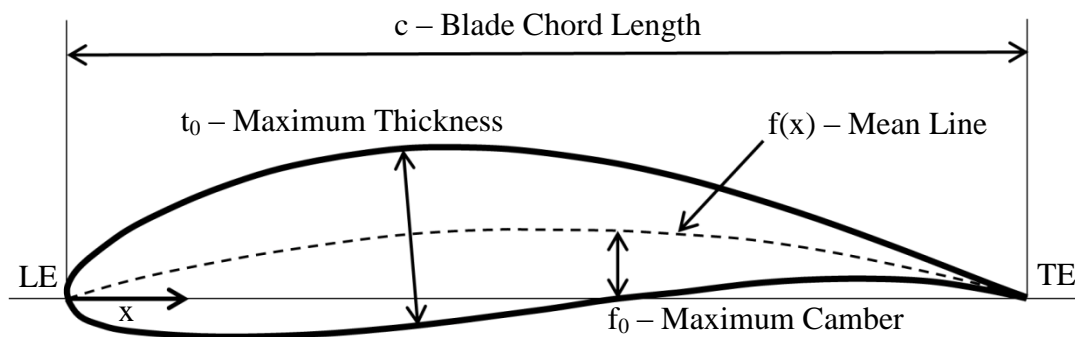


Figure 1.5 – A sample profile is shown with annotations including chord length, maximum thickness, maximum camber, mean line, leading edge (LE) and trailing edge (TE). Mean line is the camber of the foil at each position x along the chord. The thickness distribution of the foil is the thickness of the foil at each position x along the chord.

The static lift and drag characteristics of a foil can be determined experimentally or theoretically. Figure 1.6 shows the configuration of a static lift and drag test, with sample lift and drag forces. When a foil is subjected to a flow, lift and drag forces change as the angle of attack of the foil changes. Angle of attack is the angle between the inflow velocity vector and the blade chord length, as shown in Fig. 1.6. The majority of experimental and theoretical research on the lift and drag characteristics of foils has been conducted for static angles of attack between -5° and 20° , which is the angle of attack range commonly encountered in the aerodynamics of flight. Example lift and drag curves from Sheldahl and Klimas (1981) are shown in Fig. 1.7 and Fig. 1.8 for the symmetric NACA 0018 profile. The NACA 0018 profile is commonly used in the wind and tidal industries, and can be found in section 3.3.4.3. For symmetric foils, the lift coefficient is generally zero at a zero angle of attack. The lift coefficient on the foil increases linearly with angle of attack until the foil begins to stall. Once the blade begins to stall, the slope of the lift curve decreases, until the maximum lift is achieved, at which point the behavior of the lift is less predictable. The drag coefficient is minimized at zero angle of attack for symmetric foils. The drag coefficient increases marginally with angle of attack until the foil stalls. At this point the drag coefficient increases sharply, with the curve resembling the shape of a bucket, as shown in Fig. 1.8. Addition of camber to a profile changes the maximum lift coefficient, the angle of attack where $C_L = 0$, and the angle of attack where drag is minimized. Modification to the thickness profile can also modify the lift and drag curves, but with less of an effect (Abbott and Von Doenhoff, 1959).

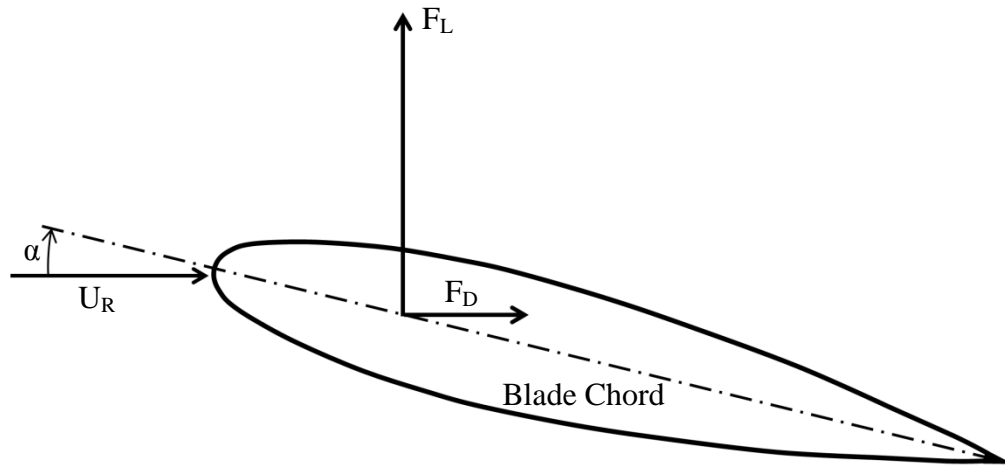


Figure 1.6 – The configuration for a static lift and drag test is shown, where F_L is the lift force, F_D is the drag force, U_R is relative velocity of the fluid, and α is the angle of attack, or the angle between the blade chord length and the relative velocity. A moment term exists along with the lift and drag forces, but it was not included in the theory in this thesis, so it is not shown.

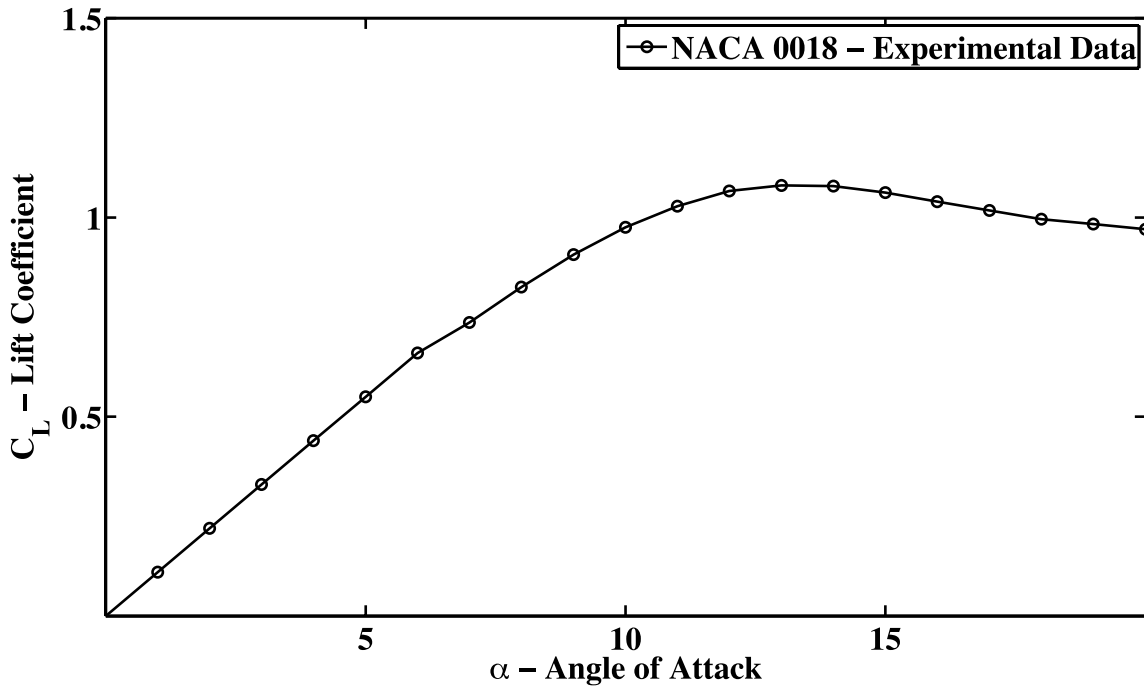


Figure 1.7 – The experimental lift curve for a NACA 0018 blade profile was taken at a Reynolds number of $Re = 1,000,000$ (Sheldahl and Klimas, 1981).

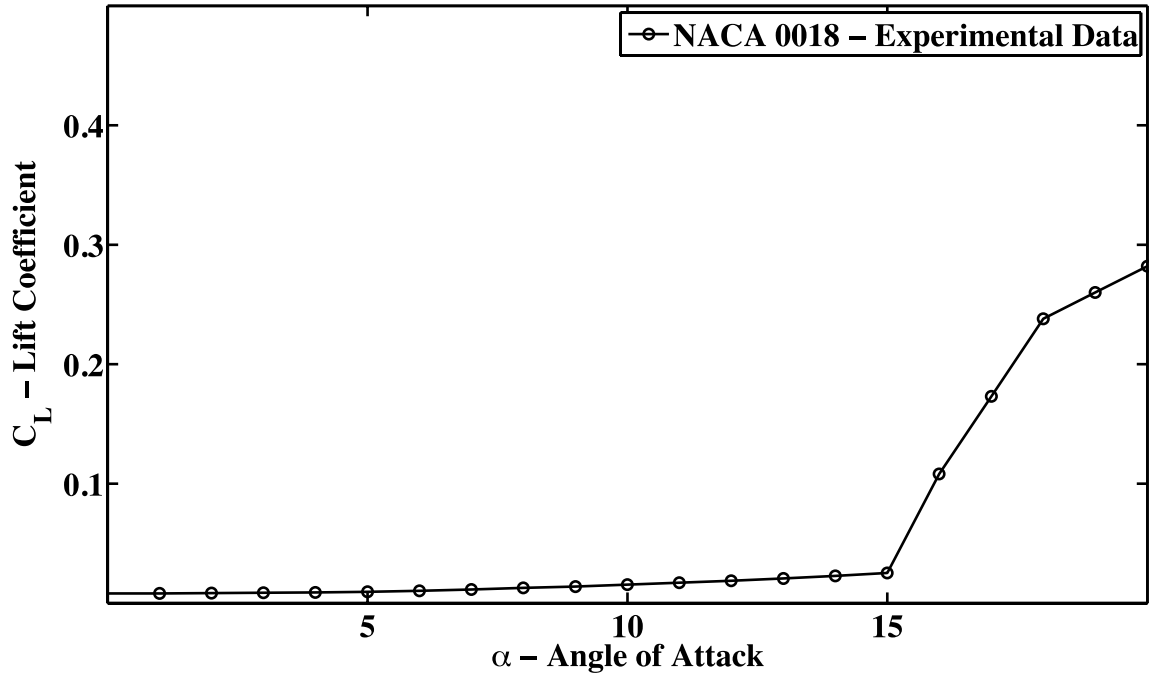


Figure 1.8 – The experimental drag curve for a NACA 0018 blade profile was taken at a Reynolds number of $Re = 1,000,000$ (Sheldahl and Klimas, 1981).

Another important characteristic of a foil is the aspect ratio, AR , which is defined as,

$$AR = \frac{b^2}{A_p}, \quad (1.1)$$

where b is the blade span and A_p is the planform area of the blade. Using Fig. 1.5 as a reference, blade span b is the length of the blade into the page, and planform area is the area of the top or bottom of the blade. For blades with rectangular planform areas, the planform area is defined as bc , where b is the blade span and c is the blade chord length.

Inserting this into eqn 1.1 yields an aspect ratio of $\frac{b}{c}$ for blades with rectangular planform areas. The aspect ratio of the turbine blade can have implications on turbine performance. Static testing has shown that lift and drag coefficients are a function of the aspect ratio. Increasing the aspect ratio of a foil increases the lift curve slope (i.e. the slope increases in the linear region of the lift curve encountered at low angles of attack) and decreases

drag in static wind tunnel testing (Abbott and Von Doenhoff, 1959). Blades with a large aspect ratio approach the performance of the two-dimensional case, or blades with infinite span (Abbott and Von Doenhoff, 1959). Increasing the aspect ratio of the blades on a tidal turbine could result in improved performance from these effects.

It is also important to note that this data is for stationary (static) blades operating in a rectilinear flow. The cross-flow turbine encounters very high angles of attack, complex flow dynamics, and curvilinear flow, all of which alter the flow characteristics significantly. However, it is necessary to understand the behavior of foils in a rectilinear coordinate system at low angles of attack under static conditions before the theory can be extended to the more complicated configuration seen in tidal turbines.

1.2.1.2 Turbine Geometry

For any given foil, the characteristics of the mounting of the blades on the turbine also impact performance (Migliore and Wolfe, 1980). Toe angle, θ_t , is the angle at which the blade profile is mounted on the turbine. A blade profile installed with a positive toe angle is shown in Fig. 1.9. Toe angle is defined as zero when the chord length is perpendicular to the turbine radius with the leading edge of the foil facing in the direction the foil is rotating. Changes in toe angle have been shown to significantly affect turbine performance (McAdam et al., 2009).

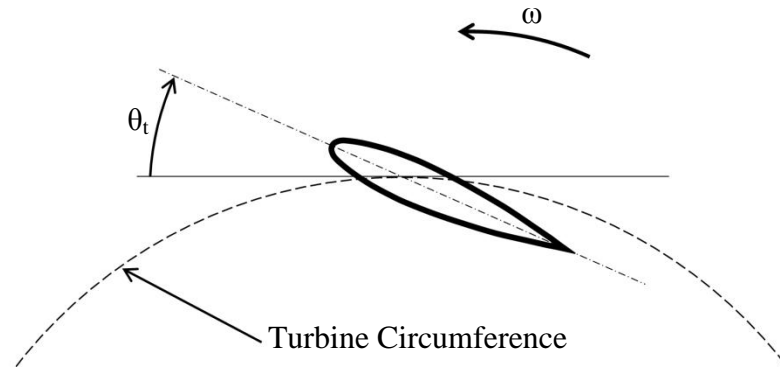


Figure 1.9 – A cross-flow turbine blade is shown mounted at a positive toe angle, θ_t . The turbine rotates with turbine angular velocity ω . The toe angle is referenced from the tangent to the turbine circumference at the blade mounting point.

Another design factor, solidity ratio, σ , is defined as,

$$\sigma = \frac{Nc}{2\pi R}, \quad (1.2)$$

where N is the number of blades, c is the blade chord length, and R is the turbine radius.

Solidity is a measure of how much of the circumference of the turbine is occupied by turbine blades. As shown in Fig. 1.10, a turbine with blades of a chord length close to zero would have a solidity ratio approaching zero. On the other extreme, a turbine with a large number of blades or with a large chord length would have a solidity ratio approaching one. The solidity ratio has a significant effect on the operating range of a cross-flow turbine. In general, high solidity turbines operate at a very low rotational speed.

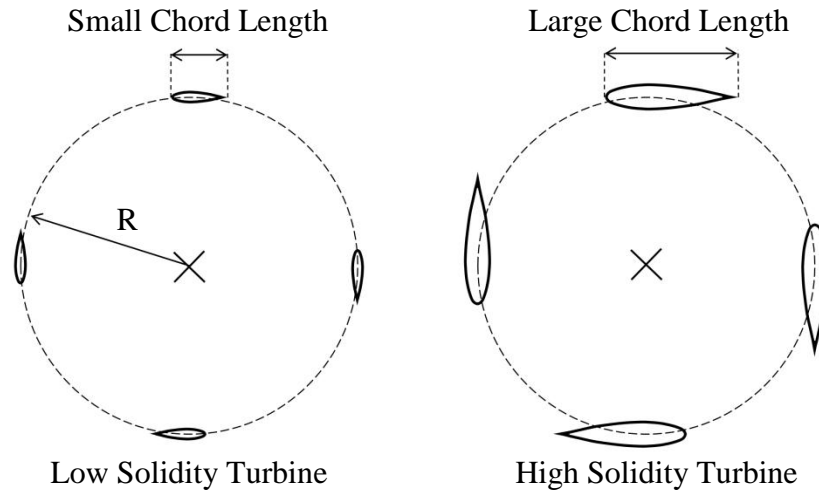


Figure 1.10 – The concept of solidity ratio is demonstrated by varying the blade chord length for turbines with the same turbine radius, R , and same number of blades. The example low solidity and high solidity turbines have solidity ratios of $\sigma \approx 0.090$ and $\sigma \approx 0.25$, respectively.

1.2.1.3 Performance Parameters

Performance parameters are quantities that define the operational characteristics of a cross-flow tidal turbine. Tip speed ratio quantifies the operational speed of the device relative to the inflow velocity. Power coefficient is the equivalent of efficiency, and characterizes the overall performance of the device. Nondimensional torque characterizes the turbine operation throughout a revolution, and facilitates comparison of the torque between devices with different physical geometries. Reynolds number has a significant effect on the lift and drag characteristics of foils.

Tip speed ratio, λ , is defined as,

$$\lambda = \frac{R\omega}{U_\infty}, \quad (1.3)$$

where ω is the turbine angular velocity, R is the turbine radius, and U_∞ is the inflow velocity. Tip speed ratio is the ratio of the tangential velocity of the blade, $R\omega$, to the

inflow velocity, U_∞ . A higher rotational speed relative to the inflow velocity corresponds to a higher tip speed ratio. Tip speed ratio is the standard quantity used to describe the rotational speed of a turbine in the tidal and wind industries, and is generally used regardless of the class of turbine.

Power coefficient, or C_P , is defined as,

$$C_P = \frac{T\omega}{\frac{1}{2}\rho A_f U_\infty^3} , \quad (1.4)$$

where T is the rotor torque, ω is the turbine angular velocity, ρ is the fluid density, A_f is the turbine cross sectional area, and U_∞ is the inflow velocity. The power coefficient is the ratio of the amount of power produced by a turbine to the maximum possible power for a given fluid traveling through a cross sectional area at a certain velocity. The power coefficient is the primary concern for turbine design, and is the focus of this thesis, both in numerical modeling and experimental testing.

Nondimensional torque is a quantity that is pertinent to blade design and model validation. The nondimensional torque can be used to estimate the torque loads on a full-scale device for structural and even foundation design, and can be used to compare experimental and numerical results. The nondimensionalized torque, T^* , is defined as,

$$T^* = \frac{T}{\frac{1}{2}\rho R A_f U_\infty^2} , \quad (1.5)$$

where T is the rotor torque, ρ is the fluid density, U_∞ is the inflow velocity, A_f is the turbine cross sectional area, and R is the turbine radius. Nondimensionalized torque is presented as a function of the turbine angular position. For experimental testing, which is

inherently noisy, multiple revolutions are averaged in a process called bin-averaging to calculate the nondimensional torque as a function of angular position. The angular position is divided into bins, in this case bins of one degree. When the angular position of a data point is within the range of a bin, the corresponding nondimensional torque value is added to the bin. The process is repeated for all data points. When all nondimensional torque values have been placed in a bin, each bin is averaged individually, and the nondimensional torque results as a function of angular position are reported.

Because of speed fluctuations encountered in the two-bladed tests, experimental torque values are overestimated at the peaks due to inertial effects. An inertial term must be included in the experimental torque calculations in order to compare experimental results with the model. The inertial term contained the turbine angular acceleration and the mass moment of inertia of the rotor and upper drive shafts of the test system. Comparing the results with the inertia yields reasonable results.

Reynolds number, Re , is defined as,

$$Re = \frac{\rho U_{ref} L_{ref}}{\mu}, \quad (1.6)$$

where ρ is the fluid density, μ is the fluid dynamic viscosity, U_{ref} is the fluid reference velocity, and L_{ref} is the object's reference length. Because of the complex dynamics of a cross-flow turbine, there is limited precedent for the reference velocities and reference lengths to use for Reynolds number calculations. In fact, there are several combinations of quantities that can be used as references: the turbine diameter with inflow velocity, the blade chord length with instantaneous blade velocity, or the blade chord length with the mean blade velocity. There are also potential effects that are a function of both

classifications of the Reynolds number; effects could be a function of the size of the entire turbine, or the size of the blade chord length. The reference velocity used for the numerical modeling section was the instantaneous blade velocity with the blade chord as length reference. This is consistent with the reference velocity and reference length recommended by Migliore and Wolfe (1980).

1.2.2 Literature

The majority of the research on cross-flow turbines has been in the area of numerical modeling, specifically two-dimensional simulations. More limited experimental work is available and is generally limited to power coefficient results for basic designs.

Numerical solution methods include both computational fluid dynamics and potential flow. Because of the large size and configuration of the cross-flow testing apparatus, the majority of testing has been performed in tow tanks, rather than flumes (Strickland et al., 1980), (Li, 2008). Model axial flow, or horizontal axis turbines, are typically smaller and have been tested in small flumes. Flumes, which force water through a channel to simulate turbine operation, generally have a small cross sectional area relative to the size of the device under test. In a tow tank, devices are towed through stationary water to simulate turbine operation. Many of the existing tow tanks were originally designed for hull drag testing and have been modified to meet hydrokinetic turbine testing requirements. Many of these tanks also have a small cross sectional area relative to the size of the device under test.

The work of Strickland et al. (1980) presents numerical and experimental data for low to medium solidity cross flow turbines ($\sigma = 0.0239$ to $\sigma = 0.0716$). A potential flow numerical method, the free vortex model (FVM), was used with lift and drag look-up

tables to model the cross-flow turbine. Experimental testing was performed in a tow tank with the following main results: rotor torque, tangential blade forces, normal blade forces, power coefficient, and streaklines. Streaklines were compared with the velocity field results from the numerical model and showed good agreement. The Reynolds number for testing and modeling was 40,000 and used the turbine diameter and inflow velocity as references.

The work of Shiono et al. (2000) presents experimental tow tank results for a variation of the NACA 63₃-018 profile for a solidity range of 0.108 to 0.537. This solidity range is considered to be medium to high. The tested blades were NACA 63₃-018 profiles with camber added so that the mean line of the profile matched the turbine radius. The experimental work presented power output or power coefficient results for variable solidity, blade number, and inflow velocity. Results also included starting torque. The testing was performed using blades with a very low aspect ratio, which could have resulted in large tip losses, especially at high rotational speeds, resulting in an underestimate of some power coefficient results. Nevertheless, these results were very useful for estimating λ_{\max} , the tip speed ratio with maximum C_p , prior to testing. This allowed for better prediction of the tip speed ratio range that would encounter positive power coefficients and generally facilitated testing.

The work of Migliore and Wolfe (1980) examined the possible effects of flow curvature on cross-flow turbine performance using numerical and experimental methods. Cross-flow turbines operate in a curved flow, but the formulations for lift and drag are typically obtained in a rectilinear coordinate system. Migliore and Wolfe used conformal mapping techniques to transform the foil in a curved flow to the virtual equivalent in a rectilinear

coordinate system (Fig. 1.11). The resulting virtual camber and virtual incidence angle were then used to calculate the lift and drag coefficients for the blade using lift and drag formulations developed in the rectilinear coordinate system.

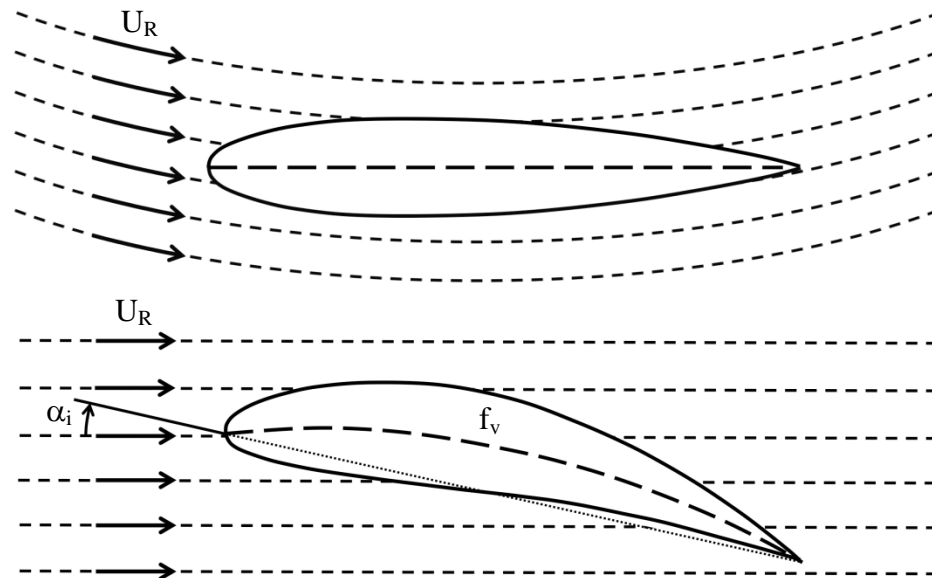


Figure 1.11 – A foil is shown in a curvilinear flow (top) and a rectilinear flow (bottom). The foil in the rectilinear flow has been transformed from the curvilinear coordinate system to a rectilinear coordinate system, with virtual angle of incidence, α_i , and virtual camber. The virtual camber is indicated by the curved mean line, with a maximum value of f_v .

Migliore and Wolfe (1980) also identified cyclic Reynolds number as an important phenomenon in cross-flow turbine modeling. Because the relative velocity encountered by the foil changes dramatically as a function of blade angular position, the reference velocity for the blade Reynolds number calculation also changes significantly, resulting in changes in the lift and drag characteristics of the foil. Because the Reynolds numbers during testing are already very low (between approximately 80,000 and 150,000), changes in Reynolds number result in significant changes to the lift and drag forces. Low Reynolds number flows are also more likely to stall and have high drag.

Any testing performed in a constricted flow, such as in a small tow tank or flume, is also subject to the blockage effect. The blockage effect has been known to influence tow tank testing results for many research areas but it has considerable implications for power coefficient results for hydrokinetic turbine testing (McAdam et al., 2009). The blockage effect changes the conditions of the test by modifying the apparent inflow velocity to the turbine or other testing device. The constricted flow accelerates the flow around the device. Because the measured inflow velocity is lower than the apparent inflow velocity, the testing results over predict the power coefficient. The magnitude of the blockage effect is a function of the blockage ratio BR , which is defined as,

$$BR = \frac{A_f}{A_c}, \quad (1.7)$$

where A_f is the turbine cross sectional area and A_c is the cross sectional area of the channel. The lower the blockage ratio, the lower the change in power coefficient as a result of the blockage effect (McAdam et al., 2009). The increase in power coefficient from the blockage effect is also a strong function of the inflow velocity, but there is no simple expression for this dependence because of the need to know the velocity field at several locations throughout the flow field, even for a simplified analysis.

Proximity of the turbine to the water surface can also result in surface effects, which could also potentially alter testing results (McAdam et al., 2009). The presence of this surface boundary condition in turbine testing further complicates the blockage effect. While blockage makes comparison with models more difficult, the free surface more closely approximates actual application of the turbines depending on the site. In this work, corrections for the blockage effect will be made as a part of the modeling effort

(Urbina, 2011a). Experimental data will be reported along with the constraint conditions of the testing, and will be compared to models that attempt to replicate these conditions.

1.2.3 Thesis Overview

This thesis is an extension of the available data for cross flow turbines. Testing was performed using six different blade profiles mounted at a range of toe angles. The results for one of the blade profiles were compared with a free vortex model developed for related work (Urbina, 2011a). This related effort includes numerical validation and improvements to the numerical model.

In order to compare the numerical model with experimental data, it was necessary to accurately model the tests under conditions similar to the tow tank. The boundary conditions of the model were modified to approximate the blockage and surface effects present in the tow tank. Model results were used to verify that the effects of the boundary conditions were appropriate. Once the boundary conditions were determined for modeling the tow tank flow conditions, the experimental testing and modeling results were compared for a range of conditions. The assessment of the overall performance of the turbine was based on comparison of power coefficient result. Nondimensional torque results were compared in order to determine the accuracy of the model at different positions during a revolution. Specifically, the nondimensional torque comparison can be used to identify areas of the model that need improvement, such as the lift and drag of foils at large angles of attack, or the dynamic stall model.

The data set in this thesis is insufficient for turbine optimization. The limitations in the data result from cost and the complexity of experimental testing. The intent of this data is

not to optimize the turbine design but to validate the model so that the optimization can be performed using the model. Final testing and more complete computational fluid dynamics modeling can then be focused on designs that are closer to the optimum design.

CHAPTER 2

NUMERICAL MODELING

2.1 Free Vortex Model

A lifting line free vortex model (FVM) developed in related work by Urbina (2011a) was used for comparison with experimental data. The model represents a two-dimensional velocity field using vorticity that is shed from the blades into the wake at each time step as the turbine operates. A vortex induces velocity on the overall flow field according to the vortex profile. The induced velocities from each vortex can be calculated at locations within the domain called control points. The induced velocity from a vortex profile is a function of the radial distance from the vortex to the control point, the vortex circulation strength and time. The Lamb-Oseen vortex profile, which was used in the model, in polar coordinates, is:

$$U_{\theta} = \frac{\Gamma}{2\pi r} \left(1 - e^{\left(\frac{-r^2}{4\nu t_e}\right)} \right), \quad (2.1)$$

where U_{θ} is the circumferential velocity induced by the vortex at a control point, r is the radial distance from the vortex to the control point, Γ is the circulation strength of the vortex, t_e is the elapsed time since the vortex was shed, and ν is the kinematic viscosity of the fluid. The radial induced velocity, U_r , is zero for this vortex profile.

The Lamb-Oseen vortex profile allows for dissipation of the vortex over time, which is a result of the presence of fluid viscosity. This effect is not explicitly modeled in potential flow methods. The induced velocity at a single control point in the domain can be calculated by evaluating the induced velocities of all vortices in the flow field at the

control point and summing the results. The velocity field can be calculated by evaluating the induced velocities at all desired control points.

The induced velocities in the flow field are especially important at the blades. The induced velocities at the blades are added to the tangential velocity of the blade from rotation and the fluid inflow velocity in order to obtain the true relative velocity at the turbine blade:

$$U_R = \sqrt{(U_\infty + U + U_T \cos \theta)^2 + (W - U_T \sin \theta)^2}, \quad (2.2)$$

where U_∞ is the inflow velocity, U is the induced velocity in the x-direction, U_T is the tangential velocity of the blade, W is the induced velocity in the z-direction, and θ is the blade angular position (Strickland et al., 1980). The coordinate system is shown in Fig.

2.1.

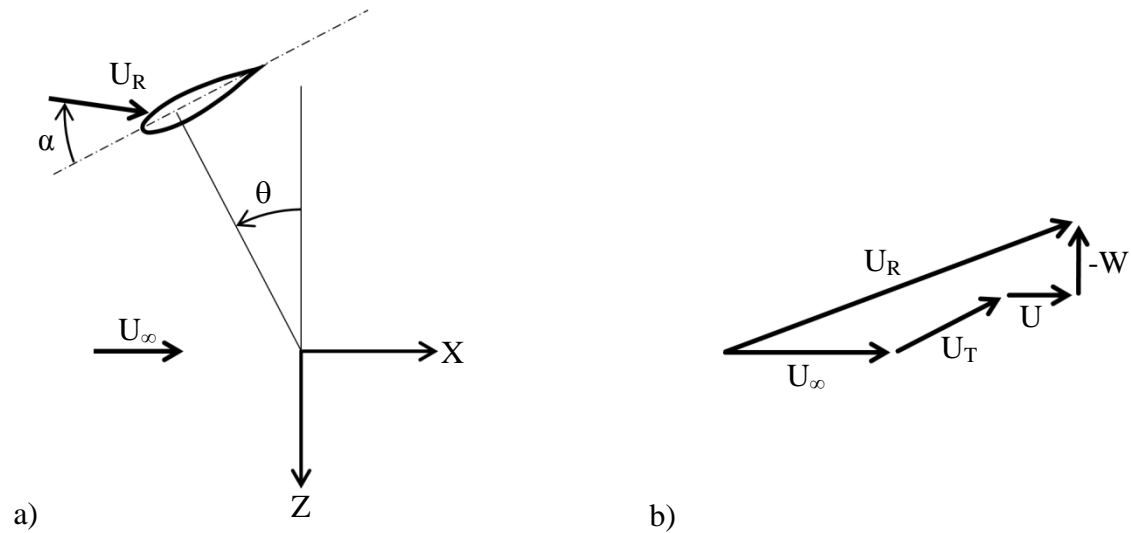


Figure 2.1 – (a) The coordinate system from Strickland et al. (1980) was used for the FVM. (b) The relative velocity at the blade, U_R , is a vector sum of the inflow velocity U_∞ , the tangential blade velocity, U_T , and the induced velocities U and W .

The angle of attack, α , is given by

$$\alpha = \tan^{-1} \left(\frac{(U+U_\infty) \sin \theta + W \cos \theta}{(U+U_\infty) \cos \theta - W \sin \theta + U_T} \right), \quad (2.3)$$

where the variables have been described above (Strickland et al., 1980). It is important to note that the angle of attack is a fluid, not a geometric quantity. It is a function of the inflow velocity, tangential blade velocity, induced velocities, and blade position. For low solidity applications with high tip speed ratios, the magnitude of the blade tangential velocity is much larger than all other velocities, and the angle of attack variation is very small. For high solidity applications with low tip speed ratios, the magnitudes of all velocities are the same order. Because the directions of the blade tangential velocity and induced velocities change significantly with rotational position, the angle of attack variation becomes large for this case. Angle of attack as a function of turbine blade angular position is shown in Fig. 2.2 for turbines with high and low solidity ratios.

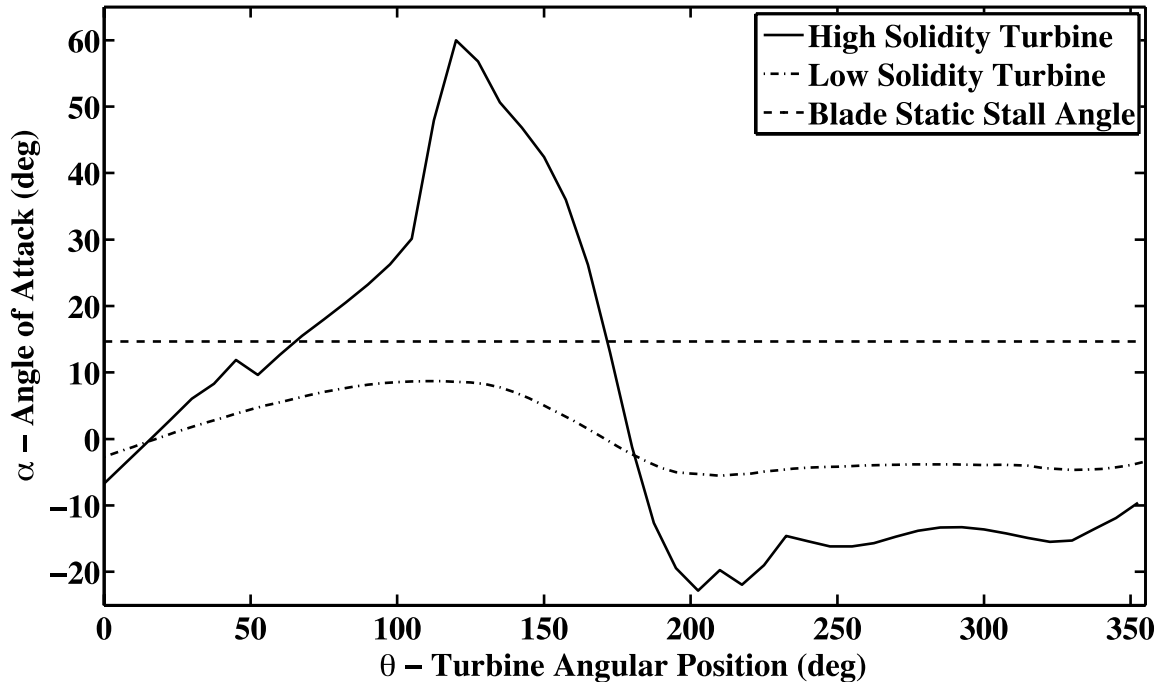


Figure 2.2 – The angle of attack as a function of turbine blade angular position from the FVM results is shown for turbines with a high solidity ratio ($\sigma = 0.147$) and low solidity ratio ($\sigma = 0.0477$). The angle of attack for turbines with high and low solidity ratios is significantly different. The blades in turbines with high solidity ratios reach angles of attack much higher than the static stall angle of attack. Turbines with a low solidity ratio tend to operate at angles of attack under the static stall angle of attack.

The angle of attack and relative velocity are then used to calculate the tangential and normal blade force coefficients, which can then be used to calculate the rotor torque. The tangential and normal blade force coefficients can be resolved as lift and drag force coefficients, which act in perpendicular and parallel directions, respectively, to the relative velocity vector. The orientation of the coefficients is the same as the orientation of the forces in Fig. 1.4 of Chapter 1. The lift force determines the amount of circulation that is shed as a vortex, according to the Kutta-Joukowski Law, which is,

$$L = \rho U_R \Gamma , \quad (2.4)$$

where L is the lift force per unit blade span, ρ is the fluid density, U_R is the relative fluid velocity, and Γ is the bound vortex circulation strength (Strickland et al., 1980).

Kelvin's Theorem must also be satisfied (Strickland et al., 1980), which is given by

$$\frac{d\Gamma}{dt} = 0, \quad (2.5)$$

where Γ is the circulation around a closed contour in the domain and $\frac{d}{dt}$ is the derivative with respect to time. Kelvin's theorem indicates that a change in the circulation of the blade must be accompanied by an equal and opposite change in the circulation of the wake (Strickland et al., 1980). In order to satisfy Kelvin's theorem and all other equations, an iterative solver is necessary. Because the induced velocities are unknown at the current time step, they are estimated by using the induced velocities from the prior time step. The induced velocities are modified, and then force coefficients and circulation are recalculated until all equations are satisfied.

A modified Beddoes-Leishman dynamic stall model was also developed by Urbina (2011a) to account for dynamic stall in the calculations. Dynamic stall is a phenomenon that occurs in high-solidity cross flow turbines as well as helicopter rotors. Turbines with high solidity ratios operate at very low tip speed ratios, so the magnitude of the tangential blade velocity is very large relative to the magnitude of the inflow velocity. This causes the device to operate at very high angles of attack for significant periods during a rotation. Static airfoil data is insufficient to simulate turbine performance because the dynamic stall effects allow the blades to delay stall until angles of attack greater than the static stall angle. Static airfoil data generally results in significant under prediction of the

power coefficient. Details of the implementation of the dynamic stall model can be found in Urbina (2011a).

2.2 Flow Blockage and Model Boundary Conditions Using Images

Boundary conditions for modeling of MHK devices were devised to represent the full range of potential device applications. Installations can range from small devices in narrow channels to applications in the Gulf Stream. The boundary conditions applied to the model were designed to model these applications. The original boundary condition that was developed for the model was the infinite fluid boundary condition. This boundary condition models a turbine that is in a flow with no boundary walls, which would be consistent with a single turbine operating in a very deep and wide channel or a device deployed to harvest ocean currents like the Gulf Stream, as long as the device is installed far from existing boundaries. The second type of boundary condition models a turbine in a flow with two walls at a specific distance from the turbine. This boundary condition is consistent with a turbine operating in a shallow constricted channel. The third type of boundary condition was developed to model the tow tank and incorporate the blockage effect into model calculations. This boundary condition has a wall on one side of the turbine and an infinite fluid on the other side. The distance from the turbine axis to the floor is used for the wall distance. The third case, the one-wall boundary condition, could also be used to model tidal sites where the turbine is located close to the bottom, such as the Cobscook Bay site in Eastport, Maine. Turbines installed permanently in these areas will most likely be moored or fixed to foundations, and will be in close proximity with the ocean floor. The one-wall boundary condition could be used to model these cases, but would most likely require a non-uniform inflow velocity profile

that results from proximity to the ocean floor. This would require little modification to the current FVM.

The presence of flow blockage in the experimental data influences the power coefficient results and complicates the comparison of model with experiment. The comparison is also complicated by the fact that the model is two-dimensional, and the testing is three-dimensional. The blades tested in this experiment have a relatively large aspect ratio. The larger the aspect ratio (the longer the blade span relative to the turbine radius), the closer the testing approximates a two-dimensional case. Even though the testing approximates a two-dimensional case, the blockage effect and surface effects remain a three-dimensional phenomenon.

2.2.1 Two Walls Using Images

Images were used to approximate the presence of two walls in the numerical model. Images are commonly used in mathematics to approximate planes of symmetry in a domain (Rae and Pope, 1984). In this model, an image is the turbine vortex field or a reflection of the turbine vortex field applied at a distance from the turbine axis based on the distance from the turbine axis to the wall. The images induce velocities on other vortices in the turbine wake. The images also induce velocities at the turbine blades.

Two walls are modeled using two images above and two images below the turbine.

Figure 2.3 shows the orientation of the images and the turbine walls for a single vortex used by Rae and Pope (1984) for corrections to wind tunnel testing. This method would theoretically include an infinite number of images. However, only four images are

necessary because the induced velocity magnitude decreases significantly as the distance from the turbine wake increases (Rae and Pope, 1984).

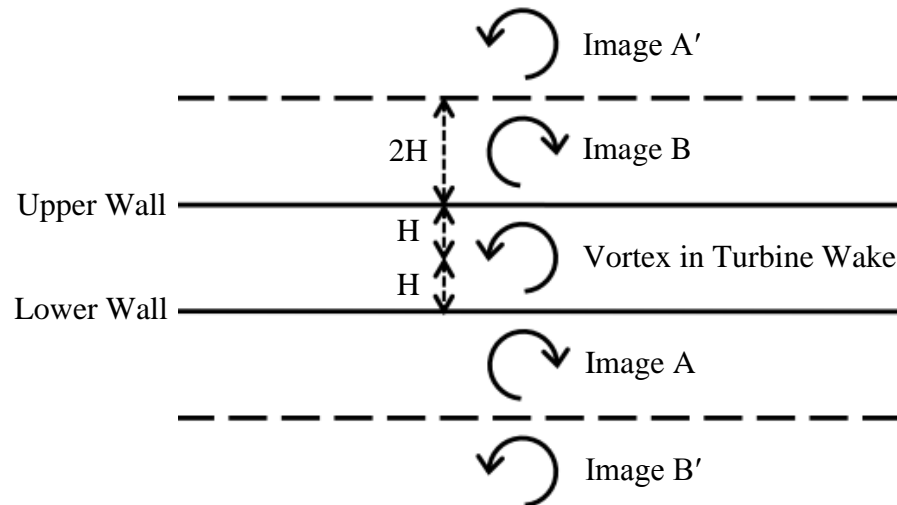


Figure 2.3 – Orientation of turbine wake images used to model two-walled case. Image A' is necessary to maintain symmetry about the upper wall, and image B' is necessary to maintain symmetry about the lower wall.

2.2.2 One Wall and Infinite Fluid Using Images

The above boundary conditions were applied to the one-wall case in a similar manner, but only one image was used, and it was applied below the turbine. The infinite fluid case is applied above the turbine. This is an approximation of the boundary condition present in the tow tank, but it is expected that the infinite fluid boundary condition approximates the free surface boundary condition better than using a wall. The free surface boundary condition would be a more accurate representation and should be considered for future work. The boundary conditions of the free surface and a seabed have been applied for boundary element methods with promising results (Whelan et al., 2009).

2.3 Model Modifications for Blade Toe Angle Variation and Virtual Incidence

Angle

There were several modifications to the FVM that were necessary to vary the toe angle of the turbine blades. First, it was necessary to ensure the correct orientation of the coordinate system used in the model to determine the sign of the toe angle. In addition, a nonzero toe angle yields blade force coefficients C_{N_b} and C_{T_b} that are not in the same coordinate system as the turbine force coefficients C_N and C_T . Coordinate transformations are then used to transform the blade force coefficients to the same orientation as the turbine force coefficients.

The FVM was also modified to include an effect of flow curvature, the virtual incidence angle correction. Flow curvature transformations from Migliore and Wolfe (1980) were used to calculate the virtual incidence angle correction values. Details of these model modifications are included in Appendix C.

2.3.1 Toe Angle Orientation

Toe angle was applied to the calculations by modifying the angle of attack before calculation of the blade forces. The coordinate system used in the model is shown in Fig. 2.4 (Strickland et al., 1980). The orientation of a positive toe angle is defined in Fig. 1.9, and is also shown in Fig. 2.4. Figure 2.4 shows that in order to obtain the relative angle of attack, α_r , the toe angle must be subtracted from the original angle of attack. The relative angle of attack is then used for blade force coefficient calculations.

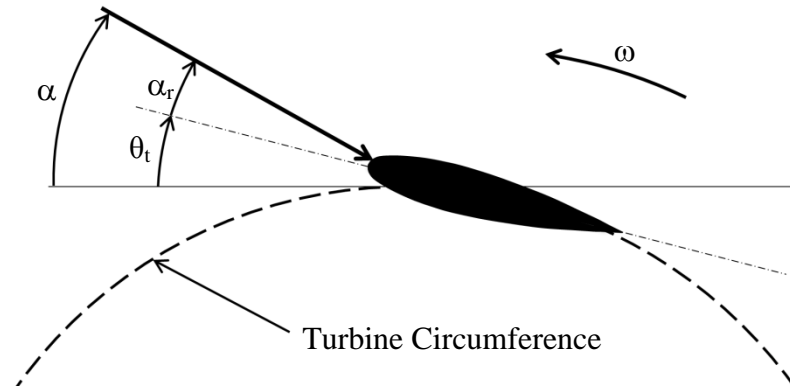


Figure 2.4 – The orientation of the angle of attack from Strickland et al. (1980) is shown with the orientation of the toe angle, θ_t , and relative angle of attack, α_r . Note that in order to obtain the relative angle of attack between the foil and the flow, α_r , the toe angle, θ_t , must be subtracted from the angle of attack, α . Turbine angular velocity, ω , is shown for reference.

2.3.2 Coordinate Transformation

For a nonzero toe angle, the resulting blade force coefficients, C_{N_b} and C_{T_b} , are in the blade coordinate system, and these coefficients must be transformed to the turbine coordinate system in order to obtain C_N and C_T . Figure 2.5 shows a turbine blade with positive toe angle, blade force coefficients, and turbine force coefficients. The transformation equations are given by

$$C_N = C_{N_b} \cos \theta_t - C_{T_b} \sin \theta_t , \quad (2.6)$$

and

$$C_T = C_{N_b} \sin \theta_t + C_{T_b} \cos \theta_t , \quad (2.7)$$

where θ_t is the toe angle.

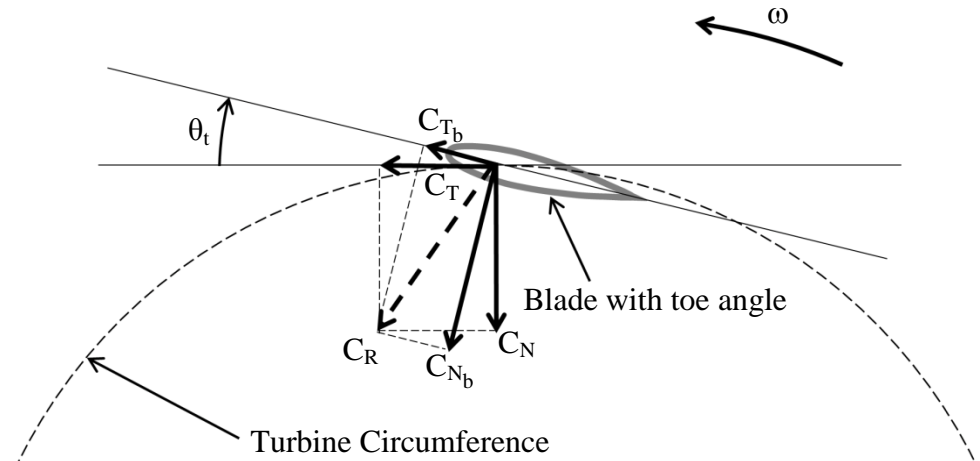


Figure 2.5 – Example normal and tangential coefficients are shown in the turbine and blade coordinate systems. C_R is the resultant force coefficient for the normal and tangential force coefficients in either coordinate system.

2.4 Model Results for Various Boundary Conditions

Figure 2.6 shows the power coefficient results for the free vortex model using all three types of boundary conditions. The results show an increase in power coefficient as the blockage effect is increased as well as an increase in λ_{max} , the tip speed ratio that yields the peak power coefficient. The case with two walls has a significantly higher efficiency than the case with no blockage. The case with one wall and an infinite fluid has an efficiency that is intermediate between the two-wall case and infinite fluid case. The power coefficient results for the one-wall case are below the Betz limit, or $C_p = 59.3\%$, and are within the typical power coefficient range for a cross-flow turbine (Hau, 2006). The results of the one-wall case will be used for comparison with the tow tank testing results.

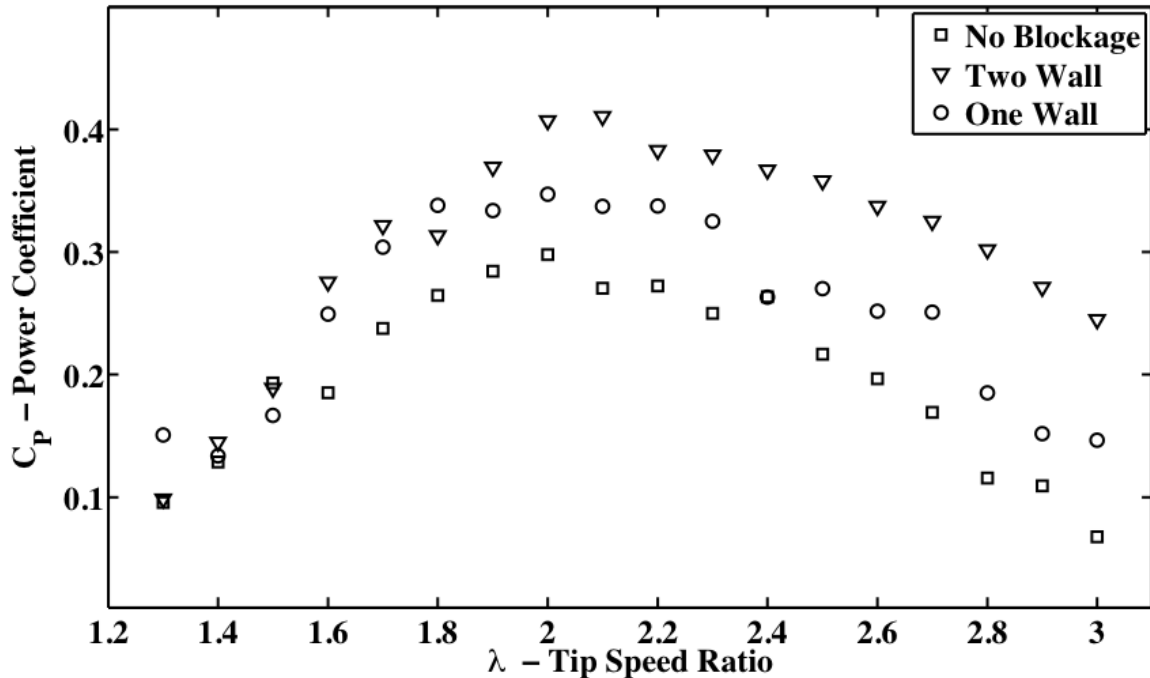


Figure 2.6 – Power coefficient results from the free vortex model are shown for the three model boundary conditions. Results are for two blades, where $\sigma = 0.147$ and $U_\infty = 0.60$ m/s.

Another important result from the model is the nondimensional torque as a function of the turbine angular position. Example results are shown in Fig. 2.7. The nondimensional torque will later be compared to the experimental tow tank results. This comparison is useful because the nondimensional torque in the model is proportional to the power coefficient. By comparing the nondimensional torque at a range of angular positions, specific angular regions in the model can be identified for further investigation and improvement. This is particularly important for understanding the role of dynamic stall and the effect of blade profile on the lift and drag at high angles of attack. These are aspects of the model that are most likely to be in need of refinement.

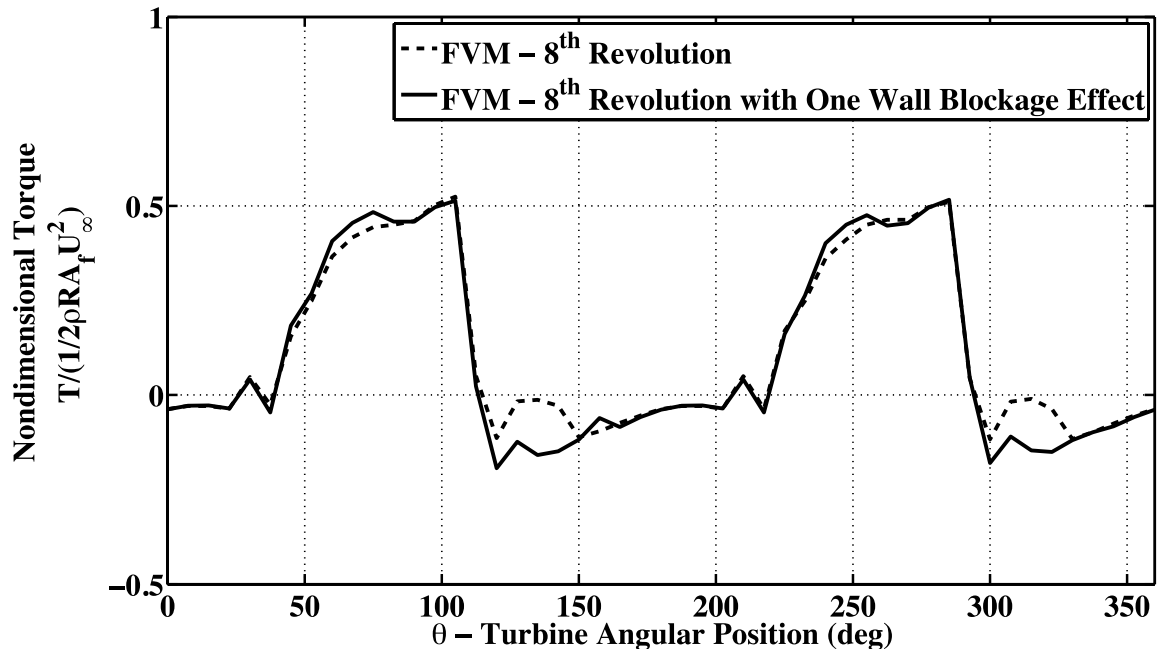


Figure 2.7 – Two-bladed nondimensional torque results from the free vortex model are shown for $\lambda = 1.50$, $\sigma = 0.147$ and $U_\infty = 0.60$ m/s.

2.5 Free Vortex Model Results with Variable Toe Angle

The effect of toe angle was also investigated using the numerical model, and power coefficient curves were developed for several different toe angles, including $\theta_t = -5^\circ$, $\theta_t = -2^\circ$, $\theta_t = 0^\circ$, $\theta_t = +2^\circ$, and $\theta_t = +5^\circ$. The modeling cases used the same geometry and flow conditions as the two-bladed tow tank testing. Figure 2.8 shows the FVM results with no blockage effect for this range of toe angles. The maximum power coefficient for this case was $C_p = 0.314$ and occurred at $\theta_t = +2^\circ$.

Figure 2.9 shows the results of the FVM with the addition of the incidence angle correction with no blockage effect for $\theta_t = -5^\circ$, $\theta_t = 0^\circ$, $\theta_t = +5^\circ$, $\theta_t = +7^\circ$, and $\theta_t = +9^\circ$. The incidence angle correction significantly affected the results, specifically the toe angle that gives the maximum power coefficient, as well as the magnitude of the maximum power coefficient. Addition of the angle of incidence correction to the FVM increased the

maximum coefficient from $C_p = 0.314$ to $C_p = 0.389$. Figure 2.10 shows the FVM results with incidence angle correction and one-wall blockage effect for $\theta_t = 0^\circ$ and $\theta_t = +5^\circ$. Addition of the one-wall blockage effect did not significantly change the results at $\theta_t = 0^\circ$. There was a significant increase in power coefficient at $\theta_t = +5^\circ$ compared to the results with no blockage effect, from 0.389 to 0.481.

Figure 2.11 compares the maximum power coefficient as a function of toe angle from the FVM results and the FVM results with angle of incidence correction, both without the blockage effect. The FVM without the incidence correction gave a maximum power coefficient of $C_p = 0.314$ at $\theta_t = +2^\circ$. The angle of incidence correction increased the maximum power coefficient to 0.389, and resulted in a maximum power coefficient at $\theta_t = +5^\circ$. These results are compared with experimental data in Chapter 4.

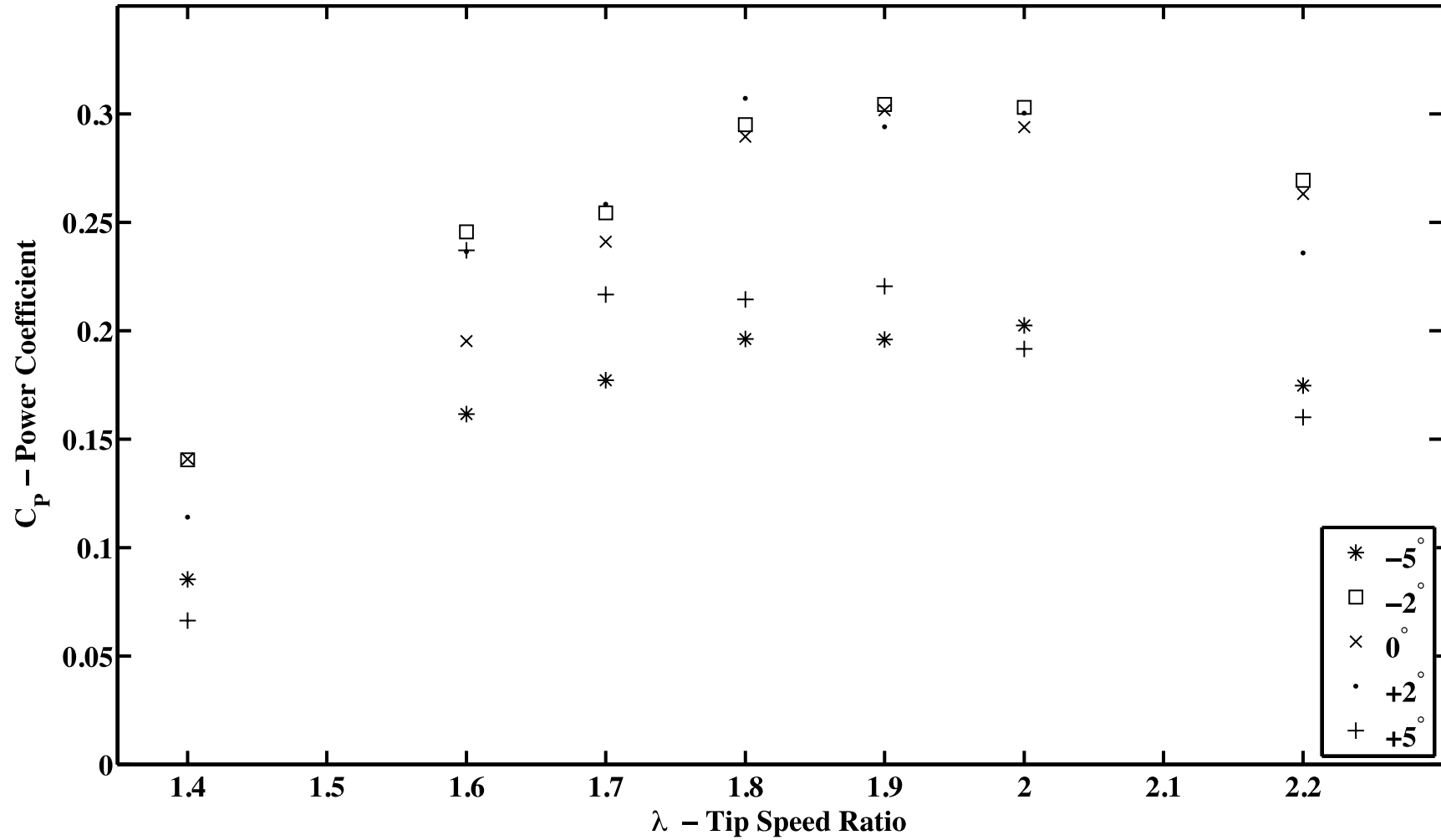


Figure 2.8 – FVM results are shown for $\theta_t = -5^\circ$, $\theta_t = -2^\circ$, $\theta_t = 0^\circ$, $\theta_t = +2^\circ$ and $\theta_t = +5^\circ$ with no blockage effect and without angle of incidence correction. Results are for two blades, $\sigma = 0.147$, $R = 0.165$ m, and $U_\infty = 0.60$ m/s.

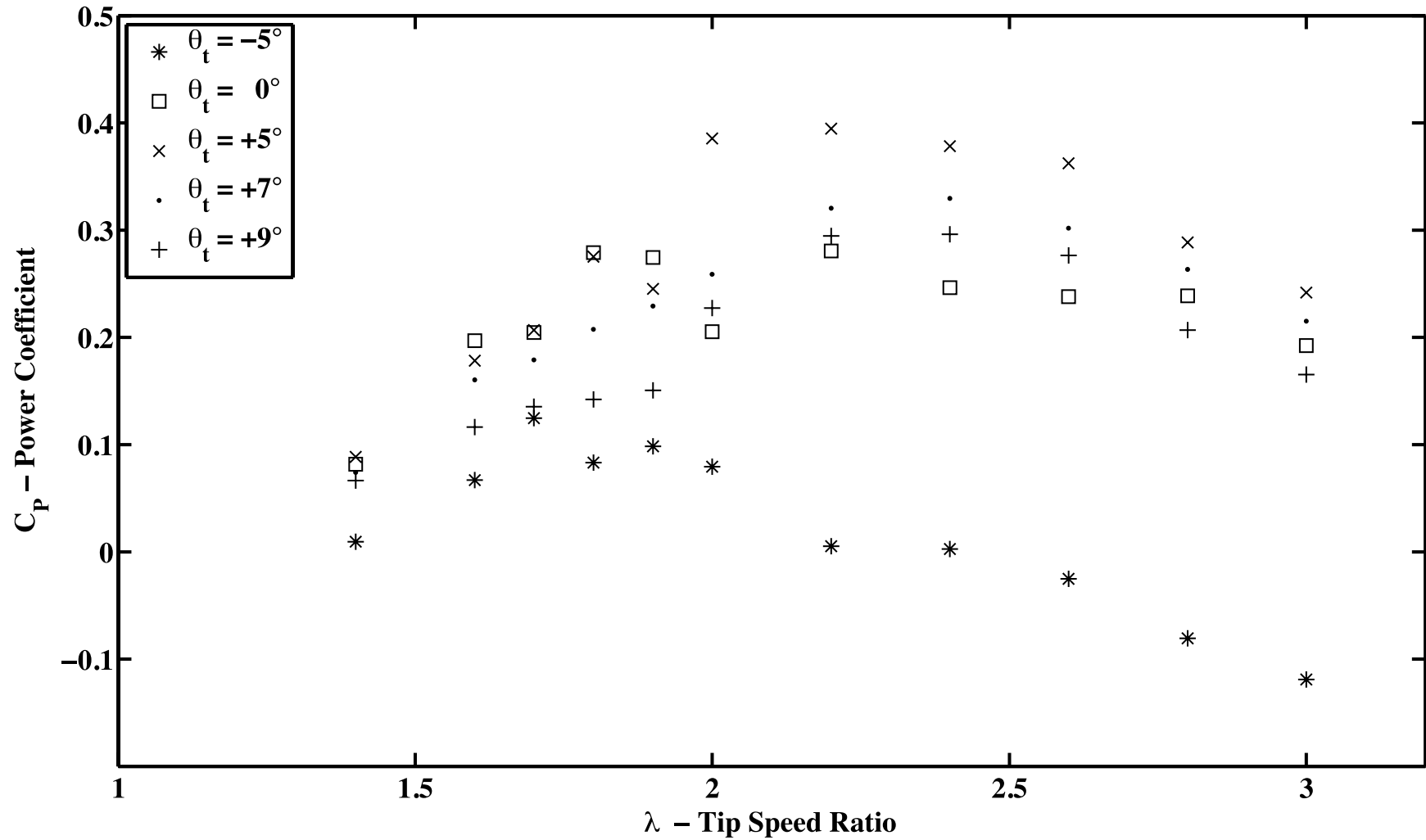


Figure 2.9 – FVM results with incidence angle correction and no blockage effect are shown for $\theta_t = -5^\circ$, $\theta_t = 0^\circ$, $\theta_t = +5^\circ$, $\theta_t = +7^\circ$ and $\theta_t = +9^\circ$. Results are for two blades, $\sigma = 0.147$, $R = 0.165$ m, and $U_\infty = 0.60$ m/s.

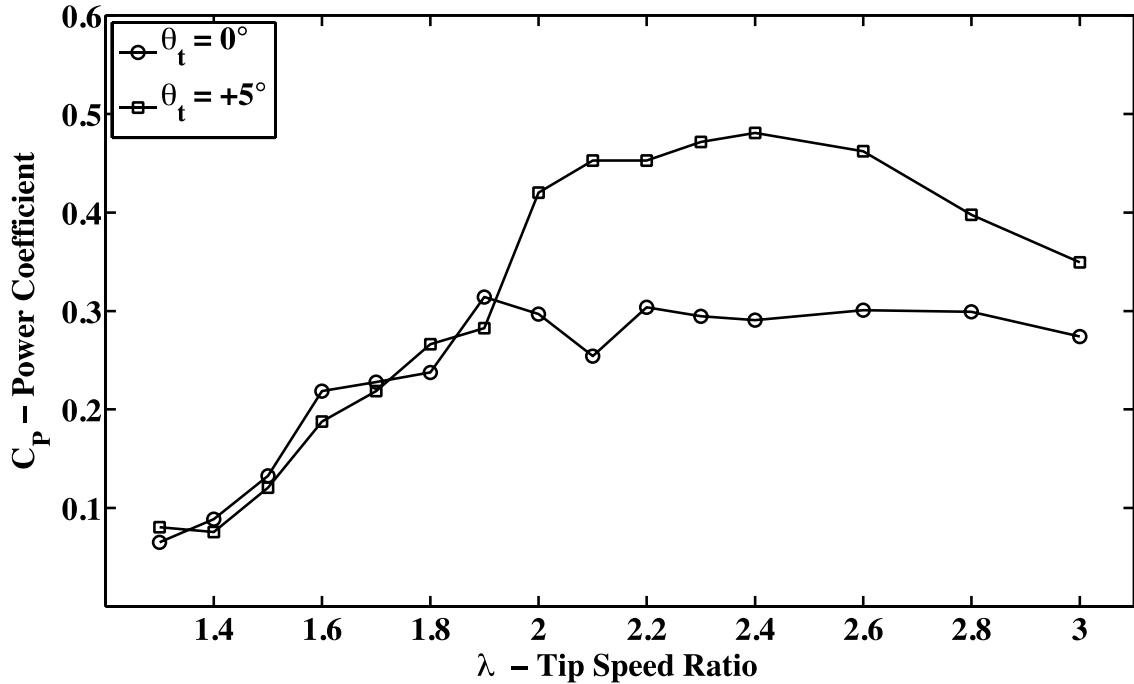


Figure 2.10 – FVM results with incidence angle correction and one wall blockage effect are shown for $\theta_t = 0^\circ$ and $\theta_t = +5^\circ$. Results are for two blades, $\sigma = 0.147$, $R = 0.165$ m, and $U_\infty = 0.60$ m/s.

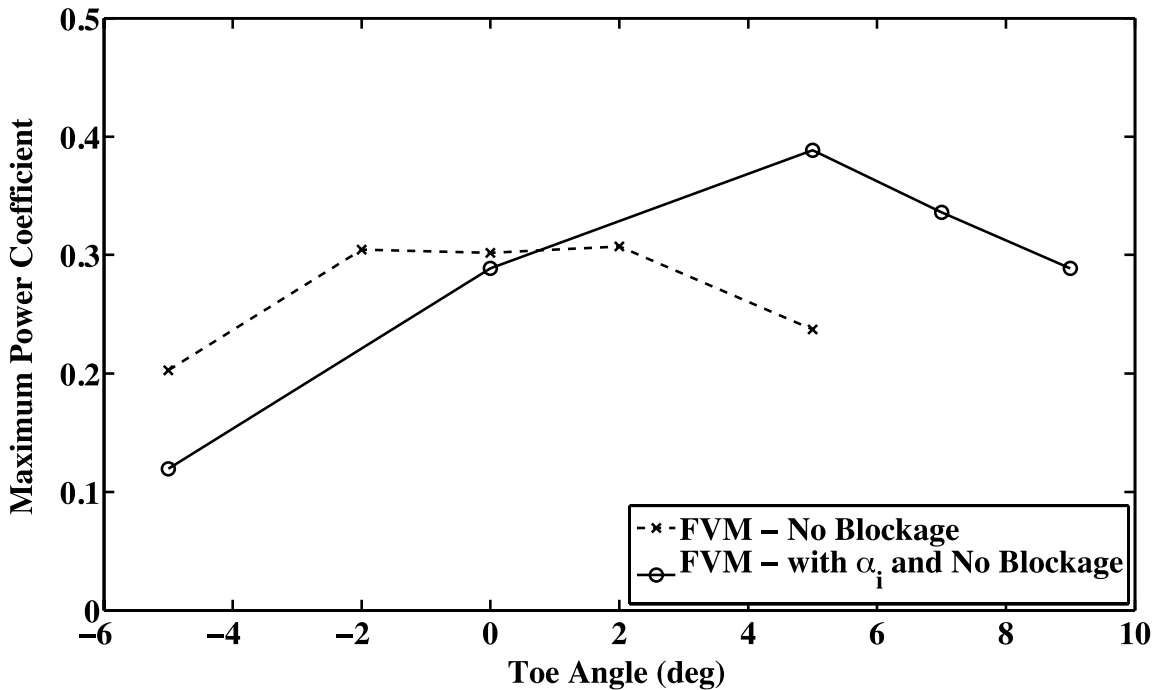


Figure 2.11 – Maximum power coefficient as a function of toe angle is shown for the FVM with no blockage effect and the FVM with angle of incidence correction and no blockage effect. Results are for two blades, $\sigma = 0.147$, $R = 0.165$ m, and $U_\infty = 0.60$ m/s.

CHAPTER 3

EXPERIMENTAL TESTING

Testing for this project was performed at the University of Maine tow tank (Fig. 3.1). The University of Maine tow tank is 2.44 meters wide, 1 meter deep, and 30 meters long. The maximum speed for this testing was 1.22 m/s, but the speed capability of the University of Maine tow tank is higher. Unlike a flume, where flowing water is used to simulate turbine operation, a tow tank moves the turbine through stationary water. To accomplish this, a 2.44 m wide, 1.22 m long, 0.25 m tall aluminum carriage is mounted on two steel rails above the water tank through a suspension system. The carriage is attached to a wire rope that is wound around a drum. The drum is turned by an AC motor, which controls the carriage velocity. Power is supplied to the carriage via a hanging track that follows the carriage movement, with 230 VAC and 120 VAC available for turbine motor control and data acquisition. A strut is attached to the front of the carriage in the center that allows for attachment of the turbine. The installed turbine is shown in Fig. 3.2.



Figure 3.1 – The University of Maine tow tank is shown with rails and carriage in the distance.

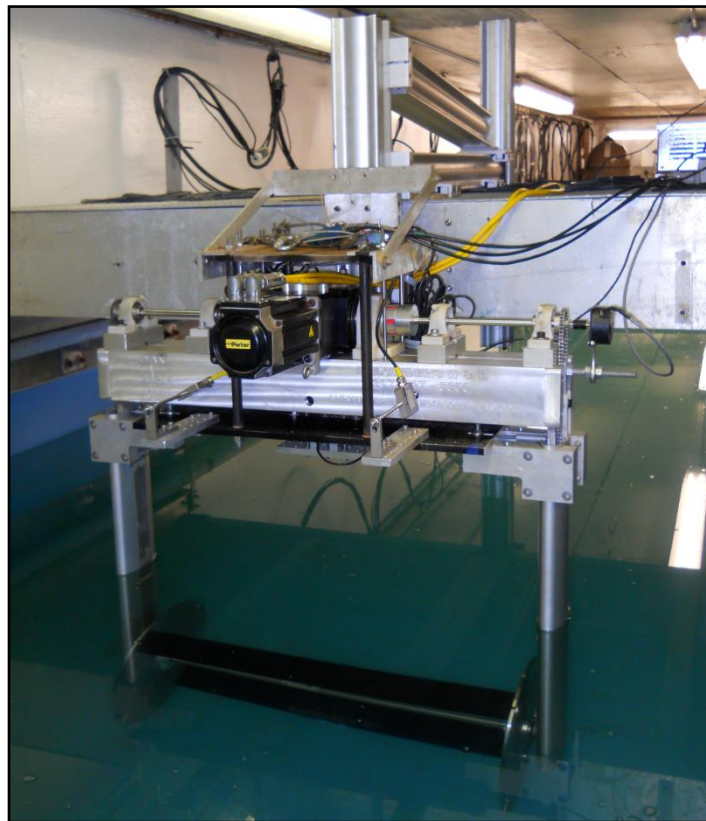


Figure 3.2 – Cross-flow turbine installed in the tow tank with instrumentation.

3.1 Experimental Setup

This section is an overview of the experimental setup. This includes a description of the apparatus, the motor control system, and the measured experimental quantities required for computation of C_P .

3.1.1 Apparatus

The model tidal turbine used in this study was designed to facilitate adjustment of critical turbine design variables. The turbine was designed to make it easy to replace blades for different blade profiles and solidity ratios, and to change toe angle, tip speed ratio, and inflow velocity. The turbine currently allows for two or four blades to be used during testing. The rotational speed and inflow velocity are controlled independently to simulate a variety of flow conditions.

A number of different sensors are monitored during testing. Torque, thrust, turbine angular position, turbine angular velocity, and inflow velocity are required for power and thrust coefficient calculations. The axes of torque and thrust measurement are shown in Fig. 3.4. The turbine uses a motor and controller that is capable of either driving the turbine or absorbing power (Fig. 3.3). The motor is coupled with a dual right angle 3:1 gear head (3 motor rotations to 1 turbine rotation), and the gear head is attached to the drive train, which operates the turbine through a chain drive. The dual right angle gear head allows for power transmission to both sides of the turbine. By using the chain drive, all instrumentation is above the water.

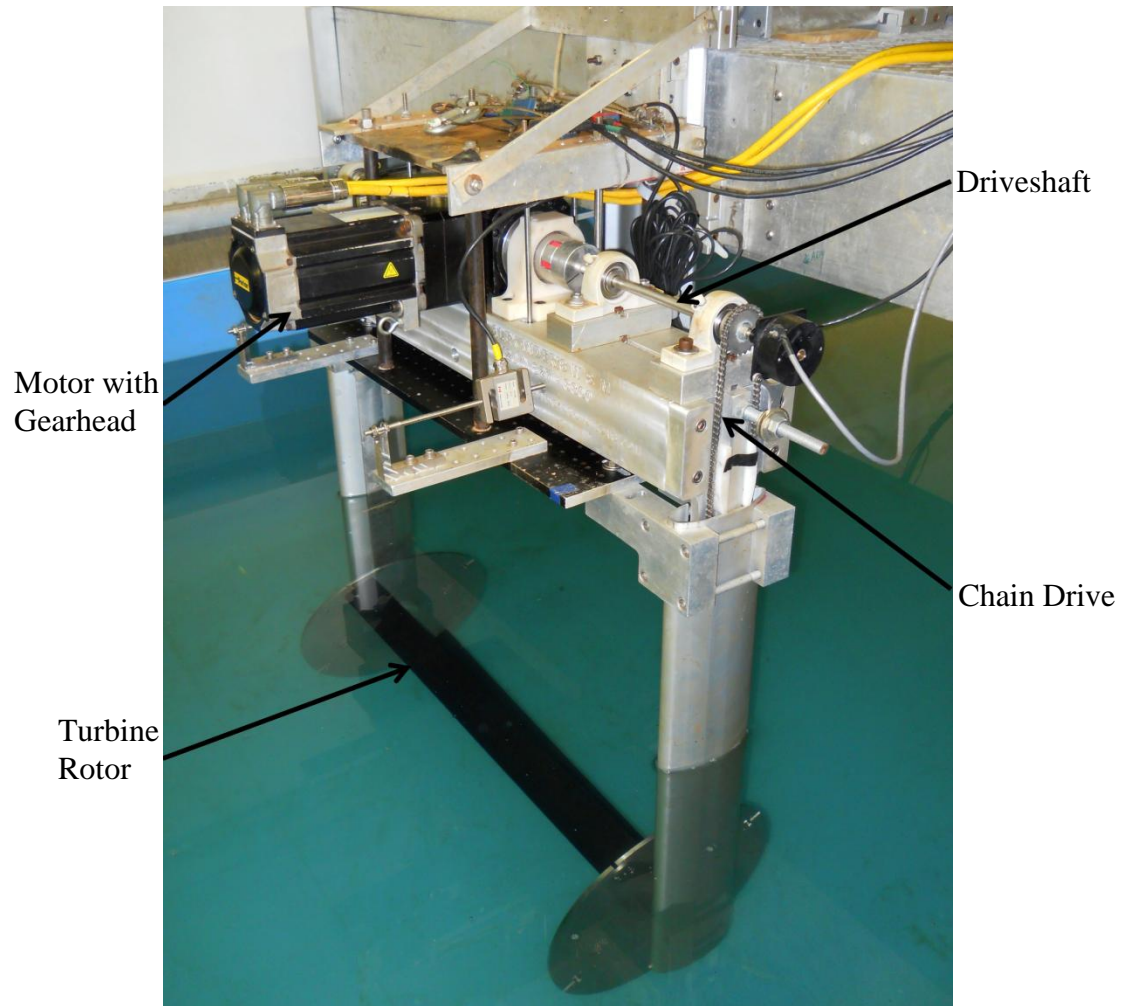


Figure 3.3 – The model cross-flow turbine test bed is shown mounted in the tow tank.

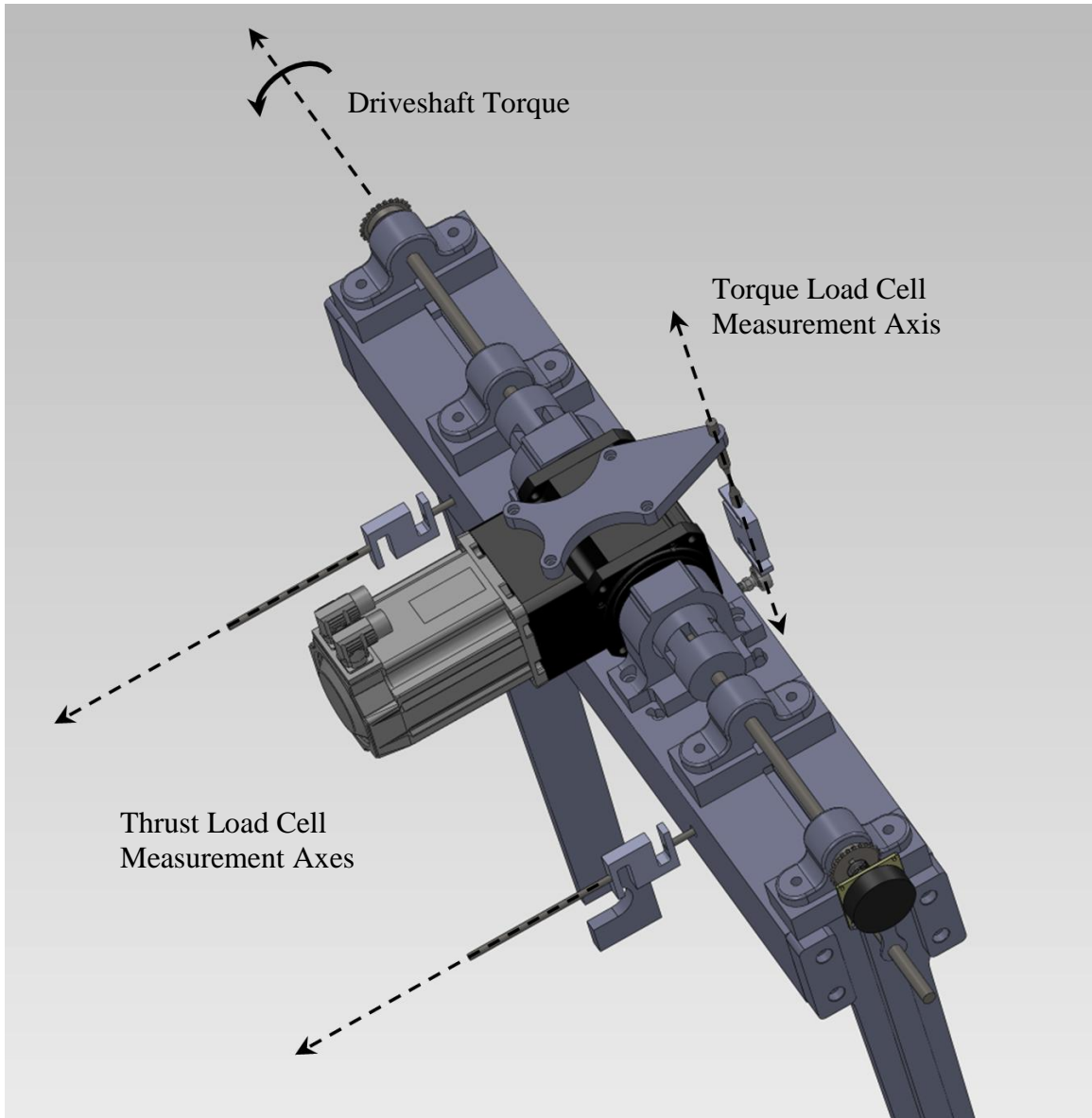


Figure 3.4 – A solid model of the upper assembly of the cross-flow turbine is shown with measurement axes. The torque in the driveshaft is measured with a load cell mounted perpendicular to the motor, at a certain distance from the driveshaft. Torque is calculated using the force in the load cell and this distance. The rotor torque is transferred to the driveshaft with a chain-drive (not shown). The thrust load cells measure the force parallel to the direction of turbine motion.

The lower portion of the turbine assembly is shown in Fig. 3.5. The turbine rotor was fitted with angle indicators for mounting of the blades. The angle indicators were designed so that the toe angle of the blades could be easily modified. A pattern of tapped holes was machined in the end plates so that the toe angle can be modified by changing the location of the alignment screws. The turbine rotor was also designed to enable easy blade interchange. The blades can be removed by removing several screws and the angle indicators, then sliding the blades out through the slot. The blade force is transferred through the blade mounting pin, into the blade angle indicator (Fig 3.6), and then into the end plate. The design of the angle indicators allowed for the blade removal slot to be included in the end plate design for quick blade interchange.

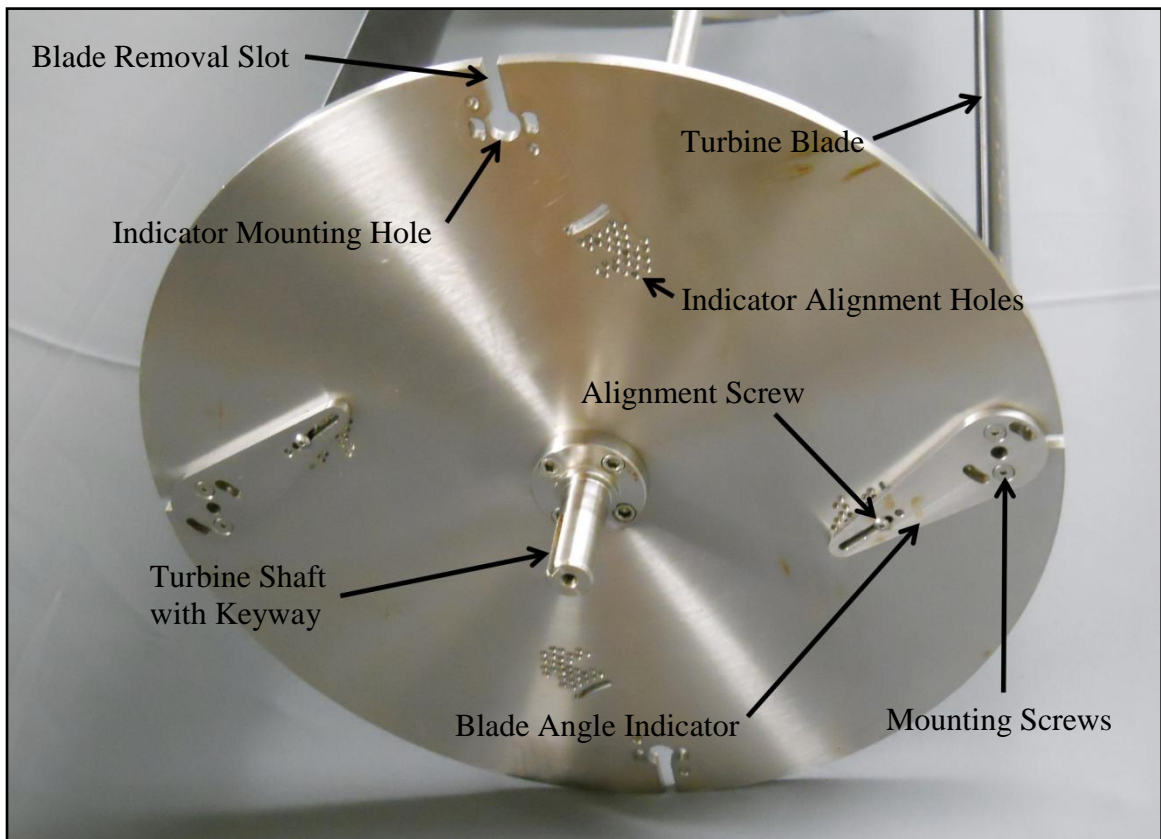


Figure 3.5 – The lower turbine assembly (turbine rotor) is shown with blades, end plates, and angle indicators.



Figure 3.6 – The center hole in the angle indicator accepts the blade mounting rod. The center hole protrudes out of the page, and when installed in the indicator mounting hole, it extends all the way through the end plate. This section transfers the blade loads from the blade to the end plate.

3.1.2 Motor Control

Unlike cross-flow turbines with helical blades, straight bladed cross-flow turbines cannot self-start in all orientations. Straight blades were selected for these tests for simplicity in manufacturing, mounting, and for the ability to modify the toe angle, which would not be possible with helical blades. The straight bladed turbine also makes it possible to investigate the torque produced by the blades at high toe angles. Since a primary goal of this work is validation of the design code, torque data as a function of turbine angular position is critical to understanding any discrepancies between the model and experimental testing. However, with straight blades the use of a simple generator to load the turbine would result in many operational cases that could not be tested. Not only does the turbine not self-start at some blade positions, but drive losses also increase resistance to turbine starting. The motor control system has the capability to power the system on start up. Once power is being produced it generates power and dumps it to a resistor

bank. For all of the test cases shown the turbine and carriage were accelerated to the desired set velocities on carriage start. Once the turbine and carriage reached the desired velocities, the turbine motor control maintained the set velocity by powering the turbine (for a negative power coefficient) or generating power (for a positive power coefficient). This system makes it possible to test conditions when the turbine efficiency is negative, or insufficient to compensate for drive losses, because the turbine can be powered throughout the duration of the test. It also makes it possible to test system losses and drag from the end plates. This is important because the value of the efficiency at all tip speed ratios is unknown prior to testing, and system losses for model turbines are significant.

3.1.3 Measured Quantities

The following measured quantities were necessary for calculation of the power and thrust coefficients. The system was set up to control the turbine and inflow velocities, but it was still necessary to measure the velocities independently. These measured velocities are then used with the turbine torque to calculate turbine performance. The resolution of the measurements was sufficient to ensure that transient effects in the torque could be detected.

3.1.3.1 Torque

The turbine rotor torque was the most difficult quantity to measure and calibrate. The turbine torque was measured with an S-type load cell attached to the motor with a bracket. The load cell was then attached to the turbine box tube, which supports the turbine. The box tube frame serves as the base for the drive train as well as the turbine assembly. The upper assembly is shown in Fig. 3.7. By attaching the load cell at a

specific distance from the rotational axis of the turbine, the force in the load cell can be multiplied by the lever arm to obtain the rotor torque.

Two types of losses were measured and accounted for in the data analysis process: drive train friction losses, and drag losses from the turbine rotor end plates. The end plates have a very high tangential velocity near the outside radius, R , and a large surface area. These factors contribute to the drag losses and a decrease in power coefficients. This effect is well established and end effects have even been tested for a cross flow turbine employing arms for mounting the blades instead of plates (Li and Calisal, 2010). The parasitic drag of the end plates was measured for this thesis by running the turbine without turbine blades, in the same manner as Li and Calisal (2010). Tests were performed over a range of rotational speeds and an inflow velocity of 1 m/s.

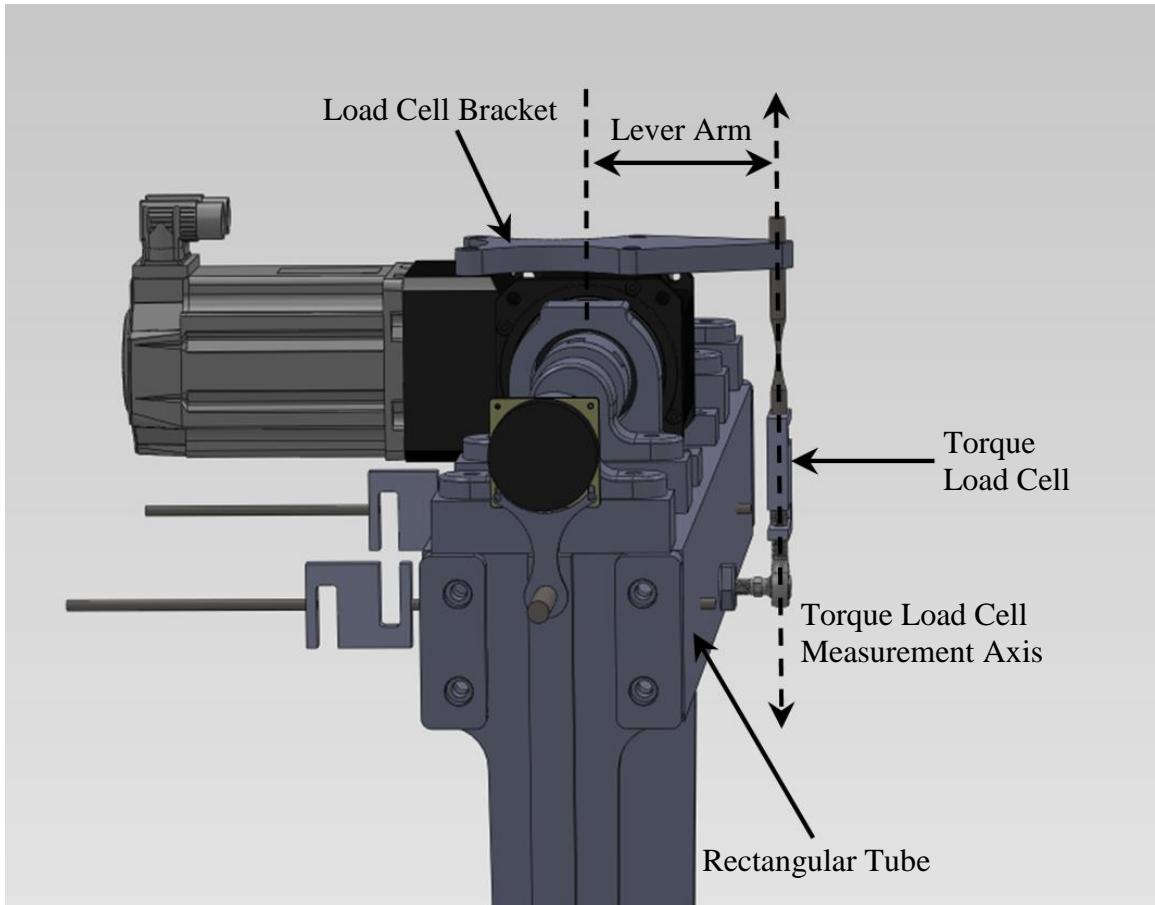


Figure 3.7 – A solid model of the upper turbine drive system is shown with the torque load cell, torque load cell lever arm, load cell bracket, motor, and rectangular tube. The system is shown without the frame and other components for clarity.

3.1.3.2 Inflow Velocity

Accurate measurement of the inflow velocity was essential. The error in the inflow velocity is critical to power coefficient calculations, because it is cubed in the power coefficient equation (Strickland et al., 1980). The inflow velocity was measured using an absolute position encoder attached to a rubber wheel that rides on the carriage rails. To obtain the inflow velocity the carriage position is measured, and the time derivative is taken during post-processing to obtain the inflow velocity. A low-pass filter was applied to the carriage position during post-processing to remove the effects of electrical noise on the results and improve the differentiation of the signal. The filter used required a very

high order (100) for the desired response, which is common for this type of filter (Losada, 2003). The phase distortion (the change in phase at different frequencies) is a linear function of the frequency for this type of filter (Losada, 2003). The function used to apply the filter reversed the phase distortion, resulting in filtered data with minimal phase distortion. Additional details of the filtering process are discussed in Appendix A.

3.1.3.3 Turbine Angular Position and Angular Velocity

Because it was also necessary to know the angular position of the turbine, the turbine angular position was measured with an absolute position encoder attached to the upper driveshaft. To obtain the turbine angular velocity, the turbine angular position signal was filtered and then differentiated with respect to time during post-processing, in the same manner as the inflow velocity.

3.1.3.4 Thrust

Thrust data was recorded in order to calculate the turbine thrust coefficient. Thrust was measured using two S-type load cells. Fig. 3.8 shows the upper assembly. The assembly was designed so that hydrodynamic shrouds shield the turbine arms from hydrodynamic forces of the flowing water. The shrouds isolate the drag force on the struts from the thrust force on the turbine rotor that is measured in the thrust load cells. Slender rods were used in the design of the dynamometer so that the vertical rods mounted to the turbine assembly and frame provide negligible resistance to the horizontal thrust forces. The entire system was calibrated in all axes with dead weights.

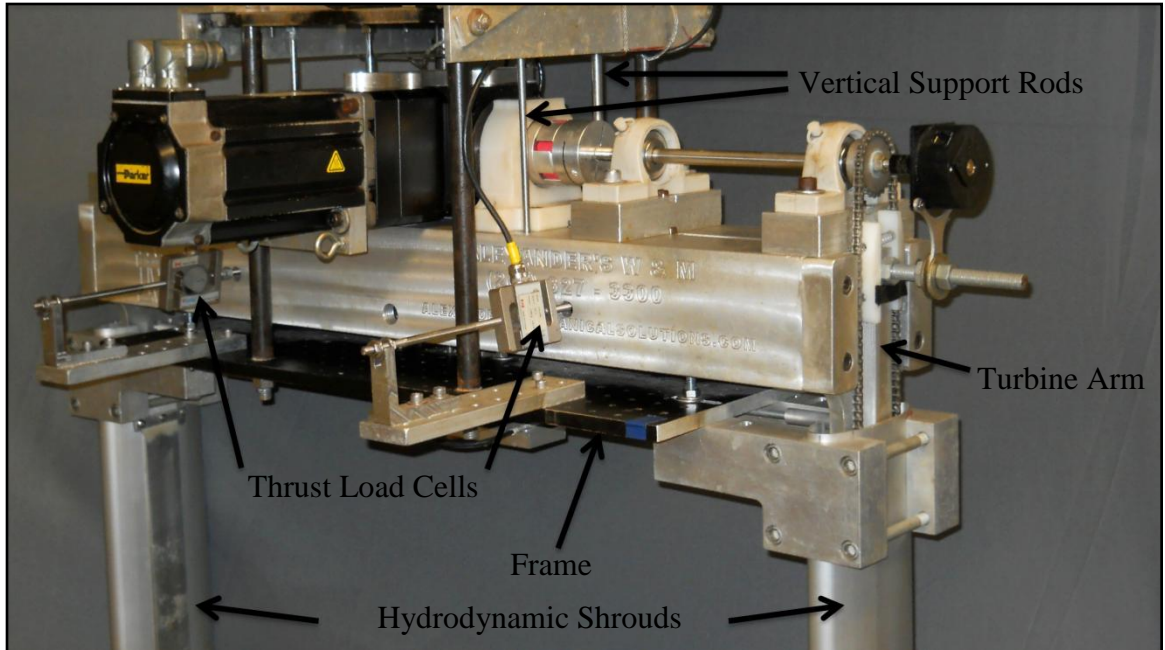


Figure 3.8 – The upper turbine assembly is shown with dynamometer, thrust load cells, and hydrodynamic shrouds.

3.1.3.5 Time

Timing was based on the sampling rate clock for velocity calculations. The real-time data acquisition system uses a 266 MHz clock with a sample rate of 2 kHz, so uncertainty in time was neglected.

3.2 Test Methods

In order to get accurate data, several tests were run prior to turbine testing. First, a series of known torques were applied to the system to simulate loading of the turbine blades. This was done by applying a series of dead weights to the turbine motor, from 0 kg to 18.14 kg. The weights were applied at a known distance from the turbine rotational axis, so each applied weight corresponded to an applied torque, according to eqn. 3.1,

$$T = Fl, \quad (3.1)$$

where F is the force in the load cell and l is the lever arm for the applied weight. The output of the torque load cell was recorded. The output was a linear function of the applied load, and linear regression was used to obtain the slope and offset. The error associated with the slope and intercept calculations were used in the uncertainty calculations. The output from a weight slightly heavier than the applied load for a typical turbine test was used in the calculations for a conservative estimate of the error, which amounted to 0.374 N. After multiplying by the lever arm of the applied load, the error in torque resulting from only the force measurement (not including the uncertainty in the lever arm length) is 0.0726 N·m. With this data a turbine test could be run, and the output of the load cell could be used along with the results from the linear regression to calculate the torque on the turbine.

3.2.1 Drive Train Friction and End Plate Drag Determination

The next set of tests determined the friction in the system. First, the turbine was rotated using the drive motor outside of the tow tank over a range of rotational speeds. The turbine angular velocity and turbine torque were recorded. Figure 3.9 shows the results of four separate series of drive train friction tests.

In addition to the turbine friction torque, it was necessary to quantify the end plate drag. To evaluate this effect, a shaft was installed across the center of the turbine with blades removed. The bladeless turbine was run in the tow tank at an inflow velocity of 1.0 m/s and a range of turbine rotational speeds. The end plate drag results are shown in Fig. 3.9. The end plate drag curve includes both the end plate drag and drive train friction terms.

The torque output of the system is a function of the turbine angular velocity, so it was necessary to include this dependence in the analysis. When analyzing actual test runs, the torque was found by entering the turbine angular velocity in the friction function, calculating the friction term, and adding it to the torque output.

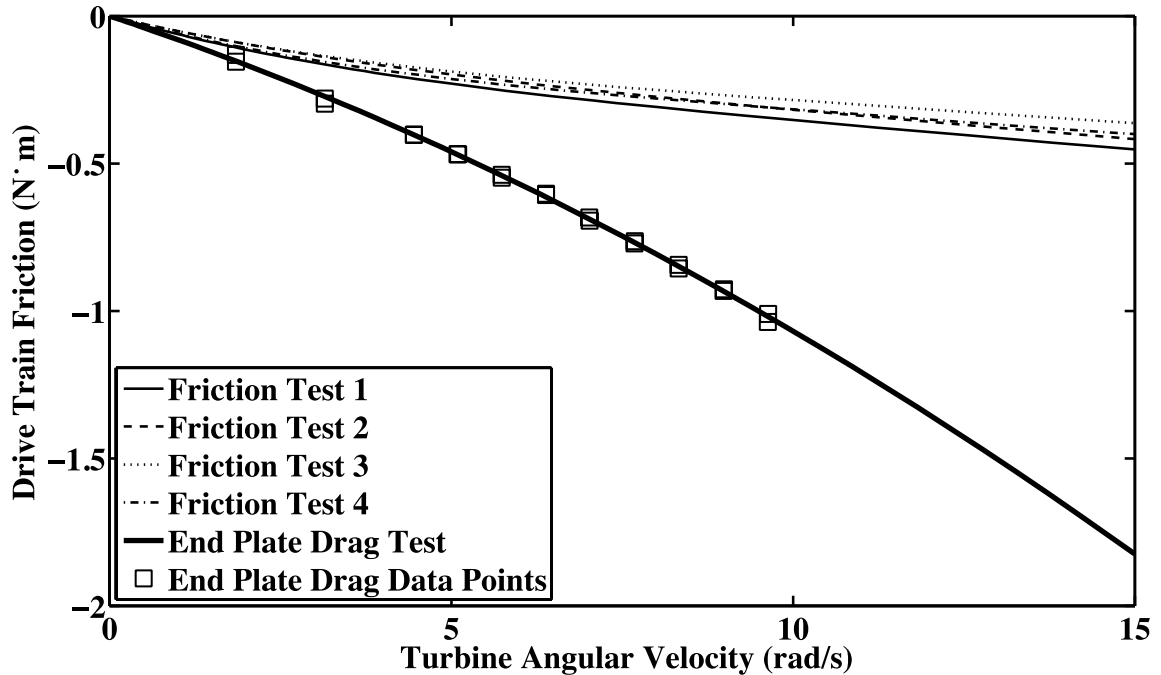


Figure 3.9 – Drive-train friction and end plate drag curves are shown as a function of turbine angular velocity. Drive-train friction curves were obtained outside the tow tank, while end plate drag tests were performed inside the tank.

3.2.2 Turbine Test Procedure

In this work a test matrix, shown in Section 3.3, was used to define the range for flow parameters and geometric configurations. For each turbine configuration, the offset, or zero value of the torque load cell was determined by running a short test. The turbine was rotated twice at a very slow rotational speed, and the mean torque load cell output was recorded and used in the analysis of the subsequent test. This test measures the preload on the load cell.

Next, the carriage and turbine are accelerated linearly to the desired inflow velocity and rotational speed. Once the acceleration period is complete, the data acquisition system records the test data. Test data is acquired with a sample rate of 2 kHz and is output to a binary file during testing. Once the test is completed, the binary file is converted back to the ASCII format for data analysis. The test results correspond to only one point on the power coefficient curve. Tests are repeated at different tip speed ratios for each set of parameters in order to quantify the desired tip speed ratio range.

3.3 Test Matrix Variables

A test matrix was developed to assess the performance of the different blade profiles. The test matrices for four-bladed tests at $U_\infty = 1.00$ m/s and $U_\infty = 1.22$ m/s are included in Table 3.1 and Table 3.2, respectively. This includes the extended toe angle range used for the NACA 63₃-018 carbon fiber blades. The toe angle range was extended based on the testing results shown in Figure 4.8. The tip speed ratio range was from $\lambda \approx 0.75$ to $\lambda \approx 1.65$.

Two-bladed tests were run for comparison with the model. Tests included the NACA 63₃-018 profile at $\theta_t = 0^\circ$ and $\theta_t = +5^\circ$. The inflow velocity for the tests was $U_\infty = 0.60$ m/s, and the tip speed ratio was varied from $\lambda \approx 1.00$ to $\lambda \approx 2.50$.

	$\theta_t = +7^\circ$	$\theta_t = +5^\circ$	$\theta_t = +3^\circ$	$\theta_t = +0.5^\circ$	$\theta_t = -2^\circ$	$\theta_t = -7^\circ$
NACA 63 ₃ -018 CF	X	X	X	X	X	
NACA 63 ₃ -018			X		X	X
NACA 63 ₃ -018 B			X		X	
NACA 0018			X		X	X
NACA 4418			X		X	X
S809			X		X	X
LNV109			X		X	X

Table 3.1 – Test matrix for four-bladed testing at $U_\infty = 1.00$ m/s for nine tip speed ratios between $\lambda \approx 0.75$ and $\lambda \approx 1.65$. CF designates carbon fiber blades and B designates tubercles.

	$\theta_t = +3^\circ$	$\theta_t = -2^\circ$	$\theta_t = -7^\circ$
NACA 63 ₃ -018 CF	X	X	
NACA 63 ₃ -018	X	X	X
NACA 63 ₃ -018 B	X	X	
NACA 0018	X	X	X
NACA 4418	X	X	X
S809	X	X	X
LNV109	X	X	X

Table 3.2 – Test matrix for four-bladed testing at $U_\infty = 1.22$ m/s for nine tip speed ratios between $\lambda \approx 0.75$ and $\lambda \approx 1.65$. CF designates carbon fiber blades and B designates tubercles.

The next section outlines the effects of changing the turbine geometry and flow parameters, and outlines the reasons for selecting the values of parameters prior to testing.

3.3.1 Inflow Velocity

The inflow velocity magnitude during testing affects the cross-flow turbine performance. If the inflow velocity is too low, the Reynolds number of the test is not high enough; lift forces decrease and drag forces increase, resulting in lower power coefficients. Increasing the inflow velocity has the opposite effect on the lift and drag blade forces. In tow tank or flume testing, higher velocities also increase the severity of the blockage effect. Thus, the inflow velocity used in testing must be high enough that blade forces are large in magnitude, but low enough that the blockage effect does not dominate the results. In tidal

turbine applications, very high inflow velocities are desirable because the generated power is proportional to the cube of the inflow velocity. With an increase in inflow velocity the generated power can increase dramatically, even with a decrease in power coefficient. Currently, the dependence of the maximum power coefficient on inflow velocity is unknown. However, the ultimate goal of the modeling effort is to model the performance of full-scale devices at proposed tidal sites, which includes high inflow velocity simulations.

Tests run at higher velocities also create unsteady operation, especially during two-bladed tests. Tests that were run at an inflow velocity of 1 m/s for four blades were decreased to an inflow velocity of 0.6 m/s during two-bladed tests in order to lower the rotor torque fluctuations. Lowering the rotor torque fluctuations allowed the motor to control the turbine rotational speed more accurately, with a corresponding reduction in speed fluctuations. This is particularly important at low tip speed ratios, where the torque peaks are highest.

3.3.2 Solidity Ratio and Number of Blades

The solidity ratio for testing can be changed by varying the blade chord length, number of blades, or turbine radius. For this testing, the turbine radius was not varied, because a smaller turbine radius produces very small torque magnitudes, and the uncertainty in power coefficient results would be too high. Changing the chord length is also impractical since it requires new blades for each solidity ratio. The solidity ratio for this testing was changed by altering the number of blades. The solidity change from four blades to two blades was useful for model verification purposes. In particular, the two-bladed torque data is useful for diagnosing blade angles where the model shows greater

error. A comparison of the FVM with two-bladed experimental torque data is performed in Chapter 4.

It is also notable that the blade profiles had different solidities, as shown below. In these cases the results of testing different profiles with different solidity ratios is useful, but the effects of changing only the solidity ratio cannot be isolated from the effects of using a different blade profile. However, the model can be used to explore future test conditions and will be used to define future experimental studies, which can then be used to isolate these factors.

3.3.3 Tip Speed Ratio and Toe Angle

The turbine power coefficient is heavily dependent on the tip speed ratio. For testing purposes it is useful to estimate the tip speed ratio that gives the peak power coefficient, λ_{\max} . Testing is then completed at a range of tip speed ratios centered around λ_{\max} . This tip speed ratio depends on the turbine solidity; the higher the solidity, the lower the value of λ_{\max} . The data from Shiono et al. (2000) contains power coefficient curves at varying solidities, and was used to estimate the location of λ_{\max} , regardless of the blade profile being tested.

Similarly, a range of toe angles was considered. No previous study systematically varied the toe angle. Data from Shiono et al. (2000) and Strickland et al. (1980) was performed at a toe angle of zero. For this thesis, the toe angle was varied from $+3^\circ$ to -7° during four-bladed testing to study the effects on power coefficient curves. The best performing foil was tested over an extended range of toe angles, up to $+7^\circ$. The toe angle was varied from 0° to $+5^\circ$ during two-bladed testing.

3.3.4 Blade Profiles

A number of foils were manufactured and tested in order to show the effects of certain blade properties. Carbon fiber blades, shown in Fig. 3.10, were designed and manufactured using a NACA 63₃-018 profile with a 7.62 cm chord length and a span of 76.2 cm (Lokocz, 2010). The carbon fiber NACA 63₃-018 blades were truncated at the trailing edge, with a truncated chord length of 6.99 cm. Because the blade mold uses a chord length of 7.62 cm, this was chord length used to define the solidity ratio of the turbine for this profile. Six sets of four 3-D printed plastic blades infused with epoxy were designed and manufactured by a collaborator. The 3-D printing method was used because it did not require molds, and the blades could be manufactured quickly. The blades have a reduced stiffness relative to the carbon fiber blades. The 3-D printed blade profiles include a profile with nearly identical dimensions to the carbon fiber blades. In addition, symmetric and cambered NACA profiles, a wind industry profile designed by NREL, and a profile with a very high lift-to-drag ratio were also produced using 3-D printing. By duplicating the NACA 63₃-018 profile, the effect of the reduced stiffness on power coefficient could be determined. In general the maximum thickness used was selected based on manufacturing constraints and the stiffness required for both the test turbine and a full-scale device. Very thin blades do not provide adequate stiffness, and are very difficult to properly mount to the test bed. For full-scale devices, the blades are designed for a maximum allowable deflection, so the required maximum thickness is a function of the blade stiffness required to remain under the allowable deflection during all operational cases.



Figure 3.10 – The NACA 63₃-018 carbon fiber turbine blade is shown with locating rod and tapped mounting holes.

The angle of attack at which stall occurs for a blade can determine the performance of the entire turbine. In general, lift no longer increases in the post-stall region, and drag increases dramatically. By delaying the onset of stall, turbine performance can be improved. This becomes more important as the blade solidity increases, because the angle of attack range also increases with solidity. For high solidity turbines, the angle of attack can be significantly larger than the stall angle. Figure 2.2 shows the variation of angle of attack in a high solidity turbine compared to the angle of attack in a low solidity turbine.

Different blade profiles were manufactured and tested to investigate the performance of foils commonly used in the industry, foils with added camber, and unique foils such as the high lift-to-drag ratio foil and NACA 63₃-018 with tubercles. The testing results serve as a baseline for the effects of modifying the types of foils traditionally used for cross-flow turbines, as well as the performance of these foils for a range of toe angles.

3.3.4.1 NACA 63₃-018

The NACA 63₃-018 foil, shown in Fig. 3.11, is a symmetric foil in the NACA 6-series, an entire series designed to encourage laminar flow and resist flow separation. This profile was selected because the design characteristics are ideal for cross-flow turbines. Testing performed by Shiono et al. (2000) used the same thickness profile. However, the blades used by Shiono et al. (2000) have camber that was added to match the turbine radius. While the operating conditions for the data obtained by Shiono et al. (2000) are not identical to the current tests, the data provides a useful comparison.

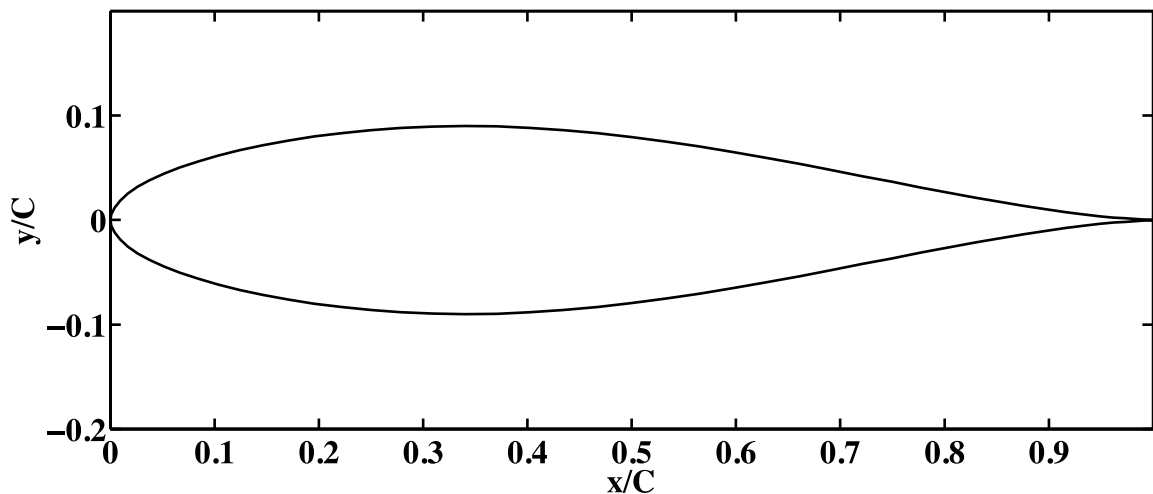


Figure 3.11 – The NACA 63₃-018 profile resists flow separation at high angles of attack. Cross-flow testing has been performed by Shiono et al. (2000) using a modified version of this profile.

3.3.4.2 NACA 63₃-018 B

The basis for this profile, shown in Fig. 3.12, is also the NACA 63₃-018 profile, and will be referred to as NACA 63₃-018 B. Tubercles, or bumps, were added to the leading edge of the NACA 63₃-018 profile in order to test possible delay of stall. In nature, the tubercles on the leading edge of humpback whale fins have been theorized to delay stall, which allows the whale fins to operate at very high angles of attack and produce very

high lift coefficients, increasing maneuverability (Custudio, 2007). The leading edge geometry of the foil was modified by adding sinusoidal protuberances with an amplitude of approximately $0.050c$ and a wavelength of approximately $0.25c$, where c is the blade chord length. The protuberances were added to the original foil at the leading edge, so that the distance from the leading edge to the tip of the protuberances is twice the amplitude of the sinusoid, or $0.10c$. The protuberances can be seen in the top view of Fig. 3.13. Additional information on the aerodynamic properties of this type of foil can be found in Custudio (2007).



Figure 3.12 – The side view of the NACA 63₃-018 blade is shown with tubercles added to the leading edge.



Figure 3.13 – The top view of the NACA 63₃-018 blade profile is shown with tubercles added to the leading edge.

3.3.4.3 NACA 0018

The NACA 0018 profile, shown in Fig. 3.14, is a symmetric blade profile in the NACA 4-Series, a family of foils commonly used in cross-flow tidal turbine and vertical axis wind turbine (VAWT) modeling and testing. The Strickland et al. (1980) testing was performed using the NACA 0012 profile, and the experimental testing performed by Migliore and Wolfe (1980) examining flow curvature effects used the NACA 0015 blade profile. These foils all have the same thickness distribution, but have different maximum thicknesses. Because the foil lift and drag have a relatively weak dependence on maximum thickness (Abbott and Von Doenhoff, 1959), comparison of these testing results is possible.

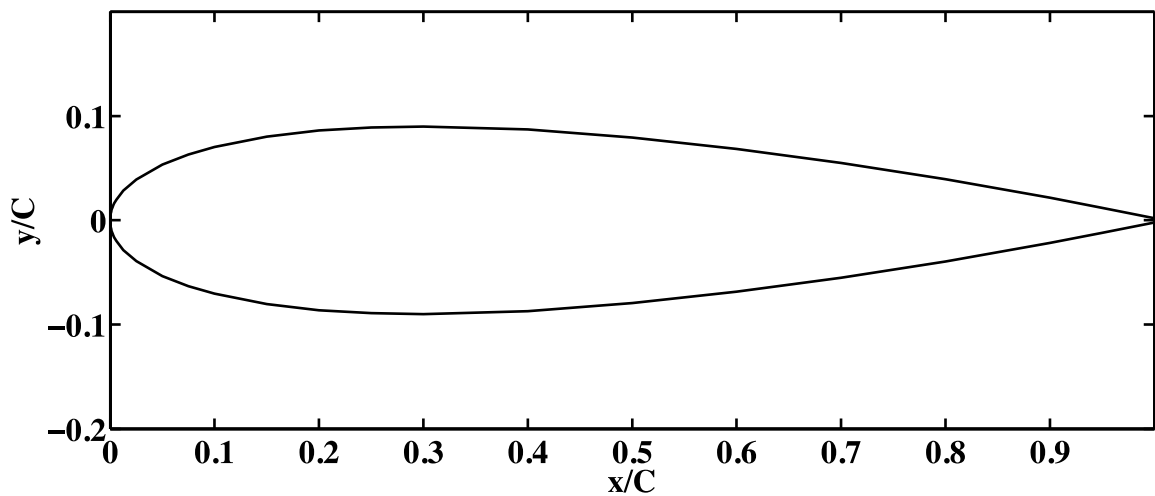


Figure 3.14 – The NACA 0018 profile has been used in cross-flow tidal and wind turbine testing.

3.3.4.4 NACA 4418

The NACA 4418 profile, shown in Fig. 3.15, has the same thickness profile as the NACA 0018 profile, but has added camber that is 4% of the blade chord length. This profile was selected to assess the effects of moderate camber on power coefficient results. By using

the NACA 0018 and NACA 4418 profiles, the effect of camber can be isolated for this thickness profile and blade chord length.

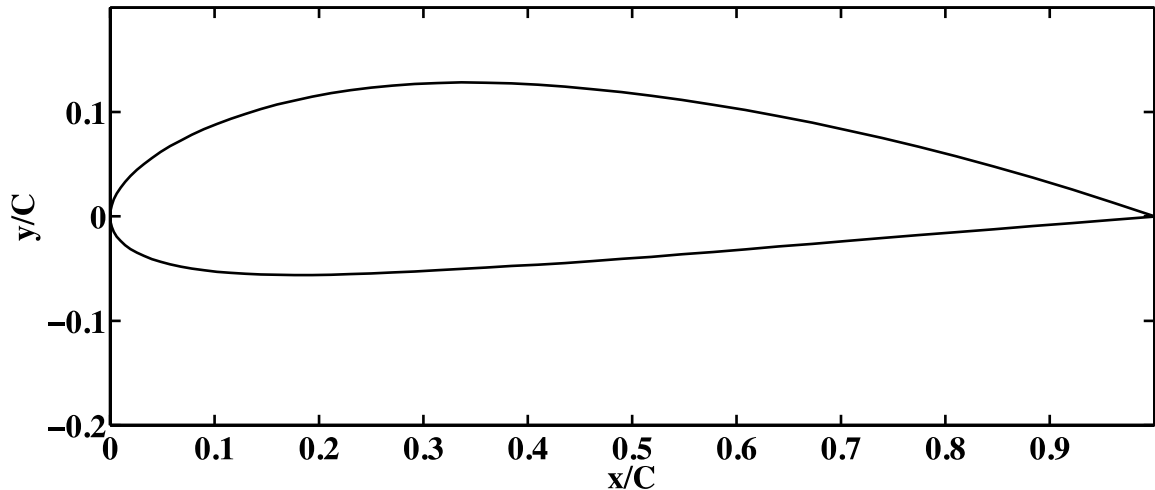


Figure 3.15 – The NACA 4418 profile has the same thickness distribution as the NACA 0018 but with added camber.

3.3.4.5 S809

The S809 profile, shown in Fig. 3.16, is a profile designed by National Renewable Energy Laboratory (NREL) that is commonly used in the wind industry for axial-flow, or horizontal-axis wind turbines (Somers, 1989). The profile is relatively thick (21% of the blade chord) and exhibited very smooth stall characteristics in wind tunnel tests (Somers, 1989).

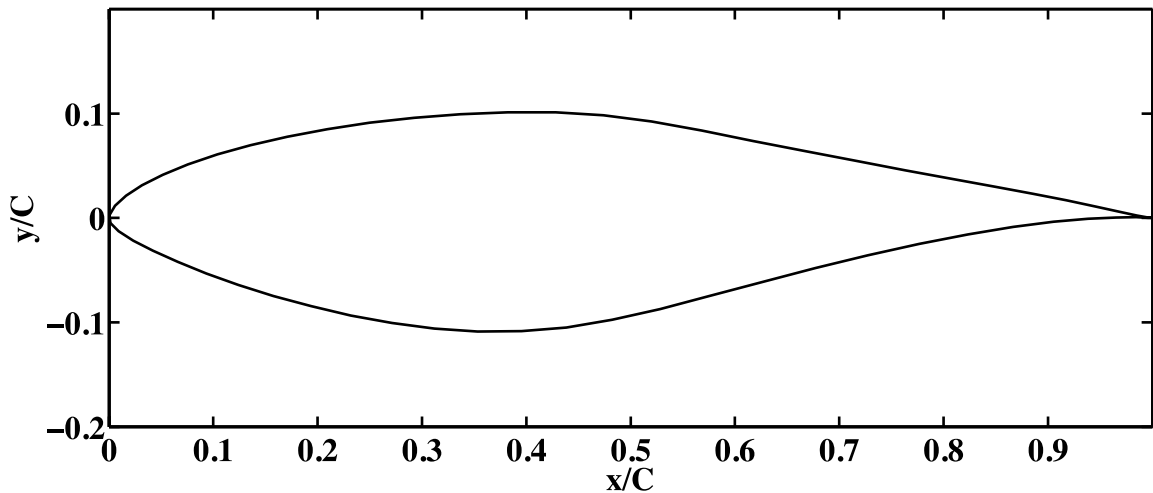


Figure 3.16 – The S809 profile, which is commonly used in the axial-flow wind turbine industry, has a large maximum thickness compared to the rest of the tested profiles.

3.3.4.6 LVN109

The LNV109 profile, shown in Fig. 3.17, was designed to have a very high lift-to-drag ratio. The profile can theoretically achieve very high lift coefficients and operate at very high angles of attack. This is a type of profile commonly used as a rear spoiler for auto racing, because it can produce a large lift force in the downward direction with very low additional drag (Bertin and Smith, 1979). The profile that was constructed had to be modified slightly to have an increased thickness distribution in order to make it thick enough to fabricate and mount on the turbine.

The results from four-bladed and two-bladed testing of these blade profiles are included in the next chapter. Power coefficient results for each profile are compared with each other, and some conclusions are drawn concerning the effects on turbine performance from changes to blade profile. Power coefficient and nondimensional torque results from two-bladed testing are also compared with the numerical model.

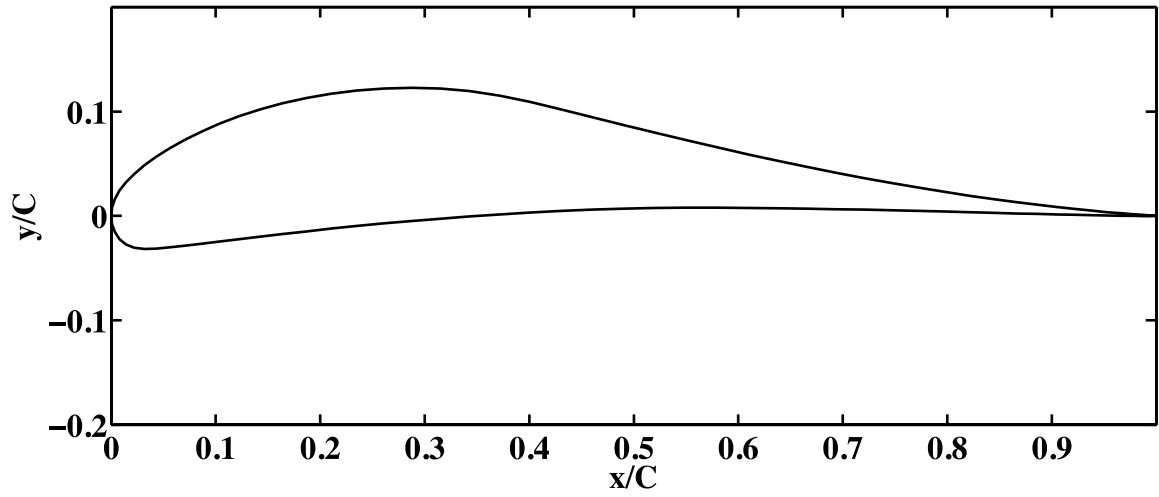


Figure 3.17 – The LNV109 profile has a very high lift-to-drag ratio while resisting separation.

CHAPTER 4

RESULTS AND DISCUSSION

Four-bladed testing was performed to get baseline performance data for each blade profile at different toe angles and flow conditions. The results from each profile are compared to determine the most favorable performance parameters. The toe angle range was extended for the best performing foil in order to better quantify the effects of changing the toe angle. Two-bladed tests were performed and power coefficient and nondimensional torque were compared with the free vortex model (FVM). For all testing cases, see the test matrix in Section 3.3.

4.1 Four-Bladed Test Results at Three Different Toe Angles

Four-bladed tests were performed at three different toe angles, $+3^\circ$, -2° , and -7° for each blade profile. The -7° toe angle was only completed for several blade profiles, and the testing results are shown in Appendix D. The power coefficients for this toe angle are very low and are only needed to ensure the maximum power coefficients as a function of toe angle are following the expected trend. Tests were performed for each case at an inflow velocity of approximately 1.00 m/s and 1.22 m/s. Published data from Shiono et al. (2000) and preliminary testing indicated that for the solidity ratio used in the testing, $\sigma = 0.294$, the peak power coefficient would occur at a tip speed ratio of approximately 1.4 for most of the profiles. Consequently, the tip speed ratio was varied between 0.75 and 1.7, with a total of nine test runs per inflow velocity. The NACA 0018 and NACA 4418 blade profiles had a longer chord length, so the solidity was higher, at $\sigma = 0.343$. Based on data from Shiono et al. (2000), the solidity ratios for all four-bladed tests were close enough that the same tip speed ratio range could be used. Four-bladed testing results

performed at $U_\infty = 1.22$ m/s are included in Fig. 4.1 through Fig. 4.7. The peak power coefficient and λ_{\max} for symmetric and cambered foils are included in Table 4.1 and Table 4.2, respectively. Only one data point was taken for each tip speed ratio, and the error bars were calculated using the uncertainty propagation equations outlined in Appendix B.

4.1.1 Symmetric Foil Results

Four separate symmetric blade sets were tested. Two sets of blades had the same profile made with different materials (NACA 63₃-018 carbon fiber and 3-D printed). The carbon fiber blades are very stiff, with the 3-D printed blades exhibiting significantly lower stiffness. Comparing the results between the NACA 63₃-018 carbon fiber and NACA 63₃-018 3-D printed blades helped to determine the validity of the testing results for the other 3-D printed blade sets. This was necessary because the design is stiffness controlled and the blade loading is not well characterized.

The maximum power coefficient and λ_{\max} from symmetric foil testing are summarized in Table 4.1. The NACA 63₃-018 blade profile has the highest efficiency, $C_p = 22.0\%$, of all the symmetric foils tested in the four-bladed testing. In spite of the significant difference in stiffness between the carbon fiber and 3-D printed blades, only a marginal reduction in power coefficient resulted from the flexible blades, from $C_p = 22.0\%$ to $C_p = 21.7\%$. The effect of the stiffness was within the range of uncertainty for the measurement. This verified that the general testing results for the 3-D printed profiles could be used to evaluate the different design parameters.

Tubercles were tested for their effect on the blade performance. The addition of tubercles to the leading edge of NACA 63₃-018 blades resulted in a lower efficiency for all testing results when compared to the unmodified NACA 63₃-018 blade profile. It should be noted that the results are specific to the tubercle geometry used. In particular the geometry described in Section 3.3.4.2 was not optimized, although it was based on the tubercle geometries tested in Custudio (2007). The specific tubercle geometry selected from Custudio (2007) exhibited resistance to stall at high angles of attack. However, resistance to stall in static aerodynamic tests does not guarantee improved performance in dynamic flow conditions, particularly regarding the dynamic stall phenomenon.

The NACA 0018 blade profile has an increased chord length and thus a higher solidity ratio than the other symmetric foils. For $\theta_t = +3^\circ$, the power coefficient peaked at a lower tip speed ratio than the lower solidity blade profiles, $\lambda_{\max} = 1.21$. For this solidity range, an increase in solidity generally results in a decrease in power coefficient. However, for these test results, the decrease was small. The maximum power coefficient for this profile was $C_P = 21.3\%$. The power coefficient values from smoothing data at other tip speed ratios suggest that the actual value may be lower, at $C_P \approx 20\%$, occurring at $\lambda_{\max} = 1.21$. Regardless, this is still a modest decrease in maximum power coefficient compared to the NACA 63₃-018 carbon fiber blade set, which had a maximum power coefficient of $C_P = 22.0\%$.

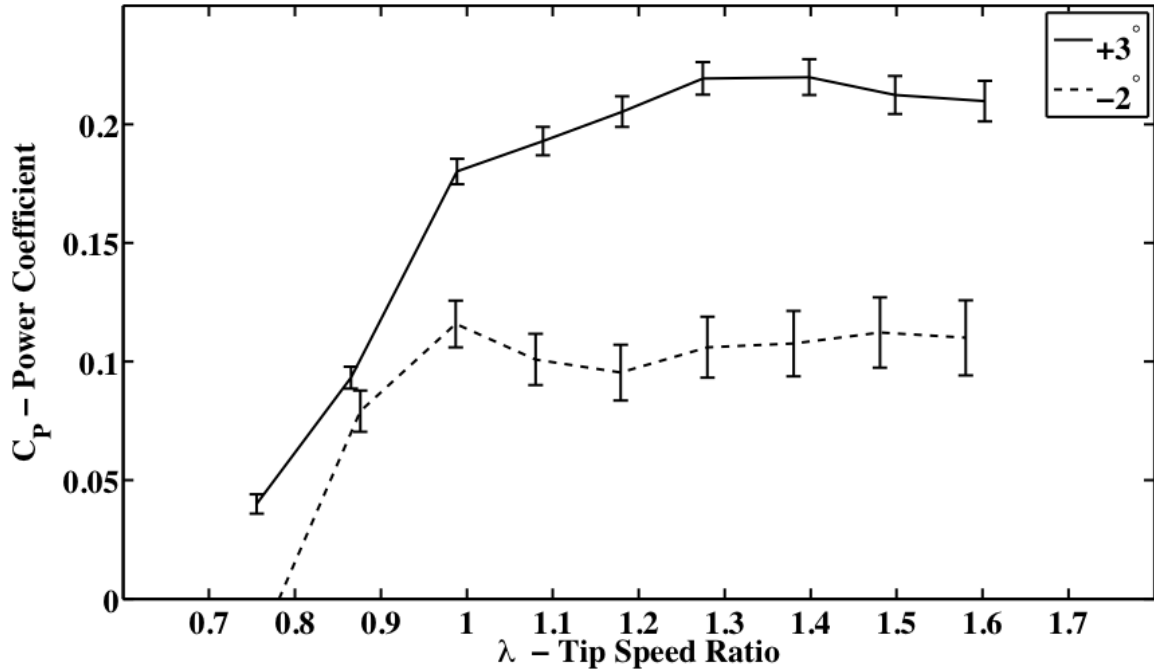


Figure 4.1 – The power coefficient curves for $\theta_t = +3^\circ$ and $\theta_t = -2^\circ$ are shown for the carbon fiber NACA 63₃-018 blade set. Four-bladed testing was performed at the toe angles $\theta_t = +3^\circ$ and $\theta_t = -2^\circ$, at an inflow velocity of $U_\infty = 1.22$ m/s, and at a solidity ratio of $\sigma = 0.294$.

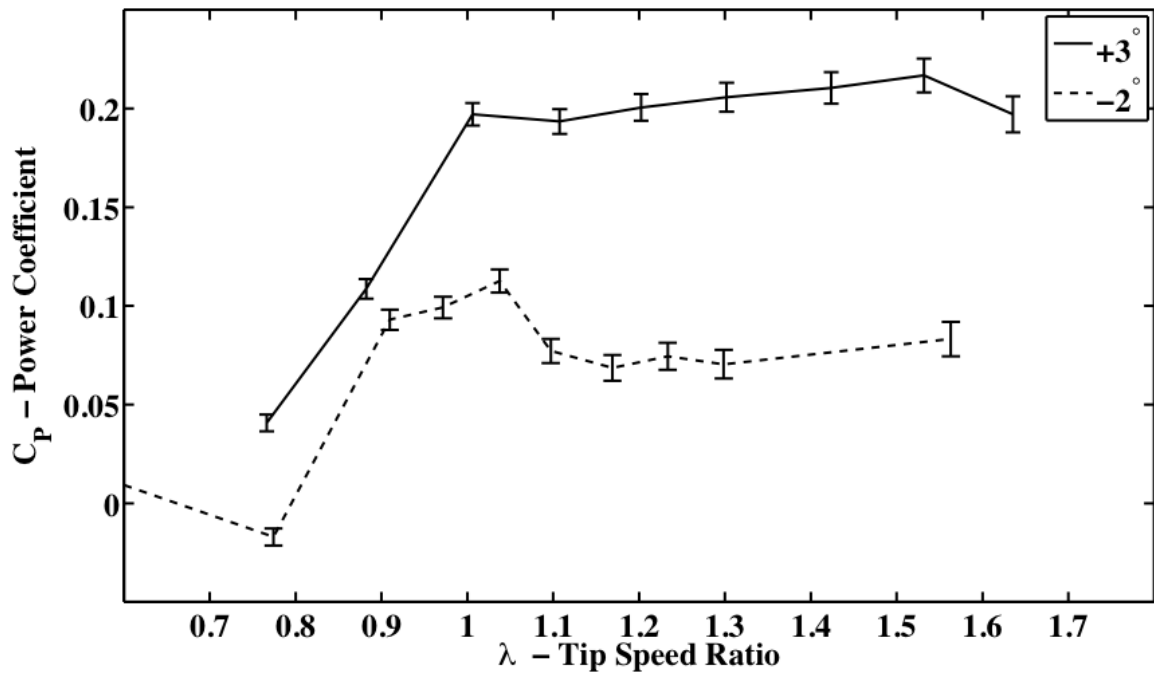


Figure 4.2 – The power coefficient curves for $\theta_t = +3^\circ$ and $\theta_t = -2^\circ$ are shown for the 3-D printed NACA 63₃-018 blade set. Four-bladed testing was performed at the toe angles $\theta_t = +3^\circ$ and $\theta_t = -2^\circ$, at an inflow velocity of $U_\infty = 1.22$ m/s, and at a solidity ratio of $\sigma = 0.269$.

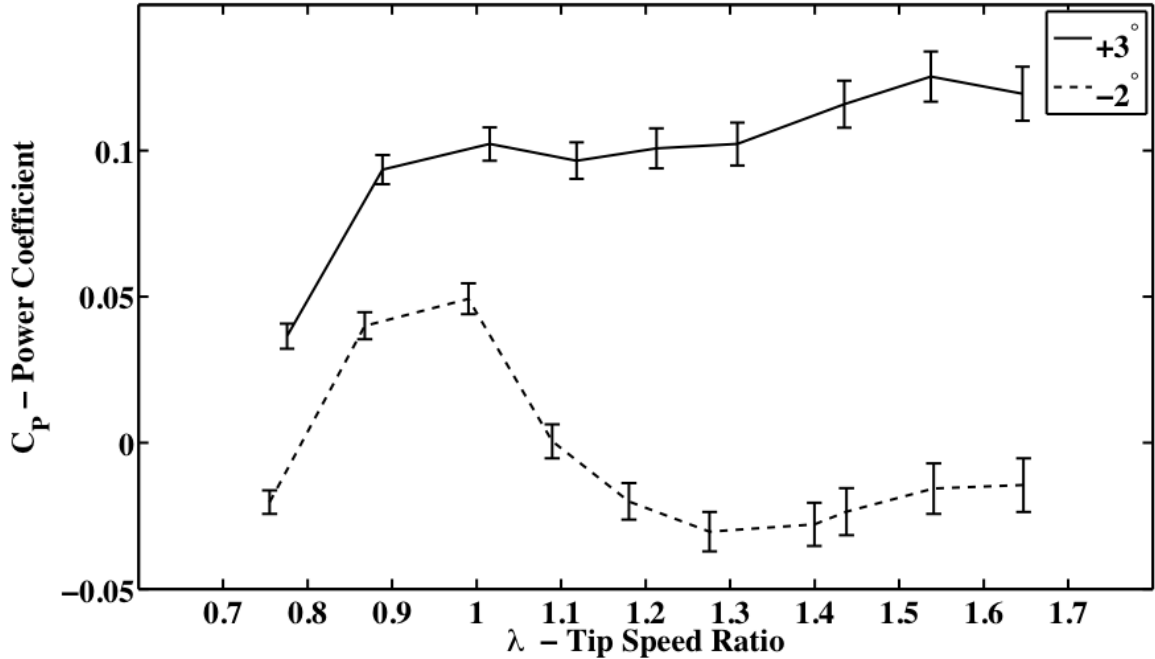


Figure 4.3 – The power coefficient curves for $\theta_t = +3^\circ$ and $\theta_t = -2^\circ$ are shown for the 3-D printed NACA 63₃-018 B blade set. NACA 63₃-018 B refers to the profile with tubercles or bumps. Four-bladed testing was performed at the toe angles $\theta_t = +3^\circ$ and $\theta_t = -2^\circ$, at an inflow velocity of $U_\infty = 1.22$ m/s, and at a solidity ratio of $\sigma = 0.269$. Note the difference in scale in this figure.

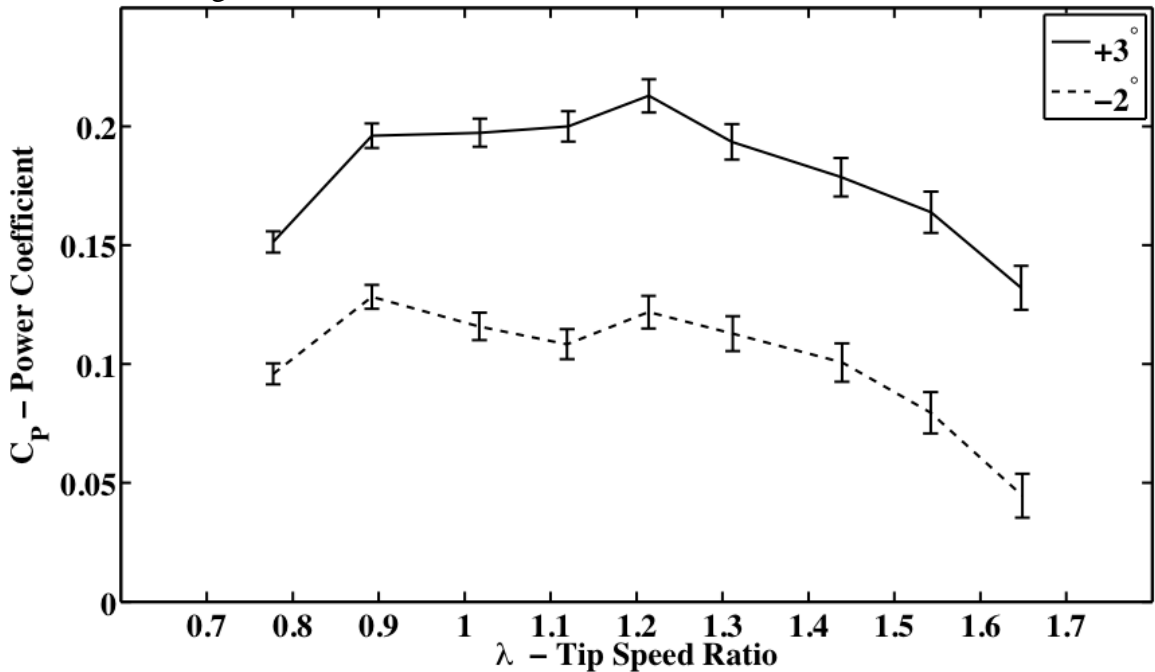


Figure 4.4 – The power coefficient curves for $\theta_t = +3^\circ$ and $\theta_t = -2^\circ$ are shown for the 3-D printed NACA 0018 blade set. Four-bladed testing was performed at the toe angles $\theta_t = +3^\circ$ and $\theta_t = -2^\circ$, at an inflow velocity of $U_\infty = 1.22$ m/s, and at a solidity ratio of $\sigma = 0.343$.

Blade Profile	Toe Angle	Maximum C_P	λ_{max}	Solidity Ratio	Chord (m)
NACA 63 ₃ -018 CF	+3°	0.220	1.40	0.294	0.0762
NACA 63 ₃ -018 CF	-2°	0.116	1.00	0.294	0.0762
NACA 63 ₃ -018 3-D	+3°	0.217	1.53	0.269	0.0699
NACA 63 ₃ -018 3-D	-2°	0.113	1.04	0.269	0.0699
NACA 63 ₃ -018 B	+3°	0.125	1.54	0.269	0.0699
NACA 63 ₃ -018 B	-2°	0.049	1.00	0.269	0.0699
NACA 0018	+3°	0.213	1.21	0.343	0.0889
NACA 0018	-2°	0.128	0.89	0.343	0.0889

Table 4.1 – Maximum C_P and λ_{max} are shown for each toe angle from symmetric foil testing results taken at an inflow velocity of $U_\infty = 1.22$ m/s. Note that the carbon fiber blade set has a chord length of $c = 0.0762$ m, which was truncated to $c = 0.0699$ m during manufacturing. The chord length of 0.0762 m was used to calculate the turbine solidity ratio.

4.1.2 Cambered Foil Results

Results for cambered foil testing are shown in Fig. 4.5, Fig. 4.6, and Fig. 4.7. The cambered foils generally performed worse than the symmetrical foils for the specific range of toe angles considered. Out of all cambered foils, the NACA 4418 profile had the maximum power coefficient, $C_P = 18.0\%$, at $\lambda_{max} = 1.31$ and $\theta_t = +3^\circ$.

The cambered NACA 4418 profile did not perform as well as the symmetrical counterpart, the NACA 0018 profile, which had the same chord length and thickness profile. The peak power coefficient was significantly lower for all toe angles. Testing at $\theta_t = +3^\circ$, shown in Fig. 4.5, yielded lower power coefficient results at low and moderate tip speed ratios and did not achieve comparable power coefficient results unless the tip speed ratio was higher than $\lambda_{max} = 1.31$.

The other two cambered profiles performed worse. Figure 4.6 shows the testing results for the S809 profile. This profile had lower power coefficients than blade profiles of a comparable solidity ratio for the range of toe angles considered. Figure 4.7 shows the

testing results for the LNV109 blade profile, which had a negative power coefficient for all test results at the range of toe angles considered.

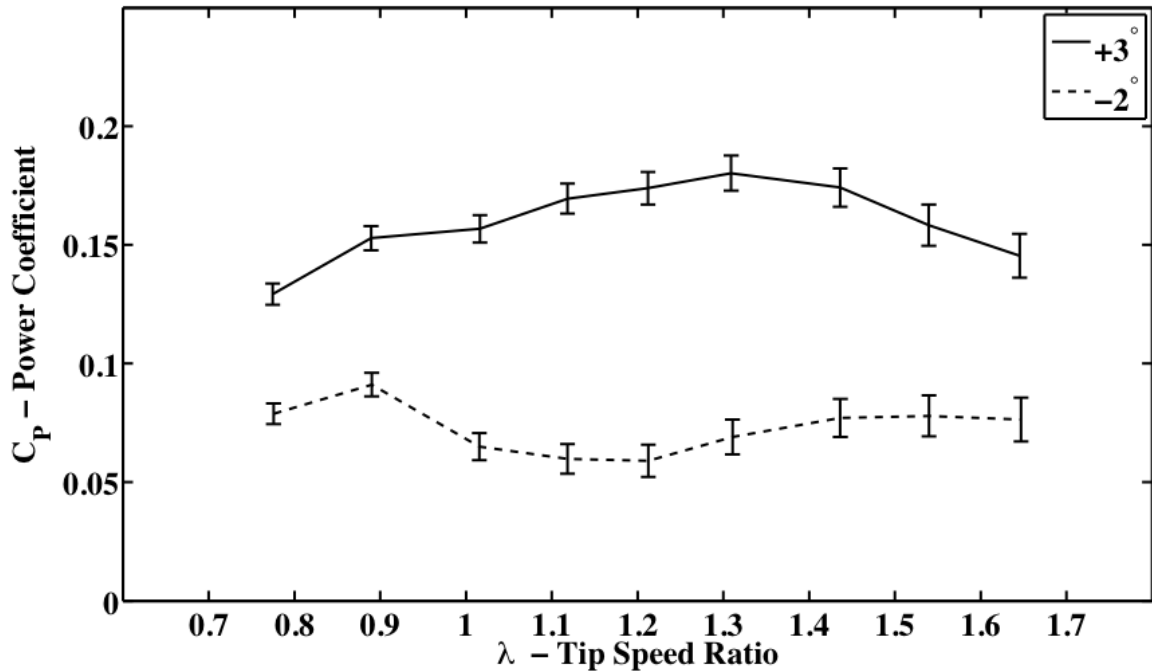


Figure 4.5 – The power coefficient curves for $\theta_t = +3^\circ$ and $\theta_t = -2^\circ$ are shown for the 3-D printed NACA 4418 blade set. Four-bladed testing was performed at the toe angles $\theta_t = +3^\circ$ and $\theta_t = -2^\circ$, at an inflow velocity of $U_\infty = 1.22$ m/s, and at a solidity ratio of $\sigma = 0.343$.

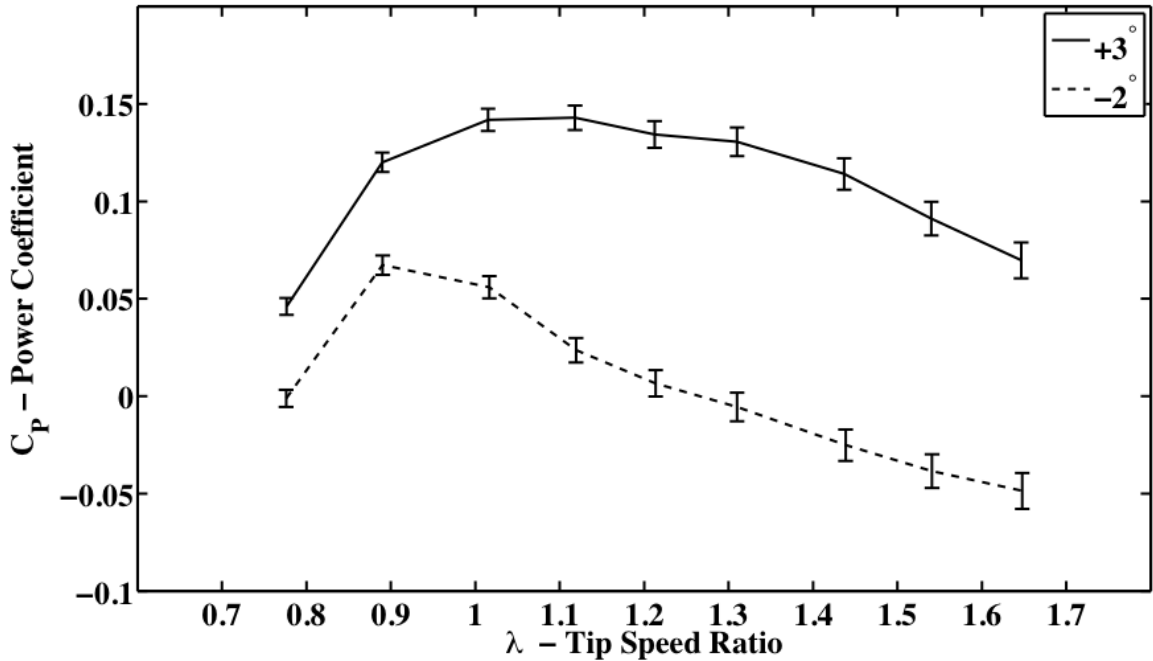


Figure 4.6 – The power coefficient curves for $\theta_t = +3^\circ$ and $\theta_t = -2^\circ$ are shown for the 3-D printed S809 blade set. Four-bladed testing was performed at the toe angles $\theta_t = +3^\circ$ and $\theta_t = -2^\circ$, at an inflow velocity of $U_\infty = 1.22$ m/s, and at a solidity ratio of $\sigma = 0.289$.

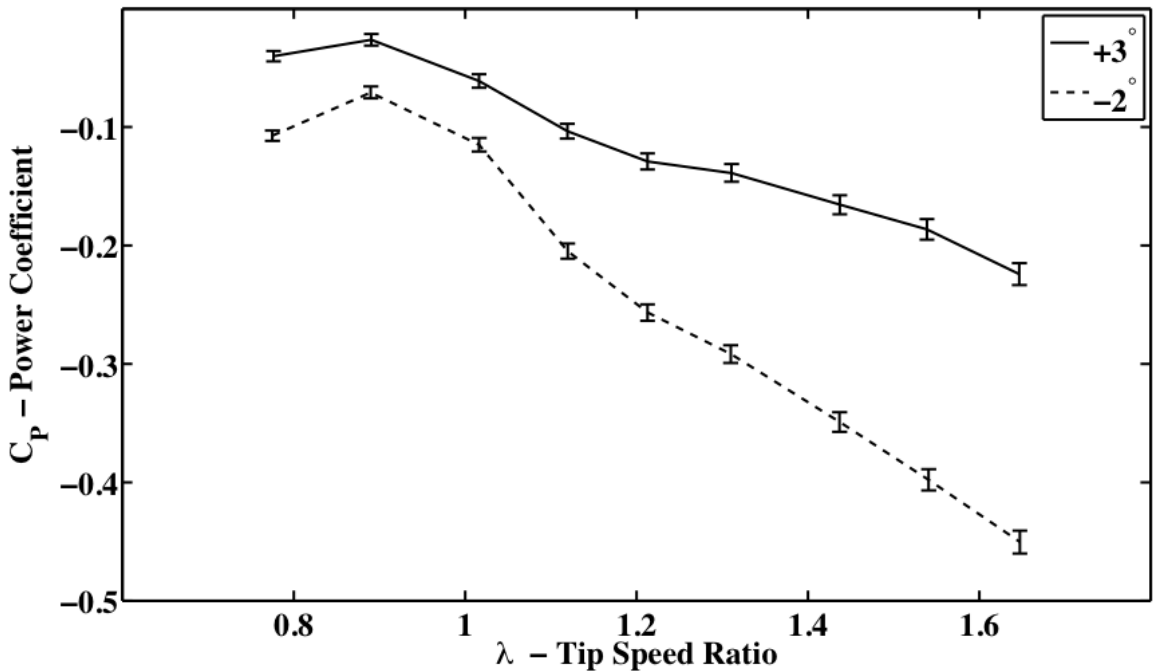


Figure 4.7 – The power coefficient curves are shown for the 3-D printed LNV109 blade set. Four-bladed testing was performed at the toe angles $\theta_t = +3^\circ$ and $\theta_t = -2^\circ$, at an inflow velocity of $U_\infty = 1.22$ m/s, and at a solidity ratio of $\sigma = 0.269$.

Blade Profile	Toe Angle	Maximum C_P	λ_{\max}	Solidity Ratio	Chord
NACA 4418	+3°	0.180	1.31	0.343	0.0889
NACA 4418	-2°	0.091	0.89	0.343	0.0889
S809	+3°	0.143	1.12	0.289	0.0749
S809	-2°	0.067	0.89	0.289	0.0749
LNV109	+3°	-0.026	0.89	0.269	0.0699
LNV109	-2°	-0.070	0.89	0.269	0.0699

Table 4.2 – Maximum C_P and λ_{\max} are shown for each toe angle from asymmetric foil testing results taken at an inflow velocity of $U_{\infty} = 1.22$ m/s.

4.2 Effect of Blade Profile on Power Coefficient

Figure 4.8 shows a comparison of the power coefficient results for blade profiles tested under the same conditions. The two best performing profiles were the NACA 63₃-018 (carbon fiber and 3-D printed), and the NACA 0018, both of which are symmetric profiles. Note that all of the foils with the lower solidity ratio had very similar power coefficients at low tip speed ratios. The values from different profiles began to diverge above a tip speed ratio of $\lambda = 0.9$. The peak power coefficients for each blade profile at $\theta_t = +3^\circ$ are summarized in Fig. 4.9.

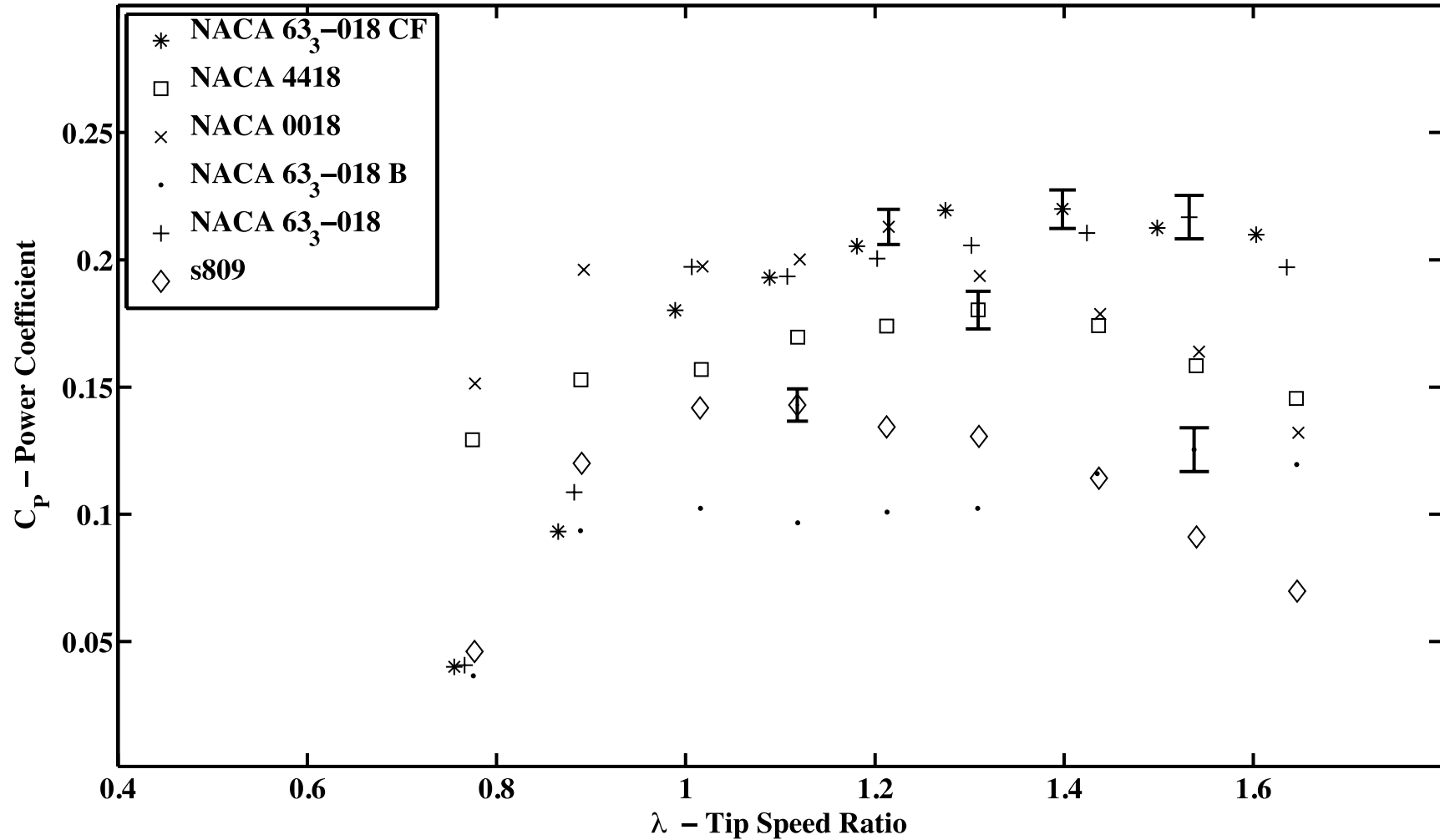


Figure 4.8 – The testing results for each blade profile, excluding the LNV109, are compared for $U_\infty = 1.22$ m/s and $\theta_t = +3^\circ$. Uncertainties are included at the point with maximum power coefficient for each profile. NACA 63₃-018 B refers to the profile with tubercles or bumps.

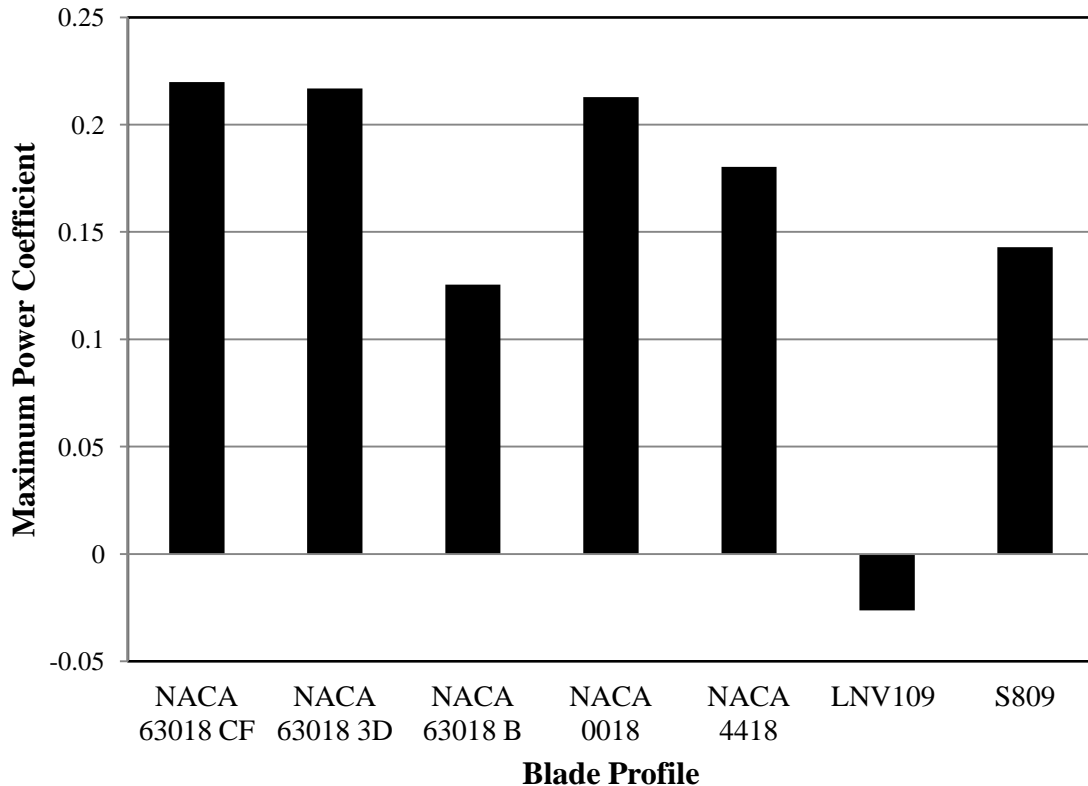


Figure 4.9 - The maximum power coefficient from four-bladed experimental testing is shown for each blade profile at $\theta_t = +3^\circ$ and $U_\infty = 1.22$ m/s.

4.3 Effect of Toe Angle on Power Coefficient

From the above data it is apparent that increasing the toe angle causes an increase in the peak power coefficient for all blade profiles tested. It is also clear that the toe angle must have a value at which the power coefficient is a maximum. At toe angles higher than the optimal toe angle, the peak power coefficient will start to decrease. To evaluate this effect, further testing was performed on the most promising profile, the NACA 63₃-018. A total of five toe angles, -2° , $+0.5^\circ$, $+3^\circ$, $+5^\circ$, and $+7^\circ$ were considered. Figure 4.10 and Fig. 4.11 show the testing results for an inflow velocity of 1.00 m/s. The peak power coefficients at each toe angle are summarized in Table 4.3, and are shown in graphical form in Fig. 4.12. The highest power coefficient was at a toe angle of $+5^\circ$, with a value of

23.4% at a tip speed ratio of 1.44. The second highest power coefficient was at a toe angle of $+3^\circ$, with a value of 22.5% at a tip speed ratio of 1.40. The power coefficient dropped significantly at $+7^\circ$, with a maximum value of 19.5% at a tip speed ratio of 1.44. Therefore the maximum power coefficient for this profile occurs at a toe angle between $\theta_t = +3^\circ$ and $\theta_t = +7^\circ$, and is close to $\theta_t = +5^\circ$.

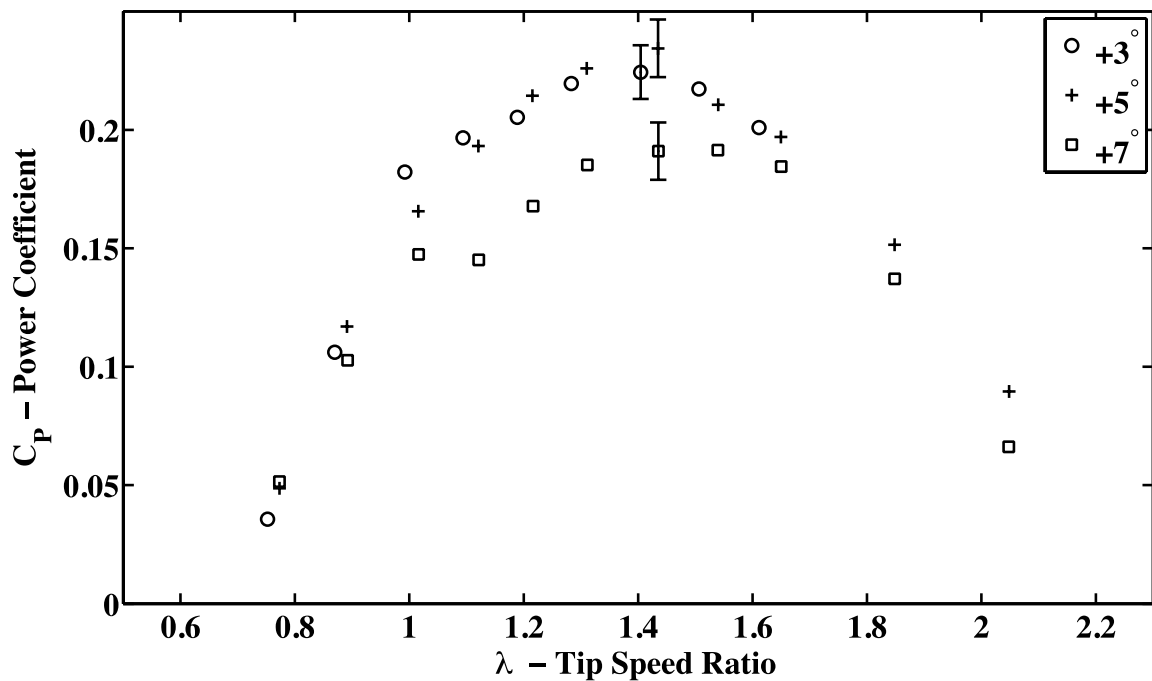


Figure 4.10 – Power coefficient curves are shown for NACA 63₃-018 carbon fiber blades for $\theta_t = +3^\circ$, $\theta_t = +5^\circ$, and $\theta_t = +7^\circ$. These four-bladed tests were taken at a solidity of $\sigma = 0.294$ and an inflow velocity of $U_\infty = 1.00$ m/s. Uncertainties are included at the peak power coefficient from each toe angle.

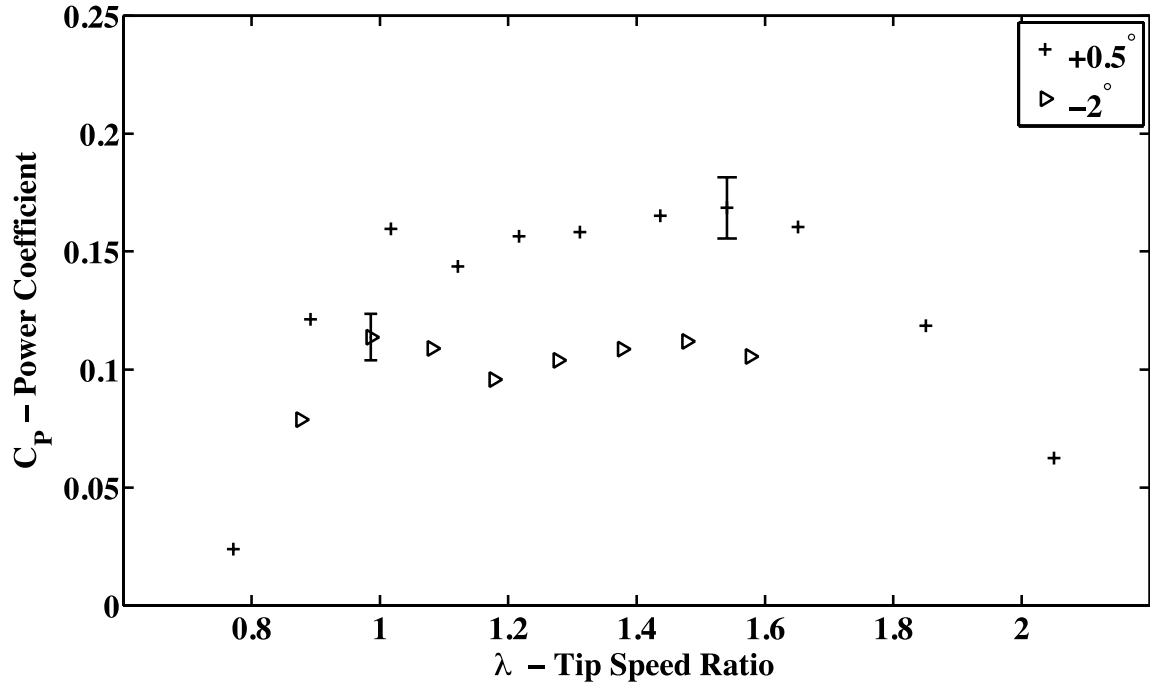


Figure 4.11 – Power coefficient curves are shown for NACA 63₃-018 carbon fiber blades for $\theta_t = +0.5^\circ$ and $\theta_t = -2^\circ$. These four-bladed tests were taken at a solidity of $\sigma = 0.294$ and an inflow velocity of $U_\infty = 1.00$ m/s. Uncertainties are included at the peak power coefficient from each toe angle.

Toe Angle	Maximum C_P	λ_{\max}
+7	0.195	1.44
+5	0.233	1.44
+3	0.225	1.40
+0.5	0.169	1.44
-2	0.114	0.99

Table 4.3 – The maximum C_P and λ_{\max} are shown for the carbon fiber NACA 63₃-018 blade profile over the extended toe angle range. Four-bladed data was taken at a solidity of $\sigma = 0.294$ and an inflow velocity of $U_\infty = 1.00$ m/s.

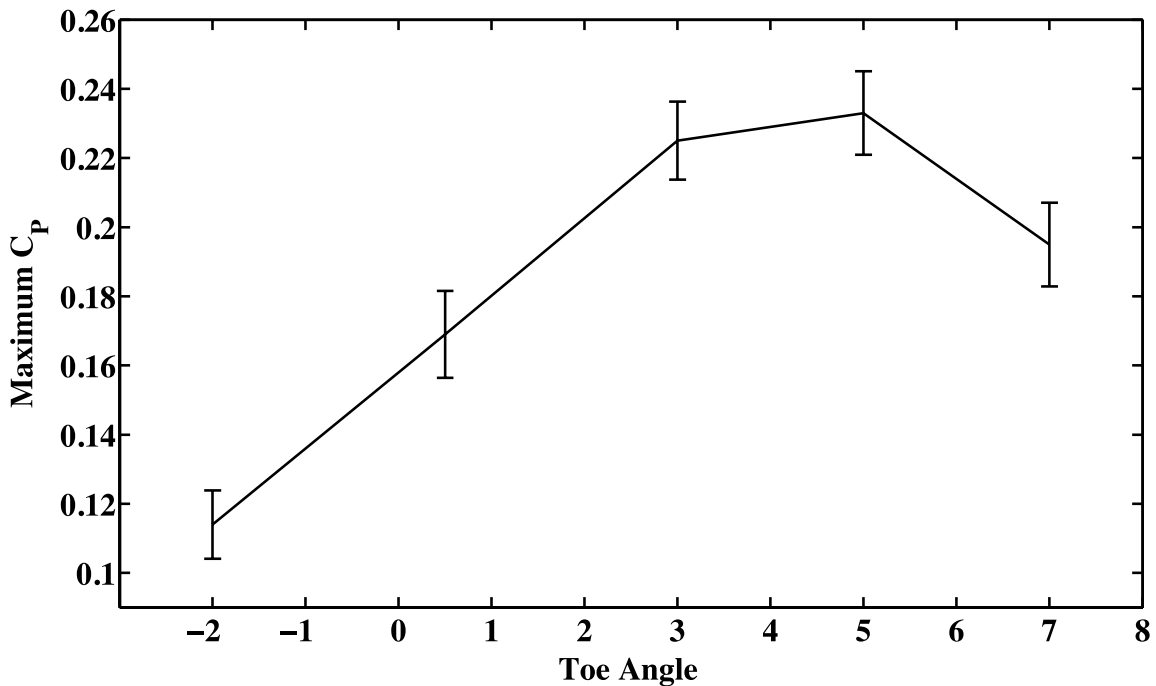


Figure 4.12 – The maximum power coefficient for the carbon fiber NACA 63₃-018 blade profile is shown as a function of toe angle. Four-bladed data was taken at a solidity of $\sigma = 0.294$ and an inflow velocity of $U_\infty = 1.00$ m/s.

4.4 Two-Bladed Tests

Two-bladed tests were performed primarily to enable comparison of the torque and power coefficients with the free vortex model. As with the toe angle study, the focus of the two-bladed tests was on the profile that performed the best in four-bladed tests, the NACA 63₃-018 profile. Because of the large magnitude of the torque fluctuations present in two bladed testing, the inflow velocity was reduced to 0.6 m/s. By lowering the inflow

velocity, smaller magnitude loads resulted in smaller speed fluctuations. The free vortex model does take Reynolds number into account, but higher Reynolds numbers are modeled more accurately than lower Reynolds numbers in general. As long as the Reynolds numbers for the blades remain sufficiently large, testing at lower inflow velocities was acceptable for model validation.

4.4.1 Testing Results for $\theta_t = 0^\circ$

Two-bladed testing was performed for the NACA 63₃-018 profile with four test runs at each tip speed ratio. The multiple data points at each tip speed ratio were averaged for comparison with the free vortex model. The power coefficient results, shown in Fig. 4.13, were higher than the results from four-bladed testing. The peak power coefficient also occurred at a higher tip speed ratio, which was expected for a case with a lower solidity. Nondimensional torque results are presented for $\lambda = 1.50$ in Fig. 4.14. The bin-averaging process is outlined in Section 1.2.1.3.

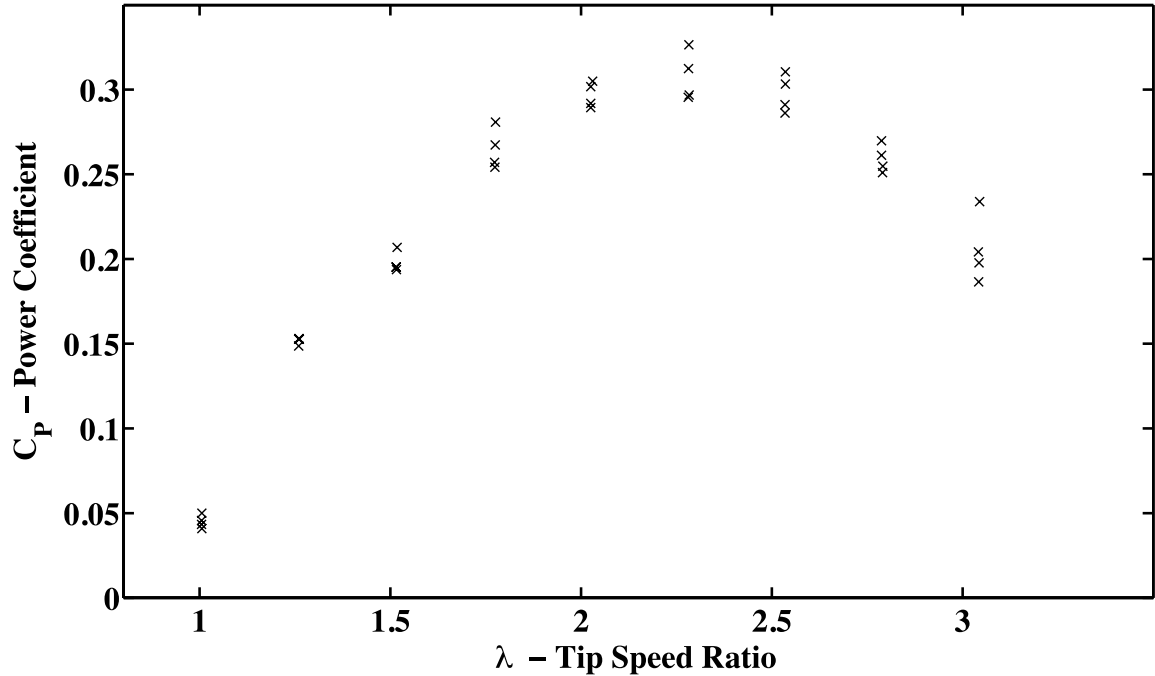


Figure 4.13 – Power coefficient results are shown for two-bladed NACA 63₃-018 testing taken at a solidity of $\sigma = 0.147$, inflow velocity of $U_\infty = 0.6$ m/s and toe angle of $\theta_t = 0^\circ$. Testing was performed four times at each tip speed ratio. The same data is shown with uncertainty in C_p in Fig. 4.17.

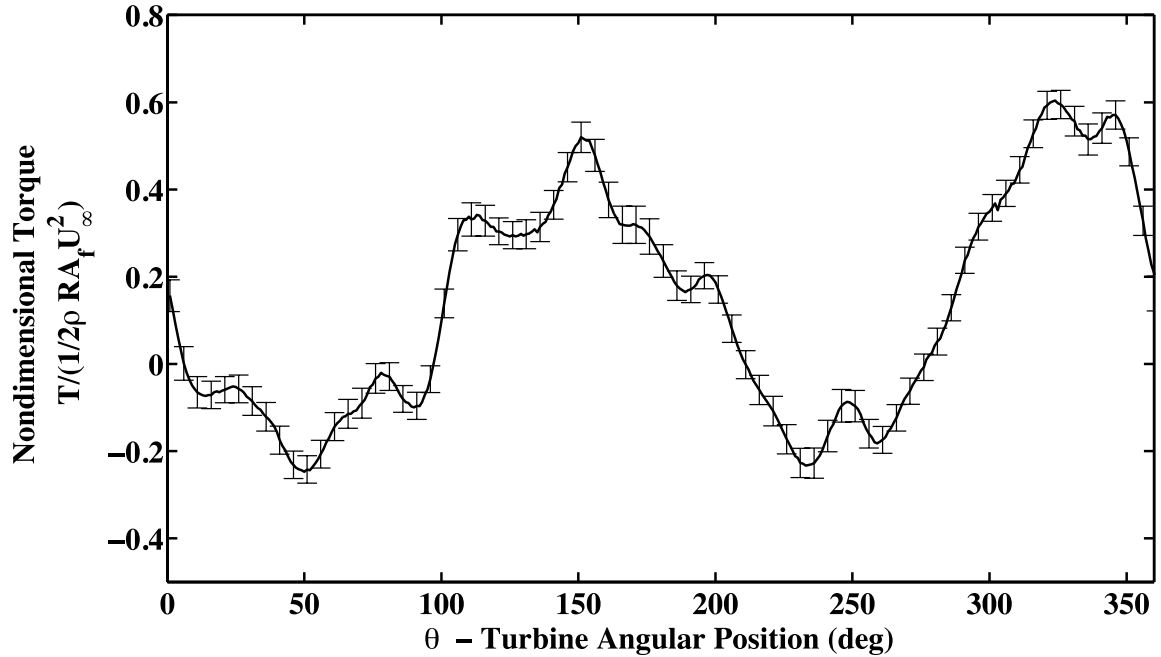


Figure 4.14 – Bin-averaged nondimensional torque from two-bladed NACA 63₃-018 experimental data is shown for $\lambda = 2.00$. Data was taken at a solidity of $\sigma = 0.147$, inflow velocity of 0.6 m/s, and toe angle of $\theta_t = 0^\circ$.

4.4.2 Testing Results for $\theta_t = +5^\circ$

Two-bladed testing results at $\theta_t = +5^\circ$ yielded higher power coefficients than the two-bladed testing performed at $\theta_t = 0^\circ$. The maximum power coefficient at $\theta_t = +5^\circ$ was $C_P = 0.370$, compared to $C_P = 0.308$ at $\theta_t = 0^\circ$. These results follow the same trend as the four-bladed testing results. The optimal toe angles for turbine efficiency were not determined for the two-bladed testing.

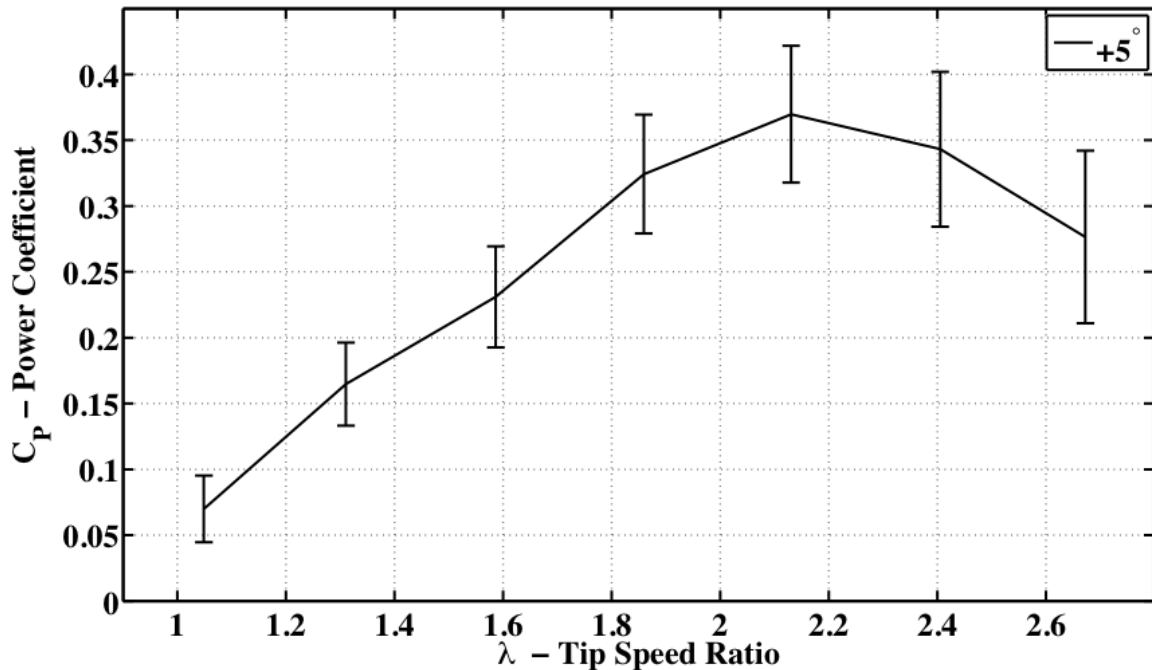


Figure 4.15 – Two bladed experimental testing results are shown for the NACA 63₃-018 profile, taken at $\sigma = 0.147$, inflow velocity of 0.6 m/s, and $\theta_t = +5^\circ$. Only one data point was taken for each tip speed ratio, and the error bars were calculated using the uncertainty propagation equations outlined in Appendix B.

4.5 Uncertainty in Experimental Results

Uncertainty in measured quantities results in uncertainties in the following calculated quantities: C_P , λ , T^* , and U_∞ . The uncertainty calculation process is shown in detail in Appendix B, and the C_P and T^* results are summarized below. Uncertainties in the C_P calculations were compared with the standard deviation of experimental results from

repeatability studies to compare the magnitudes of calculated result with experimental test repeatability.

Uncertainties in the calculated quantities result from uncertainties in measurements; the uncertainties are unrelated to the fluctuations in turbine angular velocity and inflow velocity that result from the highly unsteady nature of these tests. The magnitude and nature of these fluctuations are also described in Appendix B.

4.5.1 Uncertainty in Power Coefficient

Uncertainty in C_P was calculated using the uncertainties in the following measured quantities: F , l , ω , D , b , and Δx , where F is the force measured in the torque load cell, l is the lever arm of the applied load used in the torque load cell calibration, ω is the turbine angular velocity, D is the turbine diameter, b is the turbine blade span, and Δx is the distance traveled during the test. The uncertainty in each length-scale measured quantity was estimated using half of the smallest increment used for the length measurements. The uncertainty in F was estimated using the accuracy of the torque load cell calibration and end plate drag tests. A small arbitrary value was chosen for the uncertainty in ω , which is explained in Appendix B. Uncertainty in time was neglected.

Calculated uncertainties in C_P were compared with the standard deviation of C_P from repeatability studies for both the two-bladed and four-bladed cases. These results are shown in Fig. 4.16 and Fig. 4.17, and are included in tabular form in Appendix B. In both cases, uncertainties were greater than three standard deviations for all but one tip speed ratio, which suggests that the calculated uncertainties are generally conservative, and can be used to describe the range of C_P results for sparse experimental data sets.

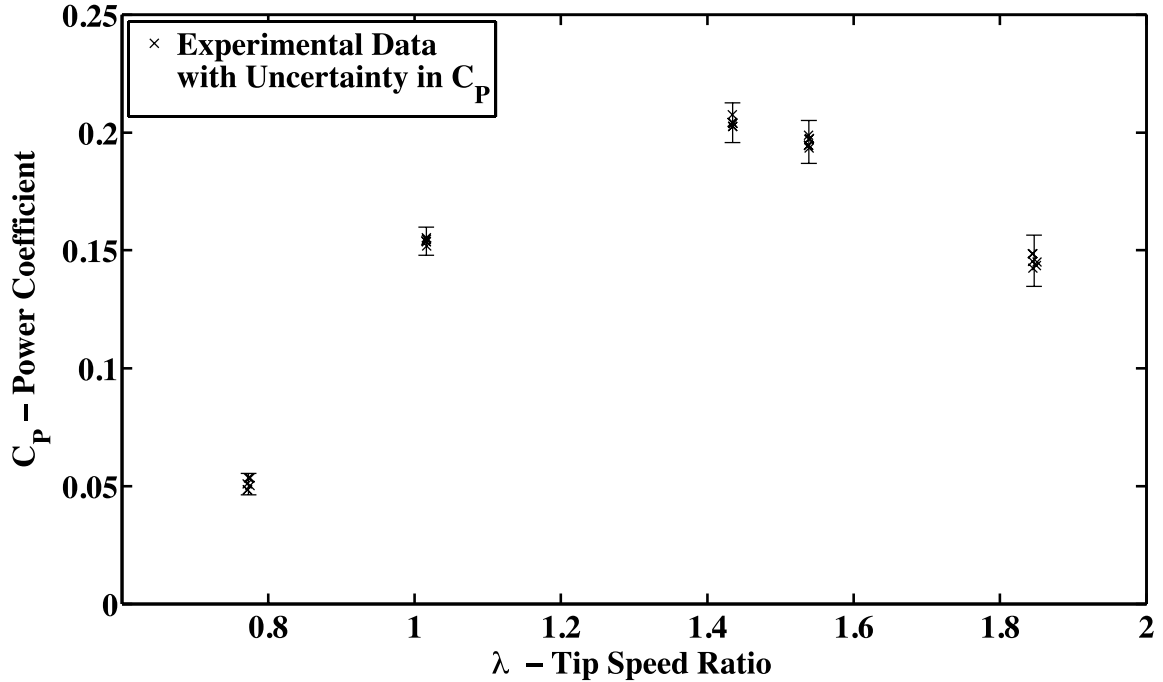


Figure 4.16 – Uncertainty in power coefficient is compared with multiple experimental data points at each tip speed ratio taken with the same turbine geometry and flow conditions. Data was taken using the NACA 63₃-018 blade profile, with four blades, $\sigma = 0.269$, $\theta_t = 0^\circ$, and $U_\infty = 1.00$ m/s.

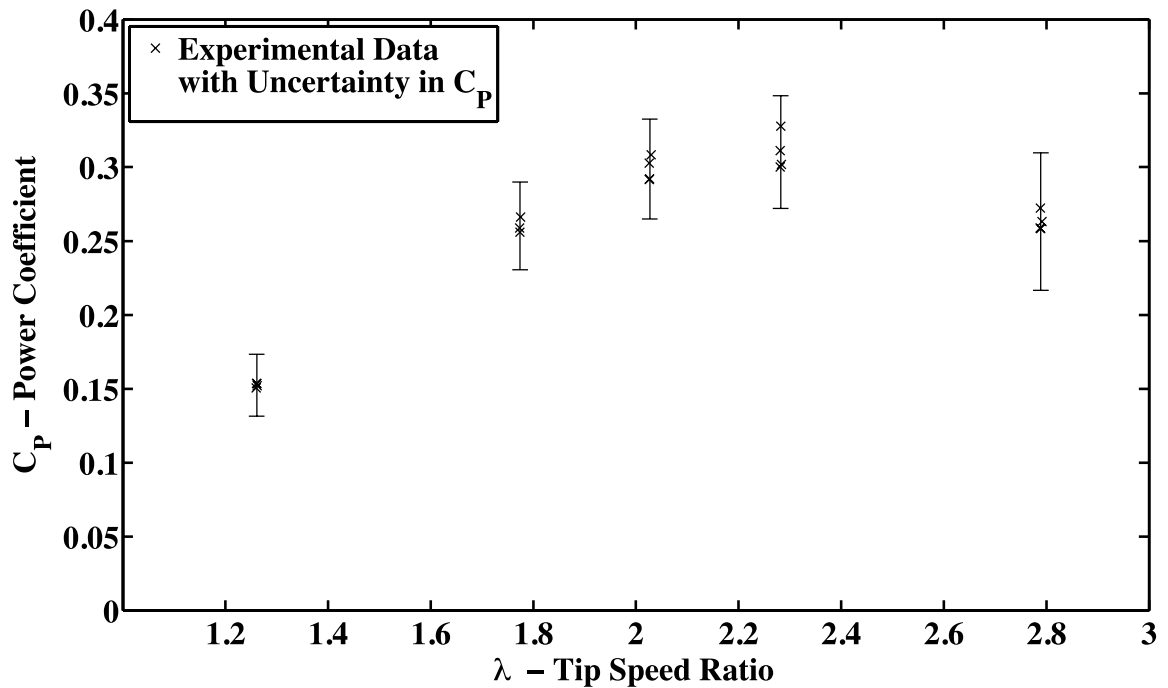


Figure 4.17 – Uncertainty in power coefficient is compared with multiple experimental data points at each tip speed ratio taken with the same turbine geometry and flow conditions. Data was taken using the NACA 63₃-018 blade profile, with two blades, $\sigma = 0.147$, $\theta_t = 0^\circ$, and $U_\infty = 0.60$ m/s.

4.5.2 Uncertainty in Nondimensional Torque

The uncertainty in T^* was calculated using the same quantities as the power coefficient, with the addition of the uncertainty in the turbine rotor mass moment of inertia, I_{rotor} , and the uncertainty in the turbine angular acceleration, $\frac{d\omega}{dt}$. Because the turbine rotor mass moment of inertia term was estimated using a solid model from SolidWorks, a conservative value of 10% of the mass moment of inertia was used for the uncertainty. This includes discrepancies between the geometries of the model and the physical turbine rotor, as well as variability in materials. The maximum turbine angular accelerations during testing generally varied from 4 to 8 rad/s^2 . Because the turbine angular acceleration is the second derivative of the measured signal, it should have a higher uncertainty than the turbine angular velocity. A conservative value of 0.6 rad/s^2 was chosen, which is about 10% of typical acceleration output. Example uncertainties in nondimensional torque are shown in the following section.

4.6 Comparison of Numerical and Experimental Results

The experimental data from two-bladed tests measured in the tow tank was compared with the numerical model. Numerical modeling results included the FVM, and the FVM with virtual incidence angle correction. Comparison of the power coefficients shows the overall performance of the model. Comparison of the nondimensional torque throughout the turbine rotation helps identify angular turbine positions where the model is performing well, or may need improvement. The nondimensional torque comparison is especially important for identifying areas of improvement that may be required in the dynamic stall model.

4.6.1 Comparison at $\theta_t = 0^\circ$

Figure 4.18 shows the comparison of experimental data with the FVM and FVM with virtual incidence angle correction, with both modeling cases employing the one-walled boundary condition for an inflow velocity of 0.6 m/s, a toe angle of $\theta_t = 0^\circ$, and a range of tip speed ratios. Compared to the experimental data, the FVM over predicts the power coefficient before the peak, from $\lambda = 1.60$ to $\lambda = 2.20$. Past the peak power coefficient, the model under predicts the power coefficient. However, the model generally follows the correct trend. Addition of the virtual incidence angle correction to the FVM improved comparison with experimental data, especially near the peak power coefficient and at tip speed ratios higher than λ_{\max} . The FVM compared better than the FVM with virtual angle of incidence correction at low tip speed ratios.

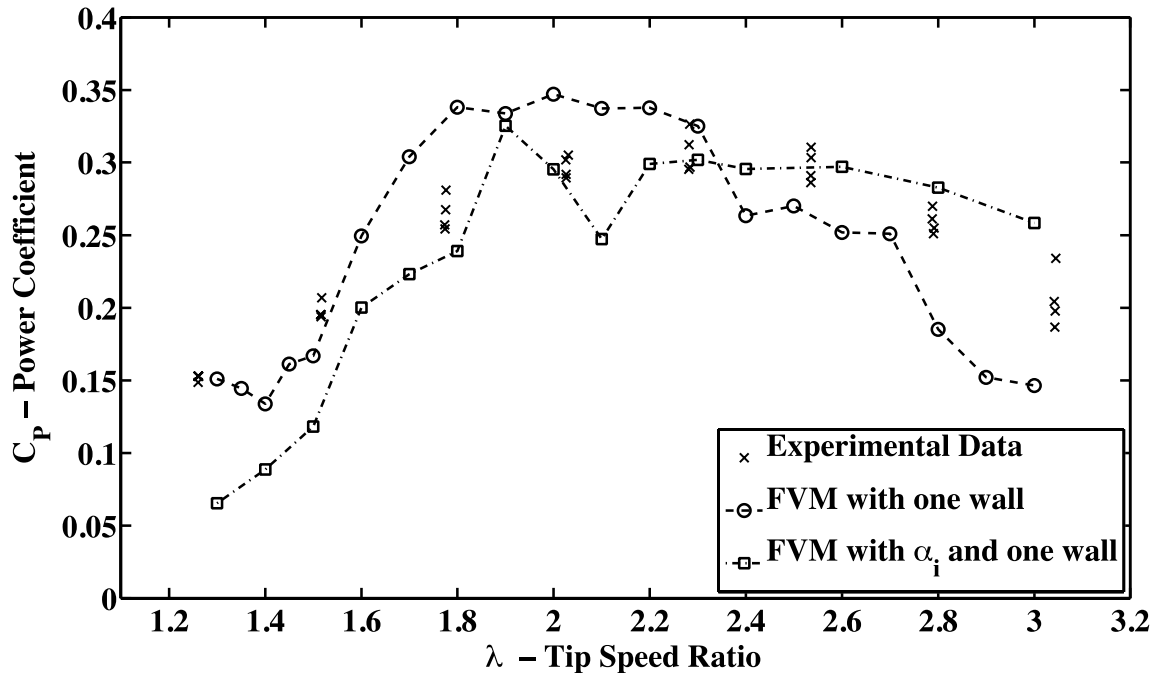


Figure 4.18 – Two-bladed experimental data at a solidity of $\sigma = 0.147$, inflow velocity of 0.6 m/s, and $\theta_t = 0^\circ$ is compared to the FVM with one wall blockage effect, and the FVM with virtual incidence angle correction and one wall blockage effect.

The nondimensional torque from experimental data, FVM, and FVM with virtual incidence angle correction were compared at $\theta_t = 0^\circ$. Figure 4.19 and Fig. 4.20 show the comparison of nondimensional torque at two tip speed ratios: $\lambda = 1.80$, and $\lambda = 2.40$. The FVM results do not have a blockage correction, and the FVM with the angle of incidence correction have the one-wall blockage correction. The FVM results without the angle of incidence correction compare well with the experimental data for $\lambda = 1.80$, but do not compare well for $\lambda = 2.40$. The FVM results with the angle of incidence correction do not compare as well at $\lambda = 1.80$, but compare better at $\lambda = 2.40$.

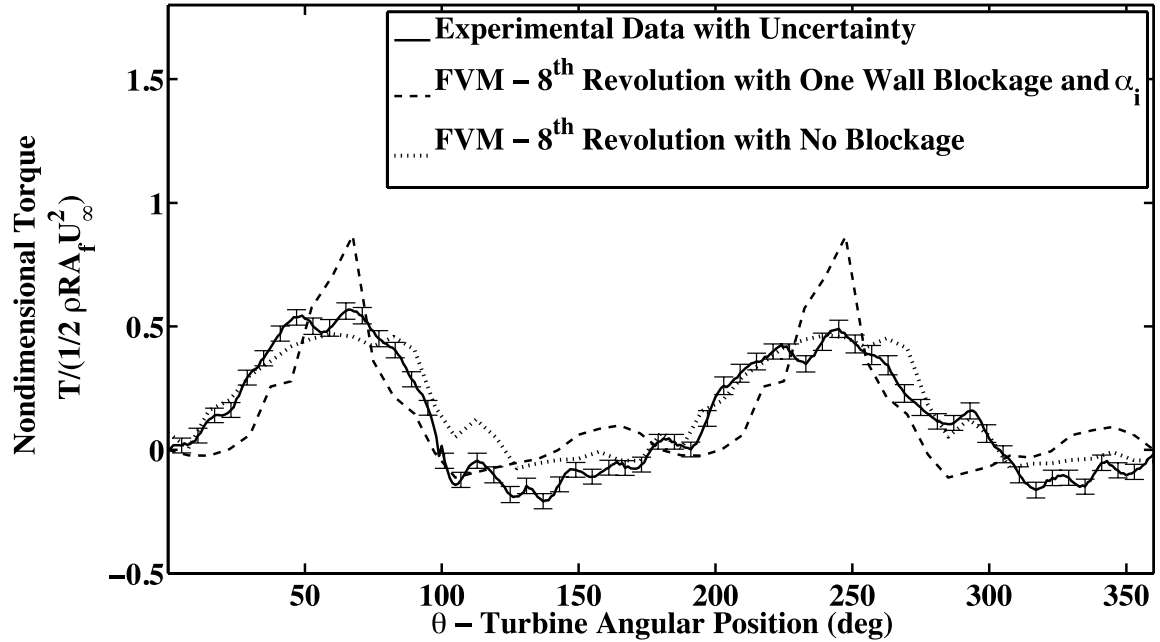


Figure 4.19 – Experimental nondimensional torque taken at $\sigma = 0.147$, $\theta_t = 0^\circ$, $\lambda = 1.80$, and $U_\infty = 0.6$ m/s is compared to the FVM with virtual incidence angle correction and one wall blockage, as well as the FVM with no blockage effect and without the virtual incidence angle correction. The eighth revolution refers to the first turbine revolution that has reached convergence.

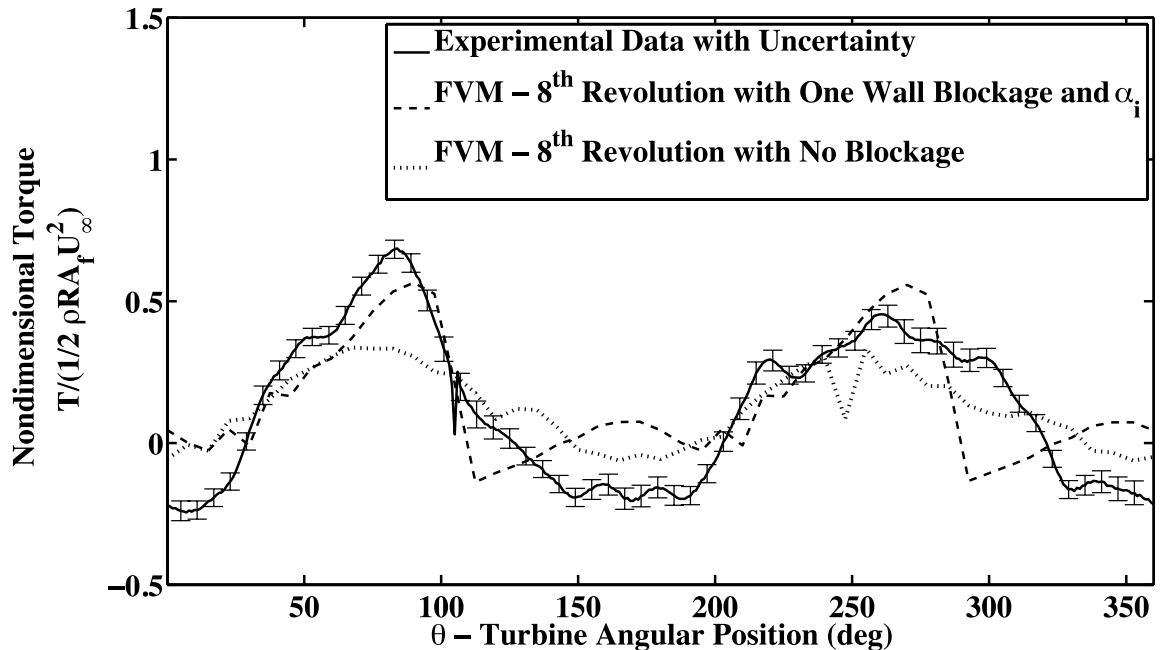


Figure 4.20 – Experimental nondimensional torque taken at $\sigma = 0.147$, $\theta_t = 0^\circ$, $\lambda = 2.40$, and $U_\infty = 0.6$ m/s is compared to the FVM with virtual incidence angle correction and one wall blockage, as well as the FVM with no blockage effect and without the virtual incidence angle correction. The eighth revolution refers to the first turbine revolution that has reached convergence.

4.6.2 Comparison at $\theta_t = +5^\circ$

Figure 4.21 shows the comparison of power coefficient results from two-bladed testing at $\theta_t = +5^\circ$ with the FVM and the FVM with virtual angle of incidence correction. While the effect of toe angle was clear from experimental results, the numerical model without the virtual angle of incidence correction was not successful in capturing the effect of the toe angle changes. The results of four-bladed testing showed that the maximum efficiency occurred at a toe angle of $\theta_t = +5^\circ$. The efficiency increase from $\theta_t = 0^\circ$ to $\theta_t = +5^\circ$ for the two-bladed tests was 0.062, and the efficiency increase from $\theta_t = +0.5^\circ$ to $\theta_t = +5^\circ$ for the four-bladed tests was 0.064 (four-bladed data was not taken at $\theta_t = 0^\circ$). The numerical model predicts that the maximum power coefficient occurs near $\theta_t = 0^\circ$, with decreasing power coefficients when the toe angle is positive or negative. This is not consistent with the trends found from two-bladed and four-bladed tow tank testing, which suggests that additional important physical effects seen in the experimental data are not included in the model.

Addition of the virtual angle of incidence correction to the FVM improved the power coefficient results, specifically the dependence of the maximum power coefficient on toe angle. Figure 4.21 shows that the power coefficients from these results were over predicted near λ_{\max} and at high tip speed ratios.

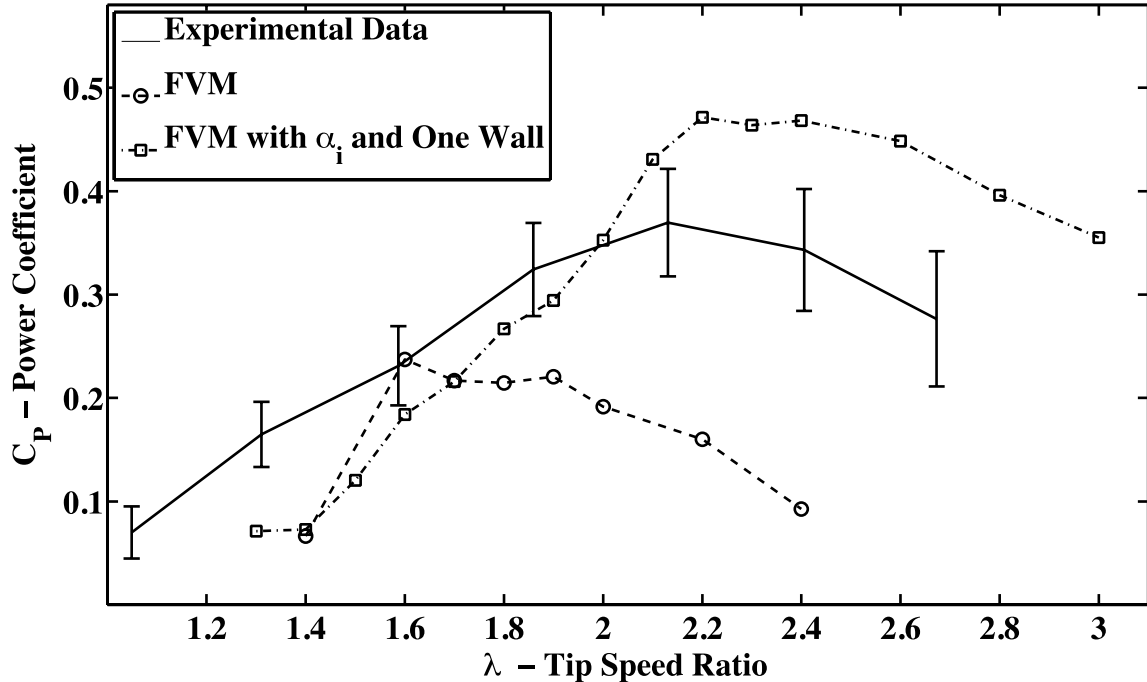


Figure 4.21 – Two-bladed experimental data at a solidity of $\sigma = 0.147$, inflow velocity of 0.6 m/s, and $\theta_t = +5^\circ$ is compared to the FVM with no blockage effect, and the FVM with virtual incidence angle correction and one wall blockage effect.

The nondimensional torque from experimental data, FVM, and FVM with virtual incidence angle correction were also compared at $\theta_t = +5^\circ$. Figure 4.22 and Fig. 4.23 show the comparison of nondimensional torque at two tip speed ratios: $\lambda = 1.80$, and $\lambda = 2.40$. The FVM results without the angle of incidence correction compare well with the experimental data for $\lambda = 1.80$, but do not compare well for $\lambda = 2.40$. The FVM results with the angle of incidence correction do not compare as well at $\lambda = 1.80$, but compare better at $\lambda = 2.40$. Calculations of flow curvature parameters using the transformation equations from Migliore and Wolfe (1980) yield average virtual incidence angle and virtual camber values that increase with tip speed ratio. This implies that flow curvature effects become more severe as the tip speed ratio is increased. The FVM results with angle of incidence correction compare better at $\lambda = 2.40$ for the toe angles of $\theta_t = 0^\circ$ and $\theta_t = +5^\circ$ because of this. Addition of the virtual camber correction to the model could

improve the comparison of the model with experimental power coefficient and nondimensional torque data throughout the tip speed ratio range tested and modeled.

(Migliore and Wolfe, 1980)

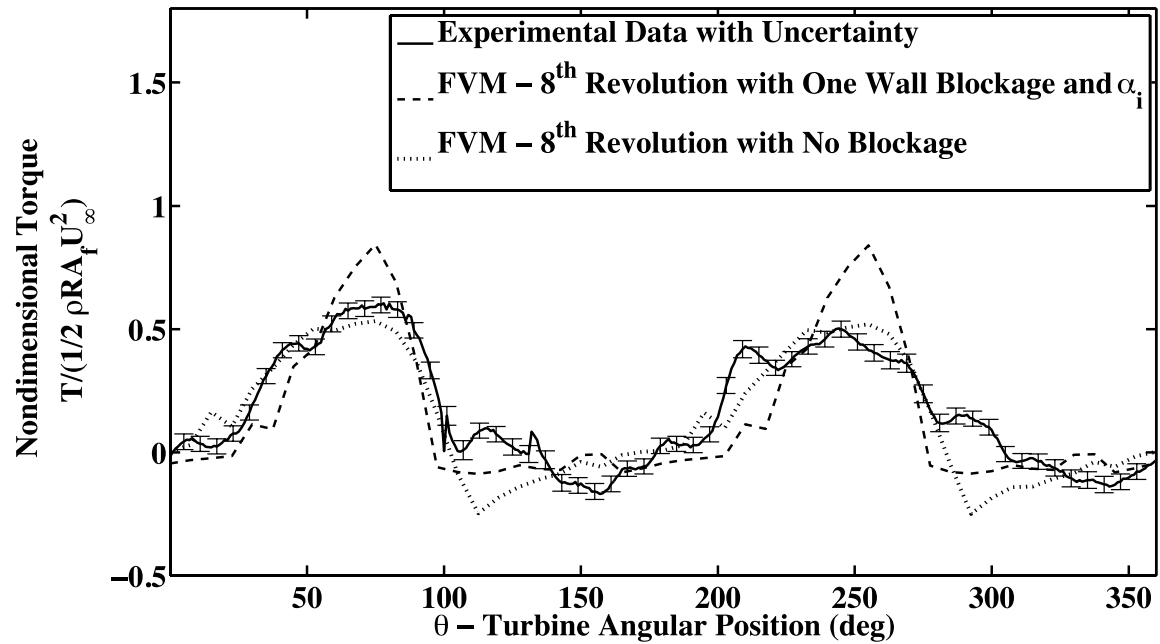


Figure 4.22 – Experimental nondimensional torque taken at $\sigma = 0.147$, $\theta_i = +5^\circ$, $\lambda = 1.80$, and $U_\infty = 0.6$ m/s is compared to the FVM with virtual incidence angle correction and one wall blockage, as well as the FVM with no blockage effect and without the virtual incidence angle correction. The eighth revolution refers to the first turbine revolution that has reached convergence.

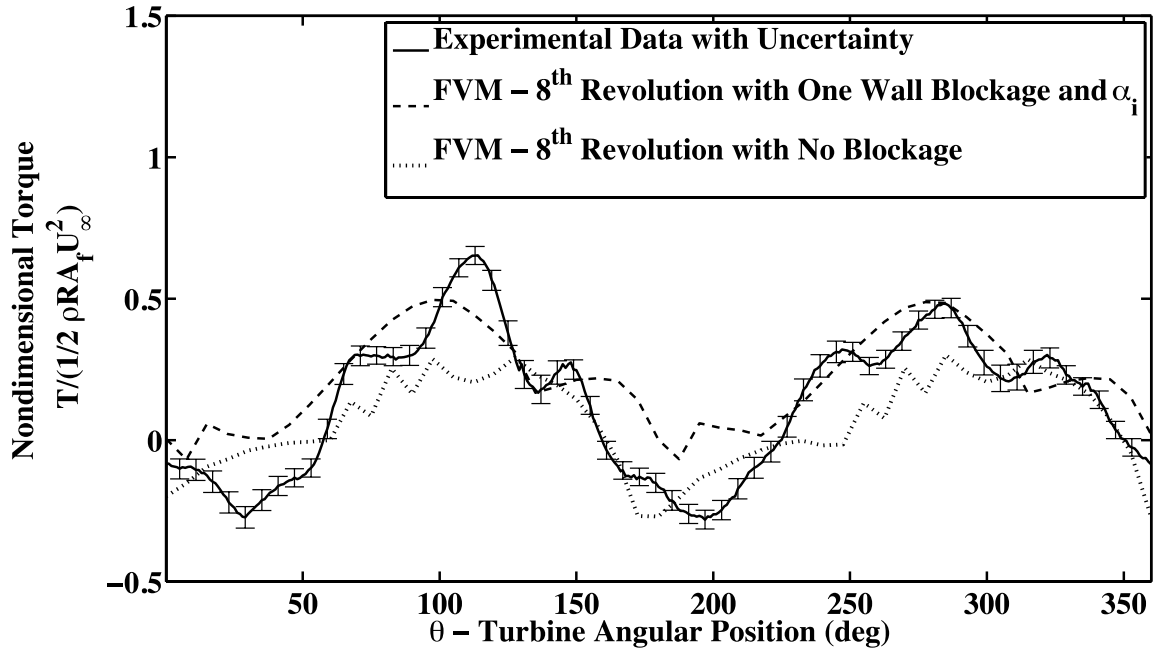


Figure 4.23 – Experimental nondimensional torque taken at $\sigma = 0.147$, $\theta_t = +5^\circ$, $\lambda = 2.40$, and $U_\infty = 0.6$ m/s is compared to the FVM with virtual incidence angle correction and one wall blockage, as well as the FVM with no blockage effect and without the virtual incidence angle correction. The eighth revolution refers to the first turbine revolution that has reached convergence.

4.6.3 Dependence of Maximum Power Coefficient on Toe Angle

Figure 4.24 shows the dependence of the maximum power coefficient on toe angle from two-bladed experimental data, the FVM with the angle of incidence correction, and the FVM with the angle of incidence correction and one-wall blockage. Four-bladed results are also included for reference. The results from the FVM with the angle of incidence correction demonstrate that this case follows the same trend as the four-bladed data. The agreement with two-bladed experimental data is very good. Addition of the one-wall blockage effect to the FVM with the virtual angle of incidence correction yielded good agreement with experiment for $\theta_t = 0^\circ$, but the power coefficients were overestimated for $\theta_t = +5^\circ$.

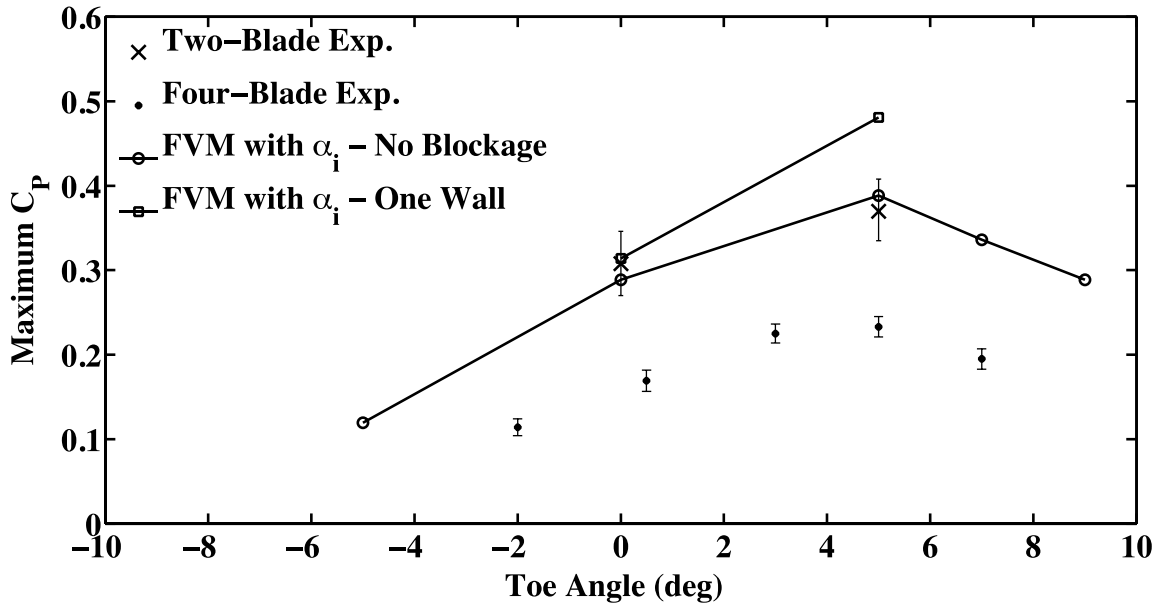


Figure 4.24 – The maximum power coefficient as a function of toe angle is shown for two-bladed experimental data, FVM with virtual incidence angle correction and no blockage effect, and FVM with virtual incidence angle correction and one wall blockage effect. Two-bladed experiment and modeling was performed at a solidity of $\sigma = 0.147$ and inflow velocity of 0.6 m/s. Four-bladed data is included for reference. Uncertainties are included in the two-bladed and four-bladed experimental data.

4.7 Conclusions

Four-bladed testing was performed for six different blade profiles using at least two toe angles for each blade under a range of flow conditions. Nine tip speed ratios were tested at inflow velocities of $U_\infty = 1.00$ m/s and $U_\infty = 1.22$ m/s. Power coefficient results were presented as a function of tip speed ratio for each set of test parameters. For all blade profiles and flow conditions which were tested at $\theta_t = +3^\circ$, $\theta_t = -2^\circ$, and $\theta_t = -7^\circ$, a toe angle of $\theta_t = +3^\circ$ resulted in the highest power coefficients. Peak power coefficients were generally lower for cambered profiles than for symmetrical profiles for the range of toe angles and flow conditions considered. In particular, results were compared for two profiles with identical thickness profiles, the NACA 0018 and NACA 4418 profiles, the

latter having added camber. The cambered profile exhibited a lower peak power coefficient ($C_P = 0.180$ at $\theta_t = +3^\circ$) than the symmetric profile ($C_P = 0.213$ at $\theta_t = +3^\circ$).

The NACA 63₃-018 blade profile was the best performing foil, and was tested at an additional range of toe angles, including $\theta_t = -2^\circ$, $\theta_t = +0.5^\circ$, $\theta_t = +3^\circ$, $\theta_t = +5^\circ$, and $\theta_t = +7^\circ$ for the four-bladed case. Results showed that the peak power coefficient occurred at $\theta_t = +5^\circ$, and that there was a decrease in efficiency as the toe angle was increased above that value. The maximum power coefficient for $\theta_t = +3^\circ$ was very close to the maximum power coefficient from the $\theta_t = +5^\circ$ testing, which implies that the ideal angle for this foil may be at an angle between the two values.

All foils were not tested at higher toe angles for several reasons. Migliore and Wolfe (1980) suggest that the effects of flow curvature are mainly a function of the curvature index, c/R , and that the detrimental effects of flow curvature can be alleviated by modifying the blade toe angle and camber. This means that for symmetric blades of a similar c/R , under similar flow conditions, the ideal toe angle should be very close to the ideal toe angle found for the NACA 63₃-018 profile. The ideal toe angle for the NACA 63₃-018 profile will serve as the starting point for future testing of symmetric blades with a similar curvature index. Cambered foils were not retested because the power coefficients were low compared to the symmetrical foils. Compared to the NACA 0018 profile, the NACA 4418 profile experienced a decrease in performance in the region that the NACA 0018 achieved the best performance. While it cannot be assumed that the cambered foils will not achieve better performance at higher toe angles, initial evidence suggested that the focus of testing should be on symmetric foils.

Overall, it is evident that at this scale, the effect of toe angle is significant. It must also be expected that the optimum toe angle could be susceptible to scale effects, specifically changes in curvature index. Full-scale devices will most likely have a lower curvature index, which means the effects of flow curvature will be less significant. These changes in scale will most likely result in a different optimum toe angle.

Two-bladed testing was completed in order to validate the FVM developed for related work by Urbina (2011a). Model testing results were taken for a lower inflow velocity than the four-bladed tests, $U_\infty = 0.60$ m/s, in order to reduce forces and turbine angular velocity fluctuations. Data was taken at $\theta_t = 0^\circ$ and $\theta_t = +5^\circ$, and power coefficient and nondimensional torque results were compared with the FVM. The infinite fluid boundary condition, one-walled boundary condition, and two-walled boundary condition were the best options available for modeling flow conditions with blockage effects. The addition of increased blockage effects in the model, such as in the two-walled case, resulted in higher power coefficients that shifted the peak to a higher tip speed ratio, as expected. The one-walled boundary condition was the most accurate representation of the tow tank, and was used for comparisons with the two-bladed experimental data.

The nondimensional torque results from the FVM, FVM with angle of incidence correction, and experiment were compared at two tip speed ratios. The FVM results compared well with experiment at $\lambda = 1.80$, but were not as accurate at $\lambda = 2.40$. The FVM results with angle of incidence correction did not compare as well at $\lambda = 1.80$, but compared better at $\lambda = 2.40$. Flow curvature effects are more significant at high tip speed ratios, which explains this phenomenon. It was also clear that inertial effects in the experimental data were important because once they were corrected in the experimental

nondimensional torque data the comparison was improved significantly. The inertial effects result in oscillations in the turbine rotor angular velocity and contributed to the higher torque peaks.

The area of greatest model development need is seen in the results of toe angle adjustments. The results of the FVM did not agree with experimental trends for nonzero toe angles, but the addition of the virtual angle of incidence correction to the FVM improved the model trends. Four-bladed NACA 63₃-018 experimental data showed a maximum power coefficient at $\theta_t = +5^\circ$. Two-bladed NACA 63₃-018 experimental tests were only performed at $\theta_t = 0^\circ$ and $\theta_t = +5^\circ$, with $\theta_t = +5^\circ$ yielding the highest maximum power coefficient. Modeling of the two-bladed case without the virtual angle of incidence correction gave the highest maximum power coefficients between toe angles $\theta_t = -2^\circ$ and $\theta_t = +2^\circ$, with the values at $\theta_t = -2^\circ$, $\theta_t = 0^\circ$ and $\theta_t = +2^\circ$ having similar magnitudes. For a toe angle of $\theta_t = +5^\circ$, the maximum power coefficient from the model was much lower and disagreed with the experimental data significantly. Model results with the virtual angle of incidence correction and no blockage were performed at $\theta_t = -5^\circ$, $\theta_t = 0^\circ$, $\theta_t = +5^\circ$, $\theta_t = +7^\circ$, and $\theta_t = +9^\circ$. The results showed substantial improvement in the dependence of maximum power coefficient on toe angle over the uncorrected data. The maximum power coefficient occurred at $\theta_t = +5^\circ$, which is consistent with four-bladed and two-bladed data. Model results with the virtual angle of incidence correction and the one-walled boundary condition were performed at $\theta_t = 0^\circ$ and $\theta_t = +5^\circ$. The results compared well with experimental data at $\theta_t = 0^\circ$, but the power coefficients were over

predicted at $\theta_t = +5^\circ$. Overall, the virtual incidence angle correction improved the comparison of power coefficient results with the experimental data.

Specific experimental limitations to this work suggest future directions for additional testing. However, the current data very clearly demonstrates limitations in the current model that can be addressed. Because of the cost and complexity of experimental testing, the data is necessarily sparse, with optimization of the design performed using a validated model.

4.8 Recommendations

Future testing should include four-blade tests. Testing of the current profiles at larger positive toe angles should be performed to ensure the toe angle data is sufficient for model validation. For cambered profiles this is needed since the toe angle with maximum power coefficient may not have been found for the cambered foils. Little comparative experimental data for the effects of toe angle on the performance of cambered blades exists. Two-bladed testing should continue for the NACA 63₃-018 profile at an extended toe angle range, up to $\theta_t = +7^\circ$, which is used in the four-bladed testing. This will support model validation and can provide important insight into the physics of flow curvature. Based on experimental testing, the FVM can be improved, with the effect of angle of incidence and camber as a priority.

4.8.1 Experimental Recommendations

Four-bladed and two-bladed testing will continue with emphasis on model validation and identifying the toe angle with the highest maximum efficiency for critical blade profiles.

Four-bladed testing for the NACA 63₃-018 profile has been completed at $\theta_t = -2^\circ$, $\theta_t =$

+0.5°, $\theta_t = +3^\circ$, $\theta_t = +5^\circ$, $\theta_t = +7^\circ$, with the maximum power coefficient occurring at $\theta_t = +5^\circ$. Two-bladed testing for the same profile has been completed at $\theta_t = 0^\circ$, and $\theta_t = +5^\circ$, with a higher power coefficient at $\theta_t = +5^\circ$. The four-bladed testing should be extended to more toe angles, including: $\theta_t = -2^\circ$, $\theta_t = +0.5^\circ$, $\theta_t = +3^\circ$, $\theta_t = +4^\circ$, $\theta_t = +5^\circ$, $\theta_t = +6^\circ$ and $\theta_t = +7^\circ$. The two-bladed testing should be extended to more toe angles, including: $\theta_t = 0^\circ$, $\theta_t = +3^\circ$, $\theta_t = +4^\circ$, $\theta_t = +5^\circ$, $\theta_t = +6^\circ$ and $\theta_t = +7^\circ$. By identifying the toe angle that provides the highest maximum power coefficient for two-bladed and four-bladed testing, conclusions can be drawn about the effects of flow curvature on the performance of cross-flow tidal turbines. This is especially important for the NACA 63₃-018 and NACA 4418 blade profiles. Two-bladed results using the NACA 4418 foil can also be used to validate the model for cambered foils.

4.8.2 Modeling Recommendations

The FVM did not accurately characterize the effects of varying the toe angle. To more accurately model the cross-flow turbine, the FVM should include the effects of flow curvature. For the curvature index used in turbine testing, the effects of flow curvature significantly affect the turbine performance (Migliore and Wolfe, 1980). Model results show that the addition of virtual incidence angle correction to the angle of attack calculation results in improved trends, specifically with respect to the toe angle. Addition of the virtual incidence angle resulted in the correct power coefficient dependence on toe angle, though the calculated power coefficient results are higher than experimental results. Without the effects of virtual camber, error in the lift and drag coefficients results in calculated blade forces that are less accurate. Addition of the virtual camber term will

result in improved lift and drag coefficients, which could reduce the forces and result in more accurate power coefficients.

The virtual incidence correction for the FVM uses conformal mapping transformations from Migliore and Wolfe (1980). The transformations are based on the velocities at different positions along the blade chord length. The transformations are based on the inflow velocity and blade tangential velocity, but do not account for induced velocities at the blades. Including the induced velocities in the transformations could improve the virtual incidence angle and camber calculations, specifically for blades on the downstream side of the turbine. At the downstream side of the turbine induced velocities are generally greatest in magnitude.

After addition of the flow curvature effects is completed, the FVM can be further validated with the tow tank results. A validated model can also be run for full-scale cases. The emphasis of the full-scale cases should be on finding the toe angle that gives the maximum power coefficient for a given blade profile, as well as comparing against any available full-scale test data.

Modeling of the virtual camber effects opens the door for modeling of blade geometries with camber. Once the virtual camber effects are modeled accurately, these methods can be easily extended to the application of camber to the model. A common blade geometry matches the blade camber to the radius of the turbine (Shiono et al., 2000). This is another geometry that should be modeled at the full-scale and experimental scale, which will be possible once the effects of virtual camber and cambered profiles are adequately modeled.

4.8.3 Summary

The experimental program in this thesis has demonstrated three important factors that must be considered in turbine modeling and validation testing for cross-flow turbines. First, the blockage effects must be considered in modeling of tow tank testing at this scale. This effect is not only significant in testing but may also have implications for applications of tidal turbines in narrow channels, as well as tidal turbines in closely spaced arrays. Secondly, the experimental effect of inertia on the turbine torque is significant. Again this may be important for turbine design since the torque fluctuations can be a major factor in durability of rotating machinery. Finally, and perhaps most significantly, the flow curvature effects influence the optimal toe angle of the blades and may be an important factor in the use of cambered foils.

The experiments have shown that the current model is insufficient for optimization of turbine design. Flow curvature needs to be added to the modeling and the results validated so that a large-scale experimental effort is not required to select foil shape and optimize the toe angle. However, even after validation of the code, a more restricted experimental optimization exercise is important in order to address these important parameters in the design of the tidal turbines.

REFERENCES

- Abbott, I. H., and von Doenhoff, A. E., 1959, "Theory of Wing Sections, Including a Summary of Airfoil Data," Dover Publications, New York, NY.
- Bahaj, A. S., Molland, A. F., Chaplin, J. R., Batten, W. M. J., 2006, "Power and Thrust Measurements of Marine Current Turbines Under Various Hydrodynamic Flow Conditions in a Cavitation Tunnel and a Towing Tank," *Renewable Energy*, Vol. 32, pp. 407-426.
- Bertin, J. J., and Smith, M. L., 1979, *Aerodynamics for Engineers*, Prentice-Hall, Englewood Cliffs, NJ.
- Charlier, R. H., 1982, "Tidal Energy," Van Nostrand Reinhold Company, New York, NY.
- Custudio, D., 2007, "The Effect of Humpback Whale-like Leading Edge Protuberances on Hydrofoil Performance," Master's Thesis, Worcester Polytechnic Institute, Worcester, MA.
- Hau, E., 2006, "Wind Turbines: Fundamentals, Technologies, Application, Economics," Springer, Berlin.
- Holman, J. P., 2001, "Experimental Methods for Engineers," McGraw-Hill, New York, NY.
- Li, Y., 2008, "Development of a Procedure for Predicting Power Generated from a Tidal Current Turbine Farm," Ph.D Thesis, University of British Columbia, Vancouver, B.C.
- Li, Y., and Calisal, S. M., 2010, "Three-dimensional Effects and Arm Effects on Modeling a Vertical Axis Tidal Current Turbine," *Renewable Energy*, Vol. 35, pp. 2325-2334.
- Lokocz, T., 2010, "Solid Mechanics of Cross Flow Tidal Turbine Blades," University of Maine.
- http://www.umaine.edu/mecheng/Peterson/Classes/Design/2009_10/Projects/TidalEnergy-TomLokocz/reports.html (accessed 3/16/2012).
- Lokocz, T., 2012, Personal communication.
- Losada, R.A., 2003, "Practical FIR Filter Design in MATLAB, Revision 1.0," The Mathworks, Inc., Natick, MA.
- McAdam, R. A., Houlby, G. T., Oldfield, M. L. G., and McCulloch, M. D., 2009, "Experimental Testing of the Transverse Horizontal Axis Water Turbine," *Proceedings, 8th European Wave and Tidal Energy Conference*, Uppsala, Sweden, pp. 360-365.

Migliore, P. G., and Wolfe, W. P., 1980, "The Effects of Flow Curvature on the Aerodynamics of Darrieus Wind Turbines," W.V.U. A.E. Report No. TR-60, West Virginia University, Morgantown, WV.

Paraschivoiu, I., 2002, "Wind Turbine Design with Emphasis on Darrieus Concept," Polytechnic International Press, Montreal.

Polagye, B., Van Cleve, B., Copping, A., Kirkendall, K., 2010, "Environmental Effects of Tidal Energy Development: Proceedings of a Scientific Workshop," U.S. Dept. Commerce, NOAA Tech. Memo. F/SPO-116, 181 p.

Rae, W. H., and Pope, A., 1984, "Low-Speed Wind Tunnel Testing," John Wiley & Sons, New York, NY.

Sheldahl, R. E., and Klimas, P.C., 1981, "Aerodynamic Characteristics of Seven Symmetrical Airfoil Sections Through 180-Degree Angle of Attack for Use in Aerodynamic Analysis of Vertical Axis Wind Turbines," Technical Report SAND80-2114, Sandia National Laboratories, Albuquerque, NM.

Shiono, M., Suzuki, K., and Kiho, S., 2000, "An Experimental Study of the Characteristics of a Darrieus Turbine for Tidal Power Generation," Electrical Engineering in Japan. Vol. 132, No. 3, pp. 38-47.

Somers, D. M., 1997, "Design and Experimental Results for the S809 Airfoil," Technical Report NREL/SR-440-6918, National Renewable Energy Laboratory, Golden, CO.

Strickland, J. H., Webster, B. T., and Nguyen, T., 1980, "A Vortex Model of the Darrieus Turbine: an Analytical and Experimental Study," Technical Report SAND79-7058, Sandia National Laboratories, Albuquerque, NM.

Urbina, R., Peterson, M.L., Kimball, R.W., DeBree, G.S., and Cameron, M.P., 2011a, "Modeling and Validation of a Cross Flow Turbine Using Free Vortex Model and a Modified Dynamic Stall Model," Submitted to: Renewable Energy.

Urbina, R., 2011b, Personal communication.

Whelan, J. I., Graham, M.R., Peiro, J., 2009, Journal of Fluid Mechanics, Vol. 624, pp. 281-291.

APPENDICES

APPENDIX A:

TEST METHODS, DATA ANALYSIS AND FILTERING

Test Methods Summary

For the purposes of this research, the primary desired quantity is C_P , the power coefficient. This section describes in detail the series of tests required for the calibration process, the testing process, and the data analysis process used to reduce the results.

In order to get quality data, it was first necessary to determine the degree of accuracy needed for each measured quantity. From eqn. 1.4, it is evident that the most important measured quantity in terms of accuracy of C_P is U_∞ , the inflow velocity, because it is cubed. Any error in inflow velocity results in an amplified error in the C_P calculation. C_P is a linear function of the torque, T , and turbine angular velocity, ω . The accuracy of both of these quantities is important, but not as critical as the accuracy of the inflow velocity. The turbine cross sectional area, A_f , can be measured with known accuracy according to the instruments used.

Calibration Procedure

After identifying the degree of accuracy required for each measured quantity, it was necessary to calibrate the measurement devices. The first calibration performed was for the inflow velocity. Two tests were necessary, and both are described in detail in the following section. The first test was designed to accurately measure the distance traveled by the carriage using an encoder wheel. The second test compared velocity calculation results from the carriage encoder wheel with data calculated using a known distance traveled and a stopwatch (thus a known average velocity).

The second quantity calibrated was the turbine torque. There were three different types of tests that were performed. First, a series of known torques were applied to the turbine. This series of tests gave the voltage output from the system as a function of applied external torque. The second type of test that was needed to accurately quantify the torque data was a friction tear, or the torque output of the system as a function of turbine angular velocity. This type of test included the effect of end plate drag, which was measured by running the turbine in the tow tank without blades. The third type of test, a “slow run” test, was needed because of the preload on the torque load cell. Before consequent turbine tests were performed, a “slow run” test was run to track the offset, or load cell output with no external loads.

Testing Procedure

The testing procedure for a cross-flow tidal turbine test run is outlined. Preliminary results are discussed, as well as the next steps taken in the testing process. It includes detailed explanations of the calculation process for torque and velocities.

Data Analysis and Filtering

This section outlines the process used to reduce calibration data and test data. The calculation process for bin-averaged non-dimensional torque data is also outlined. Sample C_P and bin-averaged non-dimensional torque results are displayed.

In addition to the calibration process, it was also necessary to examine the frequency response of the system for the proper application of low-pass filters. Tests were run to obtain the natural frequencies in the torque load cell data, which determined the proper cut-off frequency for the low-pass filter. Inflow velocity and turbine angular velocity were examined to determine the frequency range that needed to be retained, and the frequency range that could be filtered out. C_P results were also compared using several different low-pass filter cut-off frequencies on the torque to determine the sensitivity of the results to changes in the cut-off frequency. This included comparison between C_P results for filtered torque data with a very low cut-off frequency, filtered data with a moderate cut-off frequency, and filtered data with a very high cut-off frequency relative to the dominant mechanical frequencies encountered during testing.

A repeatability study was also performed to examine the precision of experiments. Five tests were run at several tip speed ratios throughout the typical range of tip speed ratios, and the variability of C_P results was examined.

Calibration Process

This section outlines the calibration process for the inflow velocity and torque load cell output. This includes calibration of the distance traveled by the turbine, which is necessary for inflow velocity calculations, a calibration of the output of torque load cell as a function of applied load, calibration of the torque output as a function of turbine angular velocity, and quantification of the torque load cell offset prior to running a test.

Determination of Carriage Wheel Encoder Radius

The inflow velocity, or carriage velocity, U_∞ , is calculated using Equation A.1,

$$U_\infty = r\omega_\infty, \quad (\text{A.1})$$

where r is the carriage encoder wheel radius, and ω_∞ is the angular velocity of the carriage encoder wheel. Figure A.1 shows the configuration of the carriage encoder. The resulting inflow velocity is the tangential velocity of the surface of the carriage encoder wheel. The inflow velocity is therefore heavily dependent on the radius of the carriage encoder wheel, and any error in the measurement of this radius results in significant inflow velocity error. To account for this, the carriage was moved a known large distance (approximately 12 m) and the total angular displacement of the carriage encoder was recorded. The carriage encoder wheel radius was calculated using eqn. A.2,

$$d = r\Delta\theta, \quad (\text{A.2})$$

where d is the total distance traveled by the carriage, and $\Delta\theta$ is the total angular displacement of the carriage encoder wheel.

By calculating the radius over a long distance, instead of measuring the wheel diameter directly, a more accurate value was obtained. Additionally, the wheel was made out of rubber, so any direct measurement (such as with a caliper) would be subject to deformation in the rubber, and therefore would not be valid. The error inherent in measuring the total distance was accounted for in the uncertainty analysis, which is presented in Appendix B.

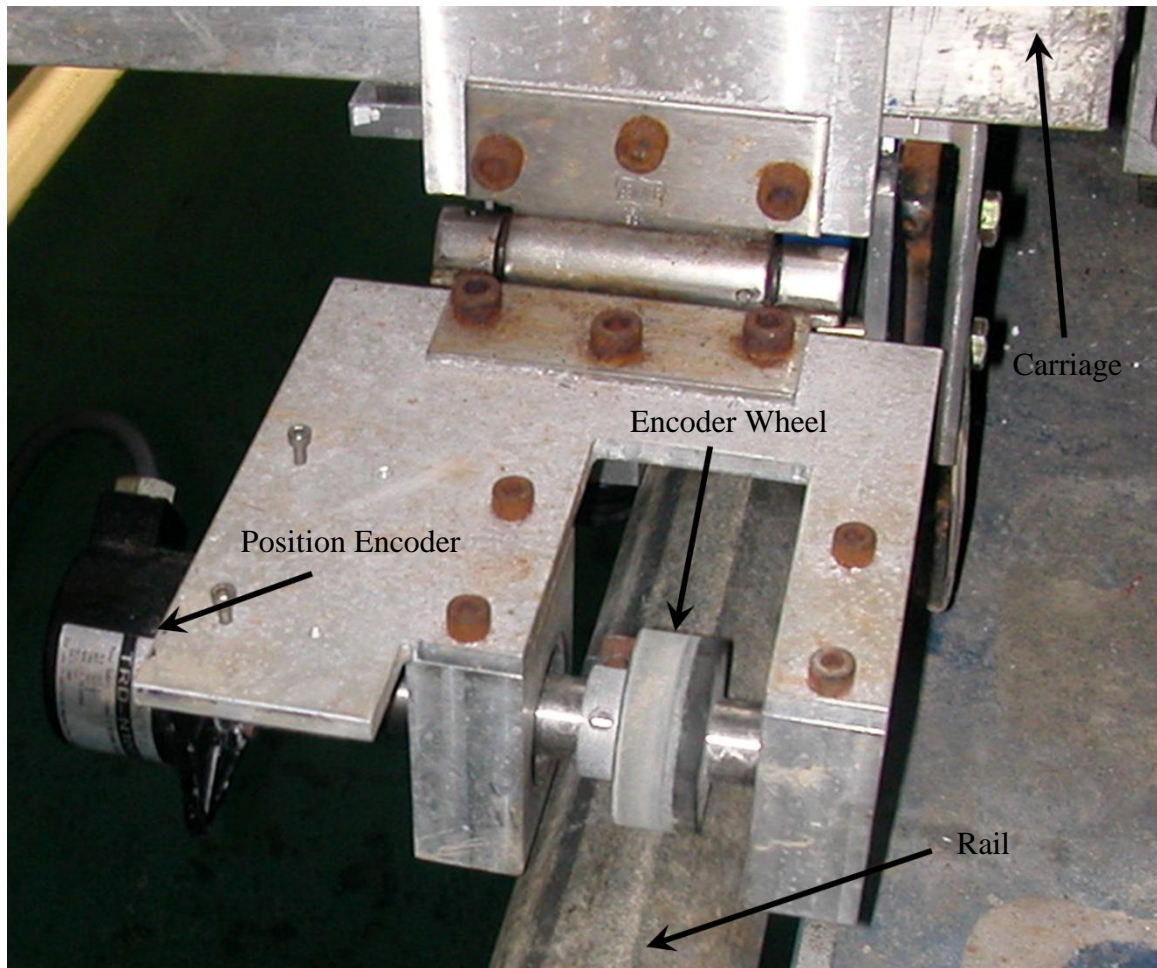


Figure A.1 – The carriage velocity encoder wheel assembly is shown riding on the tow tank rail.

Verification of Inflow Velocity Calculation

Tests were run that recorded the carriage speed using the data acquisition system as well as manual distance and time measurements using a tape measure and a stopwatch. The carriage velocity was set to 1 m/s, and the average velocity calculated from the acquired data was compared to manual measurements. The process was repeated for a range of speeds from ~0.45 to ~1.3 m/s. The calculations were compared, and showed good agreement with a maximum percent error of less than 3%. All but two values were within 1.5%. Results are shown in Table A.1. The discrepancy between the two methods can be explained mainly by the presence of human reaction time in the hand timed measurements, which are for reference only, and cannot be used to fully quantify the uncertainty in velocity measurements. Presumably, the time base from the real-time data acquisition system is nearly perfect because extraneous computer processes do not interrupt the real-time controller. Additionally, the tests were fairly short (5 m) because of space restrictions. Longer tests would reduce the error in the time-base of the manual measurements, which would improve the agreement of the two calculation methods. For this reason the error in velocity calculation that was accounted for in the uncertainty

propagation calculations was an estimate of the error in the carriage position measurement.

Distance – ft (m)	Manual Time (s)	Manual Speed - ft/s (m/s)	Measured Speed - ft/s (m/s)	% difference
16 (4.8768)	10.84	1.4760 (0.4499)	1.4652 (0.4466)	0.735
16 (4.8768)	9.02	1.7738 (0.5407)	1.7789 (0.5422)	0.285
16 (4.8768)	7.62	2.0997 (0.6400)	2.0882 (0.6365)	0.552
16 (4.8768)	6.68	2.3952 (0.7301)	2.3925 (0.7292)	0.115
16 (4.8768)	5.93	2.6982 (0.8224)	2.6960 (0.8218)	0.0780
16 (4.8768)	5.25	3.0476 (0.9289)	3.0037 (0.9155)	1.46
16 (4.8768)	4.83	3.3126 (1.0097)	3.3085 (1.0084)	0.124
16 (4.8768)	3.96	4.0404 (1.2315)	3.9388 (1.2006)	2.57
16 (4.8768)	3.83	4.1775 (1.2733)	4.2426 (1.2931)	1.53

Table A.1 – Manual carriage speed measurements are compared to the results obtained using the data acquisition.

Torque Load Cell Slope Calibration

Used within the correct load range, the output voltage from a load cell is a linear function of the applied force. Because of the complexity of the loading in the torque load cell of the test turbine, it was first necessary to verify that the voltage output from the load cell was a linear function of applied torque. After verification, linear regression was used to calculate the slope and offset from the acquired data points.

The goal of the tests was to simulate a known external loading on the turbine blades by applying a torque somewhere in the system. The system was designed such that an external load applied on the drive shaft or motor would be analogous to an external load applied directly on the blades (as would be the case in a turbine test). For this test, loads were applied to the motor, and the output was measured with a very slow motor rotation, which produced repeatable results. The test configuration is shown in Figure A.2.

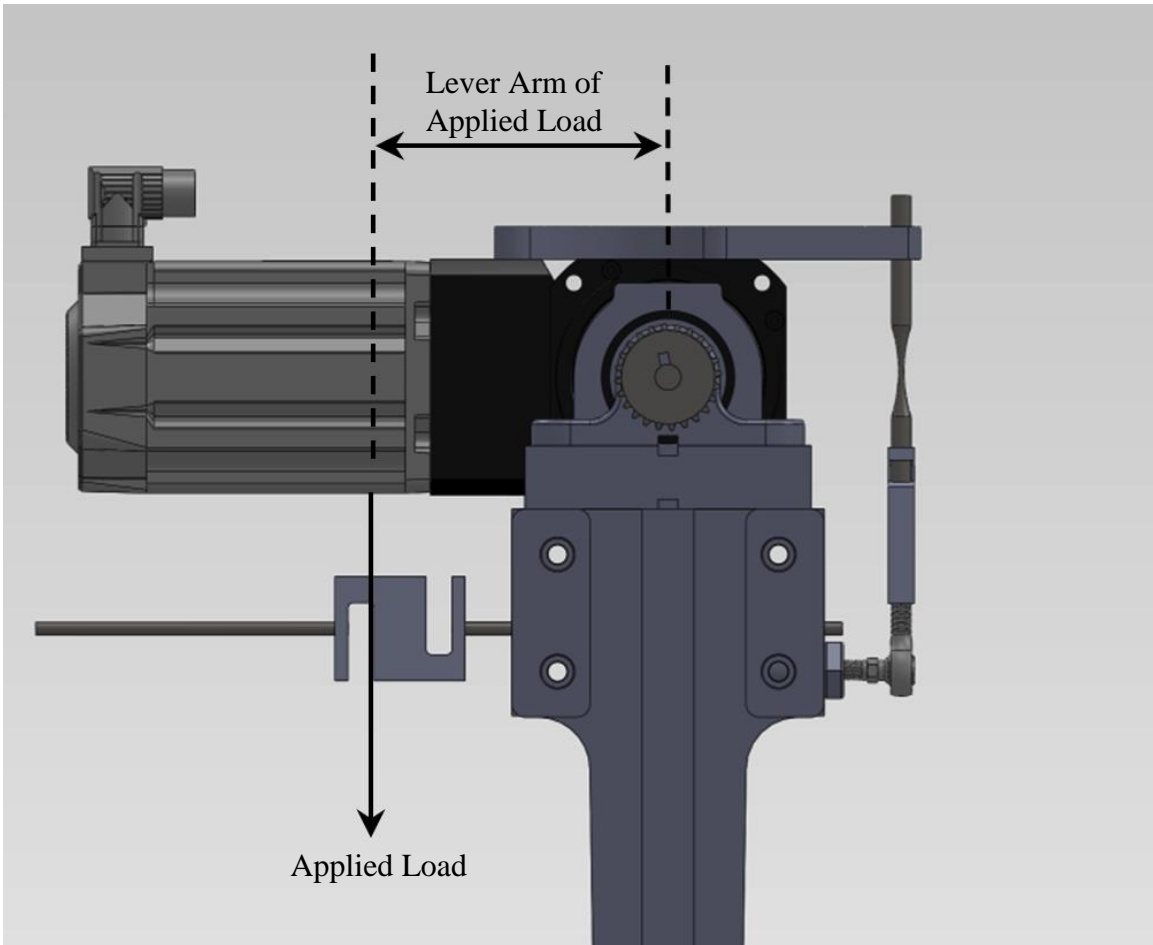


Figure A.2 – The configuration of the torque load cell is shown during the slope calibration process. The applied load F and applied load lever arm l determine the torque applied in the calibration, according to eqn. 3.1.

Specifically, tests were performed by placing weights on the motor, rotating the turbine at a rotational rate of 0.1 Hz, and calculating the average torque load cell output over a 25 second period. The process was repeated using 5 lb. weights, up to 30 lbs. According to eqn 3.1, multiplication of the applied load by the lever arm of the applied load gives the applied torque. The resulting load cell output as a function of applied torque is shown in Figure A.3. The resulting output from the system is in an unconverted binary format. For simplicity in the data acquisition process, the data was not converted to voltage from this format, because the system could be calibrated directly using the unconverted format. This was possible because unconverted binary output remained a linear function of the applied load.

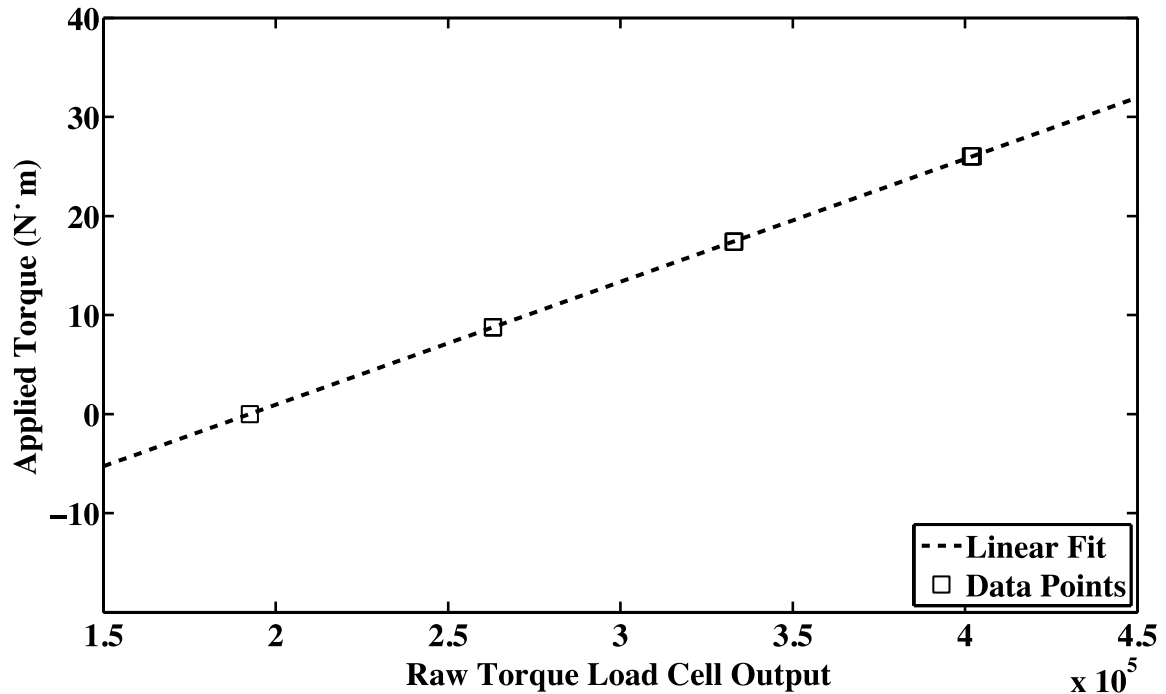


Figure A.3 - Torque load cell calibration results are shown. Raw torque load cell output refers to the unconverted binary format of the resulting data. The data was not converted to voltage because the output could be calibrated in this format. Error estimates for the linear regression line are included in Appendix B.2.

Dependence of Torque Load Cell Output on Turbine Rotational Speed

The ultimate testing goal is to assess the performance of the blades being tested, without the added effects of the test setup. The drive train friction and end plate drag in the system are highly dependent on rotational speed, and can cause a significant reduction in torque and power coefficient results at high speeds if left unaccounted for. The drive train friction is mainly friction in the bearings of the drive system. End plate drag is the viscous drag on the end plates that does not represent the performance of the blades alone. By removing the test setup effects from power coefficient results, a full-scale turbine can be designed using data from blade performance alone. Specific factors can be added in to account for drive train friction, end effects, and other elements present in the design of the actual device.

Drive train friction and end plate drag curves were obtained by testing the load cell output with the turbine rotating at various rotational speeds. First, the drive train friction as a function of rotational speed was obtained by rotating the turbine outside of the tow tank, mounted on a post, with blades installed. Tests were run for approximately 20 seconds at a constant rotational rate, and the average velocity and torque load cell output values were calculated. Tests were run from 0.1 Hz up to 2 Hz in 0.2 Hz increments, with two data points for each rotational speed. This group of tests was performed before installing the turbine in the tow tank and nearly every time the turbine was taken out of the tow tank, until it was clear that there was little variability in the friction curves. Figure A.4 shows the curves for different drive train friction tests. The curves were also created

every time the turbine was disassembled and re-assembled. The maximum difference in torque between the curves with the largest discrepancy was approximately 0.1 N·m, which has been accounted for in the uncertainty propagation calculations for C_P . The largest discrepancy was used to ensure a conservative estimate of the uncertainty in C_P . Torque uncertainty values could eventually be used that are speed dependent, which would lower the uncertainty in C_P .

The data in Figure A.4 showed that a single end plate viscous drag and drive train friction curve could be determined using one type of test, because of the small variability in the drive train friction curve. In order to accomplish this, it was necessary to run the turbine in the tow tank without blades installed. To accomplish this, a shaft and rigid couplings were machined to fit across the center of the turbine. End attachments were adapted from a previous generation of the turbine and used to attach to the inside of the end plates. The assembly is shown in Figure A.5.

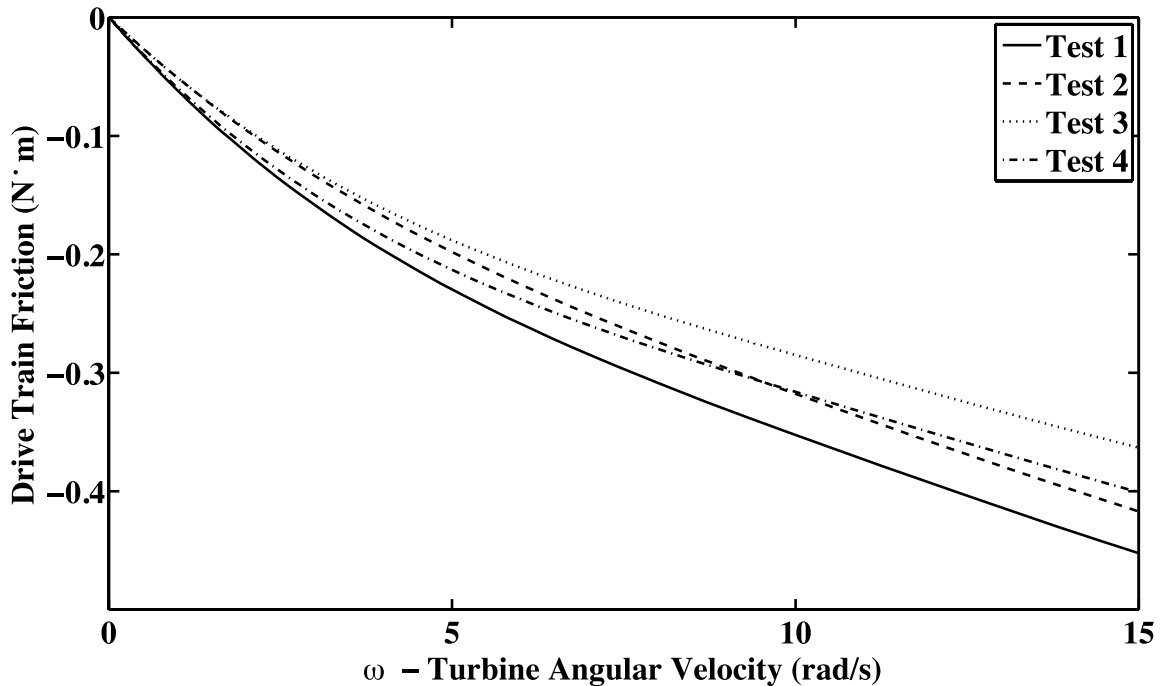


Figure A.4 - Drive train friction as a function of turbine angular velocity is shown for four separate groups of tests, which were performed before and after disassembling and assembling the drive train several times.

The shaft was installed between the end plates without blades, and then tests were run in the tow tank at a constant carriage speed of 1 m/s. Rotational rate was again varied, up to 1.6 Hz. Two tests were run for each data point. Rotational rate, inflow velocity, and torque load cell output were measured throughout the tests, and average values were calculated for the final results. Figure A.6 shows the test results of all drive train friction tests with and without end plate drag. The end plate drag and drive train friction curve in Figure A.7 is the function used in the data analysis process. The instantaneous turbine angular velocity is calculated, then the friction and end plate drag function is evaluated

for that turbine angular velocity, and the instantaneous drive train friction and end plate drag term is accounted for.



Figure A.5 – The straight bladed model Darrieus turbine rotor is shown with NACA 63₃-018 blades installed and rod across the center.

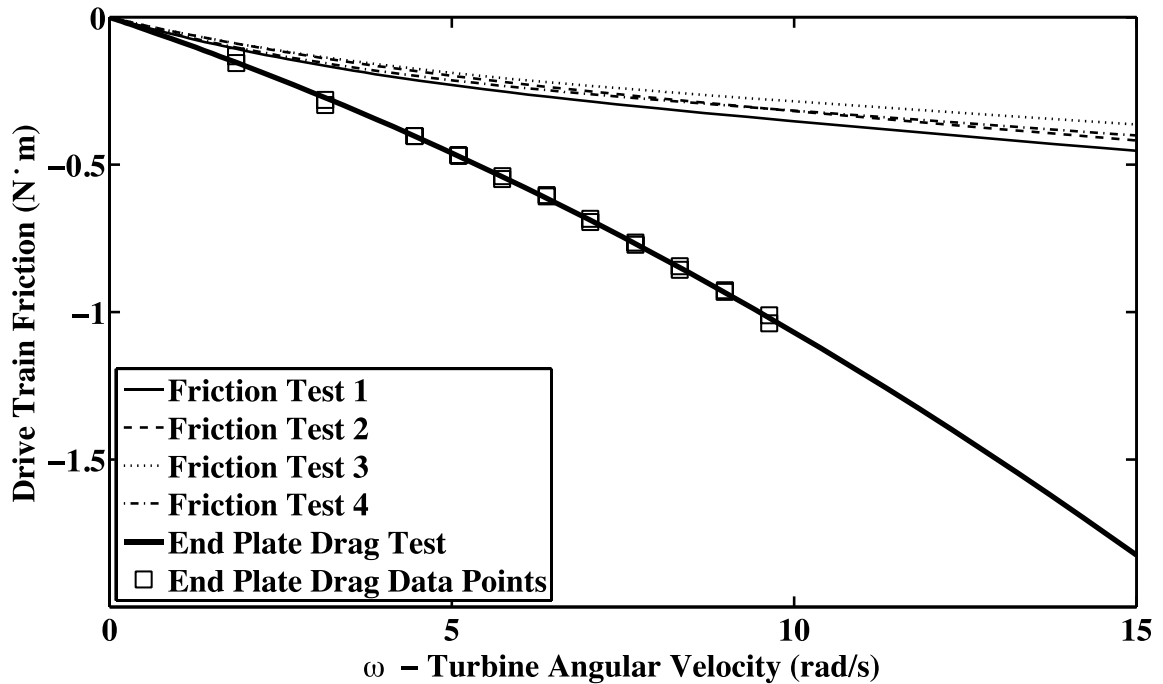


Figure A.6 - Drive train friction as a function of turbine angular velocity is shown for four separate tests. End plate drag as a function of turbine angular velocity is shown. Two data points were taken at each turbine angular velocity, and a polynomial was fit to the data.

Slow Run Tests

Every time the turbine was installed in the tow tank, the zero value of the torque load cell, or offset, changed noticeably. As a result, it was necessary to track the offset before running a test or series of tests. Static friction in the motor bearings did not allow the use of a torque load cell offset value from a stationary turbine test, because of high variability. To account for this, “slow run” tests were performed before each test was run down the tow tank. For these tests, the carriage was stationary, and the turbine was rotated at approximately 0.1 Hz for 25 seconds. This recorded two full rotations of the turbine, and the resulting average torque load cell and average turbine angular velocity were calculated. The average torque load cell values from these tests corresponded to the torque load cell output close to, but not exactly at zero turbine rotational rate. Because the turbine rotational rate was so slow, the effects of viscous drag on the blades were negligible.

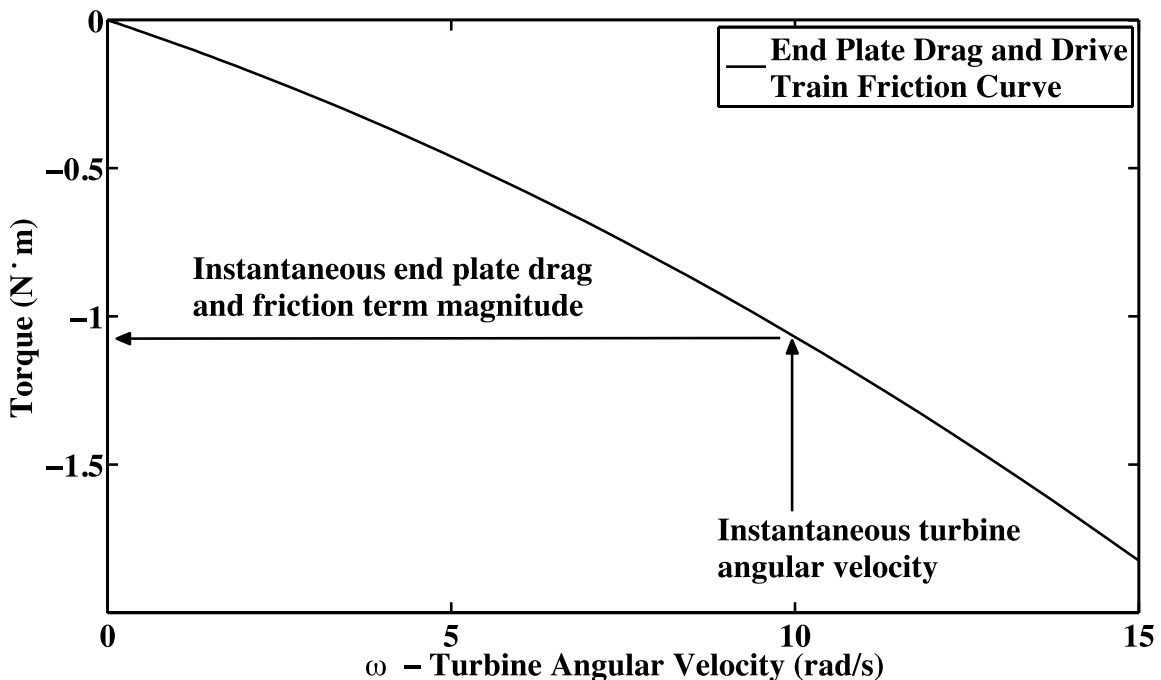


Figure A.7 – The instantaneous turbine angular velocity is entered in the end plate drag and drive train friction function, and the instantaneous torque can be calculated. This torque term represents all of the losses the system resulting from end plate drag and drive train friction.

Tidal Turbine Test Procedure

Once the system was calibrated, turbine tests were performed. Before each test, a “slow run” was performed, in order to track the offset of the subsequent turbine test. Next, the inflow velocity and tip speed ratio were chosen based on power coefficient results from past test data, current numerical modeling, and (Shiono et al., 2000). The turbine rotational rate was calculated from the inflow velocity and tip speed ratio. The test length was chosen based on the inflow velocity, because higher speeds require longer

acceleration times and distances. Typical tests were run at 1 m/s, with tip speed ratios between 0.5 and 3, and test lengths between 15 and 20 m. Once all parameters were set, the turbine test was run, with an initial acceleration period, quasi-steady operational period with data collection, and deceleration period. Tests were repeated for the same inflow velocity and various tip speed ratios, and after data analysis the resulting product is a C_P curve, shown in Figure A.8, which is a repeat of Figure 4.13. The results in Fig. A.8 are for an inflow velocity of $U_\infty = 0.6$ m/s and a toe angle of $\theta_t = 0^\circ$, with several data points taken at each tip speed ratio. In general, C_P curves were created for several inflow velocities in order to study blockage effects, surface effects, and Reynolds number effects on the lift and drag of the blades.

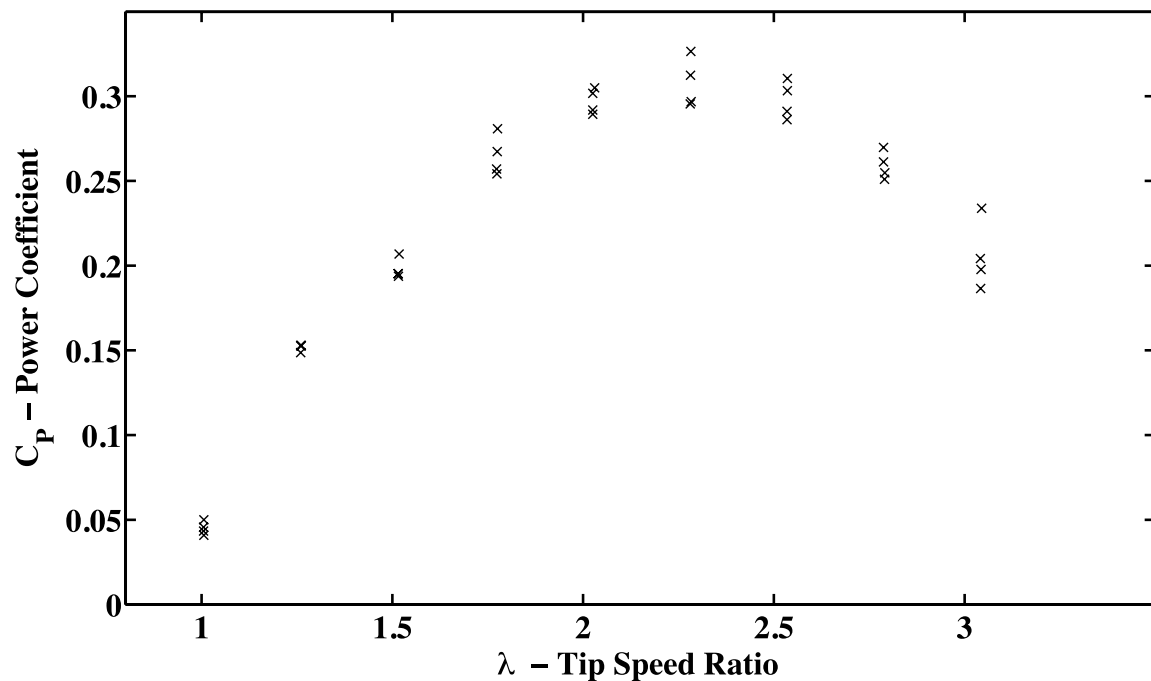


Figure A.8 – Example power coefficient results are shown for two-bladed testing taken at a solidity of $\sigma = 0.147$, inflow velocity of $U_\infty = 0.6$ m/s and toe angle of $\theta_t = 0^\circ$. Testing was performed four times at each tip speed ratio.

Data Analysis and Filtering

This section shows details of the following calculations: inflow velocity and turbine angular velocity, torque, nondimensional torque, nondimensional torque with rotor inertia, and power coefficient. The filtering process for velocity and torque calculations is also shown in detail.

Inflow Velocity and Turbine Angular Velocity Calculation Methods

For inflow velocity and turbine angular velocity calculations the type of acquired data was in angular position form. At nearly constant velocities, the angular position data resembles a sawtooth, with a discontinuity at 360° , where the encoder value switches from 360° to 0° . Filtering was required because of the errors prone in differentiating a noisy signal. Filtering signals with discontinuities creates errors near the discontinuity, so the signals were modified to remove the discontinuities. The main work in this section of

data analysis was to turn the angular position sawtooth into a single line, apply a low pass filter to the modified data, then calculate the velocity from the filtered data. Figure A.9 shows the calculation results for unfiltered and filtered turbine frequency, which is a direct function of the turbine angular velocity. The unfiltered frequency calculations are clearly unacceptable for use in calculation of C_p . Note the difference in scale between the two plots.

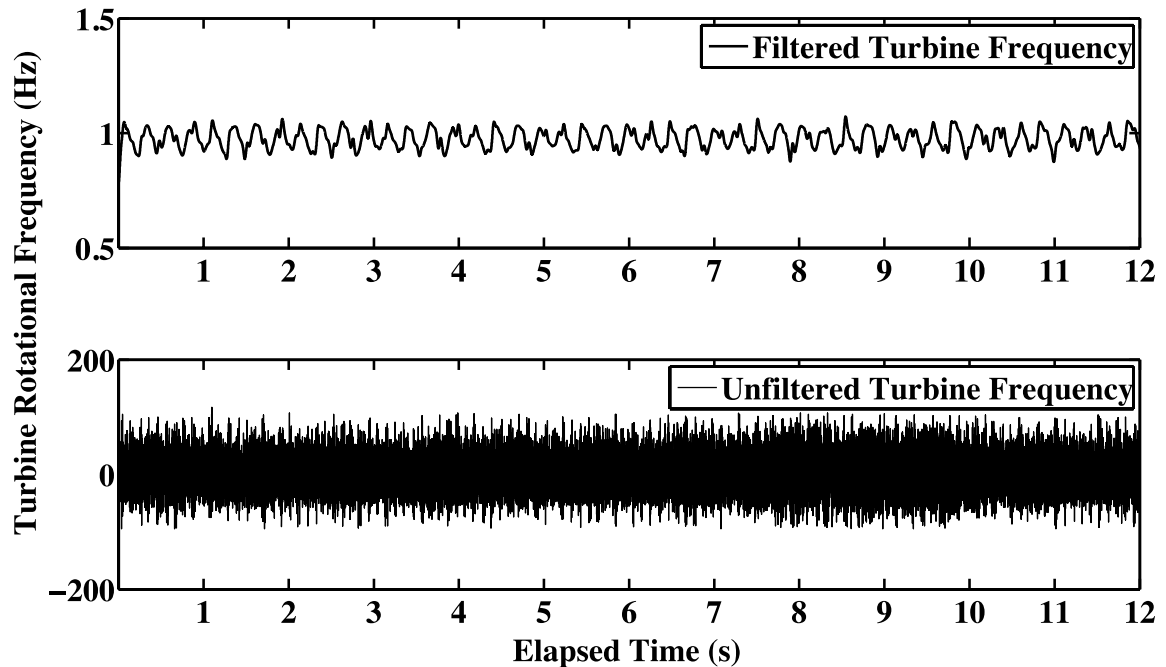


Figure A.9 - Unfiltered and filtered turbine rotational frequency (in Hz) are compared. Note the difference in the y-scale between the two graphs.

Modification of Sawtooth Signal

The angular position from the encoders was first converted to radians for convenience. The sawtooth signal was changed into a “line” by detecting peaks, and then adding 2π , 4π , 6π , and so on. The added values were stored for later use. Figure A.10 shows the original and modified signals, and Fig. A.11 compares filtered and unfiltered angular position data.

Low Pass Filter for Velocity Calculations

Built-in Matlab functions were used to create coefficients for a finite impulse response (FIR) linear-phase low pass filter with a Hamming window. The filter coefficients were applied in such a way that no phase distortion was induced in the data. The key element of the low-pass filter design was the cut-off frequency. Two separate cut-off frequencies were used for U_∞ and f , the turbine rotational frequency. The variation in speed of the carriage during test runs resulted in very low frequencies present in U_∞ , so a cut-off frequency of 4 Hz was chosen. Variations in the turbine rotational rate were slightly higher in frequency and needed to be retained, so a cut-off frequency of 8 Hz was chosen for calculation of f .

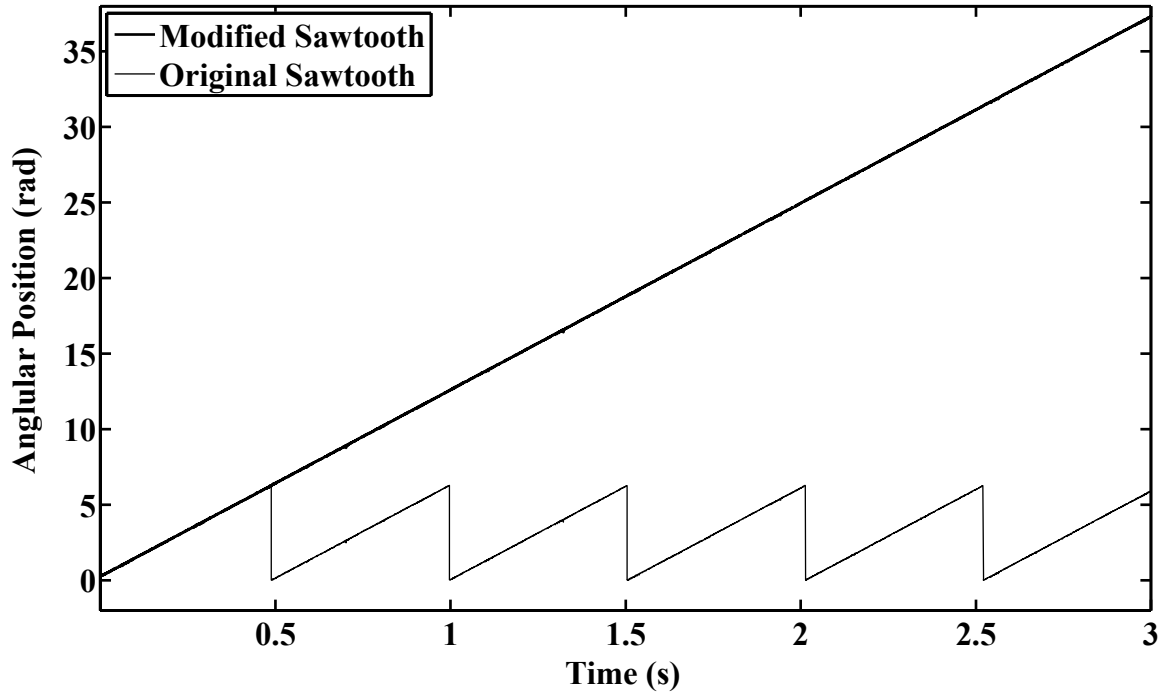


Figure A.10 – The angular position of an encoder signal is shown before and after the modifications. A signal with no discontinuities was necessary for filtering before differentiation.

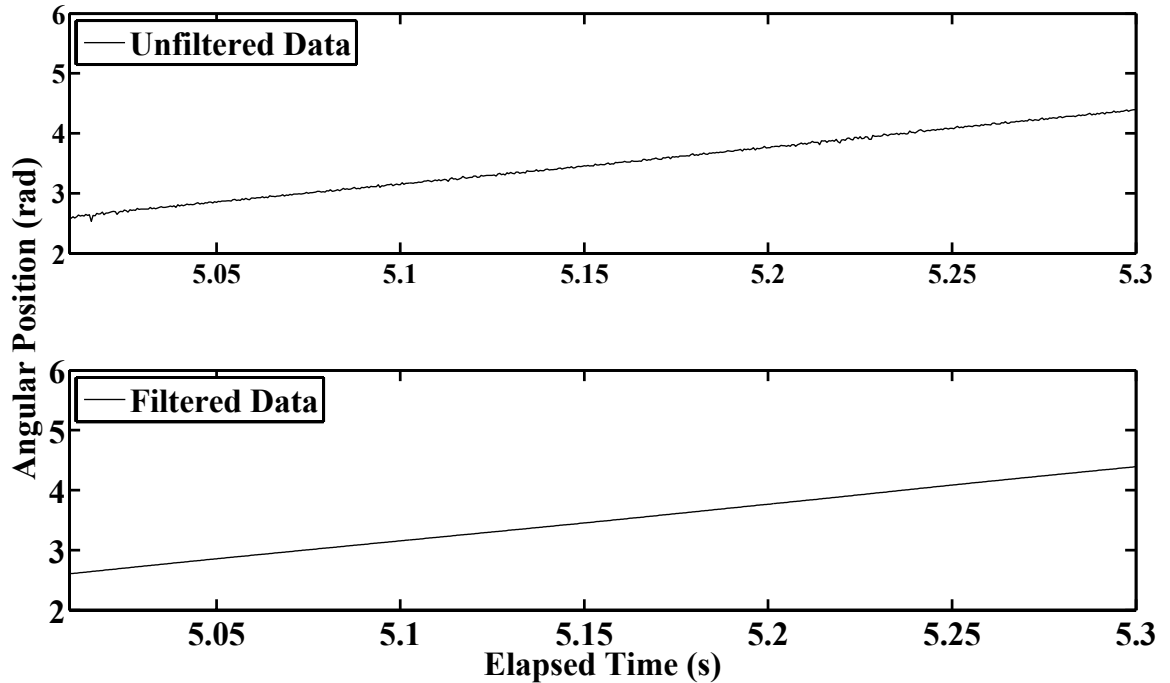


Figure A.11 - Filtered and unfiltered angular position over an elapsed time are compared. Note the chatter in the unfiltered data compared to the unfiltered data.

Turbine Angular Velocity and Inflow Velocity Calculations

Time data and filtered angular position data in radians were used to calculate the angular velocity for both encoders, ω , according to eqn. A.3,

$$\omega = \frac{\Delta\theta}{\Delta t}, \quad (\text{A.3})$$

where $\Delta\theta$ is the change in angular position of the encoder, and Δt is the change in time over the given interval, in this case the change in time between each sample, or 0.0005 seconds. The resulting angular velocity is technically an average angular velocity over a finite time interval, but in this case the time interval is very small, and for the purposes of this research the angular velocity can be considered instantaneous. The turbine angular velocity was converted from radians to Hz using eqn. A.4,

$$f = \frac{\omega}{2\pi}. \quad (\text{A.4})$$

The carriage encoder angular velocity data was converted to tangential, or inflow velocity, using eqn. A.1. Figure A.12 shows example inflow velocity results from a test. Small velocity fluctuations are present, but ultimately the inflow velocity remains close to the set velocity.

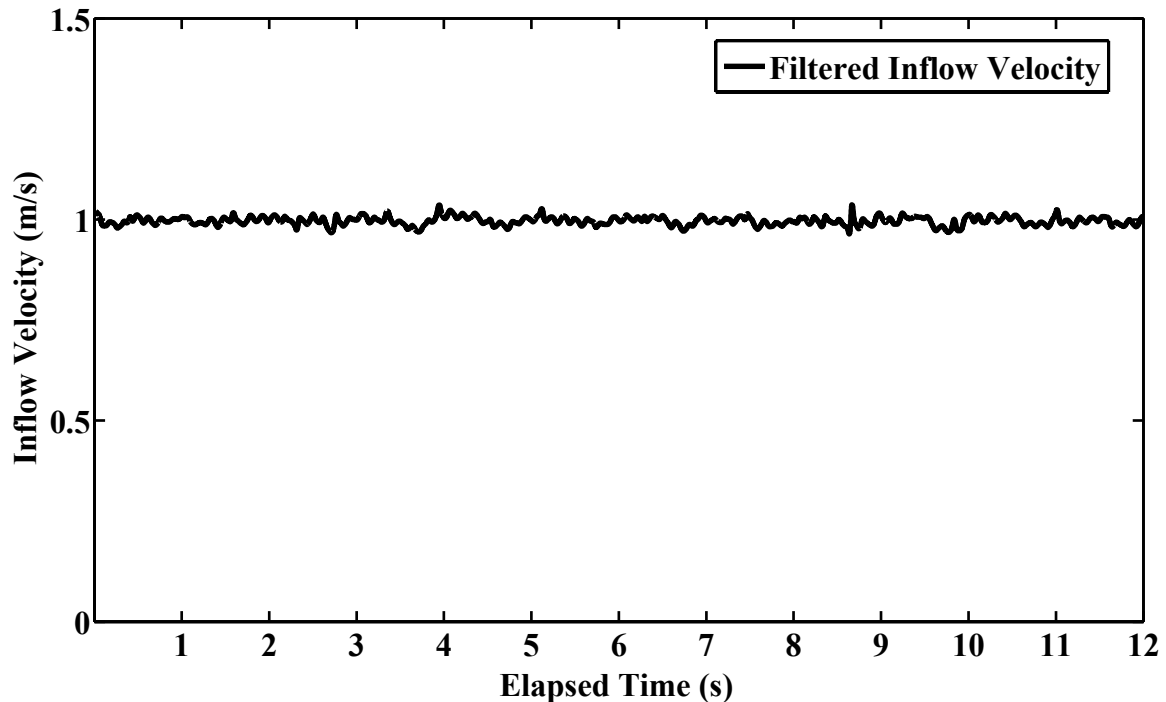


Figure A.12 - Filtered inflow velocity is shown from a four-bladed test at $\lambda = 1$ and $U_\infty = 1$ m/s. Filtering significantly improved the accuracy of the inflow velocity and turbine angular velocity calculations.

Torque Calculation

The next step was to apply the calibration procedure to torque data from an actual test run. Example results were used from four-bladed tests performed with the NACA 63₃-

018 carbon fiber blades for a toe angle of $\theta_t = +5^\circ$. The tip speed ratio was set to one, and the inflow velocity to 1 m/s.

The next step in the process was to determine the external rotor torque T_{ext} by removing the offset and the effects of drive train friction and end plate drag, according to eqn. A.5,

$$T_{ext} = m (\text{output} - \text{offset}) - T_{loss} , \quad (\text{A.5})$$

where output is the raw output from the torque load cell, m is the slope from the load cell calibration (or the slope of the line shown in Fig. A.3), the offset term is the average raw torque load cell output from the “slow run” performed immediately before the test run, and T_{loss} is the friction term containing drive train friction and end plate drag and is a function of ω , the instantaneous angular velocity of the turbine. The dependence of friction and end plate drag on angular velocity is shown in Fig. A.7. All quantities in eqn. A.5 are instantaneous. The resulting instantaneous external rotor torque load from the test run is shown in Figure A.13.

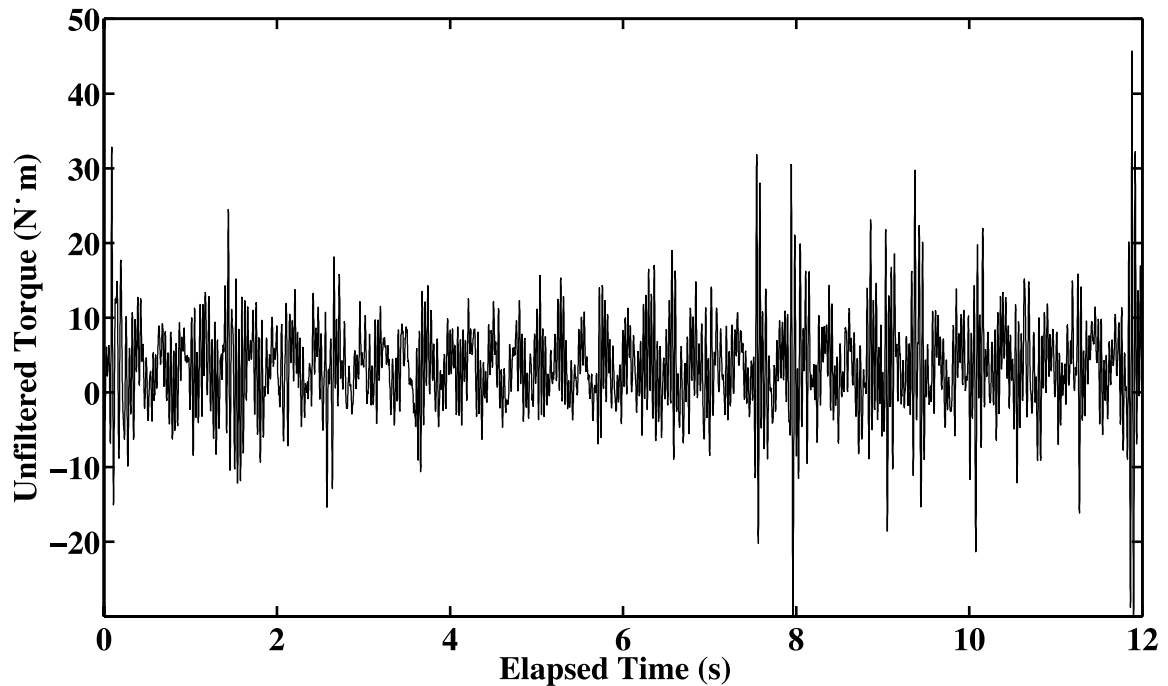


Figure A.13 – Sample unfiltered torque data from a four-bladed test is shown after application of eqn. A.5. Note the significant fluctuations in the unfiltered torque data that is a result of vibrations.

Filtering and Torque Data in the Frequency Domain

Initial torque data appeared to have a low signal to noise ratio, and the magnitude and frequency of the noise implied that it was mechanical in nature, not only electrical. A routine was created to compute the Fast Fourier Transform (FFT) of a signal in order to analyze the torque results in the frequency domain. The mean value was subtracted from the signal prior to calculating the FFT in order to preserve the low frequency signals that would be distorted by the presence of a large mean value.

Tests were run to determine the mechanical noise present in the system as a result of roughness and bumps on the carriage rails. The carriage was run at various inflow speeds with the turbine motor control turned off (the turbine was stationary). The FFT of torque from the test results at an inflow velocity of 1.0 m/s is shown in Figure A.14. These results were compared with a regular test run at 1 m/s with the turbine operating at a tip speed ratio of approximately 0.75, shown in Figure A.15. The frequency range between 18 Hz and 33 Hz contained the largest magnitude mechanical noise during both types of tests. The magnitude of the noise during regular turbine operation was slightly higher in this region than the tests run with the motor control turned off. This was expected, and can be explained by forces from the turbine blades and motor exciting the system more than the system had been excited with those forces absent. The excitation forces that need to be measured are at much lower frequencies than the mechanical noise region, so the mechanical noise can be filtered out. This analysis led to the design of a low pass filter for the torque data that minimized data loss and removed the frequencies inherent in the test setup.

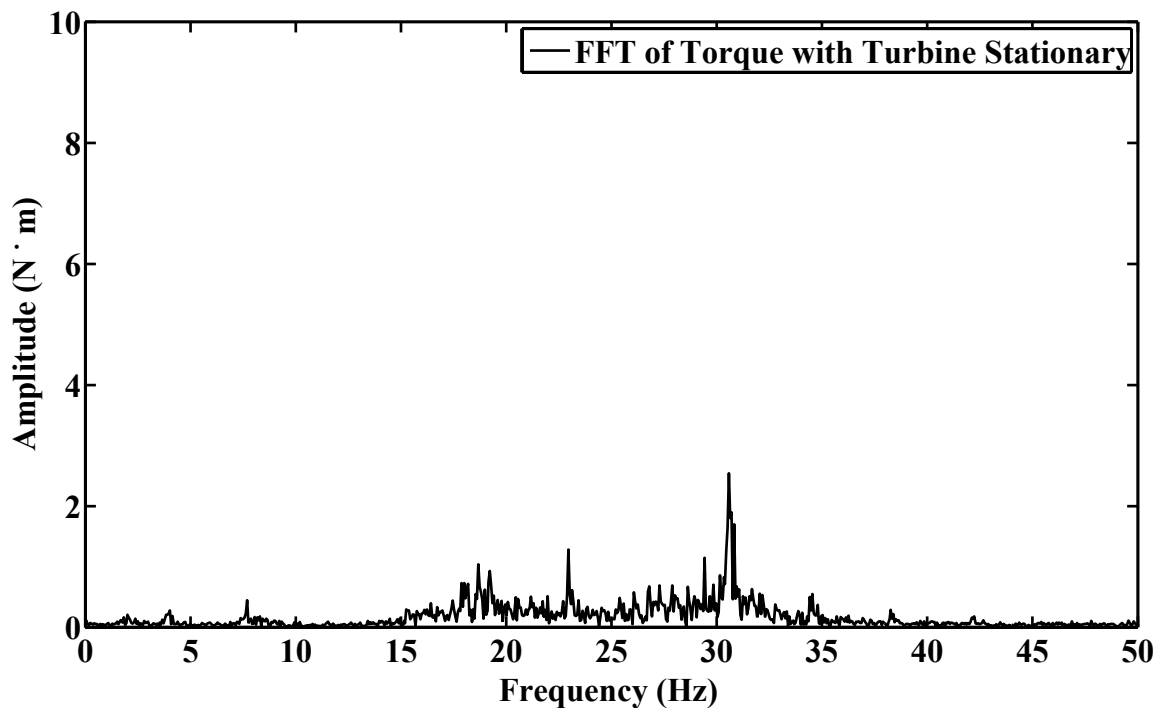


Figure A.14 – An FFT of the torque in the measurement system is shown. The test turbine was run down the tow tank with the turbine motor control turned off in order to capture structural vibrations in the absence of hydrodynamic forces.

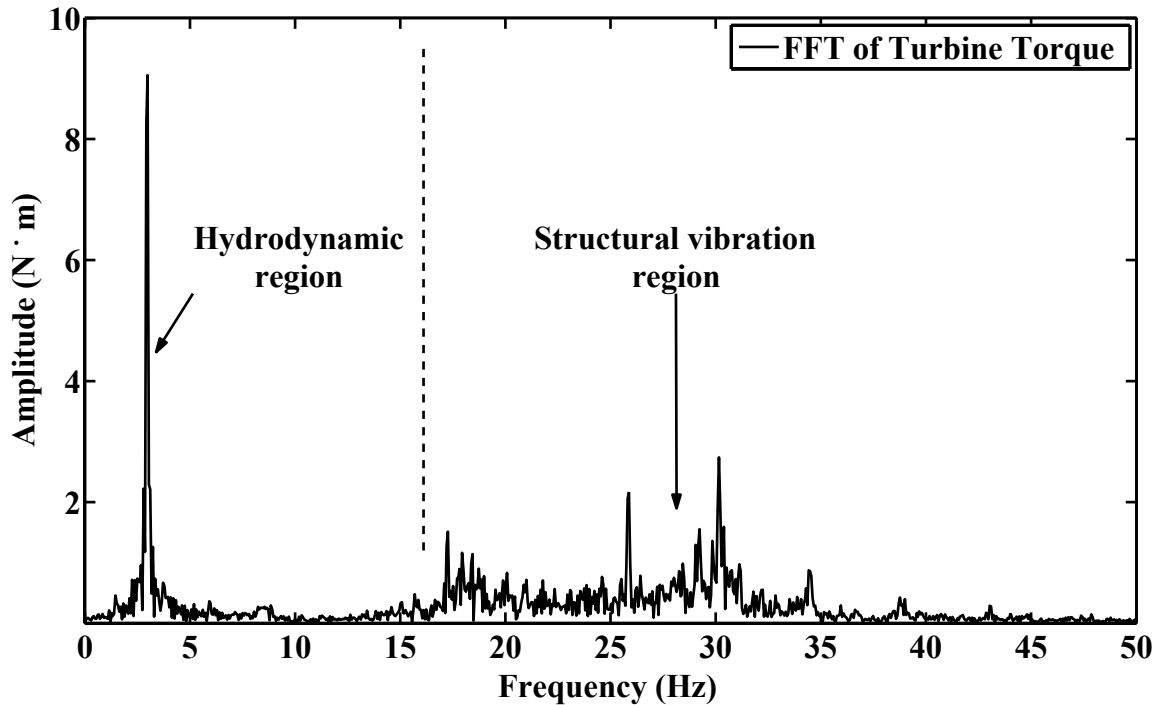


Figure A.15 – An FFT of the turbine torque is shown for a four-bladed test. Comparing with Fig. A.14 shows the hydrodynamic frequency range and the structural vibration frequency range.

The low-pass filter that was applied to the velocity data was modified slightly and used to filter the torque data. The main difference was the cut-off frequency. After testing the filter using several cut-off frequencies, a value of 17 Hz was chosen. The justification for this can be seen in Figure A.16. The cut-off frequency was chosen to be slightly lower than the natural frequency of the system because a cut-off frequency higher than 17 Hz resulted in insufficient noise removal in the 28 Hz to 32 Hz region. The resulting filtered data is compared to unfiltered data in Figure A.17. Further analysis showed that significant changes to the cut-off frequency did not significantly change the C_P for a given test.

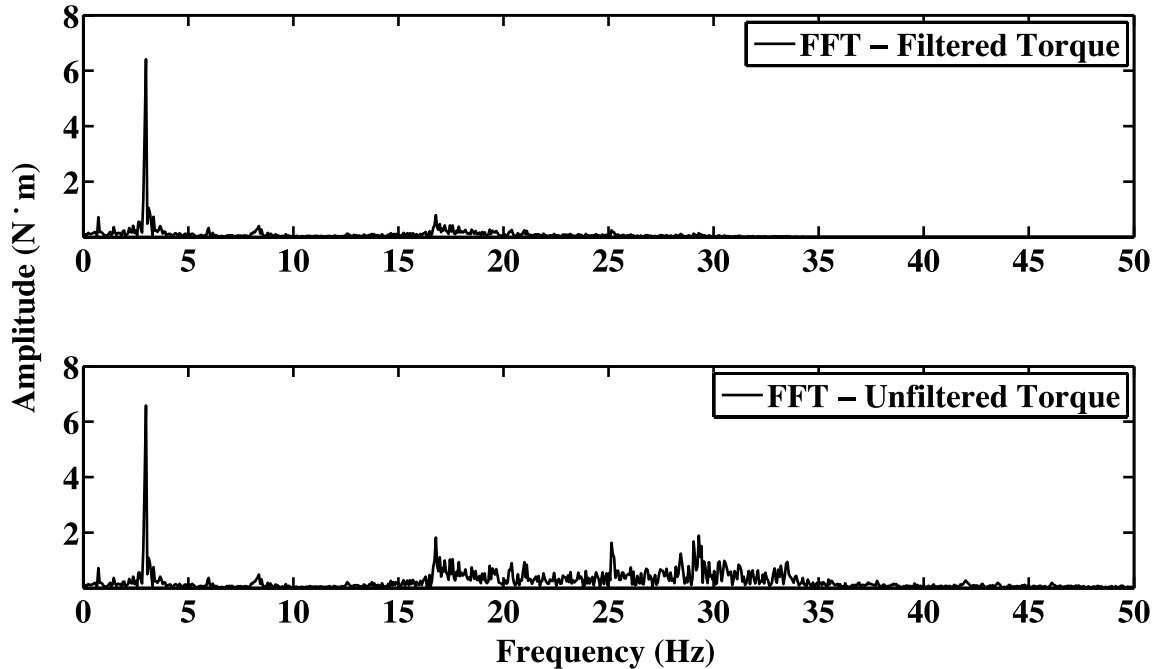


Figure A.16 – An FFT was performed on filtered and unfiltered torque data from a four-bladed test. Note the significant decrease in the structural vibration frequency range (above 17 Hz) that results from application of the filter.

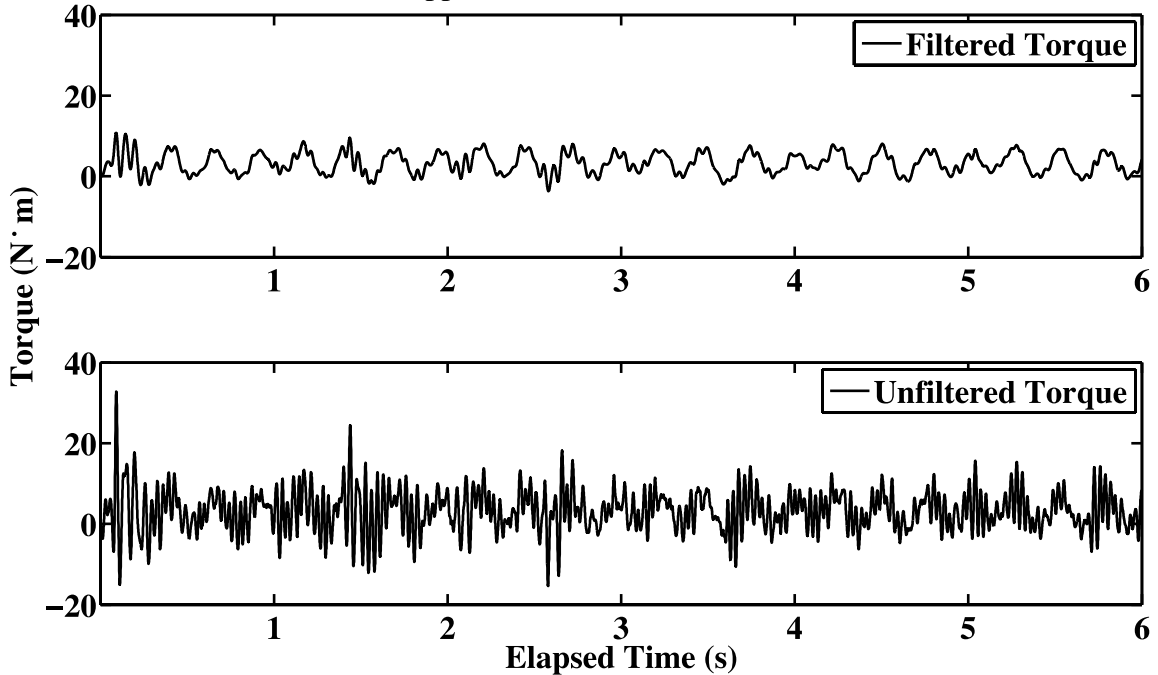


Figure A.17 - Unfiltered and filtered torque data from a four-bladed test are shown in the time domain. Note the significant decrease in noise after application of the filter.

Power Coefficient Calculation

The power coefficient, C_p , was calculated according to eqn. 1.4. Instantaneous torque, inflow velocity, and turbine angular velocity were used to calculate instantaneous C_p . The

instantaneous velocities and C_P were then averaged to get a final resulting C_P value at a given tip speed ratio and inflow velocity. Repeating this process for a range of tip speed ratios at the same inflow velocity gives a C_P curve, the main result of the testing for a certain set of parameters.

There were some concerns with losing data to filtering of noise in the torque data, so an analysis was performed on the cut-off frequency used in the low pass filter. A C_P curve was created using several cut-off frequencies: 2 Hz, 17 Hz (the value proposed for the data analysis section), and 45 Hz. Relative to the mechanical noise present in the system, these values are considered low, moderate, and high in magnitude. Figure A.18 shows the results, and by inspection there is very little change in C_P with modification of the cut-off frequency applied to the torque data. Consequently, the accuracy of the cut-off frequency applied to the torque data is not critical for accurate C_P results. However, it is important for accurate quantification of the blade torque for the design of turbines. The moderate cut-off frequency value of 17 Hz was chosen in order to remove the mechanical noise present in the measurement system while retaining the behavior of the turbine.

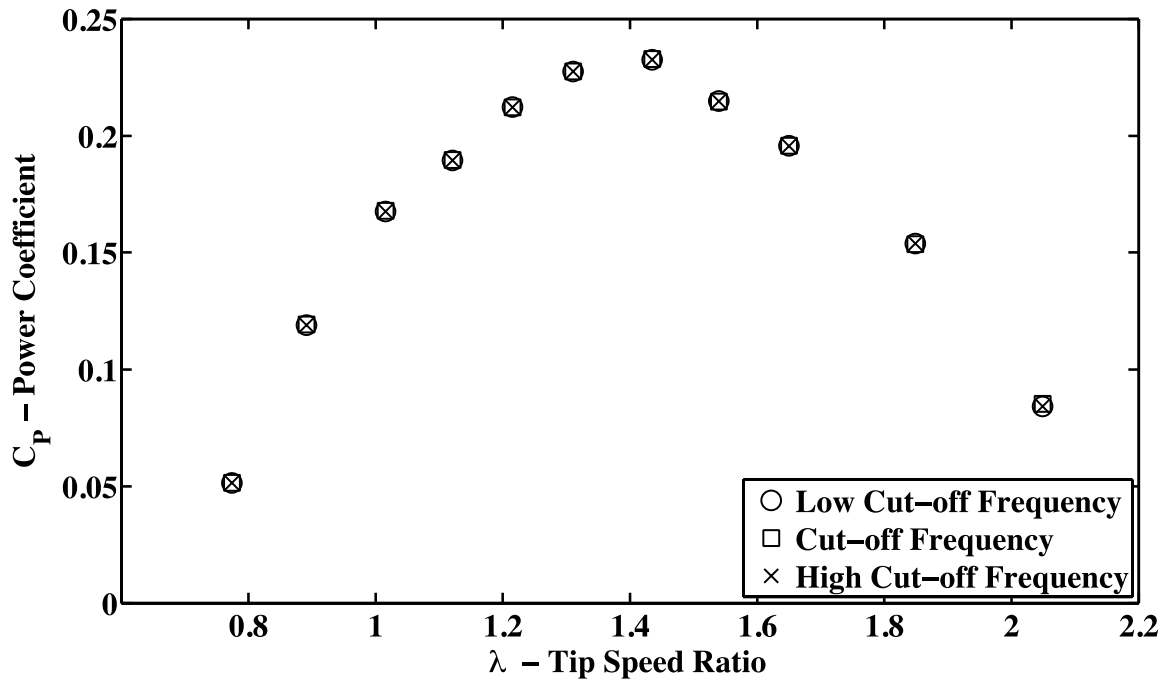


Figure A.18 – C_P results from a series of four-bladed tests are shown with low-pass filter cut-off frequencies of 2 Hz, 17 Hz, and 45 Hz. The C_P results were not significantly affected by changes in the cut-off frequency of the low-pass filter.

Bin-Averaged Nondimensional Torque

Bin-averaged non-dimensional torque is an important quantity for visualization of the torque loads present in the turbine system, as well as for load estimation in turbine design. First, torque data was normalized using eqn 1.5 (Strickland et al., 1980). Next the data was bin-averaged. Conceptually, bin-averaged torque data is the average torque within a certain turbine angular position range, or bin. For this research, a bin size of 1° was used, so there was a total of 360 bins. For example, the first 100 test data points have

an angle value between 0° and 1°, so those 100 torque values are placed in the first bin. The next 90 test data points have an angle value between 1° and 2°, so those 90 torque values are placed in the second bin. The process is repeated until all data points have been placed in a bin, and then the average nondimensional torque is calculated for each bin. An example bin-averaged nondimensional torque curve is shown in Figure A.19.

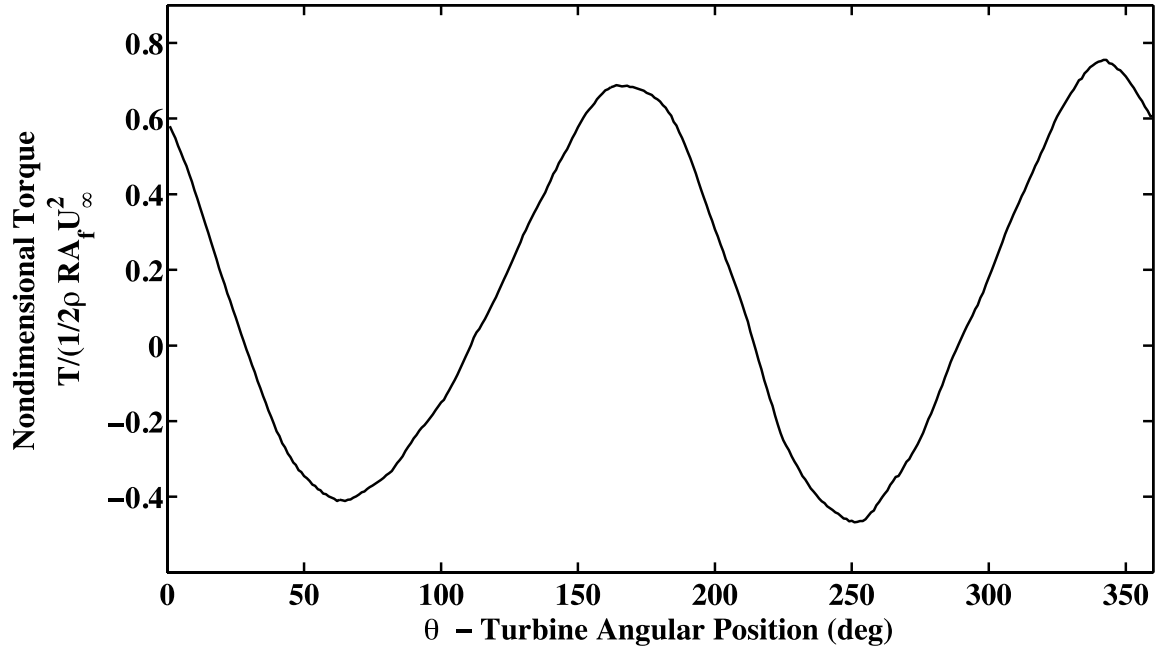


Figure A.19 – An example bin-averaged non-dimensional torque curve from a two-bladed test is shown. Results are from the NACA 63₃-018 profile at $\theta_t = 0^\circ$, $U_\infty = 0.6$ m/s, and $\lambda = 2.30$.

Bin-Averaged Nondimensional Torque with Rotor Inertia Term

One of the challenges with the system was fluctuation in the turbine angular angular velocity. This was a product of using a straight bladed cross-flow turbine. Especially at low tip speed ratios, the turbine operation is highly unsteady, with large torque peaks that cause the turbine speed to oscillate about the set speed with a magnitude of up to 5 percent of the set speed. This problem was exacerbated when the blade number was reduced from four to two. There was not a lot of modification that could be done to the motor control without overloading the motor, so some of the problem was accounted for in the data analysis. The rotor inertia term is,

$$T_{inertia} = I_{rotor} \frac{d\omega}{dt}, \quad (A.6)$$

where $T_{inertia}$ is the torque measured in the system resulting from angular acceleration of the turbine rotor, I_{rotor} is the sum of the mass moments of inertia of the turbine rotor and upper and lower driveshafts, and $\frac{d\omega}{dt}$ is the angular acceleration of the turbine rotor. The angular acceleration $\frac{d\omega}{dt}$ was calculated by filtering the turbine angular velocity, ω , and then calculating the time derivative $\frac{d\omega}{dt}$. The mass moment of inertia of the system, I_{rotor} ,

was calculated using SolidWorks, with a value of $0.248 \text{ kg}\cdot\text{m}^2$. The inertial term was calculated instantaneously and added to the measured torque data. In general the magnitude of the maximum and minimum torques was reduced. The corrected torque was then bin-averaged and nondimensionalized using eqn. 1.5. A comparison of nondimensional torque results with and without the inertial term is shown in Figure A.20.

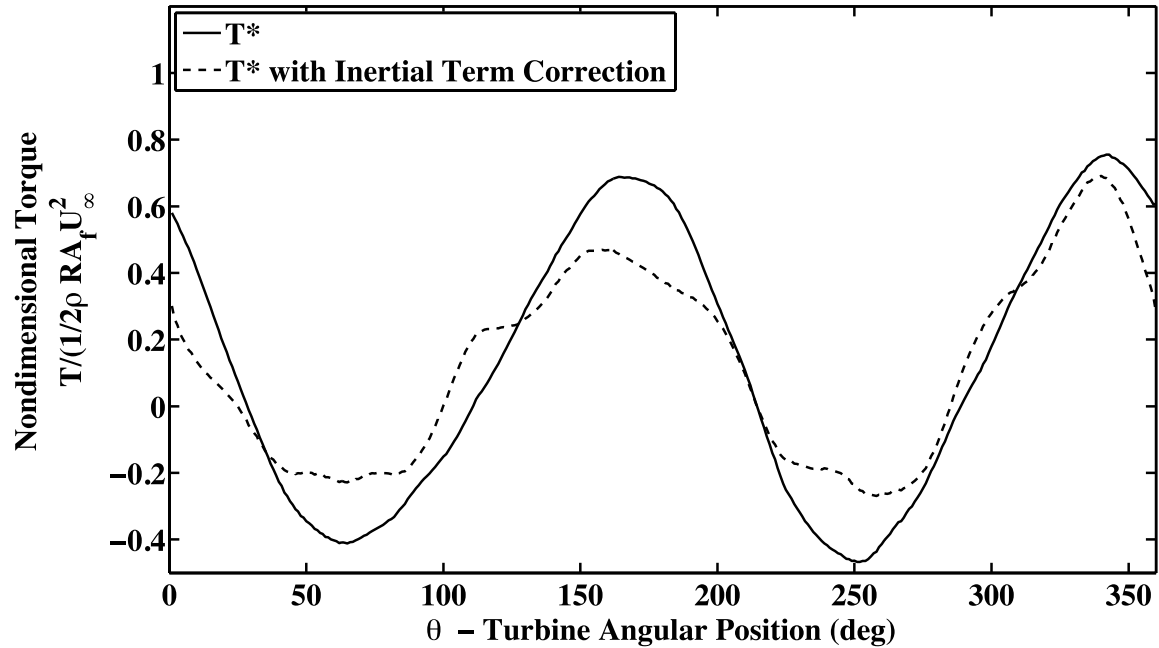


Figure A.20 – Bin-averaged non-dimensional torque from a two-bladed test is shown with and without accounting for the inertial term, $T_{inertia}$. Results are from the NACA 63₃-018 profile at $\theta_t = 0^\circ$, $U_\infty = 0.6 \text{ m/s}$, and $\lambda = 2.30$.

APPENDIX B:

UNCERTAINTY ANALYSIS AND REPEATABILITY STUDY

General Uncertainty Propagation Equation

The accuracy of C_P was estimated by applying uncertainty propagation calculations to a modified form of eqn. 1.4, the equation for C_P . The general equation for uncertainty propagation from Holman (2001) is,

$$w_R = \sqrt{\left(\frac{\partial R}{\partial x_1}\right)^2 w_{x_1}^2 + \left(\frac{\partial R}{\partial x_2}\right)^2 w_{x_2}^2 + \left(\frac{\partial R}{\partial x_3}\right)^2 w_{x_3}^2 + \dots + \left(\frac{\partial R}{\partial x_n}\right)^2 w_{x_n}^2}, \quad (\text{B.1})$$

where $R = f(x_1, x_2, x_3, \dots, x_n)$, w_R is the uncertainty in R , w_{x_n} is the uncertainty in the measurement of quantity x_n , and $\frac{\partial}{\partial x_n}$ is the partial derivative with respect to x_n . In this case variable R corresponds to C_P , and x_n corresponds to the measured quantities used to calculate C_P .

The C_P equation was modified for use in the uncertainty propagation calculations by using all variables that were measured individually. For example, instead of using the turbine cross sectional area, the product of the turbine radius and blade span was used, because those two quantities were measured individually to define the turbine cross sectional area. The modified equation is given by,

$$C_P = \frac{Fl\omega}{\frac{1}{2}\rho D b \left(\frac{\Delta x}{\Delta t}\right)^3}, \quad (\text{B.2})$$

where F is the force in the torque load cell, l is the lever arm of the applied load used in the torque load cell calibration, ω is the turbine angular velocity, ρ is the water density, D is the diameter of the turbine rotor, b is the turbine blade span, Δx is the distance traveled during the test, and Δt is the elapsed time during the test.

Uncertainty in Measured Quantities for Uncertainty in C_P Calculations

The uncertainty in the water density, w_ρ , was considered negligible. The water temperature in the tow tank was only measured occasionally. During winter months the water temperature in the tow tank was approximately 5°C. During the summer months the temperature was at most approximately 15°C. This results in a negligible change in the water density.

The uncertainty in the elapsed time, $w_{\Delta t}$, was also considered negligible, because the time measurement of the real-time data acquisition system was nearly perfect.

The uncertainty in the force in the torque load cell, w_F , was estimated using the uncertainties in the slope calibration of the load cell and the drive train friction tests. The uncertainty in the drive train friction tests was taken as approximately 0.085 N·m, or the largest deviation between the curves shown in Fig. A.4. The uncertainty in torque was converted to force by dividing by the lever arm of the applied load used in the torque load cell calibration, according to eqn. 3.1. This yielded a drive train friction uncertainty value of 0.437 N. The uncertainty in the load cell calibration was calculated using the

uncertainty from the slope and offset results from the linear least squares fit. The data points and linear regression line are shown in Fig. A.3. The uncertainty used for the load cell slope calibration was simply the standard error obtained from the linear regression, with a value of 0.190 N. The sum of the uncertainties in the drive train friction and load cell calibration tests amounted to an uncertainty of 0.629 N (0.14 lbs.), which is the torque load cell force uncertainty value used in the uncertainty propagation calculations.

The uncertainty in the turbine lever arm, w_l , was $7.94 \cdot 10^{-4}$ m (.03125 in.), or half of the smallest increment on the tape measure used to measure it. The smallest increment on the tape measure was 1/16 in.

The uncertainty in the turbine angular velocity, w_ω , was estimated using a conservative value of 0.1 rad/s (5.73 degrees/s). The average of the instantaneous angular velocities from a single test was compared to the average velocity of the same test, computed using two data points, one at the first zero angular position of the encoder, and one at the last zero angular position of the encoder. The total angular displacement between these two points was calculated using the total number of revolutions of the encoder, and the turbine angular velocity was calculated using the total angular displacement and the elapsed time. Comparing the two different methods gave a percent error of 0.029% for $\omega = 8.66$ rad/s. This includes any error from differentiating the signal using the first method of angular velocity calculation. For the same turbine angular velocity, the uncertainty estimate of 0.1 rad/s would give an uncertainty of 1.15%, so the estimate is very conservative.

The uncertainty in the turbine diameter, w_D , was 0.00254 m (0.1 in.). The mounting holes on the turbine end plates were machined precisely, and any error in the hole placement is on the order of thousandths of an inch. A larger uncertainty value was estimated in order to account for any error in the placement of the mounting pin in the turbine blades. This estimate is also conservative, considering the blade thickness is approximately 0.0137 m (0.54 in.), and the error would need to be greater than 5% of the blade thickness.

The uncertainty in the measurement of the turbine blade span, w_b , was $7.94 \cdot 10^{-4}$ m (.03125 in.), or half of the smallest increment used to measure the blade span, in this case a tape measure with increments of 1/16 in.

The uncertainty in the distance traveled during the test, $w_{\Delta x}$, was estimated using the accuracy of the measurement of the distance traveled during the distance calibration. The distance was measured using a tape measure with an accuracy of 0.00159 m (1/16 in.). The smallest increment on the tape measure was used rather than half the smallest increment in order to have a more conservative estimate. The uncertainty in the Δx does not include the effect of flow blockage.

Partial Derivative Terms and Equation for Uncertainty in Power Coefficient

Partial derivatives with respect to each measured quantity were calculated, with the following results:

$$\frac{\partial C_P}{\partial F} = \frac{l\omega}{\frac{1}{2}\rho D b U_\infty^3}, \quad (\text{B.3})$$

$$\frac{\partial C_P}{\partial l} = \frac{F\omega}{\frac{1}{2}\rho D b U_\infty^3}, \quad (\text{B.4})$$

$$\frac{\partial C_P}{\partial \omega} = \frac{Fl}{\frac{1}{2}\rho D b U_\infty^3}, \quad (\text{B.5})$$

$$\frac{\partial C_P}{\partial D} = \frac{Fl\omega}{\frac{1}{2}\rho D^2 b U_\infty^3}, \quad (\text{B.6})$$

$$\frac{\partial C_P}{\partial S} = \frac{Fl\omega}{\frac{1}{2}\rho D b^2 U_\infty^3}, \quad (\text{B.7})$$

$$\frac{\partial C_P}{\partial \Delta x} = \frac{3Fl\omega}{\frac{1}{2}\rho D b U_\infty^3 \Delta x}. \quad (\text{B.8})$$

Inserting eqn. B.3 through eqn. B.8 in eqn. B.1 yields:

$$w_{C_P} = \left[\left(\frac{l\omega}{\frac{1}{2}\rho D b U_\infty^3} \right)^2 w_F^2 + \left(\frac{F\omega}{\frac{1}{2}\rho D b U_\infty^3} \right)^2 w_l^2 + \left(\frac{Fl}{\frac{1}{2}\rho D b U_\infty^3} \right)^2 w_\omega^2 + \left(\frac{Fl\omega}{\frac{1}{2}\rho D^2 b U_\infty^3} \right)^2 w_D^2 + \left(\frac{Fl\omega}{\frac{1}{2}\rho D b^2 U_\infty^3} \right)^2 w_b^2 + \left(\frac{3Fl\omega}{\frac{1}{2}\rho D b U_\infty^3 \Delta x} \right)^2 w_{\Delta x}^2 \right]^{\frac{1}{2}}. \quad (\text{B.9})$$

Applying eqn. B.9 to the data at each tip speed ratio and entering average quantities for F , ω , and U_∞ gives uncertainty values for the entire C_P curve. Example C_P curves with uncertainty error bars are shown in Fig. 4.1, and are repeated below in Fig. B.1.

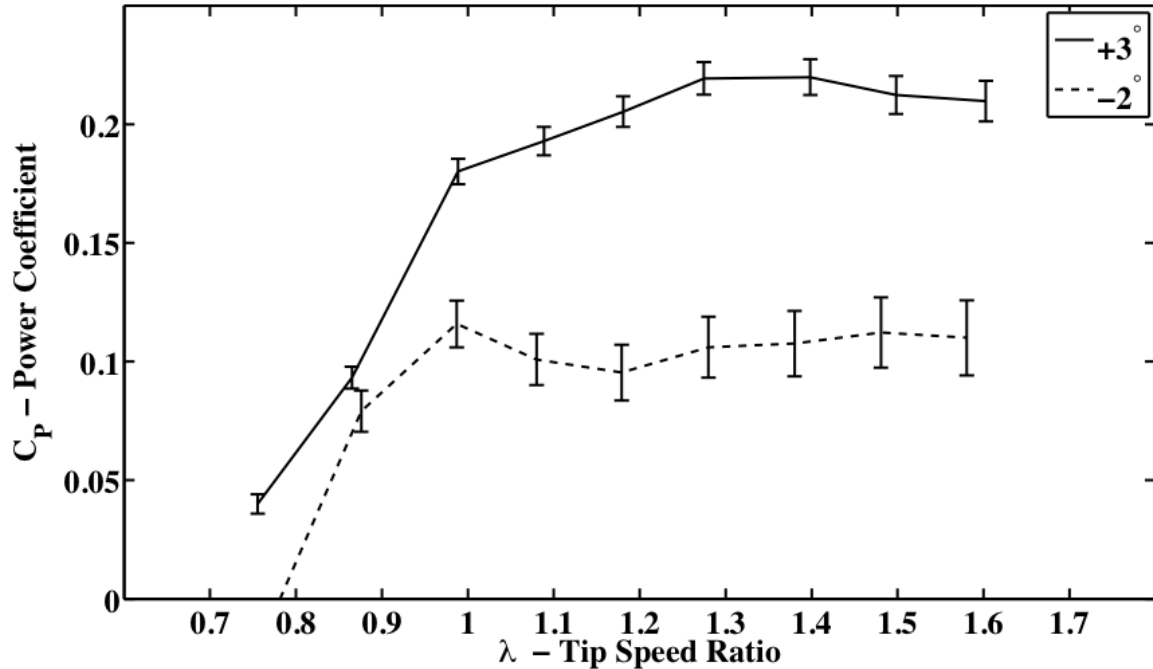


Figure B.1 – The power coefficient curves for $\theta_t = +3^\circ$ and $\theta_t = -2^\circ$ are shown with uncertainty error bars for the carbon fiber NACA 63₃-018 blade set. Four-bladed testing was performed at the toe angles $\theta_t = +3^\circ$ and $\theta_t = -2^\circ$, at an inflow velocity of $U_\infty = 1.22$ m/s, and at a solidity ratio of $\sigma = 0.294$.

Uncertainty in Measured Quantities for Uncertainty in T^* Calculations

The uncertainty in T^* was calculated using the same quantities as the power coefficient, with the addition of the uncertainty in the turbine rotor mass moment of inertia, I_{rotor} , and the uncertainty in the turbine angular acceleration, $\frac{d\omega}{dt}$. Because the turbine rotor mass moment of inertia term was estimated using a solid model from SolidWorks, a conservative value of 10% of the mass moment of inertia was chosen for the uncertainty. This takes into account minor discrepancies between the geometries of the model and the physical turbine rotor, as well as variability in materials. Additionally, the experimental data was reduced with several different turbine rotor inertia values, varying up to 15%, and there was only a small change in the calculated nondimensional torque results. Thus, the nondimensional torque results are relatively insensitive to moderate uncertainty in the rotor mass moment of inertia.

Because the turbine angular acceleration, $\frac{d\omega}{dt}$, is the second derivative of the measured signal, it should have a higher uncertainty than the turbine angular velocity.

Differentiation is a calculation that can be prone to error. The maximum turbine angular accelerations during testing generally varied from 4 to 8 rad/s². A conservative value of 0.6 rad/s² was chosen, which is about 10% of typical acceleration output.

Partial Derivative Terms and Equation for Uncertainty in T^*

The nondimensional torque equation in terms of measured quantities is:

$$T^* = \frac{(Fl + I_{rotor} \frac{d\omega}{dt})}{\frac{1}{4}\rho D^2 b (\frac{\Delta x}{\Delta t})^2}, \quad (\text{B.10})$$

where the torque load cell force, F , and turbine angular acceleration, $\frac{d\omega}{dt}$, are bin-averaged quantities. Partial derivatives with respect to each measured quantity were calculated, with the following results:

$$\frac{\partial T^*}{\partial F} = \frac{l}{\frac{1}{4}\rho D^2 b U_\infty^2}, \quad (\text{B.11})$$

$$\frac{\partial T^*}{\partial l} = \frac{F}{\frac{1}{4}\rho D^2 b U_\infty^2}, \quad (\text{B.12})$$

$$\frac{\partial T^*}{\partial D} = \frac{2(Fl + I_{rotor} \frac{d\omega}{dt})}{\frac{1}{4}\rho D^3 b U_\infty^2}, \quad (\text{B.13})$$

$$\frac{\partial T^*}{\partial b} = \frac{(Fl + I_{rotor} \frac{d\omega}{dt})}{\frac{1}{4}\rho D^2 b^2 U_\infty^2}, \quad (\text{B.14})$$

$$\frac{\partial T^*}{\partial \Delta x} = \frac{2(Fl + I_{rotor} \frac{d\omega}{dt})}{\frac{1}{4}\rho D^2 b U_\infty^2 \Delta x}, \quad (\text{B.15})$$

$$\frac{\partial T^*}{\partial I_{rotor}} = \frac{\frac{d\omega}{dt}}{\frac{1}{4}\rho D^2 b U_\infty^2}, \quad (\text{B.16})$$

$$\frac{\partial T^*}{\partial (\frac{d\omega}{dt})} = \frac{I_{rotor}}{\frac{1}{4}\rho D^2 b U_\infty^2}. \quad (\text{B.17})$$

Inserting the partial derivatives and uncertainties into eqn. B.1 yields:

$$W_{T^*} = \left[\left(\frac{l}{\frac{1}{4}\rho D^2 b U_\infty^2} \right)^2 W_F^2 + \left(\frac{F}{\frac{1}{4}\rho D^2 b U_\infty^2} \right)^2 W_l^2 + \left(\frac{2(Fl + I_{rotor} \frac{d\omega}{dt})}{\frac{1}{4}\rho D^3 b U_\infty^2} \right)^2 W_D^2 + \left(\frac{(Fl + I_{rotor} \frac{d\omega}{dt})}{\frac{1}{4}\rho D^2 b^2 U_\infty^2} \right)^2 W_b^2 + \left(\frac{2(Fl + I_{rotor} \frac{d\omega}{dt})}{\frac{1}{4}\rho D^2 b U_\infty^2 \Delta x} \right)^2 W_{\Delta x}^2 + \left(\frac{\frac{d\omega}{dt}}{\frac{1}{4}\rho D^2 b U_\infty^2} \right)^2 W_{I_{rotor}}^2 + \left(\frac{I_{rotor}}{\frac{1}{4}\rho D^2 b U_\infty^2} \right)^2 W_{\frac{d\omega}{dt}} \right]^{\frac{1}{2}}. \quad (\text{B.18})$$

Using bin-averaged values for the force in the load cell and the turbine angular acceleration yields an uncertainty for each turbine angular position, in this case 360 values.

Uncertainty in Tip Speed Ratio and Inflow Velocity

The uncertainties in tip speed ratio and inflow velocity result from uncertainties in the turbine angular velocity, ω , and the distance traveled by the carriage, Δx . Any errors from

the change in time, Δt , are neglected. The same uncertainties in ω and Δx are used as those from the C_P and T^* uncertainty calculations.

The equation for tip speed ratio is put in the form:

$$\lambda = \frac{\omega D}{2\left(\frac{\Delta x}{\Delta t}\right)}. \quad (\text{B.19})$$

Taking partial derivatives with respect to ω , D , and Δx and inserting into eqn. B.1 yields:

$$w_\lambda = \sqrt{\left(\frac{D}{2U_\infty}\right)^2 w_\omega^2 + \left(\frac{\omega}{2U_\infty}\right)^2 w_D^2 + \left(\frac{\omega D}{2U_\infty \Delta x}\right)^2 w_{\Delta x}^2}, \quad (\text{B.20})$$

where $\frac{\Delta x}{\Delta t}$ is equal to the inflow velocity U_∞ . Because Δt is neglected in the uncertainty calculations, the uncertainty in the inflow velocity, U_∞ , is:

$$w_{U_\infty} = \sqrt{\left(\frac{\partial U_\infty}{\partial \Delta x}\right)^2 w_{\Delta x}^2} = \frac{w_{\Delta x}}{\Delta t}. \quad (\text{B.21})$$

Overall, the uncertainties in tip speed ratio and inflow velocity were very low.

Repeatability Study and Comparison with Uncertainty in Power Coefficient

A repeatability study was performed to ensure reliability of the data collection process. Multiple data points were taken at each tip speed ratio, and the results were then averaged. For an unsteady system, the tests cannot be considered identical, but as long as the average inflow velocity and average tip speed ratio are very close, the tests can be considered comparable. The uncertainty in C_P was calculated for each averaged point, and the scatter in the data was compared to the magnitude of the uncertainties applied to the average C_P at each tip speed ratio. Figure B.2 shows the data points from the repeatability study. Figure B.3 shows the averaged test results with uncertainty error bars at each tip speed ratio. Comparing Fig. B.2 to Fig. B.3 shows that the uncertainty bars are slightly larger in magnitude than the scatter of the data. Table B.1 compares the standard deviation of the sample with the uncertainties. At all tip speed ratios except for one, the uncertainties are slightly larger than three standard deviations. This implies that a large percentage of the data will fall within the uncertainty range calculated. This justifies the use of a small number of data points with uncertainty bars as estimates of the scatter in C_P results. The repeatability of the test data is also encouraging, because some of the test points were taken several days apart.

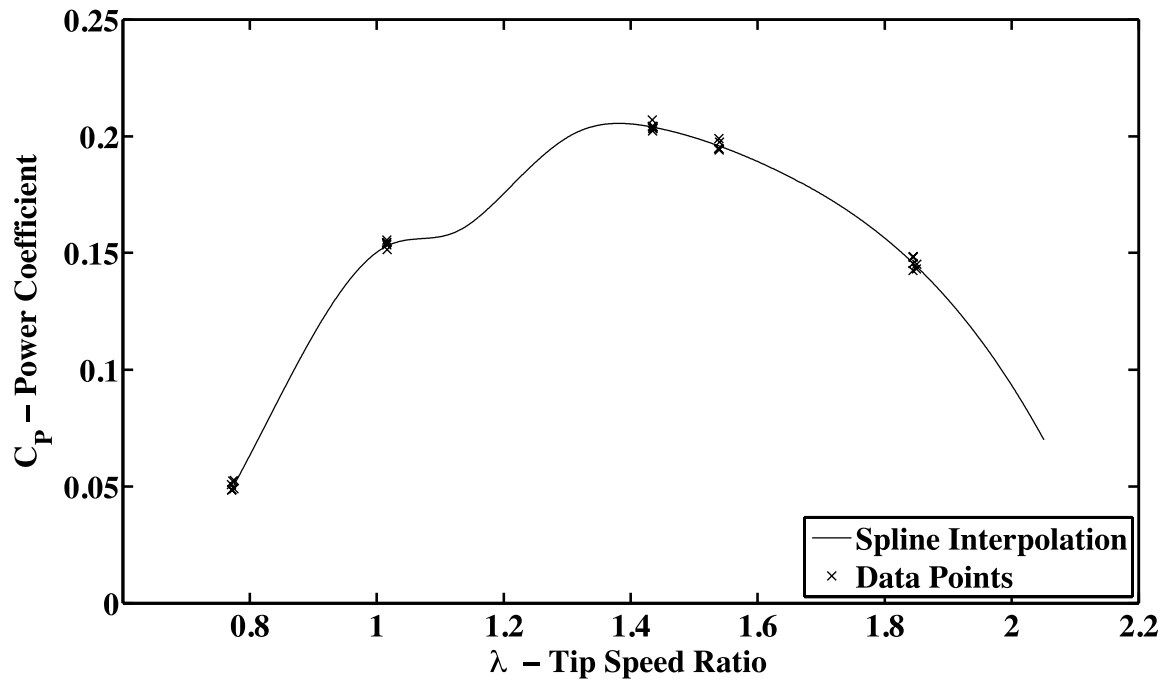


Figure B.2 – The C_P results of the repeatability study are shown for four-bladed testing of the NACA 63₃-018 profile at $\theta_t \approx +5^\circ$ and $U_\infty = 1.00$ m/s. The spline interpolation used the average C_P value at a given tip speed ratio from the repeatability study, as well as some data points from Fig. B.3.

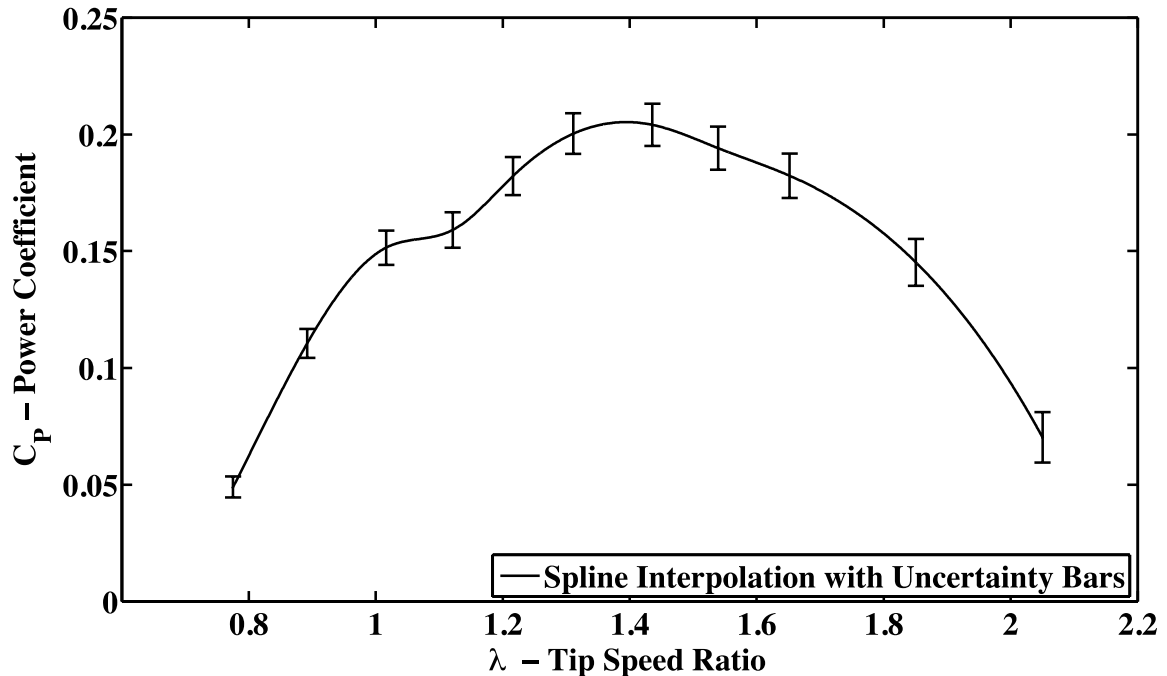


Figure B.3 – Uncertainty in C_p is shown for four-bladed testing of the NACA 63₃-018 profile at $\theta_t \approx +5^\circ$ and $U_\infty = 1.00$ m/s. Additional tests were taken for the repeatability study (shown in Fig. B.2) under the same test conditions, but not at all of the tip speed ratios in this curve.

$\bar{\lambda}$	\bar{C}_p	σ_{C_p}	$3\sigma_{C_p}$	w_{C_p}
0.775	0.0507	0.00168	0.00504	0.00449
1.02	0.1530	0.00135	0.00406	0.00733
1.44	0.2039	0.00146	0.00439	0.00903
1.54	0.1958	0.00191	0.00572	0.00921
1.85	0.1442	0.00225	0.00675	0.0101

Table B.1 – Sample standard deviation of power coefficient is compared to the uncertainty in power coefficient calculated using uncertainty propagation equations. The uncertainties are larger than three standard deviations for every point except one. The uncertainty is still close to three standard deviations in magnitude for this point.

Velocity Fluctuations

In addition to the uncertainties in C_p , T^* , λ , and U_∞ that result from the uncertainties in measured quantities, fluctuations are present in the turbine angular velocity and inflow velocity. These fluctuations are unrelated to the calculated uncertainties, and are purely a result of the unsteady nature of cross-flow turbine operation, specifically for the straight-bladed Darrieus type turbine. For this type of turbine, fluctuations in both velocities are highest at low tip speed ratios, when the blade forces are highest in magnitude. In order to maintain adequate response, the proportional term in the proportional-integral motor

control was set as high as possible without resulting in faults. However, at low tip speed ratios, the turbine angular velocity and inflow velocity fluctuated by as much as 10% of the mean velocities. This is still representative of turbine operation in applications, which will most likely encounter fluctuations in inflow velocity and turbine angular velocity resulting from the variable flow of ocean currents.

APPENDIX C:

FLOW CURVATURE COORDINATE SYSTEM

The virtual incidence angle correction was added to the FVM using equations developed by Migliore and Wolfe (1980). The functions were transcribed from FORTRAN IV to Matlab by Urbina (2011b). The functions depend on the following quantities: tip speed ratio (λ), turbine blade angular position (θ), blade mounting point (x_{mount} and y_{mount}), mean line shape (camber), and curvature index (c/R). In this case $x_{\text{mount}} = 0.333c$ and $y_{\text{mount}} = 0$, which corresponds to a mounting point on the blade chord length, positioned at a distance of 1/3 of the blade chord away from the leading edge of the foil. In order to apply the equations correctly, it was necessary to examine the coordinate system used in Migliore and Wolfe (1980) and the coordinate system used in the FVM, which is based on the model used by Strickland et al. (1980). The turbine angular position is shown in both coordinate systems in Fig. C.1. In order to input the correct turbine position to the flow curvature functions, 90° was subtracted from the turbine angular position in the Strickland coordinate system, θ_s . The orientation of a positive virtual incidence angle from the flow curvature transformations was the same as the orientation of positive angle of attack in the FVM coordinate system (Fig. 2.1), so the virtual incidence angle was added to the angle of attack for calculations.

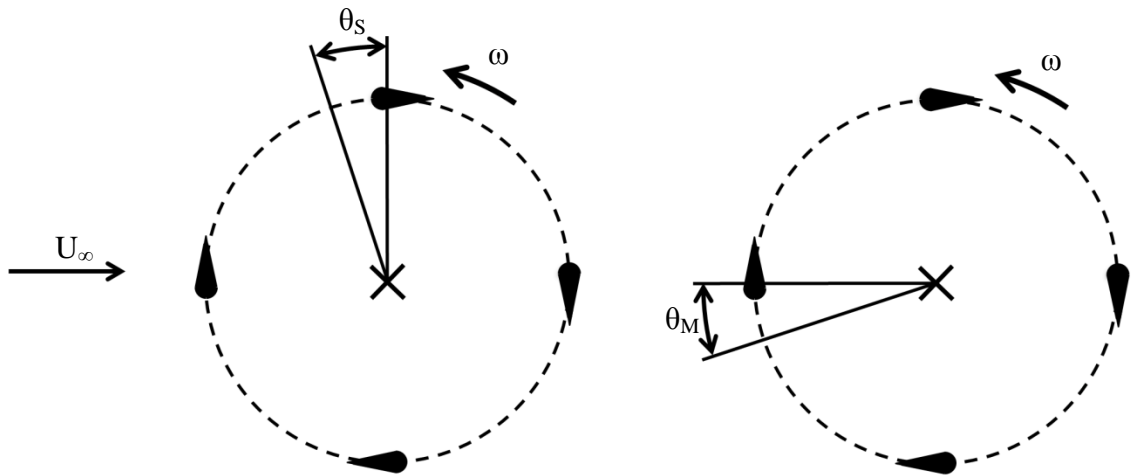


Figure C.1 – The coordinate systems used by Strickland and Migliore were different, so it was necessary to modify the turbine angular position, θ , input to the conformal mapping calculations in order to apply the virtual incidence angle at the correct turbine angular position.

APPENDIX D:

ADDITIONAL TEST RESULTS

Some additional four-bladed testing results are included. Included are testing results for six of the blade profiles at a toe angle of $\theta_t = -7^\circ$, as well as a comparison of the results between the NACA 63₃-018 carbon fiber and 3-D printed blade sets. The stiffness of the two NACA 63₃-018 blade sets is significantly different, so the effect of blade stiffness on power coefficient results was isolated.

Figure D.1 shows the power coefficient results for four profiles at $\theta_t = -7^\circ$, and one profile at $\theta_t = -5^\circ$. The power coefficients are very low, and the profiles exhibit similar behavior. Generally, the peak power coefficient is reached at a very low tip speed ratio, and the power coefficient decreases significantly with increasing tip speed ratio after the peak.

Figure D.2 shows the results for the NACA 63₃-018 blade sets with different stiffness values. Despite the significant difference in stiffness, there was virtually no change in power coefficient between the two results. The more flexible 3-D printed blades had a slightly lower peak efficiency, but overall the difference in C_p at each tip speed ratio is within the uncertainty of C_p . This data suggests that at the model scale, a flexible blade does not result in detrimental turbine performance. This also implies that the data taken using the 3-D printed blades is just as valid as the data taken using the carbon fiber blades. While the 3-D printed blades were expensive to produce, they can be used for rapid prototyping of foils, and can be manufactured quickly.

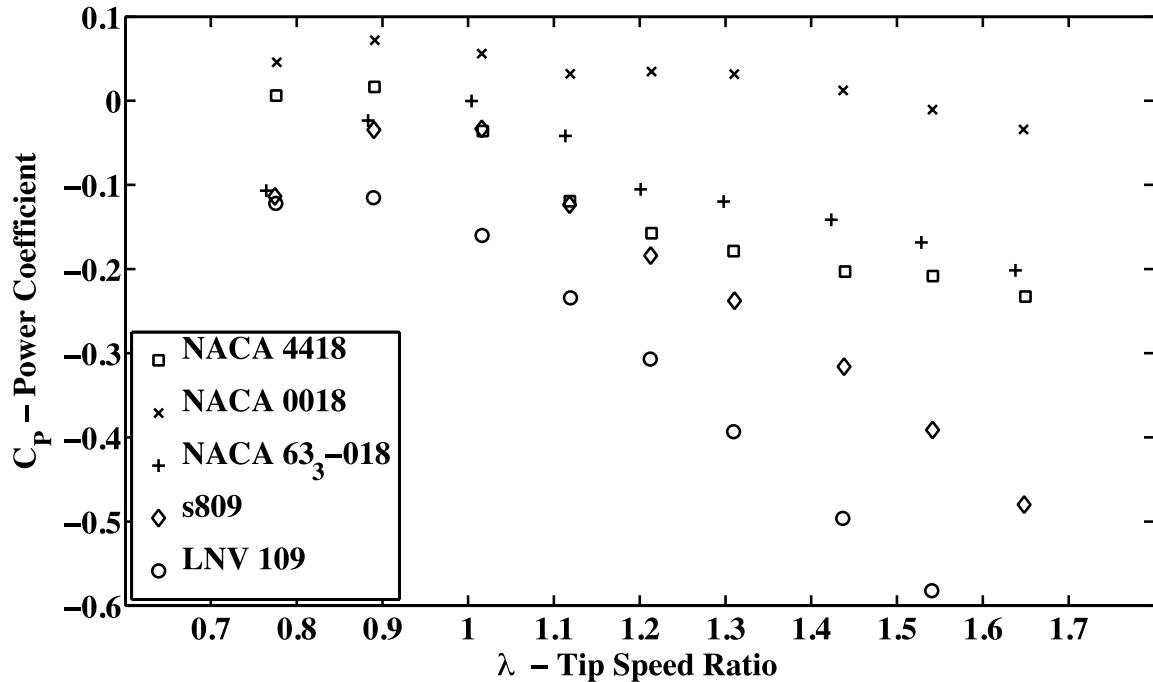


Figure D.1 – Four-bladed testing results are shown for five of the blade sets. Testing was performed at $\theta_t = -7^\circ$ at an inflow velocity of $U_\infty = 1.22$ m/s for a range of blade solidity ratios. The NACA 0018 profile was set at the incorrect angle of $\theta_t = -5^\circ$, but is included for comparison nonetheless.

The carbon fiber and 3-D printed NACA 63₃-018 blades were very similar, but additional differences need to be mentioned. The 3-D printed blades have a chord length of $c = 6.99$ cm, with a very smooth trailing edge. The carbon fiber blades were made with a chord length of $c = 7.62$ cm, which was then truncated at the trailing edge to a chord length of $c = 6.99$ cm. The chord length of the carbon fiber blades was significantly thicker than the 3-D printed blades. Despite these minor differences in geometry, the performance of the blades was very similar.

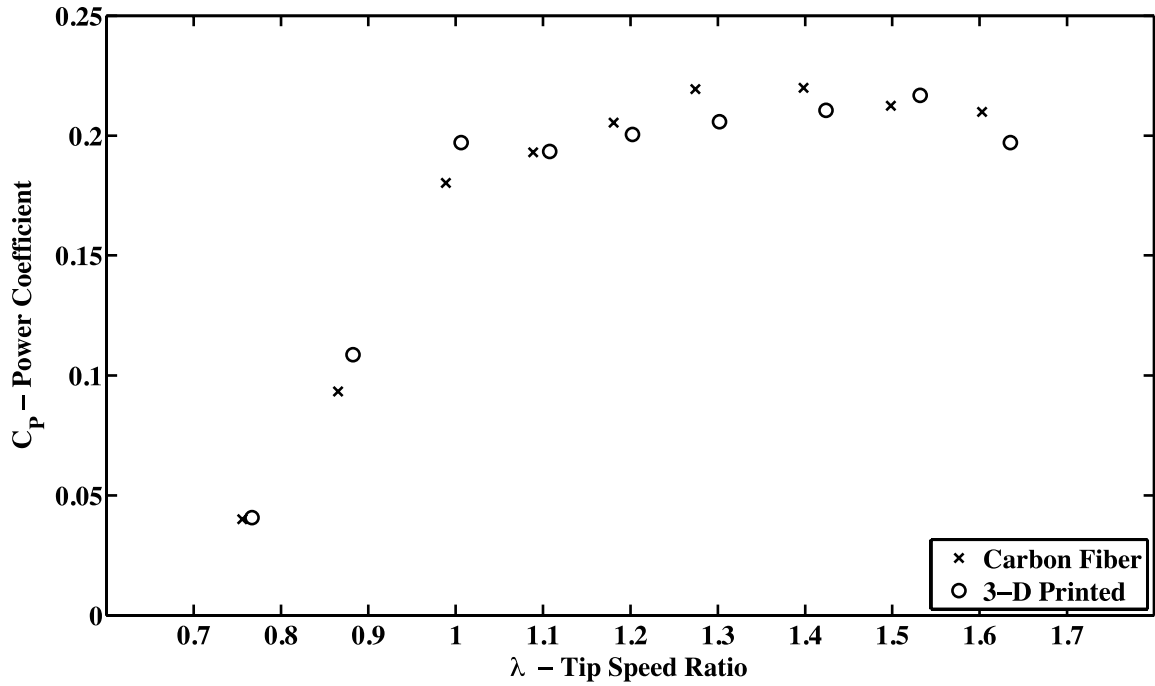


Figure D.2 – Four-bladed testing results are shown for the NACA 63₃-018 carbon fiber and 3-D printed blade sets. Testing was performed at $\theta_t = +3^\circ$, at an inflow velocity of $U_\infty = 1.22$ m/s.

APPENDIX E:
TOW TANK GEOMETRY

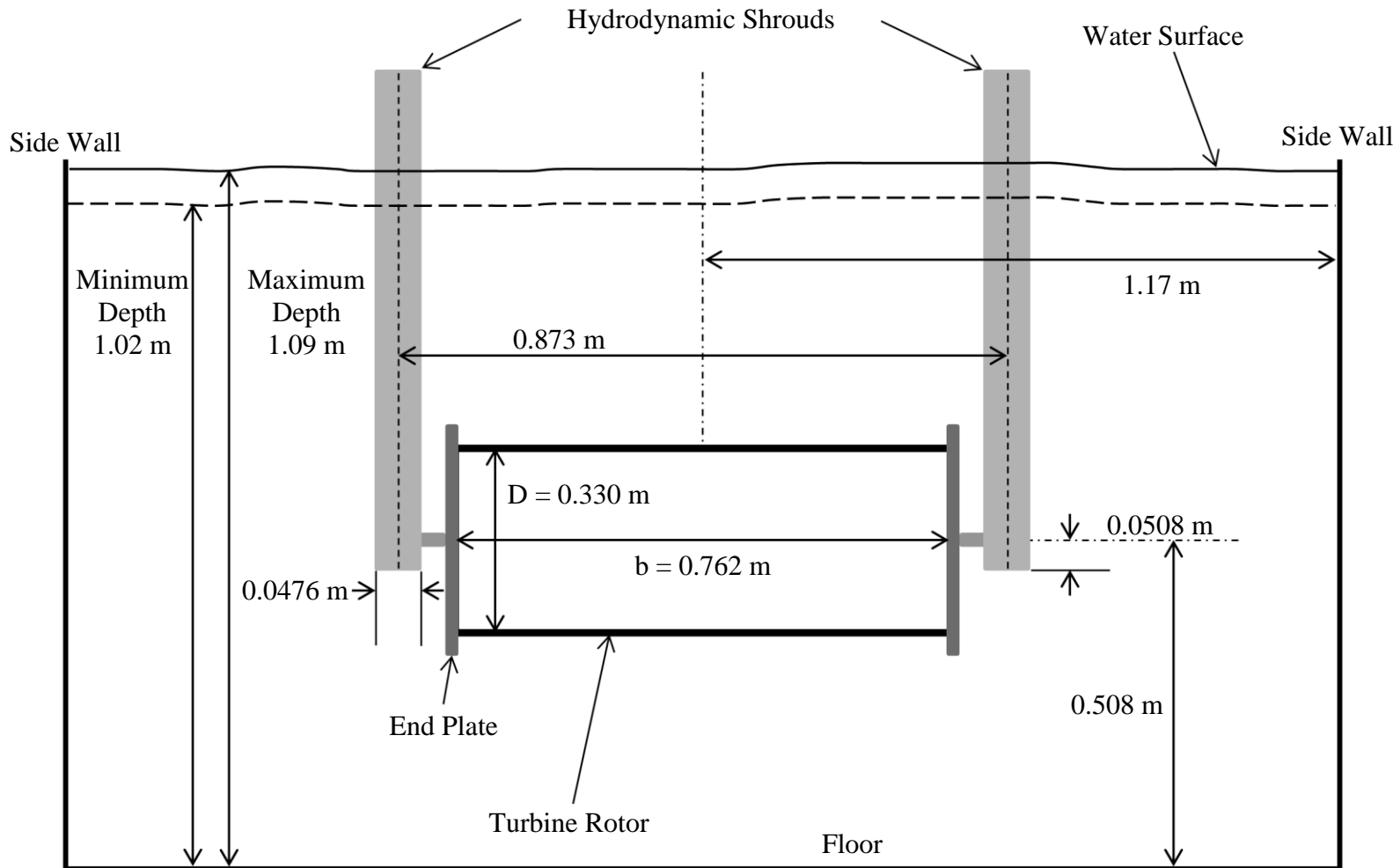


Figure E.1 – A schematic of the cross-flow turbine installed in the tow tank shows the geometry used for testing. The turbine direction of motion corresponds to out of the page.

BIOGRAPHY OF THE AUTHOR

Geoffrey deBree is a Windham, Maine native, graduating from Windham High School in 2005. Geoffrey graduated from the University of Maine in May, 2009 with a B.S. in Mechanical Engineering. Geoffrey is a member of Pi Tau Sigma, the Mechanical Engineering honor society. His hobbies include snowboarding, soccer, and playing music. Upon graduation, Geoffrey plans on pursuing a career in alternative energy, with a particular interest in projects being developed in the great state of Maine. He is a candidate for the Master of Science degree in Mechanical Engineering from the University of Maine in May, 2012.

Appendix 3-3

**DESIGN, OPTIMIZATION, AND TESTING OF A CROSS-FLOW
TIDAL TURBINE**

By

Megan Colleen Swanger

B.S. Norwich University, 2006

A THESIS

Submitted in Partial Fulfillment of the

Requirements for the Degree of

Master of Science

(in Mechanical Engineering)

The Graduate School

The University of Maine

August 2013

Advisory Committee:

Michael Peterson, Prof. of Mechanical Engineering, University of Maine, Co-Advisor

Richard W. Kimball, Prof. of Engineering, Maine Maritime Academy, Co-Advisor

Douglas Read, Prof. of Engineering, Maine Maritime Academy

THESIS ACCEPTANCE STATEMENT

On behalf of the Graduate Committee for Megan Colleen Swanger, I affirm that this manuscript is the final and accepted thesis. Signatures of all committee members are on file with the graduate school at the University of Maine, 42 Stodder Hall, Orono, Maine.

Michael Peterson, Prof. of Mechanical Engineering, University of Maine Aug 8, 2013

Richard W. Kimball, Prof. of Engineering, Maine Maritime Academy Aug 8, 2013

LIBRARY RIGHTS STATEMENT

In presenting this thesis in partial fulfillment of the requirements for an advanced degree at The University of Maine, I agree that the library shall make it freely available for inspection. I further agree that permission for “fair use” copying of this thesis for scholarly purposes may be granted by the librarian. It is understood that any copying or publication of this thesis for financial gain shall not be allowed without my written permission.

Signature

Date:

**DESIGN, OPTIMIZATION, AND TESTING OF A CROSS-FLOW
TIDAL TURBINE**

By Megan Colleen Swanger

Thesis Co-Advisors: Dr. Michael Peterson

Dr. Richard Kimball

An Abstract of the Thesis Presented
in Partial Fulfillment of the Requirements for the
Degree of Master of Science
(in Mechanical Engineering)
August 2013

This thesis is a summary of testing conducted with a Darrieus style cross-flow tidal turbine. Many locations around the world have locations suitable for tidal turbine energy, including the Cobscook Bay in Eastport, Maine. Cross-flow turbines are likely to have a smaller impact on the environment compared to axial flow turbines due to their operation at lower tip speed ratios. Since very little experimental data is available presently for cross-flow turbines, this study provides an expansive set of performance data for two NACA series blade profiles of the same chord length. One blade profile was used in two different orientations during testing. The University of Maine tow tank was utilized to perform testing in order to determine the peak power coefficient for each blade profile. Tests of two and four blade turbines were conducted at fixed inflow velocity for a range of tip speeds and blade toe angles. Turbine performance was compared to determine the most efficient solidity ratio and profile. Power coefficient curves compared consistently with previously published data.

Testing was also performed to determine the effects of viscosity and free surface effects by varying water temperature and water column height on turbine performance. This data was collected with the blade profile that provided the most efficient results set to its optimal toe angle. Results determined that both viscous and free surface interactions had considerable effect on efficiency results.

ACKNOWLEDGEMENTS

I would like to thank my advisor, Dr. Michael “Mick” Peterson, for introducing me to this project and constantly helping me all along the way. I would also like to thank my advisory committee: Dr. Richard Kimball and Dr. Doug Read, for their vast knowledge and guidance. I greatly appreciate the time you all have spent providing input and directing me down the correct path.

I would like to thank Maine Tidal Power Initiative and all of its members for providing such a positive experience that has expanded my knowledge and made me a more conscientious engineer. I’d also like to thank the U.S. Department of Energy for their funding to our project through grant EE-000298, Ocean Renewable Power Company for providing the blades and funding to conduct the experimental tests, Alexander’s Welding and Machine for manufacturing the turbine, and the Maine Army National Guard for providing tuition assistance.

I would like to thank the graduate students who worked alongside me: Geoffrey deBree and Matthew Cameron, for developing the experimental test setup, Thomas Lokocz, for designing the blade manufacturing system, and Raul Urbina, for answering my many questions and keeping me focused. I’d also like to thank the undergraduate students that put in countless hours to the project: Thomas McKay, Nathan Rocker, James Staszko, and Kai Whitehead. In addition, I would like to thank Travis Wallace for his generous support and advice during this project.

Finally, I would like to thank my family who has always been supportive of everything I do. I am always ever grateful for your presence in my life.

TABLE OF CONTENTS

ACKNOWLEDGEMENTS	v
LIST OF TABLES	ix
LIST OF FIGURES	x
LIST OF SYMBOLS	xiv
LIST OF ABBREVIATIONS.....	xvi
Chapter	
1. INTRODUCTION	1
1.1 General.....	1
1.2 Tidal Power Harnessing.....	2
1.3 Mechanical Geometry and Technical Definitions	4
1.3.1 Turbine Geometry.....	4
1.3.2 Blade Geometry	6
1.3.3 Effects of Lift, Drag, and Angle of Attack	8
1.3.4 Performance Characteristics	9
1.4 Model Scaling.....	10
1.5 Thesis Overview	12
2. EXPERIMENTAL TEST METHODS	14
2.1 Experimental Setup.....	14
2.1.1 Facility	14
2.1.2 Apparatus	16

2.1.3 Operation.....	17
2.2 Measured Values.....	17
2.3 Experimental Test Methods	19
2.3.1 Preliminary Tests	19
2.3.2 Experimental Testing Procedure.....	21
3. SYMMETRICAL FOIL RESULTS	23
3.1 Geometry of NACA 0018 Blades	23
3.2 Two-Blade Test Results	24
3.3 Four-Blade Test Results.....	29
3.4 Conclusions.....	35
4. CAMBERED FOIL RESULTS	37
4.1 Geometry of NACA 4418 Blades	37
4.2 Two-Blade Test Results	38
4.3 Comparison to Symmetric Foils	43
5. REVERSE CAMBER FOIL RESULTS.....	45
5.1 Geometry of Reverse Camber NACA 4418 Blades	45
5.2 Two-Blade Test Results	46
5.3 Comparison to Symmetric and Regular Camber Foils	51
5.4 Conclusions.....	54

REFERENCES	55
APPENDIX A. SCALING CALCULATIONS	55
APPENDIX B. EXPERIMENTAL TEST MATRIX	58
APPENDIX C. EFFECTS OF TEMPERATURE	63
APPENDIX D. EFFECTS OF WATER COLUMN HEIGHT	65
APPENDIX E. FILTERING METHODS	68
BIOGRAPHY OF THE AUTHOR.....	72

LIST OF TABLES

Table B.1	Experimental test matrix for two-bladed NACA 0018 foils at a water temperature of 67 ⁰ F with $U_{\infty} = 0.8$ m/s, $\sigma = 0.171$, and water column height at 40 inches	58
Table B.2	Experimental test matrix for four-bladed NACA 0018 foils at a water temperature of 67 ⁰ F with $U_{\infty} = 0.8$ m/s, $\sigma = 0.343$, and water column height at 40 inches	59
Table B.3	Experimental test matrix for two-bladed NACA 0018 foils at a water temperature of 48 ⁰ F with $U_{\infty} = 0.8$ m/s, $\sigma = 0.343$, and water column height at 40 inches	60
Table B.4	Experimental test matrix for two-bladed cambered NACA 4418 foils at a water temperature of 48 ⁰ F with $U_{\infty} = 0.8$ m/s, $\sigma = 0.171$, and water column height at 40 inches	61
Table B.5	Experimental test matrix for two-bladed reverse cambered NACA 4418 foils at a water temperature of 48 ⁰ F with $U_{\infty} = 0.8$ m/s, $\sigma = 0.171$, and water column height at 40 inches	62
Table D.1	Experimental test matrix for two-bladed NACA 0018 foils at water column heights from 30 to 44 inches in two degree increments.....	65

LIST OF FIGURES

Figure 1.1	Renewable electricity generation for the United States from 2008-2012 (EIA, 2011).....	1
Figure 1.2	The second largest tidal barrage in the world, La Rance Tidal Power Plant, located in Brittany, France.....	2
Figure 1.3	Model of Ocean Renewable Power Company’s cross-flow turbine generator unit	4
Figure 1.4	Side view of a Darrieus style turbine used in this testing	5
Figure 1.5	Diagram of the side view of the turbine to identify how toe angle, α_t , is determined and referenced	6
Figure 1.6	An example of a straight blade profile for a cross-flow turbine.	7
Figure 1.7	Representation of lift and drag forces on a symmetrical blade at a positive angle of attack	8
Figure 1.8	The Cobscook Bay in Eastport, Maine where Ocean Renewable Power Company installed their TidGen™ Power System.....	12

Figure 2.1	University of Maine tow tank located at the Aquaculture Research Center (ARC)	14
Figure 2.2	Cross-sectional schematic of the tow tank and turbine router	15
Figure 2.3	Turbine beam mount on tow tank carriage at the University of Maine tow tank at the Aquaculture Research Center.....	15
Figure 2.4	Turbine endplate with attached angle indicators and blades	16
Figure 2.5	Model of the turbine motor, rectangular box tube, torque load cell, thrust load cells, and turbine encoder	18
Figure 2.6	Drive-train friction and end plate drag curves as a function of turbine angular velocity	20
Figure 2.7	End plate drag curve as a function of motor frequency	21
Figure 3.1	Profile view of the symmetrical NACA 0018 blade.....	23
Figure 3.2	Power coefficient contour plot for two-blade testing of 3-D printed NACA 0018 blades with solidity ratio $\sigma = 0.171$ and inflow velocity $U_\infty = 0.8$ m/s.....	25

Figure 3.3	Power coefficient curves for two-blade testing of 3-D printed NACA 0018 blades from toe angles from -3° to 0° with solidity ratio $\sigma = 0.171$ and inflow velocity $U_{\infty} = 0.8$ m/s.....	26
Figure 3.4	Power coefficient curves for two-blade testing of 3-D printed NACA 0018 blades from toe angles from 0° to $+6^{\circ}$ with solidity ratio $\sigma = 0.171$ and inflow velocity $U_{\infty} = 0.8$ m/s.....	27
Figure 3.5	Power coefficient curves for two-blade testing of 3-D printed NACA 0018 blades from toe angles from 0° to $+6^{\circ}$ with solidity ratio $\sigma = 0.171$ and inflow velocity $U_{\infty} = 0.8$ m/s.....	28
Figure 3.6	Experimental testing by Sheldahl and Klimas (1981) for NACA 0018 foils showing lift coefficient related to angle of attack.....	29
Figure 3.7	Power coefficient contour plot for four-blade testing of 3-D printed NACA 0018 blades with solidity ratio $\sigma = 0.343$ and inflow velocity $U_{\infty} = 0.8$ m/s.....	31
Figure 3.8	Power coefficient curves for four-blade testing of 3-D printed NACA 0018 blades from toe angles from -4° to 0° with solidity ratio $\sigma = 0.343$ and inflow velocity $U_{\infty} = 0.8$ m/s.....	32

Figure 3.9	Power coefficient curves for four-blade testing of 3-D printed NACA 0018 blades from toe angles from 0^0 to $+4^0$ with solidity ratio $\sigma = 0.343$ and inflow velocity $U_\infty = 0.8$ m/s.....	33
Figure 3.10	Power coefficient curves for four-blade testing of 3-D printed NACA 0018 blades from toe angles from $+4^0$ to $+10^0$ with solidity ratio $\sigma = 0.343$ and inflow velocity $U_\infty = 0.8$ m/s.....	34
Figure 3.11	Power coefficient curve comparison for two-blade and four-blade testing of NACA 0018 blades from toe angles from $+4^0$ to $+6^0$ and inflow velocity $U_\infty = 0.8$ m/s	36
Figure 4.1	Profile view of the symmetrical NACA 4418 blade.....	37
Figure 4.2	Power coefficient contour plot for two-blade testing of 3-D printed NACA 4418 blades with solidity ratio $\sigma = 0.171$ and inflow velocity $U_\infty = 0.8$ m/s.....	39
Figure 4.3	Power coefficient curves for two-blade testing of 3-D printed NACA 4418 blades from toe angles from -4^0 to 0^0 with solidity ratio $\sigma = 0.171$ and inflow velocity $U_\infty = 0.8$ m/s.....	40

Figure 4.4	Power coefficient curves for two-blade testing of 3-D printed NACA 4418 blades from toe angles from 0^0 to $+6^0$ with solidity ratio $\sigma = 0.171$ and inflow velocity $U_\infty = 0.8$ m/s.....	41
Figure 4.5	Power coefficient curves for two-blade testing of 3-D printed NACA 4418 blades from toe angles from $+6^0$ to $+10^0$ with solidity ratio $\sigma = 0.171$ and inflow velocity $U_\infty = 0.8$ m/s.....	42
Figure 4.6	Power coefficient comparison curves for two-blade testing of 3-D printed NACA 4418 blades and NACA 0018 blades	44
Figure 5.1	Profile view of the reverse camber NACA 4418 blade	45
Figure 5.2	Power coefficient contour plot for two-blade testing of reverse camber 3-D printed NACA 4418 blades with solidity ratio $\sigma = 0.171$ and inflow velocity $U_\infty = 0.8$ m/s	47
Figure 5.3	Power coefficient curves for two-blade testing of reverse camber 3-D printed NACA 4418 blades from toe angles from 0^0 to $+4^0$ with solidity ratio $\sigma = 0.171$ and inflow velocity $U_\infty = 0.8$ m/s.....	48

Figure 5.4	Power coefficient curves for two-blade testing of reverse camber 3-D printed NACA 4418 blades from toe angles from $+4^{\circ}$ to $+7^{\circ}$ with solidity ratio $\sigma = 0.171$ and inflow velocity $U_{\infty} = 0.8$ m/s.....	49
Figure 5.5	Power coefficient curves for two-blade testing of reverse camber 3-D printed NACA 4418 blades from toe angles from $+7^{\circ}$ to $+10^{\circ}$ with solidity ratio $\sigma = 0.171$ and inflow velocity $U_{\infty} = 0.8$ m/s.....	50
Figure 5.6	Comparison of peak power coefficient curves for two-blade testing of 3-D printed NACA 0018 blades, NACA 4418 blades, and reverse camber NACA 4418 blades.....	52
Figure 5.7	Comparison of power coefficient curves for two-blade testing of 3-D printed NACA 0018 blades, NACA 4418 blades, and reverse camber NACA 4418 blades at $+6^{\circ}$ toe angle.....	53
Figure C.1	Comparison of power coefficient curves for two-blade testing of 3-D printed NACA 0018 blades at $+6^{\circ}$ toe angle	64
Figure D.1	Comparison of power coefficient curves for two-blade testing of 3-D printed NACA 0018 blades at $+6^{\circ}$ toe angle for varying water column height.....	66

Figure E.1	Comparison of filtered and unfiltered turbine frequency in Hz over time (Image source: deBree, 2010)	68
Figure E.2	Angular position output from the turbine encoder over time displayed as the original sawtooth and the modified sawtooth used to eliminate discontinuities (Image source: deBree, 2010)	69

LIST OF SYMBOLS

A	Area
A_c	Channel Cross-Sectional Area
A_t	Turbine Cross-Sectional Area
α	Angle of Attack
BR	Blockage Ratio
α_t	Toe Angle
C_p	Power Coefficient
L	Chord Length
d	Water Depth
λ	Tip Speed Ratio
μ	Fluid Dynamic Viscosity
n	Number of Blades
ρ	Fluid Density
R	Turbine Radius
Re	Reynolds Number
σ	Solidity Ratio
T	Rotor Torque
T'	Nondimensional Torque
U_∞	Inflow Velocity
ω	Turbine Angular Velocity
Fr	Froude Number

g	Gravitational Acceleration
F_L	Lift Force
F_D	Drag Force
F_T	Tangential Force
F_N	Normal Force
F_R	Resultant Force
L_D	Turbine Diameter Length
U_R	Relative Fluid Velocity
Fr_p	Froude Number of Prototype
Re_p	Reynolds Number of Prototype
ρ_p	Fluid Density of Prototype
μ_p	Fluid Dynamic Viscosity of Prototype
V_p	Inflow Velocity of the Prototype
L_p	Turbine Diameter Length of the Prototype
Fr_m	Froude Number of Model
Re_m	Reynolds Number of Model
ρ_m	Fluid Density of Model
μ_m	Fluid Dynamic Viscosity of Model
V_m	Inflow Velocity of Model
L_m	Turbine Diameter Length of Model

LIST OF ABBREVIATIONS

ASCII	American Standard Code for Information Interchange
ARC	Aquaculture Research Center
EIA	Energy Information Administration
LE	Leading Edge
MHK	Marine Hydrokinetics
NACA	National Advisory Committee for Aeronautics
ORPC	Ocean Renewable Power Company
TSR	Tip Speed Ratio
TE	Trailing Edge

CHAPTER 1

INTRODUCTION

1.1 General

Around the world, countries have started to make the transition to renewable energy. In the United States, the President has proposed an aggressive goal of generating 80% of our electricity from clean energy sources including tidal power by 2035. Since 2008, renewable energy generation has been steadily on the rise in the U.S., as seen in Fig 1.1.

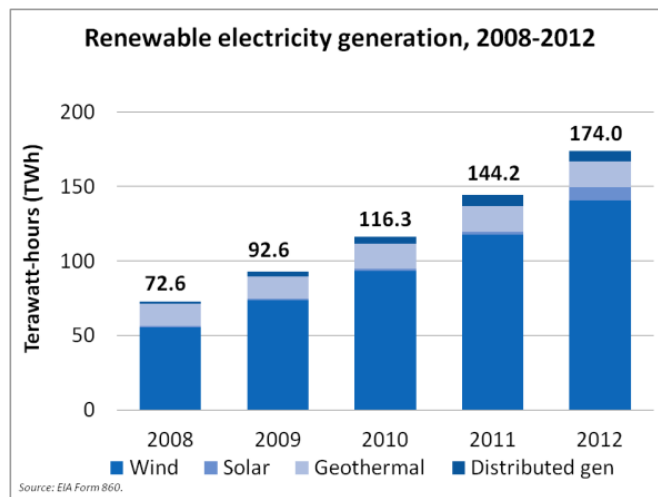


Figure 1.1 - Renewable electricity generation for the United States from 2008-2012 (EIA, 2011)

Although ocean energy is not a continuous source of power, it is extremely reliable, changing direction every six hours. The United States consumes approximately 4,000 terawatt hours (TWh) of electricity each year. The Department of Energy estimates the waves and tidal currents around the United States have the potential of generating a

maximum of 1,420 TWh which is more than a third of the total U.S. annual electricity consumption (DOE, 2012). The purpose of this thesis is to present experimental data in order to provide useful information to implement and expand the use of marine hydrokinetic (MHK) turbines.

1.2 Tidal Power Harnessing

Tidal power is typically harnessed in one of three ways: tidal barrage, tidal fence, or tidal turbine. Tidal barrages are dam-like constructions that stretch out across an inlet to collect tidal water through sluice gates during the incoming high tide (Fig. 1.2). The water is stored in a basin until the water empties through turbines on the ebb tide.

Although tidal barrages are efficient sources of tidal energy, they place a large impact on the environment in which they are emplaced.. Both species migration and navigation can be impeded by barrages. Turbidity and salinity of the water can also be affected, changing the overall ecosystem.



Figure 1.2 – The second largest tidal barrage in the world, La Rance Tidal Power Plant, located in Brittany, France. (Image source: <http://www.energybc.ca/profiles/tidal.html>)

Tidal fences are typically installed by mounting vertical axis turbines in a channel resembling large turnstiles. They are not as obstructive as a barrage, but may still impact the movement of larger marine animals and generally have a lower power output. Some researchers found that the fences could be designed with space between the caisson wall and rotor to allow fish to safely pass (Pelc, Fujita, 2002).

Tidal turbines are most commonly designed in either axial or cross-flow configurations. Axial flow turbines, although more efficient than cross-flow turbines, may be more harmful to marine life due to operation at higher tip speed ratios (TSR). Tip speed ratio, λ , as described in Eq. 1.1, is a non-dimensional value for characterizing operational turbine speed where R is the turbine radius, ω is the turbine angular velocity, and U_∞ is the inflow velocity. Axial flow turbines typically operate at a TSR range from 5 to 7 for maximum efficiency (Lokocz, 2012).

$$\lambda = \frac{R\omega}{U_\infty} \quad (1.1)$$

Cross-flow turbines have many desirable qualities despite having a lower efficiency than the axial design. One major difference is that the cross-flow turbine rotates in a constant direction independent of the direction of flow, simplifying the issue of reorienting the turbine during the change of tides which is necessary for axial flow turbines. Another advantage is that maximum efficiency is obtained at TSR much lower than axial turbines (around 1 to 2 TSR) thus reducing the risk to marine life in terms of mechanical strike (Polagye et al., 2010). One example of a cross-flow turbine in implementation, produced by Ocean Renewable Power Company (ORPC), can be seen in Fig. 1.3.

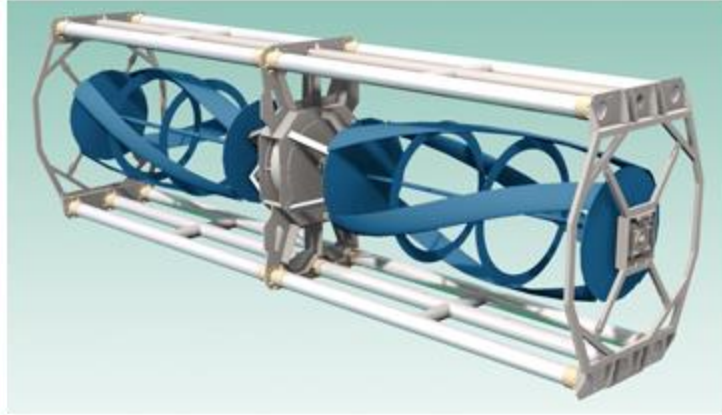


Figure 1.3 – Model of Ocean Renewable Power Company’s cross-flow turbine generator unit. (Image source: http://orpc.co/orpcpowersystem_turbinegeneratorunit.aspx)

1.3 Mechanical Geometry and Technical Definitions

1.3.1 Turbine Geometry

The Darrieus style turbine was chosen for the acquisition of the data set presented in this thesis. This simple design used straight blades arranged horizontally and parallel to the central axis of the turbine as seen in Fig. 1.4.

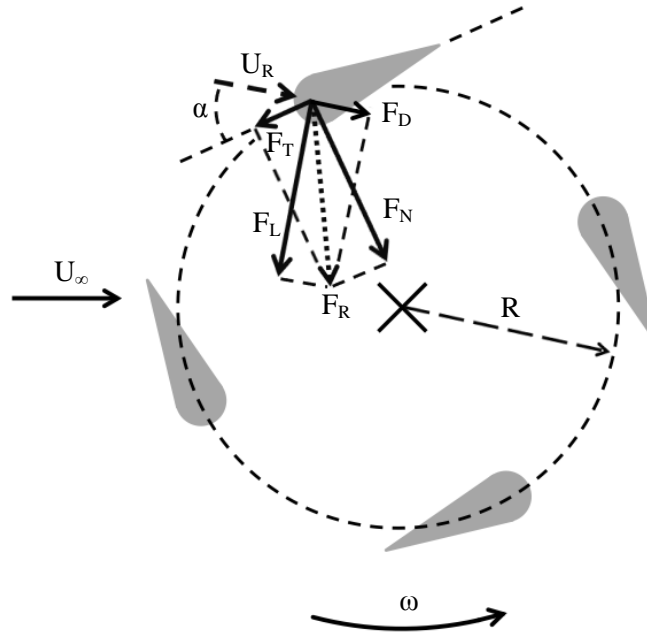


Figure 1.4 – Side view of a Darrieus style turbine used in this testing. The variable R is the turbine radius, ω is the angular velocity of the turbine, U_∞ is the inflow velocity of the water, α is the angle of attack, U_R is the relative velocity vector, F_D is the drag force, F_L is the lift force, F_R is the resultant force of the lift and drag forces, and F_T and F_N are the components of F_R that are tangential and normal to the chord length. (deBree, 2012)

For operation of this turbine, water passes through the turbine at an inflow velocity, U_∞ , which rotates the blades around the central axis. As the blades turn lift and drag forces on the blades produce torque. When the average torque for a revolution is positive, power is generated by the turbine. For cross-flow turbines, it is mostly the lift forces that produce the power in the system. To obtain the maximum lift, the blades can be mounted at different angles and be manufactured to have a camber, or bend, to obtain more power. This thesis will explore the effects of toe angle and camber to determine the optimal setup. Toe angle is defined as zero degrees when blades are mounted with the chord length perpendicular to the radius and the leading edge oriented toward the direction of rotation (Fig. 1.5).

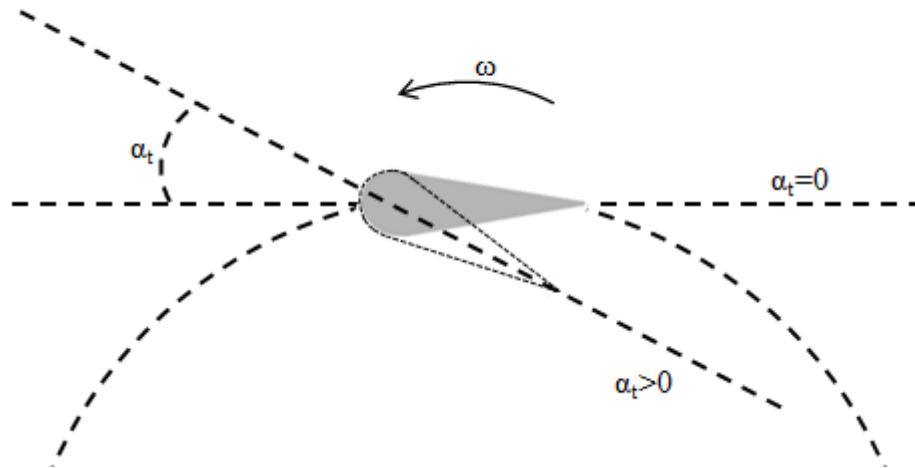


Figure 1.5 – Diagram of the side view of the turbine to identify how toe angle, α_t , is determined and referenced. The grey shaded foil is mounted where the toe angle is zero. The dashed outlined foil shows how the blade orientation could be changed to acquire a positive toe angle.

1.3.2 Blade Geometry

Straight blades in the cross-flow turbine can be manufactured in many different ways that can improve the overall turbine performance. Blade characteristics that are integral in cross-flow optimization include the blade shape, number of blades, and chord length.

These characterizations determine the solidity of the turbine, which is a ratio measurement of the blade area to the swept area of the blade (Shiono et al., 2000). The solidity ratio, σ , is calculated through Eq. 1.2, where n is the number of blades, L is the blade chord length, and R is the turbine radius. Most documented research has shown testing with a solidity ratio between approximately 0.1 and 0.5. Testing outside this range has a significantly decreased efficiency of 10% or less.

$$\sigma = \frac{nL}{2\pi R} \quad (1.2)$$

An example of a blade profile in Fig. 1.6 depicts the chord length, which extends from the leading edge (LE) of the blade to the trailing edge (TE) of the blade. Other important blade dimensions include blade thickness, camber line, and camber.

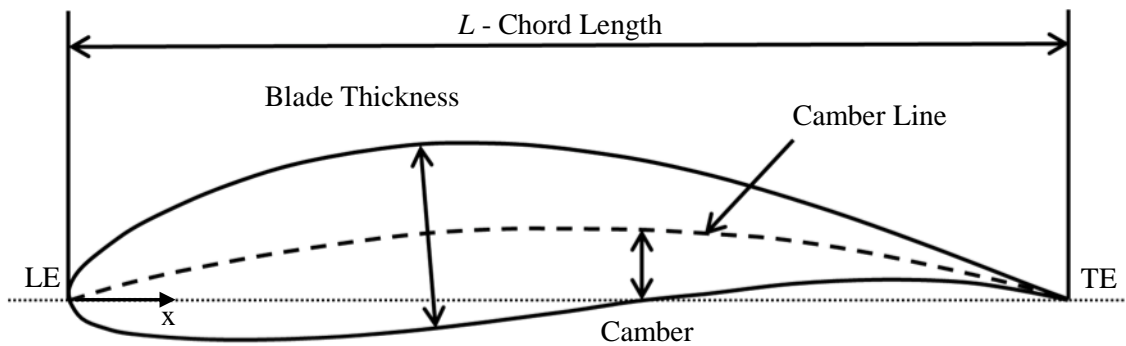


Figure 1.6 - An example of a straight blade profile for a cross-flow turbine. Geometry includes chord length, leading edge (LE), maximum thickness, maximum camber, camber line, and trailing edge (TE).

The turbine rotates in the direction of the leading edge. The distance between the leading edge and trailing edge is the chord length. Blade thickness changes along the length of the chord length. In this figure the blade has a slight curve which labels it as a cambered or asymmetric blade. Blades that lack this camber shape are termed symmetric blades. The midpoint of the upper and lower halves of the foil is the camber line. The distance from the camber line to the x-axis is the camber. Typically, the maximum camber is referenced when identifying blade characteristics (Nakayama, 1998).

This turbine apparatus has been tested with many different types of blades. The first testing by Bates (2010) included wooden blades. These foils were upgraded by manufacturing 3-D printed plastic blades and carbon fiber blades (Lokocz, 2010).

Testing by deBree showed that although the carbon fiber blades were much more rigid

than the 3-D printed plastic blades, there was negligible difference in their performance, varying by only 0.3%.

1.3.3 Effects of Lift, Drag, and Angle of Attack

The elements of lift and drag can change greatly depending on the angle of attack of the blades, therefore increasing or decreasing the overall efficiency of the turbine. Angle of attack is defined as the angle between the chord line and the relative velocity vector as seen in Fig. 1.7 where F_L is the lift force and F_D is the drag force. In general, the lift coefficient and drag coefficient are both zero at an angle of attack of zero degrees for symmetrical blades. As the angle of attack increases, so does the lift coefficient until maximum lift is reached and stall occurs. The drag coefficient increases to the stall point as well, but not to the magnitude of the lift coefficient. After the stall point, the drag coefficient increases rapidly and turbine performance is not easily predictable. When using cambered blades, the angle at which the lift coefficient is zero changes.

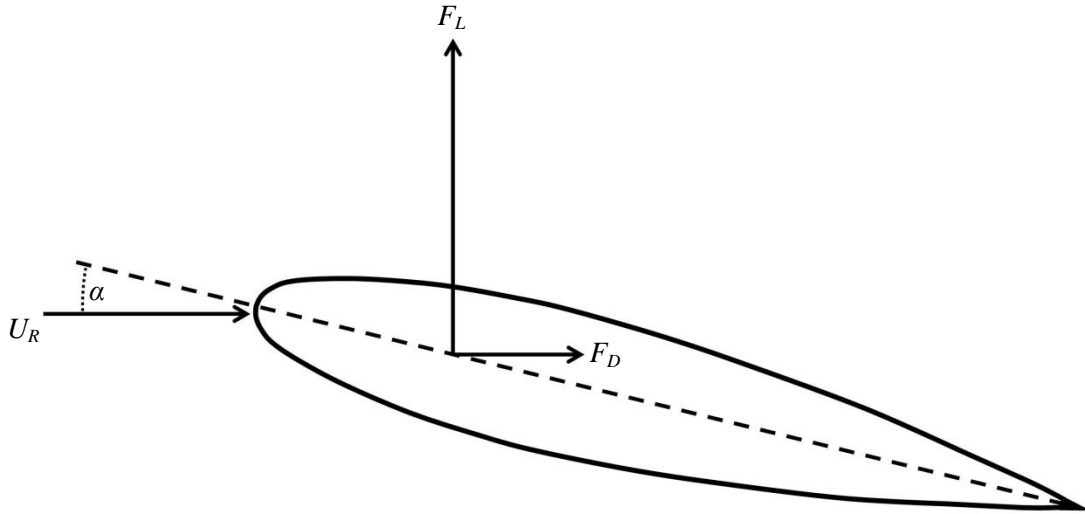


Figure 1.7 – Representation of lift and drag forces on a symmetrical blade at a positive angle of attack. F_L is the lift force, F_D is the drag force, α is the angle of attack, and U_R is the relative velocity of the fluid.

1.3.4 Performance Characteristics

For cross-flow turbine designs, there are several parameters that can be used to describe the performance characteristics. Tip speed ratio, as mentioned earlier in this chapter, describes the ratio of angular velocity of the turbine to the inflow velocity. Another parameter, the power coefficient, describes the overall efficiency of the turbine. It is the main focus in turbine design. The power coefficient is calculated by comparing the power produced by the turbine to the maximum possible power available for a fluid at a given velocity moving through a cross sectional area of the turbine (Eq. 1.3). In this equation, T is the instantaneous torque, ω is the angular velocity of the turbine, ρ is the density of the fluid, A_t is the cross sectional area of the turbine, and U_∞ is the inflow velocity. The power coefficient is averaged for each instantaneous torque value to find the overall average power coefficient for a certain TSR and inflow velocity.

$$C_p = \frac{T\omega}{\frac{1}{2}\rho A_t U_\infty^3} \quad (1.3)$$

Another parameter that is used in turbine design is the nondimensionalized torque, which can be used to estimate loads on a full scale turbine. In Eq. 1.4, nondimensionalized torque, T' , is defined where T is the rotor torque, ρ is the density of the fluid, A_t is the cross sectional area of the turbine, R is the radius of the turbine, and U_∞ is the inflow velocity.

$$T' = \frac{T}{\frac{1}{2}\rho A_t R U_\infty^2} \quad (1.4)$$

To calculate the nondimensional torque for experimental testing, the data was bin-averaged to determine the nondimensional torque as a function of angular position.

1.4 Model Scaling

Variations in Reynolds number affect the lift and drag produced. As the Reynolds number increases the effect of Reynolds number variations on the lift and drag coefficients decreases. Reynolds number is a parameter that can be used to scale turbine devices (Eq. 1.5).

$$Re = \frac{\rho U_\infty L_D}{\mu} \quad (1.5)$$

In this equation, ρ is the density of the fluid, U_∞ is the fluid reference velocity, L_D is the reference length, and μ is the dynamic viscosity of the water. For this thesis, the fluid reference velocity was the inflow velocity and the length reference was the turbine diameter. In many cases, experimental testing has found that limitations in flow velocity prohibit replications of full scale Reynolds number conditions (McAdam et al., 2009). As a result, Froude number scaling is commonly used instead of Reynolds number scaling. Both cannot be scaled at the same time since Reynolds number relies on a velocity-length product while Froude number is dependent upon velocity divided by square root of the length. For proper Reynolds number scaling, the inflow velocity would have to increase as the size of the model decreased which becomes inhibitive when designing experimental tests on a model. Since the model in this study is more than ten times smaller than the prototype, velocities would need to be upwards of 23m/s to ensure dynamic similitude, which is not possible in a typical tow tank.

In this study, the Froude number was used to verify scaling parameters, which provides a conservative amount of power produced in testing since a lower Reynolds number in model testing would reduce turbine performance compared to the full scale prototype (McAdam et. al, 2009). The Froude number, Eq. 1.6, relates the inflow velocity, U_∞ , to the square root of gravitational acceleration, g , and the turbine diameter, L_D . Eq. 1.7 relates how the scale model and prototype compare in terms of dynamic similitude, where the Froude numbers of the scale model, denoted with subscript (m), and prototype, subscript (p) are equal.

$$Fr = \frac{U_{\infty}}{\sqrt{gL_D}} \quad (1.6)$$

$$\frac{U_{\infty(m)}}{\sqrt{gL_{D(m)}}} = \frac{U_{\infty(p)}}{\sqrt{gL_{D(p)}}} \quad (1.7)$$

In this thesis, the model is the cross-flow turbine located at the University of Maine tow tank. The model is being compared to the dimensions of Ocean Renewable Power Company's cross-flow turbine located in the Cobscook Bay in Eastport, Maine (Fig. 1.8). With the model operating at an inflow velocity of 2.62 ft/s, the model was properly Froude scaled to the prototype. See Appendix A for scaling calculations.

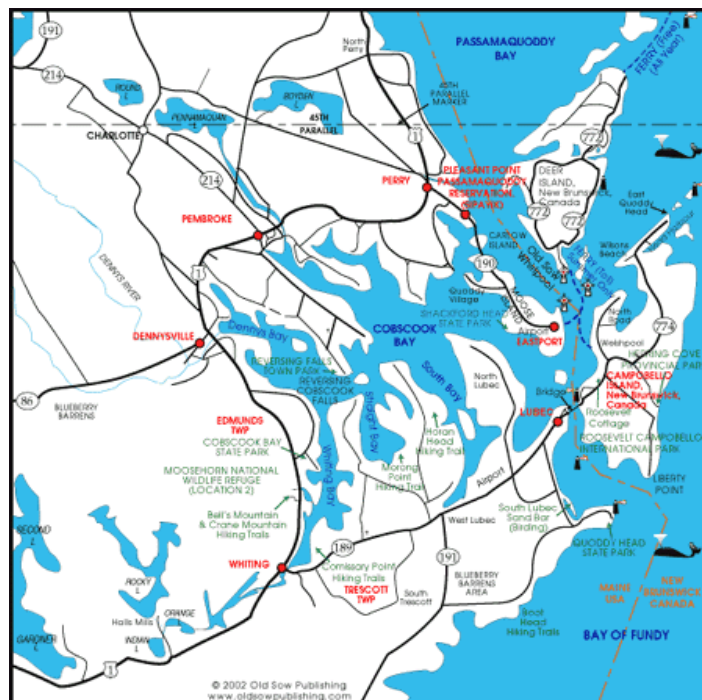


Figure 1.8 – The Cobscook Bay in Eastport, Maine where Ocean Renewable Power Company installed their TidGen™ Power System. Information specific to this setup was used for scaling purposes. (Image source: www.cobscookbay.com)

1.5 Thesis Overview

This thesis provides a detailed data set for two and four-bladed cross-flow turbines. Two different blade profiles were used at varying toe angles to compile an extensive set of data. The first profile chosen was the NACA 0018, a symmetrical blade with 3.5" chord length. The second profile, NACA 4418, was selected due to its similarities to the NACA 0018. The NACA 4418 has the same chord length and thickness as the NACA 0018, but has a slight camber equal to 4% of the chord length. The NACA 4418 was also tested in the reverse camber orientation, which will be discussed in a later chapter.

The objective of this thesis was to explore several hypotheses that would determine the optimal parameters for cross-flow turbine operation. The first hypothesis was that two-blade symmetrical foil turbines are more efficient than four-blade symmetrical foil turbines. The next study involved the comparison of the symmetrical foils with the cambered foils. Since the symmetrical and cambered foils have the same chord length, the solidity ratio remained constant in both sets of data. The results from this study led into the final hypothesis, which anticipated that the symmetrical blades would be more efficient than both the cambered and reverse cambered blades.

CHAPTER 2

EXPERIMENTAL TEST METHODS

2.1 Experimental Setup

2.1.1 Facility

Experimental testing was executed at the University of Maine tow tank at the Aquaculture Research Center (ARC) (Fig. 2.1). The tank is 100 feet long, 8 feet wide, and has a maximum depth of 3.5 feet (Fig. 2.2). The turbine was mounted to an aluminum carriage resting on steel rails running the length of both sides of the tow tank. The carriage measured 4 feet long, 8 feet wide, and 1 foot high and moves along the rails by a wire wound around a drum powered by an AC motor. The carriage is powered by an extending cable that is hung from a track attached to the ceiling. On the front of the carriage, a beam is fixed to allow attachment and detachment of the turbine as needed (Fig 2.3).

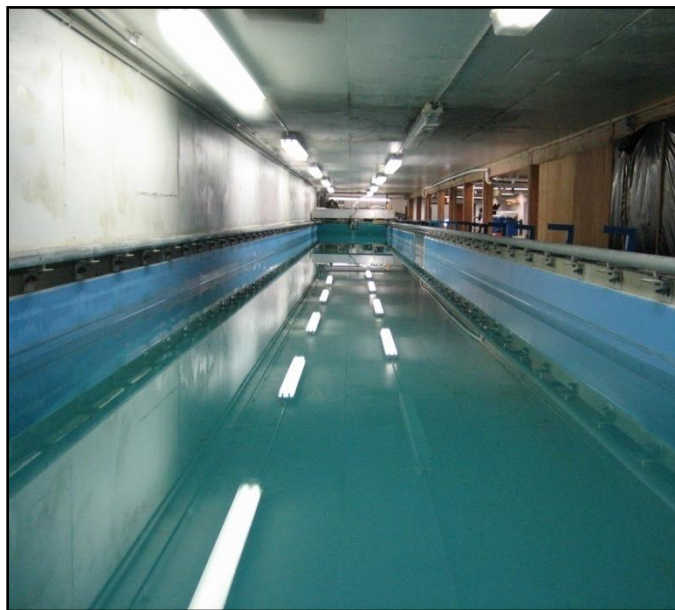


Figure 2.1 – University of Maine tow tank located at the Aquaculture Research Center

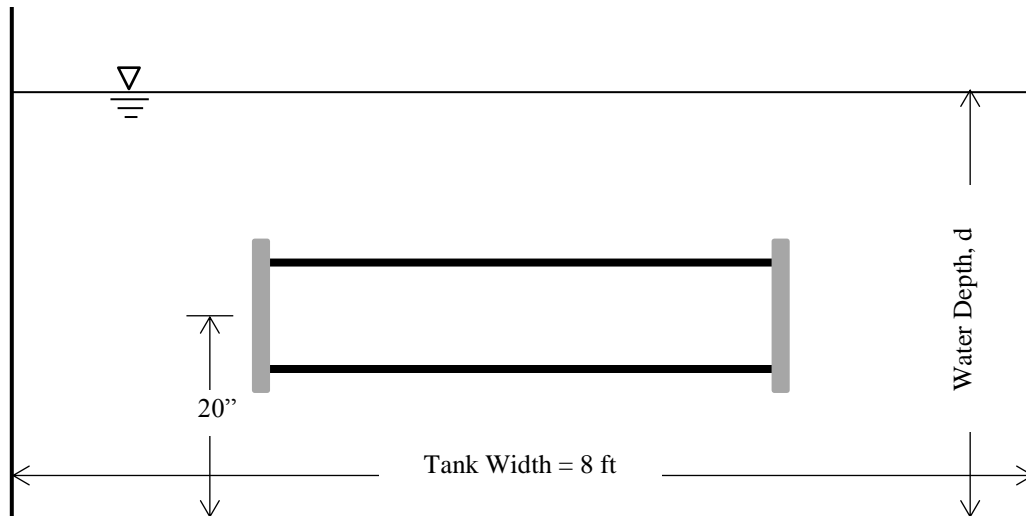


Figure 2.2 – Cross-sectional schematic of the tow tank and turbine router. Tank width and distance from the center of the turbine to the bottom of the tank remained constant for all testing. The turbine is centered along the tank width. Water depth, d , was 40 inches for all testing with the exception of the varying depth study where water depth ranged from 30 inches to 44 inches.



Figure 2.3 – Turbine beam mount on tow tank carriage at the University of Maine tow tank at the Aquaculture Research Center (ARC)

2.1.2 Apparatus

Originally designed by Bates (2010) and later upgraded by deBree (2012) and Cameron (2012), the turbine is designed to allow for expedient adjustment or changing of blades. Currently, the end plates allow the turbine to be set up in two and four-blade configurations with blades spanning 30 inches (Fig. 2.3). Angle indicators were designed along with indicator alignment holes to provide an easy method of adjusting the toe angle from -10° to $+10^{\circ}$ with one degree increments from -10° to -7° , half degree increments from -6.5° to $+3^{\circ}$, and one degree increments from $+3^{\circ}$ to $+10^{\circ}$. Toe angles were verified using the Coordinate Measuring Machine (CMM). By removing the angle indicators, the blades can be removed, added, or swapped out with a new profile quickly and easily.

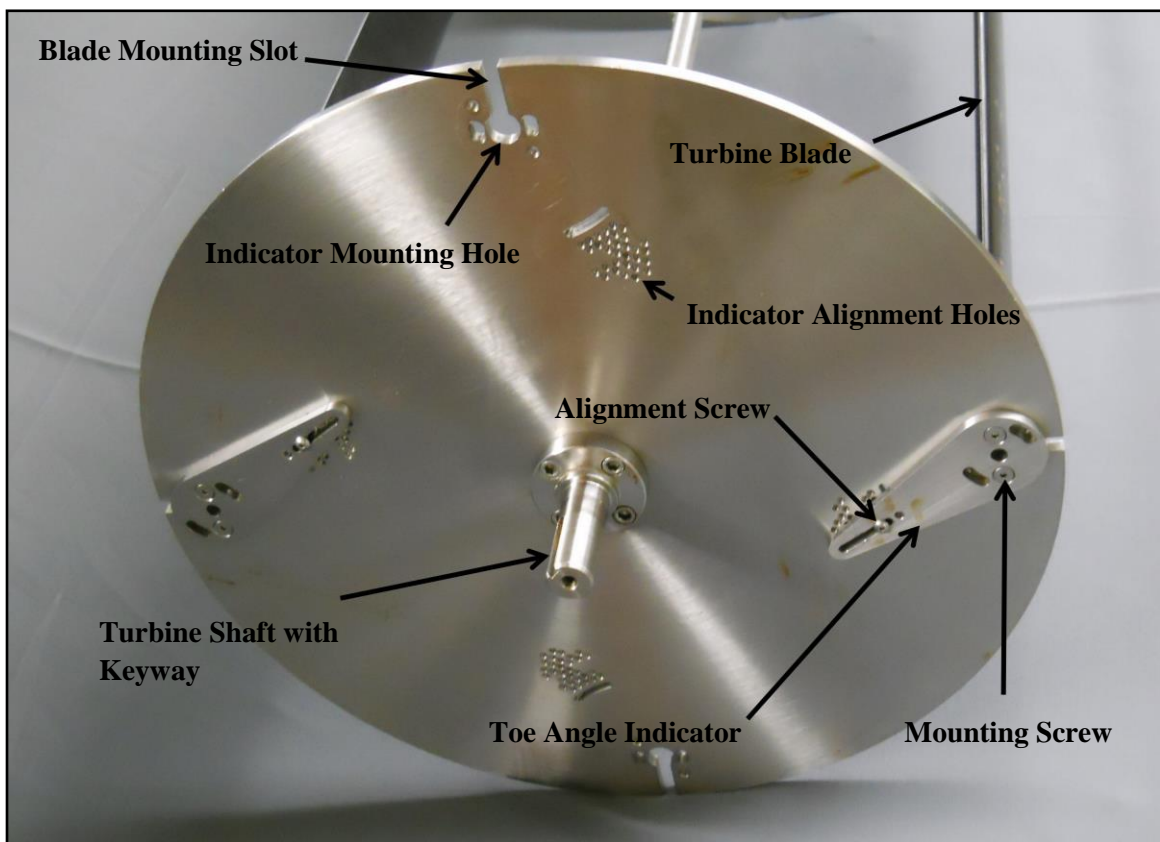


Figure 2.4 – Turbine endplate with attached angle indicators and blades (deBree, 2012)

2.1.3 Operation

The turbine operated with a motor and controller coupled with a gear head mounted to a rectangular box tube that provided support to the turbine. The gear head was connected to a drive train which rotated the turbine via chain drive that extended down to the turbine rotor through aluminum shrouds. All operation was conducted by remote desktop connection from a laptop to the onboard carriage computer.

LabView was utilized to control operation of the system through a program originally developed by Bates (2010), then upgraded by deBree (2012) and Cameron (2012). The program allowed input variables of inflow velocity and TSR. Other inputs to the system were controlled mechanically to include water column height, turbine height in the water column, toe angle, and the number of blades. Water column height was controlled by adding or draining water from the tow tank, turbine height was adjusted by moving the turbine up or down on the beam mount, and toe angle was adjusted and blades were added or removed from the endplates.

For all experimental testing, the following inputs were held constant: water column height, turbine height in the water column, and inflow velocity or carriage velocity. For the purpose of clarity, a ‘test set’ refers to a complete group of data for a certain blade profile and solidity at a range of toe angles. Each test set was organized in a test matrix (Appendix B) to define the range of TSR in order to capture the peak efficiency.

2.2 Measured Values

During each test run, the time, turbine angular velocity, and inflow velocity were measured along with the turbine torque to determine the efficiency of the turbine. Time

was recorded by a sampling rate clock. Turbine angular velocity was measured using a position encoder attached to the driveshaft by filtering the signal (Appendix E) and differentiating with respect to time from the gathered data. Inflow velocity was measured using a position encoder similar to the turbine encoder. Again, position was measured, the signal was filtered, and the data differentiated with respect to time. Turbine torque was measured using a load cell attached to the rectangular box tube, while the thrust data was collected using two horizontal load cells opposite the torque load cell (Fig. 2.4).

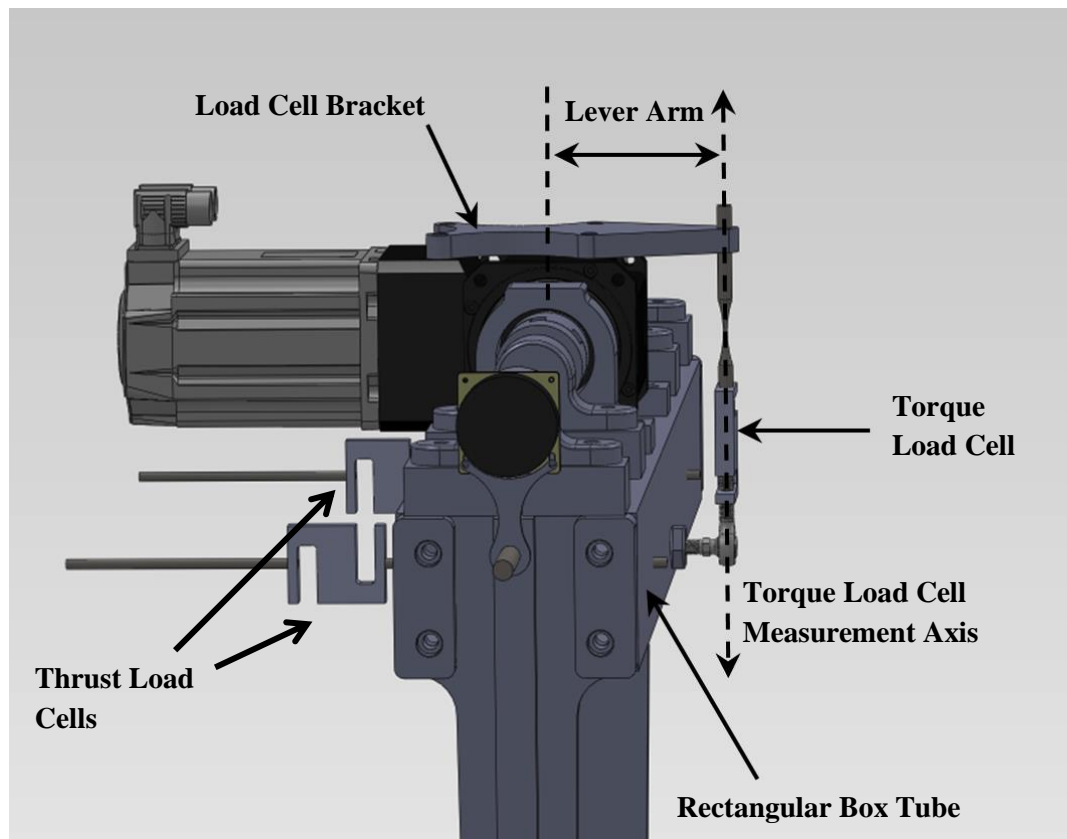


Figure 2.5 – Model of the turbine motor, rectangular box tube, torque load cell, thrust load cells, and turbine encoder.

2.3 Experimental Testing Methods

2.3.1 Preliminary Tests

Prior to the execution of each test set, several preliminary tests were performed to ensure accuracy of the system. The first test was to determine the uncertainty in the data. With the turbine attached to a dry mount outside of the water, known weights ranging from 0 to 18.14 kg were added to the turbine motor at a fixed distance from the turbine rotational axis. Each weight corresponded to an applied torque as determined by Eq. 2.1 where T is the applied torque, F is the force on the load cell, and l is the length of the lever arm.

$$T = Fl \quad (2.1)$$

The torque load cell output was a linear function of the load applied, so the slope and offset were found by using a linear regression. From the slope and intercept error the uncertainty was determined. To calculate the error, the output was used from a weight just heavier than the load for an actual test run (0.374 N). This was multiplied by the lever arm of the applied load to determine the error of the torque from the force measurement, which was 0.0726 N·m (deBree, 2012).

Another important preliminary test was to determine the friction torque and end plate drag. To find the friction, the turbine was rotated out of the water on a dry mount. Operating the turbine at a variety of rotational speeds, the torque and angular velocity were determined and plotted as seen in Fig. 2.5.

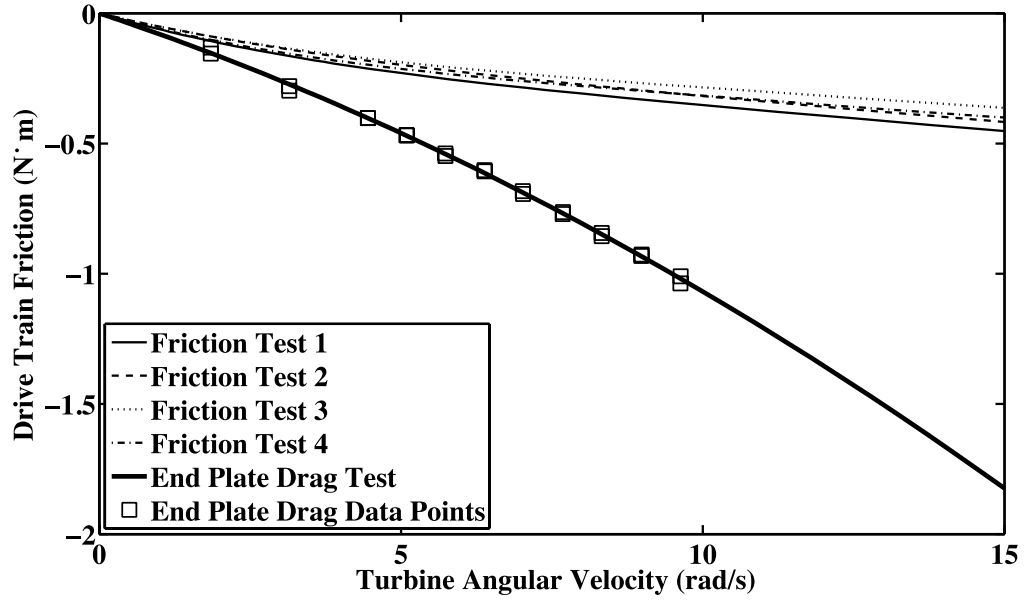


Figure 2.6 - Drive-train friction and end plate drag curves as a function of turbine angular velocity. Drive-train friction curves were obtained outside the tow tank on the dry mount post, while end plate drag tests were performed inside the tank. Both tests were performed with blades removed and center bar mounted (deBree, 2012). The center bar, with a diameter of only 0.01905 m, had a drag force of 1.39 N and was therefore determined to be negligible in the calibration.

The end plate drag was the final preliminary test before performing test matrix data collection. The blades were removed and a bar was installed in the center of the turbine. With this setup, tests were performed at an inflow velocity of 0.8 m/s at the same TSR range as identified in the test matrix about to be run. The data was analyzed and plotted as the end plate drag curve (Fig. 2.6).

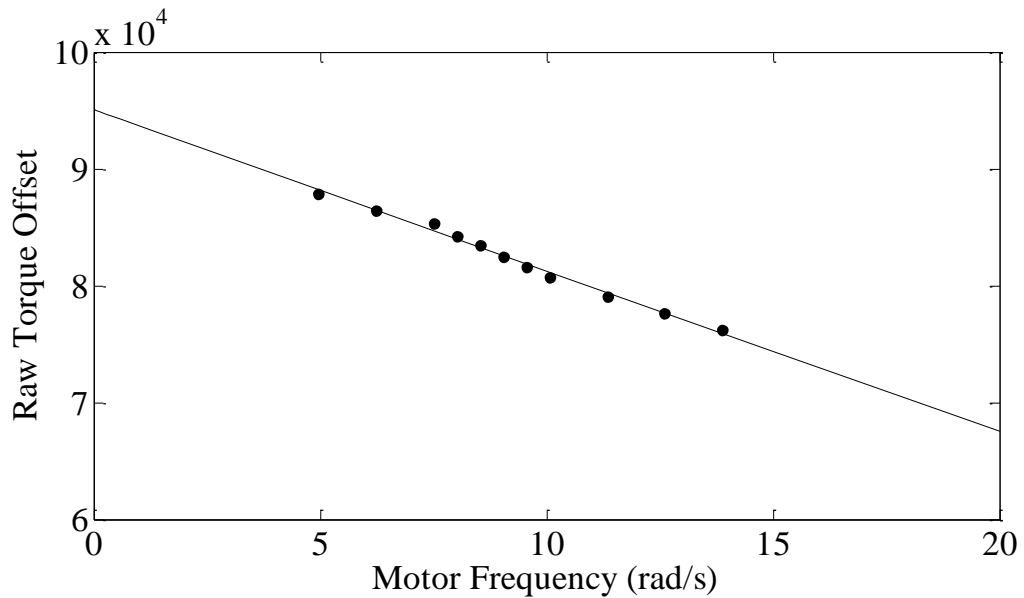


Figure 2.7 – End plate drag curve as a function of motor frequency.

2.3.2 Experimental Testing Procedure

Each test set was organized and listed in a test matrix (Appendix B) to define the TSR for each toe angle and blade profile. The bar was removed from the center of the turbine and the blades were installed. The torque offset was determined by rotating the turbine slowly to find the preload on the torque load cell. The mean torque of the torque load cell was then used for the analysis of the data in the test set by establishing the preload on the system.

For each experimental test, the carriage was accelerated down the length of the tank to the specified velocity and TSR with the turbine attached to the turbine beam mount on the carriage. For all testing, the length of each run was set to 65 feet. The data started recording after the acceleration period at a sampling rate of 2 kHz. Data was written to a binary file during the test, and then converted to ASCII once the test run is complete.

Each power coefficient curve corresponds to a single toe angle where individual points represent an experimental test at a single TSR.

CHAPTER 3

SYMMETRICAL FOIL RESULTS

The symmetrical NACA 0018 foils were tested in two and four-blade configurations at multiple toe angles. Power coefficient curves were compared for each setup to find the peak efficiency and optimal toe angle. The goal of this comparison was to determine if a lower solidity turbine was more efficient than higher solidity turbines, similar to testing performed by Shiono et al. (2000).

3.1 Geometry of NACA 0018 Blades

The symmetrical profile of the NACA 0018 blade is shown in Fig. 3.1. The blades used in the testing had a 3.5 inch chord length. This blade design, and similar symmetrical profiles, such as the 0009, 0012, and 0015 used by Sheldahl and Klimas (1981), are commonly used in Darrieus vertical axis wind turbines (VAWT).

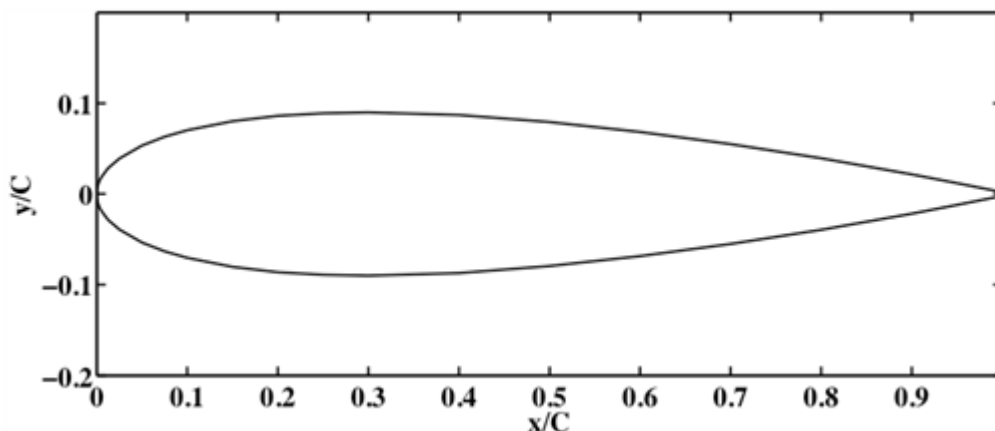


Figure 3.1 – Profile view of the symmetrical NACA 0018 blade

3.2 Two-Blade Test Results

Two-blade tests were conducted at toe angles from -3° to $+10^{\circ}$ in increments of one degree. Inflow velocity for all testing was set at 0.8 m/s with the turbine centered in the water column, which had a temperature of 67°F . With a solidity ratio of 0.171, it was estimated that the max power coefficient would be reached at a TSR between 1.6 to 2, based on experimental solidity data by Shiono et al. (2000). As a result, testing was done at a TSR range from 1 to 2.75 to ensure the peak was acquired.

The maximum power coefficient of 42.4% occurred at the $+6^{\circ}$ toe angle at a TSR of 1.6 as seen in Fig. 3.2 through 3.5. The $+6^{\circ}$ and $+5^{\circ}$ toe angles had very similar efficiency curves, varying at peak C_p by only 0.4% and no more than 2% in other parts of the curve. The results show that the efficiency increases steadily from -3° toe angle to the peak at $+6^{\circ}$. From toe angles of $+7^{\circ}$ to $+10^{\circ}$, although the efficiency decreases it does not decrease steadily, most likely due to blade stall after maximum lift is reached. Sheldahl and Klimas (1981) performed experimental testing for the lift and drag coefficients of the NACA 0018 blades at varying angle of attack that show this peak in the lift coefficient (Fig. 3.6).

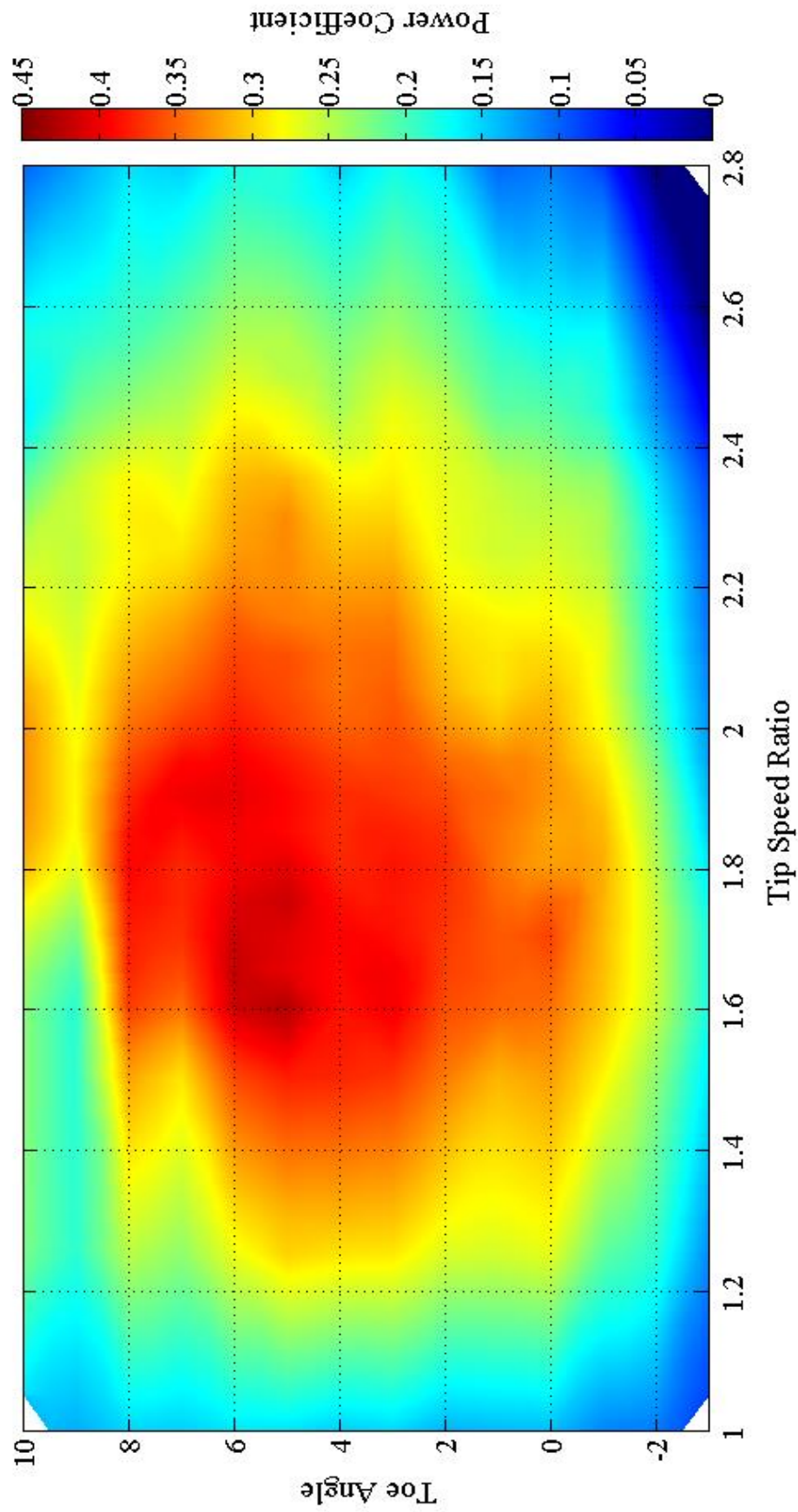


Figure 3.2 – Power coefficient contour plot for two-blade testing of 3-D printed NACA 0018 blades with solidity ratio $\sigma = 0.171$ and inflow velocity $U_\infty = 0.8$ m/s.

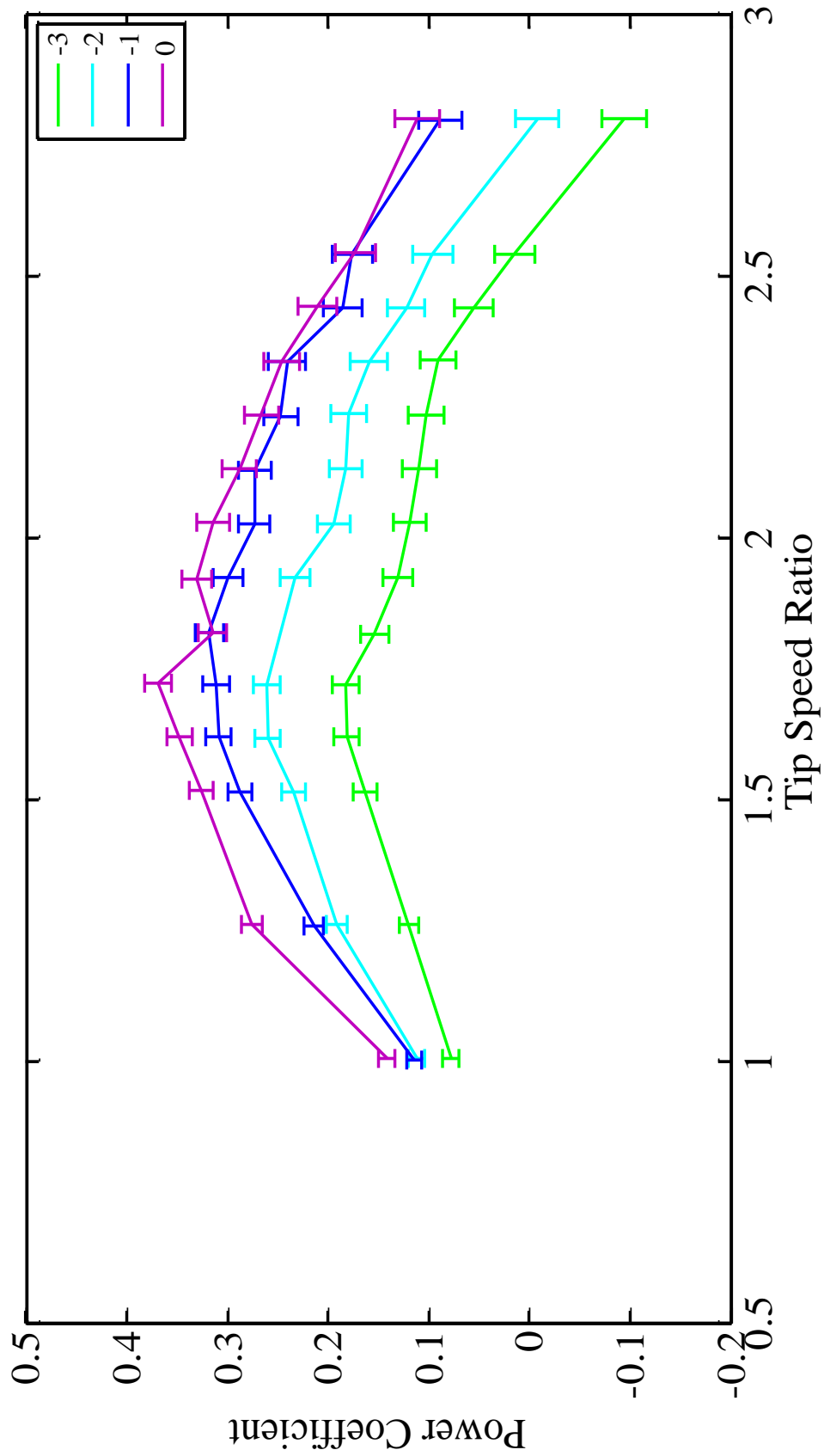


Figure 3.3 – Power coefficient curves for two-blade testing of 3-D printed NACA 0018 blades from toe angles from -3° to 0° with solidity ratio $\sigma = 0.171$ and inflow velocity $U_\infty = 0.8$ m/s.

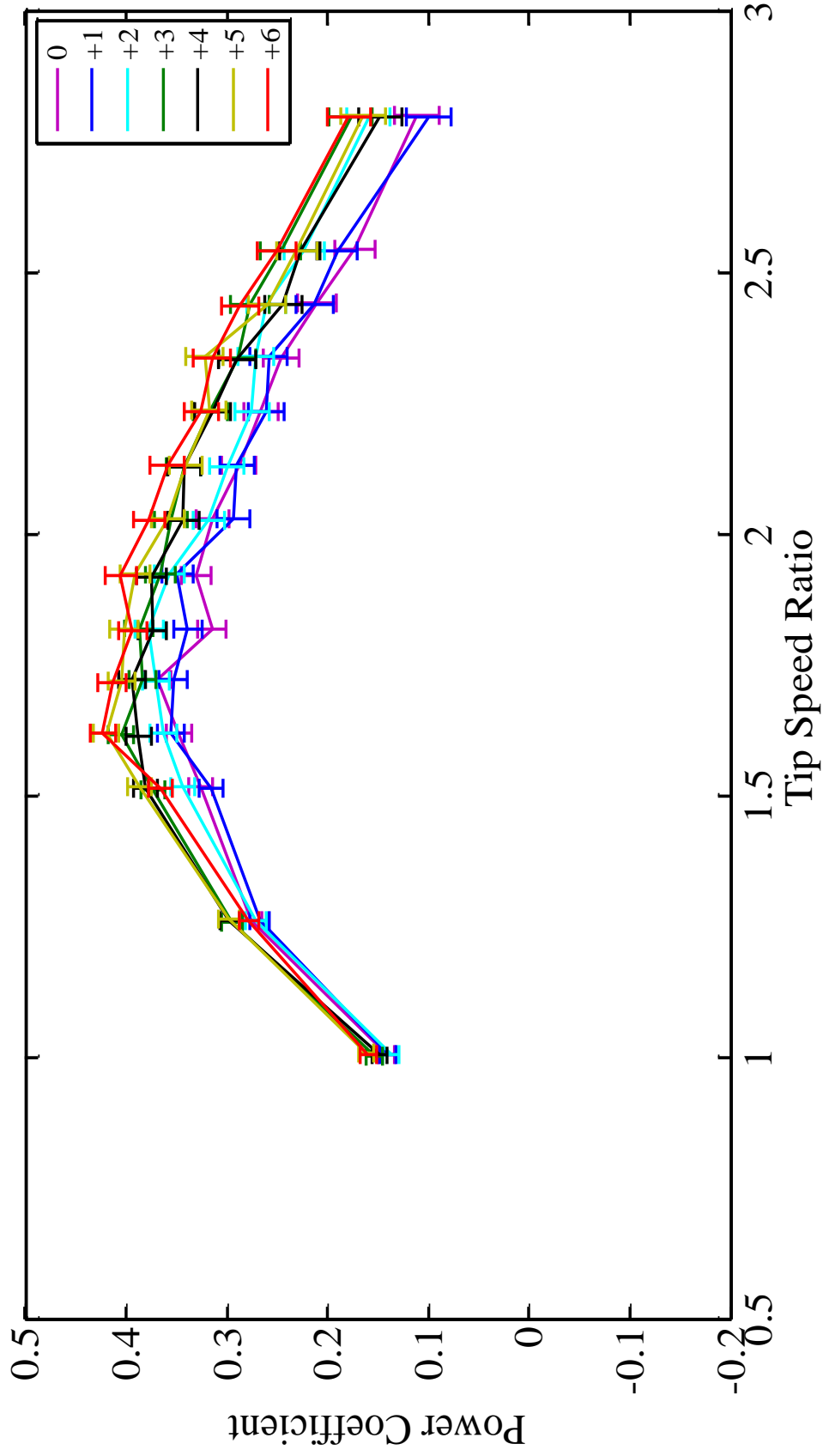


Figure 3.4 – Power coefficient curves for two-blade testing of 3-D printed NACA 0018 blades from toe angles from 0° to +6° with solidity ratio $\sigma = 0.171$ and inflow velocity $U_\infty = 0.8$ m/s.

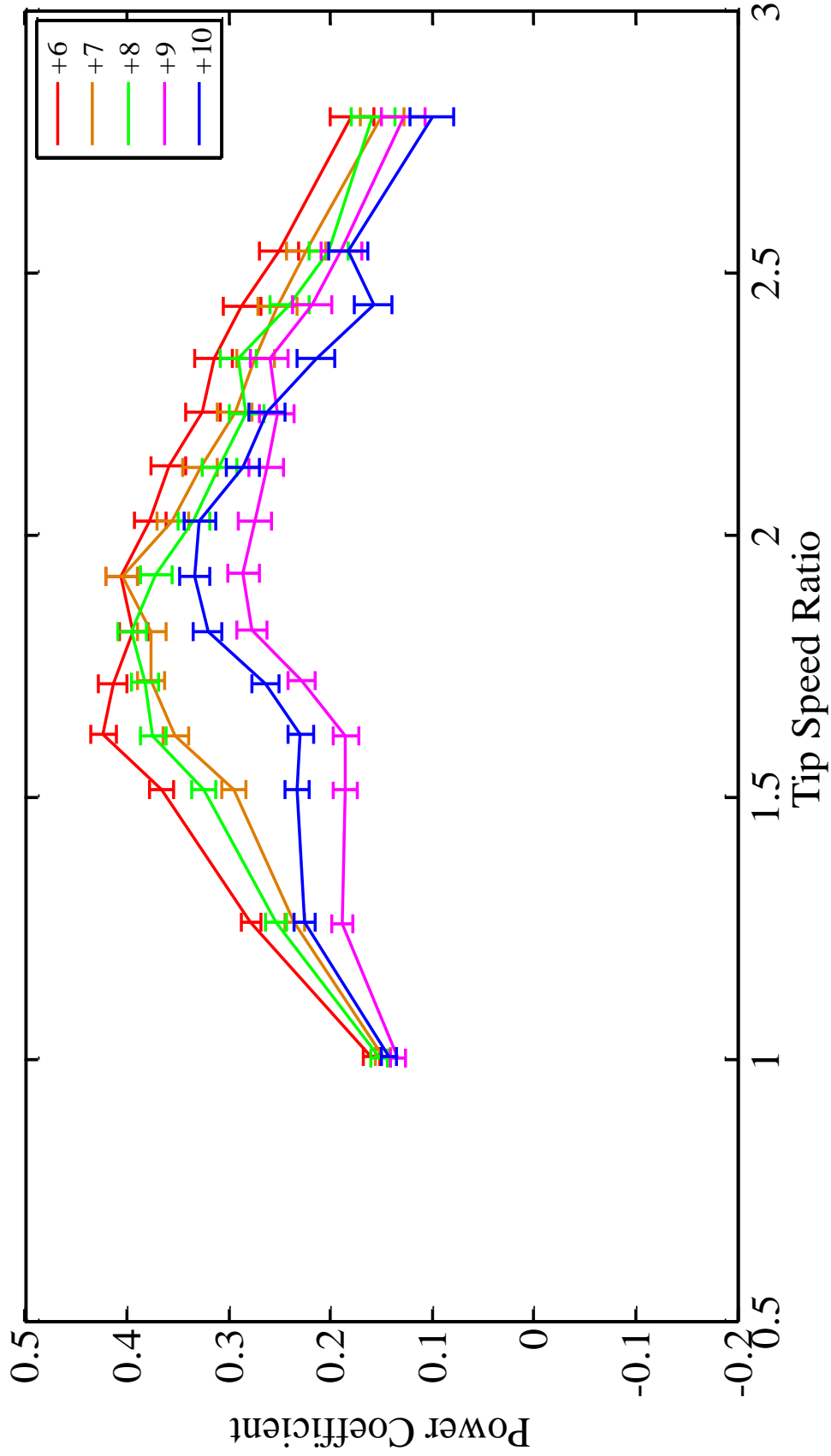


Figure 3.5 – Power coefficient curves for two-blade testing of 3-D printed NACA 0018 blades from toe angles from 0° to $+6^\circ$ with solidity ratio $\sigma = 0.171$ and inflow velocity $U_\infty = 0.8$ m/s.

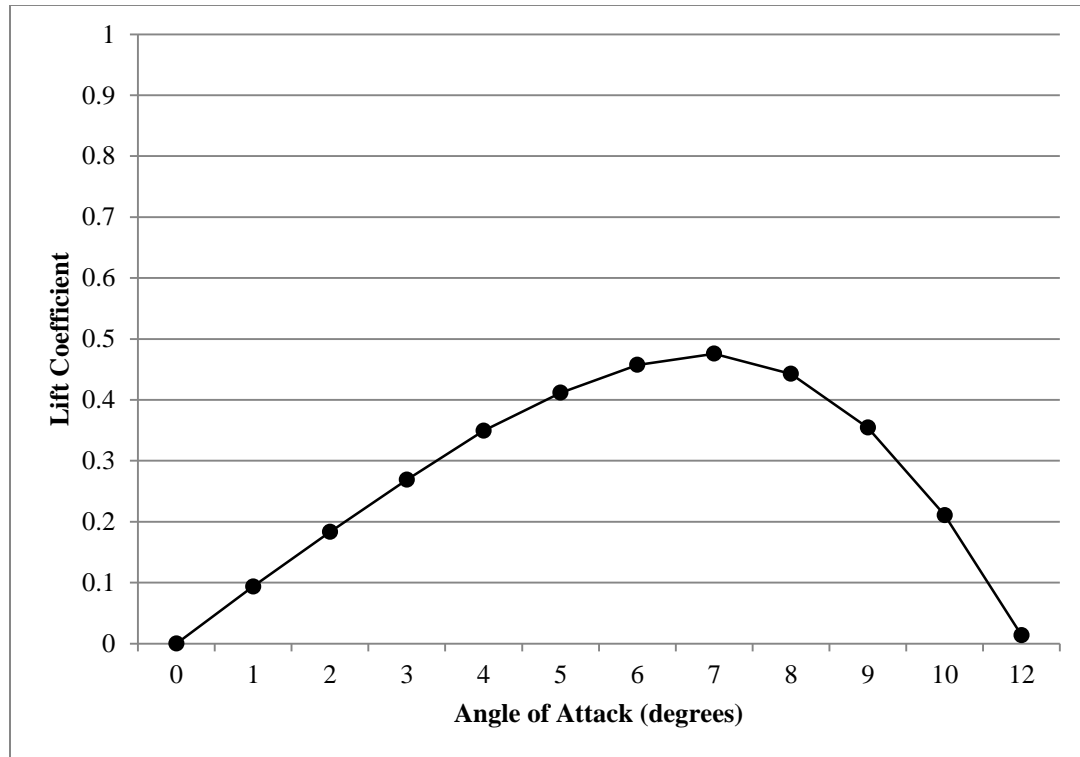


Figure 3.6 – Experimental testing by Sheldahl and Klimas (1981) for NACA 0018 foils showing lift coefficient related to angle of attack.

3.3 Four-Blade Test Results

Four-blade tests were conducted at toe angles from -4° to $+10^{\circ}$ in increments of one degree. Inflow velocity for all testing was set at 0.8 m/s with the turbine centered in the water column, with a water temperature of 67°F . With a solidity ratio of 0.343, it was estimated that the max power coefficient would be reached at a TSR between 1 to 1.5, based on experimental solidity data by Shiono et al. (2000). As a result, testing was done at a TSR range from 0.4 to 1.9 to ensure the peak was acquired.

The maximum power coefficient of 23.7% occurred at the $+4^{\circ}$ toe angle at a TSR of 1.1 as seen in Fig. 3.7 through 3.10. The $+4^{\circ}$ and $+5^{\circ}$ toe angles had very similar efficiency curves, varying at peak C_p by 2% and no more than 1.9% in other parts of the curve. The

results show that the efficiency increases steadily from -4° toe angle to the peak at $+4^{\circ}$. Similarly to the behavior seen in the two-blade results, after maximum lift is reached at $+4^{\circ}$, the data becomes less predictable as it decreases from $+5^{\circ}$ to $+10^{\circ}$.

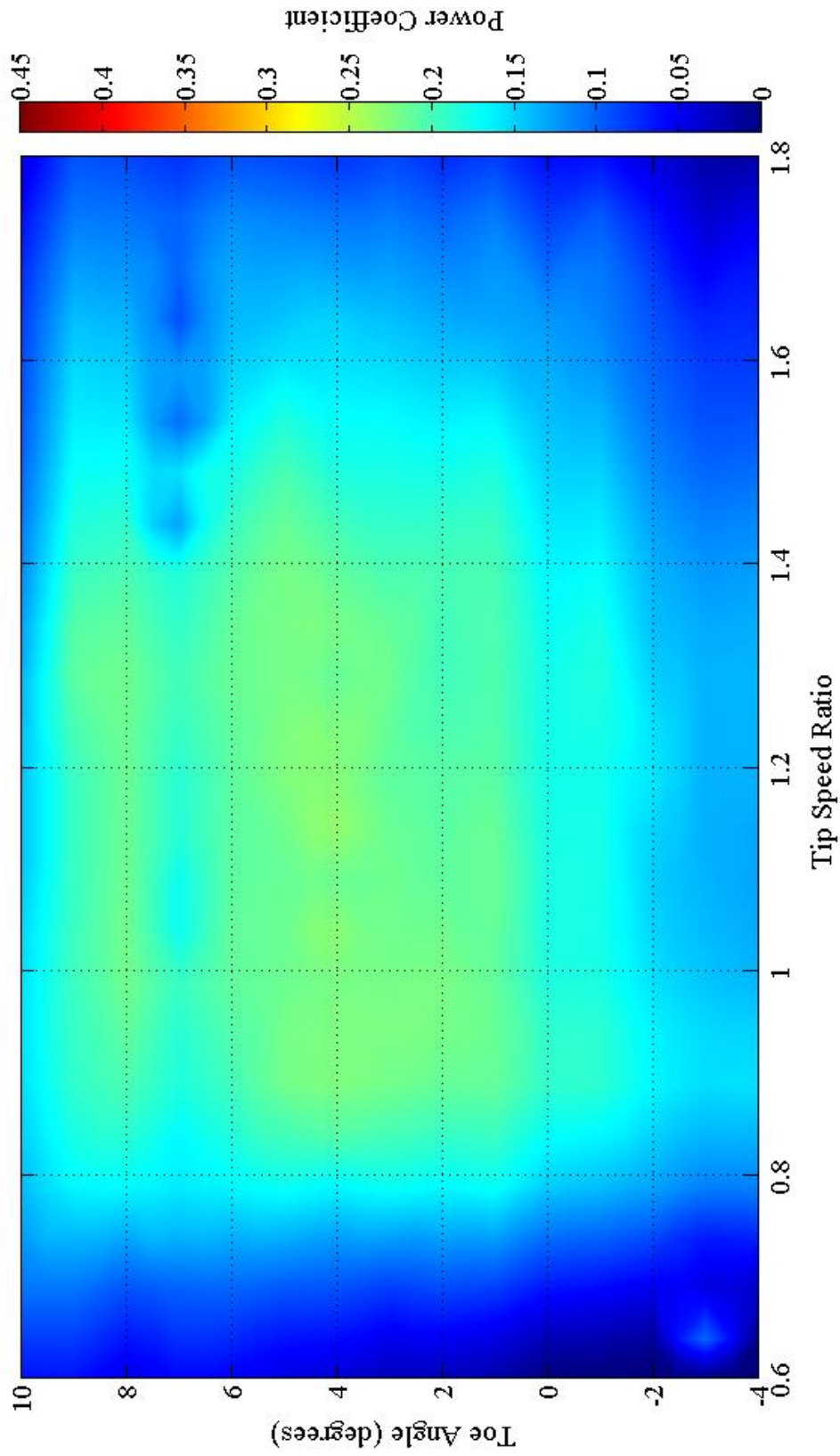


Figure 3.7 – Power coefficient contour plot for four-blade testing of 3-D printed NACA 0018 blades with solidity ratio $\sigma = 0.343$ and inflow velocity $U_\infty = 0.8$ m/s.

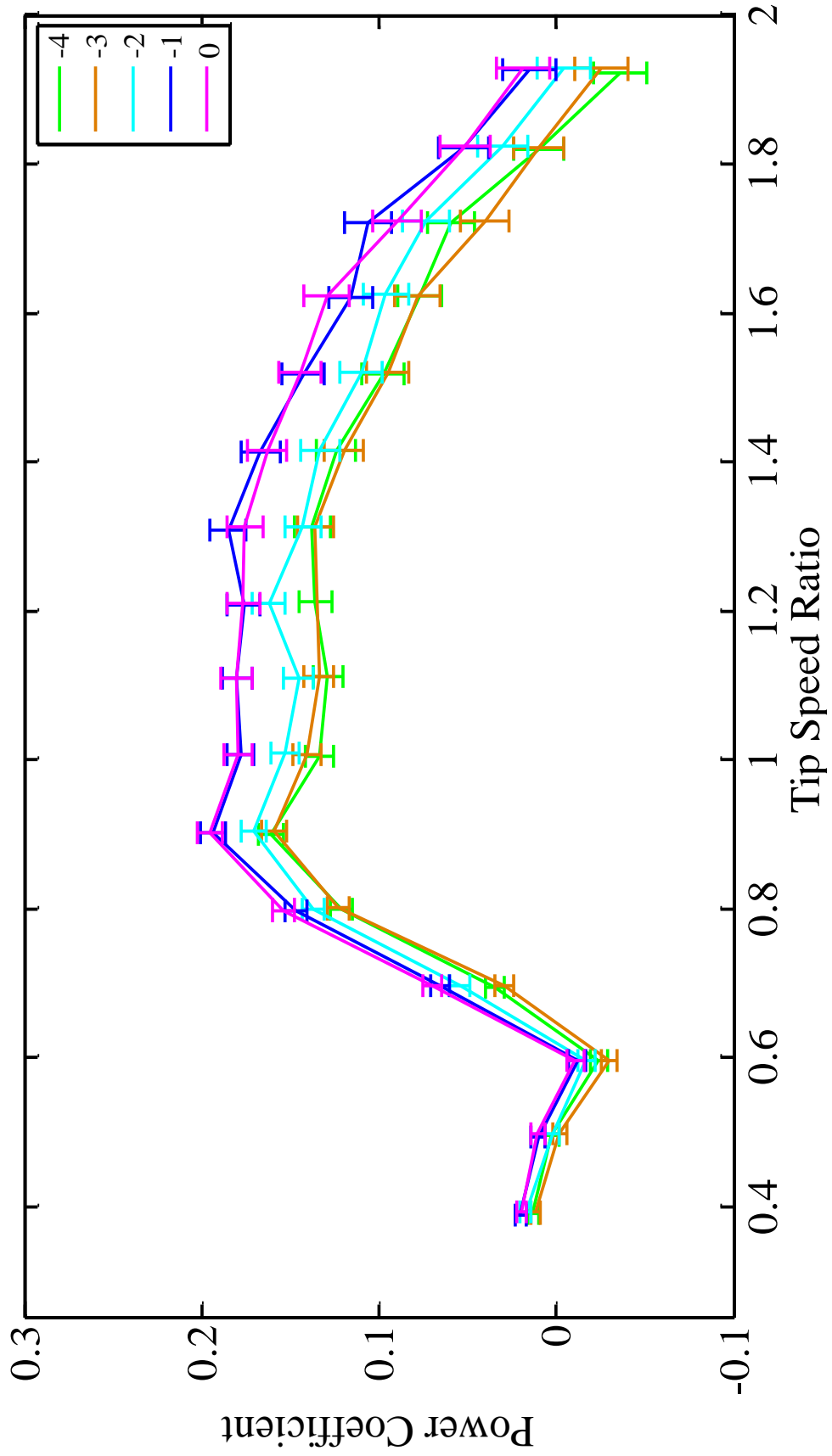


Figure 3.8 – Power coefficient curves for four-blade testing of 3-D printed NACA 0018 blades from toe angles from -4° to 0° with solidity ratio $\sigma = 0.343$ and inflow velocity $U_\infty = 0.8$ m/s.

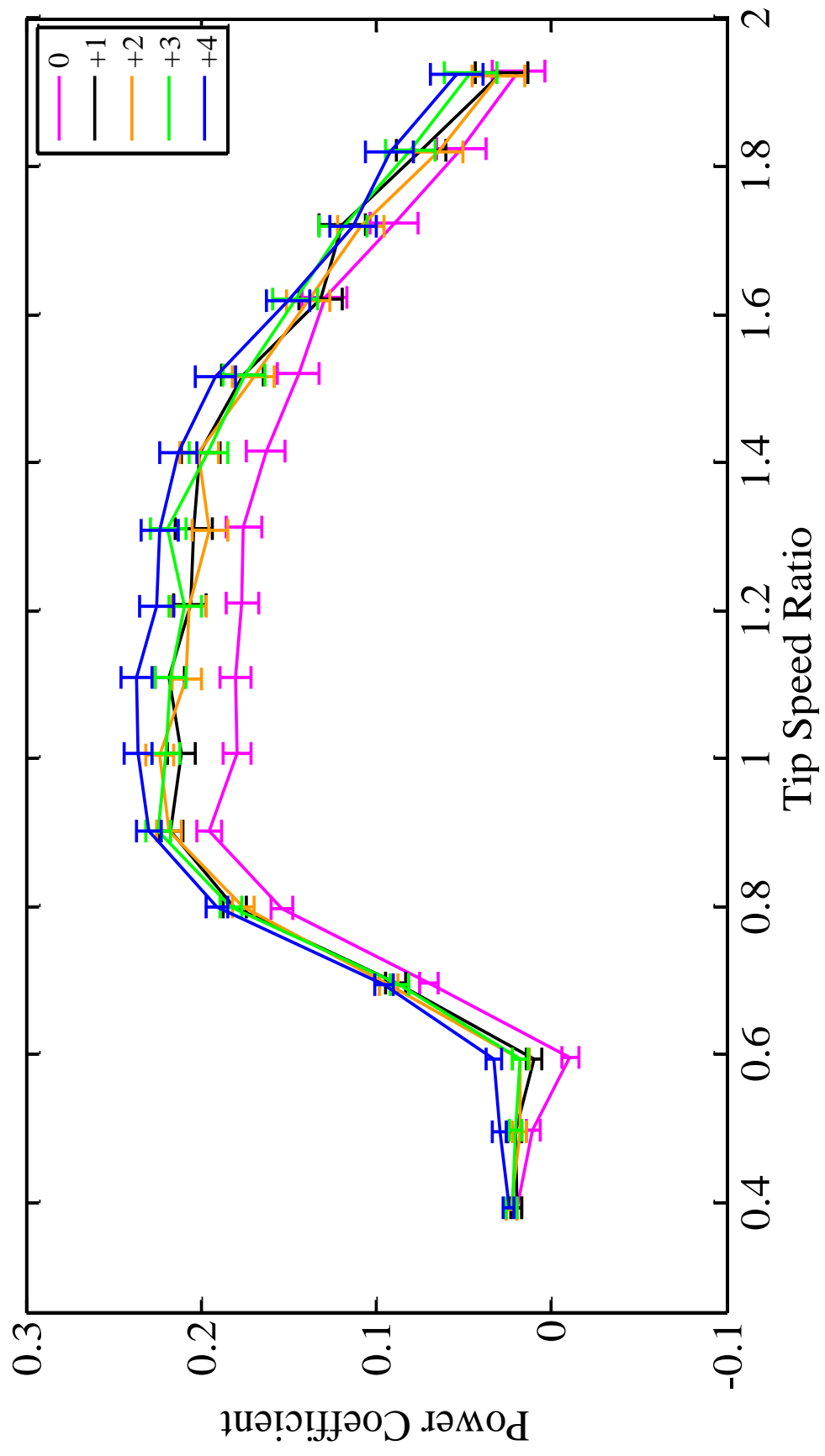


Figure 3.9 – Power coefficient curves for four-blade testing of 3-D printed NACA 0018 blades from toe angles from 0° to +4° with solidity ratio $\sigma = 0.343$ and inflow velocity $U_\infty = 0.8$ m/s.

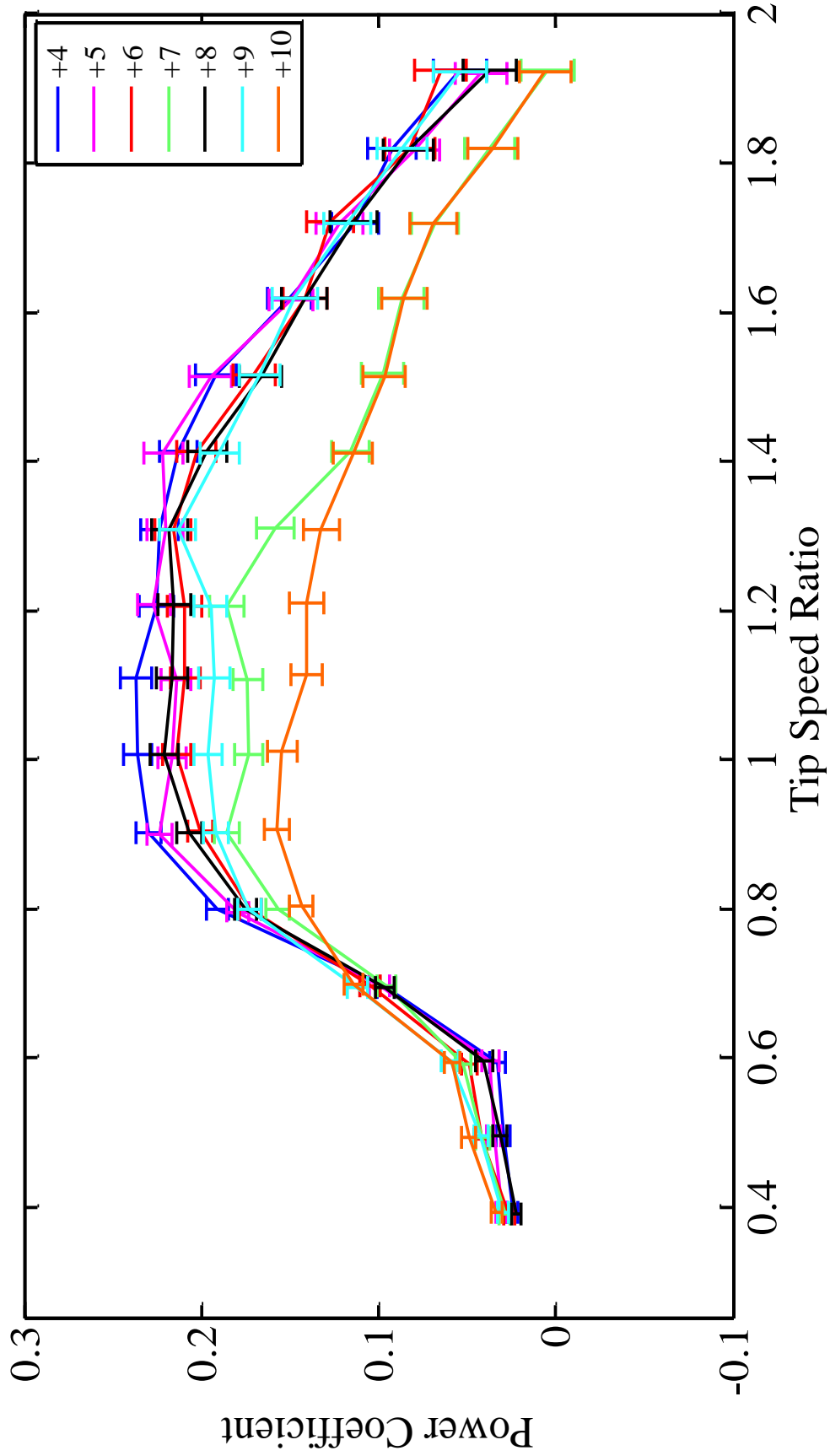


Figure 3.10 – Power coefficient curves for four-blade testing of 3-D printed NACA 0018 blades from toe angles from +4° to +10° with solidity ratio $\sigma = 0.343$ and inflow velocity $U_\infty = 0.8$ m/s.

3.4 Conclusions

As anticipated, the two-blade test results were considerably more efficient than the four-blade tests. At the peak, the two-blade turbine was better by a difference of 18.7%. The plots hold a very similar shape between the two different setups, but with a substantial shift in the data. As seen in Fig. 3.11, the two-blade curve passes directly through the four-blade curve around a TSR of 1.1 where the four-blade data peaks. Testing by Shiono et al. (2000) shows this same shift and intersection of data at similar solidities. The results show that although the two-blade turbine is more efficient, it must be operated at higher TSR to achieve peak efficiency; however, this is still a much lower TSR than other axial designs.

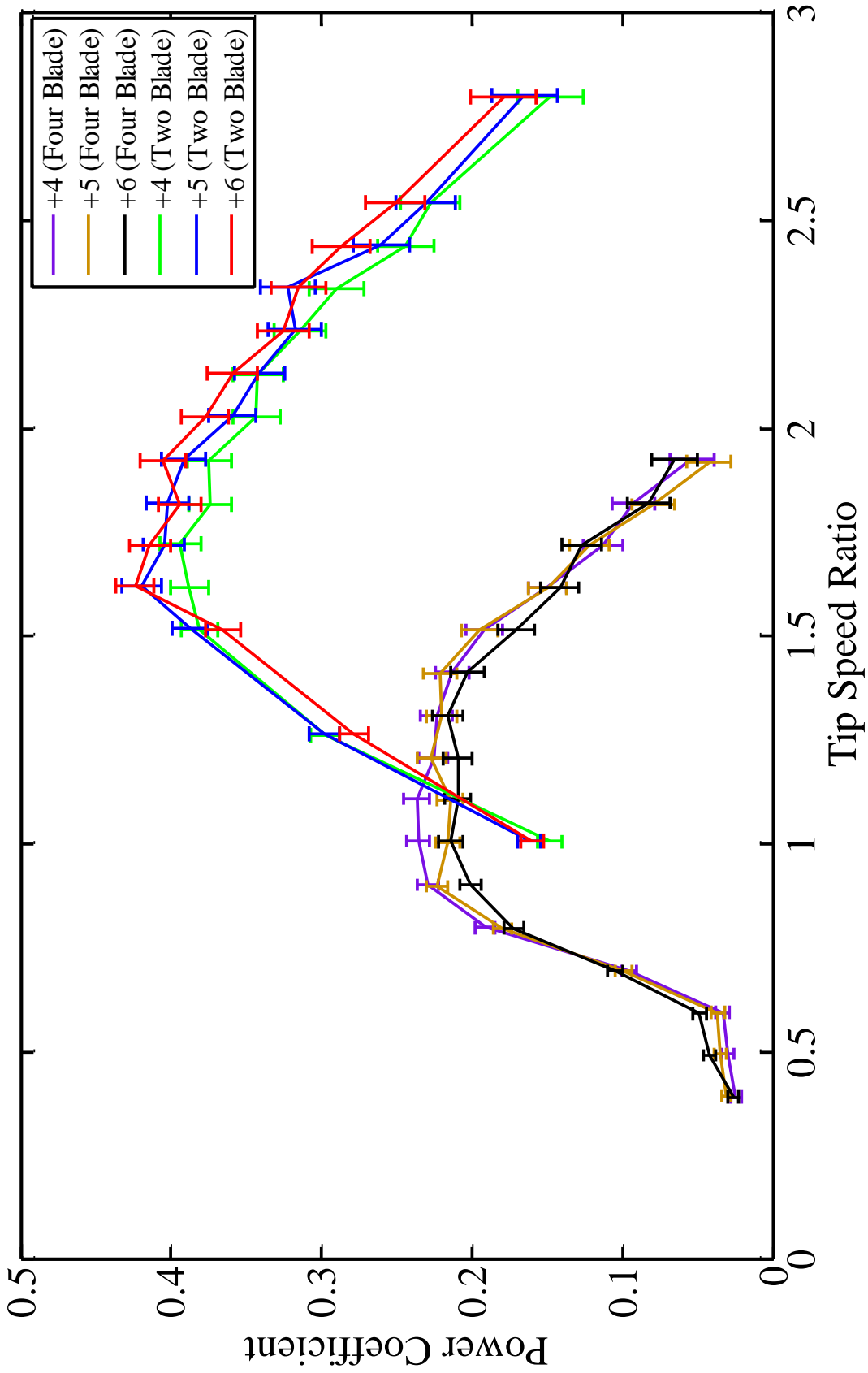


Figure 3.11 – Power coefficient curve comparison for two-blade and four-blade testing of NACA 0018 blades from toe angles from +4° to +6° and inflow velocity $U_\infty = 0.8$ m/s.

CHAPTER 4

CAMBERED FOIL RESULTS

The cambered NACA 4418 foils were tested in the two-blade configuration at multiple toe angles. Power coefficient curves were compared for each setup to find the peak efficiency and optimal toe angle. The goal of this test set was to determine if cambered foils were more efficient than symmetrical and reverse camber foils, which will be discussed in the following chapter.

4.1 Geometry of NACA 4418 Blades

The cambered profile of the NACA 4418 blade is shown in Fig. 4.1. The blades used in the testing had a 3.5 inch chord length, identical to the symmetrical NACA 0018. The NACA 4418 foil is extremely similar to the NACA 0018, having the same thickness but adding a slight camber at 4% of the total chord length. This blade was chosen because of its strong similarities with the NACA 0018 it is compared against.

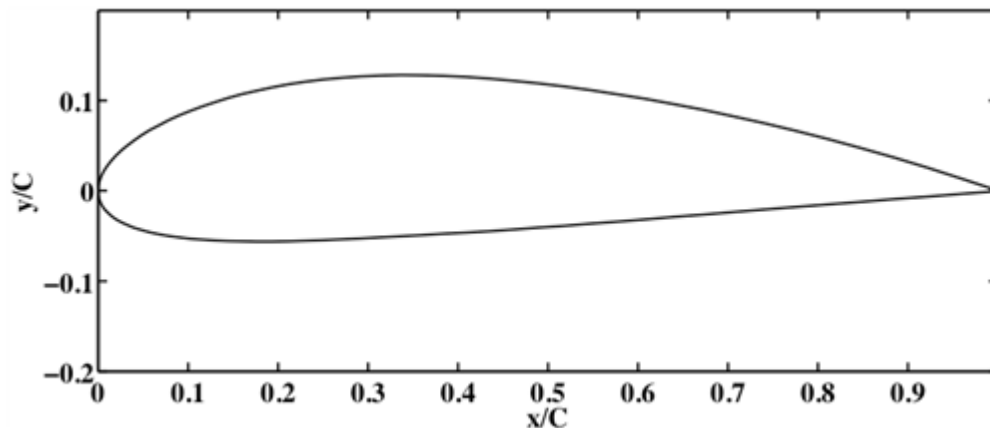


Figure 4.1 – Profile view of the symmetrical NACA 4418 blade

4.2 Two-Blade Test Results

Two-blade tests were executed at toe angles spanning from -4° to 0° in two degree increments, from $+3^{\circ}$ to $+7^{\circ}$ in one degree increments, and one test was taken at $+10^{\circ}$. Inflow velocity was set at 0.8 m/s for all testing with the turbine centered in the water column. With an identical chord length as the NACA 0018 foils, this setup possessed a solidity ratio of 0.171. Again, based on the solidity data by Shiono et al. (2000), the TSR range was set from 1 to 3 in order to capture the peak expected to be between a TSR of 1.6 and 2.

This test set was taken during the winter months when the water temperature was 48°F , a difference of 19°F less than summer test conditions. As a result of the temperature drop, the viscosity and density increased, which directly affects the efficiency of the turbine (see Appendix C). To provide comparable data with the NACA 4418 cambered and reverse cambered foils, the two-blade symmetrical NACA 0018 foils were tested again at the 48°F water temperature for the study in this chapter. The peak power coefficient occurred at a $+6^{\circ}$ toe angle at a TSR of 1.6. The maximum power coefficient was 37.5%, which can be seen in Fig. 4.2 to 4.5.

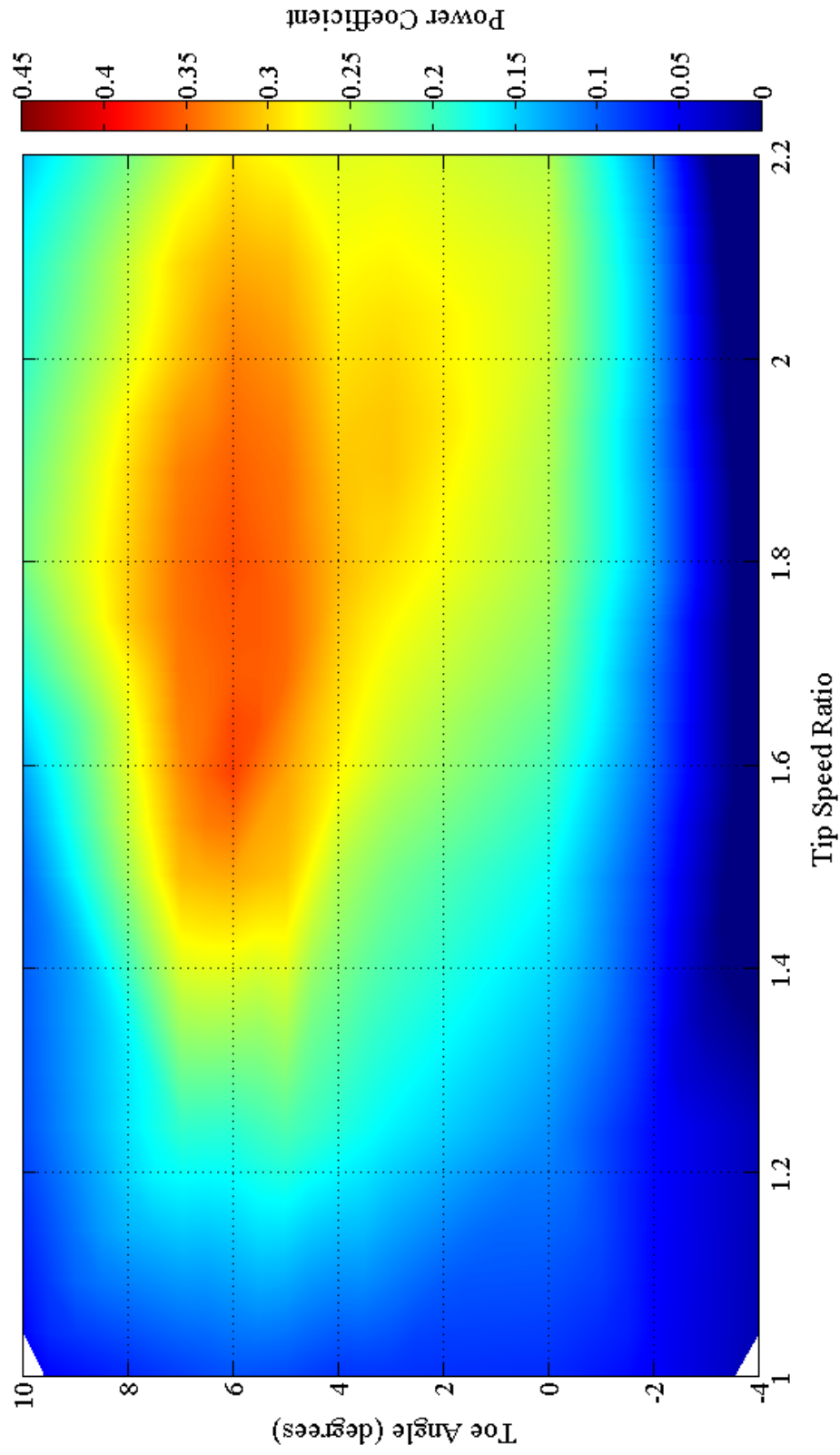


Figure 4.2 – Power coefficient contour plot for two-blade testing of 3-D printed NACA 4418 blades with solidity ratio $\sigma = 0.171$ and inflow velocity $U_\infty = 0.8$ m/s.

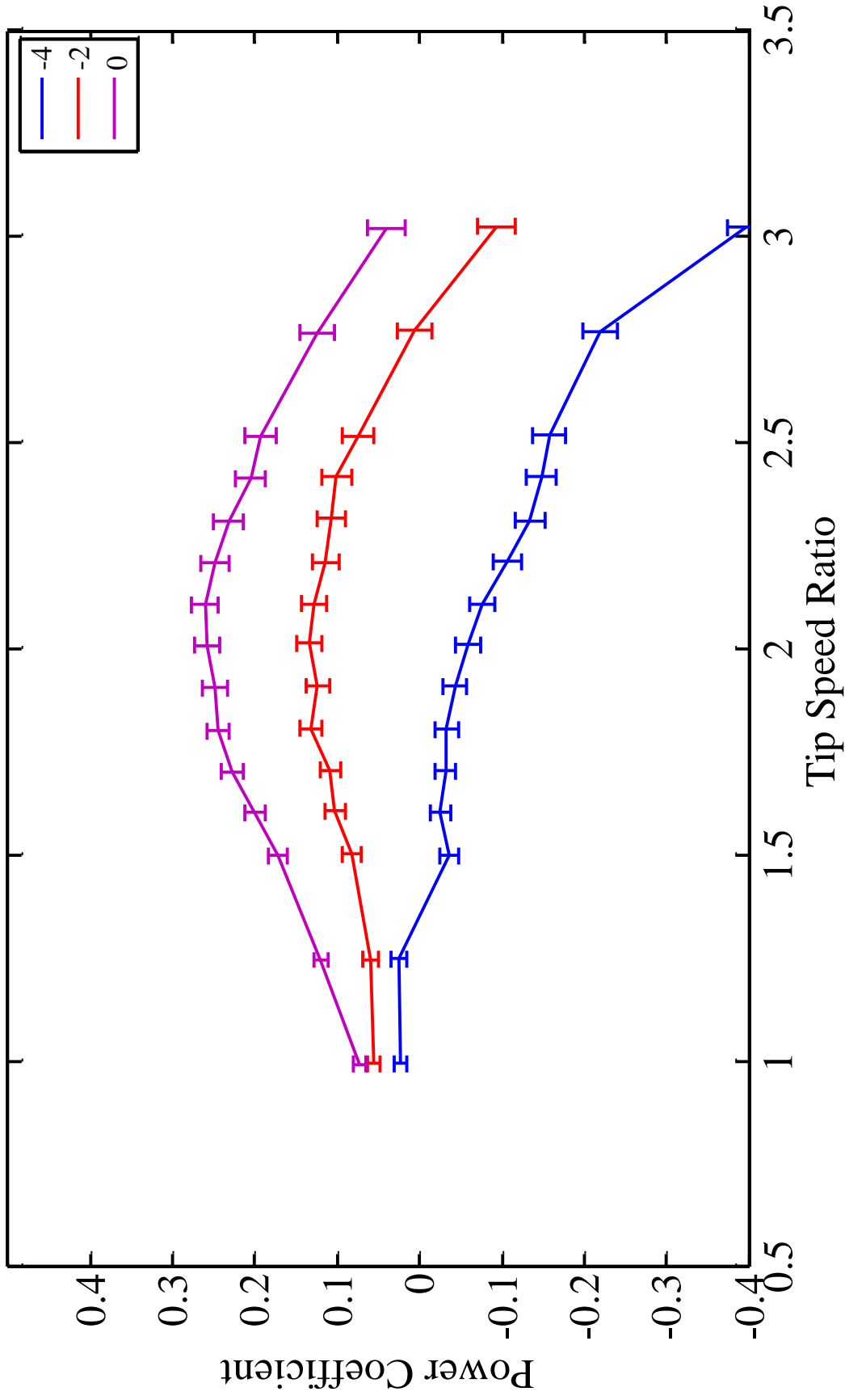


Figure 4.3 – Power coefficient curves for two-blade testing of 3-D printed NACA 4418 blades from toe angles from -4° to 0° with solidity ratio $\sigma = 0.171$ and inflow velocity $U_\infty = 0.8$ m/s.

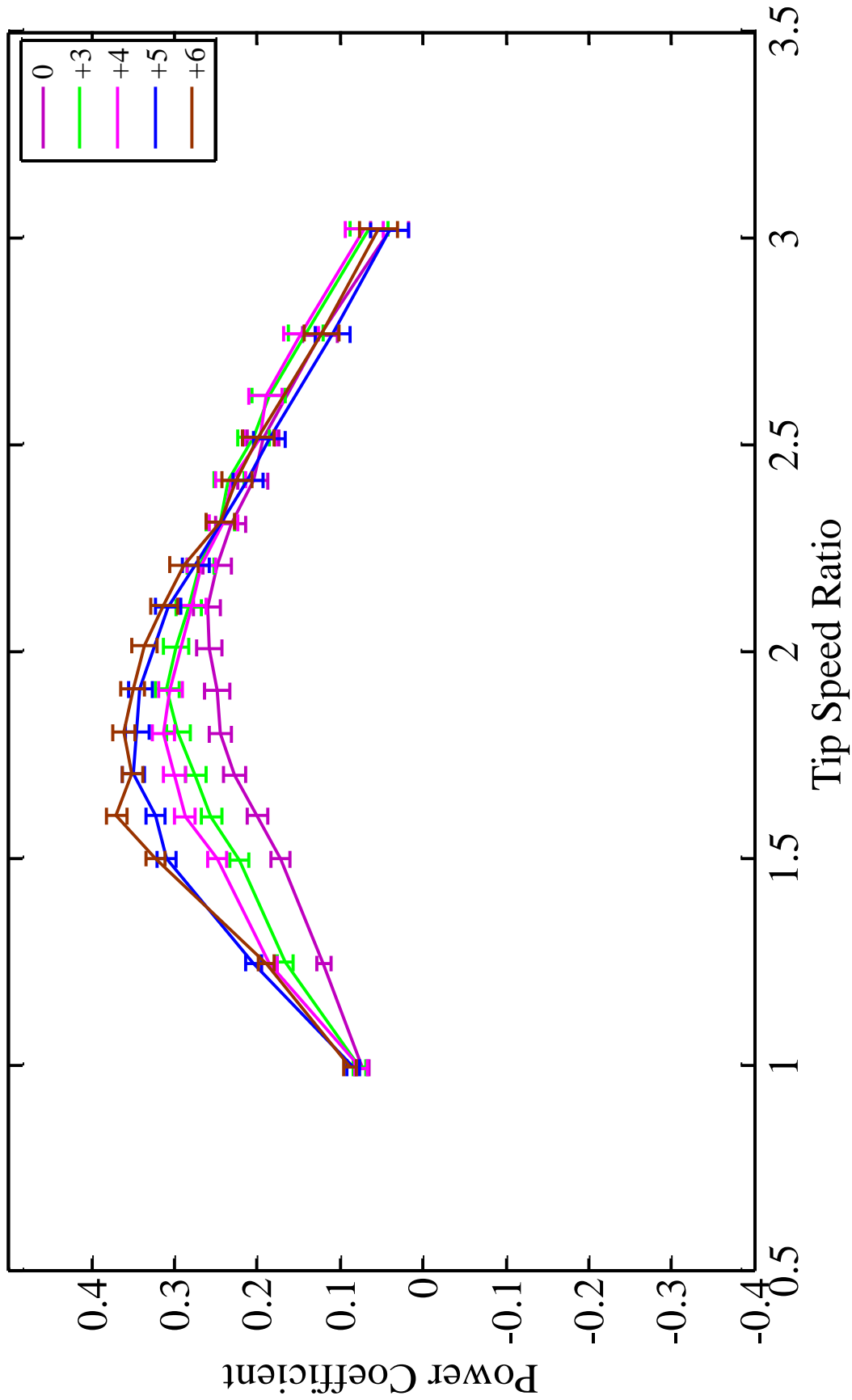


Figure 4.4 – Power coefficient curves for two-blade testing of 3-D printed NACA 4418 blades from toe angles from 0° to +6° with solidity ratio $\sigma = 0.171$ and inflow velocity $U_\infty = 0.8$ m/s.

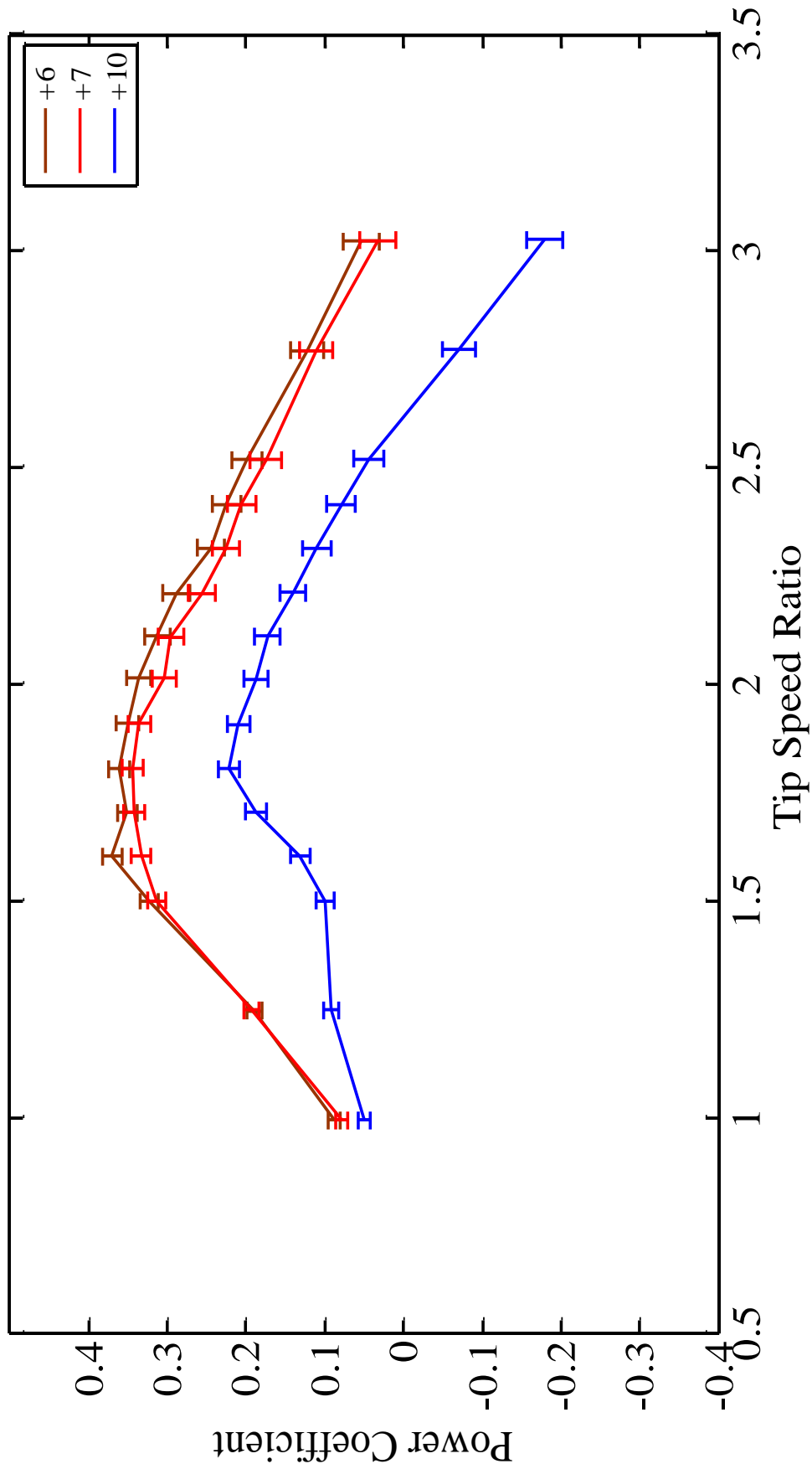


Figure 4.5 – Power coefficient curves for two-blade testing of 3-D printed NACA 4418 blades from toe angles from +6° to +10° with solidity ratio $\sigma = 0.171$ and inflow velocity $U_\infty = 0.8$ m/s.

4.3 Comparison to Symmetrical Foils

Although the addition of camber can significantly change lift and drag characteristics in certain cases (Abbott and von Donhoff, 1959), for these selected foils it does not improve the turbine performance in this study and actually results in a decrease in efficiency. With the NACA 0018 foils reaching a maximum power coefficient of 41.2% and the NACA 4418 peaking at 37.5%, the symmetrical foils are more efficient by a difference of 3.7%. Over the span of the curves the difference between efficiencies at corresponding tip speed ratios is substantial, showing the NACA 0018 foils to be over 5% more efficient at most tip speed ratios and reaching almost 8% at some points.

As mentioned before, this study was conducted during the winter months when the water temperature was approximately 20⁰F cooler than the summer tests. It is important to note that not only were the cambered foils not as efficient as the symmetrical foils in winter testing, but both were less efficient than the results from symmetrical testing during the summer. This is most likely from the viscosity change due to the large drop in temperature. Comparison of winter and summer data for the symmetrical NACA 0018 blades can be found in Appendix C.

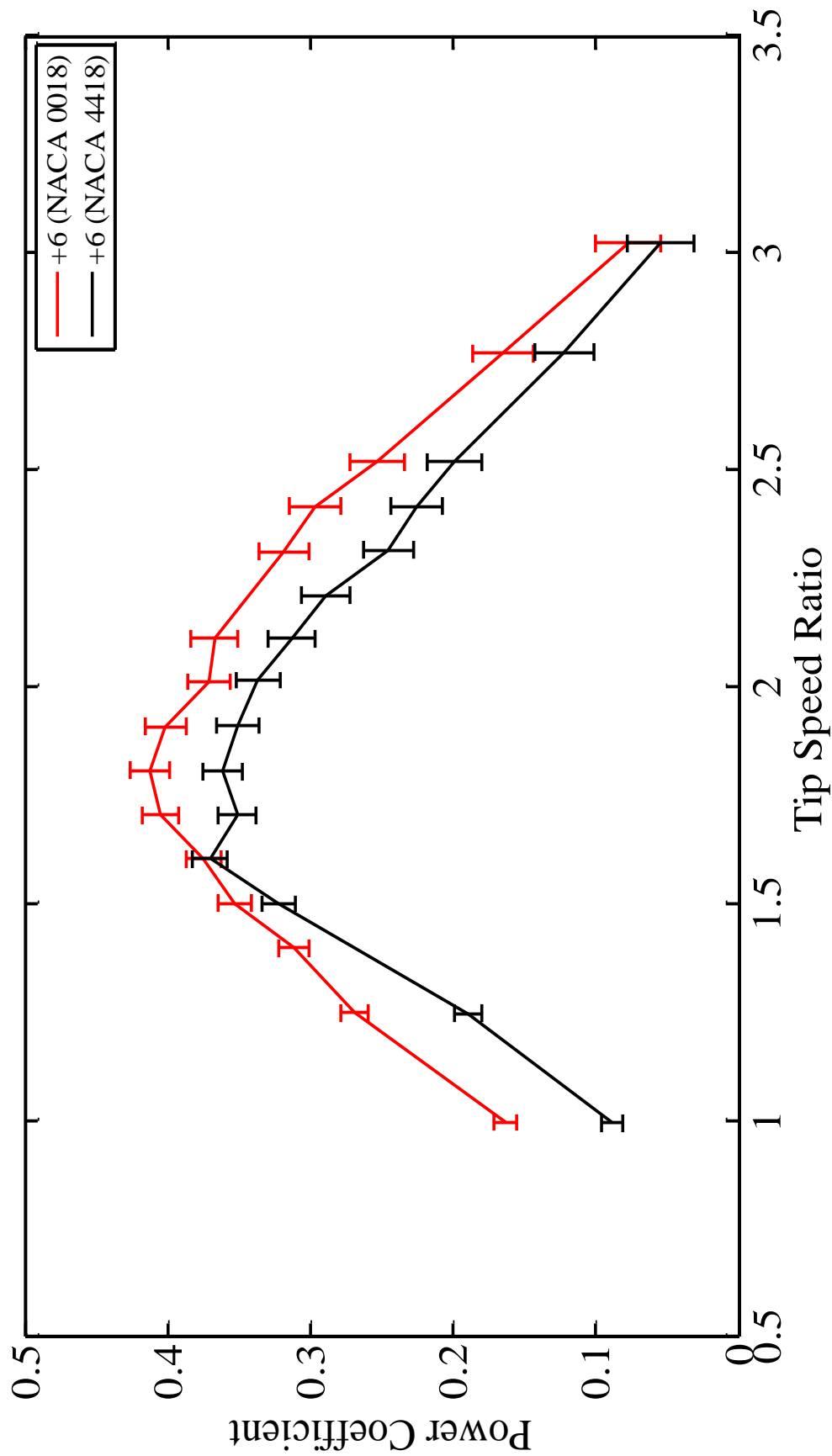


Figure 4.6 – Power coefficient comparison curves for two-blade testing of 3-D printed NACA 4418 blades and NACA 0018 blades. The peak power coefficient occurred at $+6^\circ$ toe angle. Solidity ratio $\sigma = 0.171$ and inflow velocity $U_\infty = 0.8$ m/s.

CHAPTER 5

REVERSE CAMBER FOIL RESULTS

The cambered NACA 4418 foils were tested again, but in the reverse cambered configuration. Since lower solidity had proven to be more efficient, this set of tests was done only with the two-blade setup. For each setup, power coefficient curves were compared to determine the peak efficiency and optimal toe angle and TSR. This set of tests was compared to both the symmetrical NACA 0018 foils as well as the cambered NACA 4418 in the typical configuration with the concave side facing inward toward the center of the turbine.

5.1 Geometry of Reverse Camber NACA 4418 Blades

The cambered profile of the NACA 4418 blade in the reverse orientation can be seen in figure 5.1. Again, there is a 4% camber over the total chord length and the same thickness as the symmetrical NACA 0018 foils.

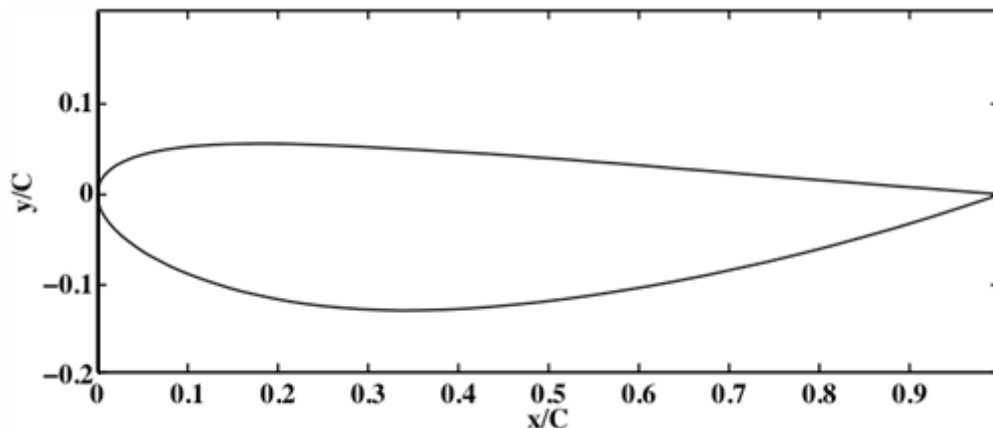


Figure 5.1 – Profile view of the reverse camber NACA 4418 blade

5.2 Two-Blade Test Results

Two-blade tests were executed at toe angles spanning from 2° to 10° in one degree increments and one test was taken at 0° . Inflow velocity was set at 0.8 m/s for all testing with the turbine centered in the water column. This test set was taken at a water temperature of 48°F . With an identical chord length as the NACA 4418 foils, this setup had a solidity ratio of 0.171. Again, based on the solidity data by Shiono et al. (2000), the peak efficiency was expected to occur around a TSR of 1.6 to 2. Initially, the TSR range was set to run from 1 to 2.75, but after a few preliminary tests the range was changed to a range of 0.6 to 2.4 to ensure an accurate representation of the curve was captured.

This test set was the least efficient compared to the symmetrical NACA 0018 and regular cambered NACA 4418 foils. The peak power coefficient was 35.1% at a toe angle of $+4^{\circ}$ and TSR of 1.7. Test set results are shown in Fig. 5.2 to 5.5.

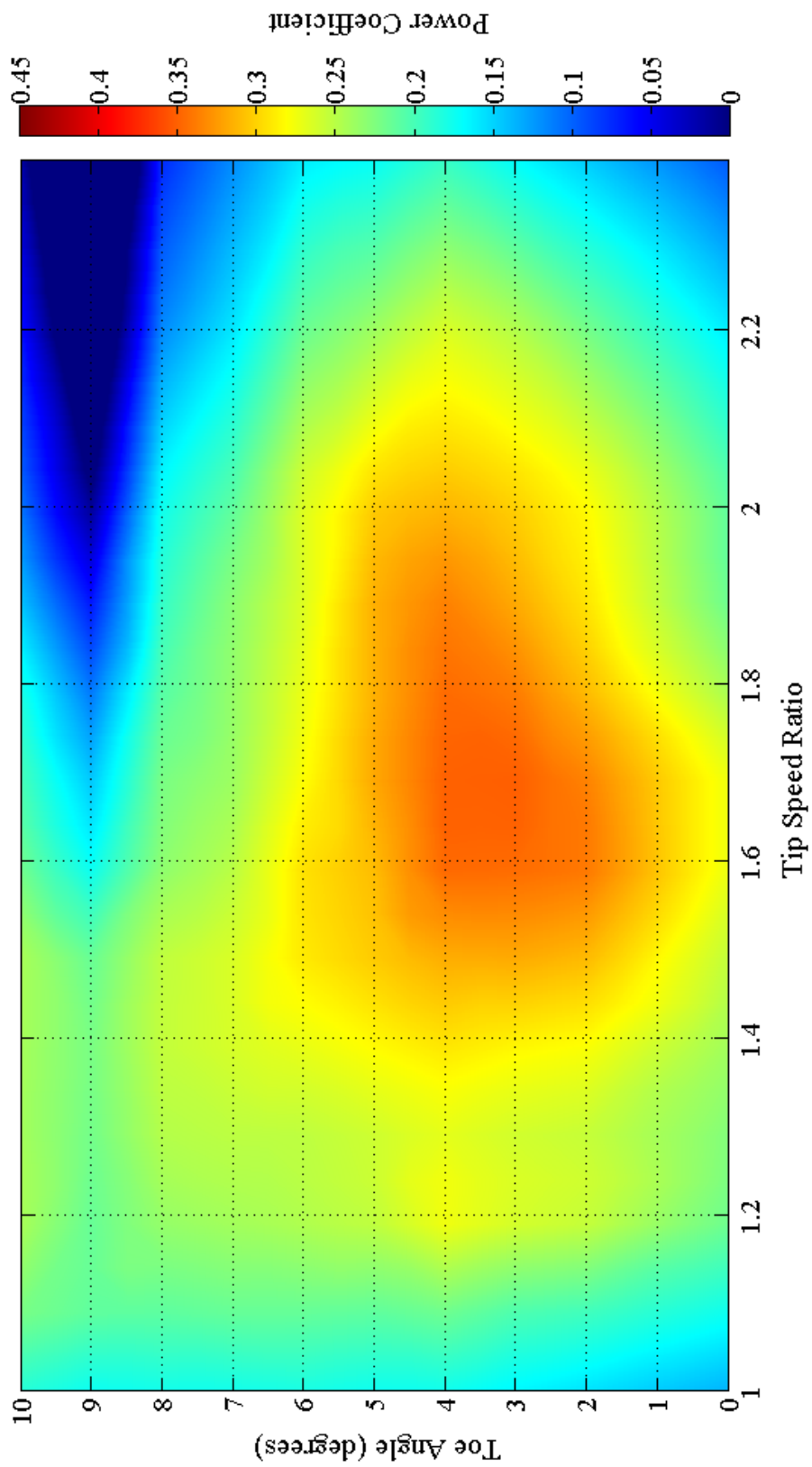


Figure 5.2 – Power coefficient contour plot for two-blade testing of reverse camber 3-D printed NACA 4418 blades with solidity ratio $\sigma = 0.171$ and inflow velocity $U_\infty = 0.8$ m/s.

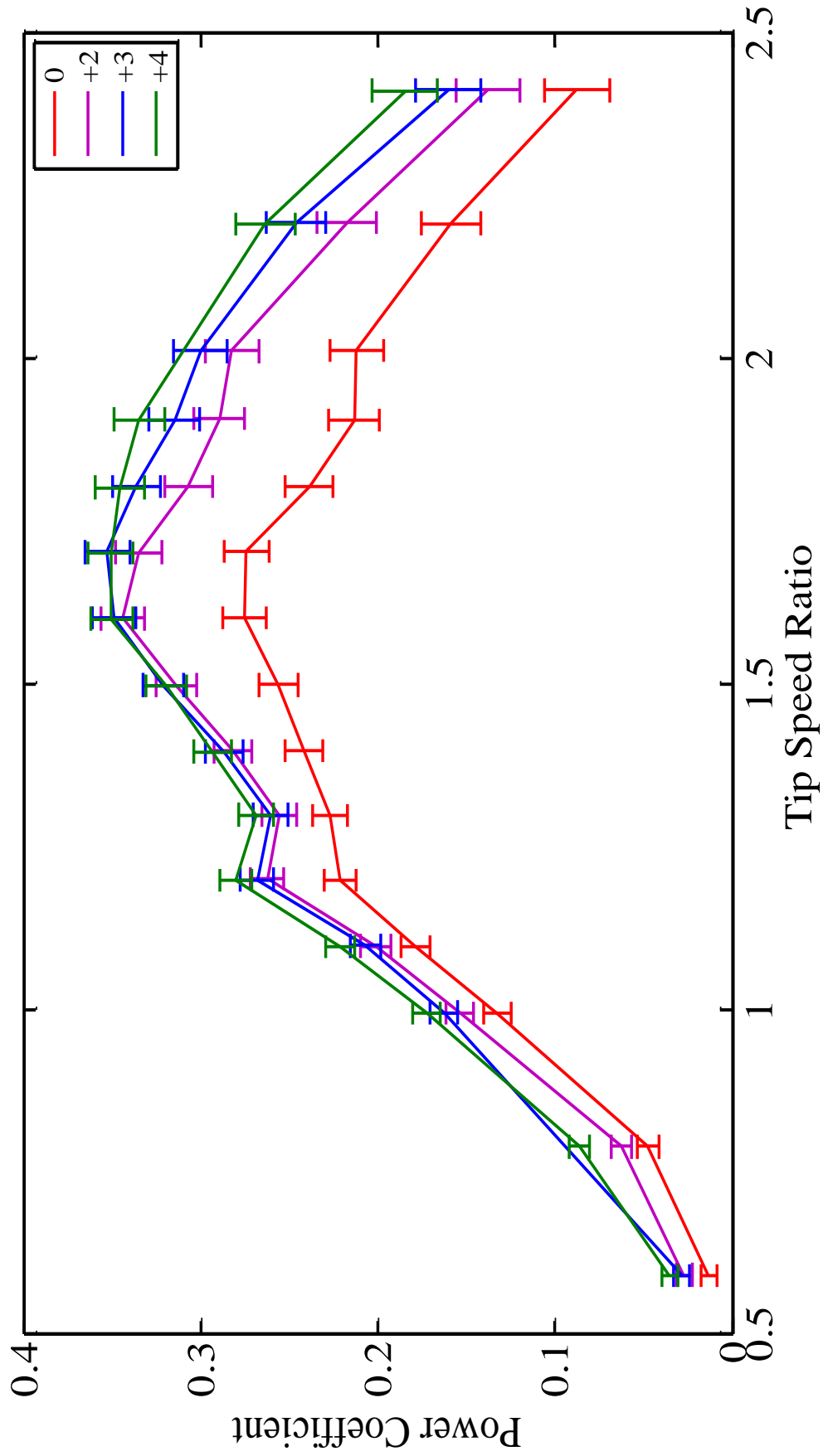


Figure 5.3 – Power coefficient curves for two-blade testing of reverse camber 3-D printed NACA 4418 blades from toe angles from 0° to +4° with solidity ratio $\sigma = 0.171$ and inflow velocity $U_\infty = 0.8$ m/s.

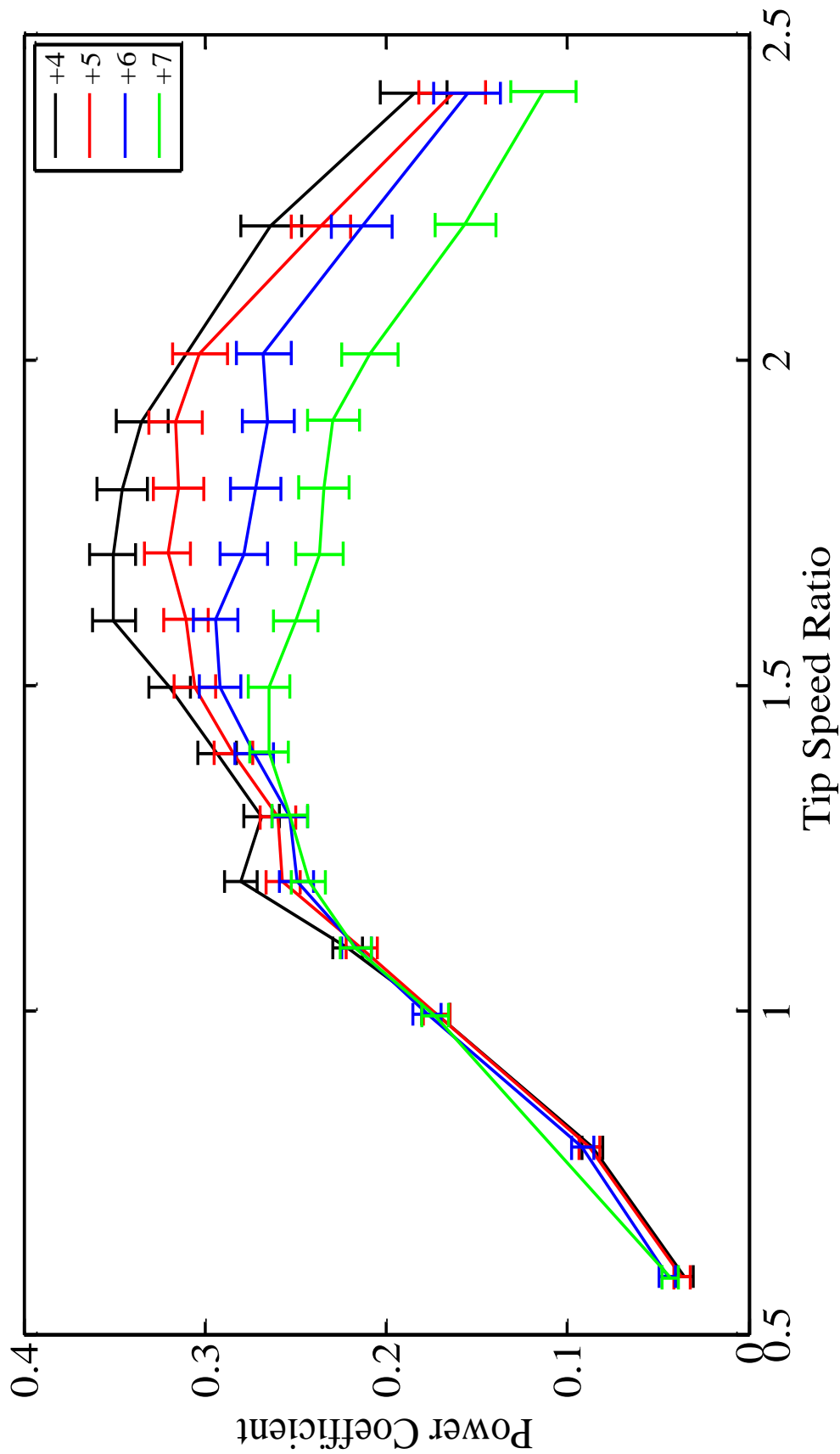


Figure 5.4 – Power coefficient curves for two-blade testing of reverse camber 3-D printed NACA 4418 blades from toe angles from +4° to +7° with solidity ratio $\sigma = 0.171$ and inflow velocity $U_\infty = 0.8$ m/s.

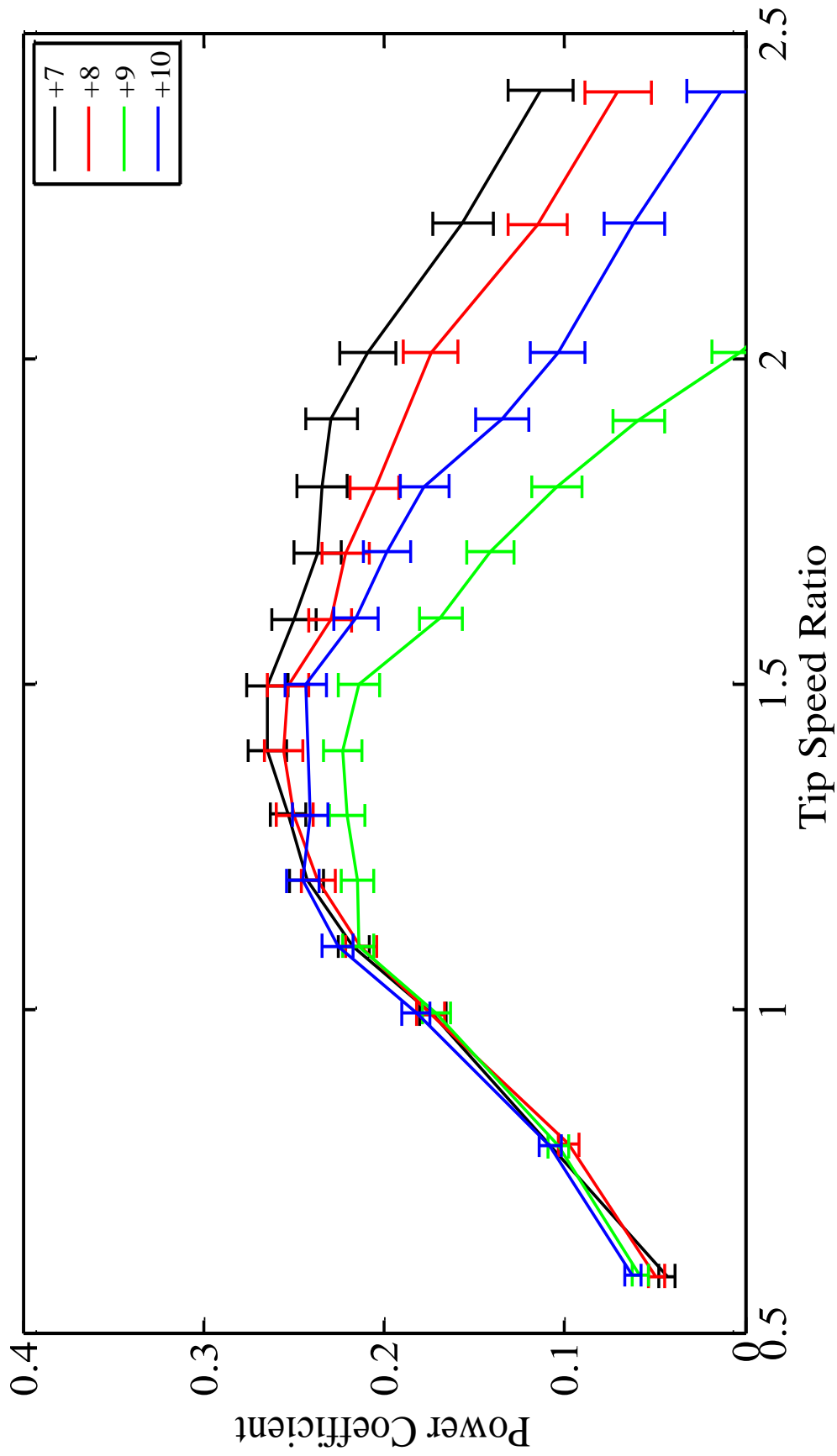


Figure 5.5 – Power coefficient curves for two-blade testing of reverse camber 3-D printed NACA 4418 blades from toe angles from +7° to +10° with solidity ratio $\sigma = 0.171$ and inflow velocity $U_\infty = 0.8$ m/s.

5.3 Comparison to Symmetric and Regular Camber Foils

The results of the reverse camber NACA 4418 foils proved to be less efficient than both the symmetrical NACA 0018 foils and the regular camber NACA 4418 foils. The comparison of the peak power coefficient curves for all three blades in Fig 5.6 shows the difference between the three profiles. At the peak of each curve, the regular camber NACA 4418 blades were more efficient by 2.4% and the symmetrical NACA 0018 blades were more efficient by 6.1%.

It is important to note that the reverse camber NACA 4418 blades reached maximum performance at a lower toe angle than the regular camber NACA 4418 and the symmetrical 0018 foils. This may be due to the fact that the reverse camber foils stall much more quickly than the symmetrical and regular camber foils, with the zero lift line at 5 degrees for the NACA 4418 foils and 0 degrees for the NACA 0018 foils. When comparing all three profiles at a $+6^{\circ}$ toe angle, as in Fig. 5.7, the performance difference became even more apparent. At this angle, the reverse camber blades were less efficient than the regular camber blades and symmetrical blades by 8.1% and 11.8%, respectively. The reverse camber NACA 4418 foils did show higher efficiencies than the other two profiles at some of the lower TSRs. At the $+4^{\circ}$ toe angle the reverse camber foils were more efficient than the regular camber foils by almost 9% at a TSR of 1, however, once the reverse cambered blades reached stall the performance dropped off rapidly.

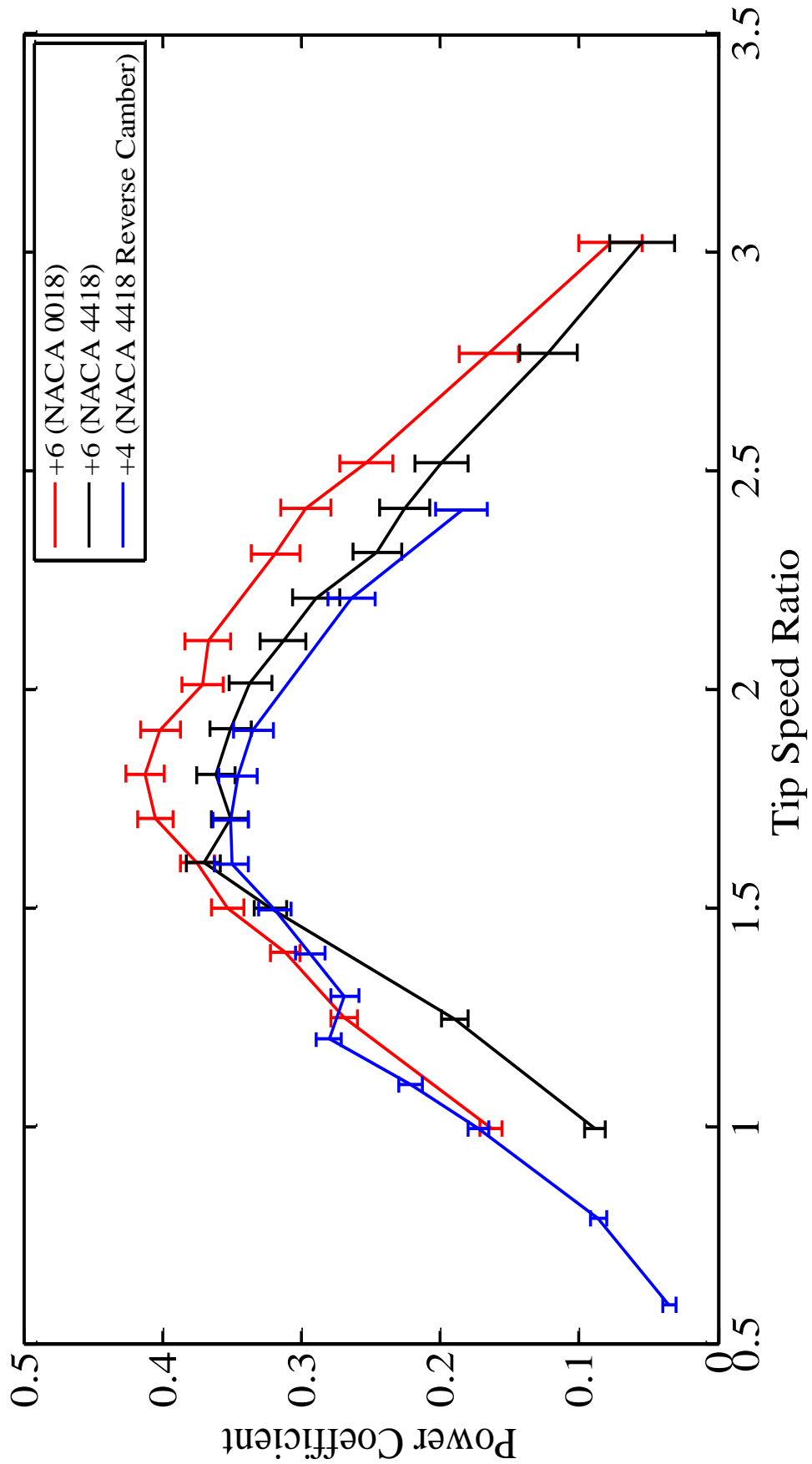


Figure 5.6 – Comparison of peak power coefficient curves for two-blade testing of 3-D printed NACA 0018 blades, NACA 4418 blades, and reverse camber NACA 4418 blades. Curves are from toe angles that showed best performance for each profile. Each profile was tested with solidity ratio $\sigma = 0.171$ and inflow velocity $U_\infty = 0.8$ m/s.

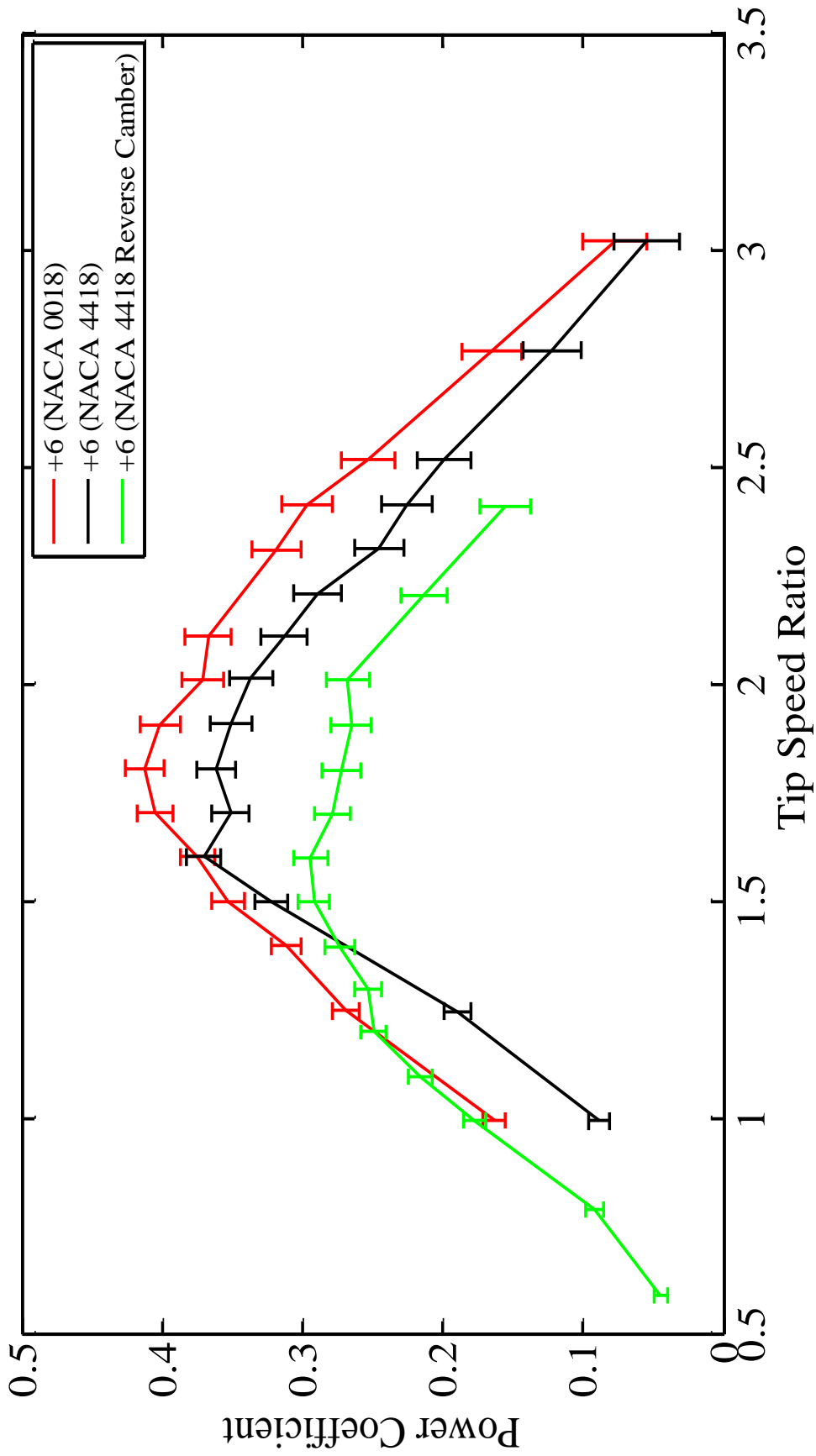


Figure 5.7 – Comparison of power coefficient curves for two-blade testing of 3-D printed NACA 0018 blades, NACA 4418 blades, and reverse camber NACA 4418 blades at $+6^\circ$ toe angle. Each profile was tested with solidity ratio $\sigma = 0.171$ and inflow velocity $U_\infty = 0.8$ m/s.

5.4 Conclusions

As anticipated, the two-blade symmetrical NACA 0018 foils were the most efficient out of all three blade profiles. The reverse camber NACA 4418 blades could be an option for systems operating at very low TSR, but the power coefficient would be less than half of the maximum performance of the symmetrical NACA 0018 foils.

Kerwin (2001) suggests that an ideal camber line would produce a constant pressure over the chord length to produce fixed lift with minimum reduction in local pressure. In this case, the camber in this study may need to be adjusted slightly to distribute the load evenly along the chord length and ensure circulation decreases to the trailing edge to avoid adverse pressure gradients and boundary layer separation.

REFERENCES

- Adamski, S., 2013, "Numerical Modeling of the Effects of a Free Surface on the Operating Characteristics of Marine Hydrokinetic Turbines," University of Washington.
- Bertin, J.J., and Smith, M. L., 1979, "Aerodynamics for Engineers," Prentice-Hall, Englewood Cliffs, NJ.
- Cameron, M., 2013. Personal communication.
- Charlier, R. H., 1982, "Tidal Energy," Van Nostrand Reinhold Company, New York, NY.
- deBree, G., 2010, Personal communication.
- Essick, J., 2009, "Hands-On Introduction to LabVIEW for Scientists and Engineers," Oxford University Press, New York, NY.
- Gillmer, T., and Johnson, B., 1982, "Introduction to Naval Architecture," Naval Institute Press, Annapolis, MD.
- Hau, E., 2006, "Wind Turbines: Fundamentals, Technologies, Application, Economics," Springer, Berlin.
- Holman, J.P., 2001, "Experimental Methods for Engineers," McGraw-Hill, New York, NY.
- Lokocz, T., 2010, "Solid Mechanics of Cross Flow Tidal Turbine Blades," University of Maine.
- Lokocz, T., 2011, Personal communication.
- McAdam, R. A., Houlby, G. T., Oldfield, M. L. G., and McCulloch, M. D., 2009, "Experimental Testing of the Transverse Horizontal Axis Water Turbine," Proceedings, 8th European Wave and Tidal Energy Conference, Uppsala, Sweden, pp. 360-365.
- Migliore, P.G., and Wolfe, W.P., 1980, "The Effects of Flow Curvature on the Aerodynamics of Darrieus Wind Turbines," W.V.U. A.E. Report No. TR-60, West Virginia University, Morgantown, WV.
- Meyer, R., 1999, "Introduction to mathematical Fluid Dynamics," Dover Publications, Inc., Mineola, NY.

Polagye, B., Van Cleve, B., Copping, A., Kirkendall, K., 2010, "Environmental Effects of Tidal Energy Development: Proceedings of a Scientific Workshop," U.S. Dept. Commerce, NOAA Tech. Memo. F/SPO-116, 181 p.

Schlichting, H., and Gersten, K., 2000, "Boundary Layer Theory," Springer, New York, NY.

Sheldahl, R.E., and Klimas, P.C., 1981, "Aerodynamic Characteristics of Seven Symmetrical Airfoil Sections Through 180-Degree Angle of Attack for Use in Aerodynamic Analysis of Vertical Axis Wind Turbines," Technical Report SAND80-2114, Sandia National Laboratories, Albuquerque, NM.

Shiono, M., Suzuki, K., and Kiho, S., 2000, "An Experimental Study of the Characteristics of a Darrieus Turbine for Tidal Power Generation," Electrical Engineering in Japan. Vol. 132, No. 3, pp. 38-47.

Strickland, J. H., Webster, B. T., and Nguyen, T., 1980, "A Vortex Model of the Darrieus Turbine: an Analytical and Experimental Study," Technical Report SAND79-7058, Sandia National Laboratories, Albuquerque, NM.

Urbina, R., Peterson, M.L., Kimball, R.W., DeBree, G.S., and Cameron, M.P., 2011a, "Modeling and Validation of a Cross Flow Turbine Using Free Vortex Model and a Modified Dynamic Stall Model," Submitted to: Renewable Energy.

Urbina, R., 2013, Personal communication.

Viehman, H., 2013, Personal communication.

Villeneuve, R., 1993, "Effects of Viscosity on Hydrofoil Cavitation," Massachusetts Institute of Technology.

Wallace, T., 2013, Personal communication.

Whelan, J. I., Graham, M.R., Peiro, J., 2009, Journal of Fluid Mechanics, Vol. 624, pp. 281-291.

White, F., 2011, "Fluid Mechanics," McGraw-Hill, New York, NY.

APPENDIX A
SCALING CALCULATIONS

Reynolds number scaling is not viable for the current test setup. With the model being considerably smaller than the prototype, the velocity of the model would have to reach speeds upwards of 23 m/s in order to have dynamic similitude, as shown by the calculations below. For the following calculations, the prototype was based off of the dimensions of Ocean Renewable Power Company's TidGen™ Turbine in the Cobscook Bay. Values of density and dynamic viscosity for the Cobscook Bay were determined based off of data from the National Oceanic and Atmospheric Administration (NOAA) based in Eastport, Maine and data collected by Viehman, 2012.

The Reynolds number for the prototype, Re_p , is calculated by Eq. A.1 where L_p is the length of the prototype diameter, V_p is the average inflow velocity of the Cobscook Bay, ρ_p is the density of the seawater, and μ_p is the dynamic viscosity of the seawater.

$$Re_p = \frac{\rho_p V_p L_p}{\mu_p} \tag{A.1}$$

$$Re_p = \frac{\left(1027.8 \frac{kg}{m^3}\right) \left(2.5 \frac{m}{s}\right) (3.6576 m)}{\left(0.001645 N \cdot \frac{s}{m^2}\right)}$$

$$Re_p = 5.71 \times 10^6$$

To ensure dynamic similitude, set the prototype Reynolds number equal to the model Reynolds number and solve for the inflow velocity of the model. In Eq. A.1, L_m is the

length of the model diameter, V_m is the inflow velocity of the tow tank, ρ_p is the density of the water, and μ_m is the dynamic viscosity of the water.

$$Re_m = \frac{\rho_m V_m L_m}{\mu_m} \quad (A.2)$$

$$Re_p = Re_m = 5.71 \times 10^6 = \frac{\left(1000 \frac{kg}{m^3}\right) (V_m) (0.3302 \text{ m})}{\left(0.001348 \text{ N} \cdot \frac{s}{m^2}\right)}$$

$$V_m = 23.3 \frac{m}{s}$$

This velocity was much too high for tow tank operations and therefore was not used for scaling. Froude number, however, scaled very closely as seen in the calculations from Eq. A.3 and Eq. A4 where V_p is the average inflow velocity of the Cobscook Bay, g is gravitational acceleration, L_p is the length of the prototype diameter, V_m is the inflow velocity of the tow tank, and L_m is the diameter of the model.

$$Fr_p = \frac{V_p}{\sqrt{gL_p}} \quad (A.3)$$

$$Fr_p = \frac{2.5 \frac{m}{s}}{\sqrt{\left(9.81 \frac{m}{s^2}\right) (3.6576 \text{ m})}}$$

$$Fr_p = 0.4174$$

$$Fr_m = \frac{V_m}{\sqrt{gL_m}} \quad (\text{A.4})$$

$$Fr_p = Fr_m \frac{V_m}{\sqrt{(9.81 \frac{m}{s^2})(0.3302 \text{ m})}}$$

$$V_m = 0.75 \frac{m}{s} \approx 0.8 \frac{m}{s}$$

By scaling with Froude number, the velocity was a more reasonable value that could be easily tested using the tow tank. As a result all testing was performed at an inflow velocity of 0.8 m/s.

APPENDIX B

EXPERIMENTAL TEST MATRIX

Toe Angle	Tip Speed Ratio (λ)													
	1	1.25	1.5	1.6	1.7	1.8	1.9	2.0	2.1	2.2	2.3	2.4	2.5	2.8
-3 ⁰	X	X	X	X	X	X	X	X	X	X	X	X	X	X
-2 ⁰	X	X	X	X	X	X	X	X	X	X	X	X	X	X
-1 ⁰	X	X	X	X	X	X	X	X	X	X	X	X	X	X
0 ⁰	X	X	X	X	X	X	X	X	X	X	X	X	X	X
+1 ⁰	X	X	X	X	X	X	X	X	X	X	X	X	X	X
+2 ⁰	X	X	X	X	X	X	X	X	X	X	X	X	X	X
+3 ⁰	X	X	X	X	X	X	X	X	X	X	X	X	X	X
+4 ⁰	X	X	X	X	X	X	X	X	X	X	X	X	X	X
+5 ⁰	X	X	X	X	X	X	X	X	X	X	X	X	X	X
+6 ⁰	X	X	X	X	X	X	X	X	X	X	X	X	X	X
+7 ⁰	X	X	X	X	X	X	X	X	X	X	X	X	X	X
+8 ⁰	X	X	X	X	X	X	X	X	X	X	X	X	X	X
+9 ⁰	X	X	X	X	X	X	X	X	X	X	X	X	X	X
+10 ⁰	X	X	X	X	X	X	X	X	X	X	X	X	X	X

Table B.1 – Experimental test matrix for two-bladed NACA 0018 foils at a water temperature of 67⁰F with $U_{\infty} = 0.8$ m/s, $\sigma = 0.171$, and water column height at 40 inches.

Toe Angle	Tip Speed Ratio (λ)															
	0.4	0.5	0.6	0.7	0.8	0.9	1.0	1.1	1.2	1.3	1.4	1.5	1.6	1.7	1.8	1.9
-4 ⁰	X	X	X	X	X	X	X	X	X	X	X	X	X	X	X	X
-3 ⁰	X	X	X	X	X	X	X	X	X	X	X	X	X	X	X	X
-2 ⁰	X	X	X	X	X	X	X	X	X	X	X	X	X	X	X	X
-1 ⁰	X	X	X	X	X	X	X	X	X	X	X	X	X	X	X	X
0 ⁰	X	X	X	X	X	X	X	X	X	X	X	X	X	X	X	X
+1 ⁰	X	X	X	X	X	X	X	X	X	X	X	X	X	X	X	X
+2 ⁰	X	X	X	X	X	X	X	X	X	X	X	X	X	X	X	X
+3 ⁰	X	X	X	X	X	X	X	X	X	X	X	X	X	X	X	X
+4 ⁰	X	X	X	X	X	X	X	X	X	X	X	X	X	X	X	X
+5 ⁰	X	X	X	X	X	X	X	X	X	X	X	X	X	X	X	X
+6 ⁰	X	X	X	X	X	X	X	X	X	X	X	X	X	X	X	X
+7 ⁰	X	X	X	X	X	X	X	X	X	X	X	X	X	X	X	X
+8 ⁰	X	X	X	X	X	X	X	X	X	X	X	X	X	X	X	X
+9 ⁰	X	X	X	X	X	X	X	X	X	X	X	X	X	X	X	X
+10 ⁰	X	X	X	X	X	X	X	X	X	X	X	X	X	X	X	X

Table B.2 – Experimental test matrix for four-bladed NACA 0018 foils at a water temperature of 67⁰F with $U_{\infty} = 0.8$ m/s, $\sigma = 0.343$, and water column height at 40 inches.

The test matrix for the symmetrical NACA 0018 foils was repeated for two-bladed testing during the winter in order to provide comparable results to the cambered NACA 4418 and reverse cambered NACA 4418 tests (Fig. B.3). Compressed experimental test matrices were developed to provide a curve with refinement at the peak power coefficient.

Toe Angle	Tip Speed Ratio (λ)															
	0.4	0.5	0.6	0.7	0.8	0.9	1.0	1.1	1.2	1.3	1.4	1.5	1.6	1.7	1.8	1.9
-4°	X	X	X	X	X	X	X	X	X	X	X	X	X	X	X	X
-2°	X	X	X	X	X	X	X	X	X	X	X	X	X	X	X	X
0°	X	X	X	X	X	X	X	X	X	X	X	X	X	X	X	X
+3°	X	X	X	X	X	X	X	X	X	X	X	X	X	X	X	X
+4°	X	X	X	X	X	X	X	X	X	X	X	X	X	X	X	X
+5°	X	X	X	X	X	X	X	X	X	X	X	X	X	X	X	X
+6°	X	X	X	X	X	X	X	X	X	X	X	X	X	X	X	X
+7°	X	X	X	X	X	X	X	X	X	X	X	X	X	X	X	X
+10°	X	X	X	X	X	X	X	X	X	X	X	X	X	X	X	X

Table B.3 – Experimental test matrix for two-bladed NACA 0018 foils at a water temperature of 48°F with $U_\infty = 0.8$ m/s, $\sigma = 0.343$, and water column height at 40 inches.

Toe Angle	Tip Speed Ratio (λ)															
	0.4	0.5	0.6	0.7	0.8	0.9	1.0	1.1	1.2	1.3	1.4	1.5	1.6	1.7	1.8	1.9
-4°	X	X	X	X	X	X	X	X	X	X	X	X	X	X	X	X
-2°	X	X	X	X	X	X	X	X	X	X	X	X	X	X	X	X
0°	X	X	X	X	X	X	X	X	X	X	X	X	X	X	X	X
+3°	X	X	X	X	X	X	X	X	X	X	X	X	X	X	X	X
+4°	X	X	X	X	X	X	X	X	X	X	X	X	X	X	X	X
+5°	X	X	X	X	X	X	X	X	X	X	X	X	X	X	X	X
+6°	X	X	X	X	X	X	X	X	X	X	X	X	X	X	X	X
+7°	X	X	X	X	X	X	X	X	X	X	X	X	X	X	X	X
+10°	X	X	X	X	X	X	X	X	X	X	X	X	X	X	X	X

Table B.4 – Experimental test matrix for two-bladed cambered NACA 4418 foils at a water temperature of 48°F with $U_\infty = 0.8$ m/s, $\sigma = 0.171$, and water column height at 40 inches.

Toe Angle	Tip Speed Ratio (λ)														
	0.6	0.8	1.0	1.1	1.2	1.3	1.4	1.5	1.6	1.7	1.8	1.9	2.0	2.2	2.4
0°	X	X	X	X	X	X	X	X	X	X	X	X	X	X	X
+2°	X	X	X	X	X	X	X	X	X	X	X	X	X	X	X
+3°	X	X	X	X	X	X	X	X	X	X	X	X	X	X	X
+4°	X	X	X	X	X	X	X	X	X	X	X	X	X	X	X
+5°	X	X	X	X	X	X	X	X	X	X	X	X	X	X	X
+6°	X	X	X	X	X	X	X	X	X	X	X	X	X	X	X
+7°	X	X	X	X	X	X	X	X	X	X	X	X	X	X	X
+8°	X	X	X	X	X	X	X	X	X	X	X	X	X	X	X
+9°	X	X	X	X	X	X	X	X	X	X	X	X	X	X	X
+10°	X	X	X	X	X	X	X	X	X	X	X	X	X	X	X

Table B.5 – Experimental test matrix for two-bladed reverse cambered NACA 4418 foils at a water temperature of 48°F with $U_\infty = 0.8$ m/s, $\sigma = 0.171$, and water column height at 40 inches.

APPENDIX C

EFFECTS OF TEMPERATURE

Initial testing was done in the summer months where the water temperature was 67⁰F. When further data was taken at a water temperature of 48⁰F, there was a noticeable change in turbine performance. Looking at the most efficient blades, the symmetrical NACA 0018 profile, a decrease is seen over the whole performance curve. The results shown in Fig. C.1 are for two-bladed testing of the symmetrical NACA 0018 foils set at the most efficient toe angle, +6⁰, and inflow velocity of 0.8 m/s. The water column height was set at 42 inches with the turbine centered in the water column. Effects of water column height on turbine performance are explained in Appendix D.

The winter results were less efficient than the summer results by an average of approximately 4% over the entire curve. The summer experimental tests, as shown in chapter 3, had a peak efficiency of 42.2% where the winter tests peaked at 37%. Since temperature is the only changing variable in this study, it can be concluded that the change in fluid viscosity is responsible for this reduction. If the effects of viscous forces are not taken into account during design, boundary separation can occur which can result in an increase in drag and decrease in lift as seen in the results here.

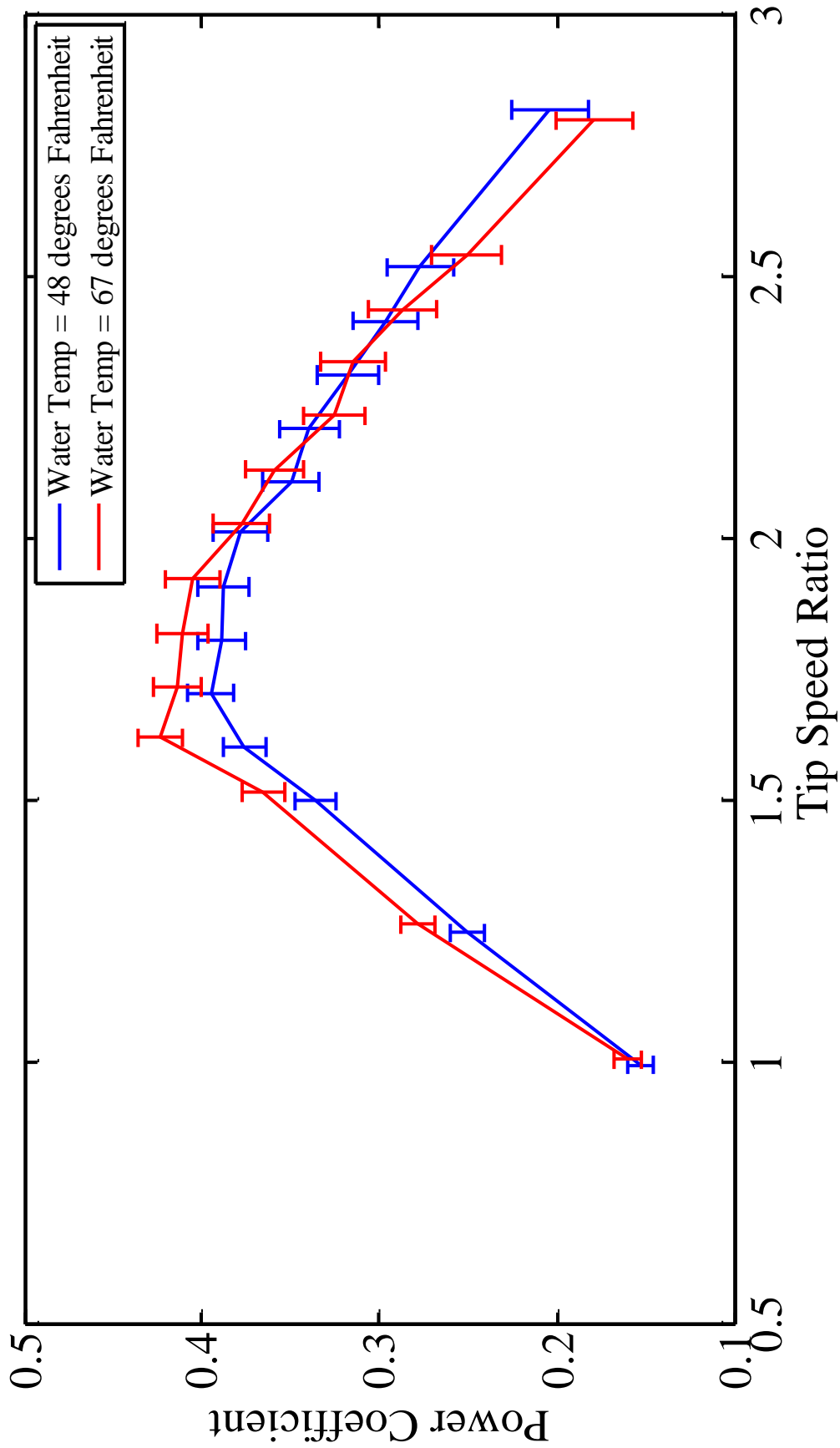


Figure C.1 – Comparison of power coefficient curves for two-blade testing of 3-D printed NACA 0018 blades at $+6^\circ$ toe angle. Testing was performed at 67°F ($\text{Re} = 258115$) and 48°F ($\text{Re} = 193886$) with solidity ratio $\sigma = 0.171$ and inflow velocity $U_\infty = 0.8$ m/s.

APPENDIX D

EFFECTS OF WATER COLUMN HEIGHT

During testing it was observed that a change in water column height can drastically change turbine performance. The power coefficient may be influenced by the distance of the turbine to the free surface or bottom of the tank because the presence of a boundary can cause flow acceleration above and below the turbine (Adamski, 2013). The series of experiments listed in Table C.1 show the tests performed at a variation of water column heights. The turbine remained stationary with the center at a distance of 20 inches from the bottom of the tank as it was in all testing. Tests were taken at a short range of tip speed ratios to capture the peak power coefficient.

Water Column Height	Tip Speed Ratio (λ)							
	1.5	1.6	1.7	1.8	1.9	2.0	2.1	2.2
30"	X	X	X	X	X	X	X	X
32"	X	X	X	X	X	X	X	X
34"	X	X	X	X	X	X	X	X
36"	X	X	X	X	X	X	X	X
38"	X	X	X	X	X	X	X	X
40"	X	X	X	X	X	X	X	X
42"	X	X	X	X	X	X	X	X
44"	X	X	X	X	X	X	X	X

Table D.1 - Experimental test matrix for two-bladed NACA 0018 foils at water column heights from 30 to 44 inches in two degree increments. Toe angle was set to $+6^\circ$, solidity $\sigma = 0.171$, and inflow velocity $U_\infty = 0.8$ m/s.

The water column height was nondimensionalized in Figure D.1 through a ratio of the water height from the center of the turbine to the free surface compared to the turbine radius.

Since the testing was performed in the tow tank in a constricted flow, the blockage effect has a large amount of influence on performance results (McAdam et al., 2009). The blockage effect is quantified by determining the blockage ratio (BR) from Eq. D.1 where A_t is the cross sectional area of the turbine and A_c is the cross sectional area of the channel.

$$BR = \frac{A_t}{A_c} \quad (D.1)$$

Under these conditions, the constricted flow causes flow acceleration around the turbine which changes the apparent inflow velocity. As a result, the actual measured inflow velocity is lower than the apparent inflow velocity and the power coefficient is artificially high. By reducing the blockage ratio, the effect on the power coefficient is reduced (McAdam et al., 2009).

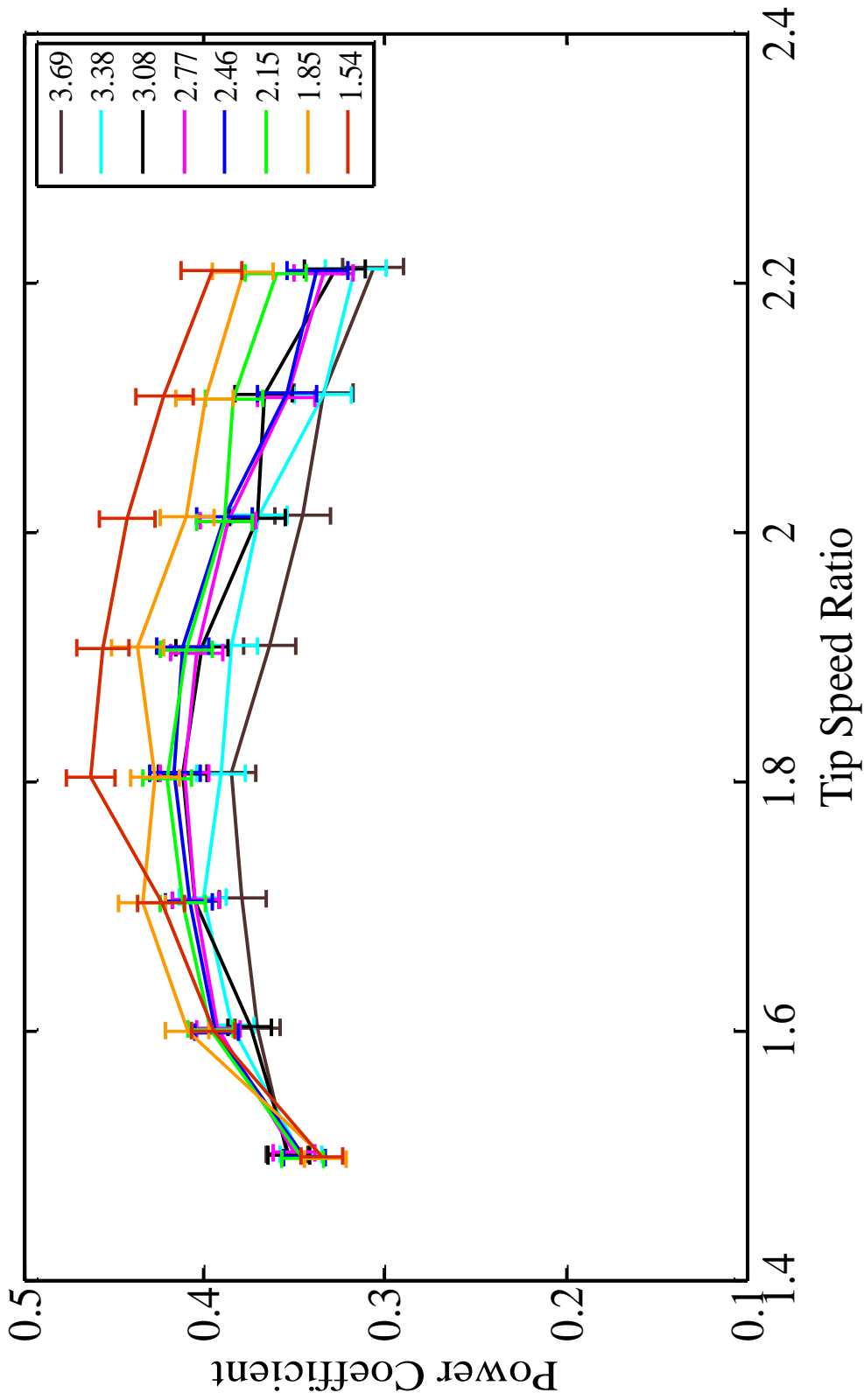


Figure D.1 – Comparison of power coefficient curves for two-blade testing of 3-D printed NACA 0018 blades at +6° toe angle for varying water column height. The center of the turbine was kept at 20 inches from the bottom of the tank. Testing was performed at 48°F with solidity ratio $\sigma = 0.171$ and inflow velocity $U_\infty = 0.8$ m/s.

APPENDIX E

FILTERING METHODS

Angular velocity of the turbine was calculated by using data collected by angular position using an encoder. Angular position is recorded from 0 to 360 degrees, after which it resets to zero again. This causes the sawtooth output seen in the figures below. Due to the noise seen in bottom portion of Figure E.1, filtering was required following the removal of the discontinuity related to the reset of the encoder upon each revolution.

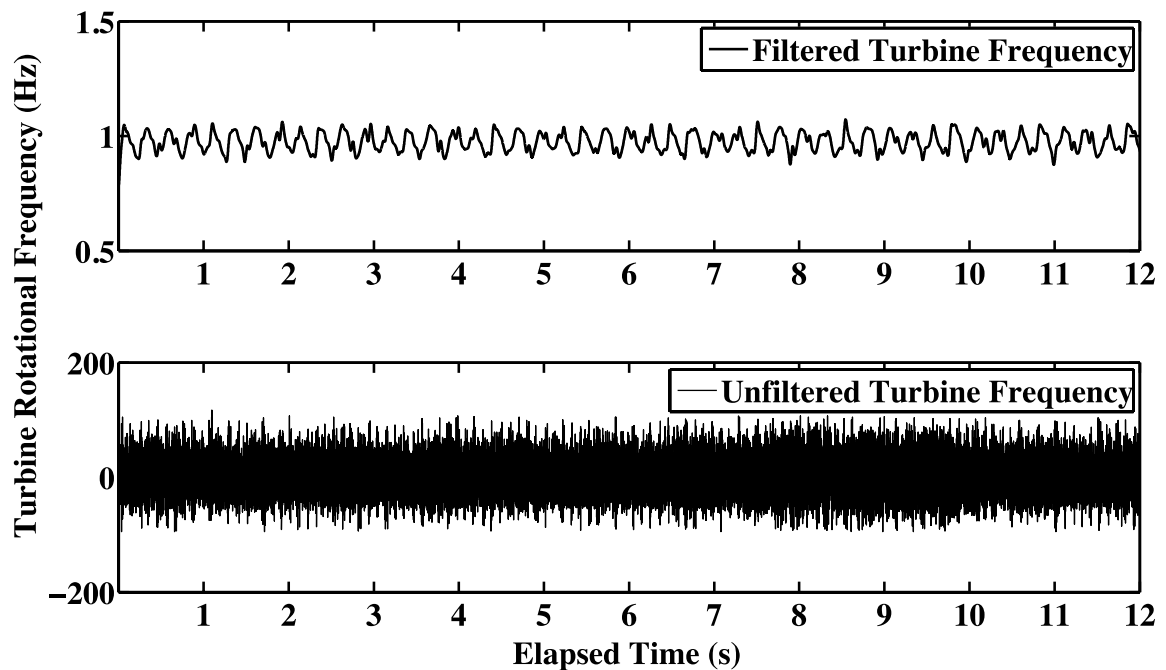


Figure E.1 – Comparison of filtered and unfiltered turbine frequency in Hz over time (Image source: deBree, 2010)

The sawtooth data from Figure E.2 was modified to a straight line by converting to radians, detecting the peak values, then adding multiples of 2π accordingly. Once discontinuities were eliminated, coefficients were created for a finite impulse response

linear-phase low pass filter with a Hamming window using standard MATLAB software functions. For the turbine rotational frequency, a cut-off frequency of 8 Hz was selected.

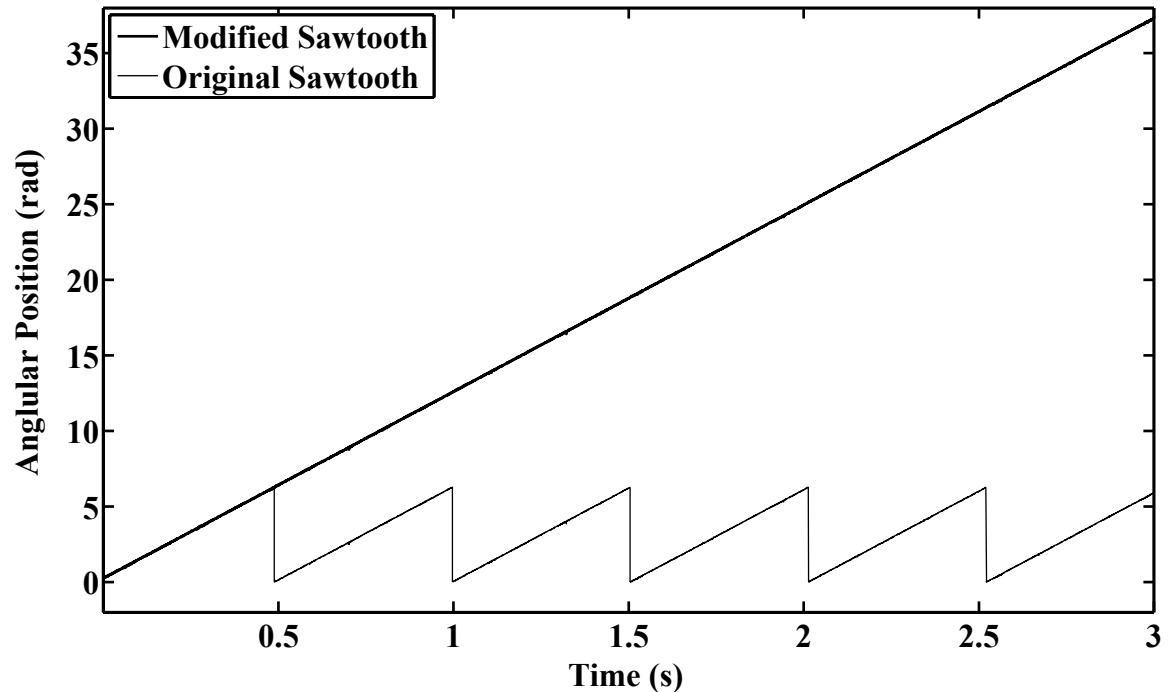


Figure E.2 – Angular position output from the turbine encoder over time displayed as the original sawtooth and the modified sawtooth used to eliminate discontinuities (Image source: deBree, 2010)

This same low pass filter was used to filter the torque data after a small change in the cut-off frequency to 17 Hz. This cut-off frequency is just a bit lower than the natural frequency of the system. Testing showed that altering the cut-off frequency had very little effect on change in the power coefficient. Comparison of the unfiltered and filtered torque data is shown in Figure E.3.

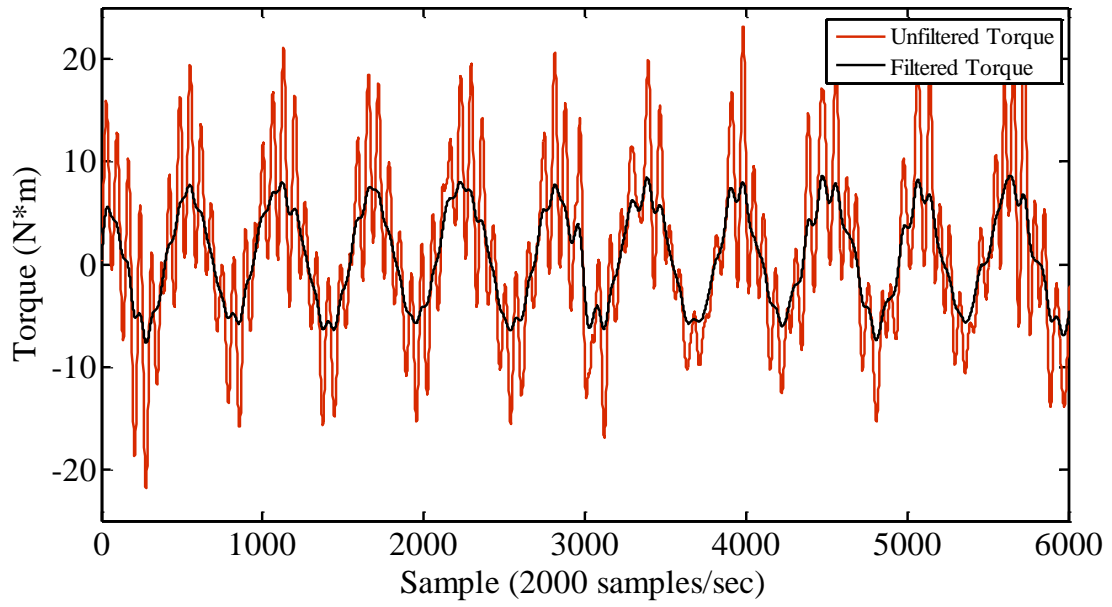


Figure E.3 – Comparison of filtered and unfiltered torque for NACA 0018 foils at $+6^\circ$ toe angle, 0.8 m/s inflow velocity, and TSR of 1.5.

BIOGRAPHY OF THE AUTHOR

Megan Colleen Swanger from Springvale, Maine graduated from Sanford High School in 2002. She went on to attend Norwich University, the Military College of Vermont, where she graduated with a B.S. in Mechanical Engineering in 2006. After graduating, she commissioned into the United States Army as a second lieutenant on active duty. She spent three years traveling around the United States and abroad as a chemical officer. After returning from her deployment to Iraq in 2009, she was promoted to captain and decided to leave active duty in 2010 to attend graduate school. She currently is serving in the Maine Army National Guard as the company commander for the 185th Engineer Support Company. She is a candidate for the Master of Science degree in Mechanical Engineering from the University of Maine in August, 2013.

**A DYNAMIC STALL MODEL FOR MODELING CROSS-FLOW TURBINES
USING LIFTING-LINE VORTEX METHODS**

By

Raul Urbina Villalpando

B.S. Universidad Panamericana, 1997

M.S. The University of Maine, 2000

A DISSERTATION

Submitted in Partial Fulfillment of the

Requirements for the Degree of

Doctor of Philosophy

(in Mechanical Engineering)

The Graduate School

The University of Maine

May 2014

Advisory Committee:

Michael L. Peterson, Professor of Mechanical Engineering, Advisor

Richard W. Kimball, Professor of Engineering, MMA

Krish P. Thiagarajan, Professor of Mechanical Engineering

Zhihe Jin, Associate Professor Mechanical Engineering

Brenden Epps, Assistant Professor, Dartmouth College

DISSERTATION RIGHTS STATEMENT

In presenting this dissertation in partial fulfillment of the requirements for an advanced degree at the University of Maine, I agree that the Library shall make it freely available for inspection. I further agree that permission for "fair use" copying of this dissertation for scholarly purposes may be granted by the Librarian. It is understood that any copying or publication of this dissertation for financial gain shall not be allowed without my written permission.

Signature:

Date:

**A DYNAMIC STALL MODEL FOR MODELING CROSS-FLOW TURBINES
USING LIFTING-LINE VORTEX METHODS**

By Raul Urbina Villalpando

Dissertation Advisor: Dr. Michael L. Peterson

An Abstract of the Dissertation Presented
in Partial Fulfillment of the Requirements for the
Degree of Doctor of Philosophy
(in Mechanical Engineering)

May, 2014

In this work, a dynamic stall model is used with lifting-line vortex method models in order to predict the hydrodynamic performance of high solidity cross-flow turbines. The dynamic stall model presented in this work is based on the Beddoes Leishman (B-L) dynamic stall model and blade force solutions which are derived using conformal mapping for one blade. The dynamic stall formulae used in the model to calculate blade forces has been modified to consider the asymptotic values. The model can therefore represent the principal phenomena to which cross-flow turbines are subject at a large range of operating conditions. The dynamic stall model has also been modified to provide predictions for a large range of angles of attack and Reynolds numbers, conditions under which cross-

flow turbines operate. The model uses Sheng's consideration of the influence of reduced-pitch rate on the angle at which the blade stalls. The dynamic stall model includes considerations for flow curvature effects. Parameters, such as blade thickness and camber, are considered in the derived formulae, which allow predictions of numerous turbine configurations and therefore make the model suitable for implementation on turbine optimization codes. This characteristic allows the method to better predict the performance of cross-flow turbines with high solidity ratios. The cross-flow turbine model was assessed with experimental data that was acquired using different blade profiles, range of toe angles and multiple solidity ratios.

This work also presents experimental data that was obtained for the hydrodynamic performance of a cross flow turbine using NACA 0018 and NACA 63018 blade families. This experimental data-set consist of measurements of the torque and power coefficient, taken at different toe angles and tip-speed ratios. The data set demonstrates the influence that the variation of the blade camber, the number of blades, and the chord-to-radius ratio has on the turbine performance. This experimental data-set is intended to complement previous data-sets for use in validation of design models and to support turbine design. Cases of negative power output and unoptimized design were also included in the experimental data set to increase the number of cases available for validating design models.

DISSERTATION ACCEPTANCE STATEMENT

On behalf of the Graduate Committee for Raul Urbina Villalpando I affirm that this manuscript is the final and accepted dissertation. Signatures of all committee members are on file with the Graduate School at the University of Maine, 42 Stodder Hall, Orono, Maine.

Dr. Michael L. Peterson/ Professor of Mechanical Engineering

May 2, 2014

DEDICATION

I want to dedicate this dissertation to my wife, Andrea, for her support, love and encouragement throughout my career. I would not have been able to finish without her. I believe that Andrea, at this point, knows more about dynamic stall and flow curvature than I do

ACKNOWLEDGEMENTS

I would like to thank my advisor, Dr. Michael “Mick” Peterson, for his guidance and support during my thesis work. “Mick” has been an important part of my professional career for the last fifteen years. I would also like to thank Dr. Richard Kimball, for his time and advice over the past six years. I am grateful to Mr. Jarlath McEntee for his technical advice especially during the early stages of my research. I would also like to express my appreciation to the Maine Tidal Power Initiative for allowing me to be part of their team and contribute to the advancement of tidal energy in Maine.

.

I would like to thank my fellow graduate students, Matthew Cameron, Geoffey deBree, Thomas Lokocz, and Colleen Swanger, with whom it has been a pleasure to work. I am equally appreciative to Nathan Rocker, Thomas McKay and Patrick Pottle for their contributions to the project. Finally, I want to thank the department of Energy, Ocean Renewable Power Company, and the Maine Tidal Power Initiative for funding this work.

TABLE OF CONTENTS

DEDICATION.....	345
ACKNOWLEDGEMENTS.....	346
LIST OF TABLES.....	349
LIST OF FIGURES.....	350
NOMENCLATURE.....	357
Chapter	
1. TIDAL TURBINES AND THEIR MODELLING.....	361
1.1. Introduction.....	361
1.2. Fluid Dynamics of the Cross-Flow Turbines.....	364
1.3. Validation of the Cross-Flow Turbine Model.....	370
2. TESTING OF HIGH SOLIDITY CROSS-FLOW TIDAL TURBINES	371
2.1 Background.....	371
2.2 Theory.....	375
2.3 Experimental Set-up.....	379
2.4 Results.....	385
2.5 Discussion.....	395
2.6 Conclusions.....	399
3. DYNAMIC STALL MODEL FOR A FREE VORTEX MODEL.....	401
3.1. Modeling Approach.....	402
3.2. Theoretical Approach.....	403
3.3. Experimental Set-Up.....	416

3.4. Results and Discussion.....	418
3.5. Conclusions.....	425
4. DYNAMIC STALL MODEL WITH FLOW CURVATURE CORRECTION.....	428
4.1. Theoretical Approach.....	430
4.1.1. Blade Forces Formulae.....	431
4.1.1.1 Lift and Drag.....	431
4.1.2. Dynamic Stall Model.....	439
4.2. Experimental Set-Up.....	443
4.3. Results and Discussion.....	445
4.4. Conclusions.....	455
5. CONCLUDING REMARKS.....	459
 BIBLIOGRAPHY.....	 464
APPENDICES.....	468
APPENDIX A. MAIN MATLAB PROGRAM ROUTINES.....	469
APPENDIX B. EXPERIMENTAL RESULTS FOR CHAPTER 4.....	477
BIOGRAPHY OF THE AUTHOR.....	480

LIST OF TABLES

Table 2.1.	Parameters of the first series of tests varying the number of blades	374
Table 2.2.	Parameters of the second series of tests varying the blade camber	374
Table 2.3.	Parameters of the third series of tests varying the chord to radius ratio	375

LIST OF FIGURES

Figure 1.1.	A schematic drawing which shows the configuration of cross flow and axial flow turbines.....	362
Figure 1.2.	Schematic showing the classification of analytical methods used for cross flow turbines.....	366
Figure 2.1.	The blade forces are shown for a given in flow.....	377
Figure 2.2.	The upstream and downstream zones with respect to the turbine are shown.....	379
Figure 2.3.	The diagram shows the instrumentation used for torque and thrust measurements.....	380
Figure 2.4.	A schematic of the cross-flow turbine installed in the tow tank shows the geometry used for testing. The turbine direction of motion corresponds to out of the page.....	381
Figure 2.5.	The straight bladed model Darrieus turbine rotor is shown with NACA 633-018 blades installed and rod across the center.....	382
Figure 2.6.	Turbine endplate with attached angle indicators and blades are shown.....	382
Figure 2.7.	The test turbine diagram shows the motor controller and transmission.....	384
Figure 2.8.	Experimental power coefficient results for a four-bladed turbine with a chord to radius ratio of 0.53 show reasonable repeatability.....	387

Figure 2.9.	The experimental power coefficient for a two-bladed turbine with a chord to radius ratio of 0.53 acquired at two different temperatures.....	387
Figure 2.10.	The experimental power coefficient results for a two-bladed turbine with a chord to radius ratio of 0.53 show the effect of varying the water column in the tow tank.....	388
Figure 2.11.	The experimental power coefficient for a two-bladed turbine with a chord to radius ratio of 0.53 acquired at two different in-flow velocities.....	388
Figure 2.12.	The experimental power coefficients for a two-bladed turbine and a four-bladed turbine with a chord to radius ratio of 0.53 are shown for different tow angles.....	389
Figure 2.13.	The experimental power coefficients for a two-bladed turbine using blades with NACA 0018 profile are shown for different tow angles and tip speed ratios.....	391
Figure 2.14.	The experimental power coefficients for a two-bladed turbine using blades with NACA 4418 profile are shown for different tow angles and tip speed ratios.....	391
Figure 2.15.	The experimental power coefficients for a two-bladed turbine using blades with NACA 4418 profile mounted in reversed position are shown for different tow angles and tip speed ratio...	392
Figure 2.16.	The experimental power coefficients for a two-bladed turbine using blades with NACA 63-3-018 profile are shown for	

	different chord-to-radius ratios.....	393
Figure 2.17.	The experimental non-dimensional torque results for a two-bladed turbine using two-inch chord blades at a toe angle of +4 degrees are shown for different tip-speed ratios.....	394
Figure 2.18.	The experimental non-dimensional torque results for a two-bladed turbine using three-inch chord blades at a toe angle of +5 degrees are shown for different tip-speed ratios.....	395
Figure 2.19.	The tangential coefficient for a NACA 0018 blade at Reynolds number of 5,000,000 is shown as a function of angle of attack...	397
Figure 3.1.	The flowchart of the analytical model is shown for each time step in the program.....	393
Figure 3.2.	The separation point in the flow across the blade diverge the streamlines depending on the angle of attack.....	394
Figure 3.3.	The normal force prediction of the modified flow equation is shown as a function of the angle of attack.....	396
Figure 3.4.	The lift force prediction of the analytical lift curve is shown as a function of the angle of attack.....	408
Figure 3.5.	The modified B-L lift curves are calculated for reduced frequencies $k=0.062$, 0.125 and 0.2150	410
Figure 3.6.	The velocity components of the relative velocity are combined in the model as shown.....	411
Figure 3.7.	The upstream and downstream zones with respect to the turbine are shown.....	415

Figure 3.8.	The model cross-flow turbine is mounted on the tow tank carriage for testing.....	416
Figure 3.9.	The nondimensional normal force from reference [5] is compared to the results of the FVM model.....	419
Figure 3.10.	The nondimensional tangential force from reference [5] is compared to the results of the FVM model.....	420
Figure 3.11.	The power coefficient from reference [6] is compared for the model results for a solidity of 0.179.....	421
Figure 3.12.	The power coefficient is compared for the model for 2 blades with a chord to radius of 0.46.....	422
Figure 3.13.	The unsteady nondimensional torque data from UMaine tow tank tests is compared for the model with and without blockage and dynamic stall at tip speed ratio of 1.8.....	423
Figure 3.14.	The unsteady nondimensional torque data from UMaine tow tank tests is compared for the model with and without blockage and dynamic stall at tip speed ratio of 1.8.....	424
Figure 3.15.	The unsteady nondimensional torque data from UMaine tow tank tests is compared for the model with and without blockage and dynamic stall at tip speed ratio of 2.0.....	425
Figure 4.1.	The flowchart of the analytical model is shown for each time step in the program.....	431
Figure 4.2.	Separation function value as a function of the effective angle of attack is shown.....	434

Figure 4.3.	The calculated lift coefficient of the analytical model for a NACA 63-3-018 as a function angle of attack is compared to experimental data for different Reynolds number of 3,000,000...	438
Figure 4.4.	The calculated lift coefficient is shown as a function angle of attack for different camber values.....	439
Figure 4.5.	The blade toe-angle and mounting point is shown.....	442
Figure 4.6.	The calculated torque for a one bladed turbine with a chord to radius ratio of 0.15 at conditions of published results (Li, 2008) indicates improvements in the predictions regarding the peak magnitude and the downstream region predictions for DVM.....	446
Figure 4.7.	The calculated torque for a three-bladed turbine with a chord to radius ratio of 0.15 at the conditions of published results (Li, 2008) shows good correlation with CFD results.....	448
Figure 4.8.	Experimental power coefficient results for a two-bladed turbine with a chord to radius ratio of 0.3 show dependency on where the maximum power coefficient is found with respect to the toe angle.....	450
Figure 4.9.	The analytical power coefficient results where flow curvature is considered show agreement with experimental data for a two-bladed turbine with a chord to radius ratio of 0.3 at a the toe angle of +4.....	450

Figure 4.10. Analytical results, when compared to experimental data show at a toe angle of +4 degrees and tip-speed ratio of 1.6, indicate improvements on the predictions when considering the flow curvature correction.....	451
Figure 4.11. Analytical results, when compared to experimental data at a toe angle of +4 degrees and tip-speed ratio of 2.4, show that the flow curvature correction has a lower contribution on the predictions.....	451
Figure 4.12. The analytical power coefficient predictions where flow curvature is considered can predict where the maximum torque is encountered when compared with experimental data for a two-bladed turbine with a chord to radius ratio of 0.46 at a toe angle of +5.....	452
Figure 4.13. The analytical results, when compared to experimental non-dimensional torque at a toe angle of +5 degrees and tip-speed ratio of 2.0, imply that there is a higher influence of the flow curvature at a chord-to-radius ratio of 0.46.....	453
Figure 4.14. The analytical results, when compared to experimental non-dimensional torque at a toe angle of +5 degrees and tip-speed ratio of 2.0, indicate that further improvements are needed to predict the torque amplitude.....	454
Figure 5.1. The calculated lift coefficient is shown as a function angle of attack for different Reynolds numbers.....	461

Figure 5.2.	The superimposed velocity profiles of two blades using single element vortex distribution with prescribed vorticity are shown.....	461
Figure B.1.	Power coefficient measured at different toe angles for a two bladed cross flow turbine with two inch chord blade and NACA 63-3-218 profile.....	477
Figure B.2.	Power coefficient measured at different toe angles for a two bladed cross flow turbine with two inch chord blade and NACA 63-3-018 profile.....	478
Figure B.3.	Power coefficient measured at different toe angles for a two bladed cross flow turbine with three inch chord blade and NACA 63-3-018 profile.....	478
Figure B.4.	Power coefficient measured at different toe angles for a two bladed cross flow turbine with two inch chord blade and NACA 63-3-218 profile (second set of tests).....	479

NOMENCLATURE

A_F	=	<i>total projected frontal area of the rotor</i>
b	=	<i>measured friction at the instantaneous tip speed ratio</i>
c	=	<i>chord length (m)</i>
C_p	=	<i>power coefficient</i>
C_C	=	<i>chordwise force coefficient</i>
C_D	=	<i>drag coefficient</i>
C_{D0}	=	<i>drag coefficient at an angle of attack of zero degrees</i>
C_{D90}	=	<i>drag coefficient at an angle of attack of ninety degrees</i>
$C_{D90, plate}$	=	<i>drag coefficient of a flat plate at an angle of attack of ninety degrees</i>
C_L	=	<i>lift coefficient</i>
C_N	=	<i>normal force coefficient</i>
$C_{N\alpha}$	=	<i>Normal coefficient slope at zero degrees</i>
C_T	=	<i>tangential force coefficient</i>
$C_{T,RL90}$	=	<i>tangential coefficient at an angle of attack of ninety degrees</i>
E_0	=	<i>cavity factor</i>
f	=	<i>blade camber (m)</i>
f'	=	<i>separation location in terms of chord</i>
f''	=	<i>delayed separation location of f'</i>
h	=	<i>distance from vortex core to evaluation point (m)</i>

I	=	<i>rotor's moment of inertia</i>
N	=	<i>number of blades</i>
NTI	=	<i>number of evaluation points in one revolution</i>
r	=	<i>reduced pitch rate ($r = \dot{\alpha} c / 2V$)</i>
R	=	<i>turbine radius (m)</i>
Re_L	=	<i>Reynolds number calculated at the blade</i>
s	=	<i>nondimensional time ($s = 2Vt/c$)</i>
S_1	=	<i>Exponential constant for separation point before stall</i>
S_2	=	<i>Exponential constant for separation point after stall</i>
S_3	=	<i>Exponential constant for reduce pitch rate before stall</i>
S_4	=	<i>Exponential constant for reduce pitch rate after stall</i>
t	=	<i>Time</i>
t_s	=	<i>time elapsed until the onset of separation</i>
T_α	=	<i>Delay constant for angle of attack due to dynamic effect</i>
T_P	=	<i>instantaneous measured torque</i>
$T_{P,AS}$	=	<i>measured torque contribution of the end plates</i>
$T_{P,B}$	=	<i>instantaneous torque produced by the blades</i>
$T_{P,R}$	=	<i>instantaneous torque produce by the rotor</i>
T_e^+	=	<i>Non dimensional single element torque</i>
T^+	=	<i>nondimensional torque</i>

U	=	<i>induce velocity parallel to the inflow (m/s)</i>
W	=	<i>induced velocity perpendicular to the inflow (m/s)</i>
U_R	=	<i>resultant velocity (m/s)</i>
U_T	=	<i>blade tangential velocity (m/s)</i>
U_∞	=	<i>undisturbed free stream velocity (m/s)</i>
V	=	<i>free stream velocity (m/s)</i>
V_p	=	<i>induced velocity (m/s)</i>
α	=	<i>angle of attack AOA or incidence (radians)</i>
α_L	=	<i>angle of zero lift (radians)</i>
α_D	=	<i>angle of minimum drag (radians)</i>
α_0	=	<i>angle of attack or incidence at zero normal force or mean AOA (radians)</i>
α_1	=	<i>breakpoint of separation</i>
α_{1max}	=	<i>Maximum value for breakpoint of separation</i>
$\dot{\alpha}$	=	<i>Angle of attack change in time</i>
β	=	<i>angle from conformal mapping related to the camber</i>
Γ	=	<i>Vorticity</i>
Γ_B	=	<i>bound vorticity</i>
Γ_S	=	<i>shed vorticity</i>
Δ	=	<i>a step change in forcing or in time</i>
ϵ	=	<i>distance of the centre of the circle form the centre of coordinates</i>
θ	=	<i>turbine rotational position</i>

$\dot{\theta}$	=	<i>rotor's angular velocity</i>
$\ddot{\theta}$	=	<i>rotor's angular acceleration</i>
θ_B	=	<i>blade rotational position</i>
κ	=	<i>reduced frequency ($k = \omega c / 2V$)</i>
λ	=	<i>tip speed ratio ($R\omega/V$)</i>
η	=	<i>Recovery factor</i>
ρ	=	<i>fluid density (kg/m^3)</i>
σ	=	<i>solidity ($Nc / 2\pi R$)</i>
ν	=	<i>Fluid viscosity</i>
ω	=	<i>angular velocity (rad/s)</i>

CHAPTER 1

TIDAL TURBINES AND THEIR MODELLING

1.1. Introduction

Although the marine hydrokinetic power industry is still in its developmental stages, tidal- energy is regarded as one of the most promising new alternative energy resources (Brito and Huckerby, 2010). Tidal energy can reduce the environmental carbon footprint and help meet future energy demands, particularly for communities near coastal areas. For example, it has been estimated that tidal energy can potentially provide 5% of the energy needs in the United Kingdom (Carbon Trust, 2007). However, any tidal energy installation is subject to environmental impact assessments and monitoring, since some of the best tidal currents available also happen to be near sensitive areas for fish spawning and feeding. A unique example is the protected area of the Severn Estuary in that has the second largest tidal range in the world (Carbon Trust, 2007). However as a protected area, any device designed for installation in this environment has to minimize the impact on these fragile ecosystems.

For tidal energy to be viable and compared favorably to other renewable energy sources, tidal turbine farms and tidal turbine designs need to be optimized for maximum power extraction with minimal environmental impact. Additionally, other design constraints, such as maximum blade tip speed, may need to be altered to reduce the impacts on local fauna. The number of turbine

design parameters and particular conditions of each tidal site, such as flow conditions, increase the number of combinations that have to be analyzed, resulting in the need for optimizers. The ability to produce efficient turbine designs with minimal environmental impact could potentially increase the likelihood of them being accepted for use in sensitive tidal areas.

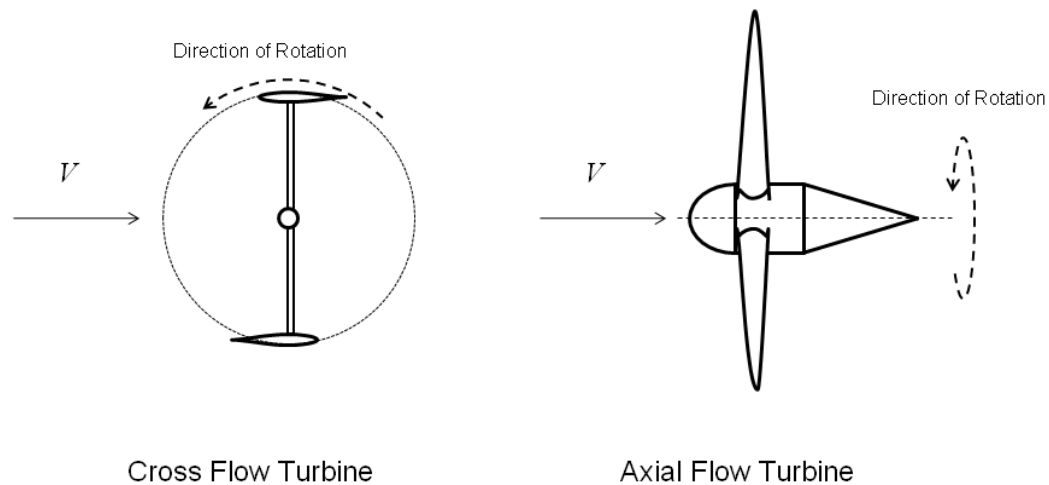


Figure 1.1. A schematic drawing which shows the configuration of cross-flow and axial flow turbines

Numerous tidal current turbine designs have been produced. These turbine designs can be classified according to their principle of operation, in to two main types: cross-flow and axial flow turbines (Khan et al., 2009), shown in Figure 1.1. The Darrieus turbine, a type of cross-flow turbine, is of particular interest because it can be designed for high solidity ratios. At high solidity ratios, the Darrieus turbine operate at lower tip speed ratios and allow for lower pressure gradients along the blade. Reducing the blade tip speeds and lowering the pressure gradients along the blade have the potential to reduce

environmental impact by minimizing mechanical strike, cavitation, and pressure gradients which adversely affects marine fauna (Dadswell et al., 1986), (Polagye et al., 2011) while still achieving turbine efficiencies that can make the tidal energy installation viable.

Darrieus turbines are much less common than axial flow designs. However, they are appealing for tidal and wind energy applications because they can accept flow perpendicular to their axis of rotation. In spite of being less common numerous analysis tools for cross-flow turbines have been developed. Free Vortex Methods (FVM) models have been one of the preferred analysis tools since they can be used to compute the induced velocity on the blade directly, and account for blade to blade interaction. FVM are also able to compute solutions efficiently and provide complete temporal and spatial velocity fields. These tools can be used to assist turbine designs, but also provide information for oceanographic studies, and fish-turbine interactions. As the industry develops further the oceanographic and environmental factors will be critical to the process of evaluating a particular site for tidal energy purposes.

This work uses a lifting-line free FVM with a modified Beddoes-Leishman (B-L) model to calculate the performance of cross-flow turbines. The FVM can also be used to model unsteady flows. The capability to model the unsteady flow is particularly important since the flow around cross-flow turbine becomes unsteady as the blades rotate. The lifting-line FVM utilizes the blade force

information of the modified B-L model to calculate the vortices needed to represent the flow velocity field around the turbine at each time step. The modified B-L model also provides blade force information, such as lift, drag, and blade circulations, for different camber and blade thickness ratios taking into account the effects of dynamic stall and flow curvature, as well as the cyclic variation of the Reynolds number, as the blades rotate around 360 degrees (Migliore and Wolfe, 1980). These considerations enable the modified B-L model to obtain reasonable predictions of the blade forces for a wide range of operating conditions. The basis of the B-L model is the calculation of the blade forces given an angle of attack and an approximate location where the flow separates on a foil. The B-L model has been modified (Simao et al., 2009) for the unsteady flow conditions at low Mach numbers in which tidal turbines operate. Blade-force calculations in the B-L model were modified based on blade forces solutions using conformal mapping; asymptotic values were used for the limit cases to assure reasonable blade forces predictions at a wide range of operating conditions.

1.2. Fluid-Dynamics of the Cross-Flow Turbines

An understanding of the blade forces is needed to estimate the turbine performance. These forces on the blade are greatly influenced by the external flow and the boundary layer created around the blade by said external flow. To calculate these forces, the interactions of the viscous layer and the outer inviscid flow have to be taken into account particularly when separation of the boundary-

layer is present. When this happens, stall, in which there is an increase of the drag force and a decrease on the lift force on the blade, can occur reducing the efficiency of turbine designs based on lift. Consequently, various techniques have been developed to estimate the boundary layer and position of the separation on the blade in an unsteady flow. Thus, the separation estimation is a critical factor in cross-flow turbines.

Analytical and numerical solutions, such as linearized theory and conformal mapping, have been developed to estimate the blade forces in a steady state flow. Actuator disk theory has also been used in Blade Element Methods (BEM) to represent the external flow produced by the blades. However, these methods do not consider the boundary layer or the unsteady nature of the flow. The boundary layer has been accounted for in panel vortex methods with viscous-inviscid interaction methods for calculating the blade forces (Drela, 1989). These methods can be used to estimate the lift and drag forces for different blade profiles; however these approaches are not accurate in the post-stall region (Berg, 1996). The boundary layer can also be modeled using vortex clouds in panel vortex methods, which have yielded encouraging results for the calculation of lift and drag forces in the post stall region (Lewis, 1991). Computational Fluid Dynamics (CFD) methods based on the Navier-Stokes equations, such as LES, DES, and URANS, have also been used to calculate the boundary layer, forces on a blade, and turbine efficiency (Li, 2008).

All of the methods listed above (Figure 1.2) can be used in turbine design or analysis. However, the appropriateness of a particular method will vary depending on the stage of the turbine design. Low computational cost methods are commonly used in design optimization to narrow the turbine design parameters that yield the highest efficiency for a given set of design constraints. Then high computational cost methods are used to define the final turbine design parameters. The low computational cost of lifting-line vortex methods (VM) and BEM is an important characteristic that makes them the preferred methods used in conjunction with optimizers (Asher et al., 2010) (Sale et al., 2009). Lifting-line VM and BEM methods can assist on providing basic turbine geometry and operating conditions at which the maximum power can be extracted (Coney, 1989). Lifting-line FVM can also be used in parametric studies to optimize turbine

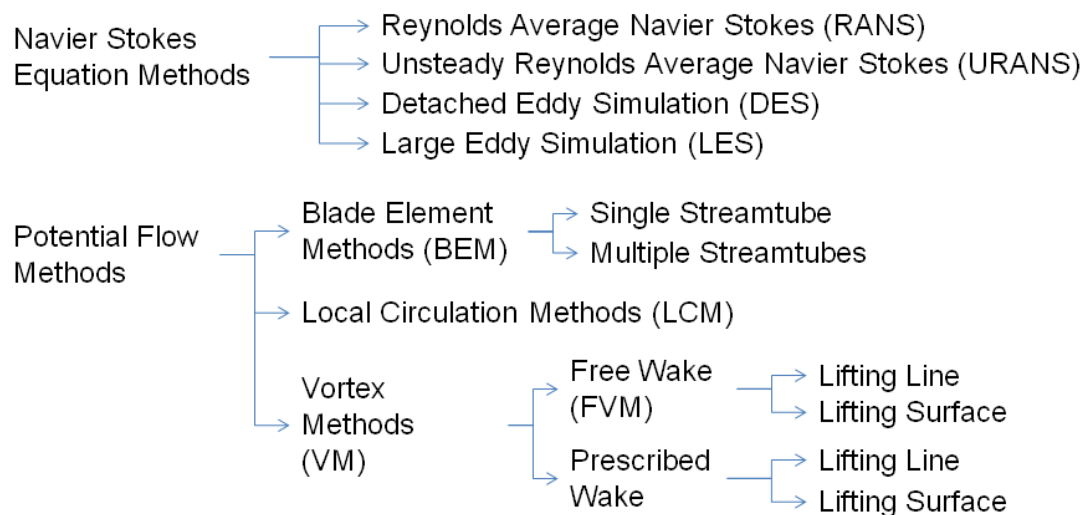


Figure 1.2. Schematic showing the classification of analytical methods used for cross-flow turbines

design with respect to parameters such as efficiency, cavitation, strength, and cost (Coney, 1989). Lifting-line FVM models have an advantage over BEM models since they make it possible to consider the effect of blade to blade interaction. In contrast, the momentum equations of the BEM models become invalid at increased rotor solidities (Strickland et al., 1980). However, since lifting-line FVM would not provide the information to design the actual blade geometry, methods such as Navier Stokes and lifting surface FVM are used to provide information to determine the final design of the blade. These methods can be used to analyze the resulting performance of the turbine.

Special considerations are required when using lifting-line FVM models because of the simplified representation of the blade which is used to model the cross-flow turbines. Phenomena such as dynamic stall and flow curvature have to be accounted for in order to obtain accurate predictions of the blade forces on the turbine. These phenomena are particularly important in modeling cross-flow turbines. Modeling the cross-flow turbine is further complicated by the fact that the blade forces are also influenced by the wake of the other blades of the turbine and previous rotations of the blade.

Dynamic stall is a phenomenon that affects the blades of a cross-flow turbine as it rotates, especially when operated at low tip speed ratios. Dynamic stall is created when unsteady loads and flow separation release large vortices that influence the forces on the blade. Dynamic stall occurs as a leading-edge vortex is shed from the blade which occurs as the blade changes its angle of

attack relative to the flow. The increase in angle of attack produces an increase in lift, a negative pitching moment, and an increase in drag on the blade. The resultant forces created by dynamic stall have a significant impact on the loading on the blades and consequently on the power output of the turbine (Simao et al., 2009). Cross-flow turbines are also subject to cyclic forces on the blades, since during turbine rotation, they experience a wide range of changes in their angle of attack. The ability to accurately predict the forces on the blade at all angles of attack is therefore critical in order to design the turbine for fatigue.

Modeling dynamic stall is an active area of research in classical fluid mechanics, and no one method is universally accepted for all applications (Sheng et al., 2008). Semi-empirical methodologies have been developed to compute the dynamic stall effect for helicopter and wind turbine applications. The Gormont dynamic stall model has been implemented for cross-flow turbines by Strickland et al (1980), Masson et al (1998), and Paraschivoiu (2002). Another semi-empirical model commonly used to account for dynamic stall is the Beddoes-Leishman (B-L) model (Leishman and Beddoes, 1989). The B-L model provides an overall representation of the unsteady phenomenon, and is commonly used for helicopter blade aerodynamic modeling at Mach Numbers above 0.5. However, cross-flow tidal turbines operate at low Mach numbers. Sheng et al. (2008) developed recommendations for extending the B-L model to lower Mach number applications. Because of the challenges in modeling the unsteady flow in lifting-line FVM and BEM methods, semi-empirical dynamic stall

models are still the best approach for accurately modeling this phenomenon. Direct numerical simulation of dynamic stall in a cross-flow turbine would increase the computational cost of the model to an unacceptable level for most applications. Therefore, numerical approximations of the dynamic stall phenomenon for lifting-line FVM and BEM are necessary to ensure that the resulting model is efficient enough for use in optimization of turbine design.

Flow curvature is a phenomenon particularly prevalent in cross-flow turbines and that has an impact on the blade hydrodynamic efficiency. Its proper consideration can improve performance calculations, even for lower blade to radius ratio (c/R) cross-flow turbines. This is due to the miscalculation of the actual blade forces at flow curvature conditions because of the difference in pressure distribution estimations found using linear flow considerations. This can be attributed to the fact that the actual and assumed velocity fields can differ greatly. Its effect is even more noticeable on the hydrodynamics of higher blade to radius ratio (c/R) cross-flow turbines. This phenomenon has been approximated by transforming the curvilinear flow field to an equivalent linear flow field with a virtually altered camber and an incidence angle (Migliore and Wolfe, 1980).

1.3 Validation of the Cross-Flow Turbine Model

To validate the model results at a range of chord to radius ratios, a lifting-line FVM model with dynamic stall and flow curvature corrections was compared to published experimental data. Additional experimental tow tank measurements were also made for comparison tell-conditions. The available experimental data used in this work for straight bladed Darrieus turbines includes a well-known data set produced by Strickland et al. (Strickland et al. 1980), Shiono et al. (Shiono et al., 2000) and Rawlings (Rawlings, 2008). These data provided a wide range of operating conditions under which to validate the proposed lifting-line FVM with the modified B-L dynamic stall model. Validating the model at a wide range of operating conditions and having reasonable blade forces predictions at the asymptotic values allows the model to be used with confidence in optimizers.

CHAPTER 2

TESTING OF HIGH SOLIDITY CROSS-FLOW TIDAL TURBINES

Numerous analytical tools have been developed to model cross-flow turbines. However, to develop better analytical tools there is a need to validate the numerical codes using experimental data from installed tidal turbines. This experimental data is specific to certain tidal designs and is generally not available to the general public. Thus, experimental data sets of scaled cross flow turbines are necessary to evaluate the analytical tools. Experimental data sets that provide information on cross flow turbines at different conditions are especially useful for validation purposes, such as conditions where negative power coefficient is acquired. The following paper provides information from an experimental data set acquired in a tow tank for different cases of camber, chord-to-radius ratio and number of blades at various toe angles and tip-speed ratios. As with all data sets some limitations that may be attributed to the tow tank where the tests were performed. Data that may will facilitate comparison to code results is presented including blockage effect, water temperature and inflow velocity.

2.1 BACKGROUND

Several experimental data sets that focus on acquiring the power coefficient and blade forces or torque produced by the turbine have been acquired for cross flow turbines. These experimental data sets for cross-flow

turbines typically measure the effects of a small number of tests (Strickland et al., 1980) (Shiono et al., 2000) (Rawlings, 2008). Some of the experimental data sets also include analytical tools that were based on, or validated by, the testing. Combined experimental and analytical approach provided greater insight into how cross flow turbines work.

One of the best known experimental data sets was acquired by Strickland et al. (Strickland et al., 1980). This work included numerical and experimental data for low to medium solidity, σ , ($\sigma = 0.0239$ to $\sigma = 0.0716$), cross flow turbines. The experimental data set included measured normal and tangential forces, power coefficient and wake measurements. The experimental data set was acquired using one, two and three blades with a NACA 0012 profile and a chord-to-radius ratio of 0.15. Testing was done at an average Reynolds number of 40,000 by varying the inflow velocity. Two analytical models were also developed: one based on blade element methods and another one based on lifting line free vortex models with a dynamic stall correction.

Another well-known experimental data set was acquired by Shiono et al. (Shiono et al., 2000). This data was acquired using a three bladed turbine with a NACA 633-018 profile for a solidity range of 0.108 to 0.537 by changing the chord to radius ratio. The tested blades were NACA 633-018 profiles with camber added so that the mean line of the profile matched the turbine radius. The inflow velocity for this work was 1 m/s.

Rawlings (Rawlings, 2008) acquired an experimental data-set using one and three-bladed turbines with two different profiles: NACA 63-4-021 and NACA 0015 with a chord to radius ratio of 0.15 and the inflow velocity in a range from 1 m/s to 2m/s. As part of the same effort, Li (Li, 2008)(Li and Calisal, 2010) produced an analytical model based on lifting line vortex method with a dynamic stall correction.

The work by Migliore et al. (Migliore and Wolfe, 1980) on cross flow turbines was acquired at a higher Reynolds number (average $Re=131,000$ for $c/R=0.14$ and average $Re=225,000$ for $c/R=0.26$). This data shows the effects that dynamic stall, Reynolds number variation and flow curvature have on the performance of a cross flow turbine. Based on these results, a flow curvature correction for improving calculations of cross-flow turbine models was developed.

The experimental data set presented in this work was acquired at a higher average Reynolds number and at a higher chord to radius ratio than the data of Strickland et al. (Strickland et al, 1980). The data set of Shiono et al. (Shiono et al., 2000) was acquired for a three bladed turbine. The new experimental data set presented in this work was acquired for two and four blades and at higher chord to radius ratios. This data include the evaluation of the effect of the number of blades (Table 2.1), blade camber (Table 2.2) and the chord to radius ratio

(Table 2.3). The purpose of this data is to provide different cases which can help to advance the development of design codes.

Table 2.1. Parameters of the first series of tests varying the number of blades

Variables		
Profile	NACA 0018	NACA 0018
Number of Blades	Two	Four
Chord Length (c)	0.0762 m	0.0762 m
Chord to Radius Ratio (c/R)	0.46	0.46
Range of Toe Angles	-3 to 10 degrees	-3 to 10 degrees
Range of Tip Speed Ratios (λ)	1 to 2.75	0.5 to 2
Water Depth	1.016 m	1.016 m
Water Temperature	19.4° Celsius	19.4° Celsius

Table 2.2. Parameters of the second series of tests varying the blade camber

Variables			
Profile	NACA 0018	NACA 4418	NACA 4418 (reversed position)
Number of Blades	Two	Two	Two
Chord Length (c)	0.0762 m	0.0762 m	0.0762 m
Chord to Radius Ratio (c/R)	0.46	0.46	0.46
Range of Toe Angles	-3 to 10 degrees	-3 to 10 degrees	-3 to 10 degrees
Range of Tip Speed Ratios (λ)	1 to 3	1 to 3	1 to 3
Water Depth	1.016 m	1.016 m	1.016 m
Water Temperature	19.4° Celsius	19.4° Celsius	19.4° Celsius

Table 2.3 Parameters of the third series of tests varying the chord to radius ratio

Variables		
Profile	NACA 63-3-018	NACA 63-3-018
Number of Blades	Two	Two
Chord Length (c)	0.0508 m	0.0762 m
Chord to Radius Ratio (c/R)	0.30	0.46
Range of Toe Angles	-3 to 10 degrees	-3 to 10 degrees
Range of Tip Speed Ratios (λ)	1 to 3.25	1 to 3.25
Water Depth	1.016 m	1.016 m
Water Temperature	8.90° Celsius	8.90° Celsius

2.2 THEORY

The hydrodynamic performance of a cross flow turbine is measured by its power coefficient. The power coefficient is the ratio of the power produced by the turbine over the available power in the fluid. To calculate the power coefficient the sum of the power extraction contribution of all the blades is combined:

$$C_P = \frac{P_{out}}{P_{in}} = \frac{\bar{T}\omega}{\frac{1}{2}\rho AU_\infty^3} \quad (2.1)$$

where C_P is the power coefficient, P_{out} is the power extracted by the turbine, P_{in} is the power available that passes through the turbine, \bar{T} is the average torque during a revolution, ω is the angular velocity, ρ is the fluid density, A is the cross sectional area of the turbine and U_∞ is the undisturbed free stream velocity in the inflow direction.

The power produced by the turbine is the sum of the power extracted by each blade. The instantaneous power extraction for a single turbine blade, $P_{out\ blade}$, is given by

$$P_{out\ blade} = \vec{F}_B \cdot \vec{V}_T \quad (2.2)$$

where, \vec{F}_B is the force vector, and \vec{V}_T is the velocity of the turbine blade.

The instantaneous rotor power coefficient of each single element, C_{pe} , is:

$$C_{pe} = T_e^+ \frac{U_T}{U_\infty} = T_e^+ \lambda \quad (2.3)$$

where the nondimensional torque is T_e^+ , the U_T is the tangential velocity of the fluid and λ is the tip speed ratio.

The nondimensional torque produced by a single blade, T_e^+ , can be written as:

$$T_e^+ = \frac{1}{2} \frac{c}{R} [\vec{C}_T + \vec{C}_N] \cdot \frac{\vec{\omega}_{1/4c}}{|\vec{\omega}_{1/4c}|} \left(\frac{U_R}{U_\infty} \right)^2 \quad (2.4)$$

where R is the turbine radius, C_T is the tangential velocity of the blade, C_N is the normal velocity of the blade, c is the chord of the turbine, $\omega_{1/4c}$ is the angular speed of the blade at one quarter of the chord and U_R is the flow velocity along the blade.

The average power coefficient, C_p , at a single revolution can then be calculated by

$$C_P = \frac{1}{N_{TI}} \sum_1^{N_{TI}} \sum_1^{N_B} C_{pe} \quad (2.5)$$

where N_B is the number of blades and N_{TI} are the number of time increments during a single revolution (Strickland et al., 1980).

The torque and power coefficient are dependent on the component of forces produced by the blade tangent to the circumference of rotation. The forces produced by the blades can be approximated using the lift and drag coefficients. In turn, the lift and drag coefficients can be calculated using the angle of attack, the camber and corrected to consider the dynamic stall and flow curvature phenomena.

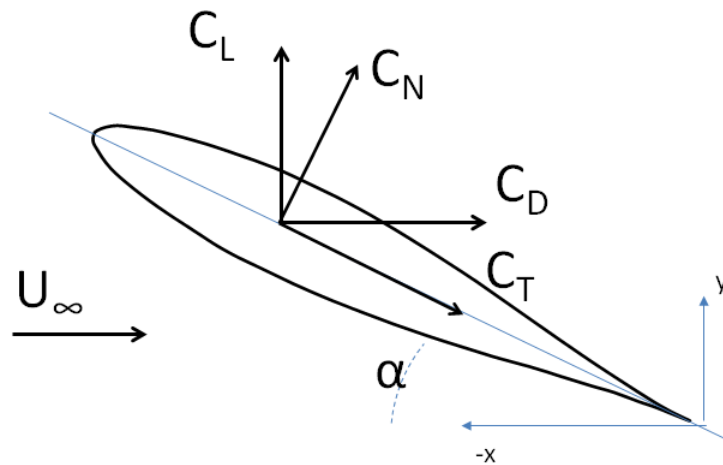


Figure 2.1. The blade forces are shown for a given in flow.

The tangential and normal coefficients in terms of lift and drag coefficients can be written as (Figure 2.1):

$$C_T = C_L \sin(\alpha) - C_D \cos(\alpha) \quad (2.6)$$

$$C_N = C_L \cos(\alpha) + C_D \sin(\alpha) \quad (2.7)$$

To properly account for the motion of the turbine in the flow, the calculated angle of attack is dependent both on the blade and flow velocities. From the geometry of the turbine the angle of attack is

$$\tan\alpha = \frac{(U_\infty + U) \sin \theta_B + W \cos \theta_B}{(U_\infty + U) \cos \theta_B - W \sin \theta_B + U_T} \quad (2.8)$$

where, U_T is the tangential velocity of the blades, θ_B is the angle of the blade with respect to the inflow or rotational position, and U and W are the induced velocities along the inflow velocity and in the perpendicular direction of the inflow, respectively.

To analyze the movement of the blade, the upstream zone is defined as when the blade goes across the flow at the front of the turbine from a rotational position (θ_B) of 0 degrees to 180 degrees (Figure 2.2). A downstream zone is defined when the blade passes across the flow from a rotational position of 180 degrees to 360 degrees.

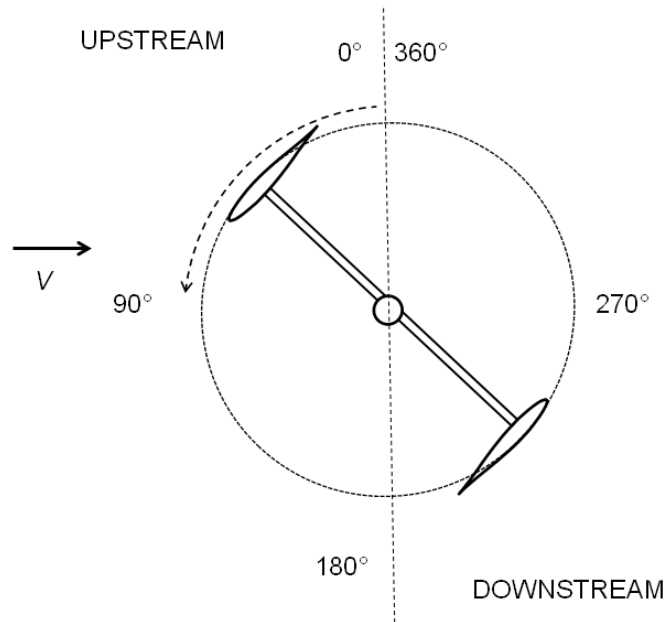


Figure 2.2. The upstream and downstream zones with respect to the turbine are shown.

2.3 EXPERIMENTAL SET UP

The hydrodynamic performance of a cross-flow turbine with different configurations was acquired in a tow tank. The data acquired during testing included the torque, thrust, turbine angular position, and inflow velocity. These measurements are required for power and thrust coefficient calculations. The power coefficient was calculated as a function of the tip speed ratio, and the torque data was calculated as a function of turbine angular position. The torque and thrust measurement instrumentation is shown in Figure 2.3. Testing was performed in a tow tank that is 2.44 meters wide, 1 meter deep and 30 meters

long (Figure 2.4). The maximum speed of the carriage during the test was 0.8 m/s and the turbine's tip speed ratio (λ) was tested from 1.1 to 3.2. The inflow velocity of 0.8 m/s was used except where noted.

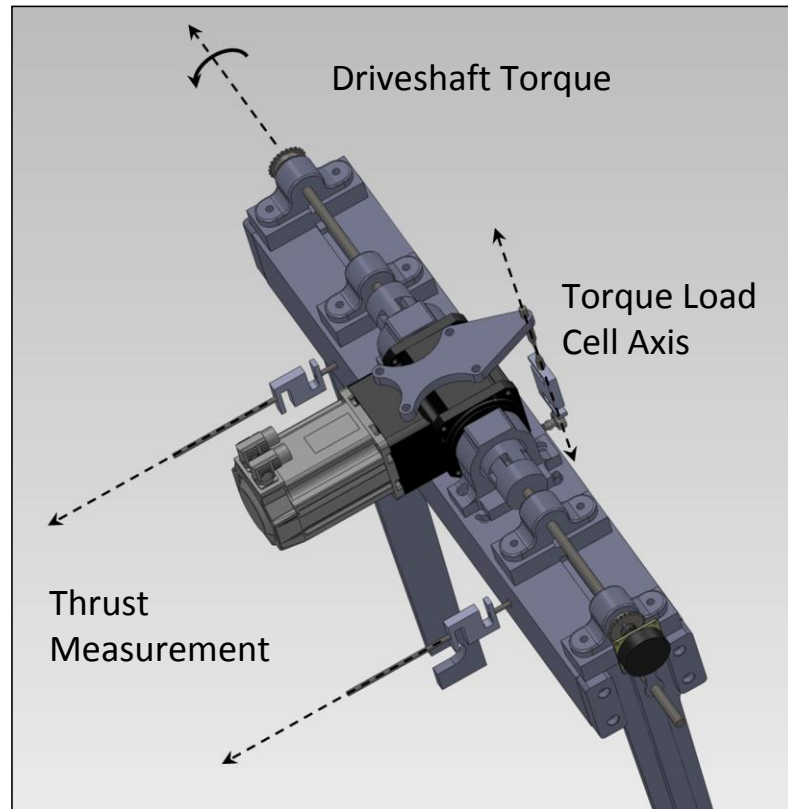


Figure 2.3. The diagram shows the instrumentation used for torque and thrust measurements (deBree, 2012).

The dimensions of the turbine were dictated by the dimensions of the tow tank used for testing. The diameter of the turbine was set at 32.5cm (Figure 2.5). Two foil sections were used for the blades with a NACA 63₃-018 profile. The first foil section had an ideal chord length of 5.08cm (chord-to-radius ratio of 0.30). The trailing edge was trimmed to facilitate manufacture and resulted in a final chord length of 4.5cm. The second foil section had an ideal chord length of 7.62

cm (chord-to-radius ratio of 0.46), with a trimmed chord length of 6.94cm. The length of the blades is 76.2cm. Additionally, two foil sections were used for the blades with a NACA 4418 and NACA 0018 profile. Both foil sections had an ideal chord length of 7.62 cm (chord-to-radius ratio of 0.46) with the trailing edge trimmed to a final chord length of 6.94cm. The blades are mounted to the turbine rotor using end plates with index patterns that facilitated varying the angle of attack from +/- 10 degrees in 1 degree increments (Figure 2.6).

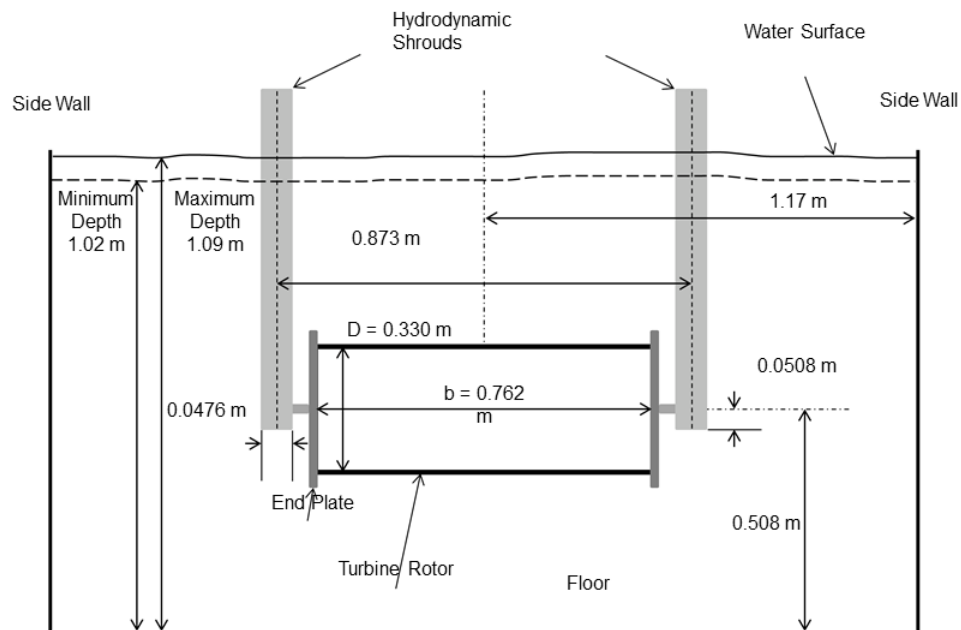


Figure 2.4 A schematic of the cross-flow turbine installed in the tow tank shows the geometry used for testing. The turbine direction of motion corresponds to out of the page (deBree, 2012).



Figure 2.5. The straight bladed model Darrieus turbine rotor is shown with NACA 633-018 blades installed and rod across the center (deBree, 2012).

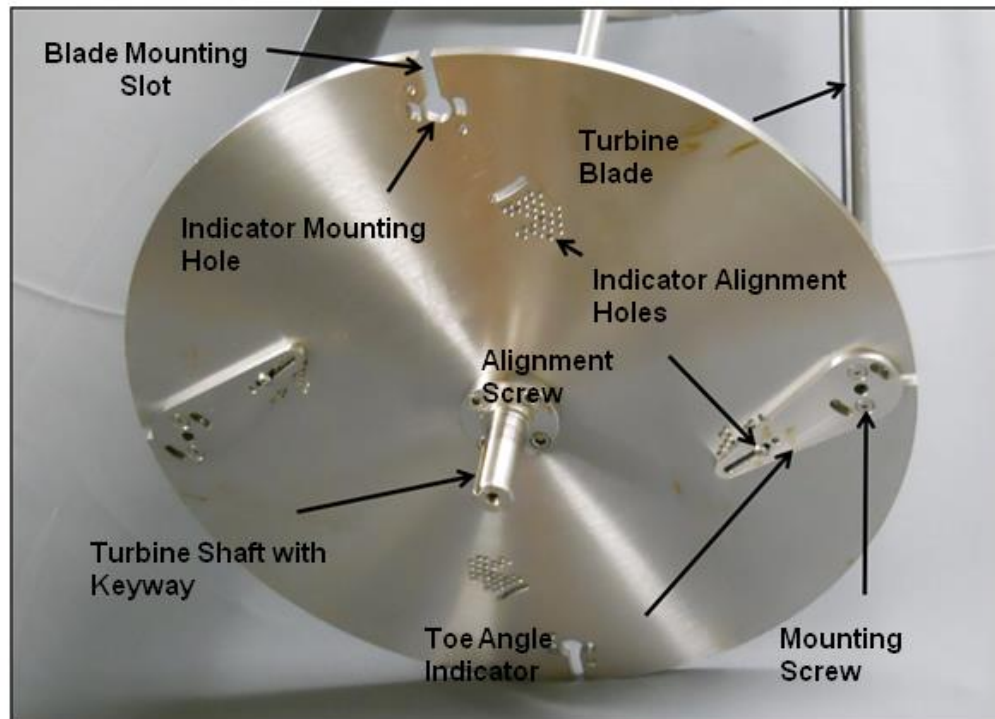


Figure 2.6. Turbine endplate with attached angle indicators and blades are shown (deBree, 2012).

Experimental data for the cross-flow turbine with straight blades was acquired at a constant angular speed by using a motor with PI controller. The use of straight blades allows the analysis of torque data as the blades rotate. However, straight bladed cross-flow turbines cannot self-start in all operating conditions, since negative torque that may stall the turbine can be produced at some operating conditions. Additionally, the torque of straight bladed cross-flow turbine oscillates from negative to positive values. This torque oscillation creates angular acceleration and deceleration making acquisition of measurements at certain tip speed ratios difficult. Variation of the angular velocity is particularly evident at low tip speed ratios. Therefore, a motor with a controller was designed with proportional integration (PI) to control the turbine angular speed. The motor with the PI controller allows the turbine angular speed to oscillate at a magnitude of up to five percent of the set speed. This is accomplished since the motor with the PI controller is capable of either driving the turbine or absorbing power (Figure 2.7), as the torque oscillates from negative to positive values when the blades rotate. The motor is coupled with a dual right angle 3:1 gear head (3 motor rotations to 1 turbine rotation). The gear head is attached to the drive train, which operates the turbine through a chain drive. A dual right angle gear head permits the transmission of power from and to both sides of the turbine, minimizing mechanical vibrations due to power transmission. The use a chain drive allows all the sensors to be placed above the water. An optical encoder was used to measure the angular position of the turbine and find the angular velocity. A load cell mounted at the motor was used to measure the torque produced by

the turbine, and two load cells were used to measure the turbine thrust (Figure 2.5).

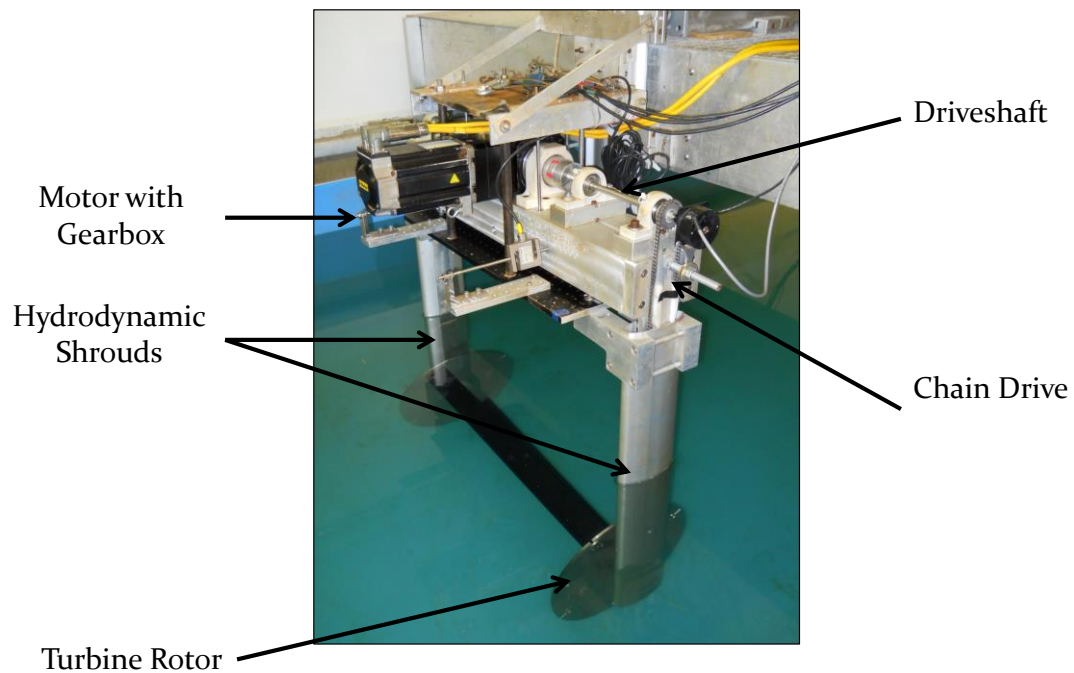


Figure 2.7. The test turbine diagram shows the motor controller and transmission (deBree, 2012).

The torque produced by the blades was calculated as a function of the turbine rotational position by considering the drive train losses, the drag losses, and the inertia forces from the turbine rotor end plates. To determine the drive train friction, the turbine was rotated using the drive motor outside of the tow tank over a range of rotational speeds. The drive train friction was measured every time the turbine blade configuration was changed. The drag of the end plates was measured running the turbine without turbine blades, using a procedure consistent with Li and Calisal (Li and Calisal, 2010b). Additionally, every time the turbine blade configuration was changed, the torque load cell offset was

measured. This measurement was repeated every fifth test run to track the torque offset value of the subsequent turbine tests. The corrected torque calculations were filtered at a cut off frequency of 17 Hz using a Butterworth filter with zero phase distortion (Matlab, 2014) to remove the mechanical vibrations. The frequency range between 18 Hz and 33 Hz was found to contain the largest magnitude of mechanical noise during both types of tests. The measured torque was further processed by bin-averaging the torque over multiple runs to produce a calculated torque as a function of the turbine rotational position (θ).

The power coefficient was calculated using measurements of the instantaneous torque, inflow velocity, and turbine angular velocity using Equation 2.1. The instantaneous angular velocity was calculated using the measured time and filtered angular position data in radians. The instantaneous power coefficient was bin-averaged to calculate the power coefficient at a given tip-speed- ratio and inflow velocity.

2.4 RESULTS

Four tests were done to evaluate the quality of the measurements taken at the tow tank and that of the post-processing routines. The first set of tests comprised of the repeatability tests shown in Figure 2.8. These tests show that there was an acceptable agreement in the measurements with good agreement at low tip-speed-ratios. A second set of tests was done to evaluate the effect of water temperature on the measurements (Figure 2.9). The effect on the power

coefficients is large from variation of the water temperature. At high water temperatures, the difference in the power coefficient may be attributed to variation of water viscosity with changes in temperature. The third test was intended to quantify the effect that the water column had on the power coefficient (Figure 2.10). The results show that at higher tip-speed ratios, there is a higher variation in the acquired power coefficient. This variation can be attributed mainly to the blockage effect. The fourth test was performed by varying the inflow velocity (Figure 2.11). This test was important to define at what inflow velocity the test data would be acquired. The intention was to maintain the inflow velocity as low as possible to minimize the velocity variations, since the velocity variations result in a phase shift in the torque data evident when the torque data is compared to analytical data (Li and Calisal, 2010b). The test results show that for the test set-up presented in this paper, there was not a significant difference in the measurements acquired at an increase in the inflow velocity from 0.8 m/s to 1.2 m/s. Therefore, an inflow velocity of 0.8 m/s was selected for tests in this work. The magnitude of effects that would be evident in some applications such as water temperature and column height is important to recognize for some applications and field data.

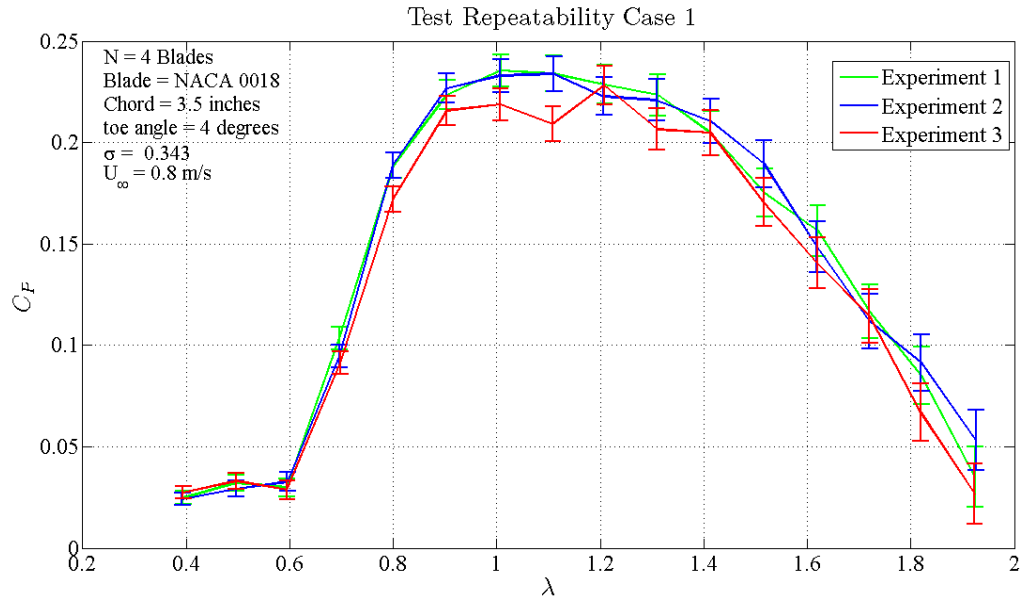


Figure 2.8. Experimental power coefficient results for a four-bladed turbine with a chord to radius ratio of 0.53 show reasonable repeatability.

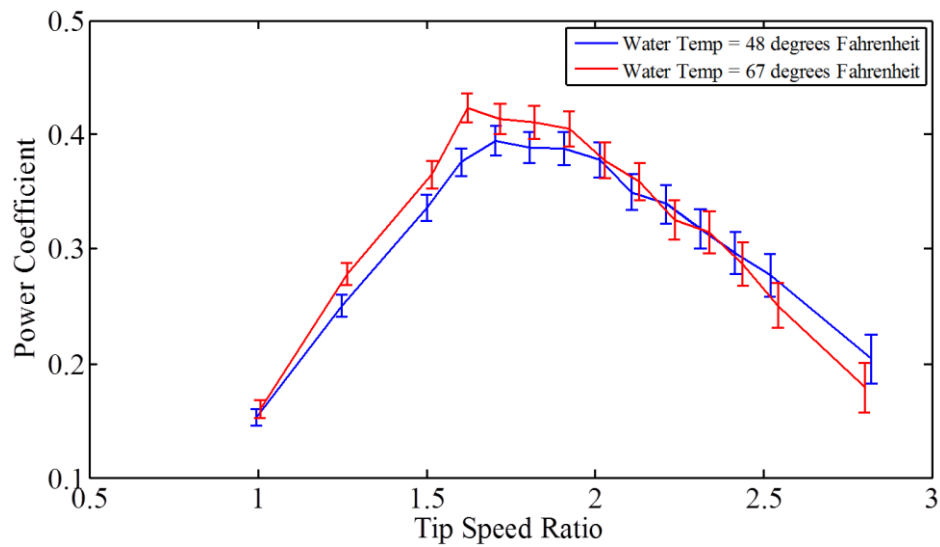


Figure 2.9. The experimental power coefficient for a two-bladed turbine with a chord to radius ratio of 0.53 acquired at two different temperatures (Swanger, 2013).

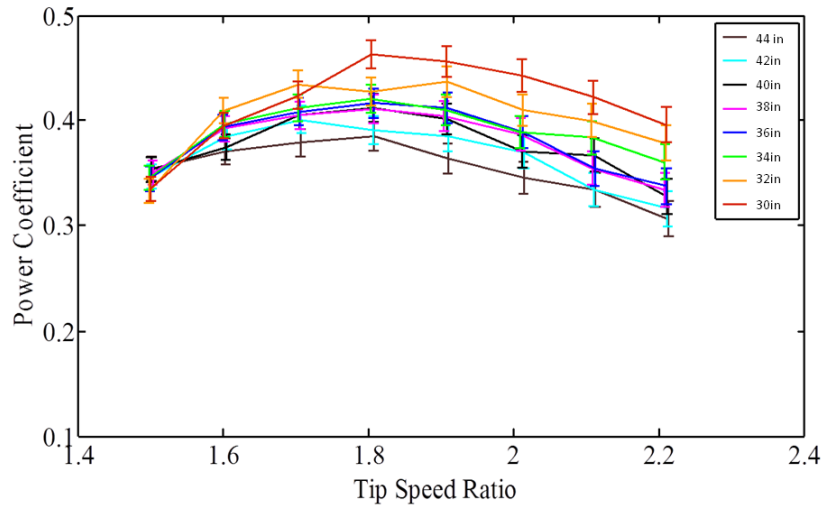


Figure 2.10. The experimental power coefficient results for a two-bladed turbine with a chord to radius ratio of 0.53 show the effect of varying the water column in the tow tank (Swanger, 2013).

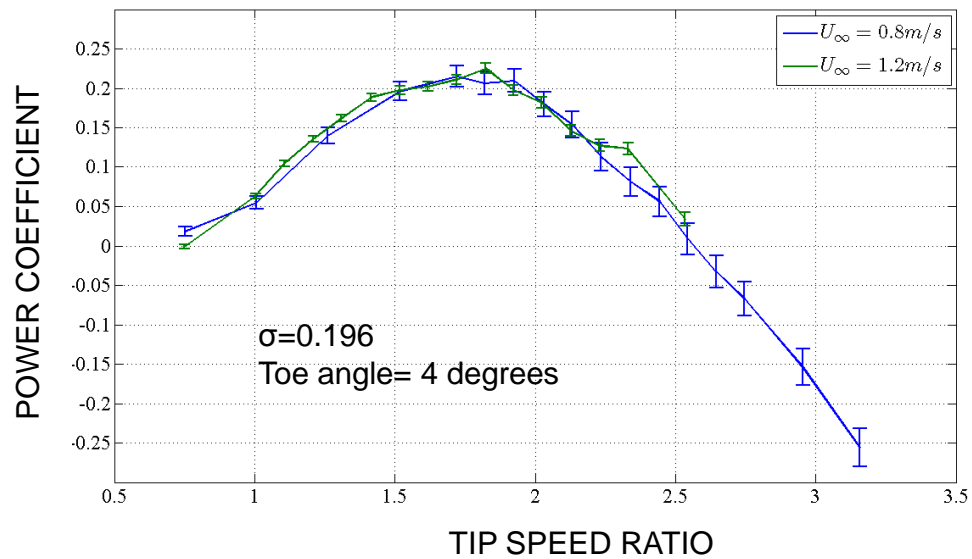


Figure 2.11. The experimental power coefficient for a two-bladed turbine with a chord to radius ratio of 0.53 acquired at two different in-flow velocities.

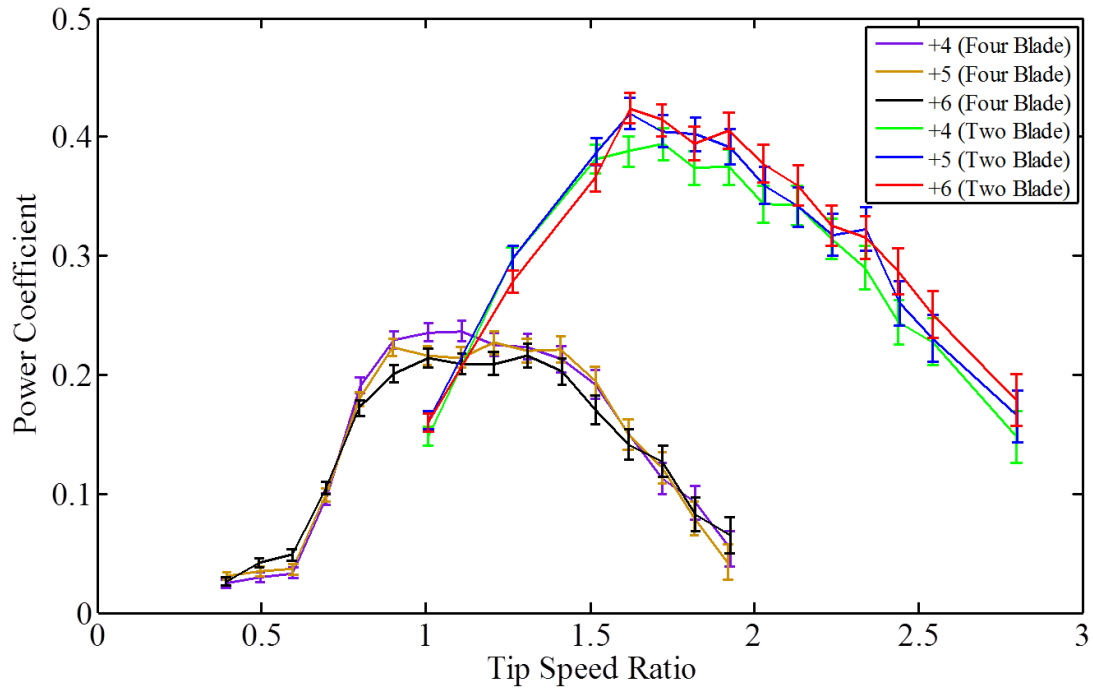


Figure 2.12. The experimental power coefficients for a two-bladed turbine and a four-bladed turbine with a chord to radius ratio of 0.53 are shown for different tow angles (Swanger, 2013).

To evaluate the effects of variables such as number of blades, camber, and blade chord to radius ratio on the turbine performance, a series of tests were performed. The two main variables in the tests were tip speed ratio and toe angle. The first series of tests (Table 2.1) were performed to evaluate the effect of varying the number of blades on the power coefficient. Data was acquired using a two-bladed turbine with NACA 0018 blades and a four-bladed turbine with NACA 0018 blades. Data was taken at a water temperature of 19° C. Figure 2.12 shows the power coefficient results for the cross-flow turbine with two and

four blades at three different toe-angles at which the maximum power coefficient was found. It can be seen that the maximum power coefficient shifts by one degree from +5 degrees in the two-bladed turbine to +4 degrees in the four-bladed turbine. Lower power coefficient was acquired with the four-bladed turbine.

The second series of tests (Table 2.2) were done to evaluate the effect of variation of camber on the power coefficient. The experimental data was acquired at 20 different tip speed ratios and 9 different toe angles. In Figures 2.13-2.15, the experimental results are shown in a contour plot to display where the maximum power coefficient can be found. Each contour plot shows data for 180 test runs. Data was taken at a water temperature of 19° C. Figure 2.13 shows the results for a two-bladed cross flow turbine using three inch blades with NACA 0018 profiles. The results for a two-bladed cross flow turbine using three inch blades with NACA 4418 profiles are shown in Figure 2.14. Additionally, Figure 2.15 shows the results for a two-bladed cross flow turbine using three inch blades with NACA 4418 profiles mounted with the camber facing in the opposite direction of the one tested in Figure 2.14. The results show that the maximum power coefficient is found when the NACA 0018 blades are used at a tip speed ratio of 1.7 and a toe angle of 5 degrees. It is evident that the cross-flow turbine using blades with a NACA 4418 profile in a reversed position is less efficient than the cross-flow turbine using blades with NACA 0018 profiles.

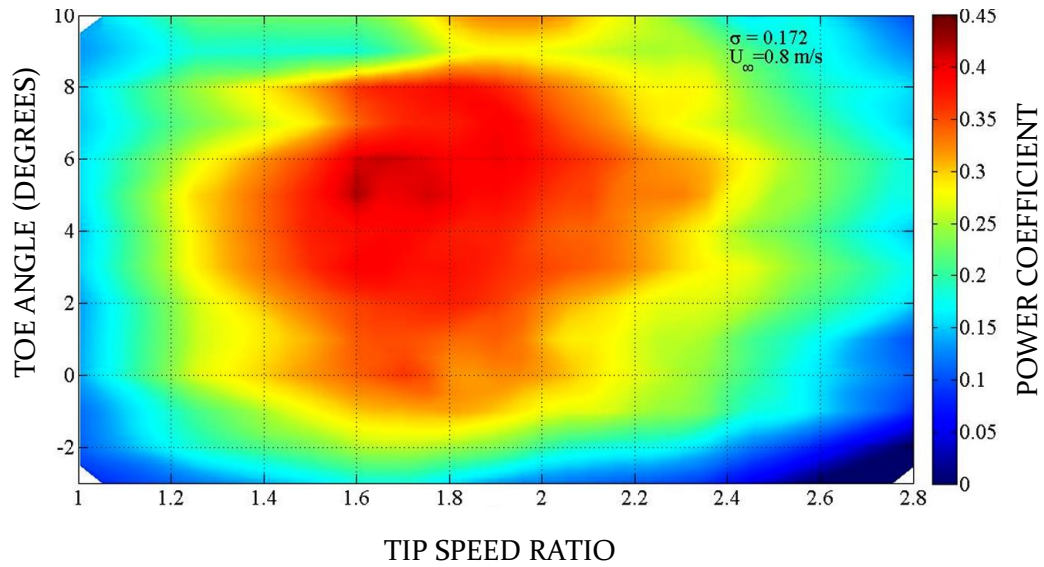


Figure 2.13. The experimental power coefficients for a two-bladed turbine using blades with NACA 0018 profile are shown for different tow angles and tip speed ratios.

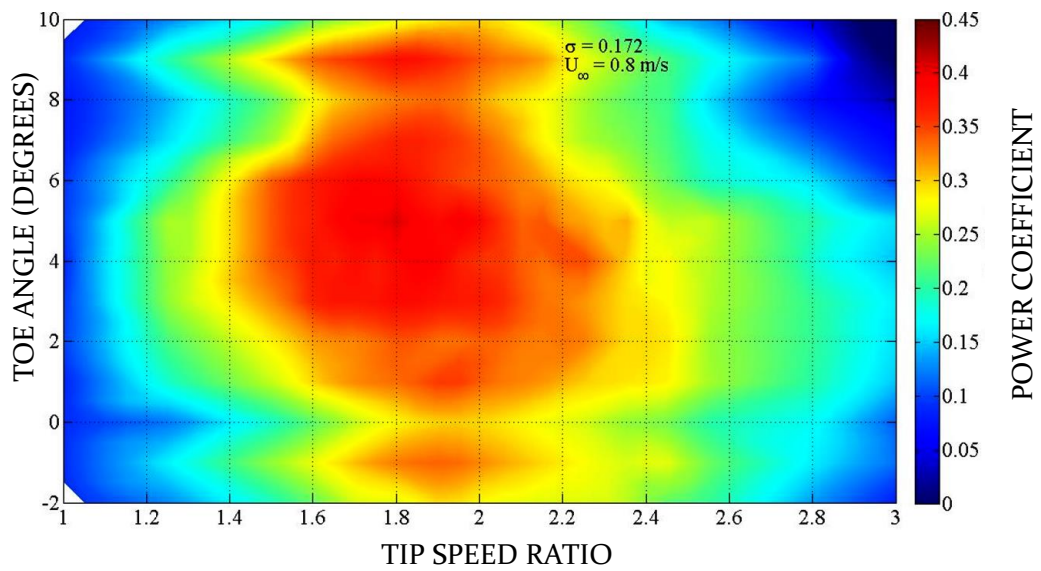


Figure 2.14. The experimental power coefficients for a two-bladed turbine using blades with NACA 4418 profile are shown for different tow angles and tip speed ratios.

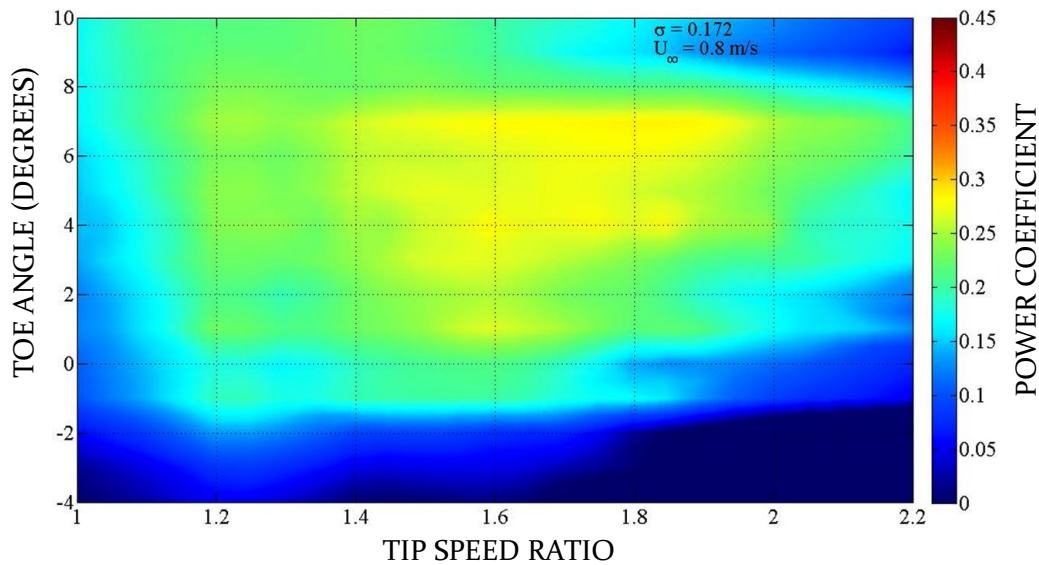


Figure 2.15. The experimental power coefficients for a two-bladed turbine using blades with NACA 4418 profile mounted in reversed position are shown for different tow angles and tip speed ratios.

The third set of tests (Table 2.3) was run to evaluate the effect of the chord to radius ratio. As in the previous series of tests, the experimental data-set was acquired at 20 different tip speed ratios and 9 different toe angles. The experimental data-set was acquired for the turbine with two-inch blades using a NACA 63-3-018 profile. Similarly, another data-set was acquired for the turbine with three-inch blades with a NACA 63-3-018 profile. Data was taken at a water temperature of 9° C. Figure 4.16 shows the power coefficient results at the toe angle configuration where the maximum power coefficient for each case of chord-to-radius ratio was found. The maximum power coefficient was acquired when the turbine was equipped with 2 inch chord blades. It is also evident that

the maximum power coefficient can be found at a lower tip speed ratio in the turbine using a higher chord-to-radius ratio.

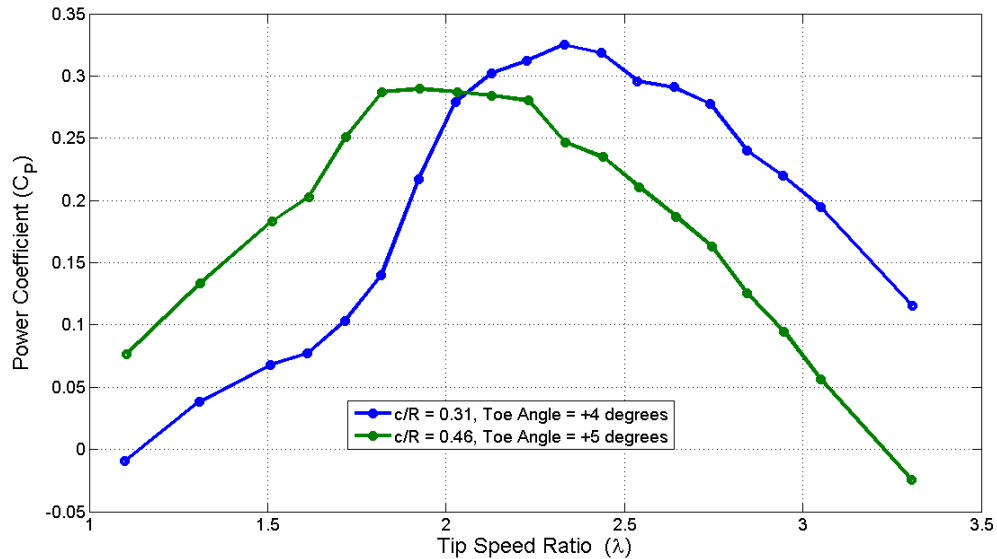


Figure 2.16. The experimental power coefficients for a two-bladed turbine using blades with NACA 63-3-018 profile are shown for different chord-to-radius ratios.

The nondimensional instantaneous torque is shown in Figures 2.17 and 2.18 for two-bladed cross flow turbines using two and three inch chord blades, respectively. The experimental results are shown as a function of the tip speed ratio and the rotational position. The experimental results show that the instantaneous torque of the turbine with two inch chord blades at a toe angle of +4 degrees (Figure 2.17), there is a phase shift as the tip-speed ratio increases. The maximum nondimensional torque for the turbine using two inch blades is lower than the turbine that uses three inch blades. Additionally the experimental results show that the maximum nondimensional torque for the turbine using two-inch blades can be found at a higher tip-speed ratio than the turbine using three-

inch blades. The maximum nondimensional torque acquired for this configuration was 0.6734 and the minimum nondimensional torque was -0.5192. For the turbine with three inch chord blades at a toe angle of +5 degrees there is a similar phase shift as the tip-speed ratio increases (Figure 2.18). The maximum nondimensional torque acquired was 0.7584 and the minimum was -0.6076. It can be seen that the peak nondimensional torque at each tip-speed ratio increases as the tip-speed ratio increases about where the maximum peak power coefficient is found. After this tip-speed ratio the value of the nondimensional torque peak starts decreasing.

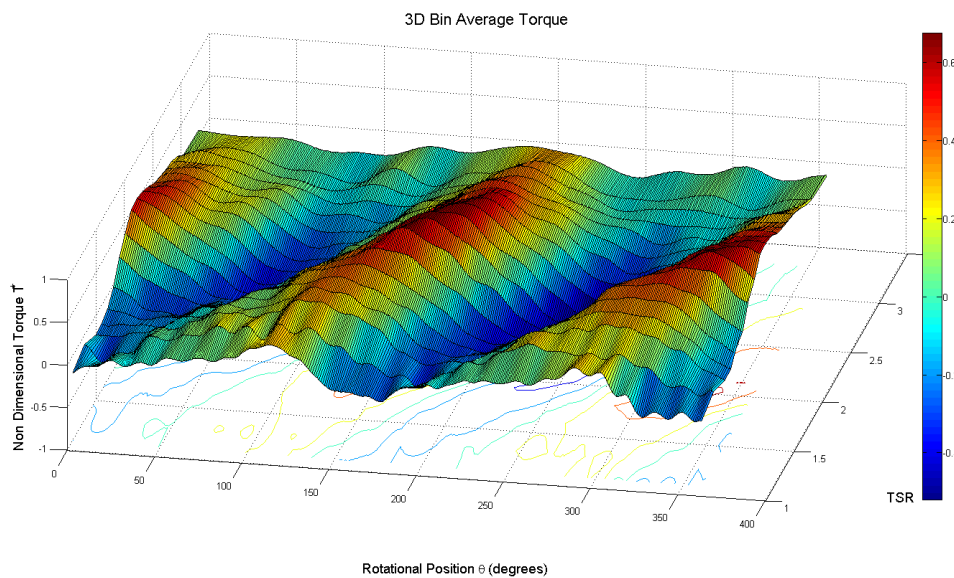


Figure 2.17. The experimental non-dimensional torque results for a two-bladed turbine using two-inch chord blades at a toe angle of +4 degrees are shown for different tip-speed ratios.

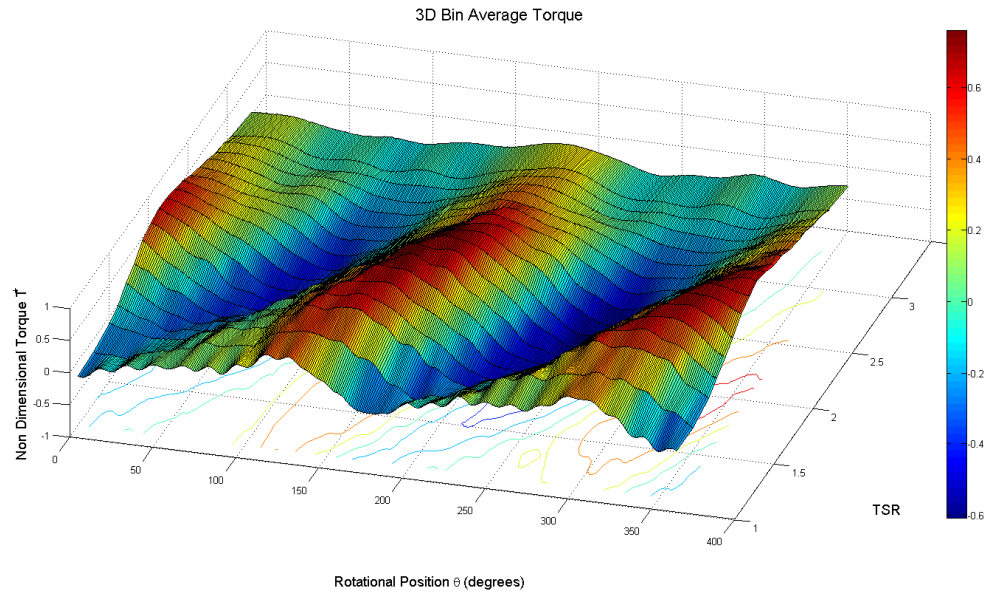


Figure 2.18. The experimental non-dimensional torque results for a two-bladed turbine using three-inch chord blades at a toe angle of +5 degrees are shown for different tip-speed ratios.

2.5 DISCUSSION

The experimental results can be understood by looking at the forces produced by the blades. The blade forces are primarily a function of the velocity of the fluid acting on the blade and the angle of attack of the fluid on the blade. For a cross-flow turbine the angle of attack changes as the blade rotates. Therefore, the blade undergoes cyclic variations from positive and negative angles of attack.

The case in which the toe angle is zero degrees is particularly interesting, because the tangential coefficient can be used to calculate the turbine torque.

The tangential coefficient can yield positive values at positive and negative angles of attack (Figure 2.16). Thus the blade can generate positive torque in both the upstream and downstream directions depending on the flow conditions. Additionally, the tangential coefficient has three regions of angle of attack which are of interest for cross flow turbines. The first region of angles of attack is where the tangential coefficient at small angles of attack remains negative until the frictional drag is overcome (Figure 2.19). In the second region of angles of attack, the tangential coefficient continues to increase as the angle of attack increases until the blade stalls. The angular position of the turbine at which the blade stalls influences the dynamic stall as the angle of attack of the blade changes. Sheng et al. (Sheng et al., 2008) related the reduced pitch rate to the angle that the blade stalls. This alters significantly the range of the second region. The third region for the angle of attack is where the blade has stalled the tangential coefficient remains negative for large angles of attack. Taking notice of these three regions is important since the toe angle and the camber can affect where the turbine generates the maximum efficiency. At large toe angles, both positive and negative, the turbine stops generating positive torque, as the turbine operates mainly in the third region of the angle of attack.

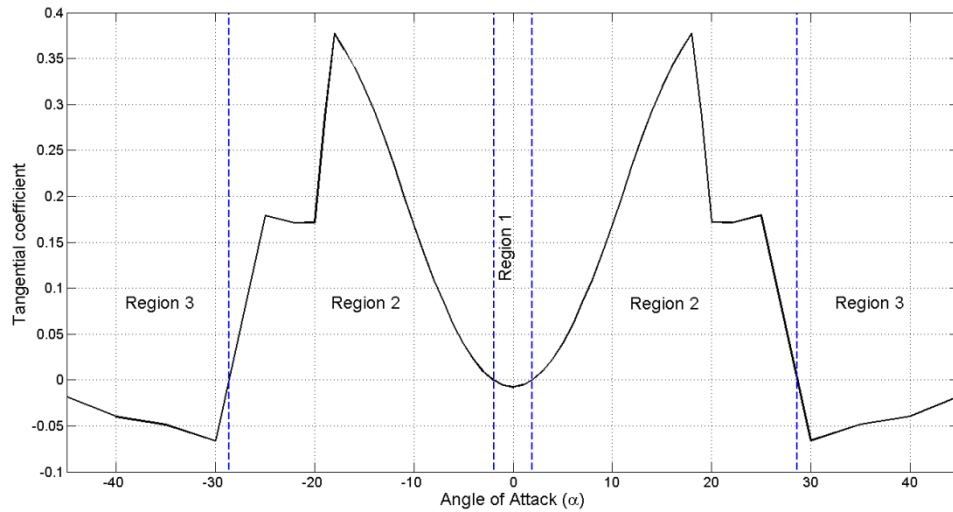


Figure 2.19. The tangential coefficient for a NACA 0018 blade at Reynolds number of 5,000,000 is shown as a function of angle of attack.

It is also important to take into account the induced velocities of the wake produced by the turbine. The induced velocities act mainly in a direction opposite of the inflow. The strength of the induced velocities is related to the shed vorticity of the blade (Strickland et al, 1980). This shed vorticity is related to change in time of the vorticity of the blade, Γ_B by

$$\Gamma_B = \frac{1}{2} C_L c U_R \quad (2.9)$$

The shed vorticity thus affects the velocity field around the turbine. The shed vorticity is related to changes on the lift coefficient (equation 2.9), the relative velocity and the length of the chord. Therefore, a change in the angle of attack has an effect on the shed vorticity resulting in a change in the lift coefficient. Similarly, as the tip-speed ratio is increased, the induced velocities in the direction opposite to the inflow increases, resulting in lower blade forces. In the

same manner, as the chord increases, the induced velocities increase. This causes the maximum torque to be found at a lower tip speed ratio as shown in Figure 2.13. For the cases shown in Figure 2.13 and 2.14 and taking into account equation 2.4, a higher power coefficient can be found when the turbine is configured with blades that have a lower chord-to-radius ratio.

The data from Figures 2.14 and 2.15 are useful to explain the torque variation. The torque increases as the tip speed ratio increases because the blade rotates faster. The reduced pitch effect does not significantly increase the angle of attack at which the blade stalls. The maximum angle of attack at which the blade stalls decreases as the tip-speed ratio increases. The result is an increase in the maximum torque. The effect of stall on the power coefficient is a decrease in torque which is compensated partly by the increased tip-speed ratio (Equation 2.4). As the tip-speed ratio continues to increase further the blade starts operating primarily in the three of the tangential coefficients, resulting in a negative average torque and power coefficient.

From Figure 2.14 and 2.15 it is also evident, that the nondimensional torque has a phase shift with regards to the rotational position as the tip speed increases. This result can be explained because as the tip-speed ratio increases, and a lower angle of attack is obtained for a given rotational position. Additionally, as the tip-speed ratio increases the induced velocities increase

further. This has the result of effectively decreasing the angle of attack shifting the location of the angle of attack with regards to the rotational position.

2.6 CONCLUSION

This chapter describes the acquisition of experimental data of a cross flow turbine at different conditions of chord-to-radius ratio, number of blades and blade camber. One of the challenges was to acquire experimental data at a large range of tip-speed ratios. The presented experimental data offers numerous cases at different toe angles and tip-speed ratios. The experimental data show that the number of blades and camber may be more important factors than the chord-to-radius ratio. This suggests that the solidity ratio may not be adequate to classify cross-flow turbines. Additionally, the experimental data shows that the toe angle is an important parameter for determining where the maximum power coefficient is found. The experimental nondimensional torque data shows that the peak magnitudes changes in phase and in magnitude as the tip-speed ratio changes at lower tip speed ratios.

In addition to chord-to-radius ratio, number of blades, and blade camber, there were other factors that were found to have an effect on power coefficient. To aid the process of validating codes, data was acquired while varying the temperature and the depth of the water in which the turbine was placed: two factors that can affect the measurement of the power coefficient. The experimental data indicates that water temperature had a greater effect on the

measured power coefficient than did the depth of the water in which the turbine was placed. Additionally, the data shows that the effect of blockage on the power coefficient measurements is greater when the tip-speed ratio is increased.

The experimental data presented in this paper offers an extensive data-set that can be used to evaluate analytical models. The presented experimental data provides insight into the basic turbine geometry at certain operating conditions at which the maximum power can be found. The goal of this work is to provide a data set that can advance the development of design codes.

CHAPTER 3

DYNAMIC STALL MODEL FOR A FREE VORTEX MODEL

An analytical model for cross-flow tidal turbines must be capable of modeling high solidity cross flow turbines. The requirements were that the overall rotor performance, aerodynamic blade forces and rotor wake needed to be predicted with reasonable accuracy. The analytical model was also designed to have low computational cost in order to allow the predictions of range of different rotor operational conditions in a reasonable time. The model is then suitable for use in optimizers and other design oriented applications rather than the analytical models which would be used on a design which is near optimal. These combined requirements narrowed the options to BEM, lifting-line FVM and LCM.

BEM have been recognized to be suited for lightly loaded blades and low rotor tip speed ratios, assuming a quasi-steady flow through the rotor (Strickland, 1975). However, lifting line FVM have additional characteristics that make them suitable for modeling cross flow turbines. FVM can take into account blade to blade interaction and unsteady flow conditions, which allows the prediction of the power coefficient for numerous blades and at high chord to radius ratios (Strickland, 1980). Consequently, a lifting-line FVM was chosen as the basis of this work.

For the model to produce accurate predictions, it is needed to take into account phenomena associated with cross flow turbines. As discussed before, dynamic stall, cyclic Reynolds variation, flow curvature and centrifugal effects have been recognized as the most relevant phenomena in cross flow turbines (Migliore and Wolfe, 1980). The main focus of this stage of this work is to implement a dynamic stall model suitable for the operational conditions of cross flow turbines. Dynamic stall models have been mainly developed for helicopter applications, which have normal operational conditions above 0.5 Mach. Sheng et al. (Sheng et al., 2008) have modified one of the most widely used dynamic stall models, the Beddoes-Leishman model, for lower Mach numbers. This modified dynamic stall model was implemented in the lifting-line FVM model. The dynamic stall model was altered to approximate the post stall blade behavior at high angles of attack.

3.1 Modeling Approach

The most significant challenge in performance prediction at operating flow conditions is the effect of dynamic stall (Migliore and Wolfe, 1980). The dynamic stall model uses semi-empirical formulas related to the reduced pitch rate, and delayed angle of attack to represent the lift and drag at a large range of angles of attack and Reynolds numbers (Figure 3.1). To calculate the angle of attack, the model uses estimations of the induced velocities of the vortex trail using vortex particles. These resulting forces are then found as resultants that can be applied at the lifting line location in the FVM model.

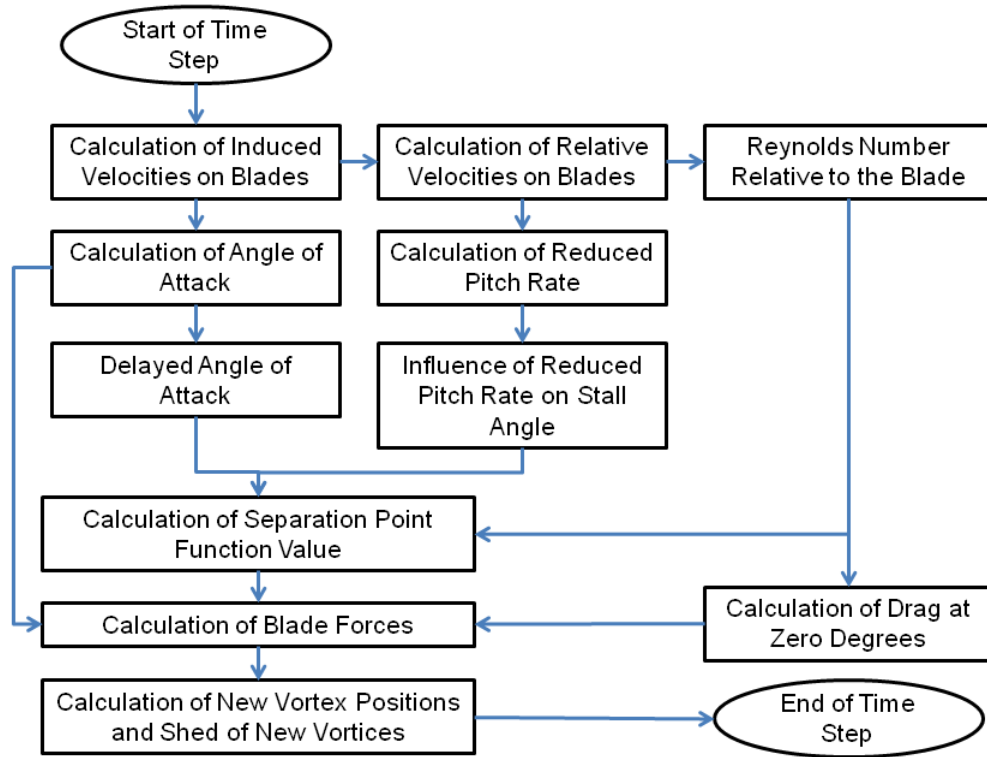


Figure 3.1. The flowchart of the analytical model is shown for each time step in the program.

3.2 Theoretical Approach

Kirchhoff first developed expressions to represent forces on a blade using streamlines representation of the flow (Thwaites, 1960). The lift coefficient, C_L , is given by

$$C_L = 2\pi\alpha \left[\frac{1 + \sqrt{f}}{2} \right]^2 \quad (3.1)$$

and the drag coefficient, C_D , is

$$C_D = 2\pi\alpha^2 \left[\frac{1 - \sqrt{f}}{2} \right]^2 \quad (3.2)$$

where α is the angle of attack shown in Figure 3.2 and f is the separation point. The geometrical definitions shown in Figure 3.2 and the variables are given in the nomenclature section.

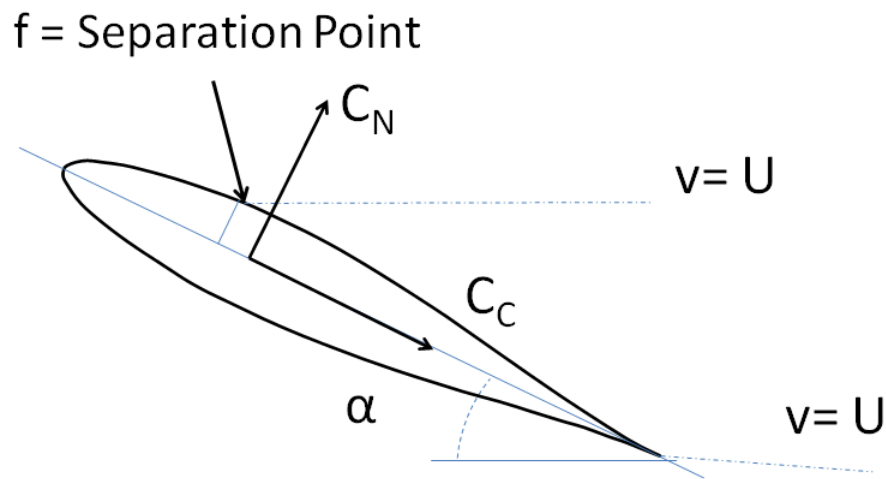


Figure 3.2. At the separation point in the flow across the blade diverge the streamlines depending on the angle of attack.

The Beddoes Leishman (B-L) formulation is based on a set of equations which are modified from Kirchhoff equations (Eq. 3.1 and 3.2). The B-L values for normal coefficient, C_N , for Mach numbers above 0.5 is

$$C_N = C_{N\alpha}(M) \left[\frac{1 + \sqrt{f}}{2} \right]^2 \alpha \quad (3.3)$$

and longitudinal coefficient, C_C^f ,

$$C_C^f = \eta C_{N\alpha} \alpha^2 \sqrt{f} \quad (3.4)$$

where $C_{N\alpha}$ is the normal force curve slope, and η is the chordwise force recovery factor. The normal and chordwise coefficients are related to lift and drag coefficients by the changes in coordinates in Figure 3.2. Sheng et al. (2008) modified the B-L equations for use at low Mach numbers in their dynamic stall model. The modified B-L for low Mach numbers formulation gives

$$C_N = C_{N\alpha} (\alpha - \alpha_0) \left[\frac{1 + \sqrt{f''}}{2} \right]^2 \quad (3.5)$$

and

$$C_C^f = \eta C_{N\alpha} (\alpha - \alpha_0)^2 (\sqrt{f'} - E_0) \quad (3.6)$$

where f' and f'' are delayed separation point functions, α_0 is the angle of attack where the lift is zero, and E_0 is a longitudinal force correction factor. The separation point function, f , is approximated by a piecewise exponential function:

$$f(\alpha) = 1 - 0.4e^{\left(\frac{\alpha - \alpha_1}{S_1}\right)}, \quad \alpha \leq \alpha_1 \quad (3.7)$$

$$f(\alpha) = 0.02 + 0.58e^{\left(\frac{\alpha_1 - \alpha}{S_2}\right)}, \quad \alpha > \alpha_1 \quad (3.8)$$

where α_1 is the angle at which steady stall is expected and S_1 and S_2 are constants which depend on the type of foil being modeled. The values for the separation point function are bounded by a maximum value of 1 for separation at the trailing edge and to zero for a fully separated flow at the leading edge.

In order to extend the range of angles of attack that these equations can be used to approximate, a method is used that takes into account Hoerner's (Hoerner and Borst, 1975) observation that the normal coefficient is close to:

$$C_N \approx [1.8 \text{ to } 2.0] \sin \alpha \quad (3.9)$$

By comparing the asymptotic values of this relationship, new expressions were derived for the normal and tangential coefficients as:

$$C_N = 2\pi \sin(\alpha - \alpha_0) \left(\frac{1 + \sqrt{f}}{2} \right)^2 \quad (3.10)$$

$$C_c = 2\pi \eta \sin^2(\alpha - \alpha_0) (\sqrt{f} - E_0) \quad (3.11)$$

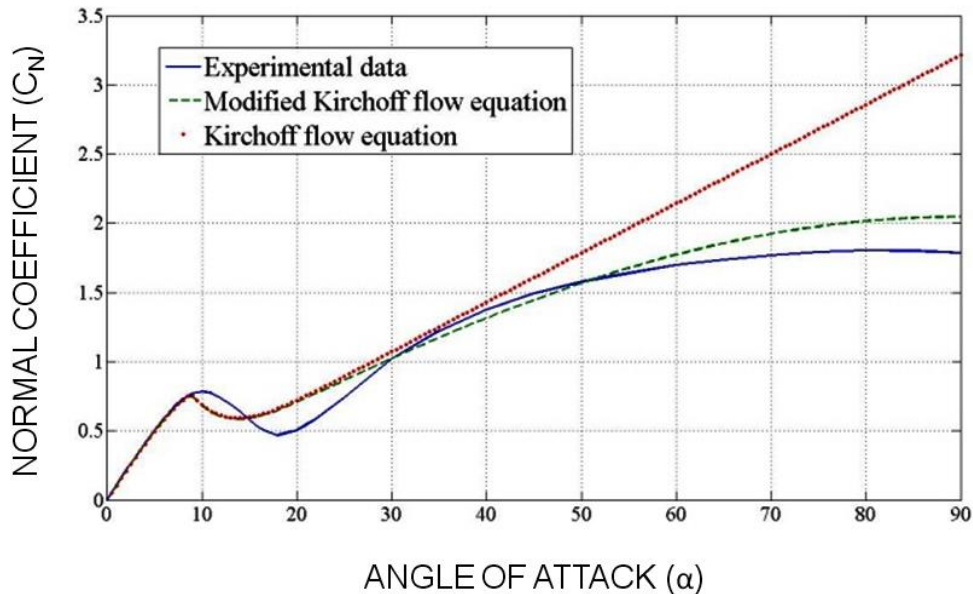


Figure 3.3. The normal force prediction of the modified flow equation is shown as a function of the angle of attack.

The analytical solution for the normal coefficient using asymptotic values (function 3.10) is shown in Figure 2.3. It can be seen that the function behaves

like a flat plate at α_0 , returning a value of zero, and a slope of 2π . At an angle of attack α_{90} the function has a value of approximately 1.8, which is near Hoerner's value of 1.98 for drag (Hoerner, 1965).

The drag coefficient, C_D , can be calculated from

$$C_D = C_N \sin(\alpha) - C_C \cos(\alpha) + C_{D0} \quad (3.13)$$

The drag at 0 degrees C_{D0} is calculated by considering the frictional drag of two flat plates in a turbulent flow. The formula for two flat plates is (Schlichting and Gersten, 1979):

$$C_{D0} = \frac{2 * 0.523}{\ln^2(0.06Re_L)} \quad (3.14)$$

The tangential and normal coefficients in terms of lift and drag coefficients can be written as:

$$C_T = C_L \sin(\alpha) - C_D \cos(\alpha) \quad (3.15)$$

$$C_N = C_L \cos(\alpha) + C_D \sin(\alpha) \quad (3.16)$$

Figure 3.4 shows the approximation for the lift coefficient. This lift is compared to the basic thin plate theory and the potential flow theory (Montgomerie, 2004) which are also used to approximate the lift data for an airfoil.

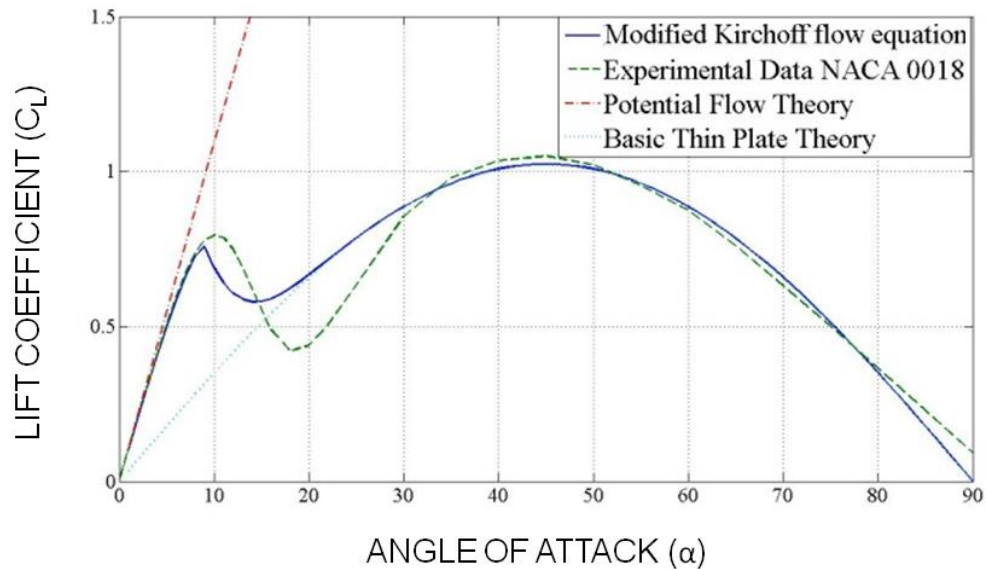


Figure 3.4. The lift force prediction of the analytical lift curve is shown as a function of the angle of attack.

Cross flow turbines undergo a cyclic variation of the Reynolds number due to the rotation of the foil in the flow (Migliore and Wolfe, 1980). This phenomenon is quite apparent at low tip speed ratios, such as $\lambda = 1$, since the flow velocity can be of the same magnitude as the rotational velocity. As a simple approximation to correct the onset of stall in the airfoil for different Reynolds numbers, a polynomial fit of experimental data was produced to calculate the static stall angle. This calculation facilitated the production of approximated lift and drag curves at the range of Reynolds numbers encountered during turbine operation.

Two major effects are considered in the dynamic stall model, a modified angle at which the foil is expected to stall and the delay on the angle of attack. The modified angle at which the foil stalls, or breakpoint of separation, at low Mach numbers is related to the reduced pitch rate (Sheng et al., 2008). The reduced pitch rate, r , is calculated from,

$$r = \frac{\dot{\alpha}c}{2V} \quad (3.17)$$

where $\dot{\alpha}$ is the rate of change in angle of attack with respect to time, c is the chord and V is the flow velocity.

The increase or decrease of the breakpoint of separation, $\Delta\alpha_1$, is approximated from experimental data in (Sheng et al., 2010). While a piecewise linear approximation was proposed by Sheng et al. (Sheng et al., 2010) a better approximation is a piecewise exponential function. The separation breakpoint is then approximated by

$$\Delta\alpha_1(r) = \alpha_1(e^{S_3 r} - 1), \quad r < 0 \quad (3.18)$$

$$\Delta\alpha_1(r) = \alpha_{1max}(1 - e^{S_4 r}), \quad r > 0 \quad (3.19)$$

where α_{1max} is the projected maximum angle of stall, and S_3 and S_4 are constants that depend on the foil shape being used.

A second consideration in the dynamic stall model is that the separation point is normally delayed under dynamic conditions (Sheng et al., 2008). Therefore, an effective angle of attack is calculated as

$$\Delta\alpha'(s) = \Delta\alpha(s)(1 - e^{-\frac{s}{T_\alpha}}) \quad (3.20)$$

where T_α is a delay constant which depends on the foil.

A new delayed separation point f' which replaces equations 3.7 and 3.8 is then defined as

$$f'(\alpha) = 1 - 0.4e^{\left(\frac{\alpha' - \alpha_{SS} - \Delta\alpha_1}{S_1}\right)}, \quad \alpha' \leq \alpha_1 \quad (3.21)$$

and

$$f'(\alpha) = 0.02 - 0.058e^{\left(\frac{\alpha_{SS} + \Delta\alpha_1 - \alpha'}{S_2}\right)}, \quad \alpha' > \alpha_1 \quad (3.22)$$

Figure 3.5 shows an example of the normal coefficient calculated for a NACA 0012 profile (Abbott and von Doenhoff, 1959) as a function of angle of attack at a range of different pitch rates.

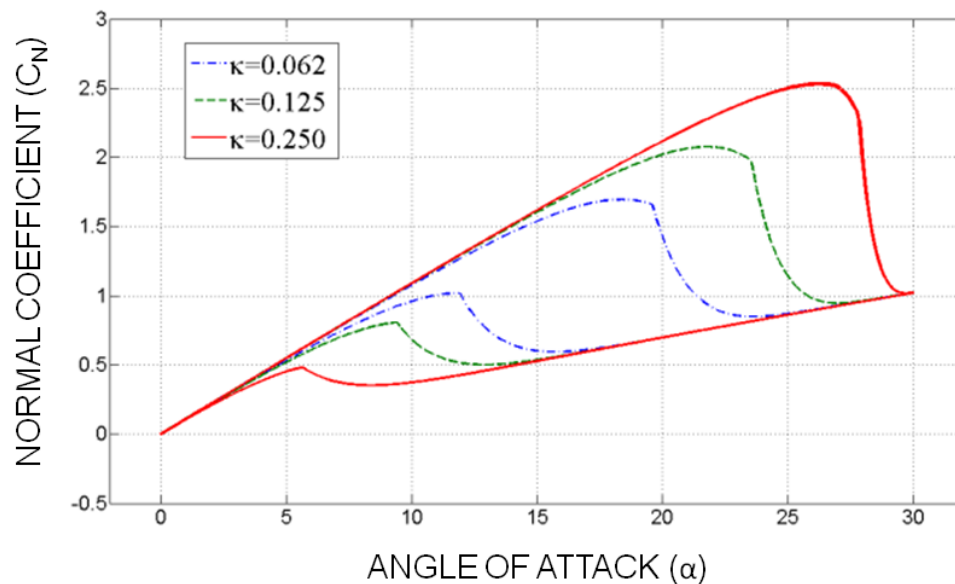


Figure 3.5. The modified B-L lift curves are calculated for reduced frequencies $k=0.062, 0.125$ and 0.2150 .

To properly account for the motion of the turbine in the flow, the calculated angle of attack is made dependent both on the blade and flow velocities. From the geometry of the turbine the angle of attack is

$$\tan\alpha = \frac{(U_\infty + U) \sin\theta_B + W \cos\theta_B}{(U_\infty + U) \cos\theta_B - W \sin\theta_B + U_T} \quad (3.23)$$

where U_∞ is the undisturbed free stream velocity in the x direction, U_T is the tangential velocity of the blades, θ_B is the angle of the blade with respect to the inflow, and U and W are the induced velocities in the x and z directions, respectively.

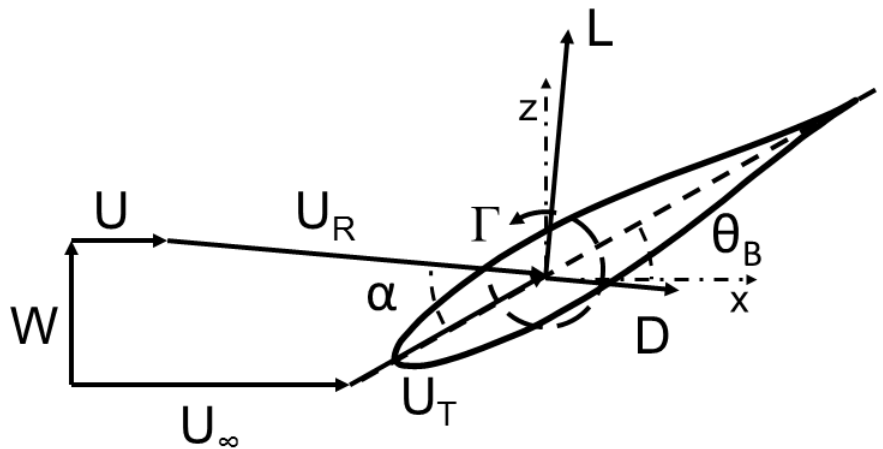


Figure 3.6. The velocity components of the relative velocity are combined in the model as shown.

The relative velocity, U_R , which is needed to estimate the lift and drag coefficients at a given Reynolds number, as well the blade forces and turbine torque, can be calculated from as shown in Figure 3.6:

$$\vec{U}_R = (U_\infty + U + U_T \cos \theta_B)\vec{i} + (W - U_T \sin \theta_B)\vec{k} \quad (3.24)$$

The relative velocity varies throughout the rotation of the blade with a maximum relative velocity found near the rotational position of the blade (θ_B) equal to zero degrees, where the velocities, U_T and U_∞ , are in same direction, and a minimum velocity found at θ_B , near 180 degrees where the velocities, U_T and U_∞ , are in the opposite direction.

The induced velocities can be calculated from the influence of all vortices filaments that include both the blade bound and wake vortices. The shed vortex strengths, Γ_S , of the blade, i , at each time step, NT , can be derived using Kelvin's theorem from the blade vorticity, Γ_B , (Strickland et al., 1980)

$$\Gamma_S(i, NT - 1) = \Gamma_B(i, NT - 1) - \Gamma_B(i, NT) \quad (3.25)$$

The instantaneous bound strength vortex of each blade can be calculated using the Kutta-Joukowski relationship (Thwaites, 1960),

$$\Gamma_B = \frac{1}{2} C_L c U_R \quad (3.26)$$

One of the key elements of the model is the ability to track the shed vortices. This is an important feature of FVM models since the velocity field can be calculated implicitly. The movement of the shed vorticity is tracked at each time step using the velocity field. The angle of attack can be calculated using the induced velocities from the shed vorticity. The induced velocity of each vortex is a function of the distance of the vortex core to the evaluation point, the time of

existence of each vortex, and the bound vorticity strength. For this model, a Lamb-Oseen vortex type is used which gives an induced velocity V_P as (Saffman, 1992)

$$\vec{V}_P = \frac{\vec{h} \times \vec{\Gamma}}{2\pi h^2} \left(1 - e^{-\frac{h^2}{4\nu t}} \right) \quad (3.27)$$

where h is the distance from the vortex core to the evaluation point, Γ is the vortex strength, ν is the kinematic viscosity and t is the time from the vortex creation to the evaluation time.

Since the model uses vortex particles to avoid tracking the vortex filaments, high velocity fields are created in the vicinity of the vortex cores. This is a problem since a simple shed vortex that is close to a blade element control point can greatly influence the calculated angle of attack. The dynamic stall model is particularly sensitive to small changes in angle of attack or reduced pitch rates that can happen when the blade passes near a velocity field of a vortex trail represented by vortex cores. The reduced pitch rate has a sharp variation especially when the blade passes through a vortex trail at the downstream. The correction implemented was to use vortex re-distribution to cell corners to represent a velocity field, created by vortices in the vicinity, of a blade element control point.

Using the resulting velocities and the tangential and normal coefficients, the force relationships, and the torque produced by the turbine are found. The

tangential force, F_T , and normal force, F_N , can be expressed in terms of the normal and tangential coefficients as:

$$F_T = \frac{1}{2} C_T \rho c U_R^2 \quad (3.28)$$

$$F_N = \frac{1}{2} C_N \rho c U_R^2 \quad (3.29)$$

where ρ is the fluid density. The nondimensional torque produced by a single blade, T_e^+ , can then be written from simple geometry as:

$$T_e^+ = \frac{1}{2} \frac{c}{R} C_t \left(\frac{U_R}{U_\infty} \right)^2 \quad (3.30)$$

where R is the turbine radius.

The instantaneous rotor power coefficient of each single element, C_{pe} , is:

$$C_{pe} = T_e^+ \frac{U_T}{U_\infty} \quad (3.31)$$

The average power coefficient, C_p , at a single revolution can then be calculated by

$$C_p = \frac{1}{N_{TI}} \sum_a^{a+N_{TI}} \sum_1^{N_B} C_{pe} \quad (3.32)$$

where N_B is the number of blades, N_{TI} is the number of calculations in a revolution and a is the start time step of a revolution. A large number of revolutions are needed to simulate a fully developed wake. So, the analytical power coefficient was obtained using the method described by Strickland et al (Strickland et al., 1980). Furthermore, in order to accommodate the blockage effect of the tow tank found on the experiments, a method of images that

included three vortex arrangements for each wall was used in the analytical model for the simulation of the free surface and tunnel floor (Pope, 1984).

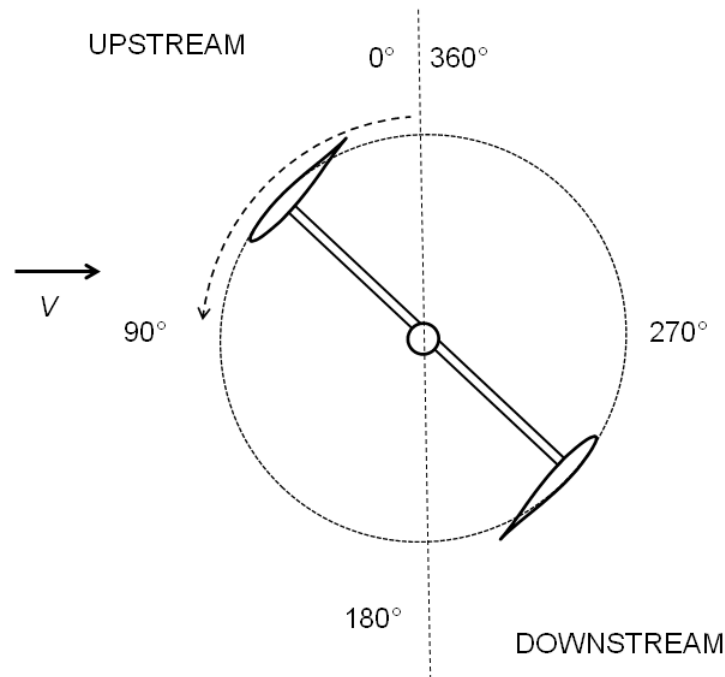


Figure 3.7. The upstream and downstream zones with respect to the turbine are shown.

In order to analyze the movement of the blade it is useful to define two zones as shown in Figure 3.7. The upstream zone is found when the blade goes across the flow at the front of the turbine from a rotational position (θ_B) of 0 degrees to 180 degrees. The downstream zone is found when the blade goes across the flow at the back of the turbine from a rotational position of 180 degrees to 360 degrees. These two zones represent the regions that the turbine

can generate positive torque. For the experimental comparison we consider these separately.

3.3 Experimental Set Up

To validate the numerical investigation at high solidities, a series of tidal current turbines with different blade profiles and geometries were designed, built, and tested in the tow tank at the University of Maine (UMaine), shown in Figure 3.8. The purpose of the experimental test was to provide data for a turbine in a free stream at high solidity rotor values. The turbine was tested in two and four blade configurations.

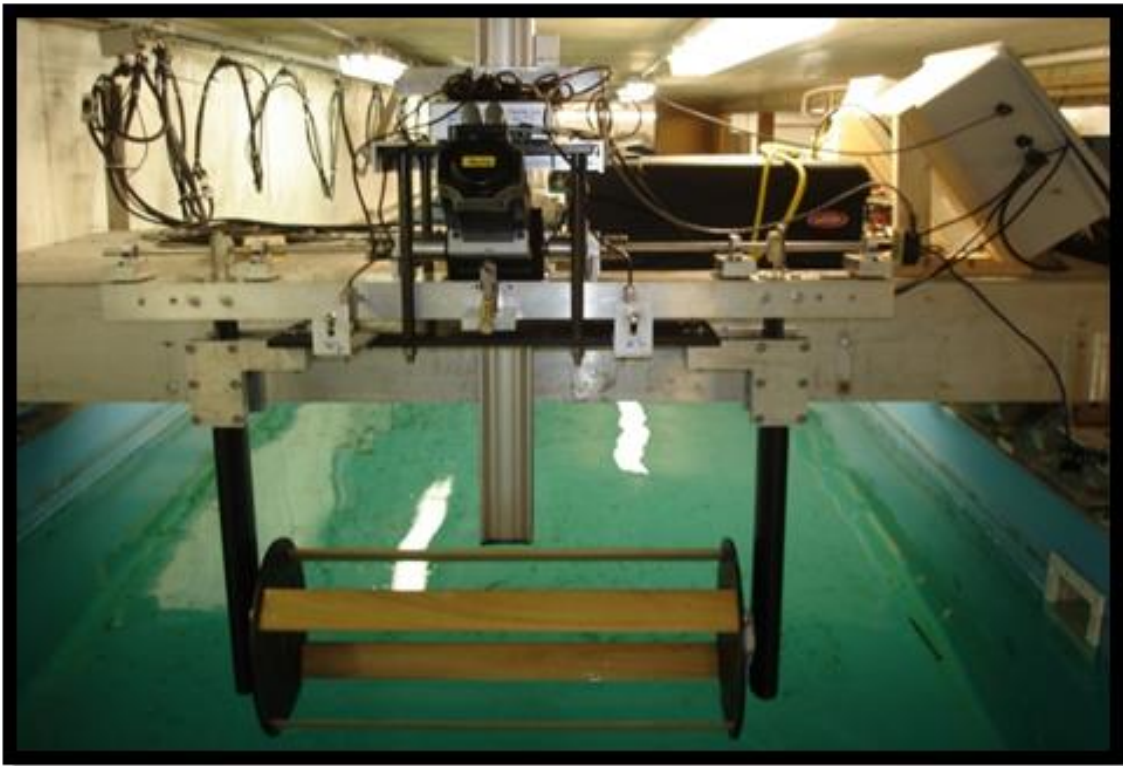


Figure 3.8. The model cross-flow turbine is mounted on the tow tank carriage for testing

The diameter of the experimental turbine is 0.325m. The foil section used for the blades is a NACA 63₃-018 profile with an ideal chord length of 7.62 cm. The trailing edge was trimmed to facilitate manufacture to give a final 6.94cm chord length. The length of the blades is 76.2cm. The maximum speed of the carriage during the test was 2 m/s and the turbine's tip speed ratio (λ) varied from 0.25 to 2.5. An optical encoder was used to measure rotational speed and angular position of the turbine. A load cell mounted at the motor was used to measure the torque produced by the turbine. The performance data acquired was processed by bin-averaging the torque over multiple runs as a function of the turbine rotational position (θ), for comparison with the analytical data. The end plate is designed to be configured for three different turbine diameters, which enables the changing of the turbine solidity. Additionally, the end plate has index patterns that facilitate varying the angle of attack from +/- 10 degrees in 1 degree increments.

The power produced by the turbine is transferred to the upper assembly where a 1.75 kW servomotor coupled with a dual right angle 3:1 gear head generator is used to dissipate the power. Power is transferred from the turbine blades through dual chains and sprockets housed in a hydrofoil shroud that is connected to the upper test bed where the power is absorbed by a motor the input measured. Cross-flow turbines are unique because they are not self-starting in all flow conditions. As the torque in a cross-flow turbine changes within a rotation of the turbine at different free stream velocities, a motor controller

maintains the servo motor at a prescribed tip speed ratio. The motor is capable of switching between power production mode and power dissipation mode. In power dissipation mode the electrical energy produced by the turbine is dumped to a resistor bank. The motor controller is configured in a manner such that the negative efficiency data can be acquired in order to characterize the performance of the turbine at higher tip speed ratios.

3.4. Results and Discussion

In order to ensure the accuracy of the model as well to evaluate the range of applicability, several conditions were used for verification and testing. Analytical results of two published experimental results and experimental data taken at the tow tank at UMaine were used to cover a broad chord to radius (c/R) ratio range. The first set of data was developed by Strickland and is reported for a turbine with two NACA 0012 blades with a c/R of 0.15, and an inflow velocity of 9.1 cm/s (Strickland et al., 1980). At this chord to radius ratio ($c/R=0.15$) the contribution of flow curvature effects is reported to be small (Migliore et al., 1980). A second set of data was acquired using a turbine with three NACA 63₃-018 blades with a c/R of 0.375, an aspect ratio of 3.55, and an inflow velocity of 1 m/s (Shiono et al., 2000). In addition to previous published experiments a third set of data was obtained for a Darrieus turbine at a higher chord to radius ratio and with blades with higher aspect ratio. The data was acquired using a turbine with two NACA 63₃-018 blades with a c/R of 0.461, and aspect ratio of 10, and an inflow velocity of 0.6 m/s.

The comparison of the analytical results against those of Strickland et al showed tangential and normal forces having good agreement with the nondimensional normal forces (Figure 3.9). The model produces reasonable predictions for the nondimensional forces at both the upstream and the downstream regions. The maximum peak magnitude in particular is predicted at the downstream. Reasonable predictions of the nondimensional tangential forces (Figure 3.10) were obtained at the upstream zone, but downstream zone predictions were inferior. A possible explanation could be that the tangential coefficient may need a better approximation for lower inflow velocities that are normally encountered in the downstream. The tangential coefficient is the likely

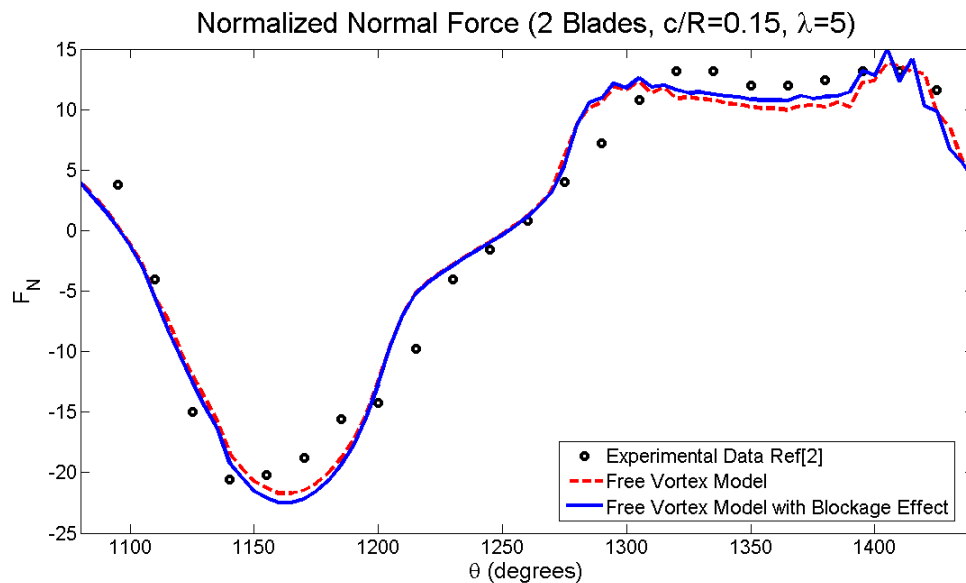


Figure 3.9. The nondimensional normal force from reference (Strickland et al., 1980) is compared to the results of the FVM model.

issue since predictions for the normal force were reasonable. Alternatively, the model may overpredict the shed vorticity at the upstream zone, lowering the angle of attack calculations and tangential force at the downstream zone. Additionally, Figures 3.9 and 3.10 show that there was not a significant contribution of the blockage effect for the configuration for Strickland et al. (1980).

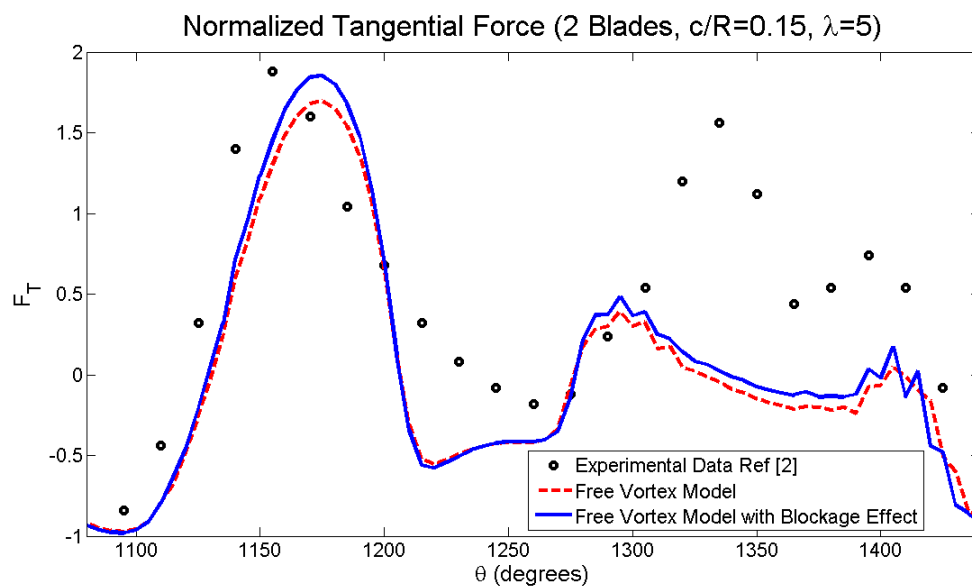


Figure 3.10. The nondimensional tangential force from reference (Strickland et al., 1980) is compared to the results of the FVM model

The comparison of the predictions of the model against the experimental results of Shiono et al.(2000) for higher solidity (0.179) for two tow tanks with widths of 1.8m and 3.0m are shown in Figure 3.11. The analytical model showed agreement in regards to where the maximum power coefficient can be found with respect to the tip speed ratio, as well as the tip speed ratios where there is an increase and decrease of power coefficient. The power coefficients were higher

than the experimental results in some regions due to the relatively low aspect ratio of the blades. The low aspect ratio can increase the induced drag and reduce the lift of the blades, thus decreasing the tangential force generated (Abbott and von Doenhoff, 1959).

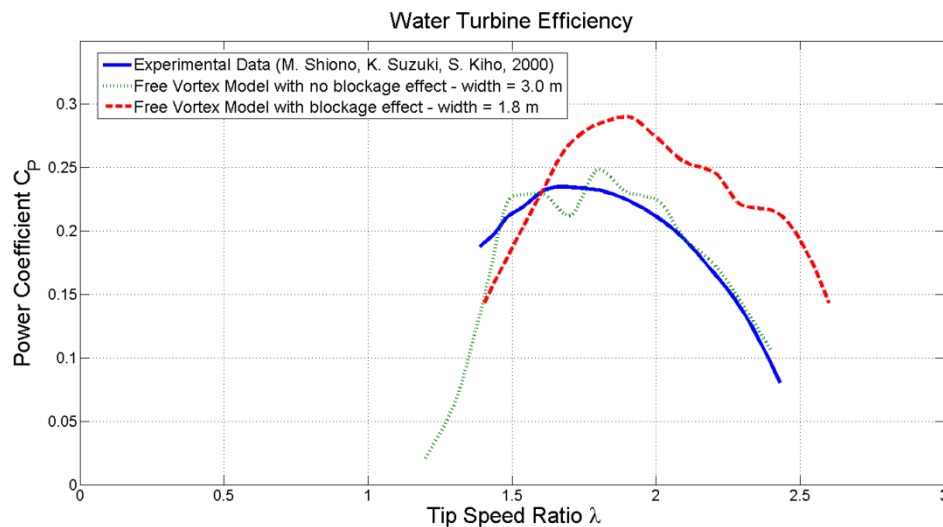


Figure 3.11. The power coefficient from reference (Shiono et al., 2000) is compared for the model results for a solidity of 0.179

1

To further validate the analytical model, the power coefficient (as a function of λ) and the nondimensional torque (as a function of θ) were acquired and compared to more results. Figure 3.12 shows a comparison of the experimental and analytical data when the blockage effect is considered as well as the results without considering blockage. The dynamic stall model has a significant effect on the tip speed ratio range at which the turbine operates. It is

¹ The analytical results for the power coefficient shown in Figures 3.11 and 3.12 differ from the ones published in Urbina et al. (2013) because the analytical results have been processed using the method described in Chapter 4.

also apparent that at lower tip speed ratios, 1.25 to 1.75, the blockage effect does not have a large contribution to the analytical results. The analytical results for tip speed ratios above 1.75 for this chord to radius ratios deviate due to the shortcomings in how the blade is modeled in lifting line FVM. At higher tip speed ratios, there is a larger effect of the blades on how the wake develops. Considering the analytical results, it may be inferred that the free surface may be acting as a free flow.

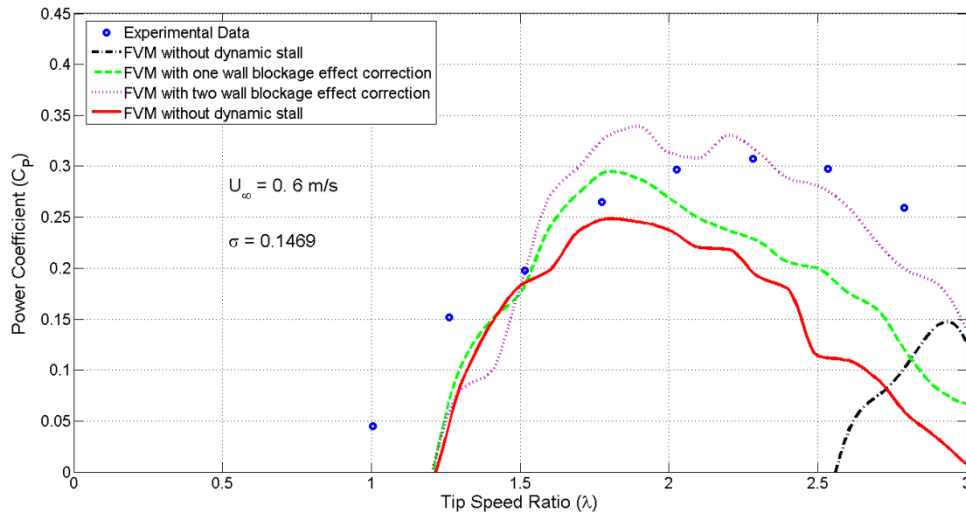


Figure 3.12. The power coefficient is compared for the model for 2 blades with a chord to radius of 0.46

To assess the model, the nondimensional torque was compared to new tow tank experiments (Figures 3.13, 3.14 and 3.15). The model gives a good estimate of the positive torque and power coefficient at $\lambda=1.5$, $\lambda=1.8$ and $\lambda=2.0$, where the turbine generates the most power at operating conditions. The inclusion of the blockage effect improves the model since delayed stall is found from calculations. This validates the assumption that the dynamic stall model

needs to consider the reduced pitch rate, since it has an influence on the angle of attack at which the blade stalls. A portion of the remaining discrepancy in the results possibly comes from a lower estimation of the torque in the downstream zone, as compared to Strickland (Strickland, 1975). Additionally, it can be seen that in the region of rotational position from 0 to 45, the model underpredicts the negative torque values due to the flow curvature effect since the turbine has a high chord to radius ratio (Migliore and Wolfe, 1980). Migliore et al. developed a flow curvature correction, which may yield better results for the tangential forces (Migliore et al., 1980). However, this correction is expected to have little impact on the power coefficient estimation because of the compensation on the effect on the sum of the tangential forces on the blades over a revolution (Cardona, 1984).

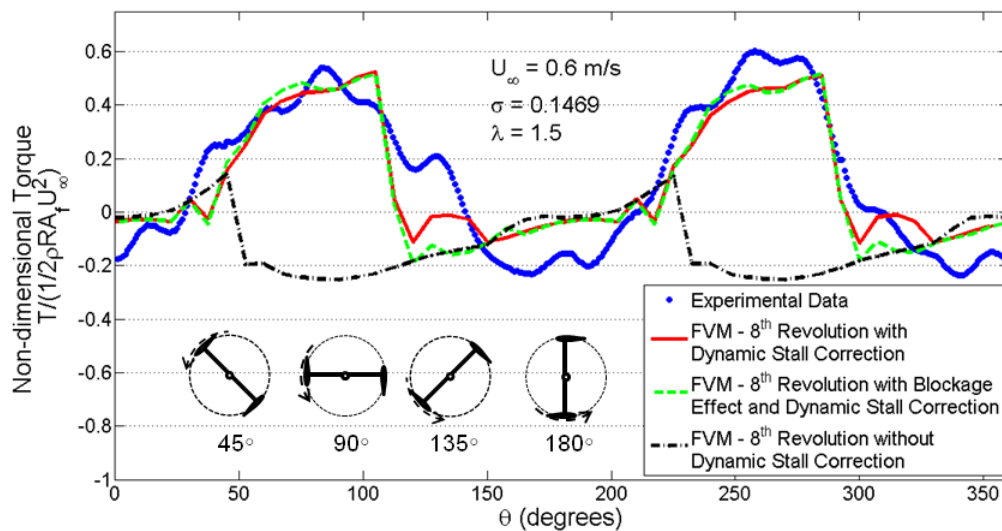


Figure 3.13. The unsteady nondimensional torque data from UMaine tow tank tests is compared for the model with and without blockage and dynamic stall at tip speed ratio of 1.5

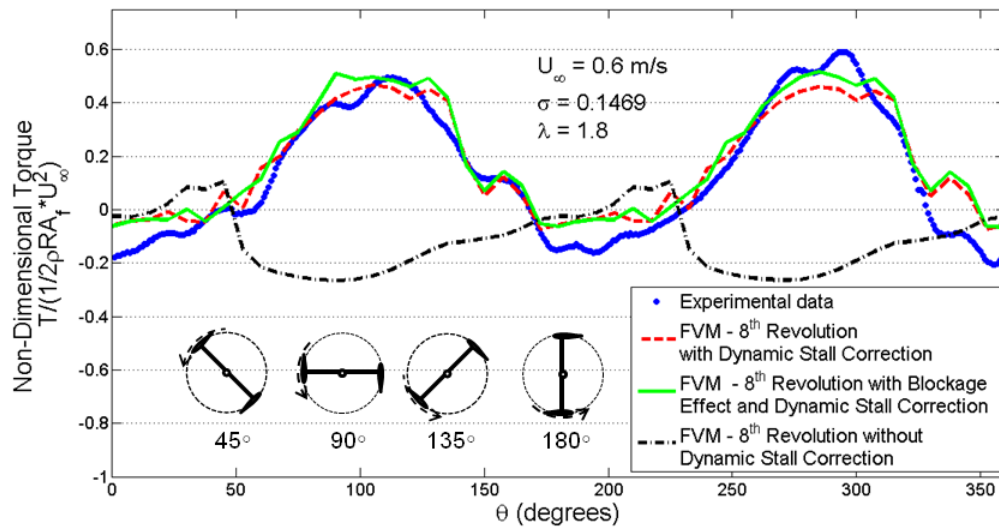


Figure 3.14. The unsteady nondimensional torque data from UMaine tow tank tests is compared for the model with and without blockage and dynamic stall at a tip speed ratio of 1.8

The analytical model compares well to experimental data at a large range of chord to radius ratio range. The model also provided reasonable estimates for the power coefficient. However, the tangential forces and torque estimates with respect to the rotational position were less accurate. The comparison with data from Strickland et al.(1980) suggests that an improved model should focus on calculations of the tangential force at the downstream zone, and thus on the calculated torque. Further considerations, such as the flow curvature corrections may also improve the torque results.

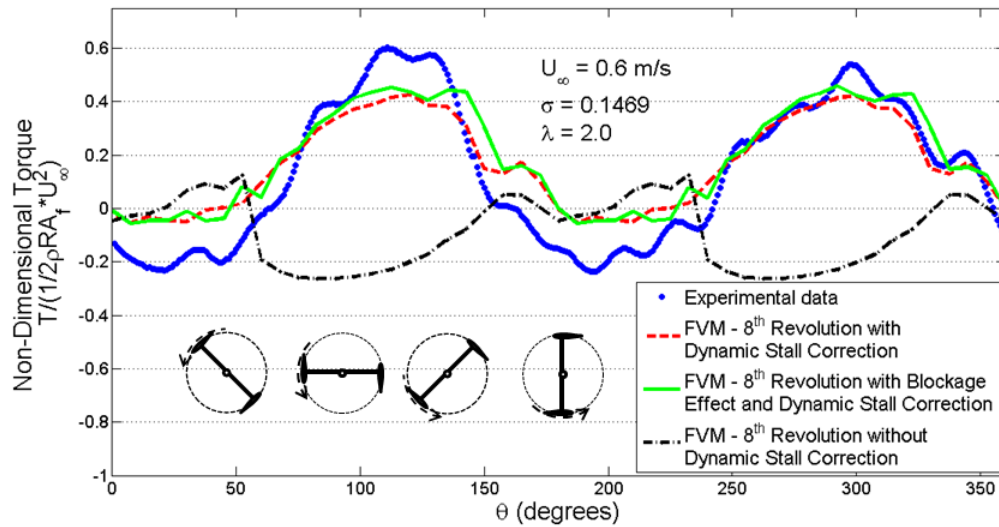


Figure 3.15. The unsteady nondimensional torque data from UMaine tow tank tests is compared for the model with and without blockage and dynamic stall at a tip speed ratio of 2.0

3.5. Conclusions

The lifting line FVM model with dynamic stall correction provides a reasonable power coefficient and blade forces estimates for cross flow turbines. The results are reasonable for a larger range of solidities and Reynolds number ratios than possible with traditional FVM models. Unlike look up tables, this method can be used when experimental data is not available for post stall angles of attack.

The blade forces calculations show good agreement with experiments at a large range of chord to radius ratios. The experiments show that dynamic stall is important for cases of relatively high stall regimes. The tangential forces and

torque estimates at the downstream zone showed inferior agreement with experiments (Strickland et al., 1980). An improved model should focus on calculations of the tangential force, particularly in the post stall region and for low Reynolds numbers. Additionally, inclusion of second order effects such as the boundary layer effects and countertorque may help provide better predictions.

One of the challenges encountered when using the lifting line model is the limited information on the lift and drag in curvilinear flows for different blade profiles. Future extension of the analytical model should consider flow curvature that may have an impact on the torque calculations (Migliore et al., 1980). This problem is particularly acute at very low Reynolds numbers. Further work should also define the parameters chordwise force recovery factor, η , and the longitudinal force correction factor, E_0 , for all post stall angles of attack at low Reynolds numbers. These two parameters are important since they are used to calculate the tangential coefficients. Both input parameters would cause the analytical model to underpredict the power coefficient for low tip speed ratios, where post stall angle of attacks are encountered. Finally, additional work may be needed to correctly define the dynamic stall on-set criteria, and to include considerations of the unsteady contributions on the lift and drag coefficient calculations.

While the model is well suited for use in optimization schemes, it is also a useful tool for broad design parameters for the turbine. A basis for detailed optimization of the turbine using tools is provided to guide high computational cost approaches such as Navier-Stokes and lifting surface FVM methods.

CHAPTER 4

DYNAMIC STALL MODEL WITH FLOW CURVATURE CORRECTION

The previous section described the implementation of an analytical model with a dynamic stall model to predict the performance of cross flow turbines. Nevertheless, other effects that are prevalent in cross-flow turbines need to be taken into account to provide better predictions if the model is to be used in conjunction with optimizers. Optimizers for cross flow turbines need to consider conditions such as toe angle and camber. Information of such conditions is important for the turbine design. To provide better predictions for different conditions of toe angles, a flow curvature correction is needed.

Flow curvature is one of the most critical effects that affect the performance of a cross turbine. Flow curvature appears as a result of variation in the direction of the instantaneous relative velocity along the blade. This variation of the relative flow velocity direction affects the lift and drag forces on the blades. The flow curvature phenomenon can be approximated by using a virtual incidence angle and a virtual camber correction.

The first effort was to use a Migliore's flow curvature correction (Migliore, 1984) in the previous analytical model. One of the reasons to use the Migliore's formulation is that it allows the mounting point of the blade and its toe or stagger

angle to be modeled. Considering the mounting point and the toe angle, allows for the blade forces to be more accurately calculated.

The analytical model presented using Migliore's formulations was compared to analytical data taken at UMaine's tow tank (deBree, 2012). However, this analytical model did not produce accurate predictions especially for cases that included a toe or stagger angle. Some limitations of Migliore's formulation were apparent. This formulation did not consider the induced velocities produced by the blade wakes. The induced velocities have a significant effect on the flow velocities at the blades, especially in the downstream region.

Therefore, a flow curvature correction was derived assuming a parabolic mean line. To include the same capabilities of Migliore's formulations, the blade forces representation in space was modified to the vectorial form. This modification made it possible to model the mounting point of the blade and its toe or stagger angle.

At the same time, the blade-forces formulae were modified to include camber considerations. This was necessary to include camber foils and flow curvature corrections. The blade-forces formulae were devised to be simple while providing reasonable predictions for a large range of angles of attack. This was accomplished by using Kirchoff's equations and conformal mapping solutions.

The blade forces formulae in turn are used in the dynamic stall model to provide the lift and drag at the blades for the unsteady flows.

4.1 Theoretical Approach

The implemented analytical model mainly considers the dynamic stall and flow curvature phenomena. The dynamic stall model uses vortex elements and a blade forces model based on conformal mapping solutions to represent the blade forces created by the unsteady flow conditions on and around the blade. As a first step, the dynamic stall model calculates an equivalent linear flow of the curvilinear flow on the blade using Migliore's formulation. The dynamic stall model uses estimations of the induced velocities of the vortex trail using vortex particles to calculate the angle of attack and the unsteady flow field. Then, an approximated boundary-layer separation location is calculated considering factors such as the reduced pitch rate, the delayed angle of attack, and the maximum change on the location of the boundary-layer separation. The dynamic stall model calculates the lift and drag force coefficients using formulae derived from conformal mapping solutions. These formulae are based on a modified Beddoes Leishman dynamic stall model which is extended to low Mach numbers (Sheng et al., 2008). The resulting force calculations of the dynamic stall model are then used to calculate the turbine efficiency. A simple flowchart of the blade forces calculations is shown in Fig. 4.1.

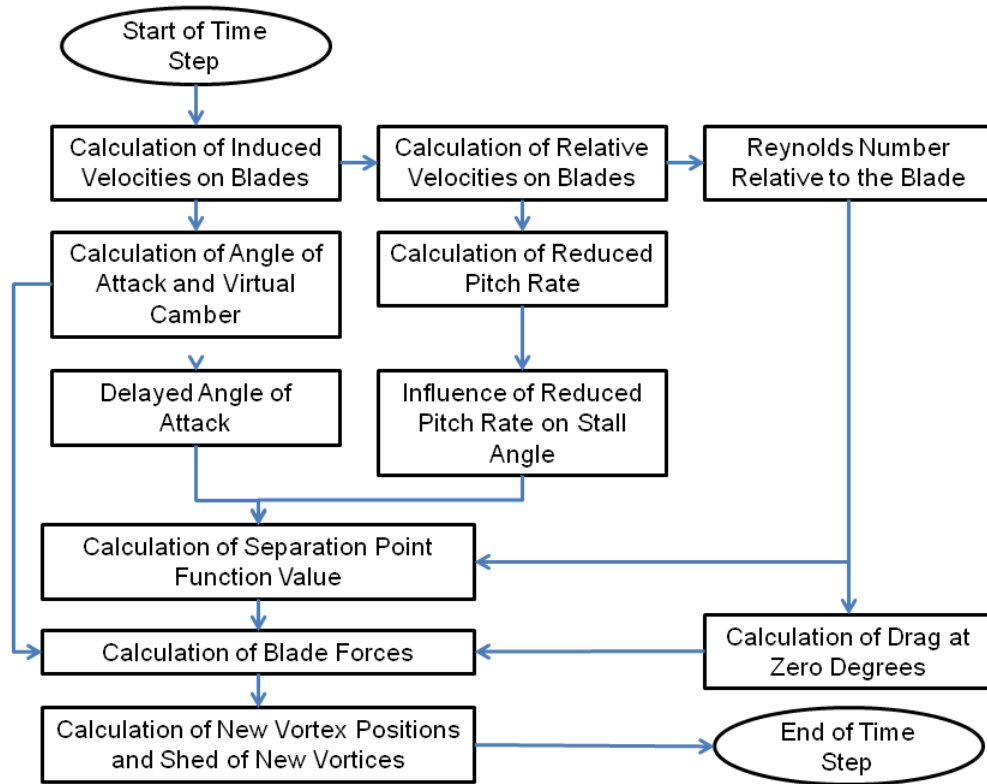


Figure 3.1. The flowchart of the analytical model is shown for each time step in the program

4.1.1 Blade Forces Formulae

4.1.1.1 Lift and Drag

To calculate the lift forces, different conformal mapping solutions that satisfy special cases (Katz, 2001)(Thwaites, 1960) are used. These special cases include the thickness and camber of the hydrofoil that are particularly important model parameters to be considered in design optimization.

The conformal mapping solutions used in these derivations are the solution for a foil with thickness

$$C_L = 2\pi(1 + \epsilon) \sin \alpha \quad (4.1)$$

where the thickness ratio, t/c , is approximately $3\sqrt{3/4}\epsilon$, C_L is the lift coefficient, α is the angle of attack, and t is the thickness of the blade. This solution contains terms needed for the conformal mapping transformation, such as ϵ which is the distance from the center of the circle to the center of the coordinates. The angle derived from conformal mapping and related to the camber, β , is contained in the following solution for a cambered foil with no thickness:

$$C_L = 2\pi \frac{\sin(\alpha + \beta)}{\cos \beta} \quad (4.2)$$

where

$$\frac{f}{c} = \frac{1}{2} \tan \beta \quad (4.3)$$

f is the camber, and c is the chord. Combining both solutions, the following equation is derived:

$$C_L = 2\pi(1 + \epsilon)(\sin \alpha + \tan \beta \cos \alpha) \quad (4.4)$$

The angle β for cambered foils can be approximated using Monk's or Pankhurst's formulae (Abbott and von Doenhoff, 1959). Using these formulae the effective angle β for cambered foils that consider virtual camber (flow curvature correction) is the sum of both effects.

The location of the separation point, shown in Fig 4.2, has a great influence on the lift and drag produced by the blade. The influence of the

separation point on the lift coefficient has been estimated by Krenk (2006) using formulae derived from conformal mapping solutions. These formulae have been modified to match experimental results closely. In particular, the angle of zero lift due to camber has been modified to a value of 0.875 of the theoretical value. This modification accounts for the discrepancy in the experimental angle of lift that varies between 0.75 and 1.0 of the value given by theory of thin wing sections (Abbott and von Doenhoff, 1959) (Jacobs et al., 1935) :

$$C_L = 2\pi(\alpha - \alpha_L) \left[\frac{1 + \sqrt{f'}}{2} \right]^2 \quad (4.5)$$

and

$$\alpha_L = - \left[1 + \frac{3}{4}(1 - 6\sqrt{z_s} + 5z_s) \right] \frac{f}{c} + \frac{3}{4}(1 - z_s) \frac{t}{c} \quad (4.6)$$

where, α_L is the angle of zero lift, f' is defined as the separation point location and z_s is defined as

$$z_s = \sqrt{1 - f'} \quad (4.7)$$

The lift coefficient that includes the effect of separation is approximated as:

$$C_L = 2\pi(1 + \varepsilon(1 - z_s)) \left[\sin \alpha + \frac{\tan \beta}{2} \cos \alpha \left[\left[1 + \frac{3}{4}(1 - 6z_s + 5z_s^2) \right] \right] \left[\frac{1 + \sqrt{f'}}{2} \right]^2 \right] \quad (4.8)$$

To extend the range of angles of attack for this equation, a correction that takes into account Hoerner's observation (Hoerner and Borst, 1975) that the lift coefficient is close to:

$$C_L \approx [1.8 \text{ to } 2.0] \sin \alpha \cos \alpha \quad (4.9)$$

is implemented. The resulting lift coefficient approximation is therefore:

$$C_L = 2\pi(1 + \varepsilon(1 - z_s)) \left[\sin \alpha + \frac{\tan \beta}{2} \cos \alpha \left[\left[1 + \frac{3}{4}(1 - 6z_s + 5z_s^2) \right] \right] \left[\frac{1 + \sqrt{f'}}{2} \right]^2 \right] \cos \alpha \quad (4.10)$$

f = Separation Point

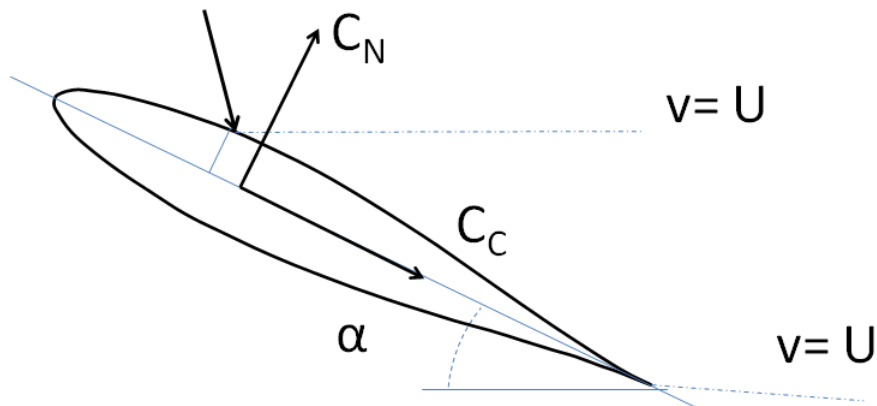


Figure 4.2 Separation function value as a function of the effective angle of attack is shown.

To calculate the turbine performance, the approximation of drag coefficient is also needed. The solution for the drag coefficient, C_D , is approximated using the following equation:

$$C_D = 2\pi(\alpha - \alpha_D)^2 \left[\frac{1 - \sqrt{f'}}{2} \right]^2 \quad (4.11)$$

where α_D is the angle of attack at which minimum drag is found. Similarly, as with the lift coefficient, to extend the range of angle of attack at which the drag coefficient formula will estimate values, Hoerner's observation that the drag is approximately (Hoerner and Borst, 1975):

$$C_D \approx [1.8 \text{ to } 2.0] \sin^2 \alpha \quad (4.12)$$

is taken into account in equation 3.10. The following is derived as a result:

$$C_D = C_{D90} \sin^2(\alpha - \alpha_D) \left[\frac{1 - \sqrt{f'}}{2} \right]^2 \quad (4.13)$$

where C_{D90} is the drag at an angle of attack of 90 degrees. By expanding the terms in equation 4.13 and using small angle approximations for α_D the following equation is derived:

$$C_D = C_{D90} [\sin \alpha - \cos \alpha \cdot \alpha_D]^2 \left[\frac{1 - \sqrt{f'}}{2} \right]^2 + C_{D0} \quad (4.14)$$

where C_{D0} is the drag at an angle of attack of 0 degrees and is defined as:

$$C_{D0} = C_{D0,plate} + 0.04 \frac{f}{c} + 0.01 \frac{t}{c} + 0.1 \left(\frac{t}{c} \right)^2 \quad (4.16)$$

where $C_{D90,flatplate}$ and $C_{D0,plate}$ are the drag values at an angle of attack of 90 and 0 degrees of a flat plate, respectively. Equation 4.16 is derived using Jacobs et al.(1935) formulae. The next step is to consider the effect of separation using the conformal mapping solution for separated flow (Thwaite, 1960):

$$C_D = 2\pi\alpha^2 \left[\frac{1 - \sqrt{f'}}{2} \right]^2 \quad (4.15)$$

The influence of the separation on the drag for a camber foil is also considered by empirically modifying formulae derived by Krenk (2006) to provide better approximations:

$$\alpha_D = -\frac{1}{14}(7 + 2z_s + 5z_s^2)\frac{f}{c} \quad (4.17)$$

Thus, the resulting drag coefficient is

$$C_D = C_{D90} \left[\sin \alpha + \cos \alpha \cdot \frac{1}{14}(7 + 2z_s + 5z_s^2)\frac{f}{c} \right]^2 \left[1 - \sqrt{f'} \right]^2 + C_{D0} \quad (4.18)$$

or

$$C_D = C_{D90} \left[\sin \alpha + \cos \alpha \cdot \frac{1}{28}(7 + 2z_s + 5z_s^2) \tan \beta \right]^2 \left[1 - \sqrt{f'} \right]^2 + C_{D0} \quad (4.19)$$

where C_{D0} is the frictional drag. It should be noted that the solutions are for blades at small angles of attack in which $\sin \alpha \approx \alpha$.

From calculations of the drag on cavities, it is known that conformal mapping underpredicts the estimated drag (Plesset and Shaffer, 1948) if no considerations are made for the separated flow. The drag is, therefore, approximated empirically as:

$$C_D = C_{D90} \sin^2 \alpha \left[\frac{1 - \sqrt{f'}}{2} \right]^2 + C_{D0} \quad (4.20)$$

where (Montgomerie, 2004)

$$C_{D90} = C_{D90,flatplate} - 1.46 \frac{t}{2c} + 1.46 \frac{f}{c} \sin \alpha \quad (4.21)$$

and $C_{D90,flatplate}$ is the drag at an angle of attack of 90 degrees of a flat plate.

The drag at 0 degrees, $C_{D0,plate}$, is calculated by considering the frictional drag of

two sides of one flat plate in a turbulent flow. The formula for two flat plates is (Schlichting and Gersten, 1979):

$$C_{D0,plate} = \frac{2 \cdot 0.523}{\ln^2(0.06Re_L)} \quad (4.22)$$

where Re_L is the Reynolds number of the blade. The tangential and normal coefficients in terms of lift and drag coefficients can be written as:

$$C_T = C_L \sin \alpha - C_D \cos \alpha \quad (4.23)$$

$$C_N = C_L \cos \alpha + C_D \sin \alpha \quad (4.24)$$

A correction is done to equation 4.23 to account for the difference between the leading edge suction and the trailing edge suction, which can be observed mainly at an angle of attack of 90 degrees.

$$C_{T,RL90} = C_{L90} \sin^2 \alpha \quad (4.25)$$

Additionally, a correction to account for the cavity factor, E_0 , (Sheng et al., 1980) is considered as:

$$E_0 = -0.16 \cos^2 \alpha \left[\frac{1 - \sqrt{f}}{2} \right]^2 \quad (4.26)$$

Thus, when equation 3.22 is the modified the following equation is the result:

$$C_T = C_L \sin \alpha - C_D \cos \alpha + C_{T,RL90} + E_0 \quad (4.27)$$

where $C_{T,RL90}$ is the tangential coefficient value at an angle of attack of ninety degrees.

The separation point function is influenced by different factors such as Reynolds number and camber. As previously commented, the cross flow turbine goes through a cyclic variation of the Reynolds number (Migliore and Wolfe,

1980). The calculation of the separation point is done by using experimental data to approximate the angle of attack at which the blade stalls. Then, a cubic hermite interpolation polynomial is used to calculate the rest of the separation point values. This simple approximation facilitates the estimation of lift and drag forces at a large range of Reynolds numbers that are encountered during turbine operation. Fig. 4.3 shows the analytical lift coefficient for a NACA 63-3-018 profile (Abbott and von Doenhoff, 1959) for Reynolds numbers 3,000,000 and Fig. 4.4 shows analytical approximations for the lift coefficient for a NACA 63-3-018 family with different camber conditions.

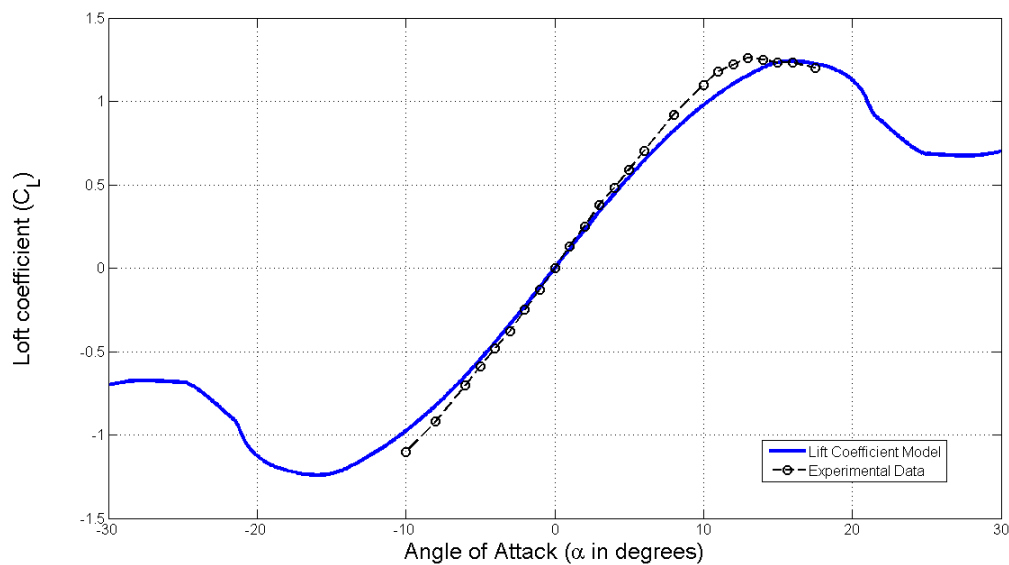


Figure 4.3. The calculated lift coefficient of the analytical model for a NACA 63-3-018 as a function angle of attack is compared to experimental data for different Reynolds number of 3,000,000.

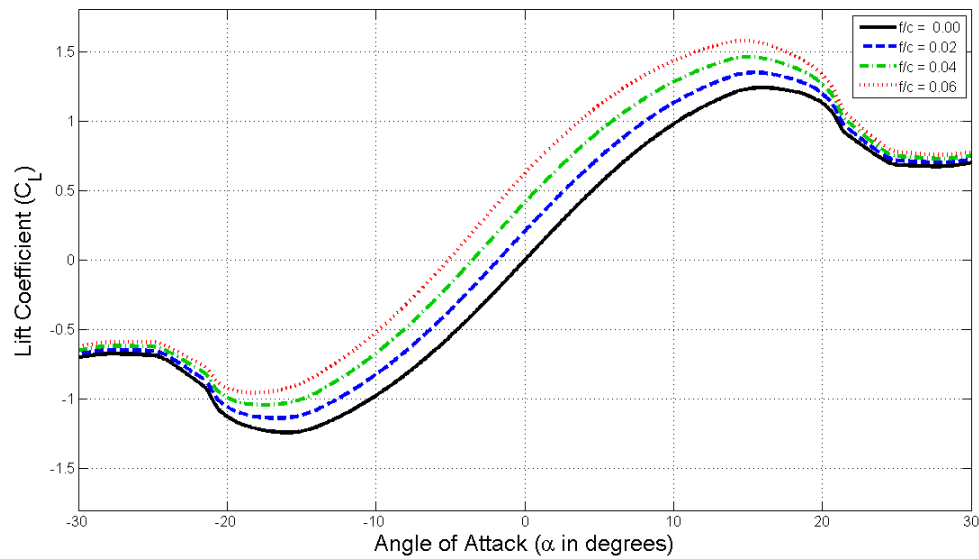


Figure 4.4. The calculated lift coefficient is shown as a function angle of attack for different camber values.

4.1.2. Dynamic Stall Model

The dynamic stall model uses two mechanisms to simulate the effects on the lift and drag forces due to the unsteady flow surrounding the blade. The first mechanism is the effect that the leading edge vortex has on the separation point location. The separation point location on the foil is changed by a modified angle at which the foil is expected to stall. The modified angle at low Mach numbers at which the foil stalls, or the breakpoint of separation, is related to the reduced pitch rate (Sheng et al., 2008). The second mechanism in the dynamic stall model is that the separation point is normally delayed under dynamic conditions (Sheng et al., 2008). The calculation of the effective angle of attack due to effect of the reduced pitch rate is done following the procedure described by (Sheng et

al., 2008) (Urbina et al., 2013). This effective angle of attack is then used to calculate an initial separation function value.

It is known that the separation point advances within an elapsed time given the presence a velocity or acceleration fluid field (Chang, 1970). Thus, a restriction on the value of the maximum velocity of the boundary-layer separation is applied using the following formula:

$$t_s = \sqrt{\frac{2.08}{\frac{du_e}{dx}}} \quad (4.28)$$

where t_s is the time elapsed and $\frac{du_e}{dx}$ is the derivative of the fluid velocity with respect to the distance over which the fluid accelerates. Because the velocity field along the blade is unknown, the velocity field is approximated by using the inviscid fluid velocity field for a Van Vorseen blade profile derived using conformal mapping (Katz, 2001) with a simple correction for the camber. The final separation point function is then used to calculate the lift and the drag of the blade.

As mentioned before, the velocity field along the blade is not uniform, but it resembles a curvilinear flow. To approximate this curvilinear flow, a flow curvature correction is used. A parabolic mean line is assumed for the flow curvature:

$$f(x) = f_0 \left[1 - \left(\frac{2x}{c} \right)^2 \right] \quad (4.29)$$

The slope of the mean line of a cambered foil is

$$\frac{df}{dx} = -\frac{8f_0x}{c^2} \quad (4.30)$$

and the change of slope is

$$\frac{d^2f}{dx^2} = -\frac{8f_0}{c^2} \quad (4.31)$$

If the slope of the camber line and the angle of attack are assumed to be equal to

$$\tan \alpha = \frac{df_0}{dx} \quad (4.32)$$

equation 4.31 can be expressed as

$$\frac{d \tan \alpha}{dx} = -\frac{8f_0}{c^2} \quad (4.33)$$

The virtual camber can be derived from the change in angle of attack along the blade,

$$\frac{f}{c} = -\frac{c}{8} \frac{d \tan \alpha}{dx} \quad (4.34)$$

The flow curvature is then evaluated at three points and the virtual camber found by a simple regression. The virtual angle of incidence is found at the midchord that has the same slope as the nose-tail line in a parabolic mean line. These effective virtual camber and virtual angle of incidence are used in equations 4.24 and 4.27 to calculate the normal and tangential forces, respectively.

The angle of attack, induced velocities, blade forces, torque and power coefficient are calculated as described in Strickland et al. (Strickland et al., 1980), and Urbina et al. (Urbina et al., 2013). The normal and tangential blade vectors are calculated using the mounting point and toe angle shown in Fig. 4.5. A large

number of revolutions are needed to simulate a fully developed wake. The analytical power coefficient is obtained by extrapolating the induced velocities due to the wake for the whole rotation of the blade. These extrapolated induced velocities are used to calculate blade forces, torque and power coefficient. Additionally, to accommodate the blockage effect of the tow tank found on the experiments, a method of images that included three vortex arrangements for each wall is used in the analytical model for the simulation of the tunnel floor or the tunnel walls (Pope 1984).

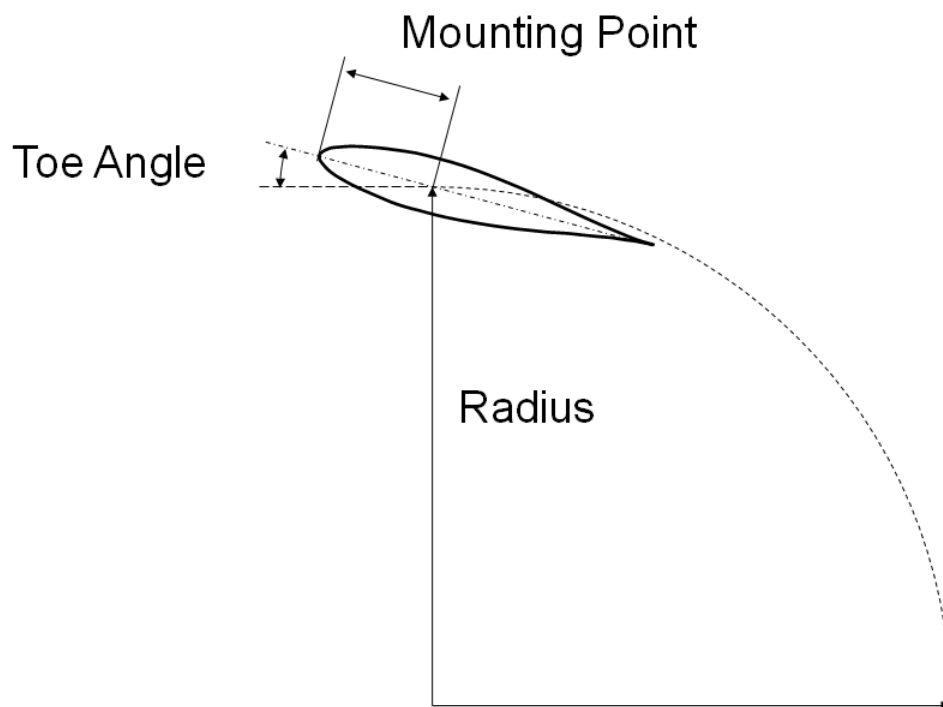


Figure 3.5. The blade toe-angle and mounting point is shown.

To analyze the forces due to the movement of the blade, it is useful to define two zones: the upstream zone and the downstream zone. The upstream zone is found when the blade goes across the flow at the front of the turbine from a rotational position (θ_B) of 0 degrees to 180 degrees. The downstream zone is found when the blade goes across the flow at the back of the turbine from a rotational position of 180 degrees to 360 degrees. These two zones represent the regions that the turbine can generate positive torque. For the experimental comparison, we consider these separately.

4.2. Experimental Set-Up

To assess the numerical investigation at high solidities, a series of tidal current turbines with different blade profiles and geometries were designed, built, and tested in the tow tank at the University of Maine (UMaine). The purpose of the experimental test was to provide data for a turbine in a free stream at high solidity rotor values. The turbine was tested in two and four blade configurations (deBree, 2012)(Swanger, 2013). The maximum speed of the carriage during the test was 0.8 m/s and the turbine's tip speed ratio (λ) varied from 1.1 to 3.2.

The dimensions of the turbine were dictated by the dimensions of the tow tank used for testing. Testing was performed in a tow tank that is 2.44 meters wide, 1 meter deep and 30 meters long. The diameter of the experimental turbine is 32.5cm. Two foil sections were used for the blades with a NACA 633-018 profile. The first foil section had an ideal chord length of 5.08cm (chord-to-radius

ratio of 0.30). The trailing edge was trimmed to facilitate manufacture and resulted in a final chord length of 4.5cm. The second foil section had an ideal chord length of 7.62 cm (chord-to-radius ratio of 0.46). The trailing edge was trimmed to facilitate manufacture and resulted in a final chord length of 6.94cm. The length of the blades is 76.2cm. The blades were mounted on end plates that had index patterns which facilitate varying the angle of attack from +/- 10 degrees in 1 degree increments.

The torque was calculated as a function of the turbine rotational position by considering the drive train losses, the drag losses, and the inertia forces from the turbine rotor end plates; and filtering the measured torque. A load cell mounted at the motor was used to measure the torque produced by the turbine. The measured torque was adjusted by considering the drag losses and endplate effects. These effects were calculated by running the turbine without turbine blades using a procedure consistent with Li and Calisal (Li and Calisal, 2010b):

$$T_P \approx T_{P,R} + T_{P,AS} \quad (4.35)$$

where T_P is the instantaneous measured torque, $T_{P,R}$ is the instantaneous torque produce by the rotor and $T_{P,AS}$ is the measured torque contribution of the end plates. Additionally, a first order correction was applied to the torque measurement to account for the angular velocity variations and friction:

$$T_{P,R} = T_{P,B} + I\ddot{\theta} + b\dot{\theta} \quad (4.36)$$

where $T_{P,B}$ is the instantaneous torque produced by the blades, I is the rotor's moment of inertia, b is the measured friction at the instantaneous tip speed ratio,

$\ddot{\theta}$ is the rotor's angular acceleration and $\dot{\theta}$ is the rotor's angular velocity. An optical encoder was used to measure rotational speed and the angular position of the turbine. The instantaneous torque produced by the blades was nondimensionalized using the following equation:

$$T^+ = \frac{T_{P,B}}{1/2\rho R A_F U_\infty^2} \quad (4.37)$$

where A_F is the total projected frontal area of the rotor. The performance data acquired was processed by bin-averaging the torque over multiple runs as a function of the turbine rotational position (θ), for comparison with the analytical data.

4.3. Results and Discussion

The analytical model was compared with experimental data to evaluate the quality of the predictions. The analytical model was evaluated at a range of chord-to-radius ratios and toe angles for different blade profiles. Three different chord-to-radius ratios were chosen, 0.15, 0.30 and 0.46, and the evaluation was done at different toe angles. The experimental results used for the evaluation consist of one published experimental data set (Li, 2008) and an experimental data set taken at the tow tank at UMaine.

The first set of data was developed by Li (Li, 2008) and is reported for a turbine with one and three NACA 63-4-021 blades with a c/R of 0.15, a toe angle of zero, and tip speed ratio of 2.75. At this chord to radius ratio ($c/R=0.15$), the

contribution of flow curvature effects is reported to be small (Migliore and Wolfe, 1980). This set of data also provides results for torque predictions using vortex method and the CFD commercial software Fluent (Ansys) (Nabavi, 2008). The Spalart-Allmaras turbulence model and a minimum time step of 0.2 milliseconds were reportedly used. These analytical torque predictions provide a good baseline to evaluate the presented analytical model. A second set of data was acquired using a turbine with two NACA 633-018 blades with a c/R of 0.30, an aspect ratio of 15, and an inflow velocity of 0.8 m/s. In addition, a third set of data was acquired using a turbine with two NACA 633-018 blades with a c/R of 0.461, an aspect ratio of 10, and an inflow velocity of 0.8 m/s.

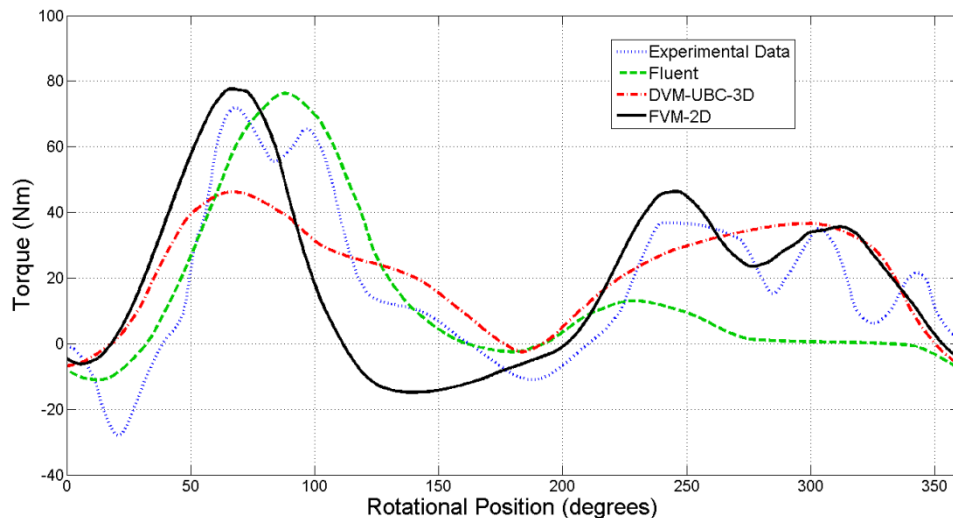


Figure 4.6. The calculated torque for a one bladed turbine with a chord to radius ratio of 0.15 at conditions of published results (Li, 2008) indicates improvements in the predictions regarding the peak magnitude and the downstream region predictions for DVM.

The first comparison of the predictions of the model was made with the experimental results of Li (Li, 2008) for a one bladed turbine, shown in Fig. 4.6. The predictions of the presented model regarding the first peak magnitude were close to the experimental and CFD results and significantly improved over the DVM results. However, there is no improvement with regards to the prediction of the location of the first peak. The presented analytical model deviates in the stall region (70-180 degrees), which may imply that further improvements need to be made to the model in this region. The predictions of the presented analytical model in the downstream region are improved over the DVM results and are significantly better than the CFD results.

The second comparison was made with the experimental results of Li (Li, 2008) for a three bladed turbine, shown in Fig. 4.7. The presented model shows an improvement over the DVM predictions regarding the torque amplitude (FVM torque amplitude of 86.636 Nm). In fact, the predicted torque amplitude is closer to the CFD predictions and in some regions they are nearly equal. However, there is no improvement of the predictions of the phase shift with respect to the experimental measurements. Regarding the predictions of the power coefficient, the FVM of 0.384 shows a small improvement, 3.2%, when compared to the prediction of the DVM-UBC model of 0.395 (Li, 2008), but a larger improvement over the traditional FVM-DVM model, 0.419. Still the CFD predictions were better, 0.369, when compared to the experiment data, 0.343 (Li, 2008).

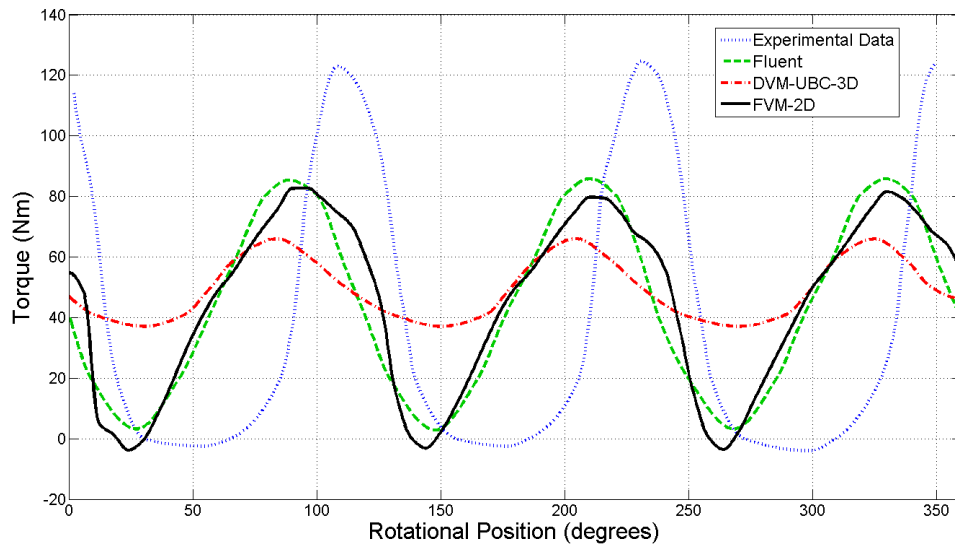


Figure 4.7. The calculated torque for a three-bladed turbine with a chord to radius ratio of 0.15 at the conditions of published results (Li, 2008) shows good correlation with CFD results.

The analytical model was further validated by increasing the chord-to-radius ratio from 0.15 to 0.30 and using a different toe angle. The toe angle has a significant impact on where the maximum power coefficient can be obtained as seen in Fig. 4.8. Under the particular conditions of this experimental data set, the maximum power coefficient can be found around a toe of 4 degrees. Fig. 4.9 shows the analytical model predictions for the power coefficient at a toe angle of 4 degrees with and without the flow curvature correction. To quantify the influence of the flow curvature correction the model was compared to experimental data for cases that included the flow curvature correction with the virtual camber, VC, virtual angle of incidence, VAI, and no flow curvature. It can be seen that the power coefficient predictions that consider flow curvature

produce better results than those that do not consider it. When compared to the experimental results, the root-mean-square error (RMSE) of the calculated power coefficient, which includes the flow curvature correction with VC and VAI, is 0.018. The RMSE for the calculated power coefficient that includes the flow curvature correction with only VAI is 0.023, and that of the one that does not include any flow curvature correction is 0.090. Fig 4.10 shows results at low tip-speed ratios. The analytical torque results nearly approximate the peak magnitude but have a deficiency on the phase prediction. These results seem to imply that there is a component of dynamic stall such as the added mass effect that is not being considered. The fact that the torque phase difference is in line with the change in time of the resultant velocity on the blade further suggests that the added mass may be the component to be considered. Additionally, at low tip speed ratios, larger variations on the rotor angular velocity were observed ($\pm 5\%$ of the set rotor angular velocity). These variations may affect the experimental measurements. This deficiency on the phase may be explained because of the Fig 4.11 shows the results at around the maximum power coefficient. At this tip speed ratio, the analytical torque results underpredict the amplitude of the peaks.

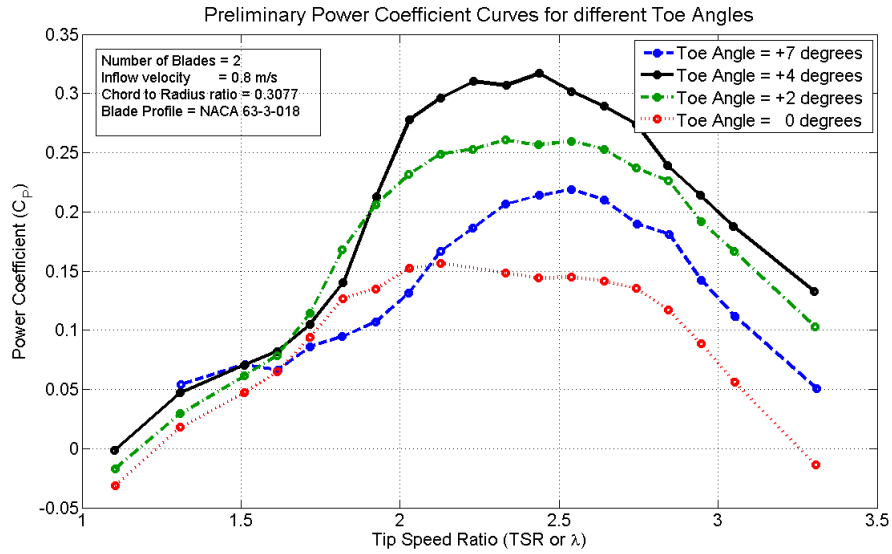


Figure 4.8. Experimental power coefficient results for a two-bladed turbine with a chord to radius ratio of 0.3 show dependency on where the maximum power coefficient is found with respect to the toe angle.

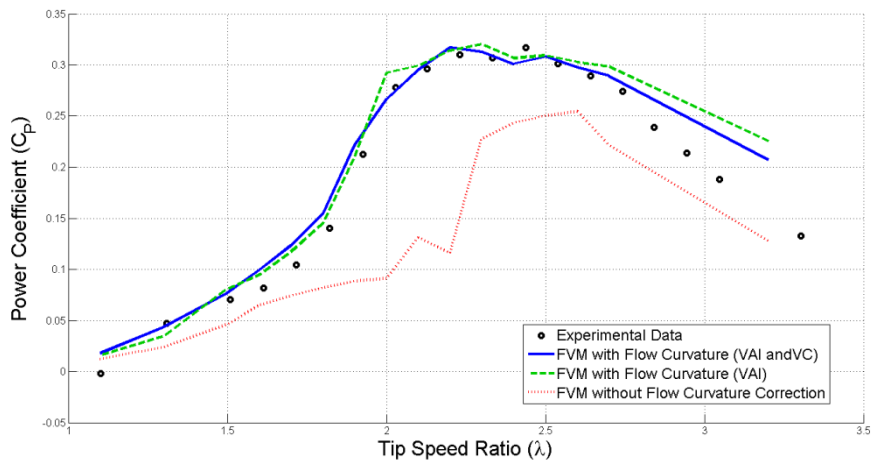


Figure 4.9. The analytical power coefficient results where flow curvature is considered show agreement with experimental data for a two-bladed turbine with a chord to radius ratio of 0.3 at a the toe angle of +4.

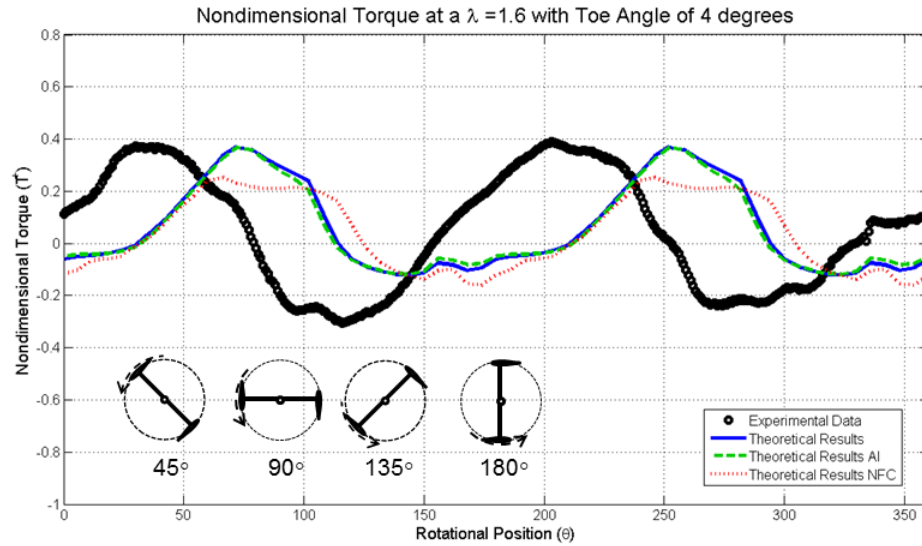


Figure 4.10. Analytical results, when compared to experimental data show at a toe angle of +4 degrees and tip-speed ratio of 1.6, indicate improvements on the predictions when considering the flow curvature correction.

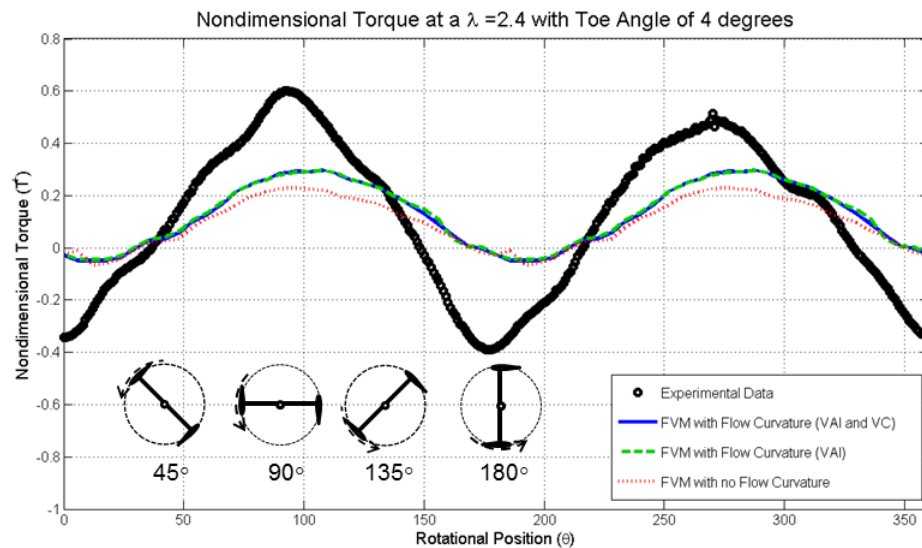


Figure 4.11. Analytical results, when compared to experimental data at a toe angle of +4 degrees and tip-speed ratio of 2.4, show that the flow curvature correction has a lower contribution on the predictions.

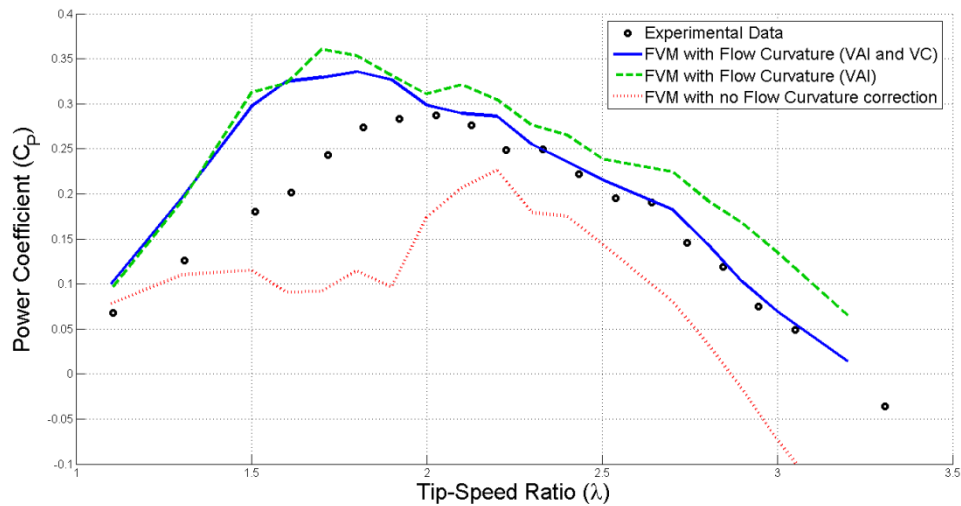


Figure 4.12. The analytical power coefficient predictions where flow curvature is considered can predict where the maximum torque is encountered when compared with experimental data for a two-bladed turbine with a chord to radius ratio of 0.46 at a toe angle of +5.

The comparison of experimental and analytical power coefficient values at the chord-to-radius ratio of 0.46 and a toe angle of +5 are shown in Fig. 4.12. It can be seen that there is a small discrepancy between the flow curvature correction that uses the virtual camber and virtual incidence angle and the flow curvature correction that only uses the virtual incidence angle. When compared to the experimental results, the RMSE of the calculated power coefficient calculation, which includes the flow curvature correction with the VC and VAI, is 0.050. The RMSE for the calculated power coefficient that includes the flow curvature correction with only VAI is 0.069, and that of the one that does not include any flow curvature correction is 0.107. This suggests that it may be more

important to consider the flow curvature phenomenon at higher chord-to-radius ratios. The analytical model seems to correctly predict the circulatory lift force that is responsible for the wake shedding at tip-speed ratios above 2.0. This is evident as the analytical model correctly predicts at which tip-speed ratios the power coefficient starts to decrease and the rate at which the power coefficient declines as the tip-speed ratio increases. However, the results for tip-speed ratios below 2.0 may indicate that further improvements may be needed for the dynamic stall model at high reduced pitch rates and high angle of attack, as well as for high virtual camber values.

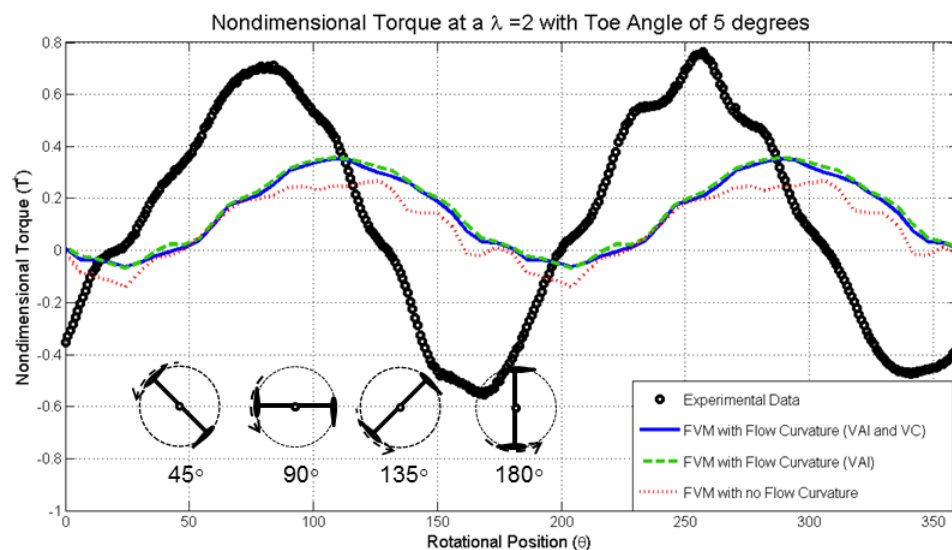


Figure 4.13 The analytical results, when compared to experimental non-dimensional torque at a toe angle of +5 degrees and tip-speed ratio of 2.0, imply that there is a higher influence of the flow curvature at a chord-to-radius ratio of 0.46.

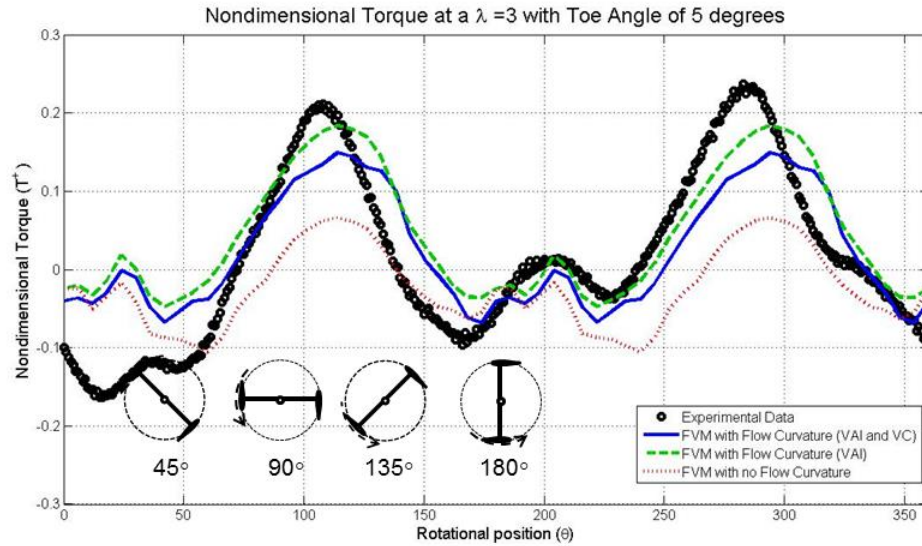


Figure 4.14. The analytical results, when compared to experimental non-dimensional torque at a toe angle of +5 degrees and tip-speed ratio of 3.0, indicate that further improvements are needed to predict the torque amplitude.

Fig. 4.13 shows the results at around the maximum power coefficient. At this tip speed ratio the analytical torque results underpredict the amplitude of the peaks. Fig. 4.14 shows results at high tip-speed ratios. The analytical torque results nearly approximate the peak magnitude and the phase. These results seem to imply that there is a component of dynamic stall such as the added mass effect that is not being considered. This component of dynamic stall possibly affects the torque magnitude near the peak power coefficient, but it does not have an influence on the total power coefficient. The added mass is due to additional flow accelerations on the foil surface induced by the temporal rate of change of flow circulation around the blade (Katz and Plotkin, 2001) (Murray and Barone, 2011). The added mass may produce forces that affect the magnitude of

the torque peaks. However, it does not affect the total power coefficient because the sum of its effect over a revolution is negligible. A correction to account for the added mass in the tangential coefficient has been implemented in Cactus (Murray and Barone, 2011). However, this correction for the added mass could not be implemented in this work because of the flow curvature correction.

4.4. Conclusions

This paper describes the implementation and comparison to experimental data of a lifting line FVM model with dynamic stall and flow curvature corrections for improving the performance predictions of a cross flow tidal-current turbine with different toe angles. Experimental comparison of the calculated torque produced by the modified dynamic stall model showed that it produces improved torque and power coefficient approximations at low chord-to-radius ratios. The combination of the blade forces model and the flow curvature correction has allowed the prediction of the power coefficient at high chord-to-radius ratios with blades mounted at different toe angles. The ability to predict the toe angle at which the blades need to be mounted to extract the maximum power coefficient is an important quality of the present analytical model. The features of the modified FVM model provides the user with the ability to estimate power coefficient and blade forces on turbines at low chord-to-radius ratios and Reynolds number with reasonable accuracy.

Assessing the analytical model at different chord-to-radius ratios has the advantage of identifying areas where the analytical model can be improved, although turbines with high chord-to-radius ratios may not be deployed on the field. The dynamic stall correction based on the reduced pitch rate and delayed angle of attack has provided better predictions of the torque magnitude at the upstream region. However, the tangential forces and torque estimates with respect to the rotational position were less accurate for higher chord to radius ratios, especially for low tip-speed ratios. This fact may imply that further improvements may be needed in the dynamic stall model for blade forces predictions at high reduced pitch rates, high angles of attack and high virtual camber values. Additional work is needed to correctly define the dynamic stall on-set criteria, especially at low Reynolds number, and improve the formulae in the post stall area. This additional work will most likely improve the results at low tip-speed ratios where the blades operate at large angle of attack ranges. Additionally, there are other phenomena, such as added mass, not being taken into account. This is true especially for cases of high chord-to-radius ratios that can improve the blade forces and therefore the calculated torque.

One of the challenges encountered when using the lifting line model is the limited information available on the lift and drag in curvilinear flows for different blade profiles. Even less information on the lift and drag at different Reynolds numbers for different blade profiles is available. This is particularly evident in the post stall region. The blade forces formulae presented here can be an alternative

for estimating lift and drag forces when experimental data is not available. The blade forces formulae also provide improved calculations for different camber values which allow for better predictions of the flow curvature phenomenon. Having better flow curvature predictions will most likely improve the calculations of the turbine performance at higher chord-to-radius ratios.

Another challenge encountered was accounting for the variation of the angular speed to allow comparison of experimental data with analytical predictions. To minimize the variations, a motor with a PI controller was implemented. However, these variations on the angular speed could only be minimized to less than $\pm 5\%$. Although a first order correction to account for the angular speed variation has been implemented, the effects which small flow velocity variations on the blade have on the blade forces were not accounted for. This first order correction to account for the angular speed variation does not affect the results on the calculated power coefficient, but it does reduce the amplitude on the torque oscillations. The effects of this error on the variation of the angular speed were more noticeable at low tip speed ratios ($\pm 5\%$). This variation on the angular speed can also change the angle of attack, inducing a phase shift on the blade.

What has been demonstrated is the ability of a computationally efficient model to characterize the most important features of the torque and power coefficient of a cross flow turbine at different toe angles. When compared to

previous FVM models, the torque and power coefficient predictions have been improved by considering the main phenomena of cross flow turbine, such as dynamic stall model and flow curvature. Additionally, the possibility to predict the performance of cross turbines with blades of different camber and at different toe angles increases the usefulness of the model. The presented FVM model can assist in determining the basic turbine geometry and operating conditions at which the maximum power can be extracted for a given configuration at low chord-to-radius ratios. Improved torque and power coefficient calculations compared to previous FVM models have been obtained. Acceptable power coefficient predictions were obtained at higher chord-to-radius ratios. However, further improvements, such as the consideration of added mass, are needed in order for the model to provide accurate calculations of the torque at higher chord-to-radius ratios. Additionally, the analytical model has approximately predicted at which toe angle the maximum power coefficient can be found for different chord-to-radius ratios. This design information on the turbine parameters could serve as the basis for higher computational cost methods, such as CFD and lifting surface FVM, to determine the final design of the blade and analyze the resulting performance of the turbine.

CHAPTER 5

CONCLUDING REMARKS

An analytical model for calculating the hydrodynamic performance of cross flow turbines has been presented. This analytical model has been compared to experimental data for different conditions of number of blades, chord-to-radius ratios and toe angles. The model presented was able to produce improved hydrodynamic predictions compared to those made by previous FVM models at low chord-to-radius ratios.

One of the challenges to improving the hydrodynamic predictions is that limited experimental lift and drag data exists for a wide range of Reynolds numbers of blades at high angles of attack, and for different camber conditions. As has been discussed in this work, all this experimental data is needed if phenomena such as dynamic stall, flow curvature and cyclic Reynolds number are to be incorporated in analytical FVM and BEM models. In particular, in order for an analytical model to predict the toe angle at which the blades are to be positioned to produce the maximum power coefficient, flow curvature is needs to be considered. In order to implement a flow curvature correction in an analytical model, experimental data at different camber is needed. In addition, if the cyclic Reynolds number is to be included in the analytical model of a cross flow turbine with one profile, this will require an extensive experimental data set for a blade profile family.

Although analytical codes, such as X-Foil (Drela, 1989), that can predict the blade forces at the conditions that cross flow turbines operate exists, they have higher computational costs than the semi-empirical blade forces model presented in this work. The semi empirical blade forces model was derived using conformal mapping solutions for one blade. This blade forces model can provide predictions at a large range of angles of attack, different camber conditions and Reynolds numbers (Figure 5.1). The blade forces model was design to easily incorporate dynamic stall phenomena. However, there are areas in which the blade forces model can be improved to provide better predictions. New relationships that consider the influence of varying Reynolds number on the separation point function should be explored. Another area that should be explored is to expand the blade model and dynamic stall model for considering separation conditions such as bubble and trailing edge separations.

Future development of the analytical model should focus on improving the representation of the flow field around the blades, which would correctly calculate the vortex-particles trajectory in the blade vicinities. A single-element blade model with a prescribed circulation distribution would be worth pursuing to improve the predictions for cross-flow turbines especially for high chord to radius ratios. This modification will allow the model to more closely represent the induced velocities especially near the leading edge and the blockage due to the blade (Figure 5.2).

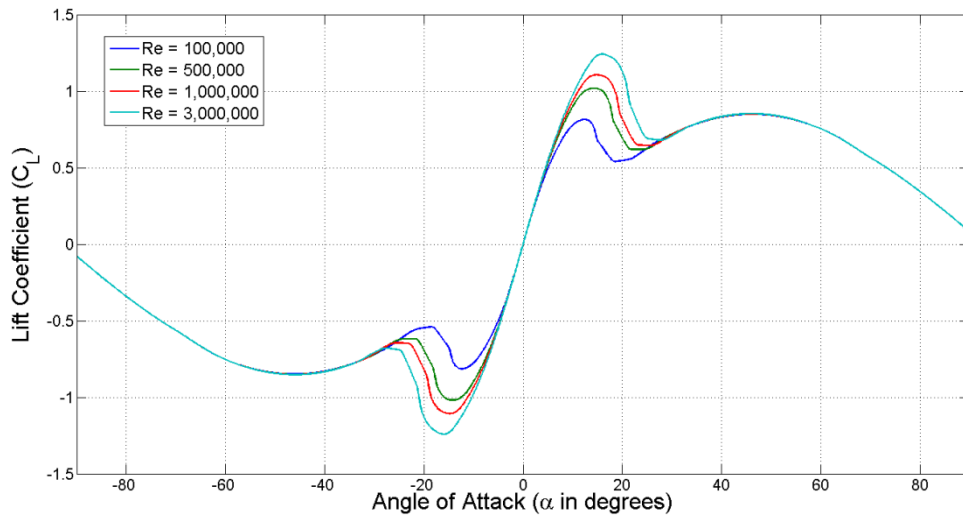


Figure 5.1. The calculated lift coefficient is shown as a function angle of attack for different Reynolds numbers

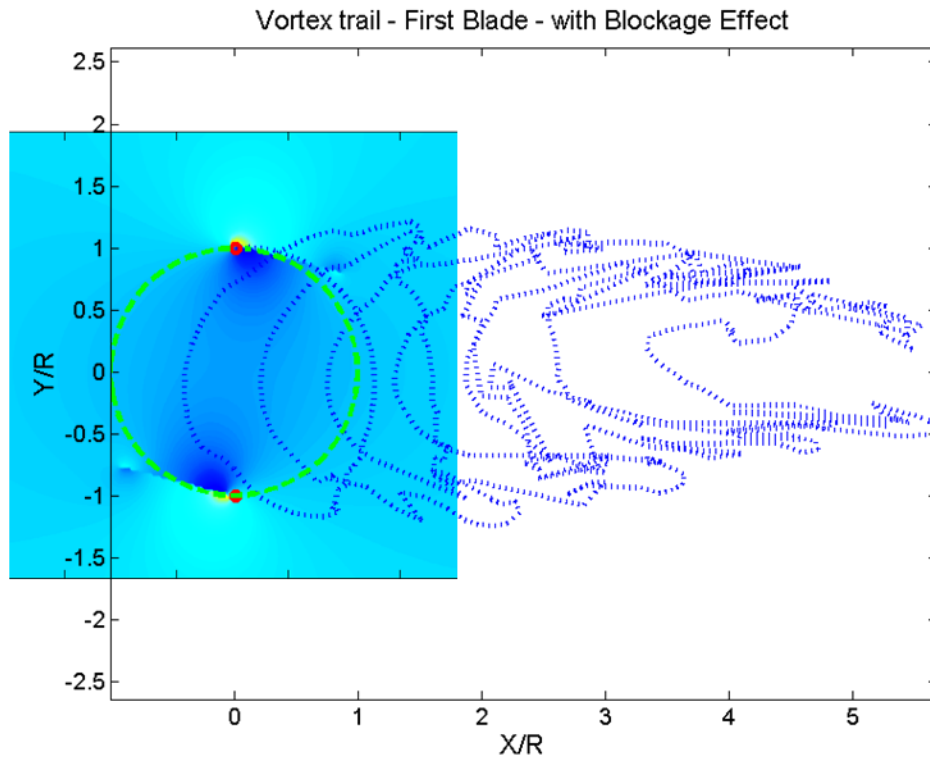


Figure 5.2 The superimposed velocity profiles of two blades using single element vortex distribution with prescribed vorticity are shown.

One of the disadvantages of lifting line methods is that they cannot produce information on the pressure distribution around the blade. The pressure distribution is needed to optimize the shape of the blade. As further work, it would be advisable to incorporate elements of panel methods in the analytical model that could provide information on the pressure distribution. In particular, panel methods that use separation point modeling (Katz & Plotkin, 2001) seem to be suitable, since the computational cost associated with them are less than those of the panel methods using cloud vortices. The panel methods that use separation point modeling functions could complement the analytical method by using functions such as the separation point function. Additionally, a blade forces model that takes into account the effect of the boundary layer may be advisable to provide better predictions at the maximum lift. Similar methods have been used to simulate vertical axis wind turbines (Zanon et al, 2012)

This work also provides experimental data for analytical code validation. This data has been used to assess the hydrodynamic performance predictions at extreme conditions. This combined approach lets us create a hypothesis of the results of this study. As an example, the experimental data shows that higher power coefficient can be acquired when the blades are mounted at certain toe angles, which the analytical code suggests may be related to the flow curvature effect. Also, the experimental data results show that higher power coefficients are found using two blades. The analytical model shows that using two blades

allow for time for the blades to encounter lower induced velocities due to the wake. Another result from the experimental data is that higher power coefficients can be acquired when using lower chord-to-radius ratios, which might not be intuitive. This result is important since using lower chord-to-radius ratio blades allow for less material to be used as well as produce lower peak torque, while still allowing for the turbine to operate at relative low tip speed ratios.

The presented analytical model has been designed to consider the main phenomena that affect cross flow turbines and has improved the predictions at low chord-to-radius ratios. The presented analytical model may be able to be incorporated in optimization schemes to provide broad design parameters for the turbine, such as the optimum toe angle and camber. The analytical model can also provide basic information of the scaling effects that can affect the turbine design. In addition, its different components, such as the blade forces model, can be incorporated in existing methods to analyze other tidal turbines such as axial flow turbines.

BIBLIOGRAPHY

- Abbott, H., & von Doenhoff, A. E. (1959). *Theory of wing sections, including a summary of airfoil data*. New York: Dover Publications.
- Asher, I., Drela, M., & Peraire, J. (2010). A Low Order Model for Vertical Axis Wind Turbines. *28th AIAA Applied Aerodynamics Conference*. Chicago.
- Berg, D. E. (1996). *Vertical-Axis Wind Turbines-The Current Status of an Old Technology*. Albuquerque: Sandia National Laboratories.
- Brito, A., & Huckerby, J. (2010). *Annual Report 2010 Implementing Agreement on Ocean Energy Systems*. International Energy Agency.
- Carbon Trust (2007). *Turning the Tide, Tidal Power in the UK*. Sustainable Development Commission.
- Cardona, J. L. (1984). Flow Curvature and dynamic stall simulated with an aerodynamic free-vortex model for VAWT. *Wind Engineering* , 8 (3), 135-143.
- Chang, P. K. (1970). *Separation of flow*, 1st ed. Oxford: Pergamon Press.
- Coney, W. B. (1989). A Method for the Design of a Class of Optimum Marine Propulsors. *Ph. Dissertation* . Cambridge, Massachusetts: Massachusetts Institute of Technology.
- Dadswell, M. J., Rulifson, R. A., & Daborn, G. R. (1986). Potential Impact of Large-Scale Tidal Power Developments in the Upper Bay of Fundy and Fisheries Resources of the Northwest Atlantic. *Fisheries* , 11 (4), 26-35.
- deBree, G.S., (2012). *Testing and Modeling of High Solidity Cross-Flow Tidal Turbines*, Master's Thesis, University of Maine, Orono, Maine
- Drela, M. (1989). XFOIL: An Analysis and Design System for Low Reynolds Number Airfoils. *Conference on Low Reynolds Number Airfoil Aerodynamics*. University of Notre Dame.
- Hoerner, S. F. (1965). *Fluid Dynamics Drag*. New Jersey: Midland Park.
- Hoerner, S. F., & Borst, H. V. (1975). *Fluid Dynamic Lift*. New Jersey: Hoerner Fluid Dynamics.
- Jacobs, E.N., Ward, .K. E., Pinkerton, R.M., (1935) *The characteristics of 78 related airfoil sections from tests in the variable-density wind tunnel*, National Advisory Committee for Aeronautics, Report No. 460.

- Katz, J. (1981). A discrete vortex method for the non-steady separated flow over an airfoil. *Journal of Fluid Mechanics* , 315-328.
- Katz, J., Plotkin, A., (2001). *Low-Speed Aerodynamics*, Second Edition, Cambridge University Press, New York.
- Khan, M. J., Bhuyan, G., Iqbal, M. T., & Quaicoe, J. E. (2009). Hydrokinetic energy conversion systems and assesment of horizontal and vertical axis turbines for river and tidal applications: A technology status review. *Applied Energy* , 86, 1823-1835.
- Krenk, S. (2006). *Airfoil theory of separation flow*, Department of Mechanical Engineering, Technical University of Denmark, to be published.
- Korotkov, O. Y., & Shumskii, G. (2000). Calculation of Dynamic Stall on an Oscillating Airfoil. *Juournal of Applied Mechanics and Technical Physics* .
- Leishman, J. G., & Beddoes, T. S. (1989). A Semi-Empirical Model for Dynamic Stall. *Journal of the American Helicopter Society* , 34, 3-17.
- Lewis, R. I. (1991). *Vortex Element Methods for Fluid Dynamic Analysis of Engineering Systems*. Cambridge: Cambridge University Press.
- Li, Y., & Çalısıl, S. M. (2010), A discrete vortex method for simulating a stand-alone tidal-current turbine: modeling and validation, *Journal of Offshore Mechanics and Arctic Engineering*, 132(3), 031102.
- Li, Y. (2008). Development of a Procedure for Predicting Power Generated from a Tidal Current Turbine Farm. *Ph. Dissertation* . Vancouver: University of British Columbia.
- Li, Y., Calısıl, S. M. (2010b), Three-dimensional effects and arm effects on modeling a vertical axis tidal current turbine, *Renewable energy*, 35 (10), 2325-2334
- Masson, C., Leclerc, C., & Paraschivoiu, I. (1998). Appropriate Dynamic-Stall Models for Performance Predictions of VAWTs with NLF Blades. *International Journal of Rotatory Machinery* , 4 (2), 129-139.
- Matlab (2014). *Search R2014a Documentation*. Retrieved from: <http://www.mathworks.com/help/signal/ref/filtfilt.html>
- Migliore, P. G., & Wolfe, W. P. (1980). *The effects of Flow Curvature on the Aerodynamics of Darrieus WInd Turbines*. Report No TR.60, West Virginia University, Morgantown.

- Migliore, P. G., Wolfe, W. P., & Fanucci, J. B. (1980). Flow Curvature Effects on Darrieus Turbine Blade Aerodynamics. *Journal of Energy* , 4 (2), 49-55.
- Montgomerie, B. (2004). *Method for Root Effects, Tip Effects and Extending the Angle of Attack Range to plus minus 180 degrees, with Application to Aerodynamics*. Swedish Defense Research Agency, Stockholm.
- Murray, J.C., Barone, M., (2011). *The development of CACTUS, a wind and marine turbine performance simulation code*, 49th AIAA Aerospace Sciences Meeting, January 4-7, Orlando, Florida
- Nabavi, Y., (2008). *Numerical study of the duct shape effect on the performance of a ducted vertical axis tidal turbine*, Master's thesis, University of British Columbia, Vancouver.
- Paraschivoiu, I. (2002). *Wind Turbine with Emphasis on Darrieus Concept*. Montreal: Presses Internationales Polytechnique.
- Plesset, M.S., Shaffer Jr., P.A. (1948). Drag in Cavitating Flow, *Reviews of Modern Physics*, Vol. 20, No. 1.
- Polagye, B., Van Cleve, B., Copping, A., & Kinkerdall, K. (2011). *Environmental Effects of Tidal Energy Development*. U.S. Dept. Commerce.
- Pope, A. (1984). *Low-speed wind tunnel testing*. New York: Wiley.
- Rawlings, G. W., (2008). *Parametric characterization of an experimental vertical axis hydro turbine*, Master's thesis, University of British Columbia, 2008
- Saffman, P. G. (1992). *Vortex Dynamics*. New York: Cambridge University Press.
- Sale, D., Jonkman, J., & Musial, W. (2009). *Hydrodynamic Optimization Method and Design Code for Stall-Regulated Hydrokinetic Turbine Rotors*. Golden, Colorado: Sandia National Laboratories.
- Schlichting, H., & Gersten, K. (1979). *Boundary Layer Theory*. New York: McGraw Hill.
- Sheng, W., Galbraith, R. A., & Coton, F. (2010). Applications of Low-Speed Dynamic-Stall Model to the NREL Airfoils. *Journal of Solar Energy Engineering* , 132, 011006 1-8.
- Sheng, W., Galbraith, R. A., & Coton, F. N. (2008). A Modified Dynamic Stall Model for Low Mach Numbers. *Journal of Solar Energy Engineering* , 130, 031013-1-10.

- Shiono, M., Suzuki, K., & Kiho, S. (2000). An Experimental Study of the Characteristics of a Darrieus Turbine for Tidal Power Generation. *Electrical Engineering in Japan* , 132 (3), 38-47.
- Simao Ferreira, C. J., van Zuijlen, A., Bijl, H., van Bussel, G., & van Kuik, G. (2009). Simulating Dynamic Stall in a Two-dimensional Vertical-axis Turbine: Verification and Validation with Particle Image Velocimetry Data. *Wind Energy* , 13 (1), 1-17.
- Stratford, B. (1959). The prediction of separation of the turbulent boundary layer. *Journal of Fluid Mechanics* , 1-16.
- Strickland, J. H. (1975). *The Darrieus Turbine: A Performance Prediction Model Using Multiple Streamtubes*. Albuquerque: Sandia Laboratories.
- Strickland, J. H., Webster, B. T., & Nguyen, T. (1980). *A Vortex Model of the Darrieus Turbine: An Analytical and Experimental Study*. Albuquerque: Sandia National Laboratories.
- Swanger, M.C., (2013). *Design, Optimization, and Testing of a Cross-Flow Tidal Turbine*, Master's Thesis, University of Maine, Orono, Maine
- Thwaites, B. (1960). *Incompressible Aerodynamics, An Account of the Theory and Observation of the Steady Flow of Incompressible Fluid past Aerofoils, Wings, and Other Bodies*. Oxfordshire: Clarendon Press.
- Urbina, R., Peterson, M.L., Kimball, R.W., deBree, G.S., Cameron, M.P., (2013). Modeling and validation of a cross flow turbine using free vortex model and a modified dynamic stall model, *Renewable Energy* Vol. 50, pp 662-669.
- Zanon, A., Giannattasio, P., Simao Ferreira, C.J., (2012), A vortex panel model for the simulation of the wake flow past a vertical axis wind turbine in dynamic stall, *Wind Energy*, 16(5), pp. 661-680, doi: 10.1002/we.1515

APPENDICES

APPENDIX A: MAIN MATLAB PROGRAM ROUTINES

```

function
[alpha,alpha_p,Ur,Gamma,Lift,Drag,CN,CC,CN_T,CC_T,rpr,f,f_p]=M2_CalG_3_
Jun30(Tur_radius,
In_Flow,alpha1,alpha_p1,f1,f_p1,V,c,iter,Delta_t,toe_angle,camber)

%%%%%%%%%%%%%%%%%%%%%%%%%%%%%%%%%%%%%%%%%%%%%%%%%%%%%%%%%%%%%%%%%%%%%%%%
%
% Calculate the relative velocity, angle of attack and forces over the
% blade
%
% University of Maine, Mechanical Engineering, Raul Urbina 2013
%
%%%%%%%%%%%%%%%%%%%%%%%%%%%%%%%%%%%%%%%%%%%%%%%%%%%%%%%%%%%%%%%%%%%%%%%%

% Assign normalized flow velocity
Ur=V;
% Assign new value of angle of attack
alpha=alpha1(iter);
% Assign new value of delayed angle of attack
alpha_p1(iter)=alpha1(iter);

% Calculate auxiliary angle of attack terms (Not needed in
calculations)
alpha_aux = alpha1 *180 / pi-toe_angle;
alpha_p_aux = alpha_p1 *180 / pi-toe_angle;

% Assign separation function value
f_aux = f1;
% Assign delayed separation function value
f_p_aux=f_p1;

% Calculate forces
[Lift,Drag,CN_T,CC_T,rpr,alpha_p,f,f_p]=BD_DynStall_June30(Tur_radius,
In_Flow,
alpha_aux,alpha_p_aux,f_aux,f_p_aux,c,V,Delta_t,iter,toe_angle,camber);

% Calculates angle of attack without toe angle (Not needed in
calculations)
alpha_p=(alpha_p+toe_angle)*pi/180;

% Calculate lift coefficient
CL=Lift;

% Calculate induced circulation
Gamma=Ur*CL*c/2;

% Calculate forces
CN = Lift*cos(alpha)+Drag*sin(alpha);
CC = Lift*sin(alpha)-Drag*cos(alpha);

```

```

function
[CL,CD,CN,CC,rpr,alpha_p1,f1,f_p1]=BD_DynStall_June30(Tur_radius,
In_Flow, alpha,alpha_p,f,f_p,c,V,Delta_t,i,toe_angle,camber)

%%%%%%%%%%%%%%%%%%%%%%%%%%%%%%%%%%%%%%%%%%%%%%%%%%%%%%%%%%%%%%%%%%%%%%%%
%
% This function calculates the blade force coefficients taken into
% account the dynamic stall phenomena. It uses a modified Beddoes -
% Lieshmann model
% University of Maine, Mechanical Engineering, Raul Urbina 2013
%
%%%%%%%%%%%%%%%%%%%%%%%%%%%%%%%%%%%%%%%%%%%%%%%%%%%%%%%%%%%%%%%%%%%%%%%%

%% Variables
% Delay on angle of attack
T_alpha=2.4;
% Delay on separation point
T_v=0.1;

% Camber
f_c=real(camber);
% Lift at 90 degrees
RL90=0.08;

%visc
visc=1e-6;

%
alpha_0=0;

%%%%%%%%%%%%%%%%%%%%%%%%%%%%%%%%%%%%%%%%%%%%%%%%%%%%%%%%%%%%%%%%%%%%%%%%
%%
%% Calculation
% Calculation of the Reynolds Effect
[alpha1,CD0,~]=M2_Reynolds_Effect(V,c,Tur_radius,In_Flow,visc);

% Calculates Reduced pitch rate and delayed angle of attack
[alpha_p1,~,rpr]=M2_Delay_RPR(alpha,alpha_p,i,V,Delta_t,c,T_alpha);

% Estimates separation point
[f1,~,~]=M2_Alpha_RPR(alpha1,alpha1,alpha_p1,rpr);

% Assigns separation point function to array
f(i)=f1;

% Calculates delayed angle of attack
[f_p1]=M2_Delay_Separation(f,f_p,i,V,Delta_t,c,T_v);

% Calculate blade forces
[CL,CD,CN,CC,~,~]=BD_LiftDragModel_May30(alpha(i),alpha(i),alpha_0,f_p1
,f_c,RL90,CD0);

```

```

function
[alpha,CD0,NRe]=M2_Reynolds_Effect(V,c,Tur_radius,In_Flow,visc)

%%%%%%%%%%%%%%%%%%%%%%%%%%%%%%%%%%%%%%%%%%%%%%%%%%%%%%%%%%%%%%%%%%%%%%%%
%
% This function calculates calculates the angle of attack.
%
% University of Maine, Mechanical Engineering, Raul Urbina 2013
%
%%%%%%%%%%%%%%%%%%%%%%%%%%%%%%%%%%%%%%%%%%%%%%%%%%%%%%%%%%%%%%%%%%%%%%%%

%%%%%%%%%%%%%%%%%%%%%%%%%%%%%%%%%%%%%%%%%%%%%%%%%%%%%%%%%%%%%%%%%%%%%%%%
%% Input variable for the Airfoil Model

%%%%%%%%%%%%%%%%%%%%%%%%%%%%%%%%%%%%%%%%%%%%%%%%%%%%%%%%%%%%%%%%%%%%%%%%
%% Naca 0018

% Angle Delay
%T_alpha=6.22*0.5;

%%%%%%%%%%%%%%%%%%%%%%%%%%%%%%%%%%%%%%%%%%%%%%%%%%%%%%%%%%%%%%%%%%%%%%%%
%%
% Normalized viscosity
N_viscosity=visc/(Tur_radius*In_Flow);

%%%%%%%%%%%%%%%%%%%%%%%%%%%%%%%%%%%%%%%%%%%%%%%%%%%%%%%%%%%%%%%%%%%%%%%%
%%

% Calculate Reynolds number
NRe=abs(V*c/N_viscosity);

% If the Reynolds number is small assigns Re=100
if(NRe<100)
    NRe = 100;
end

% Calculates Frictional Drag
CD0 = 2*0.523./(log(0.06*NRe)).^2;

```

```

%%%%%%%%%%%%%%%%%%%%%%%%%%%%%%%%%%%%%%%%%%%%%%%%%%%%%%%%%%%%%%%%%%%%%%%%
%%
%% Reynolds number effect evaluation
pp_f.form='pp';
pp_f.breaks=log([100 1000 20000 40000 80000 160000 360000 700000
1000000 2000000 5000000]);
pp_f.pieces=10;
pp_f.order=4;
pp_f.dim=1;
% Coefficients the angle of attack at which the blade stalls
pp_f.coefs=[ -0.0031    0.0260        0    0.1000
              0.0163    0.0001    0.0703    0.2000
             -8.3406   11.5005    0.5110    0.8510
             -2.8326    1.9026    4.4323    3.9530
              1.2232   -1.8916    2.9870    6.9960
              0.0635   -0.2074    2.1279    8.5650
              0.2658   -0.2866    1.9167   10.1880
             -0.7670    0.3800    1.8882   11.4140
              0.0187   -0.1124    1.8665   12.1010
             -0.0092   -0.0585    1.7376   13.3470];

% Cubic spline evaluation
re_shift=14.68-ppval(pp_f,log(NRe));

% Static Stall point angle
alpha1=14.68-re_shift;

```

```

function
[alpha_pm,delta_alpham,rm]=M2_Delay_RPR(alpha,alpha_p,i,V,delta_t,c,T_alpha)

%%%%%%%%%%%%%%%%%%%%%%%%%%%%%%%%%%%%%%%%%%%%%%%%%%%%%%%%%%%%%%%%%%%%%%%%
%
% This function calculates the reduced pitch rate and the delayed
% angle attack account the dynamic stall phenomena. It uses a modified
% Beddoes - Liesmann model
%
% University of Maine, Mechanical Engineering, Raul Urbina 2013
%
%%%%%%%%%%%%%%%%%%%%%%%%%%%%%%%%%%%%%%%%%%%%%%%%%%%%%%%%%%%%%%%%%%%%%%%%
%%%%

%% Main Routine
delta_alpha=zeros(1,i);

% Calculates Delayed Angle of Attack and Reduced Pitch Rate
%alpha_m(i)=alpha(i);
% Step 1
if (i==1)
    % delta_alpha(1)=0;
    alpha_p(1)=alpha(1);
    r(1)=0;

    % Steps 2 to 4
elseif ((i>1)&&(i<4))
    % Reduced pitch rate
    if (abs(alpha(i)-alpha_p(i-1))<=abs(360+alpha(i)-alpha_p(i-1)))
        delta_alpha(i)=(alpha(i)-alpha_p(i-1))*(1-exp(-
2*V*delta_t/c/T_alpha));
        % Delay
        alpha_p(i)=alpha_p(i-1)+delta_alpha(i);
        % Calculation of modified on set criteria
        r(i)=(alpha(i)-alpha(i-1))*c/(delta_t*2*V)*pi/180;

    else
        delta_alpha(i)=(360+alpha(i)-alpha_p(i-1))*(1-exp(-
2*V*delta_t/c/T_alpha));
        % Delay
        alpha_p(i)=alpha_p(i-1)+delta_alpha(i);
        % Calculation of modified on set criteria
        r(i)=(alpha(i)-alpha(i-1))*c/(delta_t*2*V)*pi/180;
    end
else
    % Steps 5 to higher
    % Reduced pitch rate
    if (abs(alpha(i)-alpha_p(i-1))<=abs(360+alpha(i)-alpha_p(i-1)))
        delta_alpha(i)=(alpha(i)-alpha_p(i-1))*(1-exp(-
2*V*delta_t/c/T_alpha));
        % Delay
        alpha_p(i)=alpha_p(i-1)+delta_alpha(i);
        % Calculation of modified on set criteria
        r(i)=(alpha(i)*11-alpha(i-1)*18+alpha(i-2)*9-alpha(i-
3)*2)/12*c/(delta_t*2*V)*pi/180;
    end
end

```

```

else
    delta_alpha(i)=(360+alpha(i)-alpha_p(i-1))*(1-exp(-
2*V*delta_t/c/T_alpha));
    % Delay
    alpha_p(i)=alpha_p(i-1)+delta_alpha(i);
    % Calculation of modified on set criteria
    rcal_1=(alpha(i)-alpha(i-1))*c/(delta_t*2*V)*pi/180;
    rcal_2=(alpha(i)+360-alpha(i-1))*c/(delta_t*2*V)*pi/180;
    if (abs(rcal_1)<=abs(rcal_2))
        r(i)=rcal_1;
    else
        r(i)=rcal_2;
    end

end

end

% Angle of Attack shift
if (alpha_p(i)>180)
    alpha_p(i)=alpha_p(i)-360;
end

% Assign variables
alpha_pm=alpha_p(i);
delta_alpham=delta_alpha(i);
rm=r(i);

```



```

function
[f,delta_alpha_n,delta_alpha_p]=M2_Alpha_RPR(alpha_ss,alpha1,alpha_p,rp
r)

%%%%%%%%%%%%%%%%%%%%%%%%%%%%%%%%%%%%%%%%%%%%%%%%%%%%%%%%%%%%%%%%%%%%%%%%
%
% This function calculates the separation point function using a
%
% modified Sheng method
%
% University of Maine, Mechanical Engineering, Raul Urbina 2011
%
%%%%%%%%%%%%%%%%%%%%%%%%%%%%%%%%%%%%%%%%%%%%%%%%%%%%%%%%%%%%%%%%%%%%%%%%

% Assigns second variable of angle of stall
alpha_ss2=1.25*alpha_ss;

% New calculation using smoother curves
if (rpr<0)
    delta_alpha_p=(alpha_ss)*(exp(35*rpr)-1);
    delta_alpha_n=alpha_ss2*(1-exp(35*rpr));
else
    delta_alpha_p=alpha_ss2*(1-exp(-35*rpr));
    delta_alpha_n=(alpha_ss)*(exp(-35*rpr)-1);
end

%%%%%%%%%%%%%%%%%%%%%%%%%%%%%%%%%%%%%%%%%%%%%%%%%%%%%%%%%%%%%%%%%%%%%%%%
%%
%% Calculates the separation point function using the static angle of
attack
alpha_fn=alpha1+delta_alpha_n;
alpha_fp=alpha1+delta_alpha_p;

    al_pchip=[-90   -70           -60           -20.0-alpha_fn   ...
              -12.5-alpha_fn -9.0-alpha_fn  -5.0-alpha_fn   ...
              -4.50-alpha_fn -3.0-alpha_fn  -alpha_fn
(alpha_fp-alpha_fn)*0.25   ...
              alpha_fp       3.0+alpha_fp   4.50+alpha_fp   ...
              5.0+alpha_fp   9.0+alpha_fp   12.5+alpha_fp   ...
              20+alpha_fp    60            70            90];
    f_pchip =[0      0.0001      0.0015      0.0035      ...
              0.0025      0.01       0.1        0.95
...
              0.6         0.4         0.2         ...
              0.1         0.01       0.0025     ...
              0.0035     0.0015     0.0001     0];

f=pchip(al_pchip,f_pchip,alpha_p);

```

```

function [f_p1]=M2_Delay_Separation(f,f_p,i,V,delta_t,c,T_v)

%%%%%%%%%%%%%%%%%%%%%%%%%%%%%%%%%%%%%%%%%%%%%%%%%%%%%%%%%%%%%%%%%%%%%%%%
%
% This function calculates a delayed separation point for normal force
%
% University of Maine, Mechanical Engineering, Raul Urbina 2013
%
%%%%%%%%%%%%%%%%%%%%%%%%%%%%%%%%%%%%%%%%%%%%%%%%%%%%%%%%%%%%%%%%%%%%%%%%

% Assign maximum separation point displacement
delta_f_max=2.2;

if (i==1)
    % delta_f(1)=0;
    f_p(1)=f(1);
else
    % Delay for separation point function in normal force
evaluation
    delta_f(i)=(f(i)-f_p(i-1))*(1-exp(-2*V*delta_t/c/T_v));

    % if displacement is very large assign maximum displacement
    if abs(delta_f(i)/delta_t)>delta_f_max
        delta_f(i)=sign(delta_f(i))*delta_f_max*delta_t;
    end
    % Delay
    f_p(i)=f_p(i-1)+delta_f(i);
end

% Assign variable
f_p1=f_p(i);

```

APPENDIX B:

EXPERIMENTAL RESULTS FOR CHAPTER 3

The maximum power coefficient was found when using a two bladed cross two turbine with two inch chord NACA 63-3-018 blades for a toe angle of +5, Figure 3. The test was repeated and there was good agreement between the two tests at a toe angle of +5.

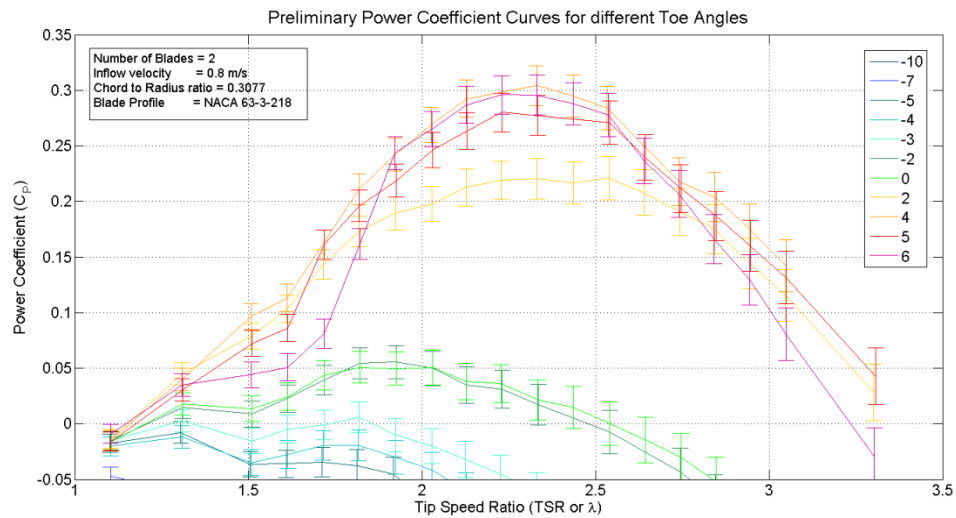


Figure B.1. Power coefficient measured at different toe angles for a two bladed cross flow turbine with two inch chord blade and NACA 63-3-218 profile.

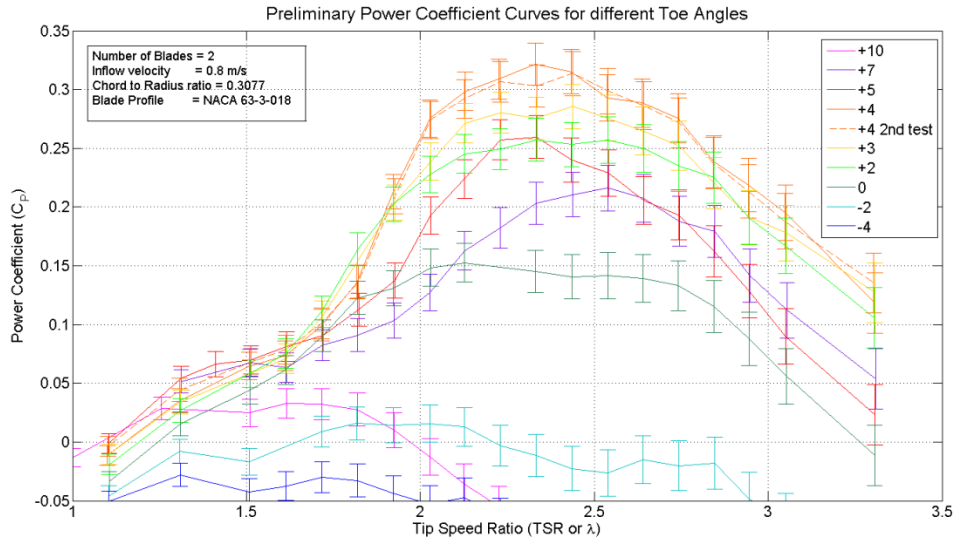


Figure B.2. Power coefficient measured at different toe angles for a two bladed cross flow turbine with two inch chord blade and NACA 63-3-018 profile.

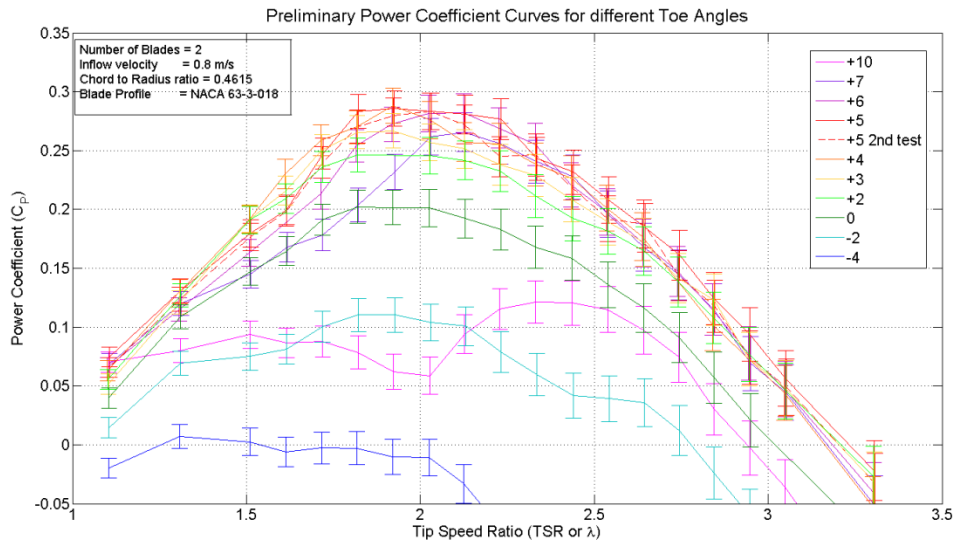


Figure B.3. Power coefficient measured at different toe angles for a two bladed cross flow turbine with three inch chord blade and NACA 63-3-018 profile.

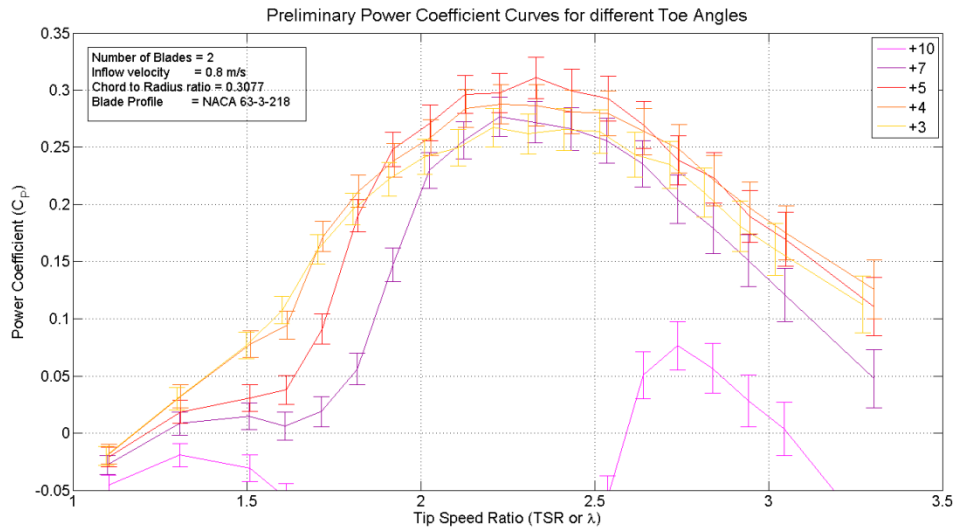


Figure B.4. Power coefficient measured at different toe angles for a two bladed cross flow turbine with two inch chord blade and NACA 63-3-218 profile (second set of tests).

BIOGRAPHY OF THE AUTHOR

Raul Urbina Villalpando was born in Mexico City, Mexico on January 08,1974. He was raised in Mexico City and graduated from Colegio Columbia in 1992. He attended Universidad Panamericana and graduated in 1997 with a Bachelor's degree in Mechanical Engineering. He entered the Mechanical Engineering graduate program at The University of Maine in the fall of 2000. After receiving his degree, Raul returned to Mexico and joined Bently Nevada-GE Energy, in the technical sales department. He entered the Mechanical Engineering doctoral program at the University of Maine in 2008. Raul is a candidate for the Doctor of Philosophy degree in Mechanical Engineering from The University of Maine in May, 2014 .

Appendix Task 4-1

Estuaries and Coasts Journal of the Coastal and Estuarine Research Federation© Coastal and Estuarine Research Federation 201310.1007/s12237-013-9703-3

Tidal Power Development in Maine: Stakeholder Identification and Perceptions of Engagement

Teresa R. Johnson¹, Jessica S. Jansujwicz² and Gayle Zydlewski¹

(1)

School of Marine Sciences, University of Maine, 200 Libby Hall, Orono, ME 04469, USA

(2)

Sustainability Solutions Initiative, University of Maine, 5710 Norman Smith Hall, Orono, ME 04469, USA

Teresa R. Johnson

Email: teresa.johnson@maine.edu

Received: 9 July 2012 Revised: 18 July 2013 Accepted: 21 August 2013 Published online: 14 September 2013

Communicated by Iris C. Anderson

Abstract

Development of renewable energy affects or is affected by numerous stakeholders. Understanding who the stakeholders are and how they are engaged in the process is necessary for improving the responsible development of renewable energy technologies. Using structured community interviews and in-depth ethnographic research (semi-structured interviews, informal interviews, observations, and document review), we identified and characterized the most salient stakeholders associated with tidal power development in Maine and documented stakeholder perceptions of developer engagement strategies. Stakeholder characterization was facilitated using a framework by Mitchell et al. (The Academy of Management Review 22:853–886, [1997](#)) that characterizes salient stakeholders using attributes of power, urgency, and legitimacy. Key stakeholders identified include fishermen, community members, tribes, regulators, developers, and scientists. Fishermen and regulators are definitive stakeholders, with legitimacy, power, and urgency in the process. Tribes are considered dominant stakeholders; they have legitimacy and power, but their interests are, at this time, not viewed as urgent. Scientists are considered to have urgency and power. The developers viewed their stakeholder engagement strategy as open and transparent. Community stakeholders, regulators, and fishermen generally perceived the developer's approach as effective; they noted the company's accessibility and their efforts to engage stakeholders early and often. Given the dynamic nature of stakeholder salience, our findings highlight the importance of

engaging dominant stakeholders so that future conflict can be more easily avoided as new information develops. Our approach can be used to inform stakeholder identification and engagement research in other renewable energy contexts.

Keywords

Renewable energy Tidal power Stakeholder engagement Stakeholder identification
Public perception

Introduction

From mitigating climate change to improving national security and providing economic stability, renewable energy is viewed as a solution to some of our most challenging social and environmental problems (El Bassam [2001](#); Elliott [2000](#)). Development of renewable energy, however, is a complex process that affects or is affected by numerous individuals, groups, and organizations. Understanding who may be affected, how they are affected, and how they are (or would like to be) engaged in the decision-making process is critically important to move renewable energy development forward in a socially and environmentally responsible manner. Attention to interested parties or stakeholders is needed to assess and enhance political feasibility (Meltsner [1972](#); Eden and Ackermann [1998](#); van Horn et al. [2001](#)), understand public attitudes (Portman [2009](#); Reddy and Painuly [2004](#); West et al. [2010](#); Devine-Wright [2005](#); Firestone and Kempton [2007](#); Firestone et al. [2009](#); Kempton et al. [2005](#)), and design more effective stakeholder processes (Hindmarsh and Mathews [2008](#); Conway et al. [2010](#)).

Opportunities for stakeholder input are considered critical in not-in-my-backyard arenas, like renewable energy (Conway et al. [2010](#); Portman [2009](#)). As Adams et al. ([2011](#)) argue, a fundamental transformation in energy strategies away from dependence on imported, nonrenewable fuels to adoption of strategies such as renewable energy development is unlikely to occur without a high level of stakeholder engagement. Stakeholder participation is distinguished from broader public participation and is defined as a process where individuals, groups, and organizations choose to take an active role in decisions that affect them (Reed [2008](#)). There are many claimed benefits of stakeholder participation in environmental decision-making (Reed [2008](#)), including developing trust (Richards et al. [2004](#)) and acceptability (Breukers and Wolsink [2007](#)); improving transparency, accountability, and understanding (Zoellner et al. [2008](#); Agterbosch et al. [2009](#)); and enhancing the quality and durability of decisions (Reed [2008](#); Breukers and Wolsink [2007](#)). It is thought that if people feel left out of the planning process and decision-making, they will be more likely to oppose the process outcome (Zoellner et al. [2008](#)). It is also claimed that stakeholder participation promotes social learning (Blackstock et al. [2007](#)) and increases the likelihood that local needs and priorities are successfully met in the decision-making process. Engaging stakeholders may serve to broaden the number of dimensions considered for problem solving (Holmes and Scoones [2000](#)) and, in particular, may allow for nontechnical information provided by nonscientists to enter the decision-making process (Glicken [2000](#)).

In practice, however, stakeholder participation may not be meeting these idealized claims (Reed [2008](#)). Integrating input from numerous and diverse stakeholders into on-going decision-making processes is a significant challenge (Glicken [2000](#)), and more effective stakeholder participation will require an improved understanding of how to engage

relevant stakeholders at the most appropriate time and in a manner that will enable them to fairly and effectively shape decisions (Reed [2008](#)).

The first step in designing more effective stakeholder engagement processes is identifying and characterizing stakeholders (Reed et al. [2009](#)). Originating from the fields of organizational management and business ethics, a stakeholder is “any group or individual who can affect or is affected by the achievement of the organization's objectives” (Freeman [1984](#), p. 46). The term refers to persons, groups, or organizations that somehow must be taken into account by leaders and managers (Bryson [2004](#)).

Although the literature offers multiple definitions of stakeholder, one common feature of all definitions is that they identify and define groups related to a specific issue (Glicken [2000](#)). Deciding how to define stakeholders in a particular management context is consequential, as the decision affects who and what counts (Mitchell et al. [1997](#)). Taking stakeholders into account is a crucial aspect of problem solving (Bryson and Crosby [1992](#); Bardach [1998](#)), and stakeholder identification is relevant to planning for stakeholder participation (Bryson [2004](#)).

The literature is replete with approaches to facilitate stakeholder identification and characterization. For example, Newman and Lamming ([1995](#)) divide stakeholders into those who will use a system directly or indirectly and those who will be involved in developing the system. While these divisions may offer a useful starting point, as Sharp et al. ([1999](#)) note, the literature does not provide help in identifying stakeholders for a particular system or relevant to a particular project. Rather, they find that “approaches are criticized for either assuming that stakeholders are ‘obvious’ or for providing broad categories which are too generic to be of practical use (Sharp et al. [1999](#), p. 388).” Given the importance of the management context, structuring effective engagement requires a better understanding of the perspectives, concerns, and information needs of the different stakeholder groups that may affect or be affected by the decision-making process.

Choices of who to include, how, when, and why are related to the questions of effectiveness and to the value of that particular stakeholder's engagement (Bryson [2004](#)).

In this study, we draw on findings from ethnographic research to identify and characterize stakeholders relevant to a tidal energy project in Maine and to document perceptions of the developer's stakeholder engagement strategy. Our focus is on the development of renewable energy technologies, specifically marine hydrokinetic devices (MHK) that capture the kinetic energy of the water when placed in the free-flowing tidal stream (Charlier and Finkl [2010](#)). MHK devices represent a new generation of tidal energy technology and significant uncertainty remains about the impacts of these technologies on social and environmental systems (Gill [2005](#); Boehlert and Gill [2010](#); Polagye et al. [2011](#); Johnson et al. [2012](#)). Despite this uncertainty, interest in tidal power development is rapidly increasing (e.g., over 80 preliminary permits issues in the USA; FERC. <http://www.ferc.gov/industries/hydropower/gen-info/licensing/hydrokinetics.asp>), and decisions are currently being made about MHK development in multi-use coastal ecosystems. Tidal power development occurs in geographically restricted coastal areas, close to shore where interaction with other human uses is high. As a consequence, multiple stakeholders may affect or be affected by tidal power development decisions (Johnson and Zydlewski [2012](#)).

The Maine-based Ocean Renewable Power Company (ORPC) is currently developing two MHK sites in eastern Maine that are furthest along in development in the USA. In

this region, the tides rise and fall on average 7 m twice per day, and there is a history of attempts to harness power from these tides (Fig. 1). The efforts of ORPC have been praised as a model for stakeholder engagement in the arena of ocean energy development (Beard 2009). In Maine, the Governor's Ocean Energy Taskforce (OETF) concluded that, “Ocean energy developers will gain trust, understanding, and possible support, from a variety of local stakeholders by adopting the best practices in public engagement... demonstrated by the ORPC-Eastport example” (Ocean Energy Task Force OETF 2009). Early in the development process, ORPC held a series of public meetings in the community and met with local authorities and opinion leaders to discuss their development plans and receive feedback on issues such as the specific site for turbine deployment in Cobscook Bay. ORPC also initiated early consultation with federal and state agencies to kick off the regulatory and permitting process (Jansujwicz and Johnson 2013).

Fig. 1

Map of Cobscook Bay

Three key questions guided our inquiry of ORPC’s Cobscook Bay Tidal Energy Project: Who are the most salient stakeholders associated with tidal energy development? What kinds of engagement strategies are considered effective for these stakeholders? How can we use this information to inform future engagement strategies?

Conceptual Framework

We used a typology developed by Mitchell et al. (1997) to organize our research findings and characterize stakeholders related to tidal energy development. In their typology, Mitchell et al. (1997) define salience as “the degree to which managers give priority to competing stakeholder claims.” In this framework, categories of stakeholders can be identified based on their power, legitimacy, and urgency. Power is relational; it refers to the ability to bring about the outcomes one desires. Legitimacy refers to those that have a legal, moral, or presumed claim. Urgency refers to individuals or organizations that deserve immediate attention from the decision-makers. All of these attributes are variable and socially constructed. These attributes lend themselves to a stakeholder typology depending on which of the attributes exist. For example, stakeholder salience, where individuals are given priority over competing stakeholders' claims, is high where all three attributes exist (legitimacy, power, and urgency); these are the definitive stakeholders. Individuals or groups viewed as having power and legitimacy are considered dominant stakeholders. Those with legitimacy and urgency are dependent stakeholders. Those with only urgency and power are considered dangerous stakeholders. Discretionary stakeholders are those with only legitimacy. Dormant stakeholders are those with power, but lack legitimacy and urgency. Demanding stakeholders are those with urgency, but lack power and legitimacy. Those lacking any of these attributes are not considered stakeholders.

We applied the typology of Mitchell et al. (1997) to our case of tidal power development in Maine. Specifically, we use the classification system to categorize stakeholders identified in our social science research, although we recognize that the variable and

socially constructed nature of the attribute-based classification system means that this is only one of several possible interpretations. As Parent and Deephouse (2007) note, the Mitchell et al. (1997) framework has been widely cited, but empirical research using the framework has been limited. We find that most citations are drawn from fields of business management and ethics, and to our knowledge, the framework has not been used to inform stakeholder identification in the arena of renewable energy development, although it has been applied to fisheries management (Mikalsen and Jentoft 2001). Our study investigates the utility of using Mitchell et al.'s framework as a tool to inform stakeholder identification and engagement for the responsible development of tidal power. In the process, we offer an empirical analysis that uses the framework of Mitchell et al. (1997). In addition to using this framework as a tool for describing stakeholders (and for applying the theory of stakeholder salience to practice), we explore the utility of using the framework as a tool to inform engagement by identifying recommendations for including salient stakeholders in the decision-making process.

Methods

We used archival documents and our observations to determine three initial stakeholder groups: developers, regulators, and community members. We used a mixed methods approach, consisting of structured community interviews and in-depth ethnographic research (semi-structured interviews, focus groups, informal interviews, observations, and document review) to develop an initial overview of the setting for tidal energy development in the area of Cobscook Bay and to characterize those that may affect or be affected by the development process. We did not want to presume a priori all of the relevant stakeholders, but instead we wanted to identify these through our research. Below we describe our specific methods to further characterize the three broad categories of stakeholders and to document stakeholder engagement experiences.

Community

In order to identify community stakeholders and their concerns, we adopted a participatory approach and partnered with the Maine Sea Grant and University of Maine Cooperative Extension and the Cobscook Bay Resource Center. Maine Sea Grant and Cooperative Extension staff members are known for having high levels of trust and access in the communities in which they work. The Cobscook Bay Resource Center is a nongovernmental organization based in Eastport, Maine, that supports community-based approaches to resource management and sustainable development. The Resource Center had previously held tidal power meetings in the community to initiate discussions about tidal power among developers and community members. They also provide support to the Cobscook Bay Fishermen's Association, which represents many of the fishermen in the area.

With these partners, we identified a nonrandom probability sample of individuals representing a diversity of stakeholder groups in the community. This included fishermen, local businesses owners, municipal leaders, teachers, and tribal representatives. From April to December 2010, we administered a semi-structured survey to a total of 38 community members from our study area (hereafter referred to as community interviews). In addition to identifying the relevant stakeholders, we were particularly concerned with the community perceptions and experiences related to the

work of ORPC because the company is currently the furthest along in-stream MHK tidal project in the USA and because the State of Maine Governor's OETF identified it as a model for community engagement. The majority of the community interviews were not recorded, but detailed notes were taken. Those that were recorded were transcribed. In June 2012, we held three focus groups, two with fishermen (n = 9) and one with community members (n = 4) from the areas surrounding the proposed project. Two were held in Eastport and one was held in Lubec. Focus groups lasted about an hour each and followed a discussion guide. In particular, participants were asked about their perceptions of the Cobscook Bay project and about their engagement with the developers. We chose interview and focus group participants purposively through document analysis, network sampling, and our observations. All interviews and focus groups were audio-recorded and transcribed. Focus groups also served to groundtruth some of the findings from the community interviews. In addition to interviews and focus groups, we made observations throughout the research process at community meetings convened by scientists and developers and public meetings held by agency regulators as a part of the formal administrative process. These included two U.S. Coast Guard public meetings on the proposed navigation regulation for the Cobscook Bay project and two informal, public meetings where MHK scientists presented their work and sought input to the research from stakeholders. Detailed field notes were taken, and when possible, meetings were audio-recorded and transcribed.

Regulators and Developers

Methods for characterizing and documenting perceptions of noncommunity stakeholder groups were similar and overlapping. In order to better understand the role of regulators and developers, we conducted 12 semi-structured interviews with federal and state agency representatives and four developers. These interviews lasted between 1 and 2 h and followed a semi-structured interview guide. Interviews were recorded and transcribed.

In addition to the two informal, public meetings and two U.S. Coast Guard public meetings, we also attended four informal consultation meetings between ORPC and federal and state regulatory and resource agencies, and one offshore renewable energy industry technical meeting, where stakeholders were given the opportunity to identify themselves and express their concerns. Public meetings and agency consultations were audio-recorded and transcribed. At each meeting, we took detailed field notes and collected additional available information (e.g., reports, handouts, presentations, etc.). These materials supplemented our handwritten notes.

Data Analysis

We coded all responses to the community interviews and entered data into an Excel spreadsheet for analysis. We also entered data from the interviews with agencies and developers and observations of meetings into an NVivo 9.0 database for qualitative analysis. We coded interviews for emergent patterns and themes following a modified grounded theory approach (Glaser and Strauss [1967](#); Strauss and Corbin [1990](#)).

Results

Stakeholder Identification

Community

When asked in the community interviews, “Who do you think would be most likely to be impacted by tidal power?,” responses were residents (48 %), followed by fishermen (33 %), and then property owners, “everyone”, and tourists (19 %). We view fishermen as a distinct subgroup within the broader community category because they were consistently identified in interviews and at public meetings as most likely to be impacted by tidal power. Community stakeholders interviewed were concerned that tidal power in Cobscook Bay would “restrict fishing,” and many shared the sentiment that “fishermen would be the most hurt by it.” In particular, scallop and urchin draggers were identified as the stakeholder group that would “lose some real estate” because of the perception that tidal power has the potential to restrict fishing ground.

Developers

Developers identified regulators, community (and particularly fishermen such as scallop draggers), and native tribes as stakeholders. In describing who should be on the “stakeholder list” one developer said:

I think the stakeholder list is long and arduous, and it's a fool's errand to just go to the agencies and negotiate at the agency level. I think it is important to negotiate at the local level, the community level, and all the other resource user level as it is to deal with your regulatory agencies.

Another developer specified what they perceived as community interests:

The obvious ones are the mariners, the fishermen, recreational boaters, anybody that might be impacted by the project location and equipment in the water. On the onshore station, the stakeholders include all the abutting landowners whether they are year-round or seasonal residents...and in that category I would put educational institutions in the area.

Adding to our a priori characterization, regulators and developers also identified scientists as an important stakeholder group. Developers talked about the wide range of professional expertise that was expected to come to bear on decisions regarding deployment of ocean energy devices. One ORPC representative acknowledged the important role of scientists for funding and “knowledge creation.” He explained that, “...having scientists involved in your project is important for helping make all that happen.”

Regulators

Agencies described themselves and other federal and state agencies as the “most active” stakeholders. A federal regulator listed agencies they viewed as relevant:

Coast Guard is very relevant, U.S. Fish and Wildlife Service, and NMFS [National Marine Fisheries Service]. There's various state agencies, the Maine Department of Marine Resources [DMR] that are very relevant, State Planning Office. Of course, FERC [Federal Energy Regulatory Commission] and the Bureau of Offshore Energy Management [BOEM].

Both federal and state agencies described their role and power as context specific and mandated by law. In general, resource agencies were identified as having a stake when a particular resource (e.g., salmon) or issue was involved. For example, a federal regulator described the role of the different agencies in decision-making for MHK development: Coast Guard, navigational issues. Maine DMR, fisheries issues, commercial fisheries interests. NMFS, the Marine Mammal Protection Act, Magnuson Stevens... Fish and

Wildlife Service [FWS], Endangered Species Act, and marine mammals as well as diving birds...Maine Department of Environmental Protection because I do believe they have to issue a 401 Water Quality Permit for these projects...FWS and NMFS also have Section 18 of the Federal Powers Act where we can prescribe fishways...Corps of Engineers, very important, they deal with navigable waterways and they have the Rivers and Harbors Act.

Agencies also included communities on the list of stakeholders but typically after discussion of the role of the various federal and state agencies. One federal regulator identified “everybody and anybody in the Eastport and Lubec community” as stakeholders. Another said:

Obviously the communities where the tidal power facilities would be constructed would, I think very much, you would have to have them in on the discussion...fishing community, I guess.

Similarly, state regulators identified recreational and commercial fishermen (particularly scallop and urchin draggers and lobstermen), and landowners potentially impacted by siting of power lines as stakeholders. A federal regulator detailed the list of community stakeholders:

In any particular project, there are always abutters, people who may own adjoining property may have visual or aesthetic concerns about a particular tidal project, people who may be affiliated with nongovernmental organizations who are concerned about the resources that might be impacted by a particular project, communities who may have issues regarding tax income that might come from a project or business opportunities, jobs, and then extending to contractors that might work on a particular project, there's a variety of stakeholders within each of those kinds of classes of stakeholders.

Another federal regulator summed up the list of stakeholders potentially affected by a project as, “users of the area” that are “defined on a case-by-case basis.” He said:

In the case of hydrokinetics, [it is] important to get the different industries involved that are other users of the area, [the] water, where potential conflicts could occur.

Although regulators mentioned navigable waterways rights (e.g., issues of boat traffic), they acknowledged that few recreational boaters use the waters of Cobscook Bay, and there is “no commercial traffic there.” Similar to developers, regulators listed Native American tribes as stakeholders. They described tribes as having “special status” and discussed how tribes were “almost always asked for their input in cases where it affects tribal resources.” However, tribes were described as having “a special class of involvement and notification,” and interaction with tribal representatives generally occurred at the federal level.

Assessment of Stakeholder Salience

Stakeholder groups identified in our social science research and characterized using the typology of Mitchell et al. ([1997](#)) ranged from not stakeholder to definitively a stakeholder (Table [1](#)). Attributes of power, legitimacy, and urgency were determined based on stakeholder perspectives and our observations. This section provides evidence to support our characterization, although we again recognize that attributes are variable and socially constructed; thus, our analysis offers only one of several possible interpretations.

Table 1

Stakeholders identified in research and their characterization based on Mitchell et al.'s typology based on their level of power, legitimacy, and urgency

Stakeholder group	Identified by:	Power	Legitimacy	Urgency	Mitchell et al.'s category
Commercial fishermen	• Developers	X	X	X	Definitive
	• Regulators				
	• Community				
Regulators	• Developers	X	X	X	Definitive
	• Regulators				
Developers	• Regulators	–	X	X	Dependent
Native tribes	• Developers	X	X	–	Dominant
	• Regulators				
Scientists	• Developers	X	–	X	Dangerous
	• Regulators				
Residents	• Community	X	X	–	Dominant
Property owners	• Developers	X	X	–	Dominant
	• Regulators				
	• Community				
Recreational	• Developers	–	X	–	Discretionary
	• Regulators				
Tourists	• Community	–	–	–	None

Community Stakeholders

Based on our analysis, we classify broader community members as generally dominant stakeholders because they are viewed as legitimate for the most part and they are perceived as potentially having power to impact the success of a project, but their stake is not viewed as urgent compared to fishermen (Table 1). This group includes residents, property owners, and those with recreation and navigation interests. Legal mandates require regulators and developers to consider how a project will lead to socio-economic and environmental impacts in the community, thus giving them legitimacy in the process. They are viewed as having power, as one representative of a tidal power development company indicates they can make or break a project:

Fundamentally, if you could have the world's greatest technology, the best turbine human kind has ever known but you don't have a site, number one and then number two, if you don't have a community that wants you there, it just isn't going to happen.

Here, the developer is alluding to problems that arise from NIMBY (not-in-my-backyard) groups, such as those seen in Cape Wind (Kempton et al. 2005). If community members are viewed as having an urgent claim, this group of stakeholders may also become a definitive stakeholder. One could also imagine the urgency of their claims increasing with new information on socio-economic or environmental impacts; this would shift them

to being definitive stakeholders. They could also be dangerous; for example, summer tourists or part-time residents who are not viewed as legitimate because they do not live year-round or rely financially on the bay, but may have significant power (e.g., political or financial) to stop a project simply if they do not want it in the community. Some of these could be classified as NIMBY groups. Unlike many offshore wind projects (e.g., Kempton et al. [2005](#)), we have not seen these groups emerge in the context of tidal power in Maine.

Another group that we have not seen emerge are nongovernmental organizations (NGOs); however, they were identified in our research as a group that may have stake in the process. One regulator pointed out that NGOs that have been involved in conventional hydro such as “the Atlantic Salmon Federation might well have concerns about marine hydrokinetic.” He also said, “Audubon Society who is very concerned about migratory birds...they might become involved...commercial fishing associations, they might become involved, but I have not heard of these organizations to date.” When asked why these groups are not currently involved in debate surrounding MHK development, the regulator added, “I think people haven't really gotten their arms wrapped around what a hydrokinetic project is or could do, or how it might impact the resources they are interested in.” It might be that as more information emerges, these groups may become more active in tidal energy development decisions and characterization would shift from discretionary to dominant or dangerous.

Fishermen

We classify fishermen as definitive stakeholders because their concerns have urgency and legitimacy. Although they hold no formal decision-making power in the process compared to the regulators' role in the permitting process, they are perceived as holding power. As one resident explained: “Loss of traditional fishing grounds will be the bone of contention. If it (tidal power) starts infringing too much (on commercial fishing) there will be a rub.” Fishermen's power comes from the cultural and economic importance of fishing to the state, and there was the perception that tidal power could compete with fishermen's interests. As one fisherman we interviewed said, “Eventually they would be competing for the bottom in our bay that has historically belonged to fishermen.” Additional semi-structured interviews and our observations at public meetings supported these findings. For example, one regulator said, “Loss of fishing grounds. I am sure that's an issue for commercial fishermen.” Impacts on this sector will be critical to any siting decision made regarding renewable energy. Their power has already been recognized to some extent by the developer; for example, the location of the testing site was moved to accommodate fishermen's concerns. ORPC has taken great effort to meet with fishermen in the region throughout the process, and in making decisions going forward, one company representative described fishermen as “one of the first [stakeholder] groups that [they] would be going to.”

Tribal Interests

Tribal interests in the community have both legitimacy and power in the process, and therefore, we classify them as dominant stakeholders. Federal agencies are required to notify and engage Native American tribes who have land in the project area that could potentially be affected by development. Tribes are perceived to have power due to their “special status” and because of their influence at the federal level when it comes to protecting tribal resources. In our case, federal agencies “reached out” to tribal

authorities. Similarly, ORPC recognized the tribes as important stakeholders and also reached out to tribal authorities as a part of their stakeholder engagement process. The location of the Cobscook Bay Tidal Energy Project near the reservation would seem to create immediate urgency for the local tribe, but they have not been vocal about the project. Instead, they were more involved in another proposed effort that is closer to their reservation. Another possible reason to explain why tribal interests have not been more engaged in the Cobscook Bay project may be that they do not consider the chosen location for turbine deployment to be an imminent threat. As a tribal representative explained:

It is placed in areas that lessen impacts to fishermen. It's not the best fishing grounds. It's placed to allow fishermen to keep fishing. Environmental impacts have been minimized.

Regulators

Agency representatives interviewed described themselves as key stakeholders and immediately listed all the state and federal agencies they perceived should be “at the table” to ensure that their statutory needs are met. Developers also identified agencies as a key stakeholder. We classify the public regulators and resource agencies as definitive stakeholders because this group holds legitimacy, power, and urgency in the process. Agencies definitive role comes from their statutory authority in the regulatory and permitting process (i.e., legitimacy). Input from agencies during the decision-making process for hydrokinetic project licensing may determine whether or not a project will go forward, although the Federal Energy Regulatory Commission (FERC) makes the final licensing decision. These agencies essentially represent all key stakeholders in the process: the fishermen, broader community members, environmental group interests, and other members of the general public. They hold significant power in the process because they have jurisdictional authority and will make recommendations or decisions (i.e., impacts to species of concern) that can influence permitting decisions and the ultimate siting of projects, including opinions about the potential social and environmental impacts. Regulators have urgency in the process because of the timing of decisions and the limited amount of information available on MHK technology with which to base their decisions. Despite uncertainty, regulators need to make major decisions about the deployment of new tidal energy technologies, the outcomes of which will affect coastal resources and the communities that depend on them.

Developers

In addition to the stakeholders identified in the interviews, we also include the developers as stakeholders with considerable urgency, legitimacy, and to a lesser extent power. We classify them as dependent stakeholders. They are legitimate because they will be impacted by any permitting or regulatory decision that is made regarding tidal power. We view them as having urgency, because the longer they are involved in the process, the more financial resources it costs them. Importantly, developers must continue to show progress to receive support from their investors. However, if there is wide acceptance for tidal power in the community (such as for economic development reasons), the developers hold some power in that they can decide not to pursue a project in a community if they feel the costs of environmental monitoring or mitigation are too excessive. If this is the case, they may be definitive stakeholders. At this time, we do not view the developers as definitive stakeholders.

Scientists

Although scientists were not identified in our a priori identification of broad stakeholder groups, developers and regulators identified them as important to the process of tidal energy development. We, including our engineering and biophysical research colleagues, can potentially direct the outcomes of the projects through the information we provide to the state, the developers, and the general public. A regulator describing his perceptions of scientists as stakeholders, said:

They've got a pretty major role in it, both the scientists developing the technology and the scientists who are out there determining what the effect of it is...a good component of the [Cobscook Bay Tidal Energy Project] is to find out what the effect is on the environment, and that's going to be conducted by scientists...in order to get the answers we need on tidal power, we need the science.

In other words, the regulator viewed scientists as stakeholders because the information they provide can impact regulatory decisions and ultimately a developer's decision regarding project feasibility.

As noted earlier, the developer also views scientists as an important stakeholder group. One representative of the developer said:

There's so much environmental work required that it's difficult to find money to do it. So it's important to have the strategic relationship with the University because the university is...a separate independent entity and is able to attract money from pools no one else can play in.

Because of the high level of uncertainty and rapidly increasing interest in tidal power, regulators and developers are turning to scientists to help them understand the potential effects of this technology in order to move the industry forward; this gives scientists some urgency in the process. We do not view ourselves as legitimate stakeholders, but we recognize that we ultimately do hold some power in the decision-making process—if not to the same extent as the regulatory agencies. We recognize also that our power and influence is likely impacted by funding and other institutional constraints. We, therefore, classify ourselves as dangerous stakeholders.

Perceptions About Engagement

The theme of engagement was heard from all stakeholder groups interviewed: developers, regulators, and community members, including fishermen, and this was a theme heard during all of the public meetings and focus groups observed. Here we first present how the developer describes its engagement strategy, and then turn to how stakeholders perceive this strategy.

Developer's Views of Engagement

ORPC views their engagement strategy as “transparent to stakeholders and based on lots of listening.” One representative of ORPC explained that for them “it has been important to be visible and open; to leverage local talents and resources.” Another described their approach this way: “We've always been pretty open. We have an open door policy in our offices. We try our best to advertise to the public, certainly respond to feedback quickly.” This is all founded on their belief that “agencies give permits, communities give permission.” Other lessons shared by the company representatives on stakeholder engagement include: engaging community leadership before moving through the permitting process; extending effort to identify and speak to the right people; scoping

community relationships early on; and being as specific as possible to avoid antagonism from those desiring more specific information. What the developers found was that the issue was not the tidal energy turbine being in the water or the testing vessel being at anchor. Rather the issue was that the community “felt uninformed or someone didn't reach out to them.” This understanding motivated the company to “make that extra effort to get some information out on the street.” Indeed, an important component of ORPC's engagement strategy is to be present in the community. One ORPC representative said: We want to be on the street, and it is part of why we hired people locally to be the face for the company up there...anytime you are walking down the street, or sitting in a restaurant, or standing in the checkout line at the IGA...someone can always stop you and say, ‘How come you did this?’ Or, ‘I heard this...’

Early in the process, ORPC identified “the need to create a relationship with the fishing community.” The original facilitator of the fishing industry relationship was a community nongovernmental organization, the Cobscook Bay Resource Center. An ORPC representative described that this has changed: “Now there's a subgroup [of fishermen] that meets with us directly” and suggests that because of this, they “gained support for [the] project.” The developer further described the relationship between ORPC and the fishermen as one based on “advice.” ORPC sought and received advice from fishermen on issues such as whom the company should talk to before they proceeded, on seasonality and other fisheries-related issues they should be aware of at different planning stages, potential hazards to navigation, and advice for how the company should communicate with the broader community about their project. The developer also described how they used input from fishermen when they put their device in the water for the first time. In describing how the company discussed siting decisions with the local fishermen, he said, “that was a very fruitful conversation because it led to the fishermen actually pointing to some places on a navigational chart, where they thought we would best fit in.” Although engaging with the community and particularly fishermen was a priority for ORPC, they acknowledged that it was a challenge “to keep both conversations and relationships current and updated.”

In addition to engaging with the community and fishermen, ORPC employees also described how it is important to work with the regulatory agencies. As one representative of the developer explained: “Much like how you build a relationship with the community, you have to build a relationship with the agency.” They are doing this through transparency and communicating information, as one representative of the company explained: “We're trying to be open with our information, we're trying to be regular with our information, keep them updated with everything that going on, and just stay at the table.”

Developers have also made an effort to engage with local tribal representatives. One representative of the developer said of the tribes, “We talked to them as much as you can...we do communicate with them, let them know what we're thinking, what we're doing.”

Community's Perceptions of Engagement

The majority of community interviewees indicated that they liked the way ORPC has worked in the community, as indicated in the following quote: “The way it's been done so far by ORPC is a collaborative effort and that is good.” In the community interviews, 79 % recommended other developers take a similar approach as ORPC. Another

community member commented: “ORPC has taken a lot of time listening to the community, especially fishermen.” Another community member praised the company's approach as “smart” for using “local people, local resources, [and] keeping people informed in the paper.”

According to the director of a local NGO, ORPC has taken a positive approach in the community because they articulated their broad goal of developing this technology...and then asked local people for their help...developed an MOU with the local city government...kept the community informed of their plans and progress...listened to local knowledge...and then, they actually acted on what they'd learned...hired local talent...invested significantly in the local community...so far they've worked at the right scale; they haven't overpromised...undertaken an incremental scaling up of tests and growth... built relationships and established credibility...identified themselves as a partner in community development (Hopkins [2009](#)).

Community members (local business owners and residents) participating in our focus groups also had positive perceptions of ORPC's approach. One of these focus group participants said:

There's been a great deal of public outreach by the tidal power developers...both on an individual basis and having community meetings. They've tried to get a great deal of input from the community about...what would be appropriate, what's acceptable. Community members felt that ORPC offered “ample opportunity” to be involved, and in terms of learning about the project, one community member said they “see stuff all the time like in the paper...[or hear] from word of mouth through one person or another that's been associated with [ORPC].” Community stakeholders also perceived company representatives as accessible and approachable: “They are downtown [in Eastport] and there's always people there, and they are very nice.” A tribal representative said: ORPC has pretty much written the boilerplate for how this should be done. Having someone in the community as a go between, like [the local community member hired by ORPC], gives their project credibility in the community. [He] is upfront and has a good relationship with community members. This is very valuable.

In general, fishermen's opinions of ORPC have also been generally positive. As noted earlier, ORPC contacted local fishermen early in the process, and some of these fishermen were later hired by the company to perform various tasks. One of these fishermen, contacted directly by ORPC to discuss possible hazards to navigation posed by the proposed project, found one of the company's public presentations informative and said that “they've taken the right approach.” Another fisherman also found public presentations by ORPC “very informative” and said of the company's approach, “They've made all efforts to approach fishermen and answer questions.” One fisherman talked specifically about how ORPC worked with the fishermen to decide on the location of the first turbine deployment. He said, “They've worked with fishermen in finding out where to place their things and they've tried to keep them out of the way of fishermen, so far.” Despite these positive perceptions, fishermen raised some concerns early on, such as fishermen who expressed uncertainty about the potential impacts on the fishing industry. For example, one fisherman said, in 2010, “I don't think they let us know everything,” and further asked, “How much bottom they will take? How much fishing grounds will be lost? What will they do for the fishermen?”

One incidence in particular, noted by several fishermen we talked to, could have ended poorly for the company. Several fishermen spoke about ORPC's decision to pursue additional preliminary permits outside of Cobscook Bay, but in a nearby area important to local fishermen, without first seeking local input. For example, one fisherman in our focus group described their reaction to this new permit:

All of the sudden, there's a chart of the bay and this great big purple area applied for tidal power. Everybody starts saying, 'Geez, where's the hearing on that?' So it kind of soured some relationships, but they've [ORPC] mended those... There's been discussions with [ORPC] since, and people understand why they done it... They promised to be more in touch, and I believe they will be.

However, not all fishermen felt that the engagement process has been completely effective or that ORPC has responded to their needs and concerns. In particular, several Lubec fishermen offered disparate views on ORPC's engagement strategy. By water, Lubec is close to Eastport and the deployment site. It is also the site of the onshore station for cable connection to the interstate grid. By land, however, Lubec is removed (approximately 1 h) from ORPC's office in Eastport. In responding to questions about their interactions with ORPC, one Lubec fisherman described their experience at the U.S Coast Guard public hearing:

We [were] told in the meeting, they said they would move the buoys [marking the location of the turbine] back from Goose Island, which they [ORPC] didn't do. Fishermen identified Goose Island as important for urchin fishing. The perceived lack of attention to the fishermen's concern about a buoy located in this area, elicited the following response from a Lubec fisherman. He said, the fact that the buoy was not moved, "kinda bugs me," and further explained... that because of this "they're not credible." A problem, from these fishermen's perspective, is that the company did not engage all of the fishermen in the bay, but primarily focused their attention on those located in the town where their office was located.

Regulator's Views of Engagement

Several regulators agreed that early engagement has been essential for improving the success of ORPC's project; one regulator explained: "I think because ORPC engaged the local community so heavily that their needs were addressed." Another regulator said, "ORPC folks have generally gone about things the right way." They commented that the first contacts that they made were locals and that "it's that local outreach and local cooperation done very early that is really important." Regulators also felt the company has effectively engaged them in the process. One regulator agreed with their strategy and stated, "...at ORPC, a lot of their project managers...they've all been very good at engaging us early and often."

Discussion

Numerous and diverse stakeholders affect and are affected by the process of tidal energy development. Our research contributes social science to better understand who may be affected, how they are affected, and how they have been engaged in the process of tidal energy development in Maine. We found that Mitchell et al. ([1997](#)) provide a useful framework for understanding the complex stakeholder environment relevant to tidal energy development, and we used the framework to organize our research findings and

facilitate identification of the most salient stakeholders whose engagement is important for tidal power development.

Given the Cobscook Bay project's coastal location and proximity to tribal lands, the community stakeholders (i.e., fishermen, residents, property owners, and tribes) we identified through our mixed methods research approach were not surprising (Table 1). In our study, fishermen were consistently identified by all three broad categories of stakeholders (community, developers, and regulators) as the group most likely to be impacted by tidal power development or likely to impact the process. Also not surprising was the fact that regulators and developers identified several of the same stakeholders. They both identified agencies and “abutting landowners,” both relevant to the regulatory context and primary, formal role of regulators and developers. More interestingly, both regulators and developers identified scientists as stakeholders, a group we had not initially included in our a priori characterization.

Applying the Mitchell et al. (1997) typology to these findings, we characterized fishermen as definitive stakeholders (Table 1), because they hold power, legitimacy, and urgency in the process. Although residents and property owners were also viewed as important interests (and their participation in the process is mandated by statute), at present, their interests do not appear as urgent as those of fishermen, and therefore, we characterized them as discretionary. To date, there has been no organized community opposition to the Cobscook Bay Tidal Energy Project and tribal interests have been minimally involved. Lack of urgency as a key attribute to characterize these community stakeholder groups may be attributed to the salience of the issue. Tidal power development is currently more urgent to the fishermen because of the perceived physical intrusion on their fishing grounds. For other community interests, tidal power development may be out-of-sight and out-of-mind, or may not be at the top of the lists of concerns compared to other presumably more pressing concerns.

Our research and analysis using Mitchell et al. (1997) suggest that future stakeholder engagement should reflect the dynamic nature of salience. Given the nascent nature of the tidal power industry and the rapidly changing technology and permitting process (see Jansujwicz and Johnson 2013), salience is likely to change as the project unfolds, thereby requiring different levels of engagement. Some groups may become more or less important than others, and therefore, the appropriate engagement strategy would need to change as well. As an example, as the environmental effects of tidal turbines are better understood, environmental NGOs might ask to be included in the discussion. Similarly, attributes of power may change, and outcomes of our research suggest that stakeholder power may not necessarily be a good indicator of whether a stakeholder or stakeholder group has the potential to influence decision-making at a particular point in the process. In fact, less powerful, local actors can deploy means to delay or halt implementation of a project (Breukers and Wolsink 2007). In our case, residents and other community interests are currently not viewed as having the same level of formal power attributed to regulators responsible for licensing decisions, and NGOs (at least at this time) are perceived as having minimal power. If mobilized, however, local residents and NGOs may ultimately have more influence than would be predicted by the static use of the Mitchell et al. (1997) typology. Thus, we suggest that on-going research should track changes in typologies of salience.

ORPC's considerable efforts to engage relevant stakeholders early and often were noted by both regulators and community stakeholders, particularly local fishermen, residents, and tribal representatives. Perhaps regulators' positive perceptions of ORPC's engagement strategy should come as no surprise. After all, as Agterbosch et al. (2009, p. 404) pointed out, in the context of an uncertain regulatory landscape, most energy distributors use “a strategy of frequent and informal contact with competent authorities,” and these “authority relations” support trust and facilitate coordinated action. Certainly, in the Cobscook Bay example, ORPC's proactive and frequent engagement with the agencies ensured that regulators statutory mandates were met and that all interests (developers, federal and state regulatory and resource agencies) were on the same page. However, in some instances, such a regulator–developer engagement strategy may be perceived as serving external economic interests and not the interests of the local community (Agterbosch et al. 2009). In our study, community stakeholders did not identify regulators as important stakeholders (perhaps this can be explained by a lack of clarity and understanding of the permitting and regulatory process); thus, this tension does not exist. Rather, evidence seemed to suggest that ORPC's current engagement strategy of public meetings, newspaper articles, and targeted meetings with specific (influential) community groups, such as the Cobscook Bay Fishermen's Association, met local needs for information.

Our results suggest that ORPC, the leading tidal power developer in the USA, has established a public engagement strategy that appears to be working well. Our empirical assessment of the Cobscook Bay process provides evidence of the claimed benefits of stakeholder participation. Most notably, we find that stakeholder engagement has shaped the decision-making process in terms of site selection for turbine deployment in Cobscook Bay and also in building (and maintaining) relationships with the community. Applying the theory of Mitchell et al. (1997) on stakeholder salience to the Cobscook Bay example, we offer insight on why ORPC's engagement process appears to be working and offer recommendations for future engagement strategies in Maine and beyond.

ORPC has engaged definitive, dominant, and discretionary stakeholders and this may explain their apparent success. By incorporating multiple viewpoints and perspectives from a number of diverse stakeholders (particularly fishermen and regulators) into their decision making process, ORPC has developed and maintained effective stakeholder relations, thereby forging an approach that appears to be resilient and adaptive to future decisions. Community response to the rapid procurement of additional preliminary permits without first seeking stakeholder input provides support for this assertion.

Although the community's initial response to the new preliminary permits was one of concern, ORPC was able to explain the reasoning behind their quick decision (i.e., they wanted to claim the permits before another, out-of-state, and perhaps less trusted company jumped in), and because of trust built in the process, they were able to successfully smooth stakeholder relations before conflict escalated. At the same time, however, because the company was not as visible outside of the community in which their office was located, community concern was evident in these more distant areas. If not addressed in a timely and effective manner, community concern could lead to more organized opposition and future conflict. This is not surprising given the proposition that if people feel left out of the planning process and decision-making, they are more likely

to oppose the process outcomes (Zoellner et al. [2008](#)). Our findings highlight the critical importance of engaging more distant stakeholder groups and groups that perhaps, at this point, do possess the attribute of urgency, so that as information develops, future conflict can be more easily avoided.

In summary, although evidence points to the benefits of the developer's current engagement approach, it is important to note that the tidal energy industry is still in its infancy, and changes will continue to occur as new information emerges. The dynamic nature of tidal energy development highlights the importance of the process, and the importance of continued engagement, transparency, and recognition of diverse stakeholder needs and communication preferences. Our stakeholder characterization offers only a snapshot, and it will be important to continue to track stakeholder salience over time as tidal power develops. In practice, we find Mitchell et al.'s typology to be a useful tool for characterizing stakeholders at different points in the process. Outcomes of our research represent a critical first step toward informing the design of more effective stakeholder processes for renewable ocean energy development and specifically tidal power. While opportunities for stakeholder participation are specific to time, site, issue, and local values (Glicken [2000](#)), our approach that combines empirical research with Mitchell et al.'s typology offers a practical strategy that can be used to inform stakeholder identification and engagement research in other renewable energy contexts.

Acknowledgments

This research was supported by the National Science Foundation award EPS-0904155 to Maine EPSCoR Sustainability Solutions Initiative at the University of Maine and Department of Energy award EE0000298 to the University of Maine. The authors would like to acknowledge their community partners, Christopher Bartlett, of the Maine Sea Grant and University of Maine Cooperative Extension, and the Cobscook Bay Resource Center, for their contributions to the community interviews. The authors are also especially grateful for Mr. Bartlett's continued support and assistance with the community meetings, focus groups, and other outreach efforts. Finally, the authors thank all of those who were interviewed and otherwise contributed to this research.

References

- Adams, M., D. Wheeler, and G. Woolston. 2011. A participatory approach to sustainable energy strategy development in a carbon-intensive jurisdiction: the case of Nova Scotia. *Energy Policy* 39: 2550–2559. [CrossRef](#)
- Agterbosch, S., R.M. Meertens, and W.J.V. Vermeulen. 2009. The relative importance of social and institutional conditions in the planning of wind power projects. *Renewable and Sustainable Energy Reviews* 13: 393–405. [CrossRef](#)
- Bardach, E. 1998. *Getting agencies to work together: the practice and theory of managerial craftsmanship*. Washington.: Brookings Institution Press.
- Beard, R.E. 2009. *Best practices and a case study in stakeholder and public engagement in siting ocean energy projects*. University of Maine Cooperative Extension and Sea Grant.
- Blackstock, K.L., G.J. Kelly, and B.L. Horsey. 2007. Developing and applying a framework to evaluate participatory research for sustainability. *Ecological Economics* 60: 726–742. [CrossRef](#)
- Boehlert, G.W., and A.B. Gill. 2010. Environmental and ecological effects of ocean renewable energy development: a current synthesis. *Oceanography* 23: 68–81. [CrossRef](#)

Breukers, S., and M. Wolsink. 2007. Wind power implementation in changing institutional landscapes: an international comparison. *Energy Policy* 35: 2737–2750.[CrossRef](#)

Bryson, J.M. 2004. What to do when stakeholders matter. *Public Management Review* 6(1): 21–53.[CrossRef](#)

Bryson, J.M., and B.C. Crosby. 1992. *Leadership for the common good: tackling public problems in a shared world*. San Francisco: Jossey-Boss.

Charlier, R.H., and C.W. Finkl. 2010. *Ocean energy: tide and tidal power*. Berlin: Springer.

Conway, F., J. Stevenson, D. Hunter, M. Stefanovich, H. Cambell, Z. Covell, and Y. Yin. 2010. Ocean space, ocean place: the human dimension of wave energy in Oregon. *Oceanography* 23: 82–91.[CrossRef](#)

Devine-Wright, P. 2005. Local aspects of UK renewable energy development: exploring public beliefs and policy implications. *Local Environment: The International Journal of Justice and Sustainability* 10: 57–69.

Eden, C., and F. Ackermann. 1998. *Making strategy: the journey of strategic management*. London: Sage.

El Bassam, N. 2001. Renewable energy for rural communities. *Renewable Energy* 24: 401–408.[CrossRef](#)

Elliott, D. 2000. Renewable energy and sustainable futures. *Futures* 32: 261–274.[CrossRef](#)

Firestone, J., and W. Kempton. 2007. Public opinion about large offshore wind power: underlying factors. *Energy Policy* 35: 1584–1598.[CrossRef](#)

Firestone, J., W. Kempton, and A. Krueger. 2009. Public acceptance of offshore wind power projects in the USA. *Wind Energy* 12: 183–202.[CrossRef](#)

Freeman, R.E. 1984. *Strategic management: a stakeholder approach*. Boston: Pitman.

Gill, A.B.. 2005. Offshore renewable energy: ecological implications of generating electricity in the coastal zone. *Journal of Applied Ecology* 42: 605–615.[CrossRef](#)

Glaser, B.G., and A.L. Strauss. 1967. *The discovery of grounded theory: strategies for qualitative research*. New York: Aldine.

Glicken, J. 2000. Getting stakeholder participation “right”: a discussion of participatory processes and possible pitfalls. *Environmental Science and Policy* 3: 305–310.[CrossRef](#)

Hindmarsh, R., and C. Mathews. 2008. Deliberative speak at the turbine face: community engagement, wind farms, and renewable energy transitions in Australia. *Environmental Policy and Planning* 10(3): 217–232.[CrossRef](#)

Holmes, T. and Scoones, I. 2000. Participatory environmental policy processes: experiences from north and south. IDS Working Paper 115.

Hopkins, W. 2009. Presentation at the 2nd Annual Global Marine Renewable Energy Conference at the Carnegie Institution for Science, Washington, D.C., April 16, 2009. Available at: <http://www.globalmarinerenewable.com/images/stories/2009Presentations/WillHopkins-2009GMRE.pdf>. Accessed 29 Jun 2012.

Jansujwicz, J. S., and Johnson, T. R. 2013. Understanding and informing permitting decisions for tidal energy development using an adaptive management framework. *Estuaries and Coasts*. doi:[10.1007/s12237-013-9678-0](https://doi.org/10.1007/s12237-013-9678-0).

Johnson, T., and G.B. Zydlewski. 2012. Research for the sustainable development of tidal power in Maine. *Maine Policy Review* 21(1): 58–64.

Johnson, K., S. Kerr, and J. Side. 2012. Accommodating wave and tidal energy—control and decision in Scotland. *Ocean and Coastal Management* 65: 26–33.[CrossRef](#)

Kempton, W., J. Firestone, J. Lilley, T. Rouleau, and P. Whitaker. 2005. The offshore wind power debate: views from Cape Cod. *Coastal Management* 33: 119–149.[CrossRef](#)

Meltsner, A. 1972. Political feasibility and policy analysis. *Public Administration Review* 32: 859–867.[CrossRef](#)

Mikalsen, K., and S. Jentoft. 2001. From user groups to stakeholders? The public interest in fisheries management. *Marine Policy* 25: 281–292.[CrossRef](#)

Mitchell, R.K., B.R. Agle, and D.J. Wood. 1997. Toward a theory of stakeholder identification and salience: defining the principle of who and what really counts. *The Academy of Management Review* 22: 853–886.

Newman, W.M., and M.G. Lamming. 1995. *Interactive system design*. Wokingham: Addison-Wesley.

Ocean Energy Task Force (OETF). 2009. Final report of the Ocean Energy Task Force to Governor John E. Baldacci. Augusta, Maine.
www.maine.gov/spo/specialprojects/OETF/Documents/finalreport_123109.pdf. Accessed 24 May 2012

Parent, M.M., and D.L. Deephouse. 2007. A case study of stakeholder identification and prioritization by managers. *Journal of Business Ethics* 75: 1–23.[CrossRef](#)

Polagye B., B. Van Cleve, A. Copping, and K. Kirkendall. 2011. Environmental effects of tidal energy development. U.S. Dept. Commerce, NOAA Tech. Memo. F/SPO-116. 181 pp.

Portman, M. 2009. Involving the public in the impact assessment of offshore renewable energy facilities. *Marine Policy* 33: 332–338.[CrossRef](#)

Reddy, S., and J.P. Painuly. 2004. Diffusion of renewable energy technologies, barriers and stakeholders, perspectives. *Renewable Energy* 29: 1431–1447.[CrossRef](#)

Reed, M.S. 2008. Stakeholder participation for environmental management. *Biological Conservation* 141: 2417–2431.[CrossRef](#)

Reed, M.S., A. Graves, N. Dandy, H. Posthumus, K. Hubacek, J. Morris, C. Prell, C.H. Quinn, and L.C. Stringer. 2009. Who's in and why? A typology of stakeholder analysis methods for natural resource management. *Journal of Environmental Management* 90: 1933–1949.[CrossRef](#)

Richards, C., K.L. Blackstock, C.E. Carter. 2004. Practical approaches to participation. SERG Policy Brief No. 1 Macaulay Land Use Research Institute, Aberdeen.

Sharp, H. A. Finkelstein, and G. Galal. 1999. Stakeholder identification in the requirements engineering process. Proceedings of 10th international workshop on database & expert systems applications (DEXA): 387–391. IEEE Computer Society Press.

Strauss, A., and J. Corbin. 1990. *Basics of qualitative research: grounded theory, procedures and techniques*. Newbury Park: Sage.

Van Horn, C., D. Baumer, and W. Gormley. 2001. *Politics and public policy*, 3rd ed. Washington: Congressional Quarterly Press.

West, J., I. Bailey, and M. Winter. 2010. Renewable energy policy and public perceptions of renewable energy: a cultural theory approach. *Energy Policy* 38: 5739–5748.[CrossRef](#)

Zoellner, J., P. Schweizer-Reis, and C. Wemheuer. 2008. Public acceptance of renewable energies: results from case studies in Germany. *Energy Policy* 36(11): 4136–4141.

Appendix Task 4-2

Estuaries and Coasts Journal of the Coastal and Estuarine Research Federation© Coastal and Estuarine Research Federation 201310.1007/s12237-013-9678-0

Understanding and Informing Permitting Decisions for Tidal Energy Development Using an Adaptive Management Framework

Jessica S. Jansujwicz¹ and Teresa R. Johnson²

(1)

Sustainability Solutions Initiative, University of Maine, 5710 Norman Smith Hall, Orono, ME 04469, USA

(2)

School for Marine Sciences, University of Maine, 200 Libby Hall, Orono, ME 04469, USA

Jessica S. Jansujwicz

Email: jessica.jansujwicz@maine.edu

Received: 9 July 2012 Revised: 14 June 2013 Accepted: 11 July 2013 Published online: 14 August 2013

Editorial responsibility: Andrea Copping

Abstract

Marine hydrokinetic (MHK) energy offers a promising new source of renewable ocean energy. However, the young industry is faced with significant challenges. Most notable is the challenge of regulatory uncertainty that is thought to hamper the successful deployment of new tidal energy technologies. Adaptive management may be one approach to deal with uncertainty and inform permitting decisions for hydrokinetic projects. In this study, we apply the concept of adaptive management to the Cobscook Bay Tidal Energy Project in Maine to better understand and inform permitting decisions. Using a social science approach of observation, interviews, and document analysis, we examine (1) agency roles and authority, (2) agency interactions, (3) regulatory change, and (4) challenges faced in the regulatory and permitting process for MHK development at the federal and state level. We found four institutional factors favorable to an adaptive approach. These include experimentation and learning, institutionalized choice to correct avoidable error, a strong commitment to interagency coordination, and an emphasis on early proactive engagement with project developers. We also identified institutional challenges or vulnerabilities. These include conflicting agency cultures, high financial costs, and long timeframes associated with baseline data collection. Lessons learned from this study can assist regulators, policymakers, and project developers design and

implement an actively adaptive management approach that can move new renewable ocean energy development forward in a way that is socially acceptable and environmentally responsible.

Keywords

Tidal power Marine hydrokinetic technology Adaptive management Regulatory Uncertainty Permitting decisions Renewable ocean energy

Introduction

Growing concern over the threat of global climate change coupled with increasing population and rising energy prices has accelerated the search for practical alternatives to fossil fuels (Campbell [2009/2010](#); Pelc and Fujita [2002](#)). In the search for new renewable energy sources, attention has increasingly turned toward the sea and the promise of ocean renewable energy. The oceans offer a vast and powerful source of renewable energy (Pelc and Fujita [2002](#)), and energy from marine wind, tides, currents, waves, and ocean thermal gradients may all hold immense potential for electrical energy generation (Boehlert and Gill [2010](#)). However, while the long-term prospects for ocean energy to supply a significant source of carbon-neutral energy appear promising (Griset [2010](#); Leary and Esteban [2009](#)), the developing industry is faced with significant challenges. Most notable is the challenge of regulatory uncertainty that is thought to hamper the successful deployment of new ocean energy technologies.

Regulatory uncertainty has been identified as the most significant nontechnical obstacle for widespread commercialization of ocean energy (Anderson et al. [2007](#); Leary and Esteban [2009](#)) and the primary barrier to the development of new wave and tidal energy technologies in the US (Bedard et al. [2007](#)). Regulatory uncertainty is often attributed to the lack of clear jurisdictional authority and to the dearth of information on the potential impacts of new ocean energy technologies. An array of federal and state agencies assert jurisdiction over ocean renewable power projects, and developers must obtain a variety of permits from numerous regulatory agencies. The Federal Energy Regulatory Commission (FERC) is the lead permitting authority for hydroelectric projects, including new wave and tidal energy technologies. However, projects are also subject to permitting by the US Army Corps of Engineers (CORPS). At the state level, mandatory conditioning authority exists in the form of coastal zone management consistency determinations, granting of leases, and easements of state owned aquatic lands, certifications under Sect. 401 of the Clean Water Act, and additional authorities under the National Historic Preservation Act (16 USC 470 et seq.), Federal Powers Act (16 USC §§ 792), Fish and Wildlife Coordination Act (16 USC §§ 661-677e), and others (Anderson et al. [2007](#); FERC [2012](#)). Additionally, federal and state agencies have the opportunity to comment on proposed projects pursuant to the Endangered Species Act (ESA; 7 USC § 136, 16 USC § 1531 et seq.), Marine Mammal Protection Act (16 USC § 1536a), and Magnuson Stevens Fisheries Conservation and Management Act (16 USC 1801 et seq.). As a result, project developers often find themselves faced with a confusing array of agency permitting requirements and considerable uncertainty exists around which regulatory processes and standards apply to their proposal. Developers charge that this regulatory complexity results in increased costs and a decreased ability to secure project financing (Griset [2010](#); Wellinghoff et al. [2008](#)).

Further complicating the regulatory landscape for renewable ocean energy is the current lack of information on the potential impacts of new technologies. This is particularly evident with emerging innovative technology designed to capture energy from the natural movement of the tides, generally referred to as marine hydrokinetic (MHK) energy. Although very small and localized as compared to wind (e.g., Jacobson and Archer [2012](#); Marvel et al. [2013](#)), tidal current energy is very predictable (Goundar and Ahmed [2013](#)), and considerable potential energy exists for generating power from tidal currents off the coast of the US and elsewhere in the world using emerging technologies (EPRI [2005](#)). However, because MHK technology is new, there have been few opportunities to evaluate their environmental impacts. Only a few devices have been deployed and tested in rivers and oceans, and even fewer environmental studies of these technologies have been completed (Cada et al. [2007](#), [2012](#)). While studies are forthcoming (e.g., Viehman et al. [2012a](#); [2012b](#) this issue), there is currently little scientific data on the nature and scale of environmental impacts of MHK technologies with which to inform policy and permitting decisions.

In combination, jurisdictional issues and knowledge constraints beg the question: Within the context of uncertainty, how can a regulatory framework balance the need for an efficient process with the need for the responsible development of new renewable ocean energy technologies? One approach to this dilemma would be to design adaptive management policies, in which there is a deliberate attempt to find some optimal balance between resource protection and the “disruptive probing” or scientific analysis necessary (Walters [1986](#)) to gain a better understanding of both the long-term impacts and long-term potential of wave and tidal energy devices. The concept of adaptive management is not new, nor is its application to tidal energy development. Oram and Marriott ([2010](#)), for example, embraced the concept of adaptive management as a means for proceeding with agency permitting of wave and tidal energy projects in the face of uncertainty. They suggest that an adaptive management approach would allow projects to be permitted and installed, while simultaneously providing agencies and other stakeholders with the opportunity to collect data on potential environmental impacts. Following an adaptive management approach, changes to the regulatory structure could then be made in response to new information and problems that may emerge during the installation process.

As an approach, adaptive management has been supported in government policies to encourage research and development in ocean renewable energy at the federal and state level (e.g., Ocean Energy Task Force OETF [2009](#)). More recently, the emerging tidal power industry has also begun to apply principles of adaptive management to project planning and implementation (e.g., FERC [2012](#)). However, although increasingly supported by the industry and government (e.g., Bornholdt [2012](#); Konnert [2010](#)), few if any case studies have empirically examined the validity of using an adaptive management approach to move tidal energy development forward in a more efficient and responsible manner. In this research, we suggest that opportunities and challenges for developing commercial-scale tidal power projects is best understood through the conceptual framework of adaptive management. To this end, we apply the concept of adaptive management to a study of MHK development in Maine, USA to better understand and inform permitting decisions for this new generation of tidal energy devices. Our study focuses on the Portland, Maine-based Ocean Renewable Power Company's (ORPC's)

Cobscook Bay Tidal Energy Project. Adaptive management is a key component of ORPC's approach (FERC [2012](#)), thus the Cobscook Bay project provides an excellent opportunity to learn from early experience with adaptive management and inform future applications of the concept to tidal energy development in Maine and beyond.

Within the context of the Cobscook Bay project, we pursued three main objectives. First, we aimed to understand and describe the regulatory and permitting process for MHK development in Maine. This included an analysis of the various federal and state agencies involved, their jurisdictional authority, roles, and decision making process. Our second objective was to examine the agency and developer perspectives on the process of tidal energy development, including their perspectives on regulatory change, knowledge gaps, and challenges faced in the project licensing process. Our final objective was to inform future regulatory and permitting decisions for tidal power projects in Maine and beyond. To accomplish this, we draw on the Cobscook Bay project to explore the concept of adaptive management. Our purpose was to highlight lessons learned from the first hydrokinetic pilot project licensed within the US to inform the practical application of adaptive management in the context of renewable energy development.

Conceptual Framework for Adaptive Management

Adaptive management is conceptualized as a way to confront uncertainty in natural resource issues (Gunderson [1999](#); Holling [1978](#); Walters [1986](#)). It recognizes that managed resources will always change as a result of human intervention, that surprises are inevitable, and that new uncertainties will emerge (Gunderson [1999](#)). As a concept, adaptive management embraces policies as experiments with the goal of learning from them so that future decisions can proceed from a better base of understanding (Lee [1993](#)). This approach involves a continual learning process based on the assumption that you cannot know that something will work until you try it (Walters [1986](#)). In other words, adaptive management is a deliberate and explicit commitment to “learn” from experience (Halbert [1993](#)) or to the process of “learning by doing” (Walters and Holling [1990](#)). As an experimental approach, adaptive management recognizes that policies must be continually modified and flexible so that they can adapt to surprise and new information as learning occurs (Gunderson [1999](#)). Indeed, an essential characteristic of adaptive management is that a direct feedback loop exists between science and management (Halbert [1993](#)). In theory, feedback from inventory, monitoring, and evaluation is used to improve decision making by allowing for management and policy decisions to be modified in light of new scientific information (Halbert [1993](#)). However, while adaptive management considers change and adaptation as inherent to management, Johnson ([1999](#)) observed that “most management institutions tend to resist change and wish to control the process of management as much as possible.” This may explain why adaptive management has been more significant as a concept than a management practice (Lee [1993](#)).

Turning to the literature, we suggest ways to move the concept of adaptive management from theory to practice. In considering future applications of adaptive management, Johnson ([1999](#)), for example, highlights the need to develop new institutional arrangements, so that adaptive management experiments are applied not just to the resource but also to the institutions themselves. According to Johnson ([1999](#)), “these

experiments would explore the relationships within and among agencies and stakeholders to find new ways to promote flexibility, cooperative management, and long-term outlook.” Lee ([1993](#)) also focuses on institutional factors that could demonstrate the viability of adopting adaptive management as a strategy for sustainable development. He suggests that there are factors that favor adaptive management but also institutional conditions or “vulnerabilities” that may limit institutional learning and responsiveness to the approach. Among the favorable institutional factors posited by Lee ([1993](#)) are the following: a mandate to take action in the face of certainty, awareness of experimentation by decision makers, commitment to improve outcomes over biological time scales, sufficient resources, availability of theory, models, and field methods for evaluation, testable hypotheses, institutional patience, and an organizational culture that encourages learning from experience. Institutional vulnerabilities include the disruptive capability of policy changes, vulnerability to political change, agency operating staff concerns, and “the requirement that the adaptive manager be an able negotiator as much as a visionary scientist” (Lee [1993](#), 80). This conceptual understanding of adaptive management is particularly applicable to our study of MHK development in Maine. In particular, our study offers an excellent opportunity to examine the institutional arrangements that may support or hinder the success of adaptive management as a flexible approach for dealing with uncertainties in tidal energy development.

Study Context

Our research takes place within the context of ORPC's Cobscook Bay Tidal Energy Project. Since 2005, ORPC has been working with the federal and state agencies to secure the necessary approvals to construct and operate a tidal energy project in Cobscook Bay, off the coast of Eastport and Lubec in Washington County, Maine. Cobscook Bay lies at the entrance to the Bay of Fundy, where the mean tidal range is about 6 m (Brooks [2004](#)). In 2005, the Electric Power Research Institute (EPRI) identified this site as one of the best sites for tidal energy development in the US (EPRI [2005](#)).

ORPC's Cobscook Bay Tidal Energy Project proposes to use the tidal currents of Cobscook Bay to generate electricity via a cross-flow kinetic system turbine generator unit mounted on the seafloor. This TidGen™ power system will capture energy from the ebb and flow of the water beneath the surface. In 2007, ORPC obtained an initial preliminary permit from FERC. This preliminary permit did not authorize construction but served to maintain ORPC's priority for the site and allowed the company to study the feasibility of the site and prepare license application materials. In 2011, ORPC completed a 1-year test of a beta pre-commercial version of their TidGen™ power system. About a year later, in March 2012, FERC granted ORPC an 8-year pilot license to construct, maintain, and operate a 330-kW tidal power project in Cobscook Bay (FERC [2012](#)). Developed by FERC in 2008, a pilot license process allows developers to test new hydrokinetic technologies, to determine appropriate sites for these technologies, and to confirm the technologies' environmental effects without compromising FERC's oversight (FERC [2008](#)). Pilot project licenses must be small, short term, avoid sensitive locations, subject to modification or shut down if unforeseen impacts occur, subject to plans for monitoring and safeguarding public safety and environmental resources, and removed

with the site restored at the end of the license term, unless a commercial license is issued (FERC 2008). Under the FERC pilot project license, ORPC was required to develop an adaptive management plan (FERC 2012). Upon obtaining the FERC pilot license, the Cobscook Bay Tidal Energy Project became the first hydrokinetic tidal energy project within the US to gain approval to connect to the interstate power grid. Construction of the first phase of the Cobscook Bay Tidal Project began in March 2012.

Methods

The research presented here is part of a larger ongoing study of tidal energy development in Maine. In this paper, we draw on social science research conducted between April 2010 and June 2012 aimed at understanding and documenting the regulatory and permitting process for tidal energy development. This research consisted primarily of semi-structured and informal interviews, discussions with key agency, industry, and other stakeholders, direct observations of the policy process, and a review of relevant documents.

To better understand the regulatory and permitting process for tidal energy development, we conducted 16 semi-structured interviews to learn directly from the participants involved. Interview participants were selected purposively through document analysis, network sampling, and our observations. Participants included 12 federal and state agency representatives, 1 private consultant, and 3 industry developers. Agencies included the FERC, the US Fish and Wildlife Service (USFWS), the National Marine Fisheries Services (NMFS), US Coast Guard (USCG), CORPS, Maine Department of Environmental Protection (DEP), and the Maine Department of Marine Resources. Interview questions were open-ended and designed to identify major themes related to the regulatory process and tidal energy development, particularly focused on the Cobscook Bay Tidal Energy Project. During the 1–2-h interviews, we asked the participants about their role in the process, their interactions with the agency and industry stakeholders, and their perceptions of the regulatory and permitting process as it has unfolded over time, including any knowledge gaps or challenges faced. Interviews were audio recorded and transcribed. Additionally, we had numerous informal interviews and discussions with agency regulators and project developers throughout the research. These interactions were recorded in extensive field notes.

We also attended meetings related to our research topic. These included two US Coast Guard public meetings on the proposed navigation regulation for the Cobscook Bay Tidal Energy Project, two informal consultation meetings between ORPC and federal and state regulatory and resource agencies, and one offshore renewable energy industry technical meeting. Public meetings and agency consultations were audio recorded and transcribed. Detailed field notes were recorded at all meetings attended. Lastly, we reviewed key documents including government publications (e.g., agency guidance, FERC license applications, and biannual project progress reports), media articles from national, regional, and local papers, and audio from local broadcasts related to tidal energy development in Cobscook Bay. Meetings, documents, and media sources provided additional insights into how the process of tidal energy development proceeded at the federal, state, and local level. They also provided insight into the various roles that

different stakeholders played in the process. Using multiple sources of data also enhanced the credibility of our results and confirmed our emerging findings (Merriam [2009](#)). Semi-structured interview transcripts, public meeting transcripts, and field notes from meetings and informal interviews and discussion were entered into a QSR–NVivo 9 database for storage and qualitative analysis. For qualitative analysis, we used a modified grounded theory approach (Glaser and Strauss [1967](#); Strauss and Corbin [1990](#)) that focused on identifying emerging themes, patterns, and relationships in the ways that participants described their experiences with the regulatory and permitting process for MHK development. The results and discussion presented below are focused on these themes including (1) agency role and authority, (2) coordination, (3) regulatory change, and (4) challenges faced in the regulatory process for tidal energy development at the federal and state level in Maine.

Results

Agency Role and Authority

The regulatory and permitting process for tidal energy development mandates involvement by an array of federal and state agencies. We draw on data from interviews supplemented by document review and our field notes to identify the role, authority, and timing of agency involvement at the federal (Table [1](#)) and state (Table [2](#)) level in Maine.

Table 1
Role, authority, and timing of involvement of federal agencies in MHK development

Agency	Role	Timing of involvement	Applicable laws and policies
Federal Energy Regulatory Commission (FERC)	<ul style="list-style-type: none"> • Authorizes construction and operation of all non-federal power projects, including hydrokinetic • Issues preliminary, pilot, and commercial licenses • Grants exclusions for hydro projects not connected to grid (Verdant Exclusion) 	Filing of Preliminary Permit application NEPA Analyses	<ul style="list-style-type: none"> • Federal Power Act • Public Utility Regulatory Policies Act • Energy Policy Act • Electric Consumers Protection Act • National Environmental Policy Act
National Marine Fisheries Service (NMFS)	<ul style="list-style-type: none"> • Consultation (informal or formal) with action agencies pursuant to Section 7 of ESA • Issues Biological Opinion to action agency for endangered species • Section 18 Fishway Prescription under FPA 	Pre-application	<ul style="list-style-type: none"> • Magnuson Stevens Conservation Act (Essential Fish Habitat, EFH) • Endangered Species Act • Fish and Wildlife Coordination Act • Federal Power Act • Marine Mammal

Agency	Role	Timing of involvement	Applicable laws and policies
			Protection Act
U.S. Army Corps of Engineers (CORPS)	<ul style="list-style-type: none"> • Consultation with applicant and other agencies • Issues permits for construction activity in navigable waters, including temporary and permanent installations 	Pre-application	<ul style="list-style-type: none"> • Section 10 of Rivers and Harbors Act • Section 404 of the Clean Water Act • Section 103 of the Marine Protection and Sanctuaries Act
U.S. Coast Guard (USCG)	<ul style="list-style-type: none"> • Reviews and provides opinions on impacts to navigation & navigation safety • Provides guidance and federal regulations that may be required • Issues permits for Private Aids to Navigation 	Application filed with FERC and CORPS	<ul style="list-style-type: none"> • Private Aids to Navigation Program (PATON)
U.S. Fish and Wildlife Service (USFWS)	<ul style="list-style-type: none"> • Reviews and provides opinions on impacts to natural resources, primarily birds. • Issues Biological Opinion to FERC for endangered species • Section 18 Fishway Prescription 	Pre-Application	<ul style="list-style-type: none"> • Endangered Species Act • Fish and Wildlife Coordination Act • Federal Power Act • Migratory Bird Treaty Act • Bald & Golden Eagle Protection Act

Table 2
Role, authority, and timing of involvement of state agencies in MHK development

Agency	Role	Timing of involvement	Applicable laws and policies
Department of Environmental Protection (DEP)	<ul style="list-style-type: none"> • Issues water quality certification • Coordinates state agency review and permit under the Maine Waterway Development & Conservation Act 	<ul style="list-style-type: none"> • Development of preapplication document 	<ul style="list-style-type: none"> • Clean Water Act Section 401 (d) • Maine Waterway Development and Conservation Act
Maine Department of Marine Resources (DMR)	<ul style="list-style-type: none"> • Reviews project application and comments on proposed plan and 	<ul style="list-style-type: none"> • Application filed with FERC • May be involved 	<ul style="list-style-type: none"> • Maine Endangered Species Act

Agency	Role	Timing of involvement	Applicable laws and policies
	impacts to trust resources • Participates in joint interagency preapplication meeting with DEP	in consultation in pre-filing • Pre-application • Integrates with DEP permit process	
Maine Department of Inland Fisheries and Wildlife (IF&W)	• Review project application and comments on impacts of proposed plan on trust resources	• Application filed with FERC • May be involved in consultation in pre-filing • Pre-application • Integrates with DEP permit process	• Fish and Wildlife Coordination Act
Maine Department of Conservation (DOC)	• Issues Submerged Lands Lease	• Early in planning process • Pre-application	• Submerged Lands Leasing Program
Maine State Planning Office (SPO)	• Consistency determination with the Coastal Management Program	• Early in planning process • Integrates with DEP permit process	• Coastal Zone Management Act
Maine Historic Preservation Commission	• Determines whether and how a proposed action may affect historic properties • Consults with FERC and Corps on ways to avoid or minimize any adverse affects	• Pre-filing	• National Historic Preservation Act (NHPA)

Interview participants highlighted major laws that structure the decision making process and place power and authority with lead federal and state agencies. Participants viewed the process of MHK development as “primarily driven by the federal agencies” with FERC assuming the lead role. FERC has authority to issue a final licensing decision; however, an array of federal and state agencies (cooperating agencies) have “mandatory conditioning authority” within the FERC process for a particular aspect of tidal energy development under a particular statute (see Tables 1 and 2). In general, the agencies with mandatory conditioning authority were perceived to wield more power in the decision making process (e.g., FERC under the Federal Powers Act; US Army Corps of Engineers under the Rivers and Harbors Act) as opposed to those provided with commenting opportunities (e.g., US Fish and Wildlife Service under the Fish and Wildlife Coordination Act). In the case of the Cobscook Bay Tidal Energy Project, permits from

FERC and CORPS are “critical to whether something gets off the ground or not,” thus these agencies are thought have more influence in the decision making process. However, the laws themselves also shaped the process by determining which agencies play a larger role in decision making. For example, as described by a federal regulator, resource agencies “only get to have that kind of power if we get to a jeopardy call or an adverse modification of critical habitat (under the ESA) otherwise its more recommendations.” This indicates that authority (and thus agencies involved and the laws applied) may shift depending upon the issue on the table. A federal official gave examples. He said: Army Corps leads the way when it comes placing structures in the water. FERC leads the way when it comes to generating electricity, and the Coast Guard leads the way when it comes to obstructing the navigational waterway.

Responsibility may also shift depending on the project and unique characteristics of the site. These factors determine the regulatory pathway in which decisions are made. For example, a federal regulator discussed how, in their agency, the “strength of decision making in the whole process really depends on what type of consultation we are doing.” If it is an informal consultation (few species and no adverse effect), NMFS's decision is “probably not the biggest decision being made in the process.” If there are only minor ESA concerns, NMFS may “fade into the background.” On the other hand, in a formal consultation (finding of adverse effect), NMFS issues a biological opinion with terms and conditions on “take.” A federal regulator sums up their influence:

Depending on the severity of the effect, we can either have a very major role, stop or potentially stop a project, or a very minor role in essentially just saying, we'd like it if you could use BMP's for sedimentation and erosion and work when the fish aren't there.

At the state level, similar trends emerge. Agencies with mandatory conditioning authority (DEP) assume a larger role in the process. According to a state regulator, “There are three decision makers, FERC, Army Corps, and DEP. The other agencies, all the other resource agencies just submit comments.” The Department of Conservation (DOC) and the Maine State Planning Office (SPO), however, submit more than comments. DOC issues a submerged lands lease and SPO makes a decision regarding concurrence or objection to a consistency determination under the Coastal Zone Management Act (Table 2). Not surprisingly, at both the state and federal level, agencies involved with the marine environment play a larger role than agencies with a focus on terrestrial or freshwater habitats. Accordingly, NMFS, USCG, and USFWS were identified as having a “big place at the table,” while “Maine Inland Fisheries and Wildlife probably would not commit a lot of resources to the project process.”

Coordination

Coordination was a dominant theme that emerged in discussions of agency involvement in the regulatory and permitting process. Interview participants spoke of coordination within agencies, interagency coordination, and coordination between agencies and project applicants. Within agency coordination was particularly salient for NMFS. Because NMFS has two divisions, the Habitat Conservation Division that implements the ESA and the Protected Resources Division that takes the lead role on the Federal Powers Act and the Magnuson Stevens Conservation Act, heavy coordination between the two divisions is necessary. Similarly, a FERC regulator spoke of the coordination that is required between the three divisions in his agency—licensing, administration, and compliance, and dam safety. He said, “going through the licensing proceeding, we work

hand in hand with Compliance to ensure that when we issue a license, that the requirements in it make sense to them.”

Interagency coordination and early proactive engagement with developers were also dominant themes. A federal regulator said:

There's a general recognition that federal agencies should work together and if there's a way to facilitate or streamline for energy related projects, we should do it. Doesn't mean we will permit everything that comes through the door, it just means if we can get through the end of a review process in an expedited manner, while meeting our regulations and responsibilities, we should.

FERC and CORPS were identified as two agencies that played a key role in coordinating the regulatory and licensing process for MHK development. A federal regulator said: At the federal level, FERC and the CORPS...all try to bring our various federal partners to the table as early as possible to work cooperatively throughout our various processes to avoid duplication of effort.

Interagency coordination was highlighted by FERC as a critical step to ensure that all agencies understood their role in FERC's licensing process:

We're working as much as we can behind the scenes to try to coordinate with the other federal agencies so that they understand better how they fit in because the goal of our licensing process is to make sure all other agencies have their own statutory needs met under our process as kind of a one stop shop.

Coordination between federal and state agencies was also important. A state regulator explained:

If there's an environmental issue out there that needs to be addressed, not only for DEP but probably for the CORPS too, we coordinate those, so you don't have two meetings on whether or not the noise from driving pilings is going to be a problem for salmon. You have one meeting on that.

By avoiding a duplication of effort, it was thought that agencies could focus their time and the applicant's time as wisely as possible. FERC and DEP tried to work together to coordinate environmental impact analysis meetings in terms of a pre-application document and the types of studies that should be done to assess impacts on fish, seabirds, whales, dolphins, and other concerns. One federal regulator emphasized the need for frequent pre- and post-meeting follow-up to make sure agencies, developers, and other stakeholders are all “on the same page.” Similarly, another federal regulator said:

We interact primarily with the other resource agencies in developing a uniform or similar set of resource issues ... so that one agency doesn't tell them [the developer] one thing, our agency tells them something different. We try to make sure we have a common understanding of the resource issues and present one view to a licensee.

Agency regulators described positive interactions with ORPC and commented on the developer's proactive engagement. One federal regulator said, “...At ORPC, a lot of their principals and project managers...they've all been very good at engaging us early and often.”

Regulatory Change

Federal Regulatory Change

Participants discussed three modifications or adaptations in the regulatory and permitting process at the federal level. One of the changes was the Verdant exclusion. In 2005, FERC issued a declaratory order for a developer, Verdant Power, who was looking to install six hydrokinetic turbines in the East River, New York, without having to get a license from FERC. The Commission found that they could do so “provided that they met the criteria that they would be small, short term, and that they are not to be connected to or displace power from the interstate power grid.” In describing this permitting option, a FERC regulator said: “The purpose of that was really to try to reduce some of the regulatory barriers.”

The second key regulatory change emerging from discussions with regulators and developers was the evolution of the pilot licensing process. Consistently, study participants discussed how the regulatory process in place for MHK projects, prior to the pilot license process, was designed for conventional hydroelectric projects (dams) and did not meet the needs of developers looking to test the economic feasibility of new tidal energy technology. A federal regulator pointed out, “prior to, (the pilot license process), there was no process. The technology was ahead of policy.” Instead, project developers had to go through existing licensing processes to obtain necessary approvals from FERC. A federal regulator with experience in conventional and MHK technology said many developers “felt that those processes were a bit more time consuming, kind of cumbersome, and expensive for these newer technology projects that were quite different than conventional.” As a result, FERC was charged with streamlining the regulatory process and reducing barriers to MHK development. The pilot license process that emerged was designed specific to tidal power to test and monitor new technology. As described by a FERC regulator:

The pilot license is unique to MHK, and that came about, basically...even though we have this Verdant Exclusion available for people to get in the water quickly, theoretically, a lot of the developers, the industry in general, felt like they still need to be able to connect to the grid to really fully test their projects. So the Commission kind of listened. We had a workshop...basically to get information from the industry and stakeholders, trying to find out what the Commission could do to try to reduce barriers and the pilot license is something that kind of came out of that.

As perceived by a project developer, the FERC pilot process was developed to stimulate a domestic renewable ocean energy industry by offering a “permitting path targeted to emerging companies with new technologies.” This process allowed developers to get into the water to test their new devices. Federal regulators also acknowledged the nascent technology and emerging process:

This is a relatively novel process aimed at streamlining some of the hurdles that they [project developers] would’ve ordinarily gone through, because FERC understood that not all these projects could be developed. The preliminary process was really largely designed to give folks, potential developers an opportunity to look at a certain site, at a certain technology, to see if it was economical.

The third change in the regulatory and permitting process was the Strict Scrutiny Policy. This policy emerged in response to concern that “a lot of developers were going and locking up sites with these (preliminary) permits and not really making any progress toward developing a license application.” There is a low bar to get preliminary permits because they do not authorize any activity. There are no National Environmental Policy

Act requirements because there is no ground disturbing, construction, or operation. FERC initially received a large number of permits, but only a very small number of permit holders actually moved into licensing. As described by a FERC regulator, the Strict Scrutiny Policy came about in response to this “flurry of activity in hydrokinetics” as a way to “bring down the numbers” by “making sure that the people who are getting the permits are serious about trying to move forward.” Under the Strict Scrutiny Policy, the applicant is required to file a schedule of activities of what they plan to do under the permit, semiannual progress reports, and then if they are going to be seeking a long-term commercial license or a short-term pilot license, they have to file “kick-off” documents within the first 2 years of the permit. As the FERC regulator said:

Really the thing is with the Strict Scrutiny Policy is we said that we would cancel permits where we’re not actually seeing progress being made, and we have had to do that on a number of occasions.

State Regulatory Change

At the state level, a Memorandum of Understanding (MOU) between FERC and the State of Maine ([2009](#)) institutionalized changes to the federal and state review process for tidal project permit applications. The purpose of the MOU was to “coordinate the procedures and schedules for review of tidal energy projects using hydrokinetic technologies” to ensure that coordinated review is “responsive to environmental, economic, and cultural concerns while providing a timely, stable, and predictable means for developers of such projects to seek necessary regulatory and other approvals” (FERC and State of Maine [2009](#)).

Participants in our study identified the MOU as a key change that added predictability to the process of tidal energy development. For example, they spoke of the commitment by the state to act “much quicker” on Sect. 401 water quality certifications. A state regulator described this process:

We figured out that a little bit of a snag we have is in part of our general rules that deal with processing of all applications. There's a time frame of fifteen working days from when we receive an application to when we have to make a determination whether or not that application is complete. When it comes to the tidal power project, we got caught in an infinite duel up here for a little while. FERC was telling ORPC, you have to submit your state application at the same time you submit your pilot license application with FERC. [DEP] can't deem their general permit application at the state level complete until FERC issues a Finding of No Significant Impact (FONSI)...FERC doesn't issue a FONSI within fifteen days of the initial, application process.

Ultimately, what emerged from efforts to coordinate at the federal and state level was an agreement to suspend the permit application until FERC made a decision. According to a federal regulator, “even though the developer filed proof that they filed an application with the state, the state basically said they were going to hold it in abeyance until FERC issued a FONSI and then they would consider the application.”

Learning by doing: Regulatory changes noted above were discussed within the context of “learning by doing.” This is exemplified by a quote from a FERC regulator who said: As a Commission we’re kind of learning as we’re going along. We’re going to try to do the best we can at adapting as we go. We’re trying to be forward thinking, in terms of what potential unique issues we’ll have with these types of projects, but we do expect

things to continue to adapt. I've seen it just within the pilots, the first two that have come through, some minor modifications or adaptations that we had to make to unique issues. A “learning by doing” approach was based on the assumption that because hydrokinetic devices are a new technology, regulators do not really know what the impacts are or what protective measures should be prescribed until the technology is deployed and monitored. Participants in our study admitted that, at least initially, they knew very little about the regulatory process for MHK development. However, they felt they gained knowledge “in doing” that would be useful in future applications. One state regulator said that he faced a “pretty steep learning curve” in understanding the FERC process, but that he was learning “by making mistakes and doing it.” He said, “I'm getting it. I'm starting to learn.” When asked about his experience and satisfaction with the Cobscook Bay Tidal Energy Project, the regulator said, “Well, I've hoped I made the state part go smooth anyway, because this is the first one, and how often when you do something the first time, do you do it exactly right?” Similarly, a federal official said:

I can tell you that internally lessons learned, hindsight being 20/20, we learned a bunch of things. Mistakes are not the right word here, but our approach would be somewhat different next time. We would take what we learned and be a whole lot more proficient in how we deal with this.

Another official in the same agency echoed this sentiment. He said, “You know, we're learning as we go along. I'm hopeful that we're going to learn enough from the Cobscook Bay project so the next one is going to be very much more streamlined.”

Many spoke of the opportunity to inform the licensing process by learning “in the water.” A federal regulator said:

The pilot process is experimental. It's designed to collect information both on the technical design of the technology but also to address environmental impacts. Our decisions have led to multiple monitoring plans, so in terms of the way this project has been going and hopefully data collection that will inform future projects, this has been very significant.

Similarly, in moving forward as the first in-water hydrokinetic project in the US, ORPC felt that they were “maturing a regulatory pathway.” They viewed their work, in partnership with the University of Maine, as “blazing the trail” by setting standards for environmental monitoring.

Much like we're pioneering technology we're pioneering the permitting process. Because it's new, and while there is a process that exists, different elements of it are somewhere undefined, and we're defining it as we get to it.

Challenges

Four key challenges to the MHK permitting and regulatory process emerged from our analysis as follows: (1) knowledge gaps and uncertainties, (2) long timeframes and high financial costs of baseline data collection, (3) timing of agency involvement, and (4) conflicting agency cultures.

Knowledge Gaps

References to “limited information” and “uncertain” or “unknown” environmental impacts of new hydrokinetic technology consistently emerged from our interview transcripts and field notes from observations, meetings, and informal discussions. Our

data also showed widespread agreement that, in contrast to conventional hydropower, there is limited environmental information to inform MHK permitting decisions. Similar to conventional hydropower project licensing, resource agencies must use the best available science to determine whether a tidal project will adversely affect a species. In the case of MHK development, however, regulators have limited scientific data with which to base their decision on. A federal regulator noted:

If we had the general sorts of studies like in a hydropower project...what sorts of impacts would accrue to resident fish that live in the reservoir, to migratory fish that move downstream as juveniles or must get upstream, past the dam—without ever having done a study of the project or a proposed project, we could say with some certainty, what the sorts of impacts were going to be. It's only a matter of finding the specifics of that site. We can't do that with hydrokinetic. We don't know the relative impact of those in a generic sense on the resources so our regulatory job is made much more difficult. Our study identified information needs that agencies, developers, and other stakeholders thought should be addressed related to tidal energy development. Overwhelmingly, our data showed that impacts to marine resources were a significant concern and a major data gap. As a federal regulator pointed out, “at the very early stages of this, there wasn't a lot of information, there were thoughts that the interactions (of the turbine) with marine species, wouldn't necessarily lead to injury or death, but there wasn't a lot of data supporting that.”

Direct and indirect impacts to fish topped the list of concerns. A federal regulator said, “The big question that always jumps out is: what are the interactions between the fish present and the technology being deployed?” Resource agencies wondered whether fish would avoid the turbines or be attracted to them. If fish swam through them, would they get disoriented, injured, or killed if struck by a turbine blade? State regulators also wondered whether turbines would affect fish migration, or serve as a magnet for predatory species. Aside from fish species such as herring and salmon, there was significant concern regarding impacts to other marine resources, specifically birds (e.g., diving ducks and eagles) and marine mammals.

Resource and regulatory agencies were also concerned about impacts to abiotic resources. For example, regulatory and resource agencies were concerned about whether the installation of the structures would affect water flow or tidal regimes. They were also concerned about physical disturbances to the environment such as impacts to the substrate. Other issues identified included the electromagnetic field effect around buried transmission cables and water quality concerns.

Agency personnel and project developers were concerned about the lack of site-specific information, ranging from area circulation models to data on local use of navigable waterways. They considered this information critical for characterizing the proposed tidal energy site. Speaking to this, an ORPC developer said:

A lot of the site information in this area is not really readily available on any coastal atlas, any kind of data portal that might be available, so we've had to kind of create our own database.

To fill this data gap, ORPC is working with “all those people that have buoys in different areas, different eyes in the water” to obtain site-specific information. Another site-specific information gap we noted was information on local marine uses. Specifically, the USCG expressed a need to better understand traffic patterns, including information on

types of vessels, frequency of transit, and types of activities those vessels were involved with. One official said, “I can tell you for Cobscook Bay that was difficult to find.” The USCG has two automated systems to determine traffic. The first one is called AIS or automated identification system and a second system for commercial fishing boats is called VMS or vessel monitoring system. VMS, often referred to by fishermen as an “electronic ankle bracelet,” manages the fisheries by knowing where the boats are and what they are doing. The USCG official explained:

VMS, it shows where they are and it shows how fast they're going and because you can't trawl very fast and you normally transmit faster than you trawl, you can kind of infer some activities just based on speed.

Although these two data systems are in place, they are not effective for documenting traffic patterns in remote areas such as Eastport, ME. With regards to the Cobscook Bay Tidal Energy Project, the USCG official said:

I got zero AIS hits and zero VMS hits in that area. So, there's no way to characterize the traffic and that's going to have a big impact on the stakeholders. If you wanted to describe all the stakeholders, those two tools can't be used.

So instead of an electronic information system that systematically records marine traffic, USCG had to rely on anecdotal information from a local law enforcement officer to characterize the waterway based on the number of scallop draggers or lobstermen who fish Cobscook Bay during various seasons.

Long Timeframes and High Financial Costs

Hydrokinetic projects are complex and take considerable time. As one state regulator described, the long-timeframe for the Cobscook Bay Tidal Energy Project, he said: “They haven't even built anything yet. That's just five years pushing paper around and collecting some information.” High cost associated with information needs of an experimental approach is also a significant challenge. Under their statutory authority, agencies require the collection of baseline information during the licensing process. As a regulator explained, “under the pilot licensing process, more study is required during the timeframe that the project is out there (in the water).” These studies, however, are capital intensive, and ORPC developers point out that there are few available funding sources to support that work. Moreover, from ORPC's perspective, “the baseline information that the agencies want has no direct relationship to the turbine in the water, and the impact of marine life with the turbine.” Thus, they question whether they should be asked to conduct the same types of studies and baseline analysis required of more conventional dam project proposals. An ORPC developer thought the agencies should provide these data “so that developers don't necessarily have to spend as much time, money, and effort on collecting data to satisfy those agencies.”

Timing of Involvement

As previously noted, agency representatives we interviewed commented that ORPC engaged them early and often. However, there was the perception by one federal agency that they were not brought into the process early enough. An official from one of the regional offices of this agency said:

We would look for a great deal more guidance, in terms of how we can collaborate together to determine exactly what the impact is and get to the bottom of things like the navigational safety plan. When they (ORPC) came to us and said “Hey, we are thinking

about this,” it was already full steam ahead. My point is that we need to be a bit more unified.

Learning from this experience, the official commented that in the future, “one of the things that we would do is get on board immediately, for example with the Army Corps of Engineers and make sure we are more connected with them and FERC.” Rather than wait to learn about the project after it had already gained momentum, the agency would seek more proactive collaboration.

Conflicting Agency Cultures

We noted tensions between the new pilot licensing process and an agency's traditional standard operating procedures. An ORPC developer said:

The pilot project process is geared to support, innovation. The resource agencies hate innovation. They want “knowns.” And, you know, stable outcomes, and ongoing regular operations as opposed to something that's experimental. And if it's experimental, it needs to be a situation that has been thoroughly vetted and then published in the right literature... which could take years.

In working with the agencies to address risk and uncertainty, ORPC found that some agency personnel were more receptive to change than others. Some were “problem solvers” who understood that the technology and process of MHK development was different than conventional hydropower possibly requiring a different approach. Others were “problem identifiers” who attempted to force the new industry into the existing regulatory structure. As one (ORPC) developer said:

Some of the agency personnel, what they are doing runs counter a little bit to how their agency has done business. So, we've got to work with the agencies so that they don't feel at risk, that we are not asking them to do something that they feel they can't do.

From their perspective, moving the permit process forward was “a constant negotiation process” to find a balance between testing new technology while safeguarding the environment. ORPC stressed that they will continue to be open with their information, keep the agencies updated on a regular basis, and try to work with agency personnel “in a way that helps them maneuver through that gauntlet internally” and “help get this done the right way.”

Discussion

In our research on the Cobscook Bay Tidal Energy Project, we identified key components of an adaptive management approach. We also identified institutional challenges that may affect adaptive management. Here, we consider favorable and “vulnerable” institutional factors (Lee [1993](#)) emerging from the Cobscook Bay case to demonstrate the viability of using adaptive management as a strategy for the responsible development of tidal power. First, we found that decision makers in our study encouraged learning from experience. There was the perception among those interviewed that feedback from monitoring and evaluation could be used to improve decision making. Decision makers recognized that a number of studies were needed to fill knowledge gaps and uncertainties related to hydrokinetics, particularly turbine resource interactions. However, there was also widespread recognition that the only way to determine the feasibility and effects of hydrokinetic projects was to “learn by doing.” In effect, this created a “chicken and egg problem.” As described by Anderson et al. ([2007](#)), a “chicken and egg” situation occurs

because regulators need to understand potential impacts before allowing technology to be deployed on a commercial scale, but some level of deployment is necessary to better understand those potential impacts. Because an adaptive approach favors action (Lee [1993](#)), it may offer a way forward. In the Cobscook Bay case, favorable institutional arrangements allowed for in situ evaluation of pilot (demonstration) projects. The pilot process is an approach that enables experimentation and learning to take place so adjustments can then be made to project design, operation, and licensing.

Second, an adaptive approach offers choices by instituting a plan to correct avoidable error (Lee [1993](#)). Regulatory policies for hydrokinetic energy are structured to avoid unacceptable risk to the local marine environment. By limiting the scope of new MHK projects, the pilot process reduces the risk for regulatory agencies charged with protecting natural resources in the public interest. Instead, regulators have the choice to stop and remove a project with the site restored if the impacts prove too high. As Lee ([1993](#), 64) notes, “This discretion is the key to the political feasibility of an adaptive policy.” While pilot licensing guidelines provide a favorable institutional arrangement, however, laws such as the ESA could significantly impact the ability to implement an adaptive management strategy, especially in an experimental context. If an endangered species is placed in jeopardy, for example, there is a limit to the use of adaptive management.

Third, our study showed that adaptive management experiments are applied not just to the resource (e.g., examination of fish turbine interactions and technological changes), but also to the institutions themselves (Johnson [1999](#)). In our study, an institutional factor favorable to adaptive management was the strong commitment to coordinate federal and state permitting activities. From a decision making perspective, adaptive management crosses jurisdictional boundaries (Lee [1993](#)), making interagency cooperation essential. Improved coordination between FERC and DEP was as an important institutional change that reduced redundancies and resolved timing issues that caused friction between state and federal processes. These changes resulted in a more expeditious and streamlined permit application review process that allowed hydrokinetic projects to get in the water faster, while still ensuring proper environmental safeguards. Additional changes will continue to occur as agencies push for earlier and more proactive engagement.

Fourth, early and proactive engagement with project developers offered a strategy to deal with risk and uncertainty. Given the high level of scientific uncertainty involved in MHK development and the sheer number of studies that could be required of an applicant, early and frequent meetings between applicants and agencies emerged as critically important. Ideally, proactive engagement could help identify what the information needs are, what information is already available, and allow various agencies to weigh in on the types of studies really necessary for a given project site. This approach is a constant negotiation process that requires patience, a key characteristic of adaptive management as identified by Lee ([1993](#)).

Lastly, our study highlighted “institutional vulnerabilities” (Lee [1993](#)) that may hamper the application of an adaptive management approach, namely high financial costs associated with baseline studies and conflicting agency cultures. Collecting baseline biophysical data over multiple seasons is required to adequately characterize a proposed tidal energy site. However, knowledge accumulates slowly, and the process is cost intensive. At the same time, industry needs to continue to show progress to attract investors. Furthermore, constraining the hydrokinetic industry is conflicting agency

cultures. Regulators want “knowns” (e.g., data on resource turbine interactions) before making decisions on permit applications. This may make innovative regulatory change difficult to accomplish within the framework of traditional agency decision making structures.

Tidal energy development is characterized by high scientific and economic uncertainty, and in this context, an adaptive approach makes sense. However, if institutional conditions do not support efficient learning from experience, adaptive management may fail to produce effective action. Drawing on the factors that favor and affect adaptive management, we recognize that there are still many questions that need to be answered before regulators can “feel really comfortable” with tidal power. However, information produced through experimentation and social learning can be used to guide management and inform the future development of new renewable ocean energy technology. Although we focus on a specific case of hydrokinetic energy development, lessons learned in the regulatory and permitting process for the Cobscook Bay Tidal Energy Project are widely applicable to ocean energy projects within Maine and beyond. Lessons learned from our study of tidal energy development in Maine can assist regulators, policymakers, and project developers design, and implement an actively adaptive management approach that can move new renewable ocean energy development forward in a way that is socially acceptable and environmentally responsible.

Acknowledgments

This research was supported by the National Science Foundation award EPS-0904155 to Maine EPSCoR Sustainability Solutions Initiative at the University of Maine. The authors would like to thank the biologists, regulators, and developers for generously sharing their time and perspectives on the process of tidal energy development.

References

- Anderson, F., G. Achterman, S. Padula, and M. Harte. 2007. A programmatic approach to wave energy planning: Opportunities for the Oregon Wave Energy Trust. Proceedings of Coastal Zone 07 Portland Oregon (July 22–26, 2007).
- Bedard, R., M. Previsic, G. Hagerman, B. Polagye, W. Musial, J. Klure, A. von Jouanne, U. Mathur, C. Collar, C. Hopper, and S. Amsden. 2007. North American ocean energy status- March 2007. Electric Power Research Institute (EPRI) Tidal Power (TP); Volume 8, 2007.
- Boehlert, G.W., and A.B. Gill. 2010. Environmental and ecological effects of ocean renewable energy development: a current synthesis. *Oceanography* 23(2): 68–81.[CrossRef](#)
- Bornholdt, M. 2012. Ocean renewable energy from a national perspective. Danvers, MA: Energy Ocean Conference 2012. June 19–21, 2012.
- Brooks, D.A. 2004. Modeling tidal circulation and exchange in Cobscook Bay, Maine. *Northeastern Naturalist* 11(2): 23–50.[CrossRef](#)
- Cada, G., J. Ahlgrimm, M. Bahleda, T. Bigford, S.D. Stavrakas, D. Hall, R. Moursund, and M. Sale. 2007. Potential impacts of hydrokinetic and wave energy conversion technologies on aquatic environments. *Fisheries* 32: 174–181.[CrossRef](#)
- Cada, G.F., A.E. Copping, and J. Roberts. 2012. Ocean/tidal/stream power: Identifying how marine and hydrokinetic devices affect aquatic environments. Hyrdoworld.com [Accessed June 10, 2012].

Campbell, H.V. 2009/2010. A rising tide: Wave energy in the United States and Scotland. *Sea Grant Law and Policy Journal* 2(2): 29–48.

EPRI. 2005. Ocean tidal and wave energy, renewable energy technical assessment guide—TAG-RE (2005). Palo Alto, CA: Electric Power Research Institute. 2005. 1010489.

FERC. 2008. Federal Energy Regulatory Commission Licensing Hydrokinetic Pilot Projects
http://www.ferc.gov/industries/hydropower/geninfo/licensing/hydrokinetics/pdf/white_paper.pdf (issued April 14, 2008).

FERC. 2012. Ocean Renewable Power Company: Order issuing pilot project license (Minor Project), Cobscook Bay Tidal Energy Project Project No. 12711–005 (February 27, 2012).

Glaser, B.G., and A.L. Strauss. 1967. *The discovery of grounded theory: strategies for qualitative research*. Chicago, IL: Aldine.

Goundar, J.N., and M.R. Ahmed. 2013. Design of a horizontal axis tidal current turbine. *Applied Energy* 111: 161–174.[CrossRef](#)

Griset, T.J. 2010. Harnessing the ocean's power: opportunities in renewable ocean energy resources. *Ocean and Coastal Law Journal* 16(2): 151–190.

Gunderson, L. 1999. Resilience, flexibility, adaptive management – antidotes for spurious certitude? *Conservation Ecology* 3(1): 7. [online] URL: <http://www.consecol.org/vol3/iis1/art7>.

Halbert, C.L. 1993. How adaptive is adaptive management? Implementing adaptive management in Washington State and British Columbia. *Reviews in Fisheries Science* 1(3): 261–283.[CrossRef](#)

Holling, C.S. 1978. *Adaptive environmental assessment and management*. London, UK: John Wiley.

Jacobson, M.Z., and C.L. Archer. 2012. Saturation wind power potential and its implications for wind energy. *Proceedings of the National Academy of Sciences* 109(39): 15679–15684.[CrossRef](#)

Johnson, B.L. 1999. Introduction to the special feature: Adaptive management – scientifically sound, socially challenged? *Conservation Ecology* 3(1): 10. [online] URL: <http://www.consecol.org/vol3/iis1/art10/>.

Konnert, T. 2010. The role of the Federal Energy Regulatory Commission in authorizing hydrokinetic technology projects. *Oceanography* 23(2): 54–59.[CrossRef](#)

Leary, D., and M. Esteban. 2009. Climate change and renewable energy from the ocean and tides: calming the sea of regulatory uncertainty. *The International Journal of Marine and Coastal Law* 24: 617–651.[CrossRef](#)

Lee, K.N. 1993. *Compass and gyroscope: integrating science and politics for the environment*. Washington, D.C.: Island Press.

Marvel, K., B. Kravitz, and K. Caldeira. 2013. Geophysical limits to global wind power. *Nature Climate Change* 3: 118–121.[CrossRef](#)

Merriam, S.B. 2009. *Qualitative research: a guide to design and implementation*. San Francisco, CA: Wiley.

Ocean Energy Task Force (OETF). 2009. Final report of the Ocean Energy Task Force to Governor John E. Baldacci. Augusta, Maine.

www.maine.gov/spo/specialprojects/OETF/Documents/finalreport_123109.pdf

[Accessed May 24, 2012].

Oram, C., and C. Marriott. 2010. Using adaptive management to resolve uncertainties for wave and tidal energy projects. *Oceanography* 23(2): 92–97.[CrossRef](#)

Pelc, R., and R.M. Fujita. 2002. Renewable energy from the ocean. *Marine Policy* 26: 471–479.[CrossRef](#)

Strauss, A.C., and J.M. Corbin. 1990. *Basics of qualitative research: grounded theory procedures and techniques*. Thousand Oaks, CA: Sage Publications.

United States Federal Regulatory Commission and State of Maine. 2009 Memorandum of Understanding (August 2009), <http://www.ferc.gov/legal/maj-ord-reg/mou/mou-ma.pdf>.

Viehman, H., G.B. Zydlewski. 2012b. Fish interactions with a commercial-scale tidal energy device in the natural environment. *Estuaries and Coasts*. (THIS ISSUE).

Viehman, H., G.B. Zydlewski, J.D. McCleave, G. Staines. 2012a. Using acoustics to understand fish presence and vertical distribution in a tidally dynamic region targeted for energy extraction. *Estuaries and Coasts*. (THIS ISSUE).

Walters, C.J. 1986. *Adaptive management of renewable resources*. New York, NY: McGraw-Hill.

Walters, C.J., and C.S. Holling. 1990. Large-scale management experiments and learning by doing. *Ecology* 71(6): 2060–2068.[CrossRef](#)

Wellinghoff, J., J. Pederson, and D.L. Morenoff. 2008. Facilitating hydrokinetic energy development through regulatory innovation. *Energy Law Journal* 29: 397–42.

Appendix Task 4-3

Maine Policy Review

Volume 21

Issue 1 *Sustainability*

2012

Research for the Sustainable Development of Tidal Power in Maine

Teresa Johnson

University of Maine, teresa.johnson@maine.edu

Gayle B. Zydlewski

University of Maine

Follow this and additional works at: <http://digitalcommons.library.umaine.edu/mpr>



Part of the [Community-based Research Commons](#), [Community Engagement Commons](#),
[Energy](#)

[Policy Commons](#), and the [Power and Energy Commons](#)

Recommended Citation

Johnson, Teresa, and Gayle B. Zydlewski. "Research for the Sustainable Development of Tidal Power in Maine." *Maine Policy Review* 21.1 (2012) : 58 -65, <http://digitalcommons.library.umaine.edu/mpr/vol21/iss1/10>.

Research
for



the Sustainable Development of Tidal Power in Maine

by Teresa Johnson Gayle B.
Zydlewski

Generating electricity from Maine's substantial tides has been a dream for generations. Today, as Teresa Johnson and Gayle Zydlewski describe, the state is poised for a new era in sustainable tidal-power development. A pilot project is already underway in the Cobscook Bay/Western Passage area near Eastport and Lubec. Tidal-power development presents technical, environmental, and social challenges, however, and

ors discuss how the Maine Tidal Power Initiative is working to develop a cooperative framework that integrates stakeholders, developers, and policymakers to tackle some of these challenges. [?](#)

INTRODUCTION

Sustainable energy futures will require a diversified portfolio of alternatives (Bosetti et al. 2009; IEA 2010) that are carbon-free and environmentally

acceptable. The energy crisis of 2008 brought to the forefront Maine's dependence on natural gas and other fossil fuels for home heating and transportation and pointed to the need to reduce this dependence to protect the economic well-being of the state. Currently, Maine's electric generation capacity is

dependent (~60%) on natural gas, oil, and coal, none of which is indigenous to the state (OETF 2009). With the need to make serious choices about its energy future, the state of Maine considered its renewable portfolio standards in 2009 and decided to include a focus on the potential for ocean energy resources. The state enacted legislation to aggressively pursue a multifaceted strategy to diversify its energy portfolio with a variety of indigenous resources, committing to prepare for offshore wind, tidal, and wave power. While the technology for offshore ocean wind energy remains decades away, tidal power is currently feasible at the small-scale level, and commercial technologies are developing rapidly. The need to sustain the Gulf of Maine's biological resources and existing marine uses while pursuing energy resources was a priority for the Governor's Ocean Energy Task Force (OETF). As such, one of the six subcommittees of the task force considered natural resources and human uses of the marine environment as potential challenges for ocean energy development and aimed to identify the best path forward to guide decision making about this new technology. Two of the largest challenges identified were the lack of knowledge about our ocean resources (baseline information) and the interaction of ocean energy development with other uses of the marine environment. The task force recognized the need to identify, manage, and resolve potential conflicts through early consultation and collaboration. A shared understanding of the proposed

technology, how and where it would be deployed, and related cost considerations were recognized as critical components of the discussion.

Much uncertainty still exists concerning the risks and benefits of developing ocean energy (see the urgent

Tidal-power devel-

call for research by Inger et al.

2009). Marine hydro-kinetic (MHK) energy captured from tides, also called tidal power, is carbon-free, but environmental

impacts of MHK devices remain uncertain. Furthermore, power

generation from the tides is restricted to areas of the globe

that have tidal currents fast

enough to generate power, e.g., peak currents of $>2 \text{ m s}^{-1}$

based hydropower.

(or four knots) in areas with semidiurnal tides (Polagye et al. 2011). Areas in the

United States with sufficient tidal energy include the Gulf of Maine, Puget Sound,

and Cook Inlet, Alaska. Tidal-power

developers have targeted these areas for innovative design and deployment.

The major challenges and uncertainties related to tidal-power development

include, but are not limited to, assessing environmental impacts, resource

availability, technology efficiencies, community acceptance, and social-

economic impacts. Tidal-power development involves complex

interactions among biophysical and social systems, along with the intersection of the

emerging technological components with the biophysical and social. Understanding

the implications of these interactions is

opment is new and

presents a different

suite of potential

effects than does

conventional river-

peak currents of $>2 \text{ m}$

necessary for decision making and moving this technology forward in a responsible way. Regulators and developers must balance the uncertain consequences to marine resources and the environment in their decisions for advancing this industry. Tidalpower development is new and presents a different suite of potential effects than does conventional riverbased hydropower. For this reason, federal and state agencies are taking a cautious approach, requiring rigorous environmental research and monitoring before approving permits. Entities proposing tidal-power development need assessments of potential environmental effects and impacts to obtain permits for pilotscale deployments. They also need to monitor effects of pilot deployments to obtain licensing for commercialscale deployments. At the intersection of biological resources and community acceptance are fish communities and the human communities that depend on them. Local communities are concerned about potential detrimental effects on their current uses of the marine environment, e.g., disruption of fishing activities or degradation of fish populations. Maine's marine resources are

important to its people, culturally and economically. Maine's working waterfronts generate more than \$740 million in income and support more than 26,000 jobs (Sheehan and Cowperthwaite 2004).

In this article, we present our integrated, stakeholder-driven research approach aimed to promote the sustainable development of tidal power. To illustrate the effort being developed by the Maine Tidal Power Initiative and Maine's Sustainability Solutions Initiative (SSI), we focus here on the integration between the human dimensions and biological research.



MAINE TIDAL POWER INITIATIVE

In response to the growing demand for knowledge necessary to develop tidal energy, an interdisciplinary team of engineers, biologists, oceanographers, and social scientists from the University of Maine and the Maine Maritime Academy are collaborating with tidal-power developers and state and federal regulators to promote the responsible development of tidal/marine hydrokinetic (MHK) energy. Organized as the Maine Tidal Power Initiative (MTPI), this group is developing a cooperative tidal-energy-development framework that integrates

stakeholders, developers, and policymakers in environmentally sensitive, multi-use coastal communities. Although our work is focused primarily on the efforts in eastern Maine, we are also working with several smaller sites that are in earlier stages of development.

Vital to the MTPI framework is the importance of tailoring to the local social and ecological conditions of each renewable energy site and how energy resource development may be guided by principles that ensure broad, sustainable benefits to all citizens. These principles must be rooted in a solid understanding of the natural environment, state-of-the-art and well-suited technologies, sound economic returns, and broad social acceptance. Although the work of the MTPI will be transferrable throughout Maine and the U.S., our sitespecific work is focused currently on Cobscook Bay/Western Passage near Eastport and Lubec, Maine, possibly the most viable commercial tidal energy site in the U.S. The team is investigating the potential for additional MHK deployment locations in Maine.

Taking SSI's sustainability science approach, which recognizes that responsible tidal-energy development, requires developing linkages and capturing feedback between social, engineering, and biophysical systems, MTPI brings together multiple disciplines and integrated research components. MTPI's seafloor geomechanics team is researching solutions and options for efficient and robust foundations for both

fixed-bottom and floating tidal-energy devices. Using local information about sediment types, they are considering the complex lateral loading from currents and scour and sediment transport around foundations using experimental modeling.

The resource assessment team is researching the commonality and uniqueness of targeted MHK developments worldwide. Water current data collected at specific sites are used with modeling methods to assess MHK tidal resources, documenting the accuracy and uncertainties associated with different methods, and assessing the impacts of energy extraction on hydrodynamics.

The turbine engineering team focuses on characterizing baseline MHK systems to provide industry benchmarks to evaluate and compare emerging turbine technology with regard to energy-extraction performance. This focus includes the laboratory design and testing of standard turbine types and the development of experimentally validated design codes to assist the design of new turbines.

The fish assessment study team uses innovative field methods to determine the effects of MHK devices on fish, particularly their behavior and water column distribution. Multiple gear types and approaches are deployed at potential tidal project and control sites to develop models and protocols that allow industry, management agencies, and stakeholders to make informed decisions.

With funding from SSI, the human dimensions research team is engaging local groups and individuals to investigate factors that influence public support. By doing this they are identifying effective and efficient engagement practices that allow stakeholders to shape the direction of research on MHK device development and make informed decisions about MHK development in their communities and beyond, while at the same time

improving the use of research in future energy policy making.

IDENTIFICATION OF INDUSTRY AND REGULATORY NEEDS

The fish assessment study team of MTPI has been stakeholder driven from the beginning. While formulating plans for tidal-device development and deployment in Eastport, the Ocean Renewable Power Company (ORPC) identified the need to consider the potential impacts of their activities on fishes, from both a technical and permitting perspective. Mechanical engineering colleagues at the University of Maine pointed ORPC in the direction of the School of Marine Sciences where there existed interest and expertise to help. With funding from the U.S. Department of Energy, within the newly formed MTPI, the fish assessment study team began identifying approaches to address the highest priority questions concerning fish interactions and responses to proposed ORPC devices. Although ORPC started discussing permitting requirements with the Federal Energy Regulatory Commission, they had not yet started discussions with state natural resource regulatory staff charged with making decisions regarding deployment. Recognizing the difference between conventional hydropower devices and the open design of ORPC, the fish assessment study team designed a scientific approach (within budgetary

constraints) to understand these basic questions:

- How do fish interact with an open design tidal device?
- Where and when are fish in the water column (particularly at the deployment depth of the device)?
- How does the tidal device affect fish distribution in the water column?

Methods included using sound to document fish distribution in the water column at all tidal stages, over multiple seasons at two sites (the planned deployment site and a control site), before and after a device would be deployed. The objective was to document the spatial and temporal changes in fish distribution in the region of a deployment of atidal device.

University of Maine scientists attended multiple meetings among ORPC and state and federal regulatory agencies (Department of Marine Resources, Department of Environmental Protection, Department of Conservation, Department of Inland Fisheries and Wildlife, U.S. Fish and Wildlife Service, and the National Oceanic and Atmospheric Administration). The MTPI fish assessment study team's approach to assessing tidal devices was discussed and adjusted to address the questions of the regulatory agencies. For example, all agencies agreed that low fish abundance in the winter months could not be assumed and that information on fish presence and distribution would need to be collected year round. The team worked with ORPC to identify and secure funding to conduct sampling during all seasons rather than only the seasons that were expected to have high abundance of fishes. In these meetings, regulators raised concerns about larger scale impacts. While the planned research would provide site-specific information about fish distribution in two locations, there was a question

about fish presence and distribution in areas that were in the bay but not near the turbine (we call these “far-field” effects). Since little is known about fishes of Cobscook Bay, we needed to understand fish communities of the bay before one (or an array of) tidal devices would be deployed. Again, ORPC asked our fish assessment study team for an approach to this question and worked to secure funds to address the questions of bay-wide fish community impacts. Research began in spring 2011.

BOOTS ON THE GROUND: IDENTIFICATION OF COMMUNITY NEEDS

As stated earlier, there is a complex interplay of the biological (fish) community and local human community needs. Therefore, we initiated a study to understand the Eastport and Lubec community perceptions about the state of tidal-power development in the region. To facilitate this, we partnered with the Cobscook Bay Resource Center and the University of Maine Sea Grant and Cooperative Extension to identify stakeholder concerns and experiences related to tidal-energy development in eastern Maine. We were concerned with the community’s broad perceptions and experiences related to tidal power. Not surprisingly, we were also interested to understand the work of the ORPC because it is currently the tidal project that is furthest along in this region and the Ocean Energy Task Force identified it as a community-based engagement model. With our research partners, we set out to interview individuals in the community to

ensure our research was informed by a diversity of stakeholder perspectives. We interviewed a total of 38 individuals representing a wide range of stakeholders from the communities around the Cobscook Bay. The majority of the stakeholder interviews were not recorded, but detailed notes were taken and then analyzed to better understand perceptions and attitudes about on-going stakeholder engagement efforts in the community, perceptions of potential positive and negative impacts, questions or concerns about tidal-power research, and familiarity with MTPI researchers and their research. Community members were interested to learn more about tidal-power development; the majority of respondents interviewed (71 percent) stated that there were some aspects of tidal power that they would like to know more about. When asked what they would like to know more about, most expressed having questions about environmental impacts (including impacts to fish and other fauna) and issues related to tidal-power technology (including questions about the specific models being tested in the area, those available globally, and the ability of these devices to produce power). Other questions centered on uncertainties about the potential energy and economic benefits that tidal power may provide. We found similar results when we asked stakeholders specifically what they thought researchers should be studying. Understanding environmental impacts topped the list of what researchers should be studying related to tidal power. More interestingly, however, was that 70 percent of respondents reported that they did not know what University of Maine researchers were studying related to tidal power. As one informant noted: “We know they are studying ...we don’t know what they are doing.” This suggested to us an opportunity to do a better job communicating our research in the community. Fortunately, stakeholders provided valuable recommendations for how to better share our

findings with the community. Most people identified public meetings as an appropriate forum, including formal briefings to stakeholders and public officials. Other more informal communication strategies were also suggested, such as face-to-face meetings and community gatherings. Respondents also recommended we write short articles in the local and state newspapers, such as the *Quoddy Tides* and the *Bangor Daily News*, and provide information through a public website.

In addition to these suggestions for where to communicate our results, we received valuable suggestions about how we should communicate (i.e., style). Most recommended that we be sure to communicate the results to a broader, nonscientific audience; for example, one individual expressed the importance of communicating publically funded research in a way that the public can understand: “Publically funded research needs to be passed to the public in such a way that their eyes don’t glaze over.” Similarly, another respondent explained:

maybe seeing those reports or a non-techno version of those reports in layman’s terms to explain what they are doing and how they are doing it, and what they are collecting, and what they are finding out, and even the questions they are asking and the answers they are finding....

Others emphasized the need to disseminate the information broadly and informally to the local community:

Boots on the ground is the best way. People associated with the project talking directly to

people....The information can’t just be given to a select few because they may not spread the word....Just talk directly with people like at coffee shops and bars. That’s how information is delivered locally.

It is interesting to note that many of the suggestions we received are not unlike the way stakeholders describe the approach that ORPC used in getting the word out about their project. One respondent suggested we might follow a similar approach:


The way it’s been done so far by ORPC is a collaborative effort and that is good. You have to talk to local people on their level. Local people need to be made comfortable.

We intend to make use of these and other valuable suggestions as we move forward with our research in hopes of achieving the broad goal of improving the linkages between knowledge and action. For example, we have already developed a website for sharing our work with the public (<http://umaine.edu/mtpi/overview/>).

FINDING FISH: RESPONDING TO COMMUNITY CONCERNS

Armed with the knowledge of what community members wanted to know and how they wanted to receive information, we decided to tailor our research on the impacts to the bay-wide fish community (requested by the local regulatory agencies) to involve community members, particularly fishermen, more directly. Because we want to better understand the fish community in Cobscook Bay, a logical start to the study was to use local knowledge. We discussed our knowledge gap and needs with local fishermen and identified a place-based approach to achieving our goal of engaging with the fishing community in a two-way exchange of information about the fishes of Cobscook Bay. Our plan was to gather their knowledge to determine sampling locations and they would receive information from us regarding

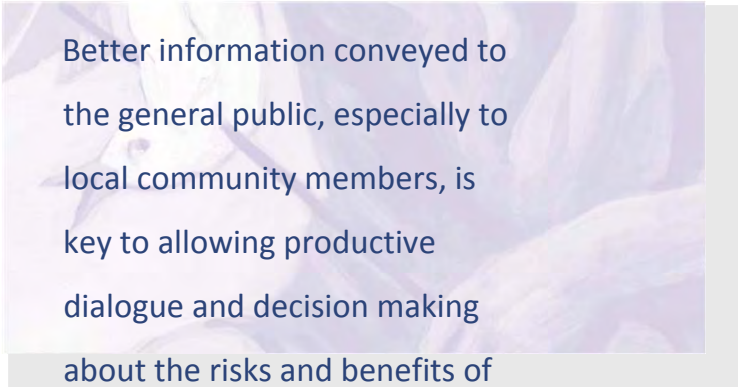
the fish in their backyard. Following recommendations from our community interviews, we organized a local meeting, sending invitations with hand-written notes to key individuals and advertising the meeting in the local paper, the *Quoddy Tides*, as had been suggested to us. A total of 13 people attended our meeting and provided suggestions and details on sites to sample. To facilitate two-way communication, we spent most of the meeting working in small groups, discussing the kinds of fish we would likely find in different parts of the bay and how we would or would not likely find them depending on when and how we sampled. The conversations were invaluable; we were able to modify our research design to improve the success of our effort. Keeping with the stakeholder-engagement model, we plan to return to the community in the winter to present the findings from our first year of sampling and solicit additional feedback about our approach as we move forward.

Following SSI's approach, we are working with federal and state regulatory agencies, tidal-power developers, and community stakeholders to better link our research to their needs. By engaging the users of the information we are being asked to provide, we are improving the chances that our research results will be more relevant to the decision-making processes that our stakeholders face, whether the stakeholder are developers interested to know if they should bother to develop in a location or regulators who need to make decisions about these projects on behalf of the public. Better information conveyed to the general public, especially to local community members, is key to allowing productive dialogue and decision making about the risks and benefits of tidal power. 



ACKNOWLEDGMENTS

Supported by National Science Foundation award #EPS0904155 to Maine EPSCoR at the University of Maine.



Better information conveyed to the general public, especially to local community members, is key to allowing productive dialogue and decision making about the risks and benefits of tidal power.

Teresa Johnson is an assistant professor in the School of Marine Sciences at the University of Maine. Her research focuses on marine fisheries management, social and ecological change in fishing communities, and stakeholder-driven collaborative research. She leads the human dimensions research team on tidal power development in the Maine Sustainability Solutions Initiative and the Maine Tidal Power Initiative.



Gayle B. Zydlewski is a research associate professor of marine sciences at the University of Maine. She studies migratory and marine fish and fish communities of Maine. Her current research focuses on how human-induced changes, such as river restoration and tidal power development, affect individual fish, fish populations, and the structure of fish communities.



REFERENCES

Bosetti, Valentina, Carlo Carraro, Emanuele Massetti, Alessandra Sgobbi, and Massimo Tavoni. 2009. "Optimal Energy Investment and R&D Strategies to Stabilize Atmospheric Greenhouse Gas Concentrations." *Resource and Energy Economics* 31:123–137.

Top 10 Ways SSI Is Using Tools to Work across Disciplinary Boundaries

Models: Using coupled social-ecological-economic simulations to understand, predict, protect, and enhance Maine's unique heritage, such as

- Social network analysis
- Bayesian belief networks and future scenarios
- Agent-based modeling
- Species-niche modeling
- Mediated modeling and participatory mapping
- Water-flow models

Social science methods: Using mixed-methods (quantitative and qualitative) to understand, predict, protect, and enhance Maine's heritage, such as

- Participant observations
- Targeted focus groups
- Interviews (structured, semi-structured)
- Surveys

Citizen science: Expanding and educating for improved science outcomes

Economics-based experimental games

Paleo-reconstruction to better understand historic landscapes and disturbance regimes

Maps for improved and long-term decision making.

Enzyme, isotope, and dissolve organic matter analyses to understand landscape effects on water

Molecular population genetics analysis

High tech tools, e.g., innovative radar tags for tracking movements of amphibians or other small-bodied organisms and automated loggers for water level

Low-tech tools, e.g., "One Orange," a stop watch and tape measure for stream flow.

"Top 10" lists provide a synthesis of common themes, methods, strategies and outcomes within SSI and reflect the collective input of more than 30 SSI faculty and students.

Community Smart Grid Utilizing Dynamic Demand Response
and Tidal Power for Grid Stabilization

published as: Anne E. Demeo and Michael L Peterson, "Community Smart Grid Utilizing
Dynamic Demand Response and Tidal Power for Grid Stabilization", *Smart Grid and
Renewable Energy*, 2013, 4, 465-472, <http://dx.doi.org/10.4236/sgre.2013.47053>
Published Online October 2013

Anne E. Demeo^{1,2}

and

Michael L Peterson²

¹ College of the Atlantic
105 Eden Street
Bar Harbor, ME 04609 U.S.
ademeo@coa.edu
207-266-1566 (corresponding author contact information)

² Department of Mechanical Engineering
University of Maine
5711 Boardman Hall, Room 219
Orono, ME 04469, U.S.

Corresponding author contact information:
Anna Demeo
P.O. Box 1277
Southwest Harbor, ME 04679
ademeo@coa.edu
207-266-1566

Abstract:

Conventional electricity generation is one of the largest contributors to climate change. Renewable energy sources are a promising part of the solution but uncertainty combined with a lack of controllability prevents renewable sources of power from being direct substitutes of conventional energy sources. This shift towards a higher penetration of renewable energy into the electric grid can be realized with the implementation of a more sophisticated smart grid, which uses dynamic demand response to alter demand to follow generation. Research on renewable energy penetration of the grid predominately focuses on wind and solar power resources but demand cannot always match availability from these sources and therefore greatly increases the need for energy storage. Tidal power differs from solar and wind in that it is a predictable renewable resource making it extremely valuable even on a relatively small scale. Introduction of tidal power into a high penetration micro-grid can serve to stabilize the grid and reduce the amount of storage required. Widely different time scales for wind, solar and tidal power availability result in low cross correlations and therefore increase stability.

This research describes an incremental approach to migrating a grid-tie island towards the formation of a smart-micro grid. The system will include a high penetration of three distributed generation systems, wind, solar and tidal and utilize commercially available energy storage and a smart-home management controller. Dynamic demand response through load balancing is implemented to minimize interactions with the electric grid. A second component of this work is to determine the optimum tidal generation capacity for the micro grid such that needed storage capacity from batteries or the utility grid is minimized.

Table of Contents

1. Introduction.....	57
2. Site	58
3. System Design	59
4. Tidal	61
5. Simulation Model.....	64
6. Simulation Results	66
6.1 Tidal	66
6.2 Dynamic Demand Response	69
7. Conclusion	71
8. Citations	73

Table of Figures

Figure 1: Map of Rouque Island.....	59
Figure 2: The Roque smart grid system is comprised of renewable energy supply, battery storage, a smart controller, load balancing capabilities, and a grid tie connection	60
Figure 3: The monthly demand is not significantly greater than the supply of wind and solar but the timing of renewables is inconsistent.	62
Figure 4: Daily net energy fluctuations for January, a typical month, vary from a maximum of 127kWh of unmet load to 58 kWh of excess renewable energy supply.....	63
Figure 5: Average monthly net energy without tidal has a median offset from zero of 36.4kWh. A tidal resource of that size reduces the size of battery storage needed.....	64
Figure 6: Simulink model for Roque smart grid: power generation from wind, solar and tidal systems is compared with island electricity demand, to predict the net surplus or shortfall of renewable energy generation	65
Figure 7: Smart Controller Flow Chart.....	66
Figure 8: Absent of tidal power the micro grid requires 11.6% of power to come from the main electric grid.	68
Figure 9: Power interactions with the main electric grid for a 4kW turbine (black) and 30kW turbine (grey): positive values indicate power taken from the electric grid while negative values show power sent to the electric grid	69
Figure 10: Power interactions with the grid absent of load balancing results in a maximum of 12.3% power taken from the grid while 2.6% of renewable energy generation is sent back to the grid.	70
Figure 11: Power interactions with the electric grid for hourly load balancing capacities of 2000W and 3000W	70

1. Introduction

Integrating renewable energy into the electric grid is a promising area of research in the widespread effort to address climate change. Conventional electricity generation is one of the largest contributors to climate change due to the production of greenhouse gasses [1]. Renewable energy sources cannot be directly substituted for conventional energy sources due to their uncontrollable and intermittent nature [2]. The conventional electricity grid functions on a generation following load principle, which entails controlling power plants to match varying power consumption [3]. Incorporating a higher penetration of renewable energy sources into the grid will require a paradigm shift to a load following generation model in which demand side management actively controls loads to offset variations in power production. This shift can only be realized with implementation of a more sophisticated electric grid.

Smart-grid is an umbrella term used to describe the technological upgrade of the grid or micro-grids to significantly increase penetration of renewable energy sources [4]. A smart-grid will dynamically monitor and control demand based on power production and consumption, known as dynamic demand response (DDR)[5]. Load balancing capacity, which is the available amount of dispatchable loads for DDR, grid energy storage and distributed renewable generation are the key components of a smart micro grid. Benefits of a smart-grid include increased penetration of renewable sources of power and an overall reduction in power consumption on the consumer side, which ultimately increases efficiency and grid security, lowers cost, and reduces carbon emissions.

Uncertainty combined with a lack of controllability prevents renewable sources of power from being direct substitutes for conventional energy sources. Research on renewable energy penetration of the grid predominately focuses on wind and solar power resources and the associated need to control demand through a smart grid network [6]. In addition to the inability to precisely characterize wind and solar power production, the reality that demand cannot always match availability from these sources greatly increases the need for energy storage.

Tidal power differs from solar and wind in that it is a predictable renewable resource. Although typically tidal sites do not offer as large of a supply as offshore wind [7], the predictability of the resource is extremely valuable as the introduction of tidal power, for small, geographically appropriate micro-grids, into a high penetration micro-grid can serve to stabilize the grid and reduce the amount of storage required. By further aggregating renewable power generation and providing a predictable input variability and uncertainty are also reduced. Widely different time scales for wind, solar and tidal power availability result in low cross correlations and therefore increase stability.

Island communities may be able to most immediately benefit from the development of smart micro-grids with predominately renewable energy penetration. Both grid-tie and autonomous islands experience high and fluctuating energy costs due to losses from underwater power cables in the first instance and fuel purchase and transportation costs for generators in the latter. These costs are a strong incentive for island communities to

integrate local energy sources. Geographically islands tend to provide an opportunity for a variety of renewable power sources including wind, tidal, wave and solar production. Moreover, many island communities operate at a scale that is suitable for smart-grid development with commercially available storage and smart-home technology.

This paper describes an incremental approach to migrating a grid-tie island towards the formation of a smart-micro grid. The system will include a high penetration of three distributed generation systems, utilize commercially available energy storage and a smart-home management controller. The primary objectives of this paper are to:

1. Determine optimum tidal generation capacity based on demand-supply balance of energy consumption and solar and wind power generation. Utilize tidal power for grid stabilization such that needed storage capacity from batteries or the utility grid is minimized.
2. Detail a non-autonomous smart-grid configuration using off the shelf storage and control equipment and off the shelf home automation management software to implement dynamic load balancing to minimize interaction with the utility grid. This will result in reduced power loss in the underwater cable, lower costs and increased efficiency. Utilize this non-autonomous smart micro-grid to aid in the refinement of an autonomous solution through monitoring of real-time power magnitude and direction at the utility grid source.

2. Site

Roque Island is a privately owned, 1300-acre island off the coast of Maine. Fifteen acres of cleared land on the southeast shore hosts six homes and a small, year round farm comprised of two large barns and several out buildings for horses and livestock for food production. Six staff members live year round on the island in three of the houses. The remaining three houses are inhabited from May through October by members of the trust, which owns the island. Population of the island averages 30 during the peak usage months of July, August and September. Average energy use for the island is 38 MWh per year. The island is connected to the mainland grid through an 1800m underwater power cable. The primary energy consumption on the farm is from the water pumping system and heating and refrigeration in the main farmhouse. The water is pumped to a central cistern then piped throughout the island. The farmhouse is 7655 square feet with an attached greenhouse. In addition to housing seasonal workers and being the main gathering place with a large communal kitchen, the farmhouse holds multiple freezers and a walk in refrigerator for food storage. Figure 1 shows a map of the island with tidal wind and solar marked.



Figure 1: Map of Rouque Island

The limited lifespan of the underwater power cable connecting Rouque to the main utility is the impetus for migrating the island community to a self-sustaining grid. An extended timeline allows an incremental approach to be taken. First, energy conservation and efficiency measures reduced overall electricity demand. Second, circuit level energy monitoring equipment was used to identify high demand sources such as a broken well pump. Attention to these loads further reduced island wide demand. Third, investment in sources of renewable energy to offset electricity demand provided 4.2 kW-installed capacity of initial solar generation. An added 5.8 kW installed capacity is scheduled for September 2013. Additionally a wind power assessment concluded that a 10kW system would be both economically and logistically feasible. Finally mechanisms to remotely and dynamically control a finite number of loads were installed.

These initial steps were used as a basis for design of the most efficient smart grid possible.

Subsequent steps of the work are detailed in this paper and include sizing the minimum tidal generation needed and comparing that need against the available resources as well as implementing control mechanisms for load balancing. Both efforts further reducing the required battery storage.

3. System Design

The smart grid system is comprised of renewable energy supply, battery storage, a smart controller, DDR, and a grid tie connection as shown in figure 2. The smart controller monitors demand and renewable power production then dynamically increases and decreases demand via a select number of dispatchable loads and battery storage. The main utility grid provides and absorbs energy when necessary until 100% renewable energy penetration can be achieved. Losses in the under water cable and low power resale rates are incentives to utilize all locally generated power as well as to limit purchasing power from the electric grid.

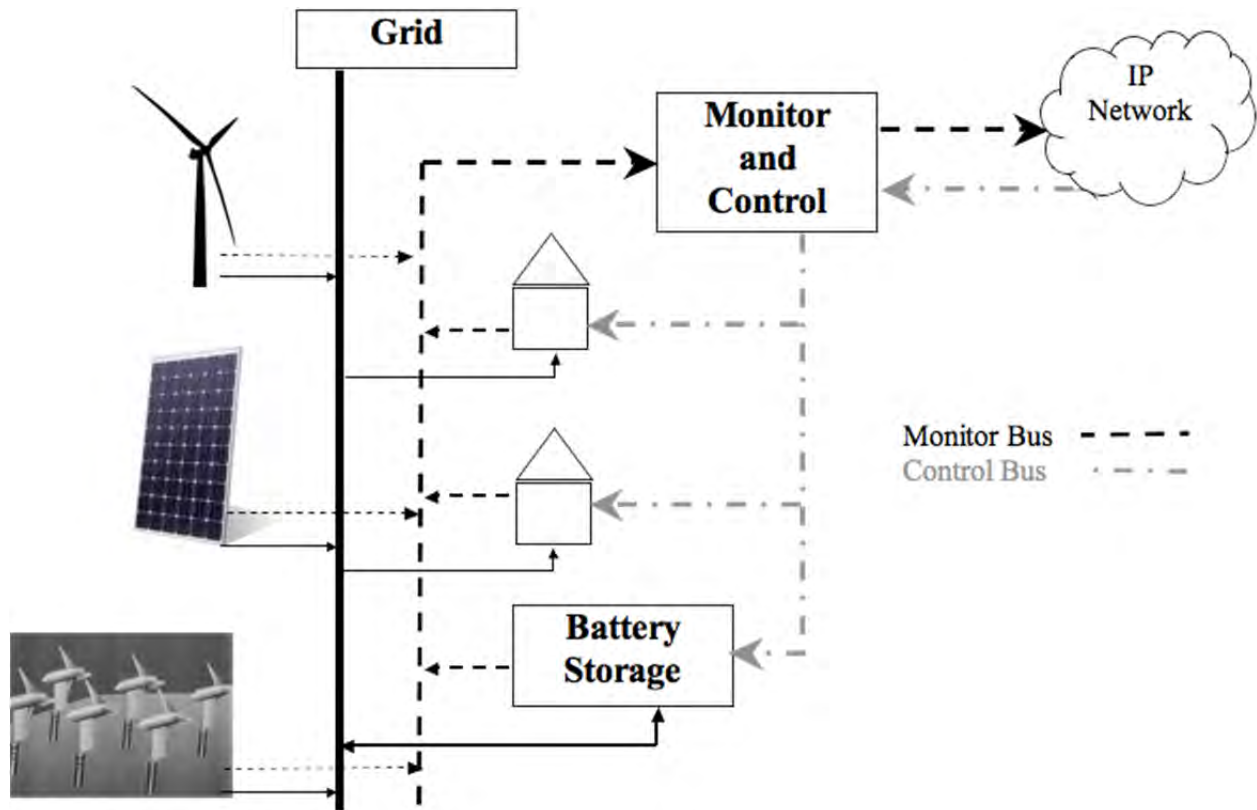


Figure 2: The Roque system is comprised of renewable energy supply, battery storage, a smart controller, load balancing capabilities, and a grid tie connection

Aggregating solar and wind energy resources with small tidal power generation significantly improves and simplifies the smart micro grid. The remaining power fluctuations are sufficiently small to be buffered with a limited battery storage unit acting both as spinning reserves and excess absorption. Battery storage provides flexibility to a micro grid as it allows time shifting between generation and consumption [8]. As a result, DDR can operate on an extended time series, bypassing many of the signal correction and conditioning issues [9] that accompany fast fluctuations of power caused by turning on and off loads.

The first order system analysis model is calculated using site-specific time series load and resource data. Circuit level power monitoring equipment (Savant Energy Monitor, Savant Systems LLC, Hyannis, MA) provides two years worth of high-resolution energy data for buildings on the island. Total island demand is monitored on a five second time scale and is 104kWh per day on average. Energy use on the island peaks from July through September, with a maximum monthly deviation in energy use across a year of 1800 kWh on average.

The Roque micro-grid is designed with 10kW installed capacity of both solar and wind power. Solar resource data is collected from an onsite small solar rooftop array (YL240P-29b, Yingli, China). Wind power data is calculated based on actual wind speed

data from an anemometer at hub height located in close proximity to the proposed turbine site. The micro-grid design is based on distributed solar, wind and tidal generation systems aggregated for renewable energy penetration approaching one hundred percent.

The system is designed to limit battery storage to twelve 12-volt 100AH batteries providing 14400-watt hours of storage or one eighth of the island daily energy consumption. A full day worth of battery storage would greatly reduce error and increase stability but the size, cost and logistics of transporting and maintaining that much storage is significant. The energy storage efficiency with the inverter is 90%. A battery charge controller is used to efficiently charge batteries and control fluctuations in power draw and charging cycles. The system is configured such that the battery is charged exclusively by renewable energy sources at no greater than the maximum charge rate. The state of charge (SOC) is instrumental to the smart controller in determining load balancing.

4. Tidal

The first objective of this work is to quantify the tidal power generation for a non-autonomous Roque Island micro-grid. The results of this investigation will determine if the proposed tidal site on the northeast side of the island is sufficient to make investment worthwhile. A tidal resource estimate was determined by weighing average monthly energy demand with proposed solar and wind generation. Analysis is absent of supply from the main utility grid as a further objective is to minimize that input.

Variability in demand and solar and wind power supply create variations in net power in both directions. Analyzing net energy on a seasonal time scale, power generation from solar and wind equate to a significant portion of demand as shown in figure 3.

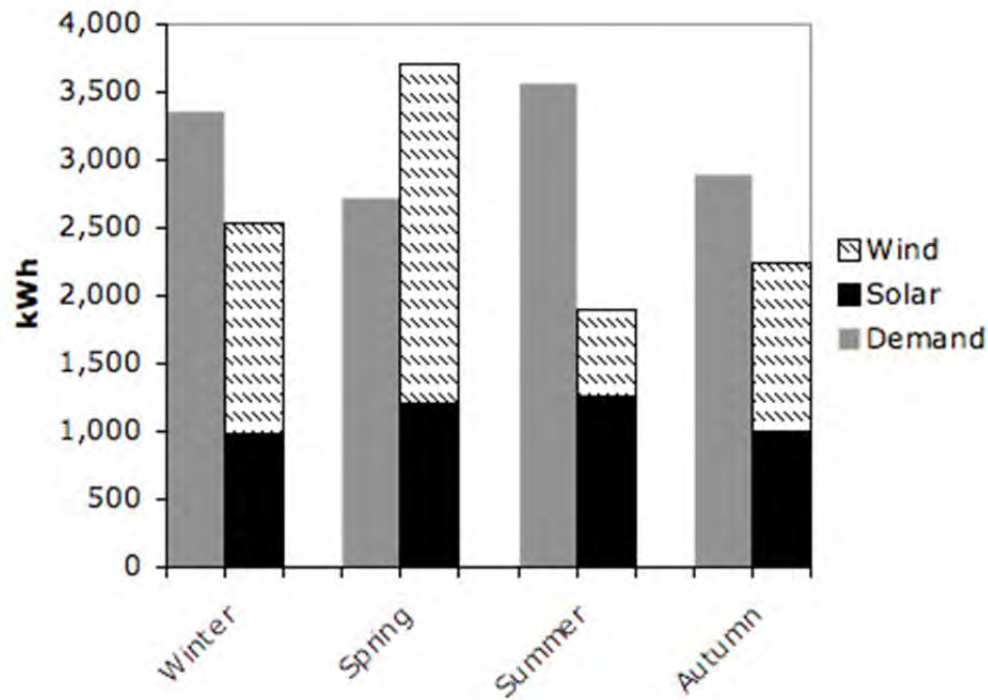


Figure 3: The monthly demand is not significantly greater than the supply of wind and solar but the timing of renewables is inconsistent.

Maximum net energy demand (demand minus supply) is 46.8% while minimum is -36%, indicating an excess of power. Monthly averages for high solar and wind penetration grids are insufficient for managing resources absent of significant energy storage due to intermittency in the supply. Day resolution of supply and demand more accurately reflect the requirements of grid management. Figure 4 shows daily net energy fluctuations from +127kWh to -58kWh for the example month of January 2012, a typical month.

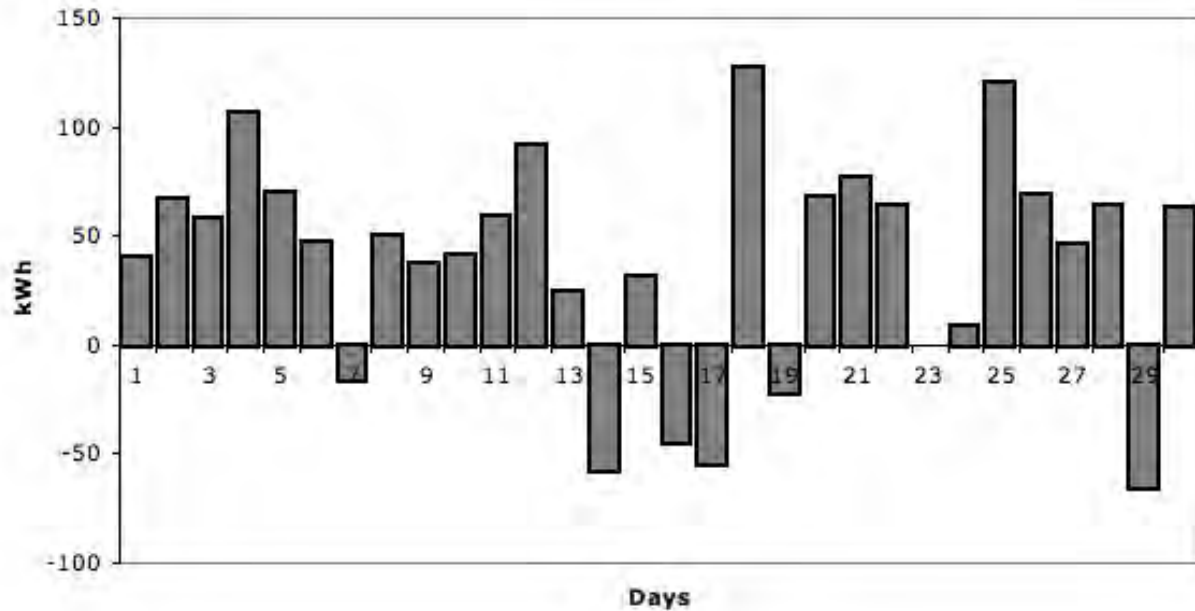


Figure 4: Daily net energy fluctuations for January, a typical month, vary from a maximum of 127kWh of unmet load to 58 kWh of excess renewable energy supply.

The net difference between average energy demand and energy production from solar and wind results in a median offset from zero of 34.6kWh as shown in Figure 5. Given a capacity factor of 30% [10] this translates to a 125kW peak capacity tidal installation. A tidal resource generation of this magnitude would center the demand-supply variability at the optimum match point and move the demand side management requirements towards the load balancing capacity of the system.

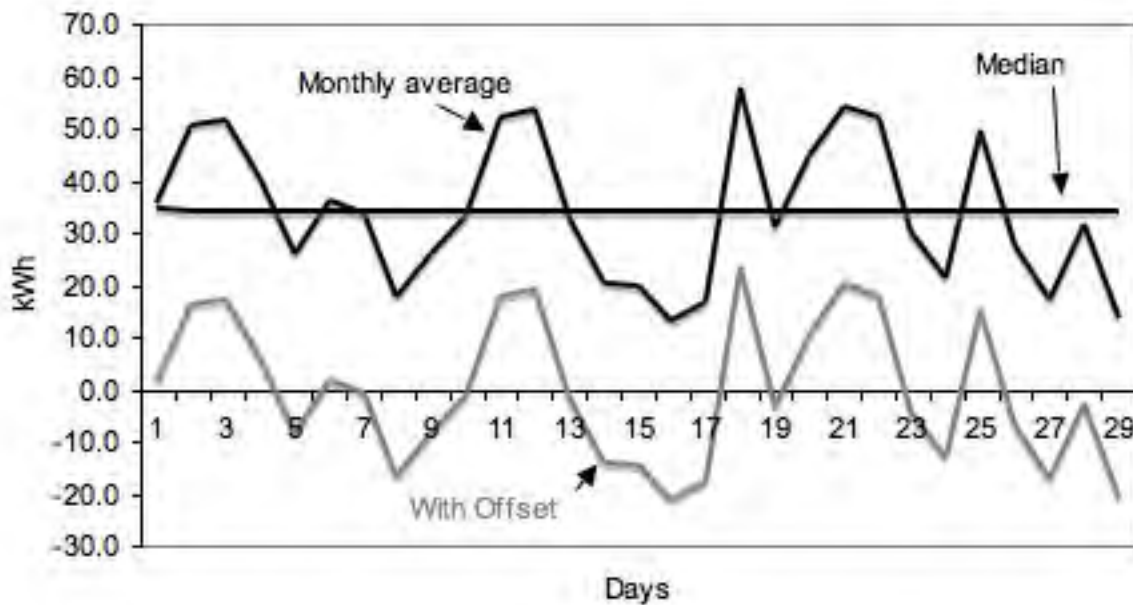


Figure 5: Average monthly net energy without tidal has a median offset from zero of 36.4kWh. A tidal resource of that size reduces the size of battery storage needed.

Initial rough estimates indicate that a 5 kW system is significantly smaller than is feasible for tidal power generation on the northwest side of the island. The proposed site is 1600M across, has an average depth of 40' and a maximum flow of 2 knots. Tidal generators achieve power densities of approximately $8\text{W}/\text{m}^2$ at flow speeds of 2 knots [11]. This corresponds to a tidal generation resource of .33MW. This resource is comparable to a similar site in Kennebec, Maine, which as about same depth and current speeds. That Kennebec site was analyzed as part of a North American tidal in-stream energy conversion feasibility study and found using very conservative assumptions to have a resource base of .4MW [12].

5. Simulation Model

A simulation of a smart grid for Roque Island was constructed using Simulink (version 8.0, Mathworks, Natick MA). The model block diagram is shown in figure 6. The model focuses on the largest seasonal supply-demand mismatch periods. Power generation from wind, solar and tidal systems is compared with island electricity demand, to predict the net surplus or shortfall of renewable energy generation. That output interfaces with battery storage and adjustable load balancing capacity to ultimately provide the amount of excess power or shortfall in power that will be sent to or taken from the electric grid. This information will establish a baseline for the system that can be further improved through increased load management, conservation measures, or adjustments in battery storage and renewable energy supply. For example, pumped water storage, as a means of absorbing

excess power, is advantageous given that water pumping is a significant demand on the system.

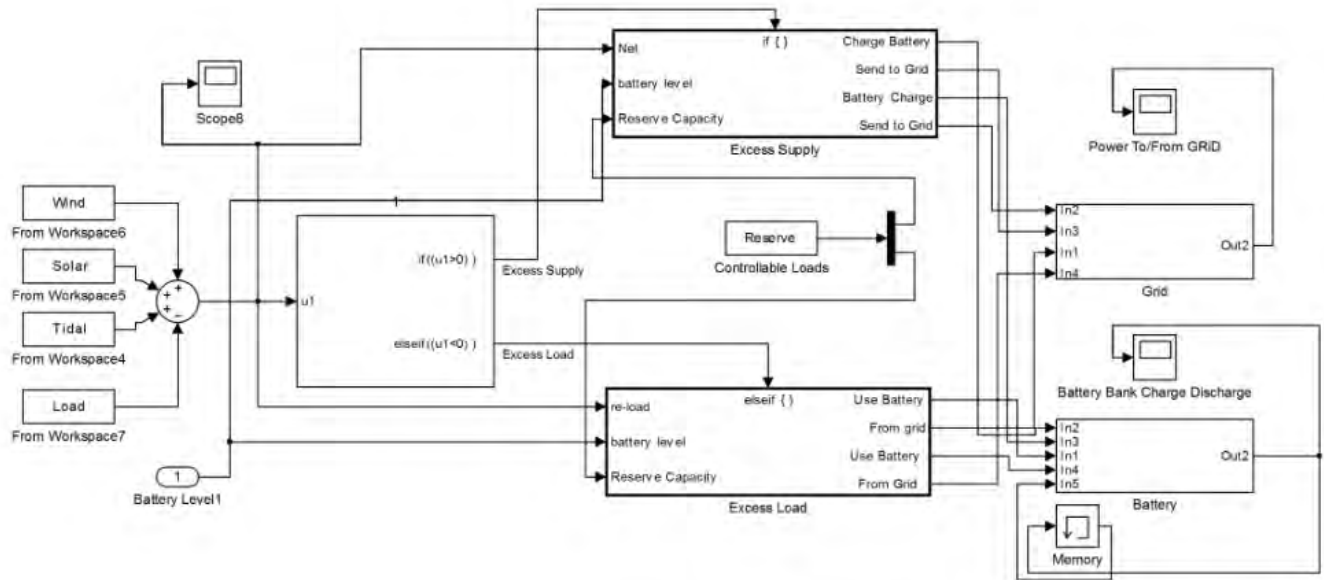


Figure 6: Simulink model for Roque smart grid: power generation from wind, solar and tidal systems is compared with island electricity demand, to predict the net surplus or shortfall of renewable energy generation

The system controller is fed high resolution current, voltage, power, power factor and direction data for every load and resource in the system including solar, tidal, wind, battery, grid connection and circuit level energy consumption. The controls are sufficient for extended time series DDR, which will further reduce peaks and troughs. SOC and charge rate are utilized for activation decisions by the smart controller. Loads for DDR are configured for on/off triggers and minimum duration between power cycles. For example a chest freezer may be set to turn on if the internal temperature is greater than T_x and turn off if it is less than T_y with a minimum hold time of Z minutes. The large thermal mass of a freezer, infrequent opening and storing of food and large energy usage makes these freezers a useful DDR load. Additional demand side management can come from pumping water to the central cistern only during peak generation times.

The system employs a proportional integral (PI) controller scheme based on the battery SOC and charge rate to determine optimum demand reductions necessary to meet unrealized supply and maintain battery storage levels. Similarly, the system gradually increases demand to capture any surplus of supply for the distributed generators. Loads are dynamically brought on or off line based on a gradual approach to the set point. Figure 7 illustrates a flow chart for the controller. Demand not matched by load balancing capacity or provided by the battery storage unit is drawn from the grid. Likewise, excess supply, with maximum demand and maximum battery SOC, is absorbed by the grid. This design

allows for slower transitions between charging and discharging phases using the battery storage as the system damper. The smart controller continuously monitors the magnitude and direction of power at the utility grid penetration point. The system attempts to offset any power through DDR and battery storage.

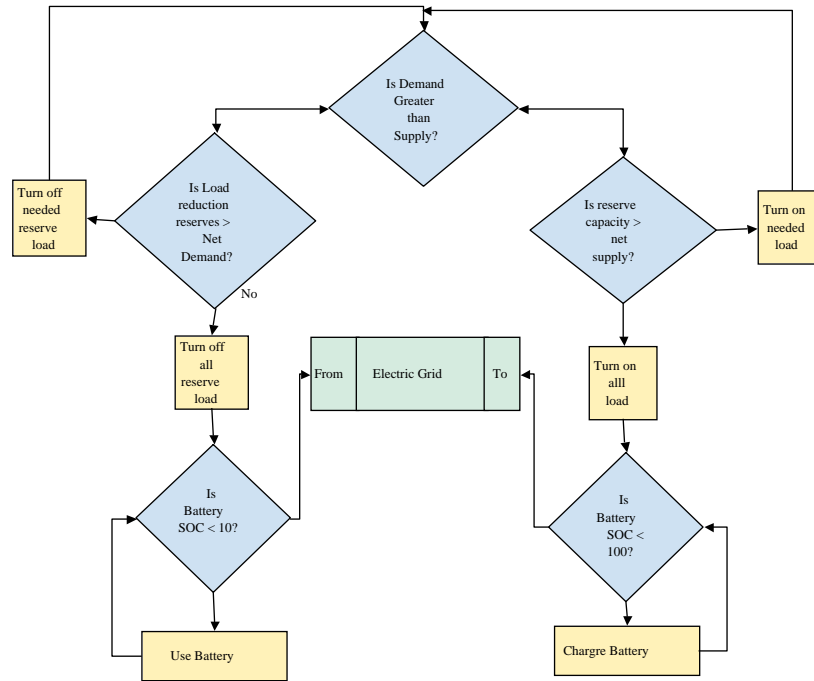


Figure 7: Smart Controller Flow Chart

6. Simulation Results

By fixing all but one input of the system, the smart grid simulation is used to determine the amount of power sent to and from the electric grid as well as the charge and discharge cycles of the battery based on the variation of a single input. In this manner, multiple scenarios can be tested prior to deployment of renewable energy generation. Two sets of simulations were done for this work. First the size of the tidal generation was varied while all other inputs were fixed. Next, the optimum tidal generator size of those simulated was fixed into the model while the size of the load balancing capacity for dynamic demand response of loads was varied.

6.1 Tidal

Several tidal turbine sizes were simulated for the micro grid. Smaller generators are modeled for lower cut-in speeds producing a lower power output over longer portion of the tidal flow period. While larger turbines are modeled for higher cut-in speeds, resulting in a higher power output but for a shorter portion of a tidal cycle. The simulations are run with a one-hour time scale then summed per day for a three-month period. Inputs to the system include battery storage capacity of 14.4kWh, solar and wind generation each with an installed capacity of 10kW and the initial anticipated hourly load capacity for the island, 2000W of hourly load balancing capacity. Table 1 summarizes the percent of excess generation and unmet load for these tidal turbines.

Table 1: % grid interaction based on tidal generator

Tidal Size	power generation per cycle	% renewable energy to grid	% load covered by electric grid
0	0	0	11.6
4 kW	65%	3.3	3.2
6 kW	65%	6.5	1.3
10 kW	65%	13.9	0.3
12 kW	65%	18.6	0.1
30 kW	25%	64.3	0.0
64 kW	25%	81.0	0.0

Without tidal power generation to augment solar and wind power generation, a relatively large amount of power is needed from the grid. Such a scenario would require more than doubling the battery capacity in the system in order to keep the grid interaction below 5%. As a baseline, Figure 8 shows the power drawn from the electric grid when the island renewable energy portfolio is absent of tidal power. For this scenario a maximum of 11.6% of power is taken from the grid to make up for shortfalls in production.

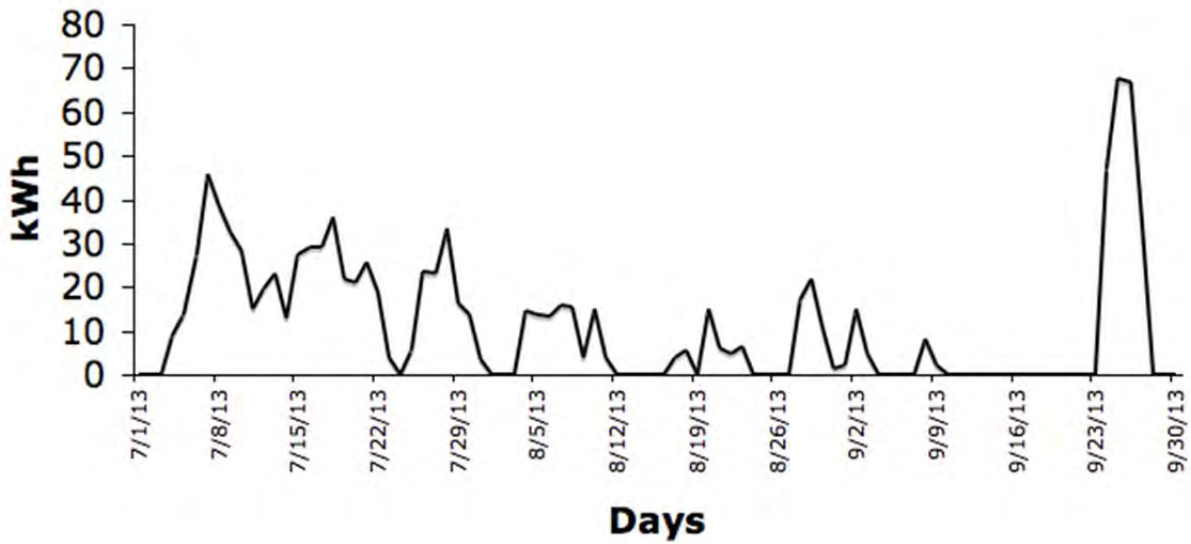


Figure 8: Absent of tidal power the micro grid requires 11.6% of power to come from the main electric grid.

Table one shows that the 4kW tidal generator provides the lowest grid interaction. The daily grid interactions for this turbine and the 30kW turbine are graphed in Figure 9. Positive values represent power taken from the grid while negative values indicate power sent to the grid.

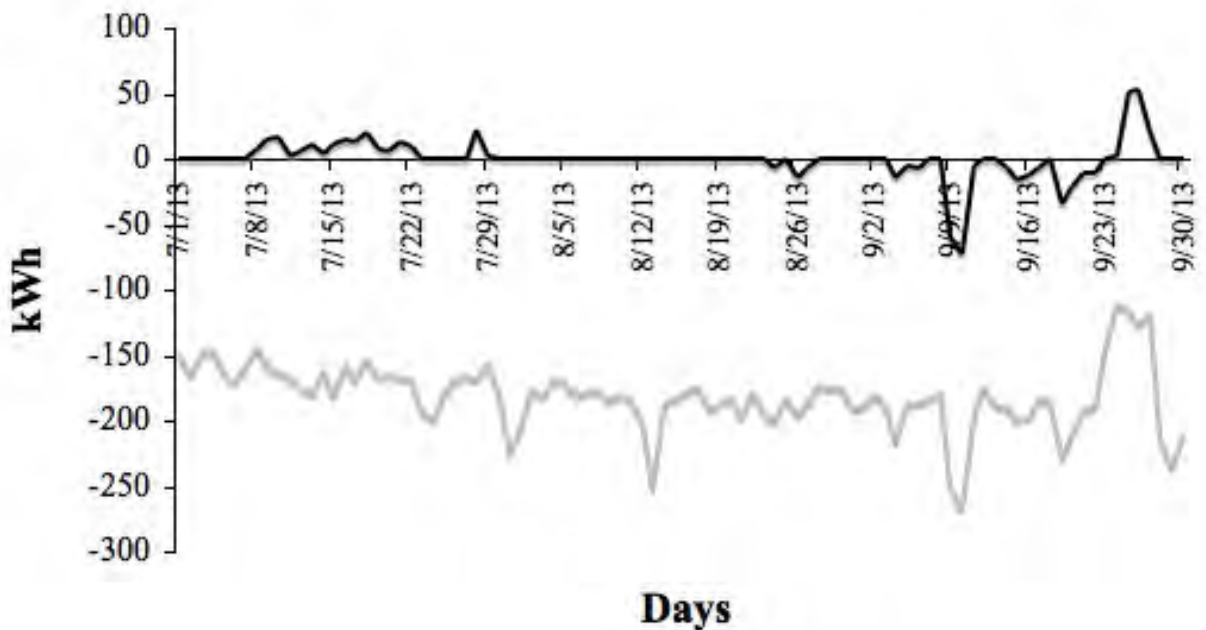


Figure 9: Power interactions with the main electric grid for a 4kW turbine (black) and 30kW turbine (grey): positive values indicate power taken from the electric grid while negative values show power sent to the electric grid

The 4kW tidal generator requires that the micro grid only take 3.3% of its power from the electric grid and send 3.2% of the total renewable energy generation back to the grid. The 30kW tidal generator eliminates grid dependence but increases the amount of renewable energy generation sent back to the electric grid to 64%. This excess power could be potential income for an island with a suitable underwater cable. However, given the cost of tidal energy and transmission losses it is unlikely that the system would justify the additional capital investment. The objective for Roque is to move towards eliminating the cable rather than replacing it, which would be required with this larger tidal generator.

6.2 Dynamic Demand Response

Since the 4kW tidal generator that provides a modest power output over a longer time provides the lowest grid interaction for the given micro grid configuration, this choice is fixed for the dynamic demand response modeling to determine the optimum load balancing capacity.

As a baseline, a simulation was run for power interactions with the grid absent of load balancing. These results are shown in figure 10. A maximum of 12.3% of power is taken from the grid to make up for shortfalls in production while 2.6% of renewable energy generation is sent back to the grid for the same seasonal period. Hourly power fluctuations to and from the grid peak just over 6000W, which is consistent with the predicted net surplus based on demand, generation sources and battery capacity.

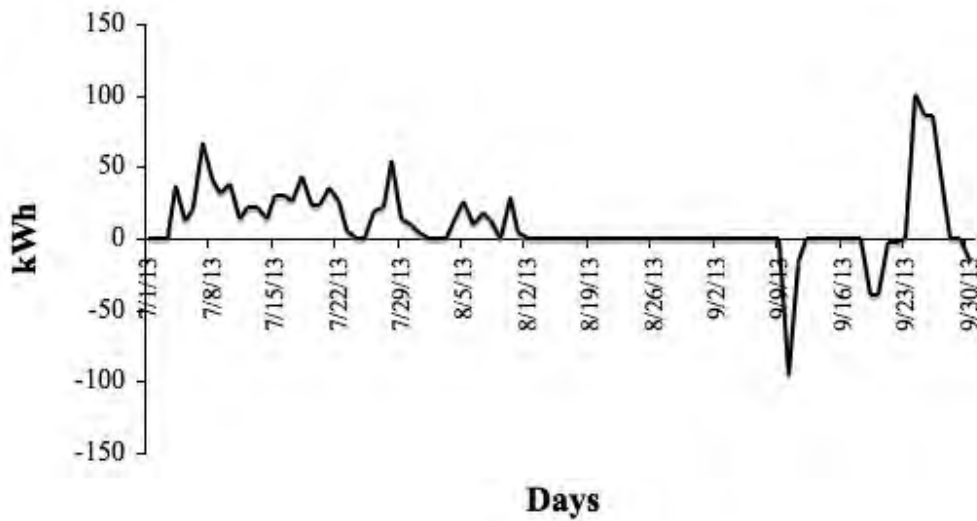


Figure 10: Power interactions with the grid absent of load balancing results in a maximum of 12.3% power taken from the grid while 2.6% of renewable energy generation is sent back to the grid.

Initial estimates for hourly load balancing capacity for the island is 2000W. Simulations were run for 2000W and 3000W. The results are shown in figure 11.

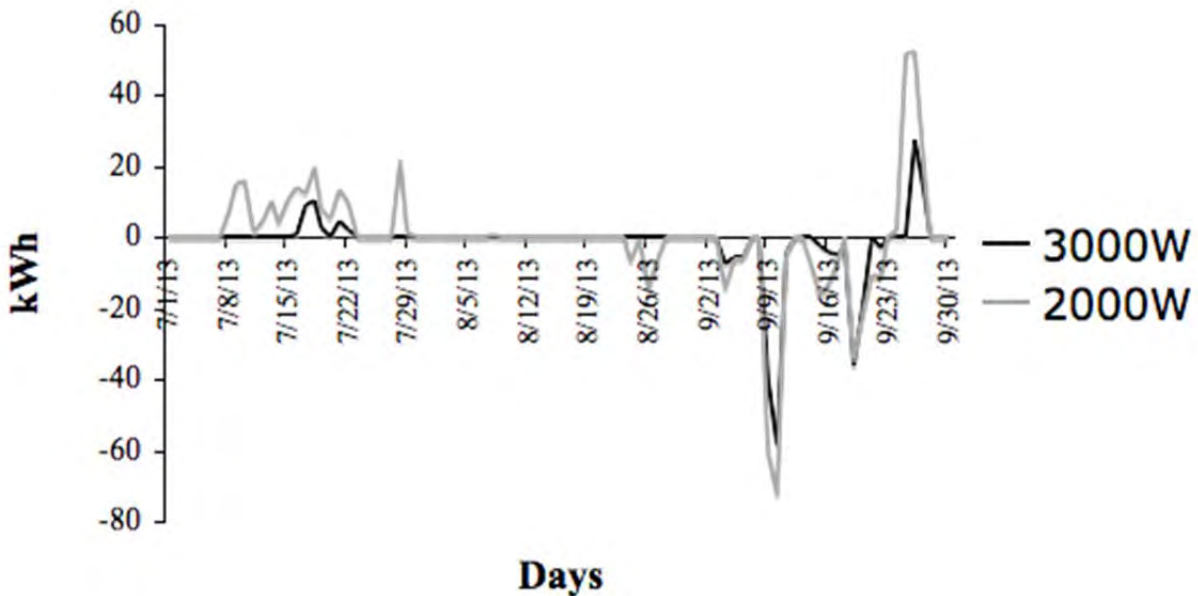


Figure 11: Power interactions with the electric grid for hourly load balancing capacities of 2000W and 3000W

Simulation using the hourly load balancing capacity for the island of 2000W requires the micro grid to take 3.2% of its power from the electric grid and send 3.3% of the total renewable energy generation back to the grid. An increase of load balancing capacity to 3000W reduces the power needed from the electric grid to .6% and the power sent to the grid to 2.5%. These results along with no load balancing are listed in table 2.

Table 2: % grid interaction based on load balancing capacity

Load Balancing	% power taken from the grid	% renewable energy to grid
0	12.3%	2.6%
2000W	3.2%	3.3%
3000W	.6%	2.5%

Dynamic demand response will alter load patterns as heating and cooling is bundled around high supply time periods. Combined with the freezers and water pumping the high percentage of dynamic demand response is realistic for this system. Monitoring of the interface point for the main electric grid will provide real power consumption and direction data with a five minute resolution. This monitoring data, fed back into the simulation model to analyze shifts in system power peaks and individual loads, will assist in optimizing load balancing capacity and incrementally reduce the time scale for load manipulation.

7. Conclusion

Renewable energy driven micro-grids that can include a tidal power generator of modest size can greatly improve the stability of the grid. If a reasonable portion of the load is interruptible and centrally controlled, the aggregation of intermittent renewable resources of solar and wind with a predictable renewable generator can provide the basis for an independent stable grid. The Roque Island grid is a living laboratory where demand has been managed with passive monitoring of energy usage on the island [13]. After first reducing demand, performance of small-scale mature renewable technologies like photovoltaics has been evaluated. Controlling the island demand by interrupting loads is operational. The goal of a nearly independent 100% renewable micro-grid now appears to be possible based on models which include small input from a reliable renewable energy source, tidal energy.

The model results support further investment in the evaluation of the tidal resource by installing flow meters and initiating cost assessment. While tidal energy is a relatively immature technology [14], it is clear that a relatively small tidal resource can have a significant impact on grid stability.

The portion of the load, which must be centrally controlled to minimize interaction with the utility grid, is relatively large even for this small grid with comparatively large interruptible loads. The scalability of the results is not clear for applications where interruptible loads such as pumping water to a cistern or cooling large freezers is a smaller portion of energy usage. However when considered on a community scale including heating, cooling, water treatment and other capital intensive energy usage may make a sufficiently large portion of the load interruptible. Regardless of the scale of the general applicability of the approach, the combination of more stable renewable energy sources and demand control has the potential to stabilize outlying portions of the grid with high cost to serve. For Roque Island, the benefits are immediate with a reduction in loss over the connecting cable for both purchased and excess power resulting in power cost reductions.

Scaling this work for mainland communities allows community scale smart-grids with high renewable energy penetration to utilize the electric grid as backup storage. This would be an opportunity for green communities to continue to experiment with grid related concepts while having a positive impact on the community through exploration of economically promising technologies. Accessibility to small scale tidal generation or river hydro-electric resources for these communities will greatly improve the stability of their micro-grid, reduce non-renewable energy usage and increase overall grid stability. While extensive modeling would be required to determine if the impact is significant, it may even be possible to pair renewable energy sources in this manner with certain types of customers in order to impact overall grid stability for high renewable penetration grids.

8. Citations

- [1] Intergovernmental Panel on Climate Change, “Climate Change 2007: The Physical Science Basis. Contribution of Working Group I to the Fourth Assessment Report of the Intergovernmental Panel on Climate Change,” S. Solomon, D. Oun, M. Manning, M. Chen & M. Marquee (Eds.), Cambridge University Press. Cambridge, United Kingdom, 2007.
- [2] G. M. Shafiullah, A. M. Oo, A. S. Ali, and P. Wolfs, Smart Grid for a Sustainable Future. 2013.
- [3], [6] E. Hart, E. Stoutenburg, and M. Jacobson, “The Potential of Intermittent Renewables to Meet Electric Power Demand: Current Methods and Emerging Analytical Techniques” Proceedings of the IEEE, 100(2), 322-334, 2012 doi: 10.1109/JPROC.2011.2144951
- [4] D. Holmberg, D. “Demand Response and Standards”. BACnet® Today & the Smart Grid | A Supplement to ASHRAE Journal, 823-828, 2011.
- [5] A. Scaglia, C. Brocca, G. Torri, and Viale Sarca, “A Model for the Design and Development of Smart Micro Grids”. In 21 WEC World Energy Congress di Montréal in Canada September, 2010.
- [7] Ocean Energy Council. ” Tidal Energy”. Retrieved from <http://www.oceanenergycouncil.com/index.php/Tidal-Energy/Tidal-Energy.html>, 2012.
- [8] R. Lassester, “Microgrids and Distributed Generation”. Journal of Energy Engineering, American Society of Civil Engineers, 133, 144-149, 2007. doi: 10.1061/(ASCE)0733-9402(2007)133:3(144)
- [9] Y. Yin, X. Luo, S. Guo, Z. Zhou and J. Wang, “A Battery Charging Control Strategy for Renewable Energy Generation Systems” IAENG Proceedings of the World Congress on Engineering Vol I, 2008.
- [10] M. Palodichuk, B. Polagye, and J. Thomson, “Resource Mapping at Tidal Energy Sites”, 2013.
- [11] D. MacKay, D. Cambridge, United Kingdom: UIT, 2009. DOI: www.withouthotair.com/
- [12] G. Hagerman, B. Polagye, R. Bedard, R., and M. Previsic, M., “Methodology for Estimating Tidal Current Energy Resources and Power Production by Tidal In-stream Energy Conversion (TISEC) Devices. EPRI North American Tidal In Stream Power Feasibility Demonstration Project, 2006.
- [13] A. Demeo, and M. Peterson, (submitted). Island Community Smart Grid Utilizing

Dynamic Demand Response and Tidal Power for Grid Stabilization. Smart Grid and Renewable Energy, 2013

[14] C.M. Johnstone, D. Pratt, J.A. Clarke, and A.D. Grant, "A Techno-economic Analysis of Tidal Energy Technology Original Research Article Renewable Energy, Volume 49, January 2013, Pages 101-106

Appendix Task 4-4

**TIDAL POWER PERMITTING
AND
SITE DEVELOPMENT FRAMEWORK**

FOR

**MAINE TIDAL POWER INITIATIVE
UNIVERSITY OF MAINE**

**DECEMBER 2013
JN: 10028.008**



**TIDAL POWER PERMITTING
AND
SITE DEVELOPMENT FRAMEWORK**

FOR

**MAINE TIDAL POWER INITIATIVE
UNIVERSITY OF MAINE**

NOVEMBER 2013

**Prepared by: CES, Inc.
465 South Main Street
P.O. Box 639
Brewer, ME 04412**



Johanna Szillery, Project Scientist



John Pond, SVP, Project Manager
Director-Environmental



Acknowledgement: This material is based upon work supported by the Department of Energy under Award Number DE-EE0000298.

Disclaimer: This report was prepared as an account of the work sponsored by an agency of the United States Government. Neither the United States Government nor any agency thereof, nor any of their employees, makes any warranty, express or implied, or assumes any legal liability or responsibility for the accuracy, completeness or usefulness of any information, apparatus, product, or process disclosed, or represents that its use would not infringe privately owned rights. Reference herein to any specific commercial product, process, or service by trade name, trademark, manufacture, or otherwise does not necessarily constitute or imply its endorsement, recommendation, or favoring by the United States Government or any agency thereof. The views and opinions of authors expressed herein do not necessarily state or reflect those of the United States Government of any agency thereof.

TABLE OF CONTENTS

1.0 INTRODUCTION.....78

2.0 SCOPE OF WORK.....79

3.0 PERMITTING AND LICENSING INFORMATION80

 3.1 Federal Energy Regulatory Commission (FERC)80

 3.2 U.S. Army Corps of Engineers82

 3.3 Maine Department of Environmental Protection.....82

 3.4 Maine Bureau of Parks and Lands83

 3.5 Municipal Ordinances83

4.0 FERC DOCKET REVIEW.....84

 4.1 Verdant Declaratory Order84

 4.2 Exemptions from Licensing.....85

 4.3 Strict Scrutiny Policy86

 4.4 Timelines.....87

5.0 DATA GATHERED AND LESSONS LEARNED FROM THE WISCASSET TIDAL RESOURCES PROJECT88

6.0 FRAMEWORK FOR TIDAL POWER PERMITTING AND SITE DEVELOPMENT 90

 6.1 Submit a FERC Preliminary Permit for the Project Area90

 6.2 Research Existing Information and Identify Information Gaps91

 6.3 Develop Study Plans for Information Gaps93

 6.4 Increase Site Knowledge Incrementally93

 6.5 Stakeholder Outreach and Involvement94

REFERENCES.....95

APPENDICES

- Appendix Task 4-2. Protected Natural Resources Reconnaissance Report, Wiscasset Tidal Resources Project, Back River, Wiscasset, Maine - S.W. Cole Engineering, Inc.
- Appendix Task 4-3. DEP Information Sheet – Regulation of Tidal and Wave Energy Projects
- Appendix Task 4-4. Wiscasset Tidal Resources Project Inter Agency Fisheries and Wildlife Consultation – S.W. Cole Engineering, Inc.
- Appendix Task 4-5. Tidal Power Site Evaluation in Wiscasset, Maine: Data Gathered and Lessons Learned
- Appendix Task 4-6. Final Report on the Wiscasset Tidal Power Project
- Appendix Task 4-7. FERC Licensing Hydrokinetic Pilot Projects



We are pleased to present this Permitting and Site Development Framework for Small Scale Tidal Power Sites. S.W. Cole Engineering, Inc. conducted research, field work, and preliminary permitting support for the Wiscasset Tidal Resources Project in Wiscasset, Maine. Using the Wiscasset Project experience, S.W. Cole developed this template to assist prospective small-scale tidal power developers through the permitting process. The purpose of CES Inc.'s work was to update and complete this template. This document is intended to be adaptable as permitting requirements and understanding of the hydrokinetic project development and permitting process grows.

1.0 INTRODUCTION

The Maine Tidal Power Initiative is a collaborative partnership among the University of Maine, the Tidal Energy Device Evaluation Center at Maine Maritime Academy, and numerous partners representing the wide range of participants in the tidal industry; tidal turbine developers, tidal site developers, ancillary technology developers, resource assessment experts, and natural resource permitting consultants. The objective of the Maine Tidal Power Initiative (MTPI) is to promote a balanced approach to tidal power development that considers the potential energy resource of a site, as well as the impact on the environment and community. MTPI promotes this mission through research in turbine engineering and design, resource assessment, environmental monitoring, and social science.

S.W. Cole Engineering, Inc. became a partner in the MTPI in 2010, as part of U.S. Department of Energy funded research which was aimed at tidal resource assessment, natural resource assessment, turbine design development, and feasibility assessment of tidal power for community-scale projects. S.W. Cole's role was to assist with permitting support of the Wiscasset Tidal Resources Project, and to begin a process framework for other community-scale tidal projects. CES, Inc.'s role was to update and finalize this process framework. The work of MTPI has been funded through numerous sources, both directly to MTPI and indirectly as cooperators.

The Wiscasset Tidal Resources Project (also referred to as the Wiscasset Project) is a community-scale project initiated by the Town of Wiscasset and The Chewonki Foundation. The aim of the Project is to explore the feasibility of community-scale tidal power generation at one of the sites in Maine identified as having high potential for tidal power, based on several metrics used by Hagerman and Bedard (2006). The Wiscasset Tidal Resources Project shares the MTPI vision of balancing the potential for tidal power generation with the environmental and sociological impacts of tidal development on the resource and community.

The Town of Wiscasset submitted a FERC preliminary permit application on November 11, 2008 and was granted a preliminary permit on May 28, 2009. The Town's preliminary permit application estimated a generating capacity of 1 to 10 MW with 4 to 40 turbines, and noted that the size, scope, and configuration of the proposed turbines would be tailored to the resource available, and to the terrestrial and aquatic environment.

S.W. Cole also worked with the Tidal Energy Device Evaluation Center (TEDEC) at Maine Maritime Academy. TEDEC is an education, research, and demonstration facility, which aims to train students with skills for the emerging tidal energy field. TEDEC also offers developers and

researchers a permitted site for testing and evaluation of a device or of potential environmental impacts. Finally, TEDEC hopes to engage the regulatory and broader community. TEDEC's unique Federal permitting status, which will be discussed later, was granted based on the mission of product development and public and community education and involvement.

Throughout this report, several terms relating to hydropower are used. Generally, hydropower harnesses the energy of flowing water, either as electrical or mechanical power. Traditional or conventional hydroelectric power creates hydraulic head by damming a water source or utilizes and enhances an existing flow by diverting a water source; this flowing water is channelized or ducted and used to turn a turbine. This power is used as is, or converted to hydroelectric power. Hydrokinetic power converts the flow of water into power in a free flow environment, without the damming or diversion associated with conventional hydroelectric power. Hydrokinetic systems are purported to have minimal impact to the environment. Wave, current, and tidal devices are a few of the ways of capturing hydrokinetic power. The term tidal turbine and tidal power is a category within hydrokinetic power, and refers to those devices which are intended to harness the predictable flow of the tides in a free-flow environment. The term tidal in-stream energy conversion is also used synonymously with tidal power. Both conventional hydroelectric power and hydrokinetic power are included in the broader term, hydropower.

2.0 SCOPE OF WORK

S.W. Cole began work on the Maine Tidal Power Initiative in July 2010 with an initial project meeting on August 13, 2010. A site visit was made to the TEDEC site (Castine Harbor and Bagaduce Narrows) in Castine on September 14, 2010; and a site visit to the Wiscasset Tidal Resources Project (Back River and Sheepscot River) in Wiscasset on October 13, 2010. Through these visits, the team gained a better understanding of the environmental resources and the communities involved in each of the projects. Based on the permitting progress and status of the TEDEC site, S.W. Cole focused permitting work on the Wiscasset Project.

S.W. Cole scientists attended a tidal power environmental and regulatory workshop hosted by Ocean Renewable Power Company (ORPC) in Eastport on October 5, 2010, and a small-scale tidal power workshop hosted by TEDEC and Maine Maritime Academy in Castine on November 13, 2010. These workshops allowed for interaction with other developers of tidal power projects, and with the biologists and resource scientists who regulate these projects.

Project research began with research on known protected species and habitats and an on-site field reconnaissance for protected natural resources (wetlands, streams, and other resource concerns) which could impact the siting and regulatory permitting of the Wiscasset Project. The Protected Natural Resources Report for the Wiscasset site is included in Appendix Task 4-2. Consultation was initiated with State and Federal resource and regulatory agencies to determine permitting and study requirements for the Wiscasset Project. These discussions ranged from general study requirements for tidal power projects, to specific opportunities and concerns as related to the Wiscasset Project.

Project consultation was also initiated with the Federal Energy Regulatory Commission (FERC) project manager for the Wiscasset Project. The project team facilitated an interagency fisheries and wildlife consultation meeting at the University of Maine on April 7, 2011. This meeting

included the key biologists, resource scientists, and regulators who will provide comments and study recommendations at the time of project licensing. These scientists and regulators commented on biological and resource considerations as they related to the Wiscasset Project.

This Report is a compilation of what was learned during this process, both directly through research and discussion, and the knowledge gained experientially, by working through the permitting process. Also included is information and experience shared by other members of the tidal community.

3.0 PERMITTING AND LICENSING INFORMATION

The Federal Energy Regulatory Commission (FERC) is the lead Federal permitting agency for hydropower projects in the United States, for both conventional hydropower and hydrokinetic projects. FERC regulates hydropower projects in several ways; project licensing for new construction, project relicensing for existing facilities, and oversight of existing projects. Under the Federal Power Act, FERC has the jurisdiction to license most non-federal projects that are proposed in a navigable waterway of the United States; proposed on Federal lands; or proposed to connect to the interstate electric transmission grid. Any of these criteria can trigger FERC involvement in the proposed project.

In addition to FERC permitting, work in navigable waterways requires coordination with, or a permit from, the U.S. Army Corps of Engineers (Corps). Additional permits and certifications are required by the State and are coordinated through the Maine Department of Environmental Protection (MDEP). A submerged lands lease will likely be required from the Maine Department of Conservation, Bureau of Parks and Lands. Permits may also be required from the local municipality. Additional information about these agencies and their jurisdiction as related to hydrokinetic project activities is covered in the following sections.

3.1 Federal Energy Regulatory Commission (FERC)

The goal of the FERC licensing process is to provide sufficient information to weigh the benefits of a proposed project with the potential impacts, and to complete an environmental analysis, as required under Federal law. Applicants provide “existing, relevant, and reasonably available” information to FERC Staff and interested parties, such as State and Federal agencies, Native American tribes, non-governmental organizations, and members of the public. This information serves as the basis for identifying issues and developing study plans and, if a license is issued, on-going monitoring plans. The licensing process also gives FERC staff information to prepare an Environmental Assessment (EA) or an Environmental Impact Statement (EIS); the Terms and Conditions issued with a FERC license are based on EA/EIS review. The Federal Powers Act (FPA) specifically mandates that an applicant for a license, prior to filing an application, “must consult” with relevant federal, state, interstate resource agencies, native tribes, and members of the public. As noted in the FPA (18 CFR Ch 1, sCh8, § 5.1), these agencies include the National Marine Fisheries Service (NMFS), U.S. Fish and Wildlife Service (USFWS), Bureau of Indian Affairs, U.S. Environmental Protection Agency (EPA), National Park Service, U.S. Coast Guard (USCG), state water resource agencies, state fish and wildlife agencies, state agency that administers the coastal zone management act (CZMA), and native tribes likely to be affected by the proposed project. Sections 3.3 and 3.4, below, define and briefly describe the state agencies in Maine for consultation. FERC staff can provide an applicant with a list of contacts to begin

the consultation process (listing potentially interested federal, state, tribal, and public stakeholders). It is the applicant's responsibility to conduct this consultation; FERC staff facilitates the stakeholder outreach process and attempts to mediate differences that may arise during the process, such as in study plan requests and license conditions. Ultimately, FERC ensures that FERC and the applicant have met the consultation requirements of the FPA, the Endangered Species Act (ESA), National Marine Sanctuaries Act, Magnuson-Stevens Fishery Conservation and Management Act, and the National Environmental Policy Act.

As related to hydropower, FERC issues preliminary permits, operating licenses, and exemptions from FERC licensing. Preliminary permits are generally the first step in the licensing process, and allow an applicant to study the feasibility of a hydropower project at a site, and to prepare application materials for a license or an exemption. Preliminary permits maintain an applicant's priority for a site area, known as "first to file" status. These permits do not authorize construction. Traditional hydropower operating licenses are issued for 30 to 50 years, and convey with them the right of eminent domain. Exemptions from FERC permitting are issued for 1) small hydropower projects, which FERC defines as five megawatts or less, and 2) hydropower projects that propose to use an existing waterway conduit. The nature and length of conventional hydropower licenses and exemptions from licensing require that the impacts of the proposed project on the environment are known. Each of these license types have separate application processes and associated anticipated processing timelines.

In 2008, in recognition of the growing hydrokinetic industry and the need for an appropriate licensing process, FERC adapted existing regulations and created the hydrokinetic pilot project licensing process. This is a streamlined process that has several advantages: 1) developers can test and evaluate hydrokinetic turbine designs; 2) developers can also test ability to connect to the grid; and 3) profit from the energy produced. From the regulatory viewpoint, FERC and resource agencies learn about the impacts of these technologies. FERC can also work within existing regulations to permit these projects, rather than craft new regulations, for a (relatively) short license term.

FERC guidelines for pilot projects have several stipulations: 1) pilot projects are small (generally less than 5 megawatts); 2) pilot projects are short term (generally 5 years); 3) pilot projects will avoid sensitive locations; 4) pilot projects will be carefully monitored for impacts to the environment and the public; and 5) pilot projects will be easily removable. Section 5.2 of this report discusses, in more detail, the contents of and procedure for the Hydrokinetic Pilot License process, as this is the main licensing avenue currently available for this technology.

The Wiscasset Tidal Resources Project was issued a FERC preliminary permit for the Sheepscot River and Back River in Wiscasset on May 28, 2009 (Permit P-13329). The preliminary permit is valid for three years and sets a deadline of two years, or May 28, 2011 for the applicant to submit a Draft Pilot License Application (DPLA). On June 15, 2011, FERC granted an 11-month extension on Wiscasset's DPLA deadline.

3.2 U.S. Army Corps of Engineers

The Corps regulates all work in navigable waters under the Rivers and Harbors Act, and regulates the discharge of dredged or fill materials into waters of the United States under the Clean Water Act. The State of Maine has a General Permit agreement with the Corps, which facilitates permitting activities between the State and the Corps for activities that “have no more than minimal individual, secondary, and cumulative adverse effects on the aquatic environment in water of the U.S.” Projects that are eligible for review under the General Permit are further defined as Category 1 or Category 2 projects. Projects which are not eligible for review under the General Permit require an Individual Permit from the Corps, which is a higher level of review. FERC preliminary permit activities and pilot license activities are eligible for review under the Corps General Permit. Larger, commercial-scale tidal power projects are likely permitted under the Individual Permit, which will be determined by the Corps Project Manager. However, permitting precedents have not yet been established for commercial-scale deployments; to date, developers of hydrokinetic technologies have been testing technologies and monitoring impacts within the FERC preliminary and pilot licenses, which fall into the Corps General Permit with the State of Maine.

The Corps will streamline the application process for hydrokinetic projects by coordinating content and format requirements with FERC; however, the emphasis of the Corps review may differ from that of FERC. The Corps’ review will focus primarily on environmental considerations, such as fisheries, water quality, and the ESA coordination; and navigational considerations and existing uses, such as commercial and recreational users. If a project does not trigger FERC jurisdiction (these criteria were noted in Section 3.1), the Corps will likely be the lead Federal permitting agency.

3.3 Maine Department of Environmental Protection

The MDEP authorizes most hydropower development through the Maine Waterway Development and Conservation Act (MWDCA). The MWDCA provides that all activities related to hydropower permitting, such as construction, maintenance, and modification, are administered by MDEP.

In 2009 and 2010, the Maine Legislature enacted laws to encourage renewable ocean energy development, to facilitate coordination among state agencies, while preserving the environmental integrity of the state’s waters. The State of Maine also has a Memorandum of Understanding with FERC to coordinate and streamline the review of hydrokinetic project applications. The resulting “General Permit for Tidal Energy Demonstration Project” is part of the MWDCA and streamlines submerged lands permitting and protected natural resources permitting for tidal energy demonstration projects. In order to qualify as a tidal energy demonstration project, as defined by the State of Maine, the project must meet FERC pilot project license criteria, and be proposed primarily to test tidal energy technology. To qualify for the Natural Resources Protection Act general permit, the project may use up to two devices, which are not already used in the Gulf of Maine for commercial energy production. The State general permit application is concurrent with FERC review of the final pilot license application. State general permit application submittals include: 1) a copy of the FERC pilot project application; 2) a copy of the environmental assessment issued by FERC; 3) proof of general liability insurance; 4) proof of

technical and financial capacity of the project team; and 5) applicant acknowledgement that remedial action may be necessary, which includes project shutdown and site remediation. The single permit issued by MDEP includes Clean Water Act (section 401) Water Quality Certification and Federal Consistency Certification for the CZMA.

The Maine Department of Marine Resources (MDMR) and the Maine Department of Inland Fisheries and Wildlife (MDIF&W) review and consult with the MDEP on hydropower permit applications to ensure compliance with wildlife and fisheries protection under the Maine Endangered Species Act. The Maine Historic Preservation Commission reviews and consults with the MDEP on projects near historic or pre-historic resources. As noted in Section 3.1, state agencies are included as part of an applicant's consultation requirements under Federal law. During the notification process that is part of all FERC licensing processes, other state, federal, or tribal agencies, organizations, or members of the public have an opportunity to indicate interest in the project activities, and be included in communications. Additional information on becoming an intervener through FERC is described in Section 3.5.

MDEP's informational publication, titled "*Regulation of Tidal and Wave Energy Projects*" (2010), is included as Appendix Task 4-3.

3.4 Maine Bureau of Parks and Lands

The Maine Department of Conservation, Bureau of Parks and Lands requires a Submerged Lands lease for the use of water over public lands, including sub-tidal lands in estuarine rivers. The state general permit application for tidal power is submitted to the Maine Department of Conservation; review timelines and post-filing procedures vary, based on project purpose (demonstration or commercial scale). This process occurs concurrently with an applicant's filing of materials with MDEP.

3.5 Municipal Ordinances

State of Maine Tidal General Permit law dictates that a municipality may not enact any standard or condition that is more stringent than those of the state law. There are likely local permitting requirements for any hydrokinetic project because impacts associated with these projects may occur in the Shoreland Zone. The Shoreland Zone is a permitting zone within 250 feet of a great pond or river; tidally influenced wetlands and waterbodies; defined freshwater wetlands; and within 75 feet of certain streams. Hydrokinetic projects have the potential to impact shared community resources, and neighboring towns may have a significant interest in nearby hydrokinetic projects. Potential applicants should consider involving local municipalities and regional organizations in their consultation process.

FERC's Rules of Practice and Procedure allow the opportunity for an interested party to become an intervener in FERC's permitting and licensing process. Intervener status grants an interested party the opportunity to be an active participant in the FERC proceeding, as well as the right to request a rehearing. Interveners receive materials filed by the applicant, by FERC as relevant to the project, and from other interested parties. A person or entity that files a timely Motion to Intervene, with no opposition filed, becomes an intervener. If opposition is filed, or if the motion is not timely, the entity becomes an intervener only if specifically granted.

In consideration of its proximity to the proposed Wiscasset Project, the Town of Westport Island filed for intervenor status during the 60-day period following FERC's acceptance of the Preliminary Permit application. In the Motion to Intervene, the Town of Westport Island noted their rationale was based on the proximity of the proposed project area to the Town's shoreline, and the potential for a project to impact the resources that are currently utilized in a variety of ways by its citizens.

We understand that the Wiscasset Tidal Resources Project worked closely with Town of Wiscasset officials, including the town manager, planner, and select board, and initiated discussions with the neighboring Town of Westport Island.

4.0 FERC DOCKET REVIEW

A review of several FERC dockets was completed to determine current FERC precedents regarding filing requirements, procedures, and study requirements for hydrokinetic projects. FERC project dockets are available on-line through their e-library system, at: <http://www.ferc.gov/docs-filing/elibrary.asp>. FERC dockets were selected that had a common tie to the Wiscasset project, such as location, proposed project size; we also researched projects which were known to have set precedents in hydrokinetic permitting.

4.1 Verdant Declaratory Order

This ruling allows the developer of an experimental technology to test, on a short-term basis, its technology without a FERC license, if that developer does not displace power from the interstate electric transmission grid. On February 2, 2005, Verdant Power (Verdant) filed a petition to be relieved of the requirements set forth under the FPA, namely a permit or license, in order to test their experimental turbine technology. Verdant's proposal was to field-test a hydrokinetic turbine design for a short time, as part of their Roosevelt Island Tidal Energy Project (RITE), in the East River of New York. In response, FERC issued a Declaratory Order, (FERC Commission, 2005) stating that an experimental device may be tested for a short period of time without a FERC license, provided that no power would be displaced from the grid and the goal was to pursue a FERC license. The FERC Order was clear in noting that the developer is required to comply with other federal and state laws as they related to the testing activity. The Verdant Order allowed Verdant to test turbines for 18 months. No additional definition of "short-term" was noted in the FERC Order.

The precedent set forth by the Verdant Order has been used in Maine for technology testing at two sites, ORPC's Eastport site, and TEDEC's testing site. Both sites have tested turbine designs as part of product development and environmental monitoring and research and powered batteries with the energy produced. Thus, the testing meets the Verdant Declaratory Order criteria, and neither ORPC nor TEDEC was required to have a FERC license for this testing. Both projects were required to comply with Corps (which includes consultation with federal and state fish and wildlife regulators) and MDEP permitting requirements. The Verdant Order allows a developer to test devices, configuration of these devices, and monitor environmental impacts using a simplified permitting process, as compared with the permitting options offered by FERC for in-water testing of a tidal device.

An applicant seeking to conduct testing under the Verdant Order should initiate consultation with FERC, the Corps, and MDEP. These agencies, in cooperation with the applicant and other interested parties, would determine the appropriate length of any testing approved under this order, and other terms and conditions under such an approval. The coordination and consultation requirements noted under Section 3.1 as part of hydropower licensing are also part of other federal laws, as noted further in Section 3.1. Testing under the Verdant Order may not involve FERC directly; however, an applicant will be required to work with many of the same federal, state, tribal, and interested members of the public (and through the similar information requests) because of work in waterways and potential work in areas with protected species.

4.2 Exemptions from Licensing

Conventional hydropower licensing includes a provision for an exemption from FERC licensing. The intent behind exemptions is to provide relief from the FPA for projects that are considered small (5 megawatts or less; up to 15 megawatts for a conduit hydroelectric facility) and that are considered to be “low impact”. Exemptions are issued in perpetuity and are geared toward established technologies with known impacts. They are issued with mandatory terms and conditions, which can be set by USFWS, NMFS, or state agencies, as they determine appropriate, to protect resources.

An applicant seeking an exemption from FERC licensing is advised to contact FERC staff to determine if an exemption from licensing is applicable to the proposed project. For reference, application guidelines are listed at: <http://www.ferc.gov/industries/hydropower/gen-info/licensing/small-low-impact/get-started/exemp-licens/project-comparison.asp>

In January 2010, TideWorks, LLC, was the first project to apply for a FERC exemption from licensing for a hydrokinetic project. TideWorks proposed a single turbine-style generator unit with an estimated capacity of 5 kilowatts, mounted to a pontoon float in the Sasanoa River, in Georgetown, Maine. The proposed turbine unit generates power using run-of-the-river natural water flow. The applicant did not propose in-water construction activities, such as pilings or buried cable. One turbine unit was proposed with no plans for additional units. In their application, TideWorks provided information on mapped Essential Fish Habitat, National Oceanographic and Atmospheric Administration habitats, aquaculture sites, and eelgrass distribution (information that is available through NOAA and MDMR). In pre-filing consultation, NMFS noted the presence of two federally-listed endangered species near the project area, Atlantic salmon (*Salmo salar*) and shortnose sturgeon (*Acipenser brevirostrum*). Also in pre-filing consultation, MDMR expressed concerns regarding the potential fisheries impact of the project, and requested a baseline study of fish populations or screen of the turbine unit.

In response to the filed application, NMFS requested TideWorks conduct a baseline fish population study. MDMR and USFWS recommended, among other items, that the turbine be screened to prevent harm to fish and other marine organisms. The screening requirement was based on screening as a typical condition required for conventional hydropower projects, and was imposed because USFWS noted there was a lack of information about the impacts of the proposed turbine unit on fishery resources. TideWorks maintained that screening of the turbine unit to the specifications requested by the agencies would in effect create a non-operational

device. TideWorks also indicated that the cost of the fisheries study recommended by the agencies was not within the budget of the project.

In December 2010, FERC organized a project teleconference with the goal of reaching compromise between agency study requests and TideWorks proposed studies. Participants included TideWorks, USFWS, NMFS, and MDMR. The discussion concluded with FERC directing TideWorks to continue working with the agencies to develop measures to protect fisheries. In follow-up discussions, TideWorks stated these agencies were not willing to change their approach. In March 2011, TideWorks requested that FERC convert their exemption application into a pilot project application. Upon review, FERC noted additional information was needed prior to this conversion. In January 2012, FERC denied TideWorks' exemption application and dismissed the conversion to a pilot license application on the basis that the project as proposed did not meet the pilot project criteria and that TideWorks failed to file the additional information requested.

It is our understanding that exemptions from FERC licensing are not practical at this time for hydrokinetic projects in part based on this project history and the intent of the exemption process. The intent of the exemption from permitting is to exempt those projects that use known technologies with understood impacts. At this time, the impacts of hydrokinetic devices on the environment are not known to the degree that they can be quantified as "low impact".

4.3 Strict Scrutiny Policy

FERC's standard policies regarding granting conventional hydropower preliminary permits do not subject project progress to "extensive" scrutiny. The preliminary permit only grants the right to investigate the feasibility of a project, does not convey land rights, and does not grant construction or operation rights. Because of the preliminary permit's narrow latitude, FERC staff has granted these permit "without requiring an extensive showing" by the applicant (FERC Commission, 2007). A conventional hydropower license, in contrast, grants the applicant the right to construct and operate a hydropower project. It also carries the possibility of obtaining land through eminent domain in cases when the applicant was not able to obtain lands by contract. As such, the process of obtaining a license for a traditional hydropower project is a "full, searching, public interest inquiry."

Following several site characterization reports in 2005 and 2006, which identified and rated locations that had potential for hydrokinetic power generation, FERC experienced a rush of preliminary permit applications. Several of these projects did not make progress toward a license application, which created concerns over "site banking". In 2007, in response to the increasing interest in, and number of applications for, hydrokinetic preliminary permits, FERC evaluated its policies on issuing and reviewing preliminary permits for hydrokinetic projects. FERC acknowledged the significant potential of hydrokinetic development and the importance of FERC's role in fostering and mediating the orderly development of this resource. Based on input from FERC staff and the interested public and agencies, FERC adopted a "strict scrutiny" policy with regard to issuing hydrokinetic preliminary permits and with regard to permit continuance and renewal. This "strict scrutiny" policy is designed to prevent "site banking".

Strict scrutiny implies that projects demonstrate progress and due diligence toward a license application during the term of the preliminary permit. This project progress criterion can be met through outreach and consultation with agency stakeholders and the public, development and implementation of study plans, research of existing data, and work on project partnerships and funding. The strict scrutiny policy applies to both the timeliness and content of submittals, which include semi-annual progress reports (6 month), responses to requests for information, updates on agency and stakeholder consultations, updates on study plan development, and subsequent preliminary permit applications.

FERC Staff have applied this strict-scrutiny policy in several ways. Natural Currents was the permit holder for the Long Island Sound Tidal Energy Project in Suffolk County, New York. After not submitting the DPLA on the initial deadline, or on the extension deadline, and late submission of several progress reports, FERC cancelled Natural Currents preliminary permit for this site. Natural Currents re-applied for a preliminary permit on the same site. FERC dismissed the preliminary permit application. In its decision, FERC staff noted that “[an applicant] must demonstrate that under the prior permit it pursued the project with due diligence and in good faith”. This includes “certain minimal steps”, such as filing timely semi-annual reports, and meeting deadlines set forth for DPLA (for Pilot license), or pre-application document (for traditional license) submission (FERC Staff, 2010).

FERC has applied strict-scrutiny to submittals as well. Natural Currents is the permit holder for the Kingsbridge Tidal Energy Project. In accordance with the preliminary permit process plan, Natural Currents submitted a DPLA in a timely manner. FERC dismissed the DPLA, noting the information in the application was insufficient; specifically, there was a lack of consultation with some regulatory agencies, there were no post-development monitoring and safeguard plans, and a “general lack of detail and specificity in [the] draft application” (FERC Staff, 2011). Natural Currents subsequent preliminary permit application for this site was denied by FERC. The Commission cited that a review of the history of this project indicated late filings of semi-annual reports and schedules, and an incomplete DPLA (FERC Staff, 2013).

In discussions with state and federal agency personnel, we understand that they track the developments of hydrokinetic projects by reviewing the 6-month progress reports submitted by the permit holder to FERC. Submittals to FERC provide a means for stakeholders to stay informed and involved in project progress.

4.4 Timelines

The FERC preliminary permit has a term of three years, a timeframe which is designed to allow an applicant to study the feasibility of a proposed hydro project. The pilot project licensing process is intended to be completed in as little as six months from DPLA submittal. To date, many aspects of the hydrokinetic permitting process have required a longer timeframe than proposed in FERC guidelines. As the understanding of the technology, its impacts, and the permitting process grow, these timelines are expected to shorten.

At this stage of the development of hydrokinetic devices, every aspect of turbine design continues to be developed and perfected, from blade geometry and material composition, to generator parts, to mooring configuration. Likewise, the methods and equipment to monitor the

environmental impacts of turbines are being developed and modified. As changes are made to turbine components and planned arrays of turbines, the environmental impacts of these changes need to be considered. Some of the knowledge, research, and experience of conventional hydropower are applicable to hydrokinetic projects; in other cases, the emerging tidal industry is developing the knowledge base and the industry standards as they develop projects. FERC, the lead regulatory oversight body, is adapting regulations and its oversight process to best serve the growing industry, while cooperating with regulatory agencies, and interested public stakeholders. Thus, the regulatory process is being developed concurrently as well.

Hydrokinetic projects currently under development are working within their second preliminary permit (projects such as the East River Tidal Energy Project in New York, NY and the Nantucket Tidal Energy Project in Edgartown, MA) or third preliminary permit. Prior to FERC's granting the first two pilot project licenses for tidal power projects, both the RITE Project and the Coombscook Bay Tidal Energy Project (CBTEP) were completing work under third preliminary permits. The amount of time required for applicants to conduct the required research, consultation, and study plan development has been longer than the three-year term of the preliminary permit. Additional information requests (AIR) from FERC and comments from stakeholders after submittal of pilot license components have extended the review timeline from the intended six months to years. In the case of the RITE, Verdant submitted their final Pilot License Application (FPLA) two years after the submittal of the DPLA. The Nantucket Tidal Energy Project submitted a DPLA on January 31, 2011, and has continued project and study development, and stakeholder outreach; however, extensions have been requested for FPLA submittal, making the pilot license process a 2.5 year process in practice for this project.

To date, FERC has granted three pilot licenses for hydrokinetic projects. The first pilot project license was granted to the Makah Bay Offshore Wave Energy Pilot Project. This project planned to convert wave energy in Makah Bay, off the coast of Washington, and was issued a license on December 20, 2007. On February 06, 2009, Finavera, the project owner, surrendered the pilot license, citing economic conditions that prevented the company from obtaining the required capital investment to begin construction. In early 2012, both the RITE Project and the CBTEP obtained FERC pilot project licenses. Construction of the first phase of the CBTEP began in March 2012, and the project began delivering power to the grid in September of 2012. CBTEP represents the first commercial grid-connected tidal power system in the U.S. and the first ocean energy project to deliver power to the grid anywhere in the U.S. and the Americas. Since license issuance, Verdant has continued to refine its turbine technology, to implement and test environmental monitoring protocols, and to pursue financing for the term of the pilot project. Construction of the first phase of the RITE project is planned for 2016.

5.0 DATA GATHERED AND LESSONS LEARNED FROM THE WISCASSET TIDAL RESOURCES PROJECT

In the case of the Wiscasset Tidal Resources Project, the need for specific information on fisheries in the area was apparent early in the project. Published resource information indicated that the proposed project area is within the range of Atlantic salmon, and discussions with fisheries biologists indicated shortnose sturgeon and Atlantic sturgeon (*Acipenser oxyrinchus*) are known to use the Sheepscot-Kennebec-Androscoggin watershed. Atlantic salmon and shortnose sturgeon are federally-listed endangered species; Atlantic sturgeon is a species of

concern and, at the time of this work, was being considered for federal endangered species listing.

A study plan was needed to determine the presence and use patterns of protected species within the proposed project area. This study plan was developed by University of Maine researchers in coordination with state and federal agencies to help begin answering these questions. The initial results of the proposed two-year study showed activity of both Atlantic and shortnose sturgeon in the proposed project area. In addition, the project team learned, upon consultation with NMFS and MDMR, that Atlantic salmon smolts are released upstream of the proposed project area, and are known to occur and migrate through the project area. The agencies indicated that, in order to consider the operation of a turbine unit within the project area, additional data were needed on the presence and seasonal, temporal, and water column use patterns of these species. Some of these discussions occurred during the interagency consultation meeting; a summary of this meeting is included in Appendix Task 4-4.

Concurrently with consultations on environmental impacts, the project team worked to identify the specific area within the larger project area (which delineated in the FERC preliminary permit) that had the greatest potential for power generation. Initially, a desktop hydrodynamic modeling study was conducted by partners at the Woods Hole Oceanographic Institution to identify areas for further work. The results of this study showed five areas which would be field sampled in a spatial velocity survey over 12 hours, using an acoustic Doppler current profiler (ADCP). The results of the spatial survey showed a potentially viable area with the highest tidal velocity of sampled sites near the Westport Island bridge, an area also known as Cowseган Narrows. The project team consulted with ORPC, a local device developer, with the results of this spatial survey. The results of this consultation suggested that more data in the Westport Island/Cowseган Narrows area would help refine the viability of the site and a suitable hydrokinetic device for the site. An ADCP was deployed for a month in this area to get a more complete data set on current power density in this area. Following this research, and in consultation with ORPC, the team determined that, at this time, a device does not exist that would be able to extract power from the currents in this area. A summary of these studies is included in Appendix Task 4-5. A presentation on the Wiscasset Project experience titled, “Tidal Power Site Evaluation in Wiscasset, Maine: Data Gathered and Lessons Learned” the Chewonki Foundation’s final report to the Town of Wiscasset is included in Appendix Task 4-6.

Based on the presence of two (and potentially a third) federally-protected species in the project area, and on the lack of a hydrokinetic device which could extract power from the site, in 2012, the Town of Wiscasset decided not to continue work on the preliminary permit or to pursue a pilot license.

Through the Wiscasset Project experience, the team learned the importance of consultation and the importance of sharing information with the broader hydrokinetic community. Through the consultation process, the presence of protected species was identified early in the project. Consultation with agencies and working with University of Maine researchers allowed the Wiscasset Project to collaborate with existing efforts, particularly with fisheries studies. Acoustic receivers and acoustic transmitters on sturgeon, which provided valuable baseline data, were part of an existing study. University of Maine researchers were able cooperate with this

existing study to leverage an existing network of equipment and accomplish needed research for the Wiscasset Project. The cost and effort to replicate this work in the absence of cooperative support would not have been feasible for the Wiscasset Project. Similarly, outreach efforts and hydrodynamic modeling were performed in conjunction with larger studies, which were identified through the collaboration process. Identifying partners and leveraging collaborative efforts was important in making progress on the Wiscasset site.

The project team learned that, in practice, FERC does not have a process to permit or license small or community scale hydrokinetic projects. This project began with S.W. Cole's involvement to aid the Wiscasset Project with community-scale tidal power development. Through this process, the team has learned that at this early stage of the permitting process, there is no difference between permitting a community scale project and commercial scale project. Both the CBTEP and RITE Projects started by testing devices with small deployments, initially under the Verdant Order, and have continued progress under their pilot licenses. Also significant for permitting considerations is that all hydrokinetic projects, because of work in navigable waters, will trigger the involvement of either FERC or Corps, which then triggers the reviews indicated in Section 3.1. At this stage, with relatively new technologies which have environmental impacts that are not well understood or quantified, studies are required to attempt to define impacts. The number and scope of these studies may be prohibitive for community scale hydrokinetic projects.

6.0 FRAMEWORK FOR TIDAL POWER PERMITTING AND SITE DEVELOPMENT

Based on the experience gained during this process, and the experiences shared by other developers in the hydrokinetic industry, this framework is offered as a process for the development of a tidal power site. This document is intended to be adaptable as permitting requirements and understanding of the hydrokinetic project development and permitting process grows.

6.1 *Submit a FERC Preliminary Permit for the Project Area*

The FERC preliminary permit establishes “first-to-file” priority for a site. It is not a prerequisite for a pilot license application; however, it does protect the investment of the prospective project owner/developer and gives priority to the permit holder in the pilot license application process. An introduction to the preliminary permit process and information on application requirements can be found at: <http://www.ferc.gov/industries/hydropower/gen-info/licensing/pre-permits.asp>

An example of a FERC-issued preliminary permit can be found at:

<http://www.ferc.gov/industries/hydropower/gen-info/licensing/hydrokinetics.asp>

Consistent with FERC's strict-scrutiny policy, preliminary permit applications for hydrokinetic projects require a high level of detail about the proposed project, including potential technologies to be used and energy production estimates; proposed studies and research during the preliminary permit period; a statement of costs and finances for the studies and work mentioned in the preliminary permit application; and maps and plans showing proposed project areas. Upon receiving a preliminary permit, the project owner submits a planned schedule of activities, which is intended to culminate in the submission of the DPLA. Standard permit conditions stipulate the permit holder also submit progress reports every six months, and a Notice of Intent (NOI) and

DPLA within two years of receiving the preliminary permit. The NOI identifies the applicant, the project, its location, its general scope and facilities, and operating capacity. The NOI also identifies any municipalities, federal agencies, and tribes which may be interested in or affected by the proposed project.

6.2 Research Existing Information and Identify Information Gaps

During the term of the preliminary permit, the applicant researches existing information on available hydrokinetic technologies; the site and its energy resource potential and environmental suitability. The applicant also initiates consultation with stakeholders, who may be able to provide information on resources and impacts. The information gathered during the preliminary permit term is intended to be useful in the decision making process as the applicant weighs the benefits, costs, and impacts of the potential development; this information also creates some of the submittals toward the pilot license application. Thus, the application requirements listed below are specifically for the pilot license application submittal, but are also beneficial research areas during the preliminary permit term.

The pilot license process and application are designed to consider thoroughly the environmental impacts and alternatives of a proposed hydrokinetic project; to develop operations, monitoring and safeguard plans; and to allow for stakeholder input and resolution of differences in information expectations. The pilot license application is derived from the conventional licensing application but places emphasis on the portions that are relevant to hydrokinetic projects.

Generally, the pilot license application content requirements include:

- 1) General content requirements
 - a. Identify affected or interested entities
- 2) General description of water source
- 3) Cumulative effects on resources
- 4) Applicable laws and status of the applicant's consultation under these laws [Laws were listed in Section 3.1]
- 5) Project location, facilities, and operation
- 6) Proposed action and action alternatives
 - a. Description of the affected environment
 - i. Geology and soils
 - ii. Water resources
 - iii. Fish and aquatic resources
 - iv. Wildlife and botanical resources
 - v. Recreation, land use, and ocean use
 - vi. Aesthetic resources

- b. Environmental analysis
 - i. Anticipated environmental effects
 - ii. Proposed project monitoring plan
 - iii. Proposed safeguard plan
- 7) Consultation/communication record
- 8) Proposed process plan and schedule
- 9) Request for waivers/designations

Informational materials from FERC describe pilot license application contents in more detail. FERC's *Licensing Hydrokinetic Pilot Projects* is the white paper that describes the newly adapted hydrokinetic pilot license process, modified from the conventional licensing application. This is included in Appendix Task 4-7, and can be found on-line at:
<http://www.ferc.gov/industries/hydropower/gen-info/licensing/hydrokinetics/energy-pilot.asp>.

Within this white paper, Appendix Task 4A-3 discusses pilot license application requirements in greater depth.

Also available from FERC is a *Hydrokinetic Pilot Project Criteria and Draft Application Checklist*, which is used by FERC to assess application completeness. This is also available on-line:

http://www.ferc.gov/industries/hydropower/gen-nfo/licensing/hydrokinetics/pdf/pilot_project.pdf

Examples of DPLA and FPLA can be found at the FERC e-library, <http://www.ferc.gov/docs-filing/elibrary.asp>, by search under a project docket number or name.

Information included in the pilot license application can include published scientific research, agency data or organizational data relevant to the species, environment, or technology used at the site. The research and information do not necessarily need to be original research conducted by the applicant. Consultation with FERC staff and relevant agencies can help to identify information sources and determine what information is relevant. In Maine, relevant agencies include; MDEP, MDIF&W, MDMR, native tribes, and Maine Historic Preservation Commission.

Coordination with and outreach to regulatory agencies, researchers, consultants, tribes, environmental groups, businesses, interested stakeholders and the public may be useful in discovering new sources of information, research, or cooperation.

Sources of existing and relevant information include:

National Wetland Inventory Maps, available at:

<http://www.fws.gov/wetlands/Data/Mapper.html>

USDA-NRCS Soil Survey Maps, available at:
<http://websoilsurvey.nrcs.usda.gov/app/HomePage.htm>

FEMA Flood Zone Maps, found at:
<https://msc.fema.gov/webapp/wcs/stores/servlet/FemaWelcomeView?storeId=10001&catalogId=10001&langId=-1>

NOAA Essential Fish Habitat Maps,
<http://www.habitat.noaa.gov/protection/efh/efhmapper/index.html>

Bedrock and Surficial Geology Maps, usually available through state geological agencies. In Maine, available through the Maine Geological Survey, on-line at:
<http://www.maine.gov/doc/nrimc/mgs/pubs/index.htm>

Maps of protected species and habitats, available through state and federal resource agencies. In Maine, preliminary site reviews for federally-protected species can be conducted on-line at:
<http://www.fws.gov/mainefieldoffice/Project%20reviews.html>

For state protected species and habitats, consult with:
Maine Department of Inland Fisheries and Wildlife, a contact list by region is on-line:
<http://www.maine.gov/ifw/aboutus/contactus.htm>

Maine Department of Marine Resources: <http://www.maine.gov/dmr/headquarters.htm>

Maine Natural Areas Program maintains a database of plant and natural community occurrences in Maine: <http://www.maine.gov/doc/nrimc/mnap/index.html>

These sources of information should be viewed as preliminary. Additional consultation and additional studies are likely to be needed as the scope of the project continues to be researched.

6.3 Develop Study Plans for Information Gaps

As gaps in existing research are found, the applicant will develop study plans, in consultation with regulatory agencies, natural resource professionals, researchers and interested members of the public. The FERC guidelines noted above can help to determine areas of missing information and potential studies that may be needed. If differences about the nature and extent of study programs or mitigation measures develop, FERC staff attempt to develop a process to resolve these.

6.4 Increase Site Knowledge Incrementally

The preliminary permit is intended to secure a potential project site, while the project developer investigates the feasibility of the project, and determines project permitting requirements. Studies of energy extraction feasibility and natural resource considerations can be done incrementally, as was done with the Wiscasset Project hydrodynamics and fisheries work. At each increment, the project owner can re-assess project feasibility and may choose to involve regulatory and public stakeholders in this assessment. This approach has been followed by several tidal developers, such as ORPC, Verdant, Natural Currents, and the Wiscasset Project.

6.5 Stakeholder Outreach and Involvement

FERC emphasizes the importance of stakeholder involvement through the licensing process for hydrokinetic projects. FERC licensing requirements include the submission of a consultation record. Consultation with stakeholders can identify information sources and gaps in information that may require study development. Consultation may also create networks for information exchange and build cooperative partnerships.

The hydrokinetic field is an emerging industry and an emerging area of research. The importance of researchers, regulators, industry partners, and the public communicating throughout the process cannot be overstated.

REFERENCES

FERC Commission. 2005. “*Declaratory Order*”; Declaratory Order – Verdant Power, Project 12178-001. April 14, 2005.

FERC Commission. 2007. “Preliminary Permits for Wave, Current, and Instream New Technology; Hydropower Projects”. Docket RM07-08-000. February 15, 2007

FERC Staff. 2008. *Licensing Hydrokinetic Pilot Projects*. April 14, 2008. Accessed at: https://www.ferc.gov/industries/hydropower/gen-info/licensing/hydrokinetics/pdf/white_paper.pdf

FERC Staff. 2010. *Order Dismissing Preliminary Permit Application*. Docket P-13663-000. April 29, 2010.

FERC Staff. 2011. “*Dismissal of Draft Application*”. Docket P-13247; April 4, 2011

FERC Staff. 2013. “*Order Denying Successive Preliminary Permit*”. Docket P-13247. May 22, 2013

Hagerman, George and Roger Bedard. 2006. *Maine Tidal In-Stream Energy Conversion (TISEC): Survey and Characterization of Potential Project Sites*. Electric Power Research Institute Report EPRI-TP-003 ME Rev 1.

Maine Department of Environmental Protection Staff. 2010. *DEP Information Sheet: Regulation of Tidal and Wave Energy Projects*. Available at: http://www.maine.gov/dep/water/dams-hydro/is_tidal_wave_reg.html

FERC web site. 2013. Licensing Processes. Describes the licensing processes available for hydropower licensing, with links to Federal Power Act (FPA) citations: <http://www.ferc.gov/industries/hydropower/gen-info/licensing/licen-pro.asp>

APPENDIX Task 4-2

Note: This document contains its own set of appendices, labeled alphabetically.

**PROTECTED NATURAL RESOURCES RECONNAISSANCE REPORT
WISCASSET TIDAL RESOURCES PROJECT
BACK RIVER, WISCASSET, MAINE**

S.W. COLE ENGINEERING, INC.

09-0428 W

MARCH 14, 2011

TABLE OF CONTENTS

1.0 Introduction	Error! Bookmark not defined.
1.1 Scope of Work	Error! Bookmark not defined.
1.2 Summary of Findings.....	Error! Bookmark not defined.
1.3 Appendices.....	Error! Bookmark not defined.
2.0 SITE LOCATION AND DESCRIPTION	Error! Bookmark not defined.
3.0 Protected Natural resource CLASSIFICATION AND DESCRIPTION	Error! Bookmark not defined.
3.1 Estuarine Wetlands	Error! Bookmark not defined.
4.0 PUBLISHED MAPPING REVIEW	Error! Bookmark not defined.
4.1 Published Mapping	Error! Bookmark not defined.
4.2 Resource Agency Correspondence/Mapping.....	Error! Bookmark not defined.
5.0 NATURAL RESOURCE REGULATIONS AND PERMITTING INFORMATION	Error! Bookmark not defined.
6.0 FINDINGS and recommendations	Error! Bookmark not defined.
7.0 CLOSING	Error! Bookmark not defined.

APPENDIX A - Limitations

APPENDIX B - Site Location Map/Protected Natural Resources Reconnaissance
Plan/Published Habitat Map/Published Mapping

APPENDIX C - Resource Agency Correspondence

APPENDIX D - Color Photographs



09-0428 W

March 14, 2011

Wiscasset Tidal Resources Project
Attention: Peter Arnold, Chewonki Foundation
485 Chewonki Neck Road
Wiscasset, ME 04578-4822

Subject: Protected Natural Resources Reconnaissance Report
Wiscasset Tidal Resources Project
Back River
Wiscasset, Maine

1.0 introduction

1.1 Scope of Work

We are pleased to present this Protected Natural Resources Reconnaissance Report for the proposed Wiscasset Tidal Resources Project in the Cowseagan Narrows area of Back River in Wiscasset, Maine. The purpose of our services was to conduct a published mapping review to identify Protected Natural Resources¹ along the shoreline of Back River and within the project area, and to conduct a field reconnaissance to identify Protected Natural Resources in the intertidal habitat of Back River and adjacent uplands. We have also reviewed pertinent permitting requirements, and begun consultation with State and Federal regulatory agencies.

We understand that our findings may be used to supplement other information that may be submitted during project permitting to the Federal Energy Regulatory Commission (FERC), the Maine Department of Environmental Protection (MDEP), the U.S. Army Corps of Engineers (Corps) and/or the Town of Wiscasset.

1.2 Summary of Findings

We identified Back River and the intertidal shoreline on either side of Cowseagan Narrows as an estuarine wetland. The intertidal zone is relatively homogeneous rockweed covered boulder and/or bedrock beach. The subtidal zone is deep water off of a steep shore. The U.S. Fish and

¹ State of Maine Department of Environmental Protection, Natural Resources Protection Act, Statute, 38 M.R.S.A. §§480-A to 480-BB, Revised 08/12/2010.

Wildlife Service (USFWS) includes the site as within mapped habitat for the Atlantic salmon, a federally-listed endangered species. We understand shortnose sturgeon and Atlantic sturgeon habitat is identified by USFWS within the Kennebec and Sheepscot estuaries, both which have a direct hydrologic connection with Back River. Shortnose sturgeon are federally-listed endangered species; Atlantic sturgeon are a species of concern, and are being considered for endangered listing.

The Maine Department of Inland Fisheries and Wildlife (IF&W) has two mapped bald eagle (federally-protected species) nests, a tidal waterfowl/wading bird habitat, and a wading bird colony in and along the Back River nearby but outside of the project area. The Maine Natural Areas Program (MNAP) noted four tidal marshes near to the site.

1.3 Appendices

This report is subject to the Limitations attached in Appendix A. Appendix B contains a Site Location Map, a Published Habitat Map, a Protected Natural Resources Reconnaissance Plan and other published mapping. Appendix C contains state and federal natural resource agency correspondence. Appendix D contains color photographs.

2.0 SITE LOCATION AND DESCRIPTION

The site is located in the Cowseagan Narrows area of Back River in Wiscasset, Maine. This area of the River is at the Route 144 bridge crossing, which is south of the downtown district of Wiscasset. A Site Location Map is attached in Appendix B as Sheet B-1. A Published Habitat Map and a Protected Natural Resources Reconnaissance Plan are attached as Sheet B-2.

Back River is a northeast-southwest oriented tidally influenced watercourse flowing between the Sheepscot River (to the north) and the Kennebec River (to the south). The Sasanoa River crosses Back River in Hockamock Bay, south of the site. In the area of the site, Back River flows north into the Sheepscot River during the ebb tide and south on the flood tide. Back River has a semidiurnal tide with a maximum tidal height range of approximately 13 feet, and an average tidal height range of between approximately 9 to 10 feet.

The land along Back River in the area of the site is generally wooded and in low density residential development, with most of the residences having a ramp and float system or pier jutting into the River. Both the east and west shorelines of the River are relatively steep with a predominance of ledge and boulders, indicative of the higher energy environment of the tidal “rip” in this area.

3.0 Protected Natural resource CLASSIFICATION AND DESCRIPTION

We conducted a site visit on November 02, 2010 to identify field observable MDEP Protected Natural Resources.

We walked and observed the intertidal area along both the east and west sides of Back River in the Cowseagan Narrows area. We collected GPS data points along the observable high tide line using the “visual assessment of debris line” and “vegetation method” portions of the Natural Resource Protection Act definition of a coastal wetland.

We also collected GPS data points along the near low water line. The published low tide in the Sheepscot River in Wiscasset, Maine on November 02, 2010 was at 2:12 PM at 0.1 foot. Our low tide line data was collected between approximately 12:30 PM and 1:00 PM. We were able to observe the low intertidal habitat under shallow water at the time of our site visit. Due to the steep nature of the shoreline, and deep water directly off the shore, the bottom habitat of the subtidal area was not observed, although we did observe some seaweed in the shallow subtidal area.

We used a mapping grade Trimble GPS to collect location data and overlaid that data onto a Maine Office of GIS aerial photograph dated July 24, 2005, taken at low tide, to make the Protected Natural Resources Reconnaissance Plan attached in Appendix B. The high and low tide lines depicted on the Plan are a connection of our GPS data points and interpretation of aerial photography, they do not represent a surveyed line. Maine GIS data of habitats mapped by resource agencies were used to make the Published Habitat Map.

3.1 Estuarine Wetlands

The intertidal habitat along the narrows is relatively homogeneous, dominated by rockweed covered ledge and boulders. The western side of the narrows is steeper and contains more ledge than the eastern side. On the western side, south of the bridge crossing, is a cliff face with a steep boulder beach at its base. North of the bridge crossing is a ledge and boulder beach ranging from about a 20% to 50+% slope. The high intertidal zone is bare to sparsely covered with rockweed (*Ascophyllum nodosum*), the mid and low intertidal densely covered with rockweed, and the shallow subtidal a transitional zone to deep water with dense rockweed and sparse kelp (*Laminaria* sp.) observed. Scuds and periwinkles were observed under the rockweed in areas.

The eastern side of the narrows is less steep, mostly ranging from about 10% to 25% slope, and with less ledge outcrop. While the eastern side is dominated by boulder beach, less steep areas

of finer sediments and salt marsh fringe wetlands also exist. Based on this, the eastern shore appears to experience less tidal energy than the western shore. Rockweed abundance in the intertidal zone is similar to the western side.

Using the Cowardin Classification system², we classified the intertidal zone of Back River as E2AB1N or estuarine, intertidal, aquatic bed, algal wetland with a regularly flooded tidal water regime. Using the Maine's Coastal Wetlands classification system³, we classified the intertidal zone of Back River as dominated by Boulder Beach with Algae (rockweed) habitat, with smaller areas of Ledge with Algae habitat, Mixed Coarse and Fine Flats with Algae habitat (eastern side only), and Salt Marsh habitat (eastern side only).

Using the Cowardin Classification system, we classified the subtidal area of Back River as a E1OWL or estuarine, subtidal, open water (unknown substrate) wetland with a subtidal water regime.

4.0 PUBLISHED MAPPING REVIEW

4.1 Published Mapping

We reviewed the USFWS National Wetland Inventory (NWI) Map, accessed on the USFWS website on January 20, 2011. The NWI Map shows the Narrows in Back River (open water) as a E1UBL, or an estuarine, subtidal, unconsolidated bottom wetland with a subtidal water regime. The eastern shore of the Narrows is mapped as a E2AB1N or an estuarine, intertidal, aquatic bed, algal wetland with a regularly flooded tidal water regime. The southernmost western shore is mapped as a E2EM1P or estuarine, intertidal, emergent, persistent wetland with an irregularly flooded tidal water regime.

We reviewed the USDA Natural Resources Conservation Service (NRCS) Soil Survey of the site, accessed on the USDA website on January 25, 2011. The NRCS maps Back River as "W" or water. The land on either side of the River in the area of the site is mapped as Lyman-Rock Outcrop-Tunbridge complex (west side) and Tunbridge-Lyman complex (east side) soils. Lyman and Tunbridge soils are shallow (10 to <20" over bedrock) and moderately deep (20 to <40" over bedrock) somewhat excessively and well drained loamy glacial till soils.

² Cowardin, Lewis M., V. Carter, F.C. Golet, E.T. LaRoe, 1979, Classification of Wetlands & Deepwater Habitats of the U.S., U.S.D.I, Fish & Wildlife Service, Washington, D.C. Jamestown, ND: Northern Prairie Wildlife Research Center Home Page. <http://www.npwrc.usgs.gov/resource/1998/classwet/classwet.htm> (Version 04DEC98).

³ Ward, Alison E., 1999, Maine's Coastal Wetlands: I. Types, Distribution, Rankings, Functions and Values. Maine Department of Environmental Protection, Augusta, ME. DEP LW 1999-13.

We reviewed the Federal Emergency Management Agency (FEMA) Flood Insurance Rate Map (FIRM) for the Town of Wiscasset, Maine, accessed on the FEMA website on January 25, 2011. FEMA maps Back River as Zone AE or “*Special Flood Hazard Areas Inundated by 100-year flood*” with “*Base flood elevations determined*”. FEMA maps the upland area along the River as being within Zone X or “*Areas of 500-year flood; areas of 100-year flood with average depths of less than 1 foot or with drainage areas less than 1 square mile; and areas protected by levees from 100-year flood.*”

Copies of published mapping are included in Appendix B.

4.2 Resource Agency Correspondence/Mapping

We wrote letters to the MNAP, IF&W wildlife division, IF&W fisheries division, Maine Department of Marine Resources (MDMR), and the USFWS regarding mapped threatened, endangered, significant, essential or rare species or habitats on or adjacent to the site. We reviewed National Marine Fisheries Service published mapping on-line.

According to a response letter from MNAP dated September 30, 2010, an “*exemplary Hemlock Forest natural community*” occurs “*on the east face of Cushman Hill, adjacent to Cushman Cove*” (north of the site). The Hemlock Forest natural community has a State Rarity Rank of S4 or “*apparently secure in Maine*”. The letter also notes that there are four tidal marsh systems near to the site that should be documented early in the project planning process. The letter further states that there is a “high probability” that other natural significant features “*occur in the littoral zone of the tidal environment.*”

According to a verbal response and an e-mailed habitat map from the IF&W Wildlife Division on September 30, 2010, bald eagle nests, which are considered Endangered, Threatened, & Special Concern Species Habitats by IF&W, are mapped on Berry Island (south of the site), and on a point of land on the western shore of Back River north of Cushman Cove (north of the site). Tidal Waterfowl/Wading Bird Habitats are mapped along Cushman Cove (north of the site) and along a cove on the western shore (south of the site). A Wading Bird Colony is mapped on Berry Island. According to Mr. Keel Kemper, IF&W assistant regional wildlife biologist, the colony is likely a Great Blue Heron rookery. Mr. Kemper stated that he feels that based on his knowledge of the project and considering existing area development, the project is not likely to have a negative impact on the wildlife resources mapped by IF&W in the vicinity of the site.

According to a response letter from the IF&W Fisheries Division, dated September 28, 2010, there is no published mapping of significant fisheries habitat in the area of the site. The letter notes that IF&W has not surveyed that area because it is estuarine, however, “*there are numerous areas in the lower Sheepscot and Back Rivers that provide transient habitat*” for both

sea run brook trout and brown trout, which are managed by IF&W. According to the letter, IF&W does not feel that a small scale tidal power project would negatively impact either species, as long as it does not block passage or destroy foraging or refuge habitat.

According to a response letter from the USFWS dated October 1, 2010, the project “*occurs within the range of the Gulf of Maine Distinct Population Segment (GOM DPS) of Atlantic Salmon (Salmo salar) in Maine, a federally-endangered species,*” and “*occurs within a HUC-10 watershed (Sheepscot Bay) that has been designated as critical habitat for Atlantic Salmon by NMFS*” (National Marine Fisheries Service). If the project will require federal permitting, or use federal funding, the federal action agency will determine if further action or information is required regarding the Atlantic salmon habitat. The letter notes that the National Marine Fisheries Service (NMFS) and USFWS share consultation responsibilities for Atlantic salmon, with NMFS handling projects in estuarine environments.

The USFWS letter also states that there are “*no other federally-listed species under the jurisdiction of the Service known to occur in the project area*”, however, it notes that occasionally bald eagles are in the area of the project. Bald eagles are no longer a federally-listed species, however, they are protected from “take”, as defined in the letter.

The MDMR referred us to their GIS mapping of the area, which is reflected on the Published Habitat Map attached in Appendix B. There are no Significant habitats mapped by MDMR on the site. Softshell clam and blue mussel habitats are mapped south of the site on the eastern shore of Back River. Also on the GIS data layer are two mapped Deer Wintering Areas on the sideslope of the land over the western side of Back River.

We accessed the National Oceanic and Atmospheric Administration (NOAA) Essential Fish Habitat (EFH) mapping website on January 26, 2011. According to the on-line mapper, “*No EFH was identified in the project area.*” However, in the specific information section for the New England region, Atlantic salmon, a federally endangered species, was listed as occurring in the Sheepscot and Kennebec Rivers, which are both within close proximity and hydrologically connected to the Back River. While not listed in any of the resources we reviewed, we understand that shortnose sturgeon (*Acipenser brevirostrum*), a federally-listed endangered species, and Atlantic sturgeon (*Acipenser oxyrinchus*) are found in the *Kennebec/Androscoggin/Sheepscot estuarine complex, which includes the Back River and the site.*

Copies of resource agency letters and mapping information are included in Appendix C.

5.0 NATURAL RESOURCE REGULATIONS AND PERMITTING INFORMATION

Based on our understanding of the project, which is development of small-scale hydrokinetic power in Back River, with attachment to the public power grid, the project will require a license or a license exemption from the Federal Energy Regulatory Commission (FERC). We understand that you currently have a FERC Preliminary Permit for the project.

In addition to FERC permitting, work in navigable waterways requires a permit from the U.S. Army Corps of Engineers. State permits and certifications will also be required, as coordinated through the Maine Department of Environmental Protection and Maine Department of Conservation Bureau of Parks and Lands. Permits may also be required from the Town of Wiscasset.

6.0 FINDINGS and recommendations

We identified the Cowseagan Narrows area of Back River and its intertidal zone along the shore as estuarine wetland. Back River is identified by NMFS as being within a HUC-10 watershed (Sheepscoot Bay) designated as critical habitat for Atlantic salmon, a federally-listed endangered species. Based on our research, it appears that shortnose sturgeon, a federally-listed endangered species, and Atlantic sturgeon, a species of concern, also may exist in the area of the site. Several mapped resources, including two bald eagle nesting habitats, a great blue heron rookery, tidal waterfowl/wading bird habitats, softshell clam habitat, tidal marshes and deer wintering areas are outside of but within proximity to the site.

We recommend commencing consultation with State and Federal agencies to determine their concerns regarding the project, and determine the extent and nature of further research that may be needed for project permitting. These agencies include: NOAA/NMFS, USFWS, MDEP, IF&W and MDMR.

7.0 CLOSING

It has been a pleasure to be of assistance to you with this phase of your project. If you have any questions, or if we may be of further assistance, please do not hesitate to contact us.

Sincerely,

S. W. COLE ENGINEERING, INC.



09-0428 W
March 14, 2011

Aleita M. Burman, Senior Wetland Scientist

AMB:amb/slh

cc: Dr. Michael Peterson
Dr. Gayle Zydlewski

P:\2009\09-0428 C - University of Maine - Castine, ME - Hydrokinetic Preliminary Site Resource Assessment - BPA\Site - Wiscasset\PNR Report.doc

APPENDIX A

Limitations

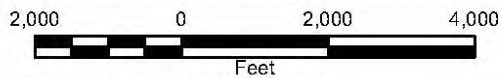
The scope of our services has been limited to the development of a Protected Natural Resources Reconnaissance Report. This report has been prepared for the exclusive use of the Wiscasset Tidal Resources Project for specific application to the proposed hydrokinetic project on Back River in Wiscasset, Maine. No warranty, expressed or implied, is made. The conclusions and recommendations presented in this report are based upon the data obtained from the areas explored.

APPENDIX B

Site Location Map/Protected Natural Resources Reconnaissance Plan/Published Habitat Map/Published Mapping



APPROXIMATE SITE LOCATION



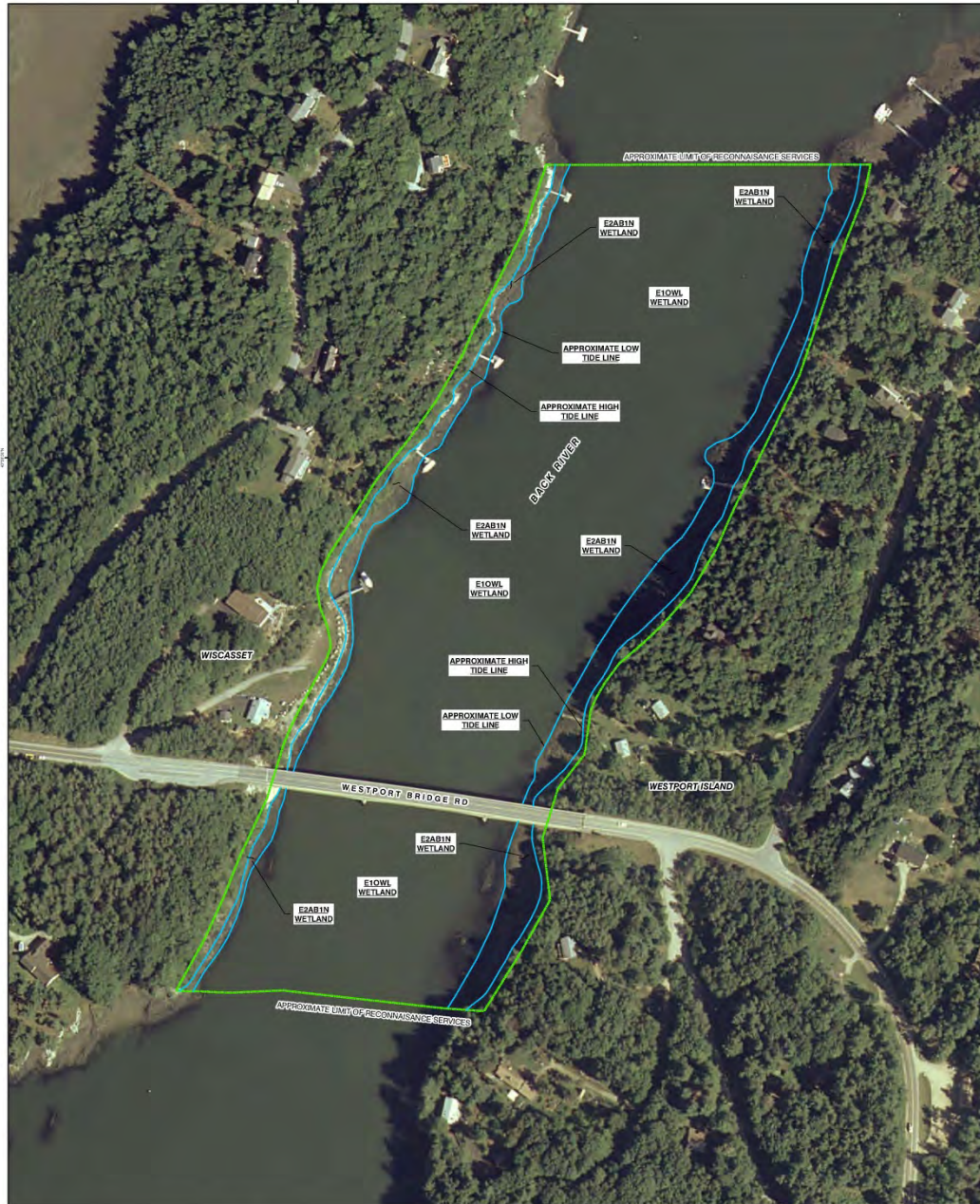
MAINE TIDAL POWER INITIATIVE

SITE LOCATION MAP

PRELIMINARY SITE RESOURCE ASSESSMENT SERVICES
 BACK RIVER
 WISCASSET AND WESTPORT ISLAND, MAINE

NOTE:
 SITE LOCATION MAP PREPARED FROM
 ESRI ArcGIS ONLINE AND DATA PARTNERS
 INCLUDING USGS AND © 2007 NATIONAL
 GEOGRAPHIC SOCIETY.

Job No.	09-0428	Scale	1:24000
Date:	02/07/2011	Sheet	B-1



- NOTES**
1. THE PURPOSE OF OUR SERVICES WAS TO CONDUCT A FIELD RECONNAISSANCE AND PUBLISHED MAPING REVIEW TO IDENTIFY PROTECTED NATURAL RESOURCES ALONG THE EAST AND WEST SHORELINE OF THE LOWMEGAN NARROWS AREA OF BACK RIVER IN WISCASSET, MAINE, AS SHOWN ON THIS PROTECTED NATURAL RESOURCES RECONNAISSANCE PLAN.
 2. OUR SERVICES WERE CONDUCTED IN GENERAL ACCORDANCE WITH THE DEFINITION OF A COASTAL WETLAND IN THE MAINE DEPARTMENT OF ENVIRONMENTAL PROTECTION'S NATURAL RESOURCES PROTECTION ACT AND THE 2009 INTERIM REGIONAL SUPPLEMENT TO THE 1987 CORPS OF ENGINEERS WETLAND DELINEATION MANUAL. THE WETLANDS WERE CLASSIFIED BASED ON METHODS DESCRIBED BY THE USDI USFWS PUBLICATION CLASSIFICATION OF WETLANDS AND URBAN/ESTUARINE WETLANDS OF THE UNITED STATES (COWARD, ET AL., 1979) AND ARE INTENDED TO GENERALLY DESCRIBE THE TYPE OF WETLANDS. THE COMMISSION BOUNDARIES ARE APPROXIMATE AND ARE BASED ON GPS DATA POINTS, AERIAL PHOTOGRAPHY REVIEW AND/OR FIELD OBSERVATIONS.
 3. BASE ORTHOPHOTOGRAPHY FROM J.W. SEWELL CO., MAINE DEPARTMENT OF MARINE RESOURCES (MDMR), MAINE OFFICE OF GEOGRAPHIC INFORMATION SYSTEMS (MIGIS/COGIS) <http://www.maine.gov/dem/mmr/mo/gis/> ENTITLED ORTHO_LMR, PHOTOGRAPHY DATED JULY 24, 2005, TAKEN AT LOW TIDE.
 4. S.W. COLE ENGINEERING, INC. CONDUCTED THE SITE VISIT ON NOVEMBER 02, 2010. SIGNIFICANT SITE FEATURES WERE LOCATED USING A MAPPING GRADE TRIMBLE GPS RECEIVER. OUR GPS DATA WAS OVERLAIN ONTO THE ABOVE REFERENCED ORTHOPHOTOGRAPHY TO MAKE THIS PROTECTED NATURAL RESOURCES RECONNAISSANCE PLAN. THE HIGH AND LOW TIDE LINES ARE A CONNECTION OF OUR GPS DATA POINTS, THEREFORE, VARIABILITY IN THE ACTUAL HIGH AND LOW TIDE LINE AND THE LINE SHOWN ON OUR PLAN MAY OCCUR. THIS PLAN DOES NOT REPRESENT A SURVEYED HIGH AND/OR LOW TIDE LINE.
 5. THIS PLAN SHOULD BE USED IN CONJUNCTION WITH THE S.W. COLE ENGINEERING, INC. PROTECTED NATURAL RESOURCES RECONNAISSANCE REPORT. THIS PLAN IS INTENDED FOR PLANNING AND PERMITTING ONLY.

LEGEND

E2ABIN	ESTUARINE, INTERTIDAL AQUATIC BED, ALGAL WETLAND WITH A REGULARLY FLOODED TIDAL WATER REGIME
E10WL	ESTUARINE, SUBTIDAL OPEN WATER UNKNOWN SUBSTRATE WETLAND WITH A SUBTIDAL WATER REGIME
[Green Line]	APPROXIMATE LIMIT OF RECONNAISSANCE SERVICES

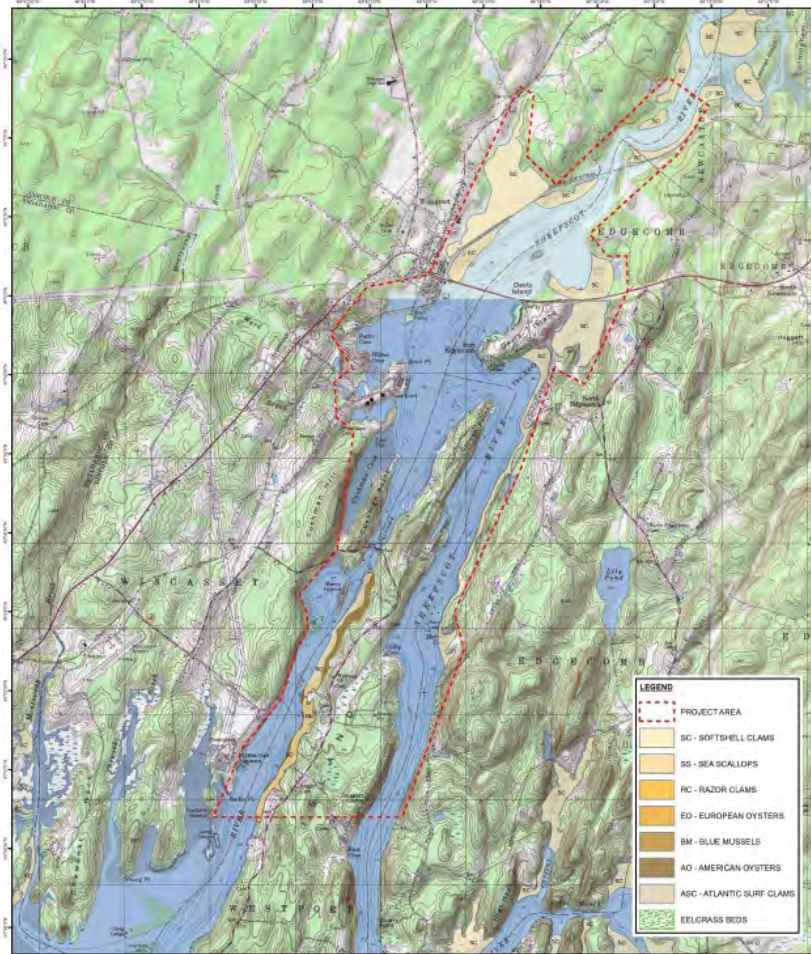


SWCOLE
SOUTHWEST COASTAL CONSULTANTS, INC.

MAINE, TIDAL, FRESHWATER
PROTECTED NATURAL RESOURCES RECONNAISSANCE PLAN

PRELIMINARY SITE RECONNAISSANCE SERVICES
BACK RIVER
WISCASSET AND WESTPORT ISLAND, MAINE

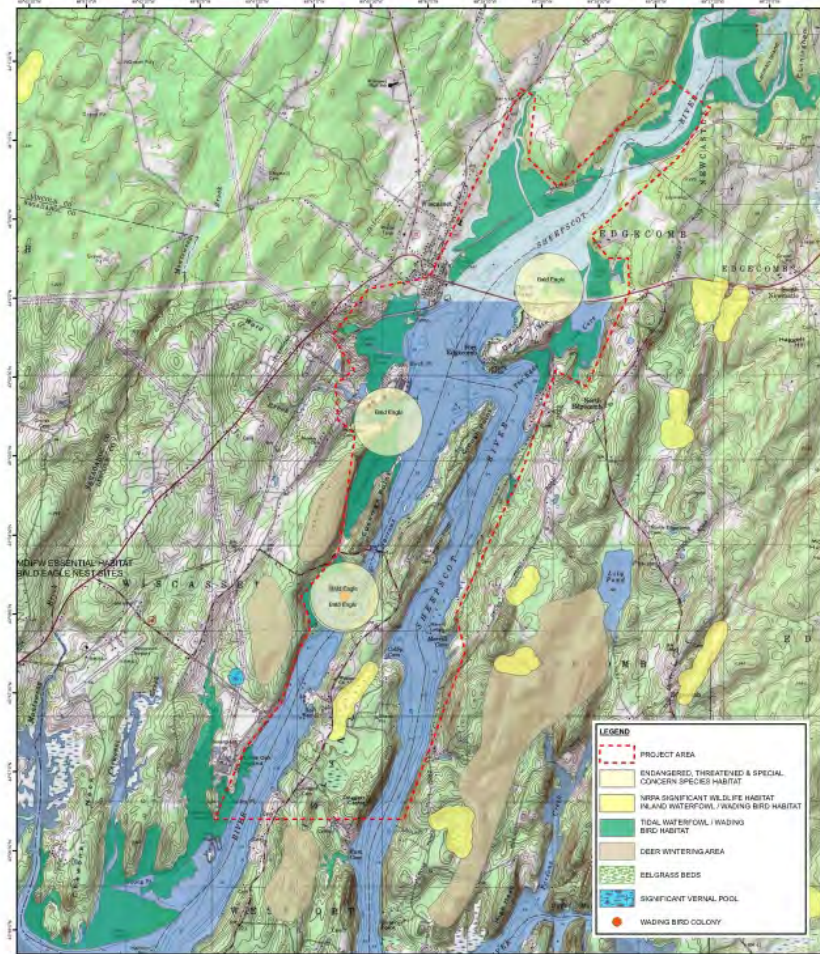
Job No. 09-0458 Sheet 1 of 150
Date: 02/07/2011 Scale: 1"=150'



MOLLUSCAN SHELLFISH HABITAT



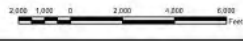
- NOTES**
1. BARE UNITS TOPOGRAPHIC MAP FROM ESRI ARCGIS ONLINE AND DATA PATENTERS INCLUDING ARCS AND © 2007 NATIONAL GEOGRAPHIC SOCIETY.
 2. MOLLUSCAN SHELLFISH FROM MAINE DEPARTMENT OF MARINE RESOURCES (MDMR), MAINE OFFICE OF GEOGRAPHIC INFORMATION SYSTEMS (MEGIS), DATED OCTOBER 13, 2010.
 3. ENDANGERED, THREATENED & SPECIAL CONCERN SPECIES HABITAT FROM MAINE DEPARTMENT OF INLAND FISHERIES AND WILDLIFE (MDIFW), DATED OCTOBER 1, 2010 AND MADE AVAILABLE THROUGH DATA REQUEST TO MDIFW OCTOBER, 2010.
 4. NPRA SIGNIFICANT WILDLIFE HABITAT INLAND WATERFOWL / WADING BIRD HABITAT FROM MAINE DEPARTMENT OF INLAND FISHERIES AND WILDLIFE (MDIFW), MAINE OFFICE OF GEOGRAPHIC INFORMATION SYSTEMS (MEGIS), DATED DECEMBER 2008.



SIGNIFICANT WILDLIFE AND ESSENTIAL HABITATS



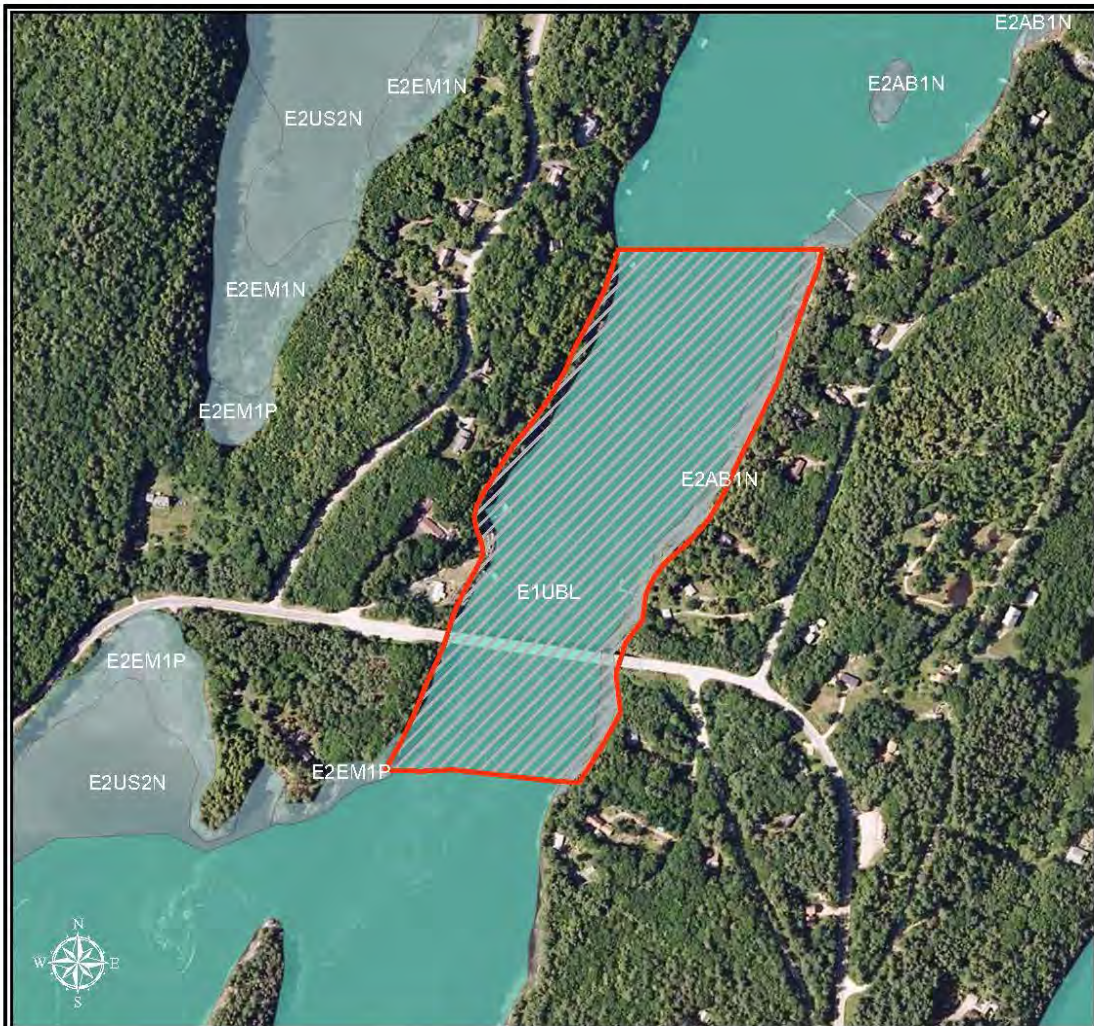
5. TIDAL WATERFOWL / WADING BIRD HABITAT FROM MAINE DEPARTMENT OF INLAND FISHERIES AND WILDLIFE (MDIFW), WILDLIFE RESOURCE ASSESSMENT SECTION, HABITAT GROUP, AND MDIFW, WILDLIFE MANAGEMENT SECTION, REGIONAL STAFF AND MADE AVAILABLE THROUGH DATA REQUEST TO MDIFW JANUARY 2011.
6. DEER WINTERING AREAS FROM MAINE DEPARTMENT OF INLAND FISHERIES AND WILDLIFE (MDIFW) AND MADE AVAILABLE THROUGH DATA REQUEST TO MDIFW OCTOBER, 2010.
7. EELGRASS BEDS FROM MAINE DEPARTMENT OF MARINE RESOURCES (MDMR), MAINE OFFICE OF GEOGRAPHIC INFORMATION SYSTEMS (MEGIS), DATED 2008.
8. SIGNIFICANT VERNAL POOLS FROM MAINE DEPARTMENT OF INLAND FISHERIES AND WILDLIFE (MDIFW) AND MADE AVAILABLE THROUGH DATA REQUEST TO MDIFW OCTOBER, 2010.




SWOLE
Sustainable Water & Environmental Solutions

MAINE TIDAL FRESHWATER
PUBLISHED HABITAT MAP
PRELIMINARY SITE RESPONSE ASSESSMENT SERVICES
BACK RIVER
WISCONSINET AND WESTPORT ISLAND MAINE

JOB No. 09-028 Scale 1:24,000
Date: 02/07/2011 Sheet: 0-1



LEGEND

 APPROXIMATE SITE LOCATION

NOTES:

1. NATIONAL WETLANDS INVENTORY MAP PREPARED FROM ESRI ArcGIS ONLINE AND DATA PARTNERS INCLUDING USGS AND © 2007 NATIONAL GEOGRAPHIC SOCIETY.

2. NATIONAL WETLANDS INVENTORY SPATIAL DATA FROM U.S. FISH AND WILDLIFE SERVICE (USFW), NATIONAL WETLANDS INVENTORY (NWI).

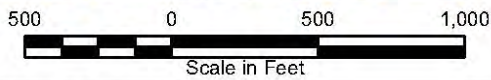


MAINE TIDAL POWER INITIATIVE

NATIONAL WETLANDS INVENTORY MAP

PRELIMINARY SITE RESOURCE ASSESSMENT SERVICES
BACK RIVER
WISCASSET AND WESTPORT ISLAND, MAINE

Job No.	09-0428	Scale	1:6000
Date:	02/07/2011	Sheet	B-4



LEGEND

 APPROXIMATE SITE LOCATION

NOTES:

1. NRCS SOIL SURVEY MAP PREPARED FROM ESRI ArcGIS ONLINE AND DATA PARTNERS INCLUDING USGS AND © 2007 NATIONAL GEOGRAPHIC SOCIETY.
2. NRCS SOIL SURVEY SPATIAL DATA FROM U.S. DEPARTMENT OF AGRICULTURE, NATURAL RESOURCES CONSERVATION SERVICE, DATED 11/21/2006, ACCESSED APRIL 2008.




MAINE TIDAL POWER INITIATIVE
NRCS SOIL SURVEY MAP

PRELIMINARY SITE RESOURCE ASSESSMENT SERVICES
 BACK RIVER
 WISCASSET AND WESTPORT ISLAND, MAINE

Job No.	09-0428	Scale	1:6000
Date:	02/07/2011	Sheet	B-5



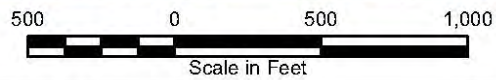
LEGEND

 APPROXIMATE SITE LOCATION

NOTES:

1. FEMA FLOOD ZONE MAP PREPARED FROM ESRI ArcGIS ONLINE AND DATA PARTNERS INCLUDING USGS AND © 2007 NATIONAL GEOGRAPHIC SOCIETY.

2. FEMA FLOOD ZONE DIGITIZED FROM SCANNED IMAGES OF FEDERAL EMERGENCY MANAGEMENT AGENCY (FEMA), FLOOD INSURANCE RATE MAP (FIRM), TOWN OF WISCASSET PANELS 2302230005B AND 2302230010B DATED 4/16/1991 AND TOWN OF WESTPORT PANELS 230222A 01 AND 02 DATED 5/31/77.



MAINE TIDAL POWER INITIATIVE
FEMA FLOOD ZONE MAP

PRELIMINARY SITE RESOURCE ASSESSMENT SERVICES
 BACK RIVER
 WISCASSET AND WESTPORT ISLAND, MAINE

Job No.	09-0428	Scale	1:6000
Date:	02/07/2011	Sheet	B-6

APPENDIX C
Resource Agency Correspondence



JOHN ELIAS BALDACCI
GOVERNOR

STATE OF MAINE
DEPARTMENT OF CONSERVATION
93 STATE HOUSE STATION
AUGUSTA, MAINE
04333-0093



ELIZA TOWNSEND
COMMISSIONER

September 30, 2010

Aleita M. Burman
S.W. Cole Engineering, Inc.
37 Liberty Drive
Bangor, Maine. 04401

Re: Rare and exemplary botanical features, Proposed Tidal Power Project, Project No. 09-0428.1, Sheepscot River, Wiscasset, Maine.

Dear Ms. Burman:

I have searched the Natural Areas Program's digital, manual and map files in response to your request of September 22, 2010 for information on the presence of rare or unique botanical features documented from the vicinity of the project site in the Town of Wiscasset, Maine. Rare and unique botanical features include the habitat of rare, threatened, or endangered plant species and unique or exemplary natural communities. Our review involves examining maps, manual and computerized records, other sources of information such as scientific articles or published references, and the personal knowledge of staff or cooperating experts.

Our official response covers only botanical features. For authoritative information and official response for zoological features you must make a similar request to the Maine Department of Inland Fisheries and Wildlife, 284 State Street, Augusta, Maine 04333.

According to our information, there is only one feature currently mapped in the area of interest. The feature is an occurrence of an exemplary Hemlock Forest natural community on the east face of Cushman Hill, adjacent to Cushman Cove. The occurrence extends from the high tide line to the crest of the hill (see attached Map 1). Note that little to no survey work for significant natural features has been conducted in this area. There is a high probability other significant natural features occur in the littoral zone of this tidal environment. The Maine Natural Areas Program has identified four tidal marsh systems within this area ranging in size from 10 to 50 acres. These systems have not been ground truthed, and if any activity is proposed that could impact them, we recommend they be documented early in the planning process (see attached Map 2).

The table below provides information on the Hemlock Forest natural community in terms of global rarity rank, state rarity rank, and element occurrence rank (see attached explanation of ranks). The element occurrence rank is a system used to rank the overall quality (i.e. condition, landscape context and size) of a natural community or rare plant occurrence. If you would like more information on this natural community, or would like to schedule a field visit to this area, please contact MNAP ecologist Don Cameron at 287-8041.

Rare and Exemplary Botanical Features in the Project Vicinity

Documented within a four-mile radius of the proposed Tidal Power Project, Wiscasset, Maine.

Feature Name	Global Rank	State Rank	State Status	EO Number	Last Seen	Habitat
Suaeda calceoliformis	G5	S2	T	3	1959-08-30	Tidal wetland (non-forested, wetland)
Bidens hyperborea	G4	S3	SC	9	1937-08	Tidal wetland (non-forested, wetland)
Hemlock forest	G4G5	S4		1	1998-06-12	Conifer forest (forest, upland)
Spartina saltmarsh	G5	S3		6	1998-09-16	Tidal wetland (non-forested, wetland)

Print Date 10/1/2010

For more information visit our website <http://www.maine.gov/doc/nrimc/mnap>

Page 1

STATE RARITY RANKS

- S1** Critically imperiled in Maine because of extreme rarity (five or fewer occurrences or very few remaining individuals or acres) or because some aspect of its biology makes it especially vulnerable to extirpation from the State of Maine.
- S2** Imperiled in Maine because of rarity (6-20 occurrences or few remaining individuals or acres) or because of other factors making it vulnerable to further decline.
- S3** Rare in Maine (20-100 occurrences).
- S4** Apparently secure in Maine.
- S5** Demonstrably secure in Maine.
- SU** Under consideration for assigning rarity status; more information needed on threats or distribution.
- SNR** Not yet ranked.
- SNA** Rank not applicable.
- S#?** Current occurrence data suggests assigned rank, but lack of survey effort along with amount of potential habitat create uncertainty (e.g. S3?).

Note: State Rarity Ranks are determined by the Maine Natural Areas Program for rare plants and rare and exemplary natural communities and ecosystems. The Maine Department of Inland Fisheries and Wildlife determines State Rarity Ranks for animals.

GLOBAL RARITY RANKS

- G1** Critically imperiled globally because of extreme rarity (five or fewer occurrences or very few remaining individuals or acres) or because some aspect of its biology makes it especially vulnerable to extinction.
- G2** Globally imperiled because of rarity (6-20 occurrences or few remaining individuals or acres) or because of other factors making it vulnerable to further decline.
- G3** Globally rare (20-100 occurrences).
- G4** Apparently secure globally.
- G5** Demonstrably secure globally.
- GNR** Not yet ranked.

Note: Global Ranks are determined by NatureServe.

STATE LEGAL STATUS

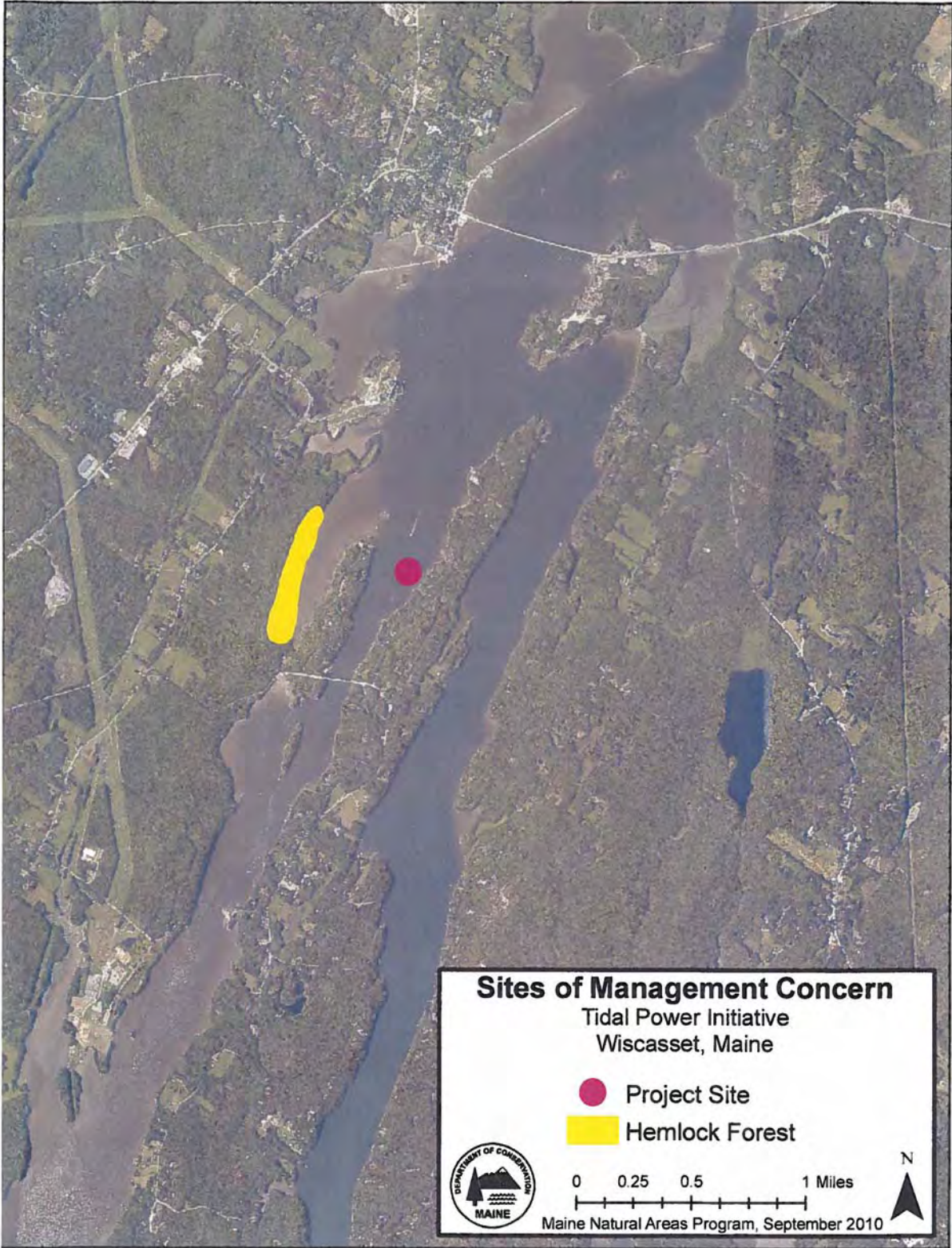
Note: State legal status is according to 5 M.R.S.A. § 13076-13079, which mandates the Department of Conservation to produce and biennially update the official list of Maine's Endangered and Threatened plants. The list is derived by a technical advisory committee of botanists who use data in the Natural Areas Program's database to recommend status changes to the Department of Conservation.

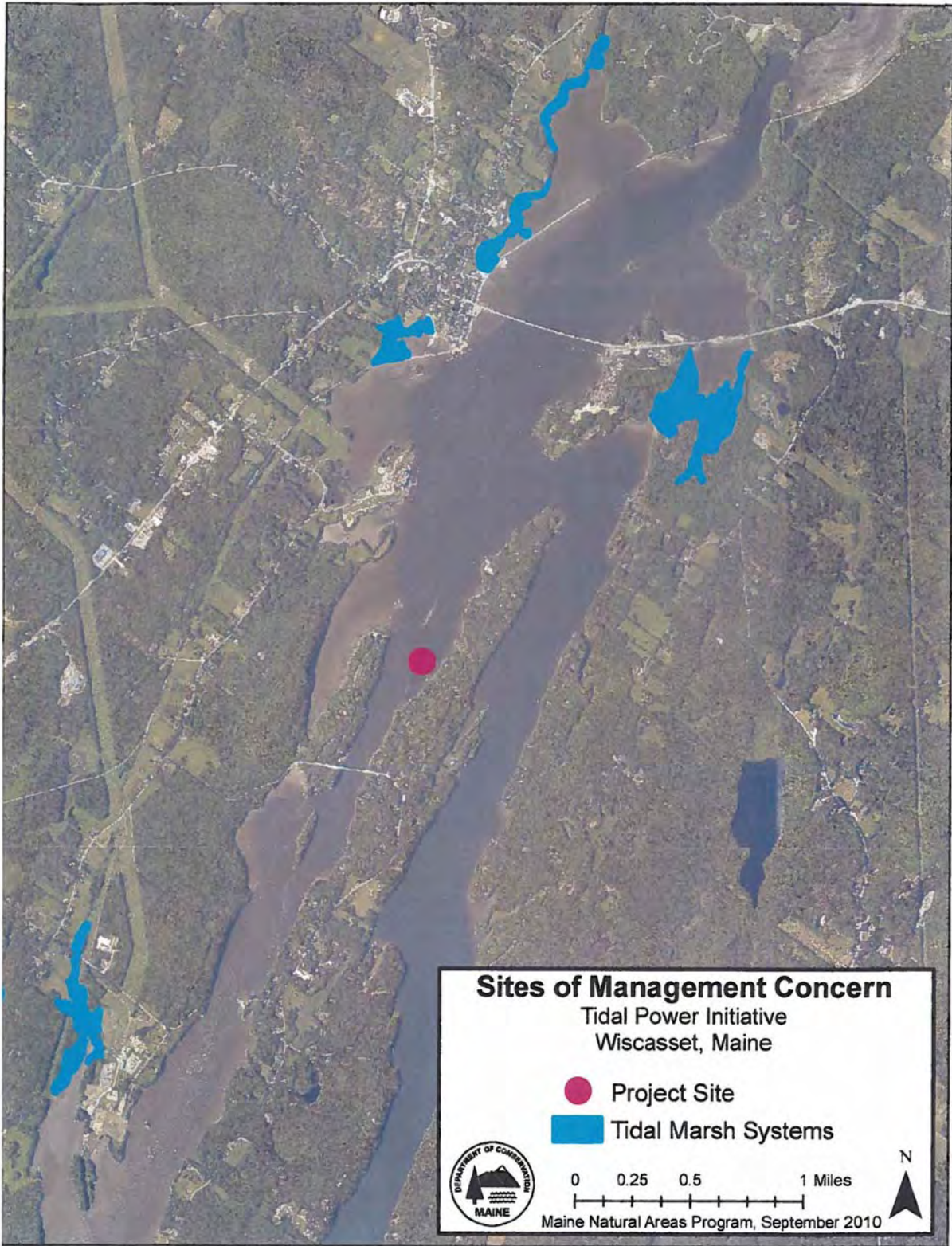
- E** ENDANGERED; Rare and in danger of being lost from the state in the foreseeable future; or federally listed as Endangered.
- T** THREATENED; Rare and, with further decline, could become endangered; or federally listed as Threatened.

NON-LEGAL STATUS

- SC** SPECIAL CONCERN; Rare in Maine, based on available information, but not sufficiently rare to be considered Threatened or Endangered.
- PE** Potentially Extirpated; Species has not been documented in Maine in past 20 years or loss of last known occurrence has been documented.

Visit our website for more information on rare, threatened, and endangered species!
<http://www.maine.gov/doc/nrimc/mnap>







Fisheries Division, Region B
Maine Department of Inland Fisheries
and Wildlife
Sidney Regional Headquarters
270 Lyons Road
Sidney, Maine 04330

September 28, 2010



Ms. Aleita Burman
S.W. Cole Engineering
37 Liberty Drive
Bangor, Maine 04401-5784

RE: Maine Tidal Power Study area, Wiscasset, Maine

Dear Lee,

The Fisheries Division of the Maine Department of Inland Fisheries and Wildlife does not have any published mapping on significant fisheries habitat in the area you describe in your letter of 22 September. We have not surveyed that area since our jurisdiction is primarily freshwater fish habitat. However, our Department does manage sea-run brook and brown trout. There are numerous areas in the lower Sheepscot and Back rivers that provide transient habitat for both species of fish; however we have not undertaken a survey of the area due to limited resources.

With the above in mind, a small scale tidal power project should not negatively impact either species unless the project blocks fish movements or destroy foraging or refuge habitat. From our knowledge of formerly proposed projects, it appears that impacts will be negligible.

While our comments may indicate that freshwater fish may not be impacted, we request that you query our sister agency the Maine Department of Marine Resources, who may have more extensive mapping and/or information on your area of interest. In addition, the federal National Marine Fisheries Service has mapped essential fish habitat in the area.

Sincerely,

A handwritten signature in blue ink that reads "Robert Van Riper".

Robert Van Riper
Regional Fisheries Biologist



United States Department of the Interior



FISH AND WILDLIFE SERVICE

Maine Field Office – Ecological Services
17 Godfrey Drive, Suite #2
Orono, ME 04473
(207) 866-3344 Fax: (207) 866-3351

FWS/Region 5/ES/MEFO

Aleita Burman
S.W. Cole Engineering, Inc.
37 Liberty Drive
Bangor, ME 04401-5784



October 1, 2010

Dear Ms. Burman:

Thank you for your letter dated September 22, 2010, requesting information or recommendations from the U.S. Fish and Wildlife Service (Service). This letter provides the Service's response pursuant to Section 7 of the Endangered Species Act (ESA), as amended (16 U.S.C. 1531-1543), the Bald and Golden Eagle Protection Act (16 U.S.C. 668-668d, 54 Stat. 250), and the Fish and Wildlife Coordination Act, as amended (16 U.S.C. 661-667d).

Project Name/Location: Wiscasset - Maine Tidal Power Initiative

Log Number: 53411-2010-SL-0377

Federally Listed Species

This project occurs within the range of the Gulf of Maine Distinct Population Segment (GOM DPS) of Atlantic salmon (*Salmo salar*) in Maine, a federally-endangered species under the joint jurisdiction of the Service and the National Marine Fisheries Service (NMFS) (74 FR 29344; June 19, 2009). The Atlantic salmon GOM DPS encompasses all naturally spawned and conservation hatchery populations of anadromous Atlantic salmon whose freshwater range occurs in the watersheds from the Androscoggin River northward along the Maine coast to the Dennys River and wherever these fish occur in the estuarine and marine environment. Also included in the GOM DPS are all associated conservation hatchery populations used to supplement these natural populations. Excluded are landlocked Atlantic salmon and those salmon raised in commercial hatcheries for aquaculture.

The proposed project site also occurs within a HUC-10 watershed (Sheepscot Bay) that has been designated as critical habitat for Atlantic salmon by NMFS (74 FR 39907; August 10, 2009). Critical habitat is designated to include all perennial rivers, streams, and estuaries and lakes connected to the marine environment within the designated watershed.

Please note that under Section 7 of the ESA, it is the federal action agency's responsibility to determine if a project may affect a federally listed species. For example, if the project receives federal funding or needs a federal permit, those actions may provide a "nexus" for Section 7

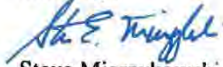
Steve Timpano
Maine Department of Inland Fisheries and Wildlife
284 State St.
State House Station 41
Augusta, ME 04333-0041
Phone: 207 287-5258

We also recommend that you contact the Maine Natural Areas Program for additional information on state-threatened and endangered plant species, plant species of special concern, and rare natural communities:

Lisa St. Hilaire
Maine Natural Areas Program
Department of Conservation
93 State House Station
Augusta, ME 04333
Phone: 207 287-8046

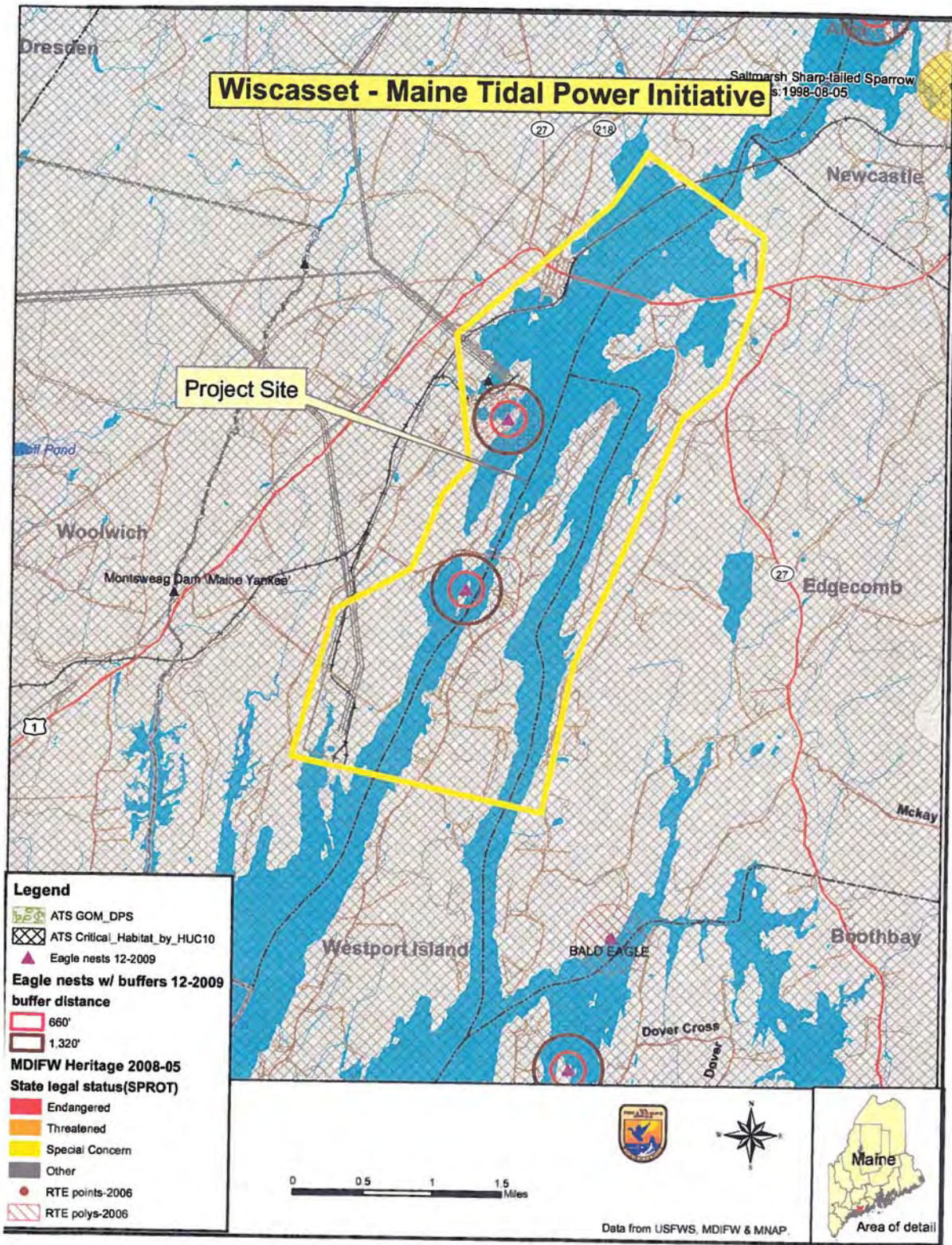
If you have any questions about this project, please contact Wende Mahaney at (207) 866-3344, Ext. 118.

Sincerely,



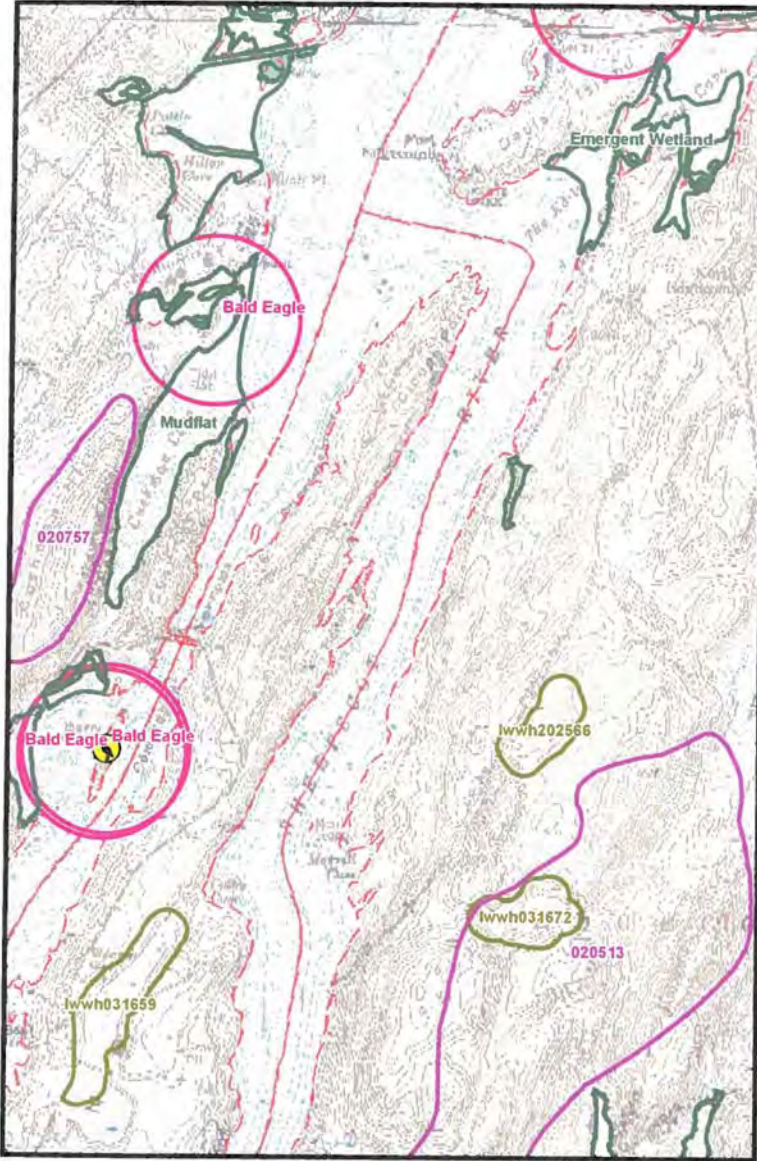
Steve Mierzykowski, Acting Field Supervisor
Maine Field Office

Enclosure



V Scanned

Search for Wildlife Observations & Habitat



-  Piping Plover / Least Tern Nesting, Feeding, & Brood-rearing Area
-  Roseate Tern Nesting Area
-  Deer Winter Area
-  Inland Waterfowl / Wading Bird Habitat
-  Tidal Waterfowl / Wading Bird Habitat
-  Seabird Nesting Island
-  Shorebird Area
-  Significant Vernal Pool
-  Endangered, Threatened, & Special Concern Species Habitat
-  Township Boundary
-  County

0 0.2 0.4 0.6 0.8 Miles

1 = 27,508

UTM Projection, Zone 19N, NAD83

N

270 Lyons Road
Sidney, ME 04330
Voice: (207) 547-5318
Fax: (207) 547-4035
September 27, 2010



APPENDIX D
Color Photographs



Photo 1: Looking south at Cowseagan Narrows area of Back River from the Route 144 bridge. Steep intertidal wetland seen at base of cliff. Photo taken by Aleita Burman on November 02, 2010.



Photo 2: Looking north at Cowseagan Narrows area of Back River from near the Route 144 bridge. Photo taken by Aleita Burman on November 02, 2010.



Photo 3: Looking north at intertidal zone of western shore. Rockweed covered boulder beach (typical). Photo taken by Aleita Burman on November 02, 2010.



Photo 4: Looking north at intertidal zone of western shore. Rockweed covered bedrock beach (typical). Photo taken by Aleita Burman on November 02, 2010.



Photo 4: Looking north at intertidal zone of eastern shore. Rockweed covered boulder beach (typical). Photo taken by Josh Brown on November 02, 2010.



Photo 5: Looking north at intertidal zone of eastern shore. Areas of rockweed covered coarse & fine flats beach with small area salt marsh in higher intertidal (typical). Photo taken by Josh Brown on November 02, 2010.





APPENDIX Task 4-3

**DEP INFORMATION SHEET
REGULATION OF TIDAL AND WAVE ENERGY PROJECTS**



DEP INFORMATION SHEET

Regulation of Tidal and Wave Energy Projects

Issued: June 2010

Contact: (207)-287-7688

Introduction

Tidal energy projects use tidal action (tidal amplitude or currents) to generate power while wave energy projects use wave action (wind-driven water level oscillations) to generate power. Historically, there were a number of small dams along the coast of Maine that used tidal action to operate a gristmill or sawmill using mechanical power until electricity became available locally. Construction was actually started on a large-scale tidal power project proposed for Passamaquoddy Bay in the 1930's, but the project was later abandoned for economic reasons. Despite the fact that designs for tidal energy systems have been patented since the 1800s, there are no commercial-scale tidal or wave energy projects in operation in the United States today and only a handful in operation world-wide.

There is currently a renewed interest in using the ocean to generate electricity, using both traditional hydropower technologies and new hydrokinetic technologies. This interest is being spurred by recent federal legislation promoting development of cleaner domestic energy sources and diversification of energy supplies through use of alternative and renewable sources and by recent studies of wave and tidal power technologies and potential sites, including sites for tidal and wave energy projects in Maine. Interest is also being spurred by the development of new composite construction materials and computer-added design improvements that may overcome some of the technical problems inherent in earlier designs.

Tidal energy projects hold the promise of producing indigenous, renewable, predictable electricity without greenhouse gas emissions and with higher power densities (power output per unit area) than either solar photo-voltaic or wind projects. Tidal energy projects also may be useful in "filling in the gaps" in generation from other intermittent energy sources, such as wind projects. However, much of the required technology is still in the research and development stage, and the economic viability and environmental impacts of these technologies are largely unknown.

In November of 2008, Governor Baldacci established the Ocean Energy Task Force to recommend a strategy for moving forward as expeditiously as practical with the development of the ocean energy resources of the Gulf of Maine. The Task Force submitted an interim report to the Governor in April 2009 and a final report in December 2009 (these reports are available online at <http://www.maine.gov/spo/specialprojects/OETF/index.htm>). Both reports resulted in emergency legislation being passed by the Maine Legislature designed to encourage ocean energy development in an environmentally responsible manner.

This information sheet describes the current status of tidal and wave energy technology and how tidal energy projects are regulated in Maine.

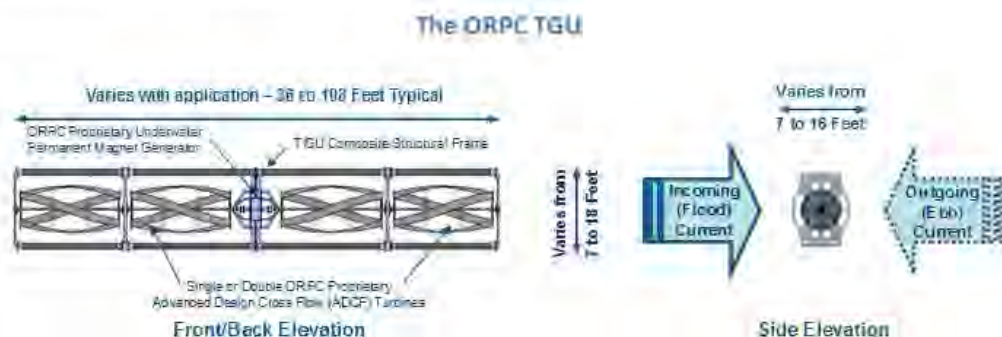
Tidal Power Technology

Existing commercial-scale tidal energy projects all use traditional tidal dam (barrage) technology, in which electricity is generated using the “head” created by holding tidal water back behind a barrier and then passing that water through a turbine when on-going tidal action creates a sufficient difference in water levels on the two sides of the barrier to power an electric generator. Combinations of two or more dams and/or reversible turbines can be used to generate power on both the incoming and outgoing tides. While a tried-and-true technology, tidal barrages have high capital costs and potentially significant environmental impacts. Also, the number of sites with sufficient tidal range and channel width characteristics to be economically viable is limited.

The nearest tidal barrage is the 20 megawatt Annapolis Royale Project in Nova Scotia, Canada, that takes advantage of the enormous tides in the Bay of Fundy.

New tidal in-stream energy conversion technologies (commonly referred to as hydrokinetic technologies) seek to use tidal currents to generate electricity without the need for a dam or barrage. There are two primary types of in-stream hydrokinetic devices, horizontal axis turbines and vertical axis turbines. Turbine designs include helical or “cross-flow” units (similar in design to the blades on a hand-powered lawnmower) and axial flow (propeller-type) units of varying diameters that are either open or closed (ducted) and that have either fixed or variable-pitch blades. Deployment configurations include single, dual or multiple units utilizing bottom foundations (either pilings or weighted platforms), monopole foundations (“underwater windmills”), or anchoring systems for units positioned in the water column. Hydrokinetic tidal systems may use conventional generator technology (wire-wound rotors and stators) or may employ permanent magnet generators, either submerged or located above the water surface.

Maine has significant tidal power potential, especially in downeast areas with a large tidal range and in high-velocity narrows. Various tidal energy devices are currently being tested in Maine and other coastal states, including New York and Alaska. The diagram below shows the Ocean Energy Power Company proprietary turbine-generator unit (TGU), which utilizes a horizontal cross-flow turbine design with an integral permanent magnet generator, and is currently being tested in Cobscook Bay in Eastport.



Wave Power Technology

Other hydrokinetic technologies seek to generate electricity from the motion of ocean waves. Many of these technologies use hydraulics to convert water level oscillations into electricity. Others employ compressed air or direct mechanical drive. Some ride on the ocean's surface (so-called "sea snakes"), while others are submerged. Some produce electricity at the device, while others pump pressurized water to on-shore generators. Finally, some are designed for shallow, near-shore locations, while others are designed for deep-water, off-shore locations.

While other states have better wave regimes than Maine, it is likely that at least some of the emerging wave technologies will be tested here, possibly in association with off-shore wind energy plants (where there is wind, there are waves).

Federal Regulation

Non-federal hydroelectric power projects, including tidal and wave energy projects that are interconnected with the interstate electric transmission grid, are subject to licensing by the Federal Energy Regulatory Commission (FERC). Traditionally, FERC has only issued 30-50 year licenses for commercial-scale projects. However, in light of the need for developers to be able to deploy projects on a short-term basis to evaluate the economic and technical feasibility and the environmental effects of various technologies, FERC has created a stream-lined pilot project licensing process to allow the licensing of demonstration hydrokinetic projects for testing purposes. Pilot projects must be small; short-term; avoid sensitive locations; subject to modification or shut-down if unforeseen impacts occur; subject to plans for monitoring and safeguarding public safety and environmental resources; and removed, with the site restored, at the end of the license term unless a commercial license is issued (more information on the licensing of hydrokinetic pilot projects is available on-line at <http://www.ferc.gov>).

All tidal and wave energy projects, whether interconnected with the electric grid or not, are subject to permitting by the U.S. Army Corps of Engineers (COE) under Section 404 of the Clean Water Act (regulating the discharge of dredged or fill materials into waters of the United States) and/or Section 10 of the Rivers and Harbors Act (regulating construction and other work in navigable waters) (for more information, go to <http://www.nae.usace.army.mil/reg/index.htm>).

State Regulation

Tidal and wave energy projects are subject to permitting by the Department of Environmental Protection (DEP) under the Maine Waterway Development and Conservation Act (MWDCA), the State's one-stop hydropower permitting law. The MWDCA requires an evaluation of the full range of potential economic and environmental impacts of a project, including impacts on public safety, wetlands, water quality, fish and wildlife resources, historic and archaeological sites, public access, and energy generation. DEP has permitting jurisdiction over all tidal and wave energy projects located in State waters (those waters within 3 miles of the mainland and any island that is part of Maine).

Tidal and wave energy projects are also subject to review under Section 401 of the Clean Water Act, which requires that any applicant for a federal license or permit for an activity that may result in a discharge to navigable waters obtain a certification from the State that the activity will not violate applicable state water quality standards. These standards consist of designated uses and numeric and narrative criteria designed to ensure that Maine's waters satisfy the "swimmable-fishable" goals of the Clean Water Act. These standards also include an antidegradation policy requiring that existing in-stream uses be maintained and protected. DEP has certification authority over all tidal and wave energy projects located in State waters.

For a summary of state and federal regulatory processes for tidal and wave energy projects, see "Siting Methodologies for Hydrokinetics," developed by Pacific Energy Ventures for the U.S. Department of Energy, at <http://www.advancedh2opower.com/default.aspx>.

Federal-State Coordination

In August of 2009, Maine became the first state on the east coast, and only the third state in the country, to sign a Memorandum of Understanding (MOU) with FERC to coordinate procedures and schedules for review of tidal energy projects in State waters or in federal waters (beyond the 3-mile state territorial limit) where the projects affect resources or uses in Maine's coastal zone.

A copy of the FERC-Maine MOU is attached to this information sheet.

Ocean Energy Legislation

In 2009, the Maine Legislature passed and the Governor signed into law *An Act To Facilitate Testing and Demonstration of Renewable Ocean Energy Technology*. This law was enacted to streamline and coordinate State permitting and submerged lands leasing requirements for renewable ocean energy demonstration projects so that the State of Maine can become an international proving ground for testing new technologies in specific locations along the coast in an environmentally responsible manner.

In 2010, the Maine Legislature passed and the Governor signed into law *An Act To Implement the Recommendations of the Governor's Ocean Energy Task Force*. This law was enacted to overcome economic, technical and regulatory obstacles and to provide economic incentives for vigorous and efficient development of promising indigenous, renewable ocean energy resources in ways that recognize the concurrent need to sustain the ongoing biological integrity of the State's waters, the vitality and productivity of ocean harvests and the differing needs and uses of the seas and other natural resources and to ensure the provision of these benefits to the people of the State by careful use of such public resources for renewable ocean energy production.

Encouragement of Tidal and Wave Power Development

The 2010 law amended the MWDCA to provide that it is the policy of the State to encourage the attraction of appropriately sited development related to tidal and wave energy, including any additional transmission and other energy infrastructure needed to transport such energy to market, consistent with all state environmental standards; the permitting and siting of tidal and

wave energy projects; and the siting, permitting, financing and construction of tidal and wave energy research and manufacturing facilities. Thus, all applications for tidal and wave energy projects must be processed in keeping with this policy.

The 2010 law also sought to encourage tidal and wave energy development by:

- Requiring that the Public Utilities Commission take into account the state's renewable energy generation goals in determining the public need for proposed transmission lines;
- Directing the Public Utilities Commission to solicit proposals for long-term contracts to supply installed capacity and associated renewable energy and renewable energy credits from one or more tidal energy demonstration projects;
- Directing the Governor's Office of Energy Independence and Security to make recommendations to the Legislature regarding terms and conditions for long-term contracts to supply installed capacity and associated renewable energy and renewable energy credits from renewable ocean energy projects; and
- Directing the Maine Port Authority to assess existing port facilities and make recommendations to the Legislature regarding acquisition of real estate needed to facilitate renewable ocean energy development opportunities.
- Directing the Bureau of Revenue Services to report to the Legislature regarding whether and under what circumstances ocean energy-generating equipment in transit within the State on April 1 is exempt from personal property tax.
- Establishing a Renewable Ocean Energy Trust fund to to protect and enhance the integrity of public trust-related resources and related human uses of the State's submerged lands.

General Permits for Tidal and Offshore Wind Energy Demonstration Projects

The 2009 law amended the MWDCA to establish a new general permit process for tidal energy demonstration projects. To qualify for a general permit as a tidal energy demonstration project, a project must use tidal action as a source of electrical power; must have a total installed generating capacity of 5 megawatts or less; and must be proposed for the primary purpose of testing tidal energy generation technology, including mooring or anchoring systems and transmission lines, and collecting and assessing information on the environmental and other effects of the technology.

The general permit process for tidal energy demonstration projects is designed to dovetail with FERC's pilot project licensing procedures for hydrokinetic technologies. In applying for a general permit, an applicant must submit: (A) a copy of a pilot project license application, as filed with FERC, along with all information required by FERC; (B) proof of general liability insurance for the project; (C) demonstration of financial and technical capacity to construct and operate the project; (D) a copy of an environmental assessment for the project issued by FERC under the National Environmental Policy Act (NEPA) that includes a "finding of no significant

environmental impact” (FONSI); and (E) an acknowledgement that the DEP may require the applicant to take remedial action under the law, including the cessation of operations and removal of project facilities, in order to protect natural resources and/or public safety.

Once all the required information has been filed, the DEP must act within 60 days on an application for a general permit and water quality certification for a tidal energy demonstration project.

Unless surrendered by the applicant or terminated by the DEP, a general permit for a tidal energy demonstration project is valid for the term of the pilot project license issued by FERC for the project. The DEP may grant one or more extensions of the general permit term to coincide with any approved extension(s) of the pilot project license or any related annual license issued by FERC.

The 2009 law also amended the Natural Resources Protection Act (NRPA) to establish a new general permit process for offshore wind energy demonstration projects, including wave energy test projects. To qualify for this general permit, a wave energy test project must use ocean wave energy to produce electricity; be proposed as part of an offshore wind energy demonstration project and be designed and sited to test production of electricity from wave energy in conjunction with and in a manner that complements electricity produced by an offshore wind energy turbine; employ up to 2 wave energy converters, each of which may use different technology, not already in use in the Gulf of Maine for commercial energy production, for the primary purpose of testing and validating the overall design of the converter and related systems; and may include a mooring or anchoring system and an ocean sensor package.

Procedural Changes

The 2010 law also made several procedural changes in existing law to streamline the review process for tidal and wave energy projects. Under these changes:

- The DEP has original jurisdiction over any tidal or wave energy general permit application, while the Board of Environmental Protection only has authority to hear any administrative appeal of the Commissioner’s decision;
- Any judicial appeal of a DEP or BEP decision on a tidal or wave energy general permit must be made directly to the Maine Supreme Court, instead of going first to Superior Court;
- The DEP may enter into an agreement for outside review of an application for a tidal or wave energy project without requiring that the applicant consent to the outside review and agree to pay all costs associated with the review; and
- Tidal and wave energy projects are not required to be consistent with Land Use Regulation Commission zoning, even if located in an unorganized territory.

Other statutory changes are discussed below.

State Submerged Lands Lease

A lease is required for the use of state-owned submerged lands in connection with the placement of any tidal or wave energy project in State waters, including any mooring or anchoring system and transmission line. Both the 2009 and 2010 laws amended the provisions of the State's submerged lands leasing program governing tidal and wave energy projects.

With respect to tidal and wave energy demonstration projects:

- Within 15 days of receiving a copy of a general permit application for a tidal or wave energy demonstration project, the Director of Public Lands shall, if requested, provide the applicant a lease option for use of state-owned submerged lands needed for the project.
- Within 30 days of receiving a copy of a general permit for a tidal or wave energy demonstration project, the Director of Public Lands shall issue a submerged lands lease for the project. The term of the lease must be consistent with that of the general permit, including any extension(s) of the permit, and the period of time needed to fully implement the approved project removal plan. The lease may include reasonable conditions, but these conditions may not impose any condition more stringent than those on the general permit and may not frustrate achievement of the purpose of the project.
- The annual rental fee for a tidal energy demonstration project for which a general permit has been issued shall be \$100 per acre of submerged lands occupied by the project, up to a maximum fee of \$10,000.

With respect to commercial tidal and wave projects:

- Within 30 days prior to filing an application for an MWDCA permit and water quality certification, an applicant for a submerged lands lease for a commercial tidal or wave energy project must participate in a joint interagency pre-application meeting with DEP and the Department of Marine Resources.
- The applicant must certify that a completed DEP permit/certification application has been or is concurrently being filed at the time of filing its submerged lands lease application.
- The Director of Public Lands shall provide notice of the lease application to the Marine Resources Advisory Council and any established lobster management policy council whose designated lobster management zone is within 3 miles of the proposed project.
- In making findings on a submerged lands lease application for a commercial tidal or wave energy project, the Director of Public Lands shall adopt all pertinent findings and conclusions in any permit issued for the project by the DEP, and may condition any lease on receipt of a DEP permit and other conditions the Director considers reasonable.

- The annual rental fee for a commercial tidal or wave energy project shall be in accordance with a fee schedule, to be established by rule, that balances state goals of assurance of fair compensation for use and mitigation of potential adverse effects on or conflict with existing uses of state-owned submerged lands that are held in trust for the people of the State with state renewable ocean energy-related goals.
- A lease for a commercial tidal or wave energy project may be issued for a term of up to 50 years (this term cannot exceed the term of any FERC license issued for the project).

Local Review

The 2009 law provides that a municipality may not enact or enforce any requirement for a tidal energy demonstration project located within the municipality that is stricter than the requirements of the general permit process, and the municipality has the burden of proving that the project is located within its municipal boundaries.

The 2010 law provides that a municipality may not enact or enforce any ordinance that prohibits the siting of a tidal or wave energy project, including associated facilities, within that municipality, and may only regulate a project or part of a project located within its boundaries.

Additional Sources

For more information on the State regulatory process and for DEP application forms, go to http://www.maine.gov/dep/blwq/docstand/dams/hydro_state_process/index.htm.

For more information on the FERC hydrokinetic pilot project licensing process, go to <http://www.ferc.gov/industries/hydropower/indus-act/hydrokinetics/energy-pilot.asp>

For tidal and waves energy reports issued by the Electric Power Research Institute, go to <http://oceanenergy.epri.com/>.

For an up-to-date report on tidal and wave energy project development in Maine waters, go to http://www.maine.gov/dep/blwq/docstand/dams/hydro_FERC_process/index.htm and click on Status of Tidal Power Project Proposals in Maine.

A copy of Public Law 270, *An Act To Facilitate Testing and Demonstration of Renewable Ocean Energy Technology*, signed into effect by the Governor on June 4, 2009, is available at <http://www.mainelegislature.org/ros/LOM/LOM124th/124R1/PUBLIC270.asp>.

A copy of Public Law 615, *An Act To Implement the Recommendations of the Governor's Ocean Energy Task Force*, signed into effect by the Governor on April 7, 2010, is available at http://www.mainelegislature.org/legis/bills/bills_124th/chapters/PUBLIC615.asp

/dams-hydro/administration/information sheet-regulation of tidal and wave energy projects

**MEMORANDUM OF UNDERSTANDING
BETWEEN
THE FEDERAL ENERGY REGULATORY COMMISSION
AND
THE STATE OF MAINE
BY AND THROUGH ITS GOVERNOR AND DEPARTMENTS OF
CONSERVATION, ENVIRONMENTAL PROTECTION, INLAND FISHERIES
AND WILDLIFE, AND MARINE RESOURCES, STATE PLANNING OFFICE,
AND GOVERNOR'S OFFICE OF ENERGY INDEPENDENCE AND SECURITY**

The State of Maine (Maine) by and through its Governor and Departments of Conservation, Environmental Protection, Inland Fisheries and Wildlife, and Marine Resources, State Planning Office, and Governor's Office of Energy Independence and Security, and the Federal Energy Regulatory Commission (Commission), as Parties to this Memorandum of Understanding (MOU), hereby acknowledge and declare as follows:

A. The Commission issues licenses under Part I of the Federal Power Act, 16 U.S.C. §§ 791a *et seq.* (FPA) for non-federal tidal energy projects also referred to as hydrokinetic technologies. This includes, but is not limited to, tidal energy projects that are or may in the future be proposed to be located in Maine state waters or in federal waters in the Gulf of Maine. The Commission's staff has established several possible means of authorizing tidal energy projects, including procedures for issuing short-term licenses for pilot projects with appropriate environmental safeguards.

B. Maine has authorities with respect to tidal energy projects that are proposed to be located in its state waters, or in federal waters where the projects affect coastal resources or coastal uses in Maine's designated coastal area, including authorities under the following federal laws: the Coastal Zone Management Act, 16 U.S.C. §§ 1451 *et seq.* (CZMA); the Clean Water Act, 33 U.S.C. §§ 1251-1387 (CWA); the National Historic Preservation Act, 16 U.S.C. §§470 *et seq.* (NHPA); as well as the FPA. Maine state law also includes provisions applicable to tidal energy projects that are proposed to be located in its state waters, affecting state waters, and upon state-owned submerged lands, including proprietary authorization, and regulatory authorization to construct and operate a tidal energy project.

C. Maine State waters and federal waters in the Gulf of Maine contain vast, untapped renewable ocean energy resources, including tidal power resources with significant potential to contribute to Maine's renewable energy mix and create related business opportunities while reducing greenhouse gas emissions that contribute to climate change.

D. Maine has enacted legislation (P.L. 2009, ch. 270) to streamline and coordinate state permitting and submerged lands leasing requirements for renewable ocean energy demonstration projects, including tidal energy demonstration projects, so

that Maine can become an international proving ground for testing promising new technologies in state waters in an environmentally responsible manner.

E. The Parties have a mutual interest in the timely processing of applications for regulatory and other approvals required for tidal energy projects using innovative hydrokinetic technologies in Maine State waters, or in federal waters where the projects affect coastal resources or coastal uses in Maine's designated coastal area, to promote clean, renewable sources of energy.

F. The Parties also desire to create a process to make it possible for developers of tidal energy projects using hydrokinetic technologies to establish short-term pilot (demonstration) projects in Maine state waters, or in federal waters where the projects affect coastal resources or coastal uses in Maine's designated coastal area, in order to study, monitor, and evaluate the economic and technical feasibility and environmental, cultural, and other effects of these technologies. The Parties intend that information developed during the pilot project licensing process will assist in the decision-making process if requests for any long-term authorizations for commercial-scale hydrokinetic tidal energy projects in Maine state waters, or in federal waters where the projects affect coastal resources or coastal uses in Maine's designated coastal area, are made.

G. The purpose of this MOU is to coordinate the procedures and schedules for review of tidal energy projects using hydrokinetic technologies in Maine state waters, or in federal waters where the projects affect coastal resources or coastal uses in Maine's designated coastal area, to ensure that there is a coordinated review of proposed hydrokinetic tidal energy projects that is responsive to environmental, economic, and cultural concerns while providing a timely, stable, and predictable means for developers of such projects to seek necessary regulatory and other approvals.

Now, therefore, the Commission and Maine agree that:

1. Maine supports the efforts by Commission staff to establish procedures to allow short-term demonstration hydrokinetic tidal energy projects with environmental safeguards through the pilot project licensing process. These procedures may, in appropriate cases, allow the licensing of hydrokinetic tidal energy projects by the Commission in a significantly shorter period than a full licensing process would require. The Parties agree that the pilot licensing process may be appropriate as a short-term means of allowing hydrokinetic tidal energy projects to proceed on a pilot (demonstration) basis while additional economic, environmental, and technical data concerning the effects and operation of such projects are gathered. The Parties also agree to share and make publicly available in accordance with applicable law and regulations all economic, environmental, and technical data gathered on these pilot projects. The Parties also agree that any shorter licensing approach established must incorporate appropriate safeguards, limitations, and monitoring to ensure that there are no significant adverse environmental, economic, or social impacts.

2. Maine and the Commission recognize that there is currently limited information available on the economic and technical feasibility and environmental, cultural, and other effects of hydrokinetic tidal energy projects, and that considerable economic, technical, and environmental analysis must occur before any proposed commercial-scale project can be approved. However, Maine and the Commission also recognize that, without *in situ* evaluation of pilot (demonstration) hydrokinetic tidal energy projects, the feasibility and effects of these projects cannot be determined. Therefore, Maine and the Commission agree that any required pre- and post-licensing studies for these pilot (demonstration) projects should be reasonable in scope, commensurate with the limited size and duration of the projects, and designed to provide information that will be relevant to the evaluation of the impacts of any proposed commercial-scale projects.

3. When Maine or the Commission becomes aware of a prospective applicant seeking a preliminary permit, pilot project license, or other license from the Commission to study or develop a hydrokinetic tidal energy project in Maine state waters, or in federal waters where the project affects coastal resources or coastal uses in Maine's designated coastal area, the party obtaining the information will promptly notify the other party to enable coordinated review of the project between Maine and the Commission. In such cases, Maine and the Commission will work together to the maximum extent feasible, with the prospective applicant and other participants in the Commission's pre-filing process to identify potential issues, to determine what information is needed, and what studies must be conducted in order to meet the requirements set forth by state and federal laws. Coordination among the Commission, Maine, and the applicant will set expectations and assist with the information needs on a proposal that will greatly assist the review process.

4. Under the Commission's "strict scrutiny" policy for processing preliminary permits for hydrokinetic projects, the Commission will process preliminary permit applications for hydrokinetic energy projects to be located in Maine state waters, or in federal waters where the projects affect coastal resources or coastal uses in Maine's designated coastal area, with a view towards limiting the boundaries of the permits, including in any areas identified by Maine as offshore wind energy test areas pursuant to state legislation (P.L. 2009, ch. 270), to prevent site-banking, and to promote competition.

5. When a prospective applicant seeks to use the pilot project license process or any other licensing process for a hydrokinetic tidal energy project to be located in Maine state waters, or in federal waters where the project affects coastal resources or coastal uses in Maine's designated coastal area, and subject to the Commission's licensing jurisdiction, Maine and the Commission agree to confer, as early in the process as practical, in order to reach agreement on a schedule for processing the application as expeditiously as practicable while ensuring sufficient time for the necessary state and federal reviews. Such a schedule, to be issued by the Commission, will include milestones for the Commission's review of the application and issuance of an environmental document, and the issuance by Maine of any certifications or concurrences

that may be required from it under federal law. To the extent feasible, Maine agrees to complete any actions required of it within the timeframes established in the schedule and, in any case, agrees to complete such actions in accordance with the decision-making schedules provided for by law. Maine and the Commission further agree that they will use their best efforts to encourage other federal agencies and stakeholders that have an interest in a proposed hydrokinetic tidal energy project in Maine state waters, or in federal waters where the project affects coastal resources or coastal uses in Maine's designated coastal area, to help develop and comply with a coordinated schedule for the review of the project. The Commission agrees to encourage the applicant for a proposed hydrokinetic tidal energy project to work with Maine to facilitate Maine's review of the project under applicable state and federal law.

6. With respect to any application to use the pilot project license process for a hydrokinetic tidal energy project to be located in Maine state waters, or in federal waters where the project affects coastal resources or coastal uses in Maine's designated coastal area, and subject to the Commission's licensing jurisdiction, Maine agrees, pursuant to state legislation (P.L. 2009, ch. 270), to take action on an application for a state permit and a request for water quality certification, for a demonstration hydrokinetic tidal project within 60 days of the State's acceptance of an application for processing. To be accepted for processing, an application must include a copy of an environmental assessment issued by the Commission for the project that includes a finding of "no significant environmental impact" pursuant to the National Environmental Policy Act, 42 U.S.C. §§ 4231 *et seq.* (NEPA). Maine further agrees, pursuant to recently enacted state legislation (P.L. 2009, ch. 270), within 30 days of the approval of a state permit and water quality certification for a demonstration hydrokinetic tidal energy project, to issue a state submerged lands lease for the project, subject to reasonable lease conditions that may not be more stringent than those contained in the state permit and that may not frustrate achievement of the purpose of the project.

7. Maine and the Commission agree that they will work to coordinate their environmental reviews of any proposed hydrokinetic tidal energy project to be located in Maine state waters, or in federal waters where the project affects coastal resources or coastal uses in Maine's designated coastal area, and subject to the Commission's licensing jurisdiction, so that documents prepared by the Commission for review under NEPA may be used by Maine agencies to satisfy the requirements of Section 401 of the Clean Water Act and the Maine Waterway Development and Conservation Act, the Maine Endangered Species Act, Mandatory Shoreland Zoning Act, and other similar requirements that are enforceable policies of Maine's approved Coastal Zone Management Program under the CZMA, or any other required actions to be taken by Maine. The Parties also agree to consult with stakeholders, including the project developers, concerning the design of studies and environmental measures, including adaptive management measures, for hydrokinetic tidal energy projects in Maine state waters, or in federal waters where the projects affect coastal resources or coastal uses in Maine's designated coastal area.

8. The Commission agrees that it will, in issuing any pilot project license or other license for a hydrokinetic tidal energy project to be located in Maine state waters, or in federal waters where the project affects coastal resources or coastal uses in Maine's designated coastal area, consider the extent to which the proposed project is consistent with pertinent state comprehensive river management plans and any subsequent amendments or addendums thereto. In addition, the Commission will consider any terms and conditions that are recommended by Maine under applicable provisions of the FPA to ensure consistency with those plans.

9. Maine and the Commission recognize that any pilot project license or other license issued by the Commission for a tidal energy project using innovative hydrokinetic technology in Maine state waters, or in federal waters where the project affects coastal resources or coastal uses in Maine's designated coastal area, must, in addition to the power and development purposes for which licenses are issued, give equal consideration to the purposes of energy conservation, the protection, mitigation of damage to, and enhancement of, fish and wildlife (including related spawning grounds and habitat), the protection of recreational opportunities, and the preservation of other aspects of environmental quality for beneficial public purposes. [16 U.S.C. § 797(e); 16 U.S.C. § 803(a)(1).]


10. Maine and the Commission will designate management contacts to work to resolve any procedural issues that arise in the review of a specific tidal energy project in Maine state waters, or in federal waters where the project affects coastal resources or coastal uses in Maine's designated coastal area. However, nothing in this MOU shall compromise or affect the rights of any party to seek relief through any available administrative or judicial process, including rights to intervene in, comment on, and appeal decisions by the Commission.

11. Nothing in this MOU requires any party to take any action that is contrary to applicable federal or state law or regulation.

12. This MOU is neither a fiscal nor a funds obligation document. Any endeavor to transfer anything of value involving reimbursement or contribution of funds between the parties to this MOU will be handled in accordance with applicable laws, regulations, and procedures including those for Government procurement and printing. Any such endeavors will be outlined in separate documents that shall be made in writing by representatives of the Parties and shall be independently authorized by appropriate statutory authority. This MOU does not provide such authority. In addition, this MOU does not establish authority for non-competitive award to the cooperator of any contract or agreement.


13. This MOU is not intended to be a binding contract enforceable in a court of law or in an administrative forum. It is intended only to lay out a process to further cooperation between the governmental entities signing this document.

14. This MOU will take effect when signed by all the parties hereto. This MOU may be modified at any time by the mutual written agreement of the Parties. The Commission or Maine may terminate the MOU upon thirty (30) days written notice to the other. During this period, the Parties shall make good-faith efforts to resolve any disagreement.



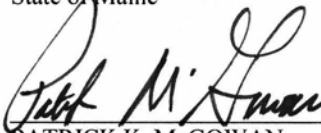
JON WELLINGHOFF
Chairman
Federal Energy Regulatory Commission

8/12/09
Date



JOHN E. BALDACCI
Governor
State of Maine

8/4/09
Date




PATRICK K. MCGOWAN
Commissioner
Maine Department of Conservation

Aug 11, 2009
Date



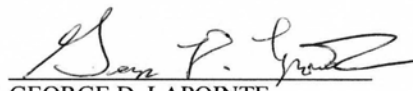
DAVID P. LITTELL
Commissioner
Maine Department of Environmental Protection

4 Aug 09
Date



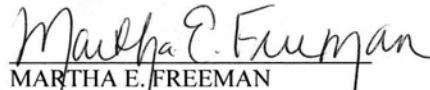
ROLAND D. MARTIN
Commissioner
Maine Department of Inland Fisheries and Wildlife

8/6/09
Date

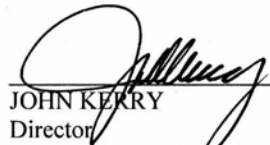


GEORGE D. LAPOINTE
Commissioner
Maine Department of Marine Resources

8/11/09
Date


MARTHA E. FREEMAN
Director
Maine State Planning Office

8/13/09
Date


JOHN KERRY
Director
Governor's Office of Energy Independence and Security

8/10/09
Date



APPENDIX Task 4-4

**WISCASSET TIDAL RESOURCES PROJECT
INTER AGENCY FISHERIES AND WILDLIFE CONSULTATION
S.W. COLE ENGINEERING, INC.**



**Wiscasset Tidal Resources Project
Inter Agency Fisheries and Wildlife Consultation**

April 7, 2011

MEETING NOTES

MEETING LOCATION: Libby Hall, University of Maine, Orono, Maine

ATTENDEES: Steve Timpano (Maine Department of Inland Fisheries and Wildlife); Garrett Staines (UMaine School for Marine Sciences); Jim McCleave (UMaine SMS); Dot Kelly (Homeowner’s Tidal Power Electric Generation Project); Rick Armstrong (Maine Maritime Academy/TEDEC); Jessica Jansujwicz (UMaine SMS); Dana Murch (Maine Department of Environmental Protection); Haley Viehman (UMaine SMS); Jeff Vieser (UMaine SMS); Raul Urbina (UMaine School of Engineering); David Bean (National Oceanic and Atmospheric Administration – National Marine Fisheries Service); Peter Tischbein (US Army Corps of Engineers); Keel Kemper (MDIFW); Norm Dube (Maine Department of Marine Resources); Jeff Murphy (NOAA – NMFS); Christine Lipsky (NOAA – NMFS); Sean McDermott (NOAA – NMFS); Glen Marquis (Ocean Renewable Power Company); Laurie Smith (Town of Wiscasset); Herb Scribner (ORPC); Gayle Zydlewski (UMaine SMS); Johanna Szillery (S.W. Cole Engineering, Inc.); Peter Arnold (Chewonki Foundation); Aleita Burman (S. W. Cole Engineering, Inc.)

NOTES BY: Johanna Szillery, 04/13/2011

~ ~ ~ ~ ~

On April 7, 2011, at 10am Johanna Szillery began the meeting and presented the meeting objectives: to begin the consultation relationship with the resource agencies and to gather feedback on the concept fisheries and avian baseline study plans, which would be presented. Johanna, Peter Arnold, and Aleita Burman presented the Wiscasset Tidal Resources Project objectives, progress to date, and near-term plans. The Project was issued a Federal Energy Regulatory Commission (FERC) Preliminary Permit in May 2009. Since then, work has involved: on-going stakeholder outreach (within the Town and with State and Federal regulatory agencies); current velocity characterization to narrow the potential project area; collaboration with researchers, technology developers, and other small-scale tidal sites; field site reconnaissance; research/review of known protected resources and habitats; project coordination with FERC. Near-term work includes: continued coordination with and reporting to FERC; month-long current velocity characterization in a likely project area; bathymetry and substrate characterization in the area; baseline fisheries study; baseline avian study.

The Wiscasset Tidal Resources Project continues to pursue a Pilot Project License. The Concept Project Plan is to deploy 1 ORPC RivGen unit, with a grid connection at the Westport Island Bridge (Route 144).

Peter Arnold presented a concept avian baseline study, which is being developed in consultation with Peter Vickery, Center for Ecological Research. The concept is to determine the bird community composition, and use/activity periods. The study plan will be developed

after researching likely avian use of the area, and tailoring observation lengths and periods to the birds' habits.

Gayle Zydlewski presented the Maine Tidal Power Initiative mission and the model for sustainability science research and policy development. Gayle reviewed historic (1970's) fisheries research for the Sheepscot and Back Rivers, and contemporary applicable research (Atlantic salmon, sturgeon). The proposed baseline fisheries study will gather information on use patterns and abundance of the local fishery, with specific attention to protected species: Atlantic and shortnose sturgeon, and Atlantic salmon. Proposed study methods involve 24-hour acoustic imaging studies from a moored boat. A control site and project deployment site will be monitored. This work is planned for May, to coincide with salmon smolt migration, and fall, to observe fish community composition. An acoustic telemetry receiver will be deployed in the project area, to monitor movements of tagged Atlantic and shortnose sturgeon throughout the year.

Meeting participants were pleased to be included in study development and project consultation at this early stage.

Dana Murch (MDEP) requested clarification on the project owner's perspectives regarding economics of the Project. For the Chewonki foundation, this represents one of their suite of sustainability initiatives. For the Town, a completed project could off-set energy expenses. Studies and work to date have been grant funded. The Project continues to actively pursue funding, and if studies are promising, the Town may choose to invest via economic development monies. Dana also asked about project size, and likely turbine technology specifications. The Project plans to work under a net metering agreement with Central Maine Power, so maximum size is 660kW. Glen Marquis (ORPC) described the RivGen turbine dimensions and mooring design.

The logistics of the grid connection were also discussed. The conceptual plan is for connection at the Westport Island Bridge. Peter Tischbein noted the potential for intertidal wetland impacts. Keel Kemper (MDIFW) mentioned an osprey nest on the Westport Island bridge, and the Friends of the Westport Osprey conservation group as an interested stakeholder to consult.

Some participants suggested two control sites, based on historic data, which showed differences in fisheries community composition in a relatively short run of the Back River. There were discussions about sturgeon activity periods and behavior, as related to data reviewed by Gayle which showed Atlantic sturgeon were detected by receivers in the Back River in March 2011, which is generally early for sturgeon movement. Additional discussion focused on the ability of fish to sense/perceive impediments, avoidance behaviors of fish (to traps, obstacles, etc), and difference between various obstacles.

Peter Tishchbein (US Army Corps) discussed Corps permitting requirements, which will review the project from both environmental and navigational considerations. Included in navigational considerations are current commercial and recreational uses of the River. He noted that it is best to identify users of the resource and include them throughout the Project process, which expedites his review of the project. For environmental review, he will seek input from other Federal agencies – NMFS, USFWS. Consultation and coordination with these agencies will expedite Corps review.

Lee Burman asked if the defined term of a FERC Pilot license (5 years) impacts Corps permitting. Peter stated an applicant needs both licenses/permits; the defined term may be a consideration in Corps review.

Dana Murch inquired whether the Project had considered a test unit (not grid connected, therefore only subject to Corps and State permitting). This is one of the options being considered. As knowledge of the site grows and turbine technologies evolve, the options will be evaluated.

Jeff Murphy and David Bean (NOAA – NMFS) discussed the NMFS review process, which can be an informal or formal consultation. The watershed is designated as critical habitat for Atlantic salmon, and shortnose sturgeon and Atlantic sturgeon are found in the Kennebec/Androscoggin/Sheepscot estuarine complex. Because of these potential for take of endangered species, the consultation will likely be formal, and is triggered by an application; however, Mr. Murphy indicated that this meeting could be considered the beginning of the informal consultation. Permit conditions are likely to be 1) impact mitigation measures, in the form of use restrictions (operation shut-downs) and 2) post- deployment monitoring. In the future, tagging and telemetry of Atlantic salmon smolts is an option; adult salmon studies are not, due to the risk of take with an endangered species. There was some discussion over potential salmon use patterns of the Back and Sheepscot Rivers, as they migrate down stream. This may be an area for future work.

Sean McDermott (NOAA-NMFS) noted that other consultations, in addition to the Endangered Species Act, are applicable and conducted through NMFS. These include: Fish and Wildlife Coordination Act, Marine Mammal Protection Act, and Magnuson-Stevens Fishery Conservation and Management Act. These consultations are initiated by the Project submitting a Pilot License Application to FERC.

Steve Timpano noted that MDIFW concerns and comments would be around birds, specifically diving birds. The Project is in the process of developing a bird monitoring plan, in cooperation with Peter Vickery of Center for Ecological Research. Several attendees suggested collaboration and data sharing with the Riverbank Pump Storage project. Norm Dube (MDMR) indicated that MDRM comments on the RiverBank project will provide some insight into MDMR concerns related to this geographic area.

Dana Murch (MDEP) noted that consultation with Maine Historic Preservation Commission is part of the consultation process. He also recommended working with the Town of Westport Island, as they may have a significant interest in the project.

Peter Tischbein commented that the Corps does consider cumulative impacts of activities to a resource. So, if the Project moves from a FERC Pilot License to an Operating License, this requires another application, and also requires another impact analysis from the Corps.



APPENDIX Task 4-5

**TIDAL POWER SITE EVALUATION IN WISCASSET, MAINE
DATA GATHERED AND LESSONS LEARNED**



Tidal Power Site Evaluation in Wiscasset, Maine: Data Gathered and Lessons Learned

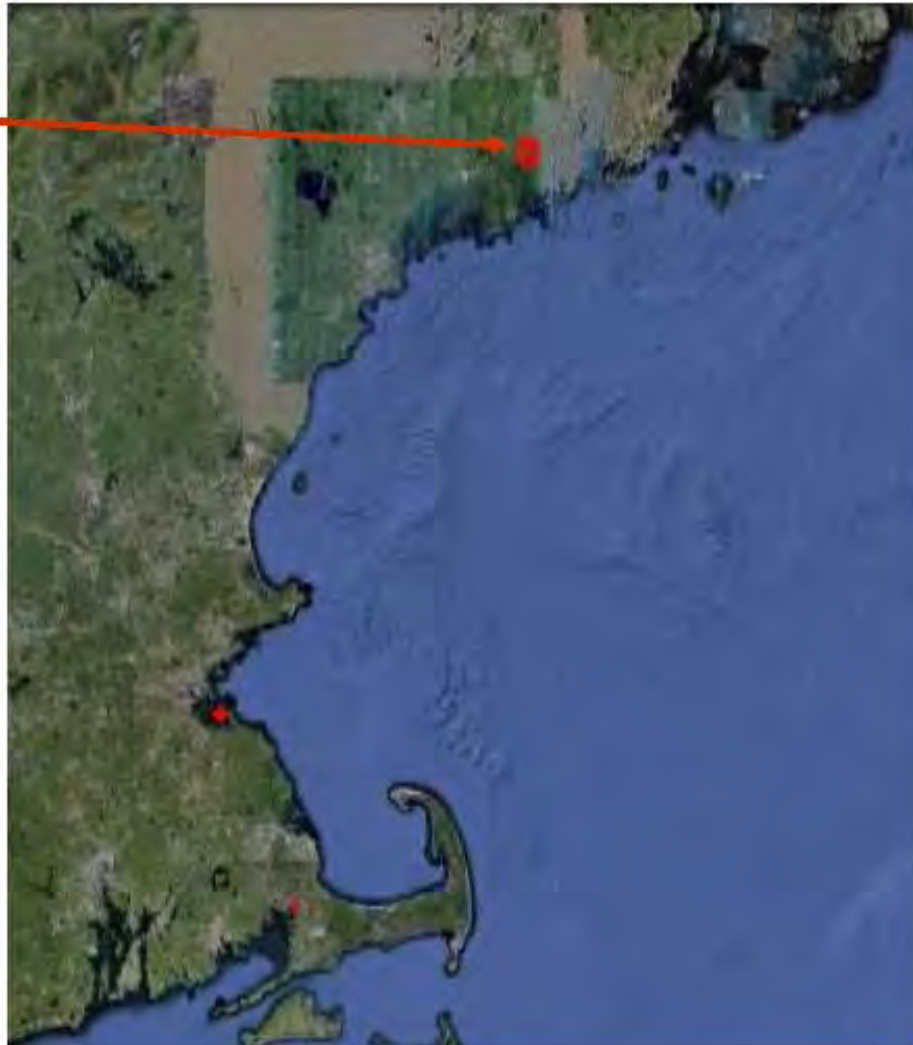
**Peter Arnold, James Churchill
Jessica Jansujwicz, Gayle Zydlewski,
Teresa Johnson, Dot Kelly, Johanna Szillery,
Garrett Staines, Carl J. Wilson,**

With Thanks to:

**The Chewonki Foundation, Maine Maritime
Academy, University of Maine, Maine Tidal
Power Institute, US. Dept. of Energy
Jay Sisson, Stanley King, Davies Allen,
Gordon Hall**

Community-Based Site Assessment

Wiscasset, Maine





**May 28, 2009 FERC Permit granted to the
Town of Wiscasset**

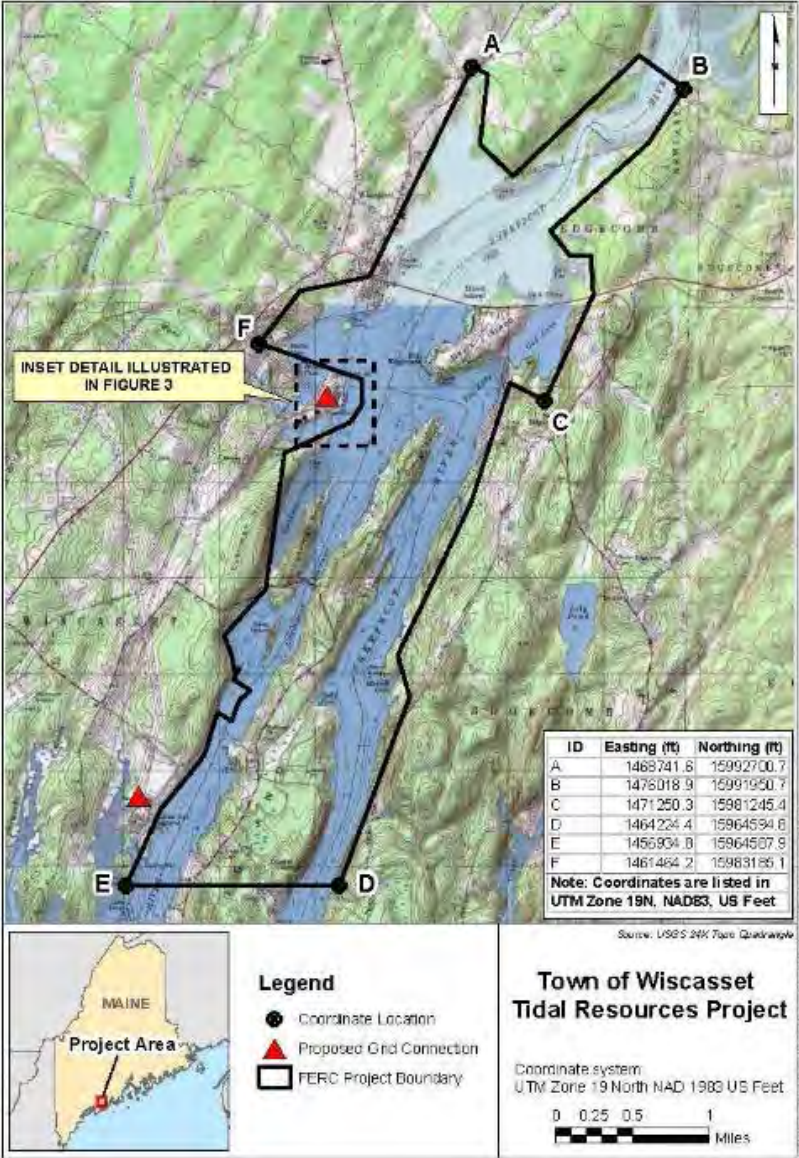
Program Manager: Peter Arnold, Chewonki Foundation

Financial Support: Gordon Hall

Dot Kelly

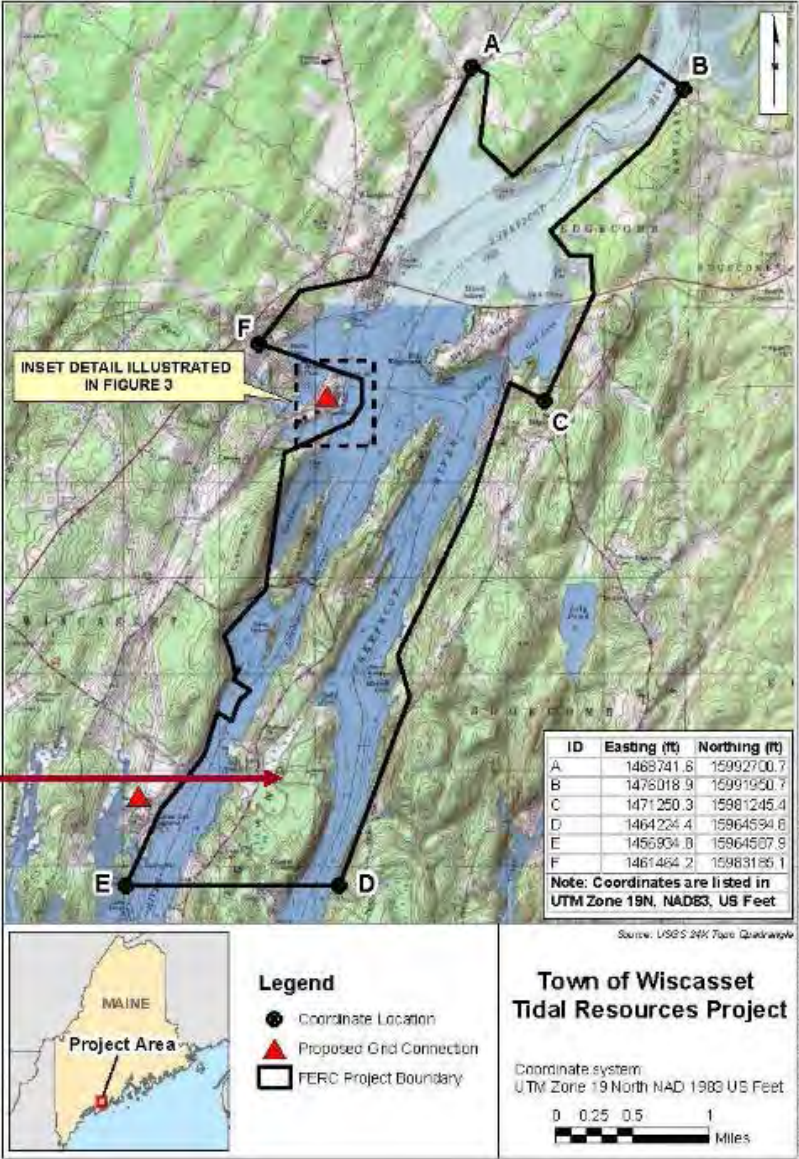
Maine Tidal Power Initiative

FERC Permit Area



FERC Permit Area

Westport Island



An aerial photograph of a large body of water, likely a reservoir or lake, with a small boat and several buoys visible. The water is a deep blue color with some ripples and reflections. The text is overlaid on the left side of the image.

Three Components of Site Assessment

- Power resource and site suitability
- Community and Social Perceptions
- Presence of Endangered Fish Species



Three Components of Site Assessment

- **Power resource and site suitability**
- Community and Social Perceptions
- Presence of Endangered Fish Species



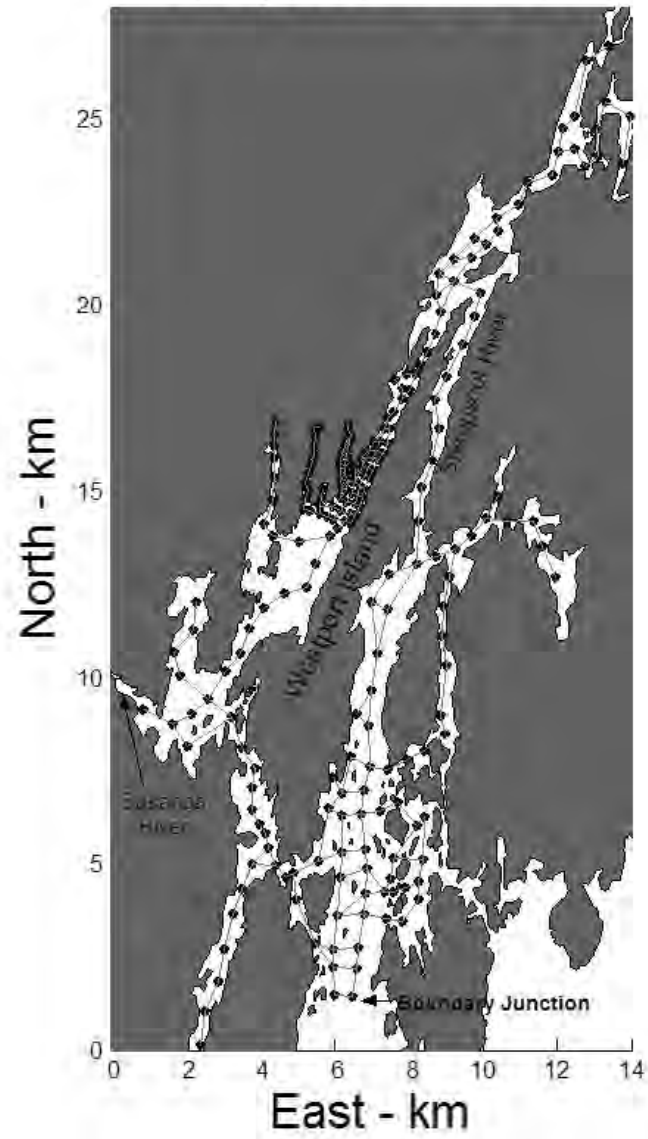
Power Resource Assessment
A Three Step Process
with “go” or “no” decision at each step

1. Hydrodynamic modeling \$
2. Shipboard velocity surveying \$\$
3. Moored velocity measurements \$\$\$

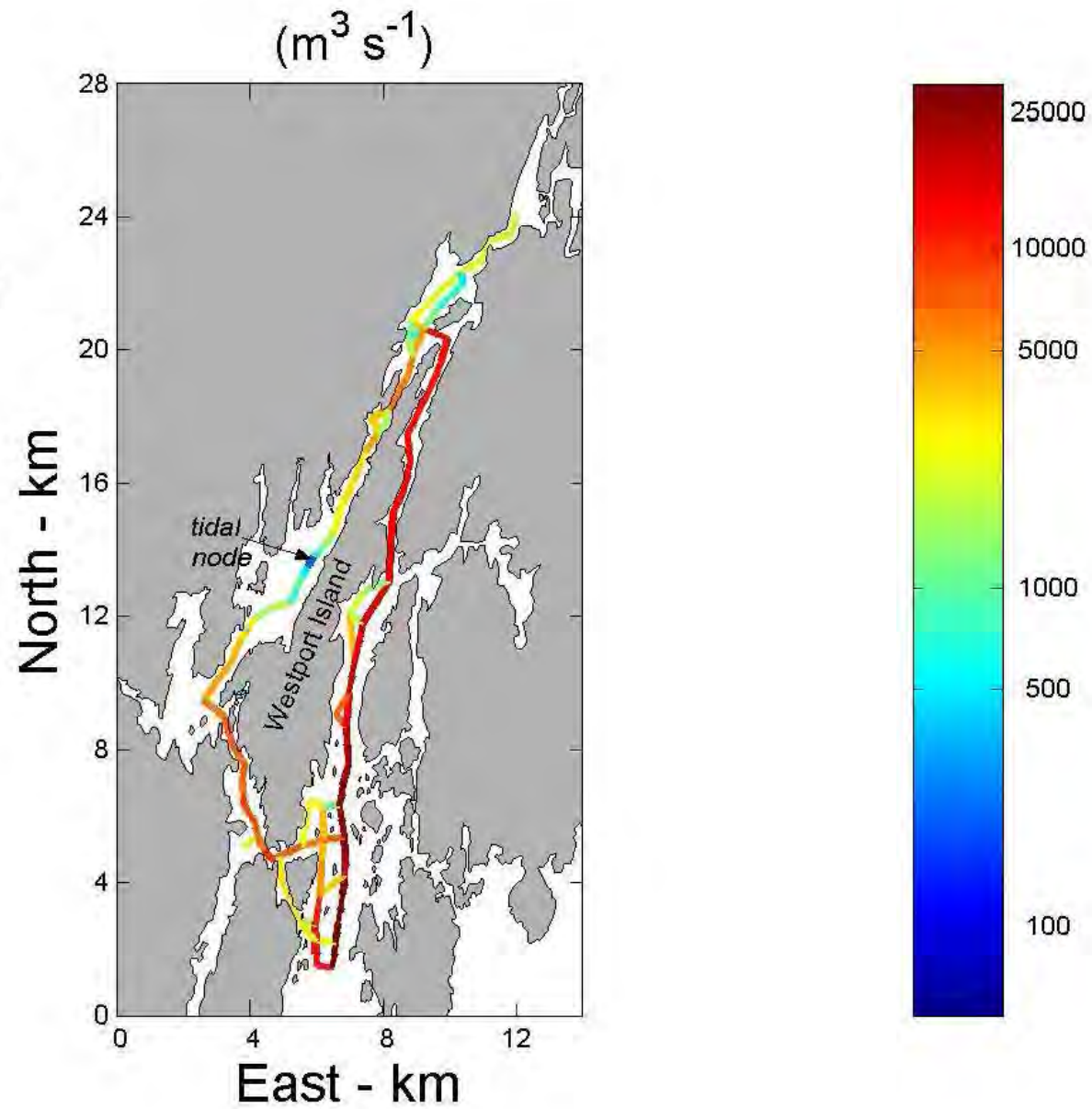
Step 1

Hydrodynamic Modeling

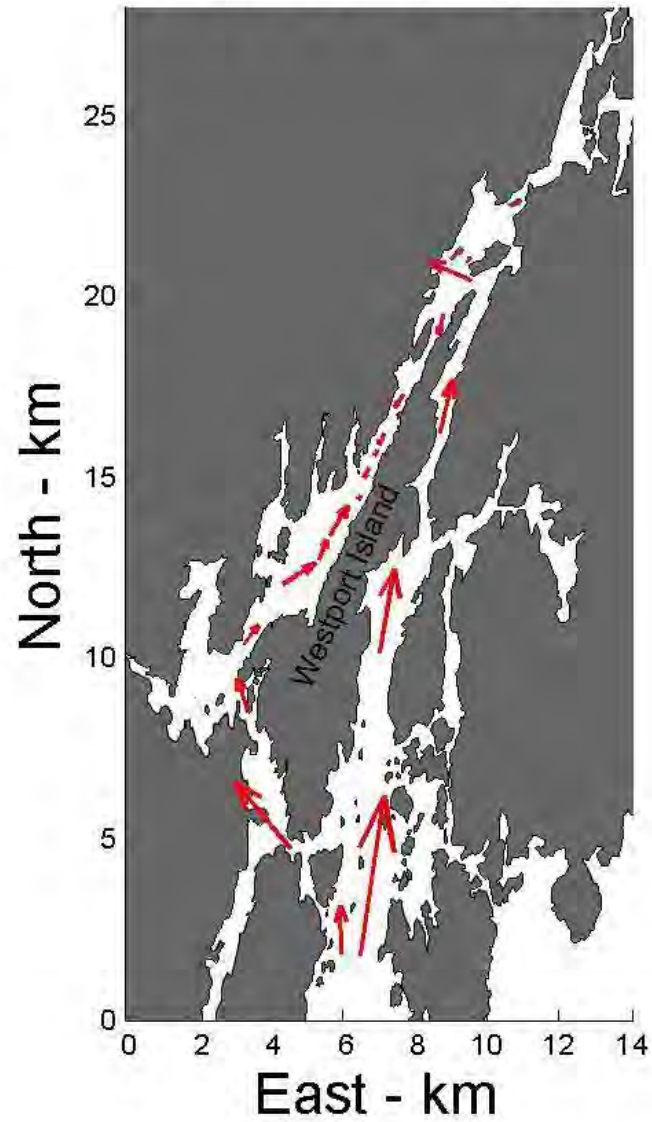
Sheepscot Model Grid



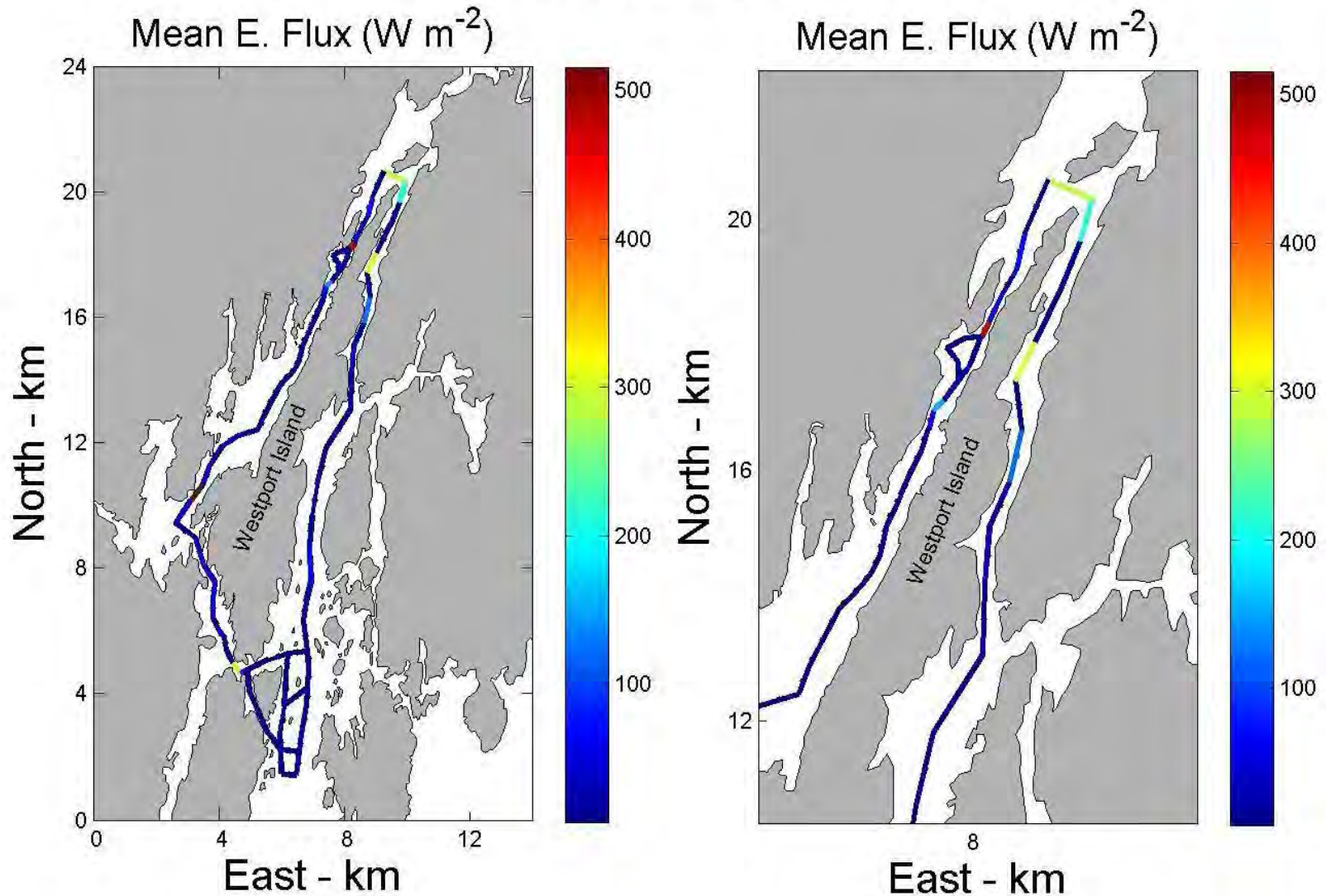
The Island Tidal Node



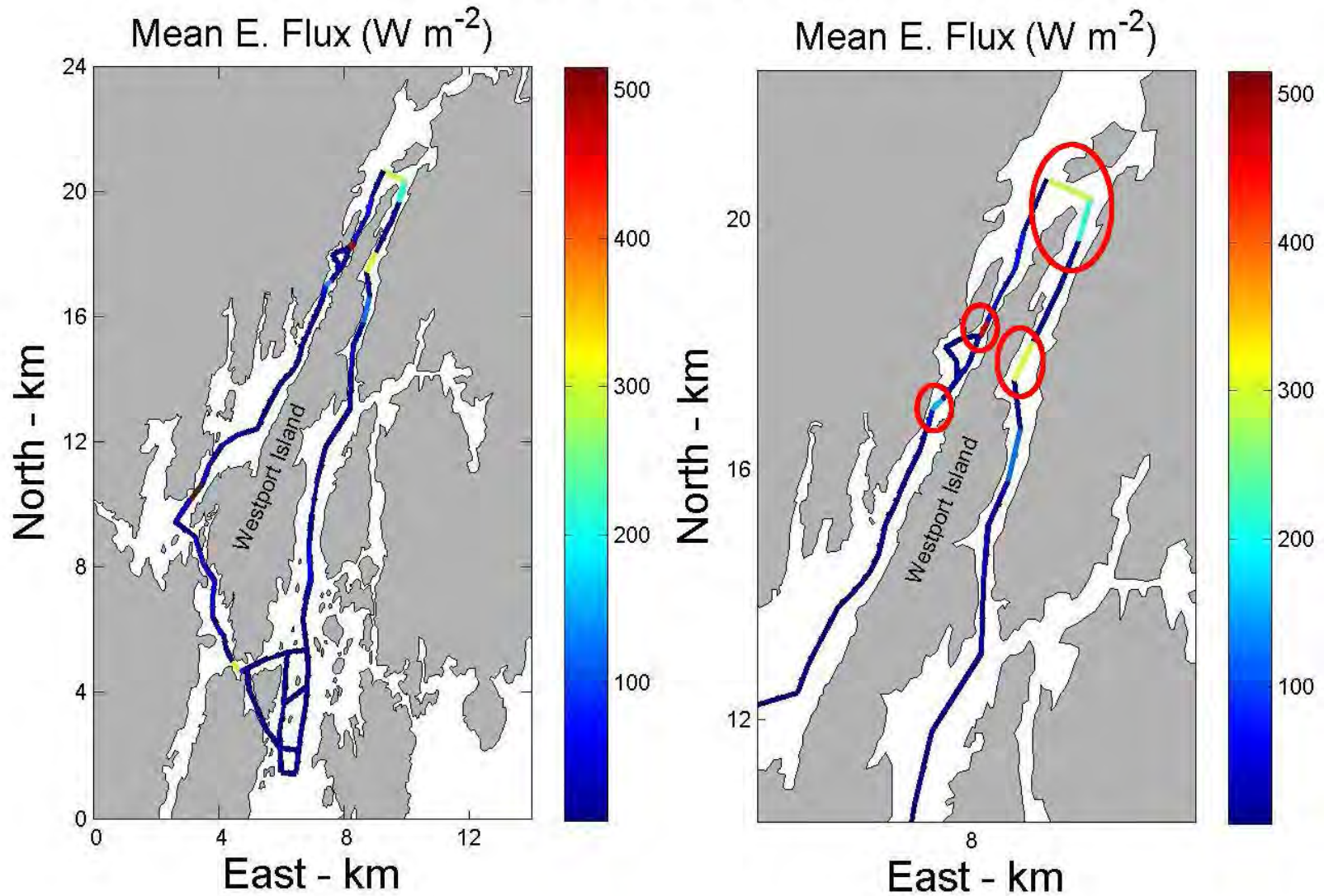
Flood Tide Transports



Tidal Power Distribution



Tidal Power Distribution



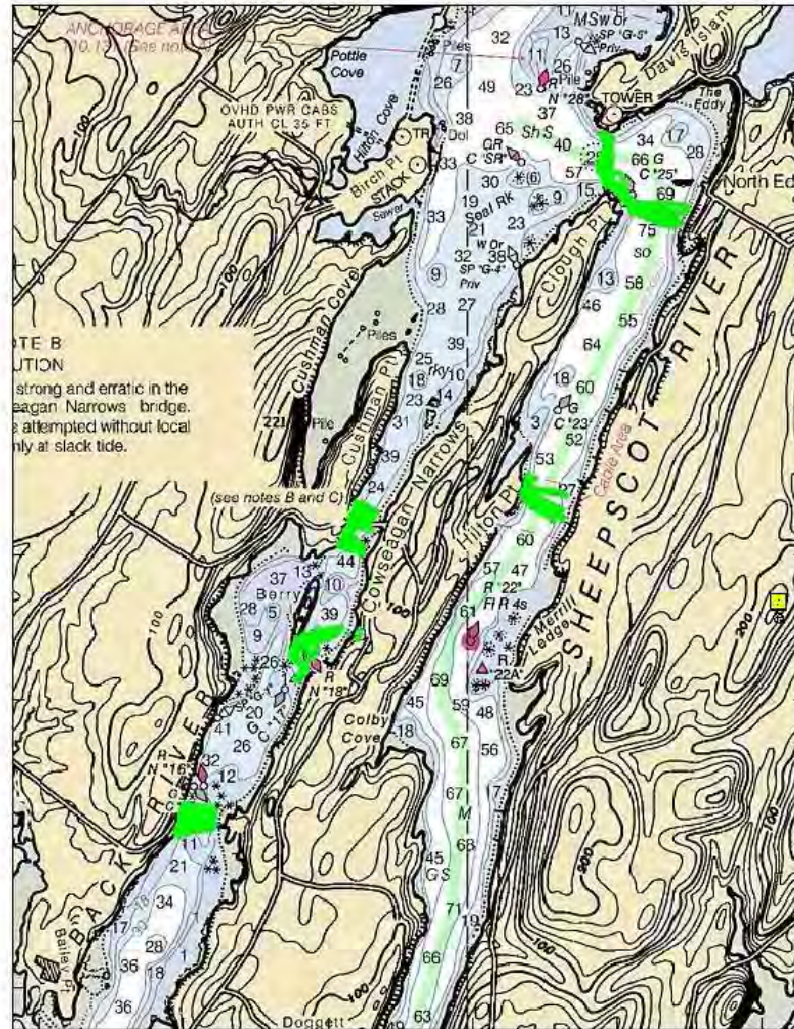
Step 2

Spatial Velocity Survey

Surveyed Areas

Our sampling focused on five areas, indicated by the sampling sites (green dots) shown here. These areas were identified as high energy locations by a numerical model and by the data from a preliminary survey conducted on September 28.

Surveying done over a
12+ hour period on
Sept. 30 2010



The Surveying Equipment



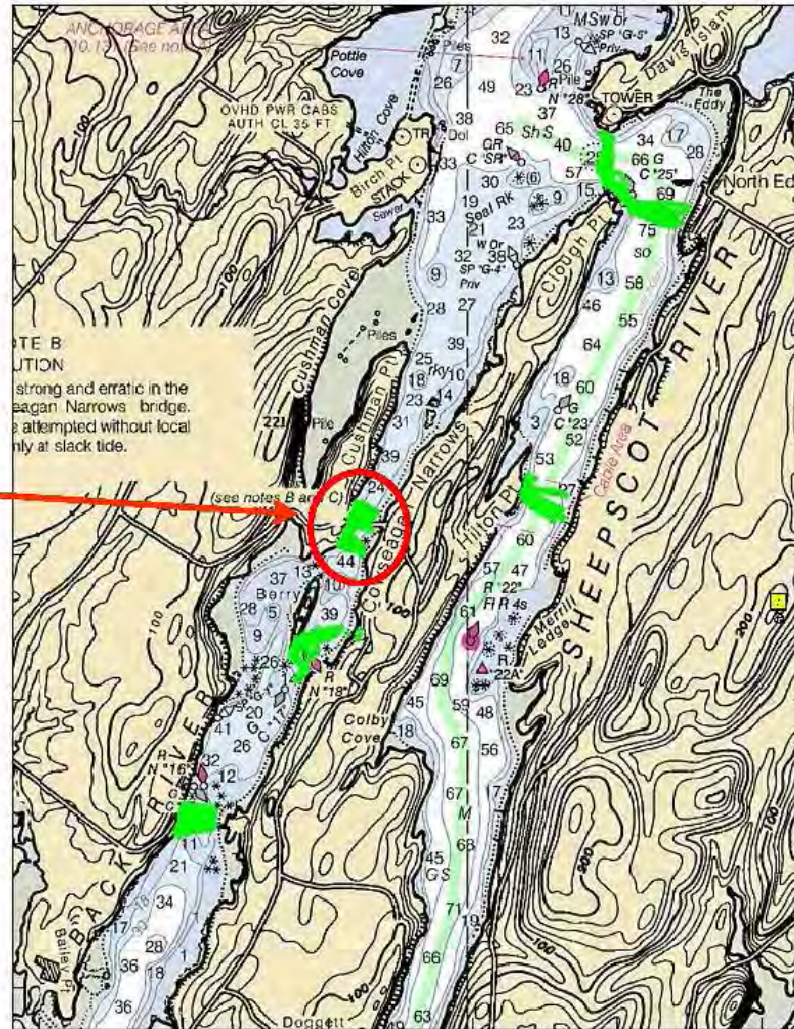
Acoustic Doppler Current Profiler
(ADCP)



R/V Seagull and Capt.
Stanley King

Surveyed Areas

The Best Area

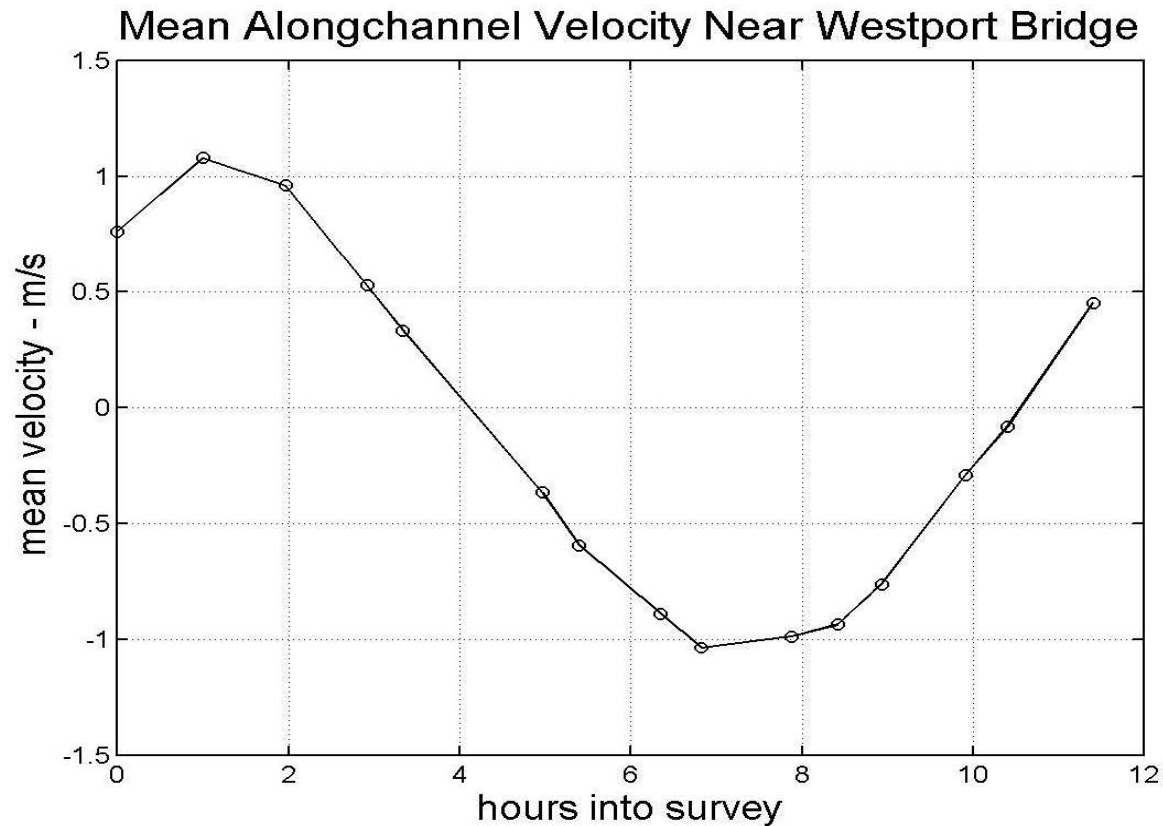


Under the Bridge



The focus here will be on the tidal flows and tidal power near the Westport Island bridge.

The Tidal Cycle

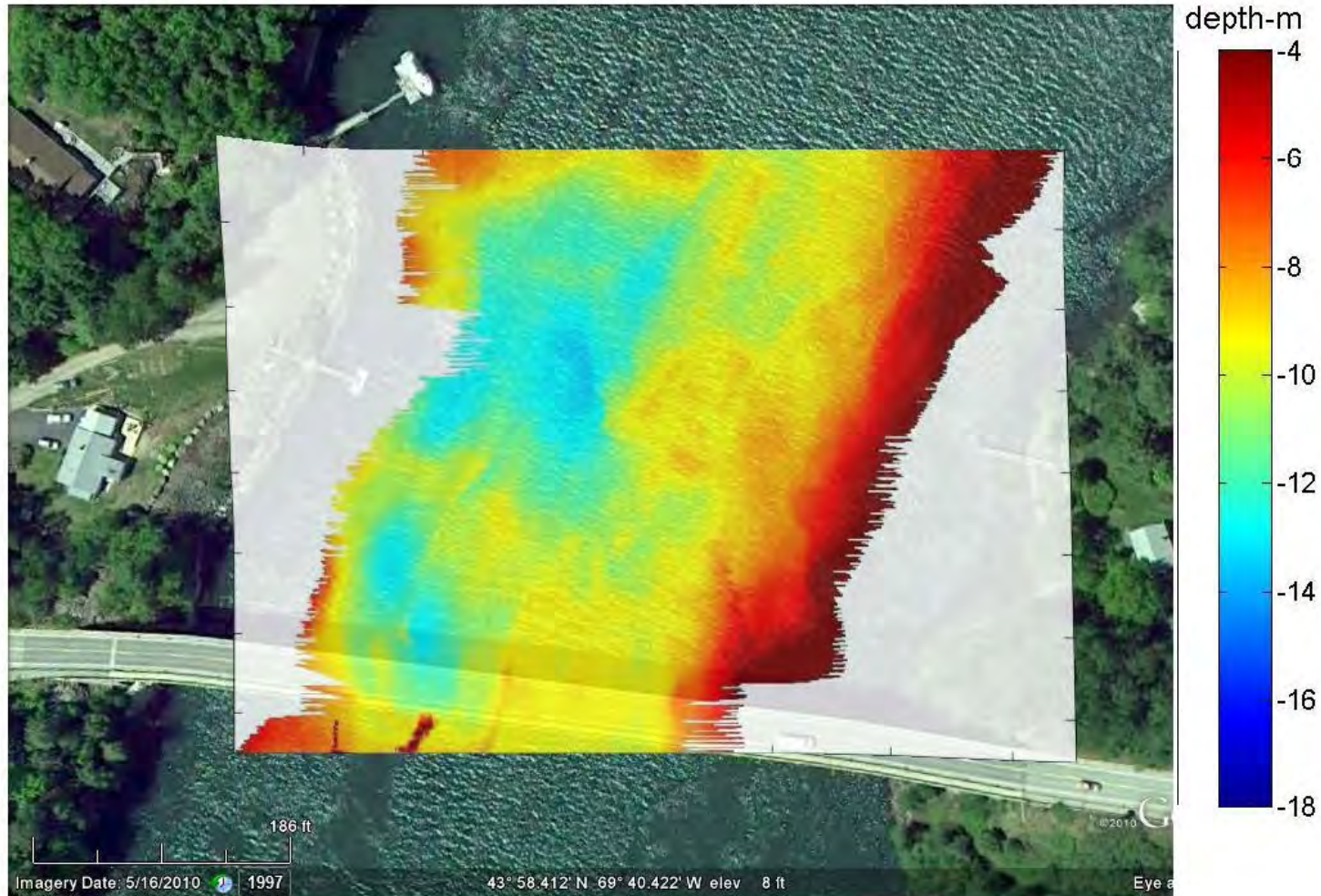


The tidal velocity nicely follows a sinusoidal cycle, with maximum ebb (positive) and flood (negative) currents of slightly greater than 1 m/s. Velocities were somewhat higher directly underneath the bridge (by about 10 %), but this is a minor point.

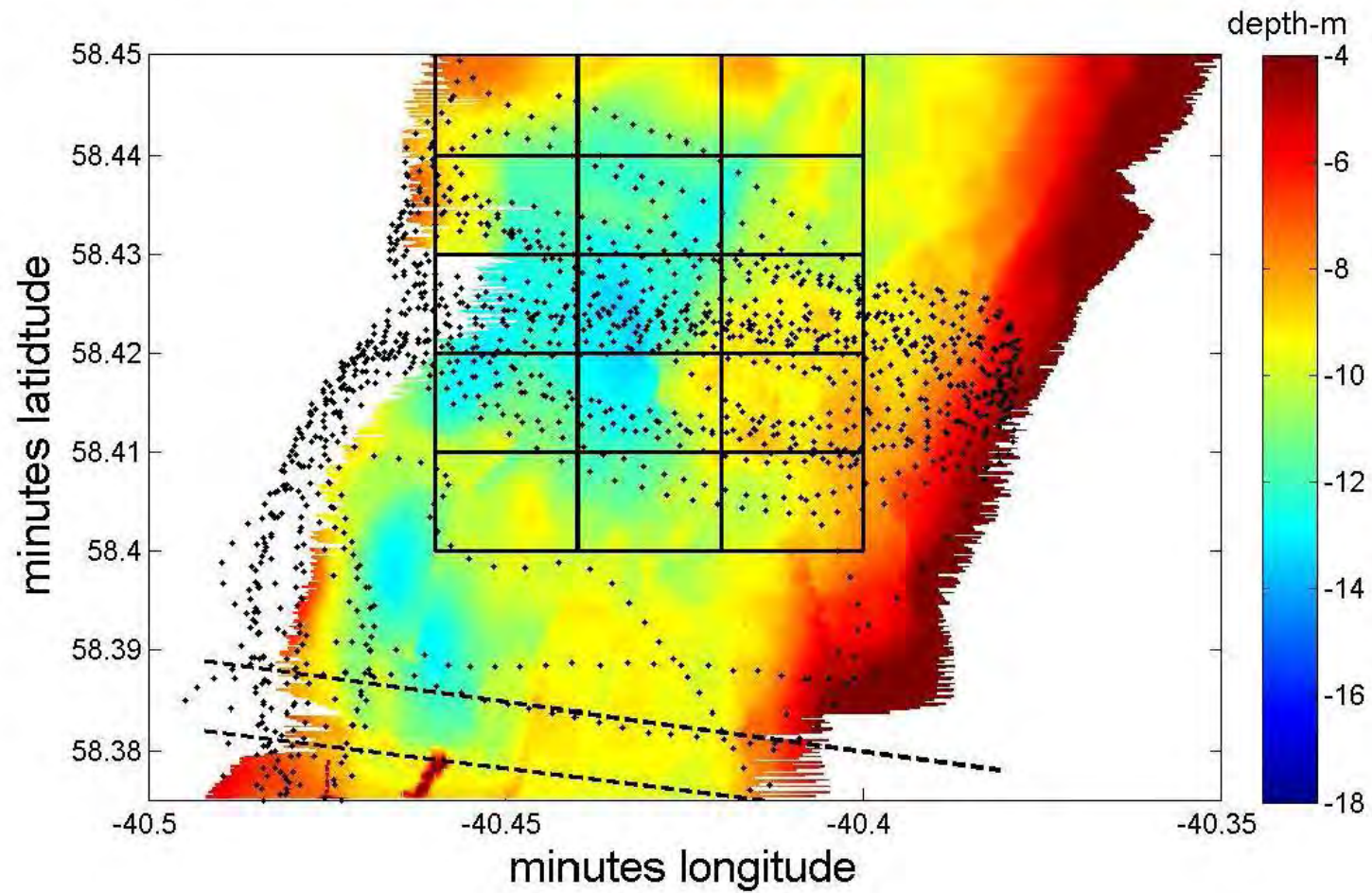
Step 3

Moored Velocity Profiling

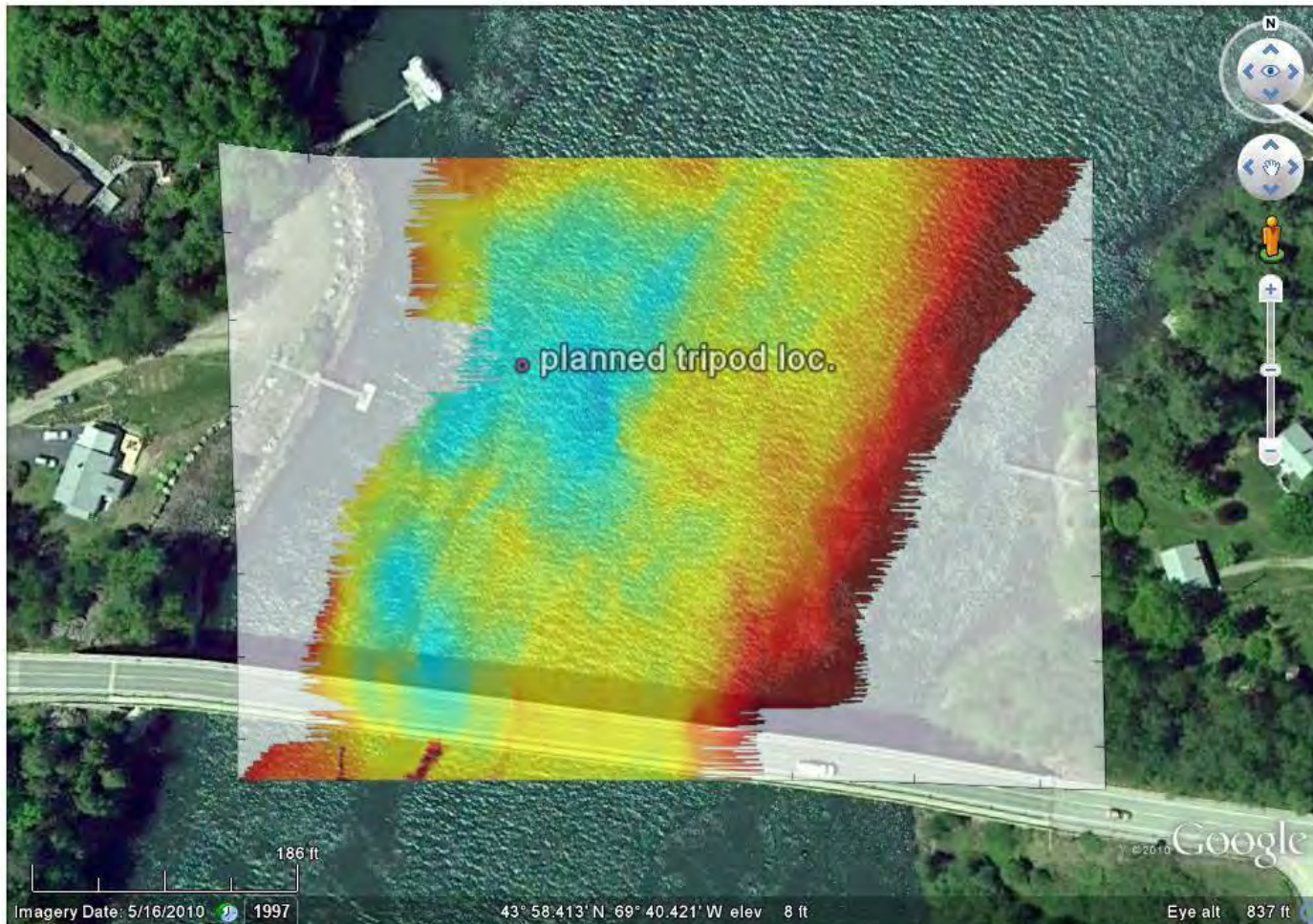
Determining the optimal bottom ADCP location based on survey velocities and multibeam data



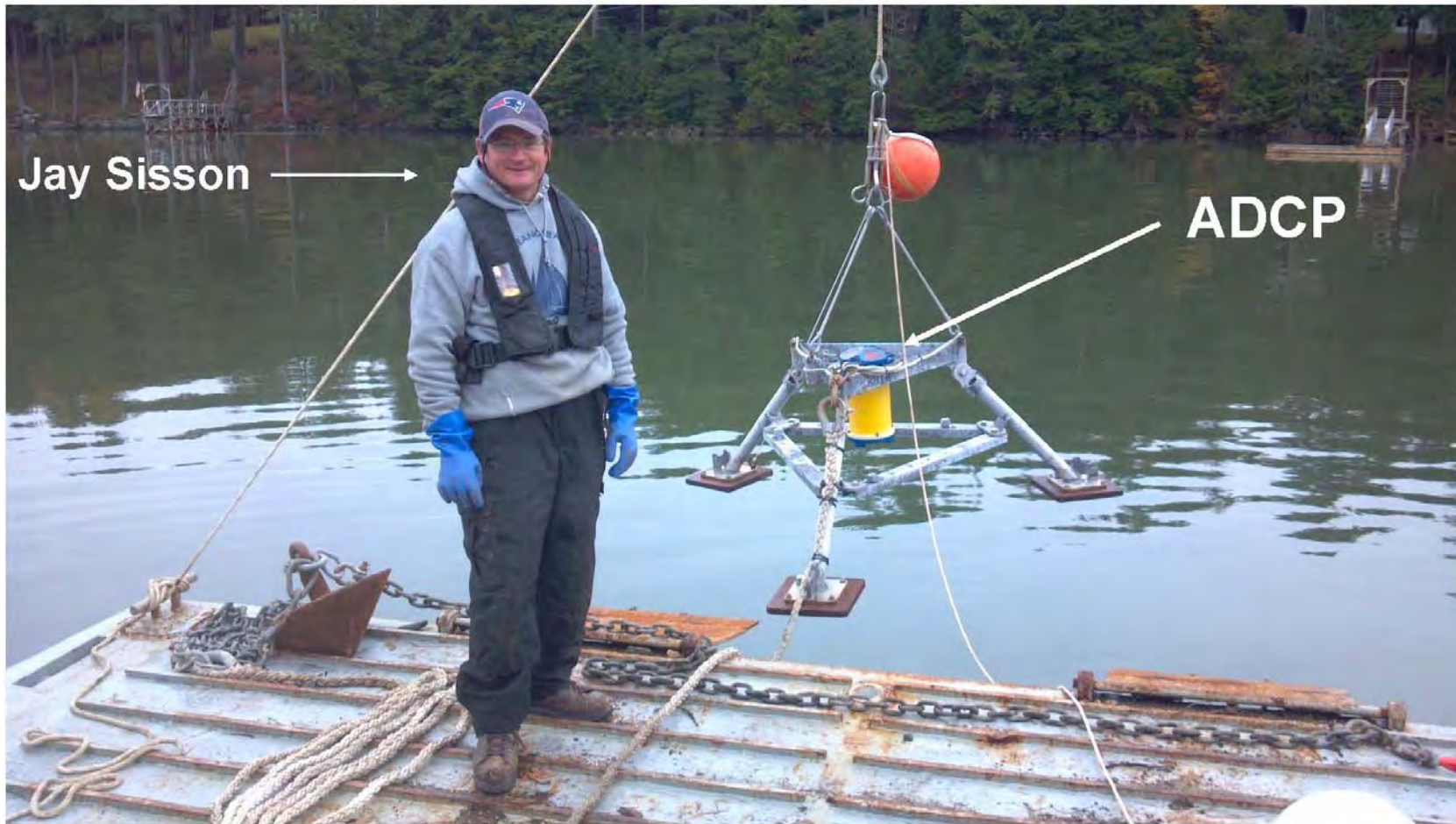
Determining Tidal Velocity Strength North of the Bridge



The Chosen Site



The Rig



Deployed Oct. 27 – Nov 29, 2011

Social Science Research

Teresa Johnson, Jessica Jansujwicz and Peter Arnold

➤ Approach

- Stakeholder “Map”
 - Who? Information needs?
- Stakeholder interactions
 - Who? Frequency? Context? How information is used?
- Stakeholder perceptions
 - Social acceptability? Information gaps? Outreach strategies?

➤ Methods

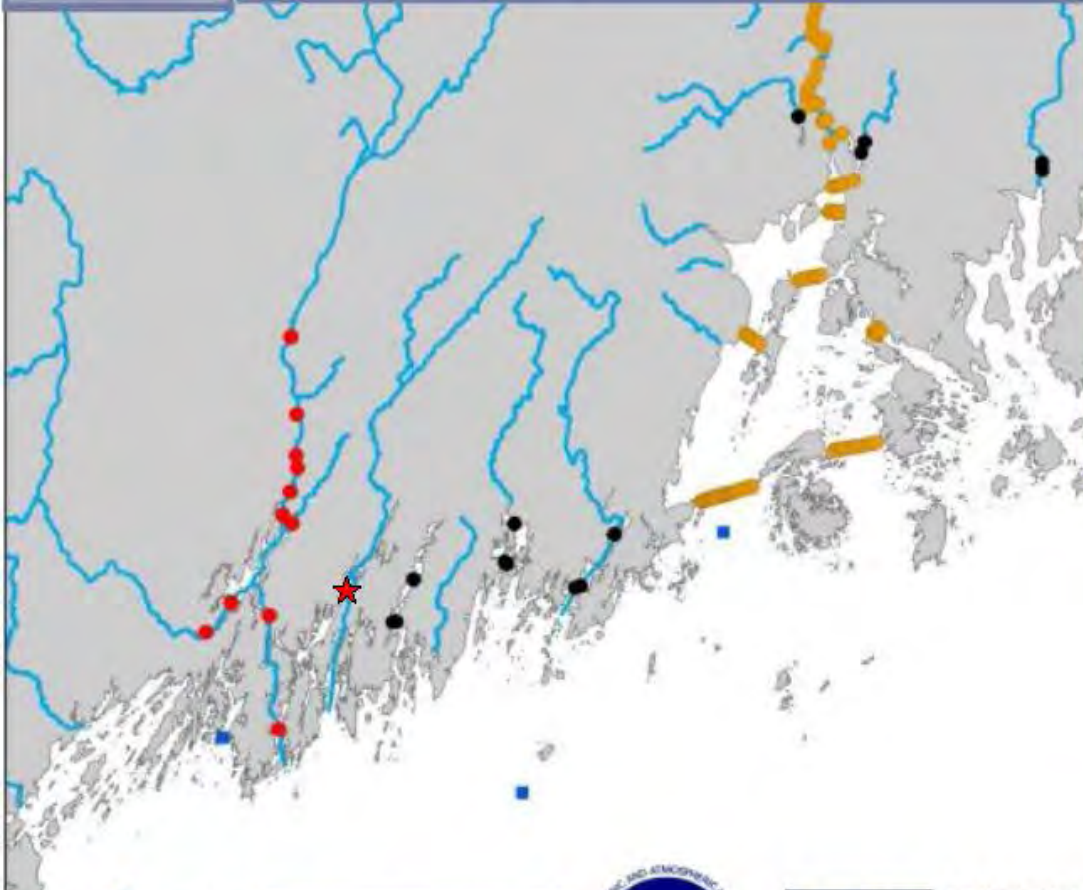
- Observations (**public meetings, agency consultation**)
- Interviews (community, technology, **policy stakeholders**)

An aerial photograph of a wide river. On the left bank, there is a dark, rocky shoreline with a wooden pier extending into the water. On the right bank, there is a white wooden structure, possibly a bridge or a walkway, extending into the water. The water is a deep blue color with some ripples and reflections. The text "Assessment of Endangered Fish Species Presence" is overlaid in the center of the image.

Assessment of Endangered Fish Species Presence

Gayle Zydlewski

Contemporary Presence: Sturgeon in the Sheepscot



- Penobscot River Array
- Coastal River Array
- Kennebec River Array
- GoMOOS Array
- New England Historic Salmon Rivers



UNIVERSITY OF
NEW ENGLAND

Biddeford Campus



Contemporary Presence: Sturgeon in the Sheepscot

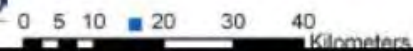


- Penobscot River Array
- Coastal River Array
- Kennebec River Array
- GoMOOS Array
- New England Historic Salmon Rivers



UNIVERSITY OF
NEW ENGLAND

Biddeford Campus



Shortnose Sturgeon

Receiver in Back River, Sheepscot

Deployed from October 2010 – July 2011

- 6 individuals detected
 - May 2 – 27
 - 0.006, .08, .6, 1.5, 3 days
- Tag origin: **Penobscot River**
 - 4 tagged on October 11, 2010
 - 2 from 2009

Atlantic Sturgeon

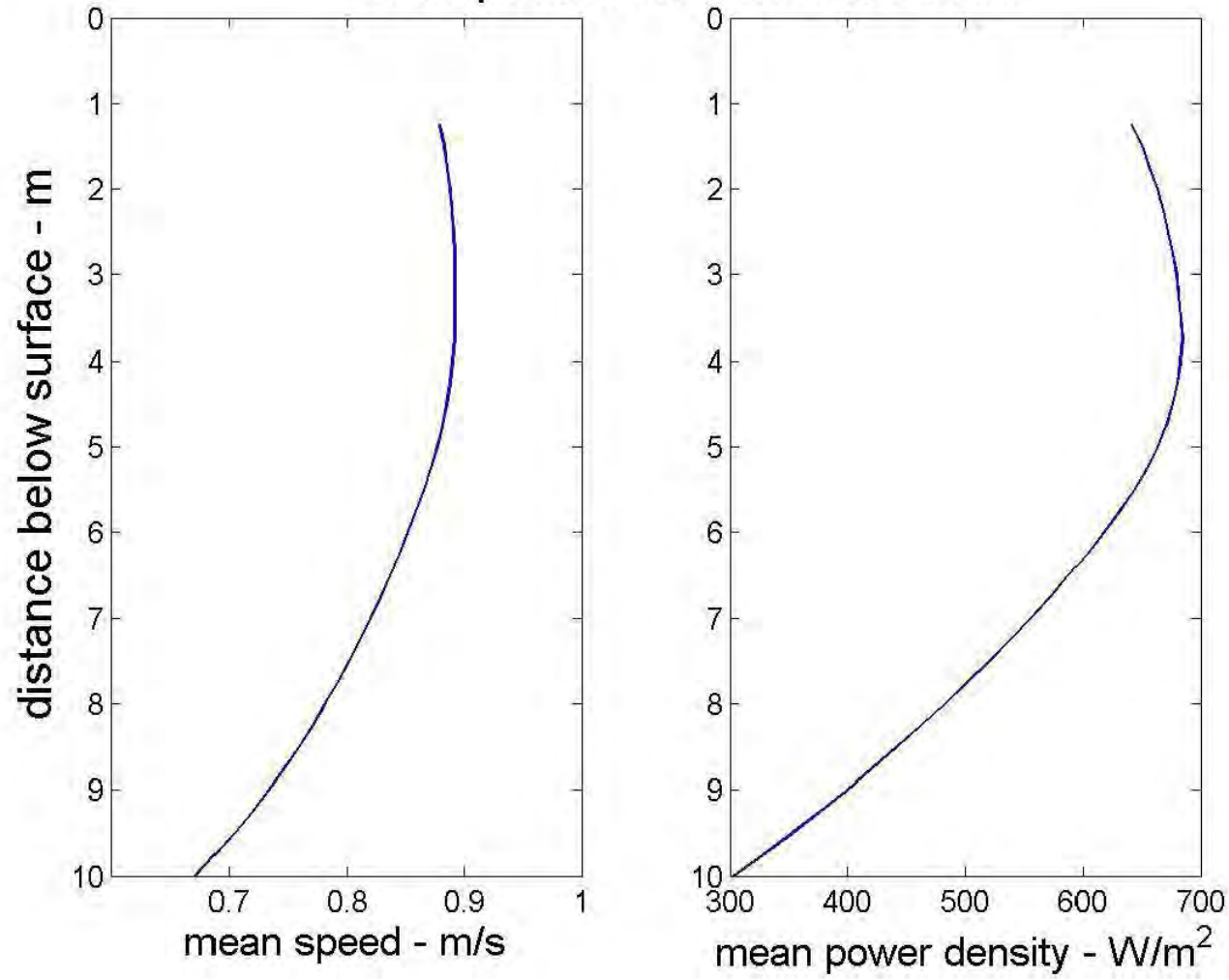
Receiver in Back River, Sheepscot

Deployed from October 2010 – July 2011

- ▶ Detected 5 individuals
 - ▶ February (1 d), March (3 h & 10 d), April (1 record), June (0.05d), Jul (7 d)
- ▶ Tag origins:
 - ▶ 2 tagged in **Merrimack River** (October 2010)
 - ▶ 3 tagged in **Saco River** (2 in August 2009, 1 in September 2010)

The Power Density

Sheepscot River Oct-Nov 2011





**Community-Based Site
Assessment in Fulfillment of a
FERC Preliminary Permit is
Feasible**



**Community-Based Site
Assessment in Fulfillment of a
FERC Preliminary Permit is
Feasible**

**Especially with partners from academia
and the non-profit research world**



Community-Based Site Assessment in Fulfillment of a FERC Preliminary Permit is Feasible

**Especially with partners from academia
and the non-profit research world**

**A suggested first (and maybe last) step is
resource assessment through
hydrodynamic modeling**



APPENDIX Task 4-6

FINAL REPORT ON THE WISCASSET TIDAL POWER PROJECT



PETER ARNOLD, MS
13 BRANCH ROAD
DAMARISCOTTA, ME 04543
(207) 406-0236

Final Report on the Wiscasset Tidal Power Project

Background

In May 2009, the Town of Wiscasset in collaboration with the Chewonki Foundation, filed for and received a FERC Preliminary Permit to study the possibility of a tidal power installation in the Sheepscot River. Since that time I have functioned as Project Manager for Wiscasset to move the study forward to the point where a decision could be made about whether to apply for a Pilot License which would allow equipment to be put into the river to create electricity using the tides.

Studies have progressed in three areas:

Fisheries

How do the endangered sturgeon and salmon, known to transit through the Sheepscot River, use the FERC study area? This research question has been addressed by fisheries biologists from the University of Maine as part of the Maine Tidal Power Initiative. These fish had never been studied in the tidal section of the river. Preliminary results have been reported NOAA as a part of an ongoing collaboration with regulatory agencies. It is anticipated that the research results will be published in the future.

Sociology

What do the citizens and governmental officials of Wiscasset think about a potential tidal power installation in the Sheepscot River? To date interviews have been conducted and the data is being compiled as part of a larger study that includes other Maine communities where FERC Preliminary Permits have been issued to study tidal power possibilities. It is expected that this material will also be published in the future.

Electricity Generation Potential

Where in the study area are the fastest currents located, what is the depth and bottom composition at that location and what is the water velocity there throughout the tidal cycle? This information was gathered in two stages. The first study, conducted by James Churchill of Woods Hole Oceanographic, involved making repeated transects through the water column at the six most promising locations in the study area through out a 12 hour tidal cycle. Those results were then modeled to approximate what the velocities might be like over a full lunar cycle.

Using the modeled data, the most promising site was identified for further study. That site was located close to the Westport Island Bridge. Carl Wilson from the Maine Department of Marine Resources next conducted a bathymetric multibeam study of the area to map bottom condictions and depths.

The information gained was presented to Ocean Renewable Power Corporation (ORPC), a Maine based tidal power equipment development company, to determine what bottom location best suited the equipment they are currently testing in Eastport. The location they identified combined good bottom characteristics with the strongest modeled current velocities. At this location an Acoustic Doppler Current Profiler was bottom deployed by James Churchill for a month to record current velocities through out the water column for a full lunar cycle.

This data was subsequently analyzed to determine the current velocity profile that in turn could be used by ORPC to determine the amount of electricity that could be made at the site using their current generation of equipment. The study indicated that the site would only produce 10% of the nameplate capacity of the ORPC equipment. Therefore, the current velocities are not high enough to make much electricity. In mathematical terms, the total power available from a current of magnitude, v , passing through a cross-section of area, A , may be expressed as: $P = \rho Av^3/2$; where P is the power and ρ is water density. The informative point here is that the power increases by the cube of the current magnitude. Just a little more velocity and the power increases very substantially. The velocity numbers for this site would not seem to justify moving forward given the capabilities of the current generation of hydrokinetic equipment.

At this time, my recommendation is that the Town of Wiscasset not apply, for either an extension of the FERC Preliminary Permit or for the next level of licensure, a Pilot License.

That said however, the project has generated a lot of information about the tidal resource that may be useful to the town or to others as the capabilities of hydrokinetic equipment improves. The exercise has also served to raise awareness of the possibility of community power generation and the possibility that a municipality can be an active player on behalf of its citizens to secure renewably generated electricity in this age of transition away from fossil fuels. This field is in its infancy and new technology is developing quickly. It may be that another technology will be able to utilize the velocities we have in the Sheepscot. I will continue to follow new potential equipment.

In order to share the lessons learned from this project, I have applied to the Energy Ocean 2012 Conference to present the results of our work on the Wiscasset Tidal Power Project at their June conference in Boston. The abstract submitted is included as an appendix to this report as are the two power point presentations done by James Churchill documenting the two phases of current velocity studies.

Respectively submitted,

Peter Arnold



APPENDIX Task 4-7

FERC LICENSING HYDROKINETIC PILOT PROJECTS

Note: This document contains its own set of appendices, labeled alphabetically.

LICENSING HYDROKINETIC PILOT PROJECTS

I. INTRODUCTION

The staff of the Federal Energy Regulatory Commission is issuing this guidance as part of the Commission's ongoing effort to support the advancement and orderly development of innovative hydrokinetic technologies. Hydrokinetic projects generate electricity from the motion of waves or the unimpounded flow of tides, ocean currents, or inland waterways. Pilot projects are small, short-term, removable, and carefully-monitored projects intended to test technologies, sites, or both. Some hydrokinetic pilot projects may be appropriate for expedited license application processing under the Commission's existing regulations.

Hydrokinetic pilot project licensing procedures were proposed in a whitepaper on August 31, 2007 and at a technical conference in Portland, Oregon on October 2, 2007. The Commission and staff received oral comments at the conference and written comments thereafter. This whitepaper uses a format of frequently asked questions (FAQs) to address the issues raised in the comments. The FAQs are divided into the following topic areas: general information; coordination with federal, State, and local resource agencies, Indian tribes, non-governmental organizations, and members of the public; information needs; monitoring, performance standards, and modification/shutdown/removal; preliminary permit/pilot project license/commercial build-out; and next steps. This paper also provides the criteria for using pilot project licensing procedures, step-by-step pilot project licensing guidance, application information needs, and standard license articles.

This document may be periodically revised as policies change and lessons are learned during pilot project development. The dates of any revisions are annotated in this document. The most current version is available on the Hydrokinetic Pilot Project Licensing Process Web Page located at www.ferc.gov.

GENERAL

Why is the Commission staff providing guidance on expedited procedures for licensing hydrokinetic pilot projects?

As stated by Chairman Joseph T. Kelliher, “there are barriers to realizing the potential of these new technologies, including financial, technological, and regulatory. The principal barrier to development of these technologies may be that they are as yet unproven. The technologies must be proven before large scale commercial deployment can occur.”

Consistent with the national interest and its own strategic objective to “Stimulate appropriate infrastructure development,” the Commission is committed to supporting the orderly demonstration and development of hydrokinetic technology.¹ According to Commissioner Philip Moeller, “This new generation of hydrokinetic technologies... is generating a lot of enthusiasm throughout the country... FERC wants to harness this enthusiasm by exploring ways to reduce the regulatory barriers to realize the amazing potential of this domestic renewable

power source.” New hydrokinetic technologies, if fully developed, have the potential to double the amount of hydropower production in the United States, bringing it from just below 10% to close to 20% of the national supply.²

Previously, the Commission has determined that experimental deployment of projects testing new hydropower technology may, in certain limited circumstances, be possible without a license under Part I of the Federal Power Act (FPA).³ That policy remains in effect. Now, for those interested in licensing hydrokinetic pilot projects, Commission staff has identified how best to apply the Integrated Licensing Process (ILP) in an expedited manner for pilot projects. These procedures will meet the needs of entities interested in testing new

technology, including interconnection with the electric grid, while minimizing the risk of adverse environmental effects.

¹ Federal Energy Regulatory Commission. Strategic Plan FY 2006–FY 2011. (Available at www.ferc.gov.)

² See Hydroelectric Infrastructure Technical Conference, Docket No. AD06-13-000 (December 6, 2006), transcript at 12; 22 (testimony of George Hagerman).

Licensing Hydrokinetic Pilot Projects

April 14, 2008

³ *Verdant Power LLC*, 111 FERC ¶61,024, *order on reh'g* 112 FERC ¶61,143 (2005).

Is this whitepaper describing a new rule?

No. Staff is proposing to adapt existing regulations and provide waivers for specific types of projects. This document provides project developers and others with staff's guidance on an efficient pathway to seek regulatory modifications and waivers to allow expedited license processing and short term testing for a specific class of projects.

What are the purposes of licensing hydrokinetic pilot projects?

The purposes of licensing hydrokinetic pilot projects are to test new, hydrokinetic technology devices; to determine the appropriate sites for hydrokinetic projects; and to gather information on environmental and other effects of the devices. Review of a project proposal would be carried out under the Commission's existing authority and regulations and the Commission would incorporate input from federal, State, and local resource agencies, Indian tribes, non-governmental organizations, and members of the public. When granted, a license would allow the developer to realize a revenue stream from generating while testing and would provide for Commission enforcement of license conditions.

What are the goals for licensing hydrokinetic pilot projects?

Staff's goal is to provide expedited procedures through which a Commission decision can be rendered in as few as six months after the filing of the application. The procedures will be oriented toward the characteristics of small, pilot projects with short license terms. They will emphasize post-license monitoring with the possibility of modifying, shutting down, or removing a device that presents an unforeseen risk to public safety or environmental resources.

What is the basis for the pilot project licensing procedures?

Staff believes that the Integrated Licensing Process (ILP, Part 5 of 18 CFR), with specific waivers granted under § 5.29(f)(2) on a case-by-case basis, is the best process to use to apply for a hydrokinetic pilot project license. The ILP time frame can be reduced while preserving opportunities for consultation and comment, environmental review and analysis, and the conditioning authority of federal and State agencies and Indian tribes. Appendix A provides a description of the procedures.

April 14, 2008

How does licensing hydrokinetic pilot projects differ from the policy applied in the Verdant Orders concerning experimental deployments?

In the *Verdant* orders, the Commission interpreted the Federal Power Act in a flexible manner that allowed an experimental deployment without a license. The Commission concluded that facilities could be installed and tested without a license if (1) the technology in question was experimental; (2) the proposed facilities were to be utilized for a short period for the purpose of conducting studies necessary to prepare a license application; and (3) power generated from the test project would not be transmitted into, or displace power from, the national grid. In contrast to projects operating under the *Verdant* decision, the pilot project procedures (1) could lead to a license under the Federal Power Act; (2) will be reviewed and overseen by the Commission; (3) will allow the transmission of electricity into the national power grid if licensed; and (4) will be available to those who wish to test technology, whether or not they intend to pursue a standard license application to follow the pilot project license.

How will a license for a hydrokinetic pilot project differ from a license for a conventional hydropower project?

Under the Federal Power Act, the Commission is authorized to issue licenses for construction, operation, and maintenance of hydropower projects.⁴ Original licenses can be issued for a term of up to 50 years. Appropriate pilot projects may have short license terms of five years in length in keeping with the early stage of the technology, expected small size of the projects, required safeguards, and the experimental nature of the efforts.

In addition to a short license term, Commission staff also envisions licenses for pilot projects having (1) an emphasis on post-license monitoring; (2) a license condition requiring project modification, shutdown, or removal in the event that monitoring reveals an unacceptable level of risk to the public or environmental harm; and (3) a license condition requiring project removal and site restoration before license expiration if a new license is not obtained. Examples of standard license articles can be found in Appendix C. Otherwise, a license for a hydrokinetic pilot project, like any hydropower project license, will authorize construction, operation, and maintenance of the project, including generation of power and transmission into the national electric grid under the conditions of the license.

Who may use these procedures?

These procedures are available on a case-by-case basis for individual hydrokinetic test projects that are proposed to be: (1) small; (2) short term; (3) not located in sensitive areas based on the Commission's review of the record; (4) removable

Licensing Hydrokinetic Pilot Projects

April 14, 2008

and able to be shut down on short notice; (5) removed, with the site restored, before the end of the license term (unless a new license is granted); and

(6) initiated by a draft application in a form sufficient to support environmental analysis.

⁴ 16 U.S.C. § 796.

How does an applicant request use of these procedures?

A potential license applicant must (1) distribute its pre-filing materials to the potentially interested State, federal, and local resource agencies, Indian tribes, non-governmental organizations, and members of the public; (2) notice the availability of the materials in local newspapers; and (3) file the materials with the Commission. The pre-filing materials should include (1) a notice of intent (NOI) to file an application; (2) a draft application (including proposed plans for monitoring, safeguarding the public and environmental resources, and assuring financing to remove the project and restore the site); (3) a request for the waivers necessary to pursue expedited processing of a pilot project license application (including a process plan/schedule and justification statement); and (4) requests for designation as non-federal representative for Endangered Species Act (ESA) and National Historic Preservation Act (NHPA) consultation. The justification statement must demonstrate that the project meets the pilot project criteria. More details are provided under the topic of Information Needs in the FAQs below, in Appendix A, and in Table A1.

How can I find out more about licensing hydrokinetic pilot projects?

Potential applicants and other interested parties can visit the Commission's web page on hydrokinetics (<http://www.ferc.gov/industries/hydropower/industry/hydrokinetics.asp>), review the Commission's standard licensing regulations and guidance (<http://www.ferc.gov/industries/hydropower/gen-info/licensing/ilp.asp>), and contact staff (please see the web site).

April 14, 2008

Coordination with Federal, State, and Local Resource Agencies, Indian Tribes, Non-Governmental Organizations, and Members of the Public

What will be the role of the federal, state, and local resource agencies, Indian tribes, non-governmental organizations, and members of the public in these procedures?

The Federal Power Act provides state and federal agencies with substantial authority in the Commission's hydropower licensing process. The pilot project procedures will not alter any of this authority. Commission staff will cooperate closely with stakeholders in developing appropriate safeguards for public and environmental resources when licensing these short-term projects. With an emphasis on these safeguards and post-licensing monitoring, we hope

that all entities can exercise their authorities in a manner that will enable the timely authorization of meritorious pilot projects.

By the regulations, the applicant will be expected to consult with affected federal, state, and local resource agencies, Indian tribes, non-governmental agencies, and members of the public in preparing a draft application. The applicant will initiate the pre-filing stage with the pre-filing materials, including proposed plans for monitoring the project, safeguarding the public and environment resources, and assuring financing to remove the project and restore the site. At this point in pre-filing, stakeholders will have an opportunity to provide comments and recommendations on the proposed plans, overall draft application, and request for waivers. The Commission will schedule a public meeting, if needed, and will consider all written or oral comments in making its determination on whether to accept the waiver request and process plan and schedule. An applicant's final application should incorporate the pre-filing comments. If the final application is filed and accepted, there will be a post-filing opportunity to file interventions, to comment on the application and monitoring and safeguard plan proposals, and to file recommendations and conditions. All stakeholders also will have the opportunity to provide comments on the Environmental Assessment before the Commission takes action on the application. Intervenors will be able to request rehearing of the Commission's decision.

Will the Commission pursue MOUs with state and federal agencies to make the pilot project procedures work as efficiently as possible?

The Commission is exploring MOUs with interested state and federal agencies.

April 14, 2008

Does the Commission encourage settlements in proceedings for licensing hydrokinetic pilot projects?

The Commission looks with great favor on settlements in licensing cases.

When parties are able to reach settlements, it can save time and money, avoid the need for protracted litigation, promote the development of positive relationships among entities who may be working together during the course of a license term, and give the Commission, as it acts on license applications, a clear sense as to the parties' views on the issues presented in each settled case. At the same time, the

Commission cannot automatically accept all settlements, or all provisions of settlements. The Commission accepts settlements, or provisions of settlements, on a case-by-case basis as discussed in its *Policy Statement on Hydropower Licensing Settlements*, issued September 21, 2006.⁵

⁵ 116 FERC ¶ 61,270 (2006).

April 14, 2008

Information Needs

How is the environment to be protected given the limited information available about these technologies?

Though information about the potential environmental effects of large-scale deployments of these devices is limited, we believe there is sufficient information to analyze the resource effects of proposed pilot projects, which the Commission will do before issuing any license for a pilot project. In addition, we believe this class of project may be able to be carried out with little risk to public safety and the environment if the projects are (1) short term; (2) small; (3) can be quickly modified, shut-down, or removed if significant, unforeseen risks to public safety or adverse environmental impacts occur; (4) are not located in areas designated as sensitive by the Commission; and (5) are removed,⁶ with the site restored, before the end of the license term. Under these conditions, the risks to the environment will be minimal, while the rewards from testing the technology and understanding interactions with the environment could be substantial.

What information is needed in the draft and final license application?

All pilot project license applications should describe the (1) existing environment; (2) details of the project proposal; (3) potential effects of the proposal; (4) proposed plans for monitoring, safeguarding the public and environmental resources, and assuring financing to remove the project and restore the site; and (5) consultation record. A complete list of draft and final application components is provided in table A1 of Appendix A.

Regarding description of the existing environment, proposal, and anticipated issues, most of the content requirements are specified in § 5.18 of the Commission's regulations. However, some of the information required by § 5.18 might not be applicable to some proposed hydrokinetic pilot projects and additional information specific to these new technologies will be needed. Although information needs will vary depending upon site location and technology type, staff has identified some expected additional information needs in Appendix B to supplement the information needs already defined in the Commission's regulations for conventional hydropower projects. These additional information needs are specific to marine, tidal, and unimpounded river environments (e.g., geology, wildlife, fisheries resources, aesthetics, electromagnetic fields, socioeconomics, navigational safety, and collision risks.)

⁶ Decommissioning and project removal would be required before the end of the pilot project license unless a standard license was granted (following a full Commission proceeding including National Environmental Policy Act review and participation by all

April 14, 2008

stakeholders).

At both the pre-filing and post-filing stages, participants will be able to comment to the Commission on the proposed plans for post-license monitoring, safeguarding the public and environmental resources, and assuring financing to remove the project and restore the site with the draft application. This opportunity will allow stakeholders to suggest modifications early in the process. The standard articles in Appendix C describe the content staff expects in the proposed plans.

What pre-filing studies will be expected as a routine part of preparing a pilot project license application?

The applicant will need sufficient information to describe site conditions and identify potential project issues. It is hoped that much of this information on site conditions will be available from existing resources. Where it is not available, it will need to be gathered. The pilot project application must identify potential environmental effects and describe the proposed plans to monitor these effects.

Will review of fish, wildlife, and environmental issues be limited to endangered species?

No. Staff intends to analyze potential effects on a wide range of fish, wildlife, and environmental issues as it does with any license application. In addition to endangered species, staff will also look at any impacts to other applicable resources including, but not limited to, water quality, water use, marine mammals, fish, birds, geology, land use, ocean use, navigation, recreation, aesthetics, and cultural resources.

Will the potential impacts of proposed projects on commercial and recreational fisherman be taken into account?

The potential impacts of proposed projects on commercial and recreational fishing will be analyzed in the Commission's Environmental Assessment and considered in the Commission's action on the license application. Staff will work with federal, state, and local resource agencies; Indian tribes; non-governmental organizations; members of the public; and commercial and recreational fishermen to ensure that these issues are understood and addressed.

Monitoring, Performance Standards, and Modification/Shutdown/Removal

April 14, 2008

How will the monitoring, performance standards, and project modification, shutdown, or removal measures be introduced into the application process so that stakeholders can review and provide input on these issues?

In its draft and final license application, the applicant will be expected to provide proposed plans for (1) post-license monitoring; (2) safeguarding the public and environmental resources; and (3) assuring financing to remove the project and

Licensing Hydrokinetic Pilot Projects

April 14, 2008

restore the site. The proposed plans would include descriptions of monitoring measures; performance standards and thresholds for modification, shutdown, or removal; and methods and timing for shutdown, modification, or removal. Stakeholders will then be able to express their views on these proposals during the both the pre-filing and post-filing stages of the licensing process and recommend modifications and additional measures.

Will forms of financial assurance other than an assurance bond be acceptable as guarantee of the financial resources to remove projects and restore the site?

The Commission will consider a variety of financial assurance instruments to cover the cost of project removal and site restoration, including, but not limited to bonds, letters of credit, and escrow accounts.

Preliminary Permit/Pilot Project License/Commercial Build-out

What is the difference between a preliminary permit and a license?

A license authorizes construction, operation, and maintenance of a hydropower project under the Commission's jurisdiction. A permit maintains priority of application for a license at a site for up to three years while the permit holder studies project feasibility and prepares an application for license. A preliminary permit does not authorize project construction or operation, nor does it provide special access to the site, but it does prevent another party from acquiring a license (or permit) for the same site during the term of the permit.

Commission staff strongly encourages potential applicants for hydropower projects to obtain a preliminary permit before applying for a license.

What are the rules of competition between preliminary permits, pilot project licenses, and standard (30- to 50-year) licenses?

The rules of competition will not change. They are:

1. If two or more applicants seek a preliminary permit for the same site, the Commission grants the permit to the applicant whose project proposal best meets the comprehensive development standard. If two project proposals are essentially equal, the Commission gives preference to the state or municipal applicant, or, if neither is a state or municipal applicant, the applicant with the earliest filing date.
2. If two or more applicants seek an original license for the same site, the Commission grants the license to the project that best meets the

April 14, 2008

comprehensive development standard. If two project proposals are essentially equal, the Federal Power Act imposes the following tie-breakers: (a) the applicant who is also a permittee for the site will prevail over all other applicants (including municipalities); (b) a state or municipal applicant will prevail over a non-municipal applicant; and (c) if there is neither a permittee nor a municipality competing, the Commission has adopted a first-to-file tie-breaker. In the case of competing relicense applications, when both are virtually the same, the incumbent licensee will be awarded the new license.

3. When a permit applicant and a license applicant seek a respective permit and license for the same site, the Commission grants the permit or license to the project that best meets the comprehensive development standard. If both proposals are essentially equal, the Commission gives preference to the license applicant.

Can a developer protect a larger build-out area, while operating under a license for a hydrokinetic pilot project?

The standard tool for attempting to preserve priority of license application for a potential build-out area is a preliminary permit. The possession of a license for a pilot project would not fundamentally change the rules for preliminary permits, including the rules of competition as outlined above.

What happens when a developer has an established preliminary permit for a proposed build-out project and later succeeds in obtaining a license for a pilot project that falls within the build-out permit boundary?

The permit would remain in place for its term with the licensed area removed from the permit area (and covered by the terms of the license).

What options are available to developers for transitions from pilot project licenses to build-out licenses?

Developers hoping to move to a commercial scale, or build-out project if the pilot project is successful should discuss the possibility as early as possible with Commission staff. We anticipate that this transition will be handled as a relicensing of the pilot project and will entail a standard licensing process including a National Environmental Policy Act review and full opportunity for participation by all stakeholders. The applicant will need to file a Notice of Intent (NOI) and pre-application document (PAD), which will include a process plan and schedule for licensing the commercial build-out. By statute, when relicensing a hydropower project, a NOI is required five years before the license expires. A licensee can request a waiver of this requirement only if the proposed project is less than 1.5 MW. In some cases, where

Licensing Hydrokinetic Pilot Projects

April 14, 2008

the NOI is filed and progress is being made toward the build-out relicensing application, the license for the pilot project may be extended by one or more years while the applicant completes the relicensing process.

Will the Commission consider any other options for the transition from a pilot project to a build-out project?

As stated earlier, this is a guidance document. It does not restrict the ability of project advocates to propose other strategies for adoption by the Commission. Such proposals should be well developed and justified. Some examples could include (1) requesting a license for a period longer than five years to accommodate a specific relicensing timeline, (2) requesting a boundary around the pilot project big enough to accommodate a future build-out plan, and (3) requesting a phased license. Those considering such a proposal should discuss the idea with staff as early in the process as possible. As in any licensing proceeding, environmental analysis and multiple stakeholder comment opportunities will be completed before any such proposal is brought before the Commissioners.

Next Steps

What are the Commission's plans for next steps in regulating these new technologies?

The Commission's licensing program is the result of decades of refinement through practice, precedent, incorporation of public comment, coordination with partner agencies and Indian tribes, and formal rulemakings. The field of hydrokinetic energy, while promising, is rapidly changing, untested, and uncertain. Under these circumstances, staff finds application of the Commission's proven regulatory system, incorporating appropriate adaptations informed by extensive stakeholder comment, to be efficient and prudent. Staff's primary purpose in providing guidance on procedures for expediting the ILP for specific hydrokinetic pilot projects is to encourage testing and reduce the uncertainties surrounding the technology. This guidance also will ensure appropriate review and environmental analysis; maintenance of public safety and environmental resource protections; and cooperation with federal, state, and local resource agencies, Indian tribes, non-governmental organizations, and members of the public under the ILP. Staff will consider additional steps as the technology, industry, and the knowledge base develop.

II. CRITERIA FOR PILOT PROJECT LICENSING PROCEDURES

In general, these criteria will be used, in conjunction with the draft application and stakeholder comments to determine whether there is good cause for granting the regulatory waivers and modifications needed to follow the expedited review proposed in the potential applicant's process plan. The criteria should be addressed in any request to use the procedures.

Pilot projects will be small. Though evaluated on a case-by-case basis, staff expects that pilot projects will be less than 5MW and often will be substantially smaller. In addition to generating capacity, staff also will consider carefully the number of generating units and the project footprint in determining whether the proposal qualifies as a pilot project.

The license will be short term. Though evaluated on a case-by-case basis, staff expects that pilot projects will have terms of five years.

Pilot projects will avoid sensitive locations. The applicant must describe potential areas of sensitivity in the proposed project area and indicate the reasons for the sensitivity. All stakeholders will have an opportunity both to comment on the applicant's description and to recommend that other areas be designated as sensitive. Commission staff will determine whether a potential use conflict makes the proposal inappropriate for an expedited review process. In many such cases, it will be possible for the applicant to pursue the project through a standard licensing process.

Pilot projects will be subject to strict safeguards for the public and environmental resources potentially leading to project modification, shutdown, or complete removal. Unacceptable risks to the public or the environment during the license period, as observed through monitoring protocols required by the license (or as otherwise becomes evident), will lead to project alteration, shut-down, or removal followed by site restoration.

Pilot projects will be required to complete project removal and site restoration before the end of the license unless the licensee obtains a new license covering the pilot project site. Licenses for pilot projects will require that the project be removed and the site restored as directed by the Commission. If a pilot project licensee opts to apply for a standard license at the end of the pilot project license term, authorization of the build-out project will be evaluated in a full Commission proceeding with National Environmental Policy Act

Licensing Hydrokinetic Pilot Projects

April 14, 2008

(NEPA) review and participation by all interested stakeholders. If build-out is licensed, there may be no need to remove the pilot devices.

April 14, 2008

Pilot project draft applications must be submitted in a form sufficient to support environmental analysis. The draft application must include a thorough description of the existing environment, incorporating a review of existing information and a description of the environmental baseline. The baseline should provide a characterization of site specifics (including items such as substrate type, a description of physical habitat, and wave patterns or flow velocity conditions, etc.). The effort may require basic pre-application surveys, measurements, or observations. The draft application should also include details of the project proposal, possible sensitive areas, potential user conflicts, and potential effects of the proposal. The information in the draft application should be sufficient to support the environmental analysis. The draft application also should include proposed plans for: (1) post-license monitoring to confirm or dismiss concerns regarding the potential effects of the project; (2) safeguarding the public and environmental resources, including performance measures, methods for modification, shutdown, or project removal should potential for an environmental harm be detected; and (3) assuring financing to remove the project and restore the site. Finally, it should include a consultation record indicating adequate consultation to date and distribution of the pre-filing materials to all potentially interested federal, state, and local resource agencies, Indian tribes, non-governmental organizations, and members of the public.

Appendix A. Hydrokinetic Pilot Project License Procedures

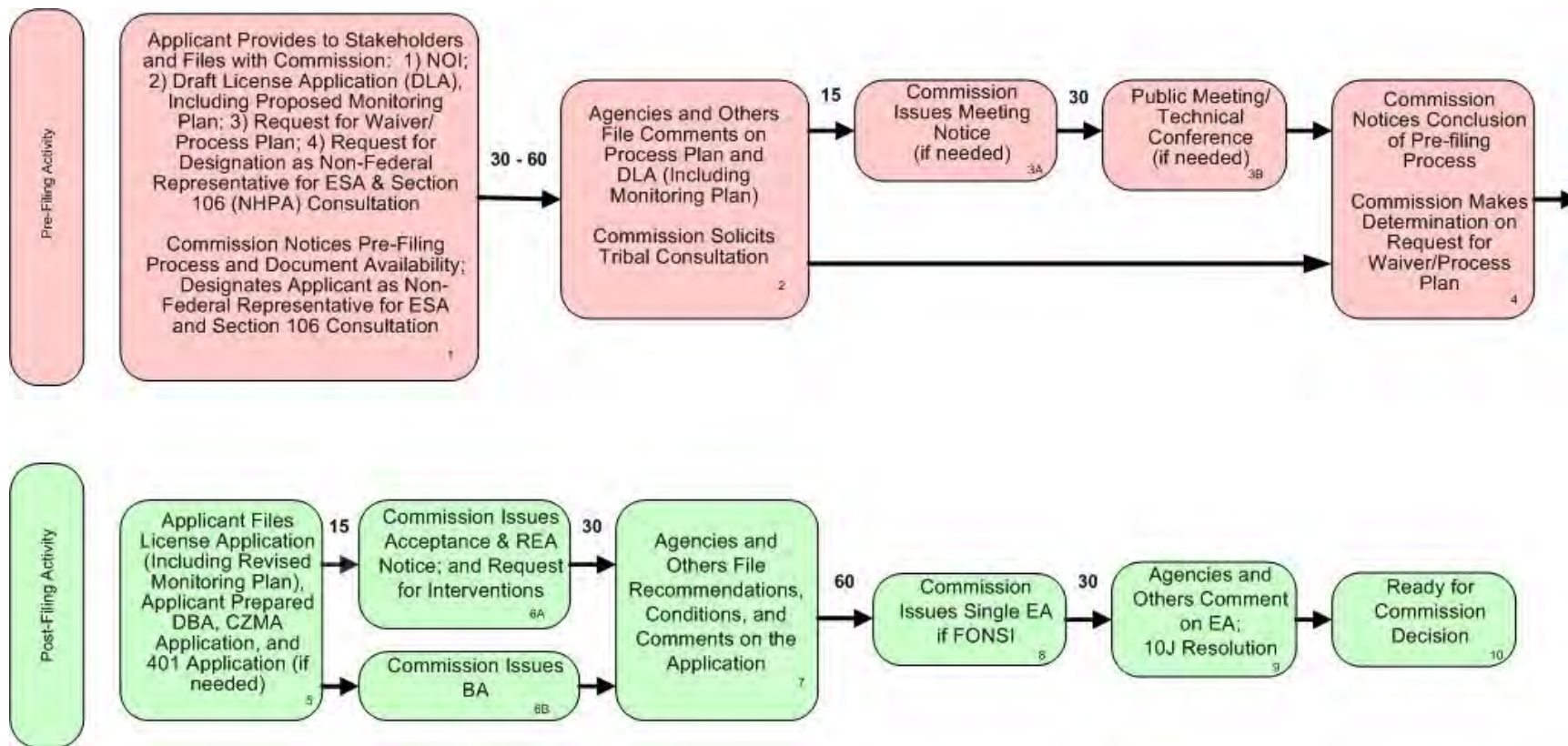


Figure 1A. Schematic of Pilot Project Licensing Procedures – revised 2/18/10

April 14, 2008

Box 1- Applicant's Pre-filing Materials and Commission Response

(Also see Table A1 below)

1) Applicant Files Notification of Intent

A potential applicant for an original license for a hydrokinetic pilot project will file a notification of its intent (NOI) to do so. The NOI will describe the principal project works to be licensed, including technology type and any transmission lines as described in § 5.5 of the Commission's regulations.

2) Applicant Files a Draft License Application

Simultaneously with the filing of its waiver request, and process plan, and notification of intent, and before filing an application (Box 5) for an original license for the hydrokinetic pilot project procedures, a potential applicant must file with the Commission and distribute to the stakeholders, a draft license application. All pilot project license applications (and draft applications) would describe the

(1) existing environment; (2) details of the project proposal; (3) potential effects of the proposal; (4) proposed plans for (a) monitoring, (b) safeguarding the public and environmental resources, and (c) assuring financing to remove the project and restore the site; and (5) the consultation record. A complete list of draft and final application components is provided in table A1 below.

The description of the existing environment must incorporate a review of existing information and a description of the environmental baseline. The baseline should provide an adequate characterization of site specifics (including items such as substrate type, a description of physical habitat, and wave patterns or flow velocity conditions, etc.) sufficient to support the environmental analysis. The effort may require basic pre-application surveys, measurements, or observations. The applicant should identify possible sensitive areas and potential user conflicts.

Contents of the proposed post-license monitoring plan should comply with the language of § 5.11 of the Commission's regulations (regarding proposed study plans). It should be complementary with the proposed plan for safeguarding public safety and environmental resources (safeguard plan). The monitoring and safeguard plans should include strategies to detect potential public safety risks and environmental effects of the project. They should measure the project against performance standards, including proposed thresholds at which the observed risk to public safety or environmental harm would trigger project modification, shutdown, or removal. A proposed plan for assuring financing to remove the project and restore the site and site restoration should be included as well. These proposed

plans should be informed by consultation with the stakeholders. Additional guidance regarding the content of the proposed plans is available in the standard articles in Appendix C below.

Table A1. Pre-Filing Materials (Box 1)

<i>Materials</i>	<i>More Information</i>
1) Notice of Intent	Appendix A. PROCEDURES
2) Draft Application	Appendix A. PROCEDURES
a. Existing Environment	Appendix B. APPLICATION CONTENTS
b. Project Proposal	
c. Potential Effects Associated with the Proposal	
d. Proposed Plans for:	
i. Post-License Monitoring of General Environmental Effects, Project Facility, and Operations	Appendix C. STANDARD LICENSE ARTICLES
1. Fish and Wildlife	
2. Project Facility and Operations	
ii. Safeguarding the Public and Environmental Resources / Project Removal	
1. Project Safety	
2. Project Removal	
3. Navigation Safety	
4. Emergency Shutdown/Removal	
iii. Financial Assurance	
e. Communication Record	
i. Record of Document Distribution	
ii. Consultation Record	
iii. Distribution List	Section III. CRITERIA & Appendix A. PROCEDURES
3) Letter of Request for Waivers and Modifications of the ILP Necessary for Expedited Processing of a Hydrokinetic Pilot Project License Application	
a. Proposed Process Plan and Schedule	
b. Justification Statement	Appendix A. PROCEDURES
4) Request Designations as Non-Federal Representative	
i. Endangered Species Act (ESA)	
ii. Section 106 National Historic Preservation Act (NHPA) Consultation	

Finally, the draft application should include a communication record comprising (1) a record documenting distribution of the pre-filing materials to the appropriate stakeholders (see 5 below); (2) a record of consultation prior to the submission of the pre-filing materials; and (3) a stakeholder distribution list.

3) Applicant Requests for Waivers Necessary for Expedited Processing of a Hydrokinetic Pilot Project License Application

An applicant seeking a hydrokinetic pilot project licensing process must request the necessary waivers and modifications to do so. The waiver request must include a proposed process plan and schedule and a justification statement. The process plan must propose a project-specific schedule for expedited review. The justification statement must demonstrate that the project meets the *Criteria for Using the Pilot Licensing Procedures*, listed in Section III above. These criteria specify that the proposed project must be: (1) small; (2) short term; (3) not located in sensitive areas; (4) removable and able to be shut down on short notice; (5) removed, with the site restored, before the end of the license term (unless a new license is granted); and (6) initiated with a draft application that is adequate as filed to support environmental analysis.

4) Applicant Requests Designation as Non-Federal Representative

With its notification of intent and draft application, a potential applicant should also request to be designated as the Commission's non-federal representative for purposes of consultation under Section 7 of the Endangered Species Act. The potential license applicant would at the same time request authorization to initiate consultation under Section 106 of the National Historic Preservation Act.

5) Applicant Distributes, Notices, and Files Pre-Application Packet

The potential applicant must provide a copy of NOI, draft license application, and the waiver request and process plan to the federal, state, and local resource agencies, non-governmental organizations, and members of the public potentially interested in the project. The potential applicant also must publish notice of the filing of its NOI, draft application, and request for waiver and process plan, no later than the filing date of the pre-filing materials with the Commission, in a daily or weekly newspaper in each county in which, or off of whose shore, the project would be located. The notice shall disclose the date of the filing of the materials with the Commission and state that comments can be filed with the Commission for up to 30-60⁷ days following the pre-filing materials filing date.

⁷ The length of the comment period was revised from 30 days to 30-60 days (February 4, 2009).

6) *Commission Notices Pre-Filing Process*

The Commission, as soon as possible, but no more than 15 days following the filing of the pre-application materials, will notice, through esubscription and in the Federal Register, the pre-filing process, docket number, and a tentative pre-filing schedule. Comments will be due 30-60 days⁸ from the applicant's filing date.

If appropriate, the Commission will designate the potential license applicant as the non-federal representative for the purpose of informal consultation under section 7 of the Endangered Species Act and for consultation under section 106 of the National Historic Preservation Act.⁹

Note that the Commission may reject the NOI, draft application, and request for waiver/process plan for an original hydrokinetic pilot project license based upon its review of the projects overall characteristics relative to the pilot project criteria, the draft application contents, or any comments filed.

Box 2 – Comments on Process Plan and Draft Application

Within 30-60 days of the date of the potential applicant's filing of its pre-filing materials, any comments on these items shall be filed with the Commission.

Tribal Consultation

Within 30 days of the filing the NOI, the Commission will solicit tribal consultation with each Indian tribe likely to be affected by the potential license application, and, if requested, Commission staff will meet with the Indian tribe on a mutually agreeable date.

Boxes 3a and 3b – Public Meeting/Technical Conference

If appropriate, within 15 days of the close of the initial comment period (Box 2), staff will provide notice of a public meeting to discuss the proposal (Box 3a). The purposes of the meeting will be defined case-by-case, but may include discussions of the project proposal, project issues, and information and monitoring needs. The meeting will include the appropriate federal, state, and local resource agencies, Indian tribes, non-governmental organizations, and members of the

⁸ The length of the comment period was revised from 30 days to 30-60 days (February 4, 2009).

⁹ The timing of Commission designation was relocated from Box 2 to Box 1 (February 4, 2009).

public potentially interested in the proposed project. The meeting (Box 3b) will be scheduled to occur within 30 days of the meeting notice.

Box 4 – Concluding the Pre-filing Process and Commission Determination on Waiver Request and Process Plan

Commission Concludes the Pre-Filing Process and Makes Determinations on the Waiver Request and Process Plan/Schedule

If a meeting is held, the Commission will issue its determination on the potential applicant's waiver request and proposed process plan within 15 days of the meeting. If a meeting is not held, the Commission will issue its determination on the proposed process plan within 30 days of the close of the initial comment period (Box 2). If the Director finds good cause for use of the pilot project licensing procedures (expediting the ILP) and accepts the potential applicant's proposed process plan (with or without modification) and draft application, staff

will indicate the decision by issuing a notice concluding the pre-filing process and approving the process plan and schedule with any modifications made by staff. If the Director does not find good cause for expediting the ILP, staff will notify the applicant of the Director's determination.

Box 5 - Filing of Application

Once pre-filing is completed, the potential applicant may file an application for an original license. Like the draft application, the application should describe the (1) existing environment; (2) details of the project proposal; (3) potential effects of the proposal; (4) proposed plans for monitoring, safeguarding the public and environmental resources, and assuring financing to remove the project and restore the site; and (5) a consultation record. The license application should incorporate comments received on the draft application. It must be sufficient to support staff's environmental analysis.

The application must include documentation of application submittals for concurrent regulatory processes such as the Coastal Zone Management Act and Clean Water Act (if needed). The required application content relevant to these and other applicable laws can be found in Appendix B of this guidance and § 5.18(b)(3) of the regulations.

To facilitate any necessary consultations pursuant to the ESA, if necessary, the applicant must file an applicant-prepared draft biological assessment (DBA) with the application.

Revised Post-License Monitoring Plan

The license application shall include a post-license monitoring plan. Contents of the post-license monitoring plan should comply with § 5.13 of the Commission's regulations (for study plans) and, in combination with the safeguard plan, should include strategies to detect potential environmental effects of the project and proposed thresholds at which the observed environmental harm would trigger project modification, shutdown, or removal. The applicant is expected to address stakeholder comments and post-license monitoring requests provided via written comments and during any public meeting or technical conference to revise the proposed post-license monitoring plan.

Box 6A - Notice of acceptance and ready for environmental analysis (REA Notice) or rejection

Within 15 days of the filing of a complete license application pursuant to Box 5 above, the Commission will publicly notice the acceptance of the application and that the proposed project is ready for environmental analysis. The notice will request interventions as well as comments, recommendations, and conditions on the project proposal.

Alternatively, if in the Director's judgment the application does not meet the filing requirements of Box 5 or Appendix B, the application will be considered deficient. At the discretion of the Director, a deficient application may be rejected or the applicant may be afforded additional time to correct the deficiencies.

Box 6B – Issuance of Biological Assessment

If necessary and appropriate, within 15 days of the filing of a complete license application pursuant to Box 5 above, Commission staff will issue a biological assessment (BA) initiating formal consultation under the Endangered

Species Act provided that the staff finds the draft applicant's BA to be adequate to initiate formal consultation. Alternatively, the Commission staff will use its NEPA document as the BA as described in Box 8 below.

Box 7 - Response to Notice of Acceptance and REA

Comments, protests, interventions, recommendations, final terms and conditions as well as final post-license monitoring requests must be filed no later than 30 days after the notice of acceptance and ready for environmental analysis.

Box 8 - Issuance of a Single Environmental Assessment

The Commission will issue a single environmental assessment (EA) no later than 60 days from the date responses are due in response to the notice of acceptance and the REA Notice in Box 6A above. If the EA results in a "Finding of No Significant Impact" (FONSI) pursuant to the National Environmental Policy

Act, the Commission will issue the EA for public comment. Each EA issued with a FONSI will include draft license articles, any needed preliminary determination of inconsistency between a fish and wildlife agency recommendation and the Federal Power Act (or other applicable law) pursuant to section 10(j) of Federal Power Act, and any mandatory terms and conditions.

If necessary and appropriate, the EA will also serve as the Commission's biological assessment for the purpose of section 7 consultation under the Endangered Species Act.

If the EA results in a "Finding of Significant Impact" under the National Environmental Policy Act, the Commission will dismiss the application. The applicant would then have the option to request a standard license application review process without the waivers and modifications available for pilot projects.

Box 9 – Comments on Single Environmental Assessment and Section 10(j) Process

Comments on Single Environmental Assessment

Comments on the EA issued, including comments in response to the Commission's preliminary determination of inconsistency pursuant to section 10(j) and attached mandatory terms and conditions, should be filed no later than

30 days after issuance of the EA, as specified in the notice accompanying the single environmental assessment.

Section 10(j) process.

Under section 10(j) of the Federal Power Act, a hydropower license issued by the Commission will include conditions for the protection, mitigation, and enhancement of fish and wildlife, including their spawning grounds and habitat. The conditions are based on recommendations filed with Commission by state and federal fish and wildlife agencies and are to be adopted unless they are found to be inconsistent with the Federal Power Act or other applicable law. (The 10(j) process is described in § 5.26 of the Commission's regulations.)

Box 10- Ready for Commission Decision

Based on the record, the Commission will act on the application

APPENDIX B. APPLICATION CONTENTS

While § 5.18 of the Commission's regulations applies in its entirety, staff has identified additional information that is specific to hydrokinetic pilot projects, particularly those proposed for the marine environment. Also, staff recognizes that some of the information required by § 5.18 may not be applicable to some proposed hydrokinetic pilot projects. Applicants should explain why any required information is not pertinent to their project. The additional provisions are as follows:

General description of water source

- § 5.18(b)(1) – Description of the body of water in which the proposed project will be located, including the specific location of the proposed project. Information on seasonal weather patterns, wave height, current speed, prevailing wave and current direction, proximity to shipping lanes, and visibility of the project works from the shoreline.

Cumulative effects

- § 5.18(b)(2) – The list of cumulatively affected resources will be based on consultation and available data.

Applicable laws

- § 5.18(b)(3) – Include a discussion of the status of compliance with or consultation under, if applicable, the Marine Mammal Protection Act.

Project location, facilities, and operation

- § 5.18(b)(4)(ii) – The description should include a device schematic and operation diagram, including the physical composition, dimensions, and general configuration of any anchoring, mooring, transmission lines, or other structures proposed to be included as part of the project or connected directly to it.
- § 5.18(b)(4)(iii) – The description should include water surface area in the project boundary, and, for tidal projects, changes in water surface levels between low and high tides using official tidal datum National Geodetic Vertical Datum, Mean High Water, Mean Higher High Water, Mean Low Water, and Mean Lower Low Water).

Proposed action and action alternatives

*Affected Environment*¹⁰

Geology and Soils

- § 5.6(d)(3)(ii) – Text descriptions and maps describing the seabed/riverbed substrates and the geomorphology of the site for the proposed project and surrounding area including the shoreline and associated beaches where applicable.
- § 5.6(d)(3)(ii)(B) – Description of the seabed or river substrate, including the types, occurrence, physical and chemical characteristics, erodability and potential for mass sediment movement, and likely sediment pathways and areas of erosion and accretion including shoreline areas and beaches. A description of any potential geologic hazards related to the project, including scouring action, slope failure, faulting, tsunamis, fluid and gas expulsion, and irregular topography.

Water Resources

- § 5.6(d)(3)(iii)(B) – The water velocities (feet per second) at the project site that correspond to the minimum, mean, and maximum recorded flows of the stream or other body of water, if applicable. Information on monthly minimum, mean, and maximum recorded temporal current speeds, wave intensities, and wave amplitudes at the proposed project.
- § 5.6(d)(3)(iii)(C) – A monthly water velocity duration curve based on available flow data and the correlation of flow (cubic feet per second) to velocity (feet per second) at the project site. Information on data collection locations and methods and all data used to determine the project's dependable capacity such as temporal wave patterns.
- § 5.6(d)(3)(iii)(G) – Information on vertical profiles of relevant water quality parameters (e.g., temperature, dissolved oxygen, etc.) throughout the water column in the project area.

Fish and Aquatic Resources

- § 5.6(d)(3)(iv) – Description of existing underwater acoustic environments, including estimated decibel levels. Identification of sensitive species located in the project vicinity.

¹⁰ § 5.18(b)(5)(ii)(A) references § 5.6(d)(3) regarding the requirements for the description of the affected environment.

- § 5.6(d)(3)(iv)(C) – Description of any important spawning or feeding grounds or refugia in the project area, including the availability and significance of such habitats.

Wildlife and Botanical Resources

- § 5.6(d)(3)(v) – Temporal and spatial distribution of marine mammal communities and availability and quality of feeding, breeding, rearing, and resting habitats. Description of existing below- and above-water acoustic environment, including estimated decibel levels.
- § 5.6(d)(3)(v)(B). Temporal and spatial distribution and seasonal migration patterns of sea bird communities and availability and quality of feeding, breeding, rearing, and resting habitats.

Recreation, Land Use, and Ocean Use

- § 5.6(d)(3)(viii) – Description of commercial and recreational fishing grounds in the project vicinity. Information on fishing seasons and gear types, and access routes used.
- § 5.6(d)(3)(viii)(A) – Description of existing uses, particularly as related to public and facility safety, including illustration by maps, drawings of existing recreation and other uses.
- § 5.6(d)(3)(viii)(F)(1) – Proximity of the project to marine sanctuaries and government-protected coastal/marine areas.
- § 5.6(d)(3)(viii)(I) and (J) – Description of recreational and non- recreational use and management within, and adjacent to, the project boundary, including shipping channels, navigational channels, marine sanctuaries, state aquatic lands, and Military Use Areas.

Aesthetic Resources

- § 5.6(d)(3)(ix) – Description of aesthetic (including acoustic) characteristics of both land and water surface components of the project area.

Environmental Analysis

- § 5.18(b)(5)(ii)(B) – This section must also include, if applicable, a description of any anticipated environmental effects of the proposed construction, installation, operation, and removal of the project. This description should be specific to the various resources described in the affected environment section, and should include: (1) any physical disturbance (vessel collision or other project-related risks for fish, marine mammals, seabirds, and other wildlife as applicable); (2) species-specific habitat creation or displacement; (3) increased vessel traffic; (4) exclusion or disturbance of recreational, commercial, industrial, or other uses of the waterway; and changes in navigational safety; (5) any above or below- water noise disturbance, including estimated decibel levels during project construction, installation, operation, and removal; (6) any electromagnetic field disturbance; (7) any changes in river or tidal flow, wave regime, or coastal or other geomorphic processes; (8) any accidental contamination from device failures, vessel collisions, and storm damage; (9) chemical toxicity of any component of, or biofouling coating on, the project devices or transmission line; and (9) any socioeconomic affects on the commercial fishing industry from potential loss of harvest or affect on access routes to fishing grounds.
- § 5.18(b)(5)(ii)(C) – The following proposed plans for the project should be included in this section: (1) a proposed project monitoring plan; (2) a plan for safeguarding the public and environmental resources (safeguard plan); and (3) a plan for assuring financing to remove the project and restore the site. The safeguard plan should include but not be limited to: (a) methods for marking project devices; (b) maps and drawings of competing uses including existing recreation; (c) methods for recovering equipment that may break loose from any anchoring devices; (d) a proposed removal and site restoration plan; and (e) a navigational safety plan developed in consultation with the U.S. Coast Guard, referencing both recreational and non-recreational use and management within, and adjacent to, the project boundary.

APPENDIX C. STANDARD HYDROKINETIC PILOT PROJECT LICENSE ARTICLES¹¹

1. General Environmental Effects and Project Facility and Operations Monitoring (Monitoring Plan)

Box 1 of these procedures includes, among other things, a requirement that the license applicant file with its NOI and Draft License Application, a Proposed Post-License Monitoring Plan that includes provisions for conducting post-license monitoring of any anticipated effects on environmental resources in the project area.

We anticipate that the Proposed Post-License Monitoring Plan would, after Commission review and modification as necessary, be approved by the Commission through an ordering paragraph within the license. Any monitoring studies not included in the Proposed Post-License Monitoring Plan but determined by the Commission to be necessary for the protection of environmental resources, would be incorporated into the license as a standard license article. Below are examples of such articles.

(a) Monitoring of Fish and Wildlife at the Project. The licensee shall, at least 90 days before starting on-site project construction or installation, file for Commission approval, a [*e.g., Marine Mammal, Seabird, or Other Listed or Sensitive Species*] Monitoring Plan to monitor [*e.g., Marine Mammal, Seabird, or Other Listed or Sensitive Species*] behavior and interaction with the in-water project facilities, including [*e.g., associated mooring and anchoring systems*] throughout the pilot license term.

The plan, at a minimum, shall include the following: (a) a detailed description of the methods and equipment that would be used for monitoring [*e.g.,*

¹¹ The following are proposed standard articles that could be included in pilot project licenses, as appropriate. Articles for addressing certain other in-water or land-based project effects on such resources as aesthetics, recreation, and erosion are not included below, because they would be technology-specific, and therefore, too variable to include as general boilerplate articles for a hydrokinetic pilot license. Generally, engineering, public safety, and administrative articles are not included, as some of these requirements may vary with technology and project location. L-Form articles are likewise not included below, because they would depend on the location of the project (*e.g., on navigable versus non-navigable waters, in-river versus the marine environment, etc.*).

Marine Mammal, Seabird, Other Listed or Sensitive Species] behavior and activity in the vicinity of the in-water facilities; (b) a detailed description of how the monitoring data will be analyzed, with specific criteria by which to evaluate adverse effects; (c) a detailed implementation schedule, including the frequency and timing of data recovery and maintenance of the monitoring equipment; and

(d) provisions for identifying, in consultation with the *[Land Management Agency]*, *[Affected Indian Tribes]*, *[Fish and wildlife agency of the state in which the project is located]*, *[state certifying agency]*, *[National Marine Fisheries Service]*, and *[U.S. Fish and Wildlife Service]*, remedial measures if monitoring identifies any adverse changes in behavior or use of ocean habitats.

An annual report shall be filed with the Commission by December 31 of each year and a copy provided to the aforementioned agencies and tribe(s) describing the monitoring results and any recommendations for modifying the project facilities or commencing the approved project removal plan if necessary to minimize adverse effects on environmental resources in the project area. Along with the annual report, the licensee shall include comments from the agencies and tribe(s) and the licensee's responses to any comments.

The licensee shall prepare the monitoring plan after consultation with the aforementioned agencies and tribe(s). The licensee shall include with the plan documentation of consultation, copies of recommendations on the completed plan after it has been prepared and provided to the agencies and tribe(s), and specific descriptions of how the agencies' and tribe's comments are accommodated by the plan. The licensee shall allow a minimum of 30 days for the agencies and the tribe(s) to comment and make recommendations before filing the plan with the Commission. If the licensee does not adopt a recommendation, the filing shall include the licensee's reasons, based on project-specific information.

The Commission reserves the right to require changes to the plan. On-site project construction or installation shall not begin until the licensee is notified by the Commission that the plan is approved. Upon Commission approval, the licensee shall implement the plan, including any changes required by the Commission.

(b) *General Project Facility and Operations Monitoring.* The licensee shall, at least 90 days before starting project construction and installation, file for Commission approval, an *[e.g., Noise, Electromagnetic Field, Sea Lion Exclusion Device, etc.]* Assessment Plan to determine if *[e.g., the project emits noise or electromagnetic fields at levels that would cause harm to marine mammals, seabirds, or fish; the sea lion exclusion device prevents haul-out onto above-water project facilities; etc.]*.

The plan shall include: (a) a detailed description of the methods and equipment that would be used to test and monitor [*e.g., ambient noise levels, project electromagnetic fields, project noise, the effectiveness of exclusion or deterrent devices, etc.*]; (b) a schedule for monitoring that considers [*ocean state conditions, seasonality of species presence/absence, etc.*]; and (c) provisions for filing a report of the results, comments from the consulted agencies and tribe(s), and the licensee's responses to any comments with the Commission and providing copies to the consulted agencies and tribe(s).

The licensee shall prepare the plan after consultation with the [*Land Management Agency*], [*Affected Indian Tribes*], [*Fish and wildlife agency of the state in which the project is located*], [*State certifying agency*], [*National Marine Fisheries Service*], and [*U.S. Fish and Wildlife Service*]. The licensee shall include with the plan documentation of consultation, copies of recommendations on the completed plan after it has been prepared and provided to the agencies and tribe(s), and specific descriptions of how the agencies' and tribe's comments are accommodated by the plan. The licensee shall allow a minimum of 30 days for the agencies and the tribe(s) to comment and make recommendations before filing the plan with the Commission. If the licensee does not adopt a recommendation, the filing shall include the licensee's reasons, based on project-specific information.

The Commission reserves the right to require changes to the plan. Project construction or installation shall not begin until the licensee is notified by the Commission that the plan is approved. Upon Commission approval, the licensee shall implement the plan, including any changes required by the Commission.

2. Safeguarding the Public and Environmental Resources / Project Removal (Safeguard Plan[s])

As part of its license application, the prospective licensee for a pilot hydrokinetic project is expected to include a Proposed Project and Public Safety Plan, Proposed Project Removal and Site Restoration Plan, Proposed Navigation Safety Plan, and Emergency Shutdown Plan (see Appendix B referring to 18 § 5.18(b)(5)(ii)(C)). If the prospective licensee determines that any of these plans are unnecessary, then it is expected to explain why in the application.

We anticipate that the plans would, after Commission review and modification as necessary, be approved by the Commission through ordering paragraphs within the license. However, should the prospective licensee decide that any of the plans are unnecessary and the Commission disagrees, then the

Commission may include standard license articles requiring the development and implementation of the plans. Below are examples of such articles.

(a) *Project Safety Plan.* At least 90 days before starting project operations, the licensee shall submit one copy of a Project Safety Plan to the Division of Dam Safety and Inspections (D2SI) – [*Portland, New York, Atlanta, etc.*] Regional Engineer, and two copies to the Commission (one of these shall be a courtesy copy to the Director, D2SI). The plan shall describe the procedures the licensee will take during any project emergency that could adversely impact life or property. Possible emergencies could include, for example, [*a vessel and project facility collision, a wave buoy break-away, release of the project’s submarine transmission cable anchoring system from the seabed, damage to project’s submarine transmission cable, etc.*].

The plan, at a minimum, shall include: (a) procedures to ensure the safety of the public near the project area; (b) description of how the project will be monitored to determine if there is an emergency; (c) procedures the licensee will take during an emergency (including immediate shutdown, if necessary); (d) procedures for reporting the emergency to local, state, and federal agencies; (e) description of contingency measures to modify operations or to implement the project removal plan; (f) a plan for annual testing of emergency equipment, including the project’s emergency shutdown system; and (g) a plan for annually coordinating with response agencies.

The licensee shall prepare the plan after consultation with the U.S. Coast Guard, [*Land Management Agency(ies)*], [*Affected Indian Tribe(s)*], [*Fish and wildlife agency of the state in which the project is located*], and [*Any other pertinent emergency response agency or interested party*]. The licensee shall include with the plan documentation of consultation, copies of comments, and recommendations on the completed plan after it has been prepared and provided to the agencies and tribe(s), and specific descriptions of how the agencies’ and tribes’ comments are accommodated by the plan. The licensee shall allow a minimum of 30 days for the agencies and the tribe(s) to comment and to make recommendations before filing the plan with the Commission. If the licensee does not adopt a recommendation, the filing shall include the licensee’s reasons, based on project-specific information. The licensee may not begin project operations until the D2SI - [*Portland, New York, Atlanta, etc.*] Regional Engineer has reviewed and commented on the plan.

(b) *Project Removal Plan.* The licensee shall, at least 120 days before starting on-site project construction or installation, file for Commission approval, a Project Removal Plan that includes, at a minimum: (a) a provision to remove all

project facilities from all project lands and waters; (b) detailed, site-specific revegetation measures for the disturbed land areas associated with removal of the land-based project facilities; (c) a provision to minimize seabed disturbances and suspended sediments during removal of any underwater facilities; (d) a provision to monitor the effects of the removal activities on *[federally listed threatened and endangered species]*; and (e) an implementation schedule that provides for all removal and restoration activities to be completed by no later than the expiration date of the license.

The licensee shall prepare the plan after consultation with the *[Land Management Agency(ies)]*, *[Affected Indian Tribe(s)]*, *[Applicable federal and state fish and wildlife management agencies]*, *[State certifying agency]*, *[National Marine Fisheries Service]*, *[U.S. Fish and Wildlife Service]*, and *[Any other interested parties]*. The licensee shall include with the plan documentation of consultation, copies of comments and recommendations on the completed plan after it has been prepared and provided to the consulted entities, and specific descriptions of how the entities' comments are accommodated by the plan. The licensee shall allow a minimum of 30 days for the consulted entities to comment and to make recommendations before filing the plan with the Commission. If the licensee does not adopt a recommendation, the filing shall include the licensee's reasons, based on project-specific information.

The Commission reserves the right to require changes to the plan. On-site project construction or installation shall not begin until the licensee is notified by the Commission that the plan is approved.

(c) *Navigation Safety Plan.* The licensee shall, at least 90 days before starting project construction or installation, file for Commission approval, a Navigation Safety Plan for purposes of protecting the public and project facilities from such events as collisions between commercial and recreational vessels and in-water project facilities; entanglement of fishing gear, anchors, dredging equipment, or other underwater devices that may damage or become entangled with project transmission, anchoring, and mooring lines; and electrocution.

The plan, at a minimum, must consider the need for: (a) a navigation or underwater activity exclusion zone boundary around the project's *[generation equipment, submarine transmission line, anchoring system, etc.]*; (b) marking the extreme corners of any exclusion zone with lights, buoys, or other indicators sufficient to warn vessels of the above and underwater project facilities and associated exclusion zone during both the day and nighttime; and (c) marking *[above-water generation equipment]* with *[fog signals, low-intensity navigation or hazard marking lights, etc.]* and painting *[above-water generation equipment]* in a

way that considers the aesthetic resources of the project area as well as the safety of the public and project facilities.

The licensee shall prepare the plan after consultation with the U.S. Coast Guard, *[Land Management Agency(ies)]*, *[Affected Indian Tribe(s)]*, *[Fish and wildlife agency of the state in which the project is located]*, *[National Marine Fisheries Service]*, *[U.S. Fish and Wildlife Service]*, and *[Any other interested parties]*. The licensee shall include in the plan documentation of consultation, copies of comments and recommendations on the plan after it has been prepared and provided to the agencies and the tribe(s), and specific descriptions of how the agencies' and tribe's comments are accommodated by the plan. The licensee shall allow a minimum of 30 days for the agencies and the tribe(s) to comment prior to filing the plan with the Commission. If the licensee does not adopt a recommendation, the filing shall include the licensee's reasons, based on project- specific information.

The Commission reserves the right to require changes to the plan. Project construction and installation shall not begin until the licensee is notified by the Commission that the plan is approved. Upon Commission approval, the licensee shall implement the plan, including any changes required by the Commission.

(d) *Emergency Shutdown and Removal*. The Director, Office of Energy Projects (Office Director), as the Commission's authorized representative, may order the licensee to cease project operation in the event that doing so is necessary for the protection of the environment or the life, health, or property of the public.

The licensee shall report by telephone to the Office Director and *[Land Management Agency(ies)]*, *[Affected Indian Tribe(s)]*, *[Applicable federal and state fish and wildlife management agencies]*, *[National Marine Fisheries Service]*, *[U.S. Fish and Wildlife Service]*, and *[Any other interested parties]* any project-related conditions causing or that may cause injury, or mortality to any federally listed threatened or endangered species under the Endangered Species Act (ESA) or marine mammal afforded protection under the Marine Mammal Protection Act (MMPA) and any other incidents affecting the environment or the life, health, or property of the public as soon as possible, but no longer than 24 hours after becoming aware of the threat or incident without unduly interfering with any necessary or appropriate emergency response or other action procedure for protecting the affected species.

Upon initial notification, the licensee shall consult with the Office Director and notified entities on the immediate course of action to take to prevent injury or minimize or eliminate the threat to the extent possible. The licensee shall propose

to the Office Director immediate measures, based on consultation with the agencies and tribe(s), and implement such immediate measures as the Office Director so directs, which may include immediate shutdown of all project operations.

No later than 7 days after becoming aware of any such threat or incident, or on any alternative schedule specified by the Office Director, the licensee shall file with the Commission and submit to the aforementioned agencies and tribe(s), a written report on the condition affecting the ESA-listed or MMPA-protected species, other environmental resources, the public, or property. The written report, in addition to any information required by the Office Director at the time of initial contact, shall include the following: (a) the location, date, time, and causes of the condition to the extent known; (b) a description of any unusual occurrences or operating conditions preceding the condition; (c) an account of any measure(s) taken to immediately alleviate the condition; (d) a detailed description of any injuries or mortalities of the ESA-listed or MMPA-protected species, or any adverse effects on other environmental resources, the public, or property as applicable; (e) a detailed description of the measures recommend by the agencies and tribe(s); and (f) a detailed description of the measures or actions that would be taken to prevent further such occurrences.

The Office Director may direct the licensee to commence project removal if no practical course of action can be taken to minimize the types of project-related adverse effects noted above.

3. Financial Assurance

To ensure that a licensee has the necessary funds available to complete project removal and site restoration in accordance with a project removal article, the Commission may include the following article in a pilot project license.

Financial Assurance. The licensee shall, at least 90 days before commencing project construction and installation, file proof of the purchase of a surety bond, or equivalent financial assurance instrument (*e.g.*, insurance, corporate guarantee, letter of credit, fully funded trust fund, etc.), to cover the entirety of the costs of removing the project in accordance with the Project Removal Plan required by this pilot license. Thereafter during the term of the license, the licensee shall maintain the bond, or equivalent financial assurance. By January 1 of each license year, or as otherwise directed by the Commission or its authorized representative, the licensee shall file proof of the maintenance of the bond, or equivalent financial assurance.

Failure to commence project removal in accordance with the procedures and timeframes authorized by the approved plan constitutes cause for the Commission to issue a demand letter to the surety for the amount required to satisfy all of the requirements of the project removal plan. Payment by the financial assurance entity of the amount required by a bond is due upon receipt of the demand letter. In lieu of payment, the surety may perform the

requirements of the plan under written instructions from the Commission, or its authorized representative within the timeframe set forth in the instructions.

The licensee agrees that all monies paid by the financial assurance entity, upon failure on the licensee's part to fulfill the requirements of the approved plan, may be retained by the United States to be applied to the satisfaction of the licensee's obligations under the plan, without prejudice to any other rights and remedies of the United States.